International Conference on Electrical, Computer & Telecommunication Engineering (ICECTE)
8-10 December 2016, Rajshahi-6204, Bangladesh

Nonlinear Adaptive Controller Design for Velocity Control of a DC Motor Driven by a DC-DC Buck Converter Using Backstepping Approach

T. K. Roy*[1], M. F. Pervej[1], F. K. Tumpa[1], and L. C. Paul[2]
[1]Dept. of ETE, RUET, Rajshahi-6204, Bangladesh
[2]Dept. of ETE, PUST, Pabna-6600, Bangladesh
*Email: roy.kanto03@gmail.com

***Abstract*—In this paper, a nonlinear adaptive controller is proposed to control the velocity of DC motors driven by DC-DC buck converters. The proposed controller is designed recursively based on the Lyapunov theory by considering the load torque of the DC motor is unknown. This unknown parameter is estimated through the adaptation law and the stability of the whole system is ensured based on the control Lyapunov function (CLF). Another main feature of the proposed control scheme is that it overcomes the over-parameterization problems of unknown parameter which generally emerges in some conformist adaptive methods. At last, the usefulness of the proposed control scheme is verified through the simulation results and performances of the designed controller are compared with an existing proportional-integral (PI) controller. Simulations results demonstrate the superiority of the proposed control scheme over an existing PI controller in term of settling time.**

Keywords—adaptive backstepping controller; control Lyapunov function ; DC-DC buck converter; DC motor

I. INTRODUCTION

DC motors are broadly used in many engineering applications such as rolling mills, doubled-hulled tankers system etc. [1]. Conventionally, DC motors are controlled by adjusting the armature voltage as a function of angular velocity or position using the pulse width modulation (PWM) technique [2]. However, owing to the hard switching strategy of the PWM, sudden deviation occurs in the voltage and current of the DC motor which is not suitable for smoothing start of a DC motor. To overcome this problem, DC-DC converters are extensively used to start a DC motor to provide a requisite voltage according to the demand [3], [4]. There are broadly three types of DC-DC converters such as buck, boost and buck-boost are available in the modern power electronic systems. Among these; the buck converter is widely used where the required output voltage is lower than the source voltage. Owing to the two energy storing elements (e.g., inductor and capacitor), DC-DC converters can generate smooth DC output voltage and current with negligible ripple. Consequently, it reduces the noise which generally produced due to the hard switching of the PWM [3]. In this way, it can improve velocity tracking performance of DC motor by providing an efficient output voltage to drive the motor. However, the performance of DC motors are highly affected by the external load torque as it is time varying. In this situation, the control of velocity of DC motors driven by DC-DC buck converters is a challenging task.

Usually, linear controllers are widely used to control the velocity of DC motors due to their simplicity and ease of implementation. A linear PI controller is proposed in [5] to control speed of a DC motor driven by a DC-DC buck converter. Another linear quadratic regulator (LQR) controller is proposed in [2] to follow the angular velocity tracking trajectory of a DC motor driven by a DC-DC buck converter. However, although these linear controllers are ease to implement, they are not appropriate to track the desired angular velocity trajectory of a DC motor under a wide range of operating points [6].

In order to address the limitations of linear controllers, researchers have paid a great deal of interest on the design of nonlinear controllers as these controllers are independent on the operating points [7]. In the literature, several nonlinear controllers such as sliding mode controller (SMC) [8], neural network [10], and backstepping [11] etc. are proposed to control angular velocity of DC motors driven by DC-DC converters. A neural network based nonlinear controller for a DC motor driven by a DC-DC buck converter is proposed in [10] where the DC motor and control parameters changing reaction under various operational conditions are monitored using a graphical user interface observer. However, the use of an observer is not a cost effective solution. For smoothing the start of a DC motor, a nonlinear SMC is proposed in [8]. Another similar controller to analyse the robustness with respect to load changes on the DC motor is proposed in [12] where the unknown load torque is estimated through an observer. However, though SMC is not sensitive to parameter variations or external disturbances, the selection of the time-varying sliding surface is very difficult due to a sudden fluctuating in the load torque on the DC motor.

To address the aforementioned limitations, the adaptive backstepping technique is one of the talented techniques as discussed in [9], [13], [15]-[17] for different applications. In [11], a backstepping controller is proposed to control the velocity of a DC motor driven by a DC-DC buck converter. An adaptive backstepping controller to control the speed of a series

978-1-5090-5785-6/16/$31.00 ©2016 IEEE

DC motor is proposed in [14]. However, for smoothing the start of DC motors, DC-DC converters are not taken into account.

The aim of this paper is to design an adaptive controller to control the velocity of DC motors driven by a DC-DC buck converter. To design the controller, load torque of DC motors is considered as unknown. The overall stability of the system is proved by formulating CLFs at different stages during the design of the controller. Finally, the performance of the designed controller is evaluated in a MATLAB/SIMULINK model and compared with an existing PI controller.

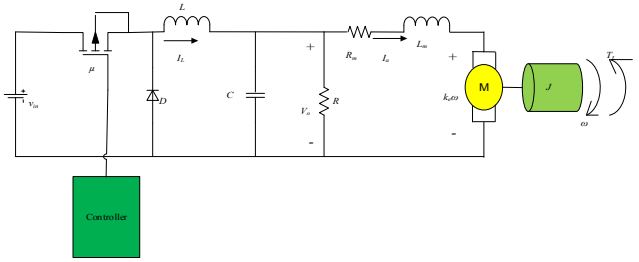

Fig. 1. DC-DC buck converter topology with combination of a DC motor

II. System Modeling and Problem Statement

Fig. 1 shows a cascade combination of a DC-DC buck converter with a DC motor. Using Kirchhoff's voltage and current laws, the dynamical model can be described by the following set of differential equations [11]:

$$\dot{\omega} = -\frac{f}{J}\omega + \frac{K_m}{J} I_a - \frac{T_L}{J} \quad (1)$$

$$\dot{I}_a = \frac{V_0}{L_m} - \frac{R_m}{L_m} I_a - \frac{K_e \omega}{L_m} \quad (2)$$

$$\dot{V}_o = \frac{1}{C} I_L - \frac{I_a}{C} - \frac{V_0}{RC} \quad (3)$$

$$\dot{I}_L = \frac{1}{L} \mu v_{in} - \frac{1}{L} V_o \quad (4)$$

where the symbols have their usual meanings which can be found in [11]. If there is a change in the load then, the corresponding load torque will also be changed. Therefore, the load torque of the DC motor may be time-varying. When this load torque of the DC motor is considered as unknown, then from (1) it can be written as: $\theta = \frac{T_L}{J}$. By incorporating this, (1)-(4) can be rewritten as:

$$\dot{x}_1 = -\frac{f}{J} x_1 + \frac{K_m}{J} x_2 - \theta \quad (5)$$

$$\dot{x}_2 = \frac{1}{L_m} x_3 - \frac{R_m}{L_m} x_2 - \frac{K_e}{L_m} x_1 \quad (6)$$

$$\dot{x}_3 = \frac{1}{C} x_4 - \frac{1}{C} x_2 - \frac{x_3}{RC} \quad (7)$$

$$\dot{x}_4 = \frac{1}{L} \mu v_{in} - \frac{1}{L} x_3 \quad (8)$$

where $x_1 = \omega$, $x_2 = I_a$, $x_3 = V_0$ and $x_4 = I_L$ are the new states of the system. Based on the mathematical model as described by (5)-(8), the design procedure of a nonlinear adaptive controller is discussed in the following section.

III. Adaptive Backstepping Controller Design

The aim of this section is to find out the control action μ in order to meet the following control objectives: (i) fixed directive of the output voltage of a DC-DC buck converter, (ii) regulate the DC motor velocity so that it can track a pre-defined reference trajectory, and (iii) robustness with respect to unknown load torque variation. To meet the abovementioned concerns, the design procedure of the proposed controller is composed of four distinct steps to obtain the final control law, μ and these steps are elaborately discussed in the following.

Step 1: According to the design purpose, velocity tracking error can be defined as:

$$e_1 = x_1 - x_{1d} \quad (9)$$

where x_{1d} is the desired velocity. The derivative of this error by inserting (5) can be written as:

$$\dot{e}_1 = -\frac{f}{J} x_1 + \frac{K_m}{J} x_2 - \theta - \dot{x}_{1d} \quad (10)$$

In (10), x_2 behaves as a virtual control variable. Thus, the average armature current tracking error of the DC motor can be defined as follows: $e_2 = x_2 - \alpha$ (11)

Substituting (11) into (10), it can be written as:

$$\dot{e}_1 = -\frac{f}{J} x_1 + \frac{K_m}{J}(e_2 + \alpha) - \theta - \dot{x}_{1d} \quad (12)$$

where α is a stabilizing function for the velocity error dynamics as represented by (12). In order to grip the unknown parameter θ as appear in (12), it is essential to define this parameter in term of the estimated value $\hat{\theta}$. Now the estimation error of this parameter can be defined as $\tilde{\theta} = \theta - \hat{\theta}$. Thus, in term of the estimation error, (12) can be rewritten as:

$$\dot{e}_1 = -\frac{f}{J} x_1 + \frac{K_m}{J}(e_2 + \alpha) - \left(\hat{\theta} + \tilde{\theta}\right) - \dot{x}_{1d} \quad (13)$$

Now, the CLF can be written as: $W_1 = \frac{1}{2} e_1^2 + \frac{1}{2\gamma} \tilde{\theta}^2$ (14)

where γ is a positive coefficient which is called parameter adaption gain. The time derivative of (14), by inserting (13) can be written as:

$$\dot{W}_1 = e_1 \left(\frac{K_m}{J}(e_2 + \alpha) - \frac{f x_1}{J} - \hat{\theta} - \dot{x}_{1d}\right) - \frac{\tilde{\theta}}{\gamma}\left(\dot{\hat{\theta}} + \gamma e_1\right) \quad (15)$$

The derivative of the W_1 as represented by (15) should be negative semi-definite in order to stabilize the error dynamics of the angular velocity. Therefore, the stabilizing function α needs to be chosen in such a way that makes $\dot{W}_1 \leq 0$ and which ensures the asymptotic stability. Thus, the stabilizing function α is chosen as follows:

$$\alpha = \frac{J}{K_m}\left(\frac{f}{J} x_1 + \hat{\theta} - k_1 e_1 + \dot{x}_{1d}\right) \quad (16)$$

where k_1 is a constant which is used to tune the output response of the system. The following adaptation law is chosen: $\dot{\hat{\theta}} = -\gamma e_1$ (17)

However, to overcome the over-parameterization problem caused by the appearance of θ in the subsequence steps, the adaptation law as represented by (17) will not be used at this step to update $\hat{\theta}$. Instead, the following tuning function is defined: $\tau_1 = \gamma e_1$ (18)

Using (16) and (18), (15) can be written as:

$$\dot{W}_1 = -k_1 e_1^2 + \frac{K_m}{J} e_1 e_2 - \frac{\tilde{\theta}}{\gamma}\left(\dot{\hat{\theta}} + \tau_1\right) \quad (19)$$

Now it is essential to obtain the time derivative of α in order to complete the next step which can be written as follows:

$$\dot{\alpha} = A + B\theta \quad (20)$$

where

$A = \frac{J}{K_m}\left\{\left(\frac{f}{J} - k_1\right)\left(-\frac{f}{J}x_1 + \frac{K_m}{J}x_2\right) + \dot{\hat{\theta}}\right\}$, $B = \frac{J}{K_m}\left(\frac{f}{J} - k_1\right)$

Step 2: The second error dynamics can be written as:

$$\dot{e}_2 = \frac{x_3}{L_m} - \frac{x_2 R_m}{L_m} - \frac{x_1 K_e}{L_m} - A - B(\hat{\theta} + \tilde{\theta}) \quad (21)$$

Here x_3 stands as a virtual control variable. Thus, the output voltage tracking error of the DC-DC buck converter can be defined as follows: $e_3 = x_3 - \alpha_1$ (22)

In terms of (22), (21) can be rewritten as:

$$\dot{e}_2 = \frac{1}{L_m}(e_3 + \alpha_1) - \frac{R_m}{L_m}x_2 - \frac{K_e}{L_m}x_1 - A - (\hat{\theta} + \tilde{\theta}) \quad (23)$$

Now, the CLF can be written as: $W_2 = W_1 + \frac{1}{2}e_2^2$ (24)

whose time derivative can be written as:

$$\dot{W}_2 = -k_1 e_1^2 + e_2\left(\frac{K_m}{J}e_1 + \frac{1}{L_m}(e_3 + \alpha_1) - \frac{R_m}{L_m}x_2 - \frac{K_e}{L_m}x_1 - A - B\hat{\theta}\right) - \frac{\tilde{\theta}}{\gamma}\left(\dot{\hat{\theta}} + \tau_1 + \gamma B e_2\right) \quad (25)$$

Now the stabilizing function α_1 can chosen as follows:

$$\alpha_1 = L_m\left(\frac{R_m}{L_m}x_2 + \frac{K_e}{L_m}x_1 + A + B\hat{\theta} - \frac{K_m}{J}e_1 - k_2 e_2\right) \quad (26)$$

Then (24) reduces to

$$\dot{W}_2 = -k_1 e_1^2 - k_2 e_2^2 + \frac{1}{L_m}e_3 e_2 - \frac{\tilde{\theta}}{\gamma}\left(\dot{\hat{\theta}} + \tau_2\right) \quad (27)$$

where $\tau_2 = \tau_1 + \gamma B e_2$ is the second tuning function. Now the time derivative of α_1 is calculated here as it is necessary in the next step which can be written as:

$$\dot{\alpha}_1 = A_{11}B_{11} + \theta(D_{11} - L_m k_2 B) + C_{11}D_{11} - E_{11} \quad (28)$$

where, $E_{11} = L_m k_2\left(\frac{1}{L_m}x_3 - \frac{R_m}{L_m}x_2 - \frac{K_e}{L_m}x_1 - A\right)$

$A_{11} = \frac{1}{L_m}x_3 - \frac{R_m}{L_m}x_2 - \frac{K_e}{L_m}x_1$, $B_{11} = R_m + \frac{f L_m}{J} - L_m k_1$

$C_{11} = \frac{K_m}{J}x_2 - \frac{f}{J}x_1$, $D_{11} = K_e - \frac{f L_m}{J}\left(\frac{f}{J} - k_1\right) - \frac{L_m K_m}{J}$

Step 3: In this step, the error dynamics can be written as:

$$\dot{e}_3 = \frac{1}{C}x_4 - \frac{1}{C}x_2 + \frac{x_3}{RC} - A_{11}B_{11} - \theta(D_{11} - L_m k_2 B) - C_{11}D_{11} + E_{11} \quad (29)$$

Here x_4 stands as a virtual control variable. Thus, another error can be defined as follows: $e_4 = x_4 - \alpha_2$ (30)

In terms of estimation error, (29) can be rewritten as:

$$\dot{e}_3 = \frac{1}{C}(e_4 + \alpha_2) - \frac{1}{C}x_2 + \frac{x_3}{RC} - A_{11}B_{11} - (\hat{\theta} + \tilde{\theta})(D_{11} - L_m k_2 B) - C_{11}D_{11} + E_{11} \quad (31)$$

At this point, we consider the following CLF

$$W_3 = W_2 + \frac{1}{2}e_3^2 \quad (32)$$

whose time derivative can be written as:

$$\dot{W}_3 = -k_1 e_1^2 - k_2 e_2^2 + e_3\left\{\frac{e_4}{C} + \frac{\alpha_2}{C} - \frac{x_2}{C} + \frac{x_3}{RC} - A_{11}B_{11} + \hat{\theta}(D_{11} - L_m k_2 B) - C_{11}D_{11} + E_{11}\right\} - \frac{\tilde{\theta}}{\gamma}\left(\dot{\hat{\theta}} - \tau_2 + \gamma(D_{11} - L_m k_2 B)\right) \quad (33)$$

The stabilizing function α_2 can be chosen as:

$$\alpha_2 = C\left\{\frac{x_2}{C} - \frac{x_3}{RC} + A_{11}B_{11} - \hat{\theta}(D_{11} - L_m k_2 B) + C_{11}D_{11} - E_{11} - k_3 e_3\right\} \quad (34)$$

Then, (33) can be simplified as:

$$\dot{W}_3 = -k_1 e_1^2 - k_2 e_2^2 - k_3 e_3^2 + \frac{e_3 e_4}{C} - \frac{\tilde{\theta}}{\gamma}\left(\dot{\hat{\theta}} - \tau_3\right) \quad (35)$$

where τ_3 is the third tuning function:

$$\tau_3 = \tau_2 - \gamma(D_{11} - L_m k_2 B) \quad (36)$$

Now it is essential to obtain the time derivative of α_2 in order to complete the next step which can be written as:

$$\dot{\alpha}_2 = A_{33} + \theta B_{33} \quad (37)$$

where, $C_{22} = \frac{B_{11}}{L_m} - k_2$, $D_{22} = C\dot{\hat{\theta}}(D_{11} - L_m B k_2) + C L_m k_2 \ddot{\hat{\theta}}$

$A_{33} = A_{22}\left(-\frac{f}{J}x_1 + \frac{K_m}{J}x_2\right) + B_{22}\left(\frac{1}{L_m}x_3 - \frac{R_m}{L_m}x_2 - \frac{K_e}{L_m}x_1\right) + C_{22}\left(\frac{1}{C}x_4 - \frac{1}{C}x_2\right) + D_{22} - C k_2\left(\frac{1}{C}x_4 - \frac{1}{C}x_2 + d_3 - A_{11}B_{11} - C_{11}D_{11} + E_{11}\right)$, $B_{33} = D_{11} - L_m k_2 B - A_{22}$

$$A_{22} = C K_e k_2 - C B_{11}\frac{K_m}{L_m} - C D_{11}\frac{f}{J} - \frac{C J L_m k_2}{K_m}\left(\frac{f}{J} - k_1\right)$$

$$B_{22} = C D_{11}\frac{K_m}{J} + C k_2 R_m + L_m k_2\left(\frac{f}{J} - k_1\right)$$

Step 4: Now the objective is to make the error variables (e_1, e_2, e_3, e_4) vanish asymptotically. To this end, the final error dynamics can be written as:

$$\dot{e}_4 = \frac{1}{L}\mu v_{in} - \frac{1}{L}x_3 + d_4 - A_{33} - \theta B_{33} \quad (38)$$

By incorporating the estimation error, (38) can be written as:

$$\dot{e}_4 = \frac{1}{L}\mu v_{in} - \frac{1}{L}x_3 + d_4 - A_{33} - (\hat{\theta} + \tilde{\theta})B_{33} \quad (39)$$

The original control signal μ is now available in (39) which needs to be designed in a manner that the errors e_1, e_2, e_3, and e_4, converge to zero as $t \to \infty$. To that aim, the final CLF is

$$W_4 = W_3 + \frac{1}{2}e_4^2 \quad (40)$$

By substituting the values of $\dot{W}_3$ and $\dot{e}_4$ the derivative of the CLF can be written as:

$$\dot{W}_4 = -k_1 e_1^2 - k_2 e_2^2 - k_3 e_3^2 + e_4\left(\frac{e_3}{C} + \frac{1}{L}\mu v_{in} - \frac{1}{L}x_3 - A_{33} - \hat{\theta}B_{33}\right) - \frac{\tilde{\theta}}{\gamma}\left(\dot{\hat{\theta}} + \tau_2 + e_4\gamma B_{33}\right) \quad (41)$$

The adaptive control law can be chosen as:

$$\mu = \frac{L}{v_{in}}\left(\frac{1}{L}x_3 + A_{33} + \hat{\theta}B_{33} - \frac{e_3}{C} - k_4 e_4\right) \quad (42)$$

Now in order to eradicate the influence of $\tilde{\theta}$ in $\dot{W}_4$; the final adaptation law can be chosen as: $\dot{\hat{\theta}} = \tau_4 - \gamma B_{33} e_4$ (43)

Finally, (40) can be simplified as:

$$\dot{W}_4 = -k_1 e_1^2 - k_2 e_2^2 - k_3 e_3^2 - k_4 e_4^2 \leq 0 \quad (44)$$

which is negative semi-definite. Simulation studies are conducted in the following section to analyze the effectiveness of the designed controller.

IV. Simulation Results

To show the effectiveness of the designed controller, a similar type system as shown in Fig. 1 is used. The physical parameters of the system are considered as follows [11]: $v_{in} = 50\,V$, $C = 200\,\mu F$, $L_m = 10\,mH$, $R_m = 2\,\Omega$, $f = 40.92 \times 10^{-6}\,N.m$, $j = 7.95 \times 10^{-6}$ kg.m^2, $k_m = 0.04913$ N.m/A, $k_e = 0.046$ V.s/rad, $T_e = 10\,N.m$. The tuning parameters of the designed controller to tune the output responses are chosen as follows: $k_1 = 3, k_2 = 5, k_3 = 7$ and $k_4 = 2$; and the adaptation gain: $\gamma = 10$ to satisfy a faster convergence speed of the unknown estimated load torque. The corresponding system responses with both controllers are shown from Fig. 2 to Fig. 4, respectively. Fig. 2 represents the angular velocity tracking response of the DC motor driven by a DC-DC buck converter. From Fig. 2, it can be seen that the designed

nonlinear adaptive backstepping controller (NABC) (blue line) can track the desired velocity perfectly whereas it is slightly oscillating when PI controller (red line) is used. Fig. 3 represents the armature current of the DC motor from where it can be seen that NABC generates more stable armature current than that of the existing PI controller.

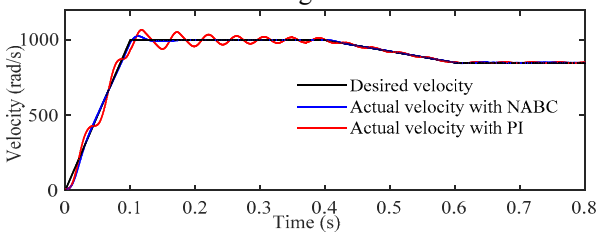

Fig. 2. Angular velocity of the DC motor driven by a DC-DC buck converter

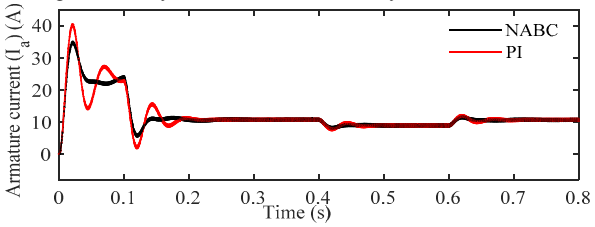

Fig. 3. Armature current of the DC Motor driven by a DC-DC buck converter

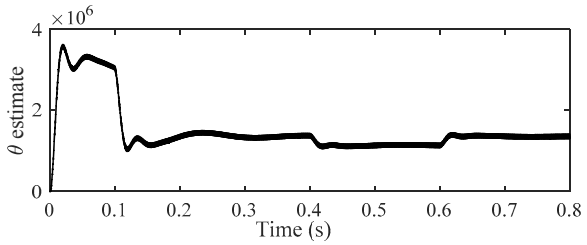

Fig. 4. Estimation of unknown parameter

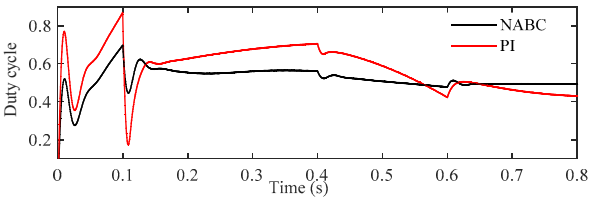

Fig. 5. Control signal

The estimation of the unknown parameter is shown in Fig. 4, from where it is clear that convergence rate is much faster due to the proper selection of the adaptation gain. The corresponding control signal of both controllers is shown in Fig. 5 from where it can be seen that the control signal with the NABC (black line) is more stable than the existing PI controller (red line).

V. CONCLUSION

In this paper, a new adaptive controller for controlling the velocity of DC motors driven by a DC-DC buck converter is proposed. The proposed controller is designed recursively by considering the load torque as an unknown parameter. The overall stability of the system is verified based on the negative semi-definite of CLFs. From the simulation results, it is evident that the designed controller has the ability to maintain the velocity tracking performance of the DC motor in a much better way than the existing PI controller as the settling time is much less with the designed controller. Future work will covenant with the design of a robust adaptive controller by considering both parametric and external disturbances.

REFERENCES

[1] V. M. H. Guzman, R. S. Ortigoza, and D. M. Carrillo, "Velocity control of a brushed DC motor driven by a DC to DC buck power converter," Int. Journal of ICIC, vol. 11, no. 2, pp. 509-521, April 2015.

[2] M. A. Ahmad, R. M. T. RajaIsmail, and M. S. Ramli,"Control strategy of buck converter driven DC motor: A comparative assessment," Australian J. Basic Appl. Sci., vol. 4, no. 10, pp. 4893–4903, 2010.

[3] R. S. Ortigoza, V. M. H. Guzman, M. A. Cruz, and D. M. Carrillo, "DC/DC buck power converter as a smooth starter for a DC motor based on a hierarchical control," IEEE Trans. on Power Electronics, vol. 30, no. 2, pp. 1076-1084, February 2015.

[4] Y. He, and F. L. Luo, "Design and analysis of adaptive sliding-mode-like controller for DC-DC converters," in IEE Proc. of Electric Power Applications, vol.153, no.3, pp.401-410, May 2006.

[5] S. E. Lyshevski, Electromechanical systems, Electric Machines and Applied Mechatronics, Boca Raton, FL, USA, CRC Press, 1999.

[6] R. Priewasser, M. Agostinelli, C. Unterrieder, S. Marsili, and M. Huemer, "Modeling, control, and implementation of DC–DC converters for variable frequency operation," IEEE Trans. on Power Electronics, vol. 29, no. 1, pp. 287-301, January 2014.

[7] H. S.-Ramirez, and M. A. O. Salazar, "On the robust control of buck-converter DC-motor Combinations," IEEE Trans. on Power Electronics, vol. 28, no. 8, pp. 3912-3922, August 2013.

[8] R. S. Ortigoza, V. M. H. Guzman, M. A. Cruz, and D. M. Carillo, "DC/DC buck power converter as a smooth starter for a DC motor based on a hierarchical control," IEEE Trans. on Power Electron., vol. 30, no. 2, pp. 1076-1084, February 2015.

[9] T. K. Roy, "Position control of a small helicopter using robust backstepping," in Proc. of the 7th ICECE, pp. 787-790, 2012.

[10] O. Bingol and S. Pacaci, "A virtual laboratory for neural network controlled DC motors based on a DC-DC buck converter," Int. J. Eng. Educ., vol. 28, no. 3, pp. 713–723, 2012.

[11] H. El Fadil and F. Giri, "Accounting of DC-DC power converter dynamics in DC motor velocity adaptive control," in Proc. IEEE Int. Conf. Control Appl., Oct. 4–6, 2006, pp. 3157–3162.

[12] J. Chiasson, "Nonlinear differential-geometric techniques for control of a series DC motor," IEEE Trans. on Control Systems Tech., vol. 2, no. 1, pp. 691-695, July 1993.

[13] T. K. Roy, M. F. Pervej, S. Rahman, and F. K. Tumpa, "Nonlinear adaptive controller design for PWM based DC-DC boost converters using backstepping control scheme," in Proc. of the 5th ICIEV, 2016.

[14] T. K. Roy, M. Morshed, F. K. Tumpa, M. F. Pervej, "Robust adaptive backstepping speed controller design for a series DC motor," in Proc. of IEEE Int. WECECE, December 2015.

[15] T. K. Roy and M. Garrat, "Altitude control of an unmanned autonomous helicopter via robust backstepping controller under horizontal wind gusts," in Proc. of 7th ICECE, pp. 771-774, 2012.

[16] T. K. Roy, M. Garrat, H. R. Pota, and H. Teimoori, "Hover flight control of a small helicopter using robust backstepping and PID," in Proc. of the 10th WCICA, 6-8 July 2012.

[17] T. K. Roy, "Robust controller for vertical-longitudinal-lateral dynamics control of small helicopter," Universal Jour. of Control and Automation, vol.2, no.1, pp. 14-24, 2014.

Inhomogeneous Line shape Broadening of Glass Laser and Improvement of the Line shape by Crystallization

Dona Basak
Department of Electrical & Electronic Engineering
Rajshahi University of Engineering & Technology (RUET)
Rajshahi-6204, Bangladesh
(donaeee07_ruet@yahoo.com or donaruet@gmail.com)

***Abstract*—Glass lasers are one type of solid state laser that uses glass as gain medium where active ions (Nd^{3+},Er^{3+}, Ho^{3+} , Tm^{3+} etc.) are doped . Materials for laser operation must possess sharp fluorescent lines, strong absorption bands, and reasonably high quantum efficiency for the fluorescent transition of interest. These characteristics are generally shown by solids (crystals or glass) which incorporate in small amount of elements in which optical transitions can occur between states of inner, incomplete electron shells. Thus the transition metals, the rare earth (lanthanide) series, and the actinide series are of interest in this connection. For this paper Nd:glass is of interest that shows inhomogeneous broadening. For inhomogeneous broadening central frequency is shifted due to local variation of electric field and thus gain reduces as gain is inversely to line width. But in case of homogeneous broadening each atom response in an identical fashion causes line broadening .However, this broadening is much less than inhomogeneous broadening and affect gain profile less severely. On the other hand, if the glass structure can be crystallize by external parameter like temperature, pressure etc. than local field variation will be compensated and we might reach to homogeneous broadening.**

Index Terms*— *Inhomogeneous broadening, Homogeneous broadening, crystallize

I. Introduction

In glass laser the gain medium is generally formed by doping Nd^{3+} ion in glass. Trivalent neodymium (Nd^{3+}) is the most successful type of active ion for solid-state lasers and thus far has been made to lase in more types of crystal and glass hosts than any other ion. It can operate as either a pulsed or continuous-wave laser with a sharp emission line. The most common emission wavelength is near 1μm, but there are several possible laser transitions in the near-infrared spectral region, and in addition a near-ultraviolet laser line [1]. The Nd ion when doped into a solid-state host crystal produces the strongest emission at a wavelength just beyond 1μm. The two host materials most commonly used for this laser ion are yttrium aluminium garnet (YAG) and glass. Nd can be doped to very high concentration in glass. The outstanding practical advantage compared to crystalline materials is the tremendous size capability for high-energy applications. The fluorescent lifetime is approximately 300μs, and, the emission line width is 18-28nm [1]. When doped in glass, the Nd: glass medium lases at wavelengths ranging from 1.054 to 1.056μm, depending upon the type of glass used.

II. Properties of Nd^{3+} in glass

Although neodymium has been made to lase in a large variety of glasses since 1961, it appears that the combines requirements of a relatively long fluorescent lifetime, high fluorescent efficiency and high durability are best provided by by a glass with an alkali-alkaline earth silicate base [2].

Neodymium compounds were first commercially used as glass dyes in 1927, and they remain a popular additive in glasses. The color of neodymium compounds—due to the Nd3+ ion—is often a reddish-purple but it changes with the type of lighting, due to the interaction of the sharp light absorption bands of neodymium with ambient light enriched with the sharp visible emission bands of mercury, trivalent europium or terbium [4]. Neodymium doped glasses generally emit wavelength of 1.054 μm with upper energy level and lower energy level of 11390 cm^{-1} and 1950 cm^{-1} respectively(See *Fig. 1*) [1][5] . Some neodymium-doped glasses are also used in lasers that emit infrared wavelengths between 1047 and 1062 nanometers. These have been used in extremely-high-power applications, such as experiments in inertial confinement fusion .

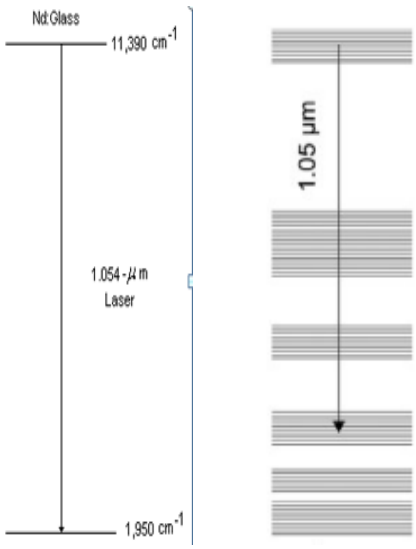

Fig 1: Energy level emitting specific radiation frequency[1][5]

It is possible to co-dope many of these elements within solid-state host, chosen to obtain the desired long lifetime as well as other suitable laser properties. The sharp fluorescent

978-1-5090-5785-6/16/$31.00 ©2016 IEEE

lines in the spectra of crystals doped with these elements result from the fact that the outer shells from the surrounding crystal lattice shield the elements involved in transitions in the optical regime[3] The host material must possess good optical properties as well good mechanical and thermal properties. Poor optical properties include variations in index of refraction, which lead to irregular beam quality in the laser output and impurities, which lead to scattering and undesired absorption of pump light or laser beam output. Poor mechanical and thermal properties lead to material deformation or fracturing of the host when the laser is operated under such high pulse-repetition rate or high steady state pumping. The host must also be able to accept the dopant material in a way that will not distort the desired properties of the dopant i.e. a long lifetime and an appropriate line shape. The host must also be capable of being grown in size, with a uniform distribution of the dopant that is required for laser gain media [6].

The rare earth ions are natural candidates to serve as active ions in solid-state laser materials because they exhibit a wealth of sharp fluorescent transitions representing almost every region of the visible and near-infrared portions of the electromagnetic spectrum. It is a characteristic of these lines that they may be very sharp, even in the presence of the strong local fields of crystals, as a result of the shielding effect of the outer electrons. The outermost electrons of these ions form a complete rare gas shell, which is the xenon shell with two 5*s* and six 5*p* electrons. This shell is optically inactive. Next inside the xenon shell is the 4*f* shell, which is filled successively in passing from one element to the next. Trivalent cerium, Ce^{3+}, has one 4*f* electron, and trivalent ytterbium, Yb^{3+}, has 13. As long as the 4*f* shell is not completely filled with 14 electrons, a number of 4*f* levels are unoccupied, and electrons already present in the 4*f* shell can be raised by light absorption into these empty levels [1]. The sharp lines observed in rare earth ion absorption and emission spectra are described to these transitions, and the sharpness of the lines is explained by the fact that the electrons making the transition lie inside the xenon shell and thus interact only weakly with outside ions. "*Table 1*", shows electron orbital distribution [3].

TABLE I: ELECTRON DISTRIBUTION OF LANTHANIDE GROUP[3]

Number	Element		Outermost electron shell					
54	Xenon	Xe	$4d^{10}$	--	$5s^2$	$5p^6$	--	--
59	Praseodymium	Pr	$4d^{10}$	$4f^3$	$5s^2$	$5p^6$	--	$6s^2$
60	Neodymium	Nd	$4d^{10}$	$4f^4$	$5s^2$	$5p^6$	--	$6s^2$
61	Promethium	Pm	$4d^{10}$	$4f^5$	$5s^2$	$5p^6$	--	$6s^2$
62	Samarium	Sm	$4d^{10}$	$4f^6$	$5s^2$	$5p^6$	--	$6s^2$
63	Europium	Eu	$4d^{10}$	$4f^7$	$5s^2$	$5p^6$	--	$6s^2$
64	Gadolinium	Gd	$4d^{10}$	$4f^8$	$5s^2$	$5p^6$	$5d$	$6s^2$
65	Terbium	Tb	$4d^{10}$	$4f^9$	$5s^2$	$5p^6$	--	$6s^2$
66	Dysprosium	Dy	$4d^{10}$	$4f^{10}$	$5s^2$	$5p^6$	--	$6s^2$
67	Holmium	Ho	$4d^{10}$	$4f^{11}$	$5s^2$	$5p^6$	--	$6s^2$
68	Erbium	Er	$4d^{10}$	$4f^{12}$	$5s^2$	$5p^6$	--	$6s^2$
69	Thulium	Tm	$4d^{10}$	$4f^{13}$	$5s^2$	$5p^6$	--	$6s^2$
70	Ytterbium	Yb	$4d^{10}$	$4f^{14}$	$5s^2$	$5p^6$	--	$6s^2$
71	Lutetium	Lu	$4d^{10}$	$4f^{14}$	$5s^2$	$5p^6$	$5d$	$6s^2$

For Nd: glass laser gain media, very large-size laser materials have been produced. It can be fabricated into special laser configurations such as slabs and fibers as well as standard rod designs. Rods of up to 2m long and 0.75m in diameter and disks of up to 0.05m thick have been successfully demonstrated [1]. The optical quality can be excellent, and beam angles approaching the diffraction limit can be achieved. Glass, of course, is easily fabricated and takes a good optical finish. The fluorescent lifetime is approximately 300μs, and, the emission line width is 18-28nm. This is wider than for Nd:YAG by factor of 40 to 60. This increased emission line width (inhomogeneous broadening) in effect reduces the laser gain. The drawback of Nd: glass laser materials is their relatively poor thermal conductivity, which restricts these lasers to relatively low pulse repetition rates for pulsed lasers and a lower operating power for continuous wave lasers [7,8,9]. Therefore, the laser thresholds for glass lasers have been found to run higher than their crystalline counterparts. This leads to thermally induced birefringence and optical distortion in glass laser rods when they are operated at high average powers. Therefore crystalline laser hosts generally offer as advantages over glasses due to their higher thermal conductivity, narrower fluorescence linewidth, and, in some cases, greater hardness. However, the optical quality and doping homogeneity of crystalline hosts are often poorer, and the absorption lines are generally narrower [10].

III. MECHANISM OF INHOMOGENEOUS BROADENING IN ND:GLASS LASER

Inhomogeneous broadening is an increase in the linewidth of an atomic transition caused by different radiating or absorbing atoms (or ions) to interact with different wavelength components. (Examples for such effects are discussed below.) This means that the absorption and emission cross sections have different spectral shapes for different atoms. The fluorescence spectrum from such a material can then exhibit peaks which are broader than those of single atoms, since it shows an average composite line-shape over many differently emitting atoms. In similar ways, absorption spectra can be broadened. See *"Fig. 2"* below-

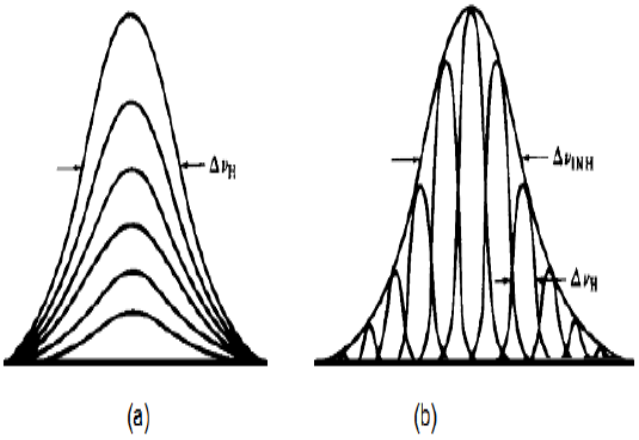

Homogeneous (a) and inhomogeneous (b) band shapes having inhomogeneous width $\Delta\nu_{INH}$ and homogeneous width $\Delta\nu_H$

Fig 2: Homogeneous and Inhomogeneous broadening[11]

Glass structure is not pure crystalline rather amorphous. Its density is not same all over the material and it does not follow a fixed structure in long range order. The figure is given below

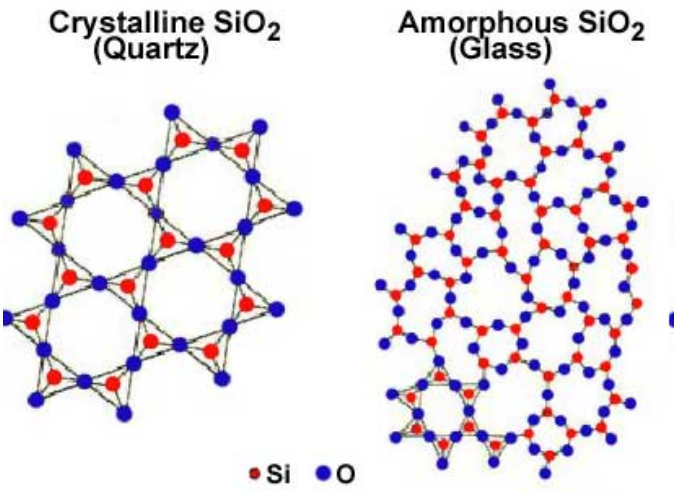

Fig 3: Atomic structure of crystalline (Quartz) and amorphous (Silica Glass) material[12]

As Nd^{3+} ion is doped in glass, it experience a local electric field produced by surrounding atoms of the material. Due to material inhomogeneity that are particularly significant in glass medium, these field differs from ion to ion. An effect of local electric field on frequency spectrum causes distortion which is known as Stark effect. An electric field pointing from left to right, for example, tends to pull nuclei to the right and electrons to the left. In another way of viewing it, if an electronic state has its electron disproportionately to the left, its energy is lowered, while if it has the electron disproportionately to the right, its energy is raised. Other things equal, the effect of the electric field is greater for outer electron shells, because the electron is more distant from the nucleus, so it travels farther left and farther right.

The Stark effect can lead to splitting of degenerate energy levels. For example, in the Bohr model, an electron has the same energy whether it is in the 2s state or any of the 2pstates. However, in an electric field, there will be hybrid orbitals of the 2s and 2p states where the electron tends to be to the left, which will acquire a lower energy, and other hybrid orbitals where the electron tends to be to the right, which will acquire a higher energy [13]. Therefore, the formerly degenerate energy levels will split into slightly lower and slightly higher energy levels. As a result a local energy level variation occurs that is responsible for different transition frequencies. For random local field variations ,the corresponding distribution of transition frequencies g(V-Vo) turns out to be given by Gaussian function .The linewidth ΔVo(FWHM) depends on the extent of variation of transition frequencies in the material and hence on amount of field inhomogeneity within the crystal or glass.

IV. Effect of Temperature on Crystallinity

Contrary to solid bodies of crystalline structure, glass has no defined melting point. It continuously transforms from the solid state to the viscous plastic state. The transition range is called the transformation range and it lies between 520°C and 550°C. Tempering and bending require a temperature of a further 100°C.

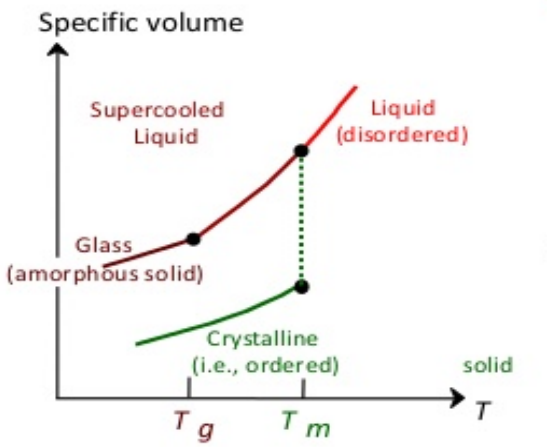

Fig 4: Change of state from amorphous to near crystalline and finally liquid for glass material [14]

"*Fig. 4",*shows a phenomenon where a glassy or amorphous state is achieved by rapidly quenching from the melt to below Tg(°C) (Glass Transition Temperature), whereas slow cooling the melt will allow crystallinity to develop in the sample (melt crystallization) [19]. Glass transition temperature (Tg) is defined as the temperature at which the mechanical properties of a plastic / adhesive radically changed due to the internal movement of the polymer chains that form the plastic / adhesive. The crystalline form can also be obtained on heating the glass through the Tg or by holding the polymer at a constant temperature between Tg and T_m(°C) (Melting Temperature) for a given length of time (isothermal crystallization)[20,21]. However due to the complex nature of crystallization, in practical situations nucleation and growth occur at different points and may proceed at different rates giving a distribution in the size and perfection of crystallites. As shown in "*Fig. 5",* crystallization rate is highly dependent on temperature and is restricted to a range of temperatures between the Tg and T_m of the polymer.

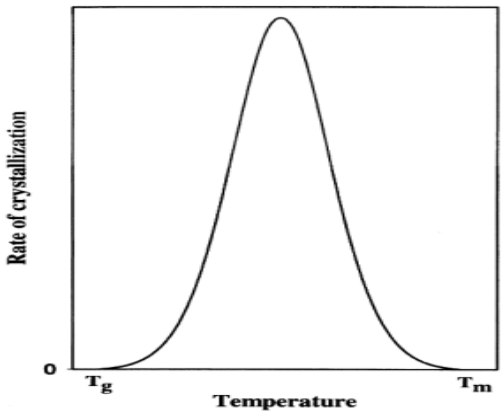

Fig 5: Dependence of crystallization rate on temperature [18]

At temperatures above T_m there is a great deal of energy in the system and the segmental motion of the polymer chains is too great for stable nuclei to form and for crystalline growth to occur [17,18]. However as the temperature is reduced below Tm there is an increase in melt viscosity and therefore an increased opportunity for nucleation to occur, growing a microstructure of few but very large crystals. As the temperature is further reduced and viscosity increases the rate of crystallization passes through a maximum where conditions favor both nucleation and growth of crystallites [17].

V. Improvement from Inhomogeneous to Homogeneous Broadening

As it is possible to make the glass similar to crystal structure, it shows a way to the remedy of inhomogeneity that is responsible for local field variation. There is now less existence of different local environment which deviate the central frequency as well as the frequency spectrum. If the temperature can be maintained when operating a glass laser between glass transition temperature (Tg) and melting temperature (Tm) with a peak crystallinity, then it can show near homogeneous spectra. This is because the problem originates from the amorphous atomic structure of silicate glass(SiO_2).

VI. Limitation of Crystallization of Glass in Glass Laser

However, the crystal structure formation makes the glass opaque. As a result its transmittance property is at loss. This is because of crystalline structure often causes scattering of light [14]. It causes a great restriction in fiber glasses for information transmission by full internal reflection.

VII. Application of Glass Laser

There are huge applications of glass lasers. This laser has high operating power .In medicine, the fact that neodymium – doped glass fibers can be made quite flexible should have the application to put into inaccessible places. The existences of efficient glass disk lasers are used in laser welding and cutting applications. Application of High radiance lasers are in plasma creation and in particular for experiments in thermos-molecular reaction.

VIII. Conclusion and Future Work

Though glass lasers shows inhomogeneous broadening it is important for its high energy applications. The gain profile shows Gaussian distribution and each Gaussian line shape function interact with other causing sidebands. As a result the net linewidth become wider than the case of homogeneous broadening. Gain is inversely related to linewidth, thus decreases as well. The main reason lies in amorphous characteristic of glass and the target of the paper is to reshape the structure to be as close as crystal structure in order to prevent local electric field variation in lattice. Glass lasers are very effective as glass fibers .Fiber Optic Communication system use glass fibers whose refractive index varies from surface to center. It also innovate some other ideas which will become the subject of research in near future. They are-

- Birefringence characteristic of glass laser
- Development of glass fibers
- Improvement of transmittance property for opaque crystal glass and reduction of scattering loss.

Acknowledgment

The author would like to thank her parents. Secondly would like to thanks to Department of EEE of RUET to give the chance of presenting the paper on it and encourage for doing further Research work.

References

[1] Semwal, Kireet, and S. C. Bhatt. "Study of Nd^{3+} ion as a Dopant in YAG and Glass Laser." *International Journal of Physics* 1.1 (2013): 15-21.
[2] E. Snitzer ."Glass Lasers," Appl. Opt.,vol. 5, pp 1487-1499,October 1966
[3] Walter Koechner, *Solid State Laser Engineering*, 5th ed., Springer Berlin, 1999.
[4] https://en.wikipedia.org/wiki/Neodymium
[5] Basics of Laser Physics: For Students of Science and Engineering, chapter 15,page 293
[6] Willium T. Silfvast, Laser Fundamentals, Cambridge University Press, 1991.. http://www.fcc.gov/Bureaus/Engineering_Technology/News_Releases/1999/nret9006.html Retrieved 2009-08-16
[7] L. R. Marshall, A. D. Hays, H. J. Kasinski, and R. Burnham; "Highly efficient optical parametric oscillators", *SPIE*, 1419: 141-152, 1991.
[8] R. D. Stultz, D. E. Nieuwsma, E. Gregor; SPIE, 1419: 64-74, 1991..
[9] J. A. Skidmore, M. A. Emanuel, R. J. Beach, B. L. Freitas, N. W. Carlson, C. D. Marshall, W. J. Benett, R. W. Solaz, D. P. Bour, and D. W. Treat; "New diode wavelengths for pumping solid state lasers", *SPIE Proceedings*, 2382: 106-116, 1997
[10] Z. J. Kiss and R. J. Pressley; "Crystalline solid lasers", *Proc. IEEE* 54(10): 1236, 1966
[11] http://chem.libretexts.org/Textbook_Maps/Physical_and_Theoretical_Chemistry_Textbook_Maps/Map%3A_Advanced_Theoretical_Chemistry_(Simons)/6%3A_Electronic_Structure/6.2%3A_Experimental_Probes_of_Electronic_Structure
[12] S.Guru.(2008) http://steelguru.com/uploads/reports/sss1-29-08-2008.jpg.
[13] https://en.wikipedia.org/wiki/Stark_effect
[14] http://www.slideshare.net/hzharraz/silica-sand-and-glass-industry
[15] Cheng, S.Z.D, Cao, M.-Y. & Wunderlich, B. (1986) Glass Transition and melting behaviour of Poly(oxy-1,4-phenyleneoxy-1,4-phenylenecarbonyl-1,4-phenylene). Macromolecules, 19: 1868-1876
[16] Cebe, P. & Hong, S.-D. (1986) Crystallisation behaviour of poly(ether-ether-ketone). Polymer, 27: 1183-1192.
[17] Cowie, J.M.G. (1991) Polymers: chemistry and physics of modern materials. 2nd ed. London: Blackie Academic & Professional.
[18] Di Loernzo, M.L. & Silvestre, C. (1999) Non-isothermal crystallisation of polymers. Progress in Polymer Science, 24: 917-950.
[19] Blundell, D.J. & Osborn, B.N. (1983) The morphology of poly(aryl-ether-ether-ketone). Polymer, 24: 953-958.
[20] Bassett, D.C., Olley, R.H. & Al Raheil, I. (1988) On crystallisation phenomena in PEEK. Polymer, 29: 1745-1752
[21] Olley, R.H., Bassett, D.C. & Blundell, D.J. (1986) Permanganic etching of PEEK. Polymer, 27: 344-348.

Removing EOG artifacts from EEG Signal Using Noise-Assisted Multivariate Empirical Mode Decomposition

Sania Zahan
Dept. of Computer Science and Engineering, Varendra University, Rajshahi, Bangladesh
Email: sania.cse@gmail.com

***Abstract*— Electroencephalogram (EEG) has significant applications on medical diagnosis and Brain Computer Interfacing (BCI). But the main obstacle of analyzing EEG signal is various types of noises to get actual information. Electro-oculogram (EOG) is a vital noise in EEG signal that can be produced by eye movements. De-noising EOG from EEG signal is the key issue in this research. Many research has been done on this purpose mainly Independent Component Analysis (ICA) based EOG separation with reference signal and wavelet based EOG separation. In this research, multivariate Fractional Gaussian noise channel will be used to establish a uniformly distributed reference scale and to derive the energy based threshold to detect the low frequency trends caused by EOG artifact. Avoiding these artifacts, we can get EOG free EEG hoping better results than existing methods.**

Keywords*— *EEG signal; EOG artifacts; Fractional Gaussian Noise channel; Energy based threshold.

I. INTRODUCTION

Human brain contains billions of neurons making up a large complex neural network which process signal information of body activity. During the processing of information, neurons change the flow of electrical currents across their membranes. These changing currents generate electric and magnetic fields that can be recorded from the surface of the scalp by attaching small electrodes. The potential difference between electrodes are then amplified and recorded as the electroencephalogram (EEG) signal [1]. EEG signal is used to diagnose various types of diseases like epilepsy, sleep disorder, brain death, Alzheimer etc. But eye blink and eyeball movement causes Electro-Oculogram (EOG) artifacts that is present all over the EEG signal. EOG signals are dominant in nature having higher amplitude. Auditory and mental arithmetic tasks with the eyes closed, leads to strong alpha waves, which are suppressed when the eyes are opened [2]. Thus the desired EEG data becomes noisy which suppress important frequency characteristics. So EEG signal must be noise free for proper analysis and diagnosis of these diseases.

In this research, I have proposed a method of decomposing EEG signal by Noise-Assisted Multivariate Empirical Mode Decomposition (N-A MEMD) [3] and then applying energy based threshold to identify frequency trends of EOG artifacts. For this purpose, a 14-channel EEG data of length 5000 has been used, acquired using international 10-20 electrode placement system [4]. Multivariate Fractional Gaussian noise (fGn) channels will be added as extra channels to the original multivariate EEG signal and then the composite signal will be processed via Multivariate Empirical Mode Decomposition (MEMD) [5]. N-A MEMD method tends to accurately align the common oscillatory modes in corresponding IMFs from multiple channels [3]. This property motivated me to extend the previously proposed method of EOG separation to N-A MEMD.

II. METHODS

A. Empirical Mode Decomposition (EMD)

In EMD [6], signal is decomposed as a linear combination of data driven set of basis functions known as the intrinsic mode functions (IMFs). Thus embedded characteristics are revealed. But same index IMFs of different channels are misaligned (mode mixing) e.g. a single IMF containing multiple oscillatory modes and/or a single mode residing in multiple IMFs [3]. It may compromise the physical meaning of IMFs.

B. Multivariate Empirical Mode Decomposition (MEMD)

In recent years, the advances in data acquisition tools have highlighted the need for direct processing of multivariate data. MEMD produces the same number of IMFs for all channels, facilitating direct multichannel modeling and reducing mode mixing problem. But even if it is applied directly, the problem is not completely eliminated. Due to the filter bank property of MEMD, Fractional Gaussian Noise channels which frequency spectrum is correlated to clean EEG, is added to the recorded EEG. Then MEMD is applied to this composite signal, resulting in proper separation of clean EEG and noise [7]. Hence Noise-Assisted MEMD method is introduced in this research.

III. PRINCIPLE AND ALGORITHM OF MEMD

MEMD processes the input signal directly in a multidimensional domain (n-space). Input signal projections are taken directly along different directions in n-dimensional spaces to calculate the local mean. Local mean calculation can be considered as an approximation of the integral of all the envelopes along multiple directions in an n-dimensional space, and the accuracy of this approximation is dependent on how uniformly the direction vectors are chosen, especially for a limited number of direction vectors [8]. The default number of directions is chosen to be 64 - to extract meaningful IMFs, the number of directions should be considerably greater than the dimensionality of the signals.

978-1-5090-5785-6/16/$31.00

A. Projections of Input Signal in n-Dimentional Spaces

The sampling scheme based on low discrepancy Hammersley sequence is used to project input signal in n-dimensional spaces [8] and hence estimates more accurate local mean. Unlike conventional uniform angular sampling schemes, this scheme belongs to a class of quasi-Monte Carlo methods, and provides relatively more uniform sampling [7].

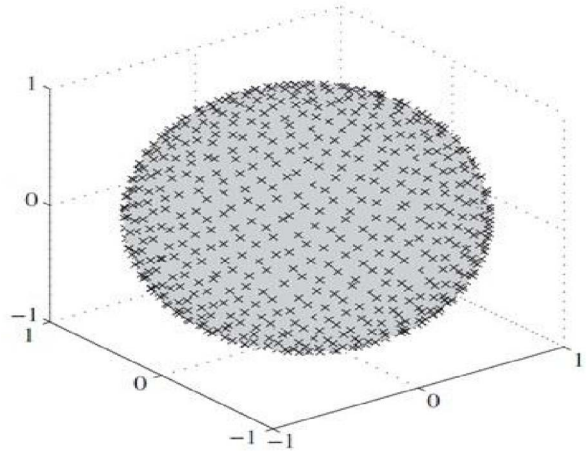

Fig. 1. Direction vectors for taking projections of multivariate signals generated by using a low-discrepancy Hammersley sequence.

The direction vectors in n-dimensional spaces can be equivalently represented as points on the corresponding unit (n-1) spheres. It is necessary since calculation of the local mean, a crucial step in MEMD, is difficult to perform due to the lack of formal definition of maxima and minima in higher dimensional domains [3].

B. Identification of Maxima and Minima

Once the projections along different directions in multidimensional spaces are obtained, their extrema are interpolated via cubic spline interpolation to obtain multiple signal envelopes. Algorithm to identify maxima and minima:

- The value of the current element of the sequence is compared with the preceding and subsequent values.
- If the current value is greater than the preceding and the subsequent values, it is identified as the function maximum.
- If the current value is smaller than the preceding and the subsequent values, it is identified as the function minimum.

Once the extrema are identified, they are connected by cubic spline lines to produce the upper and lower envelopes. These envelopes are then averaged to obtain the local mean. The mean value is further subtracted from the initial sequence. This results in the extraction of the required empirical function in the first approximation. To obtain the final IMF, new maxima and minima are again identified and all the above steps repeated. This repeated process is called sifting. The sifting process is repeated until a certain given stoppage criterion is met. Each multivariate IMF must satisfy two basic conditions:

- In the whole data set, the number of extrema and the number of zero crossings must differ at most by one.
- At any point, the mean value of the envelope defined by the local maxima and the envelope defined by the local minima is zero.

Algorithm 1: Multivariate Extension of EMD

- Generate the pointset based on the Hammersley sequence for sampling on an (n-1)-sphere [8].
- Calculate a projection, denoted by $p^{\theta_k}(t)\}_{t=1}^{T}$, of the input signal $\{v(t)\}_{t=1}^{T}$ along the direction vector X^{θ_k}, for all k (the whole set of direction vectors), giving $p^{\theta_k}\}_{k=1}^{K}$ as the set of projections.
- Find the time instant $\{t_i^{\theta_k}\}_{k=1}^{K}$, corresponding to the maxima of the set of projected signals $p^{\theta_k}\}_{k=1}^{K}$.
- Interpolate $[t_i^{\theta_k}, V\left(t_i^{\theta_k}\right)]$ for all values of k, to obtain multivariate envelope curves $e^{\theta_k}(t)\}_{k=1}^{K}$.
- For a set of K direction vectors, calculate the mean *m(t)* of the envelope curves as

$$m(t) = \frac{1}{k}\sum_{k=1}^{K} e^{\theta_k}(t) \qquad (1)$$

- Extract the "detail" *d(t)* using *d(t) = x(t) - m(t)*. If the "detail" *d(t)* fulfills the stoppage criterion for a multivariate IMF, apply the above procedure to *x(t)-d(t)*, otherwise apply it to *d(t)* [3].

Once the first IMF is extracted, it is subtracted from the input signal and the same process (Algorithm 1) is applied to the resulting signal yielding the second IMF and so on. The process is repeated until all the IMFs are extracted and only a residue is left. In multivariate case, the residue corresponds to a signal whose projections do not contain enough extrema to form a meaningful multivariate envelope.

IV. Filter Bank Property of MEMD

Filter banks represent a collection of bandpass filters designed to isolate different frequency bands in the input signal. The IMFs obtained from standard EMD algorithm provide frequency responses similar to that of a dyadic filter bank [11] [12]. The frequency response and the corresponding filter bank property of MEMD were illustrated by applying MEMD on a $N = 500$ realizations of an eight-channel white Gaussian noise each of length $T = 1000$; the power spectra of its resulting first fine IMFs (1-9) were then ensemble averaged to yield an averaged power spectra; the stopping criteria used is given in [12], with the value of $S = 5$; it is then plotted in the top of *Fig. 2*. Next, the same realizations were separately processed via standard EMD and the estimated averaged power spectra of its IMFs are shown in the bottom of *Fig. 2*.

It can be seen that the overlapping of frequency bands of same-index IMFs associated with different channels is much more prominent in the case of MEMD as compared with standard EMD [3].

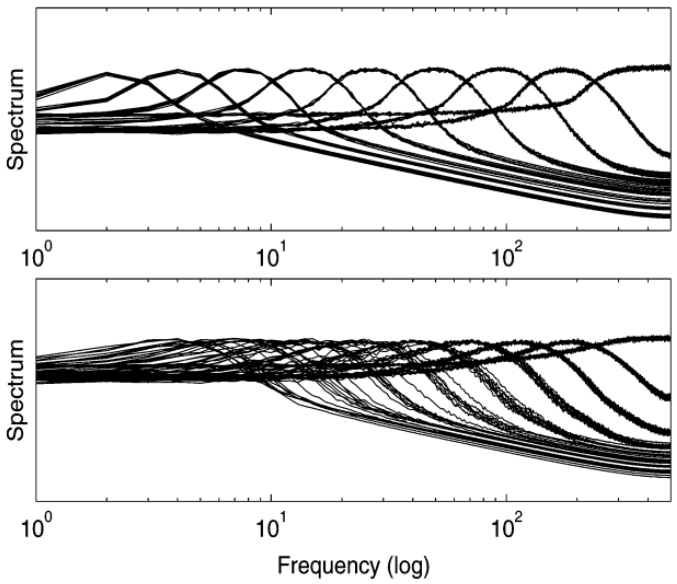

Fig. 2. Averaged spectra of white noise realization via MEMD (top) and standard EMD (bottom)

V. Principle and Algorithm of Noise-Assisted MEMD

N-A MEMD makes use of the quasi-dyadic filter bank properties of MEMD on white noise. An extra channel containing independent multivariate fGn is added to the original multivariate signal, and it is then processed via MEMD. The details of the NA-MEMD method are outlined in Algorithm2:

A. Algorithm 2: Noise-Assisted MEMD

- Create an uncorrelated Fractional Gaussian white noise time-series (*m*-channel) of the same length as that of the input.
- Add the noise channel created in Step 1 to the input multivariate (*n*-channel) signal, obtaining an (n + m) channel signal.
- Process the resulting (n + m)-channel multivariate signal using the MEMD algorithm listed in Algorithm 1, to obtain multivariate IMFs.
- From the resulting (n + m)-variate IMFs, discard the m channel corresponding to the noise, giving a set of n-channel IMFs corresponding to the original signal [3].

Since required noise free EEG signal resides in similar dyadic frequency spectrum, the method can perfectly separate the frequency bands, hence is able to reduce the EOG artifacts.

VI. Generation of Intrinsic Mode Functions

A multivariate EEG signal with 14-channel of length T = 5000 is used. Two uncorrelated fGn channels of same length are added as the 15th and 16th channels to the signal. Now the signal is decomposed using N-A MEMD. The IMFs are shown in *Fig.3.* Higher order IMFs contain lower frequency oscillations than lower order IMFs signal. Thus high frequency neurobiological signals containing valuable information are separated from the low frequency trend of EOG artifacts.

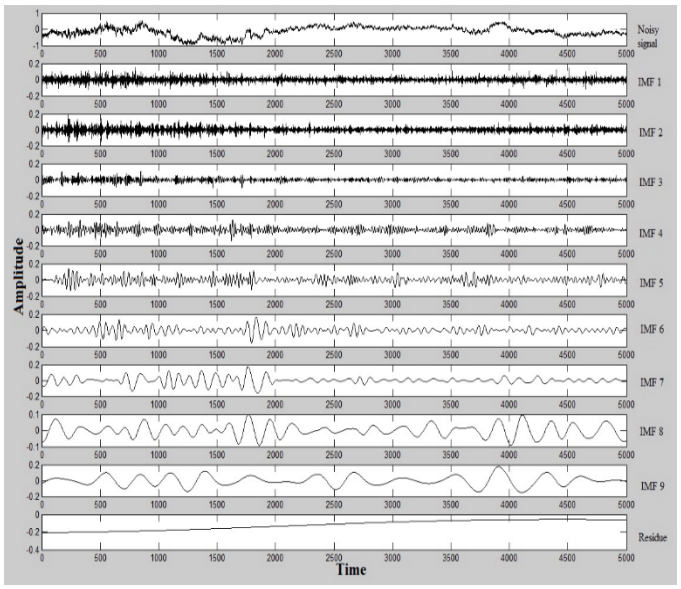

Fig. 3. The waveforms of noisy EEG signal and its first 9 IMFs out of 14 and residue

VII. Principle of Energy Based Threshold

N-A MEMD decomposes all the vectors simultaneously with equal number of IMFs in a perfect filter bank structure. The fGn channel is used here as reference signal to compare the energy to detect the EOG related trends in EEG signal.

Recorded EEG is considered as a superposition of relatively faster oscillating EEG signal and slowly varying EOG artifacts. The energy of the EOG signals is much higher than the EEG signals. Hence EOG signal is treated as the low frequency trend of the recorded EEG signals. I propose a data adaptive detrending method to separate the EOG artifacts from the recorded EEG signals. The trend of EOG is determined by comparing the energy of individual IMF of the EEG channel with the same index IMF of the reference signal (fGn). Higher order IMFs contain the lower frequency components. The high frequency EEG signal of the channel can be easily separated by summing up the lower order IMFs as:

$$\hat{S}_{EEG}^{(n)} = \sum_{j=1}^{C^{(n)}-1} d_j^{(n)}(t) \qquad (2)$$

Where $d_j^{(n)}(t)$ is the j^{th} IMF of the n^{th} channel. Here the objective is to find the critical (threshold) IMF with index $C^{(n)}$ such that the IMFs of indices $C^{(n)}$, $C^{(n)}$+1, … , j, are responsible for low frequency EOG artifacts. Then the EOG can easily be separated as:

$$\hat{S}_{EOG}^{(n)} = \sum_{j=C^{(n)}}^{J} d_j^{(n)}(t) + r_j^{(n)}(t) \qquad (3)$$

Where $r_j^{(n)}(t)$ is the final residue of the n^{th} channel. The algorithm to find the index $C^{(n)}$ of the threshold IMF for individual EEG channel as:

A. Algorithm 3: Estimating threshold

- Calculate the energies of the IMFs of fGn and its 95% confidence interval (CI).

- Find the index $C^{(n)}$, highest order IMF of an EEG channel that does not exceed the lower limit of CI.

After computing the index $C^{(n)}$ of threshold IMF (for EEG channel), the clean EEG is reconstructed using Eq. (2).

VIII. Identification of Threshold Point

The energy of each IMF of both fGn channel and EEG channels is calculated using the following equation:

$$Energy_i = log_2 IMF_i^2 \qquad (4)$$

Where IMF_i is the i^{th} IMF of a channel. Now the 95% confidence interval (CI) for fGn channel is calculated.

The energy of each IMF of an EEG channel is compared to the lower limit of the same index CI value. If the energy exceeds the lower limit, the IMF is an EOG component. Thus the highest order IMF which energy does not exceed the limit is identified and considered as the threshold point $C^{(n)}$. The energy diagram of fGn and channel-1 EEG signal with upper and lower limit CI value is shown as in *Fig. 4.*

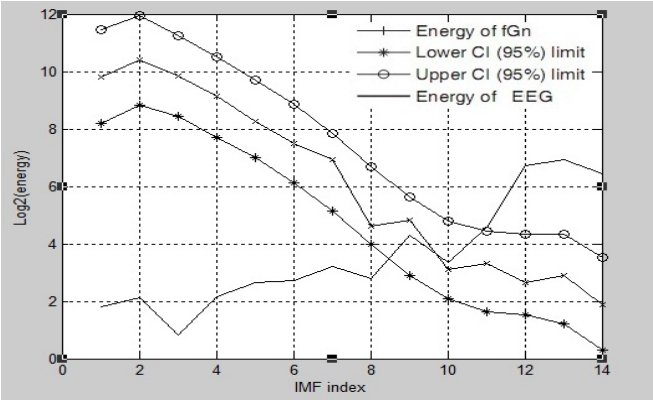

Fig. 4. Selection of threshold IMF index of EEG chan-1. The 6th IMF is selected to as the threshold one

It is visible that the energy line of EEG intersects the lower CI limit near 8. So the 8th IMF is selected as the threshold IMF and index $C^{(n)} = 8$. EEG signal is obtained by adding the IMFs up to the threshold point using Equation (2) and EOG using Equation (3).

IX. Experimental Results

The SNR of noisy EEG signal is:

$$S/N_{Original} = 122.21\ dB$$

The SNR of de-noised EEG signal obtained from both EMD and N-A MEMD method is calculated and the values are:

$$S/N_{EMD} = 134.79\ dB$$

$$S/N_{NAMEMD} = 202.73\ \text{dB}$$

In previous research [13] the decomposition was done using noise assisted EMD. But EMD fails to realize the effect of signals overlapped in multiple channels. Thus in the process of thresholding, some important information is lost. As depicted above the SNR value for N-A MEMD is much higher than ordinary EMD. Hence it is clear that N-A MEMD performs better than EMD to reduce noise from signals.

X. Conclusions

This study is devoted to analyze a method to identify the ocular artifact spike zones in EEG signal applying Noise Assisted Multivariate EMD and energy based threshold. A data driven adaptive threshold method applied only to the ocular artifact zone does not affect the low frequency components and also preserves the shape of the EEG signal in the non-artifact zones which is of very much importance in clinical diagnosis. The proposed method minimizes the complexity of the work and easily identifies the artifact zones for removing the artifacts. Signal to Noise Ratio is used as performance metrics in this paper. Higher SNR value is obtained using this method than the other previously implemented methods, therefore the suppression of ocular artifacts in dB is best. In all cases, artifacts were adequately attenuated, without removing significant and useful information.

References

[1] https://www.uni-salzburg.at/fileadmin/oracle_file_imports/1749179.PDF 30.08.2005 .

[2] "Removal of Ocular Artifacts in the EEG through Wavelet Transform without using an EOG Reference Channel", P. Senthil Kumar, R. Arumuganathan, K. Sivakumar, and C. Vimal, Int. J. Open Problems Compt. Math., Vol. 1, No. 3, December 2008.

[3] "Filter Bank Property of Multivariate Empirical Mode Decomposition", Naveed ur Rehman and Danilo P. Mandic, IEEE TRANSACTIONS ON SIGNAL PROCESSING, VOL. 59, NO. 5, MAY 2011.

[4] H.H. Jasper. The ten-twenty electrode system of the International Federation. *Electroencephalography and Clinical Neurophysiology*, 371-375, 1958.

[5] "MULTIVARIATE EMD BASED APPROACH O EOG ARTIFACTS SEPARATION FROM EEG", M.K.I Molla, T. Tanaka and T.M Rutkoski, IEEE international conference on acoustics, speech and signal processing (ICASSP), pp. 653-656, 2012.

[6] "Hilbert-Huang Transform and Its Applications", N. E. Huang and S. S. P. Shen, Eds. Singapore: World Scientific, 2005.

[7] J. Cui and W. Freeden, "Equidistribution on the sphere," SIAM J. Sci. Comput., vol. 18, no.2, pp. 595-609, 1997.

[8] N. Rehman and D. P. Mandic, "Multivariate empirical mode decomposition", in Proc. Roy. Soc. A, 2010, vol. 466, pp. 1291-1302, 2010.

[9] N. Rehman and D. P. Mandic, "Empirical mode decomposition for trivariate signals", IEEE Trans. Signal Process., vol.58, no.3, pp. 1059-1068, Mar. 2010.

[10] Z. Wu and N. E. Huang, "A study of the characteristics of white noise using the empirical mode decomposition method," in Proc. Roy. Soc. A, 2004, vol. 460A, pp. 1597-1611.

[11] D. Looney and D. P. Mandic, "Multi-scale image fusion using complex extensions of EMD," IEEE Trans. Signal Process., vol.57, no.4, pp. 1626-1630, 2009.

[12] N. E. Huang, M. Wu, S. Long, S. Shen, W. Qu, P. Gloersen, and K. Fan, "A confidence limit for the empirical mode decomposition and Hilbert spectral analysis," in Proc. Roy. Soc. Lond. A, 2003, vol. 459, pp. 2317-2345.

[13] "Separation of Ocular Artifacts from EEG Signal using Noise Assisted Bi-variate Adaptive Filtering", Most. Sheuli Akter, Md. Rabiul Islam, Bimal K. Pramanik, Md. S. Islam and Md. Ekramul Hamid, International Journal of Bio-Science and Bio-Technology, Vol. 5, No. 4, August, 2013.

International Conference on Electrical, Computer & Telecommunication Engineering (ICECTE)
8-10 December 2016, Rajshahi-6204, Bangladesh

Human Identification on the Basis of Gait Analysis Using Kohonen Self-Organizing Mapping Technique

Sagor Chandro Bakchy, Md. Rabiul Islam and Abu Sayeed
Department of Computer Science & Engineering,
Rajshahi University of Engineering & Technology, Rajshahi-6204, Bangladesh.
Email: sagorchandro.10@gmail.com, rabiul_cse@yahoo.com, abusayeed.cse@gmail.com

Abstract—Gait recognition is one of the most recent emerging technique of human biometric which can be used for security based purposes. In comparison with other bio-metric techniques gait analysis has some special security features. Most of the biometric techniques use sequential template based component analysis for recognition. Here we have proposed a developed technique for gait identification using the feature Gait Energy Image (GEI). It is implemented using Kohonen Self- Organizing Mapping (KSOM) neural network. GEI representation of gait contains all information of each image in one complete gait cycle and requires less storage and low processing speed. As only one image is enough to store the necessary information in GEI feature, recognition process is a bit easier than any other feature of gait recognition. Gait recognition has some limitations like viewing angle variation, walking speed, clothes, carrying load etc. Robust View Transformation Model (RVTM) is used to solve the problem of viewing angle. RVTM transforms the viewing angle data from various angle to specific angle. RVTM enhances recognition performance. Our proposed method compares the recognition performance with template based feature extraction which needs to process each frame in the cycle. We use GEI which gives all possible information about all the frames in one cycle and results in better performance than other feature of gait analysis.

Keywords— Gait analysis, Gait Energy Image, Kohonen Self-Organizing Mapping network, Unsupervised learning.

I. Introduction

Gait is a human biometry that indicates human unique walking style, body movements, and the activity of muscles at the time of walking or running. Human walking is a periodic incident. Starting from stepping the right leg then putting the left leg and again putting the right leg on the ground is considered as one gait cycle or gait period. Human has 32 sets of gait feature data like stribe, torso, hand, angle of joints, distance of foots and foot length etc. Gait analysis includes image processing like other bio-metric technique. In recognizing people using gait analysis first video is captured from distance with a static camera. Gait recognition approach is mainly divided into two major categories as model based approach and motion based approach [1]. Model based approach focuses on area related information likely stride, torso while motion based approach works with silhouette. Silhouette is the vivid portion of foreground in front of a dim background and is extracted from the video [2]. GEI is then found from the silhouettes. Silhouettes are extracted from video frame captured by camera using background subtractions. Gait analysis implementation has three basic types. These are i) Machine Vision (MV), ii) Floor Sensor (FS), iii) Wearable Sensor (WS). Machine vision based technique is the most common way that captures video of the surveillance area [3]. Floor sensor detect motion of human when he/she walks over the sensor mat on the ground. People wear a sensor in the part of leg and respective data are recorded. In GEI based recognition each extracted silhouette contains average information about several frames in the nearby frames [4]. Gait recognition performance is affected by some external facts like wearing trouser, carrying load, viewing angle and some internal fact like temporary or permanent injury, drunkenness and pregnancy.

II. Related Works

Concept of gait analysis is very old. Aristotle (384–322 BCE) is the person who commented about the manner in which human walk. Willhelm(1804–1891) and Eduard (1806–1871) Weber, working in Leipzig who made the next major contribution based on very simple measurements. Verne Inman (1905–1980) and Howard Eberhart (1906–1993) made major advances in America shortly after the Second World War. In recent years the first and initially most popular mechanism for measuring gait was computer vision. One vision approach proved to be practical for tracking people in large, open spaces if cameras can be placed high above the area. Another project uses Markov models to sequence the various postures of a person while walking.Computer vision has also been used for people counting systems [5]. The vision approaches are generally limited by the requirement for a specific camera vantage point or other physical attribute. Thus, in cases where the vision requirements cannot be met, other approaches are more practical. One such method utilizes continuous wave radar [6]. The strength of the wave radar approach is to determining the presence or absence of humans. The work in this paper focuses a step further on how to identify specific people after the detection of a person has occurred. Many related projects use accelerometers to identify a person based on gait. Accelerometers are attached to the person either at the leg or the small of the back. All these approaches, use accelerometer data, not gyroscope data for recognition purpose using gait analysis [7]. Also Gafurav's method uses only use accelerometer data for gait recognition rather than gyroscope data [8].

III. Proposed Methodology

In this work the CASIA-B multiview dataset was used. The dataset contains preprocessed silhouette for training into the

978-1-5090-5785-6/16/$31.00 ©2016 IEEE

machine. Our system has training and testing period. The main concept is shown in figure 1.

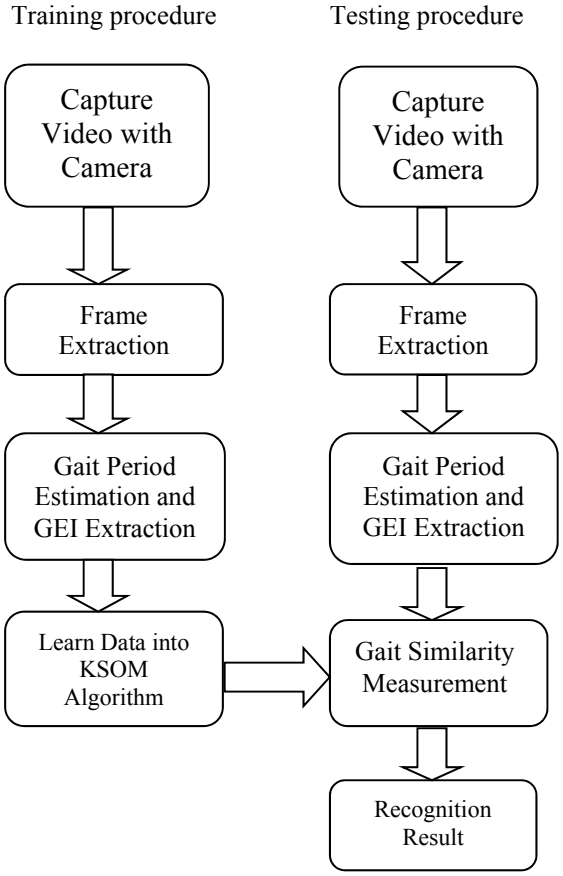

Figure 1: Gait Recognition System using Kohonen Self-Organizing Neural Network.

The Kohonen self organizing mapping technique [n] is a unsupervised learning network and used for training the machine. In the training period frames are extracted from the captured video. The GEIs are trained into KSOM neural network and stored them into database. In the testing period an input image sequence is then taken to be tested with the pre-existing data in the database and output is found from the output node of the network. The basic concept of Kohonen network is shown below in figure 2.

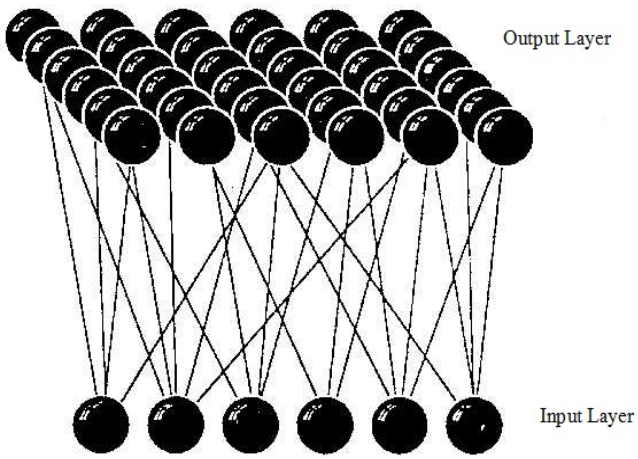

Figure 2: Kohonen network I/O layer.

IV. Implmentation

Gait Energy Image (GEI)

Human walking style is a periodic nature [9]. Each cycle contain several frames. GEI is mainly average of all silhouete (frames) in one gait cycle. GEI representation contains most possible information of the image sequences. GEI is less affected by the noise because only one image to be processed. B_t (x, y) at time t in a sequence, the gait energy image (GEI) is defined as follows.

$$G(x,y) = \frac{1}{N}\sum_{t=1}^{N} B_t(x,y) \quad (1)$$

Where N is the number of frames in one complete gait cycle of a walking person, t is the frame number in the sequence (moment of time), x and y are coordinate values in the 2D image.

If we consider a noisy silhouette image that is formed by the addition of noise $\boldsymbol{\eta_t(x,y)}$ to an original silhouette image $f_t(x,y)$ that is B_t (x, y) = f_t (x,y)+ $\boldsymbol{\eta_t(x,y)}$. Under these constraints, we further assume that $\boldsymbol{\eta_t(x,y)}$ satisfies the distribution that is described by the following equation.

$$\boldsymbol{\eta_t(x,y)} = \begin{cases} \boldsymbol{\eta_{1t}(x,y)}: \boldsymbol{P\{\eta_t(x,y) = -1\} = p,} \\ \boldsymbol{P\{\eta_t(x,y) = 0\} = 1 - p, if\ f_t(x,y) = 1} \\ \boldsymbol{\eta_{2t}(x,y)}: \boldsymbol{P\{\eta_t(x,y) = 1\} = p,} \\ \boldsymbol{P\{\eta_t(x,y) = 0\} = 1 - p, if\ f_t(x,y) = 0} \end{cases} \quad (2)$$

We have

$$E\{\eta_t(x,y)\} = \begin{cases} -p, & \text{if } f_t(x,y) = 1 \\ p, & \text{if } f_t(x,y) = 0 \end{cases} \quad (3)$$

Example of GEI extraction from the sequence of one gait cycle is given in figure 3. Here several images were taken from one gait cycle and the last one is the derived GEI.

Training

At the time of training we used the pre processed binary shilleute of CASIA-B multi-view dataset. CASIA-B dataset has about 124 person's walking data with variation in walking stsyle, carrying load and bags or wearing cloths. GEI were extracted from all the frames of one or few gait cycles from CASIA-B data set. This GEI frame is then trained into KSOM neural network as database. This database is used in next to find similarity in the testing period.

V. Experimental Result

Recognition was done using the sample data with the database to check match. Because real life data causes difficult and contains much error. In testing image of same person but of different style was choosen to check how much accurecy machine can ensure. In comaprision with template based methods GEI based recognition requires only one image to be

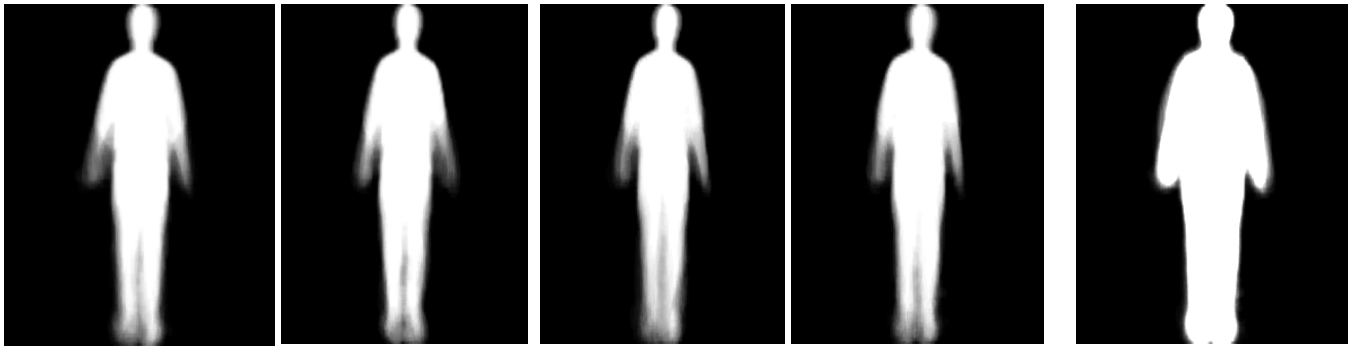

Figure 3: GEI Extraction of the frames in one complete gait cycle

processed. As a result the necessary time for recognition is mitigated and better performance is obtained than other methods. Required time for recognition decreases in a large scale. The time comparision for data matching in template based and GEI based method is shown in the following table:

Table 1: Time comparison of Template based and GEI Based recognition.

Method	No. of Subject	Total Image	Time Needed	Processed Image
Template	32	352	2.84	352
GEI	32	352	1.61	32

We had trained machine with different number of objects at different time. Each time result was different depending on the number of total image in the database. On an average gait recognition result was found as listed in the the following table:

Table-2: Gait recognition rate using KSOM Algorithm.

Trained Subject	Tested Subject (a)	Recognized Subject (b)	Result c=b/a*100
10	09	05	55.55
32	23	13	56.52
45	35	21	60.02

From the table we found that recognition rate increases with the increase in number of subjects. The comparison of performance with other method is shown in below figure 4 reveals that our proposed methodology has improved performance than some other established method. The FG and Singular Value Decomposition (SVD), Gait Energy Image (GEI) -TSVD both method has nearly 36% accuracy rate. Yu's method has recognition rate of 32% and Robust View Transformation Method (RVTM) has 51% accuracy. Ours proposed methodology has nearly 57% of recognition rate [10].

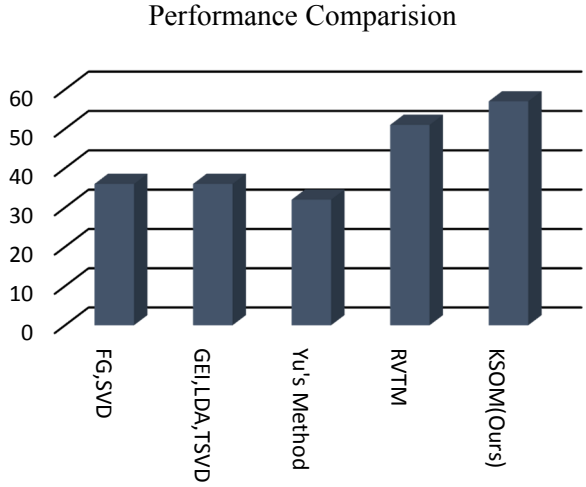

Figure 4: Gait Recognition Rate Comparison Graph

VI. Results and Discussions

We used KSOM in this work. We have tested with some of the sample data. We found about 57% accuracy using CASIA-B dataset. As gait has many limitations, recognition rate is not satisfactory in any of the method implemented till the day. In future, the system will be developed by using real life data for training and testing to attain an improved recognition result. As we have used GEI feature our system worked fast and with less storage. As a result we have found a better performance than any other methods.

References

[1] A. Samadani, A. Ghodsi, and D. Kulic, "Discriminative functional analysis of human movements," Pattern Recognition iterature, vol. 34, no. 15, pp. 1829 – 1839, 2013.

[2] Alexandros Andre Chaaraoui, Jose Ramon Padilla-Lopez, Francisco Florez-Revuelta, "Fusion of Skeletal and Silhouette-Based Features for Human Action Recognition with RGB-D Devices",vol.00,no.pp.91-97,2013.

[3] Ovidiu Ghita, Derek Molloy, and Robert Sadleir,"Irish Machine Vision and Image Processing Conference",Dublin City University, Ireland,8-9 September 2011.

[4] Md. Rokanujjaman, Md. Altab Hossain, Md. Azmal Hossin, "Part-based gait identification using fusion technique",vol.-00,pp.1-5,2014.

[5] A. Ferrero, M. Prioli, S. Salicone, and B. Vantaggi,"A 2D Metrology Sound Probability Possibility Transformation", "IEEE transaction on Instrumentation and Measurement", Volume 62 Number 5 May 2013
.

[6] Avihai Aharon Akram, Daniel Rozban, Amir Abramovich, Yitz hak Yitzhaky, Natan S. KopeikaTerahertz, "Frequency Modulated Continuous Wave Radar Using Glow Discharge Detector", "IEEE Sensors Journal", Volume: 16, Issue: 23, Pages: 8440 - 8447, Year: 2016.

[7] Sebastijan Sprager, Matjaz B. Juric, "An Efficient HOS-Based Gait Authentication of Accelerometer Data", "IEEE Transactions on Information Forensics and Security", Volume: 10, Issue: 7, Pages: 1486 - 1498, 2015.

[8] Gafurov, et al. "Spoof Attacks on Gait Authentication System." IEEE Transactions on Information Forensics and Security, Volume 2, pgs 491-502, 2007.

[9] Qi Yang, Yali Tian, "Gait recognition based on KDA and SVM", "Information Technology and Artificial Intelligence Conference (ITAIC)", 6th IEEE Joint International, Volume: 1, Pages: 160 - 163,2011.

[10] Raymond H. Chan, Tony H. Chan, Hau Man Yeung, Roger Wei Wang, "Composition Vector Method Based on Maximum Entropy Principle for Sequence Comparison", "IEEE/ACM Transactions on Computational Biology and Bioinformatics", Volume: 9, Issue: 1, Pages: 79 - 87, 2012.

Wireless Security in Selection Decode-and-Forward Relay Networks

D. K. Sarker, M. Z. I. Sarkar and M. S. Anower
Department of Electrical and Electronic Engineering
Rajshahi University of Engineering and Technology
Rajshahi-6204, Bangladesh.
Email: dks_ms@yahoo.com

***Abstract*—In this paper, a confidential communication scenario is considered through selection decode-and-forward cooperative relay networks over Rayleigh fading channel in which a source communicates with a destination via multiple relays. A best relay is selected using selection combining technique which communicates with the destination. An eavesdropper observes their communication and tries to decode confidential information. In this situation, an interest is given to ensure secure communication between the best relay and the destination so that eavesdropper is unable to decode any information from the main channel (i.e. channel between relay and destination). The performance of the proposed model is analyzed based on the closed-form analytical expressions of the ergodic secrecy capacity and the secure outage probability taking into account the distances of relays from the source, destination and the eavesdropper. Analytical results show that the additional diversity provided by the best relay situated in a strategic location significantly improves the secure outage performance of the selection decode-and-forward relay networks.**

***Index Terms*—Cooperative relay network, ergodic secrecy capacity, selection decode-and-forward, secure outage probability.**

I. Introduction

Now a days, cooperative communication through relay networks has attracted a lot of interest to the researchers due to the growing needs of various wireless communication applications. In these networks, the application strategies of relays play a pivotal role for achieving spatial diversity [1]–[3]. On the other hand, the security becomes an important issue in wireless communication networks due to the fact that the wireless communication networks are frequently used to transmit personal and confidential information and the wireless medium is susceptible to eavesdropping and fraud.

Recently, an energy-efficient secure decode-and-forward (DF) relay scheme was proposed in [4] to develop a unified mixed integer nonlinear optimization problem formulation, where the secrecy rate and secure energy efficiency performances were investigated. A cognitive DF relay and jammer selection network was proposed in [5] to study the secure outage probability of four relay selection policies namely random relay and random jammer (RRRJ), random jammer and best relay (RJBR), best relay and best jammer (BRBJ), and best relay and no jammer (BRNJ). In order to investigate the effect of of relays on the secure outage performance of multiuser downlink DF system, authors studied a relay assisted multiuser downlink DF system in [6] employing the maximal ratio combing (MRC) technique. In [7], authors studied a full-duplex relay network to analyze the achievable secrecy rate based on DF strategies with zero forcing. Note that in [4]–[7], no works have been done considering the distances of relays from the destination and eavesdropper to locate the strategic position of the relays for achieving better and secure system performance. In this paper, authors solve the problems of enhancing security with the best relay depending on the location of source, destination and eavesdropper. Moreover, to investigate the secure outage performance of the proposed model, the closed-form analytical expressions for the ergodic secrecy capacity and the secure outage probability are derived employing selection combining technique. The effects of distances between relays and destination, and relays and eavesdropper are investigated on the security of selection decode-and-forward (SDF) cooperative relay networks.

The remainder of this paper is organized as follows. Section II describes the system model and problem formulation. Numerical results are shown in Section III and Section IV provides the concluding remarks.

II. System Model and Problem Formulation

A confidential communication is considered through SDF cooperative relay networks over Rayleigh fading channel as shown in Fig.1. A source S sends confidential information to a destination D via K relays. The communication between source and destination occurs in the presence of an eavesdropper E. In the first-hop transmission, the source S transmits information to K relays. During the second-hop transmission,

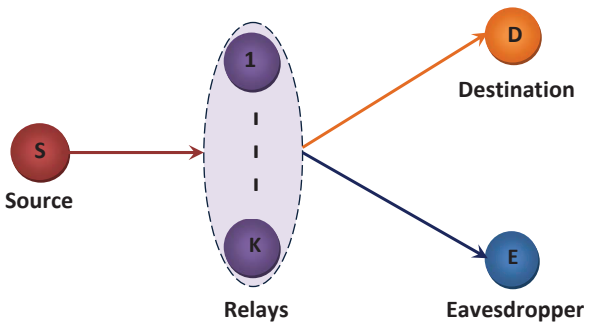

Fig. 1. System Model.

selection diversity is used for selecting the best relay (i.e., the relay with highest SNR) which forwards the source message to the destination. The propagation channels in the two hopes are considered independent but not identically distributed (i.n.i.d.). The channels are affected by small-scale fading which is modeled as Rayleigh fading. The channel gains for the source to kth relay, the best relay to destination and the best relay to eavesdropper are denoted by h_{sr_k}, h_{r_bd} and h_{r_be}, respectively. The channel mean power for the source to kth relay link, the best relay to destination link and the best relay to eavesdropper link are given by $\alpha_{sr_k} = P_{so}\delta_1^{-\mu}$, $\alpha_{r_bd} = P_{ro}\delta_d^{-\mu}$ and $\alpha_{r_be} = P_{ro}\delta_e^{-\mu}$, respectively [8], where δ_1, δ_d and δ_e denote the distances between source and relay, relay and destination, and relay and eavesdropper, respectively. P_{so} and P_{ro} denote the powers of source and each relay, respectively and μ denotes the path loss exponent. The instantaneous SNRs for the source to kth relay, best relay to destination and best relay to eavesdropper links are given by $\gamma_{sr_k} = \overline{\gamma}|h_{sr_k}|^2$, $\gamma_{r_bd} = \overline{\gamma}|h_{r_bd}|^2$ and $\gamma_{r_be} = \overline{\gamma}|h_{r_be}|^2$, respectively, where $\overline{\gamma}$ denotes the average SNR.

In the high SNR regime, the equivalent output SNR for the source to kth relay and best relay to destination links can be approximated as [3]

$$\gamma_{od} = \min\{\gamma_{sr_k}, \gamma_{r_bd}\}. \tag{1}$$

Similar to (1), the equivalent output SNR for the source to kth relay and best relay to eavesdropper links can be approximated as

$$\gamma_{oe} = \min\{\gamma_{sr_k}, \gamma_{r_be}\}. \tag{2}$$

In the selection combining scheme, the signal with largest received SNR is selected. Hence, the instantaneous SNRs at the output of relay selection combiner for main channel and eavesdropper channel are respectively given by

$$\gamma_d^{sc} = \max_{k=1,2,\ldots,K} \gamma_{od}, \tag{3}$$

$$\gamma_e^{sc} = \max_{k=1,2,\ldots,K} \gamma_{oe}. \tag{4}$$

Since γ_{sr_k}, γ_{r_bd} and γ_{r_be} are independent Rayleigh distributed random variables, therefore the cumulative distribution functions (CDFs) of γ_{od} and γ_{oe} are respectively given by [3];

$$F_{\gamma_{od}}(\gamma_d) = 1 - e^{-(\beta_k+\lambda_d)\gamma_d}, \tag{5}$$

$$F_{\gamma_{oe}}(\gamma_e) = 1 - e^{-(\beta_k+\lambda_e)\gamma_e}, \tag{6}$$

where $\beta_k = \frac{1}{\overline{\gamma}\alpha_{sr_k}}$, $\lambda_d = \frac{1}{\overline{\gamma}\alpha_{r_bd}}$ and $\lambda_e = \frac{1}{\overline{\gamma}\alpha_{r_be}}$. Differentiating (5) and (6) with respect to γ_d and γ_e, the probability density functions (PDFs) of γ_{od} and γ_{oe} can be expressed as

$$f_{\gamma_{od}}(\gamma_d) = (\beta_k + \lambda_d)e^{-(\beta_k+\lambda_d)\gamma_d}, \tag{7}$$

$$f_{\gamma_{oe}}(\gamma_e) = (\beta_k + \lambda_e)e^{-(\beta_k+\lambda_e)\gamma_e}. \tag{8}$$

From (3), the PDF of γ_d^{sc} is given by [3]

$$f_{\gamma_d^{sc}}(\gamma_d) = \sum_{k=1}^{K} f_{\gamma_{od}}(\gamma_d) \prod_{i=1;i\neq k}^{K} F_{\gamma_{od_i}}(\gamma_d). \tag{9}$$

Substituting (5) and (7) into (9), we have

$$f_{\gamma_d^{sc}}(\gamma_d) = \sum_{k=1}^{K}(\beta_k + \lambda_d)e^{-(\beta_k+\lambda_d)\gamma_d} \times \prod_{i=1;i\neq k}^{K}\left[1 - e^{-(\beta_k+\lambda_d)\gamma_d}\right]. \tag{10}$$

Using the following identity of [3]

$$\prod_{i=1}^{M}(1 - v_i) = \sum_{i=0}^{M}\frac{(-1)^i}{i!}\underbrace{\sum_{q_1=1}^{M}\cdots\sum_{q_i=1}^{M}}_{q_1\neq q_2\neq\ldots\neq q_i}\prod_{t=1}^{i} v_{q_t}, \tag{11}$$

equation (10) can be expressed as follows:

$$\begin{aligned} f_{\gamma_d^{sc}}(\gamma_d) &= \sum_{k=1}^{K}(\beta_k + \lambda_d)\sum_{i=0}^{K}\frac{(-1)^i}{i!}\underbrace{\sum_{q_1=1}^{K}\cdots\sum_{q_i=1}^{K}}_{q_1\neq q_2\neq\ldots\neq q_i} \\ &\quad\times e^{-\left[(\beta_k+\lambda_d)+\sum_{t=1}^{i}(\beta_{q_t}+\lambda_{d_{q_t}})\right]\gamma_d} \\ &= \Lambda_d e^{-\Phi_d\gamma_d}, \end{aligned} \tag{12}$$

where $\Lambda_d = \sum_{k=1}^{K}(\beta_k + \lambda_d)\sum_{i=0}^{K}\frac{(-1)^i}{i!}\underbrace{\sum_{q_1=1}^{K}\cdots\sum_{q_i=1}^{K}}_{q_1\neq q_2\neq\ldots\neq q_i}$

and $\Phi_d = \beta_k + \lambda_d + \sum_{t=1}^{i}(\beta_{q_t} + \lambda_{d_{q_t}})$.

Similarly, the PDF of γ_e^{sc} is given by [3]

$$f_{\gamma_e^{sc}}(\gamma_e) = \sum_{k=1}^{K} f_{\gamma_{oe}}(\gamma_e) \prod_{j=1;j\neq k}^{K} F_{\gamma_{oe_j}}(\gamma_e). \tag{13}$$

Substituting (6) and (8) into (13), and using the identity of equation (11), the PDF of γ_e^{sc} can be obtained as follows:

$$\begin{aligned} f_{\gamma_e^{sc}}(\gamma_e) &= \sum_{k=1}^{K}(\beta_k + \lambda_e)\sum_{j=0}^{K}\frac{(-1)^j}{j!}\underbrace{\sum_{q_1=1}^{K}\cdots\sum_{q_j=1}^{K}}_{q_1\neq q_2\neq\ldots\neq q_j} \\ &\quad\times e^{-\left[(\beta_k+\lambda_e)+\sum_{l=1}^{j}(\beta_{q_l}+\lambda_{q_l})\right]\gamma_e} \\ &= \Lambda_e e^{-\Phi_e\gamma_e}, \end{aligned} \tag{14}$$

where $\Lambda_e = \sum_{k=1}^{K}(\beta_k + \lambda_e)\sum_{j=0}^{K}\frac{(-1)^j}{j!}\underbrace{\sum_{q_1=1}^{K}\cdots\sum_{q_j=1}^{K}}_{q_1\neq q_2\neq\ldots\neq q_j}$

and $\Phi_e = \beta_k + \lambda_e + \sum_{l=1}^{j}(\beta_{q_l} + \lambda_{e_{q_l}})$.

A. Ergodic Secrecy Capacity

The ergodic secrecy capacity for SDF cooperative relay network can be expressed as

$$\begin{aligned}\langle C_s\rangle =&\frac{1}{2}\mathbb{E}\left[\log_e\left(\frac{1+\gamma_d^{sc}}{1+\gamma_e^{sc}}\right)\right],\\ =&\frac{1}{2}\left[\int_0^\infty \log_e(1+\gamma_d) f_{\gamma_d^{sc}}(\gamma_d)d\gamma_d\right.\\ &\left.-\int_0^\infty \log_e(1+\gamma_e) f_{\gamma_e^{sc}}(\gamma_e)d\gamma_e\right]. \end{aligned} \quad (15)$$

Substituting (12) and (14) into (15) we obtain

$$\begin{aligned}\langle C_s\rangle =& \frac{1}{2}\left[\int_0^\infty \log_e(1+\gamma_d)\Lambda_d e^{-\Phi_d\gamma_d}d\gamma_d\right.\\ &\left.-\int_0^\infty \log_e(1+\gamma_e)\Lambda_e e^{-\Phi_e\gamma_e}d\gamma_e\right]. \end{aligned} \quad (16)$$

Performing integration using the following identity of [9, eq. (4.222.8)], the closed-form expression for ergodic secrecy capacity is shown in (17) at the bottom of this page.

$$\begin{aligned}&\int_0^\infty \log_e(1+ax)\,x^b e^{-x}dx = \sum_{\tau=0}^{b}\frac{b!}{(b-\tau)!}\\ &\times\left[\frac{(-1)^{b-\tau-1}}{a^{b-\tau}}e^{\frac{1}{a}}\mathrm{Ei}\left(-\frac{1}{a}\right)+\sum_{\psi=1}^{b-\tau}\frac{(\psi-1)!}{(-a)^{b-\tau-\psi}}\right],\end{aligned}$$

B. Secure Outage Probability

The secure outage probability for SDF cooperative relay network is defined as

$$\begin{aligned}P_{out}(R_s) &= P_r(C_s\le R_s), \qquad R_s>0\\ &= 1-\int_0^\infty\int_\varpi^\infty f_{\gamma_d^{sc}}(\gamma_d)f_{\gamma_e^{sc}}(\gamma_e)d\gamma_d d\gamma_e, \end{aligned} \quad (18)$$

where R_s denotes the target secrecy rate and $\varpi = e^{2R_s}(1+\gamma_e)-1$. Substituting (12) and (14) into (18) we have

$$\begin{aligned}P_{out}(R_s) &= 1-\int_0^\infty\int_\varpi^\infty \Lambda_d e^{-\Phi_d\gamma_d}\Lambda_e e^{-\Phi_e\gamma_e}d\gamma_d d\gamma_e\\ &= 1-\int_0^\infty\int_\varpi^\infty \Lambda_d e^{-\Phi_d\gamma_d}d\gamma_d\Lambda_e e^{-\Phi_e\gamma_e}d\gamma_e\\ &= 1-\Lambda_d\Lambda_e\frac{e^{-\Phi_d(e^{2R_s}-1)}}{\Phi_d}\int_0^\infty e^{-(\Phi_d e^{2R_s}+\Phi_e)\gamma_e}d\gamma_e. \end{aligned} \quad (19)$$

Performing integration, the closed-form expression for the secure outage probability is shown in (20) at the bottom of the next page.

III. Numerical Results

In this section, the analytical results are verified via Monte-Carlo simulation. For this purpose, the simulation results have been generated and averaged by 110,000 realizations. The simulation and analytical results of ergodic secrecy capacity as a function of average SNR of main channel (i.e., channel between relay and destination) are shown in Fig.2 for investigating the effect of number of relays K, SNR of eavesdropper channel γ_e, distance between relay and destination δ_d and distance between relay and eavesdropper δ_e with μ=2 and α_{sr_k}=α_{r_bd}=α_{r_be}=3. It is observed that the ergodic secrecy capacity decreases with γ_e and significantly increases with K. On the other hand, the ergodic secrecy capacity decreases with δ_d and increases with δ_e and the effect of δ_d is greater than that of δ_e. So, by placing the relays in a strategic position depending on the location of eavesdropper, better secrecy rate can be achieved mitigating the problem of eavesdropping. In

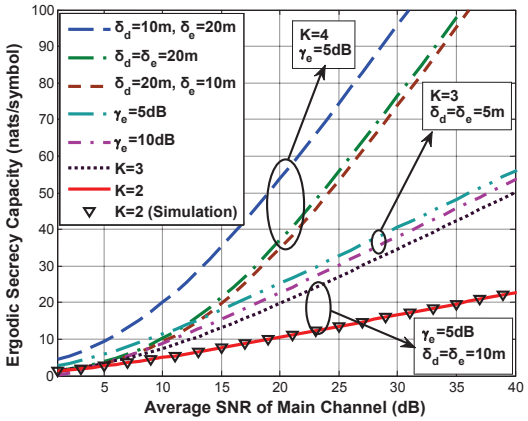

Fig. 2. The simulation and analytical results of ergodic secrecy capacity as a function of average SNR of destination channel.

Fig.3, the secure outage probability as a function of average SNR of destination channel is plotted to investigate the effect of K, γ_e, δ_d and δ_e with μ=2 and α_{sr_k}=α_{r_bd}=α_{r_be}=3. In this observation, it is seen that the secure outage probability increases with γ_e and significantly decreases with K. On the other hand, the secure outage probability increases with δ_d and

$$\begin{aligned}\langle C_s\rangle = \frac{1}{2}\Bigg[&-\sum_{k=1}^{K}(\beta_k+\lambda_d)\sum_{i=0}^{K}\frac{(-1)^i}{i!}\underbrace{\sum_{q_1=1}^{K}\cdots\sum_{q_i=1}^{K}}_{q_1\neq q_2\neq\ldots\neq q_i}\frac{e^{\beta_k+\lambda_d+\sum_{t=1}^{i}(\beta_{q_t}+\lambda_{d_{q_t}})}\mathrm{Ei}\left(-\beta_k-\lambda_d-\sum_{t=1}^{i}\left(\beta_{q_t}+\lambda_{d_{q_t}}\right)\right)}{\beta_k+\lambda_d+\sum_{t=1}^{i}(\beta_{q_t}+\lambda_{d_{q_t}})}\\ &+\sum_{k=1}^{K}(\beta_k+\lambda_e)\sum_{j=0}^{K}\frac{(-1)^j}{j!}\underbrace{\sum_{q_1=1}^{K}\cdots\sum_{q_j=1}^{K}}_{q_1\neq q_2\neq\ldots\neq q_j}\frac{e^{\beta_k+\lambda_e+\sum_{l=1}^{j}(\beta_{q_l}+\lambda_{e_{q_l}})}\mathrm{Ei}\left(-\beta_k-\lambda_e-\sum_{l=1}^{j}\left(\beta_{q_l}+\lambda_{e_{q_l}}\right)\right)}{\beta_k+\lambda_e+\sum_{l=1}^{j}(\beta_{q_l}+\lambda_{e_{q_l}})}\Bigg]. \end{aligned} \quad (17)$$

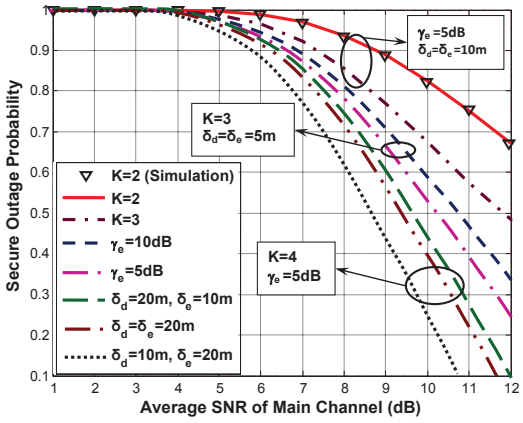

Fig. 3. The simulation and analytical results of secure outage probability as a function of average SNR of destination channel.

decreases with δ_e and the effect of δ_d is greater than that of δ_e. So, by placing the relays in a proper position depending on the location of eavesdropper, more secure and reliable system performance can be achieved. In order to investigate the effect

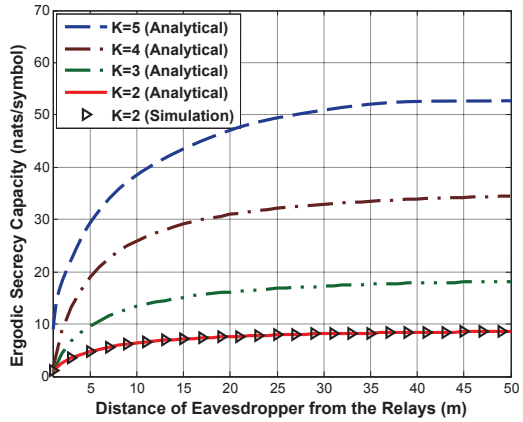

Fig. 4. The simulation and analytical results of ergodic secrecy capacity as a function of the distance of eavesdropper from the relays with μ=2 and α_{sr_k}=α_{r_bd}=α_{r_be}=3.

of relays and location of the eavesdropper simultaneously, the simulation and analytical results of ergodic secrecy capacity as a function of δ_e is shown in Fig.4. It is observed that although the ergodic secrecy capacity increases with δ_e and K, the effect of K is much greater than that of δ_e. From this observation, it can be said that depending on the location of eavesdropper, the expected secrecy rate can be maintained protecting eavesdropping by varying the number of relays.

IV. Conclusion

A focus is given on the derivation of closed-form analytical expressions for the ergodic secrecy capacity and the secure outage probability of relay networks in which a best relay is selected employing selection combining technique. The validity of analytical expressions are justified via Monte-Carlo simulation. Based on the observations and from the numerical results, it can be concluded that the additional diversity provided by best relay significantly increases diversity gain which causes an improvement in the ergodic secrecy capacity and a reduction in the secure outage probability of proposed model. By placing relays in a strategic position depending on the location of the destination and eavesdropper, better and secure system performance can be achieved protecting the problem of eavesdropping.

Acknowledgement

This work is supported by the Research Support and Publication Division of University Grant Commission, Bangladesh.

References

[1] D. K. Sarker, M. Z. I. Sarkar, and M. S. Anower, "Security in cooperative spatial multiplexing system with zero-forcing filtering," in *Proc. IEEE Int. Conf. Elect. Inf. and Commu. Technology (EICT), 2015, Khulna, Bangladesh*, Dec. 2015, pp. 273–277.

[2] S. Majhi and A. Banarjee, "Asymptotic outage analysis of incremental decode and forward cognitive radio relay network," in *Proc. IEEE Int. Conf. Commu. Syst. and Networks (COMSNETS), 2015, Bangalore, India*, Jan. 2015, pp. 1–8.

[3] T. Q. Duong, V. N. Q. Bao, and H.-J. Zepernick, "On the performance of selection decode-and-forward relay networks over Nakagami-m fading channels," *IEEE Commun. Letts.*, vol. 13, no. 3, pp. 172–174, March 2009.

[4] D. Wang, B. Bai, W. Chen, and Z. Han, "Energy efficient secure communication over decode-and-forward relay channels," *IEEE Trans. on Communications*, vol. 63, no. 3, pp. 892–905, Jan. 2015.

[5] Y. Liu, L. Wang, T. T. Duy, M. Elkashlan, and T. Q. Duong, "Relay selection for security enhancement in cognitive relay networks," *IEEE Commun. Letts.*, vol. 4, no. 1, pp. 46–49, Feb. 2015.

[6] X. Lei, L. Fan, R. Q. Hu, D. S. Michalopoulos, and P. Fan, "Secure multiuser communications in multiple decode-and-forward relay networks with direct links," in *Proc. IEEE Int. Conf. Global Communication, 2014, Austin, TX*, Dec. 2014, pp. 3180–3185.

[7] R. Bassily and S. Ulukus, "Secure communication in multiple relay networks through decode-and-forward strategies," *Journal of Communications and Networks*, vol. 14, no. 4, pp. 352–363, Aug. 2012.

[8] M. Haenggi, "On routing in random Rayleigh fading networks," *IEEE Trans. on Communications*, vol. 4, no. 4, pp. 1553–1562, July 2005.

[9] I. S. Gradshteyn and I. M. Ryzhik, *Table of Integrals, Series, and Products*, 7th ed. San Diego, CA: Academic, 2007.

$$P_{out}(R_s) = 1 - \sum_{k=1}^{K}(\beta_k+\lambda_d)\sum_{i=0}^{K}\frac{(-1)^i}{i!}\underbrace{\sum_{q_1=1}^{K}\cdots\sum_{q_i=1}^{K}}_{q_1\neq q_2\neq\ldots\neq q_i}\sum_{k=1}^{K}(\beta_k+\lambda_e)\sum_{j=0}^{K}\frac{(-1)^j}{j!}\underbrace{\sum_{q_1=1}^{K}\cdots\sum_{q_j=1}^{K}}_{q_1\neq q_2\neq\ldots\neq q_j}$$
$$\times\frac{e^{-\left[\beta_k+\lambda_d+\sum_{t=1}^{i}(\beta_{q_t}+\lambda_{d_{q_t}})\right](e^{2R_s}-1)}}{\left[\beta_k+\lambda_d+\sum_{t=1}^{i}(\beta_{q_t}+\lambda_{d_{q_t}})\right]\left[(\beta_k+\lambda_d+\sum_{t=1}^{i}(\beta_{q_t}+\lambda_{d_{q_t}}))e^{2R_s}+(\beta_k+\lambda_e+\sum_{l=1}^{j}(\beta_{q_l}+\lambda_{e_{q_l}}))\right]}. \quad (20)$$

2nd International Conference on Electrical, Computer & Telecommunication Engineering (ICECTE)
8-10 December 2016, Rajshahi-6204, Bangladesh

A Frequency Converter Control Strategy of DFIG Based Wind Turbine to Meet Grid Code Requirements

Md. Rashidul Islam[1*], M.R.I. Sheikh[2], Zinat Tasneem[3]
[1,2]EEE Department, Rajshahi University of Engineering & Technology, Rajshahi 6204, Bangladesh
[3]MTE Department, Rajshahi University of Engineering & Technology, Rajshahi 6204, Bangladesh
*E-mail: rashu_ruet@yahoo.com

Abstract— **Fixed speed wind turbine generator systems suffer from various problems specially in transient conditions. So, in recent years the use of doubly fed induction generators (DFIGs) has increased significantly. DFIGs are sensitive to external faults. However, no attempts have been made to investigate the impact of increasing the carrier frequency of frequency converter/inverter for variable speed wind generators during voltage dip conditions. In this paper a suitable control strategy is developed for frequency converter/inverter to improve the low voltage ride through (LVRT) capability of DFIG based wind turbines. Simulation results indicate that the proposed topology improve the LVRT capability under grid codes. PSCAD/EMTDC software has been used for simulations under real wind speed data.**

Keywords—low voltage ride through (LVRT); frequency converter; DFIG; grid codes; voltage dip.

I. INTRODUCTION

Electrical energy conversion from fossil fuel is not environment friendly and its stock is also limited. So, renewable energy resources draw the attention. The use of wind energy is growing rapidly and it is expected to provide 10% of the global electricity generation by the year 2020 [1].

Fixed speed wind turbine generator systems suffer from various problems, so variable speed wind turbine generator system (WTGS) is becoming more popular recently [2]. When compared to fixed-speed induction generators, the DFIG has the advantages of maximum power capture, less mechanical stresses, and less acoustical noise. Compared with the full-converter variable-speed generators, the DFIG is a preferable choice in terms of size, cost, reduced losses and weight associated with the small converter [3].

Complete shutdown of a large wind farm is not desirable and may cause serious problems on the power system operation. Therefore, to avoid the shutdown of large wind farm a new set of grid codes [4]–[7] have been defined recently, which includes the low voltage ride-through (LVRT) requirements for WTGSs during the network disturbances. Various FACTS devices are introduced to improve the LVRT capability for fixed speed WTGS but it increases the overall cost. On the other hand, LVRT capability of variable speed WTGS equipped with full or partial rating power electronic converters is very good during faults [8].

Enhance the LVRT capability of DFIGs for unbalanced faults is discussed in [9-10]. This is done either by modifying the DFIG converter controls or by using additional power electronic hardware. A proposed method for LVRT capability improvement due to balanced voltage dips is presented in [11].

LVRT issue in DFIGs has been addressed by several countermeasures in the literature. The conventional method of using a crowbar [12], machine demagnetization through modified RSC control [13], compensation of rotor back-emf voltages [14], hardware modification and series voltage compensation by the voltage source converters (VSCs) [15] are the ride-through approaches proposed in the literature. Each system has some advantages and disadvantages.

However, no attempts have been made to investigate the impact of increasing the carrier frequency of frequency converter/inverter to a practical range for variable speed wind generators during voltage dip conditions. This paper proposed a method to enhance the LVRT capability of DFIGs under balance voltage dip condition. When the grid voltage experiences a low voltage then the proposed strategy are activated. Main contribution of this proposed method is that it limits the transients of DFIGs and reduces the time to recover to normal operating condition.

II. MODEL SYSTEM

The model system used for the LVRT analysis is shown in Fig. 1. Here, a DFIG (10 MVA) is connected to 11-kV system. The output of the wind turbine is supplied to the utility grid though a 0.69/11-kV step-up transformer. Rotor of that DFIG is fed through a 0.34/0.69-kV step down transformer and two back-to-back converters that use IGBTs and a capacitor connected on the DC side acts as the DC voltage source has real and reactive power control abilities. DFIG parameters are shown in Table I.

978-1-5090-5785-6/16/$31.00 ©2016 IEEE

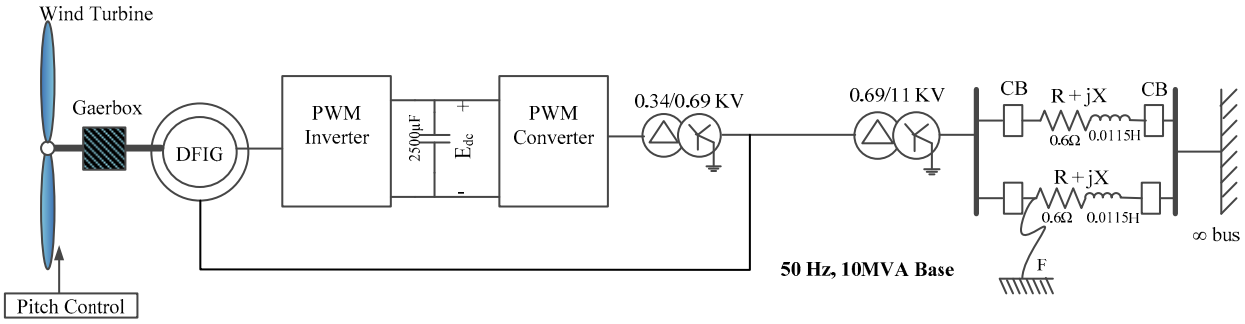

Fig. 1. Schematic diagram of the study system.

TABLE I
PARAMETERS OF DFIG

Rated power	10[MW]	Wound rotor resistance	0.01[pu]
Rated voltage	0.69[kV]	Magnetizing inductance	3.5[pu]
frequency	50[Hz]	Stator leakage inductance	0.15[pu]
J	1.50	Wound rotor leakage inductance	0.15[pu]
Stator resistance	0.01[pu]		

III. Wind Turbine Model

Mechanical power captured from the wind can be calculated using the well-known aerodynamic equation [16],[17]:

$$P_m = {}^1\!/_2\, A\rho V^3 C_P(\lambda,\beta) \qquad (1)$$

Where A is the turbine rotor area, ρ is the density of the air, V is the wind speed, C_p is the performance coefficient, β is the blade pitch angle, $\lambda=\omega R/V$ is the tip speed ratio, R is the radius of the rotor and ω is the mechanical angular speed of the blades.

IV. Modeling Of Frequency Converter

The electrical scheme of variable speed WTGS -DFIG topology is shown in Fig. 2. The pulse width modulation (PWM) frequency converter consists of grid side ac/dc converter, dc-link capacitor, and generator side dc/ac inverter. Simple two-level (2L) topology is considered for both converter and inverter as two-level converter/inverter topology is frequently used in wind power application [8].

The proposed pulse generation system of 2L converter is shown in Fig. 3. The switching strategy of 2L inverter is also the same. In both converter and inverter, the triangular carrier signal is used as the carrier wave of PWM operation. The carrier frequency is chosen 1000 Hz for both converter and inverter. The dc-link capacitor is chosen 25000 μF. The rated dc-link voltage is 0.7 kV.

When a network disturbance occurs, the terminal voltage, V_{grid}, of the high voltage side of the transformer decreases considerably. In Fig. 3 f_{c_normal} (1000 Hz) is the carrier frequency of both converter and inverter at normal condition and f_{c_fault} is the increased carrier frequency during the time when V_{grid} drops below the preset value, V_{grid_ref} at per unit. It gives excellent transient performance as demonstrated in Section V. This is the main feature of this work. To get the best result, f_{c_fault} is increased from 2000 Hz to 11000 Hz at an interval of 500 Hz. Also V_{grid_ref} is set from 0.95 pu to 0.99 pu at an interval of 0.05 and check all the transient behaviors. f_{c_fault} is increased to a practical value where switching loss is considerable. Not only the proper selection of f_{c_fault} is important but also the proper selection of V_{grid_ref} with respect to f_{c_fault} is equally important to get the best result.

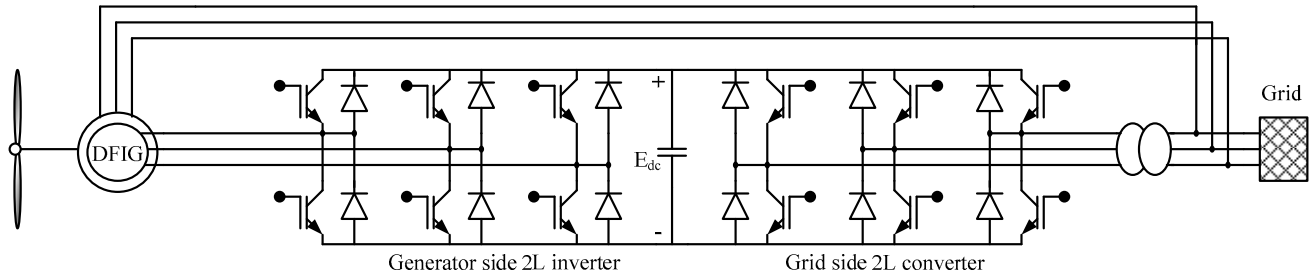

Fig. 2. Electrical scheme of variable speed wind turbine-DFIG.

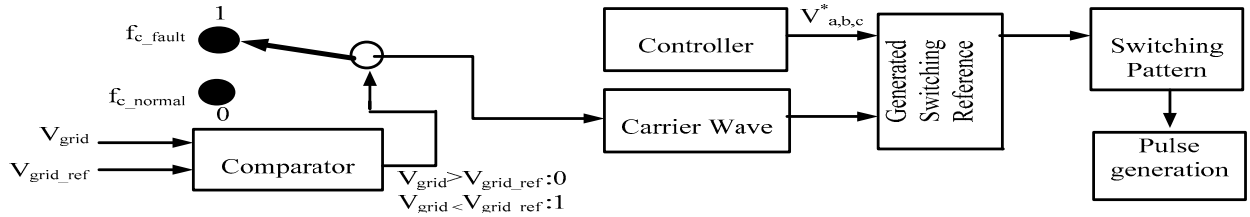

Fig. 3. Pulse generation system for both converter and inverter.

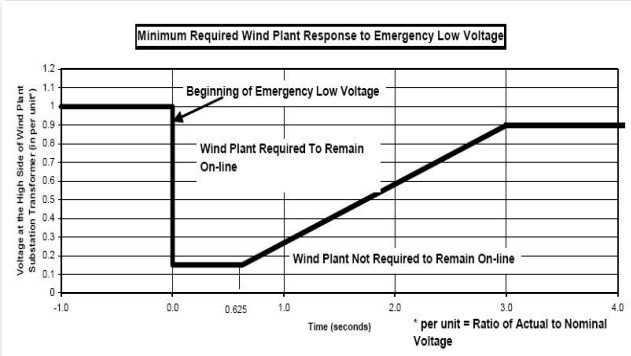

Fig. 4. Low voltage ride-through standard set by FERC, U.S. [6].

V. Simulation Results

In this study, the simulation results are described in light of the U.S. grid code, set by Federal Energy Regulatory Commission (FERC). If the voltage does not fall below the minimum voltage indicated by the solid line as shown in Fig. 4 and returns to 90% of the nominal voltage within 3 s after the beginning of the voltage drop, the plant must stay online [6]. Symmetrical three-line-to-ground fault (3LG) is considered as a network disturbance, which occurs at fault point F in Fig. 1. Simulations were run for 350 s. The 3LG fault occurs at 200 s for 50ms. Fig. 5 shows that the proposed method limits the transients of DFIGs. This proposed method is discussed in Section IV. Two cases shown in Table II are considered in the simulation study to show the effectiveness of the control strategy of the proposed system to meet the wind farm grid code requirements.

TABLE II
CASE STUDY

Case I	Case II
f_{c_fault} = 8000 Hz	f_{c_fault} = 8000 Hz
V_{grid_ref} = 0.98 pu	V_{grid_ref} = 0.96 pu

Fig. 5 shows the terminal voltages during fault of high voltage side of that 0.69/11 kV transformer in Fig. 1. It compares the transient voltage responses with and without the proposed method. Case 1 is considered for the proposed method for Fig. 5, Fig. 6 and Fig. 7. It is clear from Fig. 5 that the LVRT capability is enhanced significantly by using this proposed strategy. The terminal voltage returns to its pre-fault level for Case 1 quickly. Reactive power of that grid is shown in Fig. 6.

Terminal voltage transient is reduced by applying that strategy, so the reactive power fluctuation is reduced during fault as shown in Fig. 6. Voltage across the DC link capacitor is much less during fault for the proposed method as shown in Fig. 7. For that proposed strategy, f_{c_fault} is not only important but also the reference V_{grid_ref} is so very important for LVRT improvement. Grid side terminal voltages during fault for Case-I and Case II are shown in Fig. 8.

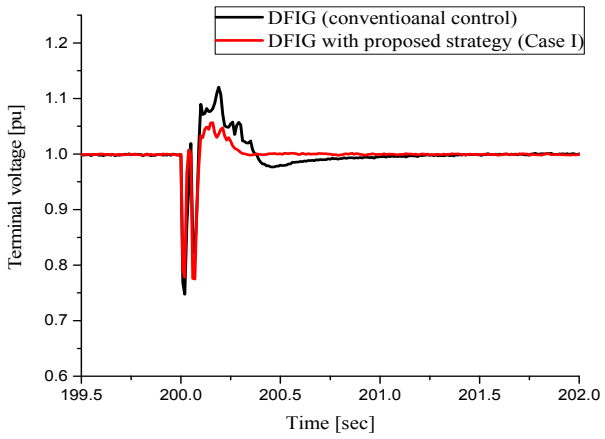

Fig. 5. Terminal voltage [pu] at grid during 3LG fault.

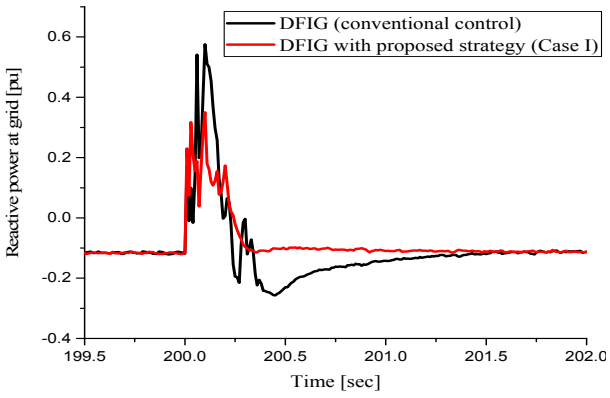

Fig. 6. Reactive power [pu] at grid during 3LG fault.

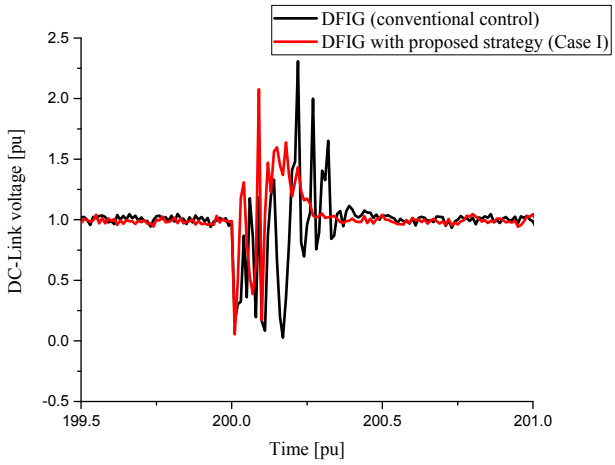

Fig. 7. DC-Link voltage [pu] of the frequency converter during 3LG fault.

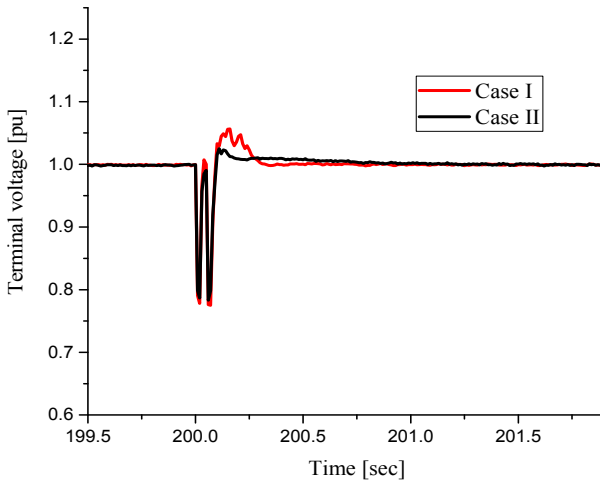

Fig. 8. Terminal voltage [pu] at grid during 3LG fault.

VI. Conclusion

This paper deals with the low voltage ride-through capability enhancement of DFIG-based WTs under balanced voltage dips. Various techniques have been used to enhance the LVRT capability of DFIGs, which are reported already in several literatures. In this paper, a new type of control strategy for frequency converter's carrier frequency of variable speed wind turbine generator systems has been presented. The LVRT characteristics of DFIG based WTGSs are evaluated in light of U.S. grid code considering symmetrical fault. After observing the terminal voltage, reactive power and DC-Link capacitor voltage it is concluded that the proposed system can be an effective solution to enhance the LVRT capability of DFIG based wind turbines.

References

[1] P. Musgrove, Wind Power. New York: Cambridge University Press, 2010.

[2] F. V. hulle, Large Scale Integration of Wind Energy in the European Power Supply Analysis, Issue and Recommendations. EWEA, Dec. 2005, Tech. Rep.

[3] A. Petersson and S. Lundberg, "Energy Efficiency Comparison of Electrical Systems for Wind Turbines," presented at the Nordic Workshop on Power and Industrial Electronics, Stockholm, Sweden 2002.

[4] R. Zavadil, N. Miller, A. Ellis, and E. Muljadi, "Making connections," *IEEE Power Energy Mag.*, vol. 3, no. 6, pp. 26–37, 2005.

[5] Ireland National Grid, Grid Code Version 2, Jan. 2007, Wind Farm Power Station Grid Code Provisions, WFPS1, pp. 213–216.

[6] Federal Energy Regulatory Commission (FERC), United States of America, Docket no. RM05-4-000-Order no. 661, Interconnection for Wind Energy, Jun. 2, 2005.

[7] Federal Energy Regulatory Commission (FERC), United States of America, Docket no. RM05-4-001; Order no. 661-A, Interconnection for Wind Energy, Dec. 12, 2005.

[8] S. M. Muyeen, R. Takahashi, T. Murata, and J. Tamura, "A Variable Speed Wind Turbine Control Strategy to Meet Wind Farm Grid Code Requirements," *IEEE Trans. Power Syst.*, vol. 25, no. 1, pp. 331–340, Feb. 2010.

[9] G-Bellmunt O, J-Ferre A, Sumper A, B-Jane J. Ride-through control of a doubly fed induction generator under unbalanced voltage sags. IEEE Trans Energy Convers 2008;23:1036–44.

[10] Flannery P, Venkataramanan G. Unbalanced voltage sag ride-through of a doubly fed induction generator wind turbine with series grid side converter. IEEE Trans Ind Appl 2009;45:1879–87.

[11] Rahimi M, Parniani M. Efficient control scheme of wind turbines with doubly-fed induction generators for low voltage ride-through capability enhancement. IET Renew Power Gener 2010;4:242–52.

[12] Kasem AH, EI-Saadany EF, EI-Tamaly HH, Wahab MAA. An improved fault ride-through strategy for doubly fed induction generator-based wind turbines. IET Renew Power Gener 2008;2:201–14.

[13] Xiang D, Ran Li, Tavner PJ, Yang S. Control of a doubly fed induction generator in a wind turbine during grid fault ride-through. IEEE Trans Energy Convers 2006;21:652 62.

[14] Rahimi M, Parniani M. Transient performance improvement of wind turbines with doubly-fed induction generators using nonlinear control strategy. IEEE Trans Energy Convers 2010;25:514–25.

[15] Joshi N, Mohan N. A novel scheme to connect wind turbines to the power grid. IEEE Trans Energy Convers 2009;24:504–10.

[16] J. G. Slootweg; H. Polinder; W. L. Kling, "Representing Wind Turbine Electrical Generating Systems in Fundamental Frequency Simulations", *IEEE Transactions on Energy Conversion*, vol. 18, no.4, pp. 516–524, 2003.

[17] V. Akhmatov, "Analysis of Dynamic Behaviour of Electric Power Systems with Large Amount of Wind Power", Ph.D. thesis, Technical Univ. of Denmark, Lyngby, Denmark, 2003.

2nd International Conference on Electrical, Computer & Telecommunication Engineering (ICECTE)
8-10 December 2016, Rajshahi-6204, Bangladesh

A Solution for the Conventional Wind Farms by Using Semi-Converter Based PMSG with a Higher Capacity

Zinat Tasneem[1], M.R.I. Sheikh[2], and Md. Rashidul Islam[3]
[1]Dept. of MTE, [2,3]Dept. of EEE
Rajshahi University of Engineering & Technology, Rajshahi-6204, Bangladesh
E-mail: tasneemzinat@gmail.com

***Abstract*—The performance of induction generator (IG) based wind farms is not satisfactory these days. The existing IG based farms create a huge problem especially in case of expanding the capacity of the wind farm. This paper introduces a new solution for the problem. It suggests that the introduction of permanent magnet synchronous generator (PMSG) with IG, not only expands the capacity of the wind farm, but also it produces a stable output. A practical case considering Synchronous Generator (SG) in combination with a wind farm having both IG and PMSG has been used. The proposed PMSG has been equipped with the full-rated power converters. The results prove the effectiveness of the proposed model. Simulations have been done by using the engineering software PSCAD/EMTDC. Real wind speed data have been considered for this study.**

***Index Terms*—IG, PMSG, SG, semi-converter, 3-level IGBT.**

I. Introduction

From the last decade, the contribution of large scale wind farms into electrical grid system has been significantly increased. Today, multi-MW size wind turbines are being installed [1], and they are very advanced power generators. At the very beginning, wind power did not have any serious impact on the power system control, but nowadays, due to its increased size, wind power has to play a much more active part in grid operation and control. The technology used in wind turbines was originally based on a squirrel-cage IG, connected directly to the grid. Power pulsations in the wind were almost directly transferred to the electrical grid by using this technology as the speed is fixed (limited slip range). Furthermore, there is no dynamic control of the active and reactive power except for a few capacitor banks which ensured unity power factor at the point of common coupling. As the power capacity of the wind turbines increases, regulating the frequency and the voltage in the grid become even more important, and it has become necessary to introduce power electronics [2] as an intelligent interface between the wind turbine and the grid. Introduction of power electronics ensured the role of a wind farm as a reliable and green energy source.

Since, the demand for wind energy is increasing day by day, it is important to assure that the power developed by the wind farm must be of good quality and the operation of the wind farm must be stable [3]. Over recent years, a new scheme for the wind generators has become popular, which includes a Variable Speed Wind Turbine with PMSG known as VSWT-PMSG. In this concept, PMSG can be directly driven by a wind turbine without gearbox and it is connected to the ac power grid through the power converters. In our previous study [4-5], it is seen that PMSG has the capability to control the real and reactive power, maintain the output voltage constant and also it is eligible to provide the necessary reactive power compensation, thus it can reduce the voltage and power fluctuations caused by the dynamic wind speed.

In this study, a 5MVA PMSG has been considered along with a 20MVA IG. This wind farm is connected to a set of Synchronous Generators (SG) of 100MVA having different types of governors. SG with thermal governor has a better response than hydro governor [6-7]. When different governors are used for SG, the condition becomes more critical since the different governors cannot respond so quickly with the response of the wind farm [7-9]. In [7] it is reported that though the thermal governor can control system frequency, but it cannot be maintained to the acceptable level when wind power capacity become 10% of total capacity. It is also presented that when several SGs with same total capacity are connected to the network, system frequency becomes more severe for 10% capacity of wind power. In [5] a reliable power system has been developed with 21% wind farm (IG-20% and PMSG-1%), 3-level converter-inverter set was chosen to be the best one, but practically 1% PMSG with 20% IG may not be feasible. Here, the capacity of PMSG has been increased to 5% and this has been possible due to a change in the converter used in PMSG. In this case, full-rated power converter works well for PMSG. In case of using PMSG with a higher capacity, 3-level converter set failed to fulfill the required conditions. Comparisons have been shown in the simulation results which prove the effectiveness of the proposed system.

II. System Layout

Two case studies have been shown in this paper. The cases are explained in the following paragraphs.

978-1-5090-5785-6/16/$31.00 ©2016 IEEE

A. Case-1, A set of SGs along with an IG and PMSG (3-level converter-inverter set) based wind farm

In this case an IG (20 MVA) along with a PMSG (5 MVA) is connected with a set of four SGs (100 MVA). Here 3-level IGBT converter-inverter set has been used for PMSG. Fig. 1(a) shows the schematic diagram of this case.

B. Case-2, A set of SGs along with an IG and PMSG (full rated power converter-inverter set) based wind farm

In this case an IG (20 MVA) along with a PMSG (5 MVA) is connected with a set of four SGs (100 MVA). The PMSG is equipped with full rated power converter-inverter set. Fig. 1(b) shows the schematic diagram of this case.

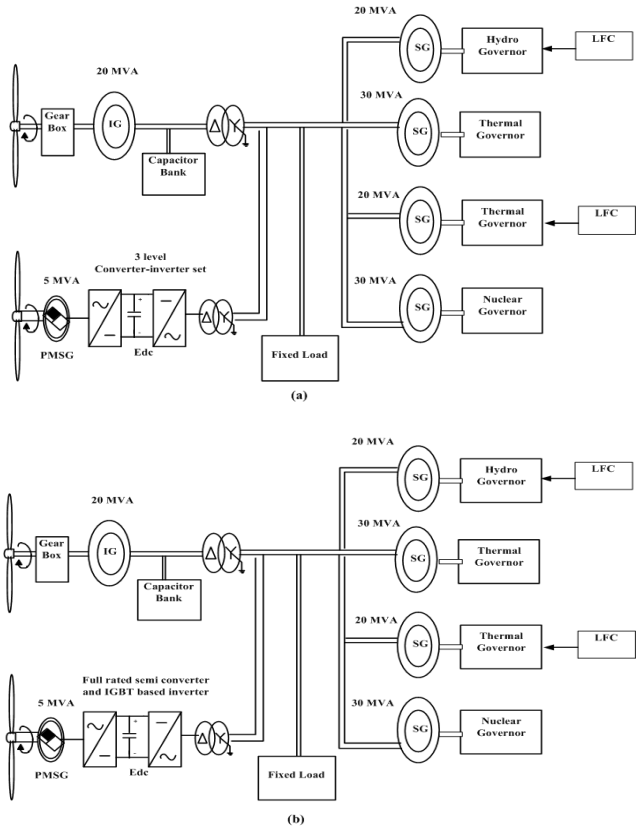

Fig. 1. Schematic diagram of (a) Case-1 and (b) Case-2.

III. Details Model of PMSG

Since two different systems are being compared in this study, hence two models for PMSG has been used in this paper. Fig. 2 and Fig. 3 show a VSWT-PMSG system which is modeled with three-level and full-rated power converter-inverter set respectively. The PMSG model available in the package software PSCAD/EMTDC is used [10]. The frequency converter consists of a generator side AC/DC converter, a DC link capacitor and a grid side DC/AC inverter, which are standard three phase two-level unit, composed of six insulated gate bipolar junction transistor (IGBTs) and anti parallel diodes at the inverter terminal and three phase three-level unit composed of twelve IGBTs and anti parallel diodes. These full-rating power converters (generator side converter and grid side inverter) are linked by a DC bus. In both models the three phase AC output of the generator is rectified and the DC output from the rectifier is fed to an IGBT-based grid side inverter. In both the converter and inverter, triangle signal is used as carrier wave of Pulse Width Modulation (PWM) operation. The carrier frequency is chosen 1000Hz. The DC link capacitor value is 30,000 μF. The rated DC link voltage is 1 pu. The grid side inverter control works to maintain the DC-link capacitor voltage at the set value, so that the active power can be exchanged efficiently from PMSG to the grid. It also controls the reactive power output to the grid in order to control the grid side voltage.

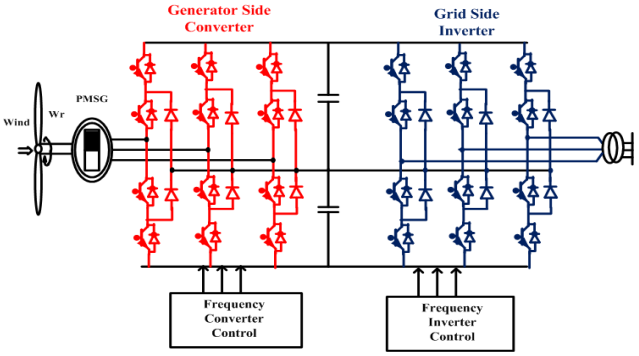

Fig. 2. Connection scheme of PMSG with 3-level IGBT based converter-inverter set.

Today, it is a trend to use a PMSG in the full-rated power converter wind turbine. As there is no reactive power needed in such a generator and active power flows in a unidirectional way from the PMSG to the grid through a power converter, only a simple diode rectifier can be applied to the generator side converter in order to obtain a cost-efficient solution. As used in Case-2. However, diode rectifier even if multiphase or 12-pulses introduces low-frequency pulsations that can trigger shaft resonance [11]. Semi-controlled rectifier solutions are also possible [12] as shown in Fig. 3.

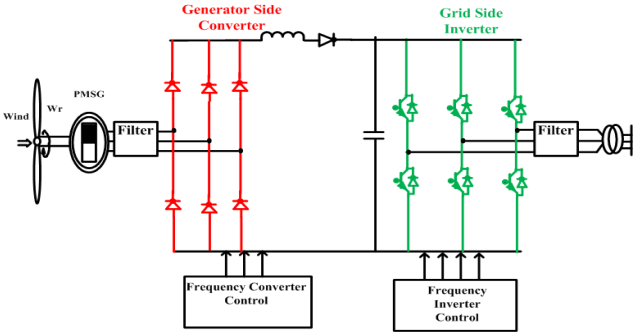

Fig. 3. Full rated power converter-inverter set (semi-converter based).

IV. Synchronous Generator Model and Governor

The governor is such a device which automatically adjusts the rotational speed of the turbine and the generator output. The turbine is operated at a constant rotational speed, when the generator load remains constant. However, when the load changes, balance between the generator output and the load is not maintained, and the rotational speed changes. When the load is removed, the governor detects the increase of the

rotational speed, and then, the valve is closed rapidly so that an abnormal speed increase of the generators is prevented. The governors of [7] and [13] are considered in this study. The synchronous generator and Load Frequency Control (LFC) model used in [7] has also been used in this study.

V. Simulation Results

Simulations have been done by using the software PSCAD/EMTDC [10] for 350 seconds. Fig. 4 shows the real wind speed data, obtained in Hokkaido Island, Japan that has been used for IG and PMSG in this simulation. Fig. 5 represents the real power response at the wind farm terminal. In case of using PMSG of 5 MVA, the response of 3-level converter-inverter set has declined than that shown in [5], rather full rated semi-converter based system provides quite a good response. Similar situation occurs in case of the other parameters, like real power, voltage at the wind farm terminal. In fact, 3-level model proves to be ineffective since it produces a negative power and less voltage in the simulation result as shown in Fig. 5 and Fig. 6 respectively.

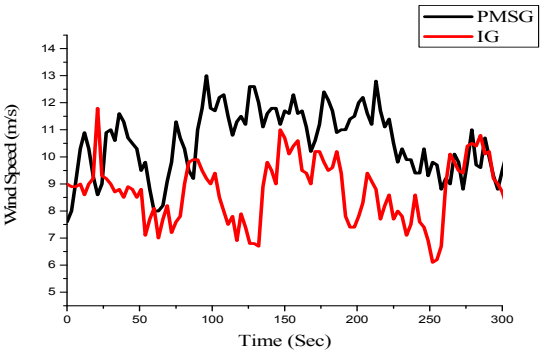

Fig. 4. Wind speed data.

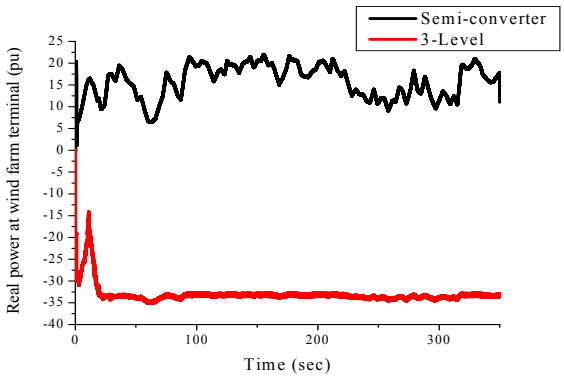

Fig. 5. Real power at the wind farm terminal.

Though, in Fig. 7, the frequency response of 3-level IGBT based system is a bit better than the semi-converter based system, but the proposed model creates a frequency

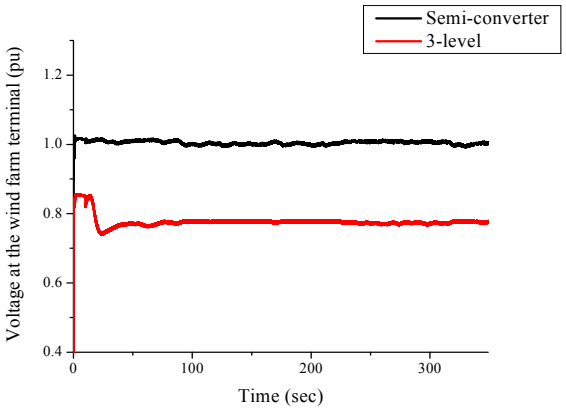

Fig. 6. Voltage at the wind farm terminal.

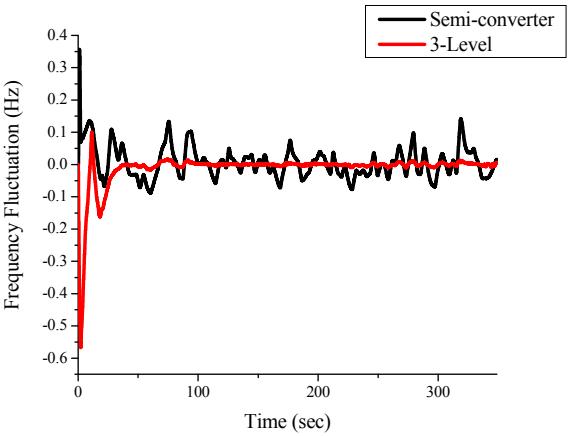

Fig. 7. Frequency fluctuation at the wind farm terminal.

fluctuation which is within the allowable limit (+/- 0.2 Hz). In the proposed model, the real power of the set of SGs can respond with that of the wind farm, i.e. when the power from the wind farm tends to decrease, the power of SG tends to increase and vice versa in order to maintain a constant power at the load side. Thus the system remains stable. This can be seen from Fig. 8. So, the power supplied to the load remains almost constant, as can be seen from Fig. 9.

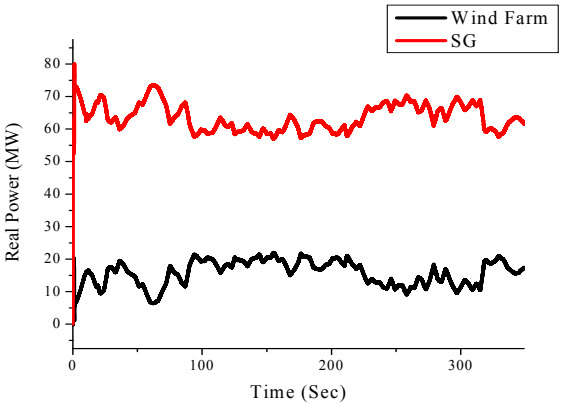

Fig. 8. Real power response at the wind farm terminal and SG terminal.

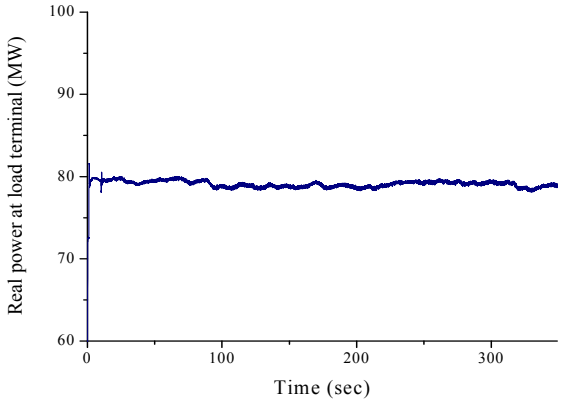

Fig. 9. Real power response at the load terminal.

Again, another situation has been considered in this study to prove the reliability of the system and that is the varying load condition. This is indicated in Fig. 10. In this condition, a 2MW of load has been added to the system at the 50th second. Similarly, another 3MW was added at 60th second. On the other hand, this extra load has been removed consequently, that is 4MW at 70th and remaining 1MW at the 80th second. Normally, frequency of the will tend to decrease in the case of addition of load and will tend to increase at the time of removal of load. Similar response can be seen from Fig. 10, but point to be noted that all the fluctuation of the proposed system lies well below the allowable limit indicated by the margins on the Y-axis. So, this system can also be applicable for varying load conditions.

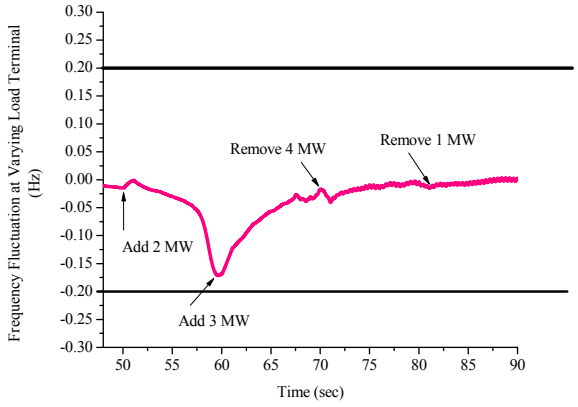

Fig. 10. Frequency fluctuation under varying load condition.

VI. Conclusion

The proposed model of the wind farm has proved its reliability in almost every sector. It can produce and comparatively stable output than the model proposed in the previous study. It helps to maintain constant power at the load terminal; moreover it also works well under varying load condition. Furthermore, it helps to increase the capacity of the PMSG used in the wind farm. Hence it is more feasible for the practical application. This type of wind farms can be economically effective, as because it does not need any external control device. Therefore, this model can also be a better option for our country to produce electricity from this green energy source.

References

[1] M. Liserre, R. Cardenas, M. Molinas, and J. Rodriguez, "Overview of multi-MW wind turbines and wind parks," *IEEE Trans. Ind. Electron.* ,vol. 58, no. 4, pp. 1081–1095, Apr. 2011.

[2] M. P. Kazmierkowski, R. Krishnan, and F. Blaabjerg, Contro l in Power Electronics-Selected Problems. New York: Academic, 2002.

[3] M. Rosyadi, M.R.I. Sheikh, S.M. Muyeen, R. Takahashi, J. Tamura, "A Control Strategy of Direct-Drive Permanent Magnet Wind Generator for Wind Farm Stabilization," *Annual Paper Meeting, Society of Rotatory Mission, Japan.* Page(s):7-12, Oct. 2010.

[4] Z. Tasneem, and M.R.I. Sheikh, "Modeling and Controlling of a Directly Driven Wind Turbine Using Permanent Magnet Synchronous Generator", (Paper ID. ET-22), *International Conference on Mechanical, Industrial and Materials Engineering 2013 (ICMIME2013),* on page(s): 261-267, Nov. 2013.

[5] Z. Tasneem, and M.R.I. Sheikh, "Stabilization of a Fixed Speed IG Based Wind Farm using Variable Speed PMSG," *Rajshahi University Journal of Science and Engineering*, vol. 43(2015), pp. 101-107, ISSN: 2408-8803 (online).

[6] M.R.I. Sheikh, M.S.R Ashrafi, and D. Datta, "Co-ordinated Frequency Control of Power System with High Wind Power Penetration," *Proc. ICEEICT 2014*, paper 205.

[7] M.R.I. Sheikh "Stabilization of a Grid Connected Wind Farm by Using SMES" a PhD thesis, Kitami Institute of Technology, Japan, September 2010.

[8] M.R.I. Sheikh, R. Takahashi, and J. Tamura, "Study on frequency fluctuations in power system with a large penetration of wind power generation," Ener. J, vol.12, pp. 77-86, 2011.

[9] M.R.I Sheikh, S.M. Muyeen, R. Takahashi, T. Murata, and J. Tamura, "Minimization of fluctuations of output power and terminal voltage of wind generator using STATCOM/SMES," *IEEE Bucharest. Bucharest*, pp. 1-6, 28 June – 02 July 2009.

[10] "PSCAD/EMTDC Manual," Manitoba HVDC Research Center, 1994.

[11] A. Faulstich, J. K. Stinke, and F. Wittwer, "Medium voltage converter for permanent magnet wind power generators up to 5 MW," in Proc. EPE , 2005, pp. 1–9

[12] D. S. Oliveira, M. M. Reis, C. Silva, L. B. Colado, F. Antunes, and B. L. Soares, "A three-phase high-frequency semicontrolled rectifier for PM WECS," IEEE Trans. Power Electron., vol. 25, no. 3, pp. 677–685, Mar. 2010

[13] "Standard Models of Electrical Power System," IEE of Japan, Technical Reports, vol. 745, pp. 40-43.

Enhancing Multicast Capacity Using Opportunistic Relaying

D. K. Sarker, M. Z. I. Sarkar and M. S. Anower
Department of Electrical and Electronic Engineering
Rajshahi University of Engineering and Technology
Rajshahi-6204, Bangladesh.
Email: dks_ms@yahoo.com

***Abstract*—An opportunistic relaying strategy is introduced in this paper to enhance the performance of multicasting. The key feature of this work is to provide an additional diversity to the multicast users selecting best relay from a group of multiple relays. It is assumed that there is no direct path between the source and the destinations and communication occurs only through the relays. The best relay is selected employing selection combining technique and the performance of multicast channels is analyzed in terms of the multicast capacity and the outage probability. In order to clarify the insight of numerical results, all the expressions are derived in analytical form and the validity of derived expressions are justified via Monte-Carlo simulation.**

***Index Terms*—Cooperative relay network, ergodic multicast capacity, opportunistic relaying, outage probability.**

I. Introduction

In wireless communication, multicasting is an effective communication mechanism for group-oriented applications such as video-conferencing, e-learning etc. On the other hand, cooperative communication techniques through relay networks have attracted a lot of interest in various wireless communication applications due to the growing needs and increasing demands [1]–[5].

In [4], based on selective relay an energy efficient cooperative multicast scheme was proposed, where authors showed that the power consumptions for relay selection can be reduced considering the conditions of nearby users. Recently, a dual-hop decode-and-forward (DF) cooperative multicast network consisting of two relays was proposed in [5], where average bit error probability was investigated considering space-shift keying. A distributed decode-and-forward N-node single-source Gaussian multicast network was reported in [6], where authors developed a source-coordinated scalable coding scheme with independent messages for multiple destinations. A layered multiplexed-coded DF relaying scheme with quadrature amplitude modulation was proposed in [7], where authors showed that their proposed scheme outperforms the conventional unlayered DF scheme in terms of achievable rates and outage. Note that in [5]–[7], no works have been done using opportunistic relaying and in [4], although a selective relay based cooperative multicast scheme is studied for reducing the relay power consumption but the capacity and outage performances has not been studied. In this paper, authors analyze the capacity and outage performance of DF cooperative multicast network through Rayleigh fading channel using opportunistic relaying. Here, the closed-form analytical expressions for the ergodic multicast capacity, the outage probability for multicasting and the complimentary cumulative distribution function (CCDF) of multicast capacity are derived to investigate the performance of wireless multicasting through selection decode-and-forward cooperative relay networks.

The remainder of this paper is organized as follows. Section II describes the system model and problem formulation. Numerical results are shown in Section III and concluding remarks of this work are provided in Section IV.

II. System Model and Problem Formulation

A multicasting scenario is considered in which a source S transmits a common stream of information to M destinations via a group of K relays. The source S and each relay are equipped with single antenna while each destination receiver is equipped with n_D antennas. It is assumed that there is no direct path between S and destinations and communication occurs only through the relays. In the first-hop transmission, the source S sends a common stream of information to K relays. During the second-hop transmission, selection diversity is used for selecting the best relay (i.e., the relay with highest SNR) and only the best relay forwards the message to M destinations. The propagation channels in the two hopes are considered independent but not identically distributed and to be affected by small-scale fading which is modeled as Rayleigh fading. The channel gain between source and kth relay $(k = 1, 2, \ldots, K)$ is denoted by h_{sr_k} and that between

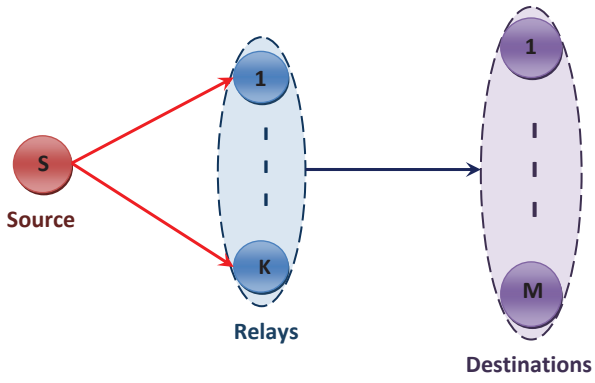

Fig. 1. Cooperative multicasting through selection decode-and-forward relay network.

978-1-5090-5785-6/16/$31.00 ©2016 IEEE

best relay and ith ($i = 1, 2, \ldots, M$) destination is denoted by $h_{r_b d_i}$. The overall instantaneous received SNRs at the kth relay and the ith destination are given by $\gamma_{sr_k} = \gamma_{o1}|h_{sr_k}|^2$ and $\gamma_{r_b d_i} = \gamma_{o2}|h_{r_b d_i}|^2$, respectively, where γ_{o1} and γ_{o2} denote the average SNRs of first and second hops, respectively. For any modulation scheme, the dual-hop channels can be modeled as an equivalent single hop channel [8]. Therefore, the equivalent output SNR at the destination, γ_{eq_k}, can be tightly approximated in the high SNR regime as

$$\gamma_{eq_k} \approx \min\{\gamma_{sr_k}, \gamma_{r_b d_i}\}. \tag{1}$$

In the case of selection combining, the signal with largest equivalent received SNR is selected. Then the instantaneous SNR at the output of the relay selection combiner of the ith destination is given by

$$\gamma_{\Sigma_{d_i}} = \max_{k=1,2,\ldots,K} \gamma_{eq_k}. \tag{2}$$

The PDF of $\gamma_{\Sigma_{d_i}}$, can be expressed as follows [9]:

$$f_{\gamma_{\Sigma_{d_i}}}(\gamma_i) = \Lambda\Phi e^{-\Phi\gamma_i}, \tag{3}$$

$$\text{where} \quad \Lambda \triangleq \sum_{k=1}^{K} \binom{K}{k} (-1)^{k-1} \sum_{l=1}^{n_D} \binom{n_D}{l} (-1)^{l-1} \quad \text{and}$$
$$\Phi \triangleq \left(\frac{k}{\gamma_{o1}} + \frac{l}{\gamma_{o2}}\right).$$

The cumulative distribution function (CDF) of $\gamma_{\Sigma_{d_i}}$ can be derived as

$$\begin{aligned} F_{\gamma_{\Sigma_{d_i}}}(\gamma_i) &= \int_0^{\gamma_i} f_{\gamma_{\Sigma_{d_i}}}(\gamma_i) d\gamma_i \\ &= \int_0^{\gamma_i} \Lambda\Phi e^{-\Phi\gamma_i} d\gamma_i \\ &= \Lambda\left[1 - e^{-\Phi\gamma_i}\right]. \end{aligned} \tag{4}$$

Let us define $d_{min} = \min_{1\le i\le M} \gamma_i$. Then the PDF of d_{min} is given by

$$\begin{aligned} f_{\gamma_{\Sigma_{d_i}}}(d_{min}) &= M f_{\gamma_{\Sigma_{d_i}}}(\gamma_i) \left[1 - F_{\gamma_{\Sigma_{d_i}}}(\gamma_i)\right]^{M-1} \\ &= M\Lambda\Phi e^{-\Phi\gamma_i} \left[1 - \Lambda\left(1 - e^{-\Phi\gamma_i}\right)\right]^{M-1} \\ &= M\Lambda\Phi e^{-\Phi\gamma_i} \underbrace{\sum_{\tau=0}^{M-1} \binom{M-1}{\tau} (-1)^{\tau} \left[\Lambda\left(1 - e^{-\Phi\gamma_i}\right)\right]^{\tau}}_{\triangleq \Xi}. \end{aligned} \tag{5}$$

Now, the term Ξ of equation (5) can be simplified as follows:

$$\begin{aligned} \Xi &= \sum_{\tau=0}^{M-1} \binom{M-1}{\tau} (-1)^{\tau} \left[\Lambda\left(1 - e^{-\Phi\gamma_i}\right)\right]^{\tau} \\ &= \sum_{\tau=0}^{M-1} \binom{M-1}{\tau} (-1)^{\tau} \left[\sum_{k=1}^{K} K! A_k \sum_{l=1}^{n_D} n_D! B_l \left(1 - e^{-\Phi\gamma_i}\right)\right]^{\tau}, \end{aligned} \tag{6}$$

where $A_k = \frac{(-1)^{k-1}}{k!(K-k)!}$ and $B_l = \frac{(-1)^{l-1}}{l!(n_D-l)!}$. The equation (6) can be expressed as [10]

$$\begin{aligned} \Xi = &\sum_{\tau=0}^{M-1} \binom{M-1}{\tau} (-1)^{\tau} \sum_{k=1}^{\tau K} K! a_k^{(\tau)} \sum_{l=1}^{\tau n_D} n_D! b_l^{(\tau)} \\ &\times \sum_{\nu=0}^{\tau} \binom{\tau}{\nu} (-1)^{\nu} e^{-\Phi\nu\gamma_i}. \end{aligned} \tag{7}$$

The coefficients $a_k^{(\tau)}$ and $b_l^{(\tau)}$ in equation (7) can be calculated recursively as follows [10]:

$$a_1^{(\tau)} = \frac{\tau}{(K-1)!}; \quad a_{\tau K}^{(\tau)} = \left[\frac{(-1)^{(K-1)}}{K!}\right]^{\tau};$$
$$a_k^{(\tau)} = \frac{1}{(-K!)^{\tau} k} \sum_{\psi=1}^{\psi_0} \left[\frac{\psi(K+1) - k}{\psi!} A_{\psi} a_{(k-\psi)}^{(\tau)}\right]$$
for $2 \le k \le (\tau K - 1)$, where $\psi_0 = \min(k, K)$ and

$$b_1^{(\tau)} = \frac{\tau}{(n_D-1)!}; \quad b_{\tau n_D}^{(\tau)} = \left[\frac{(-1)^{(n_D-1)}}{n_D!}\right]^{\tau};$$
$$b_l^{(\tau)} = \frac{1}{(-n_D!)^{\tau} l} \sum_{\xi=1}^{\xi_0} \left[\frac{\xi(n_D+1) - l}{\xi!} B_{\xi} b_{(l-\xi)}^{(\tau)}\right]$$
for $2 \le l \le (\tau n_D - 1)$, where $\xi_0 = \min(l, n_D)$.

Therefore, the PDF of d_{min} can be expressed as

$$f_{\gamma_{\Sigma_{d_i}}}(d_{min}) = \Upsilon e^{-\chi\gamma_i}, \tag{8}$$

$$\begin{aligned} \text{where} \quad \Upsilon \triangleq M\Lambda\Phi &\sum_{\tau=0}^{M-1} \binom{M-1}{\tau} \sum_{k=1}^{\tau K} K! a_k^{(\tau)} \sum_{l=1}^{\tau n_D} n_D! b_l^{(\tau)} \\ &\times \sum_{\nu=0}^{\tau} \binom{\tau}{\nu} (-1)^{\tau+\nu} \\ \text{and} \quad \chi \triangleq \Phi(1+\nu). \end{aligned}$$

A. Ergodic Multicast Capacity

The ergodic multicast capacity is given by

$$\begin{aligned} \langle C_m \rangle &= \frac{1}{2}\mathbb{E}\left[\log_e\left(1 + \min_{1\le i\le M} \gamma_i\right)\right] \\ &= \frac{1}{2}\int_0^{\infty} \log_e(1+\gamma_i) f_{\gamma_{\Sigma_{d_i}}}(d_{min}) d\gamma_i, \end{aligned} \tag{9}$$

where $\mathbb{E}[\cdot]$ denotes the expectation operator. Substituting equation (8) into equation (9), we have

$$\langle C_m \rangle = \frac{1}{2}\int_0^{\infty} \log_e(1+\gamma_i) \Upsilon e^{-\chi\gamma_i} d\gamma_i. \tag{10}$$

Performing integration by using the following identity of [11, eq. (4.222.8)]

$$\int_0^\infty \log_e(1+ax)\,x^b e^{-x}dx = \sum_{\delta=0}^{b}\frac{b!}{(b-\delta)!} \times \left[\frac{(-1)^{b-\delta-1}}{a^{b-\delta}}e^{\frac{1}{a}}\mathrm{Ei}\left(-\frac{1}{a}\right) + \sum_{k=1}^{b-\delta}\frac{(k-1)!}{(-a)^{b-\delta-k}}\right],$$

the closed-form analytical expression for ergodic multicast capacity is shown in equation (11) at the bottom of this page.

B. Outage Probability for Multicasting

The outage probability P_{out} is defined as the probability that the instantaneous multicast capacity falls below a given target rate R and it can be defined as follows:

$$\begin{aligned} P_{out}(R) &= P_r(C_m \le R), \quad R>0 \\ &= \int_0^x f_{\gamma_{\Sigma_{d_i}}}(d_{min})d\gamma_i, \end{aligned} \tag{12}$$

where $x = e^{2R}-1$. The significance of this definition is that when the multicast target rate is set to R, the multicasting will be ensured only if $C_m > R$, otherwise the multicasting will not be guaranteed. Substituting equation (8) into equation (12), we have

$$P_{out}(R) = \int_0^x \Upsilon e^{-\chi\gamma_i}d\gamma_i. \tag{13}$$

Performing integration, the closed-form analytical expression of outage probability for multicasting is shown in equation (14) at the bottom of the next page.

C. CCDF of Multicast Capacity

The CCDF of multicast capacity is defined as follows:

$$\begin{aligned} CCDF_{C_m} &= P_r(C_m > R), \quad R>0 \\ &= \int_x^\infty f_{\gamma_{\Sigma_{d_i}}}(d_{min})d\gamma_i. \end{aligned} \tag{15}$$

Substituting equation (8) into equation (15), we have

$$CCDF_{C_m} = \int_x^\infty \Upsilon e^{-\chi\gamma_i}d\gamma_i. \tag{16}$$

Performing integration, the closed-form analytical expression for the CCDF of multicast capacity is shown in equation (17) at the bottom of the next page.

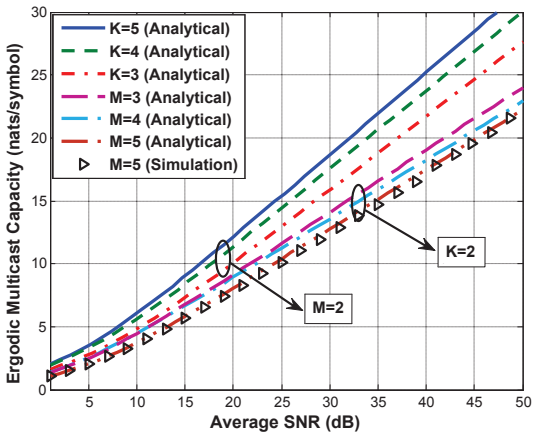

Fig. 2. The simulation and analytical results of ergodic multicast capacity as a function of average SNR with $n_D = 6$.

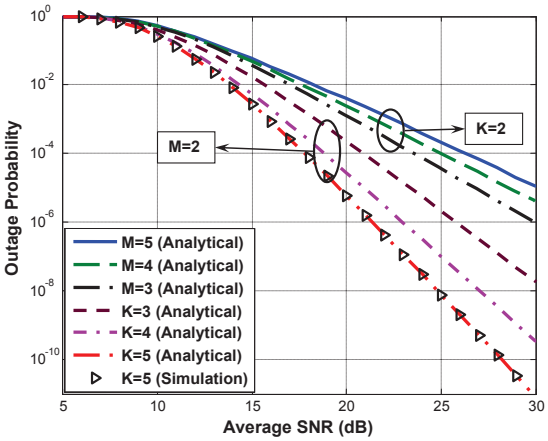

Fig. 3. The simulation and analytical results of outage probability for multicasting as a function of average SNR with $n_D = 5$.

III. Numerical Results

In this section, the analytical results are justified via Monte-Carlo simulation. For this purpose, the simulation results are generated by 110,000 realizations. The simulation and analytical results of ergodic multicast capacity and outage probability are shown in Figs.2 and 3 as a function of average SNR for the selected values of K and M, respectively. It is observed that the ergodic multicast capacity increases with K and decreases with M while the outage probability increases with M and decreases with K. Moreover, the changes in

$$\langle C_m\rangle = -\frac{M}{2}\sum_{k=1}^{K}\binom{K}{k}(-1)^{k-1}\sum_{l=1}^{n_D}\binom{n_D}{l}(-1)^{l-1}\left(\frac{k}{\gamma_{o1}}+\frac{l}{\gamma_{o2}}\right)\sum_{\tau=0}^{M-1}\binom{M-1}{\tau}(-1)^{\tau}\sum_{k=1}^{\tau K}K!a_k^{(\tau)}\sum_{l=1}^{\tau n_D}n_D!b_l^{(\tau)} \times \sum_{\nu=0}^{\tau}\binom{\tau}{\nu}(-1)^{\nu}\frac{e^{\left(\frac{k}{\gamma_{o1}}+\frac{l}{\gamma_{o2}}\right)(1+\nu)}}{\left(\frac{k}{\gamma_{o1}}+\frac{l}{\gamma_{o2}}\right)(1+\nu)}\mathrm{Ei}\left(-\left(\frac{k}{\gamma_{o1}}+\frac{l}{\gamma_{o2}}\right)(1+\nu)\right). \tag{11}$$

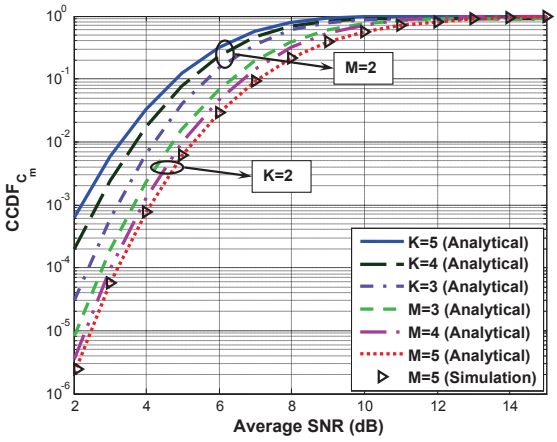

Fig. 4. The simulation and analytical results of CCDF of multicast capacity as a function of average SNR with $n_D = 5$.

ergodic multicast capacity with the variation of K is more significant than that of M. In order to highly ensure the outage performance of the proposed model, the simulation and analytical results of CCDF is presented in Fig.4 as a function of average SNR for selected values of K and M. It is seen that the CCDF of multicast capacity increases with K and decreases with M. Moreover, matching between the simulation and analytical results in the figures justify the validity of the derived analytical expressions.

IV. Conclusion

A multicast scenario is considered in a selection decode-and-forward cooperative relay network and focus on the derivation of closed-form analytical expressions for the ergodic multicast capacity, secure outage probability and the CCDF of multicast capacity. The key feature of this work is to provide an additional diversity to the destination users selecting best relay from a group of K relays. Based on the observations and from the numerical results, it can be concluded that the best relay provides an additional diversity which increases the diversity gain significantly. Hence, an improvement in the ergodic multicast capacity or reduction in the outage probability is observed from the numerical results.

Acknowledgement

This work is supported by the Research Support and Publication Division of University Grant Commission, Bangladesh.

References

[1] J. Du, M. Xiao, M. Skoglund, and M. Medard, "Wireless multicast relay networks with limited-rate source-conferencing," *IEEE Journal of Selec. Areas in Communications.*, vol. 31, no. 8, pp. 1390–1401, Aug. 2013.

[2] D. K. Sarker, M. Z. I. Sarkar, and M. S. Anower, "Wireless multicasting in cooperative multiplexing system with zero-forcing filtering," in *Proc. IEEE Int. Conf. Elect. and Electronic Engg. (ICEEE), 2015, Rajshahi, Bangladesh*, Nov. 2015, pp. 57–60.

[3] S. Majhi and A. Banarjee, "Asymptotic outage analysis of incremental decode and forward cognitive radio relay network," in *Proc. IEEE Int. Conf. Commu. Syst. and Networks (COMSNETS), 2015, Bangalore, India*, Jan. 2015, pp. 1–8.

[4] J. Lee, Y. M. Lim, K. Kim, and S. G. Choi, "Energy efficient cooperative multicast scheme based on selective relay," *IEEE Commun. Letts.*, vol. 16, no. 3, pp. 386–388, Jan. 2012.

[5] P. Som and A. Chockalingam, "Decode-and-forward cooperative multicast with space shift keying," in *Proc. IEEE Wireless Commu. and Networking Conf. (WCNC 2014), Istanbul*, April 2014, pp. 689–694.

[6] S. H. Lim, K. T. Kim, and Y.-H. Kim, "Distributed decode-forward for multicast," in *Proc. IEEE Int. Symp. Info. Theory (ISIT), Honolulu, HI*, June-July 2014, pp. 636–640.

[7] J. Chattha and M. Uppal, "Layered multiplexed-coded relaying in wireless multicast using QAM transmissions," *IEEE Commun. Letts.*, vol. 20, no. 4, pp. 760–763, Feb. 2016.

[8] T. Q. Duong, V. N. Q. Bao, and H.-J. Zepernick, "On the performance of selection decode-and-forward relay networks over Nakagami-m fading channels," *IEEE Commun. Letts.*, vol. 13, no. 3, pp. 172–174, March 2009.

[9] V. N. Q. Bao, D. H. Bac, L. Q. Cuong, L. Q. Phu, and T. D. Thuan, "Performance analysis of partial relay selection with multi-antenna destination cooperation," in *Proc. IEEE Wireless Commu. and Networking Conf. (WCNC 2014), Istanbul*, Sept 2011, pp. 101–105.

[10] G. Fedele, "N-branch diversity reception of M-ary DPSK signals in slow and nonselective Nakagami fading," *European Trans. on Telecommunication*, vol. 7, pp. 119–123, 1996.

[11] I. S. Gradshteyn and I. M. Ryzhik, *Table of Integrals, Series, and Products*, 7th ed. San Diego, CA: Academic, 2007.

$$P_{out}(R) = M\sum_{k=1}^{K}\binom{K}{k}(-1)^{k-1}\sum_{l=1}^{n_D}\binom{n_D}{l}(-1)^{l-1}\left(\frac{k}{\gamma_{o1}}+\frac{l}{\gamma_{o2}}\right)\sum_{\tau=0}^{M-1}\binom{M-1}{\tau}(-1)^{\tau} \times \sum_{k=1}^{\tau K} K! a_k^{(\tau)} \sum_{l=1}^{\tau n_D} n_D! b_l^{(\tau)} \frac{\left(1-e^{-\left(\frac{k}{\gamma_{o1}}+\frac{l}{\gamma_{o2}}\right)(1+\nu)(e^{2R}-1)}\right)}{\left(\frac{k}{\gamma_{o1}}+\frac{l}{\gamma_{o2}}\right)(1+\nu)}. \quad (14)$$

$$CCDF_{C_m} = M\sum_{k=1}^{K}\binom{K}{k}(-1)^{k-1}\sum_{l=1}^{n_D}\binom{n_D}{l}(-1)^{l-1}\left(\frac{k}{\gamma_{o1}}+\frac{l}{\gamma_{o2}}\right)\sum_{\tau=0}^{M-1}\binom{M-1}{\tau}(-1)^{\tau} \times \sum_{k=1}^{\tau K} K! a_k^{(\tau)} \sum_{l=1}^{\tau n_D} n_D! b_l^{(\tau)} \frac{e^{-\left(\frac{k}{\gamma_{o1}}+\frac{l}{\gamma_{o2}}\right)(1+\nu)(e^{2R}-1)}}{\left(\frac{k}{\gamma_{o1}}+\frac{l}{\gamma_{o2}}\right)(1+\nu)}. \quad (17)$$

Guiding Properties of a Hybrid Core Porous Fiber (HCPF) for Terahertz Wave Propagation

***Abstract*—This paper presents the guiding properties of a porous core photonic crystal fiber for Terahertz (THz) wave propagation. The reported porous core fiber has a hybrid (triangular + circular) air hole arrangement at the core region with hexagonal cladding. Simulation results show a low EML of 0.425 dB/cm at 0.7 THz frequency with negligible (< 10^{-2} dB/cm) confinement and bending losses for the proposed porous fiber. Numerical results also show a 0.46 THz band of near zero flat dispersion at 0.9±0.05 ps/THz/cm. Changes in the guiding properties for tuning the design parameters of the core region of the hybrid core porous fiber (HCPF) are reported elaborately in this paper.**

Keywords—hybrid core; porous fiber; low loss; near zero dispersion; guiding properties; terahertz propagation

I. INTRODUCTION

Terahertz (THz) frequency regime is usually defined in the frequency domain of 0.1-10 THz [1, 2]. The potential applications of this frequency regime includes sensing [3], spectroscopy [4], astronomy [5], monitoring drugs [6] and explosives [7], non-invasive imaging [8], hybridization of DNA [9], communications [10] etc. However, the present THz technologies are bulky and still mostly depend on free space propagation due to the lack of a proper low loss guiding medium for this frequency domain. A suitable waveguide for THz wave propagation is yet to be finalized, although a significant improvement can be seen in the development of THz sources and detectors. In past two decades, scientists and researchers have proposed several types of waveguides for THz wave propagation. Some of the well-known waveguides are metallic waveguides [11], metallic slot waveguides [12], hollow core dielectric waveguides [13], solid core dielectric waveguides [14], porous core dielectric waveguides [15] etc.

Recently developed porous core waveguides have shown noteworthy guiding properties for THz wave transmission. Different porous fiber design structures have been proposed in the last few years. So far, researchers have proposed hexagonal [16], octagonal [17], spiral [18], hybrid [10], triangular [2] air hole arrangements in the design methodology of porous core waveguides. In 2016, Ali *et al.* [1] reported a hybrid core porous fiber for the first time by combining two different air hole arrangements at the porous core. Their designed waveguide showed remarkable guiding properties with low loss (< 0.04 cm^{-1}) with 3.75 THz band of near zero flat dispersion. However, the core diameter of the reported fiber is too large to fabrication easily. In another reported porous core design of 2016, a triangular air hole arrangement is used with elliptical air holes at the core [2]. This waveguide reported a high birefringence of 7×10^{-2} at 1THz frequency with low effective material loss (EML) i.e., 0.1 cm^{-1}. In 2015, some reported porous core waveguides show high birefringence (7.5×10^{-2} at 1THz) using slotted core [19], bend insensitive porous fiber using spiral air hole arrangement [18] etc. In 2014, Imran *et al.* [10] showed ultra-low loss (0.056 cm^{-2}) porous fiber with near zero flat dispersion of ±0.18 ps/THz/cm using hybrid air hole distribution. In 2016, dual-hole unit-based hexagonal porous core fiber has been reported that shows a high birefringence of 3.3×10^{-2} and an EML of 0.43 dB/cm at the operating frequency of 0.85 THz.

In our work, we have designed a hybrid core porous fiber (HCPF) using only circular air holes. The porous core of the fiber has hybrid air hole distribution using triangular and circular arrangements. The cladding of the fiber has four hexagonal rings of air holes. Simulation results exhibit an EML of 0.425 dB/cm at 0.7 THz operating frequency and near zero flat dispersion of 0.46 THz band at 0.9±0.05 ps/THz/cm. The effects of tuning the design parameters (up to ±1%) of the core on the guiding properties are discussed elaborately in this paper. The reported HCPF design and discussion of the guiding properties will certainly open up new ideas and perspectives in this field of research.

II. HCPF DESIGN METHODOLOGY

The proposed HCPF has a combination of triangular and circular air hole arrangements at the porous core region. The design methodology has primarily chosen to follow the novel hybrid core structure proposed by Ali *et al.* [1] in 2016. In this previously reported design the cladding of the fiber had three air hole rings and a core area over 17%. In the newly proposed HCPF, the cladding has four hexagonal rings and a core area of 8.38% for optimal design parameters. This solves the issue of large core diameter presented in the previous hybrid core porous fiber design. The previously reported triangular arrangement in the fiber core has shown better near zero dispersion and lower losses [1, 20]. Thus, in this hybrid design, a triangular distribution is considered for the centre core region. The fiber design is simulated by COMSOL Multiphysics (version 4.2). Only circular shaped air holes are used in the cladding and the hybrid core. Four hexagonal air hole rings are arranged the cladding where, the number of air holes in the rings are 18, 24, 30 and 36 respectively. Core diameter of the fiber is D_{core}. The pitch of the cladding air holes is $\Lambda_2 = (D_{core}/4.4)$ and radius is $r_2 = (0.45\ \Lambda_2)$. A Perfectly Matched Layer (PML) boundary is surrounding the fiber (with 13% thickness). The two circular rings in the outer region of the core has 18 and 12 air holes. Six air holes are distributed in triangular arrangement inside these circular rings.

978-1-5090-5785-6/16/$31.00 ©2016 IEEE

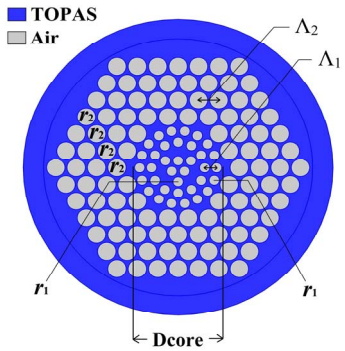

Fig. 1. Air hole distribution of the proposed HCPF design.

The pitch of the core region is $\Lambda_1 = (D_{core}/7)$ and radius is r_1 which changes with the core porosity. The designed air hole distribution of the fiber is symmetric type, thus the guiding properties for both polarizations (x and y) will be similar. TOPAS (cyclic-olefin copolymer) is the host material of the proposed porous fiber. 67938 mesh elements with 5276 boundary elements are used in the simulator (COMSOL) to represent the proposed HCPF design. Regarding the design structure of the proposed HCPF, a capillary stacking fabrication method [10] can be used to practically fabricate this waveguide. In this method it should be possible to easily fabricate the circular shaped air holes in hybrid arrangement of the proposed design.

III. Guiding Properties of the Proposed HCPF

Finite element method (FEM) is used for solving the equations for the reported geometrical structure. Effective material loss (EML), fraction of power, waveguide dispersion, confinement and bending losses are calculated for the reported HCPF. Fig. 2 shows the EMLs at different core diameters (D_{core}) and core porosities. For having lower core porosity, such as 43%, the waveguide shows a higher EML. Although, the lowest EML can be found at 53% core porosity, 47% porosity is chosen for optimum porosity. This is due to the fact that, for higher core porosity as 53%, the air holes at the core get too close to one another which may raise fabrication difficulties. Thus, 47% core porosity is taken as optimum value where the EML is lower and also air holes at the core region stay at a suitable distance for fabrication. The design parameters for 47% core porosity are chosen as optimal design parameters. Simulation results for confinement (Fig. 3) and bending (Fig. 4) losses show that the losses are negligible ($<10^{-2}$ dB/cm) after 550 µm core diameter at 47% porosity. On the other hand, EML increases for higher core diameters. Thus, 550 µm core diameter and 47% core porosity is taken as optimum design parameters. At these parameters, the proposed HCPF exhibits an EML of 0.54 dB/cm (at 1 THz frequency) with negligible confinement and bending losses. The design parameters of the core region have the most significant effects on the guiding properties of a porous core fiber. In this paper, we have studied this effect on the guiding properties. Waveguiding properties are calculated for varying the two key parameters of the core; i.e., core pitch (Λ_1) and radius (r_1). Changes in the waveguide properties are shown for tuning these parameters up to ±1% from their optimum values.

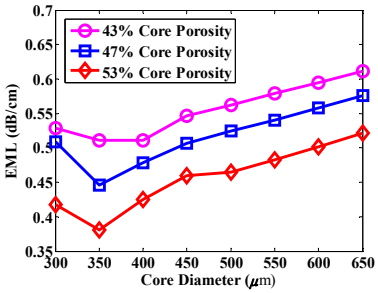

Fig. 2. EMLs for different D_{core} at different core porosities.

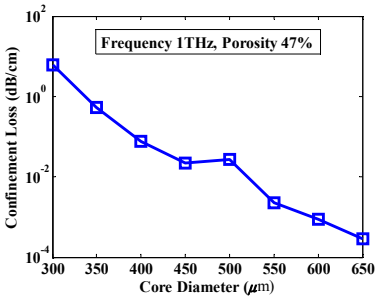

Fig. 3. Confinement loss at 47% core porosity with respect to different D_{core}.

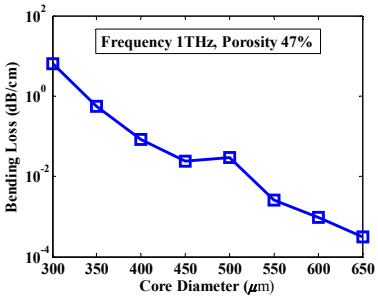

Fig. 4. Bending loss (radii 1 cm) at 47% core porosity for different D_{core}.

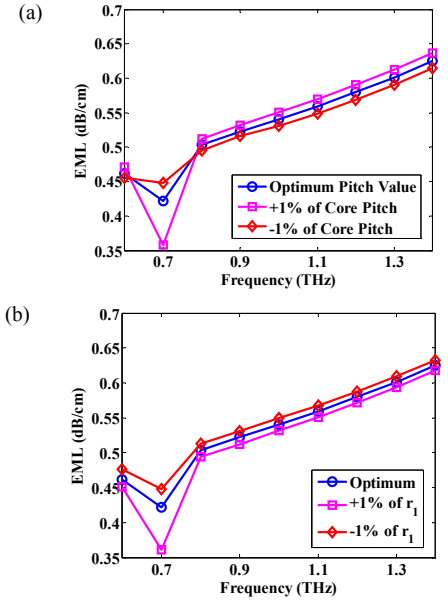

Fig. 5. Effects on EML for changing core (a) pitch, Λ_1 (b) air hole radius, r_1.

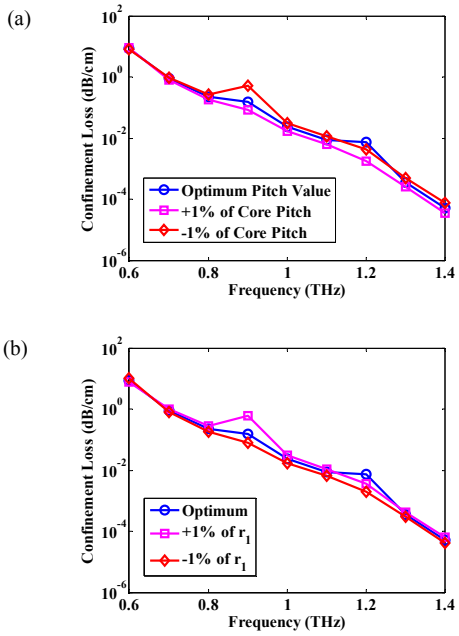

Fig. 6. Effect on confinement loss for changing the (a) pitch, Λ_1, (b) radius, r_1.

At first, the impact on EML is calculated for changing the pitch (Λ_1) and the radius (r_1). Fig. 5 shows the effects of pitch variation (Fig. 5. (a)) and radius variation (Fig. 5. (b)) on EML. When the core pitch is increased, the distance between air holes in the porous core increases and exposes more material (TOPAS) area. As a result, the EML increases slightly. However, porosity increases for the increase in the radius of the air holes in the core. In case of the proposed design, the porosity is increase to 47.97% and decreased to 46.09% from the optimum porosity 47% for 1% increase and decrease of the core air hole radius (r_1) respectively. Thus, a lower EML can be found for increased r_1 value and larger EML is found for smaller r_1 (Fig. 5. (b)). However, the changes in EML are very small compared to the EML loss. These figures show that a low EML of 0.425 dB/cm can be found at 0.7 THz frequency. It can be also seen that the EML at 0.7 THz rapidly changes with the changing pitch and radius. Fig. 6 and 7 graphically describe the effects on confinement loss and bending loss for changing the core pitch and radius respectively. It is observed that the changes in both losses are negligible for the variations in core parameters.

Fig. 8 shows the effects of changing the pitch (Λ_1) and radius (r_1) on the fraction of power of the core air holes. Due to the changes in the size and position of the air holes in the core region, a change can be seen in the fraction of power of the core air holes. However, the amount of change is very small (< 1%) for the proposed HCPF design. Fig. 9 shows the impacts on waveguide dispersion for the variations in core air hole pitch (Λ_1) and radius (r_1). Changes in the pitch and radius affect the effective refractive index and as a result, changes in the dispersion can be seen. For using larger pitch value, the level of the near zero flat dispersion increases and for smaller pitch values it decreases (Fig. 9 (a)). However, the changes in the dispersion characteristics for the variation in core air hole radius are negligible (Fig. 9 (b)). At optimum design parameters the reported HCPF exhibits a 0.46 THz band of near zero flat dispersion at 0.9±0.05 ps/THz/cm. Fig. 10 shows the fundamental mode field distribution of the proposed waveguide. The reported waveguide design has very small amount of asymmetry in the core region. As a result, the guiding properties of the waveguide will be similar for both X and Y polarizations [1, 2]. In this figure, fundamental mode field distribution for only Y polarization has been described.

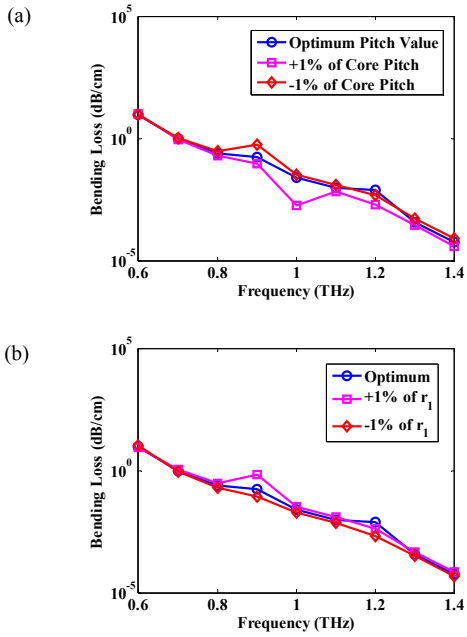

Fig. 7. Effect on bending loss for the variations in core air hole (a) pitch, Λ_1 and (b) radius, r_1.

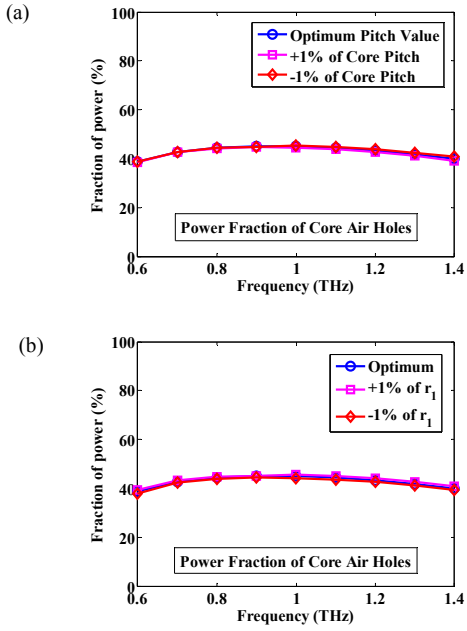

Fig. 8. Effect on the power fraction of core air holes for the variations in core air hole (a) pitch, Λ_1 and (b) radius, r_1.

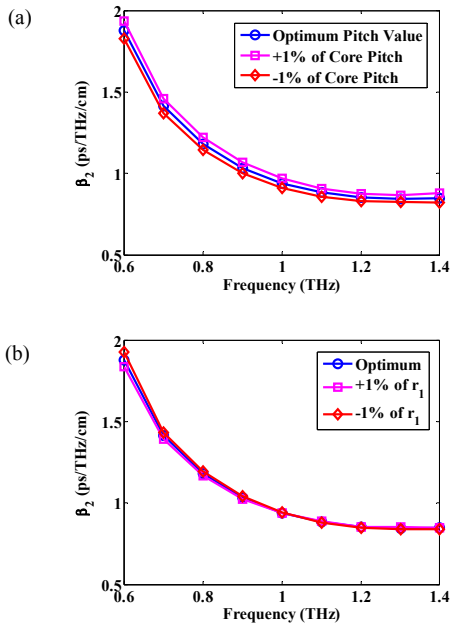

(b)

Fig. 9. Effect on the flat dispersion characteristics for the variations in core air hole (a) pitch, Λ_1 and (b) radius, r_1.

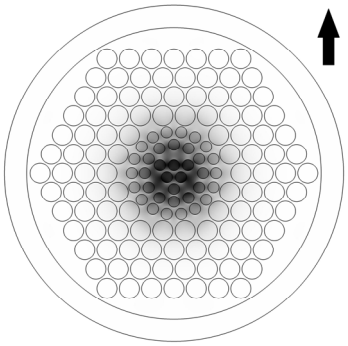

Fig. 10. Fundamental mode field distribution for Y polarization.

IV. Conclusion

The reported hybrid core porous fiber (HCPF) shows a low EML (0.425 dB/cm at 0.7 THz) with negligible confinement and bending losses. Results depicts a near zero flat dispersion at 0.9±0.05 ps/THz/cm over 0.46 THz band. This can be beneficial for communication applications by using this band. Simulation results show a very clear view of the impacts of core region parameters on the guiding properties of the waveguide. Results depicts that a smaller pitch value can result in a lower EML and also decrease the dispersion level for near zero flat dispersion. The studies of this work exhibit noteworthy direction for designing porous core fibers for THz wave transmission.

References

[1] Sharafat Ali, Nasim Ahmed, Syed Aljunid, Badlishah Ahmad, "Ultra-flat low material loss porous core THz waveguide with near zero flat dispersion," *Electronics Letters,* vol. 52, pp. 863-865, 2016.

[2] S. Rana, Sharafat Ali, Nasim Ahmed, Raonaqul Islam, Syed A. Aljunid, "Ultra-High Birefringent and Dispersion-Flattened Low Loss Single-Mode Terahertz Wave Guiding," *IET Communications,* vol. 10, pp. 1579-1583, 2016.

[3] Y. F. He, P.I. Ku, J.R. Knab, J.Y. Chen, A.G. Markelz, "Protein Dynamical Transition Does Not Require Protein Structure," *Physical Review Letters,* vol. 101, pp. 178103, 2008.

[4] J. Q. Zhang, D. Grischkowsky, "Waveguide terahertz time-domain spectroscopy of nanometer water layers," *Optics Letters,* vol. 29, pp. 1617-1619, 2004.

[5] L. Ho, M. Pepper, P. Taday, "Terahertz spectroscopy: Signatures and fingerprints," *Nature Photonics,* vol. 2, pp. 541, 2008.

[6] C. J. Strachan, P.F. Taday, D.A. Newnham, K.C. Gordon, J.A. Zeitler, M. Pepper, T. Rades, "Using Terahertz Pulsed Spectroscopy to Quantify Pharmaceutical Polymorphism and Crystallinity," *Journal of Pharmaceutical Science,* vol. 94, pp. 837-846, 2005.

[7] D. J. Cook, B.K. Decker, M.G. Allen, "Quantitative THz Spectroscopy of Explosive Materials," in *OSA Conference*, USA, 2005, pp. PSI-SR-1196.

[8] Q. Chen, Z.P. Jiang, G.X. Xu, X.C. Zhang, "Near-field terahertz imaging with a dynamic aperture," *Optics Letters,* vol. 25, pp. 1122-1124, 2000.

[9] M. Nagel, Bolivar, P. H., Brucherseifer, M., Kurz, H., Bosserhoff, A., & Büttner, R., "Integrated THz technology for label-free genetic diagnostics," *Applied Physics Letters,* vol. 80, pp. 154-156, 2002.

[10] M. I. Hasan, S. M. Abdur Razzak, G. K. M. Hasanuzzaman and Md. Samiul Habib, "Ultra-Low Material Loss and Dispersion Flattened Fiber for THz Transmission," *IEEE Photonics Technology Letters,* vol. 26, pp. 2372-2375, 2014.

[11] M. N. M. Wächter, and H. Kurz, "Metallic slit waveguide for dispersion-free low-loss terahertz signal transmission," *Applied Physics Letters,* vol. 90, pp. 061111, 2007.

[12] Y.-C. H. s. C.-H. Lai, H.-W. Chen, Y.-J. Huang, H.-C. C hang, and C.-K. Sun, "Low-index terahertz pipe waveguides," *Optic Letters,* vol. 34, pp. 3457-3459, 2009.

[13] A. Dupuis, K. Stoeffler, B. Ung, C. Dubois, and M. Skorobogatiy, "Transmission measurements of hollow-core THz Bragg fibers," *Journal of Optical Society of America,* vol. 28, pp. 896-907, 2011.

[14] F. C. P. J. Roberts, H. Sabert, B. J. Mangan, T. A. Birks, J. C. Knight, and P. S. J. Russell, "Loss in solid-core photonic crystal fibers due to interface roughness scattering," *Optic Express,* vol. 13, pp. 7779-7793, 2005.

[15] M. Uthman, B. M. A. Rahman, N. Kejalakshmy, A. Agrawal, K. T. V. Grattan, "Design and Characterization of Low-Loss Porous-Core Photonic Crystal Fiber," *IEEE Photonics Journal,* vol. 4, pp. 2315-2325, 2012.

[16] R. Islam, Hasanuzzaman GKM, Habib Selim, Rana Sohel, Khan MAG, "Low-loss rotated porous core hexagonal single-mode fiber in THz regime," *Optical Fiber Technology,* vol. 24, pp. 38-43, 2015.

[17] S. Rana, GKM Hasanuzzaman, Samiul Habib, Shubi F. Kaijage, Raonaqul Islam, "Proposal for a low loss porous core octagonal photonic crystal fiber for T-ray wave guiding," *Optical Engineering,* vol. 53, pp. 1151071-1151074, 2014.

[18] R. Islam, Sohel Rana, Redwan Ahmad, and Shubi Felix Kaijage, "Bend-Insensitive and Low-Loss Porous Core Spiral Terahertz Fiber," *IEEE Photonics Technology Letters,* vol. 27, pp. 2242-2245, 2015.

[19] R. Islam, S. Habib, GKM. Hasanuzzaman, R. Ahmad, S. Rana and S.F. Kaijage, "Extremely High-Birefringent Asymmetric Slotted-Core Photonic Crystal Fiber in THz Regime," *IEEE Photonics Technology Letters,* vol. 27, pp. 2222-2225, 2015.

[20] Sharafat Ali, Nasim Ahmed, Syed Aljunid, Badlishah Ahmad, "Hybrid Porous Core Low Loss Dispersion Flattened Fiber for THz Propagation," *Photonics and Nanostructures - Fundamentals and Applications,* vol. 22, pp. 18-23, 2016.

An Investigation of SAR inside Human Heart for Antenna Directivity, Surface Current Variations and Effect on Antenna Frequency in Presence of Heart

Md. Mamun Ur Rashid[1], Ajay Krishno Sarkar[1], Liton Chandra Paul[2]
[1]Department of Electrical & Electronic Engineering
[2]Dept. of Electronic & Telecommunication Engineering
[1]Rajshahi University of Engineering & Tech., Bangladesh
[2]Pabna University of Science & Technology, Bangladesh
i.mamunrashid@gmail.com, sarkarajay139@gmail.com, litonpaulete@gmail.com

Amal Bouazizi[3], Rikta Sen[1], Bijoy Podder[1]
[3]Department of Electrical Engineering
[1]Department of Electrical & Electronic Engineering
[3]National Engineering School of Sfax, Tunisia
[1]Rajshahi University of Engineering & Tech., Bangladesh
amalbouazizi90@yahoo.fr, rikta.sen06@gmail.com, bijoypoddereee@gmail.com

***Abstract*— In this work, the impact of human heart on an 800 MHz inset fed rectangular microstrip patch antenna characteristics were investigated using CST Microwave Studio. The antenna was simulated over a mimic human heart muscle and the distance between them was varied to analyze the changes in Specific Absorption Rate (SAR) upon antenna performance parameters (specifically, directivity & surface current) for discreet and waveguide port feeding. The results exhibited that the center frequency of the antenna was shifted to lower value and an increase in SAR values when the antenna was closer to heart for both the feeding techniques. However, the discrete port had more values of SAR than the waveguide port but for both cases SAR decreased with the increment of antenna distance from heart. SAR values for up to 4 mm distance in between the antenna and human heart did not satisfy IEEE and ICNIRP standards. For increasing surface current, the SAR values decreases due to less penetration of flux inside the tissue for both feeding techniques. Increasing directivity resulted decrement of SAR values due to the fact that more reflection of the wave from the tissue happened for more directivity. This work demonstrates how mobile phone antennas of GSM band affect human heart and how human heart affects antenna resonance frequency when mobile phones are kept in chest pocket.**

Keywords—antenna; human heart; SAR; waveguide port; discrete port; surface current; directivity

I. INTRODUCTION

With the momentous rise of the wireless communication, human interaction with EM devices has become a pioneering area in research to study the safety aspects of the devices and to prevent the potential hazardous effects associated with EM radiation on human tissue. Previous research efforts are significantly devoted to the interactions between mobile phone antennas and human body parts such as: head and hand especially [1]- [7]. However, a systematic characterization and analysis of the impact of human heart on mobile phone antenna performance has not been previously carried out.

This paper has investigated the impact of human heart on an 800 MHz antenna performance when mobile phones are kept in chest pocket and SAR inside the heart tissue was estimated changing the distance of heart from the antenna using CST Microwave Studio. The 800 MHz inset fed rectangular microstrip patch antenna was simulated over a human tissue model consisting skin, fat and heart muscle tissue layers and the distance between them was varied by 2 mm ranging from 2 mm to 20 mm to analyze the changes in antenna characteristics. All simulations were carried out by using both the discreet port and waveguide port to demonstrate the effect of two feeding techniques on antenna performance over human heart and SAR.

II. METHODOLOGY

The substrate of the antenna was FR4 (lossy) having relative dielectric constant ($\mathcal{E}_r$) and annealed copper (Cu) was used for the patch, ground plane and microstrip feeding line of the antenna. The operating frequency of the antenna (f_r) was considered as 800 MHz and the height of the dielectric substrate (h) was 3.15 mm. Patch width (W), patch length (L), patch length extension (ΔL), effective patch length (L_{eff}), effective dielectric constant ($\mathcal{E}_{reff}$), substrate width (W_s), substrate length (L_s), ground plane width (W_g) and ground plane length (L_g) of the antenna were calculated for the known values of f_r and $\mathcal{E}_r$ using the following formulas [8]-[9]:

- Calculation of Patch Width (W):

$$W = \frac{c}{2f_r}\sqrt{\frac{2}{\varepsilon_r + 1}} \tag{1}$$

  Where, c = velocity of light in free space

- Calculation of Effective Dielectric Constant ($\mathcal{E}_{reff}$):

$$\varepsilon_{reff} = \frac{\varepsilon_r + 1}{2} + \frac{\varepsilon_r - 1}{2}\left(1 + \frac{12h}{W}\right)^{-\frac{1}{2}} \tag{2}$$

978-1-5090-5785-6/16/$31.00 ©2016 IEEE

- Calculation of Patch Length Extension (ΔL):

$$\Delta L = 0.412h\left(\frac{\varepsilon_{reff}+0.3}{\varepsilon_{reff}-0.258}\right)\left(\frac{W/h+0.264}{W/h+0.8}\right) \quad (3)$$

- Calculation of Effective Patch Length (L_{eff}):

$$L_{eff}=\frac{c}{2f_r\sqrt{\varepsilon_{reff}}} \quad (4)$$

- Calculation of Patch Length (L): $L = L_{eff} - 2\Delta L$ (5)
- Calculation of Substrate Width (W_s), Substrate Length (L_s), Ground Plane Width (W_g) and Ground Plane Length (L_g):

$$W_s = W_g = 6h + W \quad (6)$$

$$L_s = L_g = 6h + L \quad (7)$$

The calculated parameters of the patch, substrate, ground plane and feeding line are summarized in table I.

TABLE I. GENERAL SPECIFICATIONS OF THE ANTENNA

Antenna Part	Parameter (Symbol)	Value (mm)
Substrate	Width (W_s)	229.1
	Length (L_s)	178.6
	Height (h)	3.15
Patch	Width (W)	114.6
	Length (L)	89.3
	Thickness (t)	0.3
Ground Plane	Width (W_g)	229.1
	Length (L_g)	178.6
	Thickness (t)	0.3
Feed Line	Width (W_f)	6.1
	Length (L_f)	103.2
	Feed inset from edge of patch (S_i)	32.6
	Spacing between feed line and patch (S_g)	2.2

III. ANTENNA DESIGN

The designed patch and the defected ground structure of the antenna are shown in Fig. 1.

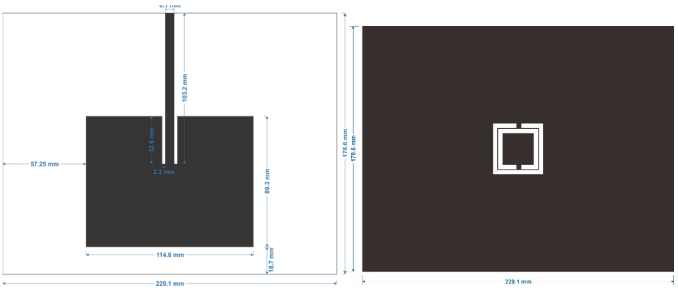

Fig. 1. Dimensions of antenna: (a) Patch; (b) Ground Plane.

The ground plane has a defect in the form of Complimentary Split Ring Resonator (CSRR). A CSRR is a negative image of the metaresonator split-ring resonator (SRR). It is made up of two concentric copper rings with a slit in each ring. The CSRR is made by removing the copper in the shape of the SRR from ground plane of microstrip antenna [10]. A square CSRR structure is etched at the center of the ground plane which is shown in Fig. 2(a) and the design parameters of the CSRR are presented in the table II.

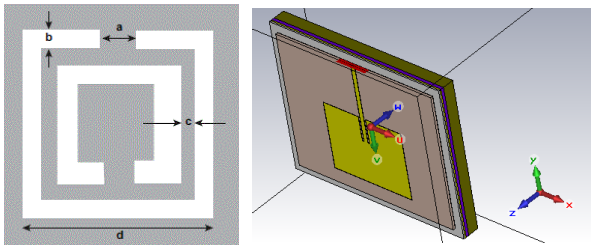

(a) (b)

Fig. 2. (a) The metamaterial CSRR structure loaded in the ground plane of the microstrip patch antenna; (b) Antenna simulated over tissue box consisting heart muscle in CST Microwave Studio.

TABLE II. DIMENSIONS OF CSRR

Dimensional Parameters	a	b	c	d
Dimensions in mm	3.4	3.4	3.4	37.2

IV. HUMAN TISSUE MODEL & TISSUE PROPERTIES

The 800 MHz antenna was simulated over human tissue model consisting of 3 layers of tissue: Skin, Fat and Heart Muscle which is shown in Fig 2(b). The permittivity, electrical conductivity, density, thermal conductivity, heat capacity and dimensions of all 3 layers of the tissue were considered from the Tissue Properties Database of the Foundation for Research on Information Technologies in Society (IT'IS Foundation) [11]. The tissue properties of all 3 considered tissue layers at 800 MHz are summarized in table III.

TABLE III. HUMAN TISSUE PROPERTIES AT 800 MHZ

Tissue Name	Skin	Fat	Heart Muscle
Permittivity	42	5.48	60.7
Electrical Conductivity	0.83	0.0485	1.17
Density (kg/m^3)	1109	911	1081
Thermal Conductivity (W/K/m)	0.37	0.21	0.56
Heat Capacity (kJ/K/kg)	3.391	2.348	3.686
Dimensions (mm)	200 x 250 x 2	200 x 250 x 4	200 x 250 x 15

V. Simulation Results

The distance between the antenna and the human tissue model is varied by 2 mm in each simulation within the range of 2 mm to 20 mm. The IEEE and ICNIRP standards of SAR are 2.0 W/Kg averaged over 10g of tissue [12]. Microstrip-line feeding configuration [8] and Transmission-line model [8] were implemented to analyze this work for convenience. The 800 MHz antenna performance parameters in free space and over the human heart are respectively summarized in table IV and demonstrated in Fig. 3 for both discrete and waveguide port feeding techniques. Contour plots of SAR distribution for 2 mm and 4 mm distances between antenna and human heart are presented in Fig. 4.

TABLE IV. 800 MHz Antenna Performance Parameters in Free Space

Port	Center Frequency (MHz)	Directivity (dBi)	Gain (IEEE) (dB)	Realized Gain (dB)	Peak Surface Current (A/m)	VSWR
Waveguide	789	6.974	5.323	5.317	37.04	1.0904367
Discrete	789	6.913	5.407	5.4	34.14	1.0880881

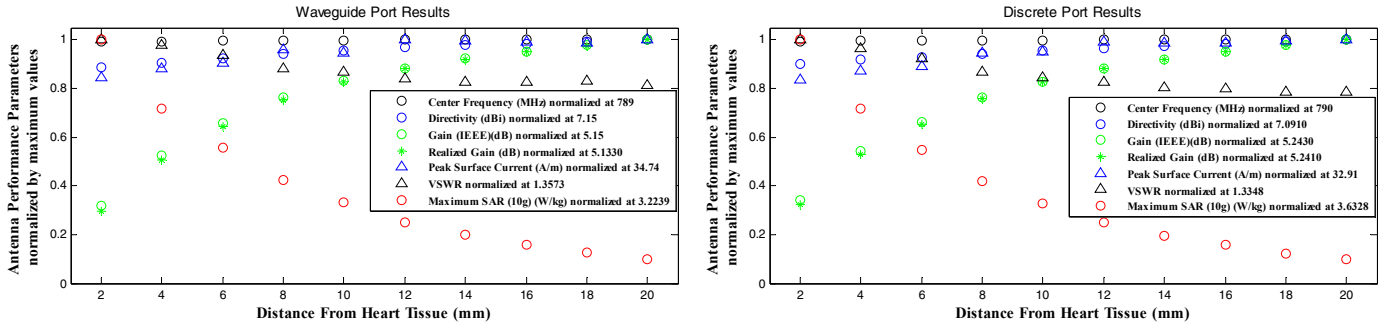

(a) (b)

Fig. 3. Antenna performance parameters normalized at maximum values versus distance of heart from the antenna for (a) waveguide port feeding; (b) discrete port feeding.

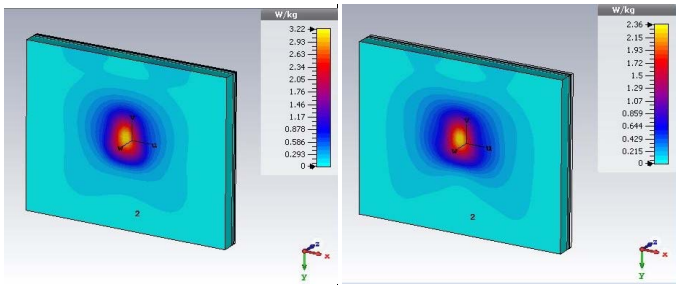

(a) (b)

Fig. 4. SAR Distribution Plots for distances between antenna and heart: (a) 2 mm; (b) 4 mm.

VI. Results Analysis & Disscussion

To observe the effect of heart on antenna radiation properties, the center frequency of the antenna for both the port was plotted against the distances between antenna and heart in Fig. 5. It is observed that the center frequency has been shifted to lower value when the antenna was closer to heart for both discreet and waveguide port feeding techniques. This is due to the greater permittivity of heart muscle compared to free-space.

The SAR values were plotted against the distances between antenna and heart for both the feeding techniques and are shown in Fig. 6. As seen from the figure SAR are greater for both discreet and waveguide port feeding when the antenna is close to the heart and SAR value for up to 4 mm distance in between antenna and human heart does not satisfy IEEE and ICNIRP standards. Discrete port feeding exhibits more variations in values of SAR than the waveguide port feeding and for both feeding cases SAR decreases with the increases of distance between heart and antenna as observed from Fig. 6.

Fig. 7 illustrates that for both the feeding techniques, SAR decreases with the increase in surface current. The decrease in SAR value is due to less penetration of flux inside the tissue as the surface current increases.

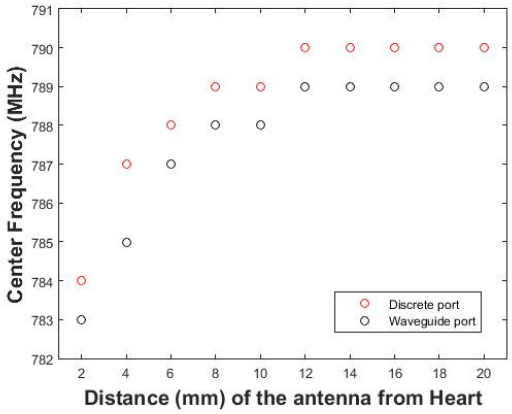

Fig. 5. Distance (mm) of antenna from heart vs. center frequency (MHz).

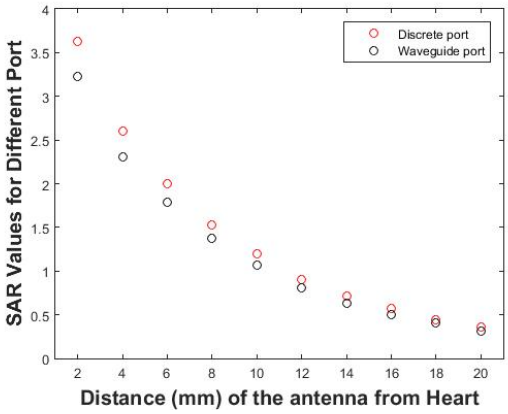

Fig. 6. Distance (mm) of antenna from heart vs. SAR for different ports.

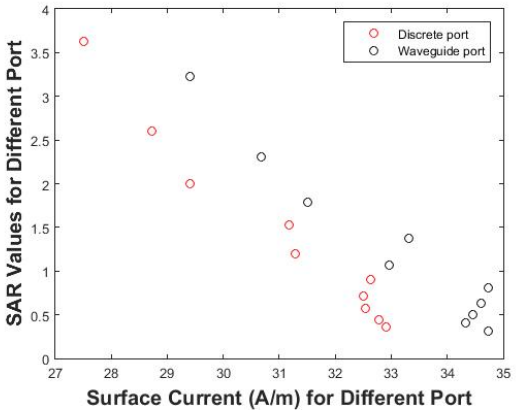

Fig. 7. Surface current (A/m) for different ports vs. SAR for different port.

Increasing directivity results decrease in SAR values as shown in Fig. 8, because the reflection of the wave from the tissue increases while directivity increases.

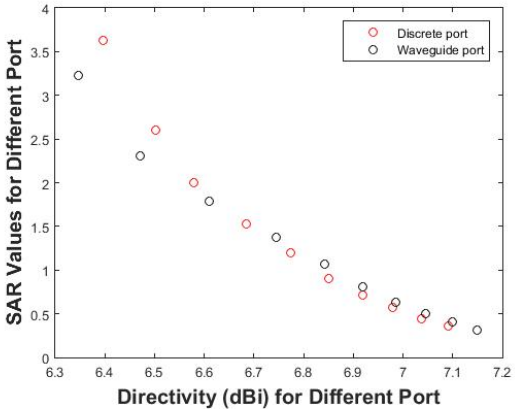

Fig. 8. Directivity (dBi) for different port vs. SAR values for different port.

VII. Conclusion

In this paper, the impact of human heart on an 800 MHz antenna characteristics and the impact of the antenna on the human heart were analyzed. The results showed significant changes in the center frequency of the antenna due to presence of heart. The SAR values decreased with the increasing distance in between antenna and heart for both the input port feeding configurations, where the discrete port results indicated more variations of SAR than waveguide port. Increasing surface current decreased SAR because of less flux penetration inside the tissue. Increasing directivity resulted an increment of reflection from the tissue and a decrement of SAR. However, further research could be done to find out the ground reason (from the mathematical point of view) on the effect of surface current and directivity upon SAR.

References

[1] T. A. J. Mary, C. S. Ravichandran, S. J. Priyadarshini and D. Sugumar, "Investigation of SAR on human head modelling using patch antenna in mobile communication for dual band frequency," *Emerging Trends in Robotics and Communication Technologies (INTERACT), 2010 International Conference on*, Chennai, 2010, pp. 121-124.

[2] M. Ahmed, "Investigating Radiation Hazard and Safety Aspects of Handheld Mobile," *Mobile Ubiquitous Computing, Systems, Services and Technologies, 2009. UBICOMM '09. Third International Conference on*, Sliema, 2009, pp. 1-9.

[3] A. Šarolić, D. Senić, Z. Živković and A. Zorica, "Influence of human head and hand on PIFA antenna matching properties and SAR," *Software, Telecommunications and Computer Networks (SoftCOM), 2011 19th International Conference on*, Split, 2011, pp. 1-5.

[4] M. A. Jensen and Y. Rahmat-Samii, "EM interaction of handset antennas and a human in personal communications," in *Proceedings of the IEEE*, vol. 83, no. 1, pp. 7-17, Jan 1995.

[5] K. Ogawa and T. Matsuyoshi, "An analysis of the performance of a handset diversity antenna influenced by head, hand, and shoulder effects at 900 MHz .I. Effective gain characteristics," in *IEEE Transactions on Vehicular Technology*, vol. 50, no. 3, pp. 830-844, May 2001.

[6] K. Ogawa, T. Matsuyoshi and K. Monma, "An analysis of the performance of a handset diversity antenna influenced by head, hand, and shoulder effects at 900 MHz .II. Correlation characteristics," in *IEEE Transactions on Vehicular Technology*, vol. 50, no. 3, pp. 845-853, May 2001.

[7] O. Kivekas, J. Ollikainen, T. Lehtiniemi and P. Vainikainen, "Bandwidth, SAR, and efficiency of internal mobile phone antennas," in *IEEE Transactions on Electromagnetic Compatibility*, vol. 46, no. 1, pp. 71-86, Feb. 2004.

[8] C.A. Balanis, Antenna Theory: Analysis and Design, John Wiley & Sons, Second Edition, 2005.

[9] S.Tignath, and L.Shrivastava, "Design and analysis of E shape defected ground antenna using MATLAB," International Journal of Advanced Research in Computer Science & Technology, vol. 1, no. 1, October-December 2013.

[10] K. Sarmah, A. Sarma, K. K. Sarma and S. Baruah, "Dual-Band Microstrip Patch Antenna Loaded with Complementary Split Ring Resonator for WLAN Applications," *Information Systems Design and Intelligent Applications: Proceedings of Second International Conference,* India, 2015, pp. 573-580.

[11] C. Gabriel. Compilation of the Dielectric Properties of Body Tissues at RF and Microwave Frequencies, Report N.AL/OE-TR- 1996-0037, Occupational and environmental health directorate, Radiofrequency Radiation Division, Brooks Air Force Base, Texas (USA), 1996.

[12] P. Stavroulakis, *Biological effects of electromagnetic fields*, 2003, Springer.

Sensitivity Enhancement of Porous Silicon Based SPR Sensor Using Graphene-M_0S_2 Hybrid Structure

M. Saifur Rahman, Md. Biplob Hossain and Md. Masud Rana
Department of Electrical and Electronic Engineering
Rajshahi University of Engineering and Technology,
Rajshahi-6204, Bangladesh
Email: saifurrahman121042@gmail.com, biplobh.eee10@gmail.com and md.masud.rana@ruet.ac.bd

***Abstract*—In this paper a theoretical porous silicon surface based plasmon resonance (SPR) sensor has been presented consisting graphene-Melybdenum sulphide (MoS_2) hybrid structure for enhancing sensor detection sensitivity. The biosensor uses perfectly matched layer (PML) boundary condition incorporating on its computational domain to improve its surface plasmon resonance characteristics. Here, graphene-MoS_2 hybrid sheet is used to detect the refractive index change of the sensor surface, which is cause of the reaction of biomolecules. Our calculations show that the graphene-MoS_2 hybrid structure on silicon porous sensor has 25% more sensitivity than the conventional silicon resonant sensor. The enhanced sensitivity is for increasing SPR angle about 25% by adding graphene-MoS_2 hybrid structure.**

Keywords— biosensor, Melybdenum sulphide (MoS_2), Porous silicon, sensitivity

I. INTRODUCTION

Electronic instrumentation has become a central means of characterizing and quantifying bio-molecular interactions in life-science now a days [1]. Electronic and communication engineering have played a remarkable research interest in many fields such as genomics, proteomics, clinical diagnosis, and chemical detection [2]. Today's Label-free optical biosensors for example surface plasmon resonance (SPR) sensor is very popular due to its sample preparation process [3]. Since porous silicon (PS) has large surface area to volume ratio (~100 m^2/cm^3) [4], [5], a good candidate material for this type of bio sensing, which facilitates surface-based interactions of probe and target binding. Recently optical sensing with PS for molecular interactions detection has been demonstrated in [6], [7], but have some drawbacks like less sensitivity, time consuming, high cost. That is why, it has become essential to implement efficient method for fast response and more sensitivity. One attractive solution is to improve sensitivity is using the gold film with bimolecular recognition elements (BRE) on account to enhance the adsorption of biomolecules on the gold surface [1], [2], [8].

In this study, we propose a SPR sensor where graphene-MoS_2 is use as the BRE, by coating it on the gold surface in the conventional SPR biosensor setup, and it analytically shows high sensitivity about 25% more than the conventional PS sensors. Graphene-MoS_2 sheet on Au (111) has been proposed and fabricated recently in [9], [10]. The special property of graphene is to stably adsorb biomolecules with carbon-based ring structures (e.g. ssDNA, enzyme, protein etc.) [13], [14], that facilates a greater refractive index change in-between the graphene-MoS_2 and sensing medium interface. When graphene is coated on Au(111) film, strong coupling is induced at the metal-graphene interface due to high charge carrier mobility of graphene about 10^6 cm^2 $V^{-1}S^{-1}$ and resulting large electric field enhancement takes place at the interface [10]. Graphene plays first interactions detection due to its property of high sensitivity, high conductivity, high carrier mobility, low intrinsic noises and high signal to noise ratio[15]-[19]. MoS_2 nano sheet has special property of high fluorescence quenching ability and different affinity toward single strand DNA (ssDNA) and double-stranded DNA (dsDNA) [11]. Therefore, it is expected that MoS_2 could adsorb biomolecules (e.g. ssDNA) using their Vander Waals force between nucleon bases and the basal plane of MoS_2 [9], [11]. Graphene and MoS_2 will be beneficial to use in sensing purpose because of the above defined characteristics of these nanomaterial's in the SPR [9].

Thus in this paper, the properties of graphene, MoS_2 and PS (small pore size few-10's nm [20]) are taken into account. Proposed biosensor uses PML boundary condition, has the advantage of confining the optical energy exactly in the layer where the biomolecules are immobilized and the binding takes place. Moreover, the Coatation of the graphene-MoS_2 hybrid sheet with gold surface, will modify the propagation constant of surface plasmon polariton (SPP); thereby change the sensitivity to refractive index. This leads to a significant increase of sensitivity of the proposed sensor as compared to conventional SPR sensors as well as waveguide.

II. THEORETICAL FABRICATION OF SPR SENSOR

The numerical structure of the proposed biosensor is given in Fig. 1. This biosensor is comprised of total seven layers. The first layer is a prism (SF10 glass) having high refractive index (n_p) of 2.125 [1], [2]. The 2^{nd} layer is Au (111) thin film that is directly deposited on the base of the prism. In order to excite the surface plasmons (SPs) at the metal-dielectric interface the electrons in the conduction band of SPR active metal must be able to resonate with the incident light of particular

978-1-5090-5785-6/16/$31.00 ©2016 IEEE

wavelength [20]. The thickness and refractive index (RI) of second layer are d_{Au} = 50 nm and n_{Au} = 0.1726+i3.4218, respectively [1],[2]. Our proposed PS, SPR sensor consists of two thin film PS layers. The third layer is lower porosity and fourth layer is higher porosity. The low and high porosity layers have porosities of 52% and 76%, and thicknesses of 300 nm and 1333 nm respectively [20]. Based on the Maxwell-Garnett effective medium approximation for cylinders (n=ω Im(ϵ)/αc, where α, ω, ϵ, c and n are porosity coefficient, radian frequency of light, complex dielectricity, speed of light and effective RI respectively [21]), the RI of the low porosity layer is 2.167 and the RI of the high porosity layer is 1.618 at 1550 nm wavelength.

A graphene or MoS_2 or graphene–MoS_2 composite layer is attached between the metal layer and affinity, for the performance enhancement of the sensor [20].The fifth layer is MoS_2 which is added on the silicon layer. The complex RI of MoS_2 (n_5) is 5.9 + 0.8i and thickness of MoS_2 is 90.65 nm [9]. The sixth layer is graphene which is added on the MoS_2 layer. It thickness and RI are d_G =0.34 nm and n_G = 3 + i1.149106,

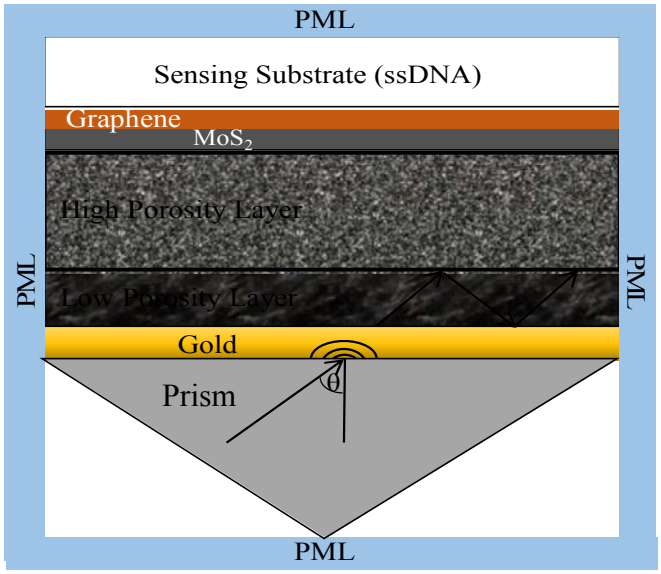

Fig. 1. Schematic diagram of proposed SPR biosensor based on Kretschman configuration

respectively [1],[2]. Therefore, total internal reflection at both interfaces of the top porous silicon layer, or gold-prism interface, is possible. The seventh layer is sensing layer (water in bare sensor) having refractive index of 1.332 [1].

III. Mathmatical Equations of SPR Sensor

A monochromatic light wave (vacuum wavelength λ=1550 nm) passes through the prism and is totally reflected at the low porous-high porous interface, generating an evanescent wave. This evanescent wave can penetrate the graphene-MoS_2 hetero layer and propagate along the x direction with propagation constant of following equation [1], [23]:

$$k_x = \frac{2\pi}{\lambda} n_p \sin\theta \tag{1}$$

Here, θ is the angle of incidence of the light with the metal surface and n_p is the RI of the prism. The SPW propagation constant k_{sp}, is described in (2), where ϵ_m is the permittivity for the gold and ϵ_s is the permittivity for the sensing sample medium [1].

$$k_{sp} = \frac{2\pi}{\lambda}\sqrt{\frac{\varepsilon_m \varepsilon_s}{\varepsilon_m + \varepsilon_s}} \tag{2}$$

Neglecting the imaginary part of k_{sp}, we can rewritte (2) as the form of Eq. (3), where n_m is the RI of the gold and n_s is the refractive index of the sample.

$$k_{sp} = \frac{2\pi}{\lambda}\sqrt{\frac{n_m^{\,2} n_s^{\,2}}{n_m^{\,2} + n_s^{\,2}}} \tag{3}$$

The absorption coefficient (A) can be given by Ekgasit approximation [12]:

$$A = \frac{2\pi}{\lambda}\frac{1}{K_{ZP}}\left\{\int_0^{d_m} Im(\varepsilon_m)\cdot|E|^2\cdot dz + \int_{d_m}^{d_m+d_s} Im(\varepsilon_s)\cdot|E|^2\cdot dz\right\} \tag{4}$$

Here, d_m and d_s are the gold and the low porous silicon layers thickness (d_{Au} =50 nm and d_s=300 nm respectively), and K_{ZP} (~K_{SP} in Eq (3)) is the wave vector in the prism. In conventional SPR sensor, the absorbing materials are only the gold layer and PS whereas after adding the graphene-MoS_2, the absorption will take place in both the metal and silicon layer. Increased absorption at the field intensity, results increase of dielectric interfaces due to which the excitation of SPs is enhanced. It might be possible to enhance the performance of the SPR sensor by depositing PS layer between Au and graphene-MoS_2 layer based on this described concept.

We used generalized Fresnel equations for N-layers optical model to obtain the performance of SPR curve, that is elaborately described in [1], [14], [22]. Most of the SPR applications, the real RI changes is considered alone owing to chemical or biochemical actions [1], [2] and therefore, the imaginary components in Eq. (3) will be neglected. And we finally get SPR angle from [1] as:

$$\theta_{sp} = a\sin\left[\frac{n_m^{\,2} n_s^{\,2}}{n_p^{\,2}(n_m^{\,2} + n_s^{\,2})}\right]^{\frac{1}{2}} \tag{5}$$

For each SPR curve, at resonant condition, the excitation of surface plasmon polariton (SPP) is known as minimum total reflectance (i.e., ATR minimum). The angle of incidence at which ATR minimum is called SPR angle, mathematically as Eq (5). The sensitivity (S) is defined as the ratio of shift in the resonance angle of incidence ($\Delta\theta_{SPR}$) to the RI change in the sensing region (Δn_a), the unit of sensitivity is ^{0}/RIU [9];

$$S^{L-M} = \frac{\Delta\theta_{SPR}^{T}}{\Delta n_a} \quad (6)$$

where $\Delta\theta_{SPR}^{T}$ is the SPR angle change of sensor, while consisting graphene-MoS_2 hetero layer and S^{L-M} is the sensitivity after adding graphene-MoS_2 hybrid sheet.

IV. Numerical Resuts and Discussions

The Lumerical Suite studio in FDTD mode is used to to design and simulate the numerical sensor shown in Fig. 1. We define the problem space as computational domain which field components are updated according to the FDTD method. Four extra layers referred to as the perfectly matched layers PMLs are added to the main computational domain. The main role of the PMLs is to enclose the domain of interest without generating any nonphysical wave reflections back into the main computation domain, which causes contamination of solution and degrades the simulation's efficiency. Hence, the PMLs must be formulated to be optically material independent. The PMLs are an artificial medium configured in a such way that waves enter into the layers without generating any reflections, as well as the amplitude of waves decays exponentially while traveling through the layers and eventually these waves vanish [22].

As an example we simulated the proposed SPR biosensor for the detection of the single-stranded DNA (ssDNA) in order to find out its numerical sensitivity. We initiated to check the performance of proposed sensor by finding it SPR curve. Fig. 2, shows reflectance vs incidence angle curve. The angle of incidence in bare sensor is 27.50 degree (—line) and the angle of incidence while 1000 nM probe ssDNA is placed as sensing dielectrics is 27.70 degree (—line).

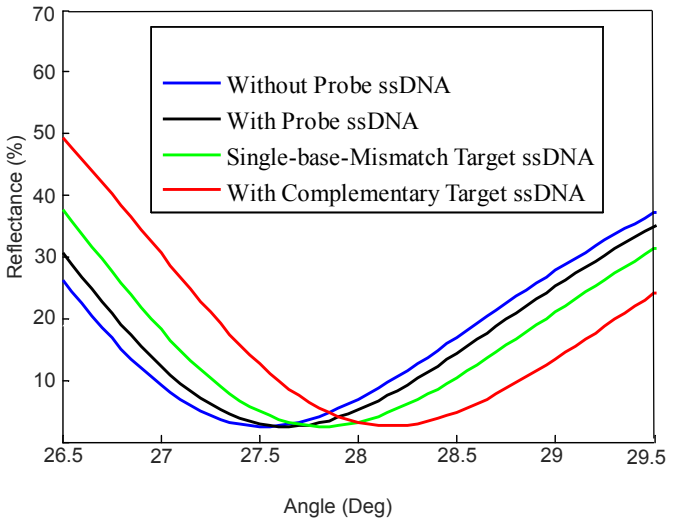

Fig. 2. The reflectance vs incidence angle characteristics of the proposed sensor for 1000 nM ssDNA

Green line (—) shows, SPR curve with single-base mismatch ssDNA of 1000 nM concentration is plaecd, then angel is 27.702. Result shows no significant change in SPR angle (change of SPR angle is 0.002 degree). When the probe molecules bring to the mismatched target, there no hydrogen bonding has taken place between probe and target DNA strands because of the presence of mismatched base pair, is shown at Fig. 1(b) in [1]. So there are no change of charges in target molecule. Red line (—), demonstrates the final stage of detection concept. It shows, 1000 nM complementary ssDNA molecules are sinking in the probe. Result shows significant change in SPR angle (28.25 degree) due to hydrogen bonding between probe and target DNA strands has taken place because of the presence of mismatched base pair, is shown at Fig. 1(a) in [1]. So there is considerable change of charges in target molecule.

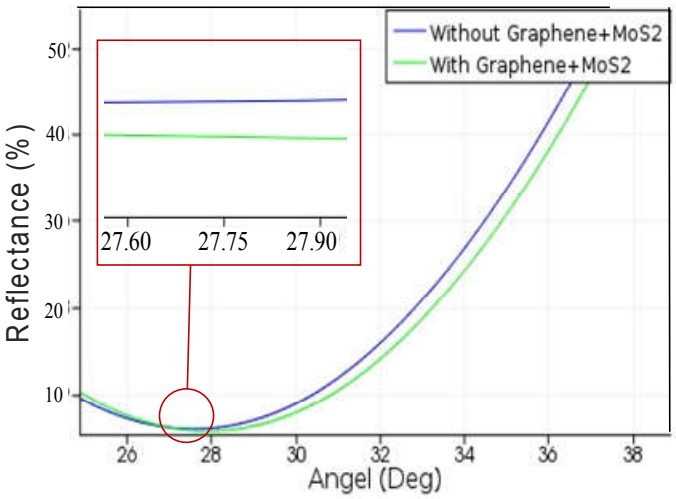

Fig. 3. SPR angel without Graphene-MoS_2 is 27.5 and with graphene-MoS_2 is 27.75 degree

The SPR angle without graphene-MoS_2 hybrid is 27.50 degree and with graphene-MoS_2 is 27.75 degree. The SPR angle has increased 0.25 degree in the right side of the SPR curve shown in Fig. 3, which accounts for enhanced sensitivity. The sensitivity equation given in Eq. (6), would have a little modification for our proposed sensor as the following Eq (7):

$$S^{L-M} = (1 + .25)\, S^{0} \quad (7)$$

where S^0 is the sensitivity of the devices without graphene-MoS_2. A detailed mathematical explanation is given in end note*. Our calculations make clear that if we add Graphene-MoS_2 hybrid structure with conventional silicon porous SPR sensor then sensitivity is increased 25%.The improved sensitivity is due to increased adsorption of biomolecules and the optical property of Graphene- MoS_2 hybrid.

Conclusion

A graphene-MoS_2 based porous silicon waveguide has presented in this paper which has 25% more sensitivity than conventional silicon sensor. Its sensitivity increased due to the absorption ability of biomolecules of Graphene and MoS_2. It reported theoretically on DNA hybridization. The biosensor

---

*$S^{L-M} = \frac{\Delta\theta_{SPR}^{T}}{\Delta n_a} = \frac{\Delta\theta_{SPR}^{0} + \Delta\theta_{SPR}^{L-M}}{\Delta c_a} = \frac{\Delta\theta_{SPR}^{0} + 0.25\Delta\theta_{SPR}^{0}}{\Delta c_a} = (1 + .25)\frac{\Delta\theta_{SPR}^{0}}{\Delta c_a} = (1 + .25)\, S^{0}$

Here, $S^{0} = \frac{\Delta\theta_{SPR}^{0}}{\Delta c_a}$; Sensor sensitivity without graphene $-$ MoS_2 layer

$\Delta\theta_{SPR}^{0}$ = SPR angle change while absence of graphene $-$ MoS_2 layer

$\Delta\theta_{SPR}^{L-M}$ = SPR angle change only due to graphene $-$ MoS_2 layer

uses perfectly matched layer (PML) boundary condition on its computational domain to improve its reflectance.

REFERENCES

[1] M. B. Hossain, and M. M. Rana, "Graphene Coated High Sensitive Surface Plasmon Resonance Biosensor for Sensing DNA Hybridization," *ASP Sensor Lett*., vol. 14, pp. 1–8, 2016.

[2] M. B. Hossain, and M. M. Rana, "DNA Hybridization Detection Based on Resonance Frequency Readout in Graphene on Au SPR Biosensor," *J. of sensors*, vol. 16, pp. 1–8, 2016.

[3] O. Brandt, and J. D. Hoheisel, "Peptide nucleic acids on microarrays and other biosensors," *Trends Biotechnol.*, vol. 22, pp. 617-622, Dec 2004.

[4] V. Lehmann, "Electrochemistry of silicon: instrumentation, science, materials and applications," Weinheim, Gernany: Wiley-VCH, 2002.

[5] M. P. Stewart, and J. M. Buriak, "Chemical and biological applications of porous silicon technology," *Adv. Mater.*, vol. 12, pp. 859-869, Jun. 2000.

[6] V. S.–Y. Lin, K. Motesharei, K.S. Dancil, M. J. Sailor, and M. R. Ghadiri, "A porous silicon-based optical interferometric biosensor," *Science*, vol. 278, pp. 840-843, Oct. 1997.

[7] S. Chan, Y. Li, L. J. Rothberg, B. L. Miller, and P. M. Fauchet, "Nanoscale silicon microcavities for biosensing," *Mat. Sci. Eng.*, vol. 15, pp. 277-282, 2001.

[8] J. Homola, "Present and future of surface plasmon resonance biosensors," *Anal. Bioanal. Chem.,* vol. 377, no. 3, pp. 528– 539, 2003.

[9] J. B. Maurya, Y. K. Prajapati, V. Singh, J. P. Saini, and R. Tripathi, "Performance of graphene–MoS_2 based surface plasmon resonance sensor using Silicon layer," *Opt Quant Electron,* Jul. 2015.

[10] A. Hoggard, L.Y. Wang, L. Ma, Y. Fang, G. You, J. Olson, Z. Liu, W.S. Chang, P.M. Ajayan, and S. Link, "Using the plasmon linewidth to calculate the time and efficiency of electron transfer between gold nanorods and graphene, ". *ACS Nano* vol. 7, pp. 11209–11217, 2013.

[11] C. Zhu, Z. Zeng, H. Li, F. Li, C. Fan, and H. Zhang, "Single-Layer MoS_2-based nanoprobes for homogeneous detection of biomolecules," *J. Am. Chem. Soc.*, vol. 135, pp. 5998–6001, 2013.

[12] S. Ekgasit, C. Thammacharoen, and W. Knoil, "Surface plasmon resonace spectroscopy based on evanescent field treatment," *Anal. Chim.*, vol. 76, pp. 561–568, 2004.

[13] K. L. Lee, C. W. Lee, W. S. Wang, and P. K. Wei, "Sensitive biosensor array using surface plasmon resonance on metallic nanoslits," *J. Biomed. Opt.*, vol. 12, no. 4, pp. 44023, 2007.

[14] L. Wu, H. S. Chu, W. S. Koh, and E. P. Li, "Highly sensitive graphene biosensors based on surface plasmon resonance," *Optics Express*, vol. 18, no. 14, pp. 14395–14400, 2010.

[15] M. B. Hossain, and M. M. Rana, "An effective compact-FDTD wideband modeling of graphene conductivity," in *Proc. IEEE Int. Conf. on Elec. Engineering and Information Comm. Tech.*, pp. 1–3, Dhaka, Bangladesh, May 2015.

[16] M. B. Hossain, and M. M. Rana, "An effective modified modeling of graphene interband conductivity," in *Proc. IEEE Int. Conf. on Elec. Engineering and Information Comm. Tech.*, pp. 1–3, Dhaka, Bangladesh, May 2015.

[17] P.T.K. Loan, W. Zhang, C.T. Lin, K.H. Wei, L.J. Li, and C.H. Chen, "Graphene/MoS_2 heterostructures for ultrasensitive detection of DNA hybridization," *Adv. Mater*.vol. 26, pp. 4838–4844, 2014.

[18] M. B. Hossain, M. Muktadhir, and M. M. Rana, "Multi-structural optical devices modeling using graphene," *Optik - International Journal for Light and Electron Optics,* vol. 127, no. 15, pp. 5841-5851, Mar. 2016.

[19] M. M. Rana, M. B. Hossain, M. R. Islam, and Y. Guo, "Surface plasmon polariton propagation modeling for graphene parallel pair sheets using FDTD," in *Proc. IEEE Int. Conf. on Applied Superconductivity and Electromagnetic Devices*, Shanghai, China, Nov.20-23, 2015.

[20] G. Rong, A. Najmaie, J.E. Sipe, and S. M. Weiss, "Porous silicon waveguides for DNA detection," in *Proc. IEEE Int. Conf. on Group IV Photonics,* pp. 13-15, Sep. 2006.

[21] J. E. Lugo, J.A. del Rio, and J. T.-Martinez, "Influence of surface coverage on the effective optical properties of porous silicon modeled as a Si-wire array," *J. App. Phys.*, vol. 81, pp. 1923-1928, 1997.

[22] D. K. Hwang, and A. D. Rey, "Optical modeling of liquid crystal biosensors," *J. Chem. Phys.*, vol. 125, pp. 174902-9, 2006.

[23] K. N. Shushama, M. M. Rana, R. Inum, and M. B. Hossain, "Graphene coated fiber optic surface plasmon resonance biosensor for the DNA hybridization detection: Simulation analysis," *Optics Communications*, vol. 383, pp. 186–190.

International Conference on Electrical, Computer & Telecommunication Engineering (ICECTE)
8-10 December 2016, Rajshahi-6204, Bangladesh

Low Voltage Ride Through Capability Enhancement of DFIG-Based Wind Turbine by a New Topology of Fault Current Limiter

Mst. Farzana Khatun[1]*, and M.R.I. Sheikh[1]

[1]Department of Electrical and Electronic Engineering, Rajshahi University of Engineering & Technology
Rajshahi-6204, Bangladesh

Email*: farzana0071@gmail.com

Abstract— **Due to rapid depletion of fossil fuel and environment concern, clean and non-polluting energy i.e. renewable energy is highly needed. Among the various renewable resources, wind energy is one of the most important and promising sources. In the recent year doubly fed induction generator (DFIG) is one of the most widely used in wind farms. But the transient stability of DFIG becomes very much sensitive and challenging concern. Three phase line-to-ground fault (3LG) is one of the worst cases of DFIG. During fault at grid side, DFIG is much affected because its stator windings are directly connected to grid. So it is important to analyse the transient stability of DFIG during fault according to fulfil the grid code requirement. To improve the transient stability and fault ride through capability of DFIG a new topology of fault current limiter (FCL) is proposed in this paper. The proposed FCL is not only limit the fault current but also faster voltage recovery. Thus improve the transient stability and fulfil the grid code requirements. For simulation analysis, PSCAD/EMTDC software is used. To determine the advantageousness of proposed FCL, its performance is compared with the conventional series dynamic resistor (SDR). Simulation results show that the proposed FCL enhances the transient stability of DFIG and better performance than SDR.**

Index Terms—**Doubly fed induction generator (DFIG), grid code, 3 line-to-ground (3LG) fault, fault current limiter (FCL), transient stability, series dynamic resistor (SDR).**

I. INTRODUCTION

Energy demand is one of the greatest problems in the modern world. But energy producing resources such as coal, oil and gas are decreasing day by day. Global warming, which is caused by fossil fuels, has become severe recently. Hence, decreasing of fossil fuel resources and environment concern has given awareness on generation of renewable energy resources. Among the various renewable resources, wind energy is one of the most attractive sources of renewable energy all over the world, mainly because it is considered to be reliable power supply, no fuel cost, non-polluting and economically viable. So, the growth of wind energy around the world in recent years has been consistently increased. At the same time different types of wind turbine technology has been developed rapidly.

Among the different types of wind turbine generation system, DFIGs have been widely used due to the advantages including variable-speed constant-frequency operation, flexible power control and a smaller converter rating around 30% of the generator rating, compared with the fixed-speed induction generators or synchronous generators based wind power system [1]–[2].

So, DFIG becomes an economical choice. But the major drawback of DFIG based wind turbine is their operation during abnormal conditions like grid faults and voltage sags, short circuit fault (phase-to-phase, phase–to-ground, three line-to-ground) and open circuit fault. When grid fault occurs, terminal voltage of DFIG goes very low and very high current flows in the stator and rotor windings of the DFIG. Because of magnetic coupling between Rotor Side Converter (RSC) and Grid Side Converter (GCS), this high fault current may damage them. Traditionally to deal with this problem, the DFIG is disconnected from the grid but it is not useful because the impact of a large scale DFIG based wind farms disconnected may disturb the stability, thus need to remain connected to the grid throughout the fault occurrence. However to remain connected DFIG must follow grid code.

To overcome these problems many controllers have been proposed such as Bi-2212 superconducting fault current limiter (SFCL) [3], energy storage systems like flywheel energy storage [4], superconducting magnetic energy storage-fault current limiter (SMES-FCL) [5]. But some disadvantages of superconducting material like cooling system is needed, temperature impact and their high installation cost compensates their high quality performance. Also flywheel energy storage systems have complex control strategy.

To solve these problems, the proposed FCL is a new technique to enhance the transient stability of DFIG based wind energy application. The performance and effectiveness of the proposed FCL are not only better but also the technique is simple and low installation cost compared to conventional other controllers.

This paper is organized as the methodology of wind turbine and DFIG given in section II. The proposed FCL and SDR model, arrangement, operation, control technique are described in section III and IV. Simulation output and corresponding discussion is described in section V. Finally, some conclusions are given in Section VI.

978-1-5090-5785-6/16/$31.00 ©2016 IEEE

II. Methodology of Wind Turbine and DFIG

The system consists of wind turbine based DFIG, transformer, double circuit transmission lines connected to the infinite bus and fault occurs at point F as shown in Fig.1. To see how much the proposed FCL is effective, its performance is compared with SDR.

In this model, DFIG consists of a wound rotor induction machine is used. Rotor side converter (RSC) and Grid side converter (GSC) of DFIG control the active power and reactive power and also control the terminal voltage of DFIG. The detailed model of DFIG was described in [6]–[7].

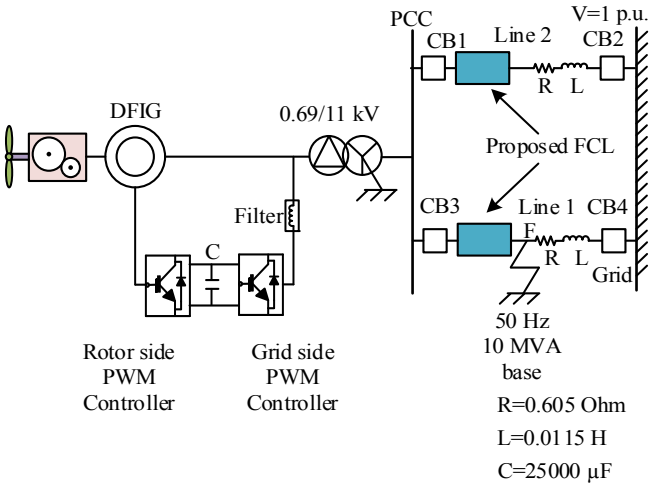

Fig.1. Schematic diagram of DFIG with proposed FCL.

In this paper, MOD-2 wind turbine model is used for wind turbine as used in [8]. Extracted power from the wind can be calculated from (1).

$$P_m = \frac{1}{2}\pi\rho R^2 V_m^3 C_p(\lambda,\beta) \quad (1)$$

$$C_p(\lambda,\beta) = 0.5(\lambda - 0.022\beta^2 - 5.6)e^{-0.17\lambda} \quad (2)$$

$$\lambda = \frac{\omega R}{V_m} \quad (3)$$

Where, P_m is the output power [W] of wind turbine, $\boldsymbol{\lambda}$ is the tip speed ratio, R the radius of the blade $[m]$, ωis the wind turbine angular speed [rad/s], β is the blade pitch angle [deg], V_w is the wind speed m/s, ρ is the air density Kg/m^3, and $C_p$is the power coefficient.

III. Proposed FCL Model Description

The details methodology of FCL is described here.

A. FCL arrangement

The proposed FCL consists of two parts. One is series connection with transmission line and another is shunt path. Series path consists of a series resistance R_s and two transistors, one is n-p-n and another is p-n-p. Shunt path consists of a resistance R_{sh} and inductance L_{sh} which is parallel to series path as shown in Fig.2. R_s is very much less than R_{sh} and L_{sh}.

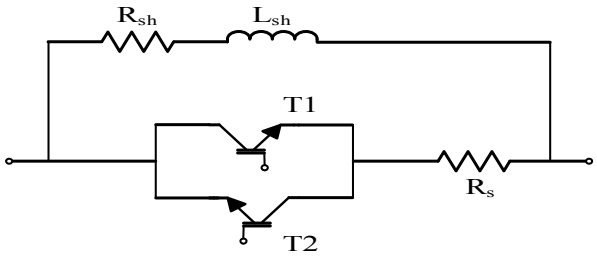

Fig.2. The proposed FCL topology.

B. FCL operation

At normal operating condition both the transistors of series path are closed. In Positive half cycle of electrical frequency, line current flow through the T1- R_s and negative half it is passed through the T2-R_s.The small value of R_s which does not effect on line current. Transistor voltage drop is also negligible to line voltage drop. So, this series connection has no effect on normal condition. Shunt impedance is enough high value than R_s, So that no current flow in the shunt path normally. But at fault condition, both the transistors are opened and current flows through the shunt path. This high value of shunt impedance limits the fault current and also improves the terminal voltage of DFIG.

C. FCL control technique

Without the faulty condition, sometimes the common coupling voltage decreases due to low demand and sometimes current is increased than its rated value. If only one term (voltage or current) have been considered for control strategy, then without fault condition FCL may worked which is undesirable. Again during fault condition, both terminal voltage and current are affected. For that reason, for controlling the FCL both the terms should be considered. Firstly the value of reference voltage, V_{ref} and current, I_{ref} is predetermined. The value of the V_{ref} is set to be 90% of the nominal value of V_{pcc}. Fault may be considered under the value of V_{ref} and above the value of I_{ref} . Thus Common coupling voltage V_{pcc} is compared with V_{ref} and line current I_{line} is compared with I_{ref} as shown in Fig.3.

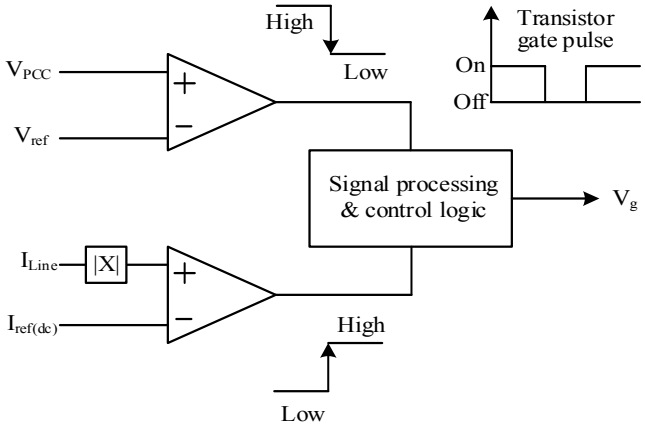

Fig.3. FCL control technique.

Output of this control circuit is used to apply in the gate of transistor as a get pulse of FCL circuit. At normal condition, this get pulse is one and transistor is closed. But at faulty condition required criteria must be fulfilled and gate pulse is zero. Both the transistor is opened and fault current flow through the shunt path. Which limit the abruptly change of voltage and current.

D. FCL design calculation

The required diagram of DFIG considering the fault condition is shown in Fig.1.
To ensure the better performance and least disturbance during fault condition, the parameter of FCL must be followed some condition [9]. During fault, active power P_{fcl} of the proposed FCL is

$$P_{fcl} = \frac{{V_{pcc}}^2 R_{sh}}{{R^2}_{sh} + \omega^2 {L^2}_{sh}} \quad (4)$$

$$R_{sh} > \frac{{V_{pcc}}^2 + \sqrt{{V_{pcc}}^4 - {P_g}^2 \omega^2 {L_{sh}}^2}}{P_g} \quad (5)$$

$$L_{sh} < \frac{{V_{pcc}}^2}{\omega P_g} \quad (6)$$

Where, V_{pcc} is the common coupling voltage (line to line, RMS), P_g is power delivered by DFIG, R_{sh} and L_{sh} is the shunt resistance and inductance.

For simulation analysis, the value of shunt resistor and inductor are considered as 2.7 [ohm] and 0.075 [Henry] respectively, which are assumed to fulfil the required condition. Series resistance is 0.001[ohm].

IV. Series Dynamic Resistor (SDR)

For determining the effectiveness of proposed FCL, it is compared with series dynamic resistor (SDR). It is also used to limit the fault current and enhance the transient stability of wind farm. [9]–[10] as shown in Fig.4.

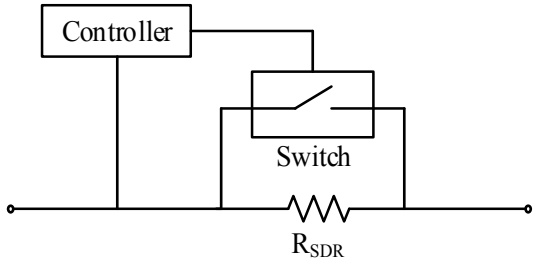

Fig. 4. SDR configuration.

A.SDR model

SDR consists of a high valued resistor which is connected in series with the transmission line and a switch is connected parallel across it. During faulty condition, this dynamic resistor (R_{SDR}) is automatically connected with the line and limited the abruptly changing of fault current. SDR also balance the active power of the system.

B.SDR operation

At normal condition, the parallel switch of SDR is closed and line current is bypassed this resistor. But, at faulty condition this switch is opened and dynamic resistor is inserted into the line. This high value series resistor limits the fault current and also maintains the terminal voltage.

C. SDR control logic

The control logic of the parallel switch of SDR is same as the control technique of the proposed FCL circuit which has been described in Fig.3. Similarly the proposed FCL transistors are used as a switch element. To compare with FCL its series dynamic resistor (R_{SDR}) is same as shunt resistor (R_{sh}) of the proposed FCL .

V. Simulation Outputs and Discussion

The performance of the proposed FCL is compared with that of SDR to determine the effectiveness of proposed FCL. Both the model is simulated by PSCAD/ EMTDC software.

For the purpose of transient analysis, A 10 MVA DFIG based wind turbine and a three phase line-to-ground (3LG) fault is occurred at point F near the PCC as shown in Fig.1. The 3LG fault of DFIG is considered as the most unfavorable condition. The 3LG fault at point F is occurred at t=0.3s for 100ms. Circuit breaker of CB_3 and CB_4 in the faulted line is opened at 0.4s and again reconnected successfully at 1.3s.
Fig. 5 shows the grid code requirement set by Federal Energy Regulatory commission [8]. Fig.6 represents terminal voltage response of DFIG when a temporary 3LG fault is occurred. Without considering any controller terminal voltage decreases after the fault started and decreases lower and lower till the circuit breakers open. But using the proposed FCL, it maintains the voltage level to ± 1 p.u of nominal voltage. SDR does not maintain the voltage level as quickly as the proposed FCL can. Thus proposed FCL can maintain grid code.

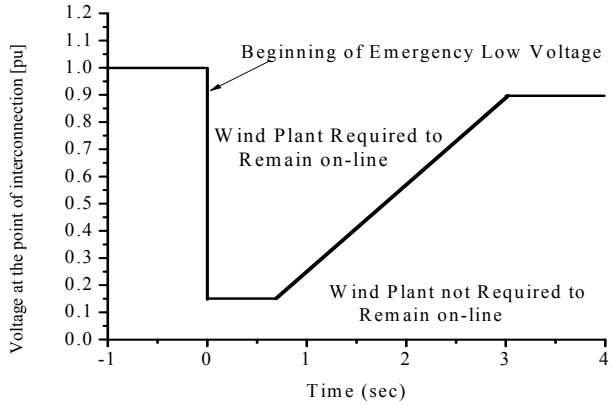

Fig.5. Low voltage ride through standard set by FERC, U.S.

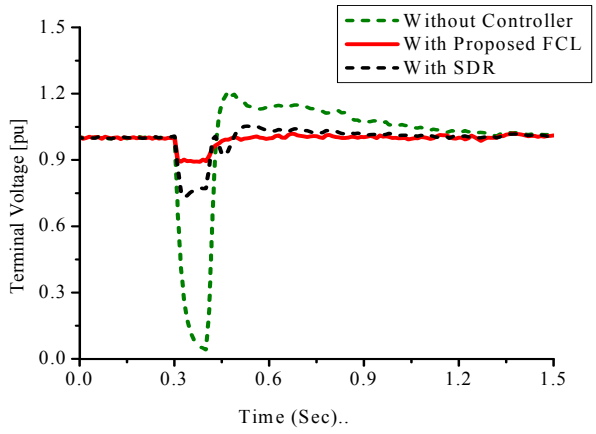

Fig.6. Terminal voltage response for 3LG fault.

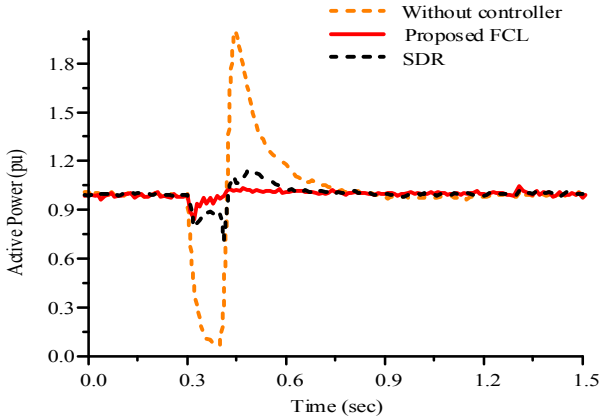

Fig.7. Active power response for 3LG fault.

In Fig.7 shows the active power response of DFIG for 3LG fault. Without any controller, when the fault occurs output power decreases and becomes very close to zero. After opening the breaker it causes huge imbalance of output power. Using the SDR output power goes very low at faulty condition and after opening the breaker it suddenly increased the output power which may have bad impact on the machine. But applying the FCL, output power fluctuation is very low at fault and after opening the breaker. The proposed FCL provided faster stability than SDR.

Fig.8 shows the faulted line current (C phase current) without any controller, with SDR and with the proposed FCL. Without any controller faulted line current increased abruptly during 3LG fault. Both SDR and proposed FCL limit the fault current. But applying the FCL fault current is better limited than SDR.

VI. Conclusion

In this paper a new topology of FCL is proposed to improve the transient stability of DFIG. The effectiveness of the proposed FCL and its performance is compared with SDR. Simulation results show that the proposed FCL model is more capable to respond to a fault and return back to the normal state within a shortest possible time. During fault condition the proposed FCL plug into a resistance and an inductance in the faulted line. Resistance obsess the extra energy and inductance limit the abruptly change of fault current. The Proposed FCL gives not only lower voltage drop but also faster voltage recovery and limit the fault current. So that the healthy line is not affected by 3LG fault and it is increased the reliability of DFIG based wind farm at faulty condition.

In future a multi-machine big power system will be simulated and verified the performance with the proposed FCL.

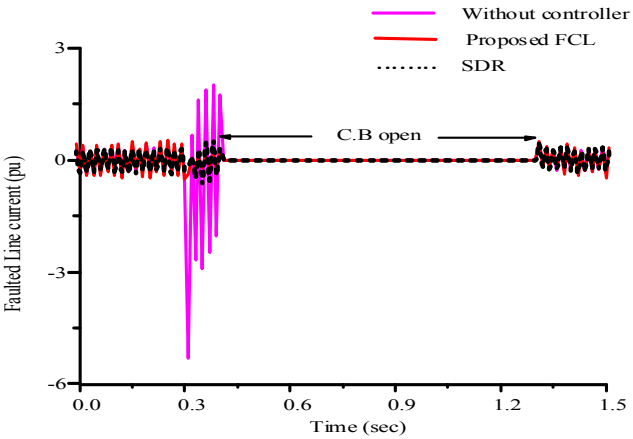

Fig.8. Faulted line current(only for phase C).

References

[1] F. Blaabjerg, M. Liserre, and K. Ma, "Power electronics converters for wind turbine systems," *IEEE Trans. Ind. Appl.*, vol. 48, no. 2, pp. 708–719, Mar./Apr. 2012.

[2] J. M. Carrasco, L. G. Franquelo, J. T. Bialasiewicz, E. Galvan, R. C. P. Guisado, A. M. Prats, J. I. Leon, and N. Moreno-Alfonso, "Power electronic systems for the grid integration of renewable energy sources: A survey," *IEEE Trans. Ind. Electron.*, vol. 53, no. 4, pp. 1002–1016, Aug. 2006.

[3] S. Romphochai, and K.Hongesombut, "Evaluation of Fault Ride Through Capability Enhancement of DFIG-Based Wind Turbine with Bi-2212 Superconducting Fault Current Limiter," *IEEE PES Innovative Smart Grid Technologies Asia 2015 (ISGT Asia 2015) Bangkok, Thailand. 4-6 November 2015.*

[4] L. Wang, J.-Y. Yu, and Y.-T. Chen, "Dynamic stability improvement of an integrated offshore wind and marine-current farm using a flywheel energy-storage system*," IET Renew. Power Gener.,* vol. 5, pp. 387–396, Sep. 2011.

[5] I.Ngamroo , "Improving FRT Capability and Alleviating Output Power of DFIG Wind Turbine by SMES-FCL," *Proceedings of 2015 IEEE International Conference on ID5111 Applied Superconductivity and Electromagnetic Devices Shanghai, China,* November 20-23, 2015.

[6] L. Yang, Z. Xu, J. Østergaard, Z. Y. Dong and K. P. Wong, "Advanced control strategy of DFIG wind turbines for power system fault ride through," *IEEE Trans. Power Systems,* vol. 27, no. 2, pp. 713-722, May. 2012.

[7] F. Mei and B. C. Pal, "Modeling of doubly-fed induction generator for power system stability study," *in Proc. IEEE Power Energy Soc. Gen. Meeting,* Jul. 2008, pp. 1–8.

[8] M.R.I. Sheikh, "Stabilization of a Grid Connected Wind Farm by Using SMES," Doctor of Engineering Thesis, Kitami Institute of Technology, Japan, September 2010.

[9] Yang, J.; Fletcher, J. E.; O'Reilly, J. E.; , "A Series-Dynamic-Resistor-Based Converter Protection Scheme for Doubly-Fed Induction Generator During Various Fault Conditions," *Energy Conversion, IEEE Transaction* , vol.PP, no.99, pp.1-11,2009.

[10] B. Gong, D. Xu, and B. Wu, "Cost effective method for DFIG fault ride through during symmetrical voltage dip*," in Proc 36th IEEE Ind. Appl. Soc. Annu.* Meeting, 2010, pp. 3263–3268.

2nd International Conference on Electrical, Computer & Telecommunication Engineering (ICECTE)
8-10 December 2016, Rajshahi-6204, Bangladesh

Improved Two-Vector Direct Power Control Algorithm-Based Three-Phase Pulse Width Modulation Rectifier

Likun Liu, Wei Xu
School of Electrical and Electronic Engineering, Huazhong University of Science and Technology(HUST), China; e-mail: weixu@hust.edu.cn.

Md. Rabiul Islam
Department of Electrical and Electrical Engineering(EEE)
Rajshahi University of Engineering & Technology(RUET)
Rajshahi-6204, Bangladesh; e-mail: rabiulbd@hotmail.com.

***Abstract*— Direct power control (DPC) has received a significant amount of research attention because of its benefits such as simplicity, robustness and excellent dynamic response. Conventional switching-table-based single-vector DPC (SV-DPC) presents irregular power ripples and variable switching frequency, due to the use of predefined switching table and hysteresis comparators. To solve these problems, two-vector DPC (TV-DPC) and three-vector DPC (THV-DPC) based three-phase pulse width modulation (PWM) rectifier are proposed. Although the performance of the THV-DPC is better than that of TV-DPC, its algorithm implementation is very complex and time consuming. In this paper, two-three combined vector DPC (TTCV-DPC) algorithm is presented which combines two and three voltage vectors by the help of the new switching table. The proposed algorithm has less complexity than the THV-DPC and better performance than the TV-DPC. Comprehensive simulations demonstrate the proposed method can get lower power ripple and lower grid-side current total harmonic distortion (THD) than that of TV-DPC.**

Keywords—Two-vector direct power control (TV-DPC), pulse width modulation (PWM), two-three combined vector direct power control (TTCV-DPC), total harmonic distortion (THD)

I. INTRODUCTION

Recently, three-phase pulse width modulation (PWM) rectifier has been widely applied to the areas of ac adjustable speed drives, active power filter, distributed generation and voltage source converter transmission. Compared to passive diode rectifier, the PWM rectifier has the advantages of bidirectional power flow, sinusoidal line current, controllable power factor, and good dc-link voltage regulation ability with a small-size capacitor [1, 2]. Various methods have been proposed to achieve power control of PWM rectifiers and they can be classified into four groups [1-3]: voltage-oriented control (VOC), voltage-based direct power control (DPC), virtual-flux oriented control (VFOC), and virtual-flux-based DPC.

Among the existing power converter control methods, DPC is one of the most commonly used approaches. Compared with VOC, DPC can achieve decoupled active and reactive power control without current loop [4]. The conventional switching table-based single-vector DPC (SV-DPC) is derived from the original direct torque control (DTC) for ac machine drives, and has now become one of the most popular control strategies because of its excellent transient performance, robustness and simplicity. However, it suffers some drawbacks of large power ripple and high grid-side current THD. Fortunately, such problems above can be solved by two-vector DPC (TV-DPC) method as proposed in [5]. It applies one active and one zero vectors during one control period, and the active vector is obtained from the switching table. However, this method increases switching loss because of asymmetry of the switching state. In [6], three-vector DPC (THV-DPC) method is introduced to further improve the performance of the rectifier, which uses a symmetrical (3+3) vectors sequence among one control period. Although the performance of the THV-DPC is better than the TV-DPC, its algorithm structure and implementation are very complex and time consuming.

In this paper, to solve aforementioned problems (e.g. large power ripple based two-vector control, great time-consumption based on three-vector control) and make full usage of merits benefited from two-vector and three-vector methods, one improved two-three-combined vector DPC (TTCV-DPC) algorithm is proposed. Through a lot of simulations, it is proved that the TTCV-DPC algorithm has much better performance indexes than those of the conventional TV-DPC algorithm, and less complexity than that of the THV-DPC algorithm.

II. PRINCIPLE OF DPC FOR PWM RECTIFIER

The conventional definition of power is based on the average time to complete the work. However, DPC is inherited from a control strategy of instantaneous power theory, and it is put forward by Japanese expert Akagi [7].

A. Model of PWM Rectifier

The topology of a three-phase two-level PWM rectifier is illustrated in Fig. 1. Three IGBT bridges are connected to the power sources through inductors L and resistors R. On the dc side, a pure resistive load R_L is connected in parallel with a capacitor C, and dc power supply e_L is series with R_L to provide the energy for the feedback of the rectifier operation.

978-1-5090-5785-6/16/$31.00 ©2016 IEEE

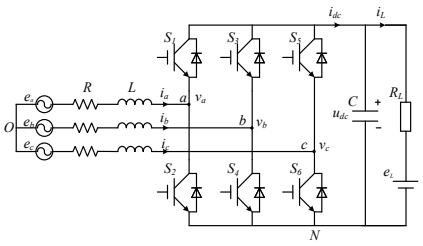

Fig. 1. Topology of a two-level PWM rectifier.

According to the Kirchhoff's law, transforming the three-phase mathematical model into two-phase stationary frame, the model of PWM rectifier can be expressed as

$$\begin{cases} L\dfrac{di_\alpha}{dt} = -Ri_\alpha + e_\alpha - u_{dc}s_\alpha \\ L\dfrac{di_\beta}{dt} = -Ri_\beta + e_\beta - u_{dc}s_\beta \\ C\dfrac{du_{dc}}{dt} = s_\alpha i_\alpha + s_\beta i_\beta + \dfrac{e_L - u_{dc}}{R_L} \end{cases} \tag{1}$$

Active power p and reactive power q can be expressed as

$$\begin{cases} p = e_\alpha i_\alpha + e_\beta i_\beta \\ q = e_\beta i_\alpha - e_\alpha i_\beta \end{cases} \tag{2}$$

From (2), the differentiations of active and reactive powers are obtained as

$$\begin{cases} \dfrac{dp}{dt} = e_\alpha \dfrac{di_\alpha}{dt} + i_\alpha \dfrac{de_\alpha}{dt} + e_\beta \dfrac{di_\beta}{dt} + i_\beta \dfrac{de_\beta}{dt} \\ \quad = \left(e_\alpha \dfrac{di_\alpha}{dt} + e_\beta \dfrac{di_\beta}{dt}\right) + \left(-\omega e_\beta i_\alpha + \omega e_\alpha i_\beta\right) \\ \dfrac{dq}{dt} = \left(e_\beta \dfrac{di_\alpha}{dt} + i_\alpha \dfrac{de_\beta}{dt}\right) - \left(e_\alpha \dfrac{di_\beta}{dt} + i_\beta \dfrac{de_\alpha}{dt}\right) \\ \quad = \left(e_\beta \dfrac{di_\alpha}{dt} - e_\alpha \dfrac{di_\beta}{dt}\right) + \left(\omega e_\alpha i_\alpha + \omega e_\beta i_\beta\right) \end{cases} \tag{3}$$

Substituting (2) and (3) into (1), the final expressions of the differentiations of active and reactive powers are derived as

$$\begin{cases} \dfrac{dp}{dt} = -\dfrac{R}{L}p + \dfrac{3E^2}{2L} - \omega q - \dfrac{\left(e_\alpha v_\alpha + e_\beta v_\beta\right)}{L} \\ \dfrac{dq}{dt} = -\dfrac{R}{L}q + \omega p - \dfrac{\left(e_\beta v_\alpha - e_\alpha v_\beta\right)}{L} \end{cases} \tag{4}$$

B. Switching Table for DPC

The overall control diagram of the switching-table-based DPC is illustrated in Fig. 2. It can be seen that active and reactive power are the inner loop control variables, and dc-link voltage is the outer loop control variable. The set value of the active power is given by the dc-link voltage set value and the sampling value after PI link with dc bus voltage product again, and the set value of the reactive power is zero to realize unity power factor operation of the PWM rectifier.

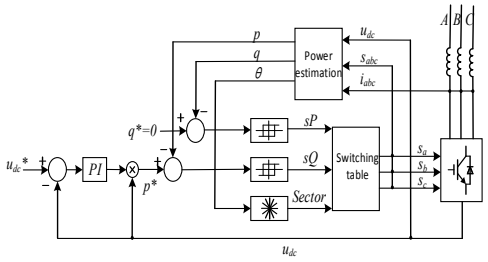

Fig. 2. Overall control diagram of the switching-table-based DPC.

A switching table is the core of DPC algorithm, and it has three input parameters. The first two are the output of the hysteresis controller, sP and sQ respectively. The values of sP and sQ are defined as

$$sP = \begin{cases} 1 & \Delta P > \text{ring-}width \\ hold & -\text{ring-}width < \Delta P < \text{ring-}width \\ 0 & \Delta P < -\text{ring-}width \end{cases} \tag{5}$$

$$sQ = \begin{cases} 1 & \Delta Q > \text{ring-}width \\ hold & -\text{ring-}width < \Delta Q < \text{ring-}width \\ 0 & \Delta Q < -\text{ring-}width \end{cases} \tag{6}$$

The third is the sector of the grid voltage vector, in which the partition method is shown in Fig. 3.

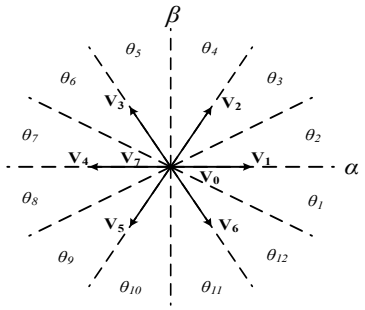

Fig. 3. The sector division in vector space.

According to (4), the differentiations of active and reactive power versus grid voltage position for various rectifier voltage vectors are illustrated in Figs. 4 and 5 separately. These two figures are very important, because it is the direct reaction of (4), and the formation of the new switching table is referred to them.

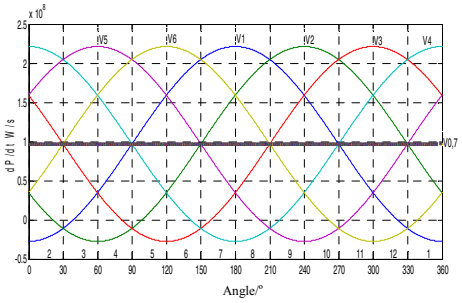

Fig. 4. Differentiation of active power versus grid voltage vector position for various rectifier voltage vectors (p=60 kW).

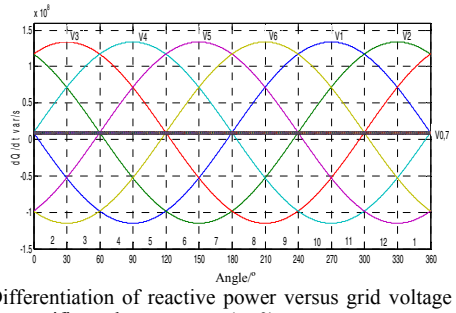

Fig. 5. Differentiation of reactive power versus grid voltage vector position for various rectifier voltage vectors (q=0).

III. Improved TTCV-DPC Algorithm

In this paper, a new switching table is proposed to improve the performance of DPC, and it introduces three vectors to two vectors switching table. The duration time of every voltage vector is calculated based on the principle of deadbeat control of active and reactive power.

A. New Switching Table

The core of the improved TTCV-DPC algorithm is how to build up one effective switching table. In this work, three voltage vectors in some sectors based two-vector switching table are optimized and chosen to build up one new switching table, as summarized in Table I. As seen from this table, it has better performance than the TV-DPC algorithm, and less complexity than the THV-DPC algorithm.

B. Calculation of Voltage Vector Duration Time

As introduced above, the selection of voltage vectors is predefined in the new switching table. Then, the duration time of active voltage vectors (including single vector and two vectors) and zero voltage vectors in the proposed TTCV-DPC algorithm should be decided separately, which is described in details as follows.

For two voltage vectors, the aim is to achieve deadbeat control of active power [8], so the duration time of active voltage vector t_a and zero voltage vector t_z can be calculated based on this principle. It should be known that the value of t_a may exceed the control period t_{sc} or even become negative during dynamic procedure. In this case, only the active voltage vector will be used during the control period to maintain system stability.

For three voltage vectors, both active and reactive power will realize deadbeat control simultaneously [9]. It is expected that by reasonably adjusting the duration time of three voltage vectors, both active and reactive power will approach as close as possible to their reference respectively [10]. So the duration time of two active voltage vectors t_{a1}, t_{a2} and zero voltage vector t_{z1} can be obtained based on this principle. This method also faces with the problem that the sum of t_{a1} and t_{a2} may exceed the control period t_{sc} or get negative during dynamic procedure. In that case, only two active voltage vectors will be used during the control period [11].

At last, the sequence of active and zero voltage vectors should be optimized and then determined to achieve minimal jumps between two adjacent vectors, which can reduce the switching loss as much as possible.

IV. Simulation and Experiment Analysis

Simulation studies are conducted to verify the improved TTCV-DPC algorithm. To prove the performance of the TTCV-DPC, the comparison of grid-side current total harmonic distortion (THD) and power fluctuation between the two control strategies are made. The results are shown in Figs. 6-8 respectively.

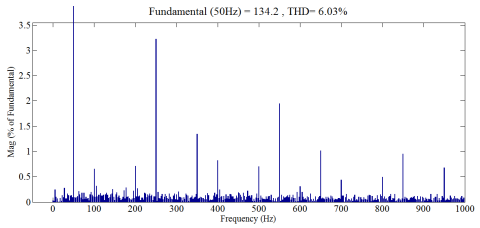

Fig. 6. The harmonic current analysis of the TV-DPC algorithm (THD=6.03%).

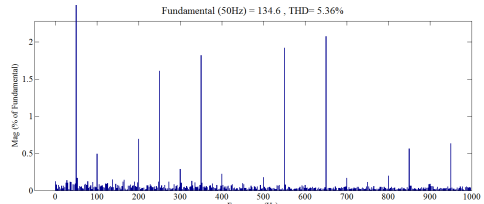

Fig. 7. The harmonic current analysis of the TTCV-DPC algorithm (THD=5.36%).

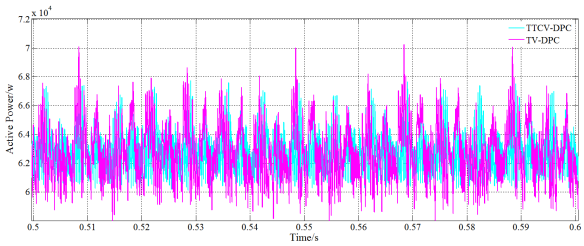

Fig. 8. The comparison of active power of the TTCV-DPC and TV-DPC algorithm.

It can be seen from Fig. 8 that the TTCV-DPC algorithm has less power ripples than the TV-DPC algorithm. In terms of grid-side current THD, the TTCV-DPC algorithm decreases by 0.67% than the TV-DPC algorithm which is shown in Figs. 4 and 5 respectively.

Apart from the simulation study, experimental platform has also been built up, which is shown in Fig.9. It is consisted of fuse protector, filter inductance, IGBT-bridge rectifier, dc-link capacitor, sensors and control board. Some relevant experiments have been done to verify theoretical investigations on the proposed TTCV-DPC algorithm, and some experiments, dc-link voltage and phase voltage and current, are shown in Fig.10.

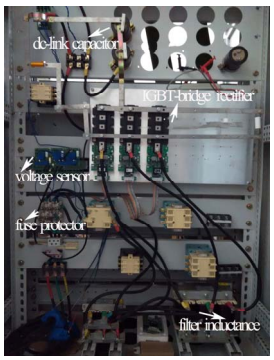

Fig. 9. The experimental platform of the PWM rectifier.

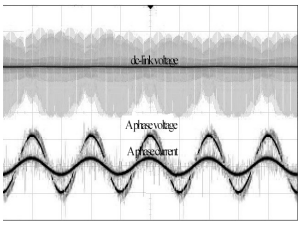

Fig. 10. The experimental waveform of dc-link voltage and phase voltage and current.

It can be seen from Fig.10 that the proposed algorithm can realize the phase position of phase voltage and phase current are the same, so that the PWM rectifier can operate under the unit power factor. Besides, the dc-link voltage is adjustable and stable, which make up the defects of the traditional rectifier.

V. Conclusion

In this paper, a novel TTCV-DPC algorithm of three-phase PWM rectifier has been proposed. The simulations illustrate less power ripples and lower grid-side current THD based on the TTCV-DPC strategy, and the relevant experiments have also confirmed the feasibility of this control strategy.

Acknowledgements

This work has been partly supported by National Natural Science Foundation of China(NSFC 51377065 and 61301035), Hubei Province Science and Technology Supporting Program (2014BAA035).

References

[1] B. Singh, B. N. Singh, A. Chandra, K. Al-Haddad, A. Pandey, and D. P. Kothari, "A review of three-phase improved power quality ac-dc converters," *IEEE Trans. Ind. Electron.*, vol. 51, no. 3, pp. 641–660, Jun. 2004.

[2] M. R. Islam, F. Rahman, and W. Xu, *Advances in Solar Photovoltaic Power Plants*, Springer-Verlag Berlin Heidelberg, Jun. 2016.

[3] Y. Zhang, J. Zhu, W. Xu, and Y. Guo, "A simple method to reduce torque ripple in direct torque controlled permanent magnet synchronous motor by using vectors with variable amplitude and position," *IEEE Trans Ind. Electron.*, vol. 58, no. 7, pp. 2848–2859, Jul. 2011.

[4] J. Rodriguez, J. Dixon, J. Espinoza, J. Pontt, and P. Lezana, "PWM regenerative rectifiers: State of the art," *IEEE Trans. Ind. Electron.*, vol. 52, no. 1, pp. 5–22, Feb. 2005.

[5] M. Malinowski, M. P. Kazmierkowski, and A. M. Trzynadlowski, "A comparative study of control techniques for PWM rectifiers in ac adjustable speed drives," *IEEE Trans. Power Electron.*, vol. 18, no. 6, pp. 1390–1396, Nov. 2003.

[6] S.A. Larrinaga and M.A. Rodriguez, "Predictive direct power control – a new control strategy for DC/AC converters," *Annual Conference of the IEEE Industrial Electronics Society (IECON)*, 2006, pp. 1661-1666.

[7] Akagi, H., Y. Kanazawa and A. Nabae, "Instantaneous Reactive Power Compensators Comprising Switching Devices without Energy Storage Components," *IEEE Trans. Ind. Appl.*, vol. IA-20, no. 3, pp. 625 – 630, May 1984.

[8] S.A. Larrinaga, M.A.R. Vidal, E. Oyarbide and J.R.T. Apraiz, "Predictive control strategy for dc/ac converters based on direct power control," *IEEE Trans. Ind. Electron.*, vol. 54, no. 3, pp. 1261–1271, Jul. 2007.

[9] X. Wang, W. Xu, Y. Zhao, and X. Li, "Modified MPC algorithm for NPC inverter fed disc coreless permanent magnet synchronous motor," *IEEE Trans.Appl. Superconduct.*, 2016, in press.

[10] Y. Lei, W. Xu, C. Mu, Z. Zhao, H. Li, and Z. Li, "New hybrid damping strategy for grid-connected photovoltaic inverter with LCL filter," *IEEE Trans. Appl. Superconductivity*, vol.24, no.5, Article#: 0601608, Oct. 2014.

[11] G. Escobar, A. Stankovic, J. Carrasco, E. Galvan, and R. Ortega, "Analysis and design of direct power control (DPC) for a three phase synchronous rectifier via output regulation subspaces," *IEEE Trans. Power Electron.*, vol. 18, no. 3, pp. 823–830, May 2003.

TABLE I. New Switching Table for DPC of PWM Rectifier

Sector / SPSQ	θ_1	θ_2	θ_3	θ_4	θ_5	θ_6	θ_7	θ_8	θ_9	θ_{10}	θ_{11}	θ_{12}
0 0	V_1 V_6 $V_{0,7}$	V_1 $V_{0,7}$	V_1 V_2 $V_{0,7}$	V_2 $V_{0,7}$	V_2 V_3 $V_{0,7}$	V_3 $V_{0,7}$	V_3 V_4 $V_{0,7}$	V_4 $V_{0,7}$	V_4 V_5 $V_{0,7}$	V_5 $V_{0,7}$	V_5 V_6 $V_{0,7}$	V_6 $V_{0,7}$
0 1	V_1 $V_{0,7}$	V_1 V_2 $V_{0,7}$	V_2 $V_{0,7}$	V_2 V_3 $V_{0,7}$	V_3 $V_{0,7}$	V_3 V_4 $V_{0,7}$	V_4 $V_{0,7}$	V_4 V_5 $V_{0,7}$	V_5 $V_{0,7}$	V_5 V_6 $V_{0,7}$	V_6 $V_{0,7}$	V_1 V_6 $V_{0,7}$
1 0	V_5 $V_{0,7}$	V_5 $V_{0,7}$	V_6 $V_{0,7}$	V_6 $V_{0,7}$	V_1 $V_{0,7}$	V_1 $V_{0,7}$	V_2 $V_{0,7}$	V_2 $V_{0,7}$	V_3 $V_{0,7}$	V_3 $V_{0,7}$	V_4 $V_{0,7}$	V_4 $V_{0,7}$
1 1	V_3 $V_{0,7}$	V_3 $V_{0,7}$	V_4 $V_{0,7}$	V_4 $V_{0,7}$	V_5 $V_{0,7}$	V_5 $V_{0,7}$	V_6 $V_{0,7}$	V_6 $V_{0,7}$	V_1 $V_{0,7}$	V_1 $V_{0,7}$	V_2 $V_{0,7}$	V_2 $V_{0,7}$

2nd International Conference on Electrical, Computer & Telecommunication Engineering (ICECTE)
8-10 December 2016, Rajshahi-6204, Bangladesh

Human Iris as a Biometric for Identity Verification

Abdul Matin[1*], Firoz Mahmud[2], Syed Tauhid Zuhori[2], Barshon Sen[2]
[1]Department of Electrical and Computer Engineering
[2]Department of Computer Science and Engineering
Rajshahi University of Engineering & Technology
Rajshahi, Bangladesh
ammuaj.cse@gmail.com, fmahmud.ruet@gmail.com, tauhid.ruet04@gmail.com, barshon.sen@ruet.ac.bd

***Abstract*—The use of human biometrics for automatic identity verification has become widespread. Mostly used human biometrics are face, fingerprint, iris, gait, retina, voice, hand geometry etc. Among them iris is an externally visible, yet protected organ whose unique epigenetic pattern remains stable throughout one's whole life. These characteristics make it very attractive to use as a biometric for identifying individuals. This paper presents a detailed study of iris recognition technique. It encompasses an analysis of the reliability and the accuracy of iris as a biometric of person identification. The main phases of iris recognition are segmentation, normalization, feature encoding and matching. In this work automatic segmentation is performed using circular Hough transform method. Daugman's rubber sheet model is used in normalization process. Four level phase quantization based 1D Log-Gabor filters are used to encode the unique features of iris into binary template. And finally the Hamming distance is considered to examine the affinity of two templates in matching stage. We have experimented a better recognition result for CASIA-iris-v4 database.**

Keywords— Biometric Identification, Iris Recognition, Pattern Recognition, 1D-Log Gabor Filter

I. INTRODUCTION

Biometric identification is a very popular trend for identity verification due to its higher accuracy and flexibility nowadays. Different biometric recognition techniques like facial recognition, iris scanning, retina scanning, fingerprint scanning, voice verification, gait recognition, hand geometry and hand writing recognition etc. have already been developed by the researchers [1] and they are being used extensively in practical life to verify an individual. This paper is explaining an iris recognition process which is one of the most reliable and secure biometric recognition technique and shows higher accuracy compared to other biometric techniques [2]. The iris pattern contains huge amount of unique features and even two eyes of an individual and identical twins also possess uncorrelated iris patters [3]. A frontal view of the human eye is shown in Fig. 1. The average diameter of human iris is about 12 mm and pupil size varies from 10% to 80% of iris diameter [4]. The externally visible surface of the multi-layered iris often varies in color and appears as a zigzag pattern [3]. The pattern of human iris remains stable throughout the whole lifetime of a person and so it is more secure to use iris features as identification metrics. Besides there are more other properties of iris as an identifier; some of which are listed below.

Properties of the Iris as an Identifier

- Random pattern of great complexity & uniqueness
- Stable features from age three to whole life
- Highly protected, internal organ of the eye
- Externally visible, from distance up to some meters
- The two eyes of an individual contain completely independent iris patterns
- Identical twins possess uncorrelated iris patterns

At first the French ophthalmologist Alphonse Bertillon proposed to use iris patterns as a basis for personal identification [5] but Cambridge Researcher, John Daugman implemented a working automated iris recognition system for the first time [2]. Though the Daugman system is the most successful and popular, some other systems have also been developed including Wildes et al. [6], Lim et al. [7], Boles and Boashash [8]. Daugman [9] used Integro-differential operator for pupil detection, Li.Ma et al., [13] used Hough transformation and extracted features using spatial filter. Wildes et al., [14] uses Hough transform and gradient edge detection for pupil detection and Laplacian pyramid for analysis of the Iris images. Boles and Boashash [8] uses zero-crossing method with dissimilarity functions of matching. Lim et al., [7] 2D Haar Transform for feature extraction and a new winner selection method designed for iris recognition. A. Poursaberi and H. N. Araabi [15] use wavelet Daubechies for feature extraction. A different iris recognition approach based on human-interpretable features was proposed by Jinaxu Chen et al. [16]. About each system faces the challenge of recognizing noisy iris images. Some issues and challenges in designing iris recognitions system were reviewed in paper [17]. The basic steps of iris recognition are almost same in all developed methods. Our experiment consist of five major steps, graphically shown in fig. 2 and they are; iris image acquisition, segmentation, normalization, feature encoding and matching. The performance of iris recognition is highly dependent on the earlier stage; segmentation where the iris region of an eye image is located.

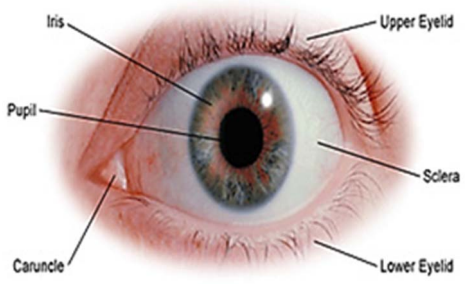

Fig. 1.Front view of a human eye

The rest stages are normalization means converting the extracted iris area into constant rectangular dimension, and feature encoding which means creating a bit-wise template containing only the most discriminating features of iris. The input of the system is an eye image and the output is a template consisting of zero and one. And only these templates are considered in matching stage to classify an individual either as genuine or imposter.

II. IRIS SEGMENTATION

The first stage if iris recognition technique is isolating iris area from an input eye image. The interior image portion of two circles is identified as iris region where one circle defines the

iris-sclera boundary and the another one defines iris-pupil boundary shown in Fig. 3. The upper and lower part of eyelids and eyelashes may corrupt the actual iris region. So their positions are also detected and isolated as noise region.

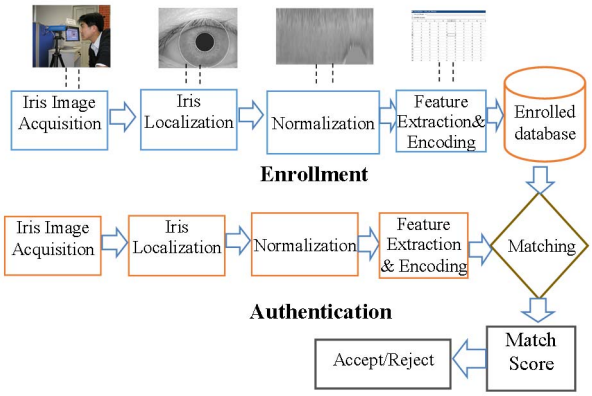

Fig. 2. A basic model for face recognition technique

A. *Specular Noise and Eyelash Detection*

Eye image may contains specular reflection and since the intensity values at specular region are normally higher than any other regions in eye image it can be easily detected by thresholding. Sometimes eyelashes may cover some pixels of iris region described in the method presented by Kong and Zhang [9]. It can be detected by convoluting separable eyelashes with Gaussian smoothing.

B. *Iris and Pupil Localization*

Accurate localization of iris and pupil in an eye image is very important for successful person identification. Hough transform is widely used for this purpose. An automatic segmentation algorithm based on the circular Hough transform is employed by Wildes et al. [6], Kong and Zhang [11]. At first, the eye image is smoothed to reduce noise using Gaussian filtering and after that gradient of intensity values is calculated both in vertical and horizontal direction. The local maxima in gradient values are suppressed and finally candidate edge pixels are isolated by thresholding process. Considering each edge pixel as a center of circle with certain radius value voting is performed in Hough space satisfying following circle equation where x_c and y_c are center coordinates and radius is r.

$$(x - x_c)^2 + (y - y_c)^2 - r^2 = 0\,. \qquad (1)$$

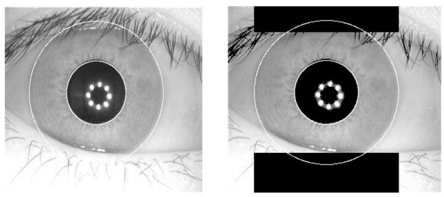

Fig. 3. Iris and pupil boundary localization (**left**), eyelids detection (**right**)

A maximum voted point in Hough space is considered as the best positioned center coordinate and the radius for which,the point became maximum is considered as the radius of iris boundary circle. Similar procedure is applied to calculate the center coordinates and radius of pupil. The circular portion between pupil boundary and iris boundary is considered as the required iris region shown in Fig. 3. For CASIA database the radius of iris is varied from 90 to 150 pixels while the pupil radius ranges from 28 to 75 pixels.

C. *Eyelids detection*

The Parabolic Hough transform is used to detect the eyelids by approximating the upper and lower eyelids with parabolic arcs which are represented as

$$(-(x - h_j)\sin\theta_j + (y - k_j)\cos\theta_j)^2 = a_j\left((x - h_j)\cos\theta_j + (y - k_j)\sin\theta_j\right), \qquad (2)$$

where a_j controls, (h_j, k_j) the curvature, is the peak of the parabola and θ_j is the angle of rotation relative to the x-axis [6][9]. Linear Hough transform is used to detect the edge line of both upper and lower eyelids. The rectangular regions in between the detected fitted lines to outer edge boundary of same side of the eye image are isolated as eyelids. The detected eyelids portions are considered as noise which are graphically shown in Fig. 3.

III. NORMALIZATION

After proper segmentation of iris region, the next step is to normalize it into a constant rectangular block to prevent its spatial inconsistency which may occur for several reasons like as iris stretching caused by dilation of pupil for illumination variation, imaging distance variation, rotation of the camera, head angle, eye rotation etc. [18]. Besides the pupil region is not always concentric within the iris region, and is usually slightly displaced [4]. So normalization is performed to minimize all of these problems. All the pixels in iris region are remapped to polar coordinates (r, θ) using homogenous rubber sheet model invented by Daugman [10] where r is the interval between [0,1] and θ is between angle [0,2π].

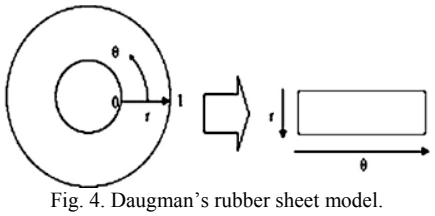

Fig. 4. Daugman's rubber sheet model.

The iris region from (x,y) Cartesian coordinates is remapped to the normalized polar representation using following formula when pupils are not concentric.

$$I\big(x(r,\theta), y(r,\theta)\big) \rightarrow I(r,\theta)\,, \qquad (3)$$

With

$$x(r,\theta) = (1 - r)x_p(\theta) + r x_l(\theta)\,, \qquad (4)$$

$$y(r,\theta) = (1 - r)y_p(\theta) + r y_l(\theta)\,, \qquad (5)$$

where the iris region image is $I(x, y)$, original Cartesian coordinates are (x, y), the corresponding normalized polar coordinates are (r, θ), and x_p, y_p and x_l, y_l are pupil and iris boundary coordinates along the θ direction. Though pupil dilation is considered in Daugman rubber sheet model but the rotational inconsistency of eye image is not considered in normalization stage rather it will be solved during matching process. Some successfully normalized patterns are shown in Fig. 5.

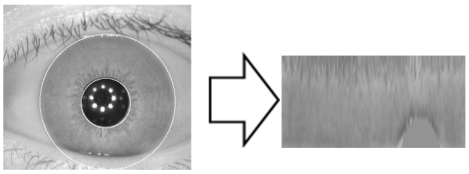

Fig. 5. Normalized iris pattern (**right**) with eye image 'S1084L01' (**left**) from CASIA-V4 database

IV. FEATURES ENCODING

The features in normalized iris pattern are encoded using 1D Log-Gabor Wavelets. At first 2D iris patterns are broken up into 1D signals and they are convoluted with the output response of 1D Log-Gabor Wavelets. To avoid noisy output of filters, intensity values at known noise area of normalized iris pattern are replaced by the average of surrounding pixels. The output of Wavelets filters is quantized into four phase levels using Daugman method [4]. Each different phase is leveled by two binary number following grey code so that only one bit changes between two consecutive phases. The frequency response of a Log-Gabor filter is given as

$$G(f) = \exp\left(\frac{-(\log(\frac{f}{f_0}))^2}{2(\log(\frac{\sigma}{f_0}))}\right), \quad (6)$$

where center frequency is f_0, and σ represents the bandwidth of the filter. Details of Log-Gabor filter are presented by Field [19].

V. TEMPLATE MATCHING

Hamming distance has been used here as the metric for bitwise matching of two iris templates. And during matching, noise masks are kept in consideration. The average of the sum of the value of bitwise exclusive OR is calculated between two templates only for the significant bits indicated by zero at corresponding position in the noise mask. The formula to calculate hamming distance is shown below.

$$\mathrm{HD} = \frac{1}{\mathrm{N} - \sum_{K=1}^{N} Xn_k(OR)Yn_k} \times \sum_{j=1} X_j(XOR)Y_j(AND)Xn_f'(AND)Yn_f', \quad (7)$$

where X_j and Y_j are two bitwise templates, Xn_j and Yn_j are the corresponding noise masks for X_j and Y_j, and the total number of bits of each template are N. Theoretically the Hamming distance for two templates of same iris should be 0.0 and for different iris it should be greater than 0.5. But practically for noisy and rotationally inconsistent eye images results differ slightly. The minimum Hamming distance is chosen as final value. Hamming distance is also calculated with shifting the templates into left and right for several times to minimize the rotational inconsistencies like as fig. 6.

VI. EXPERIMENTAL RESULTS

In this work CASIA-Iris-Interval Version 4 database has been used where there are 1565 8 bit gray-level JPEG images of both left and right eyes of 249 different individuals [20]. The rate of success of automatic segmentation using Hough transform has become 91.56% which is better than some previous result shown in Table 1.Only the successfully segmented irises have been normalized into 20 × 240 pixels rectangular patters and they have been successfully encoded to 20 × 480 pixels binary template.

TABLE 1. AUTOMATIC IRIS SEGMENTATION RESULT

Methods	Segmentation rate (%)
Libor Masek[21]	83.00
Proposed Work	91.56

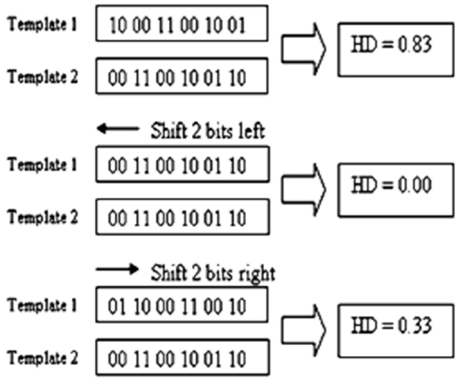

Fig. 6. An illustration of hamming distance with shifting.

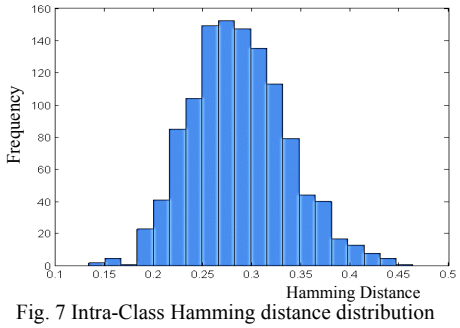

Fig. 7 Intra-Class Hamming distance distribution

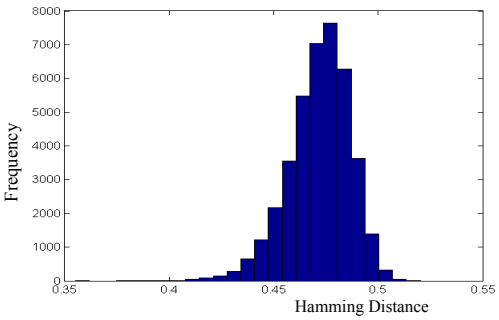

Fig. 8. Inter-Class Hamming distance distribution

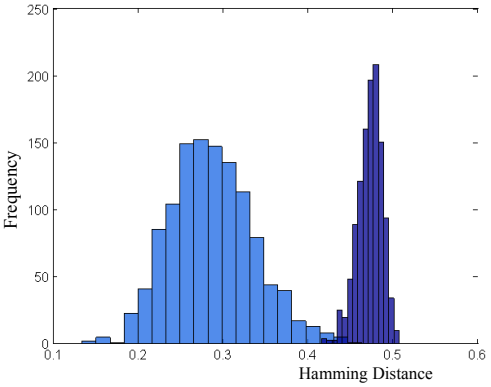

Fig. 9. Intra-Class & Inter-Class Hamming distance distribution

A. Intra-Class Comparisons

Component Comparison between images of an identical eye taken by sensor camera from different angles is termed as intra-

class comparison. In this work 1160 intra-class comparisons of iris templates were successfully performed and their hamming distance distribution is shown in Fig. 7.

B. Inter-Class Comparisons

Inter-Class comparison is defined as the comparison between two images of different eyes. Total 40,000 intra-class comparisons were executed successfully for this work and the histogram of distribution is shown in Fig. 8. Among all the results of intra-class comparisons and inter-class comparisons very few values were seen to overlap. Their combined hamming distance distribution for 1164 comparisons is shown in Fig. 9.

C. False Accept and False Reject Rates

Some of our experimented false accept rates (FAR) and false reject rates (FRR) for different threshold value have been shown in table 2. The value of FAR and FRR has become optimal for the threshold value 0.42 for the CASIA database.

We have also experimented the recognition accuracy of iris considering 200 images as training set and another 200 images as testing set. And we have derived a better recognition accuracy than some previous result shown in table 3.

TABLE 2. FAR & FRR OF CASIA-IRIS-V4 DATABASE

Threshold	FAR (%)	FRR (%)
0.20	0.000	97.337
0.30	0.000	37.801
0.38	0.000	3.952
0.40	0.000	1.890
0.42	0.172	0.945
0.44	3.090	0.258
0.48	69.785	0.000
0.50	99.142	0.000

TABLE 3. IRIS RECOGNITION ACCURACY COMPARISON

Features	Methods	Recognition Rate (%)
Iris Features	Boles et al., [8]	92.64
	Daugman[22]	98.60
	Masek et al.,[23]	94.91
	Proposed Method	99.17

VII. CONCLUSION

Nowadays the access to most of the highly secured places are controlled by human iris based verification technique because of its higher accuracy and robustness. Our experiment of Hough transformed based iris recognition technique also strongly supports the claim about its higher accuracy and reliability. This research work was conducted using CASIA –iris-version 4.0 database with the experimented parameters provided by L. Masek [18] for CASIA-version 1.0. The experimental result for updated database showed better result both in segmentation and recognition. It was also observed that correct segmentation is the most vital phase of iris recognition technique. So special concern need to be given on iris image acquisition and segmentation. Finally it can be clarified that the significance of human iris as a person identification is highly acceptable and appreciable. Though the experiment was conducted in constrained database we are optimistic to consider more dynamic dataset for future work to evaluate its global performance.

VIII. REFERENCES

[1] S. Sanderson, J. Erbetta. Authentication for secure environments based on iris scanning technology. IEE Colloquium on Visual Biometrics, 2000.

[2] Y. Wang, T. Tan, Y. Wang, and D. Zhang, "Combining face and iris biometric for identity verification", Proc. 4th Int. Conf. on Audio- and Video-Based Biometric Person Authentication (AVBPA) 1, 805-813, 2003

[3] E. Wolff. Anatomy of the Eye and Orbit. 7th edition. H. K. Lewis & Co. LTD, 1976

[4] J. Daugman. How iris recognition works. Proceedings of 2002 International Conference on Image Processing, Vol. 1, 2002.

[5] A. Bertillon. La couleur de l'iris, Revue scientifique, France, 1885.

[6] R. Wildes, J. Asmuth, G. Green, S. Hsu, R. Kolczynski, J. Matey, S. McBride. A system for automated iris recognition. Proceedings IEEE Workshop on Applications of Computer Vision, Sarasota, FL, pp. 121-128, 1994.

[7] S. Lim, K. Lee, O. Byeon, T. Kim. Efficient iris recognition through improvement of feature vector and classifier. ETRI Journal, Vol. 23, No. 2, Korea, 2001.

[8] W. Boles, B. Boashash. A human identification technique using images of the iris and wavelet transform. IEEE Transactions on Signal Processing, Vol. 46, No. 4, 1998.

[9] J. Daugman. How iris recognition works. Proceedings of 2002 International Conference on Image Processing, Vol. 1, 2002

[10] Richard P. Wildes, "Iris Recognition: An Emerging Biometric Technology," *Proceedings of the IEEE*, vol. 85, no. 9, pp. 1348-1363, 1997.

[11] W. Kong, D. Zhang, "Accurate iris segmentation based on novel reflection and eyelash detection model," *Proceedings of 2001 International Symposium on Intelligent Multimedia, Video and Speech Processing*, Hong Kong, 2001.

[12] P. and H. N. Araabi, "Iris Recognition for Partially Occluded Methodology and Sensitivity Analysis", EURASIP journal on Advances in Signal processing, vol. 2007, **(2005)**, Article ID 36751

[13] L. Ma, T. Tan, Y. Wang and D. Zhang, "Efficient Iris Recognition by Characterizing Key Local Variations", IEEE Transactions on Image processing, vol. 13, no. 6, **(2004)** June.

[14] John Daugman, "Iris Recognition," *Tutorial, International Conference on Biometrics*., 2012.

[15] P. and H. N. Araabi, "Iris Recognition for Partially Occluded Methodology and Sensitivity Analysis", EURASIP journal on Advances in Signal processing, vol. 2007, **(2005)**, Article ID 36751.

[16] Jianxu Chen, Feng Shen, Danny Z, Chen and Patrick J. Flynn, "Iris Recognition Based on Human-Interpretable Features," *IEEE Transactions on Information Forensics and Security*., Vol. 11, Issue 7, pp. 1476-1485, 2016.

[17] Kamal Hajari, Kishor Bhoyar, "A Review of Issues and Challenges in Designing Iris Recognition Systems for Noisy Imaging Environment," *International Conference on Pervasive Computing (ICPC)*., 2015.

[18] L. Masek. L. Human Iris Patterns As A form Of Biometric Identification. School of Computer Science and Software Engineering, The University of Western Australia, 2003.

[19] D. Field. Relations between the statistics of natural images and the response properties of cortical cells. Journal of the Optical Society of America, Vol. 4, No. 12, pp. 2379-2394, 1987.

[20] Casia iris image database version 4.0, Available: "http://www.cbsr.ia.ac.cn/english/IrisDatabase.asp" [Accessed: 5th June, 2016]

[21] L. Masek, "Recognition of Human Iris Patterns for Biometric Identification", 2013

[22] J. Daugman, "Statistical Richness of Visual Phase Information: Update on recognizing persons by Iris patterns", International Journal of computer vision, vol. 45, no. 1, (2001), pp. 25-38.

[23] L. Ma, Y. Wang, and T. Tan, "Iris Recognition Based on Multichannel Gabor Filtering,"Proc. Fifth Asian Conf. ComputerVision,vol. I, pp. 279-283, 2002.

Designing a Double Sourced Converter

Adnan Mohammad
Department of Electrical and Electronic Engineering
Bangladesh University of Engineering and Technology (BUET)
Dhaka, Bangladesh
Adnanmohammad1@hotmail.com

***Abstract*— This paper proposes a double sourced converter which performs both rectifier (ac to dc) and chopper (dc to dc) actions in a single circuit instead of two separate converters. Switching signals for two different modes are simulated by designing a controller to get the desired output from the proposed converter. In both modes of operation the output is dc. All necessary simulations are performed in PSIM.**

Keywords—rectifier, chopper, double sourced converter and PWM circuit.

I. INTRODUCTION

Ac to dc converter is defined as rectifier which converts bidirectional signal to unidirectional signal [1]. The main supply system is ac in nature. So, rectifiers are used to get dc supply from the ac system. Controlled rectifiers are used to get variable and low dc voltage from the ac source [1].

A dc chopper or buck converter is a dc to dc converter which provides a low dc output voltage from higher dc input voltage [2-4]. Switching with changing pulse widths performs the step down action on the output of a dc chopper [5]. Both of the circuits include LC filter to achieve pure dc component [6-7].

Rectifiers and chopper have huge applications in dc power supplies, dc drives, HVDC transmission system and etc. The main difference between a controlled rectifier and chopper is the input source they use (ac and dc sources respectively). Recent research realizes these two converters in a common circuit [5]. In this paper, a converter is proposed to get dc output from either dc or ac input using one circuit instead of two separate converters. Step down operation can be performed depending on the width of switching pulses. The great advantage of this design is that, this converter can be used in both ac and dc systems to get the dc output.

Based on a control signal the converter changes its mode of operations (either rectification or chopper). Input can be either dc or ac but the output is always dc. Finally, rectification and dc chopper actions of the proposed converter are simulated in PSIM.

II. OPERATION OF THE PROPOSED CONVERTER AND CONTROLLER DESIGN

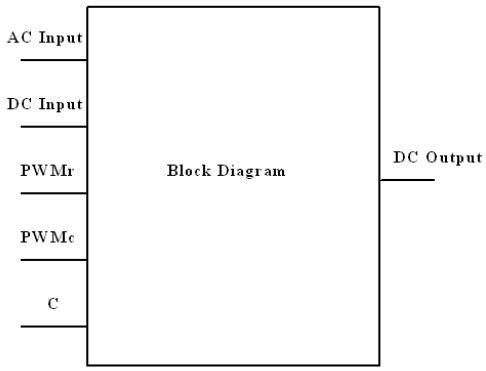

Fig. 1 Block diagram of the proposed double sourced converter.

Fig.1 shows the block diagram of proposed converter. The output of this converter is dc but the input can be either dc or ac. Depending on control signal C, the input will be selected and the converter will act as either rectifier or dc chopper. PWMr and PWMc are the switching signals for rectifier and chopper respectively.

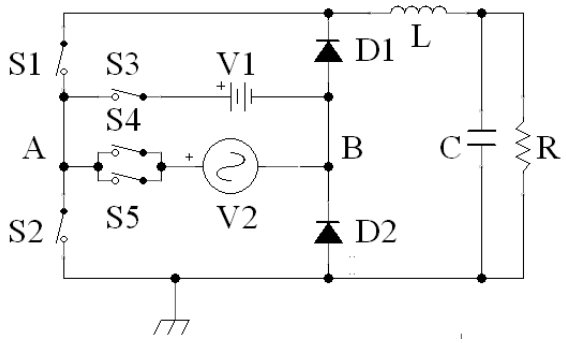

Fig. 2 The proposed double sourced converter.

Fig.2 shows the circuit of proposed converter. V1 and V2 are dc and ac input to the converter. S3 to S5 are isolation switches which isolate rectification and chopper actions. For rectification purpose all switching devices except S3 will be in operation and for dc chopping circuitry S1, S3, D1 and D2 will be in operation. In this circuit, L is the inductor and C is the capacitor which are used to form a low pass filter to get pure dc output voltage. The dc output is taken across a load resistor R.

978-1-5090-5785-6/16/$31.00 ©2016 IEEE

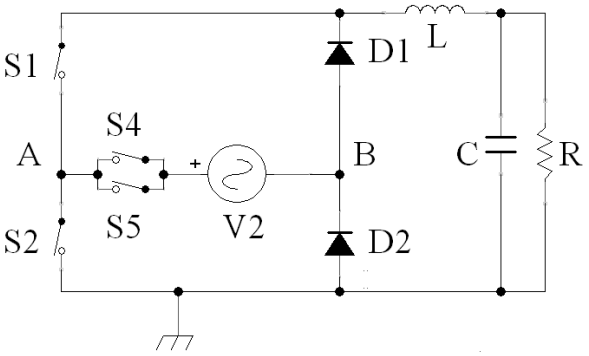

(a)

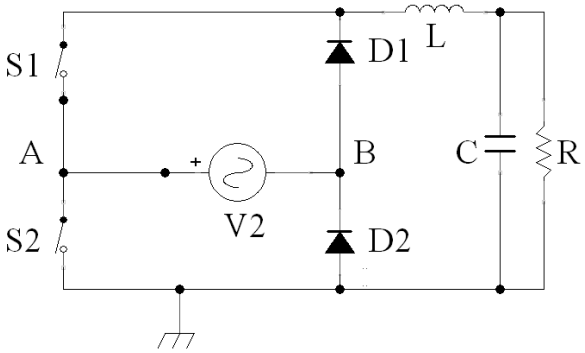

(b)

Fig. 3(a) Rectifier circuit in the proposed converter and (b) The equivalent rectifier circuit.

If S3 of Fig. 2 is out of operation then, the equivalent circuit becomes a rectifier with isolation switches S4 and S5 (Fig.3(a)). In this mode of operation, each of the isolation switches (S4 and S5) will conduct in each half cycle of the sinusoidal input (S4 in positive cycle and S5 in negative cycle) and treated as a short circuit. The equivalent rectifier treating S4 and S5 shorted is shown in Fig.3 (b). S1 and S2 are operated by a particular PWM. In positive cycle of ac input, S1 and D2 are operated and in negative cycle of input D1 and S2 are operated. The rectified dc voltage is available across the load (R). The operations in both cycles are shown in Fig. 4.

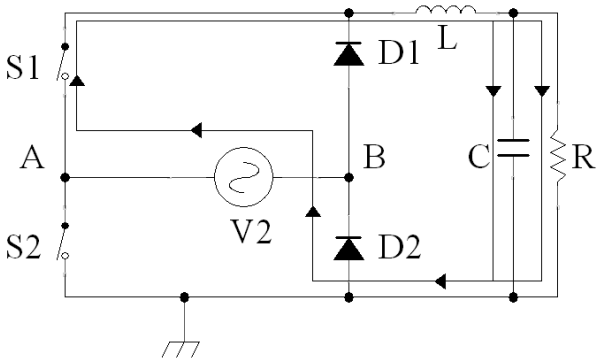

Fig. 4 (a) Rectifier operation in positive cycle of input.

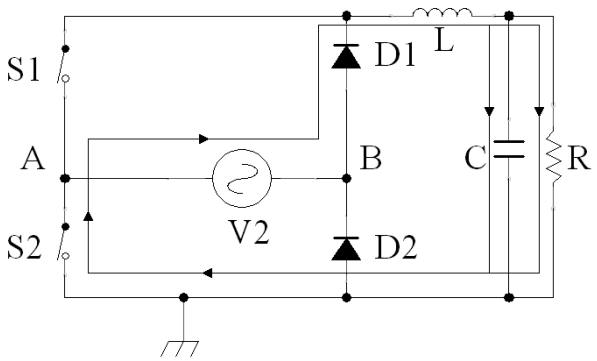

Fig. 4 (b) Rectifier operation in negative cycle of the input.

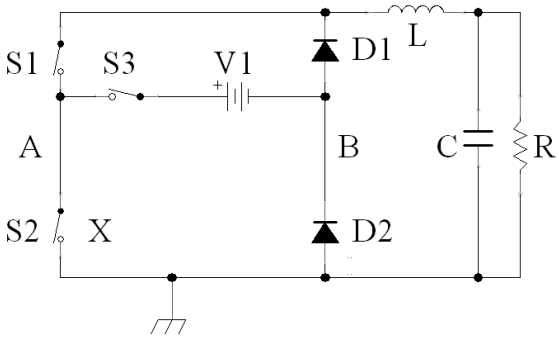

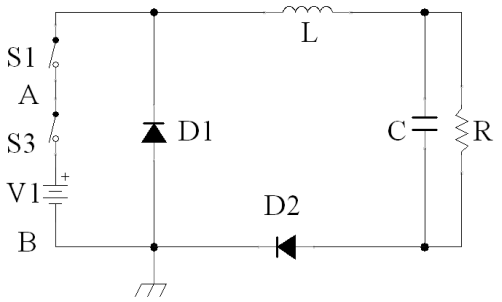

Fig. 5 Dc chopper in the proposed converter.

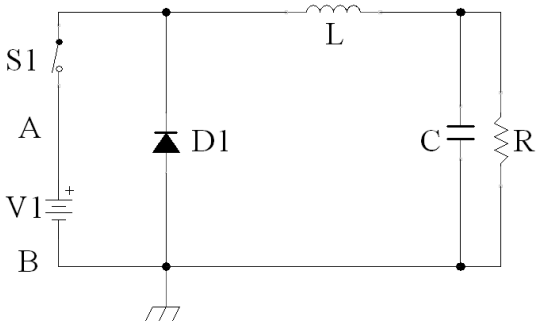

Fig. 6 The equivalent buck chopper circuit.

If S2, S4 and S5 of Fig. 2 are out of operation then, the equivalent circuit becomes a dc chopper with isolation switch S3 (Fig.5). *X* in the Fig.5 indicates that, S2 is out of operation. S3 will be in continuous operation during this mode. Fig.5 also shows the dc chopper (buck converter) with an extra isolating switch S3 and a diode D2. In conduction state, diode D2 and

switch S3 can be replaced by short circuits. The corresponding equivalent circuit will be exactly like a buck converter (Fig.6).

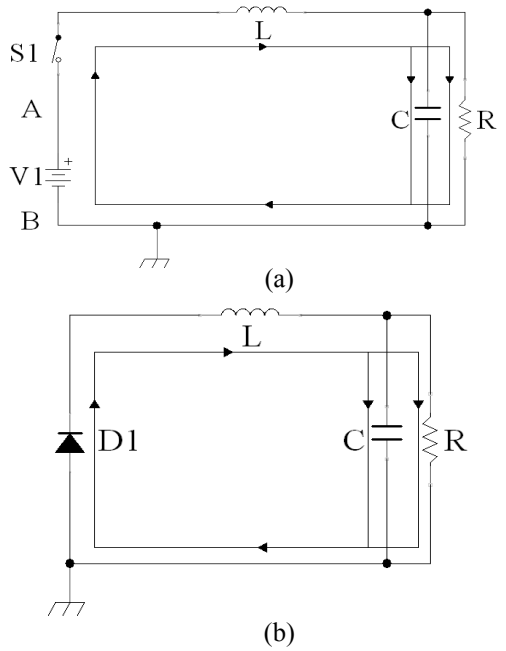

Fig. 7 The operation of buck converter (a) ON switch and (b) OFF switch.

In case of dc chopper operation the current flows from source (V1) to the load via S1 (ON), filter inductor L and filter capacitor C. During this ON switch mode of operation, the inductor stores energy [5]. The ON state mode of operation is shown in Fig.7. At OFF switch state of operation the stored energy in the inductor flows via L, C, R and D1 (freewheeling diode). This is the operation of a buck converter [5].

After showing all the equivalencies this is important to design a controller circuit for operating the proposed converter To do so, Table I is introduced.

TABLE I. DESIGN OF THE CONTROLLER CIRCUIT

C (Control Signal)	Converter`s Operation	Switch				
		S1	S2	S3	S4	S5
1	Rectifier	PWMr.Pp	PWMr.Pn	Low	C.Pp	C.Pn
0	Chopper	PWMc	Low	High	Low	Low

Table I shows the signals for operating the converter. Based on these parameters some equations can be derived for the controller. It clearly shows the state of switches during rectifying and chopper operations. *C* is the control signal, *PWMr* is the pulse width modulated signal for rectification and *PWMc* is the pulse width modulated signal for chopper action. *Pp* and *Pn* are positive and negative cycle detector signal respectively.

$$S1 = C.PWM_r.Pp + \overline{C}.PWM_c \quad (1)$$

$$S2 = C.PWM_r.Pn \quad (2)$$

$$S3 = \overline{C} \quad (3)$$

$$S4 = C.Pp \quad (4)$$

$$S5 = C.Pn \quad (5)$$

C is the control signal which will operate the converter in different modes. Table I shows that, if the control signal is High (1) the converter will act as a rectifier. For low (0) control signal the converter will act as a dc chopper. It is important to note that, Pp and Pn are signals from a comparator which detects positive or negative cycle of the sinusoidal input. Detection of positive and negative input cycles is very necessary for avoiding malfunction of the converter.

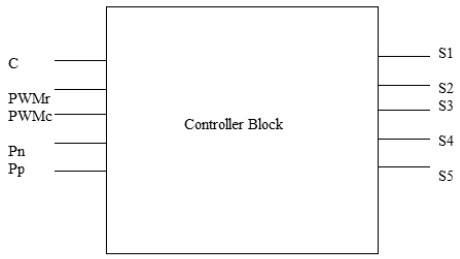

Fig. 8 The controller block.

Fig.8 shows the controller block for the converter. The block is designed using (1) to (5). There are five inputs and five outputs for the five switches of the converter.

III. SIMULATION

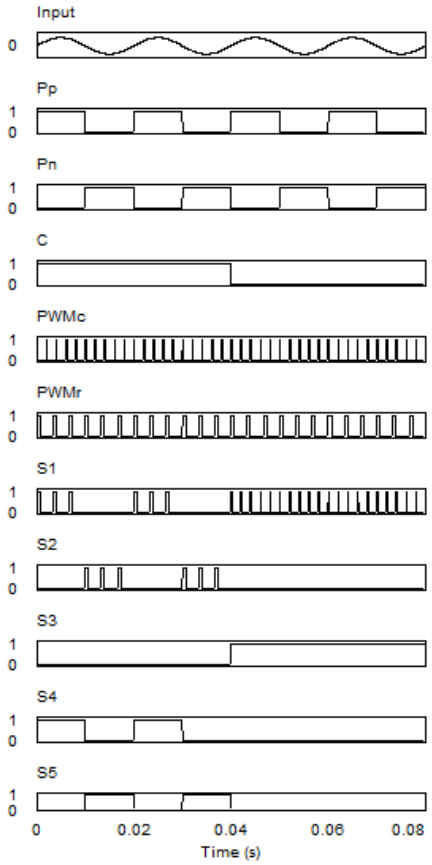

Fig. 9 Generation of switching signals.

Fig. 9 shows the simulated switching signals for the proposed converter. The simulated circuit is given in Fig. 10. A transformer is connected with the input sinusoidal wave so that,

desired low level of the sine wave can be generated for operating the comparator (Fig. 10). From Fig. 9 and Fig. 10 it is seen that, the comparator provides positive pulse (Pp) during positive cycle of input. Correspondingly, a negative cycle detector signal (Pn) is produced. Pn provides high output during the negative half cycle of ac input.

While operating the converter as a rectifier, S4 and S5 act as isolation switches. Isolation of two modes of operation (rectifier and dc chopper) is very important for perfect operation. In this mode of operation, control signal C is high (according to Table I it indicates the rectifier action) and S3 is out of operation (these are shown in Fig. 9). The operations of S4 and S5 are dependent on Pp and Pn. It is also clear from Fig.9 and (4) to (5). S4 operates during the positive half cycle of the input and S5 during negative half cycle providing required isolation. During rectification, S1 and S2 are operated with PWMr.

In chopper operation the required control signal is low (0). For chopper action, S1 and S3 are operated and all other switches are at OFF state. S1 is operated with PWMc. This is also shown in Fig. 9.

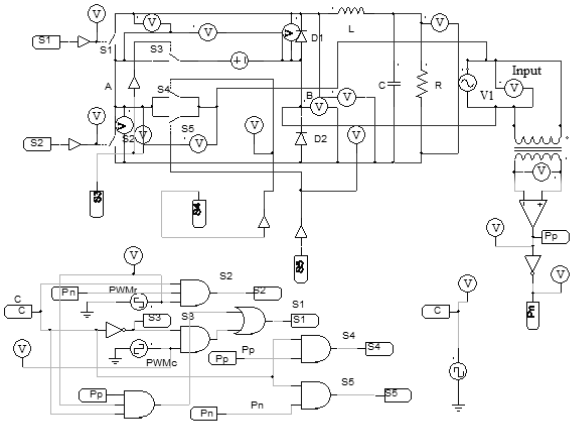

Fig. 10 Simulation circuit in PSIM.

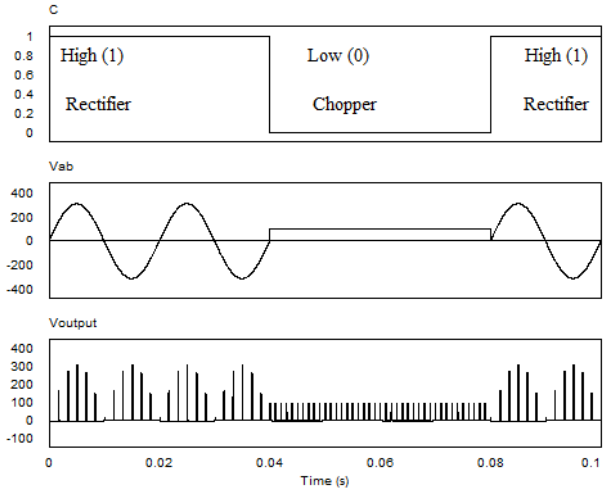

Fig. 11 Control signal, input to the converter and unfiltered output voltage.

Fig. 11 shows the inputs to the converter across 'A' and 'B' terminals for different control commands. Ac and dc sources get connected to AB terminals for high and low control signal respectively. The corresponding dc output voltage at different modes (before filtering) is also shown. In Fig. 12, the filtered dc voltage is given. So, the input to the converter can be either ac or dc but the output is always dc.

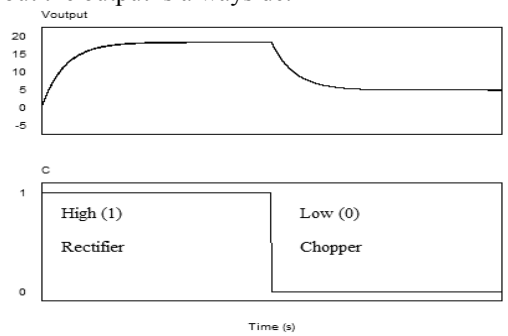

Fig. 12. Control signal and filtered dc output.

IV. CONCLUSION

This paper designs such a single power electronic converter which performs both rectifier and chopper actions. Hence, the great advantage is that, it eliminates the use of two separate converters for rectifier and chopper purposes. The output can be reduced by adjusting the pulse widths. The results are satisfactory. The converter is useful for battery charging application and designing dc drives. In future, it will be implemented in hardware.

REFERENCES

[1] A. Mohammad, A. A. Manzur and A. I. Aziz, "Comparisons among different Types of Single Phase Step Down AC to DC Converters," in International Journal of Computer Applications, vol. 121, no. 5, pp. 13-17, Jul. 2015.

[2] S. K. Mahobia and G. R. Kumrey, "Study and Performance of Single-Phase Rectifiers with Various Type of Parameter," in International Journal in Engineering Technologies and Management Research, vol. 3, no.1 (2016), pp. 9-14, Jan. 2016.

[3] Vikramarajan Jambulingam, "Speed Control of DC Motor Using MOSFET Based Chopper," in International Journal of Engineering Development and Research, vol. 4, Issue 2, pp. 1337-1341, Jun. 2016.

[4] Kirana kumar Venkanagouda Patil and Shankaralingappa C. B. "DC Motor Control Using Chopper for Remote Laboratory Set-Up," in International Journal of Innovative Research in Electrical, Electronics, Instrumentation and Control Engineering, vol. 4, Issue 7, pp.43-47, Jul. 2016.

[5] Mohammad, Adnan; Rahaman, Md.Shafieur; Ahmed, Omar; Aziz, Ashique Ibni; Muntakim, Tahmid Ul; Shaon, Mohammad Shahjalal, "Realization of existence of two buck chopper circuits in a single phase switch controlled full wave rectifier," in 2015 International Conference on Electrical Engineering and Information Communication Technology (ICEEICT), pp.1-5, 21-23 May 2015.

[6] T. J. Liang, L. S. Yang, and J. F. Chen, "Analysis and design of a single phase ac/dc step-down converter for universal input voltage," IET Electr Power Appl., vol. 1, no. 5, pp. 778–784, Sep. 2007.

[7] K. Nishimura, K. Hirachi, S. Komiyama, and M. Nakaoka, "Two buck choppers built-in single phase one stage PFC converter with reduced DC voltage ripple and its specific control scheme," in Proc. IEEE Appl. Power Electron. Conf. Expo., 2008, pp.1378–1383.

Designing a Double Sourced Converter

Adnan Mohammad
Department of Electrical and Electronic Engineering
Bangladesh University of Engineering and Technology (BUET)
Dhaka, Bangladesh
Adnanmohammad1@hotmail.com

***Abstract*— This paper proposes a double sourced converter which performs both rectifier (ac to dc) and chopper (dc to dc) actions in a single circuit instead of two separate converters. Switching signals for two different modes are simulated by designing a controller to get the desired output from the proposed converter. In both modes of operation the output is dc. All necessary simulations are performed in PSIM.**

Keywords—rectifier, chopper, double sourced converter and PWM circuit.

I. INTRODUCTION

Ac to dc converter is defined as rectifier which converts bidirectional signal to unidirectional signal [1]. The main supply system is ac in nature. So, rectifiers are used to get dc supply from the ac system. Controlled rectifiers are used to get variable and low dc voltage from the ac source [1].

A dc chopper or buck converter is a dc to dc converter which provides a low dc output voltage from higher dc input voltage [2-4]. Switching with changing pulse widths performs the step down action on the output of a dc chopper [5]. Both of the circuits include LC filter to achieve pure dc component [6-7].

Rectifiers and chopper have huge applications in dc power supplies, dc drives, HVDC transmission system and etc. The main difference between a controlled rectifier and chopper is the input source they use (ac and dc sources respectively). Recent research realizes these two converters in a common circuit [5]. In this paper, a converter is proposed to get dc output from either dc or ac input using one circuit instead of two separate converters. Step down operation can be performed depending on the width of switching pulses. The great advantage of this design is that, this converter can be used in both ac and dc systems to get the dc output.

Based on a control signal the converter changes its mode of operations (either rectification or chopper). Input can be either dc or ac but the output is always dc. Finally, rectification and dc chopper actions of the proposed converter are simulated in PSIM.

II. OPERATION OF THE PROPOSED CONVERTER AND CONTROLLER DESIGN

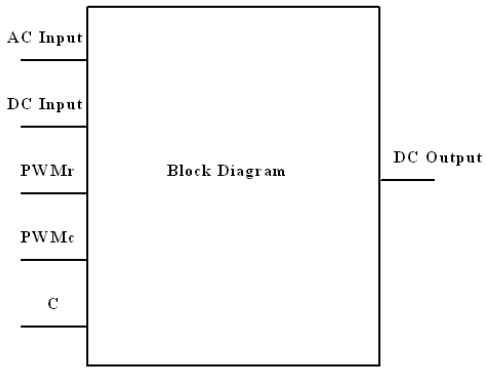

Fig. 1 Block diagram of the proposed double sourced converter.

Fig.1 shows the block diagram of proposed converter. The output of this converter is dc but the input can be either dc or ac. Depending on control signal C, the input will be selected and the converter will act as either rectifier or dc chopper. PWMr and PWMc are the switching signals for rectifier and chopper respectively.

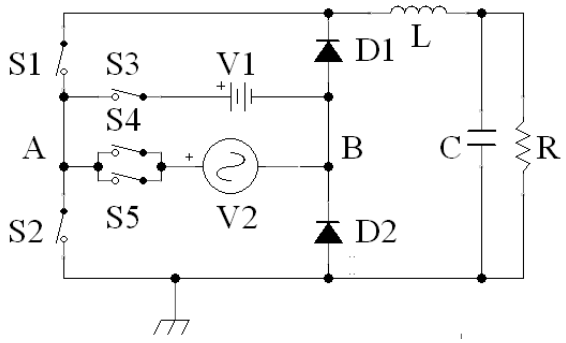

Fig. 2 The proposed double sourced converter.

Fig.2 shows the circuit of proposed converter. V1 and V2 are dc and ac input to the converter. S3 to S5 are isolation switches which isolate rectification and chopper actions. For rectification purpose all switching devices except S3 will be in operation and for dc chopping circuitry S1, S3, D1 and D2 will be in operation. In this circuit, L is the inductor and C is the capacitor which are used to form a low pass filter to get pure dc output voltage. The dc output is taken across a load resistor R.

978-1-5090-5785-6/16/$31.00 ©2016 IEEE

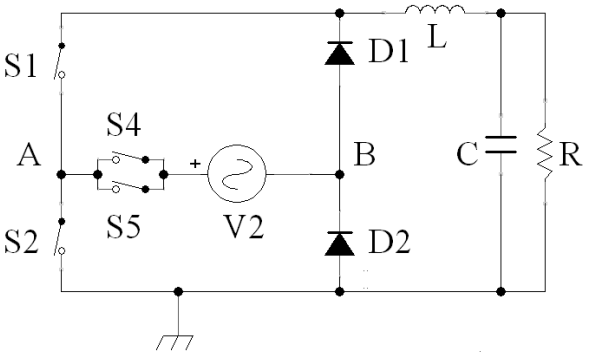

(a)

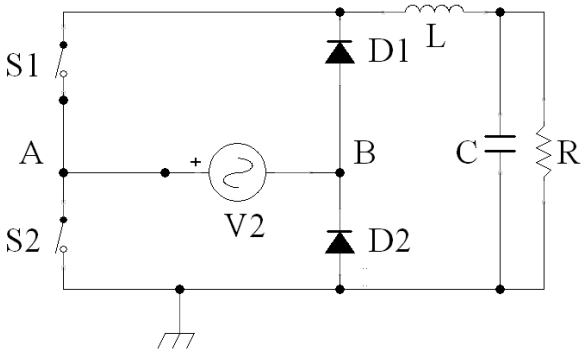

(b)

Fig. 3(a) Rectifier circuit in the proposed converter and (b) The equivalent rectifier circuit.

If S3 of Fig. 2 is out of operation then, the equivalent circuit becomes a rectifier with isolation switches S4 and S5 (Fig.3(a)). In this mode of operation, each of the isolation switches (S4 and S5) will conduct in each half cycle of the sinusoidal input (S4 in positive cycle and S5 in negative cycle) and treated as a short circuit. The equivalent rectifier treating S4 and S5 shorted is shown in Fig.3 (b). S1 and S2 are operated by a particular PWM. In positive cycle of ac input, S1 and D2 are operated and in negative cycle of input D1 and S2 are operated. The rectified dc voltage is available across the load (R). The operations in both cycles are shown in Fig. 4.

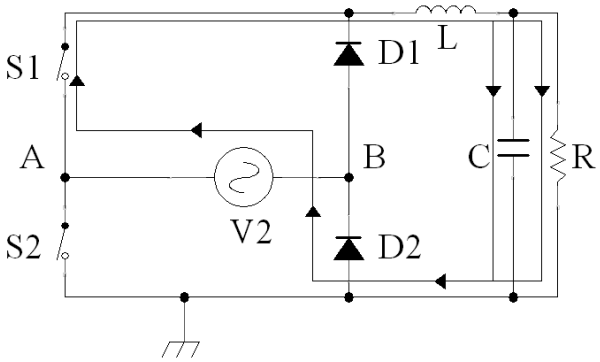

Fig. 4 (a) Rectifier operation in positive cycle of input.

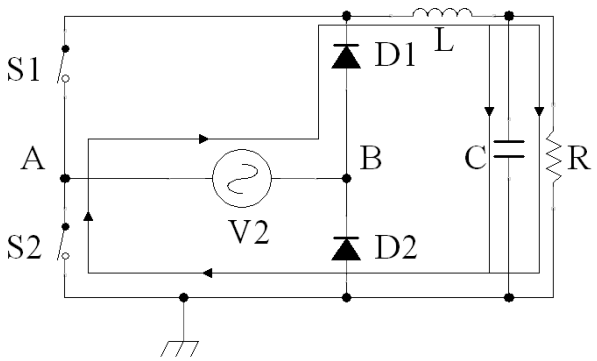

Fig. 4 (b) Rectifier operation in negative cycle of the input.

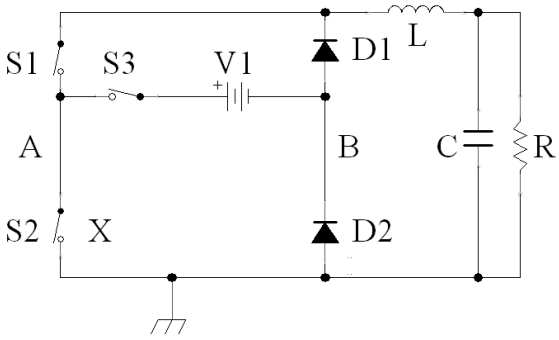

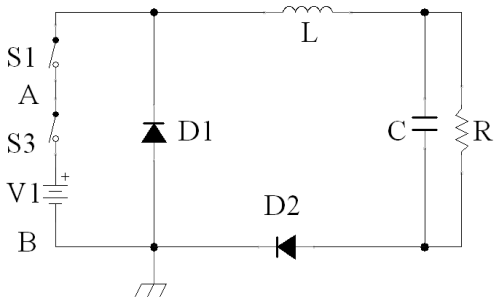

Fig. 5 Dc chopper in the proposed converter.

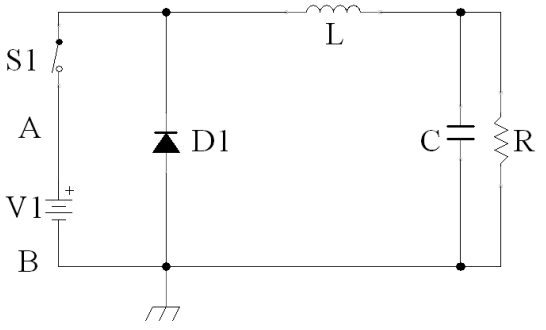

Fig. 6 The equivalent buck chopper circuit.

If S2, S4 and S5 of Fig. 2 are out of operation then, the equivalent circuit becomes a dc chopper with isolation switch S3 (Fig.5). *X* in the Fig.5 indicates that, S2 is out of operation. S3 will be in continuous operation during this mode. Fig.5 also shows the dc chopper (buck converter) with an extra isolating switch S3 and a diode D2. In conduction state, diode D2 and

switch S3 can be replaced by short circuits. The corresponding equivalent circuit will be exactly like a buck converter (Fig.6).

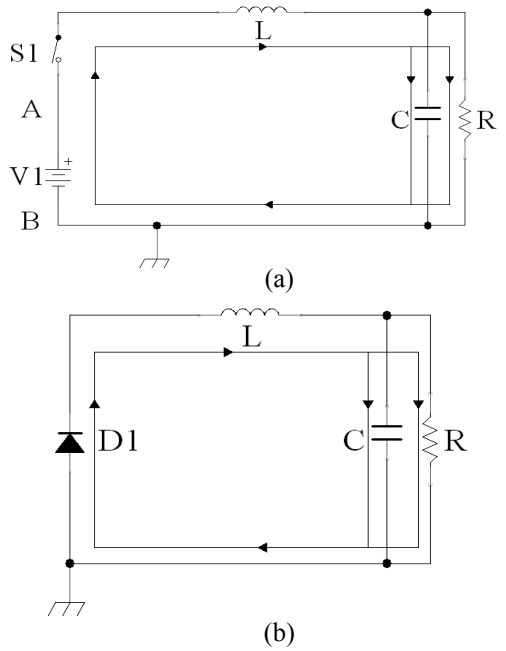

Fig. 7 The operation of buck converter (a) ON switch and (b) OFF switch.

In case of dc chopper operation the current flows from source (V1) to the load via S1 (ON), filter inductor L and filter capacitor C. During this ON switch mode of operation, the inductor stores energy [5]. The ON state mode of operation is shown in Fig.7. At OFF switch state of operation the stored energy in the inductor flows via L, C, R and D1 (freewheeling diode). This is the operation of a buck converter [5].

After showing all the equivalencies this is important to design a controller circuit for operating the proposed converter To do so, Table I is introduced.

TABLE I. DESIGN OF THE CONTROLLER CIRCUIT

C (Control Signal)	Converter`s Operation	Switch				
		S1	S2	S3	S4	S5
1	Rectifier	PWMr.Pp	PWMr.Pn	Low	C.Pp	C.Pn
0	Chopper	PWMc	Low	High	Low	Low

Table I shows the signals for operating the converter. Based on these parameters some equations can be derived for the controller. It clearly shows the state of switches during rectifying and chopper operations. *C* is the control signal, *PWMr* is the pulse width modulated signal for rectification and *PWMc* is the pulse width modulated signal for chopper action. *Pp* and *Pn* are positive and negative cycle detector signal respectively.

$$S1 = C.PWM_r.Pp + \overline{C}.PWM_c \quad (1)$$

$$S2 = C.PWM_r.Pn \quad (2)$$

$$S3 = \overline{C} \quad (3)$$

$$S4 = C.Pp \quad (4)$$

$$S5 = C.Pn \quad (5)$$

C is the control signal which will operate the converter in different modes. Table I shows that, if the control signal is High (1) the converter will act as a rectifier. For low (0) control signal the converter will act as a dc chopper. It is important to note that, Pp and Pn are signals from a comparator which detects positive or negative cycle of the sinusoidal input. Detection of positive and negative input cycles is very necessary for avoiding malfunction of the converter.

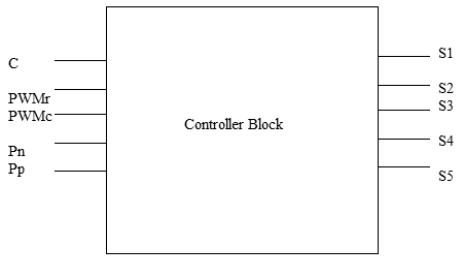

Fig. 8 The controller block.

Fig.8 shows the controller block for the converter. The block is designed using (1) to (5). There are five inputs and five outputs for the five switches of the converter.

III. SIMULATION

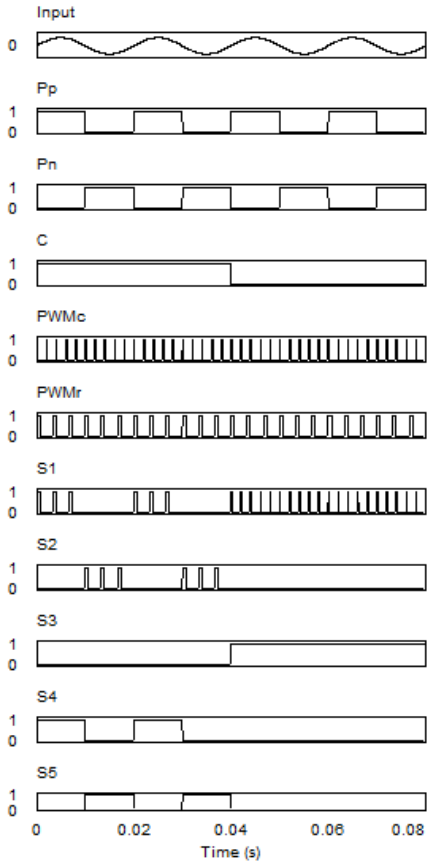

Fig. 9 Generation of switching signals.

Fig. 9 shows the simulated switching signals for the proposed converter. The simulated circuit is given in Fig. 10. A transformer is connected with the input sinusoidal wave so that,

desired low level of the sine wave can be generated for operating the comparator (Fig. 10). From Fig. 9 and Fig. 10 it is seen that, the comparator provides positive pulse (Pp) during positive cycle of input. Correspondingly, a negative cycle detector signal (Pn) is produced. Pn provides high output during the negative half cycle of ac input.

While operating the converter as a rectifier, S4 and S5 act as isolation switches. Isolation of two modes of operation (rectifier and dc chopper) is very important for perfect operation. In this mode of operation, control signal C is high (according to Table I it indicates the rectifier action) and S3 is out of operation (these are shown in Fig. 9). The operations of S4 and S5 are dependent on Pp and Pn. It is also clear from Fig.9 and (4) to (5). S4 operates during the positive half cycle of the input and S5 during negative half cycle providing required isolation. During rectification, S1 and S2 are operated with PWMr.

In chopper operation the required control signal is low (0). For chopper action, S1 and S3 are operated and all other switches are at OFF state. S1 is operated with PWMc. This is also shown in Fig. 9.

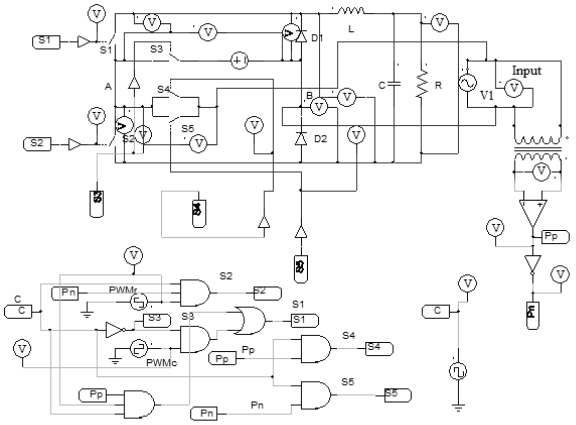

Fig. 10 Simulation circuit in PSIM.

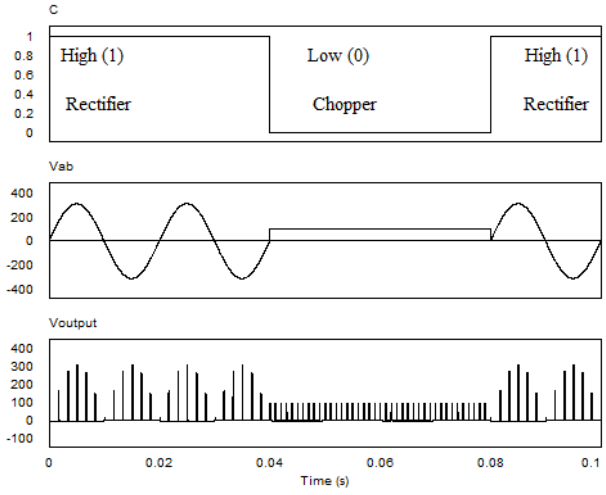

Fig. 11 Control signal, input to the converter and unfiltered output voltage.

Fig. 11 shows the inputs to the converter across 'A' and 'B' terminals for different control commands. Ac and dc sources get connected to AB terminals for high and low control signal respectively. The corresponding dc output voltage at different modes (before filtering) is also shown. In Fig. 12, the filtered dc voltage is given. So, the input to the converter can be either ac or dc but the output is always dc.

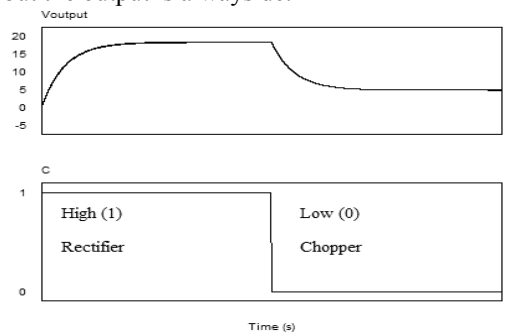

Fig. 12. Control signal and filtered dc output.

IV. CONCLUSION

This paper designs such a single power electronic converter which performs both rectifier and chopper actions. Hence, the great advantage is that, it eliminates the use of two separate converters for rectifier and chopper purposes. The output can be reduced by adjusting the pulse widths. The results are satisfactory. The converter is useful for battery charging application and designing dc drives. In future, it will be implemented in hardware.

REFERENCES

[1] A. Mohammad, A. A. Manzur and A. I. Aziz, "Comparisons among different Types of Single Phase Step Down AC to DC Converters," in International Journal of Computer Applications, vol. 121, no. 5, pp. 13-17, Jul. 2015.

[2] S. K. Mahobia and G. R. Kumrey, "Study and Performance of Single-Phase Rectifiers with Various Type of Parameter," in International Journal in Engineering Technologies and Management Research, vol. 3, no.1 (2016), pp. 9-14, Jan. 2016.

[3] Vikramarajan Jambulingam, "Speed Control of DC Motor Using MOSFET Based Chopper," in International Journal of Engineering Development and Research, vol. 4, Issue 2, pp. 1337-1341, Jun. 2016.

[4] Kirana kumar Venkanagouda Patil and Shankaralingappa C. B. "DC Motor Control Using Chopper for Remote Laboratory Set-Up," in International Journal of Innovative Research in Electrical, Electronics, Instrumentation and Control Engineering, vol. 4, Issue 7, pp.43-47, Jul. 2016.

[5] Mohammad, Adnan; Rahaman, Md.Shafieur; Ahmed, Omar; Aziz, Ashique Ibni; Muntakim, Tahmid Ul; Shaon, Mohammad Shahjalal, "Realization of existence of two buck chopper circuits in a single phase switch controlled full wave rectifier," in 2015 International Conference on Electrical Engineering and Information Communication Technology (ICEEICT), pp.1-5, 21-23 May 2015.

[6] T. J. Liang, L. S. Yang, and J. F. Chen, "Analysis and design of a single phase ac/dc step-down converter for universal input voltage," IET Electr Power Appl., vol. 1, no. 5, pp. 778–784, Sep. 2007.

[7] K. Nishimura, K. Hirachi, S. Komiyama, and M. Nakaoka, "Two buck choppers built-in single phase one stage PFC converter with reduced DC voltage ripple and its specific control scheme," in Proc. IEEE Appl. Power Electron. Conf. Expo., 2008, pp.1378–1383.

2nd International Conference on Electrical, Computer & Telecommunication Engineering (ICECTE)
8-10 December 2016, Rajshahi-6204, Bangladesh

Stability Improvement of Simultaneous AC-DC Power Transmission System

Md. Habibur Rahman[1], M.R.I. Sheikh[2], Md. Alimul Islam Salim[3]
Dept. of ECE[1], Member, IEEE[2], Dept. of EEE[2,3]
Rajshahi University of Engineering & Technology (RUET), Bangladesh[1-3].
habibieee@yahoo.com[1], ris_eee@ruet.ac.bd[2] islamsalim111004@gmail.com[3]

***Abstract*--This paper presents the concept of simultaneous ac-dc power transmission system with newly designed self adaptive Voltage Dependent control (VDCOL) procedure. Long ac transmission lines cannot be loaded to their thermal limits due to instability occurs in the power system. It is difficult to load long ac lines to their thermal limits as a sufficient margin is kept against transient instability. With the model proposed in this thesis, it will be possible to load these lines close to their thermal limits. The transmission lines and the conductors are allowed to carry usual ac along with dc superimposed on it. This thesis with newly designed controller gives us the feasibility of composite ac–dc power transmission line to get the advantages of parallel ac–dc transmission in order to transient stability and dynamic stability and dampen out oscillations. Simulation has been carried out during 1-phase and 3-phase fault in MATLAB software package (Simulink) to prove system stability enhancement.**

Keywords*—*ac-dc power transmission, MATLAB simulation, simultaneous ac-dc transmission, load Flow, new VDCOL control.

I. INTRODUCTION

The demand of electricity is tremendously increasing all over the world. In these case environmental, right-of-way, and cost concerns have delayed the construction of a new transmission line. The wheeling of this available energy through existing long ac lines to load centers has a certain upper limit due to stability considerations. Thus, these lines are not loaded to their thermal limit to keep sufficient margin against transient instability. On the basis of new concepts that allow full utilization of existing transmission facilities without decreasing system availability. To achieve this goal is simultaneous ac-dc power transmission in which the conductors are allowed to carry superimposed dc current along with ac current ac and dc power flow independently [1], and the added dc power flow does not cause any transient instability. Simultaneous ac-dc power transmission was first proposed through a single circuit ac transmission line. In these scheme, a new VDCOL controller is introduced to enhance system stability of a simultaneous ac-dc power transmission system.

II. BASIC OF AC-DC POWER TRANSMISSION

Fig. 1 depicts the basic scheme for simultaneous ac-dc power flow through a double circuit ac transmission line. The dc power is obtained through line commutated 12-pulse rectifier bridge used in conventional HVDC and injected to the neutral point of the Zig-Zag connected secondary of sending end transformer and is reconverted to ac again by the conventional line commutated 12-pulse bridge inverter at the receiving end. The inverter bridge is again connected to the neutral of Zig-Zag connected winding of the receiving end transformer. The double circuit ac transmission line carriers both three-phase ac and dc power. Each conductor of each line carries one third of the total dc current along with ac current [2]. Resistance being equal in all the three phases of secondary winding of Zig-Zag transformer as well as the three conductors of the line, the dc current is equally divided among all the three phases.

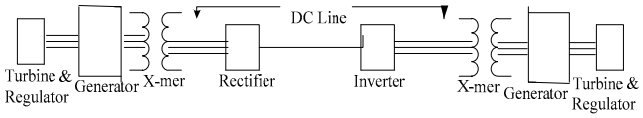

Fig. 1. Basic Scheme for composite AC-DC Transmission [1].

Two fluxes produced by the dc current ($I_d/3$) flowing through each of a winding in each limb of the core of a Zig-Zag transformer are equal in magnitude and opposite in direction. The equivalent circuit of the scheme under normal steady-state operating condition is given in Fig. 2 [1], [3]. The dotted lines in the figure show the path of ac return current only. The second transmission line carries the return dc current, and each conductor of the line carries ($I_d/3$) along with the ac current per phase V_{dro} and V_{dio} are the maximum values of rectifier and inverter side dc voltages and are equal to 3 times converter ac input line-to-line voltage.

A. Equivelent Circuit With Equations

First, Let I_{dc} be the dc link current, R_{cr} and R_{ci} be the commutation resistances of the rectifier and the inverter respectively. Let α be the ignition angle of the rectifier and γ be the extinction angle of the inverter. Let P_{d}_rectifier= Rectifier end dc power, P_{d}_inverter = Inverter end dc power. Let R_{dc} be the dc link resistance. Let V_{d}_rectifier = Rectifier terminal voltage, V_{d}_inverter = Inverter terminal voltage.

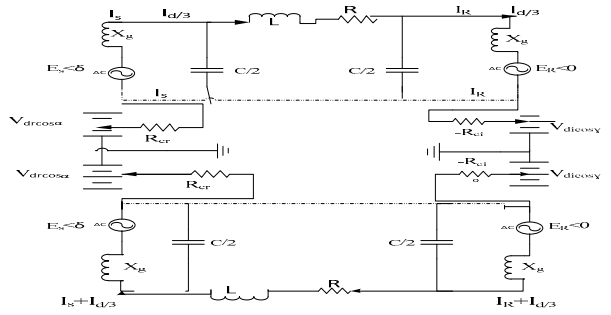

Fig. 2. Equivalent circuit diagram of DC Transmission [3].

$$I_{dc}=[V_{droCos\alpha}-V_{dioCos\gamma}]/[R_{cr}+R_{dc}-R_{ci}] \quad (1)$$

$$P_{d\_rectifier}=V_{d\_rectifier}\times I_{dc} \quad (2)$$

$$P_{d\_inverter}=V_{d\_inverter}\times I_{dc} \quad (3)$$

$$Q_{d\_rectifier}=P_{d\_rectifier}\times\tan(\theta_{rectifier}) \quad (4)$$

$$Q_{d\_inverter}=P_{d\_inverter}\times\tan(\theta_{inverter}) \quad (5)$$

$$P_{total\_sending\_end}=P_{s\_ac}+P_{d\_rectifier} \quad (6)$$

$$P_{total\_receiving\_end}=P_{r\_ac}+P_{d\_inverter} \quad (7)$$

$$Q_{total\_sending\_end}=Q_{s\_ac}+Q_{d\_rectifier} \quad (8)$$

$$Q_{total\_receiving\_end}=Q_{r\_ac}+Q_{d\_inverter} \quad (9)$$

Total Transmission Loss

$$P_{loss}=P_{total\_sending\_end}-P_{total\_receiving\_end} \quad (10)$$

$$I_{total}=\sqrt{(I_{ac}^2+(\frac{I_{dc}}{3})^2)} \quad (11)$$

The total current [4] I in all the conductors are` asymmetrical but the two original zero-crossings in each one cycle in current wave are possessed for $(I_d/3I_a)$ <1.414.

III. Proposed AC-DC Network

Fig. 3 shows the following network that carries both ac-dc power simultaneously. Two Synchronous generators is used to produce 11kV ac voltage. Turbine & Regulators is used to control the generator voltage & field excitation, Generic & Multiband power system stabilizer is used in this case. Increasing generating voltage to 132kV and transmit 100kM. Conductor size, line resistance, reactance of 3 phases are same. A three phase fault breaker & load are connected in HVAC transmission line. Parallel with ac circuit a 100 kM dc line is also built by using a rectifier and inverter circuit. AC filters are used in both sides to mitigate higher order harmonics. This filter consists of three types of elements i.e capacitor banks, tuned filters and high pass damped filter which filter out higher order harmonics [7]. A master current controller is used to set the current for rectifier and inverter. Both Rectifier and Inverter circuit consists of a transformer with two thyrestor based electronic circuit.

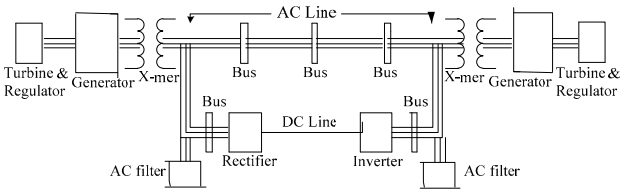

Fig. 3. Block diagram of proposed transmission network

Both transformers are connected in Zig-Zag to reduce transformer saturation. Both Rectifier and Inverter control and protection with master control circuit is used to control switching of 12 pulse thyristor firing angle. In Rectifier, controller circuit operates 12 pulse thyristor firing angle during normal operation but during abnormal conditions like DC fault and at low ac voltage, protection circuit blocks the 12 pulse thyristor firing angle thus reduce overheating and power system transient instability. A three phase fault breaker is connected in HVAC line and a ac fault breaker is connected in dc line.

IV. VDCOL Control Procedure

Voltage stability of ac-dc hybrid power grid is closely related to Voltage dependent current order limiter (VDCOL). The effects of VDCOL to voltage stability along with serious voltage reduction during or after faults are analyzed in detail. Considering that VDCOL with fixed parameters is difficult to adapt the complexity of operation conditions and ac faults in the receiving-end power grid of dc system, a kind of dynamic self-adaptive VDCOL control strategy [5] is proposed based on the voltage of ac side of converter transformers at inverter side. Simulations of power grid of Bangladesh show that the new type of VDCOL is beneficial to voltage stability of receiving-end power grid.

If there is fault in the inverter end, voltage would decrease greatly, if the VDCOL is not activated, the power control mode will increase the current to keep the power constant. Increased current will increase the reactive power consumption of converter; it will increase the risk of subsequent commutation failures if the ac system is relatively weak. if the dc voltage reaches threshold value; current order is decreased down rapidly to predefined lower value to prevent the consecutive commutation failure during inverter side ac fault.

A. New VDCOL Controling Equations.

Faraday's equation [6] clearly describes voltage and current with respects to flux of a magnetic circuit. Thus,

Faraday's Differential Equation, $$V = N\frac{d\Phi}{dt} \quad (12)$$

Faraday's Integral Equation, $$V = \frac{1}{N}\int V.dt \quad (13)$$

AC voltage, $$V = \sqrt{2}V\,\mathrm{Sin}(2\pi ft) \quad (14)$$

So, Flux, $$\Phi = \frac{1}{N}\int \sqrt{2}V\,\mathrm{Sin}(2\pi ft).dt \quad (15)$$

Integrating, $$\Phi = -(\frac{\sqrt{2}V}{2\pi fN})\,\mathrm{Cos}(2\pi ft) \quad (16)$$

Peak values of flux, $$\Phi_{pk} = \frac{\sqrt{2}V}{2\pi fN} \quad (17)$$

Or, $$\Phi_{pk} = \frac{V}{4.44fN} \quad (18)$$

From another relation, $$di = \frac{V}{L}dt \quad (19)$$

Finally after integrating, Current, $i = \frac{V}{L}t$ (20)

B. New VDCOL Controling Algorithm

Applying the above equations from [12]-[20], Conversion of Converter AC Voltage to Controlling current has been shown and the control algorithm can be explained by Fig. 4.

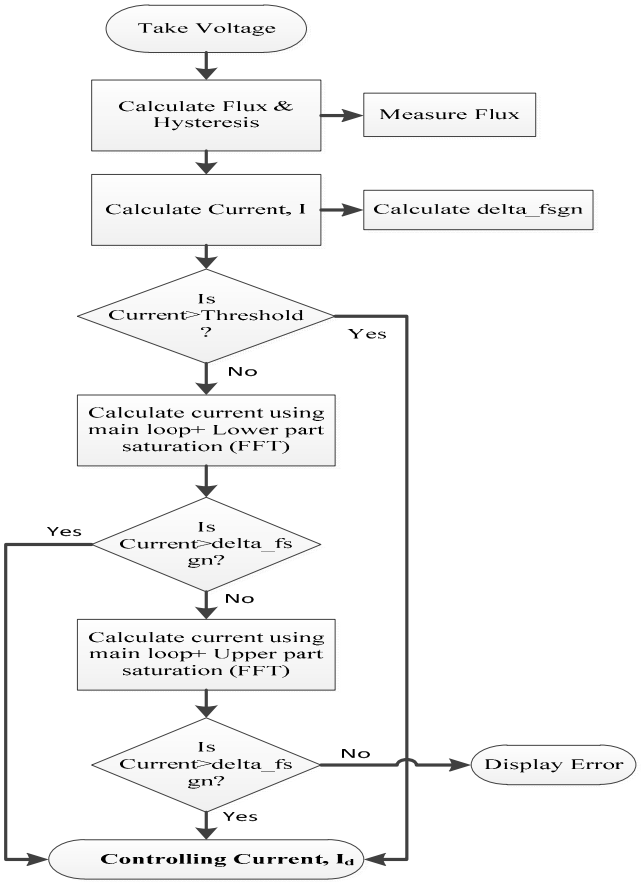

Fig. 4. New VDCOL control algorithm

New VDCOL controller is self adaptive because it automatically detects voltage and limit the thyristor commutation angle and fault current by using [2], [6] as follows.

$$P_s = \frac{V_s * V_R}{X} \sin \partial \quad \text{.....[21]}$$

Where, ∂ =firing angle.

X=Reactance per phase per circuit.

V. Simulation Results

Using MATLAB Simulink, this circuit is simulated both at normal and faulty conditions. Simulation results has been taken separately by ac, dc and simultaneous ac-dc circuit with new VDCOL control procedure.

A. Line AC-DC Voltage and Current

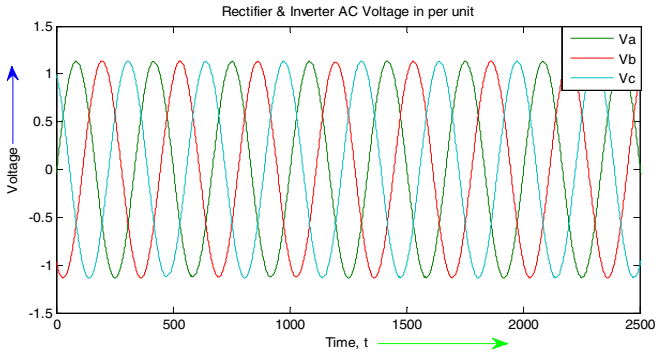

Fig. 5. Rectifier and Inerter AC voltage in per unit (time in ms).

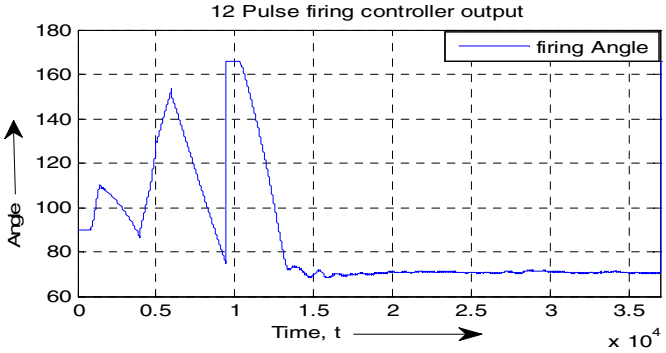

Fig. 6. Rectifier and Inverter 12 pulse firing angle controller signal

B. Simulation Results During 1-phase Fault

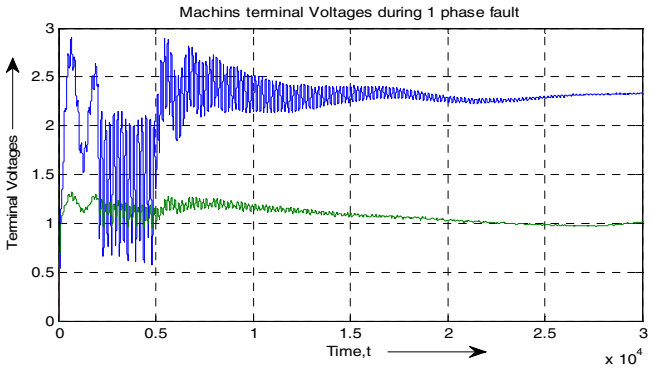

Fig. 7. Machines terminal voltage during 1-phase fault in pu.

C. Simulation Results During 3-phase Fault

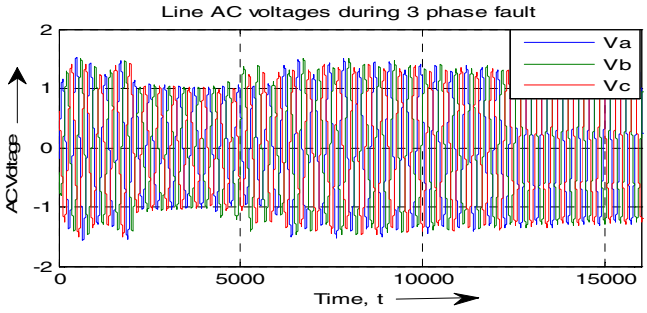

Fig. 8. Line AC voltage during 3-phase fault in pu ,time in ms.

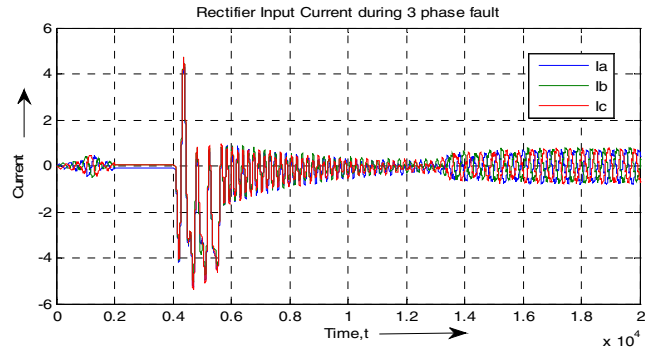

Fig. 9. Line AC current during 3-phase fault in pu, time in ms.

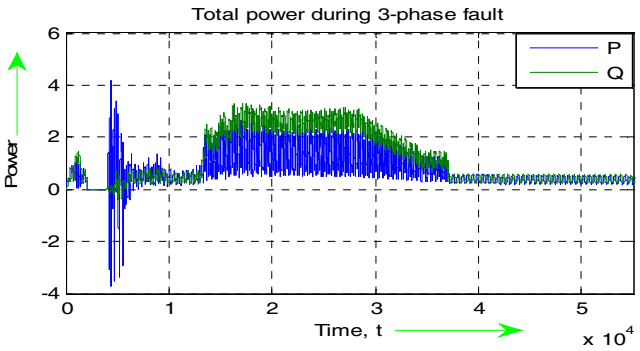

Fig. 10. Total power during 3-phase fault in pu, time in ms.

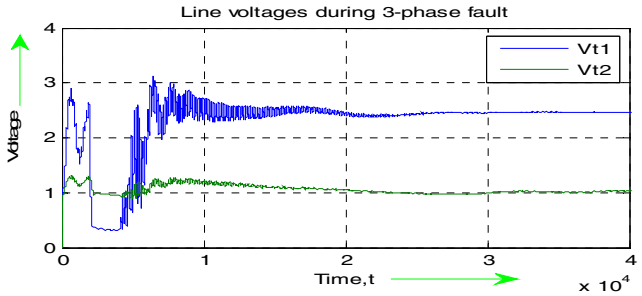

Fig. 11. Machines terminal voltage during 3-hase fault in pu.

D. Results Analysis

From the above results, It is shown that the proposed network with new self adaptive VDCOL controller is stable at any condition. Both machines are stable and whole network become stable at 70^0 firing angle of rectifier and inverter switching circuit is shown in Fig. 6. Here phase shifted discreet 12 pulse PWM technique is used for gate signal controlling. During 1-phase fault, the fault breaker opens the circuit at 0.1s and again close it at 0.2s and within 0.5s the system becomes stable is shown in Fig. 8 & Fig.9 respectively. During 3-phase faults fault breaker characteristics remains same and whole network i.e. Machines terminal voltage, Line voltage, Current, Power, is shown in Fig. 7, Fig. 10 and Fig. 11 respectively. Everything becomes stable within 1s. Thus the new VDCOL is self adaptive which automatically detect the Rectifier and Inverter voltages and then by using the proposed technique gives output as I_{order}/I_d which is the controlling current and inject this current into the rectifier and inverter control and protection circuit to regain system stable. This result can be more improved by using new modulation techniques to control thyristor/IGBT/FET firing angle.

VI. Conclusion

A simple scheme of simultaneous ac-dc power transmission with newly designed VDCOL controller through the same transmission line has been presented. The simulation works ensure that simultaneous ac-dc power can be transferred in long distant is possible avoiding thermal limit and transient stability problem. The proposed power system network is very simple and there is no physical alteration in insulator strings, towers and arresters of the original line. New VDCOL controller is self adaptive because it automatically detects voltage and limit the commutation current compered to conventional VDCOL controller. During 1 or 3-phase faults in the network, line voltage becomes lower then the new VDCOL decreases the current in such a value to avoid commutation failure thus system steady state and transient stability is improved. In LV, MV distribution system and HV transmission system the proposed scheme can be applied in a workplace with flexibility. This paper can modified by applying different algorithms like Fuzzy Logic, Neural network for further enhancement of transient stability.

Acknowledgement

We are very thankful to professors and engineers with whom we had useful discussions regarding HVAC, HVDC, Performance of MV transmissions lines.

References

[1] Abhishek Chaturvedi1, V. K. Tripathi, T Vijay Muni, Neeraj Singh, " Power System Stability Enhancement by Simultaneous AC-DC Power Transmission," Int. J. of Advanced Research in Electrical, Electronics and Instrumentation Engineering, vol. 2, no. 5, pp.1758-1765, May 2013.

[2] K. P. Basu, "Stability enhancement of power system by controlling HVDC power flow through the same AC transmission line," IEEE symposium on Industrial Electronics & Applications, Kuala Lumpur, vol.2, pp. 56-59, 4-6 Oct. 2009.

[3] P. Vijay Kumar Babu, P. Bhaskara Prasad , M.Padma Lalitha, "Power Upgrading of Transmission Line by Combining AC–DC Transmission," Int. J. of Engineering Research and Applications, vol. 2, no. 6, pp.1699-1704, Dec. 2012.

[4] H. Rahman, B. H. Khan, "Power Upgrading of Transmission Line by Combining AC-DC Transmission," IEEE Transactions on Power Systems, vol. 22, no. 1, pp.45-49, Feb. 2007.

[5] Xiaoming Liu, Yutian Lia, "New VDCOL control strategy for voltage stability in receiving end power grid of DC system," Advanced Materials research, vol.5, no.4, pp.3256-3261, Mar. 2010.

[6] Faraday's Law, [Online] Available: http://info.ee.surrey.ac.uk /Workshop/advice/coils/Faraday/#fgivev (Accessed- 20th August 2016).

[7] Mathworks, [Online] Available: http://www.mathworks.com /help/physmod/sps/examples/thyristor-based -hvdc-transmission-system-average-model.html (Accessed- 25th August 2016).

[8] XinXing XU,NengLing Tai, "Scheme of simultaneious AC-DC power transmission in medium voltage distribution network," 2015 IEEE TENCON conference procedings, China, vol. pp.1-4, 1-4 Nov. 2015.

International Conference on Electrical, Computer & Telecommunication Engineering (ICECTE)
8-10 December 2016, Rajshahi-6204, Bangladesh

Minimization of Output Fluctuations of Wind Farm Integrated Hybrid Power System Using New Pitch Controller

Fariya Tabassum[1], M.R.I. Sheikh[2] and M. Hasanuzzaman[3]
[1,2]EEE Department, Rajshahi University of Engineering &Technology, Rajshahi – 6204, Bangladesh
Email: tabassum.fariya27@gmail.com[1]

Abstract—**In this paper a central supervisory control system based on wind speed data is proposed for calculating reference power for the blade pitch angle of each wind turbine. Low Pass Filter (LPF) technique is used to generate proposed blade control system of wind farm. The wind farm consists of 5 induction generators (IG) and is connected to a multi machine power system composed of 4 synchronous generators (SG) and a load. An extra LPF is used for calculating reference power for IG4 and IG5. Simulations have been done by PSCAD/EMTDC program by using real wind speed data. Simulation results clearly indicate that proposed blade control system can maintain frequency with less energy losses**.

Keywords- **Wind turbine, grid, system frequency, blade angle control, wind speed data.**

1. Introduction

Due to the limitation of fossil fuels and their harmful effect on the environment, recently the concentration on renewable energy sources is increasing all over the world. Wind energy is considered as one of the most important types of renewable energy resources that have been widely used in electricity generation compared to the others resources such as biogas, solar and geothermal. 2015 was an exceptional year for the wind industries as annual installations crossed the 60 GW mark for the first time in history. More than 63 GW of new wind power capacity was brought on line [1].In general, the Fixed Speed Wind Turbines with Squirrel Cage Induction Generator (FSWT-SCIG) is most widely used in wind farms. This type of wind turbine is very popular and has some superior characteristics like brushless and rugged construction, low cost, maintenance free and operational simplicity [2]. The controller of this type wind turbine is only equipped with conventional blade pitch angle. The conventional pitch controller is used to maintain the output power of the wind generator at its rated level when the wind speed is over the rated speed. On the other hand, when the wind speed is within the rated speed, the blade pitch angle is maintained constant (= 0 degree) to capture the maximum power from the wind.

Various methods have been proposed for smoothing wind power fluctuations and minimizing frequency fluctuations. In [3], a pitch angle control system is designed based on the sliding mode control which has a complicated control strategy. By connecting an Electro-Mechanical Switched Capacitor (EMSC) based static synchronous compensator (STATCOM) into the grid, reactive power and terminal voltage can be controlled effectively with varying wind speed [4]. But the system's overall cost will increase. The adaptive control scheme of the superconducting magnetic energy storage (SMES) units based on the set-membership affine projection algorithm (SMAPA) is used for smoothing wind farms output power in [5]. But SMES device has high initial installation cost, large space and high maintenance cost are required. Fuzzy logic controller (FLC) based superconducting magnetic energy storage (SMES) system is used in [6] for suppressing the voltage sag/swell in distribution systems with wind power penetration. When the wind speed is higher than the rated speed the power regulation using PID is implemented in [7] for the pitch control as well as the torque control along with the feed forward control strategies. Though a supervisory control system is proposed in [8] by using low pass filter (LPF), however it is not profitable as energy losses are more in this case.

In this paper a new strategy of pitch control system is proposed. Exponential weighted moving average (EWMA) technique is used here to generate proposed blade control system and central supervisory control system based on wind speed data is used for calculating reference power for the blade angle of each wind turbine. Moreover Low pass filter (LPF) is used whiling calculating blade angle for IG4 and IG5 which reduces frequency fluctuation and gives higher output power.

978-1-5090-5785-6/16/$31.00 ©2016 IEEE

The proposed method has the advantage of low cost and less complexity compared with other smoothing methods as the pitch control system is equipped in most present wind turbines. In addition, the conventional pitch control method can be simply switched to the proposed one. The simulation analyses have been performed using PSCAD/EMTDC. Thus this system may be a good system for wind power applications.

2. Power System Model

The model system used in the simulation analyses is shown in Fig. 1. The model system consists of a wind farm (WF), a hydro power plant, SG1, with a salient pole synchronous generator (HG), two thermal power plants, SG2 and SG3, with cylindrical rotor synchronous generator (TG), a nuclear power plant, NG, with cylindrical rotor synchronous generator (SG4) and a static load of 80 MW. SG1 and SG3 are operated under Load Frequency Control (LFC), SG2 is under Governor Free (GF) and SG4 is under Load Limit (LL) modes. LFC is used to control frequency fluctuations with a long period more than a few minutes and GF is used to control fluctuations with a short period less than a minute. LL is used to constant the output power.

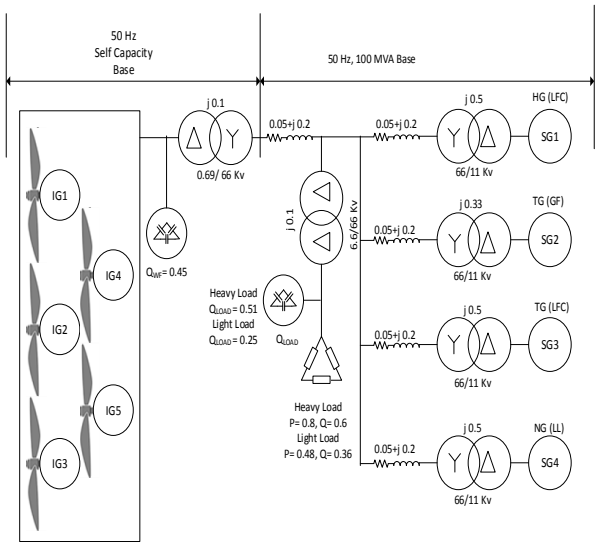

Fig.1. Model System

The wind farm consists of five fixed speed wind turbine with squirrel cage type induction generators (IG1 to IG5). Q_{WF} and Q_{Load} are capacitor banks. Q_{WF} is used at the at the terminal of wind farm to compensate the reactive power demand of the wind generators at steady state and to compensate the voltage drop due to the impedance of transmission lines, Q_{Load} is connected at the terminal of load. In the analysis, core saturations of induction generator and synchronous generators are not considered. The parameters of IG and SG are taken from [2]. The governor, AVR and LFC control models have been used as those used in [2].

3. Proposed Pitch Controller Model

3.1 Model for Generating Variable Reference Power

The MOD-2 characteristic [9] is used for the wind turbine model. The generated power from the wind generator can be obtained from Eq. (1). In Eq. (2) and (3) it is converted into per unit system. Eq. (4) shows the total generated power of wind farm in per unit. It is considered that, the wind farm is consists of five wind generator. Eq. (5) shows the average loss calculation. Finally the reference power has been calculated by using Eq. (6) and Eq. (7).Where the base wind speed is considered as 11.9 ms^{-1}.

Generated power from the wind generator no. 1, $P_1 = \frac{1}{2}\rho\pi R^2 {V_{W1}}^3$ (1)

In per unit, $P_{1pu} = \frac{\frac{1}{2}\rho\pi R^2 {V_{W1}}^3}{\frac{1}{2}\rho\pi R^2 (11.9)^3}$ (2)

So, $P_{1pu} = \left(\frac{V_{W1}}{11.9}\right)^3$ (3)

Total wind farm power, $= P_{1pu} + P_{2pu} + P_{3pu} + P_{4pu} + P_{5pu}$ (4)

$Loss = P_n - P_{refn}$ Here, n = any integer among 1 to 5

For total $\boldsymbol{n}$ no. of generators, $AvgLoss = \frac{Loss}{n}$ (5)

$P_{ref1} = P_{1pu} - AvgLoss$ (6)

In general $P_{refn} = P_{npu} - AvgLoss$ (7)

Fig. 2, Fig.3and Fig.4 show the PSCAD modeling of total wind farm output power calculation technique, average loss calculation technique and variable reference power calculation technique respectively.

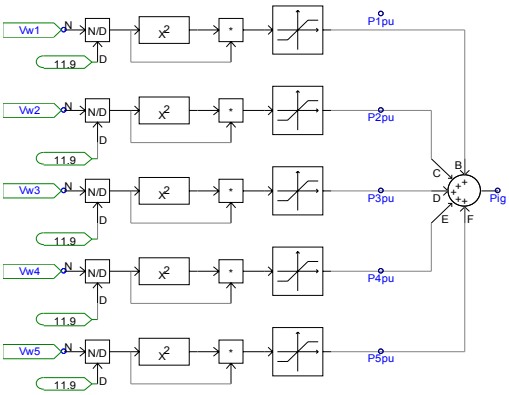

Fig. 2. PSCAD modeling for total wind farm output power calculation

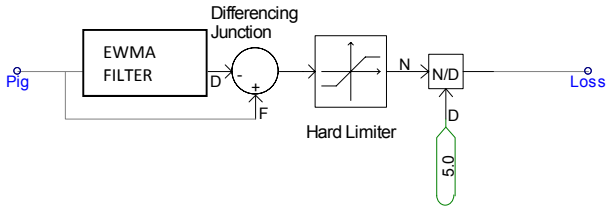

Fig. 3.PSCAD modeling for average loss calculation

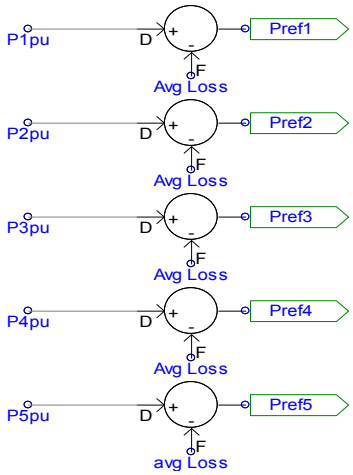

Fig. 4. PSCAD modeling for variable reference power calculation

4.2 **Model for calculating blade pitch angle (β)**

The PSCAD modeling of blade pitch angle (beta) control system for proposed model is shown in Fig. 5. The pitch servo is modeled with a first order delay system with a time constant T. in general, the pitch actuation system cannot respond instantly for the mechanical limitation so a rate limiter is needed to obtain the realistic response. 10 deg./s is the assigned value of the rate limiter for this model. A hard limiter is used which will restricts the rotation of blade from 0 to 90 degree. An extra LPF is used to calculate the blade angle for wind turbine no. 4 and 5. This will increase the output energy of the wind farm. The model is shown in Fig. 5 (b)

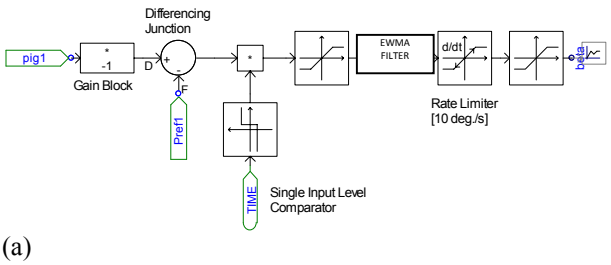

(a)

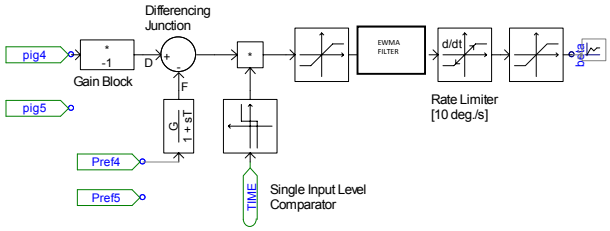

(b)

Fig. 5.PSCAD modeling for blade pitch angle (beta) calculation

4. **Simulation Results**

To investigate the performance of the proposed pitch control system, simulation analyses have been done by using PSCAD/EMTDC with simulation time 600 sec. Fig. 6 shows the real wind speed data used in the simulation analysis. The output of IG1 and IG2 in per unit (pu) are shown in Fig. 7 and Fig. 8 respectively.

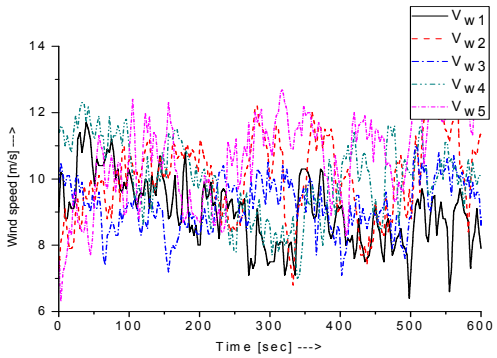

Fig. 6. Wind speed data

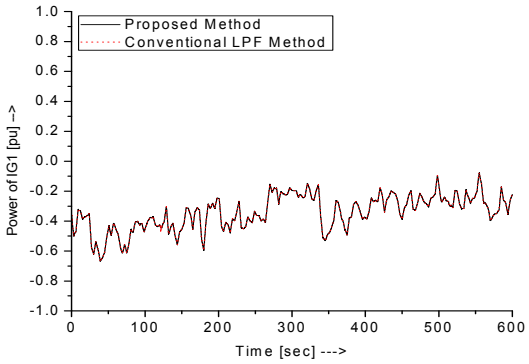

Fig. 7. Output power of IG1

Fig. 9 shows the output power of the wind farm. The power system frequency and wind farm energy are shown in Figs. 10 and 11 respectively. It is seen from Fig. 11 that more energy can be generated by the proposed system.

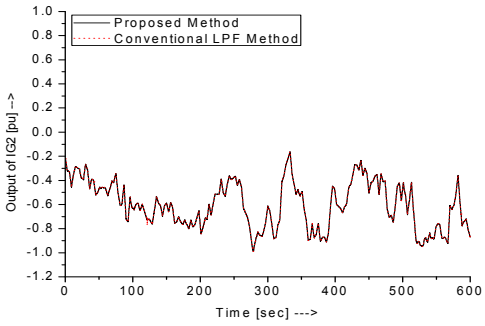

Fig. 8. Output power ofIG2

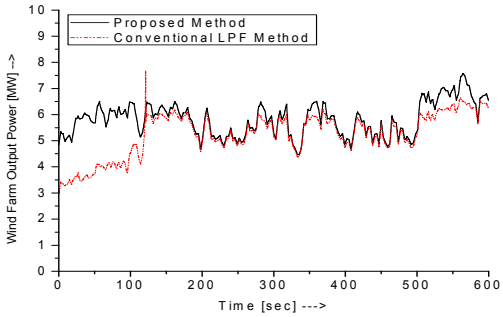

Fig. 9. Output power of wind farm

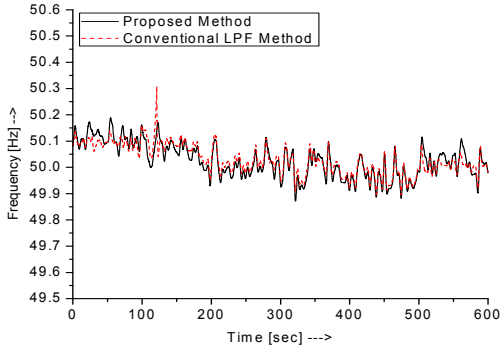

Fig. 10. Frequency response of the power system

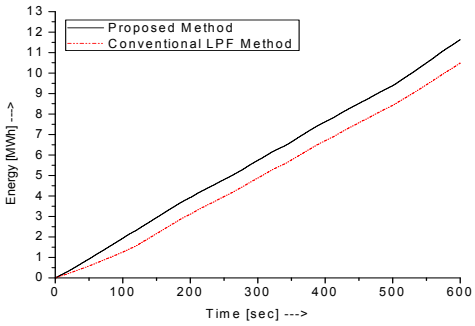

Fig. 11.Wind farm energy

5. Conclusions

In this paper, the comparative results between conventional LPF method and proposed method have been discussed. For calculating reference power for the blade pitch angle of each wind generator, a central supervisory control system is proposed. Here, the power system frequency and the energy of the wind farm are considered as the index for selecting the best method. From the simulation analysis it is seen that, the proposed method can control the frequency fluctuation more effectively and also give larger wind farm output when compared with the conventional LPF method. Hence, it can be concluded that the proposed method can be a good tool for power system application.

References

[1] The Global Wind Energy Council (GWEC), Global Status of Wind Power, Big Markets dominate in 2015. [Online] Available: http://www.gwec.net

[2] M. R. I. Sheikh "Stabilization of a Grid Connected Wind Farm by Using SMES" PhD Thesis, September 2010, Kitami Institute of Technology (KIT), Japan

[3] Yang Mi, Xiaowei Bao, Enyu Jiang, Weihua Deng, Jianxin Li, Limin Wang, Lufei Ren, Peng Wang, "The pitch angle control of squirrel-cage induction generator wind power generations system using sliding mode control", in *2014 16th European Conference on Power Electronics and Applications (EPE'14-ECCE Europe), 26-28 Aug. 2014, Lappeenranta,* pp. 1 - 10, DOI: 10.1109/EPE.2014.6910732, Publisher: IEEE

[4] N. Mondol, M. R. I. Sheikh, M. R. Hasan, "stabilization of wind firm integrated hybrid power system by using statcom", *in International Conference on Electrical & Electronic Engineering (ICEEE), 4-6 Nov. 2015,Rajshahi,* pp. 105 - 108, DOI: 10.1109/CEEE.2015.7428230, Publisher: IEEE

[5] Hany M. Hasanien, "A Set-Membership Affine Projection Algorithm-Based Adaptive-Controlled SMES Units for Wind Farms Output Power Smoothing", IEEE Trans. Sustain. Energy. Vol.5, Issue 4,pp. 1226 – 1233, DOI: 10.1109/TSTE.2014.2340471

[6] Sayed M. Said, Mohamed M. Aly, Mamdouh Abdel-Akher, "Application of superconducting magnetic energy storage (SMES) for voltage sag/swell suppression in distribution system with wind power penetration" in *2014 16th International Conference on Harmonics and Quality of Power (ICHQP), 25-28 May 2014, Bucharest,* pp. 92 – 96, DOI: 10.1109/ICHQP.2014.6842877, Publisher: IEEE

[7] K. M. S. Y. Konara, M. L. Kolhe, "Pitch controller modeling for wind turbine power regulation using feed forward control strategies", in *Power and Energy Engineering Conference (APPEEC), 2015 IEEE PES Asia-Pacific, 15-18 Nov. 2015,Brisbane, QLD,* pp. 1 - 5, DOI: 10.1109/APPEEC.2015.7381018, Publisher: IEEE

[8] Md. Amzad Hossain "Output Fluctuations Minimization of Wind Integrated Hybrid Power System by Co-Ordinated Control of Governor and Blade" a master thesis, Rajshahi University of Engineering & Technology (RUET), Bangladesh, 2015.

[9] S. M. Muyeen, J. Tamura, and T. Murata, "*Stability augmentation of a grid connected wind farm",* London, Springer-Verlag, 2009.

International Conference on Electrical, Computer & Telecommunication Engineering (ICECTE)
8-10 December 2016, Rajshahi-6204, Bangladesh

Optical Character Recognition using Back Propagation Neural Network

Shyla Afroge, Boshir Ahmed, Firoz Mahmud
Department of Computer Science & Engineering
Rajshahi University of Engineering & Technology Rajshahi-6204, Bangladesh.
Email: shyla.ruet@gmail.com, boshir_bd@ruet.ac.bd, fmahmud.ruet@gmail.com

***Abstract*—This paper represents an Artificial Neural Network based approach for the recognition of English characters using feed forward neural network. Noise has been considered as one of the major issue that degrades the performance of character recognition system. Our feed forward network has one input, one hidden and one output layer. The entire recognition system is divided into two sections such as training and recognition section. Both sections include image acquisition, preprocessing and feature extraction. Training and recognition section also include training of the classifier and simulation of the classifier respectively. Preprocessing involves digitization, noise removal, binarization, line segmentation and character extraction. After character extraction, the extracted character matrix is normalized into 12x8 matrix. Then features are extracted from the normalized image matrix which is fed to the network. The network consists of 96 input neurons and 62 output neurons. We train our network by proposed training algorithm in a supervised manner and establish the network. Eventually, we have tested our trained network with more than 10 samples per character and gives 99% accuracy for numeric digits (0~9), 97% accuracy for capital letters (A~Z), 96% accuracy for small letters (a~z) and 93% accuracy for alphanumeric characters by considering inter-class similarity measurement.**

Keywords— OCR; Character Recognition; BPN Network; English Alphanumeric Characters; Image Acquisition.

I. INTRODUCTION

Pattern recognition is the assignment of a physical object or event to one of several pre-specified categories [4]. It is an active and challenging field of research which has a very large scientific and practical interest. As [2] notes, it includes applications in "feature extraction, radar signal classification and analysis, speech recognition and understanding, fingerprint identification, character (letter or number) recognition and handwriting analysis ('notepad' computers)". Character recognition is one of the most fascinating research fields of image processing and pattern recognition. Character recognition is generally known as optical character recognition because it uses optical means to acquire the characters. Optical character recognition has huge applications including conversion of any handwritten document into structural text form, automatic number plate recognition, reading aid for blind, bank cheques etc. Character is the basic building block of any language that is used to build different structure of a language [4]. Character recognition is a process which associates with a symbolic meaning with objects (letters, symbols & numbers) drawn on an image [3]. OCR contributes immensely to the achievement of automation process and improves the interface between man and machine in numerous applications [8].

978-1-5090-5785-6/16/$31.00 ©2016 IEEE

Artificial Neural Network approach for character recognition is now gaining importance because of ANN's highly parallel architecture and fault tolerance. Zao et. al. [8] proposed an SMT (Surface Mount Technology) product character recognition using back propagation neural network.

A. F. Mollah et al. [9] presented an OCR system for camera based handheld devices. M. F. Kader et. al. [4] proposed a neural network based size and color invariant character recognition system using feed forward neural network. Prerna Kakkar et. Al. [3] presented a novel approach for recognition of English characters based on artificial neural network. Kauleshwar Prasad et al. [8] presented a handwriting recognition system to recognize English characters using Matlab's neural network toolbox. Anita Pal et. al. [5] presented a handwritten English character recognition system using neural network.

The rest of the paper is arranged as follows: Methodology is described in section II. Implementation is described in section III. Experimental results are shown in section IV. We conclude our paper in section V. Limitations and future works are described in section VI.

II. METHODOLOGY

A. Back Propagation Neural Network

Back propagation method is used for training a multi-layer artificial neural network with mathematical foundation. The method is used in multi-layer forward network with gradient – descent based on delta –learning rule along with a supervised training learning method [3]. It uses non linear Thresholding function. The main objective of this network is to train the network to balance between the input patterns that are used in training and their responses to the input patterns.

B. Stages of Proposed OCR System

The proposed OCR system is divided into two sections. The first is the training section and the second is the recognition section. The stages of the proposed system are shown in the Fig. 1.
Both training and recognition system includes image acquisition, preprocessing and feature extraction. Training and recognition section also includes training of the classifier and simulation of the trained classifier respectively.

1) Image Acquisition

The proposed OCR starts with image acquisition process (see Fig. 2) that takes an input of a digital image by using a digital camera or scanner. Specific format such as JPEG, BMT, are

taken as the input image. This image is used for testing the network.

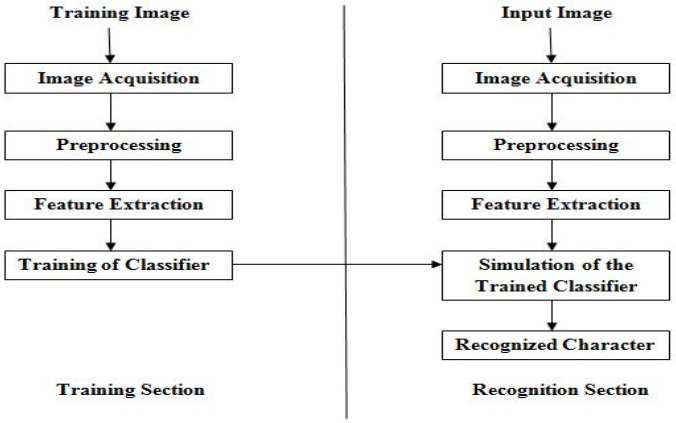

Fig. 1. Stages of the proposed OCR system

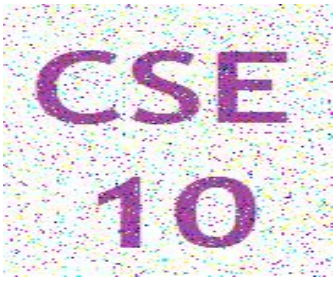

Fig. 2. Input Image

2) Pre-processing

The raw data is subjected to a number of preliminary processing steps to make it usable in the descriptive stages of character analysis. Pre-processing aims to produce data that are easy for the OCR systems to operate accurately. The following steps are the preprocessing steps.

a) Gray image conversion

A gray image has pixel value from 0 to 255. The lowest value of the range represents the black pixel intensity and highest value represents the white pixel intensity. In this stage a RGB images is converted into a gray scale image.

The following equation is used to convert an RGB image to a Gray scale image.

$$g(x,y) = 0.299xR(x,y) + 0.587xG(x,y) + 0.114xB(x,y) \quad (8)$$

Where $R(x,y)$ is Red component, $G(x,y)$ is Green component, $B(x,y)$ is the Blue component of the color image and $g(x,y)$ is the gray scale image.

b) Noise reduction

Noise reduction improves the quality of the document. The main approach is to use the median filtering technique. This technique takes the input image and a mask of size 3x3, 5x5 or 7x7 and calculates the median according to the mask for each pixel of the input image. And finally replaces the pixel with the median value that corresponds to the centre of the mask.

c) Thresholding

Thresholding is the process of setting background values for pixels below a threshold value and using a different set of values for the foreground. It is of two types such as Global thresholding and Local thresholding

The following equation is used for thresholding:

$$f(x,y) = \begin{cases} 255 & if\ f(x,y) > T \\ 0 & otherwise \end{cases} \quad (1)$$

Where T is a threshold value

d) Binarization

Binarization is one kind of thresholding where the gray scale image is converted into a binary image. Because the transformed image is defined by the two levels, it is called binary image.

e) Line Extraction

Segmentation is the process of partitioning an image into disjoint and different regions. This task is done by finding the boundaries. There are several approaches for finding the character boundaries. In this stage, an image of sequence of characters is decomposed into sub-images of individual character .

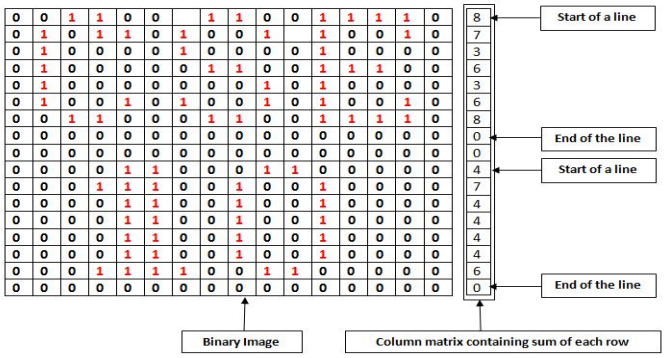

Fig. 3. Line Extraction Approach

In Line extraction text region from top to bottom is scanned and the sum of row pixels is calculated. If the sum is zero then a line is extracted which is shown in fig. 3.

f) Character Extraction

In character extraction text region from left to right is scanned and the sum of column pixels is calculated. If the sum is zero then a character is extracted. The character extraction approach is shown in Fig. 4.

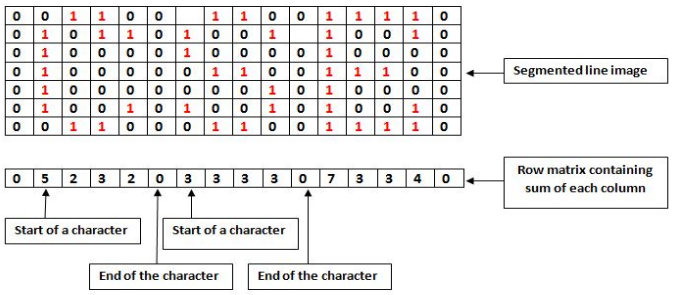

Fig. 4. Character Extraction Approach

g) Normalization

Normalization is process of equating the size of all extracted character bitmaps (binary image) .There is lots of variations in the size of characters. In order to make the extracted characters in equal dimension of matrix, normalization is performed. The normalized character matrix is of size 12x8.

3) Feature Extraction

Feature extraction is the process of extracting and differentiating features from the matrices of characters. In feature extraction stage each character is represented as a feature vector, which becomes its identity. The major goal of feature extraction is to extract a set of features, which maximizes the recognition rate with the least amount of elements.

The normalized character matrix of size 12x8 that consist only 1 and 0 is converted to a column matrix. This columnized matrix acts as feature vector which is fed to input layer of the back propagation neural network.

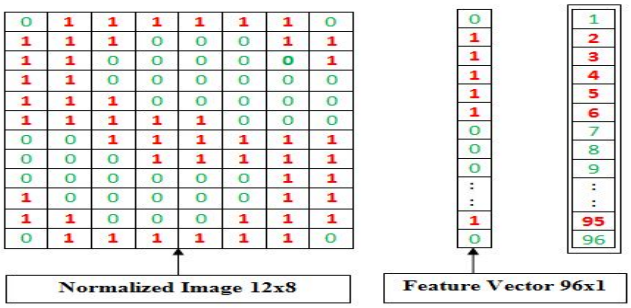

Fig. 5. Feature extraction

4) Training of Classifier

The classification stage is the decision making part of the recognition system. A feed forward back propagation neural network is used in this work for classifying and recognizing the English characters. The pixels derived from the normalized character in the segmentation stage form the input to the classifier. The classes of recognition problem are shown in the following table:

TABLE 1. CLASSES RECOGNITION PROBLEM

0	1	2	3	4	5	6	7
8	9	A	B	C	D	E	F
G	H	I	J	K	L	M	N
O	P	Q	R	S	T	U	V
W	X	Y	Z	a	b	c	d
e	f	g	h	i	j	k	l
m	n	o	p	q	r	s	t
u	v	w	x	y	z		

The network is trained with 558 samples of 62 characters where each character has 9 samples. Each character sample is written in nine different types of fonts.

5) Simulation of Trained Classifier

In this stage, the features extracted from the testing images are simulated with the trained network. Finally, the network recognizes the test characters.

The network architecture is shown in the following figure:

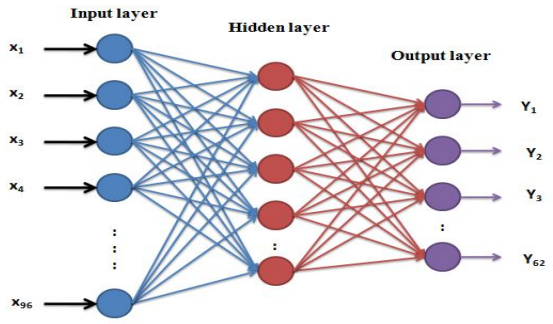

Fig. 6. Architecture of the network

III. IMPLEMENTATION

Initially, the algorithms of line and character extraction are made. MATLAB is used as tool for implementing the algorithms. Then the neural network is designed. Since there is no specific way to find the correct model of neural network, it is found by trial and error. Different models of neural network are taken, trained and the output accuracy is noted. The system is divided into two sections. Both for training and recognition section, scanned image is taken. After this, the image is converted into gray scale image and noise is removed. Then the filtered image is converted into binary image. Global thresholding is used for this purpose. Lines are extracted from the binary image. Characters are extracted from the extracted line images. These extracted characters are then normalized into a fixed size image. Features are extracted from these normalized images.

For training section, these features are used to create an input dataset which is used to train the network in a supervised learning manner with a target dataset.

For recognition section, these features are used to create a test dataset which is then used to simulate with the trained network. Finally the system recognizes the characters.

IV. RESULT ANALYSIS

Images of 62 characters of 558 samples are taken for training the network. Each character is in nine different fonts and contains 7-10% salt and pepper type noise.10 samples of each character are taken to create a test dataset where each character is in ten different fonts and contains 7-10% salt and pepper type noise.Finally, the trained network is simulated with the test data set which recognizes the test characters. The network is simulated for both individual classes and combined classes. The network specification is given below:

TABLE 2. SPECIFICATION OF THE NETWORK

Input layer	1
Hidden layer	1
Output layer	1
No. of neuron in input layer	96
No. of neurons in hidden layer	79
No. of neurons in output layer	62

Performance plot during training phase at goal 0.01 is shown in Fig.7.

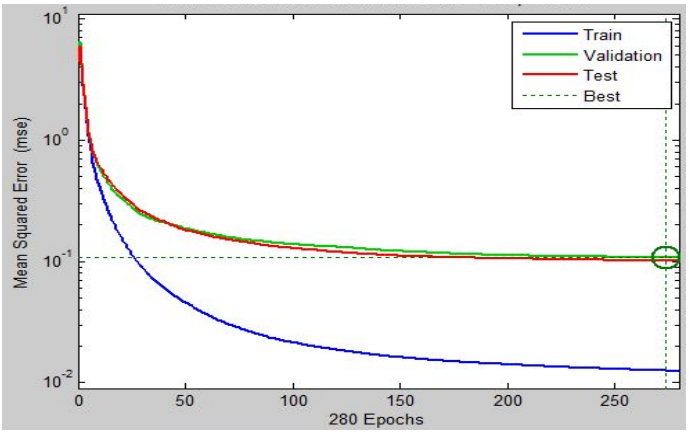

Fig. 7. Performance plot during training at goal 0.01

TABLE 3. PERFORMANCE PARAMETER (0.01)

No. of epoch	280
Goal	0.01
Mean square error	0.0128

Percentage of recognition
= (*(total no. of test characters-no. of misclassified characters)/total no. of test characters) x100%*

TABLE 4. PERCENTAGE OF RECOGNITION

Class	**No. of test characters**	**No. of correct classification**	**No. of misclassification**	**% of recognition**
0~9	100	99	1	99%
A~Z	260	252	8	97%
a~z	260	249	11	96%
0~9,A~Z,a~z	620	576	44	93%

Based on the proposed method described in the preceding sections, our system is able to recognize 10 English digits (0~9), 26 capital letters (A~Z), 26 small letters (a~z). The proposed system is able to recognize only numeric digits (0~9) with 99%, only capitals letters (A~Z) with 97 %, only small letters (a~z) with 96% and alphanumeric characters (0~9, A~Z, a~z) with more than 93% accuracy on average by considering inter-class similarity measurement. Among all characters, the recognition rate of inter-class similar characters is lower than the others.

V. CONCLUSION

In this paper, we have proposed an artificial neural network based character recognition system for recognition of English alphanumeric characters. Our system produces very good result for individual classes but produces satisfactory result when the classes are combined together.

VI. LIMITATIONS AND FUTURE WORK

The method described in this work cannot distinguish between text and non-text in the image. The character extraction approach described in the work is unable to extract characters for those languages in which characters are connected to form words. In the future, we plan to work for Bangla Character Recognition since Bangla is our mother language.

REFERENCES

[1] R. C. Gonzalez, R. E. Woods and S. L. Eddins, “Digital Image Processing Using MATLAB”, Fifth Impression.
[2] R. Bell and T. Jackson, “Neural Computing : An Introduction”
[3] P. Kakkar and U. Dutta, “A novel Approach to Recognition of English Characters Using Artificial Neural Networks ”, International Journal of Advanced Research in Electrical, Electronics and Instrumentation Engineering, Vol 3, Issue 6, June 2014.
[4] M. F. Kader and K. Deb, “Neural network based English alphanumeric character recognition”, International Journal of Computer Science, Engineering and Applications (IJCSEA) Vol.2, No.4, August 2012
[5] A. Pal and D. Singh, “Handwritten English Character Recognition Using Neural Network”, International Journal of Computer Science & Communication, Vol. 1, No. 2, July-December 2010, pp. 141-144
[6] A. P. Ottawa, Restoration of Documents With Show-through Distortion, Ontario, Canada, 2000.
[7] Keechul Jung, Kwang In Kim, Anil K. Jain.”Text Information Extraction in Images and Video: A Survey”.
[8] K. Prasad, D. C. Nigam, A. Lakhotiya and D. Umre, “Character Recognition Using Matlab’s Neural Network Toolbox”, International Journal of u- and e- Service, Science and Technology, Vol. 6, No. 1, February, 2013.
[9] A. F. Mollah, N. Majumder, S. Basu and M. Nasipuri, “Design of an Optical Character Recognition System for Camera based Handheld Devices”, IJCSI International Journal of Computer Science Issues, Vol. 8, Issue 4, No 1, July 2011.
[10] B. K. Prasad and G. Sanyal, “A Model Approach to Off-line English Character Recognition”, International Journal of Scientific and Research Publications, Volume 2, Issue 6, June 2012.
[11] R. Verma and Dr. J. Ali, “A-Survey of Feature Extraction and Classification Techniques in OCR Systems”, International Journal of Computer Applications & Information Technology Vol. I, Issue III, November 2012.

2nd International Conference on Electrical, Computer & Telecommunication Engineering (ICECTE)
8-10 December 2016, Rajshahi-6204, Bangladesh

Smoothening of WindFarm Output Fluctuations Using New Pitch Controller

A.G.M. Rakibul Hasan[1],and M.R.I. Sheikh [2]
[1,2]EEE Department, Rajshahi University of Engineering & Technology, Rajshahi-6204, Bangladesh
Emails: rgenius0@gmail.com[1], ris_eee@ruet.ac.bd [2]

Abstract—**Recently, renewable energy sources, like wind power generation, are widely being used in the world. Among various renewable resources, wind energy seems to be promising solution to provide reliable power supply with improved system efficiency. It is essential for wind farm to control the frequency as well as power. Some methods for smoothing the wind generator output fluctuations using several types of energy storage systems have been proposed, but these methods have a cost of problem. This paper proposes a new pitch control system for smoothing the wind generator output fluctuations. The simulation results show that the wind farm output fluctuations due to the wind speed variations can be smooth more effectively by the new pitch controller than the conventional pitch controller. It is confirmed that the wind farm output gives rise to fluctuations of system frequency more as the power capacity of wind farm becomes large. The wind farm output fluctuations, as well as energy and the power system frequency can be made more accurate by using new pitch controller. PSCAD software has been used for simulation analyses.**

Keywords: new pitch controller; system frequency; wind power capacity; energy generation.

I. INTRODUCTION

The method normally used, in which the angle of the rotor blades can be actively adjusted by the machine control system is known as pitch control. Pitch controller is used to maintain the output power of the wind generator at rated level by controlling the blade pitch angle of turbine blade when the wind speed is over the rated speed. In the conventional operation of wind power generators, when the wind speed is between the rated speed and the cut out speed, the wind power generator output is controlled at the rated value by a pitch control system. On the other hand, when the wind speed is between the cut in speed and the rated speed, the blade pitch angle is maintained constant 0^0, If the power capacity of wind generators becomes large, wind generator output can have an influence on the power system frequency [1]. Some methods for smoothing the wind generator output fluctuations using several types of energy storage systems have been proposed [1], but these methods have a cost of problem. Frequency can be maintained by using pitch controller and governor control system when several interconnected synchronous generators (SGs) are operated in different governor control modes. The pitch controller and governor control system model are effective when variable load and different types of governor control system are considered [2]. Using an Exponential Weighted Moving Average (EWMA) filtering approach, pitch control system is effective for output power fluctuations. By using this pitch control system, the wind farm output fluctuations and the power system frequency deviation can be decreased [3]. But this conventional pitch controller produces less energy. Output frequency fluctuations of wind farm integrated power system can be maintained in the acceptable range up to 10% of the total capacity of wind generator connected with the grid system by using conventional pitch controller. For the case of thermal governor connected system frequency fluctuations remain in the acceptable range up to 20% of total capacity by this pitch controller model without using energy storage devices [4]. But this pitch controller may not be suitable for hydro governor connected system. Only thermal result is appropriate for 20% in that pitch controller. In case of hydro, nuclear, gas turbine it combined effect is 10% -12% not 20% as described. In case of a country it has not only dependent on thermal power generator but also depend on hydro, nuclear, gas turbine power generator. In this paper newly design pitch controller is used in which energy losses is almost negligible. The wind farm output fluctuations due to the wind speed variations can be smoothed more effectively by the new pitch controller than conventional pitch controller. In simulation analyses response of energy and power is very high at new pitch controller. The response of power system frequency is also very good. Since the wind integrated power system increases gradually to fulfill the growing demand, this study will be helpful for taking preventive measures for the power grid companies which helps to improve the stability and quality of electric power. Considering these points of view, this study plays an important role for power system applications.

The organization of this paper as follows, section II presents the model system. Description of New pitch control model is given in section III. Simulation results and conclusions are present in section IV and V respectively.

978-1-5090-5785-6/16/$31.00 ©2016 IEEE

II. Model System

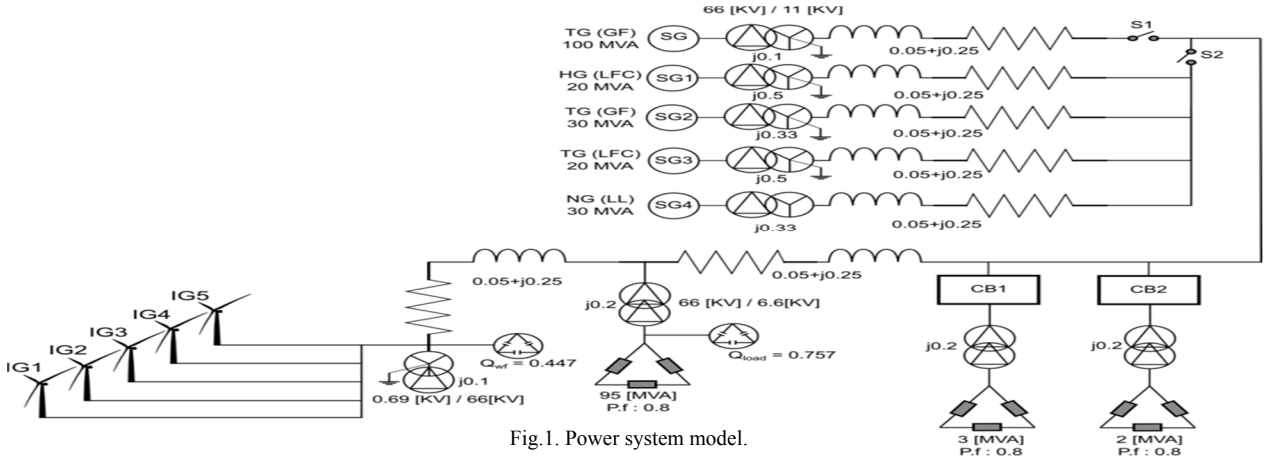

Fig.1. Power system model.

The model system used is shown in Fig.1. It consists of a wind farm, a hydro power generator SG1, two thermal power generators SG2 and SG3, a nuclear power generator SG4 and a load. The wind farm consists of five wind power generators (squirrel cage induction machines, IGn, n=1,2.....5). Hydro power generator SG1 and thermal power generator SG3 are operated under Load Frequency Control, another thermal power generator SG2 is under Governor Free control and nuclear power generator SG4 is under Load Limit operation. In general, Load Frequency Control is used to control frequency fluctuations with a long period more than a few minutes and Governor Free is used to control fluctuations with a short period less than a minute. Load Limit is used to output constant power.Q_{WF} and Q_{Load} are capacitor banks. Q_{WF} is used at the terminal of WF to compensate the reactive power demand of WF at steady state. The value of the capacitor is chosen so that power factor of the wind power station during the rated operation becomes unity. Q_{Load} is used at the terminal of load to compensate the voltage drop by the impedance of transmission lines. Core saturations of induction generator and synchronous generators are not considered [1].

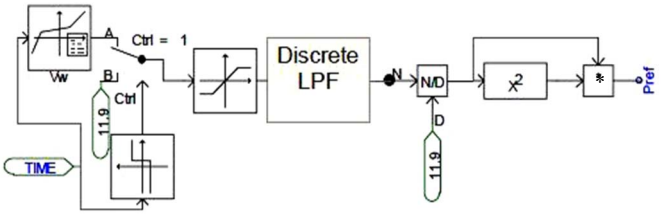

Fig 2.Reference power generator system [6]

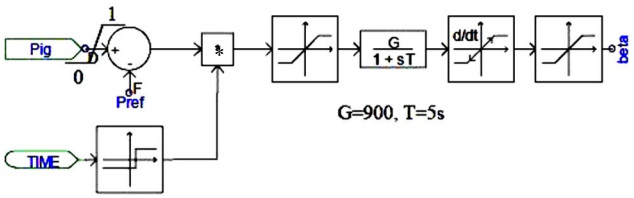

Fig. 3.Conventional Pitch angle controller [6]

III. New Pitch Control Model

As the conventional pitch controller as shown in Figs 2 and 3 works only when the wind speed is larger than the rated speed, thus the wind generator output fluctuate due to wind speed variations between cut in and rated speed and also the power system frequency may fluctuate, so this technique proposes a new pitch control system for smoothing the wind generator output fluctuations when the wind speed is between the cut in and the rated speed. The pitch control system is to protect the turbine from generator overload and too high mechanical stress in case of strong winds. The function of the new pitch controller is shown in Figs. 4 and 5.Speed deviation calculated by the speed controller. The speed controller is an integral component of every wind turbine. Its main purpose is to keep the operating point of the wind turbine at c_{pmax} . In the speed controller, first the speed reference ω_{ref} for maximum power point tracking is calculated. The reference value ω_{ref} is subtracted from the actual turbine speed ω to obtain the speed deviation $\Delta\omega$. The deviation is fed through a PI controller and there after multiplied by ω. Finally, this signal is low-pass filtered and limited in magnitude, giving the reference active power P_{ref} . The speed controller aims at keeping the turbine operating point at c_{pmax} . This is possible within a certain wind speed range. At too high wind speeds the turbine will not be able to operate at its optimal point since the blades are pitching to prevent generator overload. At too low wind speeds, maintaining an operation at c_{pmax} , and consequently at λ_{max} would require a tip speed lower than the turbine minimum rotational speed. Therefore, at too high wind speeds as well as too low, the operating point moves away from c_{pmax} [7]. The speed controller system is the calculation of ω_{ref} from the generated power P_g , which is done according to

$\omega_{ref} = A_o + A_1 P_g + A_2 P_g^2$

where A_0, A_1 and A_2 are coefficients determined so that the turbine will operate at $c_{p,opt}$. To determine the coefficients,

$$\lambda = \frac{v_{tip}}{v_{wind}} = \frac{\omega R}{v_{wind}} = \frac{\lambda}{R}.v_{wind}$$

If we use per-unit quantities instead of physical units,

$$\omega_{pu} = \frac{\lambda}{\omega_n R}.v_{wind}$$

Where ω_n is the nominal rotation speed used as speed base value. therefore

$$\omega_{pu} = \frac{\lambda\, opt}{\omega_n R}.\, v_{wind} = K_1.\, v_{wind}$$

where K_1 is a constant. Neglecting losses in the wind power plant we get

$$P_{wind,\,pu} = P_{g,\,pu} = \frac{\frac{1}{2}}{Sn} c_p \rho A\, .v^3_{wind}$$

With the nominal power S_n used as base power in optimal operation, $c_p = c_{p,opt}$

$$P_{g,\,pu} = \frac{\frac{1}{2}}{Sn} c_{p;opt} \rho A\, .\, v^3_{wind} = K_2\, .\, v^3_{wind}$$

The wind turbine is able to operate at $c_{p,opt}$ for all three wind speeds within the medium range, and one of them should preferably give nominal rotational speed. In this interval, the pitch angle should normally be zero and therefore K_1 and K_2 are calculated for the $c_p(\lambda)$ curve corresponding to $\beta = 0^0$ Under these conditions, rated wind speed will give rated rotational speed and rated power

$$K_1 = \frac{1}{v_{wind,n}}$$

$$K_2 = \frac{1}{v^3_{wind,n}}$$

Wind turbine model with a rated wind speed of 12 m/s has been used. With additional wind speeds 6 and 9 m/s, we get the following values:

A_0=0.370047, A_1=1.098151 and A_2=0.468198,K_1=0.083333 and K_2=0.000579

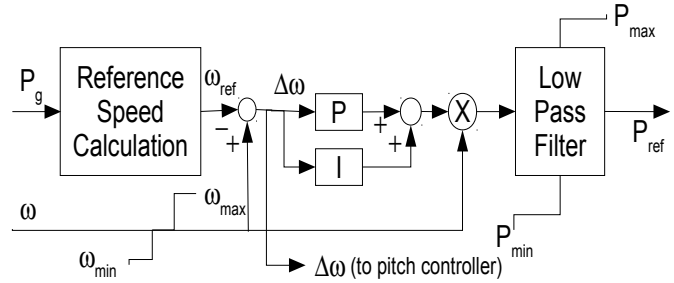

Fig. 4. Wind turbine speed controller.

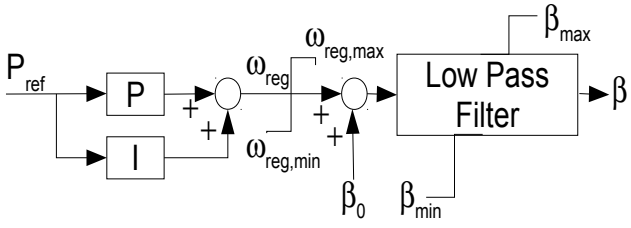

Fig. 5 . Wind turbine new pitch control system.

IV. Simulation Results

The Simulation analyses have been carried out to investigate the performance of the new pitch controller with using real wind speed data shown from Fig. 6. The simulation analyses have been performed using PSCAD/EMTDC. The wind speed data applied to each wind generator. The simulation results are shown from Fig. 7, through Fig.11. Fig.7 shows the wind farm output power for different cases, which fluctuates due to the wind speed variations. However, new pitch controller provide more as well as smooth output power. Fig. 8 shows the output frequency. It is seen from response that frequency also more smooth compares to conventional pitch controller. Figs. 9 and 10 show the blade pitch angles for IG1 and IG2 respectively. Fig. 11 shows the energy generation. As we used new pitch controller the energy generation is very high. For conventional pitch control system power generation is 8.25 MW (approximately) but for new pitch control system it is 10 MW (approximately). So the new pitch controller actually gained more 1.75 MW power. As seen from our research that the pitch controller of conventional system losses more energy compared to proposed system, this proposed system provide more energy. It is confirmed that the wind farm output gives rise to fluctuations of system frequency more as the power capacity of wind farm becomes large. The wind farm output fluctuations, as well as energy and the power system frequency more accurate by the new pitch controller.

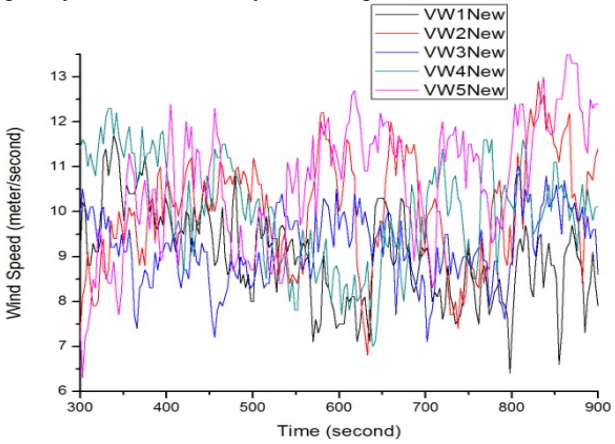

Fig.6.Response of wind speed data.

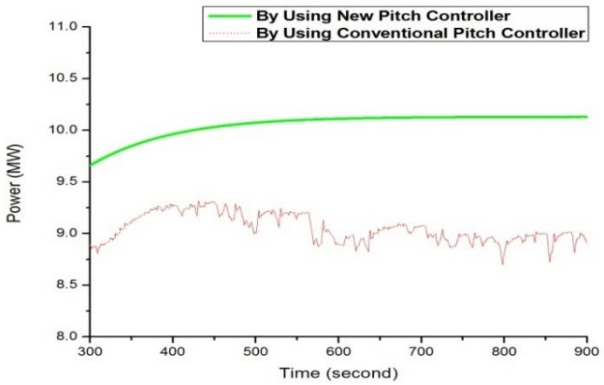

Fig. 7. Response of wind farm output power.

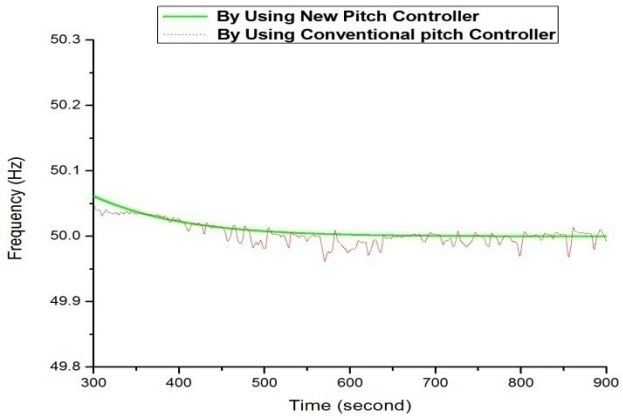

Fig. 8.Response of power system Frequency.

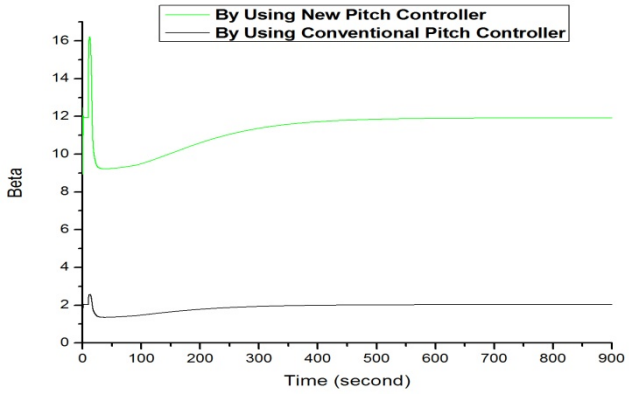

Fig.9. Response of pitch angle (IG 1).

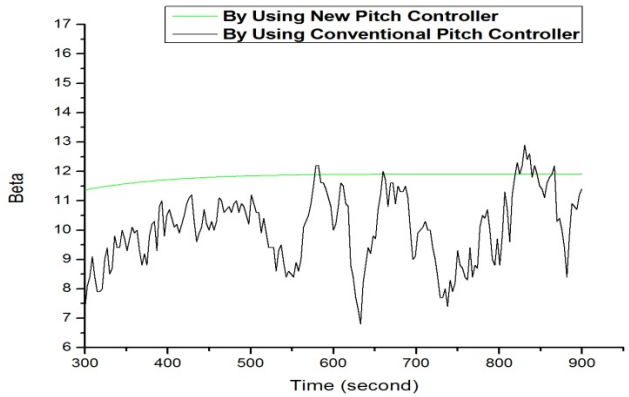

Fig.10. Response of pitch angle (IG 2).

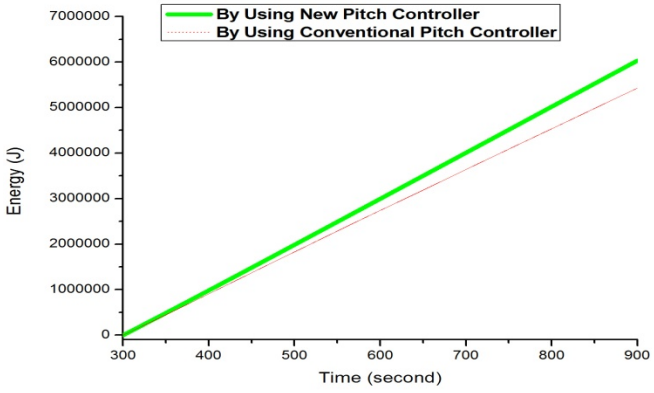

Fig.11.Response of wind farm Energy.

V. Conclusion

The wind farm output fluctuations due to the wind speed variation have been smoothed more effectively by the new pitch controller than the conventional pitch controller. It has been observed that the output power, system frequency and energy show an improved result by using new pitch controller. As all results are software simulated, so this may differ from actual physical implementation. But we believe this result will not differ in a great extent as the simulation environment was PSCAD/EMTDC. It is confirmed that as the wind farm integration increases day by day, it will hamper the power system frequency. By using the new pitch control system, the wind farm output fluctuations and thus the power system frequency deviation can be decreased effectively.

References

[1] M.R.I. Sheikh, "Stabilization of a Grid Connected Wind Farm by Using SMES" PhD Thesis, Kitami Institute of Technology (KIT), Japan. September 2010.

[2] M.R.I. Sheikh, D. Datta, and M.S.R. Ashrafi, "Minimization of Output Fluctuations of Hybrid Power System by Using Modified Pitch Controller." 8th International Conference on Electrical and Computer Engineering Dhaka, Bangladesh. 20-22 December, 2014.

[3] M.R.I. Sheikh ,M.A.Motin, F. Eva, M. Shahed, "Smoothing Control of Wind Farm Output Fluctuations by Using EWMA Pitch Controller", The 9th International Forum on Strategic Technology (IFOST), Cox's Bazar, Bangladesh. October 21-23, 2014.

[4] D. Datta , M.R.I. Sheikh , M.S.R Ashrafi, "Stabilization of Wind Power Output Fluctuations by Using New Pitch Controller". The 9th International Forum on Strategic Technology (IFOST), Cox's Bazar, Bangladesh. October 21-23, 2014.

[5] "PSCAD/EMTDC Manual'', Manitoba HVDC Research Center (http://www.hvdc.ca).

[6] Md. Amzad Hossain, "Output Fluctuations Minimization of Wind Integrated Hybrid Power System by Co- ordinated Control of Governor and Blade" a M. Sc. Thesis, RUET, October 2014,.

[7] A New Wind Turbine Control Method to Smooth Power Generation Modelling and Comparison to Wind Turbine Frequency Control, A M. Sc Thesis, Chalmers University of Technology , Sweden 2012.

[8] O. Wasynczuk, D. T. Man, J. P. Sullivan, "Dynamic Behavior of a Class of Wind Turbine Generator During Random Wind Fluctuations," *IEEE Trans. on Power Apparatus and Systems,* Vol.PAS-100, No.6, pp.2873-2845, 1981.

[9] *IEE of Japan*, Technical Reports Vol.754: Standard Models of Electrical Power System.

[10] T.Inoue, "MW Response of Thermal Power Plant from Viewpoint of Power System Frequency Control", *Trans. IEE of Japan*, Vol.124-B, No3, pp. 343-346, 2004.

[11] A.Murakami, A.Yokuyama, Y.Tada, "Basic Study on Battery Capacity Evaluation for Frequency Control in Power System with a Large Penetration of Wind Power Generation", *Trans. IEE of Japan*, Vol.126-B, No2, pp. 236-242, 2006.

[12] Simpow user Manual 11.0 Stri,2010.

International Conference on Electrical, Computer & Telecommunication Engineering (ICECTE)
8-10 December 2016, Rajshahi-6204, Bangladesh

A New Machine Learning Approach to Select Adaptive IMFs of EMD

Md. Burhan Uddin
Dept. of Computer Science and Engineering
BRAC University
Dhaka, Bangladesh
burhan420@gmail.com

Jia Uddin
Dept. of Computer Science and Engineering
BRAC University
Dhaka, Bangladesh
jia.uddin@bracu.ac.bd

Razia Sultana
Dept. of Computer Science and Engineering
BRAC University
Dhaka, Bangladesh
rsnishi.1992@gmail.com

Safat Islam
Dept. of Computer Science and Engineering
BRAC University
Dhaka, Bangladesh
skyscraper1709@gmail.com

***Abstract*—An adaptive algorithm for selection of Intrinsic Mode Functions (IMF) of Empirical Mode Decomposition (EMD) is a time demand in the field of signal processing. This paper presents a new model of an effective algorithm for the adaptive selection of IMFs for the EMD. Our proposed model suggests the decomposition of an input signal using EMD, and the resultant IMFs are classified into two categories the relevant noise free IMFs and the irrelevant noise dominant IMFs using a trained Support Vector Machine (SVM). The Pearson Correlation Coefficient (PCC) is used for the supervised training of SVM. Noise dominant IMFs are then de-noised using the Savitzky-Golay filter. The signal is reconstructed using both noise free and de-noised IMFs. Our proposed model makes the selection process of IMFs adaptive and it achieves high Signal to Noise Ratio (SNR) while the Percentage of RMS Difference (PRD) and Max Error values are low. Experimental result attained up to 41.79% SNR value, PRD and Max Error value reduced to 0.814% and 0.081%, respectively compared to other models.**

Keywords—intrinsic mode functions; empirical mode decomposition; support vector machine; Pearson's correlation coefficient

I. INTRODUCTION

Signal processing has spread its foot print thorough out most of the technological achievements and advancements. Use of signal processing in home automation to deep space exploration shows its extended reach in our life. Advance robotics, medical research and diagnostics, artificial intelligence all these respective fields has signal processing as backbone since long ago. Signal processing is used acquiring desired information as outcome from a set of raw data [1].

In analysis of non-stationary signals Wavelet transformation has been used over Fourier based transformation in regards of their performances [14]. In recent times EMD (Empirical Mode Decomposition) has proven its might on non-stationary signal processing leaving behind the wavelet transformation with locality and adaptability issues [2,3,6]. EMD decomposes a signal into a finite set of frequency modulated components which are IMFs (Intrinsic Mode Function). The EMD is adaptive and efficient in decomposing a signal. The decomposed IMFs are separated in two sets: noise free IMFs and noise dominant IMFs. For separation of the IMFs different researchers have used different approaches. Phuong and others in their paper have used Naïve Bayes classifier [3], it is a probabilistic and decision based classifier for the separation of relevant and non-relevant IMFs. On contrary to that, in paper [5] and [6] have proposed an energy based thresholding and classification method. We have followed the thresholding technique proposed by [6] for our SVM training. As the comparison results [4] show it as being better.

There are several attractive features in a SVM. Due to its excellent empirical performance, it plays a vital role in the field of machine learning. SVM is also immune to the issues like limitations of data dimensionality and limited samples [7,8]. When the dataset tends to infinity traditional statistical classifier provides ideal results [9], but in most real cases samples are small and limited. For realistic evaluation, we have chosen the SVM for IMF classification. Savitzky-Golay filter (SGF), also known as least-squares smoothing filter is used to smoothen noise dominant IMFs. In [11] the experimental results illustrate SGF works better in low to medium range SNR conditions

In this paper for the adaptive selection of IMFs we have proposed an effective algorithm which exploits the features of energy based threshold value and the empirical potential of SVM. Adaptively classified noise dominant IMFs are de-noised by using the SGF filter. The signal is reconstructed with both noise free and de-noised IMFs. Later comparative results are drawn from the values of SNR (Signal to Noise Ratio), PRD (Percentage Root Mean Square Difference) and MAX ERROR of input and reconstructed signal with respect to other models.

978-1-5090-5785-6/16/$31.00 ©2016 IEEE

The paper is organized as follows. Section II presents our proposed model briefly. The experimental setup and result are in section III. Finally, the paper concludes in section IV.

II. Proposed Model

Fig. 1 illustrates a complete flow diagram of our proposed model, where the input signals are decomposed using EMD. The empirical decomposition results in a finite set of IMFs. A threshold value using the Pearson Correlation Coefficient value is derived from the IMFs, and then they are separated into noise free and noise dominant IMFs. Noiseless and de-noised IMFs are used to reconstruct the signal. Later we briefly describe the Pearson Correlation based classification to show a comparison of the model.

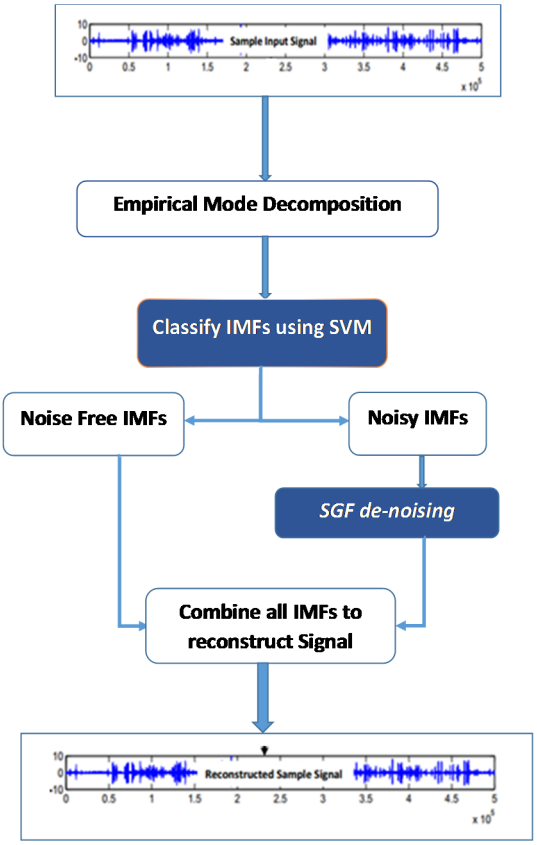

Fig. 1. Flow Diagram of the Proposed Model.

A. Empirical Decomposition and Threshold Derivation

Decomposition of the input signal using EMD results generates a finite set of IMFs. The PCC value is calculated for each of the resultant IMFs. Following the proposal of [6], a threshold value is derived (eqn.1). If Pearson's correlation coefficient of the IMFs is *Pi* and the threshold is expressed as *T*, expression of the threshold is,

$$T = \frac{\max(Pi)}{10 \times \max(Pi) - 3} \; [i = 1,2,3 \ldots] \tag{1}$$

Relevant IMFs are selected in compared to the derived *T*. IMF is relevant if $Pi \geq T$, irrelevant if not. This aids in training the SVM.

B. IMFs Classification using SVM

In order to train the SVM we used a subset of the decomposed IMFs. The SVM object was trained using the following features of IMFs, such as standard deviation [13] and root mean square (RMS) [12]. Then the trained SVM object is used to classify a large set of IMFs, into two categories, noise free and noisy IMFs.

C. De-noise the Noisy IMFs

Savitzky-Golay filter is used to de-noise the noisy IMFs. In our experimental setup the filter is used with frame size of 41 and 3rd order polynomial.

D. Signal Reconstruction

The filtered signal is reconstructed using noise free and de-noised IMFs.

$$S_R = \sum IMF_{nf} + \sum IMF_{dn} \tag{2}$$

where S_R represents the reconstructed signal and, IMF_{nf} and IMF_{dn} are noise free and de-noised signals respectively. We have used the original signal and the reconstructed signal to compare performance of our proposed model and other state of the art models.

III. Experimental Setup and Result

MATLAB® version 14 simulation tool is used to evaluate the performance of the proposed model. In order to validate our proposed model, we have used the dataset in [10]. We tested the dataset with a medium level randomized white noise. Performance of our proposed model and other state of art models were compared using three distinct statistical parameters, such as PRD, SNR and Max Error. Fig. 2 demonstrates a visual difference in performance of different models and our proposed model using a sample signal.

$$PRD = \sqrt{\frac{\sum_{n=0}^{N}(S(n) - S_R)}{\sum_{n=0}^{N}(S(n))^2}} \times 100\% \tag{3}$$

PRD values represent the percentage RMS difference of the reconstructed signal. The mathematical formula or PRD is as given equation 3, where *S(n)*: original signal and S_R: reconstructed signal. Table I displays calculated PRD values for the signals reconstructed using five different methods. In sense, lower PRD value represents better performance and closer resemblance to original signal. Each column represents values of respective methods headed by their names. The rows represent 5 distinct signals out of the used input signal set. The values show a clear trend of efficiency as the columns progress.

Our proposed model establishes a clean dominance over other methods traditional methods compared.

$$SNR = 20 \times \log \frac{X_O}{X_N} \quad (4)$$

The mathematical equation of SNR is as given equation 4, where X_O represents the signal and X_N represents the noise added. Equation 5 is the mathematical formula for Max Error, where S_R: reconstructed signal and S_O: original signal. As presented in Table I-III our proposed model out performs other state of art models. Fig. 3 demonstrates the performance of proposed model with respect to SNR. Our proposed model gives a consistent performance over a large data set as depicted in Fig. 3, but for better readability only 5 sample signals is presented in Table II.

$$ME = |S_R - S_O| \quad (5)$$

Max Error also works as a good performance evaluating parameter as suggested in [11]. The mathematical formula for Max Error (eqn. 5) calculation is simple, S_R: reconstructed signal and S_O: original signal. The Table III shows that our proposed model achieved the most efficient performance considering Max Error values over all the others models.

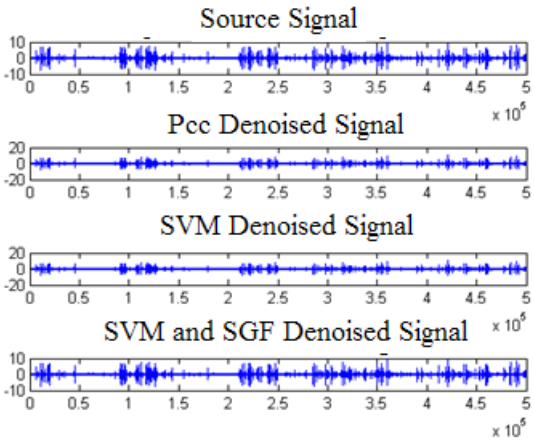

Fig. 2. Source and Reconstructed Signals.

TABLE I. CALCULATED PRD VALUES OF THE DIFFERENT METHODS

Signal	First 3 IMFs are Used in Construction	First 7 IMFs are Used in Construction	SVM Classified IMFs are Used in Construction	PCC Classified IMFs are Used in Construction	Proposed Model (SVM+SGF) Construction
1	35.0789	7.6093	16.6681	16.6681	0.8141
2	88.4465	11.0027	17.5735	17.5735	1.0142
3	102.0182	10.5388	17.7765	17.7765	1.1053
4	440.5524	16.0600	16.0570	16.0570	1.1787
5	15224.5472	38.0415	17.9300	17.9300	1.3754

[a.] Lower PRD value represents better performance.

TABLE II. CALCULATED SNR VALUES OF THE DIFFERENT METHODS

Signal	First 3 IMFs are Used in Construction	First 7 IMFs are Used in Construction	SVM Classified IMFs are Used in Construction	PCC Classified IMFs are Used in Construction	Proposed Model (SVM+SGF) Construction
1	9.4480	22.3739	15.5945	15.5945	41.7895
2	3.5444	19.1736	15.1356	15.1356	39.8797
3	2.9079	19.5477	15.0452	15.0452	39.1339
4	0.2411	15.9189	15.9207	15.9207	38.5749
5	0.0000	8.8114	14.9718	14.9718	37.2353

[b.] Higher SNR value represents better performance.

TABLE III. CALCULATED MAX ERROR VALUES OF THE DIFFERENT METHODS

Signal	First 3 IMFs are Used in Construction	First 7 IMFs are Used in Construction	SVM Classified IMFs are Used in Construction	PCC Classified IMFs are Used in Construction	Proposed Model (SVM+SGF) Construction
1	3.8788	0.7877	1.6079	1.6079	0.0862
2	6.5583	1.3310	2.7769	2.7769	0.1377
3	6.7789	1.3331	2.5055	2.5055	0.3358
4	7.4993	1.7521	1.7569	1.7569	0.0909
5	10.0021	3.9285	2.0450	2.0450	0.1432

[c.] Lower Max Error value represents better performance.

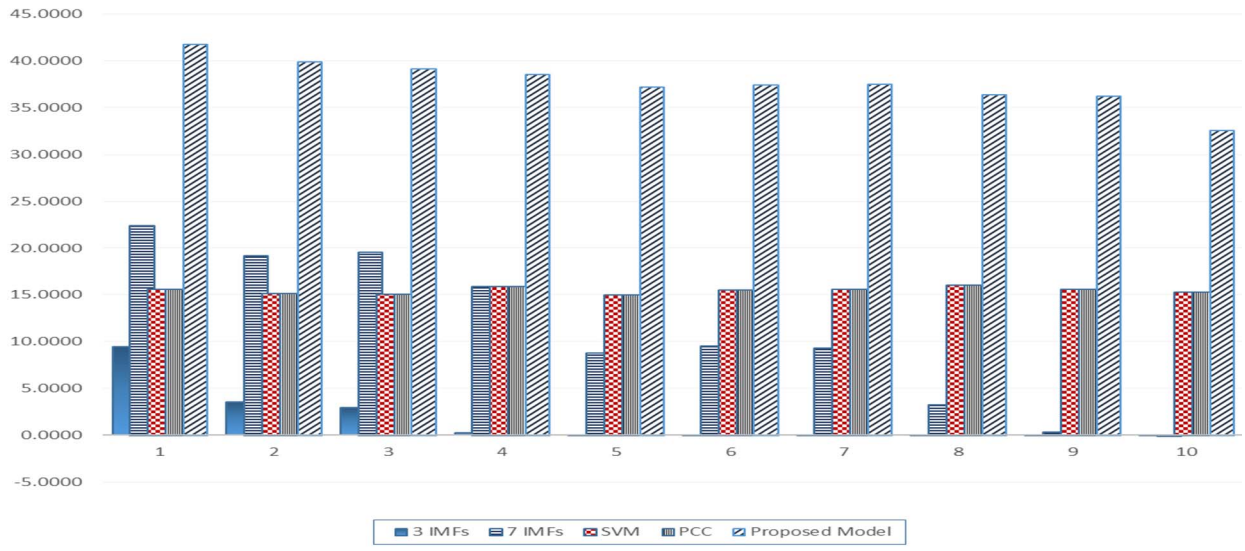

Fig. 3. SNR values for different methods.

IV. Conclusion

This paper presents a new approach to select adaptive IMF of EMD. In the proposed model we have used a machine learning tool, SVM for classification of noisy and noiseless IMFs. Savitzky-Golay filter is used to de-noise the noisy IMFs. Later the signal is reconstructed with both noise free and de-noised IMFs. Three statistical parameters SNR, PRD and Max Error were used as measuring tools in experimental evaluation. The experimental results exhibits that the proposed model out performs other state of art models by achieving a maximum 41.79% SNR, PRD and Max Error are reduced to 0.814% and 0.081% respectively, in medium noisy environments.

References

[1] S.W. Smith, "The Breadth and Depth of DSP. In The Scientist and Engineer's Guide to Digital Signal Processing," San Diego, CA: California Technical Pub, 1997, pp. 1-10.

[2] N. E. Huang, Z. Shen, S. R. Long, M. C. Wu, H. H. Shih, Q. Zheng, N. Yen, C. C. Tung, and H. H. Liu, "The empirical mode decomposition and the Hilbert spectrum for nonlinear and nonstationary time series analysis," in *Proc. of the Royal Society of London A:Mathematical, Physical and Engineering Sciences*, 1998, vol. 454, pp. 903–995.

[3] P. Nguyen, M. Kang, J. M. Kim, B. H. Ahn, J. M. Ha, B. K. Choi, "Robust Condition Monitoring of Rolling Element Bearings Using De-Noising and Envelope Analysis with Signal Decomposition Techniques," *Expert Systems With Applications,* 2015, vol. 42, pp. 9024–9032.

[4] D.B. Souza, J. Chanussot, and A. Favre, "On selecting relevant intrinsic mode functions in empirical mode decomposition: An energy-based approach," in *Proc. IEEE International Conference on Acoustics, Speech and Signal Processing (ICASSP),* 2014, pp. 325-329 .

[5] Z.K. Peng, Peter, W. Tse, and F.L. Chu, "A comparison study of improved hilbert-huang transform and wavelet transform: Application to fault diagnosis for rolling bearing," *Mechanical Systems and Signal Processing*, 2005, vol. 19, no. 5, pp. 974-988,

[6] A. Ayenu-Prah and N. Attoh-Okine, "A criterion for selecting relevant intrinsic mode functions in empirical mode decomposition," *Advances in Adaptive Data Analysis, Theory and Applications,* 2010, vol. 2, no. 1, pp. 1–24.

[7] B. E. Boser, I. M. Guyon, and V. N. Vapnik, "A training algorithm for optimal margin classifiers," In *Proc. of the Fifth Annual Workshop on Computational Learning Theory*- COLT 1992, pp. 144-152.

[8] V. Vapnik, The Nature of Statistical Learning Theory, NY: Springer-Verlag, 1995

[9] D.K. Srivastava, L. Bhambhu, "Data Classification Using Support Vector Machine," *Journal of Theoretical and Applied Information Technology*, 2010, vol 12. no. 1, pp. 435-445.

[10] J. Uddin, R. Islam, J. Kim, and C. Kim, "A Two-Dimensional Fault Diagnosis Model of Induction Motors using a Gabor Filter on Segmented Images". *International Journal of Control and Automation (IJCA*), 2015, vol. 9, no. 1, pp. 11-22.

[11] M. Almahamdy and H. B. Riley, "Performance Study of Different Denoising Methods for ECG Signals." *Procedia Computer Science,* vol. 37, pp. 325-332.

[12] M. Hamedi, S. Salleh, and A.M. Noor, "Facial neuromuscular signal classification by means of least square support vector machine for MuCI" *Applied Soft Computing*, 2015, vol. 30, pp. 83-93.

[13] P. Bhuvaneswari and J. S. Kumar, "Support Vector Machine Technique for EEG Signals," *International Journal of Computer Applications (IJCA)*, 2013, vol. 63, no. 13, pp. 1-5.

[14] V. Venkatachalam and J.L. Aravena, "Nonstationary signal enhancement using the wavelet transform," in *Proc. of the Twenty-Eighth Southeastern Symposium on in System Theory*, 1996, pp. 98–102.

978-1-5090-5785-6/16/$31.00 ©2016 IEEE

Double Compartment Microbial Fuel Cell Design using Salt Bridge as a Membrane with Sucrose and Starch as a Substrate

Sheikh Shehab Uddin, Kazi Shoffiuddin Roni
Electrical and Electronic Engineering Department
American International University Bangladesh
Dhaka 1213, Bangladesh
usshehab@gmail.com, xeonr@ymail.com

Abu Hena MD Shatil
Electrical and Electronic Engineering Department
American International University Bangladesh
Dhaka 1213, Bangladesh
abu.shatil@aiub.edu

***Abstract*—Most of the microbial fuel cell (MFC) designs need the separation of the cathode and anode cell by using proton exchange membrane (PEM). The majority used nafion or ultrex CMI-7000 as a PEM. But both of these membranes are too much costly and not too available to use. As an alternate of nafion, we use salt bridge in this study as a PEM which is pervious to other ions & substrate. Different organic materials like sucrose, glucose, starch can be used as substrate. This research paper analyses the performance of a double compartment microbial fuel cell for different substrate concentrations as well as surface area of the chambers with salt bridge as a membrane. Sucrose and starch were treated here as substrate and potassium permanganate was used as electron acceptor. Dhaka city's drain water was utilized as the container of bacteria. Better output was observed for sucrose as substrate due to higher solubility in water than starch.**

Keywords— Microbial Fuel Cell; Nafion membrane; Salt bridge; Sucrose; Starch; Potassium permanganate

I. INTRODUCTION

Bangladesh gets 7988 MW of electricity from gas and 600 MW of electricity as imported from India as of August 2016 [1]. But the amount of reserved gas is 14.16 trillion cubic feet (tcf) which will be finished within 2031 [2]. It's the high time to move to renewable sources to ensure the energy security for future generation. Bangladesh can utilize the bulk amount of bacteria filled polluted drain and river water to generate electricity through Microbial Fuel Cell (MFC). A new form of renewable energy by generating electricity from what would otherwise be considered waste was represented by Microbial fuel cell (MFC) technology. MFCs are electrochemical devices that are similar to conventional fuel cells in which energy from a chemical reaction is converted into useful electricity. This technology can use bacterium already present in wastewater as catalysts to generating electricity while simultaneously treating wastewater [3,4]. Microbes are employed by Microbial fuel cell (MFC) to generate electricity from biochemical energy produced during metabolism of organic substrates. Anode and cathode chambers are the compulsory parts of an MFC connected by an external circuit and detached by proton exchange membrane (PEM). Decomposition of organic substrates by microbes produces electrons and protons in the anode chamber. Those electrons and protons are transported through external circuit and proton exchange membrane respectively to the cathode [5]. Microbes utilize organic substrate as their energy source and outcome of this process is in release of high energy electrons those are transferred to electron acceptors. Microorganisms shuttle electrons onto anode surface that results in production of electricity [6]. For using in the MFC as microbe's bacteria is the most preferred to generate electricity while accomplishing biodegradation of organic matters and wastes [7,8]. Hydrogen can be produced in Microbial Fuel Cell and it happens smoothly from the fermentation of glucose in the presence of *Clostridium butyricum* [9].

$$C_{12}H_{22}O_{11} + 13H_2O \text{ ---> } 12CO_2 + 48H^+ + 48e^-$$

II. MICROBIAL FUEL CELL MECHANISM

Organic and inorganic matters are oxidized to generate current by bacteria which is used as biocatalysts in Microbial Fuel Cell (MFC) [10].

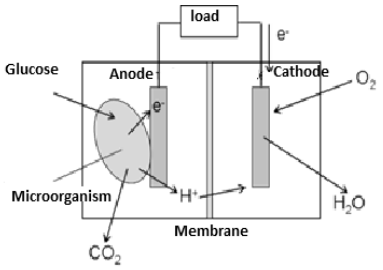

Fig. 1. MFC mechanism

Electrons which are produced from the substrates by bacteria are transferred to the negative terminal (anode) and go to the positive terminal (cathode) through a load. Several chemicals like neutral red, methylene blue, thionine are used as mediators to accelerate the generation of current in MFC. The above figure interprets that electrons gained from the substrate materials are transferred to the anode electrode by the bacteria present in anode chamber. Protons are also

978-1-5090-5785-6/16/$31.00 ©2016 IEEE

produced in oxidation reaction and passed to the cathode by proton exchange membrane. The transport of electrons from anode chamber to cathode chamber is occurred by direct contact or by mobile electron shuttles. Finally, the electrons are participating with the electron acceptor and the protons in cathode chamber [11].

III. Standard Electrode Potentials

The half-cell reactions can analyze reactions occurring in the microbial fuel cell.

$$2CH_3COO^- = CH_3\,CH_3 + CO_2 + 2e^- \quad (1)$$

For sucrose oxidation, we therefore have,

$$E_{AN} = E^0_{AN} - (RT/2F)\ln[(CH_3COO^-)^2 / (CH_3\,CH_3)] \quad (2)$$

For the cathode potential E_{cat} if we consider the case where Permanganate is used as the electron acceptor for the reaction, we can write

$$MnO^{4-} + 8H^+ + 5e^- = Mn^{2+} + 4H_2O \quad (3)$$

$$E_{cat} = E^0_{cat} - (RT/5F)\ln[(Mn^{2+}) / (MnO^{4-})(H^+)^8] \quad (4)$$

The Cell EMF is computed as,

$$E_{emf} = E_{cat} - E_{An} \quad (5)\ [5]$$

IV. Proposed Model With New Chemical Component

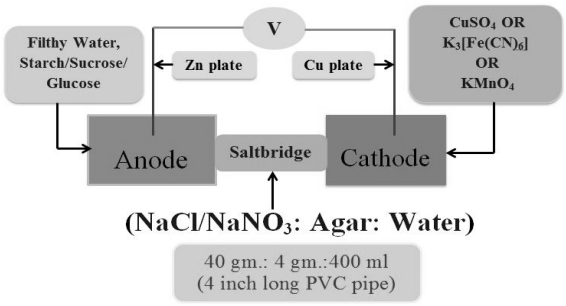

Fig. 2. An alternative model of MFC

For constructing a Microbial Fuel Cell, the configuration shown in figure 1 is the most efficient model as of now. But the chemicals as well as the components which are used in that model are unavailable in this corner of the globe. The production of some of these components like Nafion membrane is limited within some of the developed nations. So it is very tough to make MFC popular as a renewable energy source in Bangladesh. It is urgent to develop a new model of Microbial Fuel Cell. The configuration shown in figure 2 is a replacement of ideal model. The proposed model is a double compartment MFC. In anode chamber bacteria filled waste water can be used. It may be drain water, slurry of biogas plant, cow dung, human waste, rice washing water. Any type of liquid containing bacteria can be used in the anode chamber. As substrate material different organic materials can be used. Sucrose, glucose, starch etc. are included as substrate material. Any type of mediators like methylene blue, thionine, neutral red etc. is excluded in this model as they are costly but less effective. So the proposed model is "mediator less" MFC. The co enzyme like Nicotinamide Adenine Dinucleotide Hydride (NADH) is neglected totally. The reason behind neglecting NADH is the cost as well as it is not so much available in the local market. Zinc plate is used as anode electrode whereas copper plate is used as cathode electrode. The Nafion membrane is replaced by salt bridge. Nafion membrane is unavailable in this corner of the world. The market of nafion membrane is limited and cost is quite high. The salt bridge is made of water, Agar ($C_{14}H_{24}O_9$) and salt. Sodium Chloride (NaCl), Sodium Nitrate ($NaNO_3$), Potassium Chloride (KCl), Potassium Nitrate (KNO_3) etc. can be used as the sample of salt. For constructing a salt bridge, the ratio of water, agar and salt is 50 mL, 1gm, 5 gm. respectively for per inch. The measurement is suitable for 0.5-inch-thick salt bridge. Electron acceptors are kept in the cathode chamber. Oxygen (O_2), Copper Sulfate ($CuSO_4$), Potassium Permanganate ($KMnO_4$), Potassium Ferricyanide ($K_3[Fe(CN)_6]$) etc. can be used in the cathode chamber.

V. Practical Setup & Data Analysis

Based on the proposed model three set ups were constructed and observed. All the cells were kept in anaerobic condition and readings were measured across no load.

A. Set up 1

Potassium Permanganate was chosen to be used in cathode chamber. The amount of Potassium Permanganate used was 400 ml. Zinc and copper plates were chosen to do their job as electrode material in anode and cathode compartment respectively. A salt bridge of 5-inch-long and 0.5-inch-thick was used here to provide a way for the protons to pass from anode to cathode. 5 gm. Agar, 25 gm. Sodium Chloride as the sample of salt and 250 ml of water were taken for constructing the salt bridge.

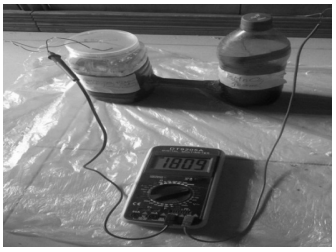

Fig. 3. Constructed Cell for Set up 1

At first all the components were taken in a pot then the materials were mixed during the heating process. The mixture was heated until it became adhesive. The amount of sucrose used was 125 gm. As the container of bacteria thick muddy layer of Dhaka North City Corporation's drain was used. At first 1 kg of muddy layer was mixed with 0.25 litre of drain water. Then 0.5 litre liquid was used from that mixture in the anode chamber. 1.809 V, 9.38 mA, 16.964 mW were measured as maximum voltage, current, power respectively for setup 1.

TABLE I. DIMENSIONS OF THE MFC CELL FOR SET UP 1

Chambers	Anode	Cathode
Length	12 cm	16 cm
Width(Anode)/Diameter(Cathode)	10 cm	6 cm
Surface Area	120 cm^2	358 cm^2
Salt bridge Length	12.7 cm	
Salt bridge Diameter	1.3 cm	
Electrode Length	14.5 cm	
Electrode Width	4 cm	
Electrode Surface Area	58 cm^2	

TABLE II. PRACTICAL FINDINGS FOR SET UP 1

Day	Voltage(V)	Current(mA)	Power(mW)
1	1.089	2.62	2.853
2	1.234	3.56	4.393
3	1.254	3.83	4.803
4	1.539	6.39	9.834
5	1.634	7.83	12.794
6	1.809	9.38	16.964
7	1.752	8.61	15.085
8	1.536	6.38	9.781

B. Set up 2

Fig. 4. Constructed Cell for Set up 2

For the second setup Potassium Permanganate was chosen to be used in cathode chamber. The amount of Potassium Permanganate used was 400 ml. Zinc and copper plates were chosen to do their job as electrode material in anode and cathode compartment respectively. A salt bridge of 5-inch-long and 0.5-inch-thick was used here to provide a way for the protons to pass from anode to cathode. The previous procedure was followed to construct the salt bridge. 250 gm of starch was taken in the anode compartment. As the container of bacteria thick muddy layer of Dhaka North City Corporation's drain was used.1.282 V, 1.515 mA, 1.944 mW were measured as maximum voltage, current, power respectively for setup 2.

TABLE III. DIMENSIONS OF THE MFC CELL FOR SET UP 2

Different Dimensions	**Measurements**
Chambers Length	16 cm
Chambers Diameter	6 cm
Chambers Surface Area	358 cm^2
Salt bridge Length	12.7 cm
Salt bridge Diameter	1.3 cm
Electrode Length	14.5 cm
Electrode Width	4 cm
Electrode Surface Area	58 cm^2

TABLE IV. PRACTICAL FINDINGS FOR SET UP 2

Day	Voltage(V)	Current(mA)	Power(mW)
1	1.282	1.515	1.944
2	1.224	1.419	1.739
3	1.227	1.406	1.725
4	1.252	1.389	1.739
5	1.176	1.099	1.292
6	1.233	1.161	1.432
7	1.237	1.284	1.588
8	1.033	1.165	1.203

C. Set up 3

Fig. 5. Constructed Cell for Set up 3

For the third setup higher quantity of sucrose and potassium permanganate was used. The amount of Potassium Permanganate used was 8 L. The amount of sucrose used was 500 gm. Zinc and copper plates were chosen to do their job as electrode material in both the compartment as before. The Salt bridges were 3-inch-thick and 3-inch long. The previous procedure was followed to construct the salt bridge. Here 2 litre of drain water was mixed with 8 Kg of muddy layer. Then 8 litre of liquid was used from the mixture. 5.36 V, 10.38 mA and 55.64 mW were obtained as maximum voltage, current and power respectively for setup 3.

TABLE V. DIMENSIONS OF THE MFC CELL FOR SET UP 3

Different Dimensions	Measurements
Chambers (Length, Width)	25.4 cm
Chambers Surface Area	645.16 cm^2
Salt bridge Length	10.16 cm
Salt bridge Diameter	7.62 cm
Electrode (Length, Width)	15.24 cm
Electrode Surface Area	464.52 cm^2

TABLE VI. PRACTICAL FINDINGS FOR SET UP 3

Day	Voltage(V)	Current(mA)	Power(mW)
1	1.327	9.59	12.73
2	1.25	9.03	11.29
3	3.74	5.85	21.88
4	3.86	9.75	37.64
5	4.27	8.57	36.60
6	4.35	8.93	38.85
7	5.36	10.38	55.64
8	4.96	9.53	47.27

VI. COMPARISONS AMONG PRACTICAL SETUPS

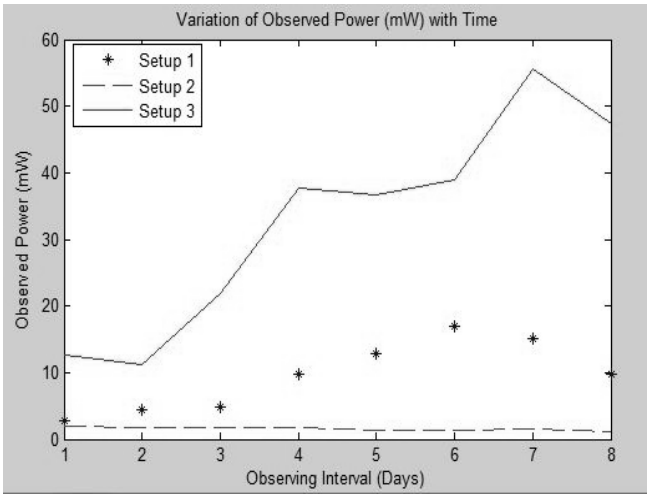

Fig. 6. Comparisons of Observed Powers (mW) from three setups

From figure 6 it is seen that setup 3 provided better power output among the three setups. The reason behind it is the use of higher amount of chemicals. In setup 2 starch is used where less impressive result was found. All the cells were kept in around 20^0c to 23^0c. It is known that starch is insoluble in water at low temperature. That may be the reason of low output from setup 3. Again all the organic materials are broken into glucose in the presence of bacteria. Starch takes one step more than sucrose to break into glucose. That may be another reason of low output from starch. But sucrose is directly converted into glucose to provide the electron. So sucrose can be a better substrate than starch for use in Microbial Fuel Cell.

VII. CONCLUSION

Membrane plays a vital role in MFC design. Except sediment MFC and specially designed single compartment MFC all the cells require PEM. The nafion is a member of Teflon (polytetrafluroethylene) which allow cations transportations including hydrogen ion across the membrane. On the other hand, salt Bridge has a high ohmic loss compared to nafion. That's why we get lower current density in our cell. While nafion can cost as much as $1500 per square salt bridge can build within $50 per square. We hope pricing will compensate the low current density. MFC cannot attain corresponding power densities due to inherent limitation. Hydrogen ion produce by microbes at a very slow rate compare to other fuel cell. Substrates like sucrose, starch increase the production of hydrogen ion at a contented rate. As in set up 3 we get the highest voltage 5.36V, which we think an effective output. The commercialize for PEM is growing rapidly & more systematic analyzes are necessary to measure the effect of the membrane in the long run.

REFERENCES

[1] (2016)Bangladesh Power Development Board Website, [Online] Available At:http://www.bpdb.gov.bd/bpdb/index.php?option=com_content&view=article&id=150&Itemid=16.

[2] (2015) The Daily Star Website. [online] Available at: http://www.thedailystar.net/backpage/gas-reserve-last-until-2031-104479.

[3] Liu H, Ramnarayanan R, Logan BE. Production of electricity during wastewater treatment using a single chamber microbial fuel cell.Environ Sci Technol 2004;28: 2281–2285.

[4] Min B, Logan BE. Continuous electricity generation from domestic wastewater and organic substrates in a flat plate microbial fuel cell. Environ Sci Technol 2004;38: 5809–5814.

[5] B.E. Logan, B. Hamelers, R. Rozendal, U. Schro ¨ der, J. Keller,S. Freguia, P. Aelterman, W.Verstraete, K. Rabaey,"Microbial fuel cells: methodology and technology,"Environ. Sci. Technol., Vol. 40,pp. 5181–5192,2006.

[6] Wrighton K C & Coates J D, Microbial fuel cells;plug-in and power-on microbiology, Microbes, Vol.4 , pp. 281-287, 2009.

[7] Park DH, Zeikus JG. Electricity generation in microbial fuel cells using neutral red as an electronophore. Appl Environ Microb 2000;66:1292–1297.

[8] Oh SE, Logan BE. Hydrogen and electricity production from a food processing wastewater using fermentation and microbial fuel cell technologies. Water Res 2005;39:4673–4682.

[9] Suzuki S. and I. Karube, Energy Production With Immobilized. Cells, *Appl. Biochem. Bioeng*., Vol. 4,pp. 281 – 310,1983.

[10] B. E. Logan, *Microbial fuel cell*, John Wiley & Sons, 2008.

[11] K. Rabaey, W. Ossieur, M. Verhaege and W. Verstraete, Wat., *Sci. Tech*.,Vol.52, pp. 59-66, 2005.

2nd International Conference on Electrical, Computer & Telecommunication Engineering (ICECTE)
8-10 December 2016, Rajshahi-6204, Bangladesh

Controlling of frequency fluctuation of wind turbine generator using wind speed controlled pitch controller

[1] A.H.M Iftekharul Ferdous, [2] M. R. I. Sheikh, [3] Md.Asaduzzaman Shobug
[1,3]Dept. of EEE, Pabna University of Science and Technology
[2]Dept. of EEE, Rajshahi University of Engineering and Technology
Pabna , Bangladesh
digonto_eee3@yahoo.com

***Abstract*— Due to the growing electricity concern, it is very much needed to use wind power for the generation of electricity. But for the random variation of wind speed, the output power of the wind generator fluctuates randomly as well as the fluctuation of the frequency occurs. As a result this decreases the energy. This paper represents a wind speed controlled pitch controller to control the wind generator output power fluctuation and also reduce the frequency fluctuations .For simulation analysis, real wind speed data is used and the simulation analysis have been performed by using PSCAD/EMTDC [1].**

Keywords— Wind turbine; Induction generator; Frequency fluctuation; Smoothing control; PSCAD.

I. INTRODUCTION

Among many types of energy sources, wind energy is one of the most prominent energy sources due to its viability and pollution free causes. One of the simplest methods of running a wind generation system is to use an induction generator connected directly to the power grid, because induction generators are the most cost-effective machines for energy conversion. For the cause of proportionality of wind turbine output to the cube of the wind velocity, the fluctuation of frequency occurs due the variation of wind speed and frequency fluctuations occurs from output power fluctuations of wind generator causes several problems on the overall power system as a result inaccuracy and lamp flickering occurs. Therefore, minimization of fluctuations of power system frequency is very important from the view point of power system security. There are many methods for smoothing the wind generator output fluctuations as well as the frequency fluctuation by using several types of energy storage systems such as EDLC [2]-[8] which are too much costly. Several works have already been done considering the application of SMES for the wind power generation and most of the cases, the energy devices are used to solve the fluctuation issues of the wind power generation system [10].
Again, another control strategy of the STATCOM/SMES is installed at a wind farm for decreasing fluctuations of output power and frequency of the wind farm [4].In most of the previous work carried out depending upon the energy devices such as SMES in minimizing frequency fluctuations is evaluated considering a multi-machine power system consisting of hydroelectric generators, diesel generators and wind generator [9].But, in most of the cases the installation cost is too much high due to the use of the energy devices.
Because of that reason, a great deal of research has been focused on the development of pitch controller design to reduce the costs of wind power for smoothing the output power and frequency fluctuation. This paper proposes a new pitch control system using the real wind speed data with rotor speed and reactive power for smoothing the wind generator output fluctuations.

II. POWER SYSTEM MODEL

The model system used in the simulation analyses is shown in "Fig. 1". The model system consists of a wind farm (WF), a hydro power generator HG (a salient pole synchronous generator, SG1), two thermal power generators (cylindrical type synchronous generators, SG2 and SG3), a nuclear power generator NG (a cylindrical type synchronous generators, SG4), and a load. The wind farm consists of five wind power generators (squirrel cage induction machines, IGn , n=1,2,3,4,5). SG1 and SG3 are operated under Load Frequency Control (LFC), SG2 is under Governor Free (GF) control and SG4 is under Load Limit (LL) operation. In general, LFC is used to control frequency fluctuations with a long period more than a few minutes, and GF is used to control fluctuations with a short period less than a minute. LL is used to output constant power. Q_{WF} and Q_{Load} are capacitor banks. Q_{WF} is used at the terminal of WF to compensate the reactive power demand of WF at steady state. In order to maintain the power factor of the wind power station unity during the rated operation, the value of the capacitor is chosen. Q_{Load} is used at the terminal of load to compensate the voltage drop by the impedance of transmission lines. Core saturations of induction generator and synchronous generators are not considered. The initial power flow and initial conditions are shown in Table I. Parameters of IGs and SGs are shown in Table II.

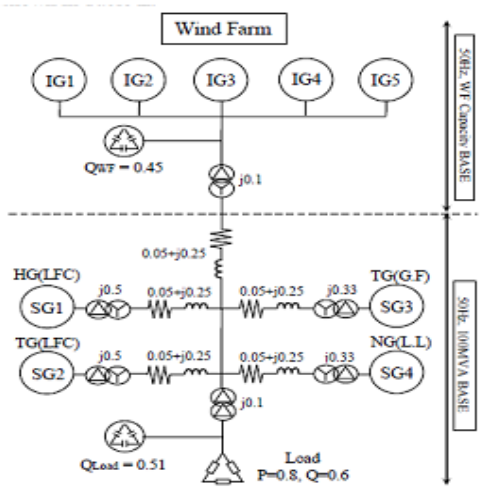

Fig 1: Model System

Table-I
Initial conditions

	IG	SG1	SG2,SG3,SG4
P	0.1	1.00	1.00
V	1.0	1.05	1.05
Q	0.0		
s (slip)	-1.733%		

Table-II

Induction Generator				
	Squirrel cage type (IGn,n=1,2,,,5)			
MVA	2 (each)			
R_1 (pu)	0.01			
X_1 (pu)	0.10			
X_m (pu)	3.5			
R_{21} (pu)	0.035			
X_{21} (pu)	0.03			
R_{21} (pu)	0.014			
X_{21} (pu)	0.098			
2H (sec)	1.5			
Synchronous generator				
	Salient pole type (SG1)	Cylindrical type		
		SG4	SG3	SG4
MVA	20	30	20	30
X_d (pu)	1.2	2.11		
X_q (pu)	0.7	2.02		
H (seconds)	2.5	2.32		

III. Modeling of Wind Turbine

The devices which are used to convert the wind energy to electrical energy are called the wind energy conversion devices. The total wind power entering the wind turbine is given by [6]:

$P_w = 0.5\rho\pi R^2 V_w^3 C_P(\lambda, \beta)$

Where, r is the air density (in kg/m3), R is the blade radius (in meters), Pw is the extracted power from the wind, and C_P is the power coefficient and the wind speed, V_W is given in miles per hour .As, C_P is too complicated to calculate; usually its value is calculated by recourse to simpler formulas. Now, C_P is calculated by the following formula [7]:

$C_P=1/2(\lambda-0.02\beta^2-5.6)\, e^{-0.17\lambda}$

Where, λ is Tip-Speed Ratio and β is the blade pitch angle.

IV. Modeling of Synchronous Generator

A. *Governor for hydro, thermal and nuclear generators [3, 5, 8]:*

The governor unit automatically adjusts the rotational speed of the turbine and thus controls the generator output. When the generator load is constant, the turbine is operated at a constant rotational speed. However, when the load changes, balance between the generator output and the load is not maintained, and the rotational speed changes, also. When the load is removed, the governor detects the increase of the rotational speed, and the valve is closed immediately so that an abnormal speed increase of the generator can be prevented. The governor models used in the simulation analysis for hydro, thermal and nuclear generators are taken from [2].

B. *Load Frequency Control Model [2, 3]:*

In the load frequency control model, the output power signal is sent to each power plant when frequency deviation is detected in the power system. Then, the governor output of each power plant is changed according to the LFC signals, and the power plant output is changed. The LFC model used here is shown in "Fig. 2", where Tc_2 (the LFC period) = 200 seconds, ω_c (LFC frequency) $=1/Tc_2 = 0.005$ Hz, ζ (damping ratio) =1. The frequency deviation is input into a low pass filter (LPF) to remove fluctuations having a short period, because the LFC is used to control frequency fluctuations having a long period. Here, the parameters are chosen by using trial and error method for obtaining the better performance from the system.

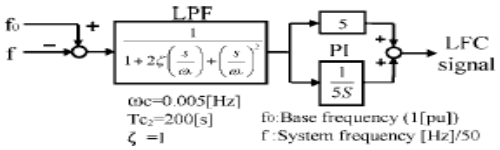

Fig 2: LFC model

V. PITCH CONTROLLER MODEL

The main function of the pitch controller is to sense the increased velocity when the wind power is beyond the rated level and maintain the output power fluctuation in an acceptable range but when the wind speed is below the rated speed, the pitch angle is zero. This paper proposes a new pitch controller model which is shown in the "Fig. 4". Here, pitch angle increases with the increases of the wind speed and controls the frequency fluctuations within $\pm$0.12[Hz]as well as controls the output power fluctuation rather than the conventional pitch controller shown in the "Fig. 3". The energy also becomes very small using the proposed pitch controller. The proposed pitch controller is modeled with a PI controller, using of the rotor speed with the wind speed in the reference and for the simplicity, a first order time delay system is used with a time constant of T_W=5s. Due to the mechanical limitations, weight of blade and rotational inertia of blade, the pitch angle cannot change instantly. Because of that, for the simulation analysis, the pitch angle is limited to change at the rate of 10 degrees per second.

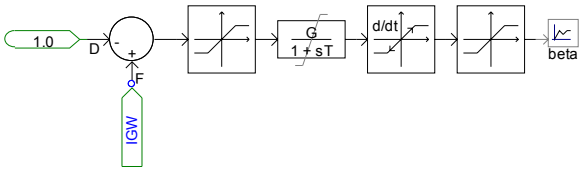

Fig 3: Conventional pitch controller

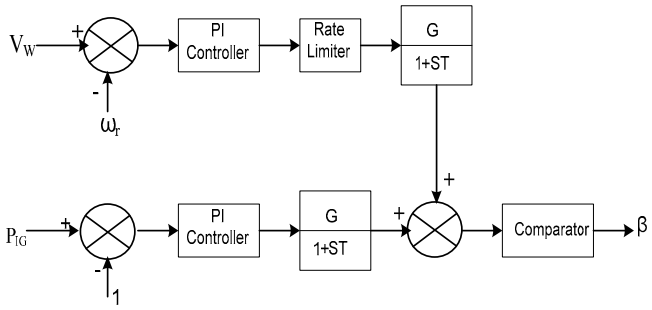

Fig 4: Proposed pitch controller

VI. SIMULATION ANALYSES

Simulation analyses has been performed in order to obtain the performance power system frequency fluctuation using real wind speed data as well as to examine the performance of the proposed wind speed controlled pitch controller. Both the proposed and conventional pitch controller is considered here to investigate the output power fluctuation. "Fig. 5" shows the wind speed data which are applied to the wind generators. The total simulation analyses have been carried out using PSCAD/EMTDC simulation tools [1] with a simulation time of 600s.

It is seen that the output power is controlled effectively here .The blade pitch angle of the proposed pitch controller shown in the "Fig. 6" & "Fig. 7," with the comparison of conventional pitch controller. "Fig. 8," shows that the output power of the wind farm which is very much better in the proposed pitch controller.

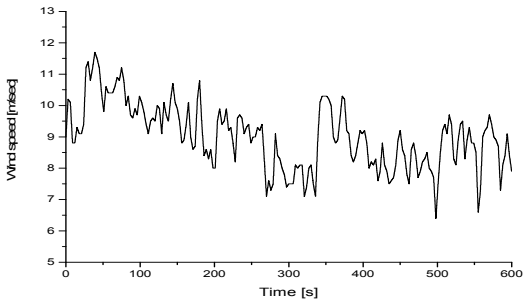

Fig 5: Real wind speed data (for IG1,IG2,IG3,IG4,IG5)

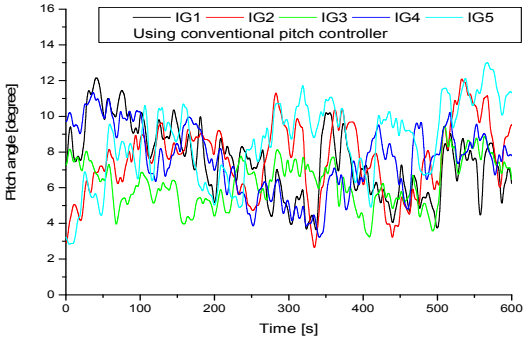

Fig 6: Pitch Angle responses of IG1-IG5

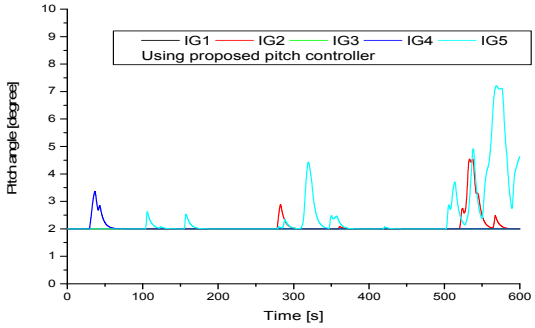

Fig 7 : Pitch Angle responses of IG1-IG5

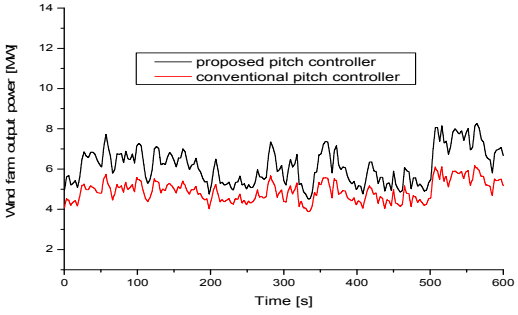

Fig 8: Output power of the Wind farm.

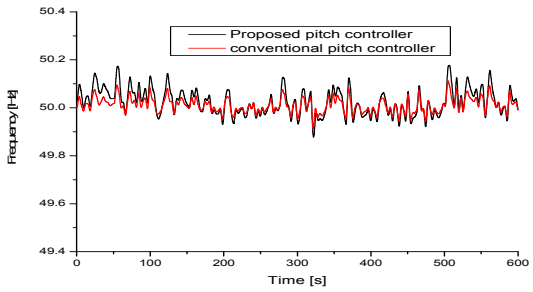

Fig 9: Frequency Fluctuation of the system

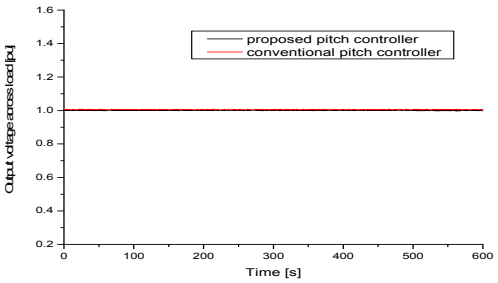

Fig 10 :Voltage across load [pu]

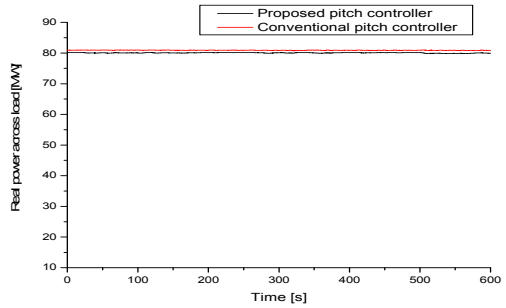

Fig 11 : Real power across load[MW]

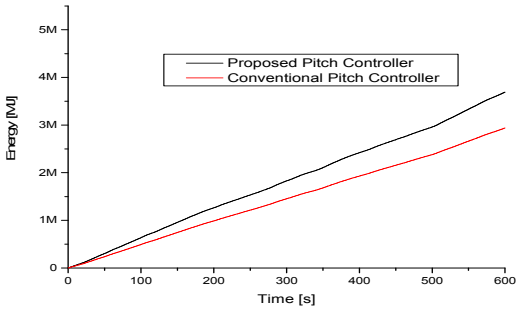

Fig 12: Energy responses

A very good result of frequency fluctuation is seen from the "Fig. 9," which shown that the fluctuation is within ± 0.13Hz which is the range of permissible power system frequency of 50±0.2 Hz. "Fig. 10" & "Fig. 11", shows the voltages and the real power across the load which is very good in comparison with the conventional pitch controller. So, the frequency can be controlled up to 20% of the total capacity of the wind power system and from the "Fig. 12", we have seen the energy generated by the wind power system using both the pitch controller. It is seen that loss of energy is considerable less in the proposed pitch controller rather than the conventional pitch controller.

VII. Discussion

From the evaluation of the frequency response, it is seen that the deviation of the frequency of the wind farm is within the range of ± 0.2[Hz] which is the permissible range of frequency deviation. This deviation of frequency is controlled within ± 0.12[Hz] by the newly proposed pitch controller. As a result, the proposed pitch controller can be considered sufficiently effective for minimizing the frequency fluctuations of the wind power system as well as smooth power can be delivered to the customers.

VIII. Conclusion

A large number of wind farms will be added with the utility network day by day but due to the continuous variation of wind causes frequency fluctuations as well as creates difficulties for the power grid companies to provide the constant power. This paper represents a new wind speed controlled pitch controller for smoothing the output power as well as smoothing the frequency fluctuation. Simulation analysis also being carried out which shows that the frequency fluctuation is controlled effectively rather than the conventional pitch controller and also cost effective rather than using any energy storage devices.

References

[1]. PSCAD/EMTDC Manual, Manitoba HVDC Research Center (1994).

[2]. M. R. I. Sheikh*, S. M. Muyeen, R. Takahashi and J. Tamura "Smoothing control of wind generator output fluctuations by PWM voltage source converter and chopper controlled SMES", Published online in Wiley Inter Science (www.interscience.wiley.com). DOI: 10.1002/etep.469.

[3]. M.R.I. Sheikh, R. Takahashi, and J. Tamura, "Study on frequency fluctuations in power system with a large penetration of wind power generation," Ener. J, vol.12, pp. 77-86, 2011.

[4]. M.R.I Sheikh, S.M. Muyeen, R. Takahashi, T. Murata, and J. Tamura, "Minimization of fluctuations of output power and terminal voltage of wind generator using STATCOM/SMES," IEEE Bucharest. Bucharest, pp. 1-6, 28 June – 02 July 2009.

[5]. Standard models of electrical power system: Technical Report Inst. Electrical Engineers of Japan (IEEJ), 1999, pp. 1–82 754

[6]. Heier S. Grid Integration of Wind Energy Conversion System. John Wiley & Sons Ltd.: Chichester, UK, 1998.

[7]. Wasynczuk O, Man DT, Sullivan JP. "Dynamic behavior of a class of wind turbine generator during random wind fluctuations." IEEE Transactions on Power Apparatus and Systems 1981; PAS-100(6): 2845–2873.

[8]. S.M. Muyeen, H.M. Hasanien, J. Tamura, "Reduction of frequency fluctuation for wind farm connected power systems by an adaptive artificial neural network controlled energy capacitor system" IET Renewable Power Generation, doi: 10.1049/iet-rpg.2010.0126, 19th March 2012.

[9]. Mohd. Hasan Ali, *Junji Tamura, and Bin Wu, "SMES Strategy to Minimize Frequency Fluctuations of Wind Generator System,"

[10]. T. Kinjo, T. Senjyu, N. Urasaki, and H. Fujita, "Terminal-voltage and output-power regulation of wind-turbine generator by series and parallel compensation using SMES," IEE Proc.-Gener. Transm. Distrib., vol. 153, no. 3, pp. 276-282, May 2006.

International Conference on Electrical, Computer & Telecommunication Engineering (ICECTE)
8-10 December 2016, Rajshahi-6204, Bangladesh

Gaussian Mixture Based Semi Supervised Boosting For Imbalanced Data Classification

Mahit Kumar Paul, Biprodip Pal
Department of Computer Science & Engineering
Rajshahi University of Engineering & Technology
Rajshahi, Bangladesh
mahit_bd@yahoo.com, biprodip.cse@gmail.com

***Abstract*—Semi supervised approaches are practical in problem domain where pattern clustering is supposed to provide good classification. Gaussian Mixture Model (GMM) can approximate arbitrary probability distribution, thus is considered as a dominant tool for classification in such domains. This paper appraises the functioning for GMM as it is applied to imbalanced datasets which consists of uneven distribution of samples from all the classes. Later, an ensemble approach is presented to boost the GMMs in a semi supervised manner via Adaptive Boosting technique. Experiment on benchmark imbalanced datasets with different imbalance ratio has been carried out. Empirical result demonstrates the efficacy of the proposed BoostedGMM classifier compared to baseline approaches like K-means and GMM.**

Keywords— Gaussian Mixture Model; AdaBoost; Classification; Clustering; Imbalance data.

I. INTRODUCTION

Supervised learning is tough when obtaining labeled data is hard. Often data labeling entails far-reaching proficient effort and is frequently time consuming too [1]. In contrast, concealed patterns are revealed by unsupervised learner from unlabeled data. But performance of reproductive classifiers can be degraded due to unlabeled data too as like attribute skewness[2] and class imbalances[3]. In this case, the midway between supervised and unsupervised learning is the semi-supervised learning (SSL). The application domains in which unlabeled data are abundant SSL is predominantly enthusiastic [4]. As the name infers, a classifier is first trained by labeled data and then used to categorize unlabeled data [1].

A probability density function (PDF) of the observations is used to symbolize a class of data patterns. Parametric method provides a convenient way to find the PDF of the observations. Parametric PDF estimators Gaussian mixture model (GMM) [5] is efficiently and broadly used in data mining, machine learning, and statistical analysis [6]. When the feature space is of high dimensionality, regardless of its acceptance and effectiveness, GMM suffers from inadequate training data [7]. Moreover, traditional methodologies of cluster analysis do not work well where new applications have tendency to produce data having very high dimensions. To eliminate this constraints, a number of techniques have been suggested, including the use of diagonal covariance matrices in the component Gaussians, universal background model (UBM) with maximum a posteriori (MAP) adaptation [8], etc. Usually, Maximum Likelihood is used to estimate the parameters in a GMM when data is accessible and the Expectation-Maximization (EM) algorithm is an effective method to accomplish this procedure.

Boosting is the point of interest of this work, which has been used to enhance GMM with a view to use with supervised classification techniques in decision fusion scenario. Boosting diminishes the variance of the unbalanced classifiers and advances the classification performance [9]. It is a strong ensemble-based learning algorithm that iteratively improves the classification accuracy using any base learner [10]. To generate models, GMM has been used as a weak learner instead of a classifier to be boosted with AdaBoost [11] algorithm, and combining these models, final model is generated. The method has been tested for imbalanced dataset. The results indicate that BoostedGMM is able to cope comparatively well with distinctive class imbalances and the performance is better than GMM, and K-means in terms of standard metrics.

II. GAUSSIAN MIXTURE MODEL

A Gaussian Mixture Model (GMM) is a parametric probability density function where iterative Expectation-Maximization (EM) algorithm estimates the parameters from training data. Weighted sum of M component Gaussian densities that forms the Gaussian mixture model is specified by the equation (1) [12]

$$p(x|\lambda) = \sum_{i=1}^{M} w_i \, g(x|\mu_i, \sum_i) \qquad (1)$$

where x represents a D-dimensional continuous valued data vector, w_i , i = 1, . . . , M , are the mixture weights, and $g(x|\mu_i, \Sigma_i)$, i = 1, . . . , M, are the component Gaussian densities. Every component density is a D-variate Gaussian function that has the form as following [12]

$$g(x|\mu_i, \sum_i) = \frac{1}{(2\pi)^{D/2}|\sum_i|^{1/2}} \exp\{-\frac{1}{2}(x-\mu_i)'\sum_i^{-1}(x-\mu_i)\} \qquad (2)$$

where, μ_i and Σ_i indicates mean vector and covariance matrix [10] respectively. Complete Gaussian mixture model is formed by the mean vectors, covariance matrices and mixture weights from all component densities. The notation λ collectively represents the above parameters as,

$$\lambda = \{w_i, \mu_i, \sum_i\} \qquad i = 1, \ldots, M \qquad (3)$$

978-1-5090-5785-6/16/$31.00 ©2016 IEEE

To estimate the parameters λ of GMM from given training vectors and a GMM configuration, several techniques are available. Undoubtedly, Maximum Likelihood (ML) estimation is the most standard and well-established method. ML estimation aims to find the model parameters that maximize the likelihood of the GMM provided the training data. For T consecutive training vectors $X = \{x_1, \ldots, x_T\}$ the GMM likelihood can be written as following [12].

$$p(X|\lambda) = \prod_{t=1}^{T} p(X_t|\lambda) \quad (4)$$

A special case of the expectation-maximization (EM) algorithm, ML parameter estimation can be obtained iteratively. In case of unsupervised clustering where the value of the variables is certainly not directly observed, EM algorithm can be used, provided the general form of the probability distribution governing variables is identified. Convergent solution to the hidden variables under the condition of maximum likelihood (ML) can also be obtained from EM. Closed forms of the probability distribution can be obtained depending upon the aimed data although there are many unknown parameters in the formula. Two steps of EM algorithm are as [13],

- The Estimation Step: Expectation of the unobserved data

$$E_{f(X|Y,\theta')}[\log f(X|Y,\theta'')] \quad (5)$$

- The Maximization Step: Finds θ" such that

$$\theta'' = argmax(E_{f(X|Y,\theta')}[\log f(X|Y,\theta'')]) \quad (6)$$

Where X and Y are unobserved and observed data respectively, θ is the parameters needed to determine the likelihood f(Y). Objective is to determine the maximum likelihood θ_{ML} that maximizes $L(\theta) = \log f(Y|\theta)$. EM algorithm essentially figures out a sequence of θ' and θ" such that $L(\theta'') > L(\theta')$ [13].

III. ADABOOST

The AdaBoost algorithm takes a weak learner A as a black box. A set of points $(x_1,y_1)\ldots\ldots\ldots(x_n,y_n)$ are the inputs for the AdaBoost algorithm provided labels $y_i \in \{-1,1\}$ for all *i*. It runs for M times and invokes the A on each of its turns. New sets of input points are fed to A to obtain new information from A on each round. New distributions D_m are defined over the n input points at each round m as n is fixed and a sample of polynomial size is selected from new distribution to give as input to A. At each round, a function or model is generated by A that outperforms than random guessing with respect to the particular distribution D_m. Finally a model is formed combining the specialist week models of each turn which are built on hard samples [11].

IV. PROPOSED BOOSTED GMM APPROACH

This paper considers GMM as the weak learner model. Initially all of the input patterns are treated equally by the proposed approach. After the first model generation, the misclassified patterns are weighted larger than those that are truly classified so that the misclassified patterns obtain higher probability of selection for the remaining model generations. This continues until the calculated error is either 0 or greater than or equal to 0.5. The BoostedGMM algorithm is summarized in Algorithm1.

Algorithm 1. BoostedGMM

1. Input: n training examples $\{x_i, c_i\}$, where $x_i \in X$, $c_i \in \{1, ..., C\}$, i = 1, ..., n; # iterations M.
2. Initialize the weights $w_i^{(1)} = 1/N$, i = 1,2, …. N;
3. For each round m = 1, … … …, M
   - Draw a sufficiently large sample from Imbalanced set D_m
   - Run GMM on this sample to produce weak learner G_m using expectation and maximization step as follows
     - Compute Expectation by following operations
       - PDF of multivariate Gaussian for cluster j from equation (2).
       - Probability of example i in cluster j

$$w_j^{(i)} = \frac{g_j(x)\emptyset_j}{\sum_{l=1}^{k} g_l(x)\emptyset_l}$$

     - Compute Maximization from following operations
       - Prior probability of cluster j

$$\emptyset_j = \frac{1}{m}\sum_{i=1}^{m} w_j^{(i)}$$

       - Mean of cluster j is

$$\mu_j = \frac{\sum_{i=1}^{m} w_j^{(i)} x^{(i)}}{\sum_{i=1}^{m} w_j^{(i)}}$$

       - n x n covariance matrix

$$\Sigma_j = \frac{\sum_{i=1}^{m} w_j^{(i)}(x^{(i)} - \mu_j)(x^{(i)} - \mu_j)^T}{\sum_{i=1}^{m} w_j^{(i)}}$$

   - Set err_m

$$err_m = \frac{\sum_{i=1}^{N} w_i^{(m)} I(y_i \neq G_m(x_i))}{\sum_{i=1}^{N} w_i^{(m)}}$$

   - Set α_m

$$\alpha_m = log((1 - err_m)/err_m)$$

   - Update weights

$$w_i^{(m+1)} = w_i^{(m)} e^{[\alpha(m) I(y_i \neq G_m(x_i))]}$$

4. Output, combined model

$$G(x) = sign(\sum_{i=1}^{M} \alpha_m G_m(x))$$

V. CLASS IMBALANCE

Imbalanced data sets involve a dissimilar class distribution. In common appreciative, class imbalance or between-class imbalance resembles major and frequently excessive imbalances. Frequently, with an order of 500:1, 1,000:1, 50,000:1 and so on, one class may out characterize another class. Fig. 1 illustrates a typical scenario. For imbalance problems the Imbalance Ratio (IR) is calculated as equation (7)

$$IR = \frac{T_{maj}}{T_{min}} \quad (7)$$

Where, T_{maj} is total instances of majority class and T_{min} is total instances of minority class.

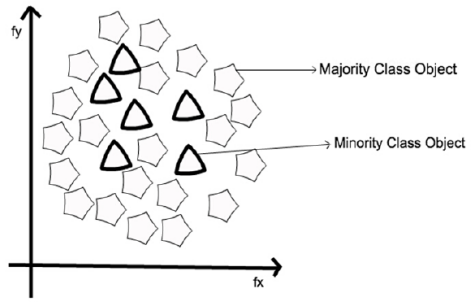

Fig. 1: Imbalanced dataset; Triangles are out represented by pentagonals.

Problems that are intrinsically based on imbalanced data frequently causes imbalance in dataset. For instance, if a data set is considered that encompasses fraud transaction samples, normal transaction samples will significantly exceed fraudulent samples. In imbalanced cases, classifiers used to provide an imbalanced degree of predictive accuracy with the majority class having better percentage of accuracy while the minority class having very poor accuracies. But a balanced accuracy (ideally 100 percent) for both of the classes on the data set is desirable [3].

VI. EXPERIMENTAL SETUP

Fivefold cross-validation has been used to assess the performance of the three mentioned methods, where each dataset is arbitrarily separated into five equal sized subdivisions. Each of the five subdivisions was used precisely once as the testing data while the rest were in corresponding training dataset. Then the results of the five folds are averaged to appraise the final performance. MATLAB has been used as coding tool of the algorithms. The machine on which experiment has been performed occupies; processor: Intel(R) Core(TM) i5-3210 CPU @ 2.50GHz; RAM: 4.00 GB, system type: 64-bit operating system.

A. Dataset

Used 11 data sets are from KEEL data-set repository [14] in this experiment. To obtain two-class imbalanced problems multiclass data sets were modified so that the blending of one or more classes befitted the positive class and the blending of one or more of the enduring classes was labeled as the negative class[15]. Performing this, we obligate different IRs: from low imbalance to highly imbalanced data sets. Table I summarizes the properties of the selected data sets. This table is ordered according to the last column in the ascending order.

B. Result Analysis

To assess the classification performance, evaluation criteria is a key factor. Fig. 2, representing the bar graph, demonstrates the comparison of all three methods in terms of the accuracy measurement with respect to the IR value using the datasets of Table I. As can be seen, the discrepancy among the methods in classification accuracy reduced as the IR value increased. The accuracy of all the methods increased by at least 20 percent as IR value is increased from 1.82 to 13. For IR values up to 5.46 the divergence of accuracy is sharp and Boosted GMM outperformed others. Although for dataset D5, D6, D7, D8, D10 the accuracy is equivalent, Boosted GMM is slightly better at rest of the cases.

In the basis of imbalanced datasets accuracy does not differentiate between the numbers of appropriately classified patterns of dissimilar classes. Hence, it may central to specious inferences, i.e., a classifier that accomplishes an

TABLE I. IMBALANCED DATASETS

Datasets		**No. of Attributes**	**Total samples**	**IR**
Name	**ID**			
glass1	D1	9	214	1.82
glass0	D2	9	214	2.06
Vehicle0	D3	18	846	3.23
ecoli2	D4	7	336	5.46
ecoli3	D5	7	336	8.19
yeast-2_vs_4	D6	8	514	9.08
ecoli-0-6-7_vs_5	D7	6	220	10
glass-0-16_vs_2	D8	9	192	10.29
ecoli-0-1_vs_5	D9	6	240	11
ecoli-0-1-4-7_vs_5-6	D10	6	332	12.28
ecoli-0-1-4-6_vs_5	D11	6	280	13

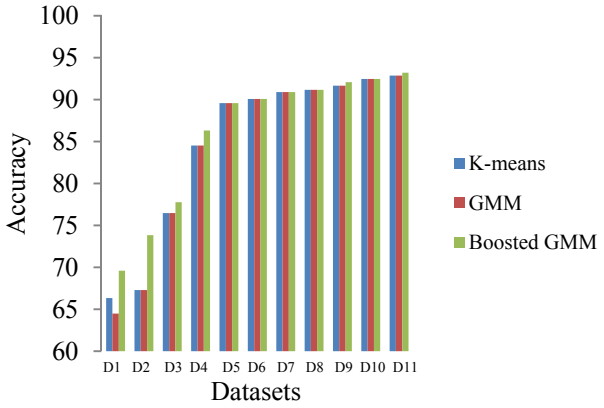

Fig. 2: IR versus accuracy analysis of experimented methods

accuracy of 90% in a data-set with an IR value of 9, is not perfect if it classifies all examples as negatives [15]. For this reason, both the F1 measure and AUC (area under the curve) has been considered to measure the positive and negative classes [16]. Table II summarizes the F1 score as well as the AUC value for the methods. Though scores are seen to fluctuate throughout the distribution, it is common to see that for each of the dataset, boosted GMM has better performance than the others. F1 and AUC score consideration demonstrates the superiority of Boosted GMM over the other methods even for the cases where the accuracies were similar.

TABLE II: F1 MEASURE AND AUC VALUES

Datasets	K-means		GMM		Boosted GMM	
	F1	AUC	F1	AUC	F1	AUC
glass1	0.6063	0.5759	0.6270	0.6068	0.6871	0.6532
glass0	0.6930	0.6736	0.6779	0.6693	0.7144	0.6935
vehicle0	0.6163	0.6286	0.7208	0.7560	0.7454	0.7760
ecoli2	0.6323	0.6667	0.5641	0.5495	0.7009	0.7375
ecoli3	0.7278	0.8395	0.5888	0.5849	0.7181	0.8182
yeast-2_vs_4	0.7125	0.8082	0.6707	0.7496	0.7089	0.7843
ecoli-06-7_vs_5	0.7084	0.8225	0.5634	0.5403	0.4683	0.4875
glass-0-16_vs_2	0.5655	0.5800	0.6082	0.6638	0.6115	0.6798
ecoli-0-1_vs_5	0.6098	0.6682	0.7064	0.8364	0.7579	0.8886
ecoli-0-1-4-7_vs_5-6	0.5908	0.6437	0.6967	0.8207	0.7522	0.8784
ecoli-0-1-4-6_vs_5	0.6105	0.6807	0.6967	0.8346	0.7537	0.8789

Table II represents that normally boosted GMM has better performance in terms of F1 measure and AUC values than K-means and GMM. In the other cases, it has fewer differences. Hence, it is observed with respect to positive and negative classes for imbalanced datasets, boosted GMM has better performance.

VII. CONCLUSION

In this paper, GMM is considered as 'weak learner' to generate strong learner applying adaboost algorithm. Different measurements remarkably specify that boosted GMM outperforms than GMM and k-means as stated. Moreover, boosted GMM has increasing performance with the increasing values of IR for imbalanced datasets. The approach is restricted when the size of the dataset is small but dimensionality is high. However, an interesting extension of this work can be preprocessing the datasets with appropriate feature selection techniques before progressing to Boosted GMM algorithm. Moreover, sample selection during boosting can be further modified to deal with particular problem area for more relevant knowledge extraction. While the accuracy is reliable, in domains where labeled examples are rare, this approach can be used together with supervised techniques for decision fusion too.

REFERENCES

[1] H. Gan, N. Sang, R. Huang, X. Tong, and Z. Dan, "Using clustering analysis to improve semi-supervised classification," Neurocomputing , vol. 101, pp. 290-298, 2013.

[2] N. Shahadat and B. Pal, "An empirical analysis of attribute skewness over class imbalance on Probabilistic Neural Network and Naïve Bayes classifier," 2015 International Conference on Computer and Information Engineering (ICCIE), Rajshahi, 2015, pp. 150-153.

[3] H. He and E. A. Garcia, "Learning from imbalanced data," IEEE Transactions on knowledge and data engineering , vol. 21, no. 9, pp. 1263-1284,2009.

[4] O. Chapelle, B. Scholkopf, and A. Zien, "Semi-supervised learning (chapelle, o. et al., eds.; 2006)[book reviews]," IEEE Transactions on Neural Networks , vol. 20, no. 3, pp. 542-542, 2009.

[5] J. A. Bilmes et al. , "A gentle tutorial of the em algorithm and its application to parameter estimation for gaussian mixture and hidden markov models," International Computer Science Institute , vol. 4, no. 510, p. 126, 1998.

[6] C. M. Bishop, "Pattern recognition," Machine Learning , vol. 128, 2006.

[7] H. Tang and T. S. Huang, "Boosting gaussian mixture models via discriminant analysis," in Pattern Recognition, 2008. ICPR 2008. 19th International Conference on , pp. 1-4, IEEE, 2008.

[8] D. A. Reynolds, T. F. Quatieri, and R. B. Dunn, "Speaker verification using adapted gaussian mixture models," Digital signal processing, vol. 10, no. 1, pp. 19-41, 2000.

[9] L. Breiman, "Bias, variance, and arcing classifiers," 1996.

[10] M. V. Joshi, R. C. Agarwal, and V. Kumar, "Predicting rare classes: Can boosting make any weak learner strong?," in Proceedings of the eighth ACM SIGKDD international conference on Knowledge discovery and data mining, pp. 297-306, ACM, 2002.

[11] G. Ratsch, T. Onoda, and K.-R. Muller, "Soft margins for adaboost," Machine learning , vol. 42, no. 3, pp. 287-320, 2001.

[12] D. Reynolds, "Gaussian mixture models," Encyclopedia of biometrics,pp. 827-832, 2015.

[13] M. Collins. "The EM algorithm", Technical report, Department of Computer and Information Science, University of Pennsylvania, 1997.

[14] J. Alcalfia-Fdez, L. Sanchez, S. Garcia, M. J. del Jesus, S. Ventura, J. M.Garrell, J. Otero, C. Romero, J. Bacardit, V. M. Rivas, et al. , "Keel: asoftware tool to assess evolutionary algorithms for data mining problems,"Soft Computing , vol. 13, no. 3, pp. 307-318, 2009.

[15] M. Galar, A. Fernandez, E. Barrenechea, H. Bustince, and F. Herrera, "A review on ensembles for the class imbalance problem: bagging, boosting,and hybrid-based approaches," IEEE Transactions on Systems, Man, and Cybernetics, Part C (Applications and Reviews) , vol. 42, no. 4, pp. 463-484, 2012.

[16] G. Forman, "An extensive empirical study of feature selection metrics for text classification," Journal of machine learning research , vol. 3, no. Mar, pp. 1289-1305, 2003.

Regenerative Braking Characteristics of PMDC Motor by Applying Different Armature Voltage

S.M. Baque Billah ,[1,*] Dr. Kazi Khairul Islam,[1]
[1]Department of Electrical and Electronic Engineering, Islamic University of Technology (IUT)
Gazipur, Bangladesh
[*]baque.ustc06@gmail.com

***Abstract*—Energy saving and prolonging mileage are very important for battery-operated electric vehicles (BEV). For saving energy in BEV's the key parts are regenerative braking performances. Permanent magnet DC (PMDC) motor based regenerative braking can be a solution to improve energy saving efficiency in BEV. In this paper, a novel regenerative braking mechanism based on PMDC motor is proposed. Based on proposed method braking can be achieved by applying different armature voltage from a battery bank without using additional converter with complex switching technique, ultra capacitor, or complex winding-changeover. An experimental setup has been used to evaluate the performance of the proposed braking system. Simulated results prove that the proposed regenerative braking technique is feasible and effective. Also this research provides simplest system for regenerative braking using PMDC motor to improve the mileage of electric vehicles.**

Keywords— regenerative braking; mileage; efficiency; battery bank; armature voltage; PMDC motor.

I. INTRODUCTION

Recently due to global warming and rising cost of petrol battery-operated electric vehicles (BEV's) are getting accepted. It is believed that in near future electric vehicles (EVs) will replace the conventional fuel based vehicles and also dominate the market due to some aspects like zero carbon emission, less expensive and quiet maneuver. Fundamentally AC and DC motor are the core part of different types of EVs [1], including two-, three- and four-wheelers. For EVs automobile manufacturer prefers AC motor instead of DC motor because of its high efficiency [2]. But for simpler speed control methods and less expensive with respect to AC motor researches till see the potentiality of DC motor in EVs [3]. As many researches show that during braking one third to one half of energy is lost [4] and regenerative braking is an energy recovery process which create braking torque to brake a EVs by energy conversion (kinetic to electrical energy) and feeding it back to the battery [5]. So designing of regenerative braking system is so much important for enhancement of viability and efficiency of DC motor based EVs. Although in [6] a regenerative braking system using series wound brushed DC motor is designed where braking efficiency is around 26.34% which is less than 30%. Instead of series wound brushed DC motor PMDC motor has some advantages, such as does not have field winding. So excitation current is not needed in PMDC motor. Since field excitation current is not required, the efficiency of these motors is generally higher than that of the wound-field motors. For that in [7] they use PMDC motor to design a scooter but can't achieve higher regenerative braking efficiency. For regenerative braking in [6] and [7] they need to use additional converter with complex switching technique and complex winding-changeover. So for simple and cost effective efficient regenerative braking system, some new method needs to be initiated [8]. Thus PMDC motor based new regenerative braking system is proposed in this paper. Based on proposed method, by applying different armature voltage regenerative braking can be achieved. This new method does not require complex converter with complex switching technique but only a low cost rotary mechanical switch and a battery bank from where rotary mechanical switch will select different voltage based on brake pedal position. An experimental setup is used to verify the PMDC motor based proposed braking technique. After analysis, results show that proposed method is feasible and effective. Due to simplicity and high efficiency, proposed braking system is superior compared to series-wound DC motor based regenerative braking system.

II. REGENERATIVE BRAKING OF PMDC MOTOR BASED ON DIFFERENT ARMATURE VOLTAGE

The PMDC motor is similar to an ordinary D.C. shunt motor except that its field is created by permanent magnets instead of salient-pole wound-field structure.

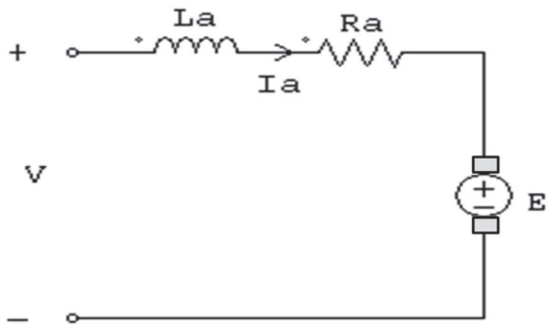

Fig. 1. Circuit diagram of Permanent magnet DC motor

Fig.1 shows the equivalent circuit of PMDC motor. The common basic two equations of PMDC motor are [9]

$$E = K * \varphi * \omega \quad (1)$$

$$T = K * \varphi * I_A \quad (2)$$

978-1-5090-5785-6/16/$31.00 ©2016 IEEE

I_A = armature current (amps)

φ = field flux per pole (Weber)

E = Back E.M.F voltage (volts)

ω = angular speed of dc motor (rad/sec)

K = constant that relates to construction of dc motor

T = induced torque (N.m)

R_a = armature resistance (Ω)

La = armature inductance (H)

Armature current is given by

$$I_A = \frac{V-E}{Ra} \quad (3)$$

In equation (3)

V = motor armature voltage.

Now rotational speed of PMDC is proportional to motor armature voltage and Speed is controlled by applying variable armature voltage [9]. Let us consider two different armature voltages V1 and V2. Those voltages will generate two different speeds N_1 and N_2 RPM and two back E.M.F voltages E_1 and E_2simultaneously. If V1 >V2 then also N_1>N_2 and from equation (1) E_1>E_2. Now if a motor feed with V1 voltage then its speed will be N_1 RPM. During this running condition if we change the motor armature voltage V1 to V2 using different Battery cell then E_1 > V2 and based on equation (3) I_A < 0 that means motor will works as a generator (Regenerative mode) and charge the battery cell (Which voltage is V2) until motor achieve the speed N_2 and back E.M.F E_2. Now based on equation (2) and (3) T<0 which indicates motor will experience a braking torque T during this regenerative mode and comparative to difference of rotational speed. This extra rotational or kinetic energy is converted into electrical energy and return back to the battery system. Based on this different armature voltage technique an effective regenerative braking system of PMDC motor can be developed which is proposed here.

III. Experimental verification

An experimental setup is used to verify this proposed technique. This setup consist of a PMDC motor ,one flywheel, battery bank, mechanical braking system, DC volt meter and DC ammeter. Fig. 2 shows the actual constructions. Battery bank allows us to select different armature voltage and calculation of energy regeneration. Now it's essential to identify some key parameters of braking and their conditions for experimental verification of proposed method. In this research armature current Ia, braking torque Tb and braking time t are considered. Now based on section II let Va is a rated armature voltage and Ira, Tra and Era are the rated armature current ,Torque and Back E.M.F respectively for this PMDC motor .For regenerative braking if focus is on three different voltages like V1,V2 and V3 where

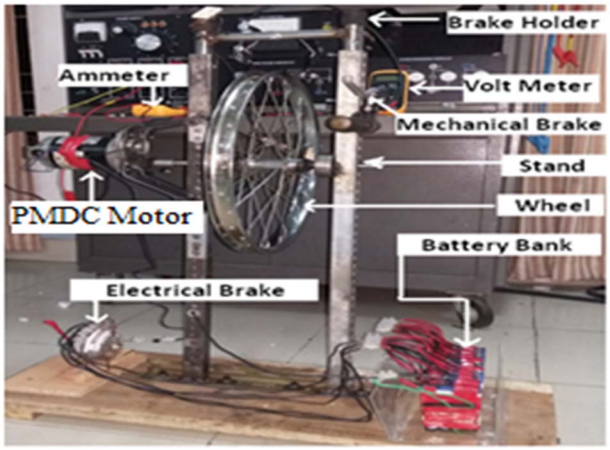

Fig. 2. Experimental Setup for Proposed Braking of PMDC motor

$$Va > V1 > V2 > V3 \quad (4)$$

Then back E.M.F Era > V1 > V2 >V3 and based on equation (2) and (3) armature current and braking torques will be negative and act like

$$Ia1 < Ia2 < Ia3 \quad (5)$$

$$T3 > T2 > T1 \quad (6)$$

In (5) and (6) Ia1,T1 is the braking current and torque when motor armature voltage shifted from Va to V1 and similarly Ia2, T2 and Ia3,T3 for Va voltage to V2 and V3 voltage respectively .Higher braking torque will create higher deceleration of vehicles and required lower braking time to stop the vehicle. So if V1,V2 and V3 armature voltage require t1,t2 and t3 braking time respectively during regenerative braking then from (6) it is cleared that

$$t1 > t2 > t3 \quad (7)$$

In this section condition (5), (6)and (7) are observed based on propose technique and numerical values are taken for simulation .For identification of proposed braking condition mechanical braking characteristics of experimental setup are also observed. Three different armature voltage V1=8v, V2=4v and V3=1.5v are taken to feed the PMDC motor for experimental verification when motor are running at rated armature voltage Va=48 V.

A. Mechanical Braking characteristics

In mechanical braking system t_{mh}=0.85s are considered as mechanical hard braking time for Experimental setup of PMDC motor. Same way t_{mm}=4.0s are considered as mechanical medium brake. That means the PMDC motor will decelerate within 0.85s during hard brake and 4.0s during medium brake. Motor generated armature voltage is observed to fine the mechanical brake characteristics because flywheel is directly connected with PMDC motor. Fig.3 (a) and (b) shows the mechanical hard and medium brake characteristics respectively.

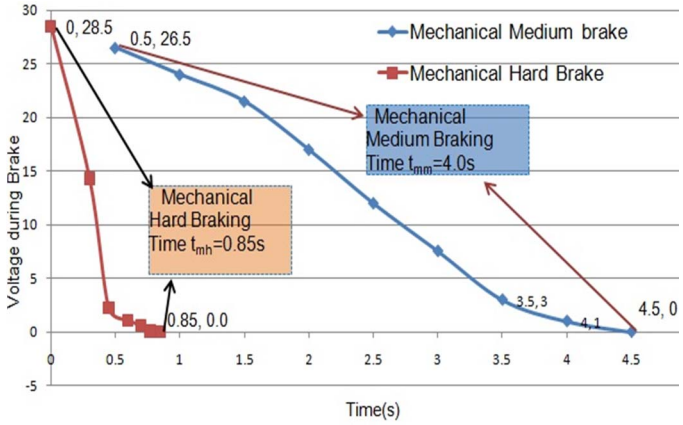

Fig. 3. Mechanical brake characteristics of experimental setup

B. Proposed Regenerative Braking Characteristics

Regenerative braking of PMDC motor based on proposed method is presented in fig.4. All figure are simulated based on numerical value taken from experimental setup. From fig.4 it's clear that regenerative braking time during 8 volt armature voltage t_{RB8}=4.75s. Similarly the estimated braking time for 4v and 1.5v armature voltage are t_{RB4}=2.75s and $t_{RB1.5}$=1.15s respectively. In fig.4 4v and 1.5v regenerative braking characteristics of PMDC motor are also presented.

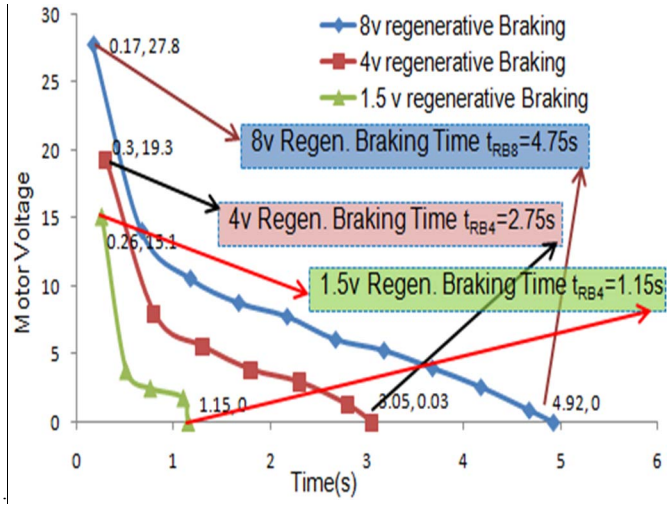

Fig. 4. Proposed Regenerative Braking Characteristics of PMDC Motor.

C. Comparison of mechanical and proposed braking

To justify the state of proposed regenerative braking, it's compared with mechanical braking system of experimental setup. Comparison shows that 1.5v armature voltage braking is comparative to mechanical hard brake and 8v braking with mechanical medium brake. Fig.5 and Fig.6 clearly shows those interpretations.

D. Current Consumption Characteristics of Experimental setup

Armature current consumption of PMDC motor is observed and numerical values are taken during normal running condition. This helps to characterize the current consumption of experimental setup and calculation of energy utilization. Here current consumption with respect to time is divided into two parts. One transient period where experimental setup takes high current with higher rate of change and another saturation period where current is low but constant. Fig.7 shows these observations.

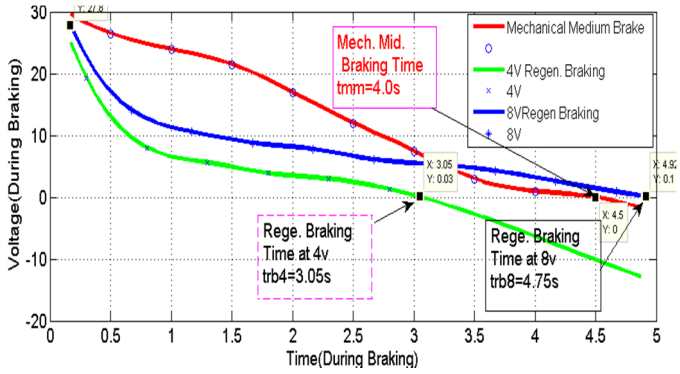

Fig. 5. Comparison with medium brake

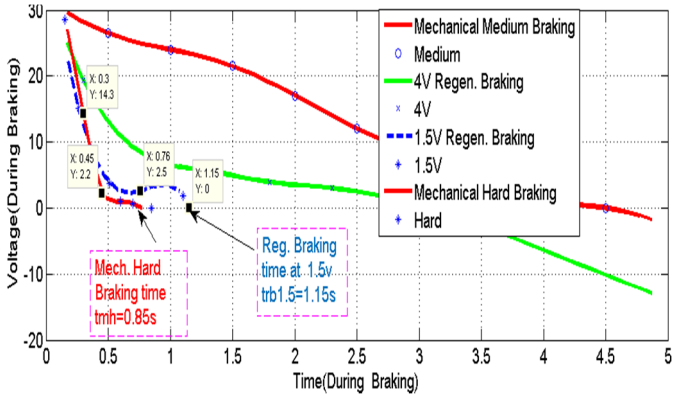

Fig. 6. Comparison with hard brake

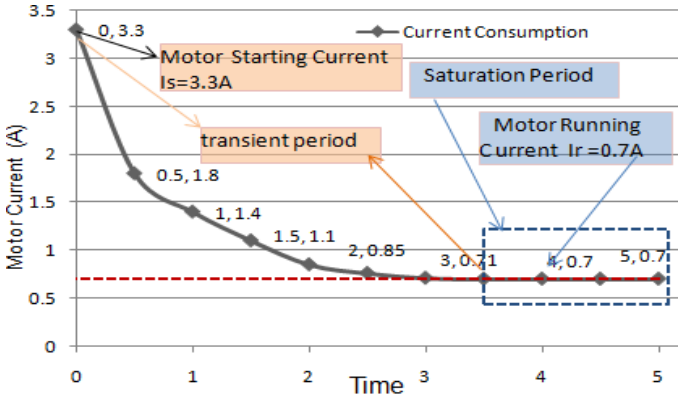

Fig. 7. Current Consumption Characteristics of Experimental setup

E. Regenerative Braking Current Characteristics of PMDC Motor

Based on proposed method regenerative Braking or battery charging current of PMDC motor is also observed. Simulated numerical data are presented in fig.8 . In fig.8 braking current I_{ST8} =-3.86A, I_{ST4} =-6.2A and $I_{ST1.5}$ =-8.89A where I_{ST8}, I_{ST4} and $I_{ST1.5}$ are braking current during 8v, 4v and 1.5 volt regenerative braking respectively. Negative polarity indicates that current will return back to the system during braking.

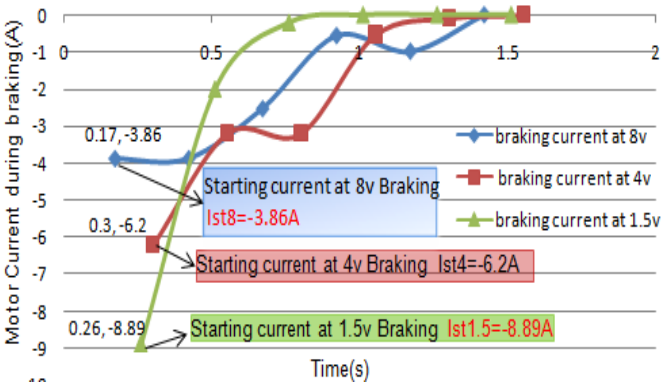

Fig. 8. Regenerative Braking current at 1.5v braking

IV. RESULT

In section III armature current Ia, braking torque Tb and braking time t are defined as a key parameters having relation (5),(6) and (7) respectively to prove that proposed method is feasible. From simulated figure fig.4 and fig.8 it's clear that proposed method is feasible because its follows the relation (7) for the regenerative braking time and relation (6) for braking current respectively.

That means $t_{RB8} > t_{RB4} > t_{RB1.5}$. and $I_{ST8} < I_{ST4} < I_{ST1.5}$.

Based on equation (2) and values of braking current, it's clear that proposed regenerative braking system also follows relation (5) for regenerative braking torque of PMDC motor.

Now for efficiency estimation, 1.5v regenerative braking are considered because most of the times vehicles use hard breaks. From the experimental data the calculated energy recovery during 1.5v braking is:

Power of regenerative Braking, $P_{RB1.5}$: 66.54w (average)

Energy of regenerative braking, $E_{RB1.5}$: 94.49j (average)

Same way after analyzing numerical data of current utilization of experimental setup the calculated powers consumed by the experimental setup are:

Power at transient period, P_T: 34.94w (average)

Power at saturation period, P_S: 21.49w (average)

Total Power, $P_T = P_T + P_S = 56.43$w (average)

Total Energy Used, $E_T =$ 220.64j (average)

From calculation it is very much clear that if a vehicle having proposed braking system using PMDC motor and does hard brake to stop and again starts to achieve rated velocity, throughout this situation vehicle will consume 220.64j energy and 94.49j energy will return back to the Battery.Fig.9 will clarify the energy consumption and regeneration of proposed braking for stop and go driving pattern in urban area. So the Efficiency of this proposed method is E_f= 42.8254.That means driving range based on proposed method will increase around 42.825% or 42.825% further than without regenerative braking and also around 16.485% more than Regenerative braking of series-wound brushed DC motors proposed in [6]. So proposed system is efficient then the system proposed in [6].

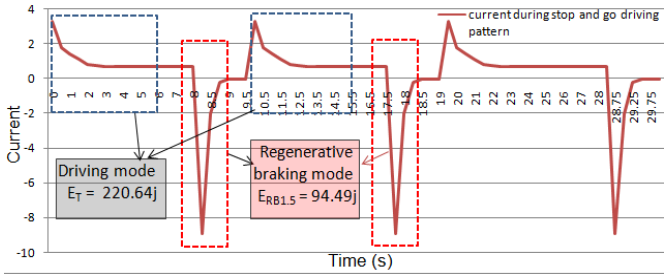

Fig. 9. Energy Consumption and Regeneration During stop and go driving pattern

V. CONCLUSION

This paper has proposed PMDC motor based simple but effective method of regenerative braking for BEV's. After simulation of experimental data, authors find that proposed method can enhance mileage around 42.825%. Finally this paper proves that regenerative braking based on motor armature voltage control is more effective and efficient then series-wound DC motor based regenerative braking system of EVs. Further research will focus on designing of rotary selector switch which can select different armature voltage from battery bank based on brake pedal position.

REFERENCES

[1] B. Fahimi and T. Sebastian, "Guest editorial special section on automotive electromechanical converters," IEEE Transactions on Vehicular Technology, vol. 56, no. 4, 2007, pp. 1470–1476.

[2] H. Baush, A. Greif, B. Lange, R. Bautz, "A 50 kW/15000 rpm switched reluctance drive for an electric vehicle: Current control and performance characteristics," ICEM 2000, 28-30 August, Espoo, Finland, pp. 603-607.

[3] Anant Kumar, Sitanshu Mishra "Speed Control of DC motor using IGBT", National Institute of Technology Rourkela 2007

[4] M. K Yoong, Y. H Gan, G. D Gan, C. K Leong, Z. Y Phuan, B. K Cheah and K. W Chew, "Studies of regenerative braking in electric vehicle," IEEE Conference on Sustainable Utilization and Development in Engineering, Kuala Lumpur, Malaysia, 2010, pp. 40 – 45.

[5] A. Caratti, G. Catacchio, C. Gambino and N. C. Kar, "Development of a predictive model for regenerative braking system," Transportation Electrification Conference and Expo (ITEC 2013), Detroit, MI, 2013, pp. 1 – 6.

[6] Y. Xiao, M. Nemec, L. J. Borle, V. Sreeram and H. H. C. Iu, "Regenerative braking of series-wound brushed DC electric motors for electric vehicles," *2012 7th IEEE Conference on Industrial Electronics and Applications (ICIEA)*, Singapore, 2012, pp. 1657-1662. doi: 10.1109/ICIEA.2012.6360991.

[7] M. Y. Tarnini, "Microcontroller based PMDC motor control for driving 0.5KW scooter," *2014 16th International Power Electronics and Motion Control Conference and Exposition*, Antalya, 2014, pp. 1204-1208. doi: 10.1109/EPEPEMC.2014.6980675

[8] X. Liu, C. Liu, M. Lu and D. Liu, "Regenerative braking control strategies of switched reluctance machine for electric bicycle," International Conference on Electrical Machines and Systems ICEMS 2008, Wuhan, China, 2008, pp. 3397 – 3400.

[9] M. H. Rashid, "Dc Drives," in Power Electronics Circuits, Devices and Applications, 2nd ed. New Delhi, India: Prentice Hall, 1998, pp. 493-540.

International Conference on Electrical, Computer & Telecommunication Engineering (ICECTE)
8-10 December 2016, Rajshahi-6204, Bangladesh

Adaptive Controller Design for Grid Current Regulation of a CSI Based PV System

T. K. Roy*, M. F. Pervej, and F. K. Tumpa
Dept. of Electronics & Telecommunication Engineering
Rajshahi University of Engineering & Technology, Rajshahi-6204, Bangladesh
*Email: roy.kanti03@gmail.com

***Abstract*—A nonlinear adaptive controller for regulating the grid of a current source inverter (CSI) based three-phase grid-connected photovoltaic (PV) system is proposed in this paper. The proposed control structure is composed of an outer current loop which is responsible for controlling the DC-side inductor current and the inner current control loop is responsible for controlling injected current into the grid. The proposed controller is designed recursively by considering some parameters of the system parameters as unknown and these unknown parameters are estimated through the adaption laws. In order to prove the overall stability of the whole system control Lyapunov functions (CLFs) are formulated at different stages of the design process. Finally, the effectiveness of the proposed control scheme is tested on a CSI based three-phase grid-connected PV system under different atmospheric conditions. Simulation results show that the proposed control scheme can effectively meet the desired control objectives.**

Keywords*—*Active power; backstepping controller; control Lyapunov function; current source inverter; reactive power

I. INTRODUCTION

Nowadays, the photovoltaic (PV) systems have received a great deal of attention owing to their distinctive advantages such as simplicity of allocation, less maintenance cost, and widely distributed throughout the earth [1]-[3]. Another advantage is that it could be used for both modes such as stand-alone and grid-connected. However, most of the PV systems are installed for the grid connected plants for the encouragements policies [3]. The main purpose of a grid-connected PV system is to transfer maximum power to the grid with a power factor as close to unity. To achieve this, each grid-connected PV system has to perform two essential functions. One is to ensure that PV modules are operated at the maximum power point (MPP) to extract the maximum power from PV arrays and the other one is, to inject a sinusoidal current into the grid with low total harmonic distortion (THD) to improve the active and reactive power quality [3].

Owing to the variations of solar irradiance and ambient temperature, the PV array module shows a nonlinear voltage-current characteristic and consequently, the output power of the PV system is unpredictable. Under this case, the MPP tracker must resist with a nonlinear and time-varying system to extract maximum power from the PV cell. To extract maximum power, many MPP tracking control algorithms have been proposed in the literature [4], [5]. A fuzzy logic controller is proposed in [6] to control the MPP of a PV array system under changing atmospheric conditions. The MPPT control strategies based on perturb and observe (P&O) method is proposed in [7]. However, P&O method has some limitations such as slow response speed, oscillations of the PV array output power and fails to quickly track the MPP under a rapid change in atmospheric conditions. To overcome these problems, an incremental conductance (IC) method is proposed in [9] due to its high tracking efficiency.

Due to the switching functions of DC-DC converters, CSI, and diode current of the PV cell a grid-connected PV system is highly nonlinear. The CSI based PV system has significant advantages over VSI as discussed in [10]. To maintain the stable operation of a CSI based grid-connected PV system under the changes in atmospheric conditions a proper controller must be installed with the system. Generally, due to the simplicity and ease of installation linear controllers are used [11]. However, this linear controller is not suitable when the operating points of the system varied due to variations in atmospheric conditions. Thus, to ensure the stable operation of a grid-connected PV system over a wide range of operating point, the design of the nonlinear controller is very important.

Several advanced control techniques are proposed to design the nonlinear controllers such as sliding mode controller (SMC) [12], model predictive controller (MPC) [13], feedback linearization controller (FBLC) etc. To analyze the dynamical stability of a three-phase grid-connected PV system, a nonlinear FBLC is proposed in [14]. Though FBLC can maintain the system stability over a wide range of operating point, for successful implementation the system parameters should be known precisely. Practically, it is quite difficult to know the exact values of the system parameters. Moreover, FBLC cancels useful nonlinearities. A nonlinear SMC can overcome the limitation of FBLC as it can provide robust performance against the parameter variation and external disturbances. To control the injected current into the grid, an SMC is proposed in [12] to ensure the stable operation of a three-phase grid-connected PV system. Though SMC has low sensitivity to parameter variations, the selection of the time-varying sliding surface is a difficult task. Moreover, the precision of control and stability of the system are badly affected by the chattering.

In order to evade the cancellation of useful nonlinearities of FBLC and chattering phenomenon of an SMC, nonlinear adaptive backstepping controller is a promising technique as proposed in [8], [15]-[20] for different applications. Moreover, the controllers as proposed in the aforementioned literature are designed only for the active power controlled, whereas reactive power control is not taken into account. In addition, the controller is designed for a voltage source inverter (VSI) based three-phase grid-connected PV system and parametric uncertainties are not taken into account within the system.

Therefore, the main aim of this paper is to control the CSI output current to inject the active and reactive power into the

978-1-5090-5785-6/16/$31.00

grid under consideration of parametric uncertainties. The performance of the designed controller is evaluated on a CSI based three-phase grid-connected PV system under the changes in atmospheric conditions.

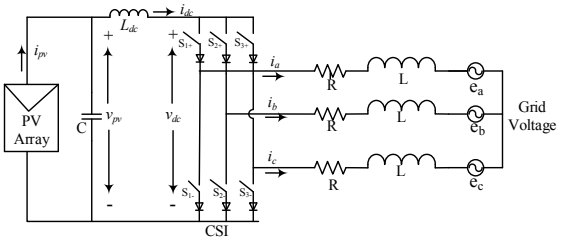

Fig.1. CSI based three-phase grid-connected PV system [10]

II. System Modeling And Problem Statement

The circuit configuration of a three-phase grid-connected PV system is shown in Fig. 1. In this configuration, a PWM based CSI is used whose output is connected to a three-phase grid via an output L filter to inject a purely sinusoidal current into the grid. Now by applying the Kirchhoff's law, the whole dynamical model of the system in abc frame can be represented by the following differential equations:

$$L\frac{di_a}{dt} = -Ri_a - e_a + \frac{v_{dc}}{3}(2S_a - S_b - S_c) \quad (1)$$

$$L\frac{di_b}{dt} = -Ri_b - e_b + \frac{v_{dc}}{3}(-S_a + 2S_b - S_c) \quad (2)$$

$$L\frac{di_c}{dt} = -Ri_c - e_c + \frac{v_{dc}}{3}(-S_a - S_b + 2S_c) \quad (3)$$

where S_a, S_b, and S_c are the input switching signals of PWM. The dynamical model as represented by (1)–(3) is nonlinear and time variant due to the input switching signals and diode current i_{pv}. In order to design the proposed controller, this model needs to be transformed into a direct-quadrature (dq) frame. Thus, using the dq transformation; a nonlinear and time-invariant model can be written as:

$$\dot{I}_d = -\frac{R}{L}I_d + \omega I_q - \frac{1}{L}E_d + \frac{v_{dc}}{L}S_d \quad (4)$$

$$\dot{I}_q = -\frac{R}{L}I_q - \omega I_d - \frac{1}{L}E_q + \frac{v_{dc}}{L}S_q \quad (5)$$

where the symbols have their usual meaning which can be found in [18]. Now the DC-side dynamics of the system can be described by the following differential equations:

$$C\frac{dv_{pv}}{dt} = i_{pv} - i_{dc} \quad (6)$$

$$L_{dc}\frac{di_{dc}}{dt} = v_{pv} - v_{dc} - i_{dc}R_{dc} \quad (7)$$

where R_{dc} is the inductor interior resistance. In the synchronous rotating dq frame, the active and reactive power can be expressed in terms of I_d and I_q as follows:

$$\begin{cases} P_g = \frac{3}{2}\left(E_dI_d + E_qI_q\right) \\ Q_g = \frac{3}{2}\left(E_dI_q - E_qI_d\right) \end{cases} \quad (8)$$

During the steady-state condition, the average value of E_q is equal to zero [10]. As a result, (8) can be rewritten as:

$$P_g = \frac{3}{2}E_dI_d, Q_g = \frac{3}{2}E_dI_q \quad (9)$$

From (9), it is clear that if the amplitude of E_d is constant, the maximum active and reactive powers delivered to the grid can be maintained by controlling the d-and q-axis currents of the grid. If it is assuming that the losses due to switching actions of the inverter are negligible then the following relation can be obtained based on power balance between the DC side and AC side of the inverter $P_{dc} = v_{dc}i_{dc} = P_g$. Using this power balance equation, (7) can be written as:

$$\frac{di_{dc}}{dt} = \frac{v_{pv}}{L_{dc}} - \frac{3}{2\,L_{dc}i_{dc}}E_dI_d - i_{dc}\frac{R_{dc}}{L_{dc}} \quad (10)$$

Now the complete dynamical model of a CSI based three-phase grid-connected PV system can be described by the following set of differential equations:

$$\frac{dv_{pv}}{dt} = \frac{1}{C}(i_{pv} - i_{dc}) \quad (11)$$

$$\frac{di_{dc}}{dt} = \frac{v_{pv}}{L_{dc}} - \frac{3}{2\,L_{dc}i_{dc}}E_dI_d - i_{dc}\frac{R_{dc}}{L_{dc}} \quad (12)$$

$$\frac{dI_d}{dt} = -\frac{R}{L}I_d + \omega I_q - \frac{1}{L}E_d + \frac{v_{dc}}{L}S_d \quad (13)$$

$$\frac{dI_q}{dt} = -\frac{R}{L}I_q - \omega I_d - \frac{1}{L}E_q + \frac{v_{dc}}{L}S_q \quad (14)$$

Here, (11)-(14) represent the complete dynamical model. Practically, it is quite impossible to know the exact value of the system parameters. If the system parameters R and L are considered as unknown then it can be written as

$$\theta_1 = -\frac{R}{L}, \text{ and } \theta_2 = \frac{1}{L}$$

By incorporating these unknown terms into (11)-(14), it can be written as

$$\frac{dv_{pv}}{dt} = \frac{1}{C}(i_{pv} - i_{dc}) \quad (15)$$

$$\frac{di_{dc}}{dt} = \frac{v_{pv}}{L_{dc}} - \frac{3}{2\,L_{dc}i_{dc}}E_dI_d - i_{dc}\frac{R_{dc}}{L_{dc}} \quad (16)$$

$$\frac{dI_d}{dt} = \theta_1 I_d + \omega I_q - \theta_2 E_d + \theta_2 v_{dc}S_d \quad (17)$$

$$\frac{dI_q}{dt} = \theta_1 I_q - \omega I_d - \theta_2 E_q + \theta_2 v_{dc}S_q \quad (18)$$

Equations (15)-(18) represent the complete dynamical model and the proposed controller is designed based on this model in the following section.

III. Proposed Controller Design

The aim of this section is to design the inverter switching control signal to achieve the following objectives:

- Inject a pure sinusoidal current into the grid with lower values of THD, and
- Control the active and reactive power injection into the grid.

To resolve the aforementioned concerns, a nonlinear adaptive controller design procedure is elaborately discussed as follows.

Step 1*:* The first tracking error between v_{pv} and v_{pvref} can be defined as:$e_1 = v_{pv} - v_{pvref}$ (19)

The dynamics of e_1 using (15) can be written as:

$$\dot{e}_1 = \frac{1}{C}\left(i_{pv} - i_{dc}\right) - \dot{v}_{pvref} \quad (20)$$

Here, i_{dc} is a virtual control variable. To stabilize the error dynamics of e_1, the first CLF can be chosen as:

$$W_1 = \frac{1}{2}e_1^2 \quad (21)$$

The derivative of W_1 using (20) can be written as*:*

$$\dot{\boldsymbol{W}}_{\boldsymbol{1}} = \boldsymbol{e}_{\boldsymbol{1}}\{\tfrac{\boldsymbol{1}}{\boldsymbol{C}}(\boldsymbol{i}_{\boldsymbol{pv}} - \boldsymbol{i}_{\boldsymbol{dc}}) - \dot{\boldsymbol{v}}_{\boldsymbol{pvref}}\} \quad (22)$$

At this stage, the stabilizing function of i_{dc} needs to be selected in such a way that $\dot{W}_1$ would be negative semi-definite, i.e., $\dot{W}_1 \leq 0$. To do that, the synthetic value for i_{dc} can be chosen as:

$$\alpha = C(i_{pv} - \dot{v}_{dcref} + k_1e_1) \quad (23)$$

where $k_1 > 0$ is a positive constant. After selecting this, (22) becomes$\dot{W}_1 = -k_1e_1^2 \leq 0$ (24)

which is negative semi-definite.

Step 2: Since α is the stabilizing function, so α and I_{dc} may not be equal. Thus, second error can be defined as follows:

$$e_2 = I_{dc} - \alpha \quad (25)$$

The time derivative of e_2 using (12) can be written as:

$$\dot{e}_2 = \frac{v_{pv}}{L_{dc}} - \frac{3}{2\,L_{dc}I_{dc}} E_d I_d - \frac{R_{dc}}{L_{dc}} I_{dc} - \dot{\alpha} \quad (26)$$

Now, the CLF can be chosen as: $W_2 = W_1 + \frac{1}{2}e_2^2$ (27)

Inserting the values of $\dot{e}_2$ from (26) and $\dot{W}_1$ from (24), respectively, it can be written as:

$$\dot{W}_2 = -k_1 e_1^2 + e_1\left(\frac{v_{pv}}{L_{dc}} - \frac{3}{2\,L_{dc}I_{dc}} E_d I_d - \frac{R_{dc}}{L_{dc}} I_{dc} - \dot{\alpha}\right) \quad (28)$$

At this instant, the stabilizing function for I_d needs to be selected in such a way that $\dot{W}_2$ would be negative semi-definite. Thus, the synthetic value for I_d can be chosen as:

$$\alpha_1 = \frac{2I_{dc}}{3E_d} L_{dc}\left(\frac{R_{dc}}{L_{dc}} I_{dc} + \dot{\alpha} - \frac{v_{pv}}{L_{dc}} + k_2 e_2\right) \quad (29)$$

After selecting this, (29) yields

$$\dot{W}_2 = -k_1 e_1^2 - k_2 e_2^2 \le 0 \quad (30)$$

Step 3: In this step, the *d*-axis current tracking error can be defined as: $e_3 = I_d - \alpha_1$ (31)

Using (13), $\dot{e}_3$ can be written as follows:

$$\dot{e}_3 = \theta_1 I_d + \omega I_q - \theta_2 E_d + \theta_2 v_{dc} S_d - \dot{\alpha}_1 \quad (32)$$

In terms of estimation errors (32) can be written as:

$$\dot{e}_3 = \left(\hat{\theta}_1 + \tilde{\theta}_1\right) I_d + \omega I_q - \left(\hat{\theta}_2 + \tilde{\theta}_2\right)(E_d - v_{dc} S_d) - \dot{\alpha}_1 \quad (33)$$

where $\tilde{\theta}_i = \theta_i - \hat{\theta}_i$ with $i = 1, 2$ is the estimation error. The *q*-axis (reactive) current tracking error define as:

$$e_4 = I_q - I_{qref} \quad (34)$$

Inserting the value of $\dot{I}_q$, the dynamics of e_4 can be written as:

$$\dot{e}_4 = \theta_1 I_q - \omega I_d - \theta_2 E_q + \theta_2 v_{dc} S_q - \dot{I}_{qref} \quad (35)$$

In terms of estimation errors (35) can be written as:

$$\dot{e}_4 = \left(\hat{\theta}_1 + \tilde{\theta}_1\right) I_q - \omega I_d - \left(\hat{\theta}_2 + \tilde{\theta}_2\right)\left(E_q - v_{dc} S_q\right) - \dot{I}_{qref} \quad (36)$$

In (33) and (36) the actual control inputs are appeared. At this stage, the objective is to design the control input signals S_d and S_q, in such a way that e_1, e_2, e_3, and e_4 converge to zero as $t \to \infty$. Thus, final CLF is considered as:

$$W_3 = W_2 + \frac{1}{2}e_3^2 + \frac{1}{2}e_4^2 + \frac{1}{2\gamma_1}\tilde{\theta}_1^2 + \frac{1}{2\gamma_2}\tilde{\theta}_2^2 \quad (39)$$

The time derivative of W_2 is

$$\dot{W}_3 = \dot{W}_2 + e_3\dot{e}_3 + e_4\dot{e}_4 - \frac{1}{\gamma_1}\tilde{\theta}_1\dot{\hat{\theta}}_1 - \frac{1}{\gamma_2}\tilde{\theta}_2\dot{\hat{\theta}}_2 \quad (38)$$

Inserting the values of $\dot{e}_2$ from (28) and $\dot{e}_3$ from (30) into (32) yields

$$\dot{W}_3 = -k_1 e_1^2 - k_2 e_2^2 + e_3\left(\hat{\theta}_1 I_d + \omega I_q - \hat{\theta}_2 E_d + \hat{\theta}_2 v_{dc} S_d - \dot{\alpha}_1\right) + e_4\left(\hat{\theta}_1 I_q - \omega I_d - \hat{\theta}_2 E_q + \hat{\theta}_2 v_{dc} S_q - \dot{I}_{qref}\right) - \frac{1}{\gamma_1}\tilde{\theta}_1\left\{\dot{\hat{\theta}}_1 + \gamma_1 e_3(E_d - v_{dc}S_d) + \gamma_1 e_4\left(E_q - v_{dc}S_q\right)\right\} - \frac{1}{\gamma_1}\tilde{\theta}_1\left\{\dot{\hat{\theta}}_1 + \gamma_1 e_3(E_d - v_{dc}S_d) + \gamma_1 e_4\left(E_q - v_{dc}S_q\right)\right\} - \frac{1}{\gamma_2}\tilde{\theta}_2\{\dot{\hat{\theta}}_2 + \gamma_2 e_3(E_d - v_{dc}S_d) + \gamma_2 e_4\left(E_q - v_{dc}S_q\right)\}$$

Choosing the following control laws

$$S_d = -\frac{1}{\hat{\theta}_2 v_{dc}}\left(\hat{\theta}_1 I_d + \omega I_q - \hat{\theta}_2 E_d - \dot{\alpha}_1 + k_3 e_3\right) \quad (40)$$

$$S_q = \frac{1}{\hat{\theta}_2 v_{dc}}\left(\hat{\theta}_1 I_q - \omega I_d - \hat{\theta}_2 E_q - \dot{I}_{qref} + k_4 e_4\right) \quad (41)$$

and adaptation laws

$$\dot{\hat{\theta}}_1 = -\gamma_1\{e_3(E_d - v_{dc}S_d) + e_4\left(E_q - v_{dc}S_q\right)\} \quad (42)$$

$$\dot{\hat{\theta}}_2 = -\gamma_2\{e_3(E_d - v_{dc}S_d) + e_4\left(E_q - v_{dc}S_q\right)\} \quad (43)$$

As a result, the time derivative of W_3 can be simplified as:

$$\dot{W}_3 = -k_1 e_1^2 - k_2 e_2^2 - k_3 e_3^2 - k_4 e_4^2 \le 0 \quad (44)$$

Equation (44) clearly indicates that the $\dot{W}_3$ is negative semi-definite and thus the whole system is asymptotically stable. The performance of the designed control scheme is shown in the following section.

IV. Results and Discussion

The aim of this section is to verify the effectiveness of the designed controller on a similar system as shown in Fig.1. To do that, an SPR 305-WHT based 100 kW PV module is considered in this paper. The parameters of the designed controller to tune the output responses are chosen as follows: $k_1 = 8$, $k_2 = 5$, $k_3 = k_4 = 7$. The performance of the controller is evaluated by considering the following two different operating conditions:

- Controller performance at standard atmospheric conditions, and
- Controller performance with changing solar irradiation.

Case I: *Controller performance at standard atmospheric conditions*

In this case study, the simulation is carried out at a standard atmospheric condition. The grid voltage and current responses of phase *A* are shown in Fig. 2. From Fig. 2, it can be seen that the grid current is not in phase with grid voltage as it is operating at a power factor of 0.80 rather than unity.

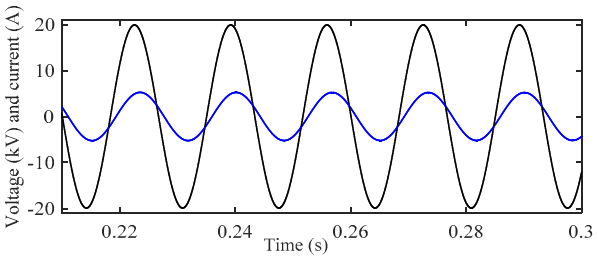

Fig. 2. Grid voltage (black line) and current (blue line) of phase *A* at standard operating condition

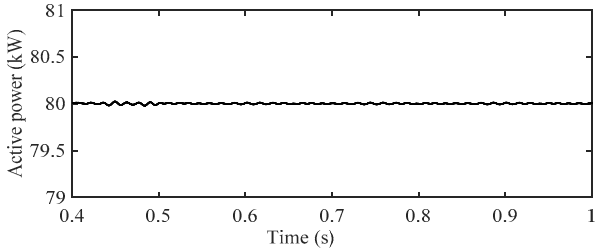

Fig. 3. Active power of the grid at standard operating condition

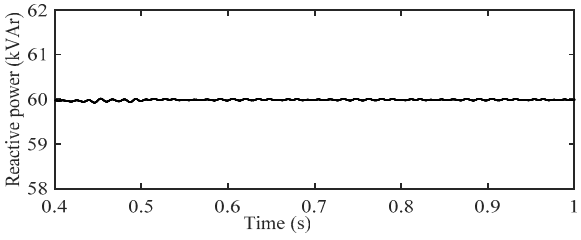

Fig. 4. Reactive power of the grid at standard operating condition

Thus, both active and reactive power will be delivered to the grid. The corresponding active and reactive power responses are shown in Fig. 3 and Fig. 4, respectively, which are injected into the grid. From Fig. 3 and Fig. 4, it can be seen that the designed controller can inject a stable active and reactive power into the power grid.

Case II: *Controller performance with changing solar irradiation*

In this case study, the simulation is carried out with changing solar irradiation while the temperature is kept constant at 25^0C. Initially, the solar irradiation level is set to 1 kW/m^2 and suddenly at t = 1 s, the solar irradiation level is

step changed to 0.5 kW/m^2 and maintained this level till t=1.3 s and at last, back to 1 kW/m^2 after t = 1.3 s. The resulting grid current is shown in Fig. 5, from where it can be seen that the grid current varies considerably in accordance with the variation of solar irradiation.

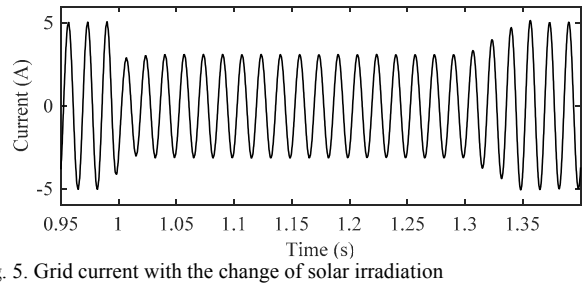

Fig. 5. Grid current with the change of solar irradiation

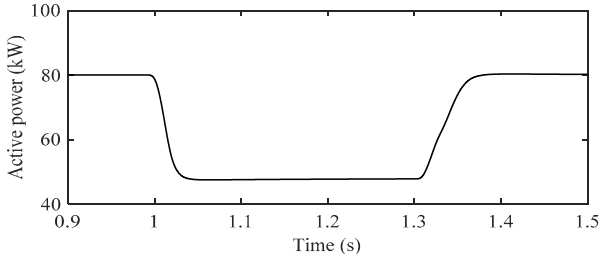

Fig. 6. Active power with changing solar irradiation

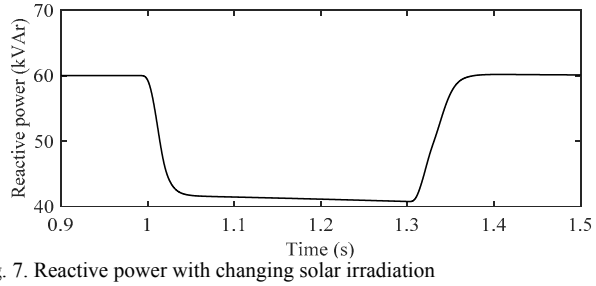

Fig. 7. Reactive power with changing solar irradiation

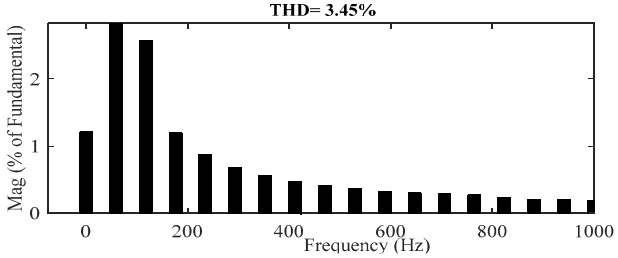

Fig. 8. THD of grid current with changing solar irradiation

Fig. 6 and Fig. 7 represent the corresponding active and reactive power of the grid. The quality of the injected power into the grid for both cases is measured in term of the THD of the injected grid current. The THD response for this case is shown in Fig. 8 from where it is clear that the designed controller can maintain the IEEE-1547 THD standard as it is less than 5%.

V. Conclusion

In this paper, a nonlinear adaptive controller is designed to enhance the power quality of a CSI based three-phase grid-connected PV system. Simulation results, under different operating situations, are included to support the theoretical frameworks of the designed controller. From simulation results, it is clear that the designed controller provides a very satisfactory performance in terms of maintaining steady-state operation under various operating conditions. Furthermore, the designed controller has shown improvements in the power quality of the system by reducing the THD of the injected current into the grid. Future work will be devoted to the design of a robust adaptive backstepping controller by considering both the parametric and external uncertainties within the system.

References

[1] A. E. Fadili, F. Giri, and A. E. Magri, "Reference voltage optimizer for maximum power point tracking in triphase grid-connected photovoltaic systems," Int. Journal of Elect. Power & Energy Systems, vol. 60, pp. 293-301, 2014.

[2] K. M. Tsang and W. L. Chan, "Three-level grid-connected photovoltaic inverter with maximum power point tracking," Int. Journal of Energy Conversion and Management, vol. 65, pp. 221-227, 2013.

[3] A. B. R.-Boué , R. G.-Valverde, F. de A. Ruz-Vila, José M. Torrelo-Ponce, "An integrative approach to the design methodology for 3-phase power conditioners in photovoltaic grid-connected systems," Int. Journal of Energy Conver. and Management, vol. 56, pp. 80-95, 2012.

[4] U. Zimmermann and M. Edoff, "A maximum power point tracker for long-term logging of PV module performance," IEEE Jou. of Photovoltaics, vol. 2, no. 1, pp. 47-55, 2012.

[5] E. Koutroulis and F. Blaabjerg, "A new technique for tracking the global maximum power point of PV arrays operating under partial-shading conditions," *IEEE Jou. of Photovoltaics*, vol. 2, no. 2, 2012.

[6] F. Bouchafaa, D. Beriber, and M. S. Boucherit, "Modeling and control of a gird connected PV generation system," 18th Mediterranean Conf. on Control & Automation, pp.315-320, 23-25 June 2010.

[7] E. Bianconi, J. Calvente, R. Giral, E. Mamarelis, G. Petrone, C. A. R.-Paja, G. Spagnudo, and M. Vitelli, "Perturb and Observe MPPT algorithm with a current controller based on the sliding mode," Int. Journal of Elect. Power & Ener. Systems, vol. 44, pp. 346-356, 2013.

[8] T. K. Roy, "Robust controller for vertical-longitudinal-lateral dynamics control of small helicopter," Universal Journal of Control and Automation, vol.2, no.1, pp. 14-24, 2014.

[9] B. Liu, S. Duan, F. Liu, and P. Xu, "Analysis and improvement of maximum power point tracking algorithm based on incremental conductance method for photovoltaic array," in Proc. IEEE Int. Conf. Power Electron. Drive Syst., pp. 637–641, 2007.

[10] P. P. Dash, and M. Kazerani, "Dynamic modeling and performance analysis of a grid-connected current-source inverter-based photovoltaic system," IEEE Trans. on Sustainable Energy, vol. 2, no. 4, Oct. 2011.

[11] R. Kadri, J. P. Gaubert, and G. Champ, "An improved maximum power point tracking for photovoltaic grid-connected inverter based on voltage-oriented control," Int. Trans. on Ind. Electr., vol. 58, 2011.

[12] I.-S. Kim, "Sliding mode controller for the single-phase grid-connected photovoltaic system," Applied Energy, vol. 83, pp. 1101-1115, 2006.

[13] A. Kotsopoulos, J. L. Darte, and M. A. M. Hendrix, "Predictive DC voltage control of single-phase PV inverters with small dc link capacitance," in Proc. Int. Symp. Ind. Electron., pp.793–797, Jun. 2003.

[14] D. Lalili, A. Mellit, N. Lourci, B. Medjahed, and E. M. Berkouk, "Input output feedback linearization control and variable step size MPPT algorithm of a grid-connected photovoltaic inverter," *Renewable Energy*, vol. 36, no. 12, pp. 3282–3291, Dec. 2011.

[15] T. K. Roy, M. F. Pervej, S. Rahman, and F. K. Tumpa, "Nonlinear adaptive controller design for PWM based DC-DC boost converters using backstepping control scheme," in Proc. of the 5th ICIEV, 2016.

[16] T. K. Roy, "Longitudinal and lateral dynamics control of a small scale helicopter using adaptive backstepping controller under horizontal wind gusts," Asian Transaction Engineering, vol. 3, no. 1, March 2013.

[17] T. K. Roy, M. Morshed, F. K. Tumpa, M. F. Pervej, "Robust adaptive backstepping speed controller design for a series DC motor," in Proc. of IEEE Int. WECECE, December 2015.

[18] T. K. Roy, "Position control of a small helicopter using robust backstepping," in Proc. of the 7th ICECE, pp. 787-790, 2012.

[19] T. K. Roy and M. Garrat, "Altitude control of an unmanned autonomous helicopter via robust backstepping controller under horizontal wind gusts," in Proc. of 7th ICECE, pp. 771-774, 2012.

[20] T. K. Roy, M. Garrat, H. R. Pota, and H. Teimoori, "Hover flight control of a small helicopter using robust backstepping and PID," in Proc. of the 10th WCICA, 6-8 July 2012.

[21] T. K. Roy, "Horizontal position control of a small scale helicopter using adaptive backstepping controller," IJCCNet, vol. 2, no. 2, 2013.

[22] T. K. Roy, "Robust adaptive control for longitudinal and lateral dynamics of a small scale helicopter," IJCCNet, vol. 1, no. 3, pp. 22 – 34, 2012.

Improvement of the Output Performance of CZTS Thin Film Solar Cell

Sudipto Saha,[1,*] Ramiraj Chowdhury,[2] and M. M. Shahidul Hassan[1]

[1]Department of EEE, Bangladesh University of Engineering and Technology
Dhaka -1000, Bangladesh

[2]Department of E&TC, Savitribai Phule Pune University
Pune-411007, India

[*]ssudiptosaha@yahoo.com

Abstract— **In this work, 1D simulation has been performed to improve the output performance of CZTS solar cells. Three device parameters: back metal work function, CZTS absorber layer thickness and acceptor doping concentration of the absorber layer have been varied to optimize the overall solar cell performance. It has been found that back metal work function plays the most critical role and Au and Pd gives superior performance when used as back metal contact. Overall the best parameters for achieving high efficiency of a CZTS solar cell is reported.**

***Index Terms*—CZTS, SCAPS, absorber layer, solar cells, Thin film, Buffer layers.**

I. Introduction

In the present time of solar cells, for highly reliable electricity generation it is necessary to build a single junction solar cell to give priority to higher conversion efficiency. The widely reliable electricity generation also requires low cost fabrication and low degradation of material properties. The CZTS is a material which fulfils all the requirements that are stated earlier with a kesterite mineral structure which contains Cu, Zn, Sn and S. Its elements are not rare and all the elements are available on the earth crust and there is no toxicity in the elements. Presently the industrial production of thin film are highly dependent on $Cu(In,Ga)Se_2$(CIGS) absorber layer because of its cell efficiency(>20%)[1] which is the highest as compared to the others available now-a-days. CdTe is another very popular absorber layer in terms of efficiency. But there are some important limitations while using the CIGS and CdTe as absorber layers in the thin film technology which consist of the higher price and unavailability of Indium in CIGS and Te in CdTe and moreover, the toxicity of cadmium is very high. These limitations will be an impediment to further development of solar cells in near future which gave birth to a search of an alternate absorber layer for thin film in solar cells. In recent years, for applications of solar cells, the CZTS has attracted much attention. Tuneable bandgap of CZTS (1.4~1.5 eV [4]), larger absorption co-efficient (over 10^4 cm^{-1} [5-7]), same beneficial properties as for CIGS in terms of grain boundaries (GB), comparatively better performance in indirect light made CZTS a point of attraction. The recorded power conversion efficiency for electrodeposited CZTS devices is 7.3% [3]. However in some previous work on CZTS some defects have also been introduced. Small grain size of CZTS leads a short diffusion length to carriers [8]. The recombination loss consequences to a low open circuit voltage (V_{oc}) which can limit the efficiency of CZTS [9]. The thermal agitation increases the carrier recombination rates and the result is the lower efficiency in higher temperature [8, 9].

CZTS thin film is complex in nature. So it needs a numerical modelling analysis in one dimension. The variability of the structure proposed and the effects of several parameters on the output performance can be predicted by a numerical simulation. The numerical simulation and the elaboration of the proposed structure of the device are discussed in the following sections.

II. Numerical Simulation

A. SCAPS-1D Numerical Simulation Program

A Solar Capacitance Simulator (SCAPS) is used for one dimensional solar cell simulation. This simulation program was exhibited at the Department of Electronics and Information Systems (ELIS) of the University of Gent, Belgium and the development of SCAPS have been contributed by several researchers like Alex Niemegeers, Marc Burgelman, Koen Decock, Stefaan Degrave, Johan Verschraegen[10,11]. The 3.20 version of SCAPS software is used to analyse both the carrier related properties of hybrid semiconductors and non-carrier related properties which consist of dielectric constant, refractive index and the absorption constant. This simulation tool has been employed to estimate the steady state band diagram, carrier transport and recombination profile based on Poisson equation and the electron and hole continuity equations. The recombination currents for bulk defects and the defects of interface are calculated with the help of Shockley-Read-Hall (SRH) model and its extension respectively.

B. Device Structure and Simulation

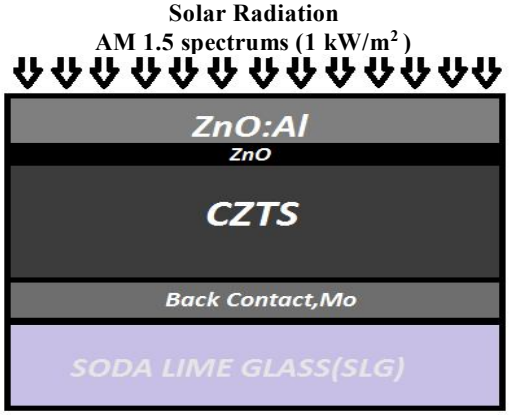

Fig. 1 CZTS solar cell structure for one dimensional simulation.

978-1-5090-5785-6/16/$31.00 ©2016 IEEE

The schematic of the vertical cross section of our simulated structure is shown in Fig. 1. In this structure molybdenum is primarily used as back metal contact having electron work function of 5.0 eV. CZTS is the absorber layer, ZnO is the buffer layer, ZnO:Al is the window layer of the simulated structure. The experimental conditions are set in a proper way before simulation. These conditions consist of temperature, bias voltage, illumination etc. The device has been enlightened with the help of AM1.5 spectrum (1 KW/m^2). The literature values and theories have enriched the device and material parameters used in the simulation in this article. In some cases, the estimations which are reasonable were also considered in the simulation. Device parameters are used in the simulation are listed in table 1[12].

TABLE I
DEVICE PARAMETERS USED IN THIS ARTICLE

Cell Properties	**Cell temperature (K)**	**Series resistance, R_S (Ω)**	**Shunt resistance, R_{SH} (Ω)**
	300	4.25	400
Front metal contact properties	**SRV* of electron (cm/s)**	**SRV of hole (cm/s)**	**Electron work function (eV)**
	1.0E+7	1.0E+5	Flat band
Back metal contact properties	**SRV of electron (cm/s)**	**SRV of hole (cm/s)**	
	1.0E+5	1.0E+7	

*SRV stands for Surface Recombination Velocity

In this article, the bandgap of CZTS is 1.46 eV [13] and the range of the constant of optical absorption of CZTS is in between 10^5(1/cm $eV^{1/2}$). In this simulation, the recombination effects and Auger electron hole capture have been considered in all the sections. Material properties of different layers used in the simulation are listed in table 2.

Here we have used the SCAPS simulation program to investigate the output performance of CZTS solar cell. We performed one dimensional simulation of the solar cell structure. Here in the simulation we have used series resistance of 4.25 Ω and shunt resistance of 400 Ω. Furthermore we have used molybdenum as back metal contact to explore the output performance of the solar cell structure. Molybdenum's electron work function is 5 eV. In the simulation the thickness of buffer layer is kept constant at 500 nm. Donor density is also kept constant 1×10^{19} cm^{-3}.

TABLE II
MATERIAL PROPERTIES OF DIFFERENT LAYERS

Material Properties	**Absorber Layer (CZTS)**	**Buffer Layer (ZnO)**	**Window Layer (ZnO:Al)**
Thickness (μm)	2.0	0.05	0.20
Bandgap (eV)	1 ~ 1.46	3.3	3.3
Electron affinity (eV)	4.5	4.6	4.6
Relative Dielectric Permittivity	10.0	9.0	9.0
CB effective density of states (1/cm^3)	2.2E18	2.2E+18	2.2E18
VB effective density of states (1/cm^3)	1.8E+19	1.8E+19	1.8E+19
Electron thermal velocity (cm/s)	10^7	10^7	10^7
Hole thermal velocity (cm/s)	10^7	10^7	10^7
Electron mobility (cm^2/Vs)	100	100	100
Hole mobility (cm^2/Vs)	25	25	25
Shallow uniform donor density N_D (1/cm^3)	1.0E+1	1.0E+19	1.0E+18
Shallow uniform acceptor density N_A (1/cm^3)	7.0E+16	1.0E+1	0

III. Result and Discussion

In this work the, SCAPS simulation program has been utilized to investigate the output performance of Front Metal (flat band) | ZnO:Al | ZnO | CZTS | molybdenum solar cell. Material parameters used in the simulation have been shown in table 2. The J-V characteristics found in the simulation is shown in Fig. 2. An efficiency of 7.89% with J_{sc}=25.85 mA/cm^2, V_{oc}=0.5448V and FF=56.05% has been found in single junction CZTS solar cell structure.

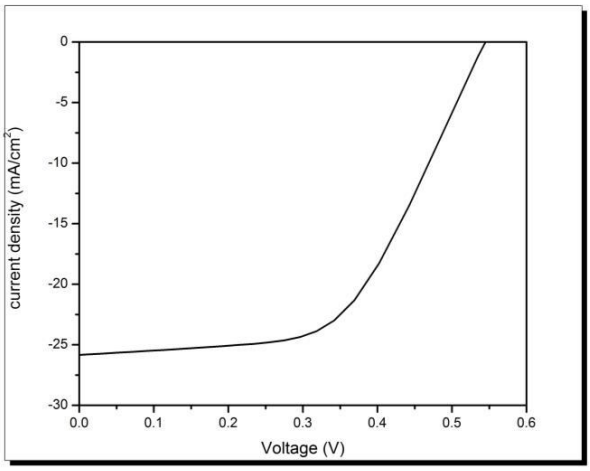

Fig. 2 Simulated J–V characteristics of Front Metal (flat band) | ZnO:Al | ZnO | CZTS | Mo solar cell.

A. Effect of back metal work function

The value of electron work function has been varied in the range of 5 to 6 eV to analyze the influence of back metal contact on solar cell performance. With the increase of back metal work function a significant change in solar cell performance has been found. The change of V_{oc}, J_{sc}, FF and efficiency with the change of back metal work function is shown in Fig. 3.

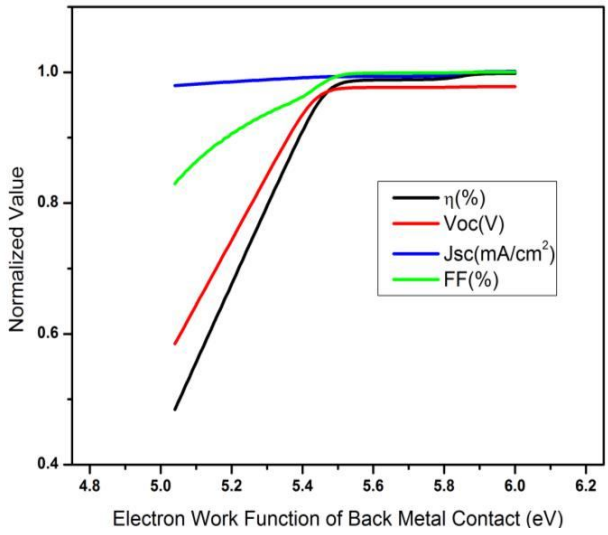

Fig. 3 Normalized output parameters of the CZTS solar cell as a function of back metal work function.

From Fig. 3 it is evident that the efficiency increases almost linearly with the rise of back metal work function from 5.05 to 5.5 eV. Here efficiency increases with a slope of 1.3% eV^{-1}. Open circuit voltage also increases linearly with the increase of back metal work function in the same range. For back metal work function ranging from 5.5 to 5.85 eV efficiency remains almost constant. For the back metal work function ranging from 5.85 to 6 eV sharp rise in efficiency has again been observed.

From the graph it can be suggested that Au and Pd are two most promising materials that can be used as back metal as their work functions are 5.47 eV and 5.6 eV respectively[12].

B. Effect of CZTS absorber layer thickness

A large number of photons containing the energy greater than and equal to the energy bandgap of materials, is absorbed by the absorber layer which contributes a good fraction of thickness in a compound semiconductor like solar cell. So for that reason it is so important to control the thickness of absorber layer to get the consistent output performance of the several number of CZTS solar cells [12].The thickness of CZTS absorber layer has been varied in the range of 0.5-5.5 µm to observe the variation of efficiency V_{oc}, J_{sc} and FF with the change of thin film thickness. Here J_{sc} and also V_{oc} increases effectively with the increase of CZTS absorber layer thickness. So the efficiency of the solar cell also increases with increase of thin film thickness. The change of V_{oc}, J_{sc}, FF and efficiency with the change of back metal work function is shown in Fig. 4.

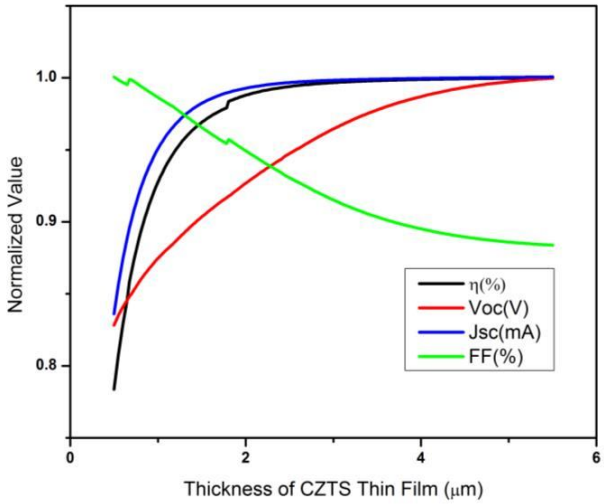

Fig. 4 Normalized output parameters of the CZTS solar cell as a function of CZTS absorber layer thickness.

Here short circuit current density is improved for absorber layer thickness up to 1.5 µm. As J_{sc} increases with the increase of thin film thickness, efficiency curve as a function of thickness follows the J_{sc} patterns and get saturated above 2.5 µm thickness of CZTS thin film. From Fig. 4 it is also evident that with the increase of thin film thickness FF decreases. From Fig. 4 it can be suggested that the thin film thickness of 2.5 µm is the most preferable one that is found in between the range of thickness 0.5-5.5µm to get maximum possible efficiency.

C. Effect of acceptor carrier concentration of CZTS thin film

Here, the solar cell structure has been simulated for N_A 5×10^{14} to 6.56×10^{16} cm^{-3} to observe the consistency issue of CZTS thin film solar cell as a function of N_A .The change of V_{oc}, J_{sc} , FF and efficiency with the change of acceptor carrier concentration of CZTS thin film is shown in Fig. 5. Acceptor concentration is closely related to electric field built up within the space charge region. With the increase of acceptor concentration, electric field increases. A higher electric field increases the V_{oc}. However with the increase of N_A magnitude of J_{sc} decreases [12]. This phenomenon is shown in Fig. 5.

From the figure N_A of 3×10^{16} cm^{-3} is considered as optimized parameter for best output performance of the photovoltaic device.

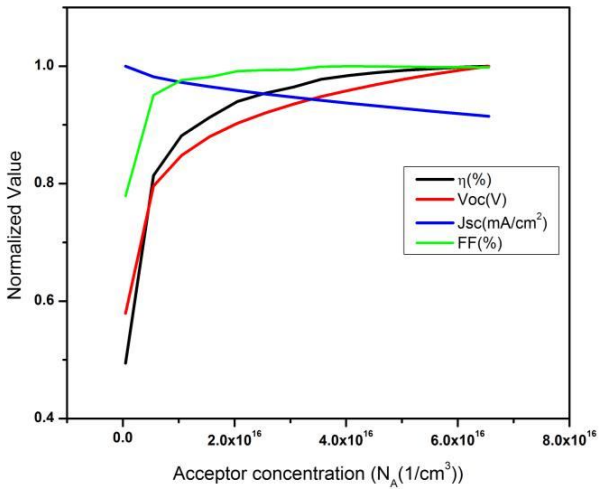

Fig. 5 Normalized output parameters of the CZTS solar cell as a function of acceptor carrier concentration of CZTS thin film.

D. Optimized CZTS thin film solar cell

J–V characteristic of optimized CZTS thin film solar cell is shown in Fig. 6. The optimized solar cell shows a much better performance resulting an efficiency of 17.84% with J_{sc}=27.4566 mA/cm^2, V_{oc}=0.9463 V, and FF=68.68%. From the above study, CZTS thin film thickness of 2.5 µm, acceptor concentration of 3× 10^{16} cm^{-3} and back metal work function of 5.47 eV has been considered as optimized parameter for best output performance of the photovoltaic device. If the series resistance can be kept below 2 Ω, the solar cell efficiency can reach up to 19.47%.

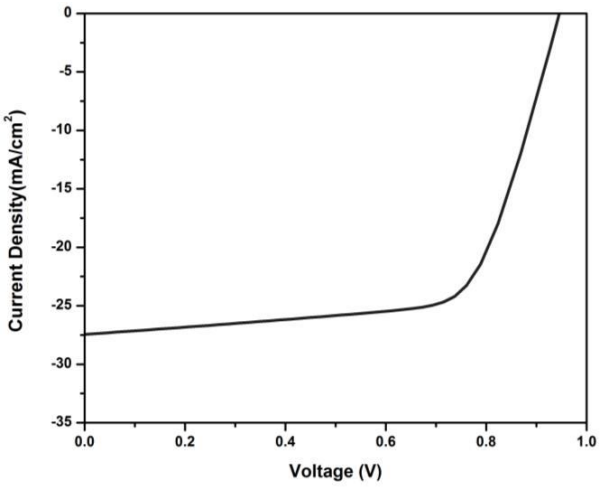

Fig. 2 Optimized J–V characteristics of CZTS thin film solar cell.

IV. CONCLUSION

The single junction CZTS solar cell while estimating with single dimension simulation, can be improved in terms of efficiency up to 17.48% (J_{sc}=27.4566 mA/cm^2, V_{oc}=0.9463 V, and FF=68.68%). For that reason, here, the simulation has optimized three device parameters-back metal work function, CZTS absorber layer thickness and acceptor doping concentration of absorber layer. The three parameters used here has been considered mutually independent though in practical, these parameters are not mutually independent . So impact of each parameter on cell performance is completely independent of impacts of the other parameters. The optimized values of the parameters mentioned above are 5.47 eV, 2.5 µm and 3×10^{16} cm^{-3} respectively. After optimization, J_{sc} has increased by 1.41 mA/cm^2, V_{oc} has increased by 0.4015 V and FF increased by 12.62%. In improving the solar cell performance, back metal work function is playing the most vital role and if Au and Pd is used as back metal contact then the CZTS thin film solar cell gives the maximum possible efficiency. Here, in this article no interface defects or layer defects have been considered. Further investigation can be done considering layer defects and interface defects.

ACKNOWLEDGMENT

The authors are very grateful to Dr Marc Burgelman at the University of Ghent for providing the software license of SCAPS-1D on request.

REFERENCES

[1] P. Jackson, D. Hariskos, E. Lotter, S. Paetel, R. Wuerz, R. Menner, W. Wischmann, and M. Powalla, "New world record efficiency for cu (in, ga) se2 thin-film solar cells beyond 20%," Progress in Photovoltaics: Research and Applications, vol. 19, no. 7, pp. 894–897, 2011.

[2] W. Shockley and H. J. Queisser, "Detailed balance limit of efficiency of p-n junction solar cells," Journal of applied physics, vol. 32, no. 3, pp. 510–519, 1961

[3] S. Ahmed, K.B. Reuter, O. Gunawan, L. Guo, L.T. Romankiw, H. Deligianni, Adv. Energy Mater. 2 (2012) 253

[4] Malkeshkumar Patel and AbhijitRay, EnhancementofoutputperformanceofCu2ZnSnS4 thin filmsolarcells — A numerical simulation approach and comparison to experiments, School of SolarEnergy, Pandit Deendayal Petroleum University,Raisan,Gandhinagar 382007,India ,2012,Physica B 407,p. 4391

[5] K.Y.B. Kishore, B.G. Suresh, P.U. Bhaskar, R.V. Sundara, Sol. Energy Mater. Sol. Cells 93 (2009) 1230.

[6] C.P. Chan, H. Lam, C. Surya, Sol. Energ. Mater. Sol. Cells 94 (2010) 207.

[7] H. Katagiri, K. Jimbo, S. Yamada, T. Kamimura, W.S. Maw, T. Fukano, T. Ito, T. Motohiro, Appl. Phys. Express 1 (2008) 41201.

[8] K.H¨ ones, E.Zscherpel, J.Scragg, S.Siebentritt, Phys.B404 (2009) 4949.

[9] D. Mitzi, O. Gunawan, T. Todorov, Sol. Energ., Mater. Sol . Cells 95 (2011) 1421.

[10] M. Burgelman, P. Nollet, and S. Degrave, "Modelling polycrystalline semiconductor solar cells," Thin Solid Films, vol. 361362, p. 527–532, 2000.

[11] M. Burgelman, K. Decock, S. Khelifi andA. Abass, " Advanced electrical simulation of thin film solar cells",Thin Solid films , 535(2013) 296-301

[12] M. Patel and A. Ray, "Enhancement of output performance of Cu2ZnSnS4 thin film solar cells — A numerical simulation approachand comparison to experiments," Elsevier Physica B, p. 4391–4397,2012.

[13] S. Saha, MD Z. E. Rafique and M. M. S. Hassan, "Performance of CZTSxSe1-x Solar Cell with Various Mole Fractions of Sulfur for Different Buffer Layers", Department of EEE, Bangladesh University of Engineering and Technology, 2016

International Conference on Electrical, Computer & Telecommunication Engineering (ICECTE)
8-10 December 2016, Rajshahi-6204, Bangladesh

Linear Pocket Profile Based Pinch-Off Voltage Model for Nano Scale n-MOSFET

Muhibul Haque Bhuyan
Department of Electrical and Electronic Engineering
Southeast University
Dhaka, Bangladesh
E-mail: muhibulhb@gmail.com

Quazi Deen Mohd Khosru
Department of Electrical and Electronic Engineering
Bangladesh University of Engineering and Technology
Dhaka, Bangladesh
E-mail: qdmkhosru@eee.buet.ac.bd

***Abstract*—This paper focuses on developing an analytical pinch-off voltage model for the pocket implanted nano scale n-MOSFETs based on symmetric linear pocket profiles both at the source and drain sides under the gate of the device. Straight line approximated equation is used to simulate the pocket profiles along the gate length at the surface of the MOS device. The effective doping concentration is derived for the whole gate length and is incorporated in the pinch-off voltage model that is obtained from the strong inversion charge expression at the surface. Then the pinch-off voltage is simulated for various drain and gate biases as well as for various device parameters. To observe the model validity, drain current vs. drain voltage curve is plotted for various gate biases by incorporating this pinch-off voltage model. The simulation results approve that the developed pinch-off voltage model can be used to study and characterize the pocket implanted advanced ULSI devices.**

Keywords—Linear Asymmetric Pocket Profile, n-MOSFET, Pinch-Off Voltage

I. INTRODUCTION

As the channel length of MOSFETs is scaled down to sub-100 nm regime, short channel effects (SCE) [1] and hot carrier reliability problems [2] have been observed. Lateral channel engineering utilizing halo/pocket implant [3-5] near the source and/or drain regions is effective in suppressing the SCE. Pocket implantation at the source and drain edges near the oxide-semiconductor interface causes inhomogeneity along the channel and produces the reverse short channel effect (RSCE) [6]. The pocket profile is usually symmetric when it is introduced from both at the source and drain sides [3-5]. It has already been observed that by introducing RSCE, SCE can be minimized [7].

In [8], analytical models for surface potential, threshold voltage, channel mobility, drain current, flicker noise etc. have been presented. But pinch-off voltage model was not given, though one may be interested to evaluate the pinch-off voltage. Because, in several design cases, pinch-off voltage is a key index. Development of the pinch-off voltage model could provide a theoretical guidance for evaluating the various properties of the device [9]. In [10], an efficient pinch-off voltage measurement technique has been presented already for uniformly doped channel MOST.

However, there is a shortage of research papers that report on the pinch-off voltage model. In a pinned photo-diode (PPD) structure, Krymiki predicted the pinch-off voltage for the first time [11]. By considering the influences of lateral electric field effect, Park modified Krymiki's model [12]. In [11-12], both researchers assumed the uniform impurity distribution of the buried layer. Of course, [9] considers the impurity concentration distribution non-uniform. Pocket implanted devices are highly non-uniform along the channel. If we use the traditional pinch-off voltage model, it will lead to a deviation from the actual value to the predicted value.

In this paper, a pinch-off voltage model has been proposed for the asymmetric pocket implanted n-MOSFET from the strong inversion charge expression. Simulation results show that the derived model could accurately predict the pinch-off voltage for various bias conditions and device parameters.

II. POCKET PROFILE

The asymmetric pocket implanted at the source side of the n-MOSFET structure, shown in Fig. 1, is considered for this work. The assumed co-ordinate system is shown at the right side of the structure.

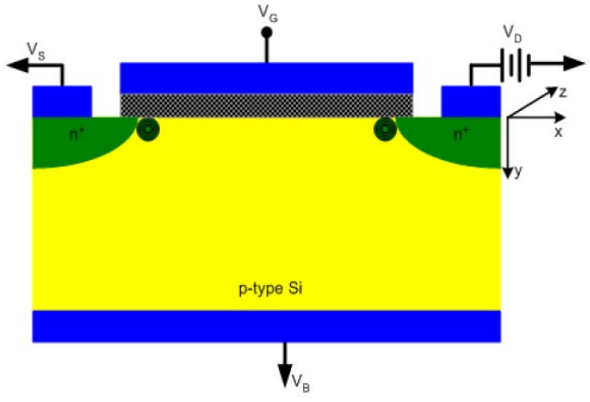

Fig. 1 Pocket implanted n-MOSFET structure with symmetric pockets both at the source and drain sides

All the device dimensions are measured from the oxide-silicon interface. In the structure, the junction depth (r_j) is 25 nm. The oxide thickness (t_{ox}) is 2.5 nm, and it is SiO_2 with fixed oxide charge density of 10^{11} cm^{-2}. Uniformly doped p-

978-1-5090-5785-6/16/$31.00 ©2016 IEEE

type Si substrate is used with substrate doping concentration, N_{sub} = 4.5×10^{17} cm^{-3}, pocket implantation at the source and drain with peak pocket doping concentration, N_{pm} = 2.5×10^{18} cm^{-3}, pocket length, L_p = 25 nm and source/ drain doping concentration, N_{sd} = 9.0×10^{20} cm^{-3}.

To preserve the long channel threshold voltage behavior for the short channel device, pocket implantation, which causes the reverse short channel effect (RSCE), is done by adding extra impurity atoms (similar to that of the substrate) near the source and drain. The peak pocket doping concentration (N_{pm}) gradually decreases towards the substrate level concentration (N_{sub}) with a pocket length (L_p) from the source and drain edges towards the center of the channel. The basis of the model of the pocket is to assume two linear doping profiles from the source and drain edges across the channel as shown in Figs. 2 and 3. The pocket parameters, N_{pm} and L_p, play vital role in determining the effect of RSCE on various device parameters.

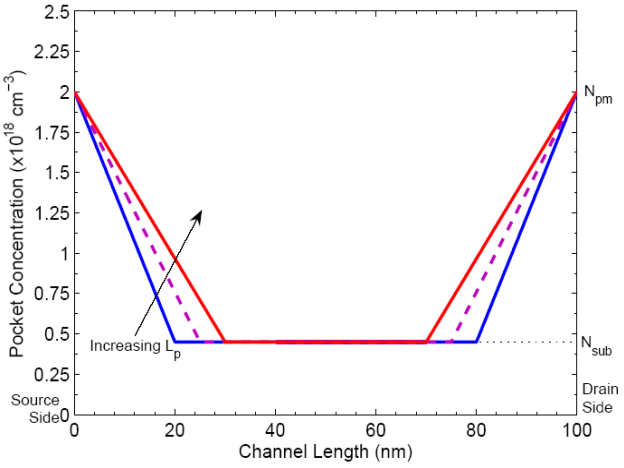

Fig. 2 Simulated pocket profiles at the surface for different pocket lengths, L_p = 20, 25 and 30 nm with N_{pm} = 2.0×10^{18} cm^{-3}

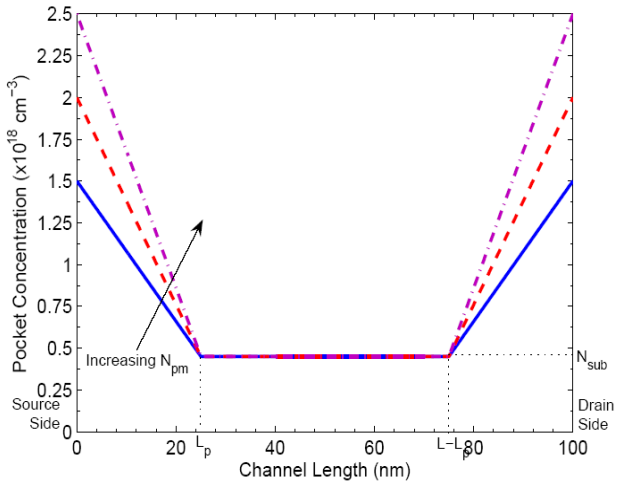

Fig. 3 Simulated pocket profiles at the surface for various peak pocket concentrations, N_{pm} = 1.5×10^{18}, 2×10^{18} and 2.5×10^{18} cm^{-3} with L_p = 25 nm

At the source side, the pocket profile is given as

$$N_s(x) = N_{sub}\frac{x}{L_p} + N_{pm}\left(1 - \frac{1}{L_p}x\right) \quad (1)$$

At the drain side, the pocket profile is given as

$$N_d(x) = N_{sub}\left(\frac{L}{L_p} - \frac{1}{L_p}x\right) + N_{pm}\left(1 - \frac{L}{L_p} + \frac{1}{L_p}x\right) \quad (2)$$

,where x represents the distance across the channel.

These two conceptual pocket profiles of equations (1) and (2) are integrated mathematically along the channel and then the result is divided by the channel length to obtain an average effective doping concentration (N_{eff}) as in equation (3).

$$N_{eff} = N_{sub}\left(1 - \frac{L_p}{L}\right) + \frac{N_{pm}L_p}{L} \quad (3)$$

When $L_p << L$ for long channel device, the pocket profile has no effect on the pinch-off voltage, V_P. But when L_p is comparable with L then pocket profile affects V_P.

III. Pinch-off Voltage Model

The pinch-off voltage (V_P) is defined as the value of the drain potential for which the inversion charge (Q_i) is zero. To model pinch-off voltage accurately, it is needed to apply the effective doping concentration directly into the inversion charge expression incorporating the threshold voltage and surface potential models obtained from [13] and [14] respectively. The derived inversion charge expression for the pocket implanted n-MOSFET is given in equation (4).

$$Q_i = -\sqrt{2q\varepsilon_{Si}N_{eff}}\left(\sqrt{\psi_s + \phi_{th}e^{(\psi_s - 2\varphi_F - V_{DS})/\phi_{th}}} - \sqrt{\psi_s}\right) \quad (4)$$

According to the above definition of V_P, from equation (4), we derive the pinch-off voltage model shown in equation (5).

$$V_P = V_{GS} - V_{th} - \gamma_A\left[\sqrt{V_{GS} - V_{th} + \left(\sqrt{2\varphi_F + \frac{\gamma_A}{2}}\right)^2} - \left(\sqrt{2\varphi_F + \frac{\gamma_A}{2}}\right)\right] \quad (5)$$

At strong inversion condition, the surface potential is assumed double of the Fermi potential, i.e. $2\varphi_F$. In equations (4) and (5), ψ_s is the surface potential, V_{th} is the threshold voltage, ϕ_{th} is the thermal voltage, V_{DS} is drain bias, V_{GS} is gate bias, γ_A is the threshold sensitivity due to the effective doping concentration. Equations for Fermi potential and threshold sensitivity are given in equations (6) and (7) respectively.

$$\varphi_F = \phi_{th}\ln\frac{N_{eff}}{n_i} \quad (6)$$

$$\gamma_A = \frac{\left(2q\varepsilon_{Si}N_{eff}\right)^{\frac{1}{2}}}{C_{ox}} \quad (7)$$

IV. Results and Discussions

Figs. 4 and 5 show that pinch-off voltage increases when gate bias increases for various peak pocket doping concentration and pocket lengths respectively. When gate bias increases carriers in the channel also increases. Hence higher drain voltage is required to pinch-off the channel, i.e. to make the inversion charge to zero. If peak doping concentration (Fig. 4) or pocket length (Fig. 5) increases then pinch-off voltage decreases. Because, effective doping will increase in both cases and hence the channel needs less voltage to pinch-off. Figs. 6 and 7 show that pinch-off voltage increases when drain bias increases for various peak pocket doping concentration and pocket lengths respectively. Similar interpretations are applied for these figures also.

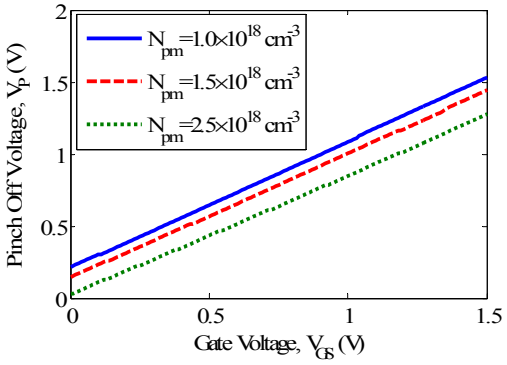

Fig. 4 Pinch voltage variation with gate voltage for various values of peak pocket doping concentration with V_{DS} = 2.0 V, L = 50 nm and L_p = 25 nm

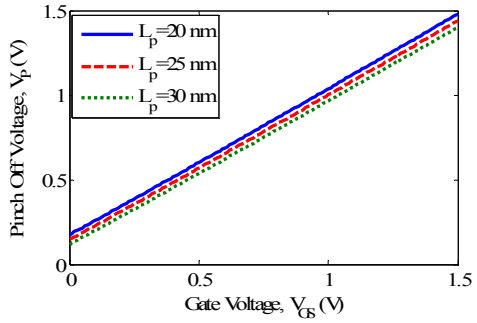

Fig. 5 Pinch voltage variation with gate voltage for various values of pocket length with V_{DS} = 2.0 V, L = 50 nm and N_{pm} = 1.5×10^{18} cm^{-3}

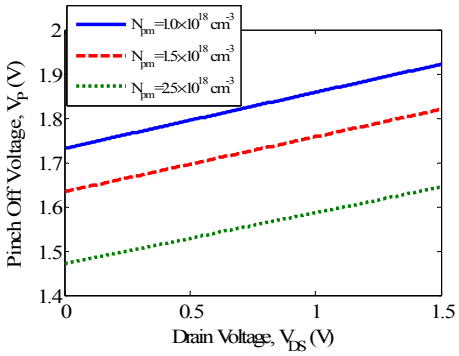

Fig. 6 Pinch voltage variation with drain voltage for various values of peak pocket doping concentration with V_{GS} = 2.0 V, L = 50 nm and L_p = 25 nm

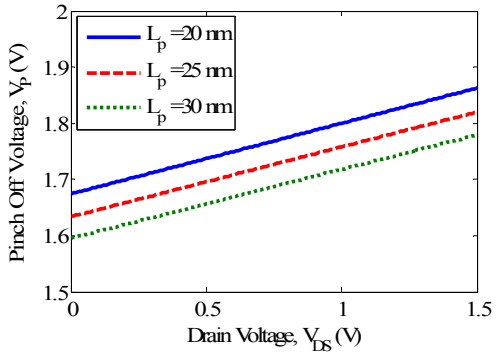

Fig. 7 Pinch voltage variation with drain voltage for various values of pocket length with V_{GS} = 2.0 V, L = 50 nm and N_{pm} = 1.5×10^{18} cm^{-3}

Fig. 8 shows that pinch-off voltage increases when gate bias increases for various substrate bias conditions. When substrate bias is made negative from zero, pinch off voltage increases, since negative bias pushes more electrons toward the channel and thus enhances the inversion charge. Therefore, higher drain voltage is required to pinch-off the channel.

Fig. 9 shows the inversion charge variation along the channel. It is observed that the peak of the inversion charge occurs at the center of the channel. This phenomenon is observed in conventional MOS devices as well. This proves the validity of our derived model for the inversion charge in equation (4) and hence the pinch-off voltage model from it in equation (5).

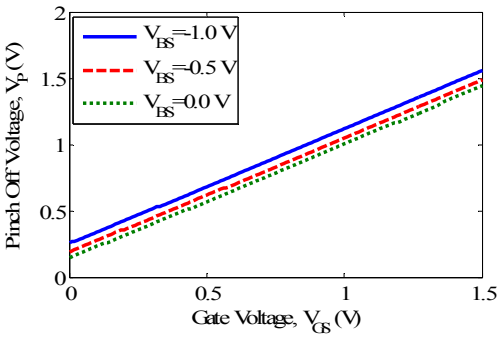

Fig. 8 Pinch voltage variation with gate voltage for various values of substrate bias with V_{DS} = 2.0 V, L = 50 nm and L_p = 25 nm

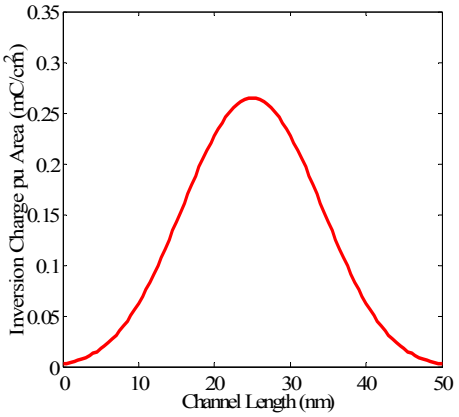

Fig. 9 Inversion layer charge variation along the channel length with gate voltage V_{GS} = 1.0 V, L = 50 nm and L_p = 25 nm

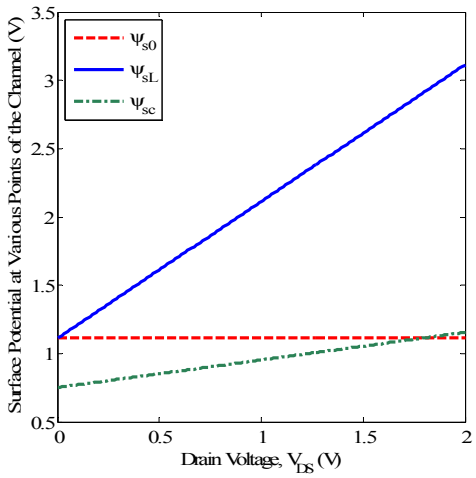

Fig. 10 Variation of surface potential with drain voltage at various points along the channel with V_{GS} = 0.0 V, L = 50 nm and L_p = 25 nm

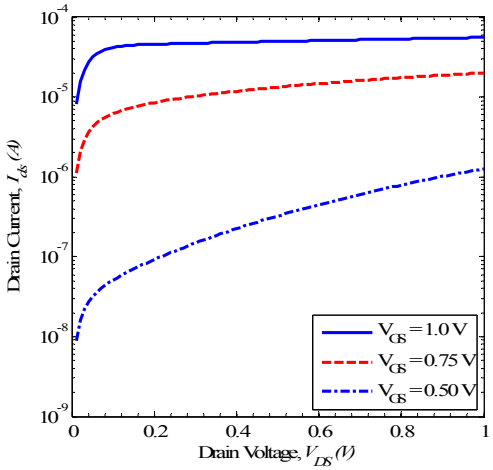

Fig. 11 Variation of drain current with drain potential for various gate voltages with L = 50 nm and L_p = 25 nm (drain current is in log scale)

From Fig. 10, it is observed that the surface potential variation at the drain side is highest when drain potential is varied. At the center this variation is moderate, but at the source almost no variation is observed. It signifies the validity of the surface potential model used in this work.

Fig. 11 shows the drain current variation with drain volage for various gate biases. As gate voltage increases, the inversion channel charge increases, the curve shifts in the upward direction, and also the locus of the pinch-off voltage shifts toward the right. It also proves our model's validity.

V. Conclusion

A pinch-off voltage model for the ultra-thin oxide and nano scaled pocket implanted n-MOSFET has been developed with symmetric linear pocket doping profiles both at the source and drain sides of the device. The proposed pinch-off voltage model has been simulated for different bias conditions and device parameters. It is found that our developed model efficiently determines the pinch-off voltages of the pocket implanted nano scaled n-MOSFET. Therefore, this model is very useful for circuit simulation.

This model can be used in to the other MOS devices, such as, SOI or DG MOSFETs with necessary modifications in the model. As a future extension of this work, type of pocket profile may be changed and comparative study may be done among these different types of pocket doping profiles and its effects on the pinch-off voltage to determine the performance of the simulator.

References

[1] M. Miura-Mattausch, M. Suetake, H. J. Mattausch, S. Kumashiro, N. Shigyo, S. Oganaka and N. Nakayama, "Physical modeling of the reverse short channel effect for circuit simulation," IEEE Transactions on Electron Devices, vol. 48, no. 10, pp. 2449-2452, Oct. 2001.

[2] A. Hokazono, S. Balasubramanian, K. Ishimaru, H. Ishiuchi, H. Chenming and L. T.-J. King, "MOSFET hot-carrier reliability improvement by forward-body bias," IEEE Electron Device Letters, vol. 27, no. 7, pp. 605-608, July 2006.

[3] B. Yu, C. H. Wann, E. D. Nowak, K. Noda and C. Hu, "Short Channel Effect improved by lateral channel engineering in deep-submicrometer MOSFETs," IEEE Transactions on Electron Devices, vol. 44, pp. 627-633, Apr. 1997.

[4] M. H. Bhuyan, F. Ferdous and Q. D. M. Khosru, "A threshold voltage model for sub-100 nm pocket implanted NMOSFET," Proceedings of the 4th IEEE International Conference on Electrical and Computer Engineering, Dhaka, Bangladesh, 19-21 December, 2006, pp. 522-525.

[5] Y. S. Pang and J. R. Brews, "Models for subthreshold and above subthreshold currents in 0.1 µm pocket n-MOSFETs for low voltage applications," IEEE Transactions on Electron Devices, vol. 49, no. 5, pp. 832-839, May 2002.

[6] M. K. Khanna, M. C. Thomas, R. S. Gupta and S. Haldar, "An analytical model for anomalous threshold voltage behavior of short channel MOSFETs," Solid State Electronics, vol. 41, pp. 1386-1388, 1997.

[7] H. Brut, A. Juge, and G. Ghibaudo, "Physical model of threshold voltage in silicon MOS transistors including reverse short channel effect," Electronics Letters, vol. 31, no. 5, pp. 410-12, March 1995.

[8] M. H. Bhuyan, "Analytical modeling of the pocket implanted nano scale n-MOSFET," PhD Thesis, Department of Electrical and Electronic Engineering, Bangladesh University of Engineering and Technology, Dhaka, Bangladesh, 2011.

[9] C. Chen, Z. Bing, W.u Longsheng, L. Xin and W. Junfeng, "Pinch-off voltage modeling for CMOS image pixels with a pinned photodiode structure," Journal of Semiconductors, vol. 35, no. 7, pp. 074012-1-7, Jul.2014.

[10] M. Bucher, C. Lallement and C. C. Enz, "An efficient parameter extraction methodology for the EKV MOST model," Journal of Semiconductors, Proc. of the IEEE Int. Conference on Microelectronic Test Structures, vol. 9, pp. 145-150, Trento, Italy, March 26-28, 1996.

[11] A. I. Krymski, N. E. Bock, N. Tu and et al., "Estimates for scaling of pinned photodiodes," IEEE Workshop on CCD and Advanced Image Sensors, 2005: 60.

[12] S. Park and H. Uh, "The effect of size on photodiode pinch-off voltage for small pixel CMOS image sensors," Microelectronics Journal, vol. 40, issue 1, pp. 137-140, Jan. 2009.

[13] M. H. Bhuyan and Q. D. M. Khosru, "Linear pocket profile based threshold voltage model for sub-100 nm n-MOSFET," International Journal of Electrical and Computer Engineering, vol. 5, no. 5, pp. 310-315, May 2010.

[14] M. H. Bhuyan and Q. D. M. Khosru, "An analytical surface potential model for pocket implanted sub-100 nm n-MOSFET," Proceedings of the 5th IEEE International Conference on Electrical and Computer Engineering, Dhaka, 20-22 December 2008, pp 442-446.

International Conference on Electrical, Computer & Telecommunication Engineering (ICECTE)
8-10 December 2016, Rajshahi-6204, Bangladesh

Feasibility Study of Low Voltage DC Distribution System for Residential Buildings in Bangladesh and Hybrid Home Appliance Design for Tropical Climate

Jyoti Prokash Das, Rifat Jahan Fatema, Md. Shamim Anower
Department of Electrical and Electronic Engineering
Rajshahi University of Engineering & Technology
Email: jpdruet111@gmail.com, rjfruet111@gmail.com, md.shamimanower@yahoo.com

***Abstract* — This paper describes a process to make the residential buildings more energy efficient. Three low voltage direct current (DC) distribution system of different voltage levels are compared with the existing alternating current (AC) system in Bangladesh. Losses in the cable, internal losses of the devices, energy consumption cost, efficiency of the converters and initial cost for new wiring are the factors which have been assessed to obtain the best system. Through the analysis it is found that 48V DC system with optimized cable area is the most economical system among the others as it saves 1,36,859.2 BDT within a life time of 20 years. Besides, a hybrid appliance is prototyped consisting of air-cooler, refrigerator and electric stove altogether for higher efficiency. The wasted heat energies from the cooling devices are stored in a thermal storage by thermoelectric modules and used later for heating purposes for the better overall efficiency.**

Keywords — AC distribution system; DC distribution system; Hybrid appliances; Thermoelectric modules; Thermal Storage.

I. INTRODUCTION

Starting in the late 1880s, Thomas Edison and Nikola Tesla were embroiled in a battle known as the war of currents. Edison developed direct current (DC) which was not easily convertible to higher or lower voltages and high transmission loss was a problem. On the other hand Tesla showed that alternating current (AC) can be stepped up easily using a transformer which reduces the transmission loss. Tesla's empirical results were the deciding factor, at least for the time being that an AC system was to prefer [1]. It would appear that AC had all but obliterated DC, but in recent years DC has seen a bit renaissance with the development in the power electronics. It offers high voltage DC transmission which allows more power to be transmitted over a long distance with less loss compared to an AC transmission and makes efficient and accurate control of electrical power possible. Though efficient AC to DC, DC to AC and DC to DC conversion technologies are now available in the market, DC to DC conversion is more efficient than AC to DC conversion.

Now most of the devices we are using today use DC internally and this requires AC to DC conversion between the AC supply and the DC side of the device. Energy storage devices also require direct current as an energy source. They are all equipped with adapters which convert 230V AC into low voltage DC and these results into unnecessary standby loss and rectifier loss [2],[3]. In case of small-scale electricity generation, such as almost all new sustainable energy sources, for example from solar cells, fuel cells, osmosis batteries, and others, DC is usually the output. Energy is wasted when converting the source's DC into AC in order to connect it to the existing 230V AC distribution network which further needs to be converted back to low voltage DC inside the DC power consuming appliances. This results in a low overall efficiency of the AC system. If the whole house is powered by DC power then these problems can be solved as DC to DC converters are more efficient. 5V, 12V, 24V and 48V DC power supply are required internally by the appliances. So comparisons are done with these voltages only expect 5V as 5V DC system will cause huge amount of feeder loss.

On the other side, there are various kinds of appliances among which kitchen appliances like electric stove, microwave oven, dishwasher, water heater etc consumes a lot of power. To make these devices more efficient a hybrid appliance has been prototyped which stores the wastage heat energy of refrigerator and air-cooler in a thermal storage and the stored heat is later used for heating purposes. This process will reduce the power consumption of the electric stove or the water heater and lead to a higher overall efficiency. Thermoelectric modules are used here for heat pumping and automatic control system is introduced too.

II. COMPARISION BETWEEN DIFFERENT DISTRIBUTION SYSTEMS

This paper shows the comparison between the existing 230V AC system and 24V DC, 48V DC and 48V DC with optimized cable area considering a lifetime of 20 years. The total energy savings and the financial impacts are determined here. Renewable energy sources or 230V AC source both can be considered as the power source but for 230V AC a central rectifier is needed (though this rectifier loss is not taken into account). Loads which are investigated are 32" LED television, washing machine, light, rice cooker, vacuum cleaner, iron, window unit AC, laptop, personal computer etc. The power ratings of these loads are within 2kW. The working

978-1-5090-5785-6/16/$31.00 ©2016 IEEE

time of these appliances is approximated by surveying at different residential buildings in Dhaka, Bangladesh. The stand by loss is different for different appliances from different producers and is taken from [4].

A. *Energy Consumption and Loss Calculation for 230V AC Distribution System in House*

The values of inductance and resistance for different cross section areas of the cables presented in Table 1 are used to calculate the losses in the cables of different cross section area.

Table 1: Inductance and Resistance for Different Core Size [5]

Core Size [mm^2]	Inductance, L [µH/m]	Resistance, R [Ohms/m]
1.0	0.6224	0.0170
1.5	0.5767	0.0113
2.5	0.5170	0.0068
4.0	0.4595	0.0043
6.0	0.4070	0.0028
10.0	0.3354	0.0017
13.3	0.2916	0.0013

The energy consumption of a house in a year can be obtained by adding the energy consumption of all appliances. The amount of energy consumption, E_C in a year by an appliance is given by,

$$E_C = E_{ON} + E_S \quad (1)$$

Where,

$$E_{ON} = \text{Working time energy consumption} = \frac{P \times T_{ON} \times 365}{1000} \text{kWh/yr} \quad (2)$$

Here, P = On power, T_{ON} = Working time per day.

and

$$E_S = \text{Standby energy consumption} = \frac{P_S \times T_S \times 365}{1000} \text{kWh/yr} \quad (3)$$

Here, P_S = Standby power, T_S = Standby time per day.

Now, the energy losses in the AC system are as the sum of the feeder cable losses and rectifier losses is given by,

$$E_{LOSS} = \frac{(E_{FL} + E_{RL}) \times T_{ON} \times 365}{1000} \text{kWh/yr} \quad (4)$$

Where, E_{FL} =Feeder loss, E_{RL} =Rectifier loss.

From the analysis, it has been found that working time energy consumption is 8242.1kWh/yr, standby power consumption is 194.65kWh/yr & energy loss is l86.20kWh/yr in which feeder loss is 35.48kWh/yr & rectifier loss is 55.41kWh. This means within the loss components standby energy is 68%, rectifier loss is 20% & feeder loss is 12%.

B. *Energy Consumption and Loss Calculation for Low Voltage DC Distribution*

Fig. 1 presents the losses for different distribution systems of different voltage level at home. The power loss of the 24V DC system is higher than for the other systems. In the case with the 48V DC system with the optimized cable area, the losses could be reduced by almost 44% compared with 48V DC system.

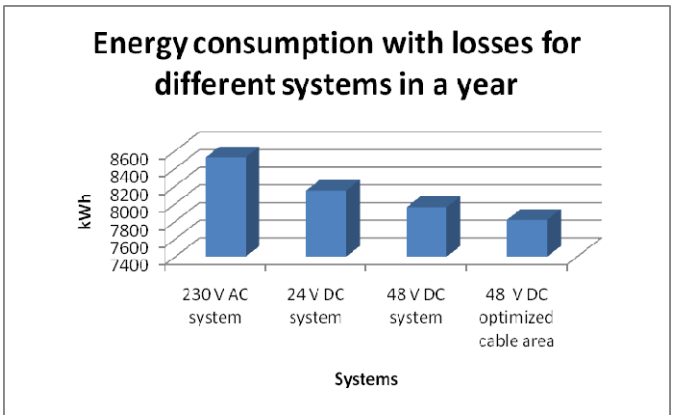

Fig. 1: Energy Consumption with Losses for Different AC and DC Voltages

The life time is assumed to be 20 years and the energy cost is determined by following DESCO tariff rate [6]. Average price of some cable and relative increment of cost compared to 1.5mm^2 wire is presented in the Fig. 2 [7].

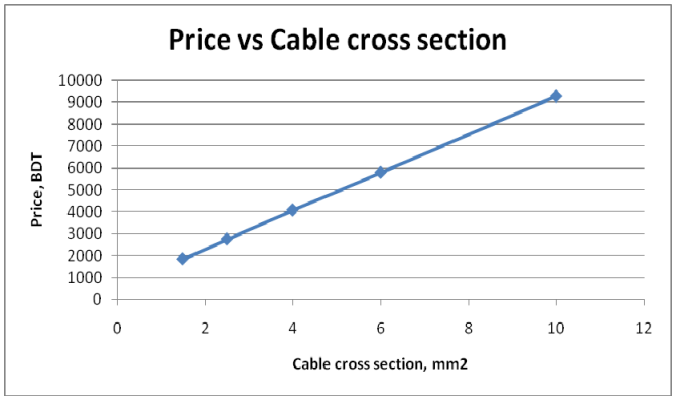

Fig. 2: Price vs. Copper Cross Section

The equation for this curve gives us an equation for the cable cost, C which is:

$$C = 266.2 + 195.9A \text{ BDT/m} \quad (5)$$

where, A = Cross sectional area of cable
Then the total cost T_C can be expressed as follows:

$$T_C = C + (E_C + E_{LOSS}) \times \text{Life time} \times \text{DESCO tariff rate} \quad (6)$$

Thus the expression in (6) leads us to obtain optimized cable area as follows:

$$A = \sqrt{\frac{\text{DESCO tariff rate} \times \text{Life time} \times 365 \times T_{ON} \times \rho}{195.9}} \frac{P}{V_{DC}}$$

where,
ρ = resistivity of cable conducting material & V_{DC} = DC voltage level.

According to this equation and taking the current ratings of the devices into account electrical wiring has been done for the 48V DC optimized cable area and for other system only the current ratings are considered. The cable costs for this are listed into Table 2.

Table 2: Investment Cost for Different Systems

System Description	230V AC System	24V DC System	48V DC System	48V DC System with Optimized Cable Area
Total Cable Cost	8264.4 BDT	14,304.2 BDT	10,560.8 BDT	12,586.4 BDT

C. Cost Analysis

In Fig. 3 the total cost of the systems is shown. Here the life time is 20 years and unit price of energy is fixed by DESCO tariff rate [5]. From this figure, it can be concluded that 48V DC system with optimized cable area is the most economical system compared with the 230V AC system and within this life time it saves almost 1,36,859.2 BDT.

III. Results & Discussions of Feasibility Analysis

Here are some specific differences & improvement which are done in this paper over the paper [5]. Blocked tariff rate is used to determine the energy related costs here which is actually practiced in the real world while fixed rate was used in [5] which have no real use now a days. Most importantly, the work done here is based on Bangladesh's scenario.

The comparisons above show some facts like 230V AC system has the highest energy consumption and losses and the lowest cable cost. Despite having the lowest cable cost 230V AC system couldn't stand against 48V DC system with optimized cable area as the energy consumption and losses were determined for a lifetime of 20 years and cable cost is just a onetime thing. 48 V DC system with optimized cable area saves almost 1,36,859.2 BDT in 20 years which is a saving of 6842.96 BDT per year and 570.25 BDT per month and this is the beneficial part of 48V DC system with optimized cable area.

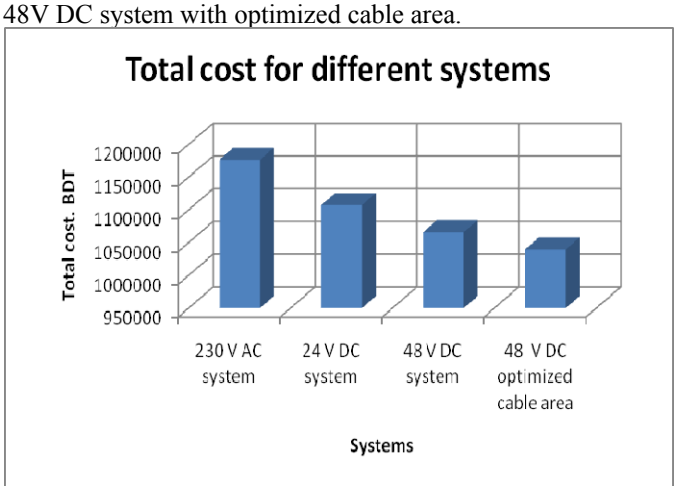

Fig. 3: Total Cost for Different Systems

IV. Hybrid Apllliances Design

In DC low voltage system, high power consuming loads causes higher loss in the feeders. So, the electrical wiring of a house has to be cleverly designed while keeping the heavy loads near to the supply to reduce feeder length and thus the losses. Moreover, the conventional appliances are modified to work along and give better efficiency. Here a refrigerator and an air-cooler are designed which run using thermoelectric modules (TEM) as heat pumps. The pumped heat of TEM is stored in a thermal storage made of aluminum which is covered with high heat resisting material and filled with paraffin to store the heat energy.

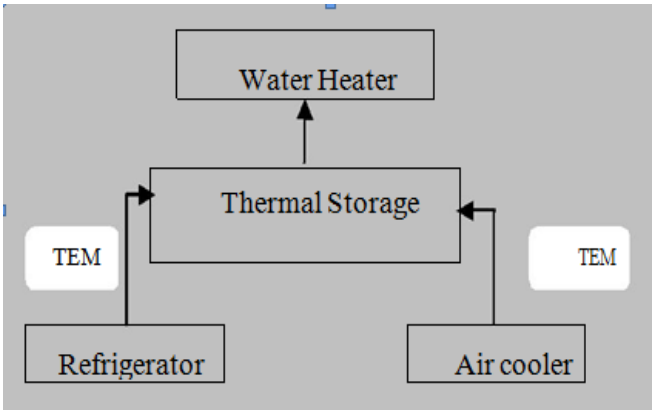

Fig. 4: Block Diagram of the Hybrid Appliances

This stored energy is later used for water heating. No compressor, power free water heater and no CFC gas make them more efficient and environment friendly respectively. This device is more suitable for hot and humid areas or simply for the tropical climate because in these areas air-cooler can extract valuable amount of heat. The physical prototype with the schematic diagram has shown in Fig. 5.

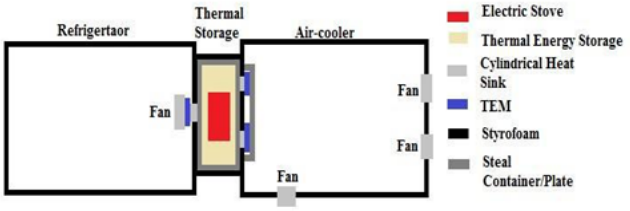

(a)

(b)

Fig. 5. The Final Prototype of the proposed hybrid system
(a) Schematic Diagram (b) Physical Representation

V. Conclusion

The benefits of using 48V DC supply for household appliances instead of 230V AC voltage have been discussed in this paper. Though loss occurs due to DC to AC and AC to DC conversion, it can be reduced by using a DC distribution system in the house. The cable cost for 48V DC with optimized cable area increases by 34.34% than in conventional AC system. But total cost decreases for 48 V DC distribution systems when the system is considered for 20 years because of no standby loss and rectifier loss. The total savings of 1,36,859.2 BDT can be achieved in 20 years by using the 48 V DC distribution system with optimized cable area compared to the 230 V AC distribution system. The appliance was also successfully prototyped.

References

[1] A. Lantero. (2014, November). *The War of the Currents: AC vs. DC Power.* [Online]. Available:http://energy.gov/articles/war-currents-ac-vs-dcpower [accessed on: 20 November, 2016].

[2] P. Vaessen. (2005, September). *Direct-Current Voltage (DC) in Households.* [Online]. Available: http://www.leonardo-energy.org/resources/442 [accessed on: 20 November, 2016].

[3] P, Pertti, K. Tero and P. Jarmo, *"DC supply of low-voltage electricity appliances in residential buildings,"* in Electricity Distribution - Part 1, 2009. CIRED 2009. 20th International Conference and Exhibition on, vol., no., pp.1-4, 8-11 June 2009.

[4] B. Mohanty, *"Standby Power Losses in Household Electrical Appliances and Office Equipment,"* in Regional Symposium on Energy Efficiency Standards and Labeling, Bangkok, Thailand, 29-31 May, 2001. [Online]. Available:http://www.un.org/esa/sustdev/sdissues/energy/op/clasp_mohanty.pdf [accessed on: 20 November, 2016]

[5] M. Amin and Y. Arafat, *"Feasibility Study of Low Voltage DC Distribution System for House,"* in the International Conference on Environmental Aspects of Bangladesh (ICEAB), Kitakyushu, Fukuoka, Japan, 2011.

[6] Desco tariff rate. (27 August, 2015). *BERC Order # BERC/ Tariff/ Bitoron-10/desco/ongsho-02/3062*. [Online]. Available:https://www.desco.org.bd/?page=tariff-rate [accessed on: 20 November, 2016]

[7] BRB Cable Industries Ltd. (2016, March). [PDF] *Price List – BRB Cable Industries Ltd.* [Online]. Available:https://www.brbcable.com>price>price_list [accessed on: 20 November, 2016]

Energy Cooperation Among BS with Hybrid Power Supply for DPS CoMP Based Cellular Networks

[1]Abu Jahid, [2]Abdullah Bin Shams and [3]Md. Farhad Hossain
[1]Department of Electrical, Electronic and Communication Engineering, Military Institute of Science and Technology, Dhaka-1216, Bangladesh,[2]Department of Electrical and Electronic Engineering, Islamic University of Technology, Gazipur-1704, Bangladesh,[3]Department of Electrical and Electronic Engineering, Bangladesh University of Engineering and Technology, Dhaka-1000, Bangladesh
Email: [1]setujahid@gmail.com, [2]abdullahbinshams@gmail.com, [3]mfarhadhossain@eee.buet.ac.bd

***Abstract*—Green cellular networking has drawn intensive attention recently for cellular operators in order to reduce the network operation cost and carbon footprints. In this paper, we consider base stations (BSs) powered by hybrid power supplies including both the conventional grid and the renewable solar energy. We propose a model for energy cooperation among BSs having individual energy storages which are connected through resistive power lines for energy sharing. Furthermore, dynamic point selection (DPS) CoMP technique is applied for selecting the best serving BS for users equipment (UE). Our goal is to maximize the green energy utilization leading to higher energy efficiency. Tempo-spatial variations of both the renewable energy generation and the traffic demand are exploited for the proposed BS cooperation. Extensive simulations are carried out for evaluating energy efficiency (EE) performance of the proposed cellular network in conjunction with DPS CoMP technique and energy sharing scheme. From simulation results we investigate the benefits of energy cooperation and effectiveness of CoMP technique in this regime.**

***Index Terms*—Energy efficiency, Energy sharing, CoMP, Hybrid power supply.**

I. Introduction

With the rapid and radical evolution of information and communication (ICT), corresponding energy consumption is also growing at a staggering rate. ICT already represents around 2% of total carbon emissions and this is expected to be increased every year with the exponential growth of the mobile traffic [1]. Since the traffic volume of cellular networks is increasing rapidly and so is its energy consumption. Therefore, the rising energy costs and carbon footprint of operating cellular networks have led to an emerging trend of addressing energy efficiency (EE) amongst the researchers, network operators and regulatory bodies such as 3GPP and ITU [2]. In a cellular system, the base stations (BSs) in its radio access network (RAN) are the most dominant energy hungry equipment adding up to 60% - 80% of the total utilization [3]. Therefore, reduction of energy consumption in BSs may significantly improve energy efficiency of cellular networks. Authors of [4] discussed load balancing concept among different BSs in order to achieve higher energy efficiency of cellular networks. However, powering radio access network using hybrid supplies combining solar energy sources with on-grid sources has become a promising alternative and is motivating the current work. Chia *et al.* [5] introduced a model for energy sharing between two cellular BSs with hybrid conventional and renewable energy sources. The proposed hybrid algorithm has some constraint when the energy profiles are non-deterministic.

978-1-5090-5785-6/16/$31.00

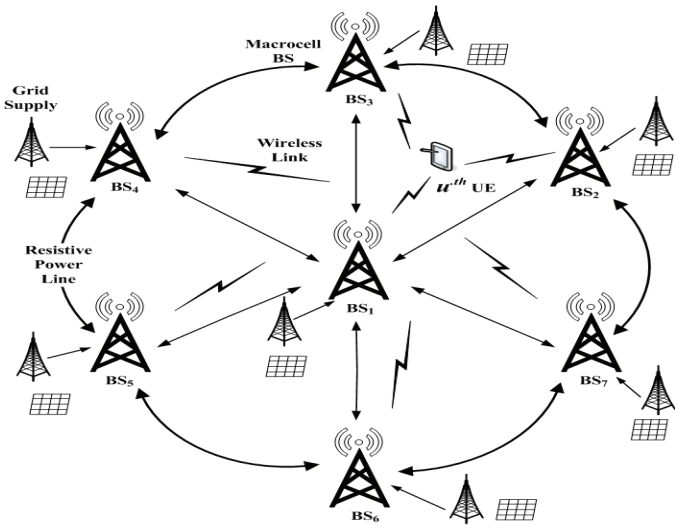

Fig. 1: Proposed Network Model.

Spectral efficiency (SE) specified as the overall system throughput, is a key performance indicator of 3GPP evolution. In recent times, advanced technologies such as Coordinated Multi-point (CoMP) transmission has been adopted by third generation partnership project (3GPP) for both downlink and uplink of LTE-Advanced (LTE-A) cellular systems [6]. However, the downlink CoMP can be categorized into three types based on data availability at multipoint; joint transmission (JT), dynamic point selection (DPS) and coordinated scheduling/coordinated beamforming (CS/CB) that are outlined by 3GPP [6].

This paper proposes energy sharing among neighboring BSs of CoMP transmission based LTE-A cellular network with hybrid power supplies. Under the proposed model, DPS CoMP technique is applied for further improving network SE. A sharing of energy among BSs would take place in the case of insufficient green energy in other BSs. A deficit may happen due to either high traffic demand or in adequate green energy generation. In this paper, our aim is to maximize the green energy utilization as well as reduction of conventional grid energy consumption in the presence of resistive power line losses and storage decay factor. In this implementation, network performance of the proposed system is evaluated in terms of energy efficiency through Monte-Carlo simulations. A thorough investigation is carried out in order to analyze the effect of CoMP based hybrid cellular system and energy

sharing based hybrid system with no CoMP, which is then compared with our proposed model.

The rest of the paper is organized as follows. In section II, a discussion of the system model is provided along with network layout and green energy model. In addition, linear energy consumption model for macrocell BS and formulation of performance metrics are also briefly explained. Section III shows the simulation results with discussion and finally, section IV concludes the paper with key findings.

II. System Model

A. Proposed Network Model

We consider a cellular network deployed using hexagonal layout, whose BSs are powered by hybrid supplies with an individual green energy storage device. In such a cellular network, BSs can share green energy among themselves through inter-connected resistive power lines. A section of the single-tier homogeneous network with seven macrocells is shown in Fig. 1. Under the proposed network model, as DPS CoMP is implemented in the system, where a BS offering the highest signal-to-interference-plus-noise ratio (SINR) is selected for serving UE. However, BSs are powered by solar energy if they have sufficient amount of green energy stored in their respective batteries; otherwise the BSs seek green power from neighboring BS. To this end, a BS switches to on-grid energy in the absence of surplus energy stored among BSs. More specifically, at the particular period of time slot, if stored green energy in a serving cell is larger than its energy demand, the BS is powered by own storage; otherwise it will share green energy from neighboring BSs having higher green power. The serving BS continuously seeks green energy among BSs until fulfill its deficit according to descending order of available green energy; otherwise the BS is powered by on-grid energy. Furthermore, under the proposed network model, the BSs share energy among themselves in a possible shortest path in order to minimize restive loss along the power lines. In addition, a neighboring BS shares energy only after fulfilling its own demand.

B. Mathematical Model of the Proposed System

For the proposed system, the green energy storage of the n^{th} BS at time t is governed by

$$s_n(t) = \mu s_n(t-1) + r_n(t) - d_n(t) \tag{1}$$

where s_n is the green energy storage, r_n is the incoming energy from solar panel, d_n is the energy demand of the particular BS and $0 \leq \mu \leq 1$ is the storage factor i.e., percentage of storage energy retained after a unit period of time. We also assume that the initial storage of the BSs follows an uniform distribution as $s_1(1) = s_2(1) = s_3(1) = ... = s_n(1) = U(0, s_{max})$, where s_{max} is the maximum capacity of the storage cells.

Now, we consider only a serving BS (BS_1) and its energy sharing in different scenarios as follows:

Case I: If $s_1(t) \geq d_1(t)$, then BS_1 will be served by its own storage so that there is no need of energy sharing from the other BSs.

Case II: If $s_1(t) < d_1(t)$, then BS_n (n^{th} neighboring BS around BS_1) would supply its surplus storage energy, i.e. energy left in the storage after fulfilling its own demand, to BS_1. Therefore, total green energy sharing in this case, $g_1(t)$ can be expressed as

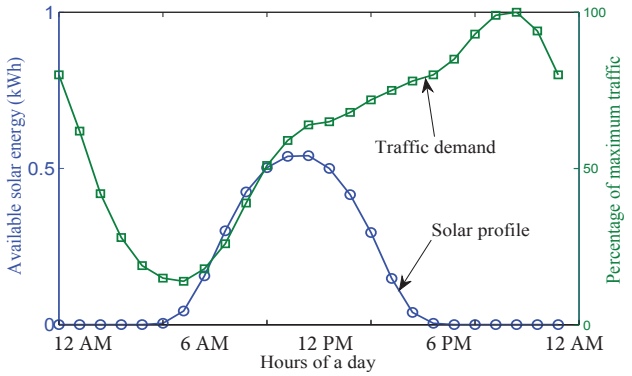

Fig. 2: Average solar energy generation and daily traffic profile.

$$g_1(t) = \frac{[d_1(t) - s_1(t)]}{\alpha} \tag{2}$$

where $0 \leq \alpha \leq 1$ is the utilization factor of the line connecting the two BSs and N denotes the total number of BSs in the system. That is, while sharing, $\alpha \times 100\%$ of the energy is dissipated as line loss. Note that the serving BS ranks the neighboring BSs in a descending order of green energy availability. Thus, for the user connected to BS_1, the green energy that can be shared by BS_1 from the j^{th} BS denoted by g_{j1} can be formulated as

$$g_{j1}(t) = [s_j(t) - d_j(t)], \quad j \neq 1 \tag{3}$$

Furthermore, if $s_j(t) - d_j(t) > g_1(t)$ then other BSs would supply their surplus storage energy to serve BS_1. Therefore, the green energy sharing in this case, $g_{j1}(t)$ is

$$g_{j1}(t) = g_1(t) \tag{4}$$

Otherwise, the neighboring BSs together supplies their surplus green energy to BS_1, though it may not be sufficient to fulfill the demand of BS_1. The total energy shared by BS_1 in this scenario can be given by

$$g_{j1}(t) = \sum_{j=2}^{M} [s_j(t) - d_j(t)] \tag{5}$$

where M is the number of neighboring BSs sharing energy with BS_1. However, provided all the neighboring BSs fail to meet the required energy demand, on-grid consumption will be required to meet the deficit of BS_1. Thus, the conventional on-grid consumption of BS_1, $c_1(t)$ in this case is

$$c_1(t) = d_1(t) - s_1(t) - g_{j1}(t) \tag{6}$$

C. Green Energy Model

We consider photovoltaic solar panel as the green energy harvester. However, the daily solar energy generation exhibits both temporal and spatial variation. In this research, we assume that solar panels of all BSs are located in the same geographical are and experiences the same energy generation rate. Average hourly solar energy generation profile of full year in Dhaka city is shown in Fig. 2. Here, solar energy profile for a particular region is estimated by adopting System Advisory Model (SAM) [7] and we set 1 kWdc capacity of solar panel. Moreover, a finite non-zero initial storage is considered and the storage capacity is rated as 350 watt-hour.

TABLE I: BS power consumption model parameters [9]

BS Type	M_{sec}	$P_{MAX}[W]$	$P_0[W]$	$\triangle P$
Macro	1	20.0	130.0	4.7

D. BS Power Consumption Model at Variable Traffic

It is worth mention that the mobile traffic volume exhibits tempo-spatial diversity and the BS energy consumption is extensively depends on the mobile traffic volumes. Based on internal surveys on operator traffic data within the Sandvine report [8], the daily traffic demand of a residential area is illustrated in Fig. 2.

It was found in [9] that the power input of a BS can be approximated a linear function of RF output power P_{MAX} and load sharing parameter χ. Hence the total power consumption considering number of sectors M_{sec} is defined as

$$P_{in} = M_{sec}(P_1 + \triangle_p P_{MAX}(\chi - 1)),\ 0 < \chi \leq 1 \quad (7)$$

where $P_1 = P_0 + \triangle_p P_{MAX}$ and P_0 is the consumption at idle state. The load dependency is accounted for by the power gradient, $\triangle_p$. The scaling parameter $\chi = 1$ indicates that a fully loaded system, i.e. BS transmitting at full power with all of their resource blocks occupied and and $\chi = 0$ indicates idle state. The parameters are summarized in Table. I.

E. Link Model

In this paper, we consider a channel model with log-normally distributed shadow fading. For a particular separation between transmitter and receiver in a large scale network, the path loss can be formulated as a function of distance by using a path loss exponent n and can be expressed as

$$PL(d) = PL(d_0) + 10nlog(\frac{d}{d_0}) + X_\sigma,\ \text{dB} \quad (8)$$

$PL(d_0)$ is usually computed assuming free space propagation model with reference distance d_0 km. X_σ is a zero-mean Gaussian random variable with standard deviation σ which is also in dB.

Thus, the received power for j^{th} UE at a distance of $d^{i,j}$ from i^{th} BS is given by

$$P_r^{i,j}(dBm) = P_t^{i,j}(dBm) - PL(dB) \quad (9)$$

where $P_t^{i,j}$ is the transmitted power at by the i^{th} BS in dBm.

Then the received SINR $\gamma_{i,u}$ at u^{th} UE from i^{th} BS can be given by

$$\gamma_{i,u} = \frac{P_{i,u}^r}{\mathcal{I}_{u,inter} + \mathcal{I}_{u,intra} + \mathcal{P}_N} \quad (10)$$

where $\mathcal{I}_{u,inter}$ is the inter-cell interference, $\mathcal{I}_{u,intra}$ is the intra-cell interference, $\mathcal{P}_N$ is the additive white Gaussian noise (AWGN) power given by $\mathcal{P}_N = -174 + 10log_{10}(B)$ in dBm with B is the bandwidth in Hz. However, LTE-A system employs orthogonal frequency division multiple access (OFDMA), which results in zero intra-cell interference.

F. Performance Metrics

The total achievable network throughput can be calculated by Shanon's capacity formula as given below

$$R_{total} = \sum_{u=1}^{U}\sum_{i=1}^{N} Blog_2(1 + \gamma_{i,u}),\ \text{bps} \quad (11)$$

where N is the number of transmitting BS for serving u^{th} UE and U is the total number of UEs in the network. we evaluate the EE performance of the network with the proposed CoMP technique in terms of bits per joule, which is defined as the ratio of aggregate throughput R_{total} of the network to the net power consumed by the network P_{net}. Thus the EE metric denoted as η_{EE} can be written as

$$\eta_{EE} = \frac{R_{total}}{P_{net}},\ \text{bit/joule} \quad (12)$$

where P_{net} the difference between the total BS power consumption and storage power. In this paper, we evaluate our proposed model in terms of EE compared with different hybrid model and conventional scheme also.

TABLE II: Simulation Parameters

Parameters	Value
System bandwidth	5 MHz (25 RBs)
Bandwidth of Resource block (RB)	180 kHz
Carrier frequency, f_c	2 GHz
Duplex Mode	FDD
Cell radius	1000 m
BS Transmission Power	43 dBm
Noise power density	-174 dBm/Hz
Number of antennas	1
Path loss exponent, n	3.574
Shadow fading SD, σ	8 dB
Access technique, DL	OFDMA
Initial Storage, $s_n(0)$	s_{max}
Maximum Storage Capacity, s_{max}	350 Wh
Storage Factor, μ	0.92 i.e. 8% loss
Line Utilization Factor, α	0.96 i.e. 4% loss
Traffic model	Randomly distributed

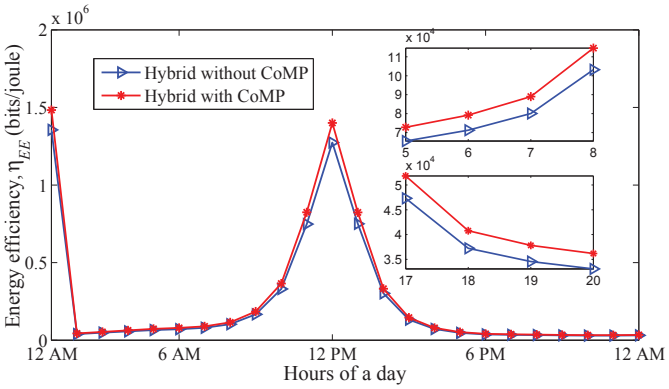

Fig. 3: EE comparison between CoMP based hybrid system and non-CoMP hybrid scheme with no energy sharing.

III. Results and Analysis

A. Simulation Setup

The results presented in this section are calculated by averaging over 10,000 independent simulations. We take into consideration of seven macrocells in a hexagonal grid fashion and UEs are randomly distributed over the geographical area. We assume number of users on individual BSs is different over a day and BSs transmit data to all the users with the same data rates. The key model parameters of the simulated system are set according to the LTE standard [6], which are summarized in Table II.

B. Result Analysis

Fig. 3 presents a comparison of the EE metric of DPS CoMP based hybrid system with non-CoMP hybrid system

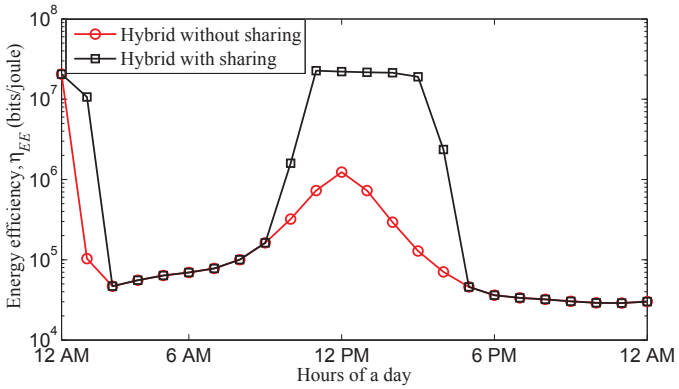

Fig. 4: EE comparison between energy sharing hybrid scheme and no sharing hybrid system without CoMP.

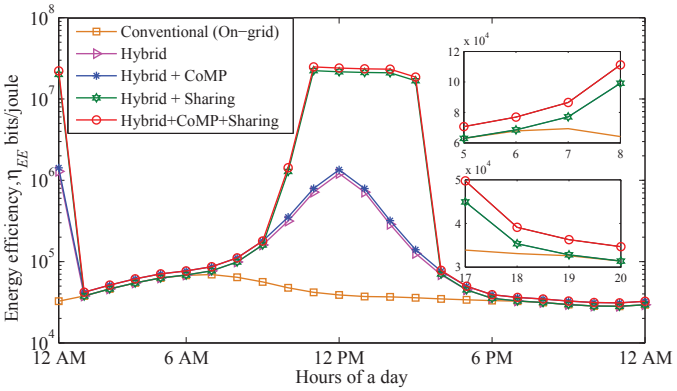

Fig. 5: EE of the proposed network compared to all hybrid scheme and conventional scheme.

over the period of one day. Under the DPS CoMP technique, UE is connected to the BS which provides the best SINR. It is important to note that the nearest BS is never fully guaranteed to provide the best possible SINR due to the randomness of shadow fading. As seen from the figure, during midnight energy efficiency falls rapidly due to unavailability of solar power and the downward trend η_{EE} curve indicates that the BS is mainly run using initial storage. As time goes, EE curve starts to increase and is typically peaks around noon, when there is adequate solar energy generation to meet the BS demand and reaches low at night, when stored energy is lower. As these two curves (i.e. hybrid with CoMP and hybrid with no CoMP) follows in a similar fashion, EE metric η_{EE} shows small changes. From the curve, it can be readily identified that the impact of CoMP has a less effect compared to non-CoMP based hybrid scheme.

Impact of green energy sharing among BSs on a hybrid scheme is demonstrated in Fig. 4. Here, we examine a particular BS and to fully realize the green energy sharing phenomenon. The BS in consideration always tends to run fully in green energy if there is sufficient energy in the storage. However, if the present green energy storage is less than demand energy, the BS would request another BS according to descending order of green energy availability. It is note-worthy that the neighboring BSs share energy only after fulfilling its own demand at a certain period that described in section II. So it can be concluded that other BSs will not sacrifice their own performance while sharing. As a consequence of green energy sharing, the overall on-grid energy consumption will be reduced. As seen from Fig. 4, EE curve falls down sharply during mid-night and starts to increase with sun light intensity. This happens because stored energy decays rapidly at night and solar energy generation reaches peak at noon. As time goes, storage gradually decreases and hence EE also decreases. From the analysis of this figure, it can be identified that sharing facility with hybrid system provides better energy efficiency over no-sharing hybrid scheme.

Finally, the EE performance of different hybrid schemes is compared to our proposed model is presented in Fig. 5. The figure includes the results for the scenario of CoMP based hybrid system as in Fig. 3 and green energy sharing based hybrid scheme as depicted in Fig. 4. The figure also includes the EE metric curve of the conventional scheme which shows inferior performance compared to our proposed model. Here, conventional scheme indicates system utilizing only grid energy but without any energy sharing or CoMP mechanism. However, the clear distinction of η_{EE} curve is shown in the zoomed figure. Note that, non-CoMP hybrid system and hybrid system without energy sharing can be regarded as hybrid system. However, Fig. 5 clearly shows that the proposed hybrid model with DPS CoMP technique and energy sharing performs significantly better than the traditional macrocell based scheme and the CoMP based hybrid scheme.

IV. Conclusions

This paper has proposed a novel energy efficiency technique for LTE-A cellular network integrating green energy sharing in conjunction with DPS CoMP technique. Under the proposed model, green energy sharing among BSs results in the minimization of on-grid consumption and thus improves EE. System performance has been evaluated through extensive simulations over 24 hours of a day and overcome the temporal disadvantage of solar energy generation using the notion of energy sharing among BSs. Our future work will include the analysis on other CoMP techniques and develop a generalized algorithm for multi-tier cellular networks with the consideration of energy savings.

References

[1] R. Mahapatra, Y. Nijsure, G. Kaddoum, N. Ul Hassan and C. Yuen, "Energy Efficiency Tradeoff Mechanism Towards Wireless Green Communications: A Survey," *IEEE Communications Surveys and Tutorials*, vol. 18, no. 1, pp. 686-705, First quarter 2016.

[2] A. P. Blanzino, C. Chaudet, D. Rossi, and J. Rougier, "A Survey of Green Networking Research," *IEEE Communications Surveys and Tutorials*, vol. 14, no. 1, pp. 3-20, 2012.

[3] M. Ismail, W. Zhuang, E. Serpedin and K. Qaraqe, "A Survey of Green Mobile Networking: From the Perspectives of Network Operators and Mobile Users," *IEEE Communications Surveys and Tutorials*, vol. 17, no. 3, pp. 1535-1556, third quarter 2015.

[4] M. F. Hossain, K. S. Munasinghe and A. Jamalipour, "Distributed Inter-BS Cooperation Aided Energy Efficient Load Balancing for Cellular Networks," *IEEE Transactions on Wireless Communications*, vol. 12, no. 11, pp. 5929-5939, 2013.

[5] Y.K. Chia, S. Sun, and R. Zhang, "Energy Cooperation in Cellular Networks with Renewable Powered Base Stations," *IEEE Wireless Communications and Networking Conference (WCNC)*, pp. 2542-2547, 2013.

[6] 3GPP, "Requirements for Further Advancements For Evolved Universal Terrestrial Radio Access (E-UTRA) (LTE-Advanced) (Release 10)," TR 36.913, V 10.0.0, 2011.

[7] "System Advisor Model (SAM)." Available: https://sam.nrel.gov/

[8] "Mobile Internet Phenomena Report," 2010. Available: http://www.sandvine.com/downloads/documents/2010 Global Internet Phenomena Report.pdf

[9] H. Holtkamp, G. Auer, V. Giannini, and H. Hass, "A Parameterized Base Station Power Model," *IEEE Communication Letters*, vol. 17, no.11, pp. 2033-2035, 2013.

Detecting Real Time Object Along With The Moving Direction For Visually Impaired People

Aniqua Nusrat Zereen and Sonia Corraya
Department of Computer Science and Engineering
BRAC University
Dhaka, Bangladesh
{aniqua.zereen, fransin.130}@gmail.com

Abstract— **Detection of real time moving object along with the moving direction in respect with visually impaired people is a challenging research area. The recent advancement in technology for real world scene capturing and portable devices like Microsoft Kinect necessitate the need of simple, reliable and faster technique for assisting blind navigation. This paper aims to develop a suitable and effective technique for moving object detection along with its moving direction in indoor environment. Depth information of the front scene of a blind people is captured using Microsoft Kinect. Three consecutive depth frames are extracted from video taken in one second and Distance along Line Profile graph is generated for four predefined lines of each depth frame. These line profile graphs are then analyzed for detecting any presence of moving object and its moving direction. After detail investigation, experimental result shows that the proposed method can successfully detect moving object along with its direction with 92% accuracy and still objects detection accuracy rate is 87%. The overall accuracy of the proposed method is 90%.**

Keywords—Blind Navigation; Microsoft Kinect; Depth Image; Escalator; Moving Direction

I. INTRODUCTION

Blind people generally have to rely on guide cane or to touch physically to sense obstacle in their moving ways, which is risky. According to natural human perceptions, moving objects movement direction is more important than object detection. When a person walks, s/he concerns about moving people and other moving objects towards him/her rather than detecting and identifying what is situated around. Again an obstacle free path can change anytime for any object's arrival on that. So information about moving object's moving direction in respect to a blind person's position is more expected and important than information about all objects in the whole scene.

Some common limitations of existing methods are limited accuracy, light source requirement, requirement of multiple hardware setups on blind person as well as in the whole environment, complex or too much informative output, longer processing time, poor performance in noisy (image or sound) environments ,costing , robustness, manual update requirement and so on. The complexity of real environment data association makes the object movement tracking more challenging [1]. Methods based on occupancy maps [4] produce more accurate result for still object rather than dynamic objects. For detecting moving objects with more accuracy some systems (e.g. in [5]-[7]) extracted the object of any type by the shape modeling and consider matching of object with that. But the main limitation of these works is the requirement of enough ground visibility [1]. Category specific models using camera (e.g. in [8]-[11]), depth information [12] or both (e. g. in [13]-[15]) outputs better result comparatively. A more reliable, single camera based obstacle detection approach is proposed in [3] however simple smooth ground surface is required for this approach to work accurately. Another obstacle detection algorithm using U-V disparity map is presented in [17] but two webcams are required for generating the disparity map. Microsoft Kinect based blind navigation system is proposed in [16] where depth image is analyzed for detecting obstacle presence and absence in the front scene and for still staircase detection only. However moving escalator would also be detected as staircase by this method which might cause dangerous accident for blind people. Again in indoor environment front scene usually contains multiple obstacles (static and dynamic).

The proposed novel approach of Object Moving Direction Identification using Depth Image for Blind is a simple, affordable and realistic blind navigation support system. For the rest of paper 'OMDIDIB' is used as a short form of **O**bject **M**oving **D**irection **I**dentification using **D**epth **I**mage for **B**lind. OMDIDIB system does not require any complex algorithm or mathematical calculation. This system can differentiate between still staircase and moving escalators along with its moving direction. Any other moving object's moving direction is also detected with respect to the blind person's view point or position. Possible outcomes of the proposed method is listed in TABLE I. Experimental result shows that the proposed method can successfully detect moving object along with its direction with 92% accuracy and still objects detection accuracy rate is 87%. The overall accuracy of the proposed method is 90%.

The rest of the paper is organized as follows. Section II is methodology which describes the experimental setup, data collection and the proposed technique. Experimental Result and discussion are presented in Section III. Finally, conclusions are drawn in section IV.

II. METHODOLOGY

To detect any object movement in any direction, whole front scene image is divided into four vertical line profiles numbering 1 to 4 from right to left. After capturing 30 frames per second configured video clip from a fixed position using Kinect three consecutive depth frames (0th, 15th and 30th frame) are extracted.

978-1-5090-5785-6/16/$31.00 ©2016 IEEE

A. *Experimental Setup*

RGB camera and depth sensor of Microsoft Kinect is used for image acquisition. Inspired by the initial setup of [16] Kinect sensor was positioned as on a standing human's chest of average heights. Ground to device height is about 1600 mm with a vertical view range of about 5000 mm (starts from 600 mm front distance of sensing device). Distance covering range of the depth image is 800 mm to 6000 mm.

B. *Data Collection*

Among many types of indoor objects, still staircase, moving escalator, still or moving human and household accessories, wall, door and obstacle free front scenes are considered for this research work. Data are collected from open access data storage of internet and also captured with Microsoft Kinect version 1 [18, 19]. A total of 600 samples depth images of 200 different front scenes (still and moving objects in twelve different directions along with moving escalators) with their respective RGB images are analyzed to test the new system. The resolution of captured and collected depth images and RGB images are 640×320 pixels.

C. *Proposed Method*

Figure 1 shows the overview of proposed system. Working flow of this new system is shown as two parts in Figure 2(a) and Figure 2(b) as a self-descriptive logical flowchart. In part-1, simple morphology processing erosion and dilation is used for noise reduction as processed depth images results better output than non-processed images as stated in [2]. After that, four vertical line profiles are extracted at pre-defined positions covering the image area. These lines are shown with number 1 to 4 from right to left in the flow diagram. Short term 'DAP graph' is used for **D**istance **A**long Line **P**rofile graph in rest of the paper.

TABLE I. POSSIBLE OUTCOMES OF THE PROPOSED METHOD OMDIDIB

Front scene contains		Type	Movement direction
No obstacle / Freeway		Still	-
Wall / Door		Still	-
Staicase/ Escalator	*Upward*	Still	-
	Downward	Still	-
Escalator		Moving	Upward
		Moving	Downward
Other Object (human, houshold accessories etc.)		Still	-
		Moving	Forward
		Moving	Backward
		Moving	Left-to-right
		Moving	Right-to-left
		Moving	Forward from left-to-right
		Moving	Forward from right-to-left
		Moving	Backward from left-to-right
		Moving	Backward from right-to-left
		Moving	In place

Next, DAP graph is generated in same axis range for each line profile of all 3 depth images. A total of twelve DAP graph is generated at this stage. Then in part-2, six logical steps are followed sequentially as described in Figure 2(b). By using Sobel edge detection method this system can determine the captured image's pattern in four categories, staircase/escalator (upward/downward), wall/door, freeway or other objects. Figure 3 shows depth image of moving escalator extracted from video. From four pre-defined line profiles, is described here. Figure 3(a) shows first line profile to determine the change in corresponding DAP graphs separately in all 3 depth images. Figure 3 (b)-(d) shows DAP graphs of corresponding first line profiles for all 3 consecutive depth images. For all 3 depth images, DAP graphs of 3(b)-(d) shows straight up or down at regular intervals shape which determines it as an upward staircase/escalator. Corresponding DAP graphs changes in particular L length of other depth images' DAP graphs (red colored area) which indicates, it is a moving escalator. Since the change in DAP graphs are decreasing with respect to line profile, the moving escalator is coming towards or downward to blind person's view point.

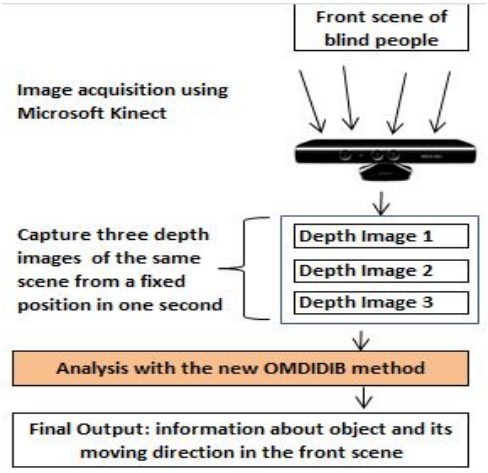

Figure 1. Overview of the proposed OMDIDIB system.

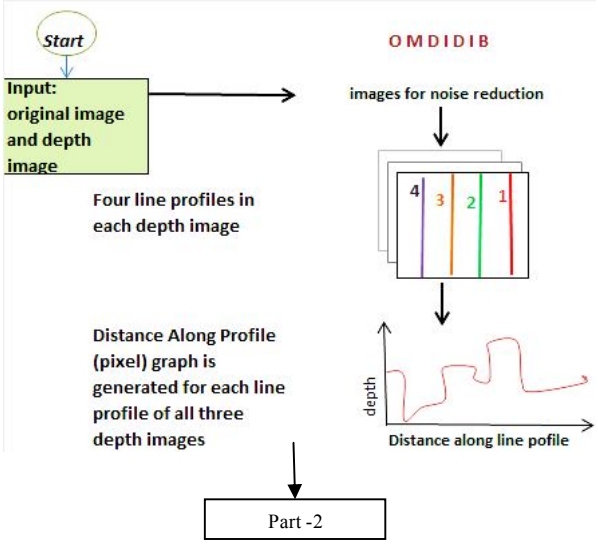

Figure 2. (a) Part-1 of OMDIDIB (Object Moving Direction Identification using Depth Image for Blind) method.

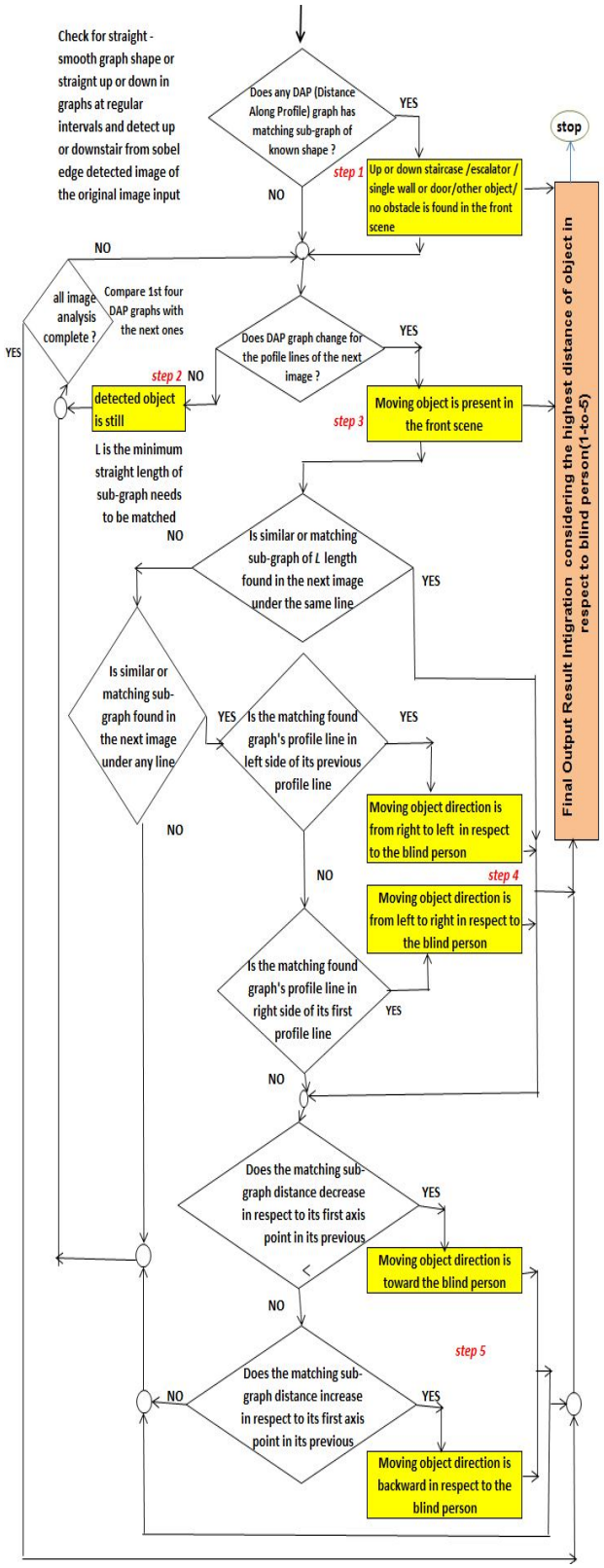

Figure 2. (b) Part-2 Flowchart of OMDIDIB (Object Moving Direction Identification using Depth Image for Blind) method.

III. EXPERIMENTAL RESULT AND DISCUSSION

For performance evaluation of the proposed method, experimental result is investigated in two levels, obstacle identification and object moving direction identification. Detail investigation result is presented in TABLE II, TABLE III and in TABLE IV. Test database is consisted of 200 different scenes taken each from one second video individually using Kinect. 3 depth frames are extracted per scene, in total 600 frames are taken to analyze the system. Below tables are showing the final result of detection and movement direction per scene's by analyzing 3 depth frames/images. When staircase and object both are present in any particular scene, then staircase has the first priority to be detected. System also prefer moving objects movement timing speed to be fast to be detected as moving, otherwise L length change in respect to distance will be too short to be detected as moving, rather it will result in still object. Images captured partially under sunlight affect system performance. Very thin object cannot be detected if it does not fall under any line profile, hence object volume size matters in some cases. Despite this, the proposed system can detect object and its movement direction separately with 87% and 92% accuracy respectively. Average accuracy is 90%. Response time of the proposed system is faster (less than 1 second) as no complex algorithm or mathematical function is used for analyzing and generating output results.

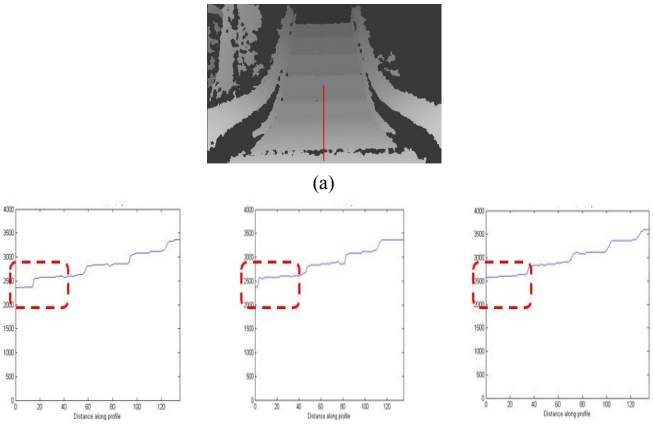

(a) (b) (c) (d)

Figure 3. (a) Depth image of downward moving escalator, (b)-(d) Analysis of single line profile of 3 consecutive depth images.

TABLE II. OBSTACLE DETECTION SUCCESS RATE AND FAILURE RATE

	Number of sample images	Percentage (%)
Success	174	87
Failure	26	13
Total	200	

TABLE III. OBSTACLE IDENTIFICATION SUCCESS RATE

System output	Actual output					
	No Obstacle / Freeway	*Wall / Door*	*Upward (stair / escalator)*	*Downward (stair / escalator)*	*Other Objects*	Total
No Obstacle / Freeway	20	2	0	0	1	23
Wall / Door	2	23	0	0	2	27
Upward (stair / escalator)	0	0	48	2	4	54
Downward (stair / escalator)	0	0	2	43	4	49
Other Objects	2	1	3	1	40	47
Rate of accuracy	87%	85%	89%	88%	85%	
Average accuracy rate	87%					

TABLE IV. OBJECT MOVING DIRECTION IDENTIFICATION SUCCESS RATE

		Moving - Escalator		Moving - Other Object	Total
		Upward	*Downward*		
Moving - Escalator	*Upward*	29	0	4	33
	Downward	0	32	2	34
Moving - Other Object		2	1	35	38
Rate of accuracy		88%	95%	93%	
Average		92%			

TABLE V. AVERAGE ACCURACY RATE AND LENGTH L IN PERCENTAGE OF LINE PROFILE FOR DIFFERENT OBJECT

Type	Object	Overall Accuracy (%)	Length L* in percentage of line profile (%)
Still	*No Obstacle / Freeway*	87	80
	Wall / Door	85	50
	Staircase / Escalator (Upward + Downward)	89	20
	Other Object	85	80
Moving	*Escalator (Upward + Downward)*	91	10
	Other Object	93	30
	Average (%)	88	45

*L is the minimum horizontal length of sub graph needs to be matched with other two images' DAP graph

IV. CONCLUSION

A novel method for real time object detection along with the moving direction for visually impaired people is presented in this paper. Up-stair, down-stair, escalators with moving direction and other moving objects' direction detection are the significant points for visually impaired peoples' independent, fast and convenient movement. Strong features of the proposed system are object sensing from blind person's view point, single camera based cheap, accurate and faster system unlike traditional multiple video camera based systems. This system is appropriate for indoor environment where escalator moves both in upward and downward direction, and other object moves in different direction in respect to blind person's position. Except direct sunlight, which is a Kinect's limitation, the proposed system can work in any light condition with 90% average accuracy rate.

REFERENCES

[1] B. Leibe, K. Schindler and L. Van Gool, "Moving obstacle detection in highly dynamic scenes," In Proceedings of IEEE International Conference on Robotics and Automation, 2009, pp. 56-63.

[2] Hsieh-Chang Huang, "A novel stair detection approach using Kinect sensor," Dawn OF Juanqi, 2015, vol. 1, pp. 59-70.

[3] Z. Yankun, C. Hong and N. Weyrich, "A single camera based rear obstacle detection system," In Proceedings of IEEE International Conference on Intelligent Vehicles Symposium, 2011, pp. 485-490

[4] A. Elfes, "Sonar-based real-world mapping and navigation," IEEE Journal of Robotics and Automation, 1987, pp. 49-265.

[5] S. Nedevschi, R. Danescu, D. Frentiu, T. Graf and R. Schmidt, "High accuracy stereovision approach for obstacle detection on non-planar roads," IEEE Intelligent Engineering Systems, 2004.

[6] M. Soga, T. Kato, M. Ohta and Y. Ninomiya, "Pedestrian detection with stereo vision," In Proceedings of IEEE International Conference on Data Engineering, 2005, pp. 24-29.

[7] L. Zhao and C. Thorpe, "Stereo and neural network-based pedestrian detection," In ITS, 2000, vol. 1, no. 3, pp. 148-154.

[8] N. Dalal and B. Triggs, "Histograms of oriented gradients for human detection," In CVPR, 2005, vol. 1, pp. 886-893.

[9] B. Leibe, A. Leonardis and B. Schiele, "Robust object detection with interleaved categorization and segmentation," International Journal of Computer Vision, 2008, vol. 77, no. 1, pp. 259-289.

[10] A. Shashua, Y. Gdalyahu and G. Hayun, "Pedestrian detection for driving assistance systems, Single-frame classification and system level performance," In IVS, 2004, pp. 1-6.

[11] B. Wu and R. Nevatia, "Detection and tracking of multiple, partially occluded humans by bayesian combination of edgelet part detectors," IJCV, 2007, vol. 75, no. 2, pp. 247-266.

[12] K. O. Arras, O. M. Mozos and W. Burgard, "Using boosted features for the detection of people in 2d range data," In Proceedings of IEEE International Conference on Robotics and Automation, 2007, pp. 3402-3407.

[13] A. Ess, B. Leibe and L. Van Gool, "Depth and appearance for mobile scene analysis," In Proceedings of IEEE 11th International Conference on Computer Vision, 2007, pp. 1-8.

[14] D. Gavrila and V. Philomin, "Real-time object detection for "smart" vehicles," In Proceedings of the Seventh IEEE International Conference on Computer Vision, 1999, vol. 1, pp. 87-93.

[15] L. Spinello, R. Triebel and R. Siegwart, "Multimodal people detection and tracking in crowded scenes," In Proceedings of AAAI Conference on Artificial Intelligence, 2008, vol. 3, pp. 1409-1414.

[16] V. Filipe, F. Fenandes, H. Fenandes, A. Sousa, H. Paredes and J. Barroso, "Blind navigation support system based on Microsoft Kinect," In Proceedings of 4th International Conference on Software Development for Enhancing Accessibility and Fighting Info-exclusion, 2012, vol. 14, pp. 94-101..

[17] M. Zhang, P. Liu, X. Zhao, X. Zhao and Y. Zhang, "An obstacle detection algorithm based on U-V disparity map analysis," In Proceedings of IEEE International Conference on Information Theory and Information Security (ICITIS), 2010, pp. 763-766.

[18] RGB-D Dataset For Visual Odometry/SLAM Under Large Lighting Variations.[online]. ttp://telerobot.cs.tamu.edu/MFG/rgbd/livo/data.html

[19] Interdisciplinary Centre for Computational Modeling University of Rzeszow. [online]. http://fenix.univ.rzeszow.pl/mkepski/ds/uf.html

International Conference on Electrical, Computer & Telecommunication Engineering (ICECTE)
8-10 December 2016, Rajshahi-6204, Bangladesh

EEG Biometrics Based on Small Intra-individual and Large Inter-individual Difference of Extracted Features

Md. Mahmudul Hasan[1*], Md. Hanif Ali Sohag[2], and Mohiuddin Ahmad[3]

[1,2,3]Department of Electrical and Electronic Engineering, Khulna University of Engineering & Technology, Khulna-9203, Bangladesh

[*]mahmudul.hasan.eee.kuet@gmail.com

***Abstract*—Biometrics refers to the process of identifying an individual from others by biological means. Most of the biometric systems are unreliable, can be imitated or even can be stolen. As a result, we need to search for a new biometrics and Electroencephalogram (EEG) based biometrics is a promising field in this aspect. By using the small intra-individual and large inter-individual difference in features with different trials, individuals can be identified with more accuracy. In this paper, a methodology for identifying an individual is proposed by determining the most effective domain and features of EEG signal. Three feed forward, back propagation multi-layer neural networks were built using the most effective features. The relative comparison shows that the network designed using the features of time domain gives the worst performance whereas the network designed using the features of both time and frequency domain gives the best performance for identifying an individual having relatively lower mean square error.**

Keywords—Electroencephalogram (EEG); biometrics; intra-individual feature; inter-individual feature; Fast Fourier Transform (FFT); Power Spectral Density (PSD); Artificial Neural Network (ANN).

I. INTRODUCTION

In the new era of science and technology the word 'biometrics' has a significant meaning which refers to the individual's physiological or behavioral characteristics or features which are unique for a specific person over time. Among the conventional biometrics fingerprint, face, and iris detection are popular nowadays and proved unique as biometric identifier by the researchers [1].

Whatever it is fingerprint, iris or voice, they all have some limitations. For instance, facial detection sometimes fails in case of twin brothers and as appearance of faces can change a lot with age, it is difficult to identify an individual after a few years. Though we use fingerprint everywhere now a days, it can be faked [2]. Even one can obtain it from another by force. An unexpected incident occurred in Malaysia in 2005 revealed how fingerprint can be found by force [3]. Facial detection failed in identifying the terrorists for the incident of Boston marathon bombing [4]. So, it is a crying need to check for a new biometric approach which can overcome the limitations of conventional biometric systems.

978-1-5090-5785-6/16/$31.00 ©2016 IEEE

Electroencephalogram (EEG) is the process which records the brain's electrical activity, they are associated with brain activities of the person's distinctive manner, and thus it is impossible to reproduce or duplicate [5]. It is very difficult to obtain EEG signal under force and threat because those signals can be influenced by mental state of the individual [6]. Besides, brain signals are associated with the subject's genetic information which makes them unique for each individual subject [7]. Therefore, brain signals are more reliable and assertive and have been proposed as a strong identification and authentication biometric [8].

Research on EEG-based identification and authentication is widely done in the recent days and some of the preliminary works carries strong evidence of EEG biometrics. EEG authentication was done by Hema [9] based on PSD features from Beta waves. He et al. [10] used the mAR features and naive Bayes model for authentication among 4 subjects. Klonovs [11] build a mobile prototype system capable of authenticating users based on the uniqueness of their brainwaves which used a mobile application named 'EEG Auth'. In this paper, the methodology is proposed to work with the most effective features from time and frequency domain and to identify a person with more accuracy.

This paper presents a general methodology of EEG-based individual identification. In this research, the BIOPAC data acquisition unit (MP36) and AcqKnowledge® 4.1 Software [12] were used for the purpose of EEG data acquisition and analysis. Different feature extraction was done using MATLAB 2012 and then three neural networks were adopted for the purpose of classification. Different scenarios were discussed for different steps in authentication.

The rest of the paper is organized as follows: section II represents proposed methodology of EEG biometrics. The signal preprocessing and analysis is described in section III. The experimental data and classification steps are briefly described in section IV and V respectively. The experimental results are discussed in section VI. Finally, section VII concludes the paper with associated future works.

II. PROPOSED METHODOLOGY

A. Proposed Model

The proposed model EEG based biometric identification for this research is shown in Fig. 1.

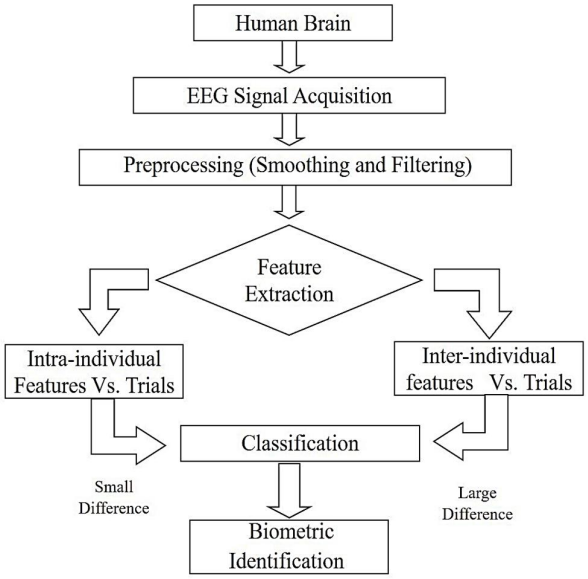

Fig. 1. Block diagram of the proposed methodology

The block diagram shows the steps of EEG signal acquisition, raw EEG signal preprocessing, feature extraction, and classification. For an individual, we considered the features with small change in different trials. For a group of people we considered the features with large change or deviation i.e.large change in inter-individual features in different trials. The selected features were used to produce feature vaectors and they were classified with the Neural network classifier.

B. Experiment Procedure

EEG data was collected in Biomedical Engineering Laboratory, Department of Biomedical Engineering of EEE Faculty, KUET, Bangladesh. Three healthy young subjects took part in the test and all of their age was between 18-24 years. They were not affected by any type of mental diseases and were controlled subject. The experiment was done on three subjects with same condition. They were all with eye closed and solved some specified simple arithmetic problem mentally such as: (23×12), (12×14), (12-32+65) etc. They were asked to solve the problems one by one sequentially.

BIOPAC electrode lead set (SS2L) with its plugs in channel 1 of MP36 data acquisition unit was used for EEG data recording. Electrode lead set was connected to the electrodes placed in occipital lobe region. The experimental setup with scalp electrode is shown in Fig. 2 for EEG recording.

Fig. 2. Pictorial view of EEG measurement

III. EEG SIGNAL PROCESSING AND ANALYSIS

A. Filtering

For using only three electrodes raw EEG signal contains noises of different frequencies including supply frequency of 50Hz. So, filtering is required before feature extraction. For filtering EEG signal band pass filter is used because it passes only the data within a specified range and attenuates the other. The raw data were filtered between ranges 0.5 Hz to 48 Hz before analysis because the line frequency was 50Hz.

B. Smoothing

The smoothing function is a transformation that calculates the moving average of a series of data points which replaces each value with a calculated mean value. The smoothing formula is shown in Eq. (1) where "p" is the number of points in the window and "q" is the sample number. We used a smoothing factor of 2 which is moderate smoothing.

$$S_{output} = \sum_{a=q-\frac{p}{2}}^{a=q+\frac{p-1}{2}} \frac{S_{input}(a)}{p} \quad (1)$$

C. Statistical and Frequency Domain Analysis

Statistical methods are the techniques used for data collection, analysis, classification and presentation of statistical data. Maximum value, mean, median, standard deviation, correlation, skewness, and kurtosis of EEG signal were used to estimate, predict, and to take decisions from the database.

In the Fourier space the raw signal is represented by magnitude of signal versus frequency. Spectral analysis is performed by computing the Fast Fourier transform (FFT). Power Spectral Density (PSD) is the term which indicates where the average power is distributed as a function of frequency. Fig. 3 shows the PSD analysis of EEG signal.

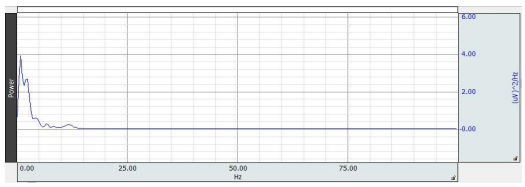

Fig. 3. PSD analysis of EEG signal

IV. EXPERIMENTAL DATA

A. Results of intra-subject feature comparision

From this offline analysis, the values of maximum, standard deviation, skewness and kurtosis for a single individual was extracted after the EEG signal had pre-processed. While extracting features in frequency domain, we considered the attributes such as mean and maximum values of PSD and mean and maximum values of FFT for measuring the difference in a specific intra-personal feature with 21 trials. Extracted effective features for EEG signal in time and frequency domain for subject 1 are shown in Table I.

TABLE I. RESPONSE OF EEG SIGNALS IN TIME AND FREQUENCY DOMAIN FOR SUBJECT1

TRIAL	Features in Time Domain				Features in Frequency Domain			
					PSD		FFT	
	Max. value (μV)	S.D (μV)	Skew (μV)	Kurt -osis (μV)	Mean Val. (μV^2)/ Hz	Max. Value (μV^2) /Hz	Mean Value (μV)	Max Val. (μV)
1	11.26	5.79	0.15	2.95	0.217	3.07	0.043	2.51
2	10.20	5.20	-0.25	3.12	0.259	5.13	0.044	1.79
3	15.79	5.85	-0.13	2.63	0.274	7.25	0.043	2.21
4	17.95	5.22	0.06	2.52	0.240	4.92	0.039	2.72
5	18.52	4.86	-0.11	2.39	0.200	3.80	0.046	2.79
6	17.43	5.82	-0.54	3.43	0.212	2.16	0.041	1.55
7	18.09	5.42	-0.09	2.58	0.243	7.53	0.048	1.31
8	18.15	5.04	0.38	3.20	0.274	5.52	0.051	1.67
9	22.32	5.34	0.38	3.45	0.220	3.44	0.045	1.41
10	22.32	5.32	0.36	3.43	0.247	5.68	0.042	2.76
11	17.74	5.64	-0.09	3.54	0.303	4.57	0.043	2.70
12	11.53	5.52	-0.13	3.05	0.252	6.07	0.042	1.93
13	12.66	5.06	0.16	3.01	0.267	3.22	0.043	2.29
14	19.59	5.88	0.21	2.55	0.216	3.81	0.048	1.86
15	19.57	5.85	0.37	2.87	0.256	8.12	0.046	2.66
16	16.28	5.79	-0.75	2.92	0.256	8.87	0.040	1.96
17	15.10	5.94	-0.84	2.99	0.257	4.64	0.044	2.57
18	17.74	5.67	-0.14	3.50	0.236	5.38	0.048	1.87
19	22.32	5.59	0.29	3.26	0.208	2.43	0.041	2.18
20	18.09	5.85	0.09	2.49	0.231	4.88	0.045	1.71
21	24.99	5.79	0.19	3.02	0.267	4.38	0.046	2.90

The extracted features which are most prominent and acceptable for intra-personal feature analysis are plotted in Fig. 4 for subject 1. Fig. 4(a) and Fig. 4(b) represent the evidence for small intra-individual and large inter-individual features in time ad frequency domain respectively.

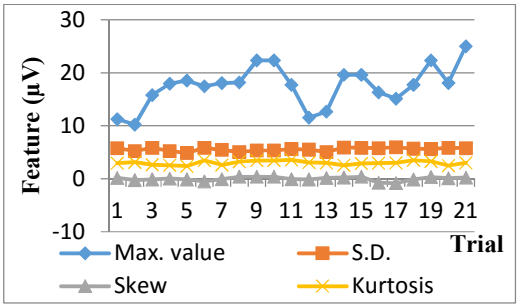

(a)

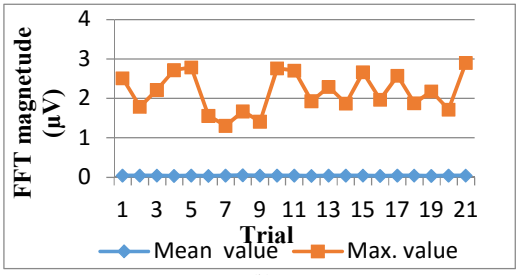

(b)

Fig. 4. Intra-individual features comparison in different trials for subject 1 (a) in time domain (b) in frequency domain

B. Results of inter-subject feature comparision

The results found from inter- subject feature comparisons in frequency domain are shown in Fig. 5. From the figure it is crystal clear that the mean values of PSD are distinct for the consecutive 21 trials for the 3 subjects. Similarly, the mean and maximum values of FFT also give strong evidence for large change in intra-individual features.

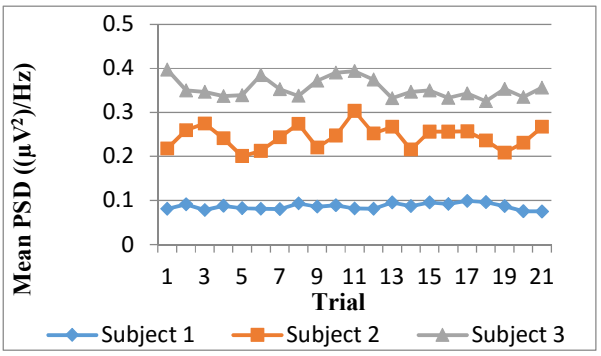

Fig. 5. Comparison of inter-individual feature in different trials in frequency domain

V. CLASSIFICATION

Three feed forward back propagation 2 layer neural network (NN) classifier were designed to classify the obtained data. We used the MATLAB built in 'nntool' for designing the neural network. The extracted features were used as input. Table II shows the input feature vectors and target for the three subjects for the network designed using frequency domain features.

TABLE II. INPUT FEATURED VECTOR AND TARGET IN FREQUENCY DOMAIN

Subject	Trial	Input Attributes in Frequency domain				Target
		PSD Max	PSD Mean	FFT Max	FFT Mean	
S-1	1 to 21	Features extracted for Subject 1				10
S-2	1 to 21	Features extracted for Subject 2				20
S-3	1 to 21	Features extracted for Subject 3				30

VI. Results and Discussion

Three Neural Networks were built for the purpose of classification and so we found three scenarios there.

A. Scenario 1:Time Domain

The first scenario indicates the neural network designed based on the features extracted in time domain. The network was able to identify all the three subjects accurately with mean square error of 0.36217. From the regression curve, we got the overall regression was 0.99427 which means that the targets and outputs were not fit enough.

B. Scenario 2:Frequency Domain

The second neural network was designed based on the features extracted on frequency domain. The network was able to identify all the three subjects accurately with mean square error of 0.0010095 at epoch 322. From the regression curve, we got the overall regression of 1 which indicates perfect fit of the targets and outputs.

C. Scenario 3:Time and Frequency Domain

The third scenario shows the neural network designed based on the features extracted from both time and frequency domain. Here we got best performance and the network was able to identify all the three subjects accurately with mean square error of 6.7232×10^{-8}. Fig. 6 shows the mean square error plot for the designed neural network. The overall regression here indicates that it is fitted enough. The relative comparisons of the three networks are shown in Table III.

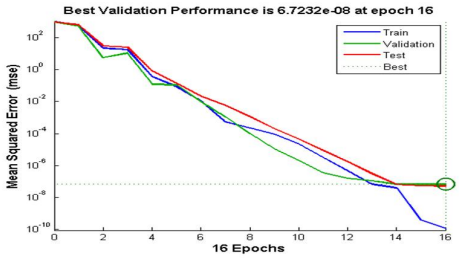

Fig. 6. Mean square error for Neural Network designed with features in time and frequency domain

TABLE III. Comparison of Performance of the Three Designed Neural Networks

Attributes		Time Domain	Frequency Domain	Time & Frequency Domain
Mean Square Error		0.36217	0.0010095	6.723×10^{-8}
Gradient		0.39033	9.9806×10^{-6}	8.457×10^{-7}
Regression (Overall)		0.99427	1	1
Accuracy of identification	Sub 1	92.2%	98.2%	100%
	Sub 2	94.5%	100%	100%
	Sub 3	94.6%	99.2%	100%

Comparing the three neural networks for three different scenarios, we can see that the network designed for time domain gives worst performance with a mean square error of 0.36217 and the network designed for frequency domain gives better performance than the first. But in case of the third network we designed gave the best performance ever.

VII. Conclusion

From the proposed methodology it is crystal clear that EEG signal alone provides strong evidence to be unique for an individual. As a result we can use the small intra and large inter individual difference in features of EEG signal with different trials to distinguish an individual from the others. The features extracted in the frequency domain give better performance in identifying a person than the time domain features. If we use an EEG headset with more number of channels, the results would be more precise. In the future era of science and technology, in case of Internet of Thing (IoT), the security of the device will be a great issue and a big problem to handle. In that case, EEG based biometrics can play an important role than the conventional biometric systems.

ACKNOWLEDGMENT

This work was partially supported by Higher Education Quality Enhancement Project (HEQEP), UGC, Bangladesh under sub project “Postgraduate Research in BME”, CP#3472, KUET, Bangladesh.

References

[1] A. Riera, A. Soria-Frisch, M. Caparrini, C. Grau, and G. Ruffini, “Unobtrusive biometric system based on electroencephalogram analysis,” EURASIP J. Adv. Sig. Proc., 2008.

[2] T. Matsumoto, H. Matsumoto, K. Yamada, and S. Hoshino, “Impact of artificial gummy fingers on fingerprint systems,” Datenschutz und Datensicherheit, 26(8), 2002.

[3] J. Kent, “Malaysia car thieves steal finger,” BBC News, 31 March, 2005.

[4] B. Schneier, “The Boston Marathon Bombing: Keep Calm and Carry On,” The Atlantic, 15 April, 2013.

[5] D. S. Bassett and M. S. Gazzaniga, “Understanding complexity in the human brain,” Trends in Cognitive Sciences, 15(5):200 – 209, 2011.

[6] S. Marcel and J. D. R. Millan, “ Person authentication using brainwaves (EEG) and maximum a posteriori model adaptation,” IEEE Trans. Pattern Anal. Mach. Intell., 29(4):743–752, May 2007.

[7] R. B. Paranjape, J. Mahovsky, L. Benedicenti, and Z. Koles, “The electroencephalogram as a biometric,” Canadian Conf. Electrical and Computer Engineering, vol. 2, pp.1363–1366, 2001.

[8] D. La Rocca, P. Campisi, and G. Scarano, “Eeg biometrics for individual recognition in resting state with closed eyes,” Proc. Int’l Conf. Biometrics Special Interest Group (BIOSIG), pp. 1–12, September 2012.

[9] C. R. Hema, M. P. Paulraj, and H. Kaur, “Brain signatures: A modality for biometric authentication,” Int’l Conf. Electronic Design (ICED), pp. 1–4, December 2008.

[10] C. He, X. Lv, and J. Wang, “Hashing the mar coefficients from EEG data for person authentication,” IEEE Int’l Conf. Acoustics, Speech and Signal Processing (ICASSP), pp. 1445–1448, April 2009.

[11] J. Klonovs, C. Kjeldgaard Petersen, H. Olesen, A. Hammershø, “Development of a Mobile EEG-based Biometric Authentication System,’’ IEEE Vehicular magazine, vol. 8, Issue: 1, pp 81-89, February 2013.

[12] Reference manuals of AcqKnowledge software guide and MP system hardware guide. (2008). BIOPAC Systems Inc., 42 Aero Camino, Goleta, CA – 0067, USA.

Impact of Energy Storage Devices on Reliability of Distribution System

Md Iamul Arafat Raihan
Junior Shift Engineer (Operations and Maintenance)
Everest Power Generation Company Limited
Meghnaghat, Narayanganj, Bangladesh
E-mail: arafatraihan17@gmail.com

***Abstract*—Modern society expects the power supply to be continuously available on demand because of its pattern of social and working habits. Hence, reliability is a key factor in power system designing and planning. Reliability of power system can be monitored at various levels of generation, transmission and distribution. This paper examines the impact of large scale energy storage on distribution system reliability. Both distributed and lumped placement of energy storage devices have been considered to calculate its impact on feeder as well as overall system reliability. DIgSILENT Power Factory 14.1 has been used as simulation tool. Results show that with introduction of energy storage devices into distribution system, duration of outage decreases in an annum. However, the inclusion of storage devices increases the frequency of outage to some extents.**

Keywords- Battery Energy Storage Systems; Reliability Indices; Distribution System Reliability; DigSILENT Power Factory

I. INTRODUCTION

Electricity is a great boon for society in many ways. Our society has become more dependent on reliable distribution of electricity and the demand of cost efficient system is increasing. This increased dependency on electricity means increased demand on the power system, which puts pressure on the system's reliability. So our goal is to maintain a better reliability in a power system & to supply electricity to its customers in an economical and reliable manner. This is where energy storage technology can play a very important role in maintaining system reliability and power quality. Energy storage system provides the added benefits of improving power quality, dynamic and transient stability and also the reliability of the supply [1].

Energy Storage refers to a process of converting electrical energy from a power network into a form that can be stored for converting back to electrical energy when needed. Such a process enables electricity to be produced at times of either low demand, low generation cost or from intermittent energy sources and to be used at times of high demand, high generation cost or when no other generation means is available. Electrical energy in an ac system cannot be stored electrically. Energy can be stored by converting it to electromagnetic, kinetic, potential energy or electrochemical energy in Battery Energy Storage System (BESS) [2].

II. POWER SYSTEMS RELIABLITY

"Reliability is the probability of a device performing its purpose adequately for the period of time intended under the operating conditions encountered"[3]. Reliability is a key factor in power system designing and planning. The objective of my research is to evaluate the reliability of distribution system in presence of energy storage devices. The reliability analysis methods can provide reliability indices at a customer site or at any system bus. An electrical power system provides the basic function of supplying customers, both large and small, with electrical energy as economically and as reliably as possible. The concept of power system reliability is extremely large and covers all aspects of the ability of the system to satisfy the customer requirements.

A. Distribution Indices

The Institute of Electrical and Electronic Engineers (IEEE) defines the generally accepted reliability indices [4].

1) System Average Interruption Duration Index (SAIDI): SAIDI measures the total duration of an interruption for the average customer during a given time period. It is normally calculated on either monthly or yearly basis.

$$\text{SAIDI}=\frac{Total\ Duration\ of\ Customer\ Interruption}{Total\ Number\ of\ Customer\ Served}$$

2) Customer Average Interruption Duration Index (CAIDI): Once an outage occurs, the average time to restore the service is found from the Customer Average Interruption Duration Index (CAIDI). CAIDI is calculated similar to SAIDI expect that the denominator is the number of customer interrupted versus the total number of utility customer.

$$\text{CAIDI}=\frac{Total\ Duration\ of\ Customer\ Interruption}{Total\ Number\ of\ Customer\ Interruption}$$

3) System Average Interruption Frequency Index (SAIFI): The System Average Interruption Frequency Index is the average number of times that a system customer experiences an outage during the year (time period under study).

$$\text{SAIFI}=\frac{Total\ Number\ of\ Customer\ Interruptions}{Total\ Number\ of\ Customer\ Served}$$

978-1-5090-5785-6/16/$31.00 ©2016 IEEE

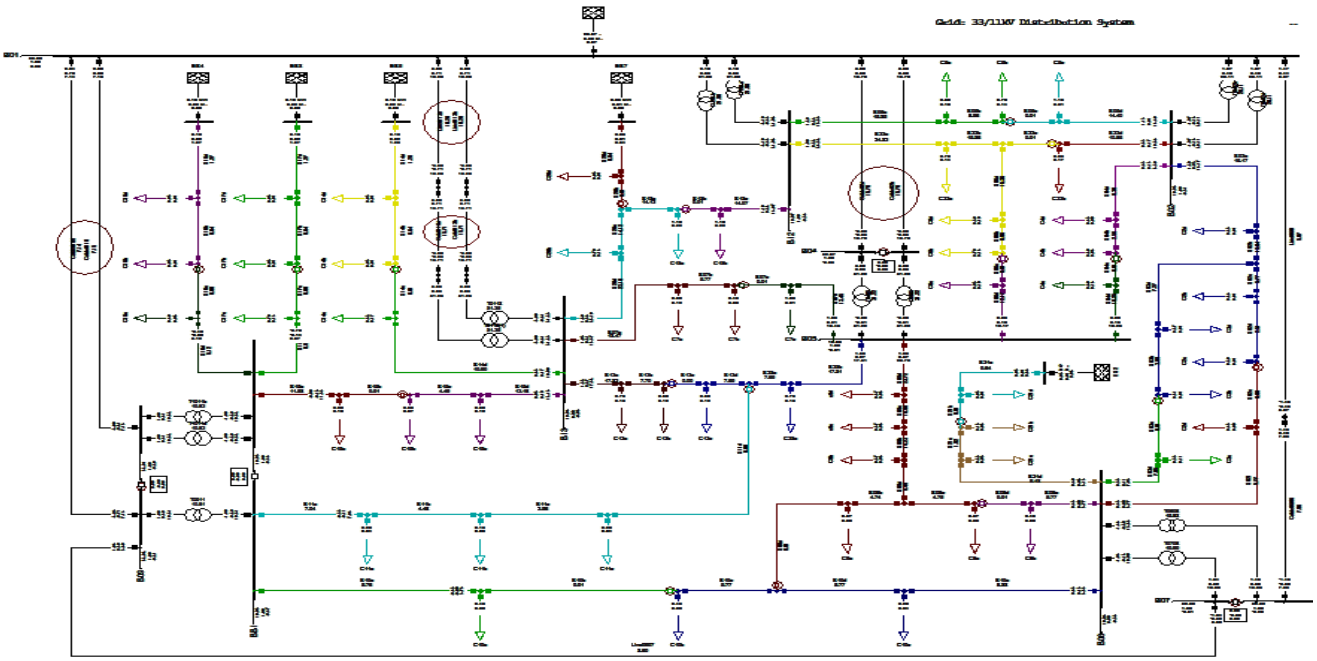

Fig. 1. 33/11 KV distribution system.

4) Customer Average Interruption Frequency Index (CAIFI): CAIFI measures the average number of interruption per customer interrupted per year.

$$\text{CAIFI} = \frac{\textit{Total Number of Customer Interruptions}}{\textit{Total Number of Customers Affected by the Interruption}}$$

III. RESULTS AND ANALYSIS

In this work, battery energy storage systems (BESSs) are placed in different bus bars of a 33/11KV distribution system in Fig. 1 to see their impact on reliability of test system. Preliminary results have been reported in [5]. Further analysis has been carried out and presented in this work.

Fig. 2 shows the default reliability index values without any BESS in system.

	Name	In Folder	Grid	SAIFI 1/Ca	SAIDI h/Ca	CAIFI 1/Ca	CAIDI h
✓	Station9_S04d	Feeders		0.07	0.2735	0.07	3.90714

Fig. 2. Value of reliability indices when no BESS is connected to the system.

Two case studies have been carried out to find the impact of BESS placement on reliability indices of the test distribution system.

A. Case Study 1: BESS Placement in Distributed Manner:

In the test system shown in Fig. 1, bus no 5, 8 and 12 are selected on random basis for testing purpose. Initially, two 1MVA BESSs have been placed at bus 5 as shown in Fig. 3.

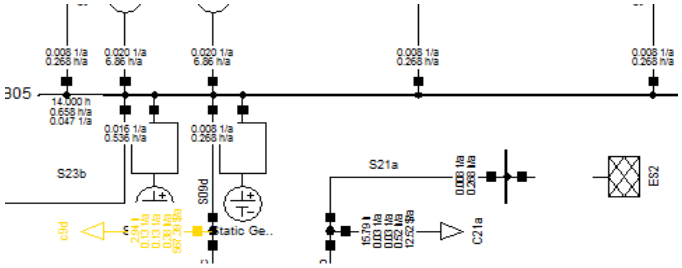

Fig. 3. Two 1MVA (=2 MVA) storage devices are connected.

	Name	In Folder	Grid	SAIFI 1/Ca	SAIDI h/Ca	CAIFI 1/Ca	CAIDI h
✓	Station9_S04d	Feeders		0.08	0.2805	0.08	3.50625

Fig. 4. The value of reliability indices when 2 storage devices are connected.

From the values showed in the Fig. 2 and Fig. 4, we can see that, after placing two storage devices in bus 5 (as in Fig. 3), the value of reliability indices changed. The values of SAIFI, SAIDI, CAIFI increased and the value of CAIDI decreased. Now we will analyze the situation more deeply by placing 4 storage devices each of 1MVA as shown in Fig.5.

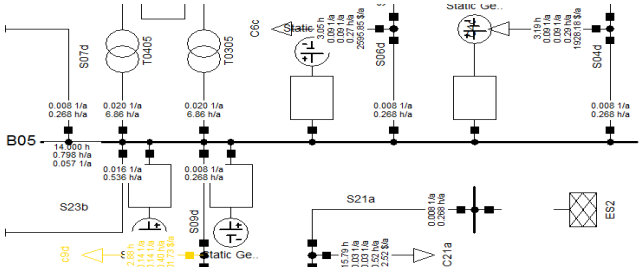

Fig. 5. Four 1MVA (=4MVA) storage devices are connected in bus 5.

	Name	In Folder	Grid	SAIFI 1/Ca	SAIDI h/Ca	CAIFI 1/Ca	CAIDI h
	Station9_S04d	Feeders		0.09	0.2875	0.09	3.19444

Fig. 6. The value of reliability indices when 4 storage devices are connected.

From Fig. 6, it can be seen that, the values of SAIFI,SAIDI and CAIFI increased and the value of CAIDI decreased again after placement of 4 storage devices.

TABLE I. COMPARISON BETWEEN CHANGES IN RELIABILITY INDICES BEFORE AND AFTER IMPLEMENTATION OF BESS

Reliability indices	Change in reliability indices when 2 storage devices are connected	Change in reliability indices when 4 storage devices are connected
SAIFI	14.28% inc	28.57% inc
SAIDI	2.56% inc	5.11% inc
CAIFI	14.28% inc	28.57% inc
CAIDI	10.26% dec	18.24% dec

inc = increase, dec = decrease

The difference in reliability indices is calculated with respect to the normal condition when no BESS is placed in the system. From the comparison in TABLE I, it can be seen that, the rate of increase and the rate of decrease of the values of reliability indices are maintaining a certain relationship with the number of devices connected. As the number of connected devices got doubled, the value of reliability indices also got almost doubled.

B. Case Study 2: BESS Placement in Lumped Manner:

Now this paper will discuss and analyze the behavior of reliability indices when BESS are connected to different buses in lumped manner.

	Name	In Folder	Grid	SAIFI 1/Ca	SAIDI h/Ca	CAIFI 1/Ca	CAIDI h
	33/11kV Distribution Syst	Network Data	33/11kV Distribution	0.13732	0.43858	0.13732	3.19379
	Summary Grid	Reliability		0.13732	0.43858	0.13732	3.19379

Fig. 7. System (Grid) reliability indices when total 8 storage devices are connected to the system in distributed manner (2 devices in Bus 05, 2 devices in Bus 08, 2 devices in Bus 12, 2 devices in Bus 13= total 8 devices and each of 1MVA= total 8MVA BESS are placed in distributed manner).

	Name	In Folder	Grid	SAIFI 1/Ca	SAIDI h/Ca	CAIFI 1/Ca	CAIDI h
	33/11kV Distribution Syst	Network Data	33/11kV Distribution	0.13386	0.42977	0.13386	3.21043
	Summary Grid	Reliability		0.13386	0.42977	0.13386	3.21043

Fig. 8. System (Grid) reliability indices when total 2 storage devices are connected to the system in lumped manner (1 device in Bus 08, 1 device in Bus 12= total 2 devices and each of 4 MVA BESS are placed in lumped manner).

TABLE II. COMPARISON OF CHANGE IN THE VALUE OF RELIABILITY INDICES OF FIG. 7 AND FIG. 8

Reliability Indices	Without Placing BESS	Placing BESS in Lumped Manner 8MVA	Placing BESS in Distributed Manner 8MVA	Difference between reliability indices for Distributed & Lumped Placement
SAIFI	0.12553	0.13386	0.13732	0.00346
SAIDI	0.41299	0.42977	0.43858	0.00881
CAIFI	0.12553	0.13386	0.13732	0.00346
CAIDI	3.289	3.21043	3.19379	0.01664

The rating of the BESS in both cases is 8 MVA but placement method is different. The value of CAIDI is higher when 8MVA BESS is connected in lumped manner. Hence, duration of outages is longer when connected in lumped manner and it is higher by 0.01664 hour. The reason behind this longer duration is the power supplied during interruption when connected in lumped manner is less compared to when connected in distributed manner. Moreover, the values of SAIFI, SAIDI, CAIFI are lower when 8 MVA battery storages are connected in lumped manner compared to distributed manner. This can be explained as SAIFI, SAIDI and CAIFI depend on the probability of outage of the storage devices. When BESS is connected in distributed manner, the number of storage device is higher than in lumped manner. So, the probability of outage of the storage devices are higher. As a result, the value of SAIFI, SAIDI, CAIFI are higher when connected in distributed manner compared to lumped manner.

Now, we will analyze another situation where BESSs are placed in a certain bus (bus 5) in different placement manners.

	Name	In Folder	Grid	SAIFI 1/Ca	SAIDI h/Ca	CAIFI 1/Ca	CAIDI h
	Station9_S04d	Feeders		0.08	0.2805	0.08	3.50625

Fig. 9. The value of reliability indices when 2 BESS, each of 1 MVA =total 2 MVA are connected in distributed manner.

	Name	In Folder	Grid	SAIFI 1/Ca	SAIDI h/Ca	CAIFI 1/Ca	CAIDI h
	Station9_S04d	Feeders		0.075	0.277	0.075	3.69333

Fig. 10. The value of reliability indices when 1 storage device of 4 MVA is connected in lumped manner.

TABLE III. DIFFERENCE BETWEEN RELIABILITY INDICES FOR DISTRIBUTED AND LUMPED BESS PLACEMENT.

Reliability Indices	Without Placing BESS	Placing BESS in Lumped Manner 1 4MVA	Placing BESS in Distributed Manner 2 1MVA	Difference between reliability indices for Distributed & Lumped Placement
SAIFI	0.07	0.075	0.08	0.005
SAIDI	0.2735	0.277	0.2805	0.0035
CAIFI	0.07	0.075	0.08	0.0035
CAIDI	3.90714	3.69333	3.50625	0.18705

From TABLE III, it can be observed that, the same thing happened here as explained earlier. The value of CAIDI is less when connected in distributed manner compared to when connected in lumped placement which gives us less duration of outage.

Now, we will examine one more case to understand the situation more clearly. Fig. 11, shows the values of reliability indices of feeders connected to bus 5 when 2 BESS of 4 MVA (total 8 MVA) are connected in lumped manner. We can observe that, these values are exactly the same as the values showed in Fig. 9. In both cases the effect on the values of reliability indices of each feeder is same. Thus, we can infer that, same reliability indices can be obtained by placing less valued storage devices in distributed manner.

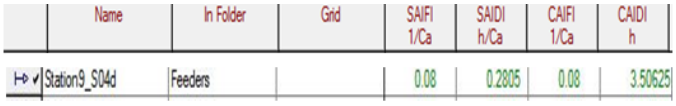

Fig. 11. The value of reliability indices when 2 BESS, each of 4 MVA =total 8 MVA are connected in lumped manner in Bus 05.

C. *Overall (33/11 KV System) Improvement of Reliability:*

To understand the overall improvement of reliability, the values of reliability indices of Fig. 12 (when no BESS is connected to the system) is compared with the values of reliability indices of Fig. 7 (when total 8 storage devices of total 8MVA are connected to the system in distributed manner).

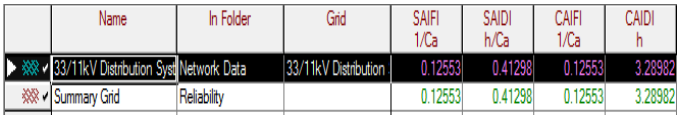

Fig. 12. System (GRID) reliability indices when no BESS is connected to the system.

TABLE IV. CHANGE IN SYSTEM RELIABILITY INDICES WHEN 8MVA STORAGE DEVICES ARE CONNECTED IN DISTRIBUTED MANNER IN %

System Reliablity Indices	Change in System Reliability, %
SAIFI	9.39% inc
SAIDI	6.19% inc
CAIFI	9.39% inc
CAIDI	2.91% dec

inc= increase, dec= decrease

From the comparison in TABLE IV, it can be observed that, the values of SAIFI & CAIFI has increased by 9.39%, the value of SAIDI has increased by 6.19%. But the value of CAIDI has decreased by 2.91%. The decrease in the value of CAIDI means that, the duration of outages has also decreased as we desired.

IV. CONCLUSIONS

When BESSs are added to a particular bus, the duration of outages of overall system is decreased as the system is a mesh interconnected network. The reduction in outage duration is significant in feeders connected to BESS integrated bus compared to overall system. Duration of outages are much lower with BESS connected in distributed manner compared to lumped manner. Hence, this work proves that distributed placement of energy storage devices is more effective for decreasing the overall duration of outages. However, with distributed placement of BESS, number of outage increases and hence, a trade-off is required.

ACKNOWLEDGEMENTS

The author would like to express his heartfelt gratitude to Dr. Tareq Aziz, Associate Professor, Department of EEE, Ahsanullah University of Science and Technology, Dhaka for his valuable support in completion of the work.

REFERENCES

[1] Ravi Gupta, N K Sharma, P Tiwari, Astha Gupta, “Application of energy storage devices in power systems”, *IJEST*, Vol. 3, No. 1, 2011, pp. 289-297.

[2] Haisheng Chen, Thang Ngoc Cong, Wei Yang, Chunqing Tan, Yongliang Li, Yulong Ding, “Progress in electrical energy storage system: a critical review”, *Progress in Natural Science*, *Elsevier,* Volume 19, Issue 3, 10 , March 2009, Pages 291–312.

[3] Roy Billinton and Ronald N. Allan, “Reliability assessment of large electric power systems”, Kluwer Academic Publishers, 1988.

[4] Reliability Indices for Utilities, available at: www.12eng.com/Reliability_Indices_for_Utilities.pdf

[5] Md Iamul Arafat Raihan, Sujit Chowdhury, Abdur Rob, Md. Raihan Khan Rabby, “Impact of Energy Storage Devices on Reliability of Distribution System,” B.Sc. Thesis, Dept. of EEE, Ahsanullah University of Science & Technology, Dhaka, November, 2015.

A Comparative Study on Power Converters for PMSG Based Wind Turbine Generation System

Md. Akmam Ul Haque
Electrical & Electronic Engineering Department
Rajshahi University of Engineering and Technology
Rajshahi, Bangladesh
noweidhaque@gmail.com

D. Datta, M.R.I. Sheikh
Electrical & Electronic Engineering Department
Rajshahi University of Engineering and Technology
Rajshahi, Bangladesh
dristidatta@gmail.com, ris_eee@ruet.ac.bd

***Abstract*— This paper focuses on modeling and simulation of a Permanent Magnet Synchronous Generator (PMSG) based wind turbine with three different types of inverter with the same configuration in its control section. In this research, a Two-Level, Three-Level and a Five-Level inverter has been used in three different simulation program to justify their performance under the same control system and same PMSG system. Based on their performance, corresponding graphical analysis has also been shown. This paper also deals with the both dynamic and transient stability of the system. Proper comparison between these three inverters has been included on the basis of their simulation performance. The performance of the system is verified by proper simulations with PSCAD Professional 4.2.0 and the obtained results are presented with brief graphical analysis.**

Keywords—PMSG, Wind Power, DC/AC Inverter, IGBT

I. INTRODUCTION

In a rapidly developing world, the urge to find an alternate, sustainable, better and efficient energy source has always been an interesting research issue over the few decades. Not only that, the changing world climate has also been a serious threat to our world. The processes of industrialization and economic development require energy. Fuels are the main energy resource in the world and are at the center of the energy demands. Therefore the utilization of the renewable energy systems is gaining expert opinion worldwide due to its sustainability and its decreasing cost of trend making them ideal for use in power generation systems. Besides, our overdependence on fossil and nuclear fuels is causing environmental pollution and safety problems which are now becoming dominant issues in our society [1]. Of the many renewable energy resources such as solar, wind, biomass, tidal etc. solar and wind energy systems are most commonly used.

Conceptual scheme of wind turbines with conventional power converter; with variable speed with a synchronous generator, is shown in Fig 1. All the power generated by the generator passes through the converter. The power converters can be arranged in different ways. Whereas the generator side converter can be a diode rectifier or a PWM (Pulse Width Modulation) voltage source converter, the grid side converter is typically a PWM source converter.

Many researches have also been done on wind power applications of power converters. In [2] a comparison has been shown between 2-level and 3-level inverter. For wind power applications of power converters it was important to evaluate a comparison between these inverters. This paper deals with the comparison between 2-level, 3-level and 5-level inverters with the same control configuration for each of the inverters.

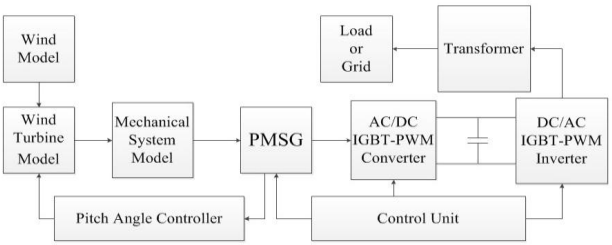

Fig. 1. Block diagram scheme of VSWT-PMSG

II. SYSTEM MODEL

A. Wind Turbine Model

Wind Turbines are the main element of a wind farm. They are used to transform wind energy into electrical energy. The wind turbine model for this paper has been taken from [3].

B. PMSG Model

The PMSG model available in the package software PSCAD/EMTDC is used [4] in this study. The power converter consists of a generator side AC/DC converter, a DC link capacitor and a grid side DC/AC inverter as depicted in Fig 1. The three phase sinusoidal signal is converted into d-q axis signal. In both the converter and inverter,. The carrier frequency is chosen 1000Hz which is a triangle signal used as carrier wave of Pulse Width Modulation (PWM) operation. The DC link capacitor value is 50,000 μF.

The grid side inverter controls the reactive power output to the grid in order to control the grid side voltage. In the control strategy, the d-axis of the reference frame is oriented along the grid side voltage. Therefore, active and reactive power can be expressed as [5]

$$P_{grid} = (V_{d\_grid}) * (I_{d\_grid}) \quad (1)$$

$$Q_{grid} = -(V_{d\_grid}) * (I_{q\_grid}) \quad (2)$$

In order to assure the active power exchange from PMSG to grid, the voltage of DC link capacitor, E_{dc}, is controlled by the d-axis current component, I_{dgrid}, of the grid. Again, the q-axis current component of the grid, I_{qgrid}, can control the reactive power, Q_{grid}, of the grid side inverter.

978-1-5090-5785-6/16/$31.00 ©2016 IEEE

III. Power Converters

Each power converter used in the three different model of simulation are consists of generator side AC/DC converter, DC-link capacitor and grid side DC/AC inverter. Each of rotor side converter has a standard 3-phase two-level unit, composed of six IGBTs and antiparallel diodes. On the other hand, the grid side DC/AC inverter used in this research are different for each of the simulations. A 2-level, 3-level and 5-level DC/AC inverter has been used respectively in three different simulations. The control arrangements are remained same, so that the behavior and comparison of the three different inverters connected in the wind application can be evaluated under the same condition of the control arrangement and system.

A. Two-Level inverter

3-phase 2-level inverters are simple in structure and commercially cheaper. But these inverters may contain high switching losses during operation. In this study, for the first simulation, a 3-phase 2 level voltage source inverter has been used, composed of 6 IGBTs. Fig 2 shows the circuit diagram topology that has been used in this research. With 2-level inverter topology inverters of 2.88 kV rms can be designed using commercially available devices which can be easily overcome with multilevel topologies.[6]

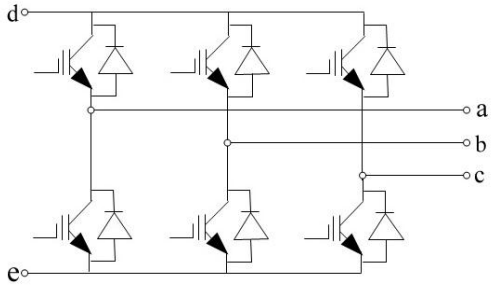

Fig. 2. Circuit diagram of 3-phase 2-level DC/AC inverter

B. Three-Level inverter

The multilevel inverters are power electronic circuits that can provide output voltage with three or more than three levels. The three-level inverter is the lowest level number multi-level inverter. Although the number of levels of output phase voltage of 3-level inverter is the same as that of line-to-line voltage of 2-level full bridge inverter, the line to line voltage of 3 level inverter consists of five voltage levels [6]. 3-phase 3-level inverter used in this research is composed of 12 IGBTS and a free-wheeling diode is used across the middle of the IGBTs. The circuit diagram is depicted in Fig 3.

C. Five-Level inverter

The five-level inverter topology is also a type of multilevel inverter. To obtain a quality output voltage or a current waveform with a minimum amount of ripple content, they require high-switching frequency along with various pulse-width modulation (PWM) strategies [7]. The 3-phase 5-level inverter used in this research is composed of 24 IGBTS. The circuit diagram is depicted in Fig 4.

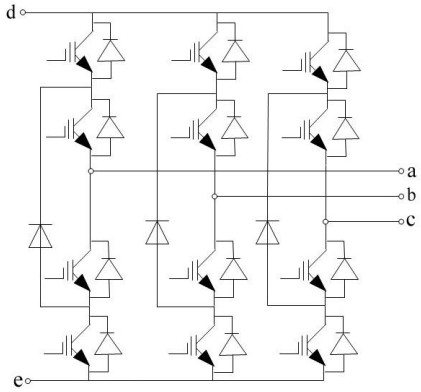

Fig. 3. Circuit diagram of 3-phase 3-level DC/AC inverter

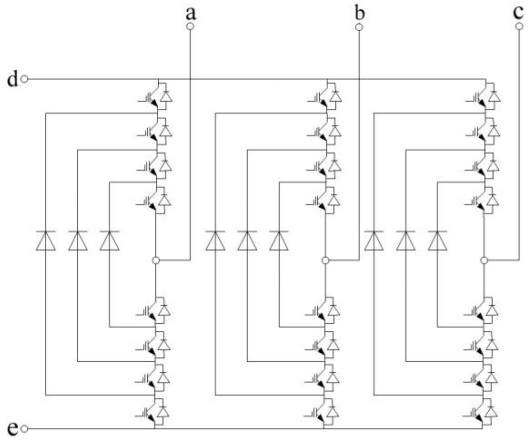

Fig. 4. Circuit diagram of 3-phase 5-level DC/AC inverter

The inverters used in this research are slightly different from NPC converter. In [6] it is said that, when the level of the FC converter increases a lot in number, these topologies are not suitable for wind turbine due to large number of capacitors. On the other hand NPC converter is not suitable for high voltage applications, where higher number of multi-levels is required [8]. Also multilevel converters have drawn tremendous interest in the power industry as they present a new set of feature that are well suited for use in reactive power compensation [7]. To reduce the number of capacitors and diodes in case of multilevel inverters the 5 level inverter has been used.

IV. Simulation Results

The simulation results are based on the dynamic behavior and transient behavior of the VSWT-PMSG. For analysis different types of real wind speed data which was obtained in Hokkaido Island of Japan has been used as shown in Fig. 5. From Fig 6-

13, the simulation results are shown. The simulation hasbeen done for 100 sec by using PSCAD/EMTDC [4].

TABLE I
SIMULATION CONDITION

Rated power of generator	3 MVA
Rated voltage of generator	0.69 kV
Frequency of generator	20 Hz
Grid side frequency	50 Hz
DC link capacitor	50000 uF
Fault time	235 sec
Fault duration	0.05 sec
PWM carrier frequency	1000 Hz (Triangular)

Table 1 shows the simulation parameters that has been used in this paper.

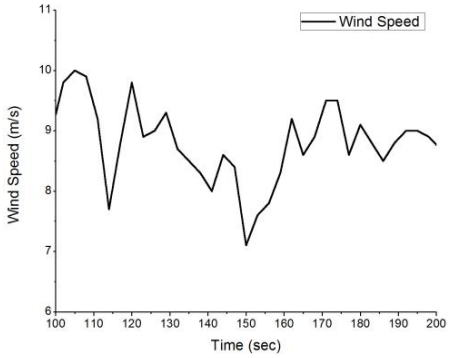

Fig. 5. Wind speed data

A. *Dynamic Stability Analysis*

For dynamic stability the simulation was carried out from 0 to 200 sec. The graphical data are shown in the Fig 6-9 for100 sec of the simulation.

Fig 6. shows the grid side voltage comparison of three DC/AC inverters. Fig 7 shows the frequency at dynamic stability analysis. Fig 8-9 are showing the performance difference for real power and reactive power, respectively.

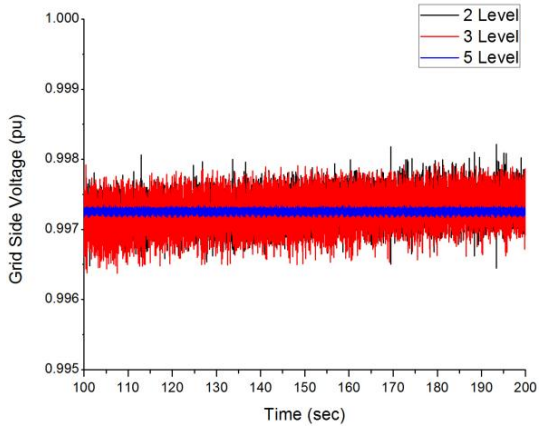

Fig. 6. Grid side voltage

From the graphical analysis stated, it can be easily evaluated that the five-level inverter is showing better performance for grid side voltage and frequency than the other two inverters. Also the real power and reactive power is much smoother for five-level inverter. But, the five-level inverter draws some reactive power, as the control system for all the inverters are remained same. Desired output can be obtained with the improved control system for the five-level inverter.

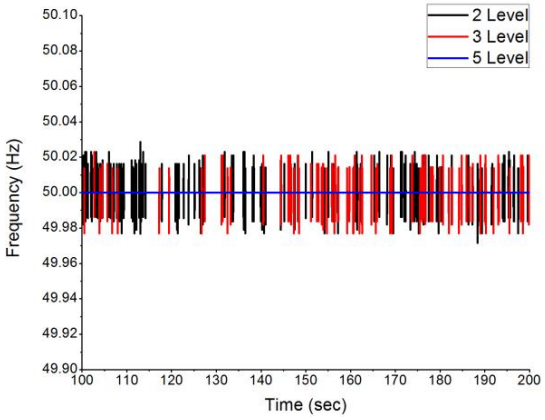

Fig. 7. Frequency

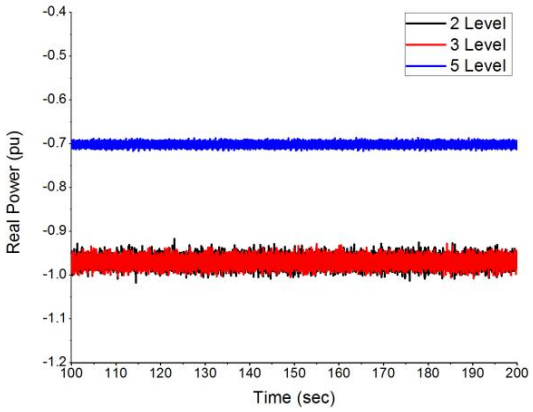

Fig. 8. Real power

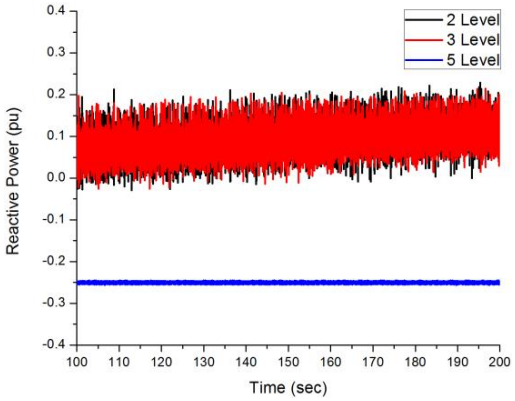

Fig. 9. Reactive power

B. *Transient Stability Analysis*

For determining transient stability, three line to ground fault (3LG) has been considered. Time to apply fault is 235 sec and the duration of fault is 0.5 sec. Figs. 10-13 shows the performance comparison of the three different inverters, when fault is occurred. In Fig 10 it can be seen that the grid side voltage during fault for 5-level inverter is much better than the other two inverters.

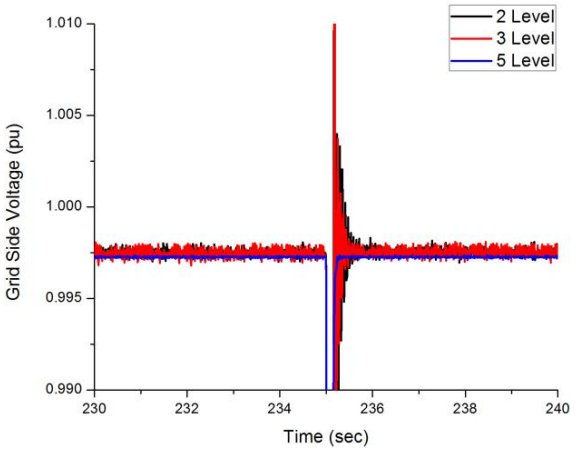

Fig. 10. Grid side voltage (during fault)

V. CONCLUSION

All the figures in this paper indicate the respective parameters for PMSG and simulated for the same wind speed. It is seen that the five-level inverter shows better performance than the two-level and three-level inverter for grid side voltage and frequency. As the evaluation of these three inverters are considered for the same control scheme, the five-level inverter draws some reactive power which can be eliminated by using improved control scheme. Overall it can be said that the five-level model has better capability of dynamic response with compared to two-level and three-level model. At the same time, the five-level inverter is more capable to responding to a fault and return back to the normal state within a short time.

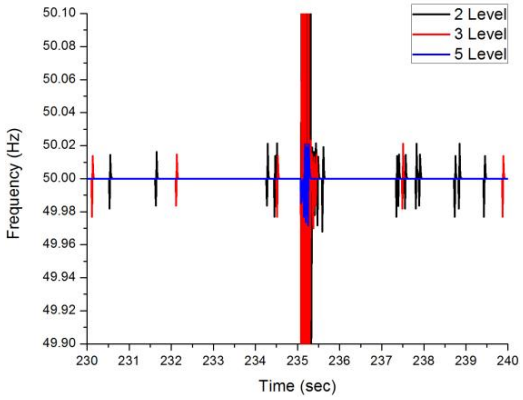

Fig. 11. Frequency (during fault)

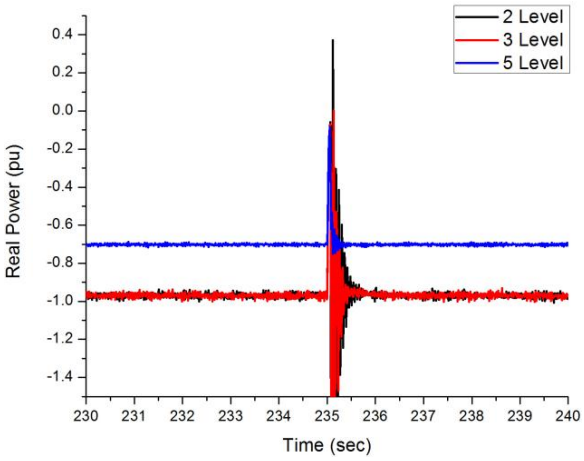

Fig. 12. Real power (during fault)

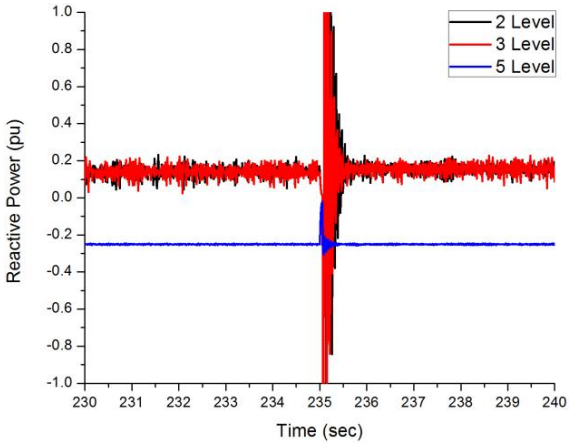

Fig. 13. Reactive power (during fault)

REFERENCES

[1] Sheikh MRI." *Stabilization of a Grid Connected Wind Farm by Using SMES*" a Ph.D thesis, Kitami Institute of technology, Japan. September 2010.

[2] Shafiul Hasan Rafi, M.R.I. Sheikh and Rusnot Ara Ferdous "*Modeling and Control Strategy for Variable Speed Wind Turbine Permanent agnet Synchronous Generator*" International Conference on Materials, Electronics & Information Engineering, ICMEIE-2015 05-06 June, 2015, Faculty of Engineering, University of Rajshahi, Bangladesh

[3] Z. Tasneem, M.R.I. Sheikh, A. N. Pinky "*Stability Augmentation of a Fixed Speed Wind Generator by Using VSWT-PMSG*", Journal of Technology Innovations in Renewable Energy, Vol3: pp.1-8

[4] "PSCAD/EMTDC Manual," Manitoba HVDC Research Center, 1994..

[5] Fernandes LM, Garcia CA, Jurado F. *Operating Capability as a PQ/PV node of a Direct-Drive Wind Turbine based on a permanent magnet synchronous generator.* Journal of Renewable Energy, Vol. 35, pp. 1308-1318, 2010

[6] Md. Rabiul Islam, Youguang Guo, Jianguo Zhu "*Power Converters for Medium Voltage Networks*"

[7] Muhammad H. Rashid "Power Electronics : Circuits, Devices and Applications"

[8] Md. Rabiul Islam, Youguang Guo, , Jianguo Zhu " Power Converters for Wind Turbines: Current and future development"

Design and Implementation of Amphibious Smart Rescue Robot

***Abstract*—Now-a-days robots make all tasks easier. Research is going on for developing robots for rescue and survey purposes. This paper presents a new type of rescue robot that can run on any rough surface including staircase. The robot also can float on the water and dive under the water. A new communication technology is used here which make it a unique rescue robot based on internet of things (IoT). So it can be easily controlled from anywhere at any time simply using computer or smartphone. Various sensors installed in this robot enable it to sense the environment. So, this amphibious robotic vehicle can be effectively used in rescue, survey at any hostile region and also in defense and research fields. Its flexible structure provide it to be modified and updated for expanding the fields of application.**

Keywords—robot, IoT, amphibious, servo motor

I. INTRODUCTION

Modern technologies are looking for providing a safer and more comfortable life for human beings. Scientists and researchers are working for this purpose. Robots are one of the best solutions and recently different types of robots are being used for using in different fields. Rescue robot has become one of the best fields of interest in robotics research sector. At present robots are being used for performing tasks in hazardous places. Some robots are designed for running on rough surface and climbing staircase [1], [2]. Some are constructed for watery regions [3]. Some robots are equipped with sensors and communication modules for surveying the remote areas [4]. But recent rescue and search operations require an assistant which can run on rough surfaces as well as can perform in watery regions especially during flood or cyclone. Remote controlling is also a fact for surveying far-off hostile and dangerous regions. Detection of environmental conditions of target regions is also a must for proper decision in rescue operation. These multidimensional requirements for effective rescue and survey operation have inspired to design and implement a smart rescue robot including all these key features. We hope this robot will meet the recent demands as well as facilitate the rescue operation. Thus the robot can play a role in our social sectors by improving social safety during disasters.

The robot uses internet to communicate with operator. For this purpose two smartphones are attached with the robot and the operator uses a laptop computer. Smartphones and computer are connected with internet. Command is transmitted from the operator's laptop and received by one smartphone of the robot. This command is further transmitted to the Arduino through Bluetooth communication. Similarly sensor readings are transmitted to the smartphone through Bluetooth and then through internet to the operator. Real time video is also transmitted from the other smartphone of the robot to the operator's laptop using Skype software. Thus this is a robot which is based on Internet of Things (IoT) [7]. In its mechanical structure there is an extension named front arm as in [1], [2], [5] which can rotate in both directions. This type of structure helps it to overcome obstacle and climb staircase. For underwater application all of its electrical and electronic components must be insulated to save them from water. We have implemented this by insulating each component to make them waterproof separately [3]. These are briefly described in the following sections. Its structural design and necessary components are explained in section II. Section III shows the principle of operation. In section IV implementation of its important features are shown. Then the future improvement are discussed in section V. Finally, Section VI concludes the paper.

Fig. 1. Robot climbing stairs.

II. SYSTEM DESIGN

The design and construction processes are discussed in this section. Here mechanical, electrical, electronic and communication apparatus are discussed in brief.

A. Mechanical structure

Main body of the robot is built using steel flat bar for increasing its strength. Mountings for all components are provided in its main structure. So all electrical and electronic components can easily be placed in their suitable positions. There are six wheels in total in this robot. These are constructed from Ebonite sheet using cutting tools and drill

978-1-5090-5785-6/16/$31.00 ©2016 IEEE

(a) (b)

Fig. 2. Wheel construction from Ebonite sheet (a) Single wheel (b) Complete wheel.

machine (Fig. 2). Every single ebonite wheel is placed one over another and joined them tightly using super glue to build a complete wheel of desired width with light weight. The back wheels are of medium size, the front wheels are of large size and the front arm wheels are of small size. The back wheels are connected with the servo motors. Front arm is connected with another servo motor through two gears having diameter ratio 5:1. Small gear is connected with the servo motor. Thus torque is increased by five times than that of servo motor. Wheels are connected with one another using four tank tracks in total. V-belts are used as tank tracks.

B. Electrical and electronic components

In this robot three servo motors (model no. MG995) and six dc motors of small size are used. These servo motors are 'Full Rotation Servo Motor' of rating 6 volts (dc). Six dc motors with six small propellers are used for underwater application. Two dc motors are used to drive the robot front, right, left or back at any speed. Other four dc motors are placed in four corners of the robot and used for balancing the robot in water. Controlling the speed of the motors we can easily and rapidly vary the position of the robot. The robot will float on water if these four motors are rotated clockwise at full speed. All these motors are controlled by Arduino Uno. Dc motors are connected with it via motor drivers. A Bluetooth module of model HC-05 is connected with Arduino to communicate with the smartphone. Temperature sensor, pressure sensor, humidity sensor, gas sensor are also connected with Arduino to sense the environment. Two rechargeable Lipo batteries are used here. One of them is used for driving motors and the other is for powering Arduino, Bluetooth module, motor drivers and the sensors. Two android smartphones are also attached with the robot; one placed at the front and the other inside the robot.

C. Waterproof design

All electrical and electronic components are waterproofed separately using polythene. There is an electronic circuit inside a servo motor. So to protect it from water the inner vacant space of servo is filled with Grease shown in Fig. 3(a). Grease is a semisolid lubricant which acts as a sealant to prevent ingress of water and incompressible materials. It also minimize friction losses. Then it is covered with polythene for extra protection. A steel rod is used to couple the servo shaft with the back wheel. Other components such as Arduino,

(a) (b)

Fig. 3. Waterproofing a servo motor (a) Filling the servo with Grease (b) Testing of servo in a jar filled with water.

Bluetooth module, motor driver, batteries are covered using polythene. In this case extra polythene is used one around another for enhancing protection. Two smartphones are covered separately using transparent polythene. Temperature and pressure sensors are waterproofed specially so that their connectivity with the environment is not hindered. Other sensors are entered in a waterproof box having a window which can be opened and closed (only during underwater operation) manually. All these separated enveloped components are connected together using flexible plastic pipes and electric wires are passed through these pipes. Six dc motors are uncovered as they can sustain under water with full efficiency.

III. WORKING PRINCIPLE

A. communication and control principle

For communication a web server is created. A HTML page is designed with necessary control keys and information boxes. Smartphone in the robot collects the commands from the server and sends them to Arduino via Bluetooth module using an android application. Again the smartphone sends sensor values to the server and these are displayed in the information boxes. These procedures are shown in Fig. 4.

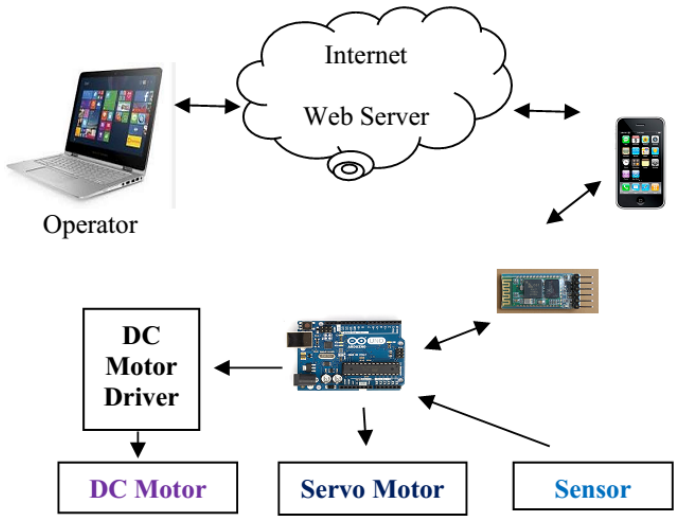

Fig. 4. Communication and control architecture.

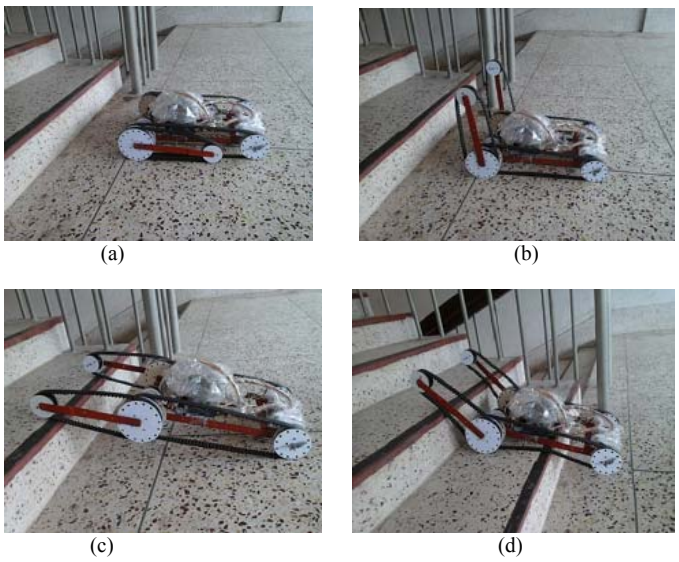

(a) (b) (c) (d)

Fig. 5. Basic steps for climbing stairs (a) Normal running stage (b) Prepare front arm to start climbing (c) Starts climbing and lifts its front side upward (d) Starts to climb the next stair.

B. Sensor functions

Temperature sensor (LM35) reads temperature in Degree Celsius, pressure sensor (MPXV5050DP) reads pressure in Pascal, humidity sensor (HSM-20G) sense humidity and converts it into voltage output for the ADC pin of Arduino. Gas sensor (MQ-9) sense Carbon Monoxide (CO), Methane and combustion gases. Arduino sends these readings to the operator to inform about the environment of hazardous area. The robot also uses GPS and Magnetic sensors of the smartphone for detecting location and direction.

C. Climbing method

For climbing stairs or overcoming obstacles the robot uses its front arm. Since high torque is produced in the front arm it can easily lift the front side of the robot upward. Then it climbs first stair and gets ready for climbing the second stair (Fig. 5). Similarly it climbs all the stairs and reaches its destination. Here necessary friction for climbing upward is provided by V-belt.

D. Underwater operation

The robot can be easily controlled when floating on water. But under the water surface communication is terminated. It then runs under water autonomously as the prescribed command. It utilizes Compass reading of the smartphone for proper direction and pressure sensor reading for calculating distance (h) between the water surface and the robot under water using the equation:

$$P = h\rho g \tag{1}$$

$$h = P / \rho g \tag{2}$$

Where P is the pressure sensor reading in Pascal, g is acceleration due to gravity having value 9.81 meter per square second and ρ is the density in kilogram per cubic meter (kg/m^3) having value 1000 kg/m^3 for water. Solving equation (2) the distance in meter is found.

IV. Experimental Test

The robot has been driven on smooth floor as a first experiment as shown in Fig. 6(a). Its movement has been successfully controlled via internet. Video transmission has also been implemented using Skype with reasonable resolution although it varies with network speed. Fig. 6(b) shows the screenshot of Laptop screen showing HTML page containing control keys and video streaming. The information boxes of the HTML page shows the environmental conditions of the surroundings. Its climbing operation has also been implemented successfully which are shown if Fig. 1, and

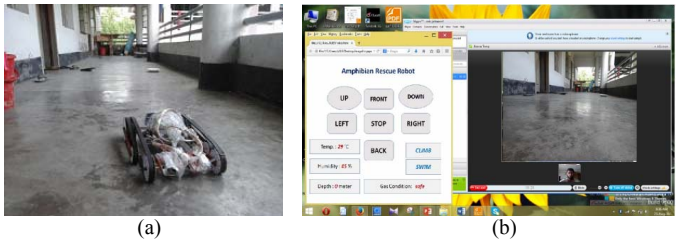

(a) (b)

Fig. 6. Implementation of smart control system and video transmission (a) Robot running on smooth floor (b) Screenshot showing video transmission using Skype video call (right) and HTML page for robot control (left).

Fig. 7. Robot overcoming obstacles.

(a) (b)

Fig. 8. Implementation of amphibious feature (a) Robot starts to swim (b) Swimming on the water.

Fig. 5. The robot was driven on a rough surface as shown in Fig. 7 and its performance was found satisfactory. These experimental results has proven its capability to search and rescue in earthquake affected areas. The robot was taken to our varsity pond to observe its amphibious feature. At first it has climbed down the stairs of the pond and then started to swim with sufficient speed and stability (Fig. 8). It was also driven under water for a short time. During the period the robot is automatically controlled. It then only records video and other information and stores them in mobile memory. After underwater surveying it floats on water and connects with the operator again. Now the robot is ready to receive command and transmit the recorded data to the operator. All these experimental results has proven that this robot is perfect for searching and rescuing in any type of hazardous regions affected by either earthquake, cyclone, flood or any other disasters.

V. Future Research

The robot may open a new window of research in robotics field. This robot is now manually controlled. But automatic control algorithm can be developed using artificial intelligence technology. Installation of image processing system may help the robot to identify situation and take action automatically at any situation. Underwater research and rescue can be enhanced using modern underwater communication technologies. Since this is an IoT robot, it may be easily synchronized with any other devices for improved search and survey operation. This type of robot can also be utilized effectively in civil defense sectors.

VI. Conclusion

In this paper, an amphibious rescue robot has been designed and implemented which has combined latest electrical, mechanical and communication technologies. Its mechanical structure, electrical and electronic apparatus for proper functioning and a new waterproof design technology were described here. The robot has used smart technologies for communication via internet. Experimental results have showed its capability to climb stair case, run on rough surface and move on and under water. Remote controlling and video streaming as well as data transmission were also examined.

References

[1] Anastasios I. Mourikis, Nikolas Trawny, Stergios I. Roumeliotis, Daniel M. Helmick, and Larry Matthies, "Autonomous Stair Climbing for Tracked Vehicles," *The International Journal of Robotics Research,* vol. 26, no. 7, pp. 737-758, July 2007.

[2] Masatoshi Hatano and Yuki Kitahara, "Research on rescue robots climbing up stairs based on the estimation of slope angles with LRF," in *Proceedings of 14th IEEE International Workshop on Advanced Motion Control (AMC)*, Apr. 2016, pp. 109 – 114.

[3] Yi Sun, Siyu Huang, Shugen Ma, and Qiquan Quan, "Development of a Waterproof Servo Unit for Amphibious Robots," in *Proceedings of IEEE International Conference on Cyber Technology in Automation, Control, and Intelligent Systems (CYBER),*June 2015, pp. 923 – 928.

[4] Hasan U. Zaman, Md. Shahriar Hossain, Mohammad Wahiduzzaman, and Shahariar Asif, "A Novel Design of a Robotic Vehicle for Rescue Operation," in *Proceedings of 18th International Conference on Computer and Information Technology (ICCIT)*, Dec. 2015, pp. 507 – 510.

[5] Mitsuhiro Kamezaki, Hiroyuki Ishii, Tatsuzo Ishida, Masatoshi Seki, Ken Ichiryu, Yo Kobayashi, Kenji Hashimoto, Shigeki Sugano, Atsuo Takanishi, Masakatsu G. Fujie, Shuji Hashimoto, Hiroshi Yamakawa, "Design of four-arm four-crawler disaster response robot OCTOPUS," in *Proceedings of IEEE International Conference on Robotics and Automation (ICRA),*May 2016, pp. 2840 – 2845.

[6] Shunzhou Wang, Huailin Zhao, and Xuyao Hao, "Design of an intelligent housekeeping robot based on IoT," in *Proceedings of International Conference on Intelligent Informatics and Biomedical Sciences (ICIIBMS)*, Nov. 2015, pp. 197 – 200.

[7] Lorin D. Dole, David M. Sirkin, Robin R. Murphy, and Clifford I. Nass, "Robots Need Humans in the Loop to Improve the Hopefulness of Disaster Survivors," in *Proceedings of 24th IEEE International Symposium on Robot and Human Interactive Communication (RO-MAN)*, Sept. 2015, pp. 707-714.

International Conference on Electrical, Computer & Telecommunication Engineering (ICECTE)
8-10 December 2016, Rajshahi-6204, Bangladesh

Low Effective Material Loss Microstructure Fiber for THz wave Guidance

Md. Ahasan Habib
Department of Electrical and Electronic Engineering
Rajshahi university of Engineering & Technology
Rajshahi-6204, Bangladesh
Email: habib.eee.116.ah@gmail.com

Md. Shamim Anower
Department of Electrical and Electronic Engineering
Rajshahi university of Engineering & Technology
Rajshahi-6204, Bangladesh
Email: md.shamimanower@yahoo.com

***Abstract*— In this paper we report a porous-core photonic crystal fiber having low material loss and nearly zero dispersion which is suitable for THz wave transmission. This proposed design exhibits a low effective material loss which is approximately 0.225 dB/cm at an operating frequency 1.0 THz and nearly zero flattened dispersion of ± 0.05 ps/THz/cm at frequency range of 0.9–1.2 THz. Moreover, other important guiding characteristics including confinement loss and power fraction of the proposed fiber is discussed. The proposed microstructure fiber has potential applications for efficient transmission of THz radiation band.**

Keywords*— *Terahertz guidance, effective material loss, confinement loss, flattened dispersion

I. INTRODUCTION

The electromagnetic waves which cover frequency ranging from 0.1 to 10 THz is defined as Terahertz (THz) radiation band. This particular frequency band has become popular to the scientists in modern age because this radiation band has potential applications in many fields such as biological imaging, spectroscopy, environmental monitoring and military security [1], [2]. This THz frequency wave can be used for also non-invasive early diagnosis of skin cancer including the basal cell carcinoma [3], dysplastic skin nevi and melanomas [4] of hardly-accessible skin areas, minimally-invasive diagnosis of colon tissue cancers [5].

In recent past, free space (unguided medium) was used for convenient guidance of THz waves. But due to some unavoidable problems such as high absorption of water vapor in the atmosphere, transmitter-receiver alignment problem *etc.* guided medium are proposed by the researchers. But the main obstacle for designing THz waveguides is the high absorption loss of the background material. To solve this problem, air holes are introduced in the background material. We know that dry air is the most transparent medium for THz wave propagation. If maximum fraction of power propagates through the air region of the waveguide core then it is possible to reduce the propagation loss of the THz waveguide. By using this concept various forms of waveguide structures have been proposed by the researchers such as metallic wires [6] and dielectric metal-coated tubes [7]. But these waveguides exhibit high bending loss as well as low coupling efficiency. So that substantial attraction is given in polymer fibers such as plastic fibers [8], Bragg fibers [9] and sub-wavelength porous fibers [10] because of their excellent THz wave propagation characteristics and design flexibility. But the material loss is high for these fibers. Then Photonic crystal fiber (PCF) became the focal point in THz regime due to the lower absorption loss [11]. But the effective material loss (EML) is not too low to transmit at a long distance of a weak signal. Then the porous core PCF came into light due to less absorption loss property than conventional PCF [12]. Another basic difference between the conventional PCF and porous core PCF is the guiding mechanism of light wave. The guiding mechanism of conventional PCF is total internal reflection (TIR) and photonic band gap (PBG) is the guiding mechanism of porous core PCF. A lot of porous core PCF (PC-PCF) with low material loss has been proposed. R. Islam and S. Rana proposed a fiber [13] having EML of 0.053 cm^{-1} and dispersion of ± 0.09 ps/ THz/ cm within 0.9 to 1.3 THz. Hasan *et al* [14] proposed a porous core PCF showing EML of 0.06 cm^{-1} and a dispersion of ± 0.18 ps/ THz/ cm within 1 to 1.8 THz. R. Islam *et al* [15] proposed a porous core PCF showing EML of 0.07 cm^{-1} and a dispersion of ± 0.55 ps/THz/cm.

In this paper, we analyze a porous core PCF which show an EML of 0.225 dB/ cm and nearly zero flattened dispersion of ± 0.05 ps/ THz/ cm. Again the design consists of only circular air holes so no problem will arise at the time of fabrication.

II. DESIGN OF PC-PCF

The cross-sectional view of the proposed microstructure fiber is shown in Fig. 1. The circular air holes in the cladding region are arranged vertically. The distance between two adjacent air-holes of the same column is denoted by pitch (Λ). The distance between two adjacent vertical axes is denoted by Λ_{cl}. The relation between the two following parameter is

978-1-5090-5785-6/16/$31.00 ©2016 IEEE

$\mathbf{\Lambda_{cl}}$ =0.87 × **Λ**. In the center column two circular air holes are used instead of single air hole whose radius is denoted by **dl**.

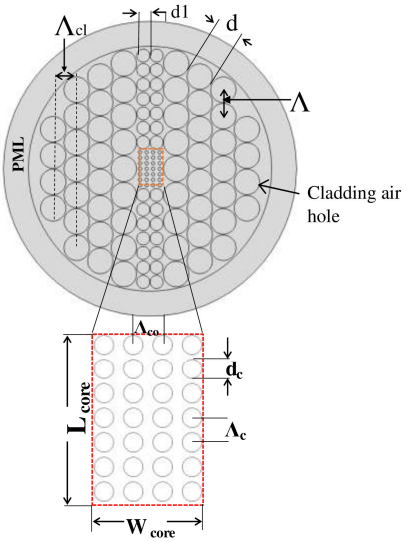

Fig. 1: Cross-sectional view of proposed microstructure fiber.

This type of structure is selected because it shows excellent modal confinement properties. In cladding region the air filling fraction (AFF) is (**d** / **Λ**) and it was kept fixed at 0.97 throughout the analysis as high AFF assures better confinement as well as reduced EML. Where **d** is the diameter of the cladding air hole. If we give close look to the structure of the proposed fiber then we can see that no air holes overlapped with each other. So this high value of AFF will not create any complexity at the time of fabrication. In this proposed design rectangular type core is used because this design permits more air holes than other structure of same area. In core region total 28 circular air holes are arranged in 4 columns and each column contains 7 air holes. The distance between two adjacent air holes of same column is $\mathbf{\Lambda_c}$ and the distance between two adjacent column is $\mathbf{\Lambda_{co}}$= 0.25× **Λ**. The core width $\mathbf{W_{core}}$ is equal to **Λ** and core length $\mathbf{L_{core}}$ is 1.5 times of **Λ**. TOPAS is used as the background material of the proposed fiber because the refractive index of TOPAS is 1.5258 which remains constant over 0.1 –2 THz frequency range [18]. Moreover, it shows low loss and low dispersion at THz bands [18].

III. Result and Discussion

The simulations are performed using commercially available Finite element method based COMSOL *V4.2* software. In this simulation software finite difference time domain (FDTD) method is used to solve the equations of finite elements. A circular perfectly matched layer (PML) is used outside the fiber which is 9% of the total radius of the fiber. The PML is used for this simulation because this layer indicates no reflection of light wave from this layer after incident of light onto it. So no interaction occurs between the source signal and reflected signal. Complete mesh consists of 36,494 elements, number of vertex elements 456, number of boundary elements 4097, number of elements 36494, minimum element quality 0.8698 which indicates that the error is very low. The mode field profile of the proposed PCF for different core porosities is shown in Fig. 2 which shows that mode fields are tightly bounded in the core region.

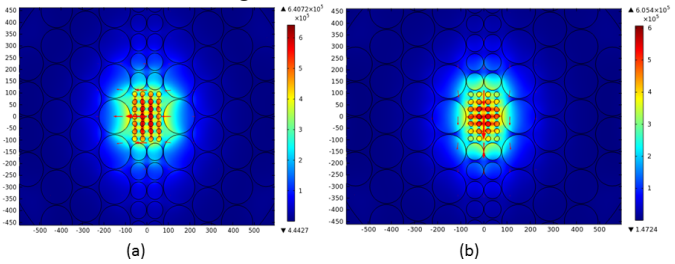

Fig. 2: Mode field distribution of the proposed fiber for (a) x-polarization and (b) y- polarization

The major challenge of designing THz waveguides is the material absorption loss which is calculated by the following theory expression [16]

$$\alpha_{eff} = \frac{\left(\varepsilon_0 / \mu_0\right)^{1/2} \int_{A_{mat}} n\,\alpha_{mat} |\mathrm{E}|^2 \, d\mathrm{A}}{2 \int_{All} S_z \, d\mathrm{A}} \quad \textbf{(1)}$$

where ε_0 and μ_0 are the permittivity and permeability of the vacuum, n is the refractive index of the material used, E is the modal electric field, α_{mat} is the bulk material absorption loss and S_z is the z-component of the Poynting vector. The numerical simulations of effective absorption loss as a function of core length for different core porosities are presented in Fig. 3, where it is observed that effective absorption loss decreases with the increase of core porosity for both polarization modes and x-polarization shows lower absorption loss compared to y-polarization. This is due to the

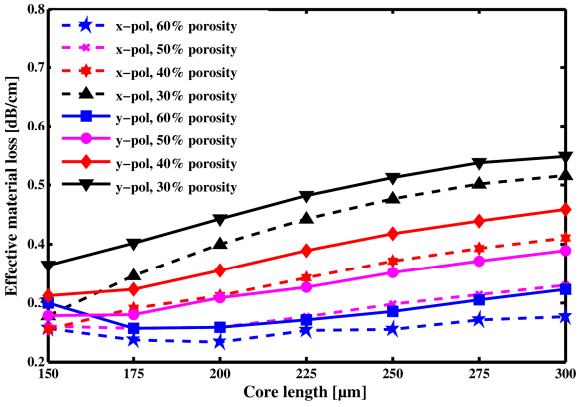

Fig. 3: EML of the proposed PCF as a function of different core porosities.

transmission of majority field through air medium instead of material for x-polarization mode. The EML of both polarization increases with the increase of core length because the effective material in core increases in both x and y direction with the increase of core length. The lowest EML is 0.225dB/cm or 0.052 cm^{-1} which is better than previously reported work in [13-15]. From fig. 3 we can see that the

effective material loss is lowest at 50% and 60% of core porosities at core length 200 µm. So the further calculations are performed only for above parameters of the proposed fiber. EML as a function of frequency for different core porosities are shown in Fig. 4.

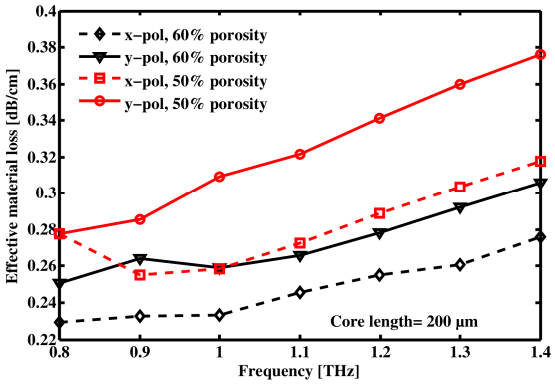

Fig. 4: EML as a function of frequency for different core porosities.

As the core is not equal in length and width so some birefringence characteristics is shown by the proposed fiber. The birefringence is calculated by using the formula [17]

$$B = |n_x - n_y| \quad (2)$$

Where B stands for birefringence, n_x and n_y indicates x and y polarization modes of the effective refractive index respectively. The birefringence characteristic is shown in fig. 5. From the fig. 5 we can see that the birefringence is maximum 0.015 at 1.4 THz which is better than reported in [15].

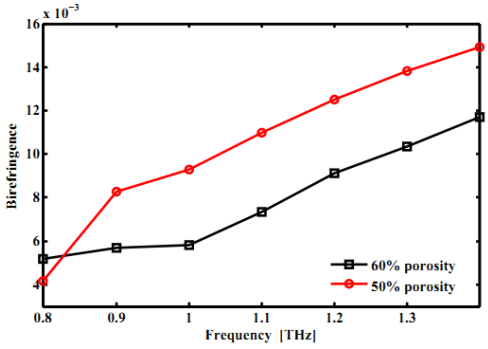

Fig. 5: Birefringence as a function of frequency at core length=200µm.

Confinement loss is an important properties at the time of practical implementation of the fiber. Confinement loss occurs due to the finite extent of the periodic cladding. This type of loss is unavoidable. The confinement loss of the mode field can be obtained by using the following equation given in [15]

$$\alpha_{CL} = 8.686 \times \frac{2\pi f}{c} \mathrm{Im}(n_{eff}) \text{ dB/ m} \quad (3)$$

Where f is the frequency of the guiding light, c is the speed of light in vacuum and $\mathrm{Im}(n_{eff})$ is the imaginary part of the effective index of the guided mode. The confinement loss of the proposed fiber is shown in fig. 6. From the fig. 6 we can see that the loss decreases with the increase of operating frequency. It is because more power passes through the air holes of the core region at higher frequency. The confinement loss of the proposed fiber is also comparable with the previous reported work in [13-15].

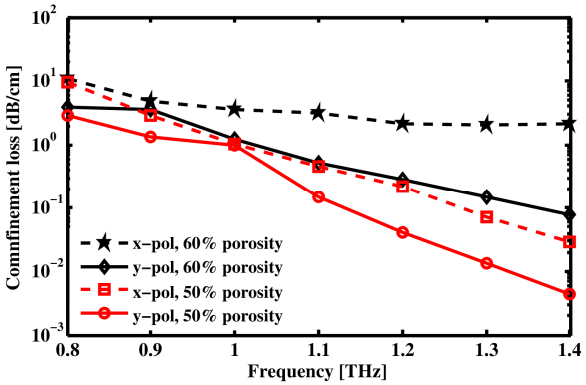

Fig. 6: Confinement loss as a function of frequency at L_{core}=200 µm

Another important property named fraction of mode power that represents the power flow distribution of different regions can be estimated by the following equation [16]

$$\eta = \frac{\int_X S_Z dA}{\int_{All} S_Z dA} \quad (4)$$

where η represents the mode power fraction and X represents the area covered by the core air holes. Fig. 7 shows the power fraction of air holes in the core region as a function of frequency. From fig. 7 we can see that the power through the core air hole increases with the increase of frequency. The power fraction is not reported in [15]. The power fraction of the proposed fiber is comparable with the previous work [13], [14].

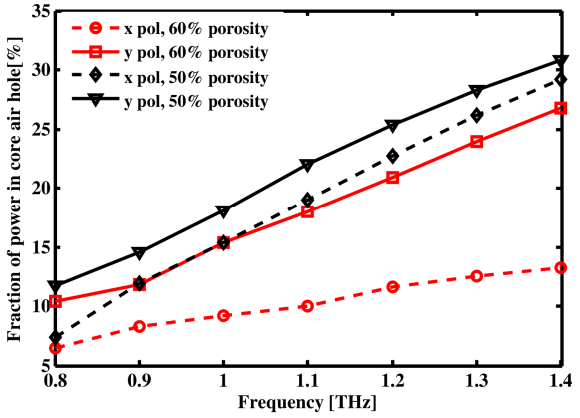

Fig. 7: Fraction of power in the core air holes as a function of frequency at L_{core}=200 µm

Now we discuss the dispersion characteristics of the proposed microstructure fiber. Due to the constant refractive index the material dispersion of TOPAS is ignored. So only the

waveguide dispersion is calculated using dispersion parameter [15]

$$\beta_2 = \frac{1}{c}\left(2\frac{dn}{d\omega} + \omega\frac{d^2n}{d\omega^2}\right) \quad (5)$$

where $\omega=2\pi f$ and c is the velocity of light in vacuum which is 3×10^8 ms^{-1}. The dispersion characteristic of the proposed microstructure fiber is shown in fig. 8. We can see that for the y polarization mode of both 50% and 60% porosity the dispersion is almost zero. For 60% porosity the dispersion is 1.06 ± 0.06 ps/ THz/ cm and for 50% porosity the dispersion is only 0.75 ± 0.05 ps/THz/cm. The dispersion is lower than the previous reported work in [13-15].

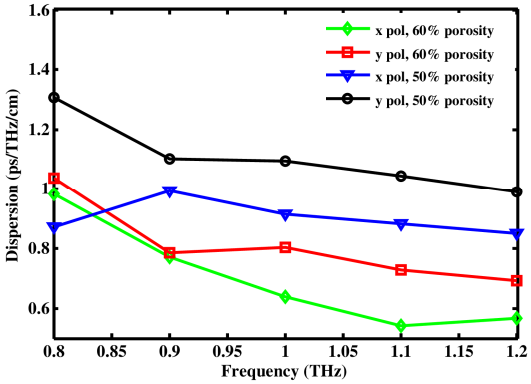

Fig. 8: Dispersion of the proposed PCF as a function of frequency for different core porosity at L_{core}= 200 µm.

Finally we want to explore the possibility for the fabrication of the proposed THz fiber. By using the edge-defined film-fed growth (EFG) technology [19], [20] the proposed structure can be manufactured. With the high velocity of growth, the EFG or Stepanov technique provides the minimal characteristic size of elements in the crystal cross section of about 0.1 mm. Besides, it allows keeping high quality of cross section. It seems that it would be very appropriate technology for practical realization of the proposed PCFs.

IV. Conclusion

In this paper a rectangular shaped porous-core microstructure fiber is proposed for the guidance of THz waves. The simulation results indicate that with optimal design parameters the proposed structure exhibits very low effective material loss of 0.225 dB/cm at 1 THz. Again nearly zero flattened dispersion of ± 0.05 ps/ THz/ cm has achieved in the frequency ranging between 0.9–1.2 THz. This structure is easy manufacturable because of its simple design and the proposed structure consists of only circular air holes. This microstructure fiber can be considered as an effective waveguide for THz wave propagation due to the excellent guiding properties.

References

[1] M. Tonouchi, “Cutting-edge terahertz technology,” Nature Photon.,vol. 1, no. 2, pp. 97–105, 2007

[2] N. F. Ren et al, “Design of subwavelengthoptical fibre for low-loss terahertz transmission,” J. Eur. Opt. Soc.-Rapid Publications, vol. 8, pp. 13068-1–13068-4, Oct. 2013.

[3] Wallace VP et al., "Terahertz pulsed imaging of basal cell carcinoma ex vivo and in vivo." Br J Dermatol. 2004 Aug; 151(2):424-32.

[4] Kirill I. Zaytsev et al., "In vivo terahertz spectroscopy of pigmentary skin nevi: Pilot study of non-invasive early diagnosis of dysplasia." Applied Physics Letters 106(5), 053702 (2015).

[5] Reid CB et al., "Terahertz pulsed imaging of freshly excised human colonic tissues." Physics in Medicine and Biology, 2011 Jul 21; 56(14):4333-53.

[6] K. Wang, and D. M. Mittleman,“Metal wires for terahertz wave guiding,” Nature, vol. 432, no. 7015, pp. 376–379, 2004.

[7] J. Harrington, R. George, P. Pedersen, and E. Mueller, “Hollow polycarbonate waveguides with inner Cu coatings for delivery of terahertz radiation,” Opt. Express, vol. 12, no. 21, pp. 5263–5268, 2004.

[8] H. Han, H. Park, M. Cho, and J. Kim, “Terahertz pulse propagation in a plastic photonic crystal fiber,” Appl. Phys. Lett., vol. 80, no. 15, pp. 2634–2636, 2002.

[9] A. Dupuis, K. Stoeffler, B. Ung, C. Dubois, and M. Skorobogatiy, “Transmission measurements of hollow-core THz Bragg fibers,” J. Opt. Soc. Amer. B, vol. 28, no. 4, pp. 896–907, 2011.

[10] L.-J. Chen et al., “Lowloss subwavelength plastic fiber for terahertz waveguiding,” Opt. Lett., vol. 31, no. 3, pp. 308–310, 2006.

[11] H. Han, H. Park, M. Cho and J. Kim, “Terahertz pulse propagation in a plastic photonic crystal fiber.” Appl. Phys. Lett., vol. 80, no. 15, pp. 2634–2636, 2002.

[12] M. Uthman et al., “Design and characterization of low-loss porous core photonic crystal fiber.” IEEE Photon. J., vol. 4, no. 6, pp. 2315–2325, Dec. 2012.

[13] R. Islam and S. Rana, “Dispersion flattened, low-loss porous fiber for single-mode terahertz wave guidance”., Optical Engineering 54(5), 055102 (May 2015).

[14] M. I. Hasan et al, “Ultra-Low Material Loss and Dispersion Flattened Fiber for THz Transmission”, IEEE Photon. Techn. Lett, vol.26, no. 23, Dec 1, 2014

[15] R. Islam et al, “A Novel Low Loss Diamond-Core Porous Fiber for Polarization Maintaining Terahertz Transmission”, DOI 10.1109/ LPT. 2016. 2550205, IEEE Photon. Techn. Lett.

[16] M. R. Hasan, M. S. Anower, M. A. Islam, and S. M. A. Razzak, “Polarization-maintaining low-loss porous-core spiral photonic crystal fiber for terahertz wave guidance”, Appl. Opt., vol. 55, no. 15, May 20, 2016.

[17] M. R. Hasan, M. S. Anower, M. I. Hasan, and S. M. A. Razzak, “Polarization Maintaining Low-Loss Slotted Core Kagome THz Fiber”, IEEE Photon. Techn. Lett, DOI 10.1109/LPT.2016.2569565.

[18] K. Nielsen et al., “Bendable, low-loss topas fibers for the terahertz frequency range,” Opt. Exp., vol. 17, no. 10, pp. 8592–8601, May 2009.

[19] K. I. Zaytsev et al., "Terahertz Photonic Crystal Waveguides Based on Sapphire Shaped Crystals," IEEE Transactions on Terahertz Science and Technology 6(4), 1-7 (2016, early access paper).

[20] P. I. Antonov, V. N. Kurlov., "New advances and developments in the Stepanov method for the growth of shaped crystals," Crystallography Reports 47(1), S43 (2002).

Linear Precoding Techniques in Enhancing Security of Cognitive Radio Networks

R. Sultana, M. Z. I. Sarkar and M. S. Hossain
Department of Electrical and Electronic Engineering
Rajshahi University of Engineering and Technology
Rajshahi-6204, Bangladesh.
Email: dola.ruet@gmail.com

***Abstract*—In this paper, the problem of security in multiple input multiple output (MIMO) system has been analysed in the presence of an eavesdropper in cognitive radio networks. Multiple primary and secondary users communicate with the primary and secondary receiver, respectively. The secrecy capacity at primary receiver (PR) and secondary receiver (SR) have been calculated. At first, we use zero-forcing (ZF) precoding at the relay which enhances the secrecy capacity of PR and SR by nullifying the impact of interference. Secondly, we use a scheme to improve the secrecy capacity of the PR and SR using the existing interference energy of the communication medium employing selective precoding (SP) at the relay. Finally, we employ phase alignment precoding (PAP) for further increase in the secrecy capacity for PR and SR by using the destructive part of interference. Our analysis shows that among the three precoding techniques, the best performance is achieved by using the PAP at the relay in terms of secrecy capacity, complementary cumulative distribution function (CCDF) and outage probability analysis.**

***Index Terms*—Primary users, secondary users, primary receiver, secondary receiver, selective precoding, zero-forcing precoding and phase alignment precoding.**

I. Introduction

In wireless communication system, the use of precoding techniques plays an important role in interference cancelation. Christos et al in [1] used ZF precoding, SP and PAP for analysing the performance of cognitive relay assisted MIMO downlink channels. In [2], relay selection has been studied for secured transmission with the presence of eavesdropper in cognitive radio network. In [3] authors design cheat proof for cooperative relay in cognitive radio network. In [4] an achievable secrecy rate of communication for PUs as well as SUs has been characterized. For detecting PU emulation, based on action recognition techniques in the frequency domain has been studied in [5]. In [6] authors maximize the secrecy throughput of the PU by designing and optimizing the beamforming, rate parameters of the wiretap code. In [7] authors propose a user scheduling scheme to achieve multiuser diversity for improving security.

In this paper, the secrecy capacity of multiple access network for compensating the interferences using ZF precoding at the relay has been characterized. Then, in order to improve the secrecy capacity, we employ SP at the relay. Finally, the PAP technique is used to enhance the secrecy capacity by accommodating the destructive part of interference.

The rest of the paper is organized as follows. The system model and the formulation of problem are discussed in Section II. In Section III, we describe the effect of interferences on the secrecy capacity without relay. In Section IV, we show, how the enhancement of secrecy capacity can be achieved using ZF, SP and PAP at the relay. Numerical results are analyzed in Section V. Finally, Section VI describes the concluding remarks of this work.

II. System Model

We consider a MIMO multiple access cognitive radio network in which M PUs are communicating with a PR and K SUs are communicating with a SR in the presence of an eavesdropper. Each PU and SU are equipped with n_{T_1} and n_{T_2} antennas, respectively while eavesdropper is equipped with n_E antennas. PR and SR are equipped with n_{R_1} and n_{R_2} antennas, respectively. PR and SR receive a scaling factor determined by the relay to limit the joint average transmit power of the system. The relay receives the information about all the channel matrices and instantaneous data symbols [8] by a high speed connection between the receivers and the relay via a backhaul network as discussed in [9]. The relay involves $n_{T_1} + n_{T_2}$ receive antennas and n_R transmit antennas.

The direct channel coefficients between PUs and PR are $\mathbf{H} \in \mathbb{C}^{n_{R_1} \times M n_{T_1}}$ and that between SUs and SR are $\mathbf{G} \in \mathbb{C}^{n_{R_2} \times K n_{T_2}}$. The cross-over channel coefficients between PUs and SR are $\mathbf{H}_P \in \mathbb{C}^{n_{R_2} \times M n_{T_1}}$ and that between SUs and PR

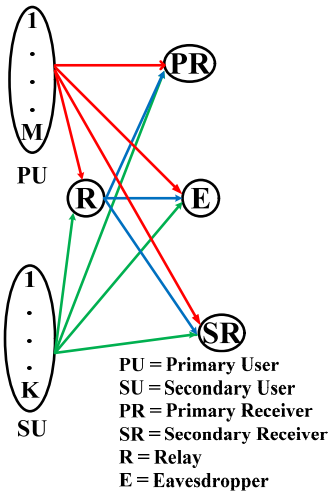

Fig. 1. System model.

978-1-5090-5785-6/16/$31.00 ©2016 IEEE

are $\mathbf{G}_M \in \mathbb{C}^{n_{R_1} \times K n_{T_2}}$. The channel coefficients between PUs and eavesdropper are $\mathbf{H}_E \in \mathbb{C}^{n_E \times M n_{T_1}}$, and that between SUs and eavesdropper is $\mathbf{G}_E \in \mathbb{C}^{n_E \times K n_{T_2}}$. The channel coefficient between relay and PR is $\mathbf{U}_M \in \mathbb{C}^{n_{R_1} \times n_r}$ and that between relay and SR is $\mathbf{U}_p \in \mathbb{C}^{n_{R_2} \times n_r}$. The channel coefficient between relay and eavesdropper is $\mathbf{U}_E \in \mathbb{C}^{n_E \times n_r}$. All the channels are assumed to be Rayleigh fading and the powers assigned to the PUs, SUs and the relay are denoted by P_1, P_2 and P_R, respectively.

In the following sections, at first, direct transmission scheme has been described to analyse the impact of interference on the secrecy capacity at PR and SR. Then, we employ ZF Precoding at the relay to nullify the effect of interferences. After that, SP at the relay has been used to enhance the secrecy capacity by using the existing constructive part of interference as an additional source of energy. Finally, we enhance the secrecy capacity employing PAP which converts the destructive part of interference into constructive one rotating the angle of correlation.

III. Direct Transmission

The SR and eavesdropper experience interferences due to the transmitted signals of PUs in the absence of the relay. Similarly, the PR and eavesdropper experience interferences due to the transmitted signals of SUs. Hence, the received signals at the receivers of PR, SR and eavesdropper are respectively given by

$$\mathbf{y}_p = \mathbf{H}\mathbf{x} + \underbrace{\mathbf{G}_M\mathbf{s} + \mathbf{z}_p}_{\mathbf{w}_p}, \tag{1}$$

$$\mathbf{y}_s = \mathbf{G}\mathbf{s} + \underbrace{\mathbf{H}_P\mathbf{x} + \mathbf{z}_s}_{\mathbf{w}_s}, \tag{2}$$

$$\mathbf{y}_e = \mathbf{H}_E\mathbf{x} + \underbrace{\mathbf{G}_E\mathbf{s} + \mathbf{z}_e}_{\mathbf{w}_e}, \tag{3}$$

where $\mathbf{x} \in \mathbb{C}^{M n_{T_1} \times 1}$ and $\mathbf{s} \in \mathbb{C}^{K n_{T_2} \times 1}$ denote the transmitted signal of PUs and SUs, respectively. $\mathbf{z}_p \sim \mathcal{CN}\left(0, N_1\mathbf{I}_{n_{R_1}}\right)$, $\mathbf{z}_s \sim \mathcal{CN}\left(0, N_2\mathbf{I}_{n_{R_2}}\right)$ and $\mathbf{z}_e \sim \mathcal{CN}\left(0, N_E\mathbf{I}_{n_{R_E}}\right)$ denote the Gaussian noises imposed on the PR, SR and eavesdropper, respectively. $\mathbf{w}_p$, $\mathbf{w}_s$ and $\mathbf{w}_e$ denote interference plus noise vectors at the PR, SR and eavesdropper, respectively. Let $\mathbf{D} = [\mathbf{H} \quad \mathbf{G}_M]$. Then, the mutual information at the PR is given by

$$I\left(\mathbf{x}; \mathbf{y}_p|\mathbf{D}\right) = h\left(\mathbf{y}_p|\mathbf{D}\right) - h\left(\mathbf{w}_p|\mathbf{G}_M\right), \tag{4}$$

where $h(\cdot)$ denotes entropy. Let the covariances of $\mathbf{x}$ and $\mathbf{s}$ are given by $\mathbf{Q}_x = \mathbb{E}\left\{\mathbf{x}\mathbf{x}^\dagger\right\} = \frac{P_1}{n_{T_1}}\mathbf{I}_{n_{T1}}$ and $\mathbf{Q}_s = \mathbb{E}\left\{\mathbf{s}\mathbf{s}^\dagger\right\} = \frac{P_2}{n_{T2}}\mathbf{I}_{n_{T2}}$, where $\mathbb{E}\{\cdot\}$ and $(\cdot)^\dagger$ denote the expectation and conjugate transpose operations, respectively. Then, the covariance of received signal $\mathbf{y}_p$ is given by

$$\mathbf{Q}_{\mathbf{y}_p} = \mathbb{E}(\mathbf{y}_p\mathbf{y}_p^\dagger) = N_1\left[\mathbf{I}_{n_{R_1}} + \mathbf{D}\Lambda_1\mathbf{D}^\dagger\right],$$

where $\Lambda_1 = \frac{1}{N_1}\mathbf{Q}_x \oplus \frac{1}{N_1}\mathbf{Q}_s = \frac{P_1}{n_{T1}N_1} \oplus \frac{P_2}{n_{T2}N_1}$. Hence, the entropy of $\mathbf{y}_p$ is given by

$$h\left(\mathbf{y}_p|\mathbf{D}\right) = \log_2 \det\left[\pi e N_1\left(\mathbf{I}_{n_{R_1}} + \mathbf{D}\Lambda_1\mathbf{D}^\dagger\right)\right].$$

Similarly, the entropy of $\mathbf{w}_p$ is given by

$$h\left(\mathbf{w}_p|\mathbf{G}_M\right) = \log_2 \det\left[\pi e N_1\left(\mathbf{I}_{n_{R1}} + \frac{P_2}{n_{T2}N_1}\mathbf{G}_M\mathbf{G}_M^\dagger\right)\right].$$

Hence, the mutual information at the PR is given by

$$I\left(\mathbf{x}_1; \mathbf{y}_p|\mathbf{D}\right) = \log_2\left(\frac{\mathbf{I}_{n_{R_1}} + \mathbf{D}\Lambda_1\mathbf{D}^\dagger}{\mathbf{I}_{n_{R_1}} + \frac{P_2}{n_{T_2}N_1}\mathbf{G}_M\mathbf{G}_M^\dagger}\right) \tag{5}$$

and the capacity at the PR with interference is given by

$$C_{PR} = \max_{\Lambda_1} \log_2\left(\frac{\mathbf{I}_{n_{R_1}} + \mathbf{D}\Lambda_1\mathbf{D}^\dagger}{\mathbf{I}_{n_{R_1}} + \frac{P_2}{n_{T_2}N_1}\mathbf{G}_M\mathbf{G}_M^\dagger}\right). \tag{6}$$

Similarly, capacity at the eavesdropper is given by

$$C_E = \max_{\Lambda_2} \log_2\left(\frac{\mathbf{I}_{n_{R_E}} + \mathbf{D}_E\Lambda_2\mathbf{D}_E^\dagger}{\mathbf{I}_{n_{R_E}} + \frac{P_2}{n_{T_2}N_1}\mathbf{G}_E\mathbf{G}_E^\dagger}\right), \tag{7}$$

where $\Lambda_2 = \frac{P_1}{n_{T1}N_E} \oplus \frac{P_2}{n_{T2}N_E}$ and $\mathbf{D}_E = [\mathbf{H}_E \quad \mathbf{G}_E]$. Therefore, the secrecy capacity at the PR is given by

$$C_{\text{PR}}^{sec} = \max_{\mathbf{Q}_x} \log_2\left[(C_{PR} - C_E)\right]. \tag{8}$$

Substituting (6) and (7) into (8), the secrecy capacity at the PR is found which is shown in equation (9) at the bottom of this page. Following the similar procedure of equation (9), the secrecy capacity at the SR with interference can be derived which is given at the bottom of next in equation (10), where $\mathbf{R} = [\mathbf{H}_P \quad \mathbf{G}]$, $\mathbf{R}_E = [\mathbf{G}_E \quad \mathbf{H}_E]$, $\Lambda_3 = \frac{P_2}{n_{T2}N_2} \oplus \frac{P_2}{n_{T1}N_2}$ and $\Lambda_4 = \frac{P_2}{n_{T2}N_E} \oplus \frac{P_1}{n_{T1}N_E}$.

IV. Transmission with Relay

Let, $\mathbf{x}_r$ denotes the transmitted signal of the relay. Assuming a simultaneous transmission of the PUs, SUs and relay, received signals at the PR, SR and eavesdropper are given by

$$\mathbf{y}_p = \mathbf{H}\mathbf{x} + \mathbf{G}_M\mathbf{s} + \mathbf{U}_M\mathbf{x}_r + \mathbf{z}_m. \tag{11}$$

$$\mathbf{y}_s = \mathbf{H}_P\mathbf{x} + \mathbf{G}\mathbf{s} + \mathbf{U}_P\mathbf{x}_r + \mathbf{z}_p. \tag{12}$$

$$\mathbf{y}_e = \mathbf{H}_E\mathbf{x} + \mathbf{G}_E\mathbf{s} + \mathbf{U}_E\mathbf{x}_r + \mathbf{z}_e. \tag{13}$$

The PUs and SUs communicate with the relay to transmit their channel estimates and data and receive a scaling factor that is determined by the precoded relay. Power scaling factor is essential to normalize power at the output of the antennas.

$$C_{\text{PR}}^{sec} = \log_2\left\{\frac{\left(\mathbf{I}_{n_{R_1}} + \max_{\Lambda_1}\mathbf{D}\Lambda_1\mathbf{D}^\dagger\right)\left(\mathbf{I}_{n_{R_E}} + \frac{P_2}{n_{T_2}N_1}\mathbf{G}_E\mathbf{G}_E^\dagger\right)}{\left(\mathbf{I}_{n_{R_1}} + \frac{P_2}{n_{T_2}N_1}\mathbf{G}_m\mathbf{G}_m^\dagger\right)\left(\mathbf{I}_{n_{R_E}} + \max_{\Lambda_2}\mathbf{D}_E\Lambda_2\mathbf{D}_E^\dagger\right)}\right\} \quad \text{bits/sec/Hz} \tag{9}$$

A. Secrecy Capacity With ZF Precoding

Let us assume that the precoded signals at the PUs and SUs are given by $\mathbf{x} = f_z\mathbf{T}_1\mathbf{b}_1$ and $\mathbf{s} = f_z\mathbf{T}_2\mathbf{b}_2$, respectively, where, $\mathbf{b}_1$ and $\mathbf{b}_2$ are the data signals, $\mathbf{T}_1$ and $\mathbf{T}_2$ are the precoding signals of PUs and SUs respectively, and f_z denotes the scaling factor provided by the ZF relay. The aim of the relay is to nullify the interference between the two systems by designing a precoder at the relay according to the ZF criterion. Let, $\mathbf{A} = \begin{bmatrix} \mathbf{H}\mathbf{T}_1 & \mathbf{G}_M\mathbf{T}_2 \\ \mathbf{H}_P\mathbf{T}_1 & \mathbf{G}\mathbf{T}_2 \end{bmatrix}$ is the channel cross-correlation matrix, $\mathbf{Y} = \begin{bmatrix} \mathbf{y}_p & \mathbf{y}_s \end{bmatrix}^T$, $\mathbf{Q} = \begin{bmatrix} \mathbf{U}_M & \mathbf{U}_P \end{bmatrix}^T$ and $\mathbf{Z}_t = \begin{bmatrix} \mathbf{z}_p & \mathbf{z}_s \end{bmatrix}^T$. Then equation (9) and (10) can be rewrite as

$$\mathbf{Y} = f_z\mathbf{A}\mathbf{b} + \mathbf{Q}\mathbf{x}_r + \mathbf{Z}_t. \tag{14}$$

Assuming a restriction to the total average transmit power to unity and based on the precoded symbols with transmitted powers $P_1 = tr[\mathbf{T}_1\mathbf{T}_1^\dagger]$, $P_2 = tr[\mathbf{T}_2\mathbf{T}_2^\dagger]$ and $P_R = tr[(\mathbf{I} - \mathbf{A})^\dagger(\mathbf{Q}\mathbf{Q}^\dagger)^{-1}(\mathbf{I} - \mathbf{A})]$, f_z can be calculated as [1]

$$f_z = \left[tr[\Upsilon^\dagger(\mathbf{Q}\mathbf{Q}^\dagger)^{-1}\Upsilon] + tr[(\mathbf{H}\mathbf{H}^\dagger)^{-1}] + tr[(\mathbf{G}\mathbf{G}^\dagger)^{-1}]\right]^{-\frac{1}{2}}, \tag{15}$$

where $\Upsilon = (\mathbf{I} - \mathbf{A})$. Compensating interferences using ZF precoding at the relay, the average received SNRs per symbol at the PR and SR are given by $\bar{\gamma}_1 = \frac{f_t^2 P_1}{N_1}$ and $\bar{\gamma}_2 = \frac{f_t^2 P_2}{N_2}$, respectively. Therefore, the secrecy capacity at the PR and SR can be derived as

$$C_{\text{PR}}^{ZF} = \log_2\left(\frac{1 + \frac{f_z^2 P_1}{N_1}}{1 + \frac{f_z^2 P_1}{N_E + ||\mathbf{G}_E||^2 P_2}}\right), \tag{16}$$

$$C_{\text{SR}}^{ZF} = \log_2\left(\frac{1 + \frac{f_z^2 P_2}{N_2}}{1 + \frac{f_z^2 P_2}{N_E + ||\mathbf{H}_E||^2 P_1}}\right), \tag{17}$$

where $\frac{f_z^2 P_1}{N_E + ||\mathbf{G}_E||^2 P_2}$ denotes the received signal-to-interference plus noise ratio (SINR) at the eavesdropper due the transmit signal of PUs. Similarly, $\frac{f_z^2 P_2}{N_E + ||\mathbf{H}_E||^2 P_1}$ denotes SINR at the eavesdropper due the transmit signal of SUs.

B. Secrecy Capacity With Selective Precoding

For some specific symbol combinations, interference existing in the communication system can be added to the desired symbols which improves the SNR at the receiver. Let the generic interference caused to jth receive antenna from the ith transmit antenna be $\rho_{i,j} = d_i\rho_{i,j}$, where d_i denotes the interfering signal and $\rho_{i,j}$ is the i,jth correlation element in matrix $\mathbf{A}$. $\rho_{i,j}$ is said to be constructive interference if the real and imaginary parts of $\rho_{i,j}$ have the same sign as the real and imaginary parts of the desired symbol, respectively. Let ξ_R and ξ_I respectively denote the real and imaginary parts of the constructive interference. Then, we have

$$\xi_R = \text{Re}\,(I_{i,j})\,\text{Re}\,(d_j) > 0 \;\text{ and }\; \xi_I = \text{Im}\,(I_{i,j})\,\text{Im}\,(d_j) > 0,$$

where $\text{Re}(x)$ and $\text{Im}(x)$ denote the real and imaginary parts of the complex number x. Therefore, as discussed in [1], precoder at the relay first forms a constructive correlation matrix $\mathbf{B}$ as follows

$$[\mathbf{B}]_{i,j} = \begin{cases} \rho_{i,j} & \text{if} \quad \xi_R > 0 \;\text{and}\; \xi_I > 0 \\ 0 & \text{if} \quad \xi_R < 0 \;\text{and}\; \xi_I < 0 \end{cases} \tag{18}$$

Following the similar procedure of previous section, the transmission power of relay can be formulated as $P_R = tr[(\mathbf{B} - \mathbf{A})^\dagger(\mathbf{Q}\mathbf{Q}^\dagger)^{-1}(\mathbf{B} - \mathbf{A})]$, and the corresponding scaling factor is given by

$$f_s = \left[tr[\Psi^\dagger(\mathbf{Q}\mathbf{Q}^\dagger)^{-1}\Psi] + tr[(\mathbf{T}_1\mathbf{T}_1^\dagger)^{-1}] + tr[(\mathbf{T}_2\mathbf{T}_2^\dagger)^{-1}]\right]^{-\frac{1}{2}}, \tag{19}$$

where $\Psi = (\mathbf{B} - \mathbf{A})$. Using the scaling factor of (19), the secrecy capacity at the PR and SR are respectively given by

$$C_{\text{PR}}^{SP} = \log_2\left(\frac{1 + \frac{(f_s^2 P_1)\mathbf{b}^\dagger\mathbf{T}_1^\dagger\mathbf{T}_1\mathbf{b}}{N_1(n_{T_1} + n_{T_2})}}{1 + \frac{(f_s^2 P_1)\mathbf{b}^\dagger\mathbf{T}_1^\dagger\mathbf{T}_1\mathbf{b}}{(N_e + ||\mathbf{G}_E||^2 P_2)(n_{T_1} + n_{T_2})}}\right). \tag{20}$$

$$C_{\text{SR}}^{SP} = \log_2\left(\frac{1 + \frac{(f_s^2 P_2)\mathbf{b}^\dagger\mathbf{T}_1^\dagger\mathbf{T}_1\mathbf{b}}{N_2(n_{T_1} + n_{T_2})}}{1 + \frac{(f_s^2 P_2)\mathbf{b}^\dagger\mathbf{T}_1^\dagger\mathbf{T}_1\mathbf{b}}{(N_e + ||\mathbf{H}_E||^2 P_1)(n_{T_1} + n_{T_2})}}\right). \tag{21}$$

C. Secrecy Capacity With Phase Alignment Precoding

Instead of zeroing the elements of channel cross correlation matrix ($\mathbf{A}$) those are responsible for destructive interference , the resulting interference can be made constructive by correcting the phase of transmitted symbols and equivalently rotating the angle of correlation between them. Hence the resulting symbols after precoding are aligned to the interested signal. The relative phase $\varphi_{i,j}$ can be expressed as $\varphi_{i,j} = b_j\frac{conj(bi\rho_{i,j})}{|\rho_{i,j}|}$, where $conj(x)$ and $|x|$ represent the conjugate and magnitude of complex number x. It is assumed that $|b_i| = 1$ and hence $|\varphi_{i,j}| = 1$ and due to this reason the amplitude of the rotated correlation remains unchanged. Since our goal is to convert the destructive interferences into constructive one, therefore, the precoder at the relay is designed according to the phase alignment criterion to zero the mean square error. $\psi = \mathbb{E}[\|\mathbf{A}\mathbf{b} + \mathbf{Q}\mathbf{x}_r - \Phi\mathbf{b}\|^2]$. Therefore, as discussed in [1], the precoder at the relay at first forms a modified correlation matrix Φ as follows

$$[\Phi]_{i,j} = \rho_{i,j}\varphi_{i,j}. \tag{22}$$

The transmission power of the relay can be formulated as $P_R = tr[(\Phi - \mathbf{A})^\dagger(\mathbf{Q}\mathbf{Q}^\dagger)^{-1}(\Phi - \mathbf{A})]$, and the corresponding

$$C_{\text{SR}}^{sec} = \log_2\left\{\frac{\left(\mathbf{I}_{n_{R_2}} + \max_{\Lambda_3}\mathbf{R}\Lambda_3\mathbf{R}^\dagger\right)\left(\mathbf{I}_{n_{R_E}} + \frac{P_2}{n_{T_2}N_1}\mathbf{H}_E\mathbf{H}_E^\dagger\right)}{\left(\mathbf{I}_{n_{R_2}} + \frac{P_2}{n_{T_2}N_1}\mathbf{H}_p\mathbf{H}_p^\dagger\right)\left(\mathbf{I}_{n_{R_E}} + \max_{\Lambda_4}\mathbf{R}_E\Lambda_4\mathbf{R}_E^\dagger\right)}\right\}, \quad \text{bits/sec/Hz} \tag{10}$$

scaling factor is given by

$$f_p = \left[tr[\Gamma^\dagger(\mathbf{Q}\mathbf{Q}^\dagger)^{-1}\Gamma] + tr[(\mathbf{T}_1\mathbf{T}_1^\dagger)^{-1}] + tr[(\mathbf{T}_2\mathbf{T}_2^\dagger)^{-1}]\right]^{-\frac{1}{2}}, \quad (23)$$

where $\Gamma = (\Phi - \mathbf{A})$. Using the scaling factor of (23), the secrecy capacity at the PR and SR are respectively given by

$$C_{\text{PR}}^{PARP} = \log_2\left(\frac{1 + \frac{(f_p^2 P_1)\mathbf{b}^\dagger\Phi^\dagger\Phi\mathbf{b}}{N_1(n_{T_1}+n_{T_2})}}{1 + \frac{(f_p^2 P_1)\mathbf{b}^\dagger\Phi^\dagger\Phi\mathbf{b}}{(N_e+||\mathbf{G}_E||^2 P_2)(n_{T_1}+n_{T_2})}}\right). \quad (24)$$

$$C_{\text{SR}}^{PARP} = \log_2\left(\frac{1 + \frac{(f_p^2 P_2)\mathbf{b}^\dagger\Phi^\dagger\Phi\mathbf{b}}{N_2(n_{T_1}+n_{T_2})}}{1 + \frac{(f_p^2 P_2)\mathbf{b}^\dagger\Phi^\dagger\Phi\mathbf{b}}{(N_e+||\mathbf{H}_E||^2 P_1)(n_{T_1}+n_{T_2})}}\right). \quad (25)$$

V. Numerical Results

In this section, we investigate the effect of different types of precoding relay (ZF, SP and PAP) on the secrecy capacity at the PR. Fig 2 depicts the simulation result of secrecy capacity at the PR versus SNR to compare the performance of ZF, SP and PAP at the relay. It is observed from Fig 2, that using PAP at the relay enhances the secrecy capacity in a larger scale compared to SP and ZF. This is because, ZF only cancels out the interference while SP uses the interference energy as an additional source of energy which increases the SNR at the PR whereas PAP uses both constructive and destructive interference power by rotating the phase angle of destructive interference.

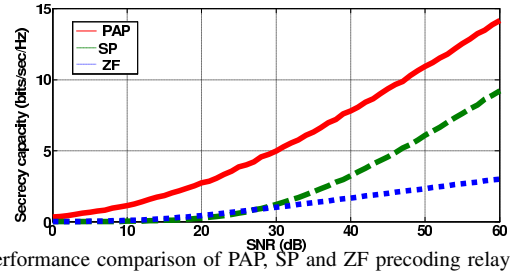

Fig. 2. The performance comparison of PAP, SP and ZF precoding relay in enhancing the secrecy capacity at the PR.

Fig 3 describes the effect of using ZF, SP and PAP at the relay on the outage probability as a function of rate. It is observed from Fig 3 that outage probability of the secrecy capacity at the PR is better for PAP than that of other two precoding relays (ZF and SP). In the case of CCDF, it is also found (Fig 4) that PAP performs better than that of other two precoding techniques.

VI. Conclusion

In this paper, we propose a scheme to use the destructive interference power in enhancing the secrecy capacity. Based on our formulation and observation of numerical results, we can conclude that, although interference reduces the secrecy capacity but employing precoding technique at the relay, it is possible to enhance the secrecy capacity. In the case of ZF at the relay, the effect of interference is removed while in the case of SP at the relay, constructive interference power can be used as an additional source of energy to enhance the secrecy capacity without increasing transmit signal power. In the case of PAP at the relay, the destructive part of interference advances the secrecy capacity one step ahead than the former two precoding techniques (ZF and SP).

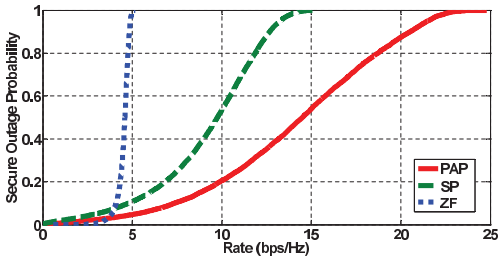

Fig. 3. Outage probability comparison of PAP, SP and ZF precoding at PR.

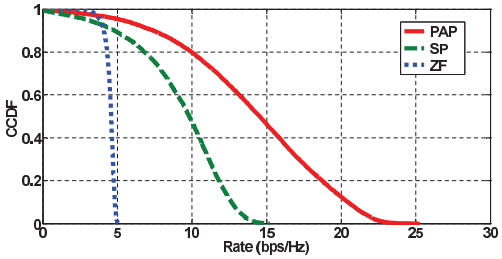

Fig. 4. CCDF comparison of PAP, SP and ZF precoding at PR.

Acknowledgement

This work was supported by the Research Support and Publication Division of University Grant Commission, Bangladesh.

References

[1] C. Masouros and T. Ratnarajah, "Interference as a source of green signal power in cognitive relay-assisted co-existing MIMO wireless transmissions," *IEEE Transactions on Communications*, vol. 60, no. 2, pp. 525–536, June 2012.

[2] Y. Zou, C. B, W.-P. Zhu, and H. L., "Relay-selection improves the security-reliability trade-off in cognitive radio syystems," *IEEE Transactions on Communication*, vol. 63, no. 1, pp. 215–228, December 2014.

[3] S. Zhong and H. Yao, "Towards cheat-proof cooperative realy for cognitive radio networks," *IEEE Tranactions on Parallel and Distributed Systems*, vol. 25, no. 9, pp. 2442–2451, May 2013.

[4] H. Jeon, McLaughlin, S. W., I.-M. Kim, and J. Ha, "Secure communications with untrusted secondary nodes in cognitive radio networks," *IEEE Transactions on Wireless Communications*, vol. 13, no. 4, pp. 1790–1805, April 2015.

[5] D. Pu, Wyglinski, and A. M., "Primary-user emulation detection using database-assisted frequency-domain action recognition," *IEEE Transactions on Vehicular Technology*, vol. 63, no. 9, pp. 4372–4382, November 2014.

[6] C. Wang and H.-M. Wang, "Primary-user emulation detection using database-assisted frequency-domain action recognition," *IEEE Transactions on Information Forensics and Security*, vol. 9, no. 11, pp. 1814–1827, September 2014.

[7] Y. Zou, X. Wang, and W. Sen, "Physical-layer security with multiuser scheduling in cognitive radio networks," *IEEE Transactions on Wireless Communications*, vol. 13, no. 4, pp. 5103–5113, Decenmer 2013.

[8] S. Sridharan, S. Vishwanath, S. A. Jafar, and S. Shamai, "On the capacity of cognitive relay assisted Gaussian interference channel," in *Proc. IEEE Int. Symp. Information Theory (ISIT08), Toronto, Canada*, 2008, pp. 549–553.

[9] Z. Ghebretensae, J. Harmatos, and K. Gustafsson, "Mobile broadband backhaul network migration from TDM to carrier ethernet," *IEEE Communications Magazine*, vol. 48, no. 10, pp. 102–109, October 2010.

2nd International Conference on Electrical, Computer & Telecommunication Engineering (ICECTE)
8-10 December 2016, Rajshahi-6204, Bangladesh

Terminal Voltage Regulation & Output Fluctuations Minimization Using Governor-Exciter Controller

D. Datta,[1] M.R.I. Sheikh ,[2] M.M. Islam,[3] A.Al. Mahdi[4]

[1,2,]EEE Department, Rajshahi University of Engineering & Technology, Rajshahi-6204, Bangladesh

[3,4,]EEE Department, Varendra University, Rajshahi-6204, Bangladesh

[*]dristidatta@gmail.com

Abstract— **Energy is essential to life and the major source of energy comes from fossil fuels. As the human population increases, our rate of consumption of these fossil fuels also increases. On the other hand, world population continues to grow and the limited amount of fossil fuels begin to diminish, it may not be possible to provide the amount of energy demanded by the world by only using fossil fuels to convert energy. The solution to the problems of limited fossil fuels and their impact on the environment is to have renewable resources play a larger role in the supply of energy. In this case wind energy is the most promising green energy. As wind turbine output is proportional to the cube of wind speed, the wind turbine generator output fluctuates due to wind speed variation. Thus this paper focuses on the comparative study between conventional wind turbine models with modified pitch controller and proposed a new technique called modified pitch governor with exciter controller to control output voltage and frequency without using any costly energy storage devices. In this study variable load is considered and real wind speed data is taken to obtain realistic response. PSCAD/EMTDC software is used for simulation analyses.**

Index Terms*—Wind turbine; new pitch controller; variable load; system frequency; wind power capacity; governor and exciter control; system model.*

I. Introduction

Renewable energy is becoming an increasingly important issue in today's world. In addition to the rising cost of fossil fuels and the threat of climate change, there has also been positive developments in this field which include improvements in efficiency as well as diminishing prices. All of this has increased the demand for alternative energy and accelerated the transition towards cleaner, more sustainable methods of electrical power. But it is a matter of great regret that, the world has limited amount of fossil fuel and nuclear power resources ([1], [2]). So, the growth of wind energy around the world in recent years has been consistently impressive.

In the conventional operation of wind power generators, when the wind speed is between the rated speed and the cut out speed, the wind power generator output is controlled at the rated value by a pitch control system [3]. On the other hand, when the wind speed is between the cut in speed and the rated speed, the blade pitch angle is maintained constant (= 0 deg), in general for the wind turbine to capture the maximum power from the wind turbine [4]. If the power capacity of wind generators becomes large, wind generator output can have an influence on the power system frequency ([5]-[8]).

From the previous study ([1], [3], [4]), it is seen that when single SG or several SGs are connected with networks, only governor control system model and conventional pitch controller cannot maintain the power system frequency to the desired level and severe situation occurs when wind power penetration becomes more than 10% of the total capacity.

In ([5], [9]) the authors applied a new pitch control system where the reference power is considered variable. Thus the frequency can be controlled up to a certain limit but voltage cannot be controlled by their pitch control systems.

But this study shows the comparison between conventional models with the proposed modified pitch controller and also proposed a new technique to control output voltage as well as frequency by variable capacitor with newly designed pitch controller with governor and exciter controller.

As the wind power penetration increases day by day, this study plays a vital role for power system application. It is seen from the simulation results that the variable capacitor with modified pitch control including governor and exciter control system model can maintain the frequency as well as voltage in acceptable limit with high wind power penetration. As a result, energy storage devices can be avoided which reduce the total cost of the system.

II. Model System For Simulation Analysis

The model system used in the simulation analysis is shown in Fig. 1. The model system consists of single (composed of small capacity multiple wind generators) wind generator (IG), one thermal power generator, SG, and three loads. Q_{WF} and Q_{Load} are capacitor banks where Q_{WF} is used at the terminal of IG to compensate the reactive power demand of wind generator at steady state. The value of the capacitor is chosen so that the p.f. becomes unity, when the wind generator operated in the rated condition. On the other hand, Q_{Load} is used at the terminal of load to compensate the voltage

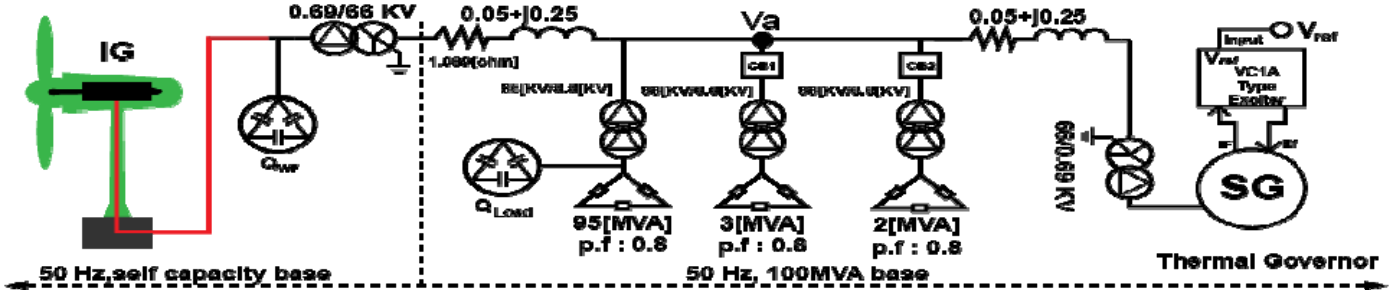

Fig. 1. Model circuit.

978-1-5090-5785-6/16/$31.00 ©2016 IEEE

drop by the impedance of transmission lines. Here circuit breakers CB1 and CB2 are used to control the load as a variable. Core saturations of induction generator and synchronous generators are not considered for simplicity. The initial power flow and initial conditions are taken from [3].

III. Synchronous Generator Model

A. Governor for Thermal Generators

The IEEJ type governor models have been used in the simulation analyses as those used in [3]. The internal input (65M) for the governor is controlled as shown in Fig. 2. In this study, conventional model of AVR for thermal generators is also used which is taken from [3].

IV. Modified Pitch Controller

In the newly designed pitch controller the power system frequency (f) is considered as the main parameter for the controllers to take decision for maintaining frequency to the desired acceptable range. The comparator and control circuit as shown in Fig. 2 is used to adjust (following eq. (1) and (2)) the initial input i.e. 65M for the governor with the addition to pitch controller.

If f > 50.2 then 65M = 0.70 (1)

Or If f < 49.8 then 65M = 0.62 (2)

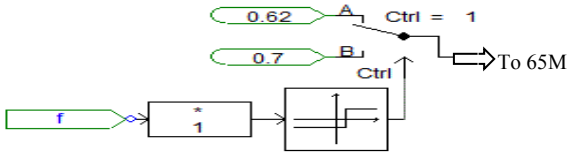

Fig. 2. PSCAD control box for controlling governor input 65M.

V. Proposed Capacitor Bank Correction System And SG's Exciter Control Technique

Generally, the value of capacitor bank for conventional model is kept constant. But for this study variable capacitor bank is considered for system voltage adjustment with wide range of voltage deviation. In our previous study [10] only fixed load have been considered, however in this study variable load also have been considered. For this reason, a new technique has been proposed to control the output voltage fluctuations by making the capacitor value variable and the adjustment for different values of capacitor have been done with respect to wind speed variation as shown in Table I. For the further smoothen of grid voltage, reference voltage of synchronous generator is also controlled to make the grid voltage approximately constant.

For this a decision circuit is used as shown in Fig. 3, where input voltage, V is sensed by the control circuit and corresponding reference voltage (as shown in Fig. 1) is generated according to the Table II.

TABLE I CAPACITOR BANK CORRECTION

Wind Speed, V_w (m/s)	Capacitor Value, C (F) as shown in Fig. 1
Below 6	6600
7	7000
8	7600
9	9000
10	12000
11	16500
12	22200
13	24000
Above 13	26000

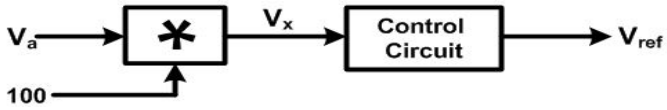

Fig. 3. Decision circuit.

TABLE II REFERENCE VOLTAGE CORRECTION

Input Voltage, V_x(Volt)	Reference Voltage, V_{ref} (Volt)
Below 99.4	1.08
99.5 to 99.7	1.07
99.8 to 99.9	1.06
100	1.05
100.1 to 100.2	1.04
Above 100.3	1.03

V. Simulation Analyses

In this paper, the following five different simulation patterns have been studied for wind generator which is experienced real wind speed shown in Fig. 4. The simulation analyses have been performed by using PSCAD/EMTDC [11].

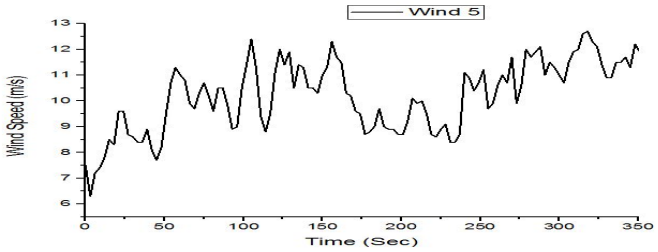

Fig. 4. Wind speed data.

TABLE III SIMULATION PATTERN

No. of Cases	Load Condition	Name of the Case
Case 01	fixed load	conventional model Vs. capacitor vary
Case 02	variable load	conventional model Vs. modified pitch controller.
Case 03	variable load	conventional model Vs. capacitor vary with modified pitch governor.
Case 04	variable load	conventional model Vs. capacitor vary with modified pitch governor and exciter control.
Case 05	variable load	Capacitor vary with modified pitch governor control Vs. capacitor vary with modified pitch governor and exciter control.

When only variable capacitor model is compared with conventional model (case 1) then the grid voltage (Fig. 5); SG's power (Fig. 6) as well as frequency (Fig. 7) fluctuation is comparatively less for variable capacitor model.

For case 02 to 05 variable load which varies between 70 MW to 80 MW has been considered which has been shown in Fig. 8. For case 02, when modified pitch controller is compared with conventional model, it is seen from Figs. 9, 10 and 11 that the response of voltage, SG's power and frequency are better respectively.

Again for case 03, the conventional model is compared with capacitor vary with modified pitch along with governor control model. Better response can be obtained from modified

model which show from Figs. 12 to Fig. 14. More smooth result can be obtained when capacitor vary with modified governor model and exciter control system. For this case (case 4) the results are shown in Figs. 15 through Fig.17.

A comparative results for case 5 is the comparison between case 3 and case 4. Fig. 18 through Fig. 20 show the simulation results for case 5. The results prove that better and smooth response can be obtained when capacitor vary along with modified pitch with governor and exciter control system is adopted.

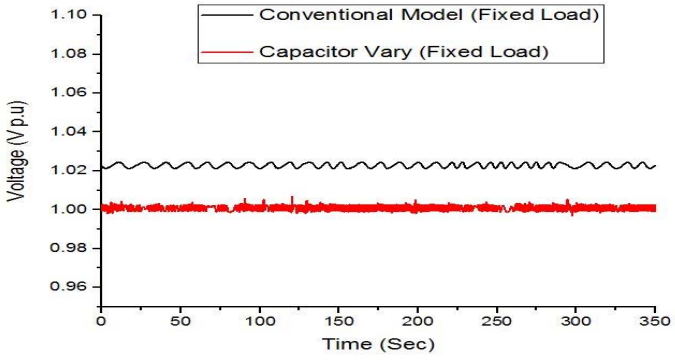

Fig. 5. Response of output voltage [case 1].

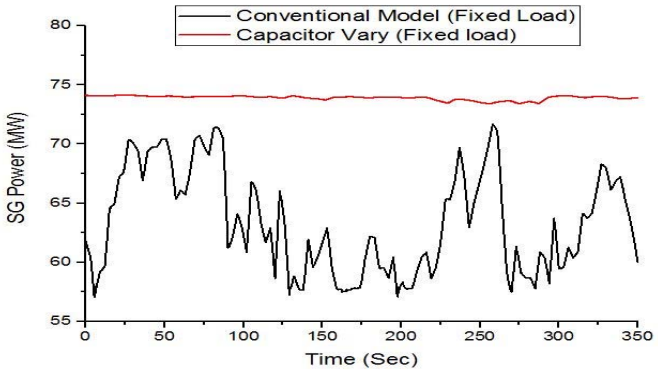

Fig. 6. Response of SG power [case 1].

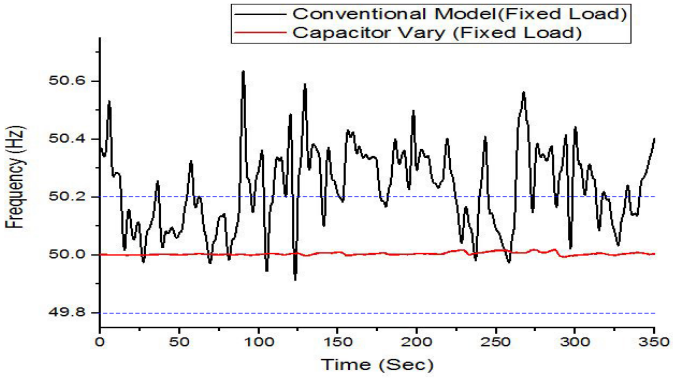

Fig. 7. Response of output frequency [case 1].

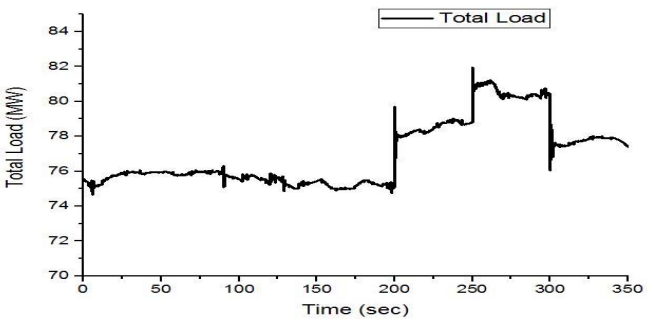

Fig. 8. Response of load changes.

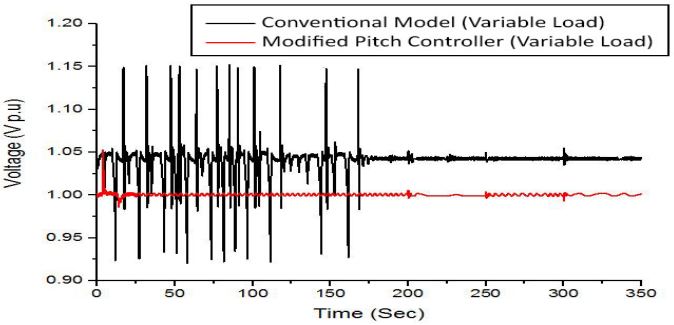

Fig. 9. Response of output voltage [case 2].

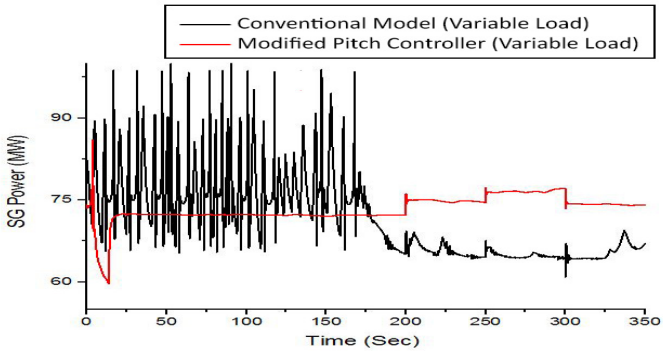

Fig. 10. Response of SG power [case 2].

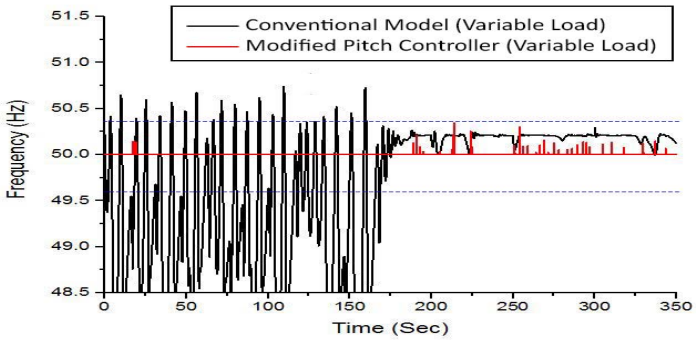

Fig. 11. Response of output frequency [case 2].

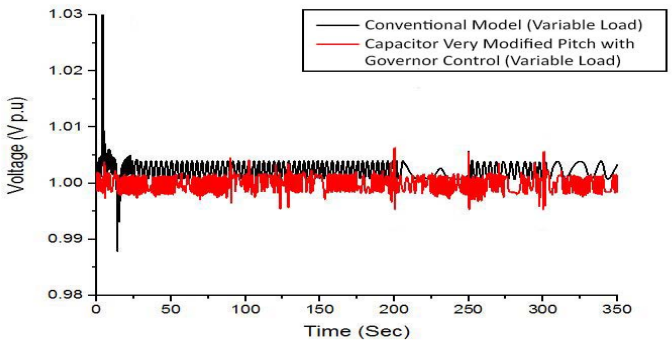

Fig. 12. Response of output voltage [case 3].

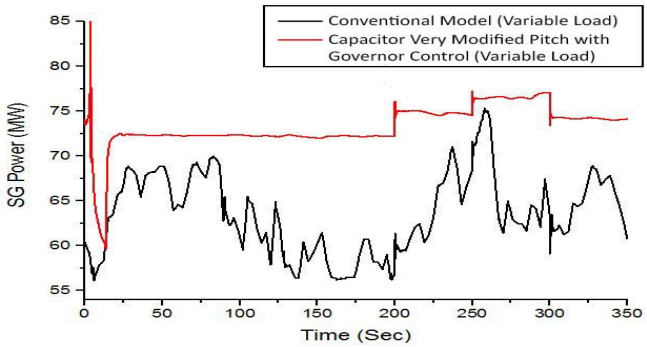

Fig. 13. Response of SG power [case 3].

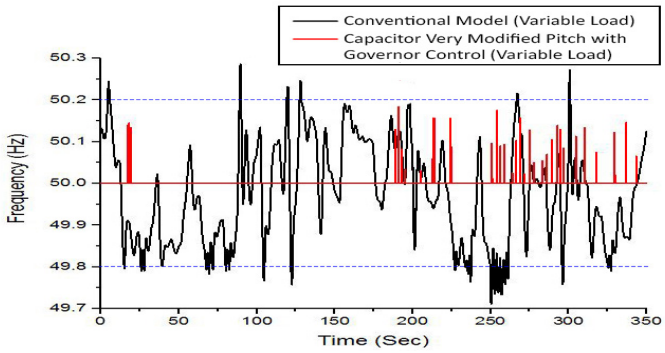

Fig. 14. Response of output frequency [case 3].

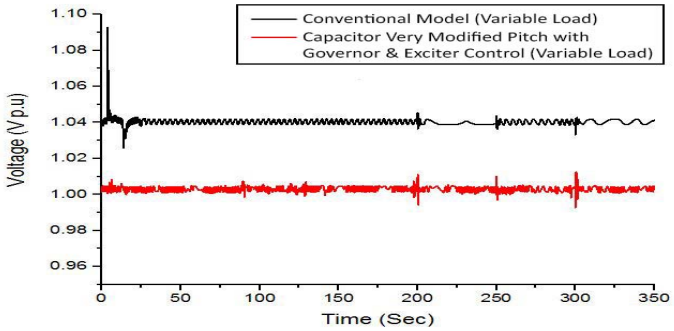

Fig. 15. Response of output voltage [case 4].

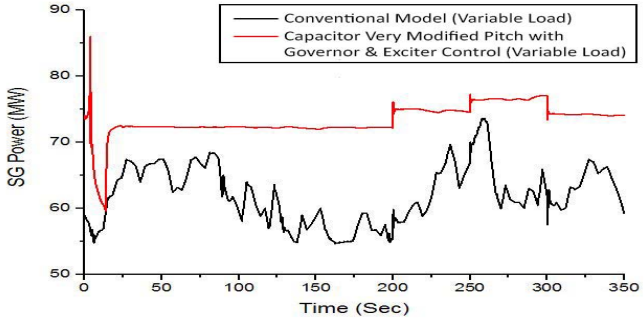

Fig. 16. Response of SG power [case 4].

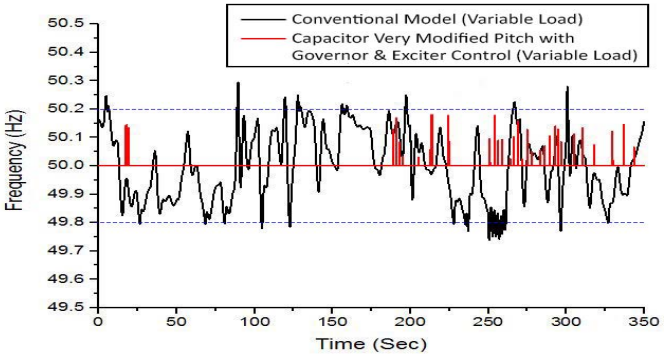

Fig. 17. Response of output frequency [case 4].

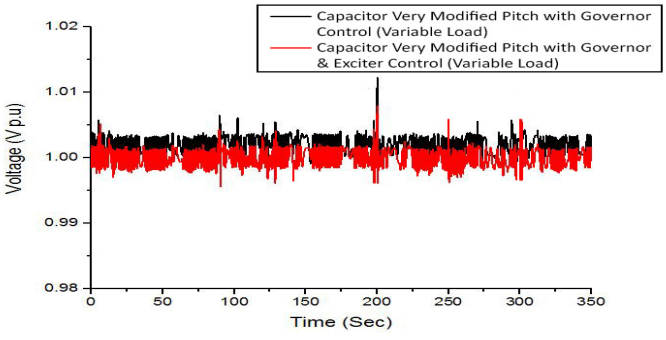

Fig. 18. Response of output voltage [case 5]

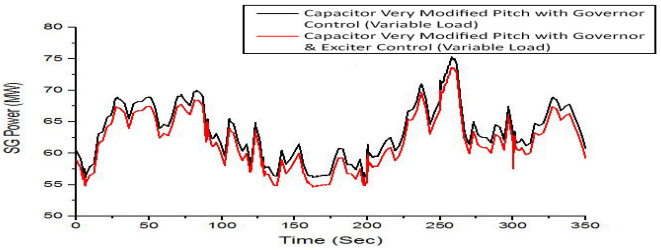

Fig. 19. Response of SG power [case 5].

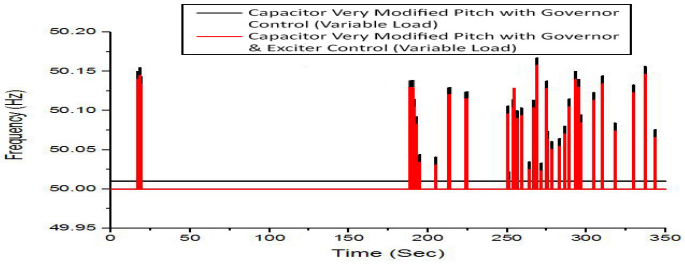

Fig. 20. Response of output frequency [case 5].

VI. Conclusions

The permissible frequency fluctuation limit of the most developed country is defined by 50Hz or 60Hz with ± 0.2 [Hz]. As frequency and grid voltage are the main factors to determine the quality of power, this paper focuses on the comparison between conventional models with respect to proposed modified pitch governor with exciter control system. It is very much clear that frequency fluctuation as well as grid voltage can remain in the acceptable limit when conventional model is modified with newly designed pitch controlling technique with governor with exciter controller. In this case any costly energy storage devices can be neglected.

References

[1] E. Haque and M.R.I Sheikh, "Grid frequency analysis with the issue of high wind power penetration", *International Conference on Electrical Information and Communication Technology,* KUET, Khulna, Bangladesh, Dec. 2013.

[2] M.R.I. Sheikh, M.S.R. Ashrafi, and D. Datta, "Co-ordinated Frequency Control of Power System with High Wind Power Penetration", *International conference on Electrical Engineering and Information & Communication Technology,* MIST, Dhaka, Bangladesh,12-14 Apr. 2014.

[3] M.R.I. Sheikh, M.M. Haque, and A. Hossain, ''Performance of governor system on minimizing frequency fluctuations with wind power generation'', *International Journal of Electrical and Computer Engineering (IJECE)*, vol. 2, no. 1, pp. 46--56, Feb. 2012.

[4] M.R.I. Sheikh, R. Takahashi, and J. Tamura, ''Study on frequency fluctuations in power system with a large penetration of wind power generation'', *International Energy Journal* , vol. 1, no. 1, Mar. 2011.

[5] T. Yamazaki, R. T. Murata, T. Tamura, Fukushima, E. Ssano, K. Shinya, and T. Matstumoto, ''Smoothing control of wind generator output fluctuations by new pitch controller'', *IEEJ Transactions on Power and Energy*, vol. 129, no. 7, pp. 880-888,Jul. 2009.

[6] C Luo, and B. T Ooi, ''Frequency deviation of thermal power plants due to wind farms'', *IEEE Transaction on Energy Conversion*,'' vol. 21, no. 3, pp. 708-716, Sep. 2006.

[7] C. Carrillo, A.E. Feijoo, J. Cidras, and J. Gonzalez, ''Power fluctuation in an isolated wind plant'', *IEEJ Transactions on Power and Energy,* vol. 19, no. 1, pp. 217-221, Mar. 2004.

[8] H. Umeki, R.Takahashi, T. Murata, and J. Tamura, ''Smoothing control of wind generator output fluctuations by new pitch controller'', *The Int. Conf. of Electrical Machines and Systems(ICEMS),*LS3C-1,2006.

[9] M.R.I. Sheikh, D. Datta & M.S.R. Ashrafi, "Minimization of Output Fluctuations of Hybrid Power System by Using Modified Pitch Controller", *IEEE Xplore Digital Library, 20-22 Dec. 2014.*

[10] D. Datta, & M.R.I. Sheikh, "Voltage Stability Augmentation of IG Based Wind Farm Using Capacitor with Exciter Control System" *IEEE International conference on electrical and computer engineering, 20-22 Dec. 2014*

[11] Manitoba HVDC Research Center. 1994. PSCAD/EMTDC Manual.

Support Vector Machine for Overcoming the Problem of Vanishing Point during Stairways Detection

Md. Khaliluzzaman and Kaushik Deb*
Dept. of Computer Science and Engineering
Chittagong University of Engineering & Technology (CUET)
Chittagong - 4349, Bangladesh
khalil_021@yahoo.co.in and *debkaushik99@cuet.ac.bd

***Abstract* — Stairways region detection from a stairways image is a challenging activity to support autonomous system and visually impaired people for navigating safely. This paper proposes a framework for investigating the problem of vanishing point during stairways candidate region verification. For that, initially stairways candidate region is detected utilizing the unique natural and geometrical features of stairways. One unique natural feature is three connected point (3CP). This 3CP is formed at every stairways step's horizontal edges end points with stairways step's width and height edge's intersection point. Another geometrical feature is stairways step's edges are exhibited in sorted order. These geometrical features are used to detect stairways candidate region from stairways images. Where, the 3CP geometrical feature of stairways is used to validate the stairways step's horizontal edge segments. After that, the validated stairways edges are justified by computing vanishing point (VP). This justification ensures that the edge segments are arrived in increasing parallel order. Finally, the *y* coordinate value of VP is utilized to verify the edge segments of stairways from other analogous looking objects and ensure the detection of stairways region. However, in some cases the vanishing point does not distinguish the stairways region from other stairways like objects such as zebra-crossing or rail-line. This paper investigates this problem and verified the stairways candidate region using the SVM classifier where Gabor filters are used to extract the features. Various stair images are utilized to evaluate the proposed framework and presented outcomes demonstrate the adequacy.**

Keywords — Autonomous system; visually impaired people; three connected point; vanishing point; SVM

I. INTRODUCTION

Accurate object detection from a particular image is the challenging task in the area of computer vision. Stair region detection from a stairways image is such a task. This activity is used for visually impaired and autonomous systems in an unknown environment. In the real time intelligent system, stairways region detection is harder for stairways shape, viewpoints, and different outdoor illumination conditions. To mitigate these problems and satisfy the requirement of intelligent autonomous systems, the detection procedure should be performed in the real time and extract every interest candidate objects from stairways image efficiently.

This section provides the descriptive summary of some procedures that are implemented as well as tested for stair detection from stair images. As far as detection of the stairways is concerned, researchers have found many comprehensive methods to detect stairways from stair image to enhance the detection precision. For example, An RGB-D based method is proposed in [2]. This method detects and recognizes the stair and pedestrian crosswalks. For that, parallel concurrent lines are extracted by applying the Hough transforms. Finally, stair and pedestrian crosswalks are recognized by using the depth information. An indoor and outdoor stair detection algorithm is introduced in [5]. In this algorithm, concurrent horizontal edges are detected the by Canny and Hough transform. The stair region is detected with using some basic criteria. However, this system is only working with a fixed distance i.e. 5 m. A Smartphone based stair detection framework in proposed in [8]. This framework is not working properly in the uneven illumination conditions. Some vision based stair detection algorithm is proposed in [1][3].

Directional filter [11] and vertical vanishing point [7] based framework for stairways detection is introduced in [10][11]. In [11], proposed an outdoor stair detection framework. This framework detects the stair region by extracting stair diagonal angles and utilizing directional Gabor filter. Later, an indoor stairways localization method is proposed in [6]. For that, planer motion tracking and directional filter is employed to detect the stair step edges. After that, a correlation process in applied to extract a hypothetical set of targets. Another stairways detection method based on the natural feature and vanishing point is exploited in [4]. This framework uses longest increasing subsequence algorithm to arrange the stairways parallel concurrent edges in the longest increasing order. Finally, vertical VP is used to ensure the detection of the stairways region. However, in some cases the vanishing point does not verified and confirmed the detection of the stairways candidate region. Previous research works such as [4][10][11] are not concentrate on this matter. This paper investigates the problem of the VP in the phase of confirming and verifying the stairways candidate region from stairways image.

A framework has been proposed in this paper for detecting stairways based on geometrical features of a stairways and investigating the problem of the vanishing point during stairways region verification. One geometrical feature of stairways is, stair step's horizontal edge (HE) end points intersect with stair step's width and height vertical edge (VE) point. This creates the 3CP shown in Fig. 1(a). Another geometrical feature is steps of a stairways are arranged in sorted order is shown in Fig. 1(b). These features are implemented in this paper to detect stairways candidate region. The extracted stairways region is verified by using the vertical vanishing point. However, in some situations the vertical vanishing point does not distinguish the stair candidate region from other analogous looking objects such as rail-line or zebra-crossing. This paper also investigates this problem. The problem investigation is the key part of this proposed framework. Finally, the stair region of interest is classified by the SVM classifier. And compare the performance of SVM classifier with the vertical VP.

978-1-5090-5785-6/16/$31.00 ©2016 IEEE

Fig. 1. Natural and unique geometrical feature of stairways: a) 3CP, and b) parallel HEs arrived in sorted order.

The paper is arranged as follows. The proposed framework is explained step by step in Section II. In Section III, the experimental results are described. Finally, the conclusion is given in Section IV.

II. Proposed Framework

This section describes the proposed framework in step by step. The framework is divided into six primary steps, i.e. (1) filtering and detecting stair edge image, (2) eliminating non-interest edges, (3) extracting longest edges with edge linking and tracking procedure, (4) detecting three connected points, (5) justifying increasing horizontal edge segments, (6) verifying and detecting the stairways candidate region by vanishing point, (7) vanishing point's problem during stairways region verification, (8) feature extraction and classification, and detecting stairways candidate region by SVM classifier. Fig. 2 shows the proposed framework.

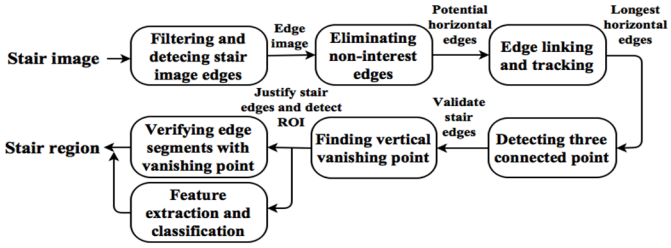

Fig. 2. Workflow of the proposed framework.

A. Filtering and extracting stairways edges

This section explains the process of extracting stairways edges from stairways image that conveys the features of the stair. Basically, the stair image is located in the environment with different lighting and noisy conditions. To extract the edges accurately from the stair image the shadow's and noise effects should be eliminated from the stairways image, and reserves the multi-directional edge information. For that, the Gabor filter which is linear directional wavelet type filter is applied on the stairways to eliminate the influence of illumination and extract the stairways potential edges. The basic form of the Gabor filter is defined in (1), (2), and (3).

$$G_{\lambda,\theta,\varphi,\sigma,\gamma}(x,y) = exp\left(-\frac{x'^2+\gamma^2 y'^2}{2\sigma^2}\right) cos\left(2\pi\frac{x'}{\lambda}+\varphi\right) \quad (1)$$

$$x' = xcos\theta + y\,sin\theta \quad (2)$$

$$y' = -xsin\theta + y\,cos\theta \quad (3)$$

here, (x, y) is the coordinate of the image pixel and the cosine factor of the wavelength is presented by λ , angular orientation is defined by θ, phase offset of the filter is ψ, the standard deviation and spatial aspect ratio are denoted by σ and γ respectively. The Gabor filters effect on the zebra-crossing image is shown in Fig. 3(b).

Since the horizontal and vertical edges are needed to satisfy the natural and geometrical features of the stair, the Canny edge detection method is used to detect the stairways edges from the filtered stairways image. Fig. 3(c) shows the result of the Canny edge detection.

B. Eliminating non-interest edges

This section extracting the potential HEs that are convey the information of the stair by eliminating the non-interest edges. Basically, the Canny edge image contains the edges with different orientations. All those edges are not required to represent the stair features. For that, initially the HEs are detected from the Canny edge image by removing the VEs from the edge image shown in Fig. 3(d).

It is seen from Fig. 3(d) that many small edges still exist in the HE image. Those small HEs are removed from HE image by employing filtering procedure. According to this procedure, if any edges are smaller than an Edge_threshold (a fixed size of edge) than the edges will be eliminated. The value of the Edge_threshold is defined by $\sqrt{\frac{\sum_{i=1}^{N}(edge(i)-edge\_mean)^2}{N}}$, which is the first standard deviation of the edge values exist in the Fig. 3(d), where, N is the number of the HEs. The result of eliminating the small HEs is shown in Fig. 4(a). In the HE image, there exist various edges in the potential HE image that are not segment of parallel horizontal edges. Those non-parallel edges are marked as non-candidate edges and removed from the edge image. Fig. 4(b) presents the outcome of removing the non-candidate edges.

C. Edge linking and tracking procedure

This section mainly contains the potential horizontal step edges. However, those potential horizontal edges may have some gaps or breaks in different regions. This paper introduces a method to fill the gaps or breaks in the horizontal edges. According to this method, the gaps of the horizontal edges with less than 3 pixels are filled automatically. Otherwise, the edge linking and tracking procedure will be employed. The procedure is shown in Fig. 5. Here, consider the value of the threshold (T) is 3. Fig. 4(c) shows the result of edge linking procedure. Finally, eliminate the edges whose consecutive edge length difference is greater than mean absolute deviation (MAD) i.e. $\frac{\sum_{i=1}^{N}|edge(i)-edge\_mean|}{N}$. After that, the edge image only holds the longest parallel HEs shown in Fig. 4(d). Assume the total number of the longest HE in the edge image is N.

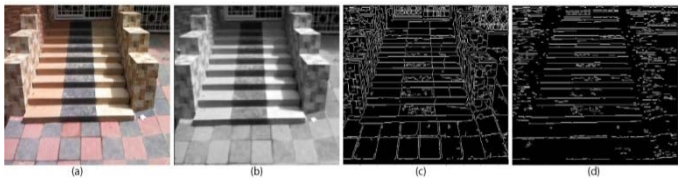

Fig. 3. Experimental example of extracting stairways edges: a) stairways image, b) Gabor filter image, c) Canny edge image, and d) HE image.

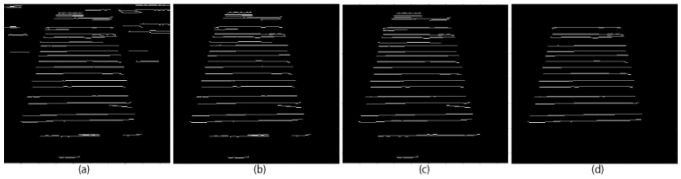

Fig. 4. Experimental example of non-interest edge elimination: a) removing vertical edges, b) filtering small edges, c) result of edge linking and tracking, and d) eliminating non-candidate edges.

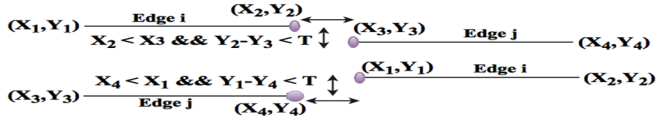

Fig. 5. Procedure of edge linking and tracking.

D. Detecting three connected points

This section describes the process of finding 3CP from stair edge image. For that, a unique geometrical property of stairways is employed in the edge image, i.e., every stairways step's horizontal edges two end points intersect with stairways steps width and height vertical edge point. This geometrical property is used in this section to validate the extracted stair horizontal edges. For that, Canny edge image is considered which contains the stair horizontal and vertical edges.

For finding the 3CPs, stairways step's width and height VEs are scanned at the two end points of the stairways HEs. However, stairways step's HEs and VEs are not all time exactly horizontal or vertical. For this reason, all time it is not possible to find the intersection points exactly at the end points of the stairways vertical or horizontal edges. The causes are shown in Fig. 6(a). For these problems, the 3CP is detected by a process. The process is shown in Fig. 6(b). The process is applied on the stair edge image to detect the 3CPs. The outcome of the 3CPs with the process is shown in Fig. 6(c).

According the process of detecting 3CPs, checking 3CPs at the one ends of the HE requires constant time, say, c. Hence, finding two 3CP at the two end points of a HE takes 2c time. Therefore, finding 3CPs for N HEs requires 2Nc time, i.e., time complexity arises about $O(N)$.

After detecting the 3CP successfully, the numbers of stair steps are determined. For that, N longest horizontal edges are used that are extracted in the previous section. The extracted HEs are considered as stairways steps HE, if the stairways steps with 3CP are 75% with respect to the N HEs. These N HEs are marked as a stairways candidate edge and used to confirm and detect the stairways region is shown in Fig. 7(a).

D. Justifying increasing horizontal edge segments

This section calculates the vertical VP from the extracted HEs that are validated by the 3CP. This VP distinguished the stairways step's HEs from other visually similar object as like rail-line or zebra-crossing. The stairways VP can be define as an intersection points with two straight lines passing through the three connected points on the right and left side of the horizontal edge segments respectively. Fig. 7(b) shows the procedure of calculating VP.

If the VP is determined from these horizontal parallel edges that are validated by the 3CPs, then these horizontal edges become smaller from bottom to top until these edges are converged. That means, these horizontal edges are appeared in sorted order. This is another natural and geometrical feature of the stair. This feature justifies the extracted increasing horizontal edge segments are from stair steps edge.

E. Verifying and detecting stair candidate region by VP

This section verifies the stairway's HE segments that are justified in the previous section. For that, VP's y coordinate value is checked as this value for any stairways the VP will be

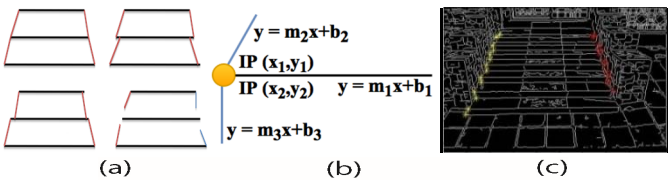

Fig. 6. Experimental example of 3CPs: a) variation of stairways step's width and height edges, b) process of detecting 3CPs, and c) detected 3CPs in the stairways edge image.

negative i.e. $y < 0$. And this y coordinate value will be resided to the range of $-ZIH \leq YCVP < 0$, here, ZIH is image height, $YCVP$ is stairways y coordinate value of the VP. If the VP of the stairways resides in the range of $-ZIH \leq YCVP < 0$, then the detected parallel horizontal edges are indicated as a stair steps edge. Otherwise, those edges may be indicated as a stairways similar visual object's edge as like rail-line and zebra-crossing. That is because the rail-line and zebra-crossing regions have the analogous feature as like stair. However, the VP of the rail-line and zebra-crossing is not imaginary i.e. positive.

In Fig. 8, extracts the rail-line and zebra-crossing step's HEs that are satisfied the property as like stairways HEs. However, the VP of these objects are (246.05, 85.03) and (224.52, 73.22) respectively that are represent in Fig. 8(e). The rail-line's and zebra-crossing's vanishing point's y coordinate value is 85.03 and 73.22. This y coordinate value distinguishes these images from stairways. The variation of the VP in the stair with respect to zebra-crossing and rail-line image is due to the physical structure of these images. The physical structure of these images is that the zebra-crossing and rail-line image does not have any slop with respect to the ground, where, stair is the opposite of the rail-line and zebra-crossing. The stairways region detected form stair image is shown in Fig. 9, where y coordinate of the vanishing point is -235. Stair detection region in the original image is shown in Fig. 9(b). Fig. 9(c) shows the final stair detection region.

Fig. 10 shows the experimental example of stairways sample images verified by VP. Those images are captured from the front side of the stairways. The camera that is used to capture the stairways images is placed at a suitable height from the ground that is not more than two meters. The camera and captured image distance must not be far away. The camera should be focused on the horizontal axis of the stair.

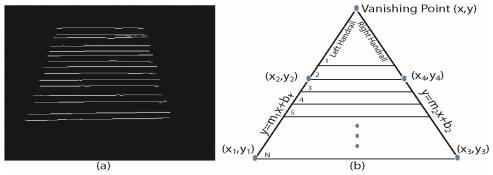

Fig. 7. Experimental example of detecting longest HEs and computing VP: a) arriving HEs in longest increasing order, and b) process of calculating vertical VP.

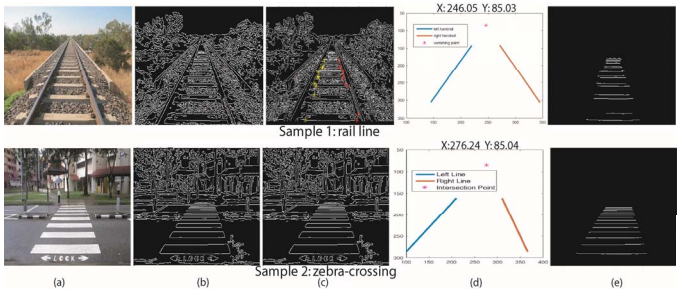

Fig. 8. Experimental example of stairways similar object: a) image, b) detected edges, c) 3CPs, d) VP with positive y coordinate value, and e) HEs in longest increasing order.

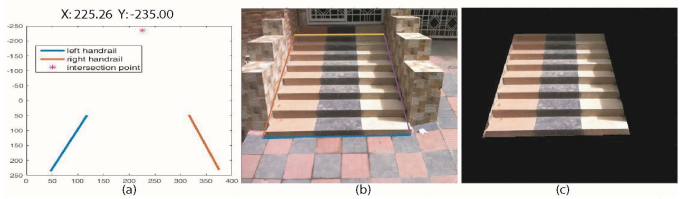

Fig. 9. Experimental example of stairways region detection: a) measuring VP, b) detected ROI in original image, and c) final detected stairways region.

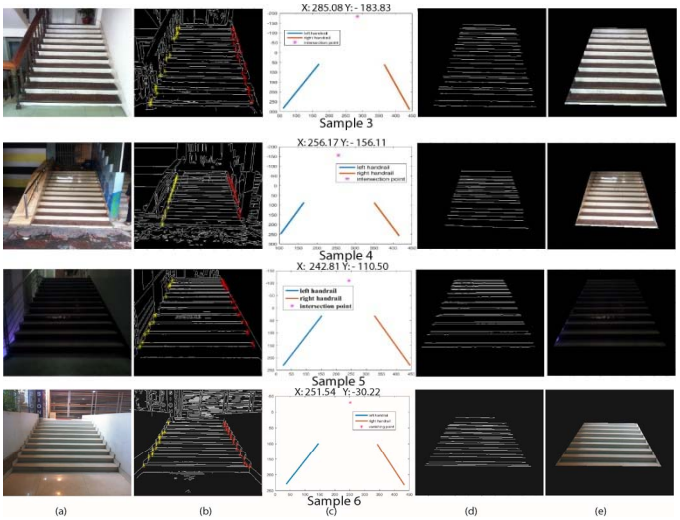

Fig. 10. Experimental example of stairways region detection: a) input stairways image, b) 3CP in edge image, c) vertical VP, d) arriving HEs in longest increasing order, and e) detected stairways region.

Fig. 10 shows the results of processing sample images that are verified by the vertical VP. The input sample image, processing 3CP, vertical VP, increasing HE, and the stair detection region are presented in Fig. 10(a), Fig. 10(b), Fig. 10(c), Fig. 10(d), and Fig. 10(e) respectively. The stairways sample 4 and stairways sample 6 are captured from indoor environment with noisy as well as low illumination conditions at different day times respectively. On the other hand, stair sample 5 and sample 7 are captured from outdoor environment at day and night time respectively. Where, sample 5 image's background is noisy and sample 7 is at the uneven illumination condition. The number of 3CP, measured vertical VP, and respective sample image's processing execution time are shown in the Table I.

G. Vanishing point's problem during stair region verification

This section investigates the problem of the VP that is occurred in the phase of the stair region verification. The problem is happened when the camera is not as closed as the stair horizontal axis and the slop of the stairways is low with respect to ground. Then, the VP of stairways will not be negative ($y > 0$) as well as will not remain within the range of $-2ZIH \leq YCVP < 0$. Since the calculated VP is not remain within the range, So the detected parallel HE segments of stairways certainly verified as a rail-line or zebra-crossing which is the wrong verification of stairways region as shown in Fig. 11.

TABLE I. 3CP, FALSE POSITIVE, FALSE NEGATIVE, VERTICAL VP AND RUN TIME OF STAIRWAYS SAMPLE IMAGES

Stair sample	Total HEs	Total 3CPs	3CPs (%)	Detection rate		Vertical VP	Run time (s)
				FP (%)	FN (%)		
3	24	21	87.50	0.00	2.00	(285.08,-183.83)	0.067
4	19	18	94.74	4.00	2.00	(256.17,-156.11)	0.064
5	23	18	78.26	2.00	3.00	(242.81,-110.50)	0.069
6	18	16	88.89	0.00	0.00	(251.54,-30.22)	0.067

* FP= False positive, FN= False negative

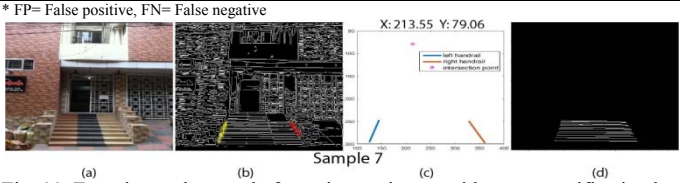

Fig. 11. Experimental example for stairways image with wrong verification by VP: a) input stair image, b) 3CPs, c) vertical VP with positive y coordinate value, and c) longest increasing HEs.

Fig. 12 shows the processing example of the same image of sample 6, however, this image is captured from front site of the stair where the camera is not as closed as the stair horizontal axis and the stair region is located at the bottom half of the captured image. And it is seem that the slop of the stair is low with respect to ground. The y coordinate of the VP of the stair sample 8 is 69.34 which is not imaginary ($y > 0$). In this type of situations the stairways regions are not verified by the VP's y coordinate value. The stairways sample 7 i.e. Fig. 11 and 8 i.e. Fig. 12 are satisfied the features of 3CP and concurrent HEs. However, they have the VP with positive y coordinate value. The total HE, 3CP, vertical VP, and processing time of sample image 7 and 8 i.e. Fig. 11 and Fig. 12 are shown in Table II.

Since the vanishing point does not distinguish the detected stair region from other similar looking objects such as zebra-crossing or rail-line. In this paper, the verification is performed by the support vector machine (SVM) classifier. Features are extracted by using the Gabor filters.

H. Feature extraction and classification

Selecting appropriate features is a vital issue in the recognition phase. The detected stair region of interest (ROI) is resized to 128x128 pixels. After that, features are extracted from the detected stair ROI by applying the Gobor filters. A 2−D Gabor filter is a Gaussian kernel function modulated by complex sinusoidal plane wave are defined in (1), (2), and (3).

In this work employs thirty-two Gabor filters in four scales and eight orientations. Since the image size is 128x128 pixels after employing the Gabor filter the feature vector will be 128x128x32=5,24,288. The down sampling is performed on the obtained feature vector to reduce its dimensionality. The feature vector is down sampled by a factor of 4. So, the size of the feature vector will be 6,55,360/(4x4) = 32,768. Still the size of the Gabor feature vector is large enough. The dimensionality reduction method is used to reduce the dimensionality of the feature vectors. The kernel principle component analysis (KPCA) [12] is employed in this paper for further reduction the dimension of the feature vectors. As the KPCA is kernel based method, its mapping depends on the kernel function such as linear, polynomial, and the Gaussian. In this paper, the Gaussian kernel is used. Finally, the features are classified by using the support vector machine (SVM)[13].

III. EXPERIMENTAL RESULTS

The experimental results of some stair images are explained in this section. All experiments were performed on the Intel(R) Xeon(R) CPU E31220@3.10GHZ processor with 4GB RAM. In this paper, the experiments were performed on 480x320 stairways images in MATLAB environments.

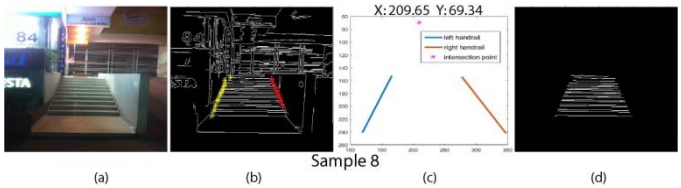

Fig. 12. Experimental example where stairways are not verified by VP: a) input stairways image, b) 3CPs, c) vertical VP and d) increasing HEs.

TABLE II. 3CP, VP, AND RUN TIME OF STAIRWAYS SAMPLE IMAGES

Stair sample	Total HE	Total 3CP	3CP (%)	Vertical VP	Run time (s)
7	12	11	91.67	(213.55,79.0	0.068
8	18	15	83.33	(209.65,69.3	0.067

The ROI of stair region is resized to a resolution of 128x128 pixels. In the experiments two dataset are considered, one for training dataset another for test dataset. The training and test dataset were used 135 and 112 stair images respectively with different types of indoor as well as outdoor stairways images. These images are captured from various environments with different illumination conditions, i.e., noisy, normal, and uneven to consider various types. Different illumination type's stairways images are shown in Fig. 13.

The detection accuracy of detecting stairways region is measured from different types of stairways images. Table III shows the detection accuracy of the candidate region of interest (ROI) with considering false positive and false negative result. False positive is a result that indicates a given condition has been fulfilled, when it actually has not been fulfilled. The false negative is a result that indicates a given condition should be fulfilled, when it actually has not been fulfilled. In our work, when system shows a portion of the stair, however, actually there is no stair in that place is a false positive. On the other hand, when system does not show a portion of the stair where the stair is actually existed is a false negative.

Table VI shows the stair ROI verification accuracy where the ROI is verified by the VP and SVM classifier. Table V shows the comparison of the proposed framework with [2], [4], and [11] for stair detection accuracy. In [4], the dynamic programming is used to find out the longest increasing subsequence of stair horizontal edges. This problem is solved in $O(n \log n)$ time. On the other hand, in this paper, the stair region is detected with the key feature of 3CP. The 3CPs are measured from the stair edge image with in $O(n)$ time, which is linear, where n is the number of horizontal parallel edges of stairways.

Fig. 13. Different types of stairways images: a) indoor stairways with uneven illumination, b) outdoor stairways with uneven illumination, and c) outdoor stairways image with noisy background.

TABLE III. STAIRWAYS ROI DETECTION ACCURACY AT DIFFERENT ENVIRONMENTAL CONDITIONS

Stair type	Environmental conditions	Total images	Detection error		Detection accuracy (%)
			False positive	False negative	
Indoor	Normal and uneven illumination	46	2.04%	1.88%	98.12
Outdoor	Normal and uneven illumination	66	3.15%	3.56%	96.44
	Average	**112**	**2.60%**	**2.72%**	**97.28**

TABLE IV. STAIR REGION VERIFICATION ACCURACY AT DIFFERENT ENVIRONMENTAL CONDITIONS BY VP AND SVM

Stair type	Total image	Correctly detected		Detection error VP		Detection accuracy (%)	
				VP	SVM		
		VP	SVM	FP	FP	VP	SVM
Indoor	46	45	46	2.18%	0.00%	97.82	100
Outdoor	66	64	65	3.03%	1.52%	96.97	98.48
	112	**109**	**111**	**2.60%**	**0.76%**	**97.40**	**99.24**

TABLE V. COMPARISON WITH RESPECT TO STAIRWAYS DETECTION ACCURACY AND AVERAGE RUN TIME

Method	Detection accuracy (%)	Avg. run time (s)
The proposed method with VP	97.40	0.066
The proposed method with SVM	99.24	0.063
[2]	97.16	0.200
[4]	96.15	0.085
[11]	93.83	0.149

V. CONCLUSIONS

A natural geometrical feature based stairways detection framework has been proposed in this paper. The key part of this paper is to investigate the problem of the vanishing point in the phase of the stairways region verification. This framework is important to improve the navigation activity of autonomous intelligent system in obscure environments. A group of stairways images were successfully tested by the proposed framework. The proposed framework detected stairways region of interest with an acceptable running time and accuracy of 0.066 (s) and 97.28% respectively. The experimental result also reveals that SVM classifier shows the better performance with respect to the vanishing point in the stairways region verification. The proposed framework can detect the traditional stair only. It is not provided satisfactory result for complex shapes stair such as spiral stair. Later, this framework will be updated for detecting spiral stair region.

References

[1] T. Schwarze, and Z. Zhong, "Stair detection and tracking from egocentric stereo vision," In 2015 IEEE International Conference on Image Processing (ICIP), September, pp. 2690-2694,IEEE, 2015.

[2] S. Wang, H. Pan, C. Zhang, and Y. Tian, "RGB-D image-based detection of stairs, pedestrian crosswalks and traffic signs," Journal of Visual Communication and Image Representation, Vol. 25, No.2, pp. 263-272, ELSEVIER, 2014.

[3] J. A. Delmerico, D. Baran, P. David, J. Ryde and J. J.Corso, "Ascending stairway modeling from dense depth imagery for traversability analysis," In 2013 IEEE International Conference on Robotics and Automation (ICRA), May, pp. 2283-2290, IEEE, 2013.

[4] K. Deb, S. T. Islam, K. Z. Sultana, and K. H. Jo, "Stairway Detection Based on Extraction of Longest Increasing Subsequence of Horizontal Edges and Vanishing Point," Contemporary Challenges and Solutions in Applied Artificial Intelligence, pp. 213-218, Springer, 2013.

[5] S. Shahrabadi, J. M. Rodrigues, and J. H. Du Buf, "Detection of indoor and outdoor stairs," Pattern Recognition and Image Analysis, pp. 847-854. Springer, 2013.

[6] D. C. Hernández, T. Kim, and K. H. Jo, "Stairway detection based on single camera by motion stereo," Modern Approaches in Applied Intelligence, pp. 338-347, Springer, 2011.

[7] G. F. McLean, and D. Kotturi, "Vanishing point detection by line clustering," IEEE Transactions on Pattern Analysis and Machine Intelligence, Vol. 17, No.11, pp. 1090–1095, 1995.

[8] S. Carbonara, and C. Guaragnella, "Efficient stairs detection algorithm Assisted navigation for vision impaired people," IEEE International Symposium on Innovations in Intelligent Systems and Applications (INISTA), pp. 313-318, June 2014.

[9] C. Zhong, Y. Zhuang, and W. Wang, "Stairway detection using Gabor filter and FFPG," International Conference of Soft Computing and Pattern Recognition (SoCPaR), pp. 578–582, October 2011.

[10] D. C. Hernández and K. H. Jo, "Stairway Segmentation Using Gabor Filter and Vanishing Point", IEEE International Conference on Mechatronics and Automation, pp. 1027-1032, 2011.

[11] D. C. Hern´andez, and K. H. Jo, "Outdoor Stairway Segmentation Using Vertical Vanishing Point and Directional Filter," International Forum on Strategic Technology, pp. 82-86, IEEE, October 2010.

[12] L.J.P. van der Maaten, E.O. Postma, and H.J. van den Herik, "Dimensionality Reduction: A Comparative Review. Tilburg University Technical Report", TiCC-TR 2009-005, 2009.

[13] Christopher J. C. Burges, "A tutorial on support vector machines for patten recognition," Data Mining and Knowledge Discovery, Vol. 2, pp.121-167, 1998.

Design of a Peripheral Interface Controller Based MPPT Charge Controller

Md Rokonuzzaman* and Md Hossam-E-Haider
Department of Electrical, Electronic and Communication Engineering (EECE)
Military Institute of Science and Technology (MIST), Mirpur Cantonment, Dhaka-1216
*ragib_isme@yahoo.com and haider8400@yahoo.com

Abstract— **This paper presents a smart charge controller (SCC) that can extract maximum power from solar panel and could make instant decision to protect the system. In the same time the designed controller can control high voltage disconnect (HVD)-reconnect, and low voltage disconnect (LVD)-reconnect. An improved maximum power point tracking (MPPT) is achieved through a Peripheral interface controller (PIC) based Perturb and Observe (P&O) algorithm. Additionally, light emitting diode (LED) used as indicator and a display is featured to show the system status. A blue-tooth device is used to work it as a data logger to monitor system status by smart phone or Laptop. Furthermore, this SCC is developed to increase the efficiency with low cost. Experimented highest efficiency 99% is recorded within the cost of BDT 2050 taka only.**

Keywords- smart charge controller (SCC), P & O algorithm, MPPT technique, PIC microcontroller .

I. INTRODUCTION

A photo-voltaic (PV) array under uniform irradiance exhibits a current-voltage characteristic with a unique maximum power point (MPP) which depends on array temperature and solar insulation irradiance [1]. So, to harness maximize energy from solar panel, it is essential to constantly track the MPP of the solar array. Last few years, research has concentrated on various MPP control algorithms to draw the maximum power of the solar array. Among them, perturb and observe (P&O) [2], incremental conductance (INC) [3], constant voltage (CV) [4], short current pulse [5], fuzzy logic control (FLC) [6], artificial neural network (ANN) [7] and some other techniques [8] have drawn attention due to the usefulness of each system. Due to low state of charge (SOC) of battery and solar panel are in cool, MPPT devices have greater benefits. For example, with typical PV module maximum power point around 17 V and low state-of-charge battery voltage at around 12 V, the potential power gain from MPPT was stated to be about 30% [1]. Whereas energy gains with hot PV modules and fully charged batteries are minimal or negative. Studies show that the life time of the battery is degraded without using charge controller. Therefore, an intelligent charge controller should be designed to prolong the battery's life time and stabilize the voltage from photovoltaic panel [9]. In this paper a charge controller is designed and developed at low cost based on PlC16F877A microcontroller as a control unit, ensuring higher efficiency on maximum power extracting and smart facilities like data logging, electronic device charging unit and remote monitoring system.

II. DESIGNED SYSTEM

In this system, for charge control and data acquisition operation PlC16F877A microcontroller is used. PlC16F877A contains five input/output (I/O) ports. Five ports are denoted by A to E. Port A is used to perform the analog to digital conversion which is used in input parts like temperature sensing circuit, battery voltage sensing circuit and current sensing circuit. Port B is used to interface with the Liquid crystal display (LCD) module whereas port C controls disconnect or reconnect operations for photovoltaic panel or load. Port D is used as input part for switching control and as output part for LED indicator. ACS712-20A current sensor is used to sense the current and a voltage divider circuit is used to sense the voltage. Current, voltage and temperature sensing unit is operated as input parts. PIC microcontroller analyzed inputted data from sensing unit and will exploit the system according to the program installed inside its memory. 'Micro C' software is used to execute the installed programming code. Output part consists: battery and load, LCD module and an indicator circuit. Circuit power at 5V is derived from a 78L05 voltage regulator connected to the battery. An LM35 temperature sensor sensed the ambient temperature. Two power IRFZ44N MOSFETs are used as solid-state switch for the panel-battery line and battery-load line. Three different LEDs of color green, blue and red are used to indicate the system status. Table I. shows the special feature that is the reason to use PlC16F877A. Electrical specification of SM-85KSM solar panel that is used for field test is mentioned in Table II. The developed specification against the older version of charge controller and specific uses of the proposed features are depicted in Table III.

TABLE I. FEATURES OF PlC16F877A

Pin	Program Memory	Data (SRAM)	EEPROM (Bytes)	I/O	CCP (PWM)
40	14.3K	368	258	33	2

TABLE II. ELECTRICAL SPECIFICATION OF SM-85KSM PANEL

Name	Rating
Maximum power	85W
Maximum voltage	17.35V
Maximum current	5.20A
Open circuit voltage, V_{oc}	19.7V
Short circuit current, I_{sc}	5.90A
Operating temperature	-40 $°C$ to +85 $°C$

978-1-5090-5785-6/16/$31.00 ©2016 IEEE

TABLE III. FEATURES OF THE DESIGNED CHARGE CONTROLLER

Feature	Model/Rating	Specification
Solar Panel	85W	Input source
Battery	12V-100Ah	Storage, Load
Microcontroller	PIC16F877A	Control unit
Current sensor	ACS712–20A	Protect over current flow
Buck converter	Self designed	
Charging	---	MPPT
MOSFET driver	IR2104	Provides proper switching
Blue-tooth device	ESP8266	Data logging
USB connector	USB 2 (480 Mbit/s)	External device charging
Display	DIS-00014 (20 × 4)	System status

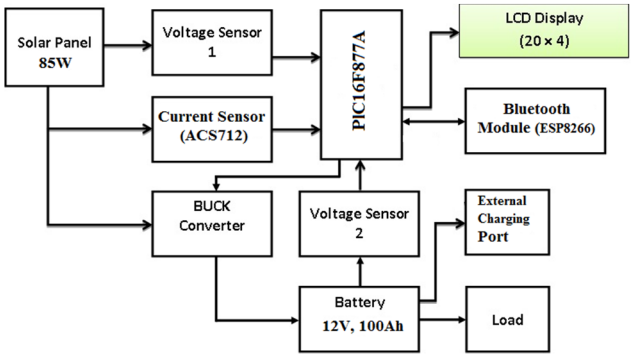

Fig. 1. Block diagram of the proposed solar charge controller

A. *Component Selection*

Fig. 1 shows block diagram of the designed charge controller. Three part of the charge controller are source, control and storage unit. 85W solar panel as source and 12V-100Ah lead acid type rechargeable battery is used as storage unit. Loads are connected through storage unit but due to full charge at available sun light panel is directly connected to the load. Panel voltage is fed to the voltage and current sensor, parallel to the buck converter circuit. At first the voltage converts analog to digital output for the control unit PIC16F877A. This controller controls both the source and load portion. Voltage divider circuit used as a voltage sensor which will sense the voltage and output is given to the microcontroller. ACS712-20A current sensor is able to sense maximum 20A current. Buck converter is designed for this proposed charge controller and it can minimize the panel voltage to the charging voltage level of the battery. Bluetooth module ESP8266 is used for data logging. An external device charging unit is connected from the battery to charge different electronic device like mobile phone, laptop etc.

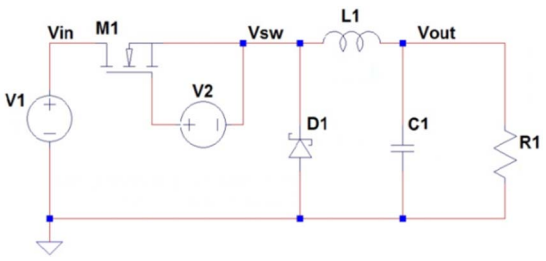

Fig. 2. Schematic diagram of a Buck converter

A buck converter circuit is used to convert panel voltage to load voltage. Since the panel voltage is always higher than the load voltage at day time. The simulated circuit diagram of a buck converter is shown in Fig. 2. Simulation has been executed by LTspice IV software. IRFZ44N MOSFET, an inductor and a capacitor with a load is used. When the MOSFET is ON, current will flow the inductor, load and output capacitor. Since the diode is reversed biased thus no current will flow through the diode. In this state magnetic energy will store in the inductor and electrical energy in the capacitor. When, this MOSFET is off stored energy in the inductor released and current complete its path through the diode and in the same time stored energy of capacitor will supply to the load and will control the current flow. LCD display with 20×4 is used to continuous monitor the panel and battery voltage, load condition with pulse width modulation (PWM). Finally a Bluetooth module is used to get all data from system to a smart phone or laptop.

a. *Inductor Selection for Buck Converter*

To design the buck converter some parameters are lifted from data sheet to calculate the inductance.

Input voltage, $V_{in} = 19.7$ V

Output voltage, $V_{out} = 12$ V

Output current, $I_{out} = \frac{\text{Panel power}}{\text{Output voltage } (V_{out})} = \frac{85\text{ W}}{12\text{ V}} = 7.08$ A

Switching frequency, $F_s = 50$ kHz

Duty Cycle, $D = \frac{V_{out}}{V_{in} \times \eta} = \frac{12\ V}{19.7\ V \times .9} = 0.68\ or\ 68\%$

Where, $\eta =$ efficiency of the converter, estimated 90% [10].

$$\text{Now, Inductor, } L = (V_{in} - V_{out}) \times D \times \frac{1}{F_s} \times \frac{1}{\Delta I_L} \quad (1)$$

Where, $\Delta I_L =$ Inductor ripple current

A good estimation for the inductor ripple current is 20% to 40% of the output current [10].

Let,

$\Delta I_L = 40\%$ of the rated current

$= 40\%$ of 7.08 A

$= 2.83$ A

Now, from equation (1),

$$L = (V_{in} - V_{out}) \times D \times \frac{1}{F_s} \times \frac{1}{\Delta I_L}$$

$$= (19.7 - 12) \times 0.61 \times \frac{1}{50{,}000} \times \frac{1}{2.83}$$

$= 0.033$ mH

$= 33.2$ µH

If $I_L = average\ inductor\ current$, then the inductor ripple current $\Delta I_L = 2I_L$[11].

Inductor peak current $= I_{out} + \frac{\Delta I_L}{2} = 7.08 + \frac{2.83}{2} = 8.5$ A

b. *Capacitor Selection for Buck Converter*

The output of buck converter has small amount of ripple voltages. Capacitor or the filter circuit is used to minimize the voltage overshoot and ripple.

Output Capacitance,

$$C_{out} = \frac{\Delta I_L}{8 \times F_S \times \Delta V_{out}} \quad (2)$$

Where, Inductor ripple current, $\Delta I_L = 2.83$ A
Switching frequency, $F_s = 50$ kHz
Let,
Output voltage ripple, $\Delta V_{out} = 20\ mV$
Now, from equation (2),

$$C_{out} = \frac{\Delta I_L}{8 \times F_s \times \Delta V_{out}}$$
$$= \frac{2.83}{8 \times 50000 \times 0.02}$$
$$= 353.75\ \mu F$$

By taking some margin, $470\ \mu F$ electrolytic capacitor are used.

c. *MOSFET selection for buck converter*

IRFZ44N MOSFET is used for better switching. Since it has very low amount of voltage drop it increases the total efficiency of the system. Voltage rating of this solid state device is greater than 20% of rated voltage. Current rating is greater than 20% of rated current. It has minimum conduction loss. IR2104 MOSFET driver is used that accept low power input from the microcontroller and produces a high current drive input for the gate of the MOSFETs. Fig. 3 shows the input voltage of MOSFETs and charging state of the battery. Red colored square pulse from the panel is almost 17 volt and the green colored curve is the charging state that is 12 volt. Theoretically, 68% duty cycle is enough to fulfill system requirement. Here, more than 68% duty cycle is used to justify the losses and to increase the efficiency of the system.

III. HARDWARE DESIGN

Fig. 4 shows field testing setup bench of the designed charge controller. System consist a 12 volt lead acid battery, four analog volts and ammeter meter, one digital multimeter, one digital oscilloscope, a display, external device universal serial bus (USB) charging unit. Oscilloscopes are displaying the wave shape of duty cycle and charging state of the battery. Multimeter displayed the converted boost voltage of solar panel.

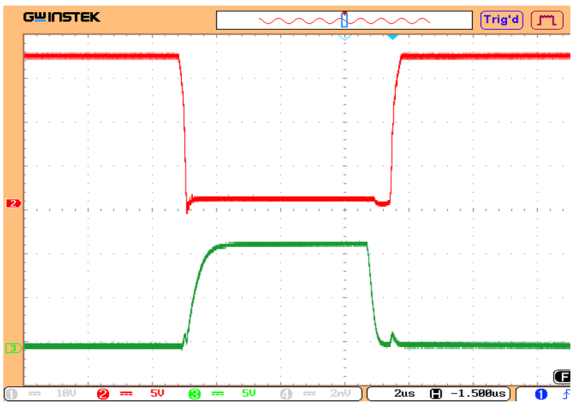

Fig. 3. Input voltage of MOSFET and charging state of battery

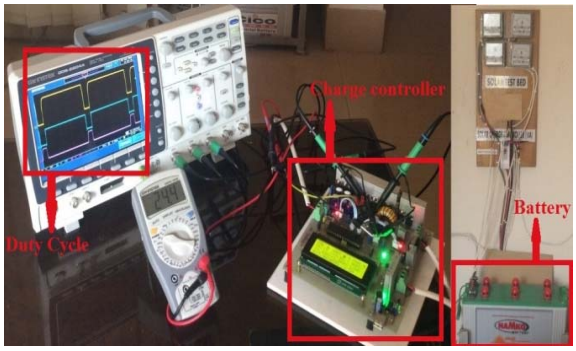

Fig. 4. Field testing setup bench

Three columns of data can visualize on display. First column shows the solar panel voltage, current and power condition. Second column shows the battery voltage, current and charging state condition. Third column shows pulse width status with load on or off condition. The same status is directly transferable to a handset or laptop through the Bluetooth device. This will be helpful to maintain or observe the system from customer end.

A. *Testing Results*

Table IV. Showing the experimental data of designed solar charge controller. Data of the panel and battery voltage, current, and power are taken respectively and values are recorded from 8.55AM to 5.00PM. From this tested value the overall efficiency of the charge controller is determined. Fig. 5 shows the efficiency recorded from the designed charge controller. In the beginning of the day at 8.55 AM panel power was 22.75W, battery power was 22.18W and charge controller efficiency was 97.47%. At the end of the day, at 5.00PM panel and battery power is recorded 6.25W and 6.02W respectively, and the efficiency measured 96.24%. Experiment shows that the efficiency level is almost over than 95%. It is also evident that due to low sunlight does not affect the efficiency of the CC and it works properly. Additionally, reverse power protection also works good due to night or less sunlight. In the same time, excessive current flow due to over load system is protects perfectly, due to low voltage control unit disconnect the load side as well as protect due to over voltage.

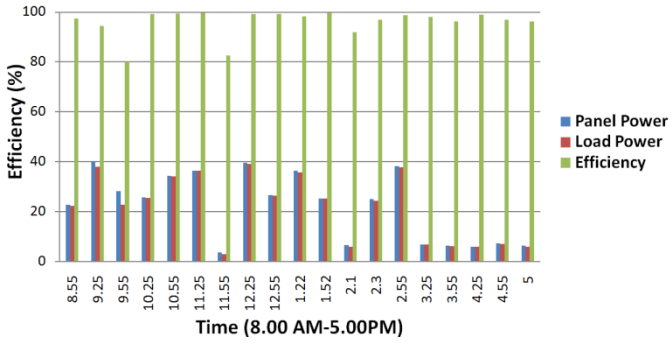

Fig. 5. Efficiency of the charge controller

TABLE IV.
EXPERIMENTAL DATA WITH EFFICIENCY OF THE DESIGNED CHARGE CONTROLLER

Sr. No	Time	Panel			Load			Efficiency (%)
		Voltage (V)	Current (A)	Power (W)	Voltage (V)	Current (A)	Power (W)	
1	08.55AM	14.4	1.58	22.75	12.6	1.76	22.18	97.47
2	09.25AM	13.9	2.89	40.17	13.4	2.83	37.92	94.40
3	09.55AM	14.2	1.99	28.26	13.0	1.74	22.62	80.05
4	10.25AM	13.6	1.89	25.70	13.3	1.92	25.54	99.35
5	10.55AM	14.0	2.45	34.30	13.6	2.51	34.14	99.52
6	11.25AM	14.1	2.58	36.39	13.9	2.61	36.27	99.73
7	11.55AM	14.2	0.26	03.69	12.2	0.25	03.05	82.61
8	12.25PM	14.2	2.78	39.48	13.9	2.82	39.19	99.30
9	12.55PM	13.8	1.92	26.49	13.5	1.95	26.33	99.35
10	01.22PM	14.0	2.59	36.26	14.1	2.53	35.68	98.38
11	01.52PM	14.3	1.77	25.31	13.5	1.87	25.25	99.74
12	02.10PM	13.9	0.47	06.53	12.8	0.47	06.02	92.09
13	02.30PM	14.0	1.79	25.06	13.5	1.80	24.30	96.97
14	02.55PM	14.5	2.64	38.28	14.1	2.68	37.78	98.71
15	03.25PM	13.4	0.51	06.83	12.9	0.52	06.71	98.16
16	04.00PM	13.4	0.47	06.29	12.9	0.47	06.06	96.27
17	04.25PM	13.3	0.45	05.98	12.9	0.46	05.93	99.15
18	04.55PM	13.3	0.55	07.32	12.9	0.55	07.09	96.99
19	05.00PM	13.3	0.47	06.25	12.8	0.47	06.02	96.24
	Average							**96.03**

IV. CONCLUSION

The most significant feature of this proposed design is the customized control on programming for the PIC microcontroller that can take any instant decision to protect the system from overcharge, low charge, high voltage disconnect, low voltage disconnect, and short circuit current. Data logging system provides the facility to analyze any certain time data. This feature also allows the user not only remotely monitor the status of the system but also record and store data. External device charging unit makes the system more feasible for remote areas customer. Experimental data shows the highest efficiency of the designed solar charge controller is 99% in some specific time, average efficiency is 96.03%, which is fully satisfy the Technical Standards Committee (TSC) of Infrastructure Development Company Limited (IDCOL), Bangladesh.

ACKNOWLEDGMENT

This work has been supported by Research and Development (R&D) fund of Military Institute of Science and Technology (MIST), Mirpur Cantonment, Dhaka-1216.

REFERENCES

[1] G. Barca, A. Moschetto, C. Sapuppo, G. M. Tina, and R. Giusto, A. D. Grasso, "A novel MPPT charge regulator for a photovoltaic stand-alone telecommunication system." International Symposium on Power Electronics, Electrical Drives, Automation and Motion, (SPEEDAM), IEEE, 2008.

[2] N. Femia, D. Granozio, G. Petrone, G. Spaguuolo, M. Vitelli, "Optimized one-cycle control in Photovoltaic grid connected applications", IEEE Trans. Aerosp. Electron. Syst., vol. 2, no. 3, Jul 2006.

[3] Kok Soon Tey and Saad Mekhilef, "Modified incremental conductance algorithm for Photovoltaic system under partial shading conditions and load variation", IEEE Transactions on Industrial Electronics, Vol. 61, No. 10, Oct 2014.

[4] G. J. Yu, Y. S. Jung, J. Y. Choi, I. Choy, J. H. Song and G. S. Kim, "A novel two-mode MPPT control algorithm based on comparative study of existing algorithms", Solar Energy, vol. 76, pp. 455–463, 2004.

[5] T. Noguchi, S. Togashi and R. Nakamoto, "Short-current pulse-based maximum-power-point tracking method for multiple Photovoltaic-and-converter module system", IEEE Trans. Ind. Electron., vol. 49, no.1, pp. 217-223, 2002.

[6] R. B. Roy, E. Basher, R. Yasmin, and M. Rokonuzzaman, "Fuzzy logic based mppt approach in a grid connected photovoltaic system," in 8th International Conference on Software, Knowledge, Information Management and Applications (SKIMA 2014). IEEE, 2014, pp. 1–6.

[7] Whei-Min Lin, Chih-Ming Hong and Chiung-Hsing Chen, "Neural-network-based MPPT control of a stand-alone hybrid power generation system", IEEE Trans on Power Electronics, vol. 26, no. 12, Dec 2011.

[8] Ali Nasr Allah Ali, Mohammed H. Saied, M. Z. Mostafa , T. M. Abdel- Moneim, "A survey of maximum PPT techniques of PV systems", 2012 IEEE Energytech-Cleveland, OH, USA pp. 1-17, 29-31 May 2012.

[9] Amin, Nowshad, Lam Zi Yi, and Kamaruzzaman Sopian. "Microcontroller based smart charge controller for standalone solar photovoltaic power systems." 34th IEEE Photovoltaic Specialists Conference (PVSC), 2009.

[10] Brigitte Hauke,. "Basic calculation of a buck converter's power stage." Texas Instruments, Dallas, Texas, Tech. Rep. SLVA477, 2011

[11] Muhammad H. Rashid, "Power electronics: circuits, devices, and applications", Pearson Education India, 2009.

International Conference on Electrical, Computer & Telecommunication Engineering (ICECTE)
8-10 December 2016, Rajshahi-6204, Bangladesh

A Comparative Performance Analysis of CdS and In_2S_3 Buffer Layer in CIGS Solar Cell

Mohammad Sijanur Rahaman Robin* and Md. Mizanur Rahaman**

*Department of Electrical and Electronic Engineering
International Islamic University Chittagong
Chittagong-4314, Bangladesh
E-mail: sijan.robin24@gmail.com

**Department of Electrical Engineering
Lakehead University, Thunder Bay, ON, Canada
E-mail: mrahman8@lakeheadu.ca

***Abstract*— Thin-film solar cells (TFSCs) have the potential to reach cost effective photovoltaic generated electricity. Cadmium Sulfide (CdS) and Indium Sulfide (In_2S_3) buffer layer based Copper Indium Gallium Selenide (CIGS) solar cell offers higher efficiency with low manufacturing cost. Therefore, this paper presents a comparative study between CdS and In_2S_3 buffer layer based CIGS solar cell. The numerical study has been performed using a Solar Cell Capacitance Simulator named SCAPS-1D. The performance of CIGS solar cell is observed by adjusting the buffer layer thickness of both CdS and In_2S_3. The efficiency of CdS/CIGS solar cell is found 25.56% that is higher than the efficiency of In_2S_3/CIGS (24.41%) solar cell for 50 nm buffer layer thickness. It is also found that, the increase in buffer layer thickness from the optimum level degrades the performance of CdS/CIGS solar cell as compared to In_2S_3/CIGS solar cell. Therefore, In_2S_3 based CIGS cell could be an ideal candidate as a substitute of toxic CdS buffer layer based CIGS solar cell.**

Keywords—Thin-film solar cell, buffer layer, CdS, In_2S_3, efficiency.

I. INTRODUCTION

Due to dramatic growing trend of world's energy consumption, the attention towards the use of renewable energy like solar cell is increasing over the years. Thin-film solar cells (TFSCs) are cost-effective, reliable and offer simple fabrication techniques [1]. A copper indium gallium selenide (CIGS) solar cell is one of the mainstream thin-film photo-voltaic technology which offers high absorption coefficient, therefore a much thinner film is required than of other semiconductor materials. Among other thin-film technologies, CIGS is a versatile material and its band gap can be tuned by associating copper indium diselenide (CIS) with copper gallium diselenide (CGS) which results ($CuIn_{1-x}Ga_xSe_2$) CIGS [2]. The laboratory CIGS solar cell efficiency is reported 21% by "solibro", 21.7% by "solar energy and hydrogen research" and highest 22.3% efficiency is reported by "solar frontier" [3-5].

CdTe is also an excellent material where more than 14 deposition techniques are used in the grown-up process of the material. CdTe has energy band gap of 1.5 eV which offers high solar spectrum absorption capability and higher carrier mobility [6]. Researchers reported maximum efficiency of 21% in CdTe solar cell but commercially available CdTe are F-doped SnO_2 (FTO) coated glass substrates which exhibits lower efficiency. Therefore, it is important to develop the fabrication process to improve the performance of CdTe thin-film solar cells [7].

Commercially available CIGS solar cells are made of various materials, but among them cadmium sulfide (CdS) buffer layer based solar cell offers various advantages such as relatively, low cost, highly efficient and availability of cellular materials. CdS is considered as the first choice to use as a buffer layer in CIGS solar cell [8]. CdS is a compound material having energy band gap of 2.42 eV. However, CdS and CdTe comprises of toxic material cadmium (Cd), hence, the use of it can guide us to health and environmental hazards [9]. In fabrication process, CdS requires wet chemical methods while other layers in CIGS require dry chemical method. This incompatible fabrication requirement leads to complexity in fabrication process of CdS [10].

Various substitutes have been taken into account as a substitute of CdS buffer layer i.e. Zinc Sulfide (ZnS), Zinc Selenide (ZnSe), Zinc Oxide (ZnO) and Indium Sulfide (In_2S_3) etc. Among the other materials, In_2S_3 is considered as an ideal substitute for toxic CdS buffer layer due to its stability, wider band gap (2.1 to 2.9 eV) and photoconductive behavior. Therefore, this In_2S_3 material not only eliminates toxic cadmium but also improve light transmission having band gap wider than that of CdS [11]. The band gap of In_2S_3 can also be increased by partially doping with oxygen or sodium [12]. The highest efficiency of In_2S_3/CIGS solar cell is reported 16.4% by Atomic Layer Deposition (ALD) process [13]. Moreover, efficiency is obtained 15.7% by Chemical Bath Deposition (CBD) process and 14.8% through evaporation technique [14]. In [15] authors reported efficiency of 19.23% with In_2S_3 based CIGS solar cell.

Therefore, this paper presents a comparative study between CdS and In_2S_3 buffer layer based CIGS solar cell. Comparative study shows that In_2S_3 can be an ideal candidate as a buffer layer of CIGS solar cell as compared to CdS/CIGS solar cell. The best possible performance of In_2S_3/CIGS solar cell is found at a band gap of 2.7 eV with optimum offer layer thickness of 50 nm. It is found that the performance of CdS/CIGS solar cell degrades with the increase of buffer layer thickness from optimum level.

II. METHODOLOGY

A. CIGS cell structure and model parameters

The schematic diagram of CdS/In_2S_3 buffer layer based CIGS solar cell is shown in Fig.1. In the solar cell configuration, a bi-layer of ZnO is used as a window layer which comprises of ZnO:Al (Aluminum doped ZnO) and i-ZnO (intrinsic Zinc-Oxide) [16]. ZnO which is used as front contact has a long range of photon transmission capability compared to other materials. CdS/ In_2S_3 is used as a buffer layer in CIGS solar cell to establish p-n junction with absorber layer which is fabricated between window and CIGS absorber layer. The band gap of CIGS absorber layer can be can be tuned with the variation of In and Ga ratio. Tuning in the absorber layer allows maximum incident sunlight absorption near to the p-n hetero-junction which results lower CIGS absorption layer compared to traditional solar cells. As molybdenum (Mo) shows constancy with processing temperature therefore it is considered ideal for back contact with metal work function of 4.95 eV [17]. Back contact collects carrier from the absorber layer and its thickness varies with the requirement of resistance of solar cell. SLG (soda-lime glass) is a good choice as substrate which determines the flexibility and rigidity of the cell. Glass is widely used as a substrate due to its low cost and ability to withstand corrosion.

.

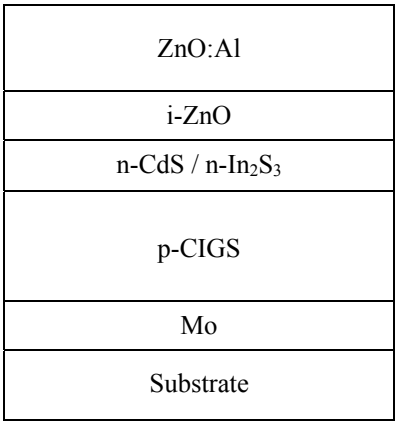

Fig.1: Simulated diagram of n-CdS / n-In_2S_3 based CIGS solar cell.

Process parameters are optimized and results are examined without the fabrication process in numerical analysis. The performance of CdS and In_2S_3 buffer layer based solar cell is carried out in simulation environment using Solar Cell Capacitance Simulator (SCAPS-ID) with the latest version (3.0.0.2) which was developed at the University of Gent [18-19]. Table-I shows the parameters used in the simulation environment for CdS/In_2S_3 solar cell. The CdS and In_2S_3 buffer layer based CIGS solar cell is simulated to observe the AC and DC characteristics of the cell before fabrication. Electrical parameters are extracted using the current density vs voltage curve of solar cell. During the analysis stage, solar cell temperature is used 300 K. Base parameters sign and symbol is shown in the Table-II.

TABLE- I
Layer properties of CIGS solar cell

Layer properties					
Layer	ZnO:Al	i-ZnO	n-CdS	n-In_2S_3	p-CIGS
Thickness (nm)	200	50	50-200	50-200	2000
E_g (eV)	3.3	3.3	2.4	2.1-2.9	1.15
χ_e (eV)	4.45	4.45	4.2	4.65-3.85	4.20
$\acute{\varepsilon}_r$	9	9	10	13.5	13.6
N_c (cm^{-3})	2.20×10^{18}	2.20×10^{18}	2.20×10^{18}	1.80×10^{19}	2.20×10^{18}
N_v (cm^{-3})	1.80×10^{19}	1.80×10^{19}	1.80×10^{19}	4.00×10^{13}	1.80×10^{19}
μ_e (cm^2/Vs)	100	100	100	400	100
μ_h (cm^2/Vs)	31	31	25	210	25
N_D (cm^{-3})	1.00×10^{20}	1.00×10^{18}	5.00×10^{17}	1.00×10^{18}	0
N_A (cm^{-3})	0	0	0	10	2.00×10^{18}
Defects properties					
Parameter	ZnO:Al	i-ZnO	n-CdS	n-In_2S_3	p-CIGS
Energetic distribution	Gaussian	Gaussian	Gaussian	Gaussian	Gaussian
Type	Donor	Donor	Acceptor	Acceptor	Donor
σ_n	1.00×10^{-15}	1.00×10^{-15}	1.00×10^{-15}	1.00×10^{-15}	5.00×10^{-17}
σ_p	5.00×10^{-13}	5.00×10^{-13}	5.00×10^{-13}	5.00×10^{-13}	1.00×10^{-13}
Interface properties					
Interface		CIGS/CdS or In_2S_3		CdS or In_2S_3/i-ZnO	
Defect type		Acceptor		Acceptor	
σn		1.00×10^{-14}		1.00×10^{-15}	
σp		1.00×10^{-14}		1.00×10^{-15}	

TABLE- II
Base parameters sign and symbols

Overall properties	
Bandgap	E_g
Electron affinity	χ_e
Dielectric relative permittivity	$\acute{\varepsilon}_r$
Conduction band effective density	N_c
Valence band effective density	N_v
Electron mobility	μ_e
Hole mobility	μ_h
Donor density	N_D
Acceptor density	N_A
Capture cross section of electrons	σ_n
Capture cross section of holes	σ_p
Surface recombination velocity of electron	SN_0
Surface recombination velocity of hole	SP_0
Metal work function	ϕ_m

III. RESULTS AND DISCUSSIONS

A. In_2S_3 band gap Optimization

The variation of open circuit voltage (V_{oc}) and short circuit current density (J_{sc}) is carried out increasing the band gap of In_2S_3 buffer layer from 2.1 to 2.9 eV. It is clearly seen from Fig. 2 that, V_{oc} increases sharply with band gap while J_{sc} increases up to 2.4 eV and afterwards decreases up to 2.6 eV. Then, after 2.6 eV band gap, J_{sc} increases and reaches the peak value at 2.8 eV. However, it drops again at 2.9 eV as shown in Fig. 2. Due to rise in the band gap in n-type region, results in the increase of number of photons to be absorbed in absorber layer. As a result, efficiency increases with band gap and nearly plateaued from 2.4 eV to 2.7 eV as shown in Fig. 3.

The optimum efficiency is found 24.41% at a band gap of 2.7 eV. Afterwards, efficiency decreases with the increase in band gap and it declines sharply at 2.9 eV. Fill factor (FF) also follows the rise-fall pattern of efficiency.

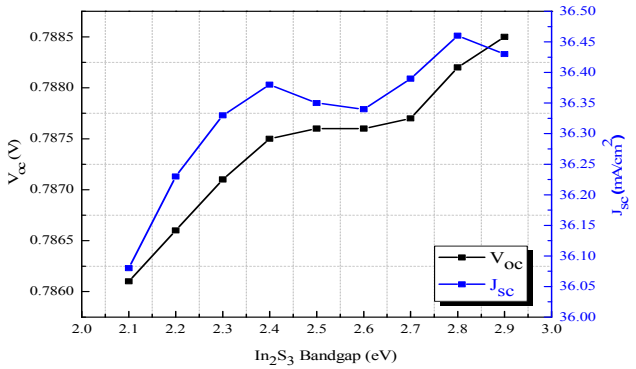

Fig. 2: Open circuit voltage and short circuit current density with In_2S_3 band gap variation.

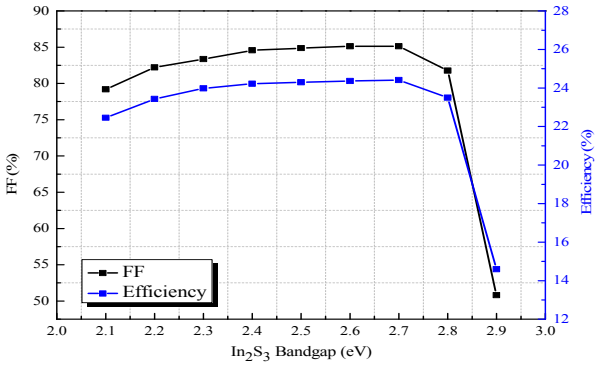

Fig. 3: Fill factor and efficiency with In_2S_3 band gap variation.

B. *Effect of Buffer layer thickness*

1) *Short Circuit Current Density* (J_{sc})*:* The CIGS solar cell performance is verified by increasing the CdS and In_2S_3 buffer layer thickness from 50 to 200 nm which is shown in Fig. 4. It is seen from Fig. 4 that, the highest J_{sc} of CdS/CIGS is found 38.41 mA/cm^2 at 50 nm while 36.39 mA/cm^2 for In_2S_3/CIGS solar cell for same buffer layer thickness. It is also seen that, J_{sc} of CdS/CIGS decreases swiftly whereas J_{sc} of In_2S_3/CIGS decreases slowly with the increase in buffer layer thickness. This happens because when buffer layer thickness increases more photons absorbed in the layer. Hence it reduces the number of photons to reach the absorber layer.

2) *Open Circuit Voltage* (V_{oc})*:* Open circuit voltage (V_{oc}) of CdS/CIGS solar cell decreases sharply with the increase of buffer layer thickness while exhibits downward trend for In_2S_3/CIGS solar cell as shown in Fig. 5. For buffer layer thickness of 50 to 100 nm, CdS layer has higher V_{oc} than In_2S_3.

3) *Fill Factor* (FF)*:* With the increase in buffer layer thickness from 50 to 200 nm, fill factor increases in a linear manner for CdS/CIGS solar cell whereas it increases slightly for In_2S_3/CIGS solar cell as shown in Fig. 6. Resulting fill factor can be considered as almost constant with further increment in In_2S_3 buffer layer thickness.

4) *Efficiency:* The effects of efficiency with buffer layer variation are shown in Fig. 7. If buffer layer thickness is increased, more photons are absorbed in this layer which results fall in efficiency. There is a noticeable decrease in efficiency for CdS/CIGS solar cell with buffer layer thickness increment and efficiency peaks of 25.56% at 50 nm thickness and it drops to 24.5% and 23.44% respectively at 100 nm and 200 nm thickness.

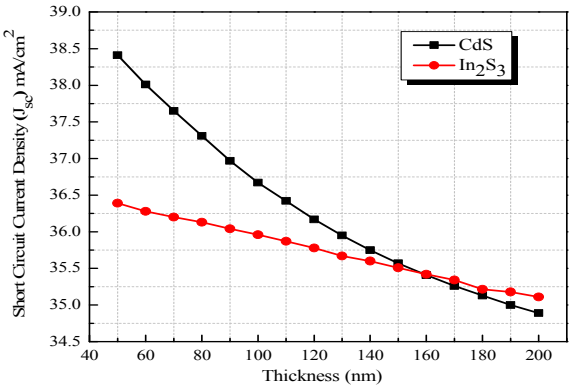

Fig. 4: Short circuit current density versus thickness variation of CdS and In_2S_3 buffer layer.

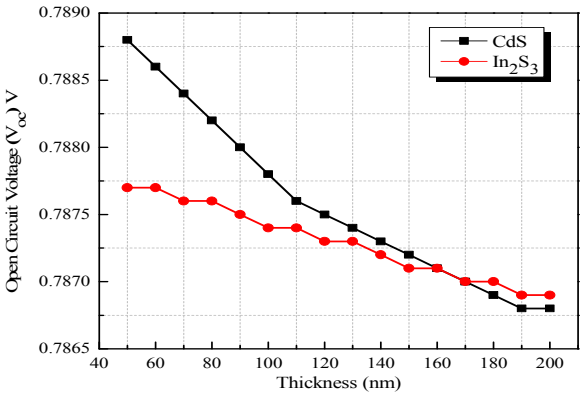

Fig. 5: Open circuit voltage versus thickness variation of CdS and In_2S_3 buffer layer.

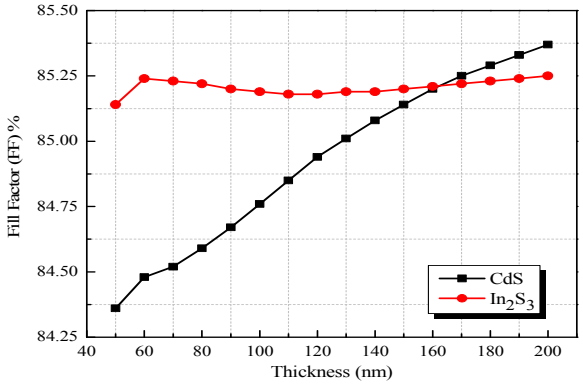

Fig. 6: Fill factor versus thickness variation of CdS and In_2S_3 buffer layer.

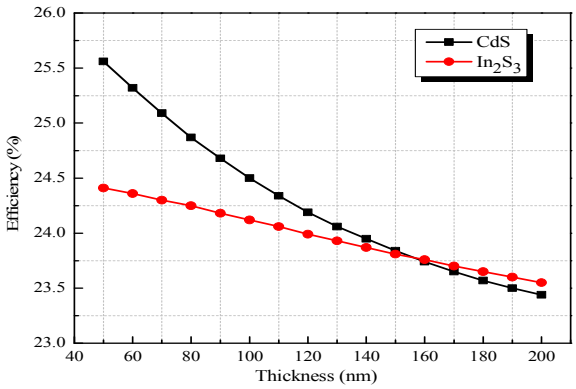

Fig. 7: Efficiency versus thickness variation of CdS and In_2S_3 buffer layer.

In case of In_2S_3/CIGS solar cell, efficiency decreases gradually with buffer layer thickness increment. The efficiency is 24.41% at 50 nm and falls to 23.55% at 200 nm. However, better efficiency is observed in In_2S_3/CIGS solar cell than CdS/CIGS for 170 to 200 nm buffer layer thickness. A comparison in solar cell electrical performance with 50 nm and 60 nm buffer layer thickness for both buffer layers is shown in TABLE-III.

TABLE -III
Electrical performance of solar cell with 50 and 60 nm buffer layer thickness

	Thickness (nm)	**V_{oc} (V)**	**J_{sc} (mA/cm^2)**	**FF (%)**	**Efficiency (%)**
CdS	50	0.7888	38.41	84.36	25.56
In_2S_3	50	0.7877	36.39	85.14	24.41
CdS	60	0.7886	38.01	84.48	25.32
In_2S_3	60	0.7877	36.28	85.24	24.36

IV. CONCLUSION

A performance comparison between CdS/CIGS and In_2S_3/CIGS solar cell has been carried out in this paper. The effects of variation of buffer layer thickness of both CdS and In_2S_3 have been observed. The optimum band gap of In_2S_3 is found 2.7 eV. For optimum 50 nm buffer layer thickness, efficiency of CdS/CIGS solar cell is found 25.56% whereas efficiency of (24.46%) is found for In_2S_3/CIGS solar cell. As efficiency of In_2S_3/CIGS solar cell is near to CdS/CIGS solar cell efficiency therefore In_2S_3 could be an effective alternative to toxic CdS buffer layer.

ACKNOWLEDGMENT

The authors cordially acknowledge Marc Burgelman and University of Gent for having us the opportunity to use SCAPS-1D software in this report.

REFERENCES

[1] A. Ibrahim, U. B. Memon, S. Roy, S. P. Duttagupta, and Amit L Sharma, "Fabrication and characterization of CDS/CDTE heterojhunction solar cell," IET International Summit, pp. 471-473, September 2015.

[2] Clas Persson, "Thin-film ZnO/CdS/CuIn1-xGaxSe2 solar cells: anomalous physical properties of the CuIn1-xGaxSe2 absorber," Brazilian Journal of Physics, vol. 36, no. 3B, pp. 948-951, 2006.

[3] D. Herrmann, P. Kratzert, S. Weeke, M. Zimmer, J. Djordjevic-Reiss, R. Hunger, P. Lindberg, e. Wallin, O. Lundberg and L. Stolt, "CIGS module manufacturing with high deposition rates and efficiencies", IEEE 40th Photovoltaic Specialist Conference (PVSC), pp. 2775-2777, June 2014.

[4] T. M. Friedlmeier, P. Jackson, Andreas Bauer, A. Bauer, D. Hariskos, O. Kiowski, R. Wuerz and M. Powalla, "Improved photocurrent in Cu(In,Ga)Se2 solar cells: from 20.8% to 21.7% efficiency," IEEE Journal of Photovoltaics, vol. 5, no. 5, pp. 1487-1491, 2015.

[5] Martin A. Green, K. Emery, Y. Hishikawa, W. Warta and E. D. Dunlop, "Solar cell efficiency tables (version 48)" Progress Photovoltaics Journal, vol. 24, pp. 905–913, 2016.

[6] M. V. Gurcia-cuenc, J. L. Morenza, E. Bertran and A. Lousia, "Electrical conduction on polycrystalline CdS film and comparision of theory and experiment," Journal of Physics D: Applied Physics, vol. 20, no. 7, pp. 958– 962, 1987.

[7] A. Cimaroli, N. Paudel, B. Paquin, D. Swanson and Y. Yan, "Effects of oxygen plasma treatment on the performance of CdTe thin-film solar cells," IEEE 42nd Photovoltaic Conference, pp. 1– 4, 2015.

[8] D. Hariskos, S. Spiering, M. Powalla, "Buffer layers in Cu(In,Ga)Se_2 solar cells and modules," Thin Solid Films vol.480–481, pp. 99– 109, 2005.

[9] M. Mostefaoui, H. Mazaria, S. Khelifia, A.Bouraioua and R. Dabou, "Simulation of high efficiency CIGS solar cells with SCAPS-1D software", International Conference on Technologies and Materials for Renewable Energy, Environment and Sustainability, pp. 736-744, 2015.

[10] A. Cimaroli, N. Paudel, B. Paquin, D. Swanson and Y. Yan, "Effects of oxygen plasma treatment on the performance of CdTe thin-film solar cells," IEEE 42nd Photovoltaic Conference, pp. 1– 4, 2015.

[11] F. Haque, N. A. Khan, K. S. Rahman, M. A. Islam, M. M. Alam,K. Sopian and N. Amin, "Prospects of zinc sulphide as an alternative buffer layer for CZTS solar cells from numerical analysis," International Conference on Electrical and Computer Engineering, pp. 504 – 507, 2014.

[12] N. Barreau, S. Marsillac, J. C. Bernedeand Assmann L., "Evolution of the band structure of β-In_2S_3–3xO3x buffer layer with its oxygen content," Journal of Applied Physics, vol. 93, pp. 5456-5459, 2003.

[13] N. Naghavi, S. Spiering, M. Powalla, B. Cavana and D. Lincot, "High-efficiency copper indium gallium diselenide (CIGS) solar cells with indium sulfide buffer layers deposited by atomic layer chemical vapor deposition (ALCVD)" Progress Photovoltaics journal, vol. 11, pp. 437–443, 2003.

[14] D. Hariskos, M. Ruckh, U. Rqhle, T. Walter, H.W. Schock, J. Hedstrfm and L. Stolt, "A novel cadmium free buffer layer for Cu(In,Ga)Se_2 based solar cells", Solar Energy Materials and Solar Cells, vol. 41–42, pp. 345-353, 1996.

[15] M. Mostefaoui, H. Mazari, S.Khelifi and R.Dabou, "Effect of a buffer layer on the performance of thin-film Cu(In,Ga)Se_2 solar cells," Journal of New Technology and Materials , vol. 04, no.01, pp. 73-76, 2014.

[16] G. Gordillo, A. A. R. Botero and E. A. Ramirez, "Development of novel control system to grow ZnO thin films by reactive evaporation," Journal of Materials Research and Technology, vol. 5, no. 3, pp. 219–225, 2016.

[17] P. Ranade, H. Takeuchi, T. J. King, and C. Hu, "Work function engineering of molybdenum gate electrodes by nitrogen implantation," Electrochemical and Solid-State Letters, vol.4 (11), pp.G85–G87, 2001.

[18] M. Burgelman, P. Nollet and S. Degrave, "Modelling polycrystalline semiconductor solar cells", Thin Solid Films, vol. 361-362, pp.527-532, 2000

[19] M. Burgelman, K. Decock, S. Khelifi and A. Abass, "Advanced electrical simulation of thin film solar cells", Thin Solid Films, vol. 535, pp. 296-301, 2013.

International Conference on Electrical, Computer & Telecommunication Engineering (ICECTE)
8-10 December 2016, Rajshahi-6204, Bangladesh

Fabrication and Characterization of Dye-Sensitized Solar Cell Using *Syzygium Cumini* Dye

Al Amin*, M. Al Emran
Electrical & Electronic Engineering
Rajshahi University of Engineering & Technology
Rajshahi-6204, Bangladesh
alamin.3eee@gmail.com*
alemraneee@gmail.com

M. F. Hossain (M, IEEE)
Electrical & Electronic Engineering
Rajshahi University of Engineering & Technology
Rajshahi-6204, Bangladesh
dr.faruk_eee@ruet.ac.bd

***Abstract*—Dye-Sensitized solar cell (DSSC) has long been regarded as one auspicious choice for the alternative way to convert the solar energy to electric energy. In this work, DSSC has been fabricated using the natural dye extracted from *Syzygium cumini* fruits. Here, nanocrystalline TiO_2 deposited on the fluorine doped tin-oxide (FTO) glass substrate has been used as dye absorber due to their high surface area and it shows high electron mobility, and carbon counter electrode has been used as a back electrode. The performance parameters of the solar cell have been achieved under AM 1.5 illumination. Optical and surface morphological studies of TiO_2 film have been observed. The solar cell efficiency of 0.161%, short circuit current density of 0.952 mA/cm^2, open circuit voltage of 735 mV and fill factor of 0.230 have been achieved in this study.**

Keywords—Natural dye; solar cell; Nanocrystalline TiO_2; Surface Morohology; Performance Parameters

I. INTRODUCTION

Nowadays the demand of electrical energy is increasing day by day with the technological development. The major parts of this energy come through the combustion of fossil fuels. Because of the combustion of fossil fuel, a huge amount of CO_2 gas is introduced into the atmosphere. As a result, the temperature of our surroundings rises, global warming and greenhouse effect occur. Further the conventional energy sources such as coal, petroleum & natural gas, fuel woods, Nuclear energy are limited in amount which is going to be end by time. So renewable energy sources can be regarded as one promising solution of the enormous problem of environment pollution and to fulfill the energy demand of our advanced society [1]. The sun is the source of all types of energy. The sun radiates solar energy approximately 3×10^{24} J per year which is ten times of the current energy demand [2, 3]. Solar cell converts the sunlight energy to electric energy. So all researchers should focus on the development of solar cell.

Dye-sensitized solar cell has been regarded as a cost-effective way to convert photon's energy to electrical energy. Here, dye is used to absorb the visible light. Every color has a range of wavelength which absorb the light exempt this range of wavelength. So it is easy to convert the photon's energy. DSSC was first developed by B. O'Regan and M. Grätzel in 1991 [4]. After that, DSSC has attracted many researchers for it's low cost, easy fabrication, non-toxic and environment friendly operation. The efficiency of DSSCs has reached up to 11.20% at 1 sun by using ruthenium(II) sensitizer ((C4H9)4N)2[Ru(4-carboxy-4´-carboxylate-2,2´ bipyridine)2(NCS)2] (N719) [5]. The ruthenium complexes have high cost [6] and it is so hard to obtain. To remove this complexity, the natural dye extracted from different natural fruits, flowers, leaves can be used as alternative of ruthenium complexes (N719) in the fabrication of DSSCs.

In this research, the natural dye extracted from *Syzygium cumini* fruits has been used as photo-sensitizer. *Syzygium cumini* dye shows good dying properties, because it contains chemical compounds such as quercetin, myricetin, gallic acid, ellagic acid [7]. The current-voltage characteristics of DSSC was investigated under AM 1.5 (100 mW/cm^2) light illumination.

II. EXPERIMENTAL DETAILS

A. Dye Extraction

The natural dye had been extracted in a very simple way. The *Syzygium cumini* fruit, which is known as jambul in Bangladesh, at first the fruits were cleaned with distilled water. Then the jambul was wrapped with cotton cloth and pressed by hand. The juice extracted from jambul was collected in a glass pot. Finally the dye was filtered for using as a photo-sensitizer.

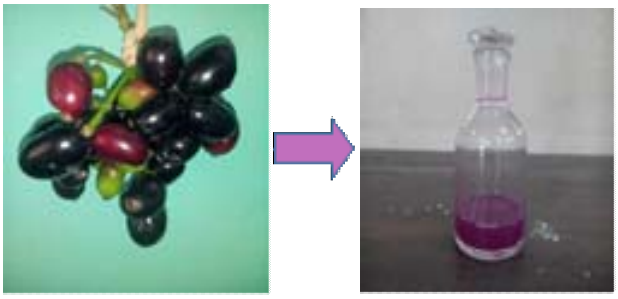

Fig. 1. Dye extraction from *Syzygium cumini* (Jambul) fruits.

978-1-5090-5785-6/16/$31.00 ©2016 IEEE

B. *Preparation of Dye-Sensitized Solar Cell (DSSC)*

The DSSC has mainly three parts such as dye-sensitized TiO_2 film deposited on the FTO glass substrate, electrolytes and carbon counter electrode. Firstly, 0.5 g of TiO_2 powder, 0.1 ml of acetylacetone and 4 ml mixture of water and ethanol (1:1) were taken into a mortar and stirred with pestle vigorously, and 0.4 ml of Triton X-114 were added into the solution. Then the diluted paste was deposited on the FTO surface by spin coating method to make the TiO_2 coating. The TiO_2 films were dried at 100 ℃ and then the films were annealed at 450 ℃ [8]. The prepared TiO_2 film was soaked by *Syzygium cumini* dye at room temperature for 24 hours.

Secondly, for the preparation of carbon counter electrode, 2.0 g of carbon powder (Bell fine APK 1101, Particle size ϕ = 10 μ m) having the surface area of 1100 m^2/g and the 0.4 g of carbon black having surface area of 68 m^2/g were dispersed in a mixture of 16 ml distilled water and 8 ml ethanol. After that, 0.25 g of carboxylmethyl-cellulose (CMC) ammonium salt as an adhesive was dissolved in this dispersion. This carbon paste was coated on the FTO conductive glass substrate by a doctor blade technique and was subsequently dried at 175 °C for 1 h. Finally, the inter-electrode space between TiO_2 electrode and carbon counter electrode was filled with the electrolytes of 0.5 M KI, 0.05 M I_2, 0.05 M 4-tert butylpridine (Aldrich) [9] in ethylene glycol. The cell area was 0.25 cm^2. The cell was performed under AM 1.5 light illumination and the I-V characteristics of the solar cell was obtained with the computer-controlled Keithley-2400 source meter.

III. Results and Discussion

The optical absorbance spectrums of the *Syzygium cumini* dye and TiO_2 film were determined with UV/VIS spectrophotometer which are shown in "Fig.2". The maximum absorbance has been observed over the wavelength of 500-600 nm. After the wavelength of 590 nm, the absorbance of *Syzygium cumini* dye goes to be down. The difference of the absorbance of TiO_2 film with and without dye sensitization has also been compared with the absorbance of dye "Fig. 2" which shows the peak over 500-600 nm, from which it has been proved that the TiO_2 film has absorbed the dye.

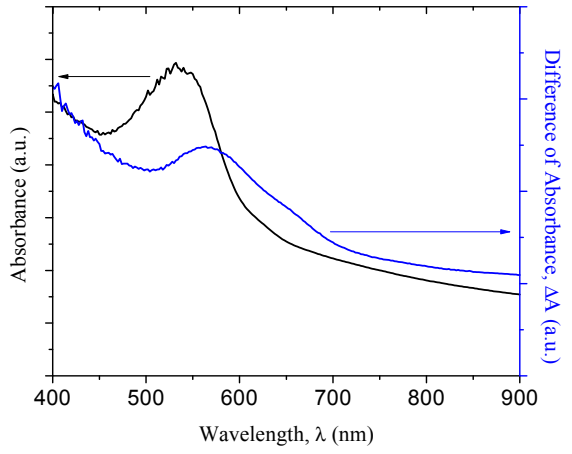

Fig. 2. Optical absorbance spectrum of *Syzygium cumini* dye, and difference of absorbance between with and without dye sensitized TiO_2 film.

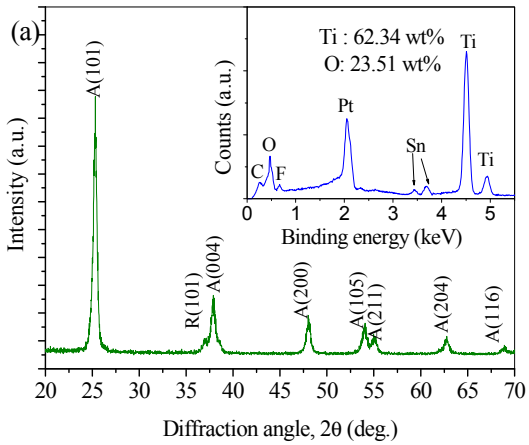

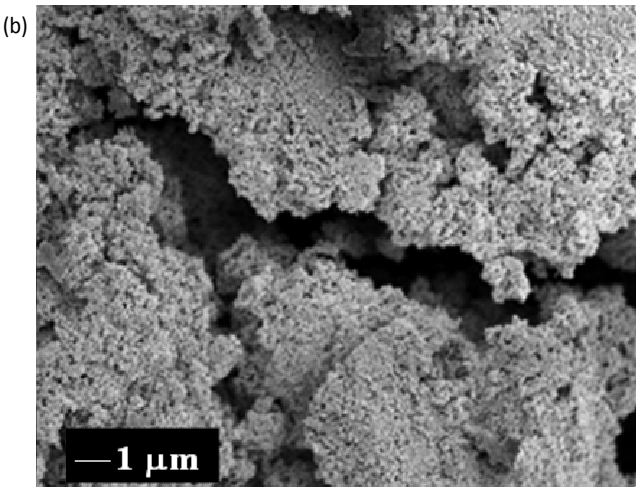

Fig. 3. Characterization of TiO_2 film (a) X-ray diffraction pattern, (inset) EDS analysis (b) FE-SEM image.

Grazing incidence X-ray diffraction (GIXRD) patterns of TiO2 electrode has been shown in "Fig. 3(a)" with incidence angle, α = 0.5°. The GIXRD pattern shows that the TiO_2 film is of polycrystalline nature. Most of the peaks show the anatase phase and highest peak A(101) is observed at 2θ value of 25.3°. Only one rutile peak R(101) is measured at 2θ value of 36.08°. The crystallite size of TiO_2 film has been measured by using the following Debye-Scherrer's equation.

$$D = \frac{0.94\lambda}{\beta cos\theta} \qquad \text{(a)}$$

Where, D = Crystallite size
λ = Wavelength of the X-ray radiation
(Cu K_α = 0.154nm)
θ = Diffraction angle
β = The full width at half maximum (FWHM)

The calculated crystallite size using anatase peak A(101) is 14.9 nm. In the inset diagram of "Fig. 3(a)", the EDS spectra of TiO_2 shows the peaks of O, Pt, Sn, Ti. The GIXRD data have been acquiesced with the EDS spectra. In EDS spectra, O peak

is found due to the oxide ion in metal oxide. The Pt, Sn, peaks exhibit due to coat Pt for FE-SEM measurement, FTO glass substrate respectively. The peak of Ti (62.34 wt%) and O (23.51 wt%) which demonstrate the high chemical purity of the composition of those products. The surface morphology of the nanocrystalline TiO_2 film has been obtained using FE-SEM method which has been shown in "Fig. 3(b)". The FE-SEM image shows the porosity structure of the TiO_2 film with discrete gain clusters.

The photocurrent density vs. photovoltage characteristics curves of the DSSC has been shown in "Fig. 4". The J-V curve has gone into down very transiently due to the effect of series resistance. It increases because of the fabrication errors. The solar cell efficiency is directly proportional to the short circuit current density (J_{sc}), open circuit voltage (V_{oc}) and fill factor (FF).

$$Efficiency, \eta = \frac{JscVoc(FF)}{P_{in}} \quad \text{(b)}$$

Where, P_{in} (100 mW/cm^2) is the incident power of light. The maximum efficiency of 0.161% has been calculated from the J-V characteristics of the DSSC, further in future the efficiency can be improved more.

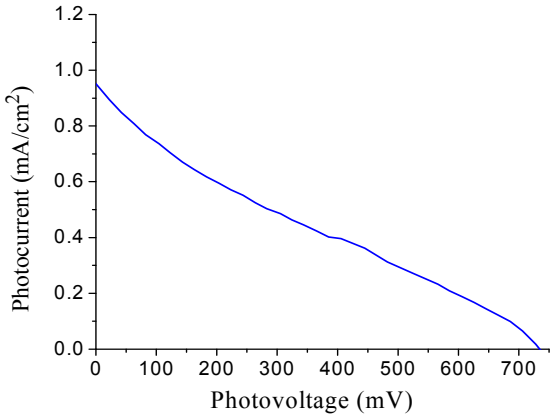

Fig. 4. J-V characteristics curve of the *Syzygium cumini* dye sensitized solar cell.

TABLE I PERFORMANCE COMPARISON OF SYZYGIUM CUMINI DSSC WITH SOME EXISTING WORKS

Dye	**J_{sc} (mA/cm^2)**	**V_{oc} (mV)**	**FF**	**Efficiency (%)**	**Ref.**
Syzygium cumini	0.952	735	0.230	0.161	This work
C. haemato-cephata	0.25	370	0.70	0.06	[10]
P. pterocarpum	0.15	400	0.71	0.04	[10]
Turmeric	0.288	529	0.48	0.03	[11]
Bloodleaf	0.260	267	0.46	0.04	[11]
Parsley	0.53	440	0.34	0.07	[12]
Walnuts	0.73	304	0.39	0.0104	[13]

IV. CONCLUSION

Electrical energy has tectonic for the social development. In this work, it has been tried to fabricate DSSCs to convert the sunlight energy to electric energy. The TiO_2 film was sensitized using *Syzygium cumini* dye as alternative of the ruthenium complexes because of it's high cost. The ruthenium complexes can be replaced possible by natural dye. The *Syzygium cumini* dye sensitized solar cell shows the efficiency of 0.161%, it is more than many existing DSSCs. Although the natural dye-sensitized solar cell has comparatively low efficiency, further the improvement works of DSSCs are going on.

ACKNOWLEDGMENT

The authors would like to thank to Professor Dr. Abu Bakar Md. Ismail, Rajshahi University, Department of Applied Physics and Electronic Engineering, for his cooperation in the characterization of electrical properties.

REFERENCES

[1] Islam MR, Islam MR, Beg MRA, "Renewable Energy Resources and Technologies Practice in Bangladesh," Renewable and Sustainable Energy Reviews, 2008, 12(2):299–343.

[2] K. R. Millington, "Encyclopedia of Electrochemical Power Sources," Amsterdam, The Netherlands: Elsevier, 2009.

[3] Umer Mehmood, M. Zaheer Aslam, R. A. Shawabkeh, Ibnelwaleed A. Hussein, Waqar Ahmad, and Adeem Ghaffar Rana, "Improvement in Photovoltaic Performance of Dye Sensitized Solar Cell Using Activated Carbon-TiO2 Composites-Based Photoanode," IEEE Journal of Photovoltaics, vol. 6, issue 5, pp. 1191-1195, 09 June 2016.

[4] B. O'Regan, M. Grätzel, "A low-cost, high-efficiency solar cell based on dyesensitized colloidal TiO2 films," Nature 353 (1991) 737–740.

[5] R. Buscaino, C. Baiocchi, C. Barolo, C. Medana, M. Grätzel, Md. K. Nazeeruddin, G. Viscardi, "A mass spectrometric analysis of sensitizer solution used for dyesensitized solar cell," Inorg. Chim. Acta 361 (2008) 798–805.

[6] Thomas W. Rees, Etienne Baranoff, "Ruthenium complexes with tridentate ligands for dye-sensitized solar cells," Polyhedron, Vol. 82, Pages 37–49, 4 Nov. 2014.

[7] V. Narayana Swamy, K. N. Ninge Gowda, R. Sudhaka, "Dyeing Properties of Natural Dye Syzygium cuminii on Silk," The Institution of Engineers (India), DOI 10.1007/s40034-014-0031-3, 2014.

[8] M. F. Hossain, S. Biswas, T. Takahashi, "Study of CdS-sensitized solar cells, prepared by ammonia-free chemical bath technique," Thin Solid Films, 518 (2009) 1599–1602.

[9] M. F. Hossain, S. Biswas, T. Takahashi, "The effect of sputter-deposited TiO2 passivating layer on the performance of dye-sensitized solar cells based on sol–gel derived photoelectrode," Thin Solid Films, 517 (2008) 1294 – 1300.

[10] Ishwar Chandra Maurya, Neetu, Arun Kumar Gupta, Pankaj Srivastava, Lal Bahadur, "Callindra haem atocephata and Peltophorum pterocarpum flowers as natural sensitizers for TiO2 thin film based dye-sensitized solar cells," Optical Materials 60 (2016) 270-276.

[11] Moustafa KF, Rekaby M, El Shenawy ET, Khattab NM., "Green dyes as photosensitizers for dye-sensitized solar cells," J Appl Sci Res 2012;8 4393-04.

[12] Taya SA, El-Agez TM, El-Ghamri HS, Abdel-latif MS "Dye-sensitized solar cells using fresh and dried natural dyes," Int J Mater Sci Appl 2013;2:37–42.

[13] El-Agez TM, El Tayyan AA, Al-Kahlout A, Taya SA, Abdel-Latif MS., "DyeSensitized solar cells based on ZnO films and natural dyes," Int J Mater Chem 2012;2:105–10.

International Conference on Electrical, Computer & Telecommunication Engineering (ICECTE)
8-10 December 2016, Rajshahi-6204, Bangladesh

Numerical Simulation for the High Efficiency p-n Si Solar Cell with HT-EBL and ET-HBL

Al Amin
Rajshahi University of Engineering & Technology
Electrical & Electronic Engineering
Rajshahi-6204, Bangladesh
alamin.3eee@gmail.com

M. F. Hossain (M, IEEE)
Rajshahi University of Engineering & Technology
Electrical & Electronic Engineering
Rajshahi-6204, Bangladesh
dr.faruk_eee@ruet.ac.bd

***Abstract*—The Hole Transport-Electron Blocking Layer (HT-EBL) and Electron Transport-Hole Blocking Layer (ET-HBL) are added on the front surface and back surface of the silicon wafer respectively for designing the high efficiency p-n homojunction Si solar cell in this simulation. The cell was simulated using A One-Dimensional Device Simulation Program for Analysis of Microelectronic and Photonic Structures (AMPS-1D) by varying the doping density and layer thickness of the p type and n type Si layer. It has been investigated that there have a great effect of doping density and layer thickness on the efficiency of solar cell and optimum efficiency has been achieved. The maximum efficiency of 28.198% has been investigated at the doping density of 1.0e+021 cm^{-3} and layer thickness of 8000 nm.**

Keywords—Solar Cell; HT-EBL; ET-HBL; Doping Density; Layer Thickness; Homojunction; AMPS-1D

I. INTRODUCTION

The energy and environment are two major areas of discussion in the current world. Energy can be harvested by burning of fossil fuel, but it has high cost and pernicious effect on environment. The burning of fossil fuel causes greenhouse effect, environment gets warm and becomes polluted. So it is more and more widely recognized that renewable energy sources, especially solar energy can be effective solution to these enormous problems [1]. There are many types of solar cell. Among them Si solar cell plays a great contribution on solar energy conversion system due to low cost and availability of Si. Ohl first traced this type of solar cell in 1941 in his laboratory [2], in which he demonstrated a grown Si p–n junction photovoltaic device. About 12 years later, a 6% efficient, diffusion-formed single-crystal Si p–n junction device was demonstrated [3] and by 1958, 14% efficient single-crystal silicon devices were available using the diffused junction technology. In 2014 Panasonic broke all record of efficiency, and designed a new model of Si solar cell by applying thin film of Si to the front and back of the Si wafer to eliminate defect at or near the wafer surface and achieved efficiency of 25.6% [4]. In Different times, many scientist have worked to enhance the sunlight energy to electric energy conversion efficiency by using different techniques and diverse materials, semiconductor-metal alloys. $In_{0.52}Ga_{0.48}N$, Copper-Indium Selenium (CIS), copper indium gallium diselenide (CIGS) are the examples of different semiconductor alloy solar cell [5-7].

Si is an important material in solar cell physics but it has already been reported that bare silicon has a high surface reflection of over 30%. The reflection can reduced by texturing and by applying anti-reflection coatings (ARC) to the surface [8]. Basic p-n homojunction Si solar cell without ARC shows efficiency of 3.8% and Form Factor (FF) of 0.74, the short circuit current density (J_{sc}) is 11.8 mA/cm^2 and open circuit voltage (V_{oc}) is 0.43 V [9], which are comparatively low. When front HT-EBL and back ET-HBL are added then the efficiency reaches at 12.45% and FF is 0.79, J_{sc} is 28.4 mA/cm^2 and V_{oc} is 0.55 V for doping density of 1.0e+15 cm^{-3} and layer thickness of 5000 nm [9], this result was investigated for 1.90 eV bandgap energy of both HT-EBL and ET-HBL. The effect of bandgap of EBL was investigated in [10] and maximum efficiency of 26.285% was achieved at 2.10 eV.

The main target of this work is how to enhance the solar cell efficiency. In this simulation model, the effect of acceptor and donor density and layer thickness of p and n region on the performance parameters of the p-Si/n-Si with front HT-EBL and back ET-HBL solar cell has been shown and the maximum efficiency of 28.198% has been obtained by varying the doping density and layer thickness.

II. SOLAR CELL DESIGNING AND SIMULATION

The physics of device transport can be captured in three governing equations: Poisson's equation, the continuity equation for free holes, and the continuity equation for free electrons. Which are written respectively in the following equations.

$$\frac{d}{dx}\left(-\varepsilon(x)\frac{d\psi}{dx}\right) = q[p(x) - n(x) + N_D^+(x) - N_A^-(x) + p_t(x) - n_t(x)] \quad (1)$$

$$\frac{\partial p_n}{\partial t} = G_p - \frac{p_n - p_{n0}}{\tau_p} - p_n\mu_p\frac{\partial \xi}{\partial x} - \mu_p\xi\frac{\partial p_n}{\partial x} + D_p\frac{\partial^2 p_n}{\partial x^2} \quad (2)$$

$$\frac{\partial n_p}{\partial t} = G_n - \frac{n_p - n_{p0}}{\tau_n} + n_p\mu_n\frac{\partial \xi}{\partial x} + \mu_n\xi\frac{\partial n_p}{\partial x} + D_n\frac{\partial^2 n_p}{\partial x^2} \quad (3)$$

978-1-5090-5785-6/16/$31.00 ©2016 IEEE

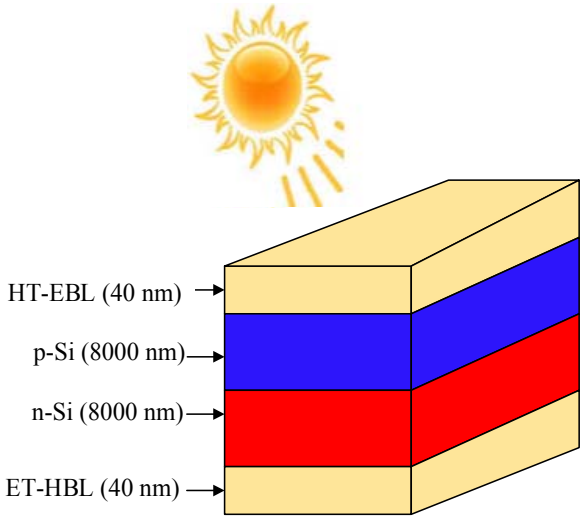

Fig. 1. Schematic diagram of the high efficiency p-n Si solar cell.

Where, ψ is the electrostatic potential, ξ is electrostatic field, p and n are free hole and free electron respectively. From the above three equations the transport characteristics can be determined, after determining it becomes a task of solving these three coupled non-linear differential equations, each of which has two associated boundary conditions. In AMPS, these three coupled equations, along with the appropriate boundary conditions, are solved simultaneously to obtain a set of three unknown state variables at each point in the device: the electrostatic potential, the hole quasi-Fermi level, and the electron quasi-Fermi level. From these three state variables, the carrier concentrations, fields, currents, etc. can then be computed. To determine these state variables, the method of finite differences and the Newton-Raphson technique are incorporated by the computer. Numerical simulation requires a model for the trap density of states (DOS) in the sample [11]. The AMPS-1D can operate in two disparate modes: the density of state (DOS) mode and lifetime mode. The definition of multiple defect states using densities, energy distribution, and capture cross-sections are allowed in DOS mode. In this work, the DOS mode has been used for this simulation.

The material parameters for simulation have been taken from the book "Solar Cell Device Physics" by Stephen J. Fonash. The device operating temperature is used as 300k and all performance parameters of cell have been taken under AM 1.5G illumination. The material parameters are listed below.

TABLE I. MATERIAL PARAMETERS

Parameter	HT-EBL	p-Si	n-Si	ET-HBL
Layer Thickness (nm)	40 nm	Variable	Variable	40 nm
Relative permittivity	11.90	11.90	11.90	11.90
Electron mobility, μ_n (cm^2/Vs)	1350	1350	1350	1350
Hole mobility, μ_p (cm^2/Vs)	450	450	450	450
Doping density of p & n region (cm^{-3})	1.0e+15	Variable	Variable	1.0e+15
Bandgap (eV)	1.90/2.10	1.12	1.12	1.90/2.10
Effective density of states in conduction band ($1/cm^3$)	2.80e+19	2.80e+19	2.80e+19	2.80e+19
Electron affinity (eV)	3.27	4.05	4.05	4.05
Effective density of states in valence band ($1/cm^3$)	1.04e+19	1.04e+19	1.04e+19	1.04e+19
ED (eV)	0.01	0.01	0.01	0.01
GDO ($1/cm^3/eV$)	1.0e+14	1.0e+14	1.0e+14	1.0e+14
TSIG/ND (cm^2)	1.0e-15	1.0e-15	1.0e-15	1.0e-15
TSIG/PD (cm^2)	1.0E-17	1.0E-17	1.0E-17	1.0E-17
EA (eV)	0.01	0.01	0.01	0.01
GAO ($1/cm^3/eV$)	1.0e+14	1.0e+14	1.0e+14	1.0e+14
TSIG/NA (cm^2)	1.0E-17	1.0E-17	1.0E-17	1.0E-17
TSIG/PD (cm^2)	1.0e-15	1.0e-15	1.0e-15	1.0e-15

TABLE II. FRONT AND BACK CONTACT PARAMETERS

Front contact	Back contact
PHIBO = 1.66 eV	PHIBL = 0.26 eV
SNO = 1.0e+7 cm/s	SNL = 1.0e+7 cm/s
SPO = 1.0e+7 cm/s	SPL = 1.0e+7 cm/s
RF = 0	RB = 1

III. RESULTS AND DISCUSSION

A. *Effect of Doping Density*

Doping density means the number of carrier in p & n region. Doping density has tremendous effect on the performance parameters of the p-n Si solar cell. The short circuit current density decreases and open circuit voltage increases with the increasing of doping density of p & n type Si material "Fig. 2". Otherwise the efficiency increases with the increases in doping density, and efficiency of 27.404% was achieved at doping density of 1.0e+21 cm^{-3}, layer thickness of 5000 nm and the 1.90 eV bandgap energy of front HT-EBL & back ET-HBL "Fig. 3".

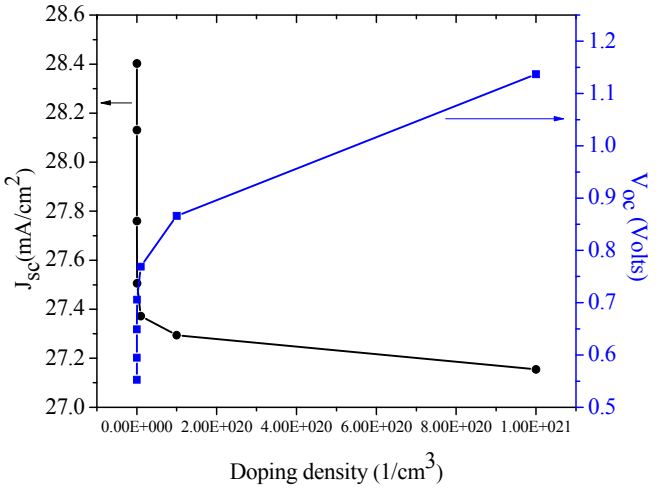

Fig. 2. Effect of doping density of the p type & n type Si on the short circuit current density (J_{sc}) & open circuit voltage (V_{oc}).

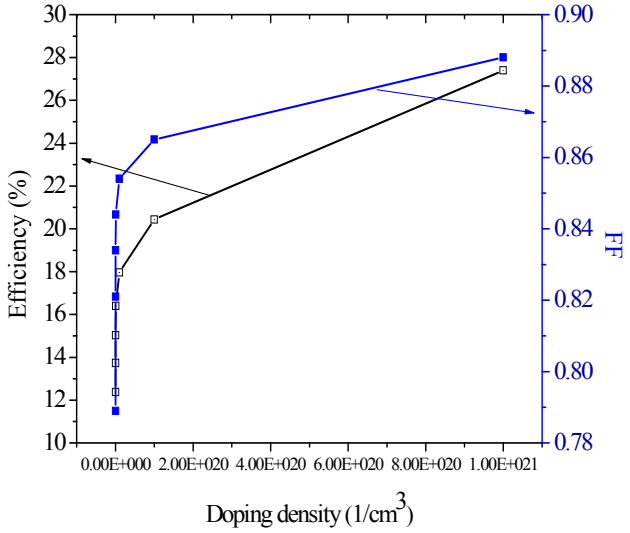

Fig. 3. Effect of doping density of the p type & n type Si on the Efficiency and fill factor (FF).

The increasing of doping density in n region means the number of free electrons increases and in p region means the number of free spaces for electron movement also increases. When sun light falls on the front surface, more electrons excite and cause more collisions. That's why the flow of electron ultimately decreases, and the open circuit voltage enhances due to the high electric field.

B. Effect of Layer Thickness

Layer Thickness means the width of p & n region. Impact of the layer thickness on short circuit current density, open circuit voltage and FF, efficiency is appreciable. When layer thickness of p & n Si increase J_{sc} increases, be 28.132 mA/cm^2 maximum at 8000 nm "Fig. 4," and the efficiency also increases, be maximum of 28.198% at 8000 nm for the 2.10 eV bandgap energy of front HT-EBL and back ET-HBL "Fig. 5". In this case the V_{oc} decreases with the increasing of layer thickness. When layer thickness increases at constant carrier concentration, the space for free electron movement increases in volume, electron can move easily. The short circuit current density increases and open circuit voltage decreases. As a result, the fill factor increases up to a layer thickness of 5000 nm, after this the FF decreases and again increases, and be maximum of 0.888 at 8000 nm layer thickness.

C. Efficiency Optimization of p-n Si solar cell

The thermodynamic equilibrium band diagram of the p-n Si solar cell with addition of front HT-EBL and back ET-HBL has been shown in "Fig. 6" which represents that the valence band and conduction band energy change from 0 to 100 nm only, further the energy remains constant.

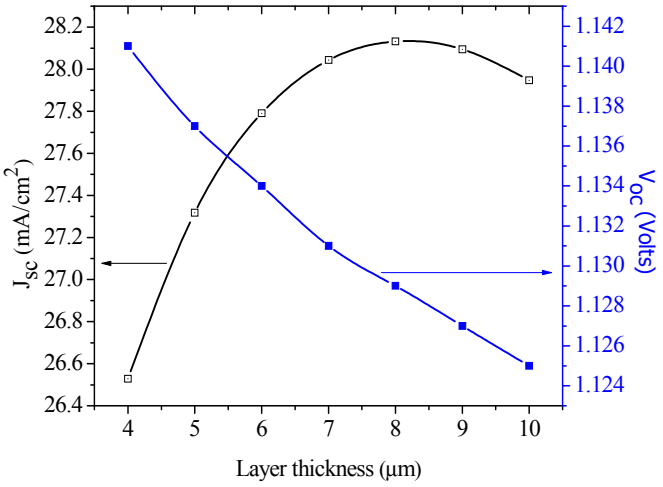

Fig. 4. Effect of layer thickness of p & n type Si on the short circuit current density (J_{sc}) & open circuit voltage (V_{oc}).

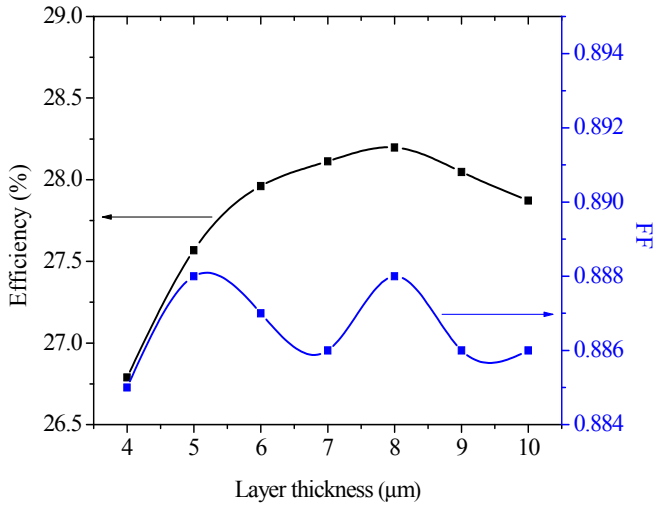

Fig. 5. Effect of layer thickness of p & n Si on the Efficiency and FF.

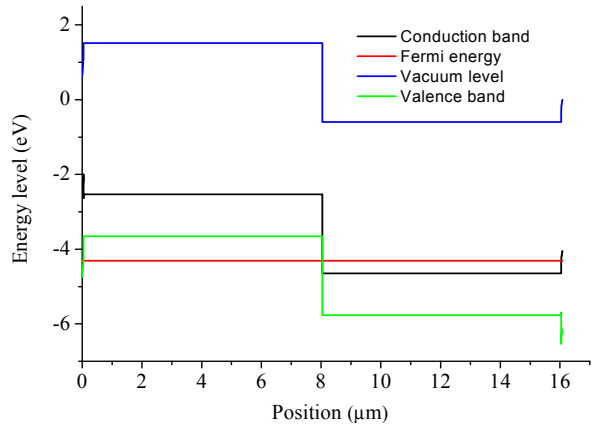

Fig. 6. The computed Thermodynamic Equilibrium (TE) band diagram of the p-Si/n-Si with the addition of a 40-nm HTL-EBL at the front contact and a 40-nm ET-HBL at the back contact for the optimum conditions.

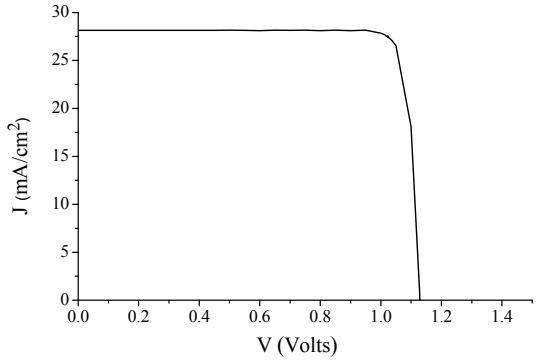

J_{sc}=28.132 mA/cm^2, V_{oc}=1.129 V,
FF = 0.888, Efficiency = 28.198%

Fig. 7. J-V characteristics curve of the high efficiency p-n Si solar cell for the optimum conditions.

The current density vs. voltage curve has been shown in "Fig. 7". The maximum efficiency of 28.198% has been obtained. For the maximum efficiency, the optimum layer thickness and doping density of p type and n type Si material has been determined 8000 nm and 1.0e+21 cm^{-3} respectively. Although the doping density is too high, it may be possible if the deposition method is developed for the desired doping concentration.

The Si solar cell with ET-HBL and HT-EBL shows comparatively higher efficiency than existing Si solar cells. The c-Si, a-Si, mc-Si and a-Si/nc-Si (thin film) show the efficiency of (25.6 ± 0.5) %, (10.2 ± 0.3) %, (11.4 ± 0.3) % and 12.7% respectively [12].

IV. CONCLUSION

The light energy to electric energy conversion efficiency is an important factor to design a solar cell in practical. In this simulation model, it has been tried to enhance the solar cell efficiency, the efficiency of p-Si/n-Si with front HT-EBL & back ET-HBL solar cell for doping density of 1.0e21 cm^{-3} and layer thickness of 8000 nm is more than basic p-n homojunction solar cell. The efficiency reach at 28.198% for the optimum conditions of layer thickness and doping concentration. So this type of solar cell can be fabricated and implemented in the laboratory.

ACKNOWLEDGMENT

The authors would like to thank to Professor Stephen J. Fonash, Pennsylvania State University, USA, for providing us the Analysis of Microelectronic and Photonic Structures of one dimensional device (AMPS-1D) simulation software.

REFERENCES

[1] Islam MR, Islam MR, Beg MRA, "Renewable Energy Resources and Technologies Practice in Bangladesh," Renewable and Sustainable Energy Reviews, 2008, 12(2):299–343.

[2] R. S. Ohl, "Light Sensitive Electric Drvice", U. S. Patent 2, 402, 662 (1941).

[3] D. M. Chapin, C. S. Fuller, G. L. Pearson, "A New Silicon *p–n* Junction Photocell for Converting Solar Radiation into Electrical Power," J. Appl. Phys. 25 (1954) 676.

[4] Kelvin Bullis, "Record-Breaking Solar Cell Points the Way to Cheaper Power," MIT Technology Reviews (2014).

[5] Dennai Benmoussa, Benslimane Hassane, Helmaoui Abderrachid, "Simulation of In0.52Ga0.48N Solar Cell Using AMPS-1D," in Proceedings of the IEEE 2013 International Renewable and Sustainable Energy Conference (IRSEC), pp. 23-26, 7-9 march 2013.

[6] Nowshad Amin, Michael Tang, Kamaruzzaman Sopian, "Numerical Modeling of the Copper-Indium-Selenium (CIS) Based Solar Cell Performance by AMPS-1D," in Proceedings of the IEEE 5th Student Conference on Research and Development, 2007. SCOReD 2007, pp. 1-6, 11-12 Dec. 2007.

[7] J. R. Ray, C. J. Panchal, M. S. Desai, U. B. Trivedi, "Simulation of CIGS Thin Film Solar Cell Using AMPS-1D," J. Nano- Electron. Phys., 3 (2011) No1, P. 747-754.

[8] Bauer G., "Absolutwerte der optischen Absorptionskonstanten von Alkalihalogenidkristallen im Gebiet ihrer ultravioletten Eigenfrequenzen," Annalen der Physik, 1934, 411(4):434 - 464.

[9] Stephen J. Fonash, "Solar Cell Device Physics," Elsevier, 2010.

[10] Md. Feroz Ali, Md. Faruk Hossain, "Effect of Bandgap of EBL on Efficiency of the p-n Homojunction Si Solar Cell from Numerical Analysis," in proceeding of IEEE 2015 International Conference on Electrical & Electronic Engineering (ICEEE), pp. 245-248, 4-6 Nov. 2015

[11] S. Fonash, J. Arch., J. Cuiffi, J. Hou, W. Howland, P. McElheny, A. Moquin, M. Rogosky, T. Tran, H. Zhu, F. Rubinelli, "A Manual for AMPS-1D for Windows 95/ NT a One-Dimensional Device simulation program for the Analysis of Microelectronic and Photonic Structures," The Pennsylvania State University, USA, 1997.

[12] Martin A. Green, Keith Emery, Yoshihiro Hishikawa, Wilhelm Warta. Ewan D. Dunlop, "Solar cell efficiency tables (Version 45)," Wiley online library, 10.1002/pip.2573, 20 December 2014.

Synchronization of Different Frequency Power Grids by Back-to-Back Modular Multilevel Converter with CSMC-SPWM Algorithm

M.A. Alim[1], M.A.G. Khan[1,2] and M.A. Munjer[1,2]
[1]Department of Electrical and Electronic Engineering
Bangladesh Army University of Engineering & Technology
[2]Rajshahi University of Engineering & Technology
Rajshahi, Bangladesh
eaar@ymail.com
agmagk@gmail.com
munjereee@yahoo.com

Abstract—**This paper presents a control process and the functioning of Back-to-Back Modular Multilevel Converter (MMC) in connecting asynchronous grids of high-voltage DC transmission system. CSMC-SPWM algorithm is used to generate gate pulses of the switching devices of back-to-back MMC for running, shifting the system from higher to any other lower level of operation and connecting of two different frequencies power grids. In this research two power grids having different frequencies of 50Hz and 60Hz are connected. The simulation results shows that the MMC operates well and synchronized properly with asynchronous grids and power can transmitted in both direction. A tap changing transformer is used to step up the output voltage of the converter during reduced number of level operation.**

Keywords—igbt; thd; csmc; hvdc; mmc; sm.; spwm ; vsc;

I. INTRODUCTION

HVDC transmission is widely recognized for long-distance or offshore grid, long submarine cable, bulk-power transmission, and asynchronous power system interconnections [1]-[5]. The line commutated current source converter is mostly used but in self commutated voltage source converter based HVDC system flexibility of the power transmission is greatly improved [6]. Compare to conventional converter, for high power applications multilevel converter promises lots of advantages. Multilevel converter produced nearly sinusoidal output voltage waveforms, lower dv/dt so less THD [7]. Because of less voltage blocking and current leading capabilities IGBTs, IGBTs are connected in series to withstand higher voltage stress and connected in parallel to increase the current leading capability [1]. Due to the complex structure of neutral-point-clamped and flying capacitor multilevel converters, cascaded H-bridge multilevel converter is widely used. The installation of cascaded H-bridge converter is easy and it can develop higher voltage but the main drawback of this converter is it does not have the ability of four quadrant operation [5],[7],[8]. MMC has the ability of four quadrant operation and very easy to install, simple structure, easy expandable, has redundancy possibilities and two way of power flow operation [7],[9],[10].

978-1-5090-5785-6/16/$31.00 ©2016 IEEE

Tor Martin Iversen confirmed redundancy possibilities in MMC without reducing output voltage of the converter [9]. M.Alim et al. also have confirmed the operation of MMC converter using a new algorithm named as Carrier and Signal (reference) Magnitude Control Sinusoidal Pulse Width Modulation (CSMC-SPWM). This algorithm drives well to have the desired level of operation according to the number of SM fault occurred [1]. In this paper CSMC-SPWM technique is used to control back-to-back modular multilevel converter for connecting two different frequencies power grids. A tap changing transformer is used to step up the output voltage so that the converter voltage remains constant during SMs faults.

II. BACK TO BACK VSC HVDC TRANSMISSION

A. Back-to-Back VSC HVDC System

In back-to-back VSC HVDC system, the two converter stations having same or different frequencies are located at the same site and there is no transmission of power with a dc link over a long distance [5].

III. MODULAR MULTILEVEL CONVERTER (MMC)

The MMC technology have been used in large HVDC transmissions system as well as in high voltage structures [7],[9]. Fig. 1 represents the general circuit of single phase and three phase equivalent circuit of n-level MMC.

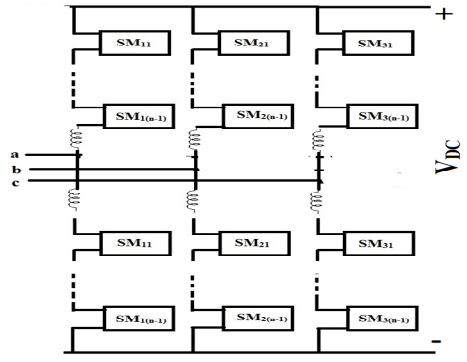

Fig. 1. Modular Multilevel Converter

The converter circuit has one leg per phase and each leg has two arms namely, positive and negative arms, with each arm having (n-1) sub-modules (SM) with a coupling arm inductor [1].

IV. CSMC-SPWM TECHNIQUE

According to the required level of operation, the amplitude of the reference signal is changed. According to the number of level the reference signal is as follows

Required Level	Reference signal
Level-02:	0.25×(2-1)×sinωt
Level-03:	0.25× (3-1)×sinωt
…	…
Level-n:	0.25× (n-1)×sinωt

The required number of carrier signals depend on the number of levels of the system. For n number of levels, total (n-1) number of carrier signals would be arranged after adding pre-defined DC value (δ_m) with the original carrier where δ_m=(n-2)/4. A 0.5 unit of magnitude difference always be maintained between two consecutive new carrier signals [6]. The original carrier signal can be represented as

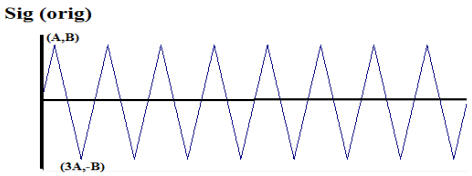

Fig. 2.Original carrier signal

$$\text{Sig (orig)}=\begin{cases} =\frac{B}{A}t & 0\leq t\leq A \\ =-\frac{B}{A}(t-2A) & A\leq t\leq 3A \\ =\frac{B}{A}(t-4A) & 3A\leq t\leq 4A \end{cases}$$

So for n levels n-1 carrier signal can be represented as

Sig1=Sig (orig)+ (δ_m-(1-1)×0.5)
Sig2= Sig (orig)+ (δ_m-(2-1)×0.5)
……
Sig(n-1)= Sig (orig)+ (δ_m-(n-1-1)×0.5) (1)

"n" level Carrier and Signal Magnitude Control Sinusoidal Pulse Width Modulation (CSMC-SPWM) contain n-1 Carrier signal named Sig1, Sig2 ….Sig (n-1). The reference signal is a sine waveform and carrier signals are triangular waves. These n-1 carrier signals maintain same frequency and amplitude. But the difference is that they had added with the different DC values. The reference signal is compared with the n-1 carrier signal. If E_{ref} is exceeded the peak amplitude of Sig1, E_{ref} is then compared with carrier signal Sig2 , until it had exceeded the peak amplitude of sig (n-1) [6].

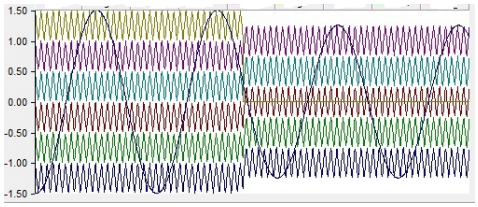

Fig. 3. Carrier signal for odd and even level

V. BACK-TO-BACK MMC WITH CSMC-SPWM CONTROLLER

Fig. 4 shows the block diagram of complete system. In this research work both VSC1 and VSC2 are controlled by the CSMC-SPWM controller. Both converters can be operated as rectifier and inverter.

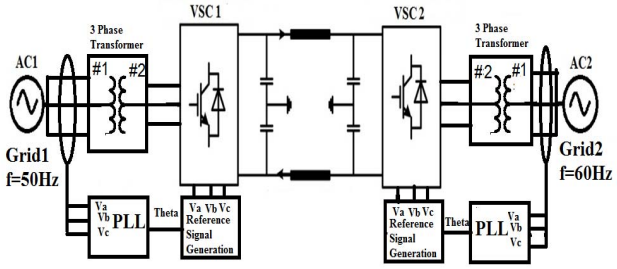

Fig. 4. Block diagram of the complete system

Fig. 5 shows the block diagram of VSC1 and VSC2 which consists of (n-1) sub module (SM) block and CSMC-PWM section. CSMC-SPWM block generates gate signals of IGBTs and also detect SMs fault and on the basis of SMs fault CSMC-SPWM block reduced number of level and bypass the faulty SMs [1].

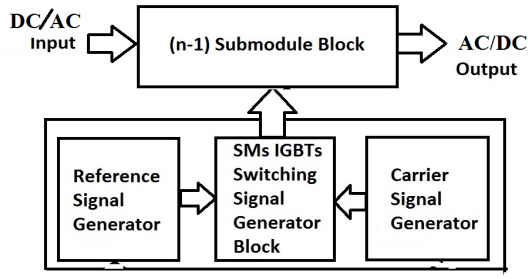

Figure. 5. Block diagram of VSC 2

Power can be transmitted from VSC1 to VSC2 or VSC2 to VSC1. When power transmitted VSC1 to VSC2, VSC1 is operated as rectifier and VSC2 is operated as inverter. In case of power transmission from VSC2 to VSC1, VSC2 then operated as a rectifier and VSC1 is operated as inverter.

Direction of power flow can be controlled by the following equation [5].

$$P=\frac{Vs.Vr}{X}sin\delta \quad (2)$$

$$Q=\frac{Vscos\delta-Vr}{X}Vr \quad (3)$$

Where δ is the phase difference between sending end and receiving end voltage. From (2) it is cleared that direction of

active is depend upon on δ and from (3) reactive power depends upon the voltage difference between sending end and receiving end. A phase locked loop (PLL) is used to synchronize between converter and grids.

VI. Simulation and Result

To verify the validity for connecting asynchronous grid, the simulation using the "PSCAD/EMTDC" software package was carried out, where the circuit parameters are summarized in Table 1. A high-voltage three phase load with a 7-level MMC as the converters were built.

TABLE I. Parameters used in CSMC-SPWM MMC

Converter	Parameters	Level 7
VSC1	Grid Frequency	50Hz
	Grid Voltage (ac)	10 kV
	Number Sub Modules (SMs)	36
	Capacitor in SM	500 µF
	Inductor	0.1 mH
	IGBT for bypass switch	36
VSC2	Grid Frequency	60Hz
	Grid Voltage (ac)	10 kV
	Number Sub Modules (SMs)	36
	Capacitor in SM	500 µF
	Inductor	0.1 mH
	IGBT for bypass switch	36

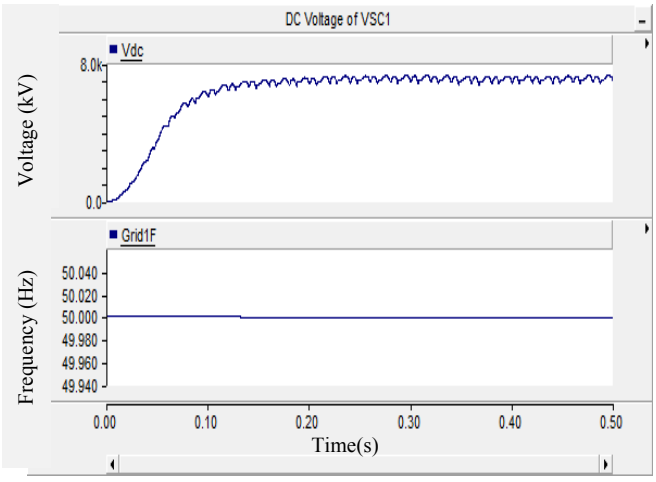

Fig. 6. DC output voltage of VSC1 and Frequency of Grid1

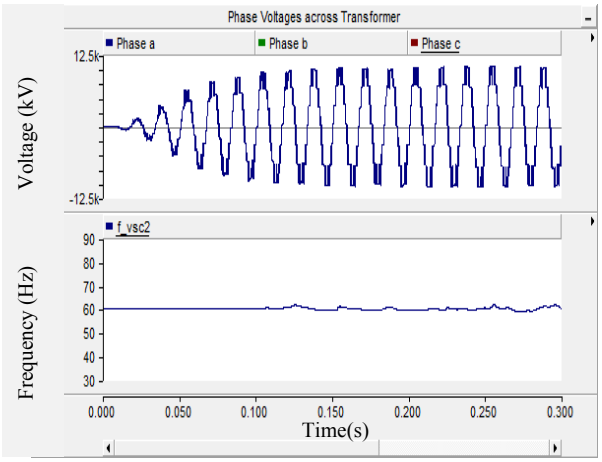

Fig. 7. 7-level and 60Hz output voltage of VSC2

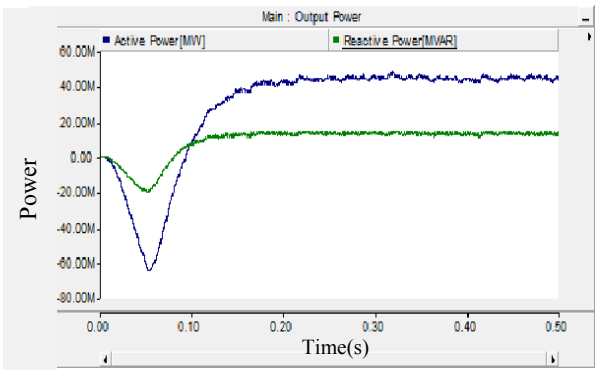

Fig. 8. Receiving end power of VSC2

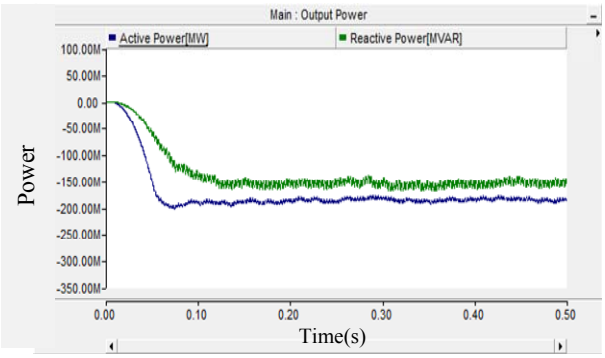

Fig. 9. Reverse direction of power flow of VSC2

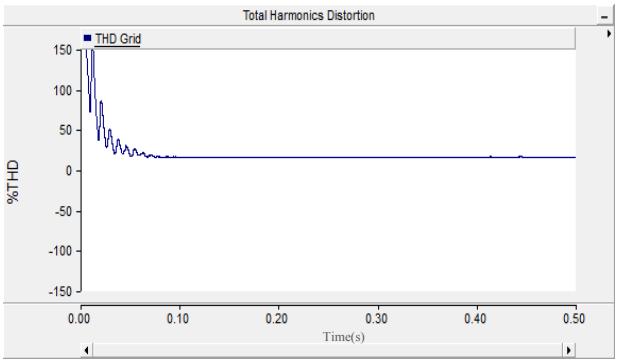

Fig. 10. THD of output voltage of VSC2

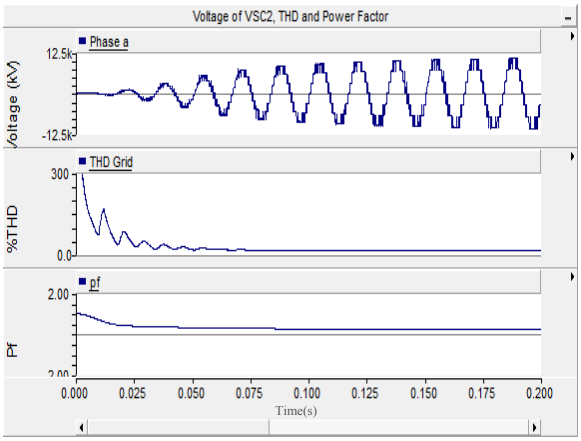

Fig. 11. 7-level output voltage, THD at very low power factor load of VSC2

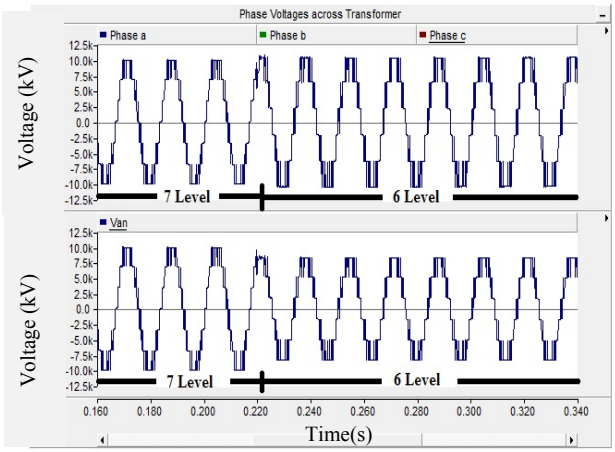

Fig 12. Output voltage of tap changing transformer (after and before VSC2)

Fig. 6 represents the simulated DC output voltage of VSC1 which is converted from ac voltage of grid1 having frequency 50 Hz. Fig. 7 shows 60Hz 7-level output voltage of VSC2. Fig. 8 and Fig. 9 show that power can transmitted in both direction. Fig. 10 represents the THD of VSC2 phase voltage which is near about 15.26%. Fig.11 shows even at low power factor load the converter drives well and in that case THD also remains low. Fig. 12 shows that even in the case of SMs fault the converter running with lower level and lower output voltage but using tap changing transformer the output voltage remains same as grid voltage.

VII. Conclusion

Connection of two grids of different frequencies has confirmed by PSCAD-EMTDC simulation software. 7 level output voltage is obtained by using CSMC-SPWM modulation technique. THD also reduced near about 15.26% without filtering which satisfies well. Power also transmitted in both direction. The major focus of this research work is to use tap changing transformer to step up the output voltage of the converter during lower level of operation due to SMs fault. The fig. 12 confirmed that after being a fault at a SM the output felt down from 7 level to 6 level. With a close look to the output at fault condition, it can be observed that level has decreased by one and the magnitude of the output voltage of the VSC2 also reduced and the tap changing transformer step up the output voltage of VSC2 to the equal of grid voltage. This method may successfully be used in asynchronous grid connection and it works properly even in large number of SMs fault, but still research is required to reduce the ripple of the output voltage during rectification mode of the converter.

References

[1] M.A. Alim, M.A.G. Khan and M.A. Munjer, "CSMC-SPWM Modular Multilevel Converter for HVDC Transmission System", *5th International Conference on Informatics, Electronics & Vision (ICIEV),* Dhaka May 13-14, 2016.

[2] M. P. Bahrman, "HVDC Transmission Overview, *IEEE/PES T&D, Transmission and Distribution Conference and Exposition*, 2008

[3] Olaf Saksvik,"HVDC Technology and Smart Grid", *The 9th IET International Conference*, Hong Kong, November 2012.

[4] Jong-Yul Kim, Jae-Young Yoon and Ho-Yong Kim, "PSCAD/EMTDC Modeling/Analysis of VSC-HVDC Transmission for Cross Border Power System Interconnection", *Journal of Electrical Engineering & Technology*, Vol. 4, No.1, 2009, pp. 35-42.

[5] Vassilios G. Agelidis, Georgios D. Demetriades and Nikolas Flourentzou, "Recent Advances in High-Voltage Direct-Current Power Transmission Systems" *IEEE International Conference on Industrial Technology, ICIT*, 2006.

[6] M.A. Alim, M.A.G. Khan, M.A. Munjer and Sumaya Kabir, "Output Voltage and Level Control Algorith During Submodule Fault of Modular Multilevel Converter for HVDC Transmission System", *IEEE International WIE Conference on Electrical and Computer Engineering,* 2016, 19-21 December, 2016, "Accepted Unpublished".

[7] Guowei Liu, Qirong Jiang and Yingdong Wei, "Study on Capacitor Voltage Balancing Control of Modular Multilevel Converter at Low Frequency", *International Journal of Computer and Electrical Engineering,* Vol. 5, No. 2, April 2013, pp. 196-200.

[8] Md Rabiul Islam,Youguang Guo, and Jianguo Zhu, "11-kV Series-Connected H-Bridge Multilevel Converter for Direct Grid Connection of Renewable Energy Systems" *Journal of International Conference on Electrical Machines and Systems,* Vol. 1, No. 2, pp.211 ~219 , 2012

[9] Tor Martin Iversen,"Multilevel Converters for a 10 MW, 100 kV Transformer-less Offshore Wind Generator" , *Department of Electric Power Engineering Norwegian University of Science and Technology*, June, 2012.

[10] W. Z. El-Khatib, J. Holboell, T. W. Rasmussen, "High frequent modelling of a modular multilevel converter using passive components", *International Conference on Power Systems Transients (IPST2013) in Vancouver*, Canada July 18-20, 2013.

[11] Sreedhar Madichetty, Abhijit Dasgupta, "Modular Multilevel Converters Part-I: A Review on Topologies, Modulation, Modeling and Control Schemes" *International Journal of Power Electronics and Drive System (IJPEDS),* Vol. 4, No. 1, March 2014 pp. 36~50.

Novel Approach of Antenna Array with Beam Steering Technology for Microwave Power Transmission from SSPS System

S. K. Saha and M. S. Hossain
Department of Electrical and Electronic Engineering
Rajshahi University of Engineering & Technology
Rajshahi-6204, Bangladesh
engr.sohag.pust@gmail.com; engg.selim@gmail.com

***Abstract*— A novel approach of antenna array with beam steering technology is addressed in this paper which can transmit microwave power from Space Solar Power Satellite (SSPS) system. Array antennas are critically important component in the development of future wireless systems with applications in communications, radar and satellite technologies. The Microwave Power Transmission (MPT) technology is a key technique for SSPS system, which is being highlighted as a technology capable of solving global environment problem as well as the energy problem. This paper presents a robust technique for MPT which is able to steer the main beam at any desired direction in the presence of array imperfections. The proposed beamforming technique is proficient to cancel the directional interferences. The simulation results show that the proposed SSPS scheme has better performance than the existing systems.**

Keywords*— Antenna array; Beam steering technology; Microwave power transmission; Robust beamforming.

I. INTRODUCTION

The SSPS system is a gigantic satellite designed as an electric power plant orbiting the Geostationary Earth Orbit (GEO), which consists of mainly three segments; Solar energy collector to convert the solar energy into DC (Direct Current) electricity, DC to microwave converter and large antenna array to beam down the microwave power to the ground. Besides, significant advancement in the design of modern array antennas, there continues to be significant and growing need for developing high performance systems that are low cost with beam steering capabilities. This paper presents a novel approach of the array antenna with the help of beam steering technology for transmission of microwave power from SSPS system. The idea of SSPS system represents one of the most promising future energy resources to provide renewable electrical energy on a large scale [1-2].

One of the most effective technologies to enable the future feasibility of SSPS system is represented by the Wireless Power Transmission (WPT) [3]. A WPT system is usually consists of a transmitting antenna, targeting to concentrate the microwave beam towards the collection area and the rectenna, which is devoted to receive and rectify the incident power [4]. Since, the large amount of power to be dealt with, at the same time extremely narrow bandwidths that have to be synthesized, large antenna arrays are usually considered for the realization of these components.

MPT is the wireless transfer of large amounts of power at microwave frequencies from one location to another [5-6]. MPT research has been driven primarily by the desire to remotely power unmanned aerial vehicles (UAVs) and by the concept of SSPS first conceived by Dr. Peter Glaser of the Arthur D. Little Company in 1968. The concept of placing enormous solar power satellite systems in space represents one of a handful of new technological options that might provide large-scale, environmentally clean base load power into terrestrial markets [7-8]. In a SSPS system, the first solar collector can be either photovoltaic cells or solar thermal turbine and the second DC-to-microwave converter of the SPSS can be either microwave tube system or semiconductor system. The third segment is a gigantic antenna array [9].

If any mismatch occurred on the environment, sources, or sensor array are violated, a disparity results between the presumed and actual signal steering vectors [10-12]. To overcome the existing difficulties, this paper proposes a novel approach of beamforming that can able to transmit microwave power from SSPS system in the presence of array imperfections.

Section II described the SSPS and MPT system. The signal model and robust beamforming algorithm is addressed in section III. Section IV presents examples of the proposed approach to make a comparison with the existing beamforming techniques. Finally, a conclusion is provided in section V.

II. SSPS SYSTEM WITH BEAM STEERING TECHNOLOGY

Fig.1 shows the functional block diagram of space solar power transformation system. It has mainly two major portions: one is SSPS and other is MPT.

A. Space Solar Power Satellite (SSPS) System

The demand of finding potential renewable energy resources to meet the increased load demand, space solar power could be a good solution. Actually, the demand of electrical energy increases rapidly than other energy demands as the world is industrialized and computerized. Under these

978-1-5090-5785-6/16/$31.00 ©2016 IEEE

circumstances, research has been carried out to look in to the possibility of building power station in space to transmit electricity to earth by way of radio waves that is the Space Solar Power Satellite. SSPS converts solar energy in to microwaves and sends that microwave in to a beam to a receiving antenna on the earth for conversion to ordinary electricity. Solar Power Satellite (SPS) is a clean, large scale, stable electric power source. SPS is also known as Satellite Power Station, Space Solar Power Station etc. The SPS would be located in the geosynchronous orbit. The microwaves would be beamed to the earth's surface, where they would be received and converted back into electricity by a large array of devices known as rectifying antenna or rectennas. Each SPS would have been massive in size. The dimensions are 10.50 km long and 5.30 km wide or with an average area of 56 sq. km. The surface of each satellite would have been covered with 400 million solar cells [11].

SPS has all the advantages of ground solar and it also generated power during cloudy weather and even at night time. In a word, SPS receiver operates just like a solar array, which received power from the space and converts it into electricity that reduces the size and complexity of the satellite.

B. Microwave Power Transmission Technology

The key technology required to enable the feasibility of SPS is that Wireless Power Transmission (WPT). The WPT is based on the energy transfer capacity of microwave beam that means, energy can be transmitted by a well focused microwave beam. Advanced in phased array antennas and rectennas have provided the building blocks for a realizable WPT system.

The microwave beam can be directed to any desired location on earth surface, which can be collected and converted back to electricity [9].

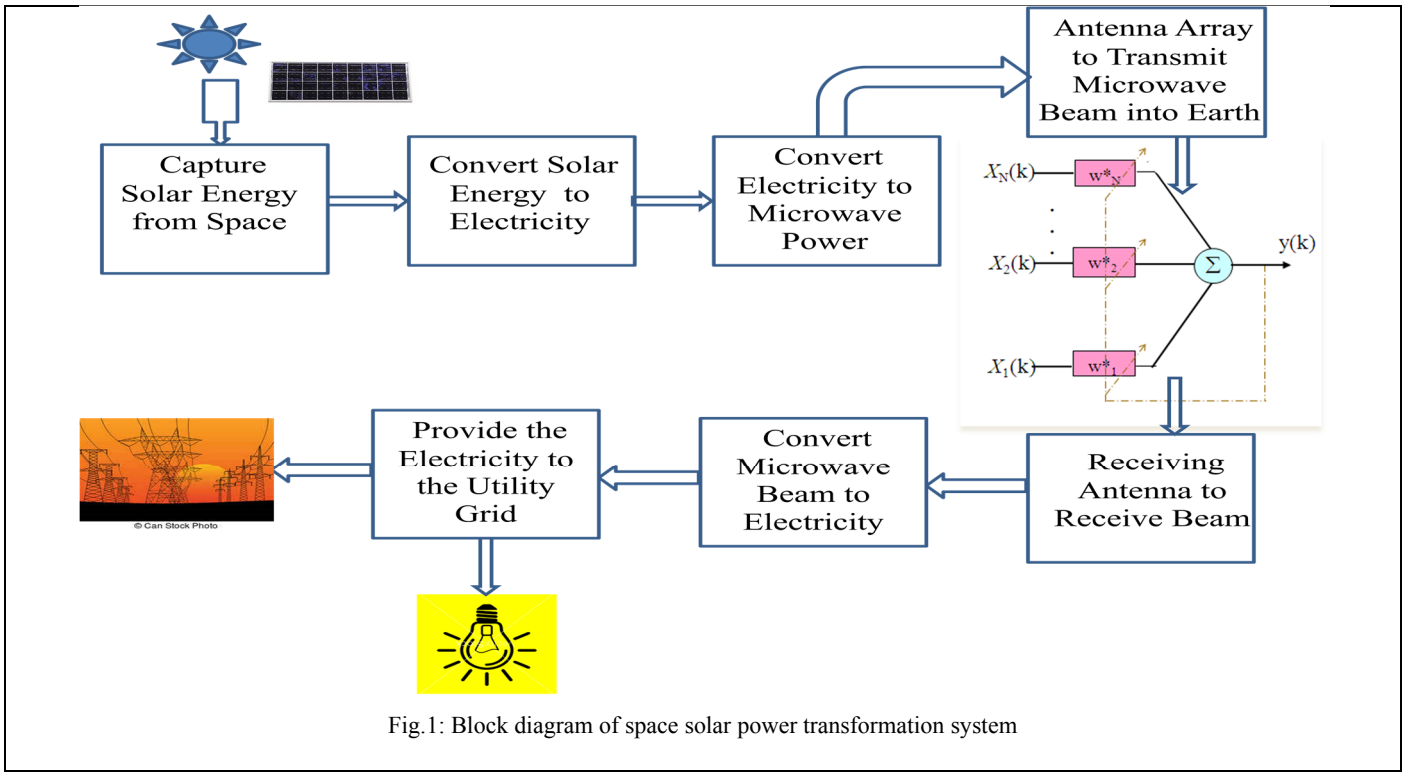

Fig.1: Block diagram of space solar power transformation system

The transmitting antenna on the satellite would have been about 1 km in diameter and the receiving antenna on the earth's surface would have been about 10 km in diameter. In order to obtain a sufficiently concentrated beam, a large amount of power must be collected and fed into a large transmitting array. The power would be beamed to the earth in the form of microwave at a frequency of 2.45 GHz [9,11].

The essential features of microwaves are larger bandwidth, smaller antenna size, sharp radiated beams and they propagate a long straight line [11].The microwave frequency in the range of 2-3 GHz is considered optimal for the transmission of power from SPS to the ground rectennas site. The amount of power available to the consumers from one SPS is 5 GW. The peak intensity of microwave beam would be 23 mW/cm^2 [11].

Transmission or distribution of 50 or 60 Hz electrical energy from the generation point to consumer end without any physical wire has yet to mature as a familiar and viable technology.

The microwave power output of the microwave device magnetron is channeled into an array of parabolic reflector antennas for transmission to the receiving end antennas. To compensate for the large loss in free space propagation and boost at the receiving end the signal strength as well as the conversion efficiency and the antennas are connected in arrays.

The overall efficiency of the WPT system can be improved by increasing directivity of the antenna array, using dc to ac inverters with higher conversion efficiency and using schottky diode with higher ratings [7-9]. The MPT system mainly consists of three aspects:

- ❖ The conversion of direct power from the photovoltaic cells to microwave power on the satellite on geosynchronous orbit above the earth.
- ❖ The formation and control of microwave beam aimed precisely at fixed locations on the earth's surface.
- ❖ The collection of the microwave energy and it's conversion into electrical energy at the earth's surface.

The key microwave components in a WPT system are the transmitter, beam control and the receiving antenna called rectennas. At the transmitting antenna, microwave power tubes such as magnetrons and klystrons are used as RF power sources. Rectenna is a component unique to WPT systems.

III. Signal Model & Beamforming Process

A. Antenna Array System Design

Let us consider the uniform linear array antenna system consisting of L antenna elements shown in Fig.1 where signals from each element are multiplied by a complex weight and summed to form the array output.

An expression for the array output is given by the following equations:

$$y(t) = \sum_{l=1}^{L} w_l^* x_l(t) \quad (1)$$

Where, * denotes the complex conjugate [10]. By using the vector notation, the weights of the array system denoted as follows:

$$w = [w_1, w_2, \ldots, w_L]^T \quad (2)$$

The induced signals on all of the elements as:

$$x(t) = [x_1(t), x_2(t), \ldots, x_L(t)]^T \quad (3)$$

The output of the array system results as:

$$y(t) = w^H x(t) \quad (4)$$

The output power of the antenna array at any time (t) is given by the magnitude square of the array output that is,

$$P(t) = |y(t)|^2 = y(t)\, y^*(t) = w^H x(t)\; x^H(t)\, w \quad (5)$$

The array correlation matrix is defined as follows:

$$R = E[x(t)\, x^H(t)] \quad (6)$$

Where, E[.] denotes the expectation operator. The elements of this matrix denote the correlation between various elements.

B. Beamforming Process

The different elements of an array induce signals, which are combined to form a single output. This combining process is known as beamforming. The beamforming are classified into two basic categories: (i) conventional beamforming which is also known as the delay-and-sum beamformer that has weights of equal magnitudes. The phases are selected to steer the array in a particular direction (ϕ_0,θ_0) known as look direction and (ii) optimal beamforming which maximizes the output SINR in the absence of errors and doesn't required the knowledge of interference directions and power levels of interferences and the level of the background noise power to maximize the output SINR.

IV. Proposed Robust Approach of Antenna Array Processor

To make optimal processor robust against array imperfections, a diagonal loading factor can be added with the array correlation matrix. The robust correlation matrix is given [10]

$$R_{robust} = R\_ac + \eta * I \quad (7)$$

Where the symbol η is known as the loading factor, which usually used 10 times of background noise [10].

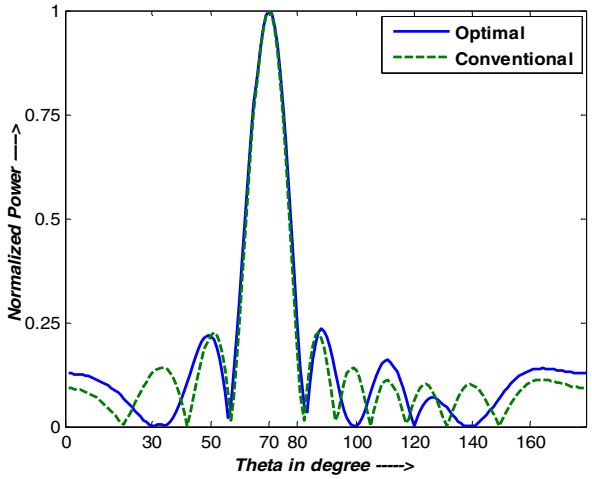

Fig.2: Normalized power comparison between conventional and optimal beamformer.

Fig.2 shows the power pattern comparison between conventional and optimal array processor. The conventional beamforming system described in the previous section needs information of the direction of interference sources. In addition, the beamforming using the weights anticipated by this system does not maximize the output SINR. These limitations are mitigated by the optimal beamforming system. It maximizes he output SINR in the absence of errors and doesn't required the knowledge of interference directions and power levels of interferences and the level of the background noise power to maximize the output SINR. The direction of the desired signal source is the only requirement.

In this example, ten-element linear array with equally half wavelength spaced are considered. One can observed from this Fig.2 that the optimal beamformer and conventional has identical pattern in main beam but optimal processor is able to cancel the directional interferences at 30^0, 100^0, 120^0 and 140^0.

Fig.3 shows that the output power pattern comparison between optimal and robust optimal beamformer. Assumed and actual steering directions were 70^0 and 69^0 respectively. One can easily be observe that the robust optimal processor

has unity gain in the desired signal direction but optimal processor treated actual signal direction as interference.

Fig.4 shows that the main beam direction remains constant at different operating frequencies, but the beam width decreases for the higher frequency. Fig.5 shows that the element pattern is constant over the entire bandwidth.

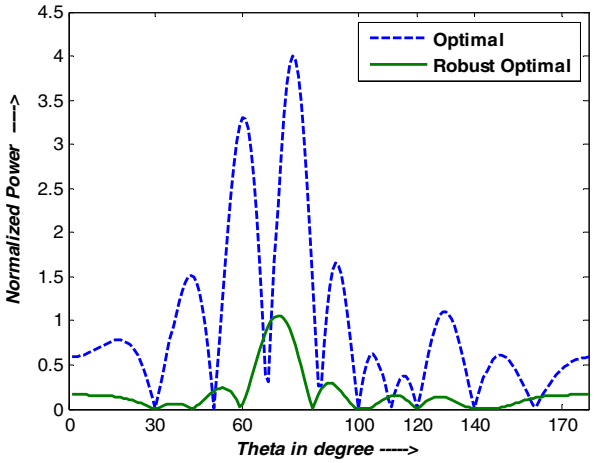

Fig.3: Output power comparison between optimal processor and robust optimal processor for 1^0 steering angle mismatch.

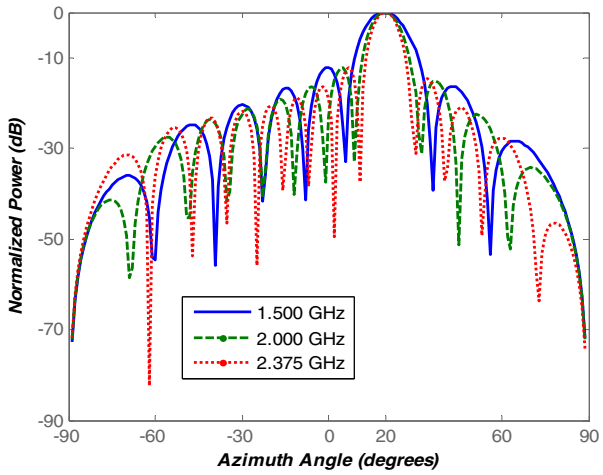

Fig: 4: Frequency variation effects on proposed processor.

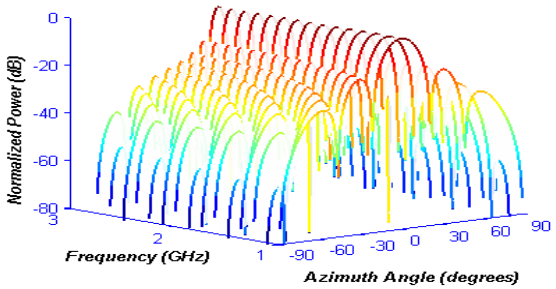

Fig.5: 3D output power pattern of the proposed processor.

V. Conclusion

The robust antenna array processor for SSPS system has been investigated in this paper. The consequences of this investigation is that, the proposed novel approach of antenna array with the help of beam steering technology is effective for transmission of microwave power from SSPS system. To mitigate the existing mismatch difficulties, this proposed robust optimal processor can be used for effective transmission of microwave power from SSPS system that is capable of solving global energy problem as well as ensured the green environment. Finally, the proposed processor is able to steer the main beam in any desired direction with array imperfections. Moreover, it can cancel the directional interferences and able to maintain the main beam in a preferred direction with different frequency band.

References

[1] J. O. McSpadden and J. C. Mankins, "Space solar power programs and microwave wireless power transmissiontechnology," *IEEE Microw. Mag.*, 3(4), pp. 46 57, Dec. 2002.

[2] A. K. M. Baki, K. Hashimoto, N. Shinohara, T. Mitani and H. Matsumoto, "New and improved method of beamforming with reduced side lobe levels for microwave power transmission," *5th Int.l Conf. on Electrical and ComputerEngineering,* Dhaka, Bangladesh, pp. 773-777, 2008.

[3] N. Shinohara, B. Shishkov, H. Matsumoto, K. Hashimoto, and A. K. M. Baki, "New stochastic algorithm for optimization of both side lobes and grating lobes in large antenna arrays for MPT," *IEICE Trans. Comm.*, E91-B, (1),pp 286-296, Jan. 2008.

[4] C. Bergsrud and S. Noghanian, "Survey of Ground Antenna Systems for Solar Power Satellite Application", *IEEE Aerospace Conference,* pp. 1-5, 2013.

[5] B. Strassner and K. Chang, "Microwave Power Transmission: Historical Milestones and System Components", *Proceedings of the IEEE*, *101*(6), pp.1379-1396, 2013.

[6] L. Shan and W. Geyl, "Optimal Design of Focused Antenna Arrays", *IEEE Transactions on Antennas and Propagation,* 62 (11), pp. 5565-5571, Nov-2014.

[7] X. Wang, X. Hou, L. Wang and M. Lu, "Employing Phase-Conjugation Antenna Array to Beam Microwave Power from Satellite to Earth", *IEEE International Conference on Wireless for Space and Extreme Environments (WISEE),* pp. 1-5, 2015.

[8] S. T. Goh, S. Zekavat and A. R. Seyad, "Space Solar Power Orbit Design and Cost Analysis", *IEEE 7th International Conference on Recent Advances in Space Technologies (RAST),* pp. 753-758, 2015.

[9] X. Lu, P. Wang, D. Niyato, D. I. Kim and Z. Han, "Wireless Charging Technologies; Fundamentals Standards and Network Applications", *IEEE Communications Surveys and Tutorials,* 18 (2), pp. 1413-1452, 2016.

[10] M. S. Hossain, G. N. Milford, M. C. Reed, and L. C. Godara, "Efficient robust broadband antenna array processor in the presence of look direction errors," IEEE Transactions on Antennas and Propagation, vol. 61, no. 2, pp. 718–727, Feb. 2013.

[11] G. Oliveri, P. Rocca, F. Viani, F. Robol & A. Massa, "Latest advances and innovative solutions in antenna array synthesis for microwave wireless power transmission", IEEE *-(IMWS), IEEE MTT-S International* (pp. 71-73), May. 2012.

[12] M. S. Hossain, G. N. Milford, M. C. Reed, L. C. Godara, "Robust Efficient Broadband Antenna Array Pattern Synthesis Techniques", *IEEE Transactions on Antennas and Propagation*, vol. 62: no. 9. pp. 4537-4546 Sept, 2014.

Robust Beamforming Synthesis Technique for Low Side Lobe Level using Taylor Excited Antenna Array

M. A. Sarker, M. S. Hossain and M. S. Masud
Department of Electrical and Electronic Engineering
Rajshahi University of Engineering & Technology
Rajshahi-6204, Bangladesh
arifrueteee11@gmail.com; engg.selim@gmail.com; engg.shahnewazmasud@gmail.com

***Abstract*—Antenna array is one of the most useable technologies in present day communication system. There are many applications like biomedical imaging, military communication and radar system where low side lobe level is an essential feature of array processor. There is a trade-off between side lobe level (SLL) and the directivity of the array. Designing an antenna array system with optimum trade-off between SLL and directivity has become a crucial problem. To suppress high SLL of output beam pattern and signal direction mismatches, some notable optimization techniques have been developed. Amplitude weighting of array elements is a well known approach for SLL control. In real-time implementation of antenna array system, the main beam may not be in the assumed direction and the actual signal is treated as an interference signal which is undesirable. Hence the robustness of an array processor against uncertainties is an important issue. In this paper, a method is proposed to keep the SLL at the desired value as well as makes the array system more applicable for real time implementation considering array uncertainties and imperfections.**

Keywords—robust beamforming; side lobe level control; fixed diagonal loading; Taylor excitation technique; signal direction mismatches

I. INTRODUCTION

Over the past few decades, researchers have taken on the challenge of providing various array designs to tailor radiation characteristics according to system requirements. An antenna array, or simply array, is an assembly of individual radiating antennas in an electrical and geometrical configuration. Antenna arrays are used to obtain high directivity, narrow beamwidth, low side-lobes, point-to-point and preferred–coverage pattern characteristics [1-2]. A linear array antenna is an assembly of radiating elements in a linear geometrical configuration. The radiation pattern depends on the number and the type of elements being used and the physical-electrical structure of the array.

Beamforming is a process which is related with an array of sensors to generate a form of spatial filtering. A beamformer can separate signals having overlapping frequency content but originate from different spatial locations [3]. The array antenna beamformer can be used for RADAR, air traffic control, SONAR, satellite, terrestrial communications, ultrasonic, optical, topographic imaging, geo-physical exploration like earth crust mapping, oil exploration, volcano monitoring, meteorology, seismology, biomedical applications like fetal heart monitoring, tissue hyperthermia, and hearing aids etc [1,4-5].

Some of the applications of beamforming require very low SLL. By amplitude tapering of the array elements, the SLL of the array can be reduced [1]. Designing an antenna array system with optimum trade-off between SLL and directivity has become a crucial problem. Taylor amplitude excitation yields a pattern that is an optimum compromise between directivity and SLL.

In realistic circumstances theoretically predicted performance of the beamformer may not be attained due to various effects and array imperfections such as look direction errors, mutual coupling effects, local scattering, distortion of wave front, signal source spreading, deficiency in array calibration and distorted antenna profile [4]. The performance of array beamformer corrupts with array deficiency, hence the inevitability of robust beamforming come into sight.

The beamformers described in [6-9] use different methods with linear array for controlling SLL which are not robust against array deficiency. To solve the problem of robustness, different robust techniques have been developed. In [11-15] some robust techniques are used to improve the beamformer performance by using linear programming, diagonal loading and frequency invariance constraints technique. These techniques do not consider the SLL of the system.

The contribution of this paper is to present a simple robust technique in a Taylor excited linear array (TELA) so that the system can keep the SLL at the desired value as well as robust against array imperfections. The proposed beamformer is simulated using MATLAB 2015a.

II. BACKGROUND AND SYSTEM MODEL

Consider a linear array beamformer as shown in Fig. 1. The beamformer consists of *N* identical antenna elements. The output of the beamformer is formed by multiplying the signals originated in each antenna with a complex weight and then accumulated towards an expected source in the look direction, in the presence of uncorrelated directional interferences and uncorrelated background noise. From Fig. 1, the array output can be written as [5],

$$y(t) = \sum_{n=1}^{N} w_n^* x_n(t) \quad (1)$$

978-1-5090-5785-6/16/$31.00 ©2016 IEEE

Where * denote the complex conjugate. The weight of the array and signals induced in each element can be written in the following vector format

$$W = [w_1, w_2, \dots \dots . w_N]^T \quad (2)$$

and

$$X(t) = [x_1(t), x_2(t), \dots \dots \dots . x_N(t)]^T \quad (3)$$

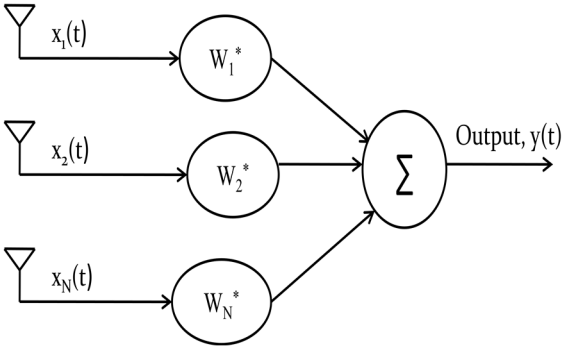

Fig. 1. Conventional Antenna Array Beamformer

Then, the output of the array structure becomes,

$$Y(t) = W^H X(t) \quad (4)$$

Consider that the noise environment consists of the random noise of power σ_n^2 and a directional interference of power P_I in look direction. Assume that there is a source of power P_S in the look direction and that the interference and the signal are uncorrelated. For this case, the array correlation matrix R is given by [5]

$$R = P_S\, S_0\, S_0^H + P_I\, S_I\, S_I^H + \sigma_n^2 I \quad (5)$$

Where I is an identity matrix and S_0, S_I are the steering vector of signal and interference respectively. Consider an N dimensional complex vector $\hat{w}$ represents the constrained weight of the array. The expression for $\hat{w}$ can be given by [5]

$$\hat{w} = \mu_0 R^{-1} S_0 \quad (6)$$

If the array weights be constrained to have a unit response in the look direction, that is

$$\hat{w}^H S_0 = 1 \quad (7)$$

Thus μ_0 is given by

$$\mu_0 = \frac{1}{S_0^H R^{-1} S_0} \quad (8)$$

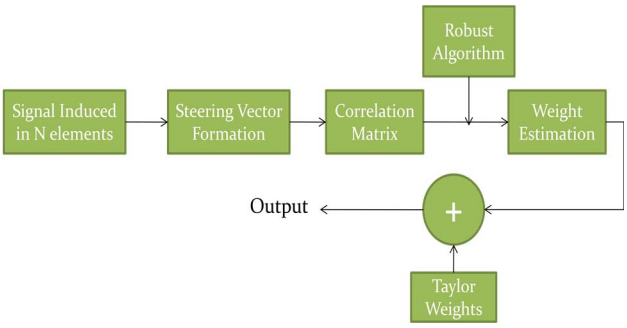

Fig. 2. Block diagram of proposed beamforming system

Fig. 2 shows the block diagram of TELA based robust beamformer. The conventional correlation matrix is modifed by the robust algorithm to get robust correlation matrix. Finaly the the robust weights are combined with Taylor weight in such a way that the proposed processor is able to keep the SLL at the desired value as well as robust against array imperfections. Substituting the value of μ_0 results of equation (8) the following expression for the weight vector is given by

$$\hat{w} = \frac{R^{-1} S_0}{S_0^H R^{-1} S_0} \quad (9)$$

Taylor distribution method is more applicable for continuous distribution [1]. The Taylor design [10] yields a pattern that is an optimum compromise between bandwidth and SLL. This technique of Taylor leads to a pattern whose first few minor lobes are maintained at an equal and specified level, the remaining lobes decay monotonically. The pattern of a line source contains an element factor and a space factor. The element factor depends upon the type and orientation of fields or currents which make up a typical segment of the source, and usually has little directivity, at least in the direction in which it would augment the directivity of the space factor. The space factor is the highly directive factor. It is dependent for its shape upon the relative variation of field or current strength along the source [10]. The normalized line source which yields the desired pattern is given by [1]

$$I(z') = \frac{\lambda}{l}\left[1 + 2\sum_{p=1}^{\bar{n}-1} SF(p, A, \bar{n}) \cos\left(2\pi p \frac{z'}{l}\right)\right] \quad (10)$$

Where z' is the position of line sources, l=Array length, $\bar{n}$ =boundary of region of uniform side lobes. The coefficients $SF(p, A, \bar{n})$ represent samples for Taylor pattern and they can be obtained by

$$SF(p, A, \bar{n}) = \begin{cases} \dfrac{[(\bar{n}-1)!]^2}{(\bar{n}-1+p)!\,(\bar{n}-1-p)!} \prod_{m}^{\bar{n}-1} \left[1 - \left(\dfrac{\pi p}{u_m}\right)^2\right] & |p| < \bar{n} \\ 0 & |p| > \bar{n} \end{cases} \quad (11)$$

Where, $u = \frac{l}{\lambda}\cos\theta$ with θ the angle measured from the end fire direction and λ be the wavelength.

III. Robust Beamforming Technique

Robustness is typically understood as an ability of adaptive beamforming algorithm to achieve high performance in the situations with imperfect, incomplete or erroneous knowledge about the source, propagation media, and antenna array [12].

There are numerous robust beamforming techniques. Diagonal loading method of the correlation matrix is a popular robust algorithm. Among different diagonal loading techniques, fixed diagonal loading (FDL) is the easiest method. In this paper we propose FDL technique of robust beamforming. This loading technique adds a fixed value diagonally with the correlation matrix to reduce the signal cancellation for look direction errors. The robust correlation matrix is given by

$$R_{robust} = R_{actual} + \lambda I \quad (12)$$

Where λ is the fixed diagonal loading factor taken to be equal to $10\sigma^2$with σ^2denoting the background noise power and I denoting the identity matrix [15]. Determination of fixed loading factor λ is a challenging task. Loading factor λcan be defined by setting its value with reference to the background noise or equal to the standard deviation of the diagonal entities of the correlation matrix. But how loading factor is related with the background noise gain constraint and the level of uncertainty of signal direction is unclear [13].

IV. Performance Analysis

A number of examples are presented in this section to evaluate the performance of the proposed processor. Taylor excitation of linear array offers the optimum trade-off between directivity and SLL of the array. Fig. 3 shows the radiation pattern of uniformly excited linear array (UELA), Chebyshev excited linear array (CELA) and TELA of 20 elements and 0.5λ spacing. From Fig. 3 it has been found that UELA has most sharp and narrow main lobe whether CELA and TELA have almost same characteristics. UELA has higher side lobe levels. The maximum side lobe level (MSLL) is almost at -13 dB. CELA and TELA have MSLL at the desired -30dB. All the side lobes of CELA are at -30 dB. Few side lobes, closer to the main lobe is at -30 dB and the others decaying monotonically in TELA.

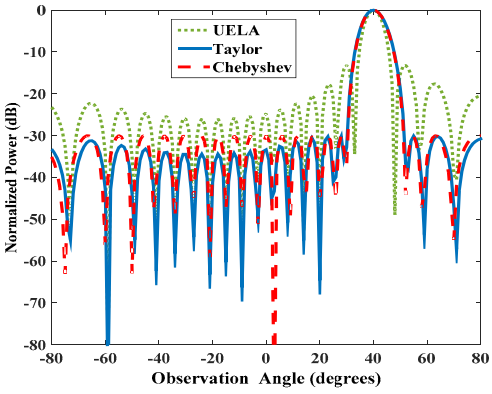

Fig. 3. Radiation pattern at 40^0 observation angle of 20 elements, 0.5λ spacing for uniform, Taylor and Chebyshevexcitation with defined SLL= -30dB.

The normalized power pattern can be observed by plotting observation angle in the X axis, frequency in the Y axis and the normalized power in the Z axis. The 3-D radiation pattern is shown in Fig. 4 which demonstred the desired signal direction clearly.

Due to various effects and array imperfections, the theoretically predicted performance of the beamformer may not be achieved. Fig. 5 indicates the normalized power pattern of Taylor excited array beamformer without robust technique. The assumed signal direction of the beamformer is 40º and actual signal directions are 38º and 42º respectively. From Fig. 5, we can see that the beamformer without robust technique creates two nulls at 38º and 42º which are undesirable. The MSLL also increased to -4 dB and this is quite low.

The look direction signal cancellation problem can be removed by using robust algorithm. Fig. 6 represents that the proposed robust TELA can operate spontaneously $\pm 2°$ of look direction error from the assume direction 40^0 keeping the MSLL at the desired -30 dB. From Fig. 6, it can also be seen that the original power pattern of TELA at actual look direction is restored using the proposed robust technique.

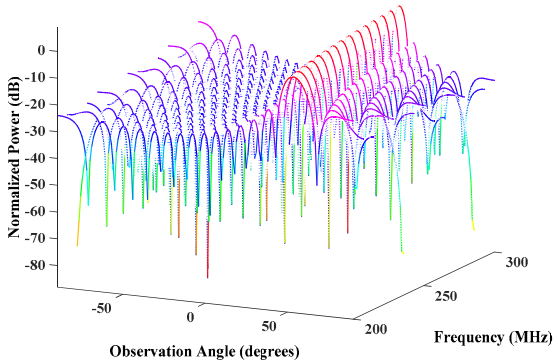

Fig. 4. Radiation pattern of an array with respect to observation angle and frequency.

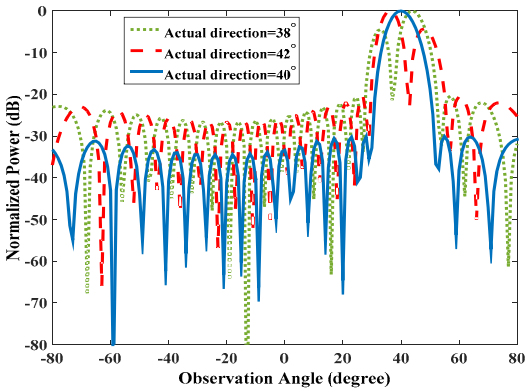

Fig. 5. Comparative radiation pattern of 20 elements, 0.5λ spacing conventional TELA at different actual direction when assume direction 40^0 with SLL= -30dB.

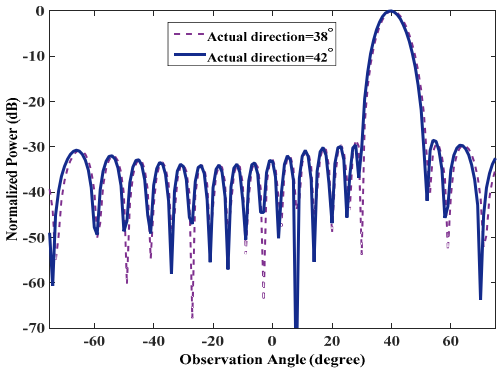

Fig. 6. Comparative radiation pattern of 20 elements, 0.5λ spacing conventional TELA at different actual direction when assume direction 40^0 with SLL= -30dB.

In Tab.I, the array characteristics like directivity, SLL and half power beamwidth (HPBW) are compared for conventional or UELA, CELA and TELA for different number of array elements and different array spacing. The directivity is increased with the increase of array elements for all three excitations. When the spacing between the elements is greater than 0.75λ, grating lobe is formed. The HPBW is decreased with the increase of both number of elements and spacing between the elements. From Tab. I, it is evident that conventional or UELA has higher MSLL whereas TELA and CELA has MSLL at the desired value. Taylor excitation bears the advantage that the sidelobes can be easily manipulated and it is more suitable for continuous source unlike Chebyshev excitation.

Table I Comparison of Directivity, HPBW and MSLL for Uniform, Taylor and Chebyshev Excitation

Properties		Directivity (dBi)				HPBW (degree)				MSLL(dB)			
		Element spacing				Element spacing				Element spacing			
	N	*0.2λ*	*0.4λ*	*0.6λ*	*0.8 λ*	*0.2λ*	*0.4 λ*	*0.6 λ*	*0.8 λ*	*0.2 λ*	*0.4 λ*	*0.6 λ*	*0.8 λ*
CONVENTIONAL ARRAY	10	6.28	9.10	10.64	9.09	30.09	14.75	9.79	7.27	-12.98	-13.01	-13.05	-12.98
	15	7.96	10.84	12.44	10.83	19.72	9.78	6.44	4.76	-13.32	-13.22	-13.16	-13.35
	20	9.16	12.08	12.08	12.07	14.7	7.25	4.75	3.55	-13.26	-13.21	-13.41	-13.37
	30	10.88	13.83	13.83	13.82	9.75	4.75	3.05	2.27	-13.31	-13.46	-13.75	-13.33
CHEBYSHEV	10	5.35	8.31	10.03	8.31	39	18.95	12.53	9.35	-30	-30	-30	-30
	15	7.14	10.14	11.89	10.14	24.96	12.31	8.19	6.12	-30	-30	-30	-30
	20	8.44	11.43	13.18	11.43	18.36	9.07	6.06	4.47	-30	-30	-30	-30
	30	10.25	13.23	14.97	13.23	12.01	5.99	3.99	2.8	-30	-30	-30	-30
TAYLOR	10	5.39	8.36	10.07	8.36	38.72	18.81	12.41	9.27	-30	-30	-30	-30
	15	7.12	10.12	11.87	10.12	25.09	12.39	8.23	6.17	-30	-30	-30	-30
	20	8.36	11.37	13.12	11.37	18.69	9.23	6.16	4.54	-30	-30	-30	-30
	30	10.12	13.13	14.88	13.13	12.39	6.16	4.09	2.89	-30	-30	-30	-30

The proposed beamforming technique of TELA can not work properly when the difference between actual signal and assumed signal is beyond ±2º. The TELA is unable to maintain the MSLL at the desired -30 dB when the difference is beyond the range of ±2º.

V. CONCLUSION

The robust algorithm based TELA beamformer has been proposed in this paper. It has been found using computer simulation that the uniformly excited array has higher directivity but higher side lobe levels. The Taylor distribution technique has narrow HPBW and easy to manipulate side lobe levels. The problem of performance degradation of conventional TELA with look direction error has been eliminated using robust technique. Thus the proposed beamforming system ensures desired MSLL even with array imperfection and uncertainties.

REFERENCES

[1] C. A. Balanis, "Antenna theory: Analysis and Design", 3rd edition, A John Wiley & Sons, 2005.

[2] S. Das, M. Bhattacharya, A. Sen, and D. Mandal, "Linear Antenna Array Synthesis with Decreasing Sidelobe and Narrow Beam-width", *ACEEE International Journal on Communications*, *3(1)*, 10-14, 2012.

[3] B. D. Van Veen and K. M. Buckley, "Beamforming a Versatile Approach to Spatial Filtering", *IEEE Aeros. Electron. Syst.Mag.*, vol. 5, pp 424, 1988.

[4] M. M. Rashid, M. S. Hossain and M. F. Ali, "Robust 2D Beamforming with Optimal Loading Technique," *2015 IEEE International Conference on Telecommunications and Photonics (ICTP)*, Dhaka, pp. 1-5, 2015.

[5] L. C. Godara*, "Smart Antennas*" New York: CRC Press, 2004.

[6] A. Safaai-Jazi and W. L. Stutzman, "A New Low Side Lobe Pattern Synthesis Technique for Equally Spaced Linear Arrays", *IEEE Transactions on Antennas and Propagation*, Vol. 64, Issue: 4, pp. 1317-1324, April 2016.

[7] N. Fadlallah, L. Gargouri, A. Hammami, R. Ghayoula, A. Gharsallah, and B. Granado, "Antenna Array Synthesis with Dolph-Chebyshev Method," *11th Mediterranean Microwave Symposium (MMS 2011)*, Yasmine Hammamet, Tunisia, September 2011.

[8] L. Sarika, P. Nandini, S. Bharathi, Y. Dhana, S. Suresh, "Side lobe Reduction in a Uniform Linear Array Antenna Using Windowing Techniques", *IJRET: International Journal Of Research in Engineering and Technology*, Vol. 3, Issue 4, May 2014.

[9] A. T. Abed, "Study of Radiation Properties in Taylor Distribution Uniform Spaced Backfire Antenna Arrays", *American Journal of Electromagnetics and Applications,* Vol. 2, No. 3, pp. 23-26, 2014.

[10] T. T. Taylor, "Design of Line-Source Antenna for Narrow Beamwidth and Low Sidelobes", *IRE Trans. Antennas Propagat.*, Vol. AP-3, No. 1, pp. 16–28, January 1955.

[11] X. Jiang, W. J. Zeng, A. Yasotharan, H. C. So and T. Kirubarajan, "Robust Beamforming by Linear Programming", *IEEE Transactions on Signal Processing*, Vol. 62, No. 7, April 2014.

[12] S. A. Vorobyov, "Principles of Minimum Variance Robust Adaptive Beamforming Design", *Signal Processing*, 93, pp. 3264-3277, 2013.

[13] M. S. Hossain, G. N. Milford, M. C. Reed, and L. C. Godara, "Efficient Robust Broadband Antenna Array Processor in the Presence of Look Direction Errors", *IEEE transaction on Antennas and Propagation*, Vol.61, no. 2, pp. 718-727, February 2013.

[14] A. Khaabbazibasmenj, S. A. Vorobyov, A. Hassanien, "Robust Adaptive Beamforming Based on Steering Vector Estimation with as little as Possible Prior Information", *IEEE Transaction on Signal Processing*, Vol. 60, No. 6, pp. 2974-2987, June 2012.

[15] Y. Zhao, W. Liu and R. Langley, "Adaptive Wideband Beamforming with Frequency Invariance Constraints", *IEEE Transaction on Antennas and Propagation*, Vol. 59, No. 4, pp. 1175-1181, April 2011.

International Conference on Electrical, Computer & Telecommunication Engineering (ICECTE)
8-10 December 2016, Rajshahi-6204, Bangladesh

Comparison of Two Types of Graphene Coated Fiber Optic SPR Biosensors

Kamrun Nahar Shushama, *Student Member, IEEE,* Md. Masud Rana, *Member, IEEE*, and Reefat Inum, *Student Member, IEEE*
Department of Electrical and Electronic Engineering
Rajshahi University of Engineering and Technology
E-mail: shushamanahar@gmail.com, md.masud.rana@ruet.ac.bd, romel.eee09@gmail.com

***Abstract*— In the present paper, surface plasmon resonance based two graphene coated fiber optic biosensors are analyzed using a four layer model. Graphene is used as third layer of a four layer model. Gold or silver is used as second layer and graphene is coated around the silver or gold. A theoretical study has been carried out for two sensors using gold and silver. Two biosensors have been studied separately and then a comparison has been made. Sensitivity has been studied for different number of graphene layers.**

Keywords*— Fiber optic sensors, Surface plasmon resonance (SPR), Graphene

I. INTRODUCTION

Surface plasmon resonance is the optical excitation of surface plasmon wave (SPW). It creates at the interface of metal and dielectric. Metals which have negative permittivities (gold, silver) and dielectric materials (liquid, gas or solid) are used. Surface plasmons remains confined at the interface and decays exponentially in the transverse directions. When the wave vector of the incident light matches that of the SPs (Surface plasmons) then resonant excitation of photon-electron coupling takes place. The evanescent part of SPR has high sensitivity to changes in complex refractive index of metal layer, surrounding dielectric medium and their geometrical sizes [1]. The most important condition for excitation of SPs is that the incident light is in the transverse magnetic (TM) polarization state [2]. The direct incident light has relatively small wave vector. So it cannot excite SPW at the metal dielectric interface. Extra momentum has to transfer to the incident light. For this high refractive index (RI) dielectric is required to fulfill the wave vector matching criteria. High wave vector prism, grating, corrugated surfaces and fibers are used for giving extra momentum to the incident light [2]. The reflectance spectra show a dip at the resonance condition. It occurs when the wave vector of the incident light matches with the SPW. SPR based fiber optic sensor in the wavelength interrogation mode has many advantages. It has advantages over SPR sensor comprising prism coupled configuration in angular interrogation mode [1]. It is attractive for researchers due to compactness, light weight, high sensitivity, ease of multiplexing and remote sensing, mechanical flexibility and the ability to transmit optical signals over a long distance. These sensors allow the miniaturization and the chemical or biological sensing in inaccessible locations [1]. The sensitivity of fiber optic sensor increases greatly by using graphene as a sensing layer [3].

Biosensors have been studied with great importance as they are very important in medical diagnostics, enzyme detection, beam polarization selection [4] food safety [5] ,[6], DNA hybridization [7], [8], protein- protein [9], [10], protein-DNA [11], [12] and so on .

Prism based SPR biosensor operating in angular interrogation mode has a number of limitations e.g., large size, presence of different optical and mechanical moving parts, no capability of online monitoring applications. By replacing the prism with an optical fiber such limitations are overcome. For a fiber-optic SPR biosensor, a thin metallic film (Au or Ag) is coated around the fiber as sensing layer. In different circumstances gold film has good resistance to oxidation and corrosion [13]. Gold shows larger shifts in resonance wavelength. It is chemically stable [13]. Its absorption coefficient is larger. This leads to broadening of resonance curve thereby reducing the performance in terms of detection accuracy. Biomolecules adsorb poorly on gold so that it limits the sensitivity of this kind of fiber optic SPR sensors [3]. On the contrary, silver shows a sharper resonance peak compared to gold and hence shows higher detection accuracy. But silver is prone to oxidation so that it reduces the detection accuracy [3]. Whenever graphene is used as sensing layer on Au or Ag film, sensitivity increases [3], [13]. Graphene is a single layer of graphite. It is one atom thick two dimensional plane where carbon atoms are arranged in honeycomb lattice. It possesses many superior properties e.g., high surface to volume ratio, high electron mobility, and stable structure between graphene layers [14]. Graphene adsorbs biomolecules with carbon-based ring structures stably so that a large refractive index changes near the graphene /sensing medium interface [15]. So for fiber-optic SPR biosensors, graphene is considered as a very good candidate as the sensing layer [3]. Graphene coated SPR based photonic crystal fiber (PCF) using gold and silver has been studied [3]. Graphene coated SPR based optical fiber biosensor has also been studied for the

configuration used in this paper [3] using gold as second layer. In this paper, SPR based graphene coated sensor for the configuration in [3] has been studied using silver as second layer. A comparison between graphene coated gold and silver sensor is shown.

II. NUMERICAL MODELING OF THE SENSORS

A numerical model of fiber optic biosensor is presented whose configuration is shown in Fig. 1 [3]. For realization of the optical fiber, a fiber core with diameter of *D* (50 *μm)*, sensing region *L* (5 *mm)* is taken. The cladding is removed and the uncladded portion of the fiber is considered to be coated with a sheet of *Au or Ag* film with the thickness of d_2 (30 *nm*).

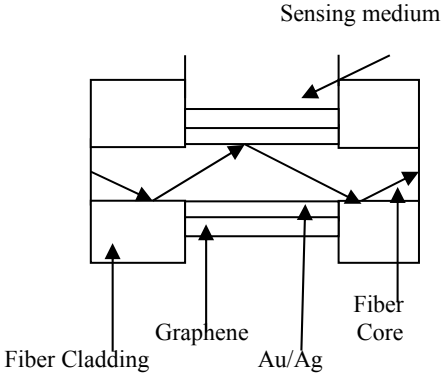

Fig. 1. Schematic diagram of the sensors.

Then Au or Ag with the thickness of d_3 ($d_3 = N \times 0.34$ *nm*, where *N* is the number of graphene layers) is coated with the graphene sensing layer. Light is launched into one end of the fiber at the axial point. Then arrives at the other end of the fiber. dP is the power arriving at the other fiber end between the incident angles θ and θ+dθ and dP can be expressed as [3],

$$dP \propto P(\theta)d\theta \quad (1)$$

$P(\theta)$ is the modal power related to the incident angle θ expressed as,

$$P(\theta) = \frac{n_{co}^2 \sin\theta\cos\theta}{(1-n_{co}^2\cos^2\theta)^2} \quad (2)$$

The refractive index of the fiber core is n_{co} (1.451). The reflectance value for a single reflection at the core/metal interface is as eq. (3).The normalized transmitted power of p-polarized light is expressed as,

$$P_{trans} = \frac{\int_{\theta_{cr}}^{\frac{\pi}{2}} R_p^{Nref(\theta)} P(\theta)d\theta}{\int_{\theta_{cr}}^{\pi/2} P(\theta)d\theta} \quad (3)$$

$Nref(\theta) = \frac{L}{D\tan\theta}$ is the total number of light reflections in the SPR fiber sensor by a ray whose incident angle is θ with the normal to the core-metal layer interface. L is the length of sensing region where D is the diameter of the fiber core. θ_{cr} is the critical angle of the optical fiber expressed as $\theta_{cr} = \sin^{-1}(n_{cl}/n_{co})$, n_{cl} is the refractive index of the fiber cladding (1.45). The reflection Rp can be achieved by using the four layer (fiber core/ metal/ sensing layer/ sensing medium) model analysis. Among the four layers, the first layer is the fiber core, the second layer is metal layer. The complex refractive index of graphene in the visible range is expressed as $n_3 = 3+i\frac{C}{3}\lambda$ where λ is the vacuum wavelength and $C \approx 5.446\ \mu m^{-1}$ [16]. The fourth layer is the sensing medium. Its refractive index SRI is n_s (water 1.33). The reflection intensity for *p*-polarized light is $R_p = |rp|^2$ where

$$r_p = \frac{(M_{11}+M_{12}q_N)q_1-(M_{21}+M_{22}q_N)}{(M_{11}+M_{12}q_N)q_1+(M_{21}+M_{21}q_N)} \quad (4)$$

$M = \prod_{K=2}^{N-1} M_k$ and

$$M_k = \begin{bmatrix} \cos\beta_k & -i\sin\beta_k/q_k \\ -iq_k\sin\beta_k & \cos\beta_k \end{bmatrix},$$

$q_k = \frac{(\varepsilon_k - n_c^2 sin^2\theta)^{1/2}}{\varepsilon_k}$, $\beta_k = \frac{2\pi d_k}{\lambda}(\varepsilon_k - n_c^2 sin^2\theta)^{1/2}$

According to Drude formula, the dielectric function of any metal ε_m is [17],

$$\varepsilon_m(\lambda) = \varepsilon_{mr} + i\,\varepsilon_{mi} = 1 - \frac{\lambda^2\lambda_c}{\lambda_p^2(\lambda_c + i\lambda)} \quad (5)$$

Where λ_p and λ_c represent the plasma and the collision wavelengths respectively.

III. RESULTS

In the simulation the following values of the optical parameters of silver and gold are used: for gold λ_p = 1.6826×10−7 m, λ_c =8.9342 ×10−6 m and for silver λ_p = 1.4541×10−7 m, λ_c= 1.7614×10−5 m [17].

A. Comparison of Parameters' Effects on two sensors

We have compared the biosensors without graphene as the fourth layer. We simulate the resonance wavelength versus increasing SRI (surface refractive index). The other parameters are kept constant. From Fig. 2 and 3 it is seen that, for both cases with graphene layers the resonance wavelength shifts to the longer wavelength. At the same time the bandwidth experiences slight broadening with increasing SRI. It is also seen that, with the same increase in SRI the resonance wavelength shifts larger for graphene on gold than graphene on Ag. For gold the resonance wavelength is 525.4 nm (2 layers of graphene, SRI 1.33) while without graphene the resonance wavelength is 509.2 (SRI 1.33). For silver, the resonance wavelength is 475.2 (2 layers of graphene, SRI 1.33) while without graphene the resonance wavelength is 458.8 (SRI 1.33).

The thickness of the gold film and graphene layers acting as sensing layer also affect the resonance wavelength of the optical fiber biosensor. The variations of resonance wavelength versus thickness of gold and silver film with two graphene layers have been simulated in Fig. 4. The thickness is varied from 30 nm to 50 nm when the SRI is 1.33 and other parameters are kept same. It is observed that,

the resonance wavelength shifts towards the longer wavelength when the thickness of the gold and silver film increases. At that time, the transmission of the resonance wavelength gets significantly larger. It is also observed that the resonance wavelength experiences smaller wavelength shift when the thickness of the gold and silver film increases. The resonance wavelength shift for gold is larger than silver. When the thickness is increased from 30 nm to 40 nm, the resonance wavelength shift for gold and silver is 41.2 nm and 28.4 nm respectively.

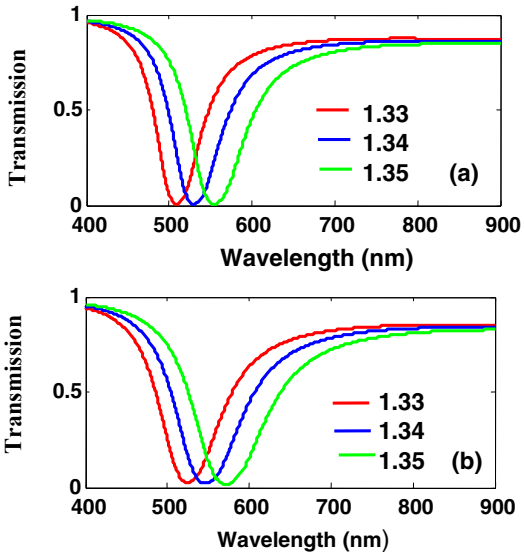

Fig. 2. Transmission spectra of gold sensor with the changing SRI without graphene layer (a) and with two graphene layers (b).

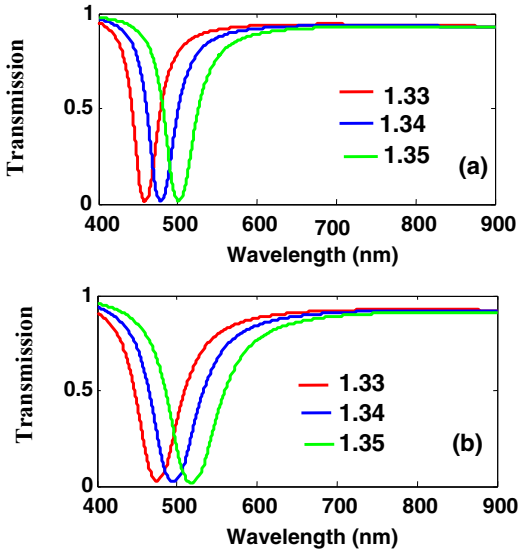

Fig. 3. Transmission spectra of Ag sensor with the changing SRI without graphene layer (a) and with two graphene layers (b).

After that, for Au and Ag biosensors we simulate the resonance wavelength versus number of graphene layers which is shown in Fig. 5. In this case, the thickness of the gold/ silver is used 30 nm and the SRI is 1.33 when other parameters are same. It is seen that, for both sensors with increasing number of graphene layers the shift in resonance wavelength is same. The resonance wavelength is larger with more graphene layers. In fact resonance wave-lengths increase with the thickness of the Au /Ag film and number of sensing layers. For both sensors, with the increased thickness of film the transmission of the dip gets higher. The transmission of the dip gets higher for silver film than gold.

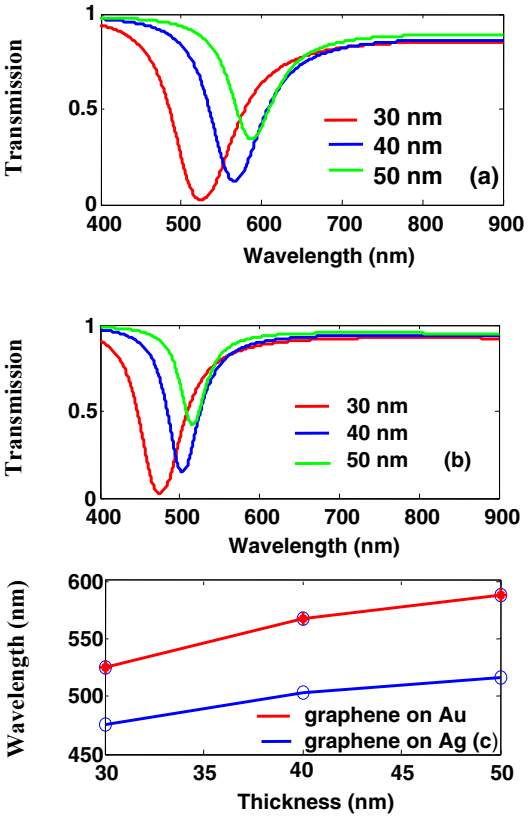

Fig. 4. Transmission versus wavelength for varying thickness of (a) Au (b) Ag. Variation of wavelength versus thickness of Au and Ag (c).

B. *Sensitivity Analysis*

Sensitivity of biosensor is defined as the change in the resonance wavelength for unit change in the refractive index of the sensing medium [2],

$$\text{Sensitivity} = \frac{\delta\lambda_{res}}{\delta n} \qquad (6)$$

These two biosensors act as refractive index sensors. By sensing refractive index changes, the sensors sense biomolecules. When biomolecules are added with the

sensing medium, the refractive index of the medium changes δn (.01). Therefore the resonance wavelength changes $\delta\lambda_{res}$. The larger is the shift of resonant wavelength for the same changes in the RI, the higher is the sensitivity of the biosensor. When graphene is used as sensing layer, the sensitivity of the biosensor increases than conventional biosensor using gold/ silver [3], [11]. The sensitivity of the graphene coated gold and silver sensors for the configuration shown in Fig. 1 with two graphene layers is 2020 nm/ RIU and 1980 nm/RIU respectively. The sensitivity of the graphene coated gold sensor is higher than the graphene

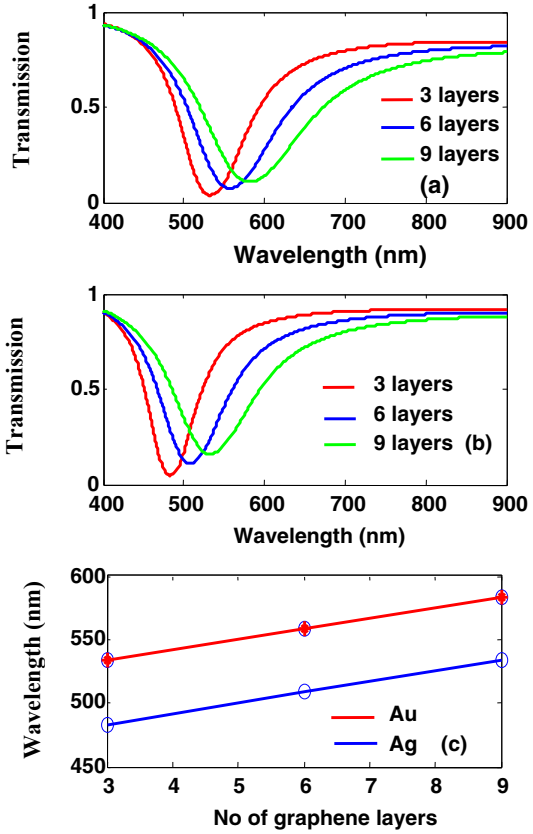

Fig. 5. Transmission versus wavelength for varying no of graphene layers on (a) Au (b) Ag. Variation of wavelength versus no of graphene layers of Au and Ag (c).

coated silver sensor. The sensitivity increases with the increase in number of graphene layers [15].

IV. Conclusion

Surface plasmon resonance based fiber optic biosensors have been used extensively for many advantages than other biosensors. Graphene enhances the sensitivity of this type of biosensors. In this paper, SPR based graphene coated fiber optic gold and silver biosensors are analyzed by varying different parameters. Their sensitivity has also been studied. It is seen that for the same configuration of the biosensor, the graphene coated gold sensor shows higher sensitivity than graphene coated silver sensor. The design of the sensors may be modified in such a way so that highest sensitivity can be obtained.

References

[1] Y. Yuan, L. Ding, and Z. Guo, "Numerical investigation for SPR-based optical fiber sensor",*Sens. Actuators B, Chem.*, vol. 157, no. 1, pp. 240–245, 2011.

[2] A.K. Mishra, S.K. Mishra, "Graphene and Beyond Graphene MoS2: A New Window in Surface-Plasmon-Resonance-Based Fiber Optic Sensing", *The Journal of Physical Chemistry* C,2016.

[3] H. Fu, S. Zhang, H. Chen, and J.Weng, "Graphene enhances the sensitivity of fiber optic surface plasmon resonance biosensor", *IEEE Sensors Journal*, vol. 15, no. 10, pp. 5478–5482, 2015.

[4] T.-J. Wang, C.-W. Tu, and F.-K. Liu, "Integrated-optic surface plasmon- resonance biosensor using gold nano particles by bipolarization detection", *IEEE Journal on Selected Topics in Quantum Electronics*, vol. 11, no. 2, pp. 493–499, 2005.

[5] J. Homola, "Present and future of surface plasmon resonance biosensors", *Anal. Bioanal. Chem.*, vol. 377, no. 3, pp. 528–539, 2003

[6] M. Pumera, "Graphene in biosensing", *Mater. Today*, vol. 14, nos. 7–8,pp. 308–315, 2011.

[7] H. Karimi, R. Yusof, R. Rahmani, "Development of solution-gated graphene transistor model for biosensors", Nanoscale Research Letters, vol. 9, no. 1,pp. 1–11, 2014.

[8] K. N. Shushama, M. Rana, "Graphene coated fiber optic surface plasmon resonance biosensor for the DNA hybridization detection: Simulation analysis", *Opt. communication,* 2017.

[9] A. Madeira, E.Vikeved, A. Nilsson, B. Sjogren, "Identification of protein-protein interactions by surface plasmon resonance followed by mass spectrometry",*Current Protocols in Protein Science*, vol. 65, pp. 19.21.1–19.21.9,2011.

[10] M. Kim, K. Park, E.-J. Jeong, Y.-B. Shin, and B. H. Chung, "Surface plasmon resonance imaging analysis of protein-protein interactions using on-chip-expressed capture protein", *Analytical Biochemistry*, vol. 351, no. 2, pp. 298–304, 2006.

[11] H. F. Teh,W. Y. X. Peh, X. Su, and J. S. Thomsen, "Characterization of protein-DNA interactions using surface plasmon resonance spectroscopy with various assay schemes",*Biochemistry*, vol. 46, no. 8, pp. 2127–2135, 2007.

[12] J. Majka and C. Speck, "Analysis of protein-DNA interactions using surface plasmon resonance",*Advances in Biochemical Engineering/Biotechnology*, vol. 104, pp. 13–36, 2007.

[13] J. Narayan Dash and Rajan Jha, "Graphene based birefringent photonic crystal fiber sensor using surface plasmon resonance", *IEEE Photonics Technology Letters*, 1041-1135, 2013.

[14] M. B. Hossain, S. Muktadhir, "Multi-structural optical devices modeling using graphene tri-layer sheets", Optik 127, 5841–5851, 2016.

[15] L. Wu,H. S. Chu, "Highly sensitive graphene biosensors based on surface plasmon resonance", *Opt. EXPRESS, 18*, 2010.

[16] R. R. Nair *et al.*, "Fine structure constant defines visual transparency of graphene", *Science*, 320, 1308, 2008.

[17] B.D. Gupta, A.K. Sharma, "Sensitivity evaluation of a multilayered surface plasmon resonance-based fiber optic sensor: a theoretical study", *Sensors and Actuators B* 107,pp. 40- 46, 2005.

International Conference on Electrical, Computer & Telecommunication Engineering (ICECTE)
8-10 December 2016, Rajshahi-6204, Bangladesh

Human Activity Recognition Based On Gaussian Mixture Model and Directive Local Binary Pattern

Swarup Kumar Dhar[1], Md. Mahmudul Hasan[1], Shayhan Ameen Chowdhury[1*]
[1]Dept. of Computer Science and Engineering (CSE), International Islamic University Chittagong (IIUC)
Chittagong-4318, Bangladesh
Email: swarup_dhar@outlook.com, mdpabel15@gmail.com, [1*]shayhan@yahoo.com

***Abstract*—Recognizing human activities has become an active research area in computer vision because of its promising need and use in many applications. In this paper, we represent a method for recognizing human activities in video. In order to recognize different activities accurately a distinctive and informative feature vector is required which can encode more distinctive information. We introduce a feature named Directive Local Binary Pattern (DLBP) which we develop on the basis of our experimental result that is orientation information is more informative than magnitude information for binary silhouette based recognition. The proposed Directive Local Binary Pattern (DLBP) incorporates orientation information with intensity differences of binary silhouette images. It is further combined with Edge Orientation Histogram (EOH) and forms a more distinctive and informative feature set. By means of the extracted features, Support vector machine is used for training and recognition which is a robust classifier. The proposed method for recognizing human activities is experimented on different videos containing various moving humans and the outcomes of our method are encouraging.**

Keywords— Human Activity Recognition; Gaussian Mixture Model; Local Binary Patter; Binary Silhouette Image; Error Correcting Output Code; Support Vector Machine

I. INTRODUCTION

With the necessity and popularity of recognition system of human activities for their vast applications such as surveillance, human-computer interaction, patient health care, robotics, the research on this field is being done by the researchers for a long time [1]. One of the important steps of recognition system is extraction of feature. For feature extraction, many methods have been also developed such as PCA, ICA, LDA [7], Histogram of Oriented Gradient (HOG) [8], Local Binary Pattern (LBP) etc. M. Z. Uddin, J. J. Lee and T. -S. Kim [7] used Linear Discriminant Analysis (LDA) of Independent Component (IC) features and Hidden Markov Model for recognizing human activities. W. -L. Lu and J. J. Little [10] used PCA-HOG for human activity recognition which shows noticeable result. H. Su, J. Zou and W. Wang [4] used Local Binary Pattern (LBP) in human activity recognition where LBP is a powerful local texture extraction operator. For recognition Hidden Markov Models (HMM) [6], Support Vector Machines (SVM) [6] are hugely used among the current computer vision approaches. W. Zhou and Z. Zhang [2] used multiple instances HMM for learning and recognition activities. To speed the recognition system, K. G. M. Chathuramali and R. Rodrigo [5] used SVM classifier. SVM has the advantages of effectiveness in high dimensional spaces, memory efficient as it uses a subset of points of training in the decision function which is called support vectors, adaptability by specifying different Kernel functions for the decision function etc.

In this paper, we propose a human activity recognition method in which we introduce a feature. This feature is capable of encoding more information than intensity differences of LBP by incorporating orientation information with the intensity difference. The extracted features are used by multiclass one-vs-one SVM classifier for training as well as recognition. Since our human activity recognition system is a multiclass classification problem, we use Error correcting output code (ECOC) combined with One-vs-One Binary Linear SVM for constructing a multiclass support vector machine.

II. THE PROPOSED METHOD

The following Fig.1 demonstrates our proposed method step by step for recognizing human activities. Finally the DLBP and EOH features are extracted from the foreground images and passed into SVM-ECOC for classification.

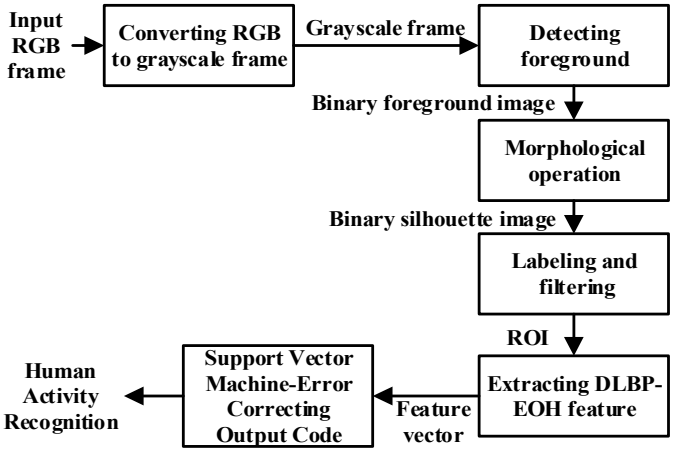

Fig. 1. The proposed framework for Human Activity Recognition.

978-1-5090-6122-8/16/$31.00 ©2016 IEEE

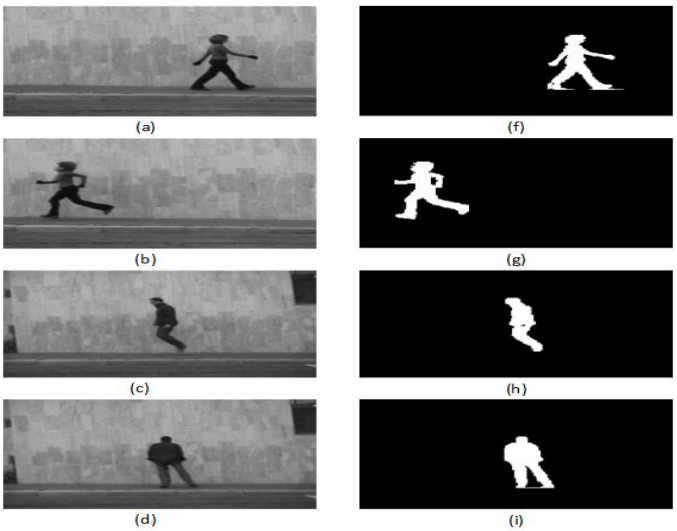

Fig. 2. Binary foreground images for corresponding gray images using GMM. (a), (b), (c), (d) are gray images and (f), (g), (h), (i) are their binary foreground images respectively.

A. RGB to Grayscale Conversion

For using Gaussian Mixture Model to detect binary foreground, we first need to convert the RGB video frames into grayscale video frames. To do that, we use the standard NTSC (National Television System Committee) conversion formula in order to compute the effective luminance or intensity of a pixel.

B. Foreground Detection Using Gaussian Mixture Model

Gaussian Mixture Model (GMM) can extract binary foreground of the moving objects from video [11]. In GMM, we use the minimum volume of the data that should be appointed for the background is 0.7 to generate the background. The initial variance of the gaussians of the mixture model we have used is 30×30. We use 40% of total video frames as initial video frames for training background model. For these 40% video frames, the learning rate we use is *1/(number of current frame)* [11]. Using this, initial estimation of the gaussians of mixture model is done on these frames which improve the degree of accuracy and performance for robust modeling of background [11]. After training these 40% video frames, for the rest of the video frames the learning rate we use is, $\alpha = 0.004$. Thus using GMM we get the binary foreground images for the corresponding grayscale images which are shown in Fig. 2.

C. Morphological Operation

The morphological operations we have performed over the foreground images are dilation, erosion and again dilation respectively to remove noises, fill up holes in the interesting subject. Then performing the morphological operations, each frame is labeled and filtered into 64×128 binary silhouette of ROI containing the human body of specific activity. After performing all these, the resulting binary ROI images are shown in Fig. 3. From these noise-free binary silhouette ROIs, the proposed DLBP and popular EOH features are extracted.

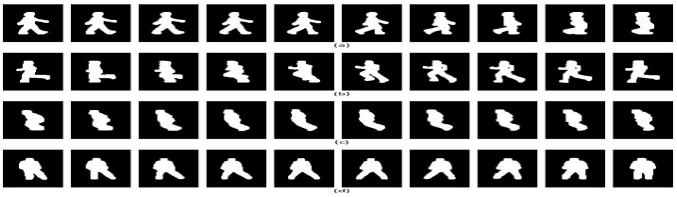

Fig. 3. Generalized ROIs from image sequence of (a) walking (b) running (c) jumping (d) siding.

D. Directive Local Binary Pattern and Edge Orientation Histogram Based Features

Before developing our proposed feature, we perform an experiment on HOG feature because HOG feature achieves satisfactory result in recognition applications. That's why, we first try to find out what is the strong information encoded in HOG which is more responsible for providing good result in binary silhouette based recognition. To do this, we try to recognize various human activities using HOG-SVM classifier taking gradient orientation and gradient magnitude separately and we apply these separately on binary silhouette images. When we take gradient orientation and ignore magnitude information by keeping the value of magnitude is equal to 1 for all pixels in HOG feature, we call it Orientation Dominant HOG-SVM classification. On the other hand, in the same way when we take gradient magnitude and ignore orientation information by keeping the value of orientation is equal to 1 for all pixels in HOG feature extraction, we call it Magnitude Dominant HOG-SVM classification. For testing a specific kind of activity, we first train the system by using 400 binary silhouette images of that kind of activity as positive training images and randomly using 400 binary images as negative training images consisting of non human binary images and other activities' binary silhouette images. In both classifications, for distributing the gradient magnitude and orientation of each pixel, the method developed by N. Dalal and B. Triggs [8] is used. We perform these two classifications with respect to four kinds of activities. These are walking, running, jumping and siding. The recognition results using Orientation Dominant HOG-SVM and Magnitude Dominant HOG-SVM classifications are shown in Table I. where we see that Orientation Dominant HOG-SVM is providing better recognition result than Magnitude Dominant HOG-SVM. As a result, we conclude that gradient orientation is the most strong and discriminative information encoded in HOG feature in case of silhouette based images.

Orientation information is lost in Uniform LBP. On the other hand, Center Symmetric LBP can contain only four orientation directions. To cope up with these limitations and generate a discriminative feature descriptor, we introduce a feature which incorporates orientation information with the intensity difference information of LBP since we have experimentally seen in HOG that orientation information is more distinctive and informative than magnitude information in case of binary silhouette based recognition. We name our proposed feature as Directive Local Binary Pattern (DLBP). It becomes more discriminative variation of LBP in case of binary silhouette based recognition.

TABLE I. DETECTION RATE FOR ORIENTATION DOMINANT HOG-SVM AND MAGNITUDE DOMINANT HOG-SVM

	Activity	Detection Rate (%)	Mean	Standard Deviation
Orientation Dominant HOG-SVM	Walking	68.5	87.9	13.10
	Running	95		
	Jumping	96.6		
	Siding	91.5		
Magnitude Dominant HOG-SVM	Walking	65.3	80	13.58
	Running	71.6		
	Jumping	91.6		
	Siding	91.5		

a. *Directive Local Binary Pattern*

The features' basic aim is to incorporate orientation information with the intensity difference information of LBP to improve the performance. For the calculation of our proposed Directive Local Binary Pattern (DLBP), at first, we calculate LBP over binary silhouette ROI. If the value of the central pixel is smaller than its neighbor pixels' value then 1 is obtained. On the other hand, if the value of the central pixel is greater than or equal to its neighbor pixels' value then 0 is obtained. From the LBP ROIs, we compute and keep only Uniform Local Binary Patterns. The Uniform local binary patterns are those local binary patterns which have at most two 0-1 or 1-0 transitions. The magnitude $m(x,y)$ of a pixel is identified by the number of continuous "1" bit of its neighbors (after comparing with the central pixel). On the other hand, the orientation $\Theta(x,y)$ of that pixel is identified by the principle direction of these "1" bit. Thus we calculate the magnitude as well the orientation of each pixel. Then we divide the orientations of the pixels into bins ranging from 0° to 360° following bilinear interpolation. The histograms of orientations $H_k(Cell_i)$ in each orientation bin k of cell $Cell_i$ are calculated by summing the all pixels' magnitudes whose orientations belong to the orientation range of bin k in cell $Cell_i$.

$$H_k(Cell_i) = \sum_{(x,y) \in Cell_i, \Theta(x,y) \in bin\,k} m(x,y) \quad (1)$$

In Fig. 4, after performing morphological operations, we get the binary silhouette ROI in Fig 4(a). In Fig. 4(b), we represent a magnified 3×3 portion. The intensity values of the magnified portion are shown in Fig. 4(c). In Fig. 4(d), LBP pattern is represented and thus finally in Fig. 4(e), we get the final LBP image. Then we keep only the uniform patterns from LBP. In Fig. 4(f), a uniform pattern is shown. Finally, from Fig. 4(f) the magnitude and orientation is calculated. The magnitude of this central pixel $m(x,y)$ is the number of continuous "1" bit in its binary pattern (here, for 01110000, $m(x,y) = 3$). The orientation of this central pixel $\Theta(x,y)$ is shown by the red arrow in Fig. 4(g) that is the principle direction of continuous "1" bit in its binary pattern (here, for the 01110000, $\Theta(x,y) = 45^o$). In our approach, a 64×128 binary ROI is divided into blocks. Each block consists of 2×2

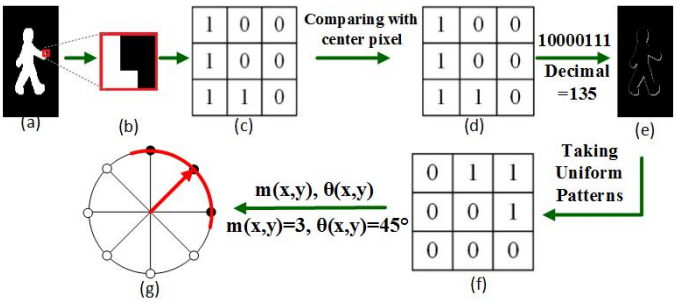

Fig. 4. Computing pixel orientation and magnitude of Directive LBP feature. (a) Silhouette image. (b) Magnified 3×3 portion. (c) Pixel intensity values. (d) Comparing with center pixel and forming binary patterns of central pixel. (e) LBP image. (f) Uniform pattern taking. (g) Orientation and magnitude computation of central pixel.

cells where each cell is of 8×8 pixels. We use 50% overlapping of blocks with each other at the time calculating histograms over blocks. We use $n=8$ bins for dividing the orientation of pixels. In binning process for distributing the gradient orientation along with its magnitude, we use bilinear interpolation between the neighboring centers of bins of orientations. The orientation of each pixel is divided into its two closest neighbor bins. Then histograms over each cell are computed which are concatenated over blocks. The histograms of the blocks of the entire image are finally concatenated to be represented as a feature descriptor. Thus for a 64×128 binary silhouette ROI, it generates a 3360D feature vector (7×15×32) where there are 7×15 overlapping blocks.

The DLBP can integrate orientation information with LBP features which is lost during computation of LBP feature but this orientation information is stronger in case of detection and recognition as orientation information is more discriminative and critical than magnitude information. It is less dimensional than HOG. CS-LBP keeps four orientation directions where DLBP contains eight orientation directions.

b. *Edge Orientation Histogram*

The feature set will be more distinctive as well as informative if we become able to combine the edge direction information with proposed DLBP feature. In order to do that a robust way is Edge Orientation Histogram (EOH) described in [9]. In our approach, for calculating EOH, we use five sobel operators to get the power of the gradient in five certain directions which are vertical, horizontal, two diagonals and non-directional. From the convolution matrix, the maximum gradient is counted and it is used to complete a histogram by keeping just the index (type) of the gradient orientation. Based on the type of orientation of the edges we generate a histogram of K bins where $K=5$ (types of gradient orientation). We use canny edge detector to eliminate the amount of non- important gradients. Then we divide a 64×128 binary silhouette ROI image into 8×8 regions where each region consists of 8×16 pixels. After that, histograms are computed over each of the regions. By concatenating these histograms, we construct feature vector. For a 64×128 binary silhouette ROI image with 8×8 regions, the EOH feature has a 320D (8×8×5) feature vector. After calculating the EOH and DLBP features, for each 64×128 binary silhouette ROI we get 3680D feature vectors

by concatenating 320D EOH feature vector and 3360D DLBP feature vector. This 3680D feature vector is used for training the classifier as well as for recognizing different activities.

E. Support Vector Machine(SVM)-Error Correcting Output Code(ECOC) Model

For training and recognition, we use one-vs-one linear SVM classifier. Since the classification we need is a multiclass classification problem, we use one-vs-one SVM learner with error-correcting output code. An error-correcting output code model (ECOC) [3] [12] has the ability to convert the problem of multiple class classification into a set of binary SVM classifiers.

III. EXPERIMENTS

In our experiment we have used Weizmann standard datasets.

1) Weizmann Dataset: Among the 10 types of human activity of Weizmann action dataset [5], we have recognized four activities using DLBP-EOH features and SVM-ECOC classifier. These are walking, running, jumping and siding.

Table II represents Confusion matrix for four types of human activities set for Weizmann Dataset after implementing DLBP-EOH, HOG and Uniform LBP respectively. Here D means DLBP-EOH implementation, H means HOG implementation and U means Uniform LBP implementation.

From Table II and Fig. 5, we have clearly seen that proposed Directive Local Binary Pattern (DLBP) combined with Edge Orientation Histogram (EOH) is capable of providing better results than Histogram of oriented gradients (HOG) and Uniform Local Binary Pattern (Uniform LBP) in case of Running and Siding activities in the binary silhouette

TABLE II. CONFUSION MATRIX FROM WEIZMANN DATASET

	Walking (%)			Running (%)			Jumping (%)			Siding (%)		
Walking	**D**	**H**	**U**	**D**	**H**	**U**	**D**	**H**	**U**	**D**	**H**	**U**
	68.64	72.37	69.74	15.35	12.50	12.50	06.36	08.77	10.09	09.65	06.36	07.68
Running	**D**	**H**	**U**	**D**	**H**	**U**	**D**	**H**	**U**	**D**	**H**	**U**
	30.60	32.84	30.97	61.57	60.07	54.10	02.24	02.99	07.09	05.60	04.10	07.84
Jumping	**D**	**H**	**U**	**D**	**H**	**U**	**D**	**H**	**U**	**D**	**H**	**U**
	12.79	08.72	09.30	07.56	07.27	09.30	60.76	63.08	65.41	18.90	20.93	15.99
Siding	**D**	**H**	**U**	**D**	**H**	**U**	**D**	**H**	**U**	**D**	**H**	**U**
	09.12	10.03	17.63	11.85	14.59	03.04	06.69	03.34	09.42	72.34	72.04	69.91

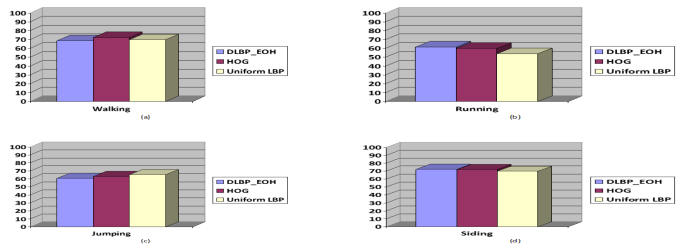

Fig. 5. Comparison using bar chart: (a) Walking, (b) Running, (c) Jumping, (d) Siding.

based activity recognition. The proposed DLBP can integrate orientation information along with intensity difference which makes it capable of storing more information. Besides, this is also concatenated with EOH to make the feature set more distinctive in a robust way. All these enable the system to improve its performance.

IV. CONCLUSION

In this paper, we have represented an approach for human activity recognition by introducing a feature. It can alleviate limitation of LBP since it can store orientation information along with intensity difference information. The proposed method shows encouraging results in case of Running and Siding activities. In Future, we have plans to add motion information with it to improve the accuracy of the system. We also plan to increase the number of recognized activities and work with multi-person interaction and partial occlusion.

REFERENCES

[1] P. Turaga, R. Chellappa, V. S. Subrahmanian, O. Udrea, "Machine Recognition of Human Activities: A Survey," IEEE Trans. on Circuits and Systems for Video Technology, vol. 18, no. 11, pp. 1473–1488, October 2008.

[2] W. Zhou, Z. Zhang, "Human Action Recognition With Multiple-Instance Markov Model," IEEE Transactions on Information Forensics and Security , vol. 9, no. 10,pp. 1581 - 1591, September 2014. R. Nicole, "Title of paper with only first word capitalized," J. Name Stand. Abbrev., in press.

[3] S. Escalera, O. Pujol, P. Radeva, "On the decoding process in ternary error-correcting output codes," IEEE Transactions on Pattern Analysis and Machine Intelligence , vol. 32, no. 1, pp. 120 - 134, November 2009.

[4] H. Su, J. Zou and W. Wang,"Human Activity Recognition Based On Silhouette Analysis Using Local Binary Patterns," 10th International Conference on Fuzzy Systems and Knowledge Discovery (FSKD), pp. 924 – 929, July 2013.

[5] K. G. M. Chathuramali and R. Rodrigo, "Faster human activity recognition with SVM," International Conference on Advances in ICT for Emerging Regions, pp. 197 – 203, Dec. 2012.

[6] J. K. Aggarwal and M. S. Ryoo, "Human activity analysis: a review," ACM Computing Surveys, vol. 43, no. 3, Article 16. 2011.

[7] M. Z. Uddin, J. J. Lee and T.-S. Kim, "Independent Component Feature-based Human Activity Recognition via Linear Discriminant Analysis and Hidden Markov Model," 2008 30th Annual International Conference of the IEEE Engineering in Medicine and Biology Society , pp. 5168 – 5171, Aug. 2008.

[8] N. Dalal and B. Triggs, "Histograms of oriented gradients for human detection," 2005 IEEE Computer Society Conference on Computer Vision and Pattern Recognition , vol. 1, pp. 886–893, June 2005.

[9] K. Levi and Y. Weiss, "Learning object detection from a small number of examples: The importance of good features," IEEE Computer Society Conference on Computer Vision and Pattern Recognition, vol. 2, pp. 53–60, July 2004.

[10] W. -L. Lu and J. J. Little "Simultaneous Tracking and Action Recognition using the PCA-HOG Descriptor," The 3rd Canadian Conference on Computer and Robot Vision, pp. 6, June 2006.

[11] P. Kaewtrakulpong, R. Bowden, "An Improved Adaptive Background Mixture Model for Real-time Tracking with Shadow Detection," 2nd European Workshop on Advanced Video Based Surveillance Systems, AVBS01, VIDEO BASED SURVEILLANCE SYSTEMS: Computer Vision and Distributed Processing, September 2001.

[12] E. L. Allwein, R. E. Schapire, Y. Singer, "Reducing multiclass to binary: A unifying approach for margin classifiers," Journal of Machine Learning Research, vol. 1, pp. 113–141, 2000.

International Conference on Electrical, Computer & Telecommunication Engineering (ICECTE)
8-10 December 2016, Rajshahi-6204, Bangladesh

Sentiment Mining from Bangla Data using Mutual Information

Animesh Kumar Paul[1], Pintu Chandra Shill
Department of Computer Science and Engineering
Khulna University of Engineering & Technology
Khulna, Bangladesh
[1]animesh10kuet@gmail.com

Abstract— **Due to the explosion of social networking sites, blogs and review sites (for example, Amazon, Twitter, and Facebook, etc.) it provides an overwhelming amount of textual information. We need to organize, explore, analyze the information for making a better decision from the side of customers and companies. Thus, sentiment analysis is the best way in which it determines the author's feelings expressed in reviews as positive or negative opinions by analyzing an enormous number of documents. In this work, we used Mutual Information (MI) for the feature selection process and also used Multinomial Naive Bayes (MNB) for the classification of Bangla and English reviews. The experimental results demonstrate that the system can achieve satisfactory accuracy for Bangla dataset compare to English dataset where Bangla dataset is generated from Amazon's Watches English dataset.**

Keywords—Sentiment Analysis, Sentiment levels, Feature Selection, Mutual Information, Multinomial Naive Bayes (MNB).

I. INTRODUCTION

With the rapid wideness of e-commerce, many companies are placing their product into online market for selling, and a huge number of user now buy a product from online. Millions of people express their shopping experience and product features and their nuances. Due to the explosion of social networking sites, blogs and review sites (for example, Amazon, Twitter, Facebook, and Consumer Reports), it provides an overwhelming amount of textual information about the present condition of the product as an active feedback from the user. From these active feedback information, manufacturing companies [1] want to know what is the feeling of their customers on their or other company's products which helps them to maintain their online reputation [2-4] and at the same time, user easily can get ideas who want to know which product will be good for them with compare to others product.

Due to the increasing amount of user-generated contents (opinion, reviews, comments, feedbacks, suggestions), analyzing all of this online information is necessary for making an effective decision from the customers and company. Explore, analyze and organize these kinds of extensive information manually is time-consuming. Automatic sentiment analysis for these user-generated information refers to the field of natural language processing (NLP), computational linguistics (CL), and text mining. Sentiment analysis [5] is the task of retrieve the opinions about the product and classify the given contextual information into different polarity (positive or negative opinion). This text classification task is also referred to as polarity classification.

The research in the field of sentiment analysis started much earlier. In [6], here it used several machine learning systems (Naive Bayes, Maximum Entropy, and SVM techniques) to classify a large corpus of movie reviews for unigrams and bigrams. The idea of the difficulties in the opinion classification was to get from [6]. In [7], it used an unsupervised method to classify the reviews as thumbs up (recommended) or thumbs down (not recommended). It uses document level opinion classification. In [8], here it used separate subjective sentences from the rest of the text, and it achieved the best result using a SVM method based. In [9], it used WordNet syntactic relations together with topic relevance to calculate the subjectivity scores for words. In [10], it is as [6], taking comments off of social networking sites about movie reviews. In [11], it summarized the opinions expressed in reviews about the different parts of a product which are distinct from the classical document summarization. In [12], it used part-of-speech information for minion the opinions because adjective has a correlation with subjectivity [13]. In [14], sentiment analysis is done at the phrase and sentence level except for the document level. In [15], it worked on Bangla sentiment analysis and it identify the sentiment information in each report, aggregates them and represents the summary information in text.

In this paper, it investigates a small part (positive and negative attitudes towards products.) of the significant problems in sentiment analysis for Bangla data. The goal is to determine the polarity of Bangla language texts using Multinomial Naive Bayes based on Feature selection method.

The association of this article is as follows: the details process of sentiment analysis is described in section II. After that, Section III describes the experimental results and analysis. Finally, some concluding remarks are presented in section IV.

II. Mutual Information based Multinomial Naive Bayes Model

The overall process of opinion mining is shown in Fig.1. It contains several steps: i) Collect the dataset, ii) Process the training dataset before passing it to Feature extraction method, iii) Select the necessary features using Mutual information

978-1-5090-5785-6/16/$31.00 ©2016 IEEE

method, iv) Train the multinomial naive bayes based on only the selected features, v) Test the model using the Testing dataset.

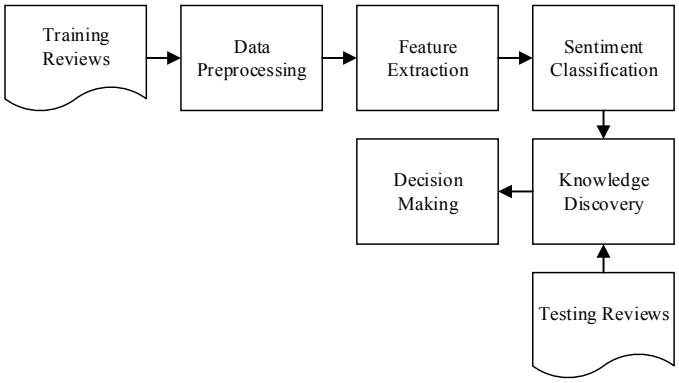

Fig. 1. Flow chart of Text Classification Process (Training + Testing)

A. Dataset

For this research purpose, we needed to use English and Bangla dataset. A set of product reviews collected from Web data: Amazon Reviews [16] are used as English corpus which contains over 68356 reviews of watch-products [16]. All the reviews are given ratings to be ranged from 1-star to 5-star such as (1, 2, 3, 4, 5). For Bangla corpus, Bangla dataset is generated from this Amazon dataset.

B. Data Preprocessing

1) English Corpus Preprocess

From the English corpus, we took only the reviews as a positive (score = 1) which have rating 4 or 5 and a negative (score = 0) which have rating 1 or 2. The same number of positive and negative reviews for English and Bangla corpus are used on training and testing phases.

a) Stopping Words

Before passing the training data to feature extraction algorithm, the training data are filtered by the stopping word means to remove all unnecessary words from the training data for getting better features as output from the feature extraction algorithm. If there will be not at least 3 characters in a word, then it will be considered as a stopping word. And also some stopping words such as away, awfully, b, back, be, became, didn't, different, do, does, doesn't, doing, don't, done, etc. are taken into consideration which is collected from different websites. All punctuation except periods, apostrophes, and hyphens, additional white spaces, URLs, repeating letters, non-English alphabetic words is removed.

2) Bangla Corpus Preprocess

For sentiment analysis, it's hard to find a standard Bangla dataset, and for this reason, a Bangla dataset is generated from the processed English dataset by translating each word one by one. Non-Bangla alphabetic words are removed.

3) Negation Handling

In the sentiment analysis, negation handling is one of the contributing factors for the classifier. Negation is one of the most common linguistic constructions [17], and the polarity of a sentence can be changed for this. For this reason, we need to consider the negation in the sentiment analysis [18, 19]. For English corpus, we consider "*no", "not", "never", "n't"* as negation term which affects the polarity of a word. For the presence of negation word in a sentence, all the words will not indicate the negative meanings [19]. For English corpus, we just transformed all words into ("not_" + word) which are after the negation word. If the given line is "I don't like this watch." after negation the given line will be "I do not not_like not_this not_watch.".

For the Bangla corpus, negation words affect the sentence polarity like English. The negation terms in Bangla are "না", "নয়", and "নি" which will change the contextual polarity. It's hard to understand which portions of the sentence will be affected by the negation word in Bangla corpus and from this thinking, we transformed all words into ("না_" + word) of a sentence. If the given line is "আমি করি না পছন্দ এই ঘড়ি।" after negation the given line will be "না_আমি না_করি না না_পছন্দ না_এই না_ঘড়ি।".

C. Feature Extraction Using Mutual Information

In the machine learning algorithms like SVM, Neural Networks, etc., feature extraction used as an integrated module in the different system. In a larger picture, it is used to identify a subset of features for further text classification stage. Feature extraction method is used to remove redundant features (decrease the dimensionality of the space of feature) which contain high disambiguation capabilities, avoid system failure, handling the skewed datasets, reduce the computational cost, and minimize the overfitting of the learning system. In the feature extraction process, it identifies the portions of a given document which will affect the contextual polarity (positive or negative sentiment) and combines those parts of the documents so that it will increase the probability of the document falling into one of these two polarities (0, 1). If we use higher dimensional features like bigrams, trigrams, these will increase the number of features in which it contains many redundant and noisy features, and those would affect the accuracy of the system. There are different feature selection approaches such as Mutual Information, $\chi 2$ Feature selection, Frequency-based feature selection, etc. Here, for feature extraction, we used mutual information for filtering the features from the training dataset both for Bangla and English.

Mutual Information (MI) [20] measures how much information the presence/absence of a term contributes to making the correct classification decision on c. Formally, the mutual information of two random variables can be shown as:

$$I(U;C) = \sum_{e_t \in \{1,0\}} \sum_{e_c \in \{1,0\}} P(U = e_t, C = e_c) \log_2 \frac{P(U = e_t, C = e_c)}{P(U = e_t) P(C = e_c)}$$

Where U is a random variable that takes values $e_t = 1$ (the document contains term t) and $e_t = 0$ (the document does not contain t), and C is a random variable that takes values $e_c = 1$ (the document is in class c) and $e_c = 0$ (the document is not in class c). We write U_t and C_c if it is not clear from context which term t and class c we are referring to.

For Maximum Likelihood Estimates (MLEs) of the probabilities, above equation is equivalent to Equation:

$$I(U;C) = \frac{N_{11}}{N} \log_2 \frac{N N_{11}}{N_{1.} N_{.1}} + \frac{N_{01}}{N} \log_2 \frac{N N_{01}}{N_{0.} N_{.1}} + \frac{N_{10}}{N} \log_2 \frac{N N_{10}}{N_{1.} N_{.0}} + \frac{N_{00}}{N} \log_2 \frac{N N_{00}}{N_{0.} N_{.0}}$$

Where the Ns are counts of documents that have the values of $e_t c$ and e_c that are indicated by the two subscripts. For example, N10 is the number of documents that contain t ($e_t = 1$) and are not an equal number ($e_c = 0$). N1. = N10 + N11 is the number of documents that contain t ($e_t = 1$) and we count documents independent of class membership ($e_c \in \{0, 1\}$). N = N00 + N01 + N10 + N11 is the total number of documents.

D. Text Classification using Multinomial Naive Bayes

Multinomial Naive Bayes (MNB) [21] is a probabilistic learning classifier which is based on Bayes' decision rule with robust and naive independence assumptions. It is a modified version of Naive Bayes that is designed more for text documents. Original Naive Bayes [22] only considers the presence and absence of particular words in a document whereas MNB uses multinomial distribution for all pairs where it uses the word counts and rectify the underlying calculations to act within. MNB shows desire efficiency with the accuracy.

In the multinomial naive Bayes for a given document, the probability of a document d being in class c is computed as

$$P(c|d) \propto P(c) \prod_{1 \le k \le n_d} P(t_k|c)$$

Where $P(t_k|c)$ is the conditional probability of term t_k occurring in a document of class c. $P(t_k|c)$ denotes a measure of how much evidence t_k contributes that c is the correct class. P(c) is the prior probability of a document occurring in class c. Choose the document that has a higher prior probability when document's terms do not provide clear evidence for one class versus another.

In text classification, our goal is to find the best appropriate class for the document. The best class in NB classification is the most likely or maximum a posteriori (MAP) class c_{map}:

$$c_{map} = arg\max \hat{P}(c|d) = argmax\, \hat{P}(c) \prod_{1 \le k \le n_d} \hat{P}(t_k|c)$$

We write $\hat{P}$ for P because we do not know the true values of the parameters P(c) and $P(t_k|c)$, but estimate them from the training set.

The above equation can be written as:

$$c_{map} = argmax\, [\log \hat{P}(c) + \sum_{1 \le k \le n_d} log\hat{P}(t_k|c)]$$

Each conditional parameter $log\hat{P}(t_k|c)$ is a weight that indicates how good an indicator t_k is for c. Similarly, the prior $\log \hat{P}(c)$is a weight that indicates the relative frequency of c.

For the priors,

$$\hat{P}(c) = \frac{N_c}{N'}$$

Where N_c is the number of documents in class c and N is the total number of documents.

We estimate the conditional probability $\hat{P}(t|c)$ as the relative frequency of term t in documents belonging to class c:

$$\hat{P}(t|c) = \frac{T_{ct}}{\sum_{t' \in V} T_{ct'}}$$

Where T_{ct} is the number of occurrences of t in training documents from class c, including multiple occurrences of a term in a document. T_{ct} is a count of occurrences in all positions k in the documents in the training set.s

We use the add-on or Laplace smoothing, which simply adds one to each count because some words may not exist for a particular class c.

$$\hat{P}(t|c) = \frac{T_{ct}}{\sum_{t' \in V}(T_{ct'} + 1)} = \frac{T_{ct} + 1}{(\sum_{t' \in V} T_{ct'}) + B'}$$

Where B = |V| is the number of terms in the vocabulary. Add-one smoothing can be interpreted as a uniform prior.

III. EXPERIMENTAL RESULT

We use Amazon's Watches [16] dataset which contains 68356 reviews, but in the empirical analysis, we used only 16000 reviews with 8000 positive and 8000 negative level. We used 13000 reviews which include 6500 positive and 6500 negative reviews for the training purpose and 3000 reviews for testing purpose which contains the equal number of positive and negative reviews.

After processing the chosen dataset, mutual information method is used to extract the optimal number of features from the training dataset. Accuracy, sensitivity, specificity depends on the number of selected features. Tiny number/a large number of selected features are unable to give better performance in distinguishing the polarity into the document. Fig.2 shown that a small number and a vast number of selected features can't be able to provide better accuracy and we need to choose an optimal number of features. We selected the top 10000 features with maximum mutual information for English and Bangla dataset.

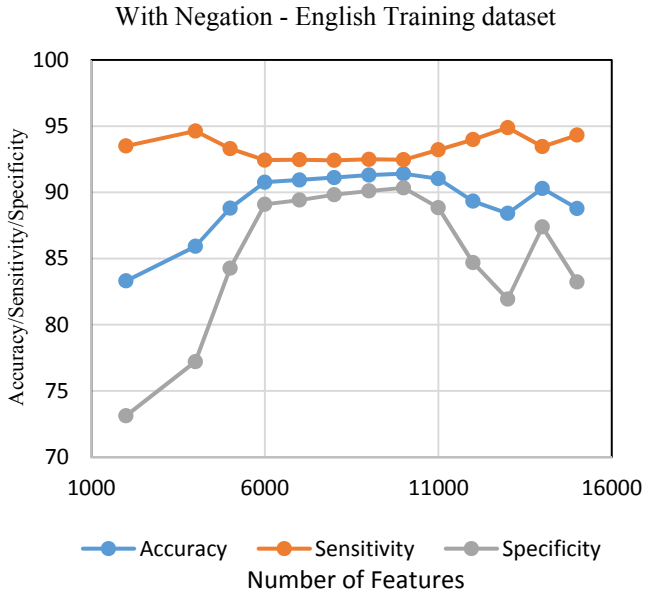

Fig. 2. System Accuracy, Sensitivity, Specificity Based on Different Number of Feature Selection.

For English [Fig.3(a)], in the testing phase using English training data for testing we get 91.1% accuracy without using negation and get 91.4% accuracy with negation. In testing phase, using English testing data, we get 85.1% accuracy without using negation and get 85.8% accuracy with negation. For Bangla [Fig.3(b)], in testing phase using Bangla training data for testing we get 88.54% accuracy without using negation

and get 87.79% accuracy with negation. In the testing phase, using Bangla testing data, we get 84.78% accuracy without using negation and get 83.77% accuracy with negation. The accuracy for Bangla dataset is close to English dataset's accuracy where Bangla and English dataset both are identical.

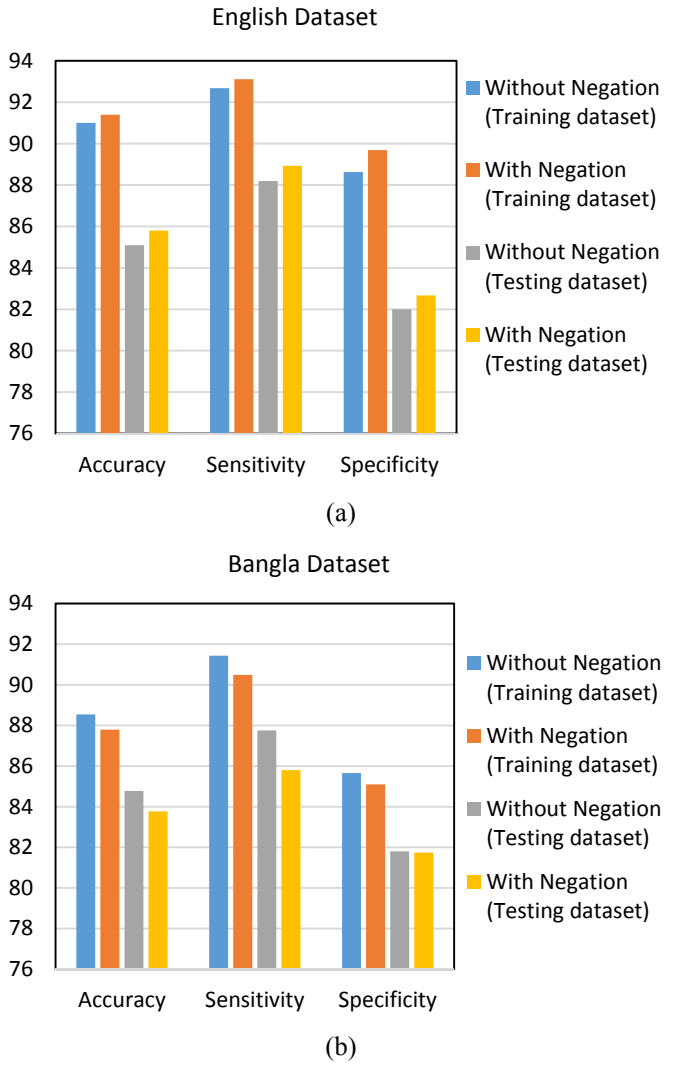

Fig. 3. Evaluation of the given system on different dataset (a) English Dataset (b) Bangla Dataset.

IV. CONCLUSION

For analyzing the reviews and classifying the sentiments, we used the Multinomial Naive Bayes (MNB) based on feature selection method (Mutual Information) for both Bangla and English datasets. In the feature selection stage, preprocessed data are passed to the Mutual Information (MI) method, and then MI selects an optimal set of features. Based on these features, MNB gives the prediction for each document to classify into positive or negative opinions. From the experimental result, the accuracy for the Bangla dataset slightly differs from the accuracy for the English dataset of the proposed system. For this method, we got a satisfactory level of accuracy for Bangla dataset compare to English dataset where Bangla dataset is generated from Amazon's Watches dataset.

REFERENCES

[1] Ann, and Khurshid Ahmad. "Sentiment polarity identification in financial news: Acohesion-based approach." ANNUAL MEETING-ASSOCIATION FORCOMPUTATIONAL LINGUISTICS. Vol. 45. No. 1. 2007.

[2] Das, Sanjiv and Mike Chen, "Yahoo! for Amazon: Extracting market sentiment from stockmessage boards", Proceedings of APFA-2001.

[3] Das, Sanjiv and Mike Chen, "Yahoo! for Amazon: Sentiment extraction from small talk on the web, Management Science", 53(9): pp.1375-1388, 2007

[4] Yubo Chen and JinhongXie, "Online Consumer Review: Word-of-Mouth as a New Element of Marketing Communication Mix, Management Science", vol 54, no 3, pp.477-491, 2008.

[5] Bing Liu, "Sentiment analysis and opinion mining, Morgan and Claypool publishers", 2012.

[6] Pang, L. Lee, and S. Vaithyanathan, "Thumbs up?:sentiment classification using machine learning techniques", in Proceedings of the ACL-02 conference on Empirical methods in natural language processingVolume 10, pp.79–86, 2002

[7] P.D. Turney, "Thumbs up or thumbs down? Semantic orientation applied to unsupervised classification of reviews", Proceedings of the Association for Computational Linguistics (ACL), pp.417–424, 2002.

[8] Pang, B., & Lee, L., "A sentimental education: Sentiment analysis using subjectivitysummarization based on Minimum Cuts". in Proceedings of the 42nd Annual Meeting ofthe Association of Computational Linguistics. 2004.

[9] Mullen, T., & Collier, N., "Sentiment analysis using support vector machines withdiverse information sources". In Proceedings EMNLP'04, pp.412-418, 2004.

[10] K. Yessenov & S. Misailovic, "Sentiment analysis of movie review comments. Methodology", pp.1–17,2009.

[11] M. Hu & B. Liu, "Mining and summarizing customerreviews", in Proceedings of the tenth ACM SIGKDD international conference on Knowledge discovery and data mining, pp.168–177. ACM, 2004.

[12] M.Hu, & B. Liu, "Mining opinion features in customer reviews", Proceedings of 19th National Conference on Artificial Intelligence, pp. 755-760, 2004

[13] Wiebe, J., Bruce, R., Bell, M., Martin, M., & Wilson, T., "A corpus study of evaluative and speculative language", Proceedings of 2nd ACL SIGdial Workshop on Discourse and Dialogue. Aalborg, Denmark, 2001

[14] T. Wilson,"Recognizing contextual polarity in phrase-level sentimentanalysis", In Proceedings of HLT-EMNLP, pp. 347–354, 2005.

[15] Das, A. & Bandyopadhyay, S.,"SentiWordNet for Bangla." In Knowledge Sharing Event-4: Task 2: BuildingElectronic Dictionary", Mysore, 2010.

[16] Web data: Amazon reviews, https://snap.stanford.edu/data/web-Amazon.html

[17] Maral Dadvar, Claudia Hauff, Franciska de Jong, ''Scope of Negation Detection in Sentiment Analysis''

[18] Jia, L., C. Yu and W. Meng, "The effect of negation on sentiment analysis and retrieval effectiveness", in 8th International Conference on Information and Knowledge Management, 2009.

[19] Wiegand, M., et al. A survey on the role of negation insentiment analysis. in '10 Proceedings of the Workshop onNegation and Speculation in Natural Language Processing 2010: Association for Computational Linguistics.

[20] Huawen Liu, Jigui Sun, Lei Liu, Huijie Zhang, "Feature selection with dynamic mutual information", Pattern Recognition 42, pp.1330 – 1339, 2009.

[21] Daniel Jurafsky & James H. Martin , "Speech and Language Processing", Chapter 7, 2015.

[22] V. Muralidharana, V. Sugumaranc, "A comparative study of Naive Bayes classifier and Bayes net classifier for fault diagnosis of monoblock centrifugal pump using wavelet analysis", Applied Soft Computing Volume 12, Issue 8, pp.2023–2029, 2012.

International Conference on Electrical, Computer & Telecommunication Engineering (ICECTE)
8-10 December 2016, Rajshahi-6204, Bangladesh

A Statistical Approach for Offline Signature Verification using Local Gradient Features

A.B.M. Ashikur Rahman
Department of CSE
Islamic University of Technology
Boardbazar, Gazipur, Bangladesh
ashikiut@iut-dhaka.edu

Golam Mostaeen
Department of CSE
University of Saskatchewan
Saskatoon, SK S7N 5C5, Canada
gom766@mail.usask.ca

Md. Hasanul Kabir
Department of CSE
Islamic University of Technology
Boardbazar, Gazipur, Bangladesh
hasanul@iut-dhaka.edu

***Abstract*—Signature is widely used as a means of personal verification which emphasizes the need for a signature verification system. Often the single signature feature may produce unacceptable error rates. Features used in this method are mainly local key-point feature that deals with the orientation around each key-point. Before extracting the features, preprocessing of a scanned image is necessary to isolate the region of interest part of a signature and to remove any spurious noise present. The system is initially trained using a database of signatures obtained from those individuals whose signatures are to be authenticated by the system. For extracting the feature, key-points of the image are detected. For each point, orientation around the point is calculated as the feature. By matching the features of sample signature and testing signature decision is taken. If a query signature is in the acceptance range then it is an authentic signature, otherwise it is a forged signature.**

Keywords— Signature Verification; Forgery Detection keypoint, descriptor; Harris corner detection; statistical approach; Local Features; Orientation.

I. Introduction

A handwritten signature is the scripted name or legal mark of a persons identity, executed by hand and it is used for the purpose of authentication which is widely used in various sectors. Hence, methods for automatic signature verification must be developed to avoid forgeries. The forgeries in handwritten signatures have been categorized based on their characteristic features [14]. The three major types of forgeries are: Random Forgery, Unskilled Forgery and Skilled Forgery. Approaches for signature verification fall into two categories according to the acquisition of the data i.e. On-line and Off-line. On-line data records the motion of the stylus when the signature is produced, and includes location, and possibly velocity, acceleration and pen pressure, as functions of time. These dynamic characteristics are specific to each individual and sufficiently stable as well as repetitive. Off-line data is a 2-D image of the signature. For signature verification a number of methods are proposed. Some of the methods uses global features which are calculated considering the whole image. Some of them uses local features which is calculated based on some interest points. But these methods cannot ensure to overcome all the challenges. Specially, same threshold is taken for different persons which often lead to error and effect accuracy. In this paper, we propose a statistical method that extracts features based on local gradient values. From the signature image we use Harris corner detection method to find interest point. Then orientation is assigned. For each key-point we calculate the feature vector based on gradient features. Our method also pick person specific threshold that increases the accuracy. So promising results have been found by our originated method even if the image is rotated in any angles or it has noise.

II. Related Works

The existing method of signature verification can be divided into two parts mainly on basis of their feature selection. One kind of them uses global features, which are extracted on basis of the total image. These features are size, ratio, height and width, total number of black pixels, center of gravity, mean, variance etc. For example A.C. Verma et al. [1] proposed a method that uses global and geometric features. Geometric data like aspect ratio, center of gravity, baseline shift etc. are considered as features. Though this method is good at detecting random forgery, it cannot detect skilled forgery as the geometric value get closer. Besides false acceptance occurs more often. Prashanth and Raja et al. [2] proposed an angular based model which uses geometric center as the feature point. Each and every block is then divided vertically and horizontally until 128 points are found. Finally the distance and angle from the point (1, 1) is calculated for each of the geometric mean obtained. Main limitation of the method is that two different signature can have geometric center on the same point. Radon transform [4] is another existing method that Computes projection sum of the image intensity along a radial line. However this method results in little high false rejection rate. Another one uses local features, which is calculated from particular points out of the whole image. Local features depends on particular portion of the input image. Mainly, some key points are detected from the input images and features are extracted for those particular key points. SURF [9] uses Local feature approach where first key point is detected using Fast Hessian and Haar wavelet. SURF descriptor is then extracted using assignment orientation and descriptor components. Though this approach makes the verification method rotation invariant, there is scope for increasing its performance with faster computation. Pal et al. [5] proposed

978-1-5090-5785-6/16/$31.00 2016 IEEE

Fig. 1: Steps of our proposed system

a method that uses Gabor filter along with SURF algorithm. Besides Madasu et al. [13] proposed a grid model that splits the image into a grid version. However as it takes the value of each block, if the signature is little bit slant, the output will vary a lot.

III. Proposed Method

For verifying signature some challenging situations occur. The difficulties in processing off-line signature are (i) the highly stylish and unconventional writing, (ii) the nature and variety of the writing pen (iii) the non-repetitive nature of variation of the signatures, because of age, illness, mood, stress levels, geographic location and perhaps to some extent the emotional state of the person. Our proposed method for signature verification follows some steps which are shown in Fig.1.

A. Preprocessing

The purpose of preprocessing phase is to make signatures standard and ready for feature extraction. For our implementation and testing of the proposed method a number of signatures from different persons are scanned at 300 DPI (dots per inch). Then those are cropped from the signature sheet so that some of them can be used for training and others for testing separately. After that those images are converted to binary form for better result. Then noise removal steps are applied.

B. Obtaining Keypoint Using Harris Corner Detection

An interest point is a point in an image which has a well-defined position and can be robustly detected. This means that an interest point can be a corner but can also be, for example, an isolated point of local intensity maximum or minimum, line endings, or a point on a curve where the curvature is locally maximum. The Harris corner detector algorithm [10] relies on a central principle: at a corner, the image intensity will change largely in multiple directions. This can alternatively be formulated by examining the changes of intensity due to shifts in a local window. Around a corner point, the image intensity will change greatly when the window is shifted in an arbitrary direction. Following this intuition the Harris corner detector uses the second moment matrix as the basis of its corner decision.

C. Orientation Assignment

We have key-points which are tested to be stable. The next thing is to assign an orientation to signature. This orientation provides rotation invariance. Then Gradient magnitudes and orientations of all points in the 16x16 neighbor is calculated using equation (3) and (4):

$$d_x = L(x+1, y) - L(x-1, y) \tag{1}$$

$$d_y = L(x, y+1) - L(x, y-1) \tag{2}$$

$$m(x, y) = \sqrt{(d_x)^2 + (d_y)^2} \tag{3}$$

$$\Theta(x, y) = \frac{d_x}{d_y} \tag{4}$$

Then, a histogram is created for this where the 360 degree of orientation are broken into 8 bins (each 45 degrees). From the histogram, the bin with highest response is assigned to a key-point as its orientation.

D. Feature Extraction of the Key-Points

In this step the feature descriptor is calculated for each of the key-point found in the previous step. We used SIFT (Scale-Invariant Feature Transform) [12] for calculating the descriptor. SIFT provides descriptors in vector form of length 128 for each key-point.

E. Distance Ratio Selection

The key-point descriptor from the previous step for two signatures is matched to see to what extent they are similar. Distances of one feature from one signature is calculated against every features of the other. Ratio between the distances of the nearest feature d_n and the second nearest feature d_s is denoted by δ. If δ is less than some threshold δ_m, then this feature is considered similar to the nearest feature.

$$\delta = \frac{d_n}{d_s} \tag{5}$$

Varying the value of δ_m we can vary the number of matches between two signatures.
Let we are given 3 signatures S_1, S_2 and S_3 for training the system. For each of the possible pair, we want to keep the number of matches in between to a predefined number β. So the distance ratio is increased via some step until we find the number of matches in between the two signatures equal or greater than β. This distance ratio is found out for each of the possible pairs.
δ_{12} = Ratio to get β matches between S_1 and S_2
δ_{23} = Ratio to get β matches between S_2 and S_3
δ_{13} = Ratio to get β matches between S_1 and S_3
The mean of the distance ratios is calculated for the usage in the next step of the proposed model using equation (6).

$$\delta_{mean} = \frac{\delta_{12} + \delta_{23} + \delta_{13}}{3} \tag{6}$$

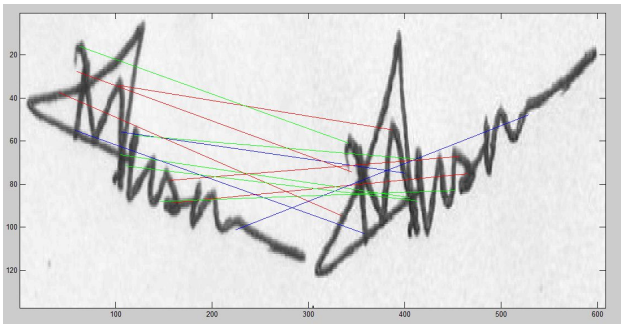

Fig. 2: Matching Based on Key-Points

F. Matching And Threshold Selection

The average distance ratio, δ_{mean} is used in all the pairs of signatures (S_1, S_2), (S_2, S_3) and (S_3, S_1) and corresponding total number of matches M_{12}, M_{23} and M_{13} are calculated.
M_{12} = number of matches between S1 and S2 using δ_{mean}
M_{23} = number of matches between S2 and S3 using δ_{mean}
M_{13} = number of matches between S1 and S3 using δ_{mean}
The mean, μ and variance, σ^2 of the matches are then calculated.

$$\mu = \frac{M_{12} + M_{23} + M_{13}}{3} \tag{7}$$

$$\sigma^2 = \frac{1}{3}\sum_{i=1}^{3}\sum_{j=1}^{3}(M_{ij} - \mu)^2, i \neq j \tag{8}$$

G. Testing

During testing phase a test signature S_t is taken and using the steps of the proposed method the feature descriptor is calculated. Then the number of matches with each of the training signatures is found out.
M_{t1} = number of matches between S_t and S_1 using δ_{mean}
M_{t2} = number of matches between S_t and S_2 using δ_{mean}
M_{t3} = number of matches between S_t and S_3 using δ_{mean}
Then the mean, M_t = Average (M_{t1}, M_{t2}, M_{t3}) is calculated. The final decision is made using equation (9):

$$decision = \begin{cases} Accept & \text{if } |M_t - \mu| \leq \sigma^2 \\ Reject & \text{Otherwise} \end{cases} \tag{9}$$

IV. Experimental Result and Performance Analysis

A. Data Set and Experimental Setup

We have implemented the proposed model and compared with a number of existing approaches. All those implementation and simulation have been done using MATLAB 2013 on a personal computer of 2.13GHz processors with 2 GB main memory. For the comparison and testing of the proposed method we have used a number of signatures from 20 different persons. For each of the person we have used 6 signatures, 5 of them are genuine and the rest one is forged. Out of those 5 genuine signatures only 3 are used for training the system. And then the system is tested using remaining 2 genuine signatures and 1 forged signature. Our first section of dataset contains ideal signatures that are with negligible amount of noises and without any rotation. The second set of dataset contains salt and pepper noise. The third set of dataset contains Gaussian noise with five different variances of 0.01, 0.02, 0.05, 0.1 and 0.2. Both of those noises are simulated using MATLAB codes. The fourth set of signature contains different rotation.

TABLE I. Performance in Presence of Gaussian Noise

Noise level (variance)	Accuracy(%)
0.01	93.84
0.02	93.84
0.05	92.30
0.10	87.60
0.20	80.00

TABLE II. Performance in Presence of Salt & Pepper Noise

Noise level (variance)	Accuracy(%)
0.02	93.84
0.05	93.84
0.10	90.70
0.15	89.23
0.20	86.15

B. Performance Measurement

We have measured the performance by calculating accuracy using equation (10):

$$Accuracy = \frac{N_s}{N} \tag{10}$$

Where N_s is the number of correctly classified signatures and N is the total number of test cases.

1) Gaussian Noise: The most common noise in images is Gaussian noise. We used weinner2 filter of size 5x5 to eliminate Gaussian noise. This filter works well to eliminate this noise. After this, we calculated features and find matches. Table I shows the details of the performance of our method:

2) Salt & Pepper Noise: For Salt & pepper noise, we used median filter of size 3x3. Median filter can perform well if the noise is not more than the half of the pixels. Otherwise it fails to eliminate noise. In practical, the noise level is not that much high. Table II shows the performance for the dataset containing Salt & Pepper noise.

3) Different Orientation: Another common problem is with the orientation of signature which may vary. We assigned orientation to each of the signatures. Orientations of both signature are matched before key-point matching. Now, both signature have same orientation even though there is a rotation. Fig. 2 shows matching between two signatures with different orientation.

C. Comparative Analysis

We implemented SURF, SIFT and one of the geometric feature based method [1] and compared the outcome in different challenging situation with our proposed method. We can

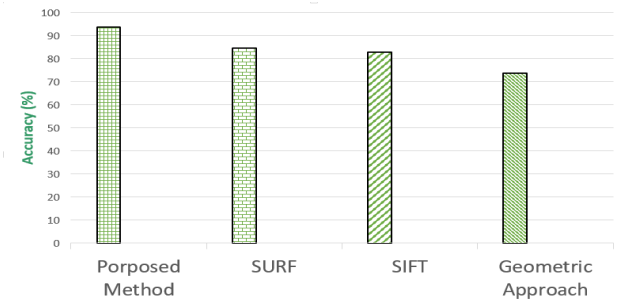

Fig. 3: Performance Comparison Without Modification

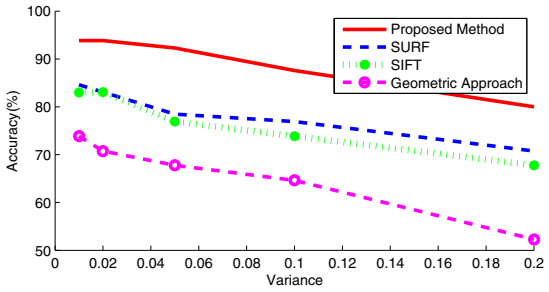

Fig. 4: Performance Comparison in Presence of Gaussian Noise

see that, existing methods cannot give a good performance in different challenging situations.

1) Without Modification: At first, we tested the dataset images which contain no modification and the result of accuracy is shown in Fig. 3 along with the performance of other three existing methods.

2) Gaussian Noise: Gaussian noise is also known as *white noise*. We can see that, as the variance of noise increases the accuracy decreases. But, the performance of our proposed method is still better than the others. Normally, Gaussian noise does not occur having variance more than 0.2. Practically it is very less than that. Fig. 4 shows the performance comparison.

3) Salt & Pepper Noise: Performance regarding Salt & Pepper Noise is almost same as Gaussian noise. Fig. 5 shows that our proposed method outperforms the existing methods.

4) Different Orientation: The accuracy is same as the unmodified dataset. For other methods this takes a little difficulty.

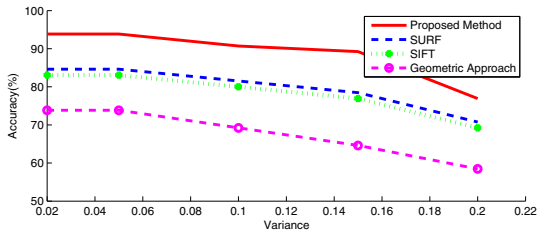

Fig. 5: Performance Comparison in Presence of Salt & Pepper Noise

As SURF and SIFT uses local features, they are also rotation invariant but problem is with the Geometric approach. It fails to perform better in different orientations.

V. Conclusion

This paper presents an investigation of the performance of off-line signature verification. There are a number of existing methods that extract different features to train and test the system. In most of them a global decision line is used for deciding if a test signature is genuine or forged. But from practical scenario some signatures are too complex where some are not. Besides some signature undergoes a lot of changes, while even given by the actual person based on different environment or mental conditions. So always using the same decision line for every persons signature does not work the best in real life. Our proposed method uses different decision line for different person. Our system learns from the training signatures variations and nature to select an optimal decision line that works efficiently. It works fine with any rotation of the training or test signature. It can learn from comparatively lesser amount of training data thus making it suitable for usage in practical scenario.

References

[1] A. C. Verma, D. Saha and H. Saikia, *Forgery Detection In Offline Handwritten Signature Using Global And Geometric Features*, International Journal of Computer and Electronics Research, 2013.

[2] C. R. Prashanth and K. B. Raja, *Off-line Signature Verification Based on Angular Features*,International Journal of Modeling and Optimization, 2012.

[3] C. R. Prashanth, K. B. Raja, K. R. Venugopal and L. M. Patnaik, *Intra-modal Score level Fusion for Off-line Signature Verification*, International Journal of Innovative Technology and Exploring Engineering (IJITEE), 2012.

[4] V. Kiani, R. Pourreza and H. R. Pourreza, *Offline Signature Verification Using Local Radon Transform and Support Vector Machines*, International Journal of Image Processing (IJIP), 2010.

[5] S. Pal, S. Chanda, U. Pal, K. Franke and M. Blumenstein, *Off-line signature verification using G-SURF*, 12th International Conference on Intelligent Systems Design and Applications, 2012.

[6] H. A. Raman Maini, *Study and Comparison of Various Image Edge Detection Techniques*, International Journal of Image Processing (IJIP), Volume 3, Issue 1, 2010.

[7] P. Rajarajeswari and N. Uma, *Off-Line Signature Verification And Forgery Detection Using Pixel Based Fuzzy Logic Technique*, Journal of Innovative Research and Solutions(JIRAS), 2013.

[8] Pemeena Priyadarsini, M. J., K. Murugesan, S. Rao Inbathini, A. Jabeena, and K. Sai Tej, *Bank Cheque Authentication Using Signature*, International Journal of Advanced Research in Computer Science and Software Engineering, 3, no. 5 (2013).

[9] Bay, Herbert, Tinne Tuytelaars, and Luc Van Gool, *Surf: Speeded up robust features*, European conference on computer vision. Springer Berlin Heidelberg, 2006.

[10] C. Harris and M. Stephens, *A combined corner and edge detector*, Alvey vision conference. Vol. 15. 1988.

[11] J. Malik, R. Dahiya and G. Sainarayanan, *Harris Operator Corner Detection using Sliding*, International Journal of Computer Applications (0975 8887), 2011.

[12] Lowe, David G. *Object recognition from local scale-invariant features.*, Computer vision, 1999. The proceedings of the seventh IEEE international conference on. Vol. 2. Ieee, 1999.

[13] Madasu, V. K., and Lovell, B. C. *An automatic offline signature verification and forgery detection system*, Pattern Recognition Technologies and Applications: Recent Advances, 63-89, 2008.

[14] Suen, Ching Y., Qizhi Xu, and Louisa Lam, *Automatic Recognition of Handwritten data on chequesFact or Fiction?*, Pattern Recognition Letters 20.11 (1999): 1287-1295.

Performance Analysis of Multiple Relay Multi-cellular Interference Networks

T. R. Jyoti[1], M. Z. I. Sarkar[2], M. I. Sarkar[1], T. U. Alam[1] and D. K. Sarker[2]
[1]Department of Electronics and Telecommunication Engineering
[2]Department of Electrical and Electronic Engineering
Rajshahi University of Engineering and Technology
Rajshahi-6204.
Email: tamanna104005@gmail.com

***Abstract*—We consider a single-input multiple-output (SIMO) multiple-access channel (MAC) multi-cellular communication scenario in which two base stations having a group of users each, are situated in two adjacent cells. In order to provide cooperative diversity at the base stations (BSs), multiple relays are used. Each group of users transmits information to its corresponding BS directly as well as via relays, but at the same time it provides interference at the BS of adjacent cell. The BSs are equipped with multiple antennas while the users of each group and relays are equipped with single antenna. We are interested to study the capacity of the each base station in both the optimal and normal cases with and without interference. Considering maximal ratio combining (MRC) at the BSs, at first, we derive the expression of combiner output signal-to-interference plus noise ratio (SINR) using optimum weighting vector. Then we use this SINR to calculate the optimal ergodic capacity. Finally, we derive the expression of normal ergodic capacity for both the base stations. Our results show that, optimization of combiner output SINR by weighting vector at the base stations enhances the ergodic capacity in multi-cellular interference channels.**

***Index Terms*—Maximal ratio combining, multiple-access channel, multi-cellular interference network, optimum weighting vector.**

I. Introduction

In the multicellular network all the cells are independent in ideal case. But, practically multicellular network is an interference network where the margin of each cell is the part of another cell in the overlapping region. Fading, noise, interference are the three key challenges faced by designers of mobile communication systems. Fading limits the coverage and reliability between a base station and a mobile user, interference decreases the channel capacity and also restricts the reusability of the spectral resource and thus limits the overall spectral efficiency.

Recently, K. Hosseini et al. [1] compared downlink multi-cell interference mitigation techniques in large-scale (LS) multiple-input multiple-output (MIMO) and network MIMO considering cooperative wireless cellular system. The theory and currently known techniques for multi-cell MIMO co-operation in wireless networks are studied in [2]. Authors reported that in dense networks where interference plays the key capacity-limiting factor, multi-cell cooperation can dramatically improve the system performance. In [3], authors showed that optimal selection of a single relay among a set of multiple amplify and forward (AF) relays minimizes the outage probability. In [4], authors demostrated that inter-cell interference cancellation (ICIC) with well-designed feedback strategies provides significant throughput gain. A. Bletsas et al. [5] studied an opportunistic relaying scheme with decode-and-forward (DF) and AF protocols under an aggregate power constraint. In [6] authors derived an algorithm to improve the network-wide sum-rate and compared its performance to the case which has no interference coordination among the base stations.

This paper addresses the communications of cellular SIMO MAC channels, where two groups of users communicate with their respective BSs directly and via multiple relays where users of one cell create interference to the base station of other cell. Our main objective is to achieve the maximum ergodic capacity by optimizing the weighting vector which can take the advantage of possible channel diversity to improve the ergodic capacity and to show the comparison of optimal and normal capacity with and without interference. By applying the MRC diversity combining technique, at first, we derive the expressions of capacity and combiner output SINR for both the destinations and then, we derive the expressions of optimal capacity for both the BSs using the optimized weighting vector.

The rest of the paper is organized as follows. The system model and problem formulation are discussed in section II. Section III describes the derivation of capacities for both the base stations. The numerical results are depicted in Section IV and Section V provides the concluding remarks of this work.

II. System Model and Problem Formulation

We consider a communication scenario in which two groups of users communicate with base station-1 (BS1) in Cell 1 and base station-2 (BS2) in Cell 2, respectively. K relays denoted by $\{R_l\}_{l=1}^{k}$ help to improve the capacity between the groups of users and the base stations providing cooperative diversity. The users of group 1 and group 2 are equipped with single antenna while the BS1 and BS2 are equipped with n_{R_1} and n_{R_2} antennas, respectively. Interference occurs in both the cases when the adjacent users of one cell transmit signal in their neighboring cell. The direct channel coefficient between group 1 and BS1 is $\mathbf{a}_{p_i}$, $i = 1, 2, \ldots, M$, and the

978-1-5090-5785-6/16/$31.00

direct channel coefficient between group 2 and BS2 is $\mathbf{q}_{c_j}$, $j = 1, 2, \ldots, N$, while the crossover coefficient between group 2 and BS1 is $\mathbf{q}_{p_j}$ and the cross-over coefficient between group 1 and BS2 is $\mathbf{a}_{c_i}$. x_i and s_j denote the transmitted signals of ith user of group 1 and jth user of group 2, respectively. $\mathbf{n}_{p_0} \sim \mathcal{CN}\left(0, \sigma_1^2 \mathbf{I}_{n_{R_1}}\right)$ and $\mathbf{n}_{s_0} \sim \mathcal{CN}\left(0, \sigma_2^2 \mathbf{I}_{n_{R_2}}\right)$ denote the Gaussian noises imposed on BS1 and BS2, respectively. During the first hop, received signals at BS1 and BS2 are respectively given by

$$\begin{aligned}\mathbf{y}_{p_1} &= \sum_{i=1}^{M} \mathbf{a}_{p_i} x_i + \sum_{j=1}^{N} \mathbf{q}_{p_j} s_j + \mathbf{n}_{p_0} \\ &= \mathbf{A}_p \mathbf{x} + \mathbf{B}_s \mathbf{s} + \mathbf{n}_{p_0}, \qquad (1) \\ \mathbf{y}_{s_1} &= \sum_{j=1}^{N} \mathbf{q}_{c_j} s_j + \sum_{i=1}^{M} \mathbf{a}_{c_i} x_i + \mathbf{n}_{s_0} \\ &= \mathbf{Q}_c \mathbf{s} + \mathbf{Q}_p \mathbf{x} + \mathbf{n}_{s_0}, \qquad (2)\end{aligned}$$

where $\mathbf{A}_p = [\mathbf{a}_{p_1}, \mathbf{a}_{p_2}, \ldots, \mathbf{a}_{p_M}]$, $\mathbf{B}_s = \left[\mathbf{q}_{p_1}, \mathbf{q}_{p_2}, \ldots, \mathbf{q}_{p_N}\right]$, $\mathbf{Q}_c = \left[\mathbf{q}_{c_1}, \mathbf{q}_{c_2}, \ldots, \mathbf{q}_{c_N}\right]$, $\mathbf{Q}_p = [\mathbf{a}_{c_1}, \mathbf{a}_{c_2}, \ldots, \mathbf{a}_{c_M}]$, $\mathbf{x} = [x_1, x_2, \ldots, x_M]^T$ and $\mathbf{s} = [s_1, s_2, \ldots, s_N]^T$. The transmitted powers are limited in the sense $\mathbb{E}[\mathbf{x}\mathbf{x}^\dagger] \leq P_1$ and $\mathbb{E}[\mathbf{s}\mathbf{s}^\dagger] \leq P_2$, where P_1 and P_2 denote average total powers at the BS1 and BS2, respectively. Received signal at the lth relay is given by

$$\begin{aligned}y_{r,l} &= \sum_{i=1}^{M} d_{l,i} x_i + \sum_{j=1}^{N} g_{l,j} s_j + \mu_l \\ \mathbf{y}_r &= \mathbf{D}_r \mathbf{x} + \mathbf{G}_r \mathbf{s} + \mathbf{n}_r, \qquad (3)\end{aligned}$$

where $d_{l,i}$ and $g_{l,j}$, $(l = 1, 2, \ldots, K)$, denote the fading coefficients between the ith user of group 1 and jth user of group 2, respectively. μ_l is the background noise of lth relay that has a Gaussian distribution with zero mean and variance σ^2, i.e., $\mu_l \sim \mathcal{N}(0, \sigma^2)$. $\mathbf{y}_r = [y_{r,1}, y_{r,2}, \ldots, y_{r,k}]^T$, $\mathbf{n}_r = [\mu_1, \mu_2, \ldots, \mu_k]^T$,

$$\mathbf{D}_r = \begin{pmatrix} d_{1,1} & d_{1,2} & \ldots & d_{1,M} \\ \vdots & \vdots & \ddots & \vdots \\ d_{k,1} & d_{k,2} & \ldots & d_{k,M} \end{pmatrix},$$

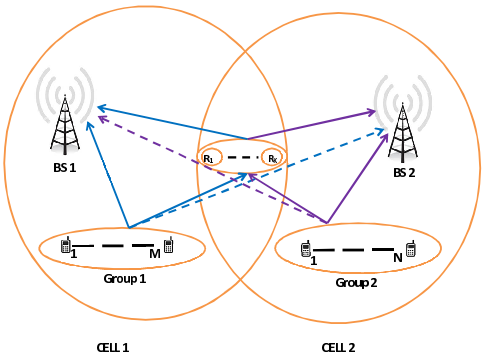

Fig. 1. System model.

and

$$\mathbf{G}_r = \begin{pmatrix} g_{1,1} & g_{1,2} & \ldots & g_{1,N} \\ \vdots & \vdots & \ddots & \vdots \\ g_{k,1} & g_{k,2} & \ldots & g_{k,N} \end{pmatrix}.$$

$(\cdot)^T$ and $(\cdot)^\dagger$ denote the transpose and conjugate transpose of a matrix or a vector. During the second hop, received signals at the BS1 and BS2 are given by

$$\begin{aligned}\mathbf{y}_{p_2} &= \mathbf{H}_p G \mathbf{y}_r + \mathbf{n}_{p_1} \\ &= \mathbf{H}_p G \mathbf{D}_r \mathbf{x} + \mathbf{H}_p G \mathbf{G}_r \mathbf{s} + \mathbf{H}_p G \mathbf{n}_r + \mathbf{n}_{p_1}, \qquad (4) \\ \mathbf{y}_{s_2} &= \mathbf{B}_c G \mathbf{y}_r + \mathbf{n}_{s_1} \\ &= \mathbf{B}_c G \mathbf{D}_r \mathbf{x} + \mathbf{B}_c G \mathbf{G}_r \mathbf{s} + \mathbf{B}_c G \mathbf{n}_r + \mathbf{n}_{s_1}, \qquad (5)\end{aligned}$$

where $G = \sqrt{\frac{\frac{(P_1+P_2)}{K}}{P_1+P_2+\sigma^2}}$ denotes the relaying gain. $\mathbf{H}_p = [h_1, h_2, \ldots, h_k]$ and $\mathbf{B}_c = [b_1, b_2, \ldots, b_k]$. h_l, b_l, $(l = 1, 2, \ldots, k)$, denote the Rayleigh fading coefficient between lth relay to BS1 and BS2, respectively. $\mathbf{n}_{p_1} \sim \mathcal{CN}\left(0, \sigma_1^2 \mathbf{I}_{n_{R_1}}\right)$, and $\mathbf{n}_{s_1} \sim \mathcal{CN}\left(0, \sigma_2^2 \mathbf{I}_{n_{R_2}}\right)$ denote the zero-mean complex additive white Gaussian noise (AWGN) at the BS1 and BS2 for the sub channels from relay to BS1 and BS2, respectively. Therefore, the overall received signals at the BS1 and BS2 are respectively given by

$$\begin{aligned}\mathbf{y}_{p_t}^1 &= \begin{bmatrix} \mathbf{y}_{p_1} \\ \mathbf{y}_{p_2} \end{bmatrix} \\ &= \begin{bmatrix} \mathbf{A}_p \\ \mathbf{H}_p G \mathbf{D}_r \end{bmatrix} \mathbf{x} + \begin{bmatrix} \mathbf{B}_s \\ \mathbf{H}_p G \mathbf{G}_r \end{bmatrix} \mathbf{s} + \begin{bmatrix} \mathbf{n}_{p_0} \\ \mathbf{H}_p G \mathbf{n}_r + \mathbf{n}_{p_1} \end{bmatrix} \\ \mathbf{y}_{p_t}^1 &= \mathbf{A}_1 \mathbf{x} + \mathbf{B}_1 \mathbf{s} + \mathbf{n}_p, \qquad (6)\end{aligned}$$

where $\mathbf{A}_1 = \begin{bmatrix} \mathbf{A}_p \\ \mathbf{H}_p G \mathbf{D}_r \end{bmatrix}$, $\mathbf{B}_1 = \begin{bmatrix} \mathbf{B}_s \\ \mathbf{H}_p G \mathbf{G}_r \end{bmatrix}$ and $\mathbf{n}_p = \begin{bmatrix} \mathbf{n}_{p_0} \\ \mathbf{H}_p G \mathbf{n}_r + \mathbf{n}_{p_1} \end{bmatrix}$.

$$\begin{aligned}\mathbf{y}_{s_t}^1 &= \begin{bmatrix} \mathbf{y}_{s_1} \\ \mathbf{y}_{s_2} \end{bmatrix} \\ &= \begin{bmatrix} \mathbf{Q}_c \\ \mathbf{B}_c G \mathbf{G}_r \end{bmatrix} \mathbf{s} + \begin{bmatrix} \mathbf{Q}_p \\ \mathbf{B}_c G \mathbf{D}_r \end{bmatrix} \mathbf{x} + \begin{bmatrix} \mathbf{n}_{s_0} \\ \mathbf{B}_c G \mathbf{n}_r + \mathbf{n}_{s_1} \end{bmatrix} \\ \mathbf{y}_{s_t}^1 &= \mathbf{Q}_2 \mathbf{s} + \mathbf{D}_2 \mathbf{x} + \mathbf{n}_s, \qquad (7)\end{aligned}$$

where $\mathbf{Q}_2 = \begin{bmatrix} \mathbf{Q}_c \\ \mathbf{B}_c G \mathbf{G}_r \end{bmatrix}$, $\mathbf{D}_2 = \begin{bmatrix} \mathbf{Q}_p \\ \mathbf{B}_c G \mathbf{D}_r \end{bmatrix}$ and $\mathbf{n}_s = \begin{bmatrix} \mathbf{n}_{s_0} \\ \mathbf{B}_c G \mathbf{n}_r + \mathbf{n}_{s_1} \end{bmatrix}$. Let us define $\mathbf{w}_1 \in \mathbb{C}^{2n_{r_1}}$ and $\mathbf{w}_2 \in \mathbb{C}^{2n_{r_2}}$ be the weighting vectors of combiner at the BS1 and BS2, respectively. Then, we have

$$\mathbf{y}_{p_t} = \mathbf{w}_1^\dagger \mathbf{y}_{p_t}^1 = \mathbf{w}_1^\dagger \mathbf{A}_1 \mathbf{x} + \mathbf{w}_1^\dagger (\mathbf{B}_1 \mathbf{s} + \mathbf{n}_p). \qquad (8)$$

$$\mathbf{y}_{s_t} = \mathbf{w}_2^\dagger \mathbf{y}_{s_t}^1 = \mathbf{w}_2^\dagger \mathbf{Q}_2 \mathbf{s} + \mathbf{w}_2^\dagger (\mathbf{D}_2 \mathbf{x} + \mathbf{n}_s). \qquad (9)$$

A. Combiner output Signal-to-interference plus Noise ratio

The signal to interference plus noise ratio (SINR) at BS1 is given by

$$\Gamma_1(\mathbf{w}_1) = \overline{\gamma}_1 \frac{\mathbf{w}_1^\dagger \mathbf{A}_1 \mathbf{A}_1^\dagger \mathbf{w}_1}{\mathbf{w}_1^\dagger \left[\overline{\gamma}_{21} \mathbf{B}_1 \mathbf{B}_1^\dagger + \left(\mathbf{I}_{n_{R_1}} \oplus \widetilde{\Upsilon}_1\right)\right] \mathbf{w}_1}, \qquad (10)$$

where $\overline{\gamma}_1 = \frac{P_1}{\sigma_1^2}$ and $\overline{\gamma}_{21} = \frac{P_2}{\sigma_1^2}$ respectively denote the average received SNR and interference to noise ratio (INR) at BS1, and $\widetilde{\Upsilon}_1 = \mathbf{I}_{n_{R_1}} + \frac{G^2\sigma^2}{\sigma_1^2}\mathbf{H}_p\mathbf{H}_p^\dagger$. Similarly, the instantaneous SINR at BS2 is given by

$$\Gamma_2(\mathbf{w}_2) = \overline{\gamma}_2 \frac{\mathbf{w}_2^\dagger \mathbf{Q}_2 \mathbf{Q}_2^\dagger \mathbf{w}_2}{\mathbf{w}_2^\dagger \left[\overline{\gamma}_{12}\mathbf{D}_2\mathbf{D}_2^\dagger + \left(\mathbf{I}_{n_{R_2}} \oplus \widetilde{\Upsilon}_2\right)\right]\mathbf{w}_2}, \quad (11)$$

where $\overline{\gamma}_2 = \frac{P_2}{\sigma_2^2}$ and $\overline{\gamma}_{12} = \frac{P_1}{\sigma_2^2}$ respectively denote the average received SNR and INR at BS2, and $\widetilde{\Upsilon}_2 = \mathbf{I}_{n_{R_2}} + \frac{G^2\sigma^2}{\sigma_2^2}\mathbf{B}_c\mathbf{B}_c^\dagger$.

III. The Capacity

A. Normal Capacity at the Base Stations

1) The Covariance: The covariance of $\mathbf{y}_{p_t}^1$ and $\mathbf{w}$, $\mathbf{R}_{\mathbf{y}_{p_t}^1}$ and $\mathbf{R}_\mathbf{w}$ for the BS1 can be calculated as

$$\mathbf{R}_{\mathbf{y}_{p_t}^1} = \mathbb{E}\left[\mathbf{y}_{p_t}^1 {\mathbf{y}_{p_t}^1}^\dagger\right] = \sigma\left[\mathbf{I}_{n_{R_1}} + \mathbf{c}\mathbf{Q}\mathbf{c}^\dagger\right], \quad (12)$$

$$\mathbf{R}_\mathbf{w} = \mathbb{E}\left[\mathbf{w}\mathbf{w}^\dagger\right] = \sigma\left[\mathbf{I}_{n_{R_1}} + \frac{P_2}{\sigma N}\mathbf{B}_1\mathbf{B}_1^\dagger\right], \quad (13)$$

where $\mathbf{w} = \mathbf{B}_1\mathbf{s} + \mathbf{n}_p$, $\mathbf{Q} = \frac{p_1}{\sigma M}\mathbf{I}_{n_M} \bigoplus \frac{p_2}{\sigma N}\mathbf{I}_{n_N}$, σ= Noise power. Similarly, the covariance of $\mathbf{y}_{s_t}^1$ and $\mathbf{z}$, $\mathbf{R}_{\mathbf{y}_{s_t}^1}$ and $\mathbf{R}_\mathbf{z}$ for the BS2 can be calculated as

$$\mathbf{R}_{\mathbf{y}_{s_t}^1} = \mathbb{E}\left[\mathbf{y}_{s_t}^1 {\mathbf{y}_{s_t}^1}^\dagger\right] = \sigma\left[\mathbf{I}_{n_{R_2}} + \mathbf{p}\mathbf{G}\mathbf{p}^\dagger\right], \quad (14)$$

$$\mathbf{R}_\mathbf{z} = \mathbb{E}\left[\mathbf{z}\mathbf{z}^\dagger\right] = \sigma\left[\mathbf{I}_{n_{R_2}} + \frac{p_1}{\sigma M}\mathbf{D}_2\mathbf{D}_2^\dagger\right], \quad (15)$$

where $\mathbf{z} = \mathbf{D}_2\mathbf{x} + \mathbf{n}_s$, $\mathbf{G} = \frac{P_2}{\sigma N}\mathbf{I}_{n_N} \bigoplus \frac{P_1}{\sigma M}\mathbf{I}_{n_M}$.

2) The Entropy: The entropy of $\mathbf{y}_{p_t}^1$ and $\mathbf{w}$, $H(\mathbf{y}_{p_t}^1)$ and $H(\mathbf{w})$ for the BS1 are given by

$$\begin{aligned} H(\mathbf{y}_{p_t}^1) &= \log_2 \det(\pi e \mathbf{R}_{\mathbf{y}_{p_t}^1}) \\ &= \log_2\left[\det \pi e\sigma(\mathbf{I}_{n_{R_1}} + \mathbf{c}\mathbf{Q}\mathbf{c}^\dagger)\right] \quad (16) \\ H(\mathbf{w}) &= \log_2 \det(\pi e \mathbf{R}_\mathbf{w}) \\ &= \log_2\left[\det \pi e\sigma(\mathbf{I}_{n_{R_1}} + \frac{p_2}{\sigma N}\mathbf{B}_1\mathbf{B}_1^\dagger)\right]. \quad (17) \end{aligned}$$

Similarly, the entropy of $\mathbf{y}_{s_t}^1$ and $\mathbf{z}$, $H(\mathbf{y}_{s_t}^1)$ and $H(\mathbf{z})$ for the BS2 are given by

$$\begin{aligned} H(\mathbf{y}_{s_t}^1) &= \log_2 \det(\pi e \mathbf{R}_{\mathbf{y}_{s_t}^1}) \\ &= \log_2\left[\det \pi e\sigma(\mathbf{I}_{n_{R_2}} + \mathbf{p}\mathbf{G}\mathbf{p}^\dagger)\right] \quad (18) \\ H(\mathbf{z}) &= \log_2 \det(\pi e \mathbf{R}_\mathbf{z}) \\ &= \log_2\left[\det \pi e\sigma(\mathbf{I}_{n_{R_2}} + \frac{p_1}{\sigma M}\mathbf{D}_2\mathbf{D}_2^\dagger)\right]. \quad (19) \end{aligned}$$

3) Mutual Information: The mutual information at the BS1 can be defined as

$$\begin{aligned} I(\mathbf{x}; \mathbf{y}_{p_t}^1) &= H(\mathbf{y}_{p_t}^1) - H(\mathbf{w}), \\ &= \log_2\left[\frac{\det \pi e\sigma(\mathbf{I}_{n_{R_1}} + \mathbf{c}\mathbf{Q}\mathbf{c}^\dagger)}{\det \pi e\sigma(\mathbf{I}_{n_{R_1}} + \frac{p_2}{\sigma N}\mathbf{B}_1\mathbf{B}_1^\dagger)}\right]. \quad (20) \end{aligned}$$

Similarly, the mutual information at the BS2 can be defined as

$$\begin{aligned} I(\mathbf{s}; \mathbf{y}_{s_t}^1) &= H(\mathbf{y}_{s_t}^1) - H(\mathbf{z}), \\ &= \log_2\left[\frac{\det \pi e\sigma(\mathbf{I}_{n_{R_2}} + \mathbf{p}\mathbf{G}\mathbf{p}^\dagger)}{\det \pi e\sigma(\mathbf{I}_{n_{R_2}} + \frac{p_1}{M\sigma}\mathbf{D}_2\mathbf{D}_2^\dagger)}\right] \quad (21) \end{aligned}$$

B. Optimal Capacity at the Base Stations

1) Optimal weighting Vector: From the Cauchy-Schwarz inequality, we obtain the optimal weighting vector $\mathbf{w}_{1_{opt}}$ at the BS1 that maximizes the combiner output SINR $\Gamma_1(\mathbf{w}_1)$ as follows

$$\begin{aligned} \mathbf{w}_{1_{opt}} &= \arg\max_{\mathbf{w}_1} \Gamma_1(\mathbf{w}_1) \\ &= c_1\left[\overline{\gamma}_{21}\mathbf{B}_1\mathbf{B}_1^\dagger + \left(\mathbf{I}_{n_{R_1}} \oplus \widetilde{\Upsilon}_1\right)\right]^{-1}\mathbf{A}_1, \quad (22) \end{aligned}$$

where c_1 is an arbitrary constant. At the BS2, the optimal weighting vector $\mathbf{w}_{2_{opt}}$ that maximizes the combiner output SINR $\Gamma_2(\mathbf{w}_2)$ is given by

$$\begin{aligned} \mathbf{w}_{2_{opt}} &= \arg\max_{\mathbf{w}_2} \gamma_2(\mathbf{w}_2) \\ &= c_2\left[\overline{\gamma}_{12}\mathbf{D}_2\mathbf{D}_2^\dagger + \left(\mathbf{I}_{n_{R_2}} \oplus \widetilde{\Upsilon}_2\right)\right]^{-1}\mathbf{Q}_2, \quad (23) \end{aligned}$$

where c_2 is an arbitrary constant.

2) Maxium Output SINR: The MRC weighting vector at the BS1, $\mathbf{w}_{1_{opt}}$, produces the following maximum output SINR

$$\Gamma_{1_{max}} = \overline{\gamma}_1\mathbf{A}_1^\dagger\left[\overline{\gamma}_{21}\mathbf{B}_1\mathbf{B}_1^\dagger + \left(\mathbf{I}_{n_{R_1}} \oplus \widetilde{\Upsilon}_1\right)\right]^{-1}\mathbf{A}_1. \quad (24)$$

Similarly, MRC weighting vector at the BS2, $\mathbf{w}_{2_{opt}}$, produces the following maximum output SINR

$$\Gamma_{2_{max}} = \overline{\gamma}_2\mathbf{Q}_2^\dagger\left[\overline{\gamma}_{12}\mathbf{D}_2\mathbf{D}_2^\dagger + \left(\mathbf{I}_{n_{R_2}} \oplus \widetilde{\Upsilon}_2\right)\right]^{-1}\mathbf{Q}_2. \quad (25)$$

The optimal capacity at the BS1 is given by

$$\begin{aligned} C_{1_{opt}} &= \log_e \det\left(\mathbf{I}_M + \Gamma_{1_{max}}\right) \\ &= \log_e \det\left[\mathbf{I}_M + \overline{\Gamma}_1\mathbf{A}_1^\dagger\left\{\overline{\gamma}_{21}\mathbf{B}_1\mathbf{B}_1^\dagger + \left(\mathbf{I}_{n_{R_1}} \oplus \widetilde{\Upsilon}_1\right)\right\}^{-1}\mathbf{A}_1\right]. \quad (26) \end{aligned}$$

Similarly, the optimal capacity at the BS2 is given by

$$\begin{aligned} C_{2_{opt}} &= \log_e \det\left(\mathbf{I}_N + \Gamma_{2_{max}}\right) \\ &= \log_e \det\left[\mathbf{I}_N + \overline{\Gamma}_2\mathbf{Q}_2^\dagger\left\{\overline{\gamma}_{12}\mathbf{D}_2\mathbf{D}_2^\dagger + \left(\mathbf{I}_{n_{R_2}} \oplus \widetilde{\Upsilon}_2\right)\right\}^{-1}\mathbf{Q}_2\right]. \quad (27) \end{aligned}$$

IV. Numerical Results

In this section, the simulation results of the analysis have been depicted on the basis of the derived expressions given in the previous Sections. Figs. 2 and 3 describe the effect of interferences on the optimal and normal ergodic capacity of BS1 and BS2, respectively. The capacity with interference is denoted by dotted line and the without interference is denoted by solid line. From these, we see that both the optimal and normal capacity decrease with interference. But the optimal

capacity is always greater than the normal capacity. This is because, due to the optimization of weighting vector at the receiver terminal maximizes signal-to-noise ratio (SINR) which in turn enhances the channel capacity.

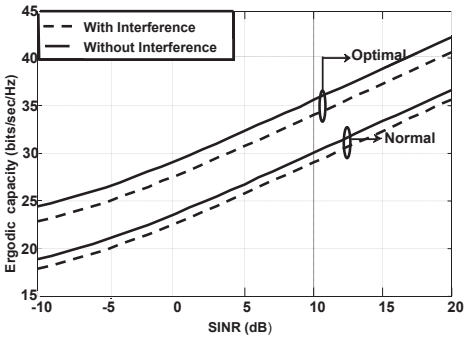

Fig. 2. The optimal and normal ergodic capacity of BS1 of as a function of SINR.

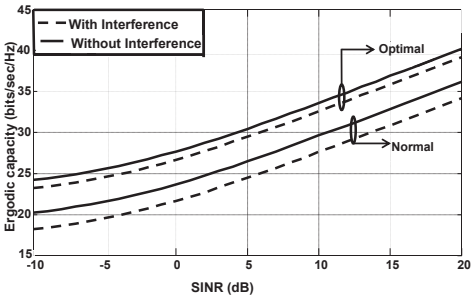

Fig. 3. The optimal and normal ergodic capacity of BS2 of as a function of SINR.

The effects of number of users are described in Figs. 4 and 5 for selected values of M and N, respectively. We see that the capacity of BS1 increases with the number of users of Cell 1 i.e., M while the capacity of BS2 decreases with M. Similarly, the capacity of BS2 increases with the number of users of cell 2 i.e. N while the capacity of BS1 decreases with N. Because, due to the increase in the number of users of a cell, capacity at the base station increases which is the characteristics of multiple access channel. Since the interference of adjacent cell increases with the number of users of other cell, therefore, we see that the capacity of other cell decreases with the increase in number of other cell.

V. Conclusion

In this paper, we focus on the derivation of optimal capacity of multi-cellular networks. Some numerical results have been presented to verify the validity of derived expressions. Based on our formulation and from the observation of numerical results, it can be concluded that both the optimal and normal capacity decrease with interference. But the optimization of weighting vector at the receiver terminal maximizes SINR which enhances the channel capacity. Although the capacity of a cell increases with the number of users but the capacity

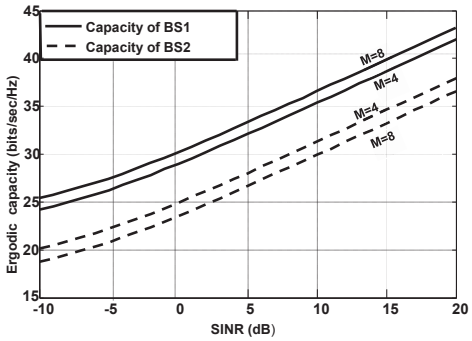

Fig. 4. The optimal ergodic capacity of BS1 versus SINR for selected values of M with $N = 4$.

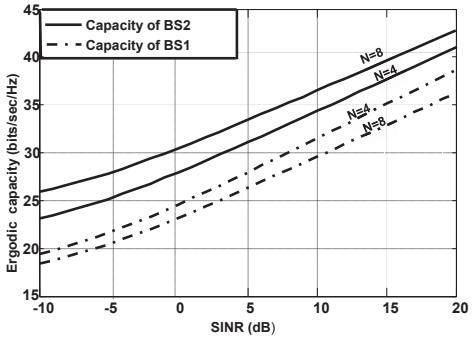

Fig. 5. The optimal ergodic capacity of BS2 versus SINR for selected values of N with $M = 4$.

of adjacent cells decrease due to the effect of additional interferences created by the additional users. Therefore, it is clear that the effect of interferences created by the users of adjacent cells can be reduced by optimizing the weighting vector at the receiver terminals.

Acknowledgment

This work is supported by the Research Support and Publication Division of University Grant Commission, Bangladesh.

References

[1] K. Hosseini, E. S. Rogers, W. Yu, and R. Adve, "Large-scale MIMO versus network MIMO for multicell interference mitigation," *IEEE Trans. on Signal Processing*, vol. 8, no. 5, pp. 930–941, May 2014.

[2] D. Gesbert, S. Hanly, H. Huang, S. S. Shitz, O. Simeone, and W. Yu, "Multi-cell MIMO cooperative networks: A new look at interference," *IEEE Journal on Selected Areas in Communications*, vol. 28, no. 9, pp. 1380–1408, December 2010.

[3] A. Bletsas, H. Shin, and M. Z. Win, "Outage optimality of opportunistic amplify-and-forward relaying," vol. 11, no. 3, pp. 261–263, March 2007.

[4] J. Zhang and J. G. Andrews, "Adaptive spatial intercell interference cancellation in multicell wireless networks," *IEEE Journal on Selected Areas in Communications*, vol. 28, no. 9, pp. 1455–1468, December 2010.

[5] A. Bletsas, H. Shin, M. Z. Win, and A. Lippman, "Cooperative diversity with opportunistic relaying," in *Proc. IEEE Third Conference on Wireless Communication and Networking, Las Vegas*, November 2006, pp. 1034–1039.

[6] D. H. N. Nguyen, "Sum-rate maximization in the multicell MIMO multiple-access channel with interference coordination," *IEEE Trans. on Wireless Communications*, vol. 13, no. 1, pp. 36–40, June 2013.

Investigation of low switching frequency control of a Three phase Cascaded H-bridge multilevel inverter

Md Mubashwar Hasan[1], A. Abu-Siada[2]
[1, 2]Department of Electrical and Computer Engineering, Curtin University, Perth, Australia
m.hasan12@postgrad.curtin.edu.au[1],
a.abusiada@curtin.edu.au[2]

Md. Rabiul Islam, Department of Electrical and Electronic Engineering, Rajshahi University of Engineering & Technology, Rajshahi 6204, Bangladesh.
Rabiulbd@hotmail.com

***Abstract*— This paper presents analysis of a three phase hybrid multilevel inverter (MLI) by applying low frequency stair case control strategy. The proposed MLI contains three cascaded stages, auxiliary stage-1, auxiliary stage-2, and main stage. The main stage contains three half-bridge cells which are connected in parallel with a common DC power supply. Each of the stages in the auxiliary stages consists of three H-bridge where the H-bridge cells contain isolated DC power supplies. The proposed hybrid MLI is tested for symmetric and asymmetric configurations of input voltage sources of the main and auxiliary stages. A scaled down prototype of the proposed hybrid three-phase hybrid MLI is developed to verify the control concept and the real time performance of the inverter.**

***Keywords*— Cascaded Inverter; Low frequency control; THD.**

I. INTRODUCTION

Cascaded MLI (CMLI) is the dominating type in the MLI topologies as it contains some distinctive characteristics over the other types of MLI topologies e.g. it does not need any capacitive voltage balancing as isolated/non-isolated DC voltage supplies are utilized instead of balancing capacitors [1, 2], creates low voltage stress on the power electronic devices [3], utilizes reduced number of semiconductor devices comparing to other types of MLI topologies [4, 5]. Cascaded H-bridge (CHB) MLI is a very well-known topology, which is implemented for several applications [6-8]. According to similar and dissimilar magnitude among the H-bridge cells in the CHB MLI topology, it can be classified into two groups: symmetric and asymmetric topology. The asymmetric topologies have capability to enhance the number of levels in the output voltage without increasing the number of semiconductor device and input DC supplies in comparison to the symmetric topology. For example, a two stage three phase symmetric CHB MLI requires twenty four semiconductor switches and six input DC supplies to generate five levels in the output line voltage while same two stage CHB structure is able to generate nine levels in the line voltage while the ratio between the voltage sources of the two stages are kept 1:3. The increment of the number of levels in the line voltage reduces the total harmonic distortion (THD). Hybridization in cascaded MLI is done to reduce the requirement of the number of power electronic devices and the input DC supplies [2, 9].

II. PROPOSED HYBRID CASCADED MLI

The proposed Hybrid MLI is shown Fig. 1, where the main stage, auxiliary stage-1 and auxiliary stage-2 are denoted by main, auxi-1 and auxi-2; respectively. Each auxiliary stage consists of three H-bridge cells while the main stage consists of three half-bridge cells as shown in Fig. 1.

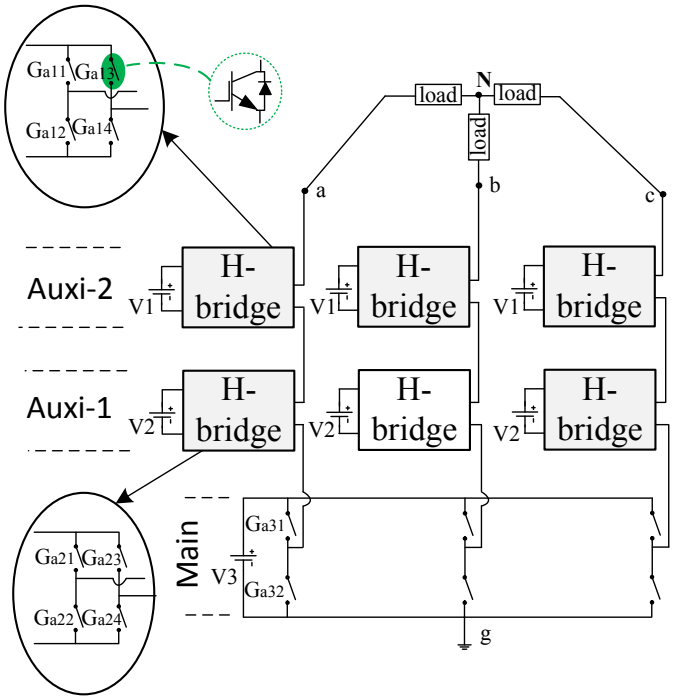

Fig. 1. Proposed three phase Hybrid cascaded MLI

The magnitudes of the auxiliary-1, auxiliary-2 stages and main stage are expressed by V_1, V_2 and V_3, respectively. Symmetric or asymmetric structure of the aforementioned three stage hybrid cascaded MLI can be made by adjusting the values of V_1, V_2 and V_3. Table 1 shows the switching logic of the proposed hybrid MLI for generating pole voltage output (V_{xg}) while it is considered as asymmetric structure when $V_1=V_{dc}$, $V_2=3V_{dc}$, $V_3=9V_{dc}$, where x is phase arm a, b,c. Here the conjugative switches are denoted by (′) sign.

978-1-5090-5785-6/16/$31.00 ©2016 IEEE

TABLE 1. SWITCHING LOGIC FOR DIFFERENT LEVEL GENERATION

V_{xg}	Sx1, Sx2′	Gx11, Gx12′	Gx13, Gx14′	Gx21, Gx22′	Gx23, Gx24′
0	0	1	1	1	1
V_{dc}	0	1	0	1	1
2 V_{dc}	0	0	1	1	0
3 V_{dc}	0	1	1	1	0
4 V_{dc}	0	1	0	1	0
5 V_{dc}	1	0	1	0	1
6 V_{dc}	1	1	1	0	1
7 V_{dc}	1	1	0	0	1
8 V_{dc}	1	0	1	1	1
9 V_{dc}	1	1	1	1	1
0V_{dc}	1	1	0	1	1
11 V_{dc}	1	0	1	1	0
12 V_{dc}	1	1	1	1	0
13 V_{dc}	1	1	0	1	0

The line voltage (V_{ab}, V_{bc}, V_{ca}) is found from the pole voltages, V_{ag}, V_{bg}, V_{cg} by the following equation,

$$\begin{bmatrix} V_{ab} \\ V_{bc} \\ V_{ca} \end{bmatrix} = \begin{bmatrix} V_{ag} - V_{bg} \\ V_{bg} - V_{cg} \\ V_{cg} - V_{ag} \end{bmatrix} \quad (1)$$

If the number of levels in the pole voltage (V_{xg}) is Np, then the number of levels in the line voltages can be expressed by

$$N_{\text{level}} = 2N_{\text{p}} - 1 \quad (2)$$

he phase voltage is obtained by

$$\begin{bmatrix} V_{aN} \\ V_{bN} \\ V_{cN} \end{bmatrix} = \frac{1}{3}\begin{bmatrix} 2 & -1 & -1 \\ -1 & 2 & -1 \\ -1 & -1 & 2 \end{bmatrix}\begin{bmatrix} V_{ag} \\ V_{bg} \\ V_{cg} \end{bmatrix} \quad (3)$$

III. LOW FREQUENCY CONTROL STRATEGY

Low frequency control strategy is applied to MLI in order to achieve better performance in terms of reduced switching losses and THD [10]. The pole voltage Vxg, is held as reference to generate the switching states (S) and it can written as

$$\left.\begin{aligned} V_{ag,ref} &= \frac{(N_p-1)*V_{dc}}{2}\left(m_i*\cos(2\pi ft)+[1-\frac{m_i}{6}\cos(6\pi ft)]\right) \\ V_{bg,ref} &= \frac{(N_p-1)*V_{dc}}{2}\left(m_i*\cos(2\pi ft-\frac{2\pi}{3})+[1-\frac{m_i}{6}\cos(6\pi ft)]\right) \\ V_{bg,ref} &= \frac{(N_p-1)*V_{dc}}{2}\left(m_i*\cos(2\pi ft+\frac{2\pi}{3})+[1-\frac{m_i}{6}\cos(6\pi ft)]\right) \end{aligned}\right\} \quad (4)$$

Where m_i, f, and t are the modulation index, line voltage frequency and instantaneous time.

The switching states can be expressed by

$$\left.\begin{aligned} S_a &= round\left(\frac{(N_p-1)}{V_1+V_2+V_3}*V_{ag,ref}\right) \\ S_b &= round\left(\frac{(N_p-1)}{V_1+V_2+V_3}*V_{bg,ref}\right) \\ S_c &= round\left(\frac{(N_p-1)}{V_1+V_2+V_3}*V_{cg,ref}\right) \end{aligned}\right\} \quad (5)$$

The number of switching states (S) for can be expressed by

$$S = 6(N_{\text{p}} - 1) \quad (6)$$

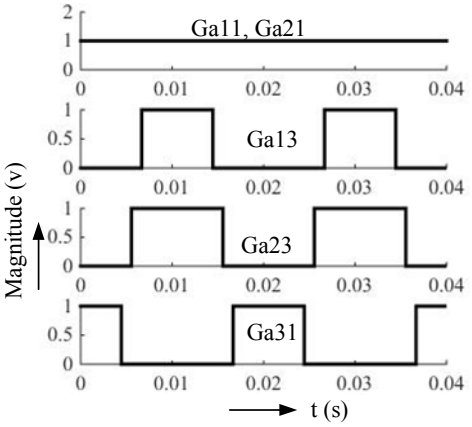

Fig. 2. Gate signals for phase arm-a

The generalized vector presentation of switching states is shown in Fig. 2 which obeys the following equations.

$$V = V_q - jV_d \quad (7)$$

$$\left.\begin{aligned} V_d &= \frac{V_1+V_2+V_3}{\sqrt{3}(N_p-1)}(S_{\text{c}}-S_{\text{b}}); \\ V_q &= \frac{V_1+V_2+V_3}{3(N_p-1)}(2S_{\text{a}}-S_{\text{b}}-S_{\text{c}}) \end{aligned}\right\} \quad (8)$$

While the proposed hybrid MLI is examined for symmetric and asymmetric structures, only the symmetric method is explained for simplicity. The magnitudes of all the DC voltage supplies would be same during symmetric structure (V_1=V_2=V_3=V_{dc}) and there exists 18-switching states (300, 310, 320, 330, 230, 130, 030, 031, 032, 033, 023, 013, 003, 103, 203, 303, 302, 301) in such symmetric structure. The switching operation can be shown by Table 2 to achieve a complete cycle of three phase line voltages. The gate signals of the switches in the phase arm-a is shown in Fig. 2. The

switching signal for the switches in phase arm-b and c are same as phase arm-a, b contains 120^0 and 240^0 phase shift.

TABLE 2. SWITCHING STATES SEQUENCE FOR A COMPLETE ONE CYCLE OF THREE PHASE LINE VOLTAGE GENERATION

Switching states *Sa,Sb,Sc*	Ga11, Ga12′	Ga13, Ga14′	Ga21, Ga22′	Ga23, Ga24′	Ga31, Ga32′	Gb11, Gb12′	Gb13, Gb14′	Gb21, Gb22′	Gb23, Gb24′	Gb31, Gb32′	Gc11, Gc12′	Gc13, Gc14′	Gc21, Gc22′	Gc23, Gc24′	Gc31, Gc32′	Vab	Vbc	Vca
300	1	0	1	0	1	1	1	1	1	0	1	1	1	1	0	3	0	-3
310	1	0	1	0	1	1	0	1	1	0	1	1	1	1	0	2	1	-3
320	1	0	1	0	1	1	0	1	0	0	1	1	1	1	0	1	2	-3
330	1	0	1	0	1	1	0	1	0	1	1	1	1	1	0	0	3	-3
230	1	0	1	0	0	1	0	1	0	1	1	1	1	1	0	-1	3	-2
130	1	0	1	1	0	1	0	1	0	1	1	1	1	1	0	-2	3	-1
030	1	1	1	1	0	1	0	1	0	1	1	1	1	1	0	-3	3	0
031	1	1	1	1	0	1	0	1	0	1	1	0	1	1	0	-3	2	1
032	1	1	1	1	0	1	0	1	0	1	1	0	1	0	0	-3	1	2
033	1	1	1	1	0	1	0	1	0	1	1	0	1	0	1	-3	0	3
023	1	1	1	1	0	1	0	1	0	0	1	0	1	0	1	-2	-1	3
013	1	1	1	1	0	1	0	1	1	0	1	0	1	0	1	-1	-2	3
003	1	1	1	1	0	1	1	1	1	0	1	0	1	0	1	0	-3	3
103	1	0	1	1	0	1	1	1	1	0	1	0	1	0	1	1	-3	2
203	1	0	1	0	0	1	1	1	1	0	1	0	1	0	1	2	-3	1
303	1	0	1	0	1	1	1	1	1	0	1	0	1	0	1	3	-3	0
302	1	0	1	0	1	1	1	1	1	0	1	0	1	0	0	3	-2	-1
301	1	0	1	0	1	1	1	1	1	0	1	0	1	1	0	3	-1	-2

IV. IMPLEMENTATION AND RESULTS

Fig. 3 shows the implemented hardware prototype of the three phase cascaded hybrid MLI, where IGBT, IGBTs, HGTG20N60B3D, 600V/40A are chosen as semiconductor switches for the main stage and the auxiliary stages. The voltage source magnitudes are managed from the external DC supplies and their magnitudes are adjusted as $V_1= V_2=V_3=V_{dc}=$ 80 V. Inductive 3-phase load (Z=55+j37.68) Ω/phase) is considered for testing the inverter performance and digital signal processor, TMS320F2812 is utilized to get the real time gate signals.

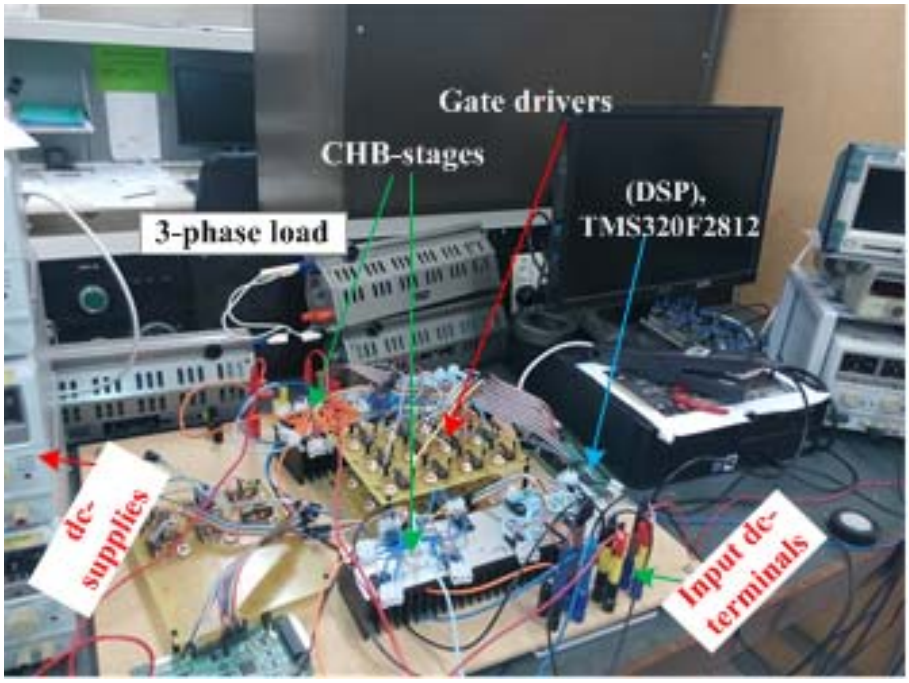

Fig. 3. Different parts of hardware setup

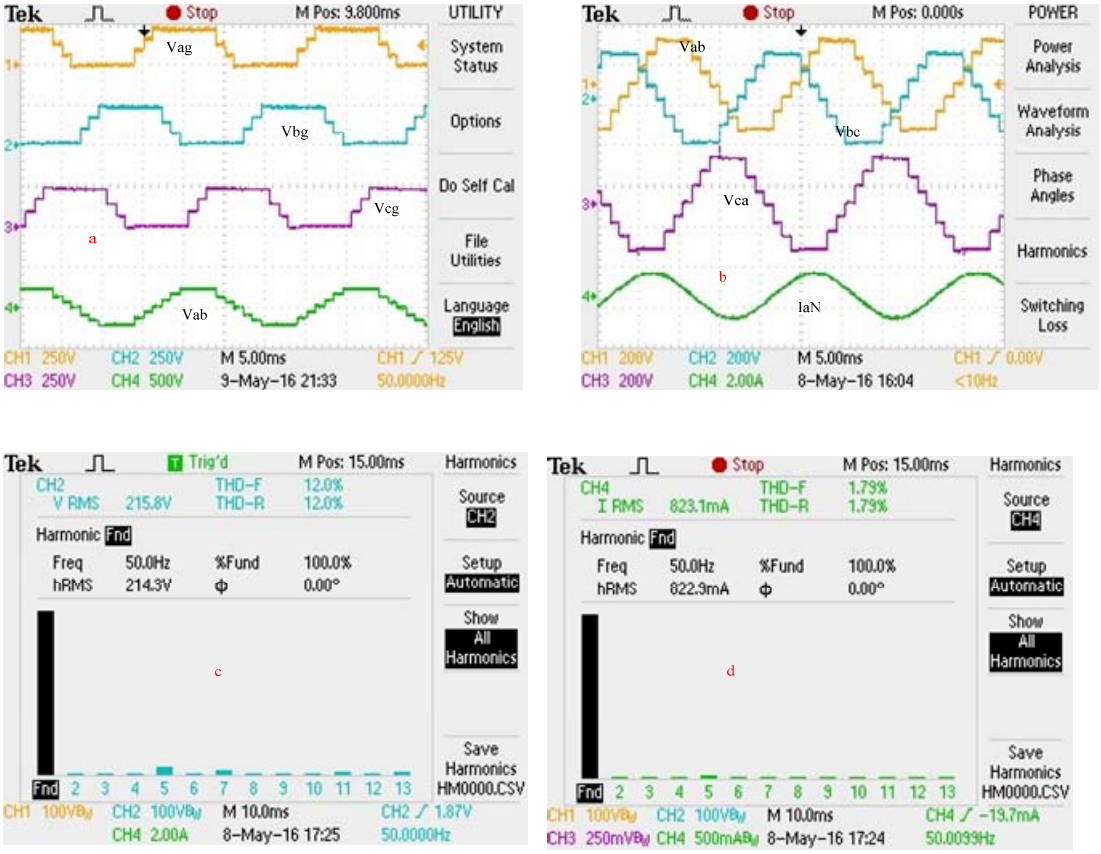

Fig. 4. Experimental result of (a) pole voltages (Vag, Vbg, Vcg), (b) Line voltages (Vab, Vbc, Vca) and line current (I_{aN}), (c) line voltage THD, (d) line current THD

Figs. 4a and 4b shows the pole voltage (V_{ag}, V_{bg}, V_{cg}), line voltage (V_{ab}, V_{bc}, V_{ca}) and line current output, respectively. The pole voltages contain four levels (240 V, 160 V, 80 V, 0) while the line voltages appear seven level (±240 V, ±160 V, ±80 V, 0) for the symmetric structure of the hybrid MLI. Figs. 4c and 4d show the THD of the unfiltered line voltage and line current respectively. Though line current THD is less than 5% but line voltage THD exceeds the IEEE THD limit and line voltage THD can be reduced by increasing the number of voltage levels. To do so, asymmetric method can be applied, e.g., the same inverter prototype is able to generate 27-levels and 240V line voltage magnitude in the line voltage while $V_1=V_{dc}=18.46V$, $V_2=3V_{dc}=55.38V$, $V_3=9V_{dc}=166.15V$ and THD is found less than 5%.

V. CONCLUSION

A simple implementation technique along with an easy control technique is presented in the paper which is expected to contribute in high voltage and high power applications. This hybrid inverter can be easily utilized for PV voltage conversion (DC/AC), if the input DC supplies are replaced by PV arrays.

REFERENCES

[1] E. Najafi and A. H. M. Yatim, "Design and implementation of a new multilevel inverter topology," IEEE Trans. Ind. Electron., vol. 59, pp. 4148-4154, 2012.

[2] M. Hasan, S. Mekhilef, and M. Ahmed, "Three-phase hybrid multilevel inverter with less power electronic components using space vector modulation," IET Power Electron., vol. 7, pp. 1256-1265, 2014.

[3] E. Babaei, S. Laali, and Z. Bayat, "A single-phase cascaded multilevel inverter based on a new basic unit with reduced number of power switches," IEEE Trans. Ind. Electron., vol. 62, pp. 922-929, 2015.

[4] M. Farhadi Kangarlu and E. Babaei, "Cross-switched multilevel inverter: an innovative topology," IET Power Electron., vol. 6, pp. 642-651, 2013.

[5] M. F. Kangarlu, E. Babaei, and M. Sabahi, "Cascaded cross-switched multilevel inverter in symmetric and asymmetric conditions," IET Power Electron., vol. 6, pp. 1041-1050, 2013.

[6] L. M. Tolbert, F. Z. Peng, and T. G. Habetler, "Multilevel converters for large electric drives," Industry Applications, IEEE Transactions on, vol. 35, pp. 36-44, 1999.

[7] M. V. Rajkumar and P. Manoharan, "FPGA based multilevel cascaded inverters with SVPWM algorithm for photovoltaic system," Solar Energy, vol. 87, pp. 229-245, 2013.

[8] K. K. Gupta, A. Ranjan, P. Bhatnagar, L. Kumar Sahu, and S. Jain, "Multilevel inverter topologies with reduced device count: a review," Power Electronics, IEEE Transactions on, vol. 31, pp. 135-151, 2016.

[9] S. Mekhilef and M. N. Abdul Kadir, "Voltage control of three-stage hybrid multilevel inverter using vector transformation," IEEE Trans. Power. Electron., vol. 25, pp. 2599-2606, 2010.

[10] M. M. Hasan, A. Abu-Siada and M. R. Islam, "Design and implementation of a novel three-phase cascaded half-bridge inverter," IET Power Electron., vol. 9, no. 8, pp. 1741-1752, 6 29 2016.

International Conference on Electrical, Computer & Telecommunication Engineering (ICECTE)
8-10 December 2016, Rajshahi-6204, Bangladesh

Performance Analysis of Graphene Based Nano Dipole Antenna on Stacked Substrate

Reefat Inum, Md. Masud Rana, and Kamrun Nahar Shushama
Department of Electrical and Electronic Engineering
Rajshahi University of Engineering and Technology
E-mail: romel.eee09@gmail.com, md.masud.rana@ruet.ac.bd, shushamanahar@gmail.com

***Abstract*—The design of a graphene based nano dipole antenna on stacked substrate is reported. A stack of substrate is formed from two different dielectric substrate materials, each of equal height. The performance of the designed antenna is investigated for three different substrate stacks such as Quartz-Silicon, GaAs-Silicon Nitride, and Polyimide-Glass. For each stack, total substrate height is varied from 80 µm to 120 µm, taking 20 µm as step size. The considered performance parameters of the designed antenna are return loss, bandwidth, radiation efficiency, gain, and directivity at a targeted resonance frequency of 1.02 THz. The simulation results confirm that Quartz-Silicon substrate pair with a height of 100 µm provides the best antenna performance. The enhanced outcomes are compared with other similar graphene antennas to ensure the effectiveness of the proposed design. The attractive properties and significant performances of the proposed graphene antenna make it a potential candidate to be used in wireless communication in nanosystems and THz sensing applications.**

Keywords—Graphene, Terahertz (THz), Planar dipole, Stacked substrate.

I. INTRODUCTION

A one atom thick planar sheet of carbon atoms tightly packed into a 2-D honeycomb crystal lattice is called graphene [1]. Due to some unique electronic properties such as very high electron mobility, very high sensitivity, and thermoelectric current effect etc. [2], graphene can be said to be the silicon of 21st century. Consequently several studies have been carried out to construct atomically precise nano-scale antennas employing surface plasmon resonance property of graphene [3]-[6]. Actually, operation at nano scales is an unfeasible option for the conventional metallic antenna due to the requirement of VHF frequency band. But the unique band structure of graphene would enable it to operate at a relatively lower frequency making it a feasible option for a nano sized antenna [7], [8].

The importance of analysis and investigation of graphene based planar dipole antenna is two folded. Firstly, Dipole is the simplest of all antenna structures. It has several advantages over other structures such as ease of construction and fabrication, light weight, low profile, inexpensive etc. [9]. Secondly, the use of graphene as the radiating element provides some extraordinary advantageous features to the planar printed dipole antenna in terms of ease of integration, reconfigurability, dynamic tuning, plasmonic nature of graphene conductivity at terahertz frequency etc. [8]. In [4], the design of a graphene dipole antenna on quartz substrate was reported which provides -28 dB return loss and 1.8 dBi directivity. Various aspects of graphene-based photoconductive antennas were investigated in [6]. The summary of this investigation in a word is that the tunable behavior of graphene antennas compensates for their lower radiation efficiency and bandwidth. Graphene-sheet resonant plasmon antenna on glass substrate was designed and analyzed in the terahertz frequency range in [10] where only input impedance and radiation pattern of the proposed antenna were reported without any optimization in the antenna geometry.

In this paper, we present a compact and miniaturized design of a graphene based planar dipole antenna on stacked substrate. The type and height of different substrate materials are considered as the key parameters to conduct the analysis at a targeted resonance frequency of 1.02 THz. A comparison of the radiation characteristics between the designed and other similar antennas shows the effectiveness of the proposed design. As the proposed graphene nano antenna radiates and resonates at THz band, an array of such several antenna elements is predicted to be applied in THz imaging system.

II. ANTENNA MODELING

Substrate, highly variable graphene parameters, and geometrical dimensions are the key factors that strongly control the properties of the designed antenna. Therefore, a vast parameter space must be considered to optimize the antenna even for very simple geometries. The antenna modeled in this work is illustrated in Fig. 1. Two graphene strips separated by a gap are placed on the stacked substrate. The strips are integrated with a source in the center gap. The inductive property exhibited by the real part of the complex

978-1-5090-5785-6/16/$31.00 ©2016 IEEE

conductivity of graphene patches permits the propagation of TM plasmonic modes at THz frequencies which can be excited by the source [11].

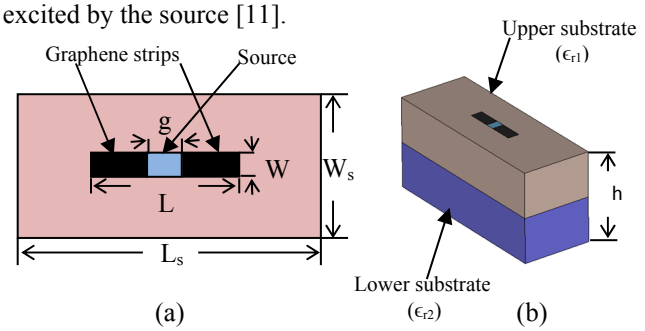

Fig. 1. Schematic diagram of the proposed antenna, (a) top view, and (b) 3-D view.

Initially, the length of the dipole is determined according to the following formula:

$$L = \frac{\lambda}{2} \quad (1)$$

where, $\lambda = \frac{c}{f}$ is the wavelength and c is the velocity of light and f is the antenna resonance frequency. Thus the length of each graphene strip of the half wavelength planar dipole antenna is calculated as:

$$L_{strip} = \frac{\lambda}{4} \quad (2)$$

However, since the electric field will fringe at the end of the dipole arms and the antenna based on graphene is expected to have a resonant character, the effective resonance length can be determined by $L_{eff} = m \times \pi B$, where B is the wave vector of the SPP wave [4]. Considering a resonance frequency of 1.02 THz, the actual dipole length to support SPP wave found after optimization is $L = 20$ µm. Next, the width of the graphene sheet is determined such that apposite propagation of plasmonic wave is ensured. A ratio of length to width approximately equal to 4 is required by the graphene sheet to sufficiently support SPP mode. Consequently, the width of the dipole arm is found to be $W = 5$ µm. The feed gap g is maintained at 1µm. To create the graphene material in the simulation environment, thickness, chemical potential, relaxation time, and temperature of graphene are taken as 10 nm, 0.31 eV, 1 ps, and 300 k respectively. The most important part of the antenna design in the context of this work is the construction of substrate in the form of a stack. Two different materials, each of equal height, arranged as upper on lower substrate, form the stack. Since the absorption cross section increases with the substrate size up to a given limit, a larger substrate is needed to enhance the performance of graphene based antennas [12]. Thus the length and width of the dielectric substrate are taken as four times of dipole length and six times of dipole width respectively. Thickness of each substrate material of the stack is primarily taken as 40 µm making a total height of 80 µm. The effect of substrate thickness on the radiation characteristics of graphene based planar dipole antenna is investigated by varying the total thickness as 80 µm, 100 µm, and 120 µm for three different substrate pairs. The complete design parameters are tabulated below:

Table I

Design parameters of the graphene based planar dipole antenna on two substrate layers.

Parameter	Value (µm)
Dipole length, L	20
Dipole width, W	5
Feed gap, g	1
Substrate length, L_s	4*L=80
Substrate width, W_s	6*W=30
Total substrate height, h	80, 100, 120

III. Simulation Results

Finite element method (FEM) based CST MWS software is used to simulate the proposed antenna model. The antenna performance parameters to be considered are the return loss, gain, bandwidth, directivity, and radiation efficiency. Three pairs of stacked substrate with a varying height are investigated to analyze the performance of the proposed antenna.

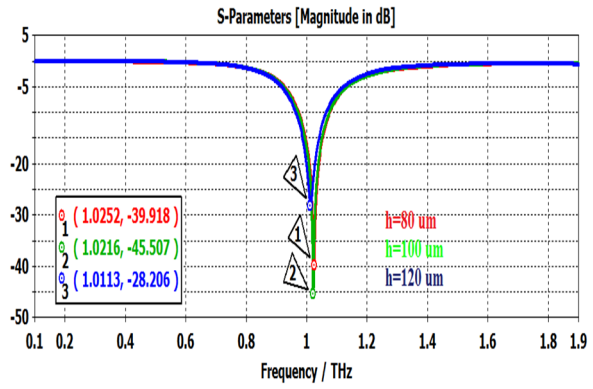

(a)

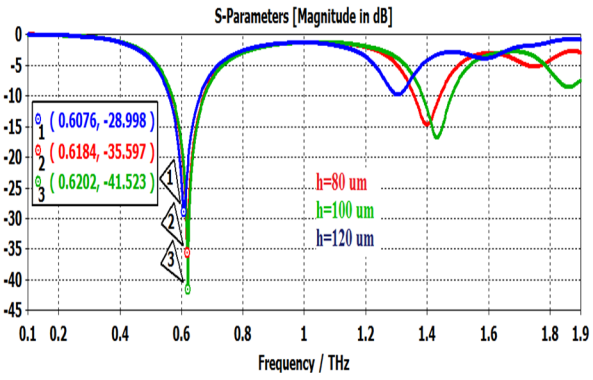

(b)

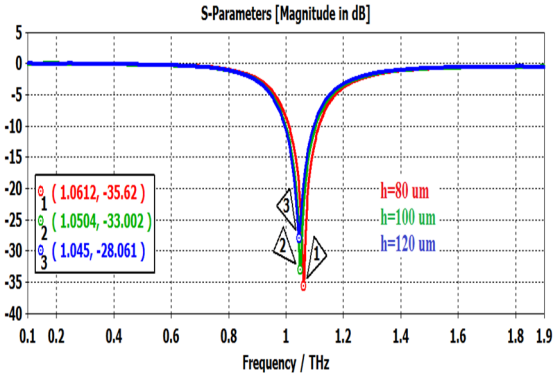

(c)

Fig. 2. Return loss of the graphene based planar dipole antenna based on (a) Quartz-Silicon, (b) GaAs-Silicon Nitride, and (c) Polyimide-Glass substrate stack for varying thickness.

The effects of substrate height on the antenna return loss for three different substrate stacks can be analyzed from Fig. 2. For the quartz (ϵ_r=3.75)-silicon (ϵ_r=11.9) substrate pairs, the best result is obtained as -45.507 dB return loss for a total height of 100 µm as shown in Fig. 2(a). The same figure also reveals that the return loss increases at 120 µm which may be due to the increased surface introduced in the larger dielectric material. Fig. 2(b) depicts that the antenna resonance frequency decreases for the GaAs (ϵ_r=12.94)-silicon nitride (Nth order model, N=2) substrate stack. In this case also the return loss improves from -35.597 dB at 80 µm to -41.523 dB at 100 µm and the worst result found at 120 µm again.

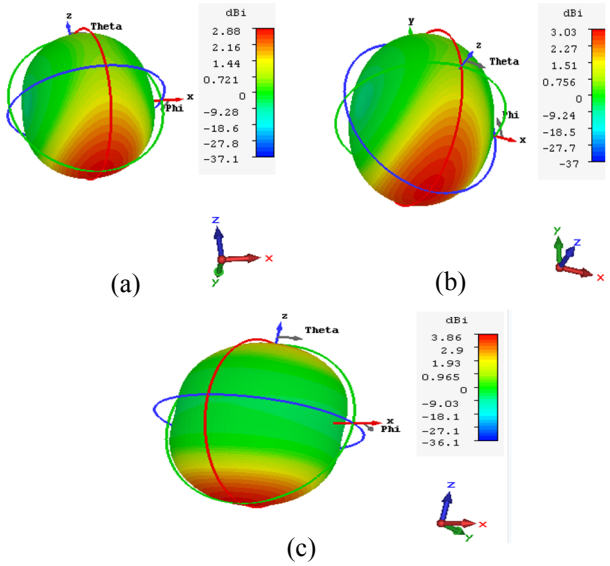

(a) (b)

(c)

Fig. 3. 3-D plot of directivity of the graphene based planar dipole antenna on (a) GaAs-Silicon Nitride substrate stack for h=100 µm, (b) Polyimide-Glass substrate pair for h=80 µm, and (c) Quartz-Silicon stacked substrate for h=100 µm.

The polyimide (ϵ_r=3.5)-glass (ϵ_r=4.82) substrate pair shifts the antenna resonance frequency to the right as is evident from Fig. 2(c). But in this case, the best performance obtained is -35.62 dB for 80 µm. The bandwidth of the designed planar dipole antenna on quartz-silicon substrate is found to be 0.11197 THz for h=100 µm. For the same height, GaAs-silicon nitride pair provides with a bandwidth of 0.10636 THz. However, bandwidth measurement is conducted at a substrate height of 80 µm for polyimide-glass stack as this pair gives best return loss at the same height. In this case the antenna bandwidth found is 0.1021 THz. The radiation efficiency and total efficiency of the designed antenna are also evaluated through numerical simulation. For h=100 µm, quartz-silicon substrate pair gives -14.76 dB as the radiation efficiency and total efficiency. The planar dipole antenna on GaAs-silicon nitride substrate stack at a height of 100 µm provides radiation efficiency of -15.57 dB and total efficiency of -21.01 dB. For a total substrate height of 80 µm, the designed antenna on polyimide-glass substrate pair shows -15.57 dB and -15.87 dB as radiation efficiency and total efficiency respectively.

Gain and directivity are two very much important parameters to judge the performance of an antenna. The 3-D plots of directivity for three different antenna types are available in Fig. 3. As in the case of antenna bandwidth and efficiency evaluation, the directivity of the graphene based planar dipole antenna is also determined systematically.

Its obvious from Fig. 3 that the best performance obtained in terms of antenna directivity is 3.86 dBi at 1.02 THz frequency which is for quartz-silicon substrate pair.

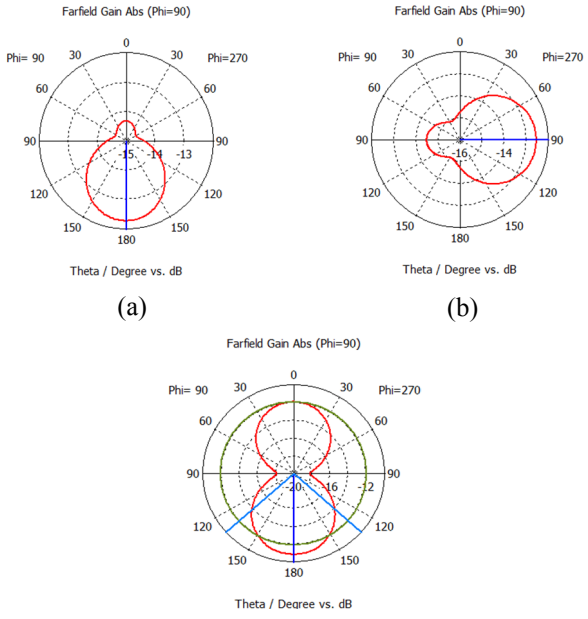

(a) (b)

(c)

Fig. 4. Polar plot of gain of the designed planar dipole antenna deposited on (a) GaAs-Silicon Nitride substrate stack for h=100 µm, (b) Polyimide-Glass substrate pair for h=80 µm, and (c) Quartz-Silicon stacked substrate for h=100 µm.

Its evident from Fig. 4(a) that the antenna on GaAs-silicon nitride substrate pair gives radiation pattern having main lobe direction at 180° and gain of -12.3 dB. Fig. 4(b) shows that the antenna on polyimide-glass substrate pair has a gain of -12.5 dB at 90° direction. The degree to which the radiation patterns of Fig. 4(a) and (b) are similar with that of conventional metallic antenna is very low. Consequently these two substrate pairs are not suitable to model a graphene based planar dipole antenna. The radiation pattern by the planar dipole designed on quartz-silicon stacked substrate is shown in Fig. 4(c). In this case, the antenna gain obtained is -10.9 at a direction of 180°. However, the best thing happened for this substrate pair is that it provides a radiation pattern which is very much similar to that of the metallic counterpart.

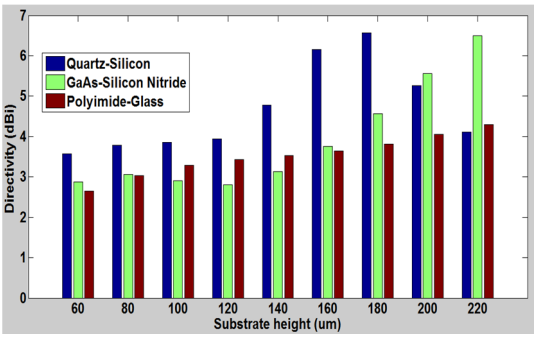

Fig. 5. Antenna directivity versus substrate height for three different substrate stacks.

Its observed from Fig. 5 that the antenna directivity is normally increased with an increase in substrate height. However, for quartz-silicon substrate pair, directivity is decreased for heights greater than 180 µm. Hence, there is a trade-off between the directive gain and miniaturization of graphene based planar dipole antenna.

Table II

Performance comparison of the proposed antenna with similar other antennas

Performance parameter	**Proposed antenna**	**[4]**	**[5]**
Return loss (dB)	-45.507	-28	-
Bandwidth (THz)	0.11197	-	-
Gain (dB)	-10.9	-	1
Directivity (dBi)	3.86	1.8	2.18
Radiation efficiency (%)	3.34	2	-

Analyzing the performance parameters of three different antenna types, graphene based planar dipole on quartz-silicon substrate stack with a total substrate height of 100 µm is proposed as a compact, miniaturized, and plasmonic antenna. However Table II compares the performance parameters of the proposed antenna with that of similar other graphene based antenna.

IV. Conclusion

The performance of graphene based antenna is investigated by designing a planar dipole antenna deposited on stacked substrate. The proposed antenna on quartz-silicon substrate with a total substrate height of 100 µm has the advantages of compactness, being low profile, miniaturized, inexpensive, and supporting SPP mode of propagation. A comparison of the proposed antenna with other existing graphene based antennas also reflects the effectiveness of the design. However, one drawback of graphene based antennas is their low radiation efficiency. This is because the surface resistance of graphene is very high compared to metals at micro and mm-waves frequency, even with the possibility of doping and electric field biasing [8]. However the dynamic tunability of such graphene based antennas with respect to chemical potential compensates for this low radiation efficiency.

References

[1] A. K. Geim and K. S. Novoselov, "The rise of graphene," *Nature Materials*, vol. 6, no. 3, pp. 183-191, Mar. 2007.

[2] A. H. C. Neto, F. Guinea, N. M. R. Peres, K. S. Novoselov, A. K. Geim, "The electronic properties of graphene," *Rev. Mod. Phys.*, vol. 81, pp. 109-162, Jan. 2009.

[3] Y. Yao *et. al.*, "Broad electrical tuning of graphene-loaded plasmonic antennas," *Nano Lett.*vol. 13, pp. 1257-1264, Feb. 2013.

[4] T. Zhou *et. al.*, "Miniaturized tunable terahertz antenna based on graphene," *Microw.Optic. Tech. Lett.*, vol. 56, no. 8, Aug. 2014.

[5] M. Dragoman *et al.,* "Terahertz antenna based on graphene." *J, Appl. Phys.* vol. 103, May. 2010.

[6] M. Z. Koohi, M. Neshat, "Evaluation of graphene-based terahertz photoconductive antennas," *Trans. F: Nanotech.,* vol. 22, pp. 1299-1305, May. 2015.

[7] J. M. Jornet, I. F. Akyildiz, "Graphene based nano antennas for electromagnetic nanocommunications in the terahertz band," *in Proc. 4th European Conf. Antennas Propag.(EuCAP),* Apr. 2010.

[8] J. P. Carrier *et al.,* "Graphene antennas: can integration and reconfigurability compensates for the loss?," *Microw. Conf.(EuMC),*Dec. 2013.

[9] J. M. Floc'h *et al.,* "On the design of planar printed dipole array antennas," *Sci. Res.*Oct. 2012.

[10] M. Tamagnone *et al.,* "Analysis and design of terahertz antennas based on plasmonic resonant graphene sheets," *J. Appl. Phys.* vol. 112, 2012.

[11] M. Tamagnone, J. P. Carrier, "Predicting input impedance and efficiency of graphene reconfigurable dipole using a simple circuit model," *IEEE Antennas Wireless Propag. Lett.* Vol. 13, pp. 313-316, Feb. 2014.

[12] I. Llatser *et al.,* "Radiation Characteristics of tunable graphennas in the terahertz band," *Radioengineering*, vol. 21, issue. 4, pp. 946, Dec. 2012.

Modelling & Simulation of a Grid Connected Hybrid Power Plant with Photovoltaic, Wind & Diesel Power for Cox's Bazar

Kazi Meharajul Kabir
Institute of Energy Technology
CUET
Chittagong, Bangladesh
kazimeharajul_kabir@yahoo.com

Alok Nath
Electrical & Electronic Engineering
FSET, USTC
Chittagong, Bangladesh
aloknatheee@gmail.com

Snehadhit Mazumder
Electrical & Electronic Engineering
FSET, USTC
Chittagong, Bangladesh
snehadhit@gmail.com

Md. Onik Islam
Electrical & Electronic Engineering
FSET, USTC
Chittagong, Bangladesh
mdanikislam38@gmail.com

Abstract—**This paper emphasis on establishing a hybrid power plant which consists of two renewable sources photovoltaic, wind energy and non renewable diesel source for the production of energy to contribute national power demand in Bangladesh. Solar power & wind power are our main source and diesel power is used as a standby power. If we will not able to fulfil our target demand, then we will use diesel energy. We consider renewable source because it provides clean energy. On the other hand, non renewable sources such as, oil, coal, gas will finish approximately within next 20 years. So, it is very necessary for us to find out new source of energy to overcome our power crisis. In this proposed system we came up with an idea to establish an environment friendly power plant combining Photovoltaic and wind energy at various sea shores throughout the country. For design and optimization, we have chosen Cox's Bazar sea shore where wind flow is available as well as solar radiation is optimal. The system is connected to national grid for contributing our national electricity demand.**

Keywords — Hybrid System; Photovoltaic; Wind; Diese;, National Grid; Cox's Bazar;

I. INTRODUCTION

Electricity is the most superior form of energy and a key factor for the economic development of any country. Bangladesh is a developing country. Recently, energy demand is increasing rapidly because of urbanization and industrialization. Therefore, the production of electricity is not sufficient enough for its rapid development. To overcome this situation, government has taken some necessary steps. For instance, proposed various power plants which are based on oil, coal, nuclear sources and many more which are non-renewable. Moreover, due to geographical position and lack of greater safety facilities and technical experts, nuclear power plant is not suitable for Bangladesh. So, power production and its environment related issues is a major concern for the country. However, most of the existing power plants are run through fossil fuels like natural gas. The gas reserve has fallen to such an alarming level that if no new reserves are discovered. It reserve may last for another 6 to 7 years[1]. We didn't create energy, only transform energy from one form to another one. So, generation of electricity from the alternative sources has become essential for Bangladesh. The vast Bay of Bengal on the south of the country along with the V-shaped coastal belt is the main source of the south westerly wind blowing over the terrain. The geographical location of the country has become an ideal place for utilization of solar energy. Wind flow is also reasonable in coastal areas and annual average solar radiation is similar throughout the coastal areas of Bangladesh. Cox's Bazar is one of the coastal area with an average annual solar radiation of 4.77 KWh/m2/day and monthly average wind speeds at a height of 20 meters is 3.55 m/s. Combination of wind and solar along with standby diesel power is a bright prospect. In Bangladesh, around 62% [2] of the total population (counting renewable energy) have access to electricity and 321 KWh [3] is per capita generation. Compared to other developing countries this power generations very low. To meet the growing electricity demand the use of fossil fuels need to be increased which in turn has negative environmental effects. Because the power sector alone contributes to 40% of total CO_2 emission of Bangladesh [4]. In this situation, it is obligatory to develop and endorse renewable energy sources which will ensure energy security without raising environmental impacts. This paper proposes a grid connected hybrid power system by utilizing two renewable energy sources solar and wind along with standby diesel power at Cox's Bazar Seashore where we can overcome the power demand also emits less CO_2 gas compared to other conventional power system.

II. DATA ANALYSIS IN COX'S BAZAR

Cox's Bazar long beach is located at 21 degrees 26.69 minutes North latitude and 91 degrees 57.89 minutes East longitude. We collected one year wind speed and solar radiation from NASA.[5] . Table I. shows the GHI value & wind speed for Cox's Bazar.

978-1-5090-5785-6/16/$31.00 ©2016 IEEE

TABLE I. GHI VALUE & WIND SPEED FOR COX'S BAZAR

Month	Clearness Index	NASA Daily Radiation (KWh/m^2/day)	NASA Average wind speed (m/s) Height(20m)
January	0.653	4.750	2.90
February	0.641	5.330	3.13
March	0.620	5.930	3.40
April	0.579	6.090	3.68
May	0.503	5.520	3.75
June	0.372	4.110	4.87
July	0.347	3.810	4.83
August	0.380	4.030	4.32
September	0.424	4.150	3.35
October	0.527	4.530	2.70
November	0.601	4.480	2.86
December	0.659	4.560	2.82
Annual Average	0.526	4.77	3.55

III. PROPOSED HYBRID SYSTEM

We will propose a grid connected hybrid system consists of two renewable sources (solar, wind) and non renewable source diesel including load , battery , converter & inverter. Our target is producing 2MW electrical power per day and average production is 83 unit per hour. In addition, the power will be supplied to control room load and excess electricity will be supplied to national grid to contribute our national power demand. Table II. Shows System Architecture. Figure 1. Shows the hybrid power plant model.

TABLE II. SYSTEM ARCHITECTURE

PV	Generic flat plate PV	200	kW
Wind Turbine	Norvento nED	100 kW	8
Generator	100kW Genset	100	kW
Battery	CELLCUBE® FB	1	Strings
Converter	ZBB EnerSection®	150	kW
Grid	Grid extension	2	Km

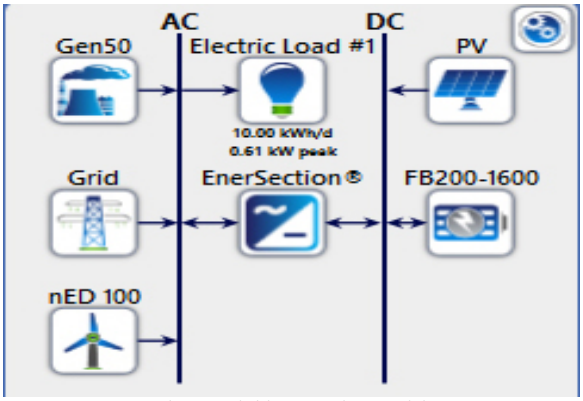

Fig. 1. Hybrid power plant model

IV. ENERGY SPECIFICATION FOR SIMULATION

A. Solar Energy

Solar panel converts light energy into the electrical energy. Sun radiation is absorbed with the panel material and electrons are emitted from the atoms that they are bounded. This released current creates solar power is converted into electrical power by solar cell [6]. When PV cells are joined physically and electrically it's called solar panel or PV module. Panels joined together form a solar array. The sunlight impinging on panels, i.e. irradiance or insulation (incoming solar radiation), is measured in units of watts per square meter (W/m2).We can use only 40% of sunlight radiation for PV module [7]. The PV system gives output as a DC Power. The PV generator can be calculated according to following equation:

$$P = A \cdot x2 + B \cdot x + C \text{ (in Watts)} \ldots\ldots\ldots\ldots\ldots\ldots..(1)$$

Where, x= solar radiation, P=power generation, and A, B, C are constants, which can be derived from measured data. Figure 2. Shows the solar radiation curve

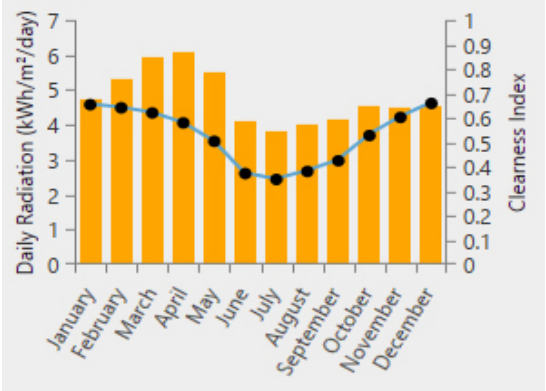

Fig. 2. Solar radiation

B. Wind Energy

Wind power involves converting wind energy into electricity by using wind turbines. It converts the kinetic energy into mechanical energy [8]. A wind turbine is composed number of propellers-like blades called a rotor. Wind comes from change of the air move around the surface of the earth[9]. The power output of a turbine is a function of the cube of the wind speed. If wind speed increases, output power also increases. We can convert only 59% wind energy into electricity according to Betz limit. The output equation for a wind generator is given

$$P = (1/2) \times \rho \times A \times v^3 \text{(in Watts)} \ldots\ldots\ldots.. (2)$$

Where, A = area perpendicular to the direction of flow (in m^2), V = wind velocity (m/s), ρ = density of air (in Kg/m^3) and P = power generation. Figure 3. Shows the wind speed curve

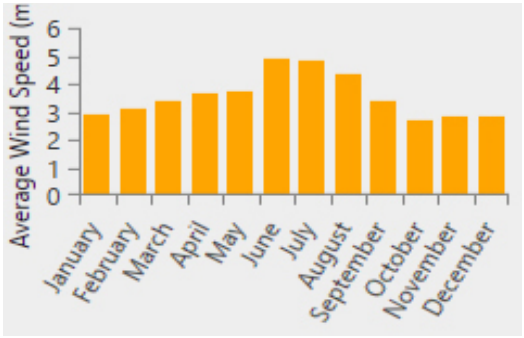

Fig. 3. Average monthly wind speed data

C. *Diesel Generator*

The Non renewable source diesel generator which operates at low load is inefficient and fuel cost low diesel generator consumes 30% of full-load fuel consumption[10]. The autonomous diesel generator has high operation cost, demands constant maintenance and the transportation of fuel to remote locations is difficult and costly, mainly rainy season in Bangladesh [11]. We used diesel generator to help fulfill our target demand. Fuel cost is 0.8$/L.

D. *Battery*

TABLE III. BATTERY CELL SPECIFICATION

Nominal Voltage	700 V
Nominal Capacity	2285.71Ah
Nominal Capacity	16000kwh
Round Trip Efficiency	65%
Float Life	20year
Maximum Capacity	3297.384Ah
Capacity Ratio	0.505c
Rate Constant	0.801k
Suggest life throughout	17520000 kWh
Max. Charge rate	1 A/Ah
Max. Charge current	230.35
Max. Discharge current	354.385

E. *Electric Load*

We used only a control room load demand, the using instrument are light, fan, computer, charger, etc.

TABLE IV. CONTROL ROOM LOAD DEMAND

Scaled annual average	10kWh/day
Scaled peak load	0.616kw
Load factor	0.68
Total annual load	3650kWh/yr

F. *Grid*

2km grid extension needed for the system to connect the National Grid.

TABLE V. GRID SPECIFICATION

Grid extension	2 km
Grid purchases capacity	100 kw
Grid sell capacity	1000 kw
Grid purchases price	0.15$/kWh
Grid sell price	0.16$/kWh

V. OPTIMIZATION RESULT

HOMER software is use to simulate the system. We used input data of solar radiation, wind speed and load on the basis of HOMER software requirement. PV sell produce 301905kWh/year. Wind turbine produce 390307kWh/year And Diesel generator produce 134920kWh/year. The main purpose of the propose system is contribute to national power demand. Grid sell is 797298kWh/year and grid purchase is 437kwh/year. Figure 4. Hybrid system production curve. Figure 5. Shows grid purchases & sell curve. Table.VI shows Electricity production. Table VII. Shows Electricity consumption

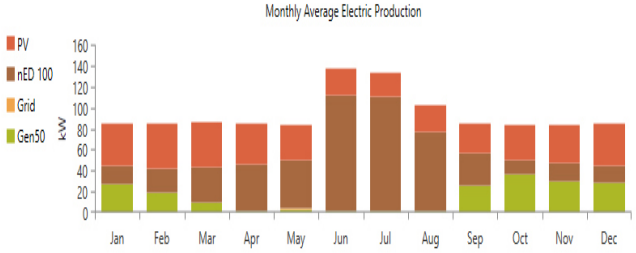

Fig. 4. Hybrid Electricity Production curve

The following result are obtained

TABLE.VI ELECTRICITY PRODUCTION

Component	Production (kWh/yr)	Friction %
PV	301,905	36.48
Wind turbine	390,307	47.16
Diesel generator	134,920	16.30
Grid Purchases	437	0.05
Total	827,569	100

TABLE VII. ELECTRICITY CONSUMPTION

Load	Consumption (kWh/yr)	Fraction %
AC	3650	0.46
DC	0	0
Grid Sells	797,298	99.54

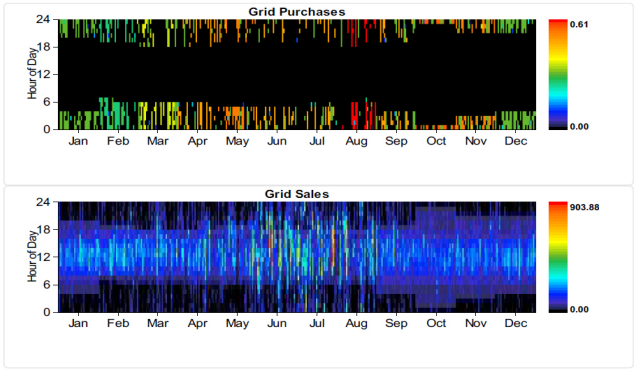

Fig. 5. Grid Purchases & Sales curve

VII. COST OF THE SYSTEM

currently 1$ = 80 BDT. Table VIII. Shows total hybrid system cost analysis

TABLE VIII. TOTAL SYSTEM COST ANALYSIS

Component	Capital	Replacement	O&M
PV	1,45,000	24,858	2,586
Wind turbine	2,40,000	67,884	51,710
100kW Genset	10,000	1,308	1,308
Converter	18,000	5,091	3,878
Grid	10,000	0	1,369
Battery	1,00,000	80,000	1,293
System	523,000	179,141	62,144

We proposed a hybrid power plant for 25 year , but battery will be replaced after 15-20 years. Figure 6. shows the overall 25 year cost curve

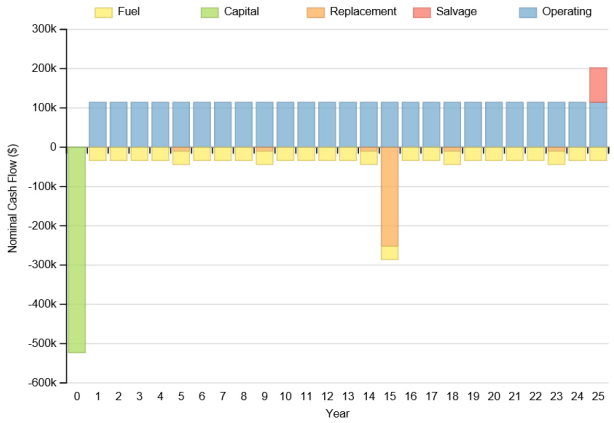

Fig. 6. The overall 25 year cost curve

VIII. CONCLUIONS

The main target of our propose system is to reduce power crisis and contribute to our national power demand, also creates different scope for producing electricity. This hybrid system is more effective than conventional quick rental coal based power plant where per unit cost is 0.23$/kWh. The per unit cost of this system is 0.13$/kWh. We used non renewable diesel power which provides some pollution. Compared to other conventional power systems it is less enough for generating electricity. But, we used diesel generator only 17%. Our collected wind speed data high are 20m, but standard wind turbine setup is 25-30 meter. If the height is increased, wind speed will be increased. Therefore, we may not need to use diesel generator for producing electricity for our target demand. Proposed hybrid system is profitable creating direct & indirect employment opportunities, but initial cost is high.

REFERENCES

[1] M. M. Hasan, M.F. Khan, "A comparative study on installation of solar PV system for grid and non grid rural areas of Bangladesh", *Developments in Renewable Energy Technology (ICDRET),2012.*

[2] http://www.powercell.gov.bd, *accessed on August 29, (2015).*

[3] www.powerdivision.gov.bd/user/brec1/30/1, *accessed on August 29,(2015).*

[4] R. M. Shrestha, G. Anandarajah, and M. H. Liyanage, "Factors affecting CO_2 emission from the power sector of selected countries in Asia and the Pacific,"*Energy Policy,* vol. 37, pp. 2375-2384, Jun 2009.

[5] NASA surface meteorology, solar & wind energy , *http://eosweb.larc.nasa.gov*

[6] (2010) Mir NahidulAmbia, Md. Kafiul Islam, Md. AsaduzzamanShoeb, Md. Nasimul Islam Maruf, A.S.M. Mohsin, "An Analysis & Design on Micro Generation of A Domestic Solar-Wind Hybrid Energy System for Rural & Remote Areas-Perspective Bangladesh.".

[7] Molla Shahadat Hossain Lipu "A Feasibility Study of Solar-Wind-Diesel Hybrid System in Rural and Remote Areas of Bangladesh" *INTERNATIONAL JOURNAL of RENEWABLE ENERGY RESEARCH, Vol.3, No.4, 201).*

[8] Potential of micro hydro power units in Bangladesh. Available at:*http://www.lged-rein.org/*

[9] How wind turbine works. Available at:*http://www.energymatters.com.au/renewable-energy/wind-energy/*

[10] S.W. Shaahid and M.A. Elhadidy, "Optimal sizing of battery storage for stand-alone hybrid (photo-voltaic + diesel) power systems", *International Journal of Sustainable Energy*, Vol. 24, pp. 155-166, 2005.

[11] Z. Nikolic, V. Shiljkut, and D. Nikolic, "Diesel-solar electricity supply for remote monasteries", *Journal of Renewable and Sustainable Energy, Vol. 5, 041815, July 2013)*

Exploiting Parallelism for Faster Implementation of Bubble Sort Algorithm Using FPGA

Ashrak Rahman Lipu[1], Ruhul Amin[2], Md. Nazrul Islam Mondal[3], Md. Al Mamun[4]
[1]Dept. of Computer Science and Engineering, RUET, Rajshahi, Bangladesh, ashrakrahman@gmail.com
[2]Dept. of Computer Science and Engineering, RUET, Rajshahi, Bangladesh, ruhul113056@gmail.com
[3]Dept. of Computer Science and Engineering, RUET, Rajshahi, Bangladesh, nimbd109@gmail.com
[4]Dept. of Computer Science and Engineering, RUET, Rajshahi, Bangladesh, cse_mamun@yahoo.com

***Abstract*—Sorting is a classic problem that has been studied for decades. From the beginning of computing, many Sorting algorithms have been investigated. Bubble sort is a very common and powerful sorting technique used in different applications. For high speed data processing, we need faster and efficient environment for any sorting algorithm. In this purpose, FPGA based hardware accelerators can show better performance for high speed data processing than the general purpose processors. In this paper, the sequential and parallel bubble sort algorithm is implemented using FPGA. We show that parallel implementation of Bubble sort algorithm is almost 10 times faster than that of sequential implementation for 20 different data inputs. However, this implementation is faster for more data inputs.**

Keywords—FPGA; Bubble Sort ; Clock Cycle; Odd-even transposition; Swappers; Schematic view

I. INTRODUCTION

Many applications in computing require things to be in order. Sorting is a procedure that is needed in numerous computing systems [1]. In computer science, sorting can be used to sort data either ascending or descending which is usually required in algorithm such as evolutionary algorithm. Sorting plays a major role in commercial data processing and in modern scientific computing. For example transaction processing, combinatorial optimization, astrophysics, molecular dynamics, linguistics, genomics, weather prediction etc are the applications of Sorting.

Several algorithms to undertake the sorting process are Selection sort, Merge sort, Insertion sort, Heap sort, Radix sort, and Bubble sort. Heap sort, Radix sort, and Merge sort are powerful to sort large number of data [2]. Meanwhile the selection sort, Insertion sort and Bubble sort are powerful for few data. As we are concern for sorting a few data we took bubble sort for our implementation.

Reconfigurable gate arrays, also known as field programmable gate arrays (FPGA), are widely used in the industry to implement a variety of digital circuits. FPGA is an integrated circuit that takes advantage of the gate-level parallelism that multi-core GPPs cannot. The design implemented in FPGA has longer design cycle than design implemented for parallel processing in GPPs. A large amount of memory is available internal to the FPGA and is accessed with a small number of pins such that the reconfiguration time is, for example, four orders of magnitude faster than the traditional approaches and at notably low cost [3].

Sorting implementation on FPGA has been implemented by many researchers. Srivasta et al. [4] proposed hybrid design for large scaling sorting on FPGA. Other research on high-speed parallel scheme is found for data sorting on FPGA in the paper [5]. The authors in the paper [6] introduced parallel bubble sort to utilize the concept in parallel computing.

To gain a better performance, fast accelerators based on FPGAs [7], GPUs [8] and multi-core CPUs [8] have been investigated in depth with increased intensity during the last few years. For these reasons the goal of this paper is to implement the bubble sort algorithm using FPGA to achieve better performance. We exploit the parallelism implementing Bubble sort algorithm using FPGA and hence we show that parallel implementation of Bubble sort algorithm is almost 10 times faster than that of sequential implementation for 20 different data inputs. In this paper we implement the mentioned algorithm for 20 data, each of 8-bit only. However, this implementation is faster for more data inputs no doubt.

The key idea of this paper is to implement parallel swapping for independent data by exploiting the parallel reconfigurable architecture of FPGA. The main contribution of our work is as follows:

- We exploit the parallelism to implement Bubble sort algorithm using FPGA.
- We have shown that parallel implementation is almost 10 times faster than that of sequential implementation for 20 different data inputs.

II. METHODOLOGY

A. Sequential Bubble Sort

The basic principle of bubble sort is to compare two consecutive numbers from leftmost to rightmost and swaps them if certain condition is met.

In Fig. 1, a list L = {6, 2, 4, 1} is taken for ascending sort. In every pass, left to right scan is done and two consecutive numbers are compared and swapped. In the example, the largest number is moved to the rightmost position for every pass. As every pass is over, the no. of unsorted data is

978-1-5090-5785-6/16/$31.00 ©2016 IEEE

decreased by one it is go on until all the data are sorted. In every pass, compare is done sequentially which can be depicted in Fig. 2.

Again, all the passes are done sequentially too. The algorithm of sequential bubble sort is given bellow:

Algorithm 1: Sequential Bubble Sort
Input : L (unsorted data list) Output: O (sorted data list) Step 1: compare and swap L sequentially Step 2: decrease L by 1 and repeat step1 until L is sorted

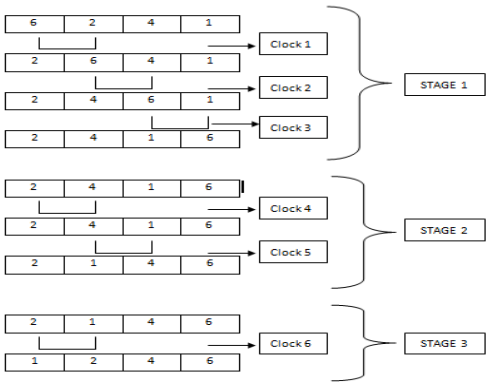

Fig. 1. Steps of sequential bubble sort algorithm for the example.

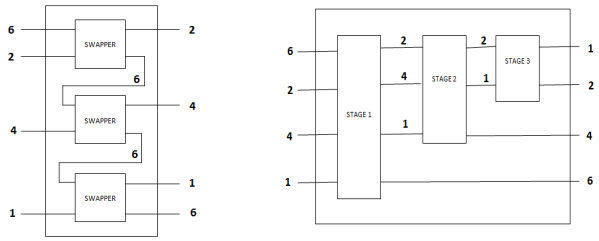

(a) (b)

Fig. 2. Block Diagram of Stages for Sequential Sort

B. Parallel Bubble Sort

The motivated idea of parallel bubble sort is parallel comparison and swapping. Parallel swapping can be applied on independent data of a list. Odd-even transposition technique is a handy in this case. To explain it, let

$$L = < a_1, a_2, a_3, \ldots\ldots, a_p, a_q, \ldots\ldots, a_n >$$

Be a list of n elements. Any pair of consecutive elements, say (a_p, a_q) is said to be odd or even pair if the position of first element p is odd or even respectively e.g. (a_1, a_2) is odd pair while (a_2, a_3) is even pair. Fig. 3 explains the technique with the above example.

From Fig. 3, every step/pass includes one odd and one even phase which work sequentially. But every phase works parallel swapping on consecutive data of the list. Fig. 4(a) depicts the odd-even transposition scheme. Again, steps/ passes are executed sequentially which is depicted in Fig. 4(b).On the basis of explanation, the algorithm of parallel bubble sort is given bellow.

Algorithm 2: Parallel Bubble Sort
Input : L (a unsorted list) Output: O (a sorted list) Step 1: sort all the odd pair in parallel Step 2: sort all the even pair in parallel Step 3: Repeat steps 1-2 sequentially (n/2) times

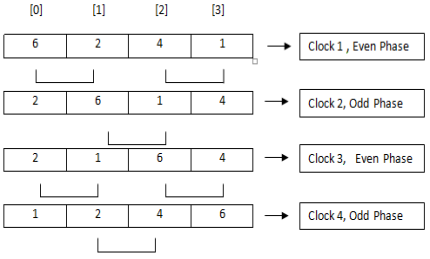

Fig. 3. Steps of parallel bubble Sort.

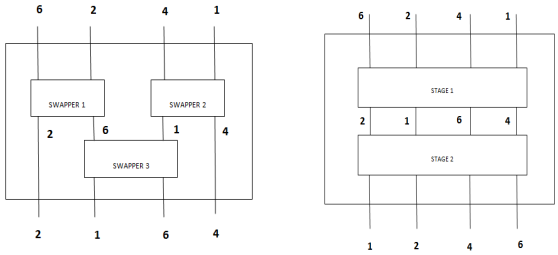

(a) (b)

Fig. 4. Block Diagram of Stages for parallel bubble Sort.

C. FPGA implementation of sequential bubble sort

A hierarchical or layered approach is followed to implement the sequential and parallel bubble sort. The system is designed bottom-to-top approach in three layers. Fig. 5 shows the required layers to implement the sort in FPGA and again shows the schematic of swapper module.

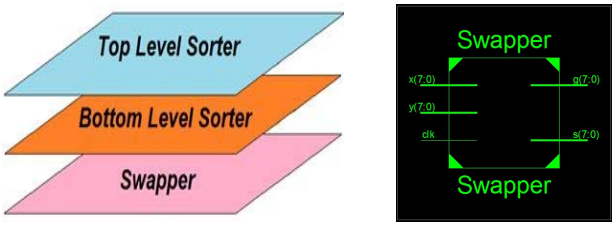

Fig. 5. Hierarchical layer and Schematic view of a swapper.

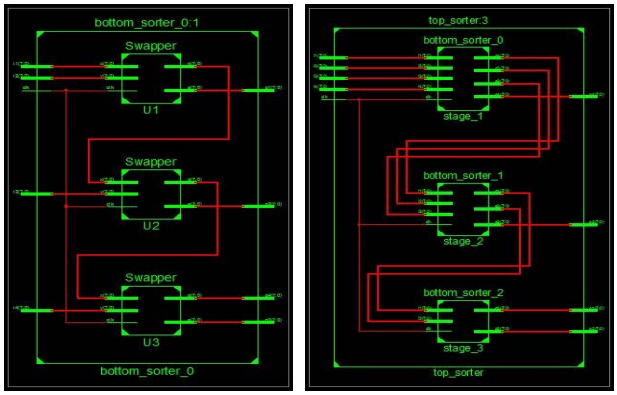

(a) (b)

Fig. 6. Wiring of bottom level and top level sorter for sequential bubble sort.

Swapper takes two input data, compare it and swaps them if swapping condition is met. Fig. 6(a), depicts the second upper layer, bottom_level_sorter of the system which is formed of swappers and their essential wiring. It is the implementation of Fig. 2 of sequential bubble sort scheme. It indicates the single step of Fig. 2(a), in which swappers run sequentially. The last layer, layer three, top_level_sorter's schematic is shown in Fig. 6(b). It is the implementation of Fig. 2(b), of sequential bubble sort. Here, bottom_level_sorters are wiring sequentially likely passes are done sequentially to form top_level_sorter or the whole system.

D. FPGA implementation of parallel bubble sort

Parallel bubble sort is also implemented as three layer system like the sequential one. It is most likely the sequential bubble sort but the orientation or wiring or connection is different. The basic building block of parallel bubble sort is the first layer swapper whose schematic is shown in Fig. 5 of sequential bubble sort. The second layer of the hierarchy, bottem_level_sorter is shown in Fig. 7(a).

In Fig. 7(a), swappers are connected in parallel exactly as described in Fig. 4(a). This type of connection forms the odd-even transposition here. FPGA implementation of last layer, layer three of parallel bubble sort is top_level_sorter which is shown in Fig. 7(b). It shows the sequential connection of bottom_level_sorter or odd-even transposition unit which implement the structure of Fig. 4(b), of parallel bubble sort. In case of FPGA implementation of the whole system, number is represented as 8 bit signed integer number.

The device utilized is Spartan-6 of 400 MHz clock speed. Xilinx ISE-14.7 software is used to design different modules, simulate to verify and to implement them FPGA. The main performance criterion in this study is execution time. We focus only to execute the sort in parallel to reduce clock cycle.

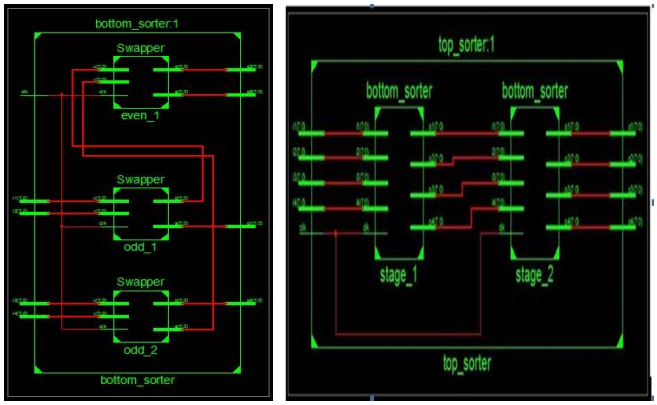

(a) (b)

Fig. 7. Wiring of bottom level and top level sorter for parallel bubble sort.

III. RESULT AND DISCUSSION

A. Sequential Bubble Sort

From the experiments, it is seen that sequential bubble sort can be applied to sort a list. Sequential bubble sort successfully sorted all the variation of inputs from 4 to 20. The example of 4 inputs is shown in Fig. 8.

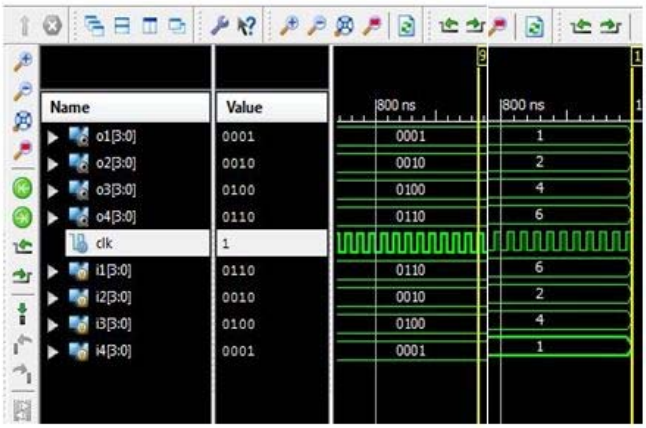

Fig. 8. Visualization of the result for four input sequential bubble sort.

From Fig. 1, it is seen that 6 clock cycles is required to completely sort the list. Its clock cycle depends on input number. If input number is N then required clock cycle is N*(N-1)/2.To improve the system i.e. reducing execution time, optimization procedure can be empowered.

B. Parallel Bubble Sort

From the experiments, it is evident that parallel bubble sort can be utilized to sort the numbers. Parallel bubble sort successfully sorts all the input from 4 to 20 numbers. Fig. 9 shows the example of 4 inputs above.

From Fig. 4, it is seen that only 4 clock cycles are needed to completely sort the list. Its clock cycle depends on input

number. If input number is N then required clock cycle is N. To improve the system i.e. reducing execution time, optimization procedure can be empowered.

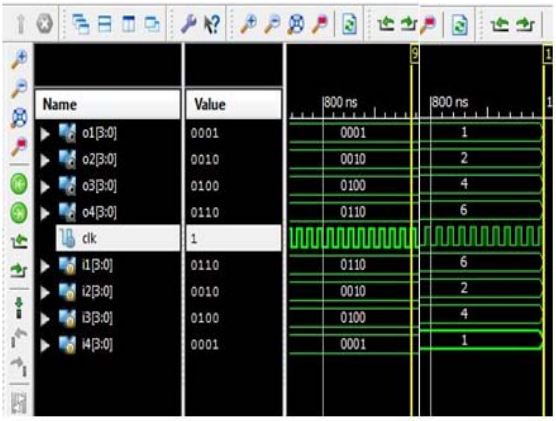

Fig. 9. Visualization of the result for four input parallel bubble sort

C. *Comparison of Sequential and Parallel Bubble Sort*

In this paper, sequential and parallel bubble sort are compared. The comparison is focused on the clock cycle only. The clock cycle of sequential and parallel bubble sort is listed at Table 1. Finally, Fig. 10 depicts the clock cycle comparison.

TABLE I. COMPARISON OF CLOCK CYCLE

SL. No	Number of Data	Clock for Parallel sort	Clock for Sequential sort
1	4	4	6
2	6	6	15
3	8	8	28
4	10	10	45
5	12	12	66
6	14	14	91
7	16	16	120
8	18	18	153
9	20	20	190

In execution clock cycle, parallel bubble sort perform better than sequential bubble sort. Parallel bubble sort sorts inputs faster than the sequential bubble sort. This is because several processes execute parallel in parallel bubble sort. Therefore, it does not have to wait for previous one completion. On the contrary, in sequential bubble sort, the next process executes after the previous process have finished. In all cases: best, average and worst, parallel bubble sort requires less clock cycles than sequential bubble sort. That's why; parallel one is faster than sequential one.

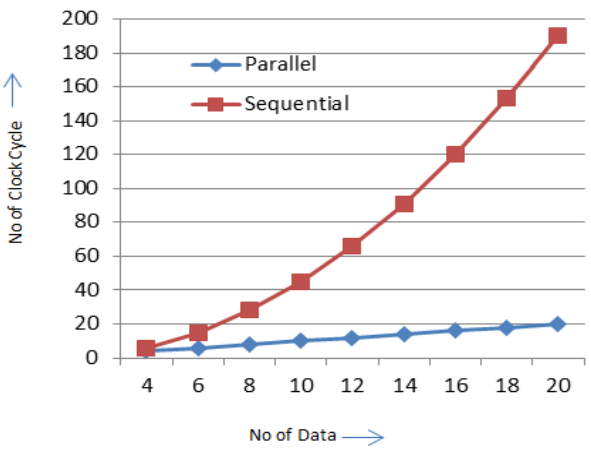

Fig. 10. Clock cycle comparison between serial and parallel bubble sort.

IV. CONCLUSION

In this paper, we have implemented Bubble sort algorithm in parallel using FPGA in order make it faster than that of sequential implementation. In fact, we exploit the parallelism for implementing the mentioned algorithm in FPGA. We have shown that parallel implementation of Bubble sort algorithm is almost 10 times faster than that of sequential implementation for 20 different data inputs. It is highly expected that this implementation is faster for more data input and hence we have a plan to implement it in future.

REFERENCES

[1] D.E. Knuth, The Art of Computer Programming. Sorting and Searching, vol. III, Addison-Wesley, 2011

[2] R. Abirami, "VHDL Implementation of Merge Sort Algorithm", International Journal of Computer Science and Communication Engineering, Vol. 3, No. 2, pp. 15-18, 2014.

[3] Chatter, Mukesh. "High performance self modifying on-the-fly alterable logic FPGA, architecture and method." U.S. Patent No. 5,838,165. 17 Nov. 1998.

[4] A. Srivastava, R. Chen, V. K. Prasanna, and C. Chelmis, "A Hybrid Design for High Performance Large-scale Sorting on FPGA" In Re ConFigurable Computing and FPGAs, pp. 1-6, 2015.

[5] S. Dong, X. Wang, and X. Wang, "A Novel High-Speed Parallel Scheme for Data Sorting Algorithm Based on FPGA" In 2nd International Congress on Image and Signal Processing, pp. 1-4, 2009.

[6] R. Rashidy, S. Yousefpour, and M. Koohi, "Parallel Bubble Sort Using Stream Programming Paradigm" In 5th International Conference on Application of Information and Communication Technologies, pp. 1-5, 2011.

[7] Asano, Shuichi, Tsutomu Maruyama, and Yoshiki Yamaguchi. "Performance comparison of FPGA, GPU and CPU in image processing." *2009 international conference on field programmable logic and applications*. IEEE, 2009.

[8] Che, Shuai, et al. "Accelerating compute-intensive applications with GPUs and FPGAs." *Application Specific Processors, 2008. SASP 2008. Symposium on*. IEEE, 2008

[9] white paper : www.xilinx.com

Real Time Google Map and Arduino Based Vehicle Tracking System

Md. Marufi Rahman[1], Jannatul Robaiat Mou[1], Kusum Tara[2], Md. Ismail Sarkar[1]
[1]Department of Electronics & Telecommunication Engineering
[2]Department of Electrical & Electronic Engineering
Rajshahi University of Engineering & Technology
Email: rahmania444.ff@gmail.com,jannatulruet@gmail.com

***Abstract*—A vehicle tracking system is very useful for tracking the movement of a vehicle from any location at any time. In this work, real time Google map and Arduino based vehicle tracking system is implemented with Global Positioning System (GPS) and Global system for mobile communication (GSM) technology. GPS module provides geographic coordinates at regular time intervals. Then the GSM module transmits the location of vehicle to cell phone of owner/user in terms of latitude and longitude. At the same time, location is displayed on LCD. Finally, Google map displays the location and name of the place on cell phone. Thus, owner/user will be able to continuously monitor a moving vehicle using the cell phone. In order to show the feasibility and effectiveness of the system, this work presents experimental result of the vehicle tracking system. The proposed system is user friendly and ensures safety and surveillance at low maintenance cost.**

Keywords— GPS; GSM; Cell phone; Google Map; Arduino.

I. INTRODUCTION

In modern days, the safety of private and public vehicles is a major concern. To ensure safety while travelling, GPS tracking system is installed in vehicle. Vehicle tracking system using GPS & GSM allows user to locate the vehicle through Short Message Service (SMS) in cell phone. Police can follow the signal emitted by the tracking system to locate a stolen vehicle. The Telegraph is a daily newspaper reported that in 2002 the rate of stolen vehicle was 3,00,000 but in 2014 it dropped below 1,00,000 because of applying security systems [1]. Eddie et al., 2013 worked on simple bus tracking system in UCSI University, Malaysia [2]. That tracking system provided students with the location information of a bus within a fixed route, but no map was used to get real location on earth. Montaser et al., 2012 proposed a design and implementation of a vehicle tracking and anti-theft system for protecting a vehicle from any intruders using GPS/GSM technology [3]. In that work, a laptop embedded with Google Earth was used for tracking and viewing the location and status of the vehicle on a map. Junaid et al., 2009 implemented a GSM based commercial automobile tracker using PIC 18F452 and developed a google earth embedded monitoring software [4]. Khondker et al., 2009 reported on cost effective GPS-GPRS based object tracking system [5]. The system allowed a user to view the present and the past positions recorded of a target object on Google Map through the internet. Ramani et al., 2013 worked on vehicle tracking and locking system based on GSM and GPS [6]. Seokju et al., 2014 worked on the design and implementation of vehicle tracking system using GPS/GSM/GPRS technology and smartphone application [7]. Parvez et al., 2010 developed a theoretical model of GSM network based vehicle tracking system [8]. Many researchers tried to develop an automated vehicle tracking system to track and display location of a vehicle in real time. The cost of operation for most of these tracking systems is higher which prevents from widespread use. On the other hand, the rate of car theft, asset theft, child kidnapping in many countries are increasing at a higher rate. But there is no healthy literature about the low cost experimental set-up in real time monitoring. A cell phone will be good alternative to replace the existing system. The main objective of this work is to reduce the cost of the tracking system using the latest technologies and making it available to the common people.

In this paper, a real time Arduino based vehicle tracking system with GPS and GPRS shield is attached to the moving vehicle to enable the owner/user to track the location of that vehicle. This proposed system will continuously monitor a moving vehicle and report the status of the vehicle. For doing so an Arduino UNO board with Atmega328 microcontroller is interfaced to a GSM module and GPS receiver. The GPS receiver will continuously give the data indicating the position of the vehicle in terms of latitude and longitude in real time. The GSM module will send the position (Latitude and Longitude) of the vehicle to cell phone from a remote place. The same data is also displayed on LCD. Google map displays the location and name of the place on cell phone in real time.

II. OBJECTIVES

The main objectives of the proposed Arduino based vehicle tracking system are:

(i) Acquisition of a geographic coordinates of vehicle in real time using the GPS receiver.
(ii) Transmission of information about the location of vehicle using the GSM module.
(iii) Display position and name of the place on Google map in real time using cell phone.

978-1-5090-5785-6/16/$31.00 ©2016 IEEE

III. System Overview

The Arduino based vehicle tracking system has two parts – the hardware and software specification. Hardware specification consists of Arduino UNO board with microcontroller, GPS and GPRS shield, LCD. In software specification, Aurdino IDE software, Google map is used.

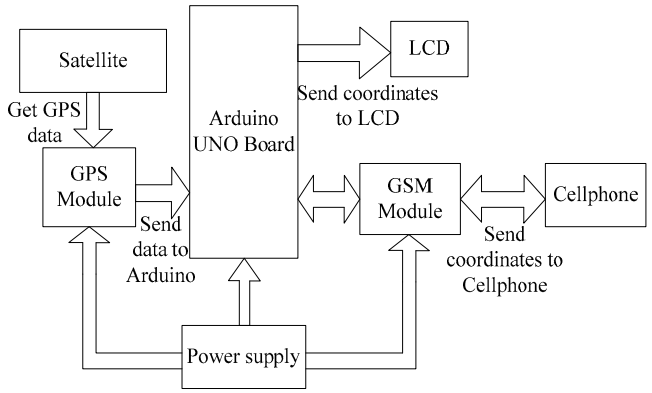

Fig. 1. Block diagram of Arduino based vehicle tracking system.

Fig. 1 presents the block of Arduino based vehicle tracking system. At first, +5 volt DC power is supplied to GSM and GPRS shield, Arduino UNO board with microcontroller to activate those devices. Arduino is used for controlling the process with a GPS receiver and GSM module. GPS receiver worked on 9600 baud rate is used to receive the data from satellites. The data is sent to the Arduino which reads coordinates by extracting $GPGGA String from GPS receiver, and forwarded to GSM in terms of coordinates (latitude and longitude). GSM module sends the coordinates to user/owner by SMS so that he can track the vehicle around the globe, and watch the live position on Google Map. And an optional 16x2 LCD is also used for displaying coordinates.

IV. Hardware Specification

A. Arduino Microcontroller

The Atmega328 microcontroller in Arduino UNO is used as the brain to control the vehicle tracking system with GPS and GSM module. A program is written using C programming language, compiled, and then saved into the flash memory of microcontroller.

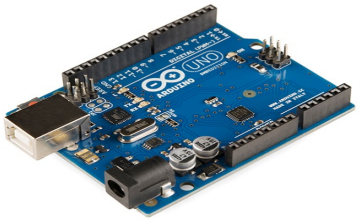

Fig. 2. Arduino UNO board. [9]

Arduino UNO board is shown in fig. 2 that interface the GPS and GSM module.

B. GPS and GPRS Shield

The Global Positioning System (GPS) is the Global Navigation System (GNSS) that receives signal from at least three satellites to compute its two dimensional (latitude and longitude) position. Therefore, GPS is a key technology for getting position. GPS was developed by the United States Department of Defense. The GPS in vehicle tracking systems is employed to provide users the coordinates of the location anywhere on earth. The GSM/GPRS module is responsible of establishing connections between a tracking system and a remote user for transmitting the information of vehicle's location, using TCP/IP connection through the GSM/GPRS network.

Fig. 3. GPS and GPRS shield.[10]

Fig. 3 shows the GSM and GPRS shield with GPS and GSM/GPRS module. At first GPS technology gives satellite navigation through a high-gain SMD antenna. Then the microcontroller based Arduino is interfaced with an embedded SIM908 chip. The SIM908 chip on the GSM and GPRS shield is a compact quad-band cellular module. The SIM card assists the system to send messages to cell phone. It is controlled via AT commands. The location of a vehicle can be monitored anytime with signal coverage.

C. Liquid Crystal Display (LCD)

A 16x2 LCD is used for displaying location values (latitude and longitude). A +5 volt DC supply is given to activate LCD.

V. Software Specification

A. Arduino IDE Software

Arduino IDE software is used for compiling the program into the microcontroller. In this software C programming language has been used for coding. For receiving data from the satellite and sending data into the cell phone, program is written using Arduino IDE software.

B. Google Map

A Google map is used to display the location of a vehicle on a cell phone in real time. The Google map automatically handles access to the Google Maps servers, displays location and place on map.

VI. Flow Chart of the System

To view the current position of the vehicle, Arduino based vehicle tracking system using cell phone has been developed.

978-1-5090-5785-6/16/$31.00 ©2016 IEEE

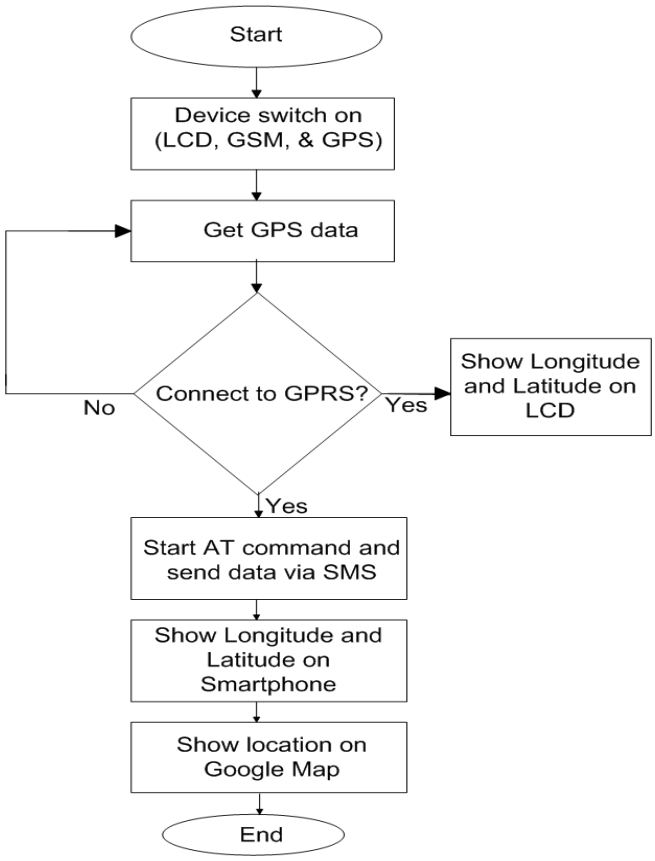

Fig. 4. Flowchart of the proposed tracking system.

Fig. 4 illustrates the flow chart of the Arduino based vehicle tracking system. At first switch is made on to give power supply to Arduino, GPS and GPRS shield, and LCD. GPS pin TX is connected to microcontroller of Arduino and GSM pins TX and RX are connected to serial ports to communicate with SIM908. Microcontroller communicates with the help of serial communication. The GPS receiver locates the latitude and longitude of the vehicle using the satellite service. If GPRS is ready then positional data is sent to the owner in the form of SMS to the owner's number. At the same time, LCD shows the location in the form of latitude and longitude.

VII. Result and Discussion

The Arduino based vehicle tracking system is embedded inside a vehicle whose position is to be determined and tracked in real time.

A. Test of the Proposed Vehicle Tracking System

Fig. 5 shows experimental set-up of Arduino based vehicle tracking vehicle tracking system. The GPS receiver receives geographic coordinates (longitude & latitude) from the satellites. Then the data is read by Arduino based microcontroller and information about location of vehicle is then transmitted through GSM network to cell phone. A test was done in RUET CSE building to detect the location of the Arduino based vehicle tracking system. The system worked well and location was sent to owner/user through SMS successfully.

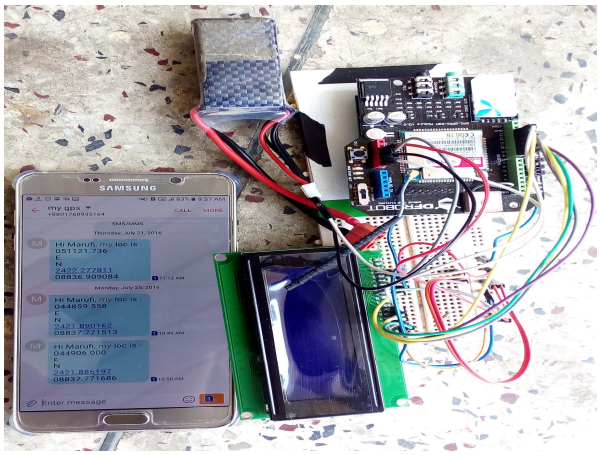

Fig. 5. Experimental set up of the proposed vehicle tracking system.

Fig. 6. Display of location (Longitude and latitude) on LCD.

Fig. 6 shows the display of coordinates of vehicle on LCD.

B. Testing the Location on Cell phone

In order to demonstrate operation of the vehicle monitoring system successfully, a cell phone was configured to get the location of the vehicle.

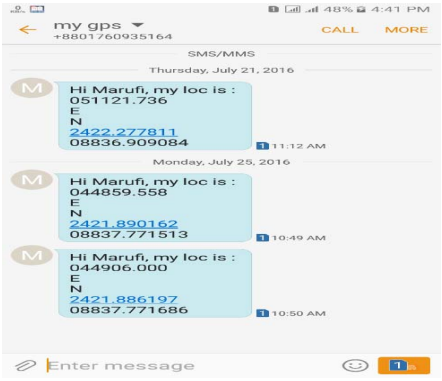

Fig. 7. Snapshot of Text SMS received by cell phone.

Fig. 7 shows the location of a vehicle on cell phone. The coordinates of vehicle are:
Longitude = 2421.886197 N
Latitude = 8837.771686 E

978-1-5090-5785-6/16/$31.00 ©2016 IEEE

C. Testing the Location on Google Map

The received longitude and latitude information was used to identify the location of the vehicle on google map.

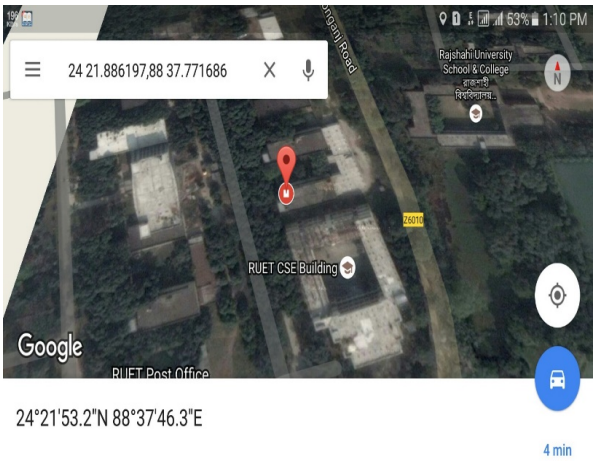

Fig. 8. Snapshot of the location which shows position of the vehicle tracking system in real time using Google map.

Fig. 8 illustrates the location of the vehicle on the Google map. Bubble indicates the position in the form of latitude and longitude of the vehicle. The place was RUET CSE building whose longitude is 2421.886197 and latitude is 8837.771686.

VIII. Advantages and Applications

A. Applications of the System

The low cost Arduino based vehicle tracking system can be used widely in tracking Cabs/Taxis, stolen vehicles, school/colleges buses etc. Furthermore, guardian can easily track down school going children for avoiding accident. If the system is equipped with a bus or train, it will save time and avoid waiting for a long time of passengers. One can also find the nearest taxi by using this technology. The system can be employed fleet management systems, and intelligent transportation systems (ITS), as well as tracking human and animal in jungles. It can be used by food delivery and car rental companies also.

B. Advantages of the System

(i) As Arduino and GPS & GPRS Shield is used, it reduces the complexity of the system.

(ii) It provides more security at low cost.

(iii) From the remote place, user/owner will get the position of vehicle through the tracking system.

(iv) The owner will monitor the vehicle and get the update information about the vehicle regularly.

IX. Conclusion and Future Scope

The proposed Arduino based vehicle tracking system using GPS and GSM technology was developed and tested successfully to track the exact location of a moving or stationary vehicle in real time. Arduino made the system user friendly. The system provides better service and cost effective solution for users. A vehicle's geographic coordinates obtained from an in-vehicle device. A cell phone has been used to display location of vehicle on Google map. The system was able to experimentally demonstrate its effective performance to track a vehicle's location anytime from anywhere. **This is easy to make and inexpensive compared to others.** The proposed system will ensure safety and security of vehicle, driver, and passengers.

The Arduino based vehicle tracking system can be further enhanced by using camera to get the real time view of the vehicle, which would be more convenient for the user to track the vehicle. The system can be made compatible with engine through SMS in future. Buzzer can also be added to check engine status. Travelling distance can be calculated and recorded using database.

References

[1] Transport, "Number of cars stolen in the UK falls to 48-year low," The Telegraph, UK, 2015. [Online]. Available: http://www.telegraph.co.uk/finance/newsbysector/transport/11558743/Number-of-cars-stolen-in-the-UK-falls-to-48-year-low.html. Accessed on: September 29, 2016.

[2] Eddie Chi-Wah Lau, "Simple Bus Tracking System", *Journal of Advanced Computer Science and Technology Research*, vol.3, no.1, 2013.

[3] Montaser N. Ramadan, Mohammad A. Al-Khedher, and Sharaf A. Al-Kheder, "Intelligent Anti-Theft and Tracking Sytem for Automobiles", *International Journal of Machine Learning and Computing,* vol. 2, no. 1, February 2012.

[4] Junaid Ali, Shaib Nasim, Taha Ali, Naveed Ahmed and syed Riaz un Nabi, "Implementation of GSM based Commercial Automobile Tracker Using PIC 18F452 and Development of Google Earth Embedded Monitoring Software" *Proceedings of 2009 IEEE student conference on Research and development (SCOReD 2009)*, Nov. 2009, Malaysia.

[5] Khondker Shajadul Hasan, Mashiur Rahman, Abul L. Haque, M Abdur Rahman, Tanzil Rahman, and M Mahbubur Rasheed, "Cost Effective GPS-GPRS Based Object Tracking System," *Proceedings of the International MultiConference of Engineers and Computer Scientists 2009 (IMECS 2009),* March 2009, Hong Kong, vol. 1.

[6] R.Ramani, S.Valarmathy, N.SuthanthiraVanitha, S.Selvaraju, M.Thiruppathi, R.Thangam, "Vehicle Tracking and Locking System Based on GSM and GPS," *Int. Journal Intelligent Systems and Applications*, vol. 9, pp. 86-93, 2013.

[7] SeokJu Lee, Girma Tewolde, Jaerock Kwon, "Design and implementation of vehicle tracking system using GPS/GSM/GPRS technology and smartphone application," 2014 IEEE World Forum on Internet of Things (WF-IoT), 2014.

[8] MZ Parvez, KZ Ahmed, QR Mahfuz, MS Rahman,*" A* theoretical model of GSM network based vehicle tracking system," 2010 International Conference on Electrical and Computer Engineering (ICECE), Dec. 2010, pp. 594-597.

[9] https://en.wikipedia.org/wiki/Arduino

[10] https://www.dfrobot.com/wiki/index.php/GPS/GPRS/GSM_Module_V3.0_(SKU:TEL0051)

Security Analysis of Co-located and Distributed MIMO Interference Networks with Linear Receivers

Kazi Newaj Faisal, Md. Zahurul Islam Sarkar, Rezwana Sultana and Md. Sifatul Muktadir
Department of Electrical and Electronic Engineering
Rajshahi University of Engineering and Technology, Rajshahi-6204, Bangladesh
Email: newajfaisal@gmail.com

***Abstract*—In this paper, we compare the performance of the linear receivers such as maximum-ratio combining (MRC), zero-forcing (ZF) and minimum mean-square error (MMSE) receivers in enhancing security for co-located MIMO (C-MIMO) and distributed MIMO (D-MIMO) interference network. We derive the expressions for secrecy achievable rates in case of MRC, ZF and MMSE receivers for both C-MIMO and D-MIMO systems. Then, we determine the effect of interference on secrecy achievable rate for C-MIMO and D-MIMO system with MRC, ZF and MMSE receivers. Our results show that, the performance of D-MIMO system in enhancing security is better than C-MIMO system in case of all three receivers. It is also observed that ZF and MMSE receivers are more affected by interferences in D-MIMO system with compared to C-MIMO system.**

***Index Terms*—Co-located MIMO, distributed MIMO, linear receivers and secrecy achievable rate.**

I. Introduction

A large number of antennas can be placed in either receivers or transmitters or both for Multiple-input multiple-output (MIMO) communication. It can attain significant performance gain in terms of achievable rate, energy efficiency, spectral efficiency, security and reliability. MIMO system can be adopted using two different schemes. In co-located MIMO (C-MIMO) scheme the antennas are co-located at both side of wireless link and in distributed MIMO (D-MIMO) the base station (BS) antennas are distributed at different geographical locations. As the wireless networks are susceptible to eavesdropping and fraud, privacy and security in wireless networks are important issues. Motivated by these issues, in this paper, we have considered secure communications in C-MIMO and D-MIMO interference networks and investigate the performance of MRC, ZF and MMSE receivers in enhancing secrecy achievable rate. Recently, the spectral efficiency of massive MIMO system for C-MIMO and D-MIMO configuration has been analyzed in [1]. The accurate expressions of uplink spectral efficiency for a single-cell D-MIMO with linear ZF receivers have been derived in [2]. In [3], the asymptotic achievable secrecy rate of a multi-cell multi-user massive MIMO system with a multi-antenna active eavesdropper is derived to investigate the strategy for reliable and secure transmission. An investigation for secure communication in a massive MIMO uplink system with massive antenna array receiver in the presence of multiple co-located or distributed antenna eavesdroppers is done in [4]. The comparison of energy efficiency and spectral efficiency for distributed MIMO and co-located MIMO uplink system is shown in [5]. The lower bound on the capacity of a MU-MIMO network was estimated in [6] for both the perfect channel state information (CSI) at the receiver using MRC, ZF and MMSE detectors. In the Section-II of this paper, we derive the secrecy achievable rate of an interference-limited C-MIMO cellular network using MRC, ZF and MMSE receivers. We also derived the expressions for secrecy achievable rate for MRC, ZF and MMSE receivers using D-MIMO network in Section-III. Finally, in Section IV, we compare the performance of MRC, ZF and MMSE receivers in enhancing security for C-MIMO and D-MIMO interference networks. The concluding remarks of this work is provided in Section V.

II. Achievable Secrecy Rate for C-MIMO Model

In this paper, we have considered a Rayleigh fading MIMO uplink system consisting two adjacent cells with a overlap between them (shown in figure 1). In Cell-1 and Cell-2, K and L number of users are transmitting to the base stations $BS-1$ and $BS-2$, equipped with M_1 and M_2 antennas, where each user has N_1 and N_2 antennas, respectively. An eavesdrpopper, equipped with N antennas, is situated in the common area of both cells. In this paper, two mathematical models for Rayleigh fading channel have been considered, i.e. C-MIMO and D-MIMO models. For the C-MIMO system, the $M_1 \times 1$ received signal vector from the users of Group-1 to BS-1 can be expressed as

$$\begin{aligned}\mathbf{y}_1^{\text{C-MIMO}} &= \sqrt{P_1/N_1}\sum_{i=1}^{K}\mathbf{H}_i\mathbf{x}_i + \sqrt{P_2/N_2}\sum_{j=1}^{L}\mathbf{Z}_j\mathbf{s}_j + \mathbf{w}_1 \\ &= \sqrt{P_1/N_1}\mathbf{H}\mathbf{X} + \sqrt{P_2/N_2}\mathbf{Z}\mathbf{S} + \mathbf{w}_1, \end{aligned} \tag{1}$$

where the channel matrices from the ith user of Group-1 and the jth user of Group-2 to BS-1 are represented by $\mathbf{H}_i$ and $\mathbf{Z}_j$, $\mathbf{H} = [\mathbf{H}_1, \mathbf{H}_2, \dots \mathbf{H}_K]$ & $\mathbf{Z} = [\mathbf{Z}_1, \mathbf{Z}_2, \dots \mathbf{Z}_L]$ are the channel matrices from the users of Group-1 and Group-2 to BS-1, $\mathbf{x}_i$ & $\mathbf{s}_j$ are the transmitted signals from the ith user of Group-1 and the jth user of Group-2 and P_1 & P_2 denote the average power transmitted by each user from Group-1 & Group-2, respectively. Similarly as (1), the expression of signal received at BS-2 and eavesdropper can be represented by the following equations respectively.

$$\mathbf{y}_2^{\text{C-MIMO}} = \sqrt{P_1/N_1}\mathbf{Q}\mathbf{X} + \sqrt{P_2/N_2}\mathbf{G}\mathbf{S} + \mathbf{w}_2, \tag{2}$$

$$\mathbf{y}_3^{\text{C-MIMO}} = \sqrt{P_1/N_1}\mathbf{V}\mathbf{X} + \sqrt{P_2/N_2}\mathbf{U}\mathbf{S} + \mathbf{w}_3, \tag{3}$$

where, $\mathbf{Q} = [\mathbf{Q}_1, \mathbf{Q}_2, \dots \mathbf{Q}_K]$, $\mathbf{V} = [\mathbf{V}_1, \mathbf{V}_2, \dots \mathbf{V}_L]$, $\mathbf{G} = [\mathbf{G}_1, \mathbf{G}_2, \dots \mathbf{G}_K]$ and $\mathbf{U} = [\mathbf{U}_1, \mathbf{U}_2, \dots \mathbf{U}_K]$. The channel coefficients from the ith user of Group-1 and the jth user of Group-2 to BS-2 are denoted by $\mathbf{Q}_i$ and $\mathbf{G}_j$, respectively.

978-1-5090-5785-6/16/$31.00

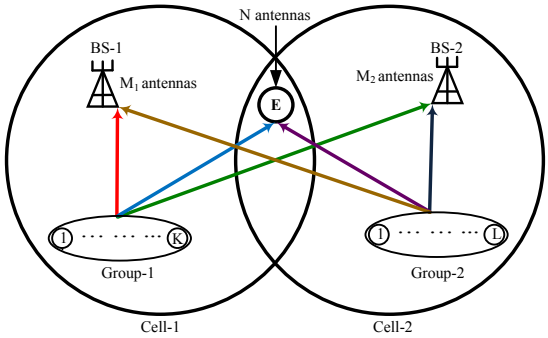

Fig. 1. System model.

Also $\mathbf{V}_i$ and $\mathbf{U}_j$ represents the channel coefficients from the ith user of Group-1 and the jth user of Group-2 to eavesdropper, respectively. The channel model uses additive white, zero-mean Gaussian noise which is denoted by $\mathbf{w}_1$, $\mathbf{w}_2$ & $\mathbf{w}_3$ vectors for the received signals $\mathbf{y}_1$, $\mathbf{y}_2$ & $\mathbf{y}_3$, respectively. The achievable rates for very large multiuser MIMO systems with perfect channel state information is derived in [6]. For our system, we have assumed a $M_1 \times KN_1$ linear detector matrix represented by $\mathbf{A}$ dependent on $\mathbf{H}$. The linear detector matrix $\mathbf{A}$ is defined as follows for the MRC, ZF and MMSE detectors;

$$\mathbf{A} = \begin{cases} \mathbf{H} & \text{for MRC} \\ \mathbf{H}\left(\mathbf{H}^\dagger\mathbf{H}\right)^{-1} & \text{for ZF} \\ \mathbf{H}\left(\mathbf{H}^\dagger\mathbf{H} + \frac{N_t}{P}\mathbf{I}_{N_t}\right)^{-1} & \text{for MMSE} \end{cases} \tag{4}$$

To separate the received signal expressed by (1) into streams, we can use the linear detector matrix as follows.

$$\mathbf{r}_1 = \mathbf{A}^\dagger\mathbf{y}_1^{\text{C-MIMO}} = \sqrt{P_1/N_1}\mathbf{A}^\dagger\mathbf{H}\mathbf{X} + \sqrt{P_2/N_2}\mathbf{A}^\dagger\mathbf{Z}\mathbf{S} + \mathbf{A}^\dagger\mathbf{w}_1 \tag{5}$$

Therefore, the received signal for kth user can be expressed as

$$\mathbf{r}_{1,k} = \sqrt{\frac{P_1}{N_1}}\mathbf{A}_k^\dagger\mathbf{H}_k\mathbf{x}_k + \sqrt{\frac{P_1}{N_1}}\sum_{i=1,i\neq k}^{K}\mathbf{A}_k^\dagger\mathbf{H}_i\mathbf{x}_i + \sqrt{\frac{P_2}{N_2}}\mathbf{A}_k^\dagger\mathbf{Z}\mathbf{S} + \mathbf{A}_k^\dagger\mathbf{w}_1 \tag{6}$$

where, $\mathbf{A}_k$ and $\mathbf{H}_k$ are the kth sub-matrices of $\mathbf{A} = [\mathbf{A}_1, \mathbf{A}_2, \ldots \mathbf{A}_K]$ and $\mathbf{H} = [\mathbf{H}_1, \mathbf{H}_2, \ldots \mathbf{H}_K]$, respectively. $\mathbf{x}_k$ is the kth row of the matrix $\mathbf{X}$. Let $\mathbf{a}_{k,n_1}$ and $\mathbf{h}_{k,n_1}$be the n_1th column of $\mathbf{A}_k$ and $\mathbf{H}_k$ matrices. Let us assume x_{k,n_1} be the n_1th element of the column matrix $\mathbf{x}_k$, then the received signal for the n_1th antenna of kth user can be derived as (7) given at the bottom of the next page. Similarly as (7), the received signal for BS-2, r_{2,l,n_2} can also be derived. The received signal at eavesdropper considering the transmitted signals of Group-1 as desired signal and the transmitted signals of Group-2 as interference signal, r_{E1,k,n_1} and the received signal at eavesdropper considering the transmitted signals of Group-2 as desired signal and the transmitted signals of Group-1 as interference signal, r_{E2,l,n_2} can also be obtained in a similar way. For this purpose, $\mathbf{B}$, $\mathbf{F}$ and $\mathbf{D}$ are used as linear detector matrices, respectively. If the channel $\mathbf{H}$ is realized as fixed then the noise-plus-interference term is a random variable which has zero mean and variance of $\sqrt{P_1/N_1}\sum_{t_1=1,t_1\neq n_1}^{N_1}\mathbf{a}_{k,n_1}^\dagger\mathbf{h}_{k,t_1}x_{k,t_1} + \sqrt{P_1/N_1}\sum_{i=1,i\neq k}^{K}\mathbf{A}_k^\dagger\mathbf{H}_i\mathbf{X}_i + \sqrt{P_2/N_2}\mathbf{A}_k^\dagger\mathbf{Z}\mathbf{S} + \mathbf{A}_k^\dagger\mathbf{w}_1$. We also assume that the channel is ergodic so that each codeword spans over a infinite number of realizations for the fast-fading factor of $\mathbf{H}$. Therefore, the ergodic achievable rate for the n_1th antenna of kth user is

$$R_{1,k,n_1}^{\text{C}} = \mathbb{E}\left\{\log_2\left(1 + \frac{\frac{P_1}{N_1}|\mathbf{a}_{k,n_1}^\dagger\mathbf{h}_{k,n_1}|^2}{\lambda}\right)\right\} \tag{8}$$

where, $\lambda = (P_1/N_1)\sum_{t_1=1,t_1\neq n_1}^{N_1}|\mathbf{a}_{k,n_1}^\dagger\mathbf{h}_{k,t_1}|^2 + (P_1/N_1)\sum_{i=1,i\neq k}^{K}|\mathbf{A}_k^\dagger\mathbf{H}_i|^2 + (P_2/N_2)\sum_{j=1}^{L}|\mathbf{A}_k^\dagger\mathbf{Z}_j|^2 + ||\mathbf{A}_k||^2$.

A. MRC Receiver

In the case of MRC detectors, from (4), we have $\mathbf{A}_k = \mathbf{H}_k$ and $\mathbf{a}_k = \mathbf{h}_k$. Therefore from (8), the achievable rate of the the n_1th antenna of kth user, $R_{1,k,n_1}^{\text{C-MRC}}$ and the achievable rate of the the n_1th antenna of kth user at eavesdropper, $R_{E1,k,n_1}^{\text{C-MRC}}$ can be determined. Therefore, the achievable secrecy rate for the the n_1th antenna of kth user is given by

$$R_{S_{1,k,n_1}}^{\text{C-MRC}} = R_{1,k,n_1}^{\text{C-MRC}} - R_{E1,k,n_1}^{\text{C-MRC}} = \mathbb{E}\left\{\log_2\left(\frac{1 + \frac{\frac{P_1}{N_1}||\mathbf{h}_{k,n_1}||^4}{\alpha_1}}{1 + \frac{\frac{P_1}{N_1}||\mathbf{v}_{k,n_1}||^4}{\beta_1}}\right)\right\} \tag{9}$$

where $\alpha_1 = (P_1/N_1)\sum_{t_1=1,t_1\neq n_1}^{N_1}|\mathbf{h}_{k,n_1}^\dagger\mathbf{h}_{k,t_1}|^2 + (P_1/N_1)\sum_{i=1,i\neq k}^{K}|\mathbf{H}_k^\dagger\mathbf{H}_i|^2 + (P_2/N_2)\sum_{j=1}^{L}|\mathbf{H}_k^\dagger\mathbf{Z}_j|^2 + ||\mathbf{H}_k||^2$ and $\beta_1 = (P_1/N_1)\sum_{t_1=1,t_1\neq n_1}^{N_1}|\mathbf{v}_{k,n_1}^\dagger\mathbf{v}_{k,t_1}|^2 + (P_1/N_1)\sum_{i=1,i\neq k}^{K}|\mathbf{V}_k^\dagger\mathbf{V}_i|^2 + (P_2/N_2)\sum_{j=1}^{L}|\mathbf{V}_k^\dagger\mathbf{U}_j|^2 + ||\mathbf{V}_k||^2$. Similarly as (9), the achievable secrecy rate for the n_2th antenna of lth user is given by

$$R_{S_{2,l,n_2}}^{\text{C-MRC}} = \mathbb{E}\left\{\log_2\left(\frac{1 + \frac{(P_2/N_2)||\mathbf{g}_{l,n_2}||^4}{\tau_1}}{1 + \frac{(P_2/N_2)||\mathbf{u}_{l,n_2}||^4}{\epsilon_1}}\right)\right\} \tag{10}$$

where, $\tau_1 = (P_2/N_2)\sum_{t_2=1,t_2\neq n_2}^{N_2}|\mathbf{g}_{l,n_2}^\dagger\mathbf{g}_{l,t_2}|^2 + (P_2/N_2)\sum_{j=1,j\neq l}^{L}|\mathbf{G}_l^\dagger\mathbf{G}_j|^2 + (P_1/N_1)\sum_{i=1}^{K}|\mathbf{G}_l^\dagger\mathbf{Q}_i|^2 + ||\mathbf{G}_l||^2$ and $\epsilon_1 = (P_2/N_2)\sum_{t_2=1,t_2\neq n_2}^{N_2}|\mathbf{u}_{l,n_2}^\dagger\mathbf{u}_{l,t_2}|^2 + (P_2/N_2)\sum_{j=1,j\neq l}^{L}|\mathbf{U}_l^\dagger\mathbf{U}_j|^2 + (P_1/N_1)\sum_{i=1}^{K}|\mathbf{U}_l^\dagger\mathbf{V}_i|^2 + ||\mathbf{U}_l||^2$.

B. ZF Receiver

In the case of ZF detectors at the receiver, from (4), we have $\mathbf{a}_{k,n_1}^\dagger\mathbf{h}_{k,t_1} = \delta_{n_1t_1}$, where $\delta_{n_1t_1} = 1$ when $n_1 = t_1$ and 0 otherwise. We also have $\mathbf{A}_k^\dagger\mathbf{H}_i = \delta_{ki}$, where $\delta_{ki} = 1$ when $k = i$ and 0 otherwise. Similarly as (9), the achievable secrecy rate for the the n_1th antenna of kth user is given by

$$R_{S_{1,k,n_1}}^{\text{C-ZF}} = \mathbb{E}\left\{\log_2\left(\frac{1 + \frac{P_1/N_1}{\alpha_2}}{1 + \frac{P_1/N_1}{\beta_2}}\right)\right\} \tag{11}$$

where, $\alpha_2 = \frac{P_2}{N_2}\sum_{j=1}^{L}|(\mathbf{H}_k^\dagger\mathbf{H}_k)^{-1}\mathbf{H}_k^\dagger\mathbf{Z}_j|^2 + [(\mathbf{H}^\dagger\mathbf{H})^{-1}]_{kk}$ and $\beta_2 = \frac{P_2}{N_2}\sum_{j=1}^{L}|(\mathbf{V}_k^\dagger\mathbf{V}_k)^{-1}\mathbf{V}_k^\dagger\mathbf{U}_j|^2 + [(\mathbf{V}^\dagger\mathbf{V})^{-1}]_{kk}$. Hence, the achievable secrecy rate for the the n_2th antenna of lth user is given by

$$R_{S_{2,l,n_2}}^{\text{C-ZF}} = \mathbb{E}\left\{\log_2\left(\frac{1 + \frac{P_2/N_2}{\tau_2}}{1 + \frac{P_2/N_2}{\epsilon_2}}\right)\right\} \tag{12}$$

where, $\tau_2 = \frac{P_1}{N_1}\sum_{i=1}^{K}|(\mathbf{G}_l^\dagger\mathbf{G}_l)^{-1}\mathbf{G}_l^\dagger\mathbf{Q}_i|^2 + [(\mathbf{G}^\dagger\mathbf{G})^{-1}]_{ll}$ and $\epsilon_2 = \frac{P_1}{N_1}\sum_{i=1}^{K}|(\mathbf{U}_l^\dagger\mathbf{U}_l)^{-1}\mathbf{U}_l^\dagger\mathbf{V}_i|^2 + [(\mathbf{U}^\dagger\mathbf{U})^{-1}]_{ll}$.

C. MMSE Receiver

In the case of MMSE detectors at the receiver, from (4), we have, $\mathbf{A}_k = \frac{{\mathbf{\Lambda}_{1,k}}^{-1}\mathbf{H}_k}{\mathbf{H}_k^\dagger{\mathbf{\Lambda}_{1,k}}^{-1}\mathbf{H}_k+1}$, where $\mathbf{\Lambda}_{1,k} \triangleq \sum_{i=1,i\neq k}^{K}\mathbf{H}_i\mathbf{H}_i^\dagger + (N_1/P_1)\mathbf{I}_{M_1}$. Again, the n_1th column of $\mathbf{A}_k$ matrix can be written as $\mathbf{a}_{k,n_1} = \frac{{\mathbf{\Lambda}_{1,k,n_1}}^{-1}\mathbf{h}_{k,n_1}}{\mathbf{h}_{k,n_1}^\dagger{\mathbf{\Lambda}_{1,k,n_1}}^{-1}\mathbf{h}_{k,n_1}+1}$, where $\mathbf{\Lambda}_{1,k,n_1} \triangleq \sum_{i=1,i\neq k}^{K}\mathbf{h}_i\mathbf{h}_i^\dagger + (N_1/P_1)\mathbf{I}_{M_1}$. Therefore, similarly as (9) the

achievable secrecy rate for the the n_1th antenna of kth user is given by

$$R_{S_{1,k,n_1}}^{\text{C-MMSE}} = \mathbb{E}\left\{\log_2\left(\frac{1+\frac{(P_1/N_1)|\mathbf{a}_{k,n_1}^{\dagger}\mathbf{h}_{k,n_1}|^2}{\alpha_3}}{1+\frac{(P_1/N_1)|\mathbf{d}_{k,n_1}^{\dagger}\mathbf{v}_{k,n_1}|^2}{\beta_3}}\right)\right\} \quad (13)$$

where, $\alpha_3 = \frac{P_1}{N_1}\sum_{t_1=1,t_1\neq n_1}^{N_1}|\mathbf{a}_{k,n_1}^{\dagger}\mathbf{h}_{k,t_1}|^2 + \frac{P_1}{N_1}\sum_{i=1,i\neq k}^{K}|\mathbf{A}_k^{\dagger}\mathbf{H}_i|^2 + \frac{P_2}{N_2}\sum_{j=1}^{L}|\mathbf{A}_k^{\dagger}\mathbf{Z}_j|^2 + ||\mathbf{A}_k||^2$ and $\beta_3 = \frac{P_1}{N_1}\sum_{t_1=1,t_1\neq n_1}^{N_1}|\mathbf{d}_{k,n_1}^{\dagger}\mathbf{v}_{k,t_1}|^2 + \frac{P_1}{N_1}\sum_{i=1,i\neq k}^{K}|\mathbf{D}_k^{\dagger}\mathbf{V}_i|^2 + \frac{P_2}{N_2}\sum_{j=1}^{L}|\mathbf{D}_k^{\dagger}\mathbf{U}_j|^2 + ||\mathbf{D}_k||^2$. Similarly as (10), the achievable secrecy rate for the the n_2th antenna of lth user is given by

$$R_{S_{2,l,n_2}}^{\text{C-MMSE}} = \mathbb{E}\left\{\log_2\left(\frac{1+\frac{(P_2/N_2)|\mathbf{b}_{l,n_2}^{\dagger}\mathbf{g}_{l,n_2}|^2}{\tau_3}}{1+\frac{(P_2/N_2)|\mathbf{f}_{l,n_2}^{\dagger}\mathbf{u}_{l,n_2}|^2}{\epsilon_3}}\right)\right\} \quad (14)$$

where, $\tau_3 = \frac{P_2}{N_2}\sum_{t_2=1,t_2\neq n_2}^{N_2}|\mathbf{b}_{l,n_2}^{\dagger}\mathbf{g}_{l,t_2}|^2 + \frac{P_2}{N_2}\sum_{j=1,j\neq l}^{L}|\mathbf{B}_l^{\dagger}\mathbf{G}_j|^2 + \frac{P_1}{N_1}\sum_{i=1}^{K}|\mathbf{B}_l^{\dagger}\mathbf{Q}_i|^2 + ||\mathbf{B}_l||^2$ and $\epsilon_3 = \frac{P_2}{N_2}\sum_{t_2=1,t_2\neq n_2}^{N_2}|\mathbf{f}_{l,n_2}^{\dagger}\mathbf{u}_{l,t_2}|^2 + \frac{P_2}{N_2}\sum_{j=1,j\neq l}^{L}|\mathbf{F}_l^{\dagger}\mathbf{U}_j|^2 + \frac{P_1}{N_1}\sum_{i=1}^{K}|\mathbf{F}_l^{\dagger}\mathbf{V}_i|^2 + ||\mathbf{F}_l||^2$.

III. Achievable Secrecy Rate for D-MIMO Model

For a D-MIMO system, the received signal vector $\mathbf{y}_1^{\text{D-MIMO}}$ at BS-1 is related with $O_1N_t \times 1$ transmitted signal vector $\mathbf{X}$ and $\mathbf{S}$ by

$$\mathbf{y}_1^{\text{D-MIMO}} = \sqrt{P_1/(O_1N_1)}\mathbf{H}_D\mathbf{X} + \sqrt{P_2/(O_2N_2)}\mathbf{Z}_D\mathbf{S} + \mathbf{w}_1, \quad (15)$$

where $\mathbf{H}_D = \mathbf{H}\boldsymbol{\Delta}_1^{\frac{1}{2}}$ and $\mathbf{Z}_D = \mathbf{Z}\boldsymbol{\Delta}_2^{\frac{1}{2}}$ are the channel matrix from O_1N_1 and O_2N_2 transmit antennas to N_r receive antennas, respectively, O_1 and O_2 denotes the number of radio ports located at the transmitting side of Group-1 and Group-2, respectively. $\boldsymbol{\Delta}_1^{\frac{1}{2}} = \text{diag}\left(\sqrt{\frac{\sigma_1}{\lambda_1^v}},\ldots,\sqrt{\frac{\sigma_1}{\lambda_1^v}},\ldots,\sqrt{\frac{\sigma_{O_1}}{\lambda_{O_1}^v}},\ldots,\sqrt{\frac{\sigma_{O_1}}{\lambda_{O_1}^v}},\ldots,\right) \in \mathbb{R}^{O_1N_1\times O_1N_1}$ and $\boldsymbol{\Delta}_2^{\frac{1}{2}} = \text{diag}\left(\sqrt{\frac{\phi_1}{\delta_1^v}},\ldots,\sqrt{\frac{\phi_1}{\delta_1^v}},\ldots,\sqrt{\frac{\phi_{O_2}}{\delta_{O_2}^v}},\ldots,\sqrt{\frac{\phi_{O_2}}{\delta_{O_2}^v}},\ldots,\right) \in \mathbb{R}^{O_2N_2\times O_2N_2}$ represent $O_1N_1 \times O_1N_1$ and $O_2N_2 \times O_2N_2$ diagonal matrix accounted for the large-scale fading effect in which the path loss is characterized by $\lambda_{O_1}^v$ and $\delta_{O_2}^v$ for some exponent v, respectively. $\{\sigma_i\}_{i=1}^{O_1}$ and $\{\phi_i\}_{i=1}^{O_2}$ are independent random variables. Similarly as (15), the received signal at BS-2 and eavesdropper can be expressed as followings.

$$\mathbf{y}_2^{\text{D-MIMO}} = \sqrt{P_1/(O_1N_1)}\mathbf{Q}_D\mathbf{X} + \sqrt{P_2/(O_2N_2)}\mathbf{G}_D\mathbf{S} + \mathbf{w}_2 \quad (16)$$

$$\mathbf{y}_3^{\text{D-MIMO}} = \sqrt{P_1/(O_1N_1)}\mathbf{V}_D\mathbf{X} + \sqrt{P_2/(O_2N_2)}\mathbf{U}_D\mathbf{S} + \mathbf{w}_3 \quad (17)$$

Similarly as C-MIMO Model, the linear detector matrix can be used to determine achievable secrecy rate.

A. MRC Receiver

Similarly as (9), the achievable secrecy rate for the n_1th antenna of kth user is given by

$$R_{S_{1,k,n_1}}^{\text{D-MRC}} = \mathbb{E}\left\{\log_2\left(\frac{1+\frac{(P_1/O_1N_1)||\mathbf{h}_{Dk,n_1}||^4}{\alpha_4}}{1+\frac{(P_1/O_1N_1)||\mathbf{v}_{Dk,n_1}||^4}{\beta_4}}\right)\right\} \quad (18)$$

where, $\alpha_4 = \frac{P_1}{O_1N_1}\sum_{t_1=1,t_1\neq n_1}^{N_1}|\mathbf{h}_{D\,k,n_1}^{\dagger}\mathbf{h}_{Dk,t_1}|^2 + \frac{P_1}{O_1N_1}\sum_{i=1,i\neq k}^{K}|\mathbf{H}_{D\,k}^{\dagger}\mathbf{H}_{Di}|^2 + \frac{P_2}{O_2N_2}\sum_{j=1}^{L}|\mathbf{H}_{D\,k}^{\dagger}\mathbf{Z}_{Dj}|^2 + ||\mathbf{H}_{Dk}||^2$ and $\beta_4 = \frac{P_1}{O_1N_1}\sum_{t_1=1,t_1\neq n_1}^{N_1}|\mathbf{v}_{D\,k,n_1}^{\dagger}\mathbf{v}_{Dk,t_1}|^2 + \frac{P_1}{O_1N_1}\sum_{i=1,i\neq k}^{K}|\mathbf{V}_{D\,k}^{\dagger}\mathbf{V}_{Di}|^2 + \frac{P_2}{O_2N_2}\sum_{j=1}^{L}|\mathbf{V}_{D\,k}^{\dagger}\mathbf{U}_{Dj}|^2 + ||\mathbf{V}_{Dk}||^2$. Similarly as (10), the achievable secrecy rate for the n_2th antenna of lth user is given by

$$R_{S_{2,l,n_2}}^{\text{D-MRC}} = \mathbb{E}\left\{\log_2\left(\frac{1+\frac{(P_2/O_2N_2)||\mathbf{g}_{Dl,n_2}||^4}{\tau_4}}{1+\frac{(P_2/O_2N_2)||\mathbf{u}_{Dl,n_2}||^4}{\epsilon_4}}\right)\right\} \quad (19)$$

where, $\tau_4 = \frac{P_2}{O_2N_2}\sum_{t_2=1,t_2\neq n_2}^{N_2}|\mathbf{g}_{Dl,n_2}^{\dagger}\mathbf{g}_{Dl,t_2}|^2 + \frac{P_2}{O_2N_2}\sum_{j=1,j\neq l}^{L}|\mathbf{G}_{D\,l}^{\dagger}\mathbf{G}_{Dj}|^2 + \frac{P_1}{O_1N_1}\sum_{i=1}^{K}|\mathbf{G}_{D\,l}^{\dagger}\mathbf{Q}_{Di}|^2 + ||\mathbf{G}_{Dl}||^2$ and $\epsilon_4 = \frac{P_2}{O_2N_2}\sum_{t_2=1,t_2\neq n_2}^{N_2}|\mathbf{u}_{D\,l,n_2}^{\dagger}\mathbf{u}_{Dl,t_2}|^2 + \frac{P_2}{O_2N_2}\sum_{j=1,j\neq l}^{L}|\mathbf{U}_{D\,l}^{\dagger}\mathbf{U}_{Dj}|^2 + \frac{P_1}{O_1N_1}\sum_{i=1}^{K}|\mathbf{U}_{D\,l}^{\dagger}\mathbf{V}_{Di}|^2 + ||\mathbf{U}_{Dl}||^2$.

B. ZF Receiver

When ZF detector is used, similarly as (11), the achievable secrecy rate for the n_1th antenna of kth user is given by

$$R_{S_{1,k,n_1}}^{\text{D-ZF}} = \mathbb{E}\left\{\log_2\left(\frac{1+\frac{P_1/(O_1N_1)}{\alpha_5}}{1+\frac{P_1/(O_1N_1)}{\beta_5}}\right)\right\} \quad (20)$$

where, $\alpha_5 = \frac{P_2}{O_2N_2}\sum_{j=1}^{L}|(\mathbf{H}_{D\,k}^{\dagger}\mathbf{H}_{Dk})^{-1}\mathbf{H}_{D\,k}^{\dagger}\mathbf{Z}_{Dj}|^2 + [(\mathbf{H}_D^{\dagger}\mathbf{H}_D)^{-1}]_{kk}$ and $\beta_5 = \frac{P_2}{O_2N_2}\sum_{j=1}^{L}|(\mathbf{V}_{D\,k}^{\dagger}\mathbf{V}_{Dk})^{-1}\mathbf{V}_{D\,k}^{\dagger}\mathbf{U}_{Dj}|^2 + [(\mathbf{V}_D^{\dagger}\mathbf{V}_D)^{-1}]_{kk}$. Similarly as (12), the achievable secrecy rate for the n_2th antenna of lth user is given by

$$R_{S_{2,l,n_2}}^{\text{D-ZF}} = \mathbb{E}\left\{\log_2\left(\frac{1+\frac{P_2/(O_2N_2)}{\tau_5}}{1+\frac{P_2/(O_2N_2)}{\epsilon_5}}\right)\right\} \quad (21)$$

where, $\tau_5 = \frac{P_1}{O_1N_1}\sum_{i=1}^{K}|(\mathbf{G}_{D\,l}^{\dagger}\mathbf{G}_{Dl})^{-1}\mathbf{G}_{D\,l}^{\dagger}\mathbf{Q}_{Di}|^2 + [(\mathbf{G}_D^{\dagger}\mathbf{G}_D)^{-1}]_{ll}$ and $\epsilon_5 = \frac{P_1}{O_1N_1}\sum_{i=1}^{K}|(\mathbf{U}_{D\,l}^{\dagger}\mathbf{U}_{Dl})^{-1}\mathbf{U}_{D\,l}^{\dagger}\mathbf{V}_{Di}|^2 + [(\mathbf{U}_D^{\dagger}\mathbf{U}_D)^{-1}]_{ll}$.

C. MMSE Receiver

When MMSE detector is used, similarly as (13), the achievable secrecy rate for the n_1th antenna of kth user is given by

$$R_{S_{1,k,n_1}}^{\text{D-MMSE}} = \mathbb{E}\left\{\log_2\left(\frac{1+\frac{(P_1/O_1N_1)|\mathbf{a}_{D\,k,n_1}^{\dagger}\mathbf{h}_{D\,k,n_1}|^2}{\alpha_6}}{1+\frac{(P_1/O_1N_1)|\mathbf{d}_{D\,k,n_1}^{\dagger}\mathbf{v}_{D\,k,n_1}|^2}{\beta_6}}\right)\right\} \quad (22)$$

where, $\alpha_6 = \frac{P_1}{O_1N_1}\sum_{t_1=1,t_1\neq n_1}^{N_1}|\mathbf{a}_{D\,k,n_1}^{\dagger}\mathbf{h}_{Dk,t_1}|^2 + \frac{P_1}{O_1N_1}\sum_{i=1,i\neq k}^{K}|\mathbf{A}_{D\,k}^{\dagger}\mathbf{H}_{Di}|^2 + \frac{P_2}{O_2N_2}\sum_{j=1}^{L}|\mathbf{A}_{D\,k}^{\dagger}\mathbf{Z}_{Dj}|^2 + ||\mathbf{A}_{Dk}||^2$ and $\beta_6 = \frac{P_1}{O_1N_1}\sum_{t_1=1,t_1\neq n_1}^{N_1}|\mathbf{d}_{D\,k,n_1}^{\dagger}\mathbf{v}_{Dk,t_1}|^2 + \frac{P_1}{O_1N_1}\sum_{i=1,i\neq k}^{K}|\mathbf{D}_{D\,k}^{\dagger}\mathbf{V}_{Di}|^2 + \frac{P_2}{O_2N_2}\sum_{j=1}^{L}|\mathbf{D}_{D\,k}^{\dagger}\mathbf{U}_{Dj}|^2 + ||\mathbf{D}_{Dk}||^2$. Similarly as (14), the achievable secrecy rate for the n_2th antenna of lth user is given by

$$R_{S_{2,l,n_2}}^{\text{D-MMSE}} = \mathbb{E}\left\{\log_2\left(\frac{1+\frac{(P_2/O_2N_2)|\mathbf{b}_{D\,l,n_2}^{\dagger}\mathbf{g}_{Dl,n_2}|^2}{\tau_6}}{1+\frac{(P_2/O_2N_2)|\mathbf{f}_{D\,l,n_2}^{\dagger}\mathbf{u}_{Dl,n_2}|^2}{\epsilon_6}}\right)\right\} \quad (23)$$

where, $\tau_6 = \frac{P_2}{O_2N_2}\sum_{t_2=1,t_2\neq n_2}^{N_2}|\mathbf{b}_{D\,l,n_2}^{\dagger}\mathbf{g}_{Dl,t_2}|^2 + \frac{P_2}{O_2N_2}\sum_{j=1,j\neq l}^{L}|\mathbf{B}_{D\,l}^{\dagger}\mathbf{G}_{Dj}|^2 + \frac{P_1}{O_1N_1}\sum_{i=1}^{K}|\mathbf{B}_{D\,l}^{\dagger}\mathbf{Q}_{Di}|^2 + ||\mathbf{B}_{Dl}||^2$ and $\epsilon_6 = \frac{P_2}{O_2N_2}\sum_{t_2=1,t_2\neq n_2}^{N_2}|\mathbf{f}_{D\,l,n_2}^{\dagger}\mathbf{u}_{Dl,t_2}|^2 + \frac{P_2}{O_2N_2}\sum_{j=1,j\neq l}^{L}|\mathbf{F}_{D\,l}^{\dagger}\mathbf{U}_{Dj}|^2 + \frac{P_1}{O_1N_1}\sum_{i=1}^{K}|\mathbf{F}_{D\,l}^{\dagger}\mathbf{V}_{Di}|^2 + ||\mathbf{F}_{Dl}||^2$.

$$r_{1,k,n_1} = \sqrt{P_1/N_1}\mathbf{a}_{k,n_1}^{\dagger}\mathbf{h}_{k,n_1}x_{k,n_1} + \sqrt{P_1/N_1}\sum_{t_1=1,t_1\neq n_1}^{N_1}\mathbf{a}_{k,n_1}^{\dagger}\mathbf{h}_{k,t_1}x_{k,t_1} + \sqrt{P_1/N_1}\sum_{i=1,i\neq k}^{K}\mathbf{A}_k^{\dagger}\mathbf{H}_i\mathbf{X}_i + \sqrt{P_2/N_2}\mathbf{A}_k^{\dagger}\mathbf{Z}\mathbf{S} + \mathbf{A}_k^{\dagger}\mathbf{w}_1 \quad (7)$$

IV. Numerical Results

In figure 2, the comparison of achievable secrecy rate for MRC, ZF and MMSE receivers in a cellular interference networks as a function of number of antennas at BS-1 is shown. It is observed that the secrecy achievable rate increases with the number of antennas at BS-1 for both the configuration and the D-MIMO system performs better than C-MIMO system in achieving secrecy rate as the number of antennas at the receiver increases. Figure 3, 4 and 5 illustrate the effect of interference on the secrecy achievable rate for both C-MIMO and D-MIMO system in case of MRC, ZF and MMSE receivers, respectively. It is found that the effect of interference on the secrecy achievable rate for D-MIMO system is less than that of C-MIMO system in case of MRC receivers. In case of ZF and MMSE receivers, it is observed that the effect of interference on secrecy achievable rate for D-MIMO system is more than that of C-MIMO system for the same number of users, number antennas at base station, number of antennas at eavesdroppers and number of radio ports for D-MIMO systems.

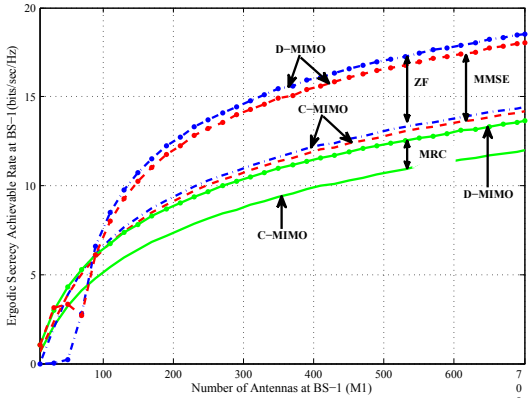

Fig. 2. Secrecy achievable rate versus number antennas at BS-1 for the MRC, ZF and MMSE receivers with $K = 4$, $N_1 = 4$, $N_2 = 4$, $L = 4$, $N = 3$, $O_1 = 4$ and $O_2 = 4$.

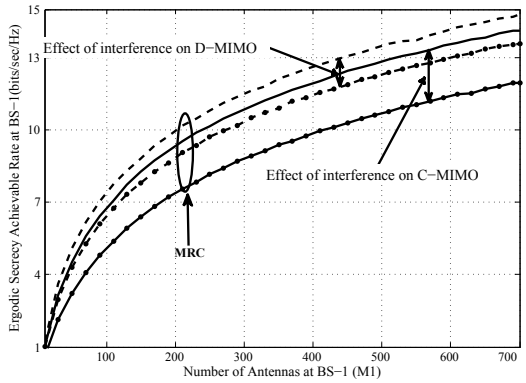

Fig. 3. Effect of interferences on the performance of MRC receivers with $K = 4$, $N_1 = 4$, $N_2 = 4$, $L = 4$, $N = 3$, $O_1 = 4$ and $O_2 = 4$.

V. Conclusion

This paper shows the performance of MRC, ZF and MMSE receivers in enhancing secrecy achievable rate for co-loacted and distributed MIMO system with large antenna arrays in a cellular inference network. Based on our formulation and from the observation of numerical results, we can conclude

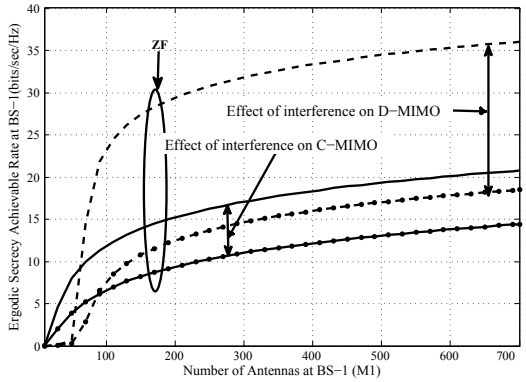

Fig. 4. Effect of interferences on the performance of ZF receivers with $K = 4$, $N_1 = 4$, $N_2 = 4$, $L = 4$, $N = 3$, $O_1 = 4$ and $O_2 = 4$.

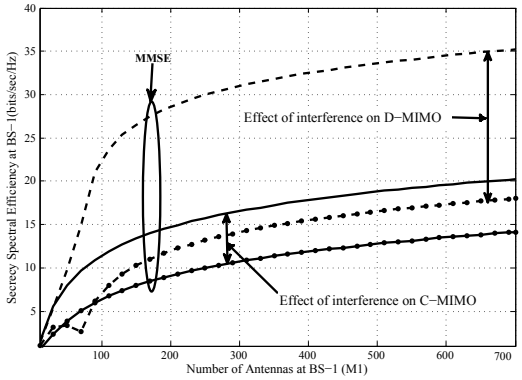

Fig. 5. Effect of interferences on the performance of MMSE receivers with $K = 4$, $N_1 = 4$, $N_2 = 4$, $L = 4$, $N = 3$, $O_1 = 4$ and $O_2 = 4$.

that more secrecy achievable rate can be obtained with the increasing number of antennas at the receiver for both the system in case of MRC, ZF and MMSE receivers. It can also be concluded that the performance of D-MIMO system in enhancing secrecy achievable rate is better than C-MIMO system in case of MRC, ZF and MMSE receivers. Although D-MIMO system with ZF and MMSE receivers show much more improvement in secrecy achievable rate but these are more affected by interferences than C-MIMO system with respective receivers as compared to the C-MIMO and D-MIMO systems with MRC receivers.

References

[1] G. N. Kamga, M. Xia, and S. Assa, "Spectral-efficiency analysis of massive mimo systems in centralized and distributed schemes," *IEEE Transactions on Communications*, vol. 64, no. 5, pp. 1930–1941, May 2016.

[2] H. Almelah and K. Hamdi, "Spectral efficiency of distributed large-scale mimo systems with zf receivers," *IEEE Transactions on Vehicular Technology*, vol. PP, no. 99, pp. 1–1, 2016.

[3] Y. Wu, R. Schober, D. W. K. Ng, C. Xiao, and G. Caire, "Secure massive mimo transmission with an active eavesdropper," *IEEE Transactions on Information Theory*, vol. 62, no. 7, pp. 3880–3900, July 2016.

[4] J. Wang, J. Lee, and T. Q. S. Quek, "Secure communication for massive mimo uplink in the presence of co-located and distributed eavesdroppers," in *2015 International Conference on Wireless Communications Signal Processing (WCSP)*, Oct 2015, pp. 1–5.

[5] C. He, B. Sheng, P. Zhu, and X. You, "Energy efficient comparison between distributed mimo and co-located mimo in the uplink cellular systems," in *2012 IEEE Vehicular Technology Conference (VTC Fall)*, Sept 2012, pp. 1–5.

[6] H. Q. Ngo, E. Larsson, and T. Marzetta, "Energy and spectral efficiency of very large multiuser mimo systems," *IEEE Transactions on Communications*, vol. 61, no. 4, pp. 1436–1449, April 2013.

2nd International Conference on Electrical, Computer & Telecommunication Engineering (ICECTE)
8-10 December 2016, Rajshahi-6204, Bangladesh

Faster Implementation of Booth's Algorithm Using FPGA

Ahmed Salman Tariq[1], Ruhul Amin[2], Md. Nazrul Islam Mondal[3], Md. Ali Hossain[4]
[1]Dept. of Computer Science and Engineering, RUET, Rajshahi, Bangladesh, salmangalib.ruet@gmail.com
[2]Dept. of Computer Science and Engineering, RUET, Rajshahi, Bangladesh, ruhul113056@gmail.com
[3]Dept. of Computer Science and Engineering, RUET, Rajshahi, Bangladesh, nimbd109@gmail.com
[4]Dept. of Computer Science and Engineering, RUET, Rajshahi, Bangladesh, ali.ruet@gmail.com

***Abstract*— Modern world has become more dependent on electronics and hence speed is a major factor in the field of their functionalities. Modern CPUs work lot faster and efficiently than older versions. Still humans require more and more time efficiency in their daily computational works. In this paper, the main focus is on the increase of time efficiency in computing. Hence this paper shows a time performance comparison between FPGA and CPU implementation. In this regard, Booth's multiplication algorithm has been implemented on both CPU and FPGA to compare the running time. The FPGA implementation is found out to be around 9 times faster than that of a modern CPU implementation.**

Keywords—FPGA; Booth's algorithm; signed binary multiplication; speed-up factor; time efficieny; CPU.

I. INTRODUCTION

Present world is very fast for the advent of modern technology. As days go, everyone demands more fast and efficient technology. Another major sector of technology is multiple use of a device i.e. programmable device. To cope with the demand and provide better facilities, Field Programmable Gate Array (FPGA) technology is prominent now. People always want better and better time performance from machines. And better time performance can be achieved with highly parallel processing capability [1]. With the re-configurability property, FPGA [7] helps to design a device that works in true parallel manner, as a result time performance, area reduction, power consuming reduction etc. [5] are achieved in the fields of various computational works. In this paper, Booth's binary multiplication algorithm has been taken as an experimental computation for testing to demonstrate how faster an FPGA can compute than a CPU.

II. THEORETICAL BACKGROUND

In case of comparison with addition or subtraction, multiplication is a much more complex operation. A wide Variety of algorithms have been developed and used in various machines (computers) for the purpose of binary multiplication. One of them is Booth's algorithm for signed binary multiplication. We have used implemented this algorithm on both FPGA by Verilog programming and on CPU by programming in C.

Let's discuss in brief; how multiplication is performed using Booth's algorithm. In case of signed multiplication, where either multiplicand or multiplier or both of them can be negative; the Booth's algorithm uses two's complement for negative number(s) of the corresponding binary equivalent [2]. The algorithm is;

INITIALIZE
  A := 0;
  Q_{-1} := 0;
  M := Multiplicand;
  Q := Multiplier;
  Count := n;

DO
  IF Q_0, Q_{-1} = 01
    THEN A := A + M ;
  ELSE IF Q_0, Q_{-1} = 10
    THEN A := A – M ;
  ARITHMETIC SHIFT RIGHT: A, Q, Q_{-1} ;
  Count := Count – 1 ;
WHILE *Count ≠ 0*

Here, n is the number of bits used in multiplicand and multiplier which is stored in variable *Count*. So, it can be realized here that the loop / iteration will take n number of steps to calculate the result of multiplication [6]. The result is finally stored in A, Q when the iteration is complete [2]. However, since this algorithm performs partial addition/ subtraction, it has $O(n^2)$ complexity.

Fig.1 shows the flowchart for Booth's algorithm for two's complement binary multiplication.

978-1-5090-5785-6/16/$31.00 ©2016 IEEE

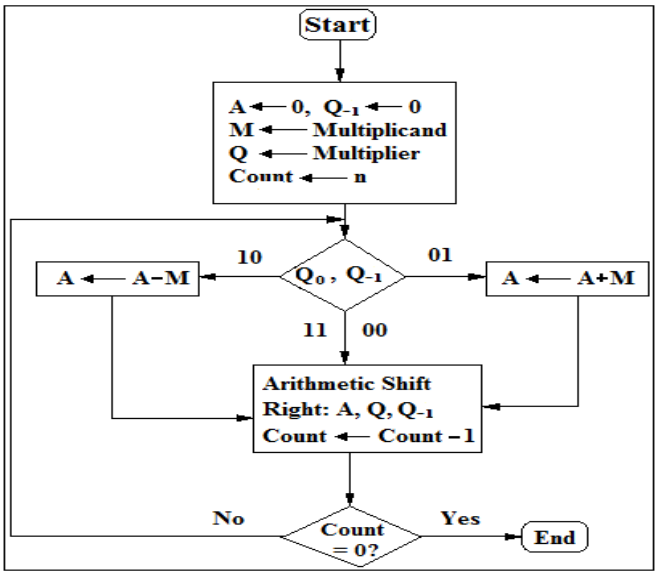

Fig.1: Flowchart for Booth's multiplication algorithm.

Let's have a look at an example. Say, we have to multiply 8 and -5; where 8 is the multiplicand (M) and -5 is the multiplier (Q). We all know that the result is simply 8 x (-5) = -40, but how is it done in binary level using Booth's algorithm?

We will consider the binary equivalents of these two numbers. 1000 is the binary form of decimal value 8 and two's complement of decimal value 5's binary is 1011 (taking 4 bits) which indicates; -5 (negative). So, initially we need to set; A = 0000, Q = 1011, M = 1000 and Q_{-1} = 0. Since we are using 4 bits for both the multiplier and multiplicand, n = 4 here, hence the number of cycle till final result is four.

Fig.2 illustrates the whole procedure step by step for the multiplication of 8 and -5.

A	Q	Q_{-1}	M		
0000	1011	0	1000	Initial Values	
1000	1011	0	1000	A ← A – M	First cycle
1100	0101	1	1000	Shift	
1110	0010	1	1000	Shift	Second cycle
0110	0010	1	1000	A ← A + M	Third cycle
0011	0001	0	1000	Shift	
1011	0001	0	1000	A ← A – M	Fourth cycle
1101	1000	1	1000	Shift	

Fig.2: Example of Booth's Algorithm [8 x (-5)].

As the figure shows, after the last cycle; value stored in A is 1101 and Q is 1000. So, the result of multiplication is; 11011000. The MSB here is 1, which indicates that the result is negative. Its one's complement = 00100111, hence; two's complement = 00101000 that is equivalent of 40. So, the actual result is - 40.

III. IMPLEMENTATIONS

A. CPU Implementation

The Booth's multiplication algorithm has been implemented on both CPU and FPGA platform. Implementation on CPU (Core i5 – 4th gen.) has been accomplished by programming with C language according to the algorithm mentioned in previous article. Fig.3 shows partial C program for implementing Booth's signed binary multiplication algorithm and Fig.4 shows the output of the program with the calculated corresponding CPU time.

```
140   printf("  A          Q          Q_1        M     \n\n");
141   for(i=3;i>=0;i--)
142   {printf("%d",A[i]);}
143    printf("        ");
144   for(i=0;i<4;i++)
145   {printf("%d",Q[i]);}
146    printf("          %d        " ,Q_1);
147    for(i=0;i<4;i++)
148   {printf("%d",M[i]);}
149    printf("\n\n");
150
151   for(k=0;k<4;k++)
152   {
153     if(Q[3]==0&&Q_1==1)     //Perform Addition for Q_0,Q_1 = 0 1
154     {
207     else if(Q[3]==1&&Q_1==0)     //Perform Subtraction for Q_0,Q_1 = 1 0
208     {
274     carry=0;
275     //Arithmetic Shifting
276     t=A[3];
277     for(i=3;i>=1;i--)
278     {
281     Q_1 = Q[3];
```

Fig.3: C program (partial) for Booth's algorithm implementation on CPU.

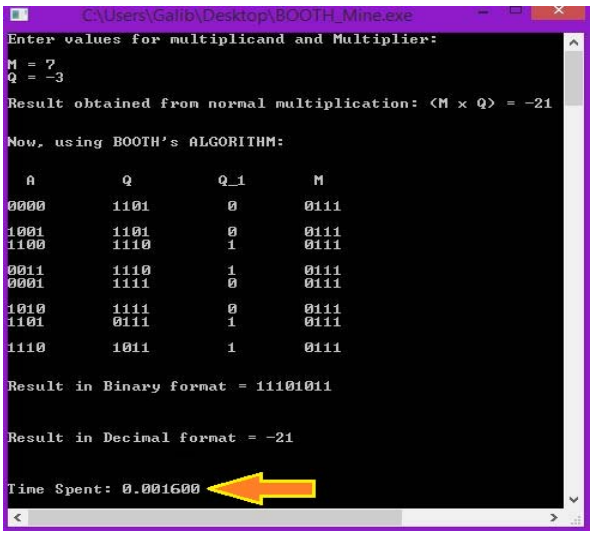

Fig.4: Console output of Booth's algorithm implementation program.

B. FPGA Implementation

The algorithm has been then implemented on Spartan-6 FPGA using Xilinx ISE 14.7 and Verilog coding. In our designed top module, there are two sub-modules inside; an adder and a subtractor. Fig.5 shows partial Verilog code and Fig. 6 shows the corresponding RTL schematic of the Booth's multiplier circuitry.

```
13    reg [3:0] count;
14    wire [7:0] sum, difference;
15
16    always @(posedge clk, posedge start)
17       begin
18          if (start)
19             begin
20                A <= 8'b0;
21                M <= mc;
22                Q <= mp;
23                Q_1 <= 1'b0;
24                count <= 4'b0;
25             end
26          else
27             begin
28                case ({Q[0], Q_1})
29                   2'b0_1 : {A, Q, Q_1} <= {sum[7], sum, Q};
30                   2'b1_0 : {A, Q, Q_1} <= {difference[7], difference, Q};
31                   default: {A, Q, Q_1} <= {A[7], A, Q};
32                endcase
33                count <= count + 1'b1;
34             end
35       end
36
37    alu adder (sum, A, M, 1'b0);
38    alu subtracter (difference, A, ~M, 1'b1);
39
40    assign prod = {A, Q};
41    assign busy = (count < 8);
42
43 endmodule
```

Design Summary | multiplier_tb.v | multiplier.v

Fig.5: Verilog code (partial) for Booth's algorithm implementation on FPGA.

Fig.6: Booth's multiplier (RTL schematic).

The simulation has been performed by creating a verilog testbench and the simulation result of Booth's multiplication algorithm is shown below in Fig.7 which is for multiplication of -7(1001) by 3(0011).

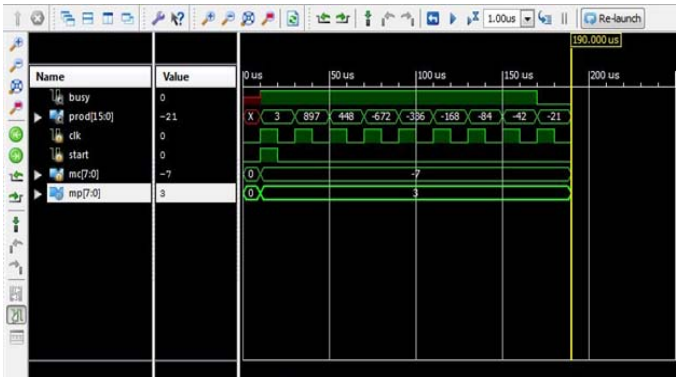

Fig.7: Simulation result of Booth's algorithm

IV. Result Analysis and Comparison

After running the C program of Booth's algorithm implementation for four combinations of inputs (multiplicand and multiplier); such as both positives, positive multiplicand and negative multiplier, negative multiplicand and positive multiplier and both negatives. The CPU time spent in these four cases has been shown in Table I.

TABLE I. CPU Run-time for Booth's Algorithm Implementation

SL. No.	Multiplicand	Multiplier	Result	Time Spent (sec)
1	7	3	21	0.0015
2	7	-3	-21	0.0016
3	-7	3	-21	0.0016
4	-7	-3	21	0.0017

Similarly, the run-times spent for those four combinations of inputs in FPGA simulation have been listed below in Table II.

TABLE II. FPGA Simulation Run-time for Booth's Algorithm Implementation

SL. No.	Multiplicand	Multiplier	Result	Time Spent (sec)
1	7	3	21	0.00018
2	7	-3	-21	0.00018
3	-7	3	-21	0.00018
4	-7	-3	21	0.00018

Now, using the data from the tables of Fig.8 and Fig.9, a graph can be plotted easily to show the comparison between the CPU and FPGA implementation of Booth's algorithm with respect to time efficiency. Fig.10 shows a column graph that illustrates the difference which proves that FPGA can operate way faster than that of CPU implementation.

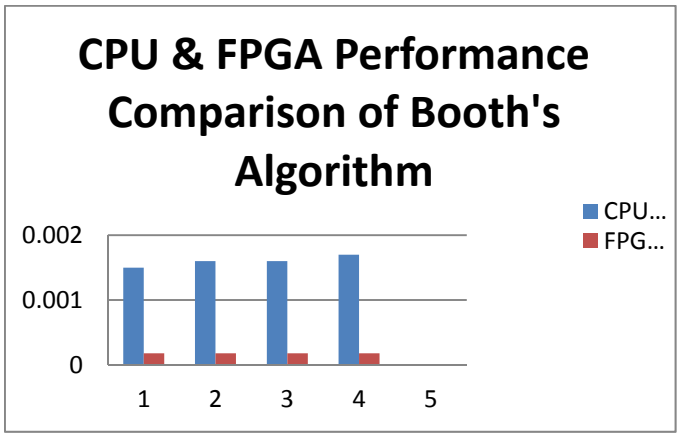

Fig.8: Performance comparison graph for Booth's algorithm implementation.

V. SPEED-UP FACTOR

From the data in Table I and Table II, speed-up factor can be measured;

Speed-up factor, F_1 = CPU time / FPGA time
= 0.0015s / 0.00018s = 8.33
F_2 = 0.0016s / 0.00018s = 8.89
F_3 = 0.0016s / 0.00018s = 8.89
F_4 = 0.0017s / 0.00018s = 9.44

SO, AVERAGE SPEED-UP FACTOR; F_A = (8.33+8.89+8.89+9.44) /4
=35.55/4
= 8.8875 ≈ 9

VI. CONCLUSION

In this paper, Booth's algorithm is implemented both on the CPU and FPGA in order to compare the implementation time. It is shown that because of highly parallel processing capability of FPGA with configurable logic blocks, FPGA implementation is around 9 times faster than that of CPU implementation. In future we have a plan to modify Booth's algorithm in order to make it more time efficient.

REFERENCES

[1] Chatter, Mukesh. "High performance self modifying on-the-fly alterable logic FPGA, architecture and method." U.S. Patent No. 5,838,165. 17 Nov. 1998.

[2] William Stallings, "Computer Organization and Architecture – Designing for Performance", 8th edition, pp. 335-342, 2014

[3] D. M. J. Purnomo, M. R. Alhamidi, A. Wibisono, and M. I. Tawakal, "Investigation of Flip-Flop Performance on Different Type and Architecture is Shift Register with Parallel Load Applications" Jurnal Ilmu Komputer dan Informasi, pp. 87-95, 2015

[4] R. Rose J. et al. " A classification and survey of field programmable gate array architectures," Proceedings of The IEEE, vol. 81,no. 7 1993

[5] Brown. S. et al, "Field Programmable Gate Arrays", Organization", 4th edition, pp. 274-282.

[6] Carl Hamacher, Zvonko Vranesic, Safwat Zaky, "Computer Organization", 4th edition, pp. 274-282.

[7] Keith Underwood, " FPGAs vs. CPUs: Trends in Peak Floating-Point Performance", 2004

[8] White paper: www.xilinx.com pp.

2nd International Conference on Electrical, Computer & Telecommunication Engineering (ICECTE)
8-10 December 2016, Rajshahi-6204, Bangladesh

Modeling of Graphene Conductivity Using FDTD in the Near Infrared Frequency

Pejush Chandra Sarker, Md. Masud Rana and Ajay Krishno Sarkar
Department of Electrical and Electronic Engineering, Rajshahi University of Engineering & Technology, Rajshahi, Bangladesh
pejush01@yahoo.com, md.masud.rana@ruet.ac.bd, sarkarajay139@gmail.com

***Abstract*—This paper investigates the modeling of graphene interband conductivity in near infared frequency range. First, the interband graphene conductivity is incorporated in surface boundary condition (SBC). Then, SBC is applied in finite-difference time domain (FDTD) method for modeling graphene sheet. Moreover, auxiliary differential equation (ADE) is used to characterize frequency dependent graphene conductivity in FDTD method. Advantages, accuracy, applicability and stability of the proposed method are analyzed by numerical examples. The method is validated by comparing the existing analytical results. This method can be easily implemented to model the graphene interband conductivity for optical device applications.**

Keywords—Finite-difference time domain; Graphene interband conductivity; Surface boundary condition;

I. INTRODUCTION

Graphene is a single layer of graphite atoms considered as in form of a two-dimensional, hexagonal lattice [1]. The graphene conductivity can be tuned by changing the chemical potential using gate electric and/or magnetic fields [1], [2]. Its capability to support highly confined surface plasmon polariton (SPP) makes a new platform of plasmonic metamaterial and transformation optic devices e.g., graphene micro-ribbon, graphene polarizer, graphene modulator [3]. Thus, the modeling of graphene is necessary to know the electro-magnetic (EM) behavior of those devices. Finite-difference time domain (FDTD) method is one of the most popular numerical methods to know the electro-magnetic (EM) behavior of those devices [4], [5]. So far, in the literature, four types of FDTD approaches have been proposed for modeling the graphene: 1) standard FDTD method [1], [6], [7], 2) the sub-cell FDTD method [8], [9], 3) surface boundary condition (SBC) [5], and 4) combination of vector wave finite-element time domain and FDTD method [10]. All the FDTD approaches in [1], [5], [7]–[10], have been proposed for only graphene intraband conductivity modeling up to far infrared frequency range. But, in the near infrared frequency range, interband term affects on dispersion relation for accurate SPP simulation [6]. In [6], conductivity of graphene sheet is considered as volumetric instead of surface conductivity. It requires extremely finer spatial grid and time steps [5]. Thus, it needs large memory resources and time for the simulation.

In this paper, SBC FDTD method has been used to model graphene conductivity in near infrared frequency band. Both intraband and interband conductivities are considered. Transmission and reflection coefficients have been calculated and also compared with analytical results. The effect of interband in near infrared frequency band has been investigated with numerical examples. Here, auxiliary differential equation (ADE) is also applied for frequency dependent graphene conductivity.

II. GRAPHENE CONDUCTIVITY MODELING

The conductivity of graphene is expressed by the Kubo formula [11]. The simplified formula is given by

$$\sigma_g = \sigma_{\text{intra}} + \sigma_{\text{inter}} \tag{1}$$

where, σ_{intra} is due to intraband contribution and σ_{inter} is due to interband contribution. The intraband conductivity is as follows [7], [12],

$$\sigma_{\text{intra}} = \frac{e^2 k_B T \tau}{\pi \hbar^2}\left(\frac{\mu_c}{k_B T} + 2\ln(e^{-\frac{\mu_c}{k_B T}} + 1)\right)\frac{1}{1 + j\omega\tau} \tag{2}$$

and the interband conductivity is as follows [6],

$$\sigma_{\text{inter}} = \frac{-je^2}{4\pi\hbar}\ln\left(\frac{2|\mu_c| - (\omega - j2\Gamma)\hbar}{2|\mu_c| + (\omega - j2\Gamma)\hbar}\right) \tag{3}$$

where, $\tau = 1/(\Gamma)$ is phenomenological electron relaxation time, ω is the angular frequency, e is the electron charge, T is the temperature, μ_c is the chemical potential, k_B is the Boltzman constant, and $\hbar$ is the reduced Planck's constant. Although, σ_{intra} is easily implemented into FDTD method, σ_{inter} cannot be easily incorporated into FDTD method. In [6], a parameterization of graphene conductivity has been developed

using Padé approximant to incorporate into FDTD method which is as follows,

$$\sigma_{\text{inter}}(\omega)=\frac{a_0+a_1 j\omega+a_2(j\omega)^2}{1+b_1 j\omega+b_2(j\omega)^2} \tag{4}$$

where, $a_0=-9.114\times10^{-28}$, $a_1=1.674\times10^{-20}$, $a_2=1.343\times10^{-36}$, $b_1=8.082\times10^{-17}$ and $b_2=2.148\times10^{-31}$.

Therefore, graphene conductivity including both intraband and interband can be expressed as follows

$$\sigma_g(\omega)=\frac{n_0+n_1 j\omega+n_2(j\omega)^2+n_3(j\omega)^3}{1+d_1 j\omega+d_2(j\omega)^2+d_3(j\omega)^3} \tag{5}$$

where, $n_0=a_0+\sigma_0$, $n_1=a_1+a_0\tau+b_1\sigma_0$, $n_2=a_2+a_1\tau+b_2\sigma_0$, $n_3=a_2\tau$, $d_1=b_1+\tau$, $d_2=b_2+b_1\tau$, $d_3=b_2\tau$, and

$$\sigma_0=\frac{e^2k_BT\tau}{\pi\hbar^2}\left(\frac{\mu_c}{k_BT}+2\ln(e^{-\frac{\mu_c}{k_BT}}+1)\right).$$

The graphene conductivity in (5) is new that is developed depending on Padé approximant in [6].

III. Graphene Conductivity in the SBC FDTD Method

A. Implementation in 1-D FDTD

A transverse electromagnetic (TEM) polarized plane wave is incident on graphene sheet. Graphene sheet is positioned at grid (k+1/2) as shown in Fig. 1. It allows a possibility of conduction current at the sheet. By applying surface boundary condition, magnetic fields at graphene sheet can be written as

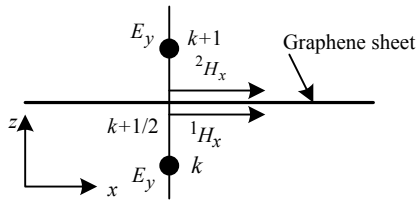

Fig. 1. A 1-D FDTD cell including graphene sheet [5].

$$^2H_x-{}^1H_x=\sigma_g E_y \tag{6}$$

where, ^1H_x and ^2H_x are the immediate magnetic fields at the down and up sides of the graphene sheet respectively. By putting the value of σ_g (6) becomes

$$\{1+d_1 j\omega+d_2(j\omega)^2+d_3(j\omega)^3\}(^2H_x-{}^1H_x)=\{n_0+n_1 j\omega+n_2(j\omega)^2+n_3(j\omega)^3\}E_y \tag{7}$$

Converting frequency domain to time domain $j\omega\rightarrow\partial/\partial t$, (7) becomes an ADE. Using central derivative at the time instant n-2 in that ADE, one obtains the following equation.

$$\begin{aligned}E_y^n(k+1/2)=&A_1E_y^{n-1}+A_2E_y^{n-2}+A_3E_y^{n-3}+A_4E_y^{n-4}-\\&B_1{}^1H_x^{n+1/2}+C_1{}^2H_x^{n+1/2}-B_2{}^1H_x^{n-1/2}+C_2{}^2H_x^{n-1/2}-\\&B_3{}^1H_x^{n-3/2}+C_3{}^2H_x^{n-3/2}-B_4{}^1H_x^{n-5/2}+C_4{}^2H_x^{n-5/2}\\&-B_5{}^1H_x^{n-7/2}+C_5{}^2H_x^{n-7/2}+B_6{}^1H_x^{n-9/2}-C_6{}^2H_x^{n-9/2}\end{aligned} \tag{8}$$

where, $A_1=(4n_3-2h^2n_1-4hn_2)/(2n_3)$,

$A_2=(8hn_2-4h^3n_0)/(2n_3)$, $A_3=(2h^2n_1-4hn_2-4n_3)/(2n_3)$,

$A_4=1$, $B_1=C_1=d_3/(2n_3)$, $B_2=C_2=(2hd_2-d_3)/(2n_3)$,

$B_3=C_3=(2h^3+4h^2d_1-2hd_2-2d_3)/(2n_3)$,

$B_4=C_4=(2h^3-4h^2d_1-2hd_2+2d_3)/(2n_3)$,

$B_5=C_5=(2hd_2+d_3)/(2n_3)$, and $B_6=C_6=d_3/(2n_3)$.

Here, the magnetic fields at every time step are approximated by the average value, e.g., $^1H_x^n=(^1H_x^{n+1/2}+{}^1H_x^{n-1/2})/2$ and spatial mesh, h=Δz is also considered. All values of fields are at (k+1/2) grid point. By discretizing the Faraday's law $\partial B/\partial t$= - $\Delta\times E$ at grid (k+1/2) [5], [12], we get,

$$\mu_1\delta_t^c\{^1H_x^n\}=\delta_z^b\{E_y^n(k+1/2)\} \tag{9a}$$

$$\mu_2\delta_t^c\{^2H_x^n\}=\delta_z^f\{E_y^n(k+1/2)\} \tag{9b}$$

where, μ_1 and μ_2 are the permeability of media to the down and up sides of graphene sheet and δ_t^c, δ_z^b, and δ_z^f are the central, backward and forward difference derivative approximations respectively [7], [12]. Rearranging (9), we get,

$$\begin{bmatrix}1 & -g_1\\ -g_2 & 1\end{bmatrix}\begin{bmatrix}^1H_x^{n+1/2}\\ ^2H_x^{n+1/2}\end{bmatrix}=\begin{bmatrix}F_1^n\\ F_2^n\end{bmatrix} \tag{10}$$

where, $g_1=\frac{C_1m_1}{1+m_1B_1}$, $g_2=\frac{B_1m_2}{1+m_2C_1}$, $m_1=\frac{2\Delta t}{\mu_1\Delta z}$,

$m_2=\frac{2\Delta t}{\mu_2\Delta z}$ and

$$\begin{aligned}F_1^n=&f_{e1}[A_1E_y^{n-1}+A_2E_y^{n-2}+A_3E_y^{n-3}+A_4E_y^{n-4}-E_y^n(k)]\\&+f_{h11}{}^1H_x^{n-1/2}+f_{h12}{}^2H_x^{n-1/2}+f_{u11}U\end{aligned} \tag{11a}$$

$$\begin{aligned}F_2^n=&f_{e2}[E_y^n(k+1)-A_1E_y^{n-1}-A_2E_y^{n-2}-A_3E_y^{n-3}-\\&A_4E_y^{n-4}]+f_{h21}{}^1H_x^{n-1/2}+f_{h22}{}^2H_x^{n-1/2}-f_{u22}U\end{aligned} \tag{11b}$$

where, $f_{e1}=\frac{m_1}{1+m_1B_1}$, $f_{e2}=\frac{m_2}{1+m_2C_1}$, $f_{h11}=\frac{1-B_2m_1}{1+m_1B_1}$,

$f_{h22}=\frac{1-C_2m_2}{1+m_2C_1}$, $f_{h12}=\frac{C_2m_1}{1+m_1B_1}$, $f_{h12}=\frac{B_2m_2}{1+m_2C_1}$,

$f_{u11}=\frac{m_1}{1+m_1B_1}$, $f_{u22}=\frac{m_2}{1+m_2C_1}$ and $U=-B_3{}^1H_x^{n-3/2}+C_3{}^2H_x^{n-3/2}-B_4{}^1H_x^{n-5/2}+C_4{}^2H_x^{n-5/2}-B_5{}^1H_x^{n-7/2}+C_5{}^2H_x^{n-7/2}+B_6{}^1H_x^{n-9/2}-C_6{}^2H_x^{n-9/2}$.

Form (10), updating equations for ^1H_x and ^2H_x at conducting surface are obtained.

B. *Implementation in 2-D FDTD*

For two dimensional problems, transverse magnetic (TM) mode (E_z, H_x, H_y) is implemented to get simulation results. A graphene conducting line is positioned at the y grid (j+1/2) parallel to the x axis as shown in Fig. 2. A pair of the tangential components (^1H_x, ^2H_x) of the magnetic field (H_x) is considered instantaneously due to the possibility of current and charge in graphene conducting line. By discretizing the Faraday's law $\partial B/\partial t = -\Delta \times E$ at the grid (i, j+1/2) just like 1-D case, we get,

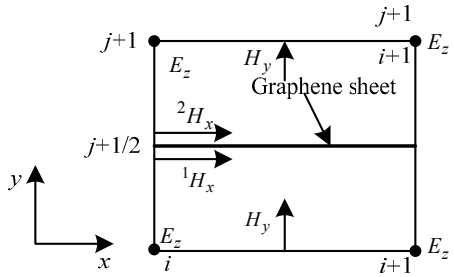

Fig. 2. A 2-D FDTD cell including graphene sheet.

$$\mu_1 \delta_t^c \{^1H_x^n\} = -\delta_y^b \{E_z^n(i, j+1/2)\} \quad (12a)$$

$$\mu_2 \delta_t^c \{^2H_x^n\} = -\delta_y^f \{E_z^n(i, j+1/2)\} \quad (12b)$$

E_z $(i, j+1/2)$ can be obtained from surface boundary condition and updating equations for ^1H_x and ^2H_x at conducting surface are obtained using (10) similar to 1-D case; where $F_1(i, j+1/2)$ and $F_2(i, j+1/2)$ are denoted by

$$F_1^n = f_{e1}[E_z^n(i,j) - A_1E_z^{n-1} - A_2E_z^{n-2} - A_3E_z^{n-3} - A_4E_z^{n-4}] + f_{h11}{}^1H_x^{n-1/2} + f_{h12}{}^2H_x^{n-1/2} + f_{u11}U \quad (13a)$$

$$F_2^n = f_{e2}[-E_z^n(i,j+1) + A_1E_z^{n-1} + A_2E_z^{n-2} + A_3E_z^{n-3} + A_4E_z^{n-4}] + f_{h21}{}^1H_x^{n-1/2} + f_{h22}{}^2H_x^{n-1/2} - f_{u22}U \quad (13b)$$

Fields at other grid points are obtained by using classical FDTD method.

IV. Numerical Analysis

Transmission (T) and reflection (Γ) coefficients are two important parameters in the propagation characteristics of electromagnetic fields. For 1-D FDTD, both coefficients are numerically obtained by calculating electric fields of both sides of graphene sheet. Electric fields are determined using Discrete Fourier Transform (DFT). Then, numerically obtained results are compared with the analytical results. Time step is selected as $\Delta t = \Delta z/(2c_0)$ to meet courant condition limit; where c_0 is the velocity of light and spatial mesh is Δz is set to $\lambda_{min}/15$. Analytically, transmission and reflection coefficients are calculated by $T = 2/(2+\eta_0\sigma_g)$ and $\Gamma = T-1$ respectively, where η_0 is the free space impedance [8], [10].

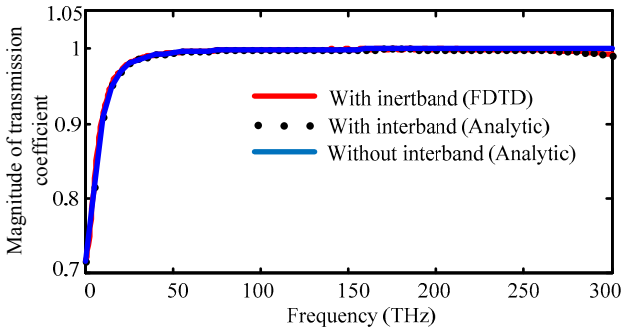

Fig. 3. Magnitude of transmission coefficients for a TEM wave including graphene sheet.

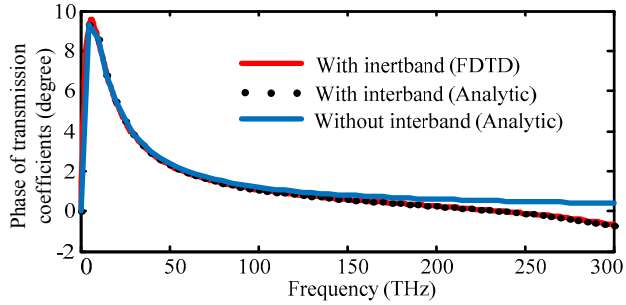

Fig. 4. Phase of transmission coefficients for a TEM wave incident of graphene sheet.

Fig. 3 and Fig. 4 show numerically and analytically obtained amplitudes and phases of transmission coefficients. Percentages of errors of amplitude and phase for transmission coefficient are 0.085% and 0.56% respectively at 1500 time steps.

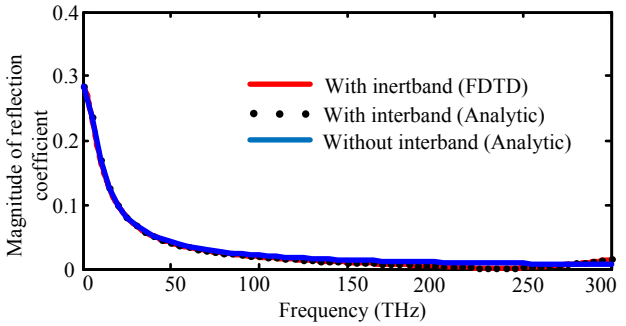

Fig. 5. Phase of transmission coefficients for a TEM wave incident of graphene sheet.

Similarly, the numerically and analytically obtained amplitude and phase of reflection coefficients for 1-D FDTD case are shown in Fig. 5 and Fig. 6 respectively. Figs. 3–6 show the strong agreement between the FDTD results and analytically obtained results. Moreover, the effect of interband conductivity in near infared frequency range is observed, especially in the phase of transmission and reflection coefficients.

For 2-D FDTD case, the problem is considered with 200×200 cells as shown in Fig. 8, where $\Delta x=\Delta y=80$ nm. Perfect match layer (PML) is used to truncate the domain. The pattern of E_z can be obtained by applying DFT at the points positioned away from an equal distance. Fig. 8 shows a difference in the electric field patterns with and without considering interband conductivity.

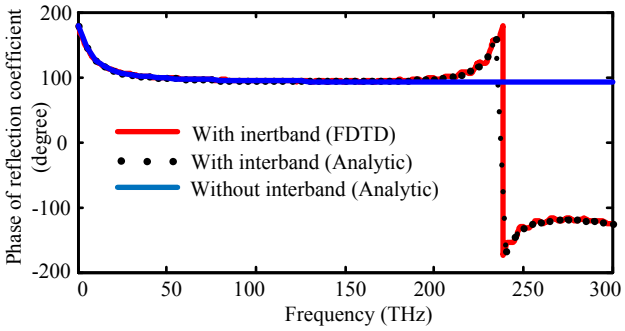

Fig. 6. Magnitude of reflection coefficients for a TEM wave incident of graphene sheet.

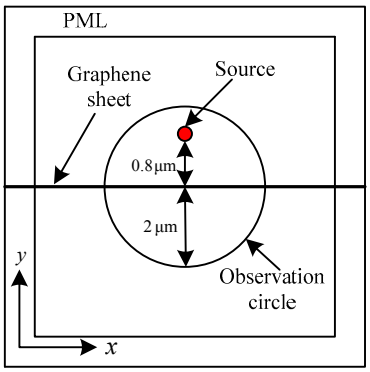

Fig. 7. Observation of scattering by graphene sheet [8].

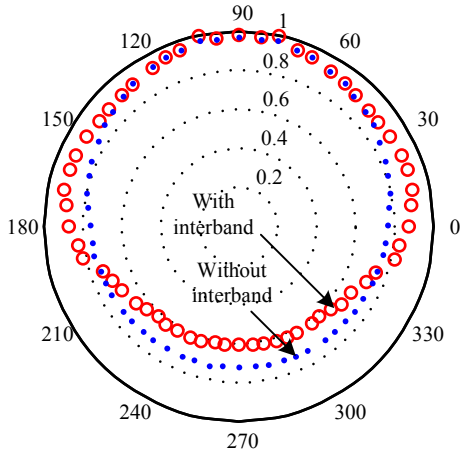

Fig. 8. Normalized pattern of E_z at the frequency, f=215 THz.

Here, for all simulations, the physical values are set at chemical potential, μ_c=0.6 eV temperature, T=300 K and phenomenological scattering rate, Γ=11 meV/$\hbar$. Gaussian pulse is used as source. Air is considered as media of two sides of graphene sheet for simulation.

V. Conclusion

This paper presents a method which shows the effect of interband conductivity in near frequency region by SBC FDTD method. In addition, ADE method is used to implement frequency dependent graphene conductivity in FDTD method. The validation of propose method has been done by comparing the results obtained from FDTD method and analytical method. The strong agreement between analytical and numerical results is observed. A significant change in radiation pattern of electric field is also obtained in near infrared frequency range in case of interband conductivity. No instability has been found during simulation.

References

[1] H. Lin, M. F. Pantoja, L. D. Angulo, J. Alvarez, R. G. Martin, and S. G. Garcia, "FDTD modeling of graphene devices using complex conjugate dispersion material model," *IEEE Microw. Wireless comp.s Lett.*, vol. 22, no.12, pp. 612–614, Dec. 2012.

[2] G. W. Hanson, "Dyadic greens functions for an anisotropic, non-local model of baised graphene," *IEEE Trans. Antennas Propag.*, vol. 56, pp. 747–757, Mar. 2008.

[3] A. Vakil, and N. Engheta, "Transformation optics using graphene," *Science*, vol. 332, pp 1291–1294, 2011.

[4] Y. Shao, J. J. Yang, and M. Huang, "A review of computational electromagnetic methods for graphene modeling," *Inter. J. Antennas Propag.*, vol. 2016, no. 7478621, 2016.

[5] V. Nayyeri, M. Soleimani, and O. M. Ramahi, "Modeling graphene in the finite-difference time-domain method using a surface boundary condition," *IEEE Trans. Antennas Propag.*, vol. 61, no. 8, pp. 4176–4182, Aug. 2013.

[6] A. Mock, "Padé approximant spectral fit for FDTD simulation of graphene in the near infrared," *Optical Mater. Express*, vol. 2, no. 6, pp. 771–781, 2012.

[7] G. D. Bouzianas, N. Kantartzis, T. Yioultsis, and T. Tsiboukis, "Consistent study of graphene structures through the direct incorporation of surface conductivity," *IEEE Trans. on Magn.*, vol. 50, no. 2, pp 161–164, Feb. 2014.

[8] X. Yu, and C. D. Sarris, "A perfect match layer for sub-cell FDTD and applications to the modeling of graphine structures," *IEEE Antennas Wireless Propag. Lett.*, vol. 11, pp. 1080–1083, 2012.

[9] G. D. Bouzianas, N. Kantartzis, C. Antonopoulos, and T. Tsiboukis, "Optimal modeling of infinite graphene sheets via a class of generalized FDTD scheme," *IEEE Trans. Magn.*, vol. 48, no. 2, pp 379–382, Feb. 2012.

[10] F. Afshar, A. A. Sharbaf, and D. D. Giannacopoulos, "A provably stable and simple FDTD formulation for electromagnetic modeling of graphene sheet," *IEEE Trans. Magn.*, vol. 52, no. 3, pp. 7203504–7203504, Mar. 2016.

[11] G. W. Hanson, "Dyadic greens functions and guided surface waves for a surface conductivity model of graphene," *J. Appl. Phys.*, vol. 103, no. 064302, 2008.

[12] M. B. Hossain, S. Muktadhir, and M. M. Rana, "Multi-structural optical devices using graphene tri-layers sheets," *Optik*, vol. 127, pp. 584–585, 2016.

International Conference on Electrical, Computer & Telecommunication Engineering (ICECTE)
8-10 December 2016, Rajshahi-6204, Bangladesh

Face Recognition System Using Soft-output Classifier Fusion Method

Rizoan Toufiq,[1,*] and Md. Rabiul Isalm[1]

[1]Department of Computer Science & Engineering, Rajshahi University of Engineering & Technology
Rajshahi, Bangladesh

[*]rizoantoufiq@yahoo.com

***Abstract*—The objective is to develop a dynamic decision selection method for face recognition system where minimum number of information about face are available to take correct decision. Statically we can develop such system where Bayesian method has been preferred in most case. It is better to fuse two or more classifier whose outputs are not highly correlated. In this work, the output of two classifiers systems are not so much correlated. We considered more than one decision for each classifier so that the correlations of the output are varied. It has been proved that the Bayesian optimal decision boundaries can be produced decision in fusion technique. It also has been proposed two methods to determine the Bayesian optimal decision are performed correctly in different database. We have proposed a different technique to calculate prior and posterior probability. Finally the fusion decision has been taken based on the probability values and it has been shown that the performance of Bayesian fusion techniques is better among the individual classifier technique. This fusion technique has been used in decision level and selected a class which is considered as correct output. Finally we have compared the performance among different classifier output and this soft-output classifier fusion method.**

Keywords— Face Recognition system, Dynamic Decision system, Bayesian Fusion technique, Classifier Fusion System, Fuzzy/Soft output

I. INTRODUCTION

The objective of this decision support systems (DSS) based face recognition is to create a correct decision. We emphasize to use a minimum amount of input data and take correct decision based on that information. In face recognition system, it is crucial to take minimum information to derivation of correct decision in a reasonable time. In each classifier has its own learning error and recognition error. In soft-output decision system reduces this error rate and enhances the performance of the recognition system. It is assumed that increase the performance of learning technique enhance the performance of recognition rate for individual classifier [1]. According to this approach, it is difficult to develop a better individual classifier which provides the more accurate result. The solution of the problem will be combined existing well performing methods using soft-output classifier fusion method named Bayesian fusion, hoping that better results will be achieved. Fusion of data or information can be carried out on different level, most of the case it occurs in data label, feature label or classifier label. In this work, fusion will be considered in classifier label in order to achieve the better performance and accuracy rate.

In recent, face recognition system is the most popular system where its permanence, universality, performance, collectability, acceptability and circumvention are very important to support our reliable system. In 2004, face identification system from a video has been proposed. In this work the Dempster-Shafer theory that is a decision support system has been used to improve the performance of face identification. A frame-based approach was used where faces were detected and identified independently in each frame. The concepts of soft labels and granular computing also have been presented in a multispectral face recognition application [2, 3]. A face recognition system based on fuzzy data fusion also a popular technique to enhance the performance [4]. In 2013, a face recognition system has been described where two novel preprocessing techniques, viz., Eccentricity-Range based Background Removal and Multi-Scaled Image Fusion, has been proposed to improve the performance of a face recognition system [5]. In recent, Independent Component Analysis (ICA), Locality Preserving Projections (LPP), Minimum Average Correlation Energy (MACE) Gabor Filters, Score Level Fusion Techniques (SLFT) have been developed and analyzed for face recognition in the presence of various noises and blurring effects [6]. Feature fusion method has been implemented in face recognition system to increase the performance of face recognition system. Here linear regression analysis also has been used to extract frequency features of image to recognize different individual face [7, 8]. There are many other systems i.e. robust face recognition, a local-based illumination insensitive face recognition algorithm, a hyperspectral face recognition system, proposed to enhance the performance of recognition stage. [9-11]. In recent, deferent type of multi-classifier fusion method based on soft-output has been developed. A novel confidence index based block linear regression classification method has been proposed where images are divided into blocks, and each block is identified using the linear regression classifier separately. Finally a confidence index model has been developed to measure the recognition confidence of each block, and the final decision has been achieved by aggregating individual results with the designed Bayesian decision fusion algorithm [12]. Fusion of multi-modalities also has been performed at the score level based on Bayesian analysis to improve the accuracy [13]. It also has been used on both local and holistic information to remove the unnecessary features [14]. A Multimodal gender recognition based on Bayesian hierarchical model has been

978-1-5090-5785-6/16/$31.00 ©2016 IEEE

experimented on the fingerprint and face image database and the effectiveness of this system has been verified for both the feature representation and generative modal [15]. A temporal Bayesian fusion has been developed for continuous real-value estimation of valence, arousal, power, and expectancy dimensions of affect by combining video, audio, and lexical modalities [16].

In this work, we used Bayesian framework technique to improve the performance of face recognition system where more than one face has been selected by each classifier and each assigned some probabilistic value, which is called soft output. First, methodology has been describe include related feature selection method and different classifier technique. After this section, we will discuss about Bayesian fusion technique which is the main part of this work. Then the implementation process has been described with experimental result. Finally we will discuss about our findings and the conclusion of our work.

II. Outlines For Methodology

The proposed system has two different phases, one is training and classifying the database images and test images by different classifiers and other is combined the output of the classifiers using soft-output classifier fusion method i.e. Bayesian fusion method.

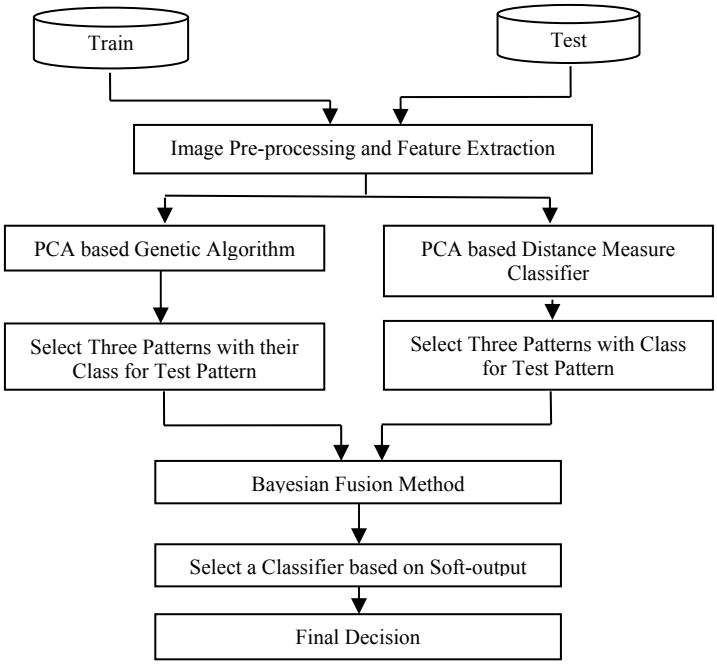

Fig. 1 Face Recognition System Using Bayesian Fusion Method.

First, we focus on image pre-processing technique where region of interest are located. The features of facial image are tried to extract in a popular analytical processes i.e. PCA. Then reduced featured has been used in training stage. For the purpose of classification, we implement two different classifiers named Genetic algorithm and PCA based distance classifier. Finally, Unknown images are taken as input and the feature vector has been extracted in similar approach. Then the unknown face features are plotted on face space and compared with the classified facial dataset. Finally each classifier generates an output set. This output set are fused using Bayesian fusion method. Most accurate class assigned for test probe has been selected and the output of this class has been accepted as final result.

In this system, we select face pattern with their class using two different classifiers for a test pattern. Then we calculate the probability how the test pattern are similar to each class pattern. Finally the class for the unknown face pattern has been selected which pattern is most likely with unknown pattern.

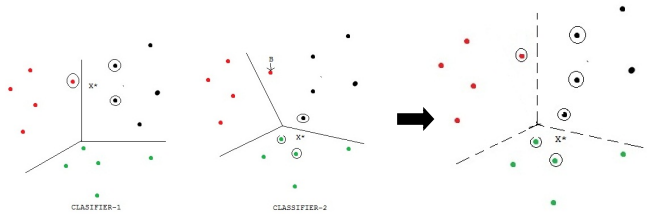

Fig. 2 Classifier-1 and Classifier-2 assigned three patterns with class

In fig.2, we see that B pattern is incorrectly classifier by classifier 2. Every classifier has been assigned three patterns with their class for an unknown pattern X*. Finally we determine that X* is belongs to i-th class using by bayesian fusion method. This classifier shape is dynamically changed for different unknown pattern.

A. Image Pre-processing and Feature Extaction

In this work, ORL facial database has been used where images has been taken against a dark homogeneous background with the subjects in an upright, frontal position, with tolerance for some tilting and rotation of up to about 20 degrees. [17].

Fig. 3 Facial databases (some sample images)

In this work, we have used nonlinear spatial filter technique i.e. median filter which is a used to remove noise typically in pre-processing step. It reduces noise but preserves edge of digital image [18, 19]. Finally we used PCA technique to find out the reduce features from the face images. The pixels with the largest variation between images have the most influence on the principal component [20-22].

B. Learning Techniques

First we discuss about the PCA base distance measure classifier technique where Euclidean distance measure technique has been used. Let the calculated weight vector of i-th train image is Ω_i and the calculated weight vector of test image is Ω then Euclidean Distance Measures can be used to classify the test image.

$$\lambda_i = \min\|\Omega - \Omega_i\| \quad (1)$$

We select the minimum value of λ and the corresponding

trained image is selected as resultant image for the test probe image. In genetic algorithm, we can generate solutions for optimization problems by natural selection, such as inheritance, mutation, selection, and crossover. Here fitness value is used to reflect the degree of "goodness" of the chromosome for solving the problem [23, 24].

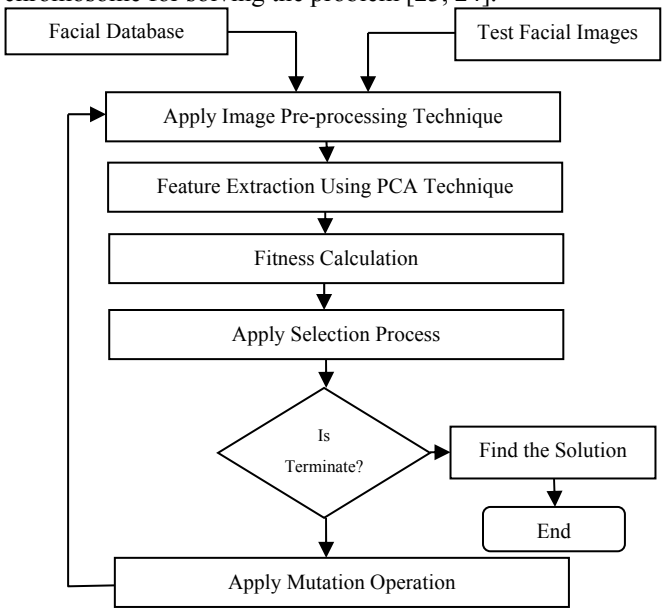

Fig. 4 Block diagram of face recognition system using PCA based GA

Feature vector has been calculated using PCA technique. PCA which is statically technique applied to reduce the dimension. Distance of each pattern from unknown pattern has been calculated. This distance value has been used to develop an objective function and converts this selection process as a maximization problem. Most fitted images are selected for next generation. Mutation operation has been applied on the present generation members. Finally one image has been selected based on the fitness value. Objective or Fitness function has been defined as

$$\lambda_i = \sqrt{(\Omega_i)^2 - (\Omega_r)^2} \quad (2)$$

$$F_i = \frac{1}{\lambda_i} \quad (3)$$

Roulette- wheel selection process has been applied to select the parent of the next generation. In this selection process, probability of fitness values and cumulative probability for a discrete random variable x has been calculated by the following equation.

$$P(x_i) = \frac{F(x_i)}{\overline{F}(x)} \quad (4)$$

$$C(x_i) = \sum_{x_i < x} P(x_i) \quad (5)$$

Fig. 5 Region of facial image focused on each generation

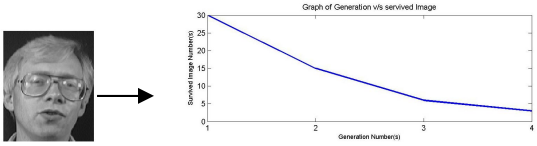

Fig. 6 Sample Output of GA

In Fig.5, the mutated pixel of the train images and test images in each generation is shown. In Fig. 6, it has been shown, the number of images survived in each generation. Finally we took three survived images for a single test images.

C. Soft-output Classifier Fusion Method

There are different kinds of fusion methods operated on classifiers. Here we used Bayesian fusion method to select the best class for a test image according to selected images by genetic algorithm and distance measure classifier. Let X* is a test pattern and X represent the images those are used in training stage. Let ω_i represents the i-th class of a pattern then we can calculate the likelihood of X* for the j-th classifier ,C_j

$$LH_j(X^* | X^* \varepsilon \omega_i) = n(X | C_j(X) = \omega_i) / n(X) \quad (6)$$

Here i = 1, 2, 3…..M, M represents the total number of class. Then we calculated Posterior Probability of X* being class ω_i for each classifier. Finally we calculated the average of these Posterior Probability of X* being class ω_i for j-th classifier

$$Poserior_j(X^* \varepsilon \omega_i) = LH_j(X^* | X^* \varepsilon \omega_i) * P(X | X \varepsilon \omega_i) \quad (7)$$

$$A(X^* \varepsilon \omega_i) = \frac{\sum_{j=1}^{K} Posterior_j(X^* \varepsilon \omega_i)}{K} \quad (8)$$

Here K represents the total Number of classifiers i.e. k =2.

Finally we has been selected the class which has the maximum posterior probability i.e.

$$\omega = Max_{1 \le i \le M}(A(X^* \varepsilon \omega_i)) \quad (9)$$

So the test pattern X* is belong to ω class.

III. Experimental Result and Performance Analysis

The ORl face database has been used in our experiment to compare our result. We select 10 persons; each has 10 individual facial images. We trained 3 randomly selected images per person and tested other 7 facial images per person. We showed the performance of the soft-output fusion method (i.e. Bayesian fusion method) comparing to the two individual classifiers. To contrast the other individual classifier, the fusion method performs better among them in every case. Here we select three best output of individual classifier to calculate the probability and combine the output. In this work, the correlation of the output of two classifiers is below 50% (on average) and the best class is selected for a test image that is truly belonging to it. Here the probability of correctly selected face for a test image belongs to best three outputs in each

classifier is high, so the finally chosen face will be correct with high probability. For this reason, the individual classifier wrongly selected the class for an unknown pattern in some case but in this same domain, the Bayesian fusion method gave correct class for the unknown face pattern. The performance of the classifiers and fusion classifier are given in tab. I.

TABLE I. PERCENTAGE ACCURACY OF THE PROPOSED BAYESIAN FIUSION METHOD. FOR THE SAKE OF COMPARISON THE PERFORMANCE OF OTHER CLASSIFIER ARE ALSO SHOWN

Performance of PCA based Distance Measure Classifier	Performance of PCA based GA Classifier	Performance of Soft-output Fusion Method
84.29%	88.57%	95.72%

IV. CONCLUSION

Different methods performing on data should produce different errors. Combination of such multiple experts should reduce overall classification error and as a consequence emphasis correct outputs. Finally it will be assumed that the fusion technique will perform better comparing among the individual classifier based face recognition system. As shown in above table, the face recognition system has been trained with 30 images and different 70 facial images have been used as test images. The recognition rate of the soft-output classifiers fusion methods named Bayesian fusion method is better than individual classifiers. The recognition rate of GA and EDM are 88.57% and 84.29% respectively when we trained 30 images. Whereas the recognition rate of soft-output fusion method is 95.72%. Here fusion method focuses only the maximum posterior probability of a class assigned by individual classifier belongs to test image.

REFERENCES

[1] G. Giacinto and F. Roli, "Methods for dynamic classifier selection", *International Conference on Image Analysis and Processing, 1999.,* pp. 659-664, doi: 10.1109/ICIAP.1999.797670.

[2] Foucher, S. & Gagnon, L. "Face recognition in video using Dempster-Shafer theory", *IEEE International Conference on Acoustics, Speech, and Signal Processing, 2004. Proceedings. (ICASSP '04)*, vol.3, no., p.iii,545-8 vol.3, 17-21 May 2004,doi: 10.1109/ICASSP.2004.1326602.

[3] Singh, R., Vatsa, M., and Noore, A., "Multiclass mv-granular soft support vector machine: A case study in dynamic classifier selection for multispectral face recognition", *Pattern Recognition, 2008. ICPR 2008*, p.1- 4, 2008, doi: 10.1109/ICPR.2008.4761877.

[4] Meng F., Zhao Y. and Yue F., "A Face Recognition Method Based on Fuzzy Data Fusion", *Computational Intelligence and Industrial Application, 2008*, vol.1, p.351-354, 19-20 Dec. 2008, doi: 10.1109/PACIIA.2008.320.

[5] Prabhu N.S., Kesari T.N., Manikantan K. and Ramachandran S., "Face recognition using Eccentricity-Range based Background Removal and Multi-Scaled Fusion as pre-processing techniques", *Nirma University International Conference on Engineering*, p.1-6, 28-30 Nov. 2013 doi: 10.1109/NUiCONE.2013.6780132.

[6] Fernandes S.L. and Bala G.J., "Recognizing facial images using ICA, LPP, MACE Gabor Filters, Score Level Fusion Techniques", *International Conference on Electronics and Communication Systems (ICECS), 2014* , p.1-5, 13-14 Feb. 2014, doi: 10.1109/ECS.2014.6892552.

[7] Toufiq, R. and Islam, M.R., "Face recognition system using PCA-ANN technique with feature fusion method", *Electrical Engineering and Information & Communication Technology (ICEEICT), 2014 International Conference on* , pp.1-5, 10-12 April 2014, doi: 10.1109/ICEEICT.2014.6919110.

[8] Li Z., Zhang Q., Duan X. and Zhao F., "Face recognition based on regression analysis using frequency features", *4th IEEE International Conference on , Information Science and Technology (ICIST), 2014* , p.192-195, 26-28 April 2014, doi: 10.1109/ICIST.2014.6920363.

[9] Liu L., Fieguth P., Zhao G. and Pietikainen M., "Extended local binary pattern fusion for face recognition", *IEEE International Conference on Image Processing (ICIP), 2014*, vol., no., p.718-722, 27-30 Oct. 2014,doi: 10.1109/ICIP.2014.7025144.

[10] Nikan S. and Ahmadi M., "Local gradient-based illumination invariant face recognition using local phase quantisation and multi-resolution local binary pattern fusion", Image Processing, IET , vol.9, no.1, pp.12-21, 2015, doi: 10.1049/iet-ipr.2013.0792.

[11] Metallinou A., Lee S. and Narayanan, S., "Decision level combination of multiple modalities for recognition and analysis of emotional expression", *IEEE International Conference on , Acoustics Speech and Signal Processing (ICASSP), 2010*, p.2462-2465, 14-19 March 2010, doi: 10.1109/ICASSP.2010.5494890.

[12] Xu Y. and Wu H., "Decision fusion for block linear regression classification based on confidence index", *First Asian Conference on Pattern Recognition (ACPR), 2011* p.199,203, 28-28 Nov. 2011, doi: 10.1109/ACPR.2011.6166708

[13] Zhang G., and Wang Y., Hierarchical and discriminative bag of features for face profile and ear based gender classification, *International Joint Conference on Biometrics (IJCB), 2011* , p.1-8, 11-13 Oct. 2011, doi: 10.1109/IJCB.2011.6117590.

[14] Asteriadis, S., Karpouzis, K. and Kollias, S., "Robust validation of Visual Focus of Attention using adaptive fusion of head and eye gaze patterns", *IEEE International Conference on Computer Vision Workshops (ICCV Workshops), 2011*, p.414-421, 6-13 Nov. 2011, doi: 10.1109/ICCVW.2011.6130271.

[15] Xiao-Yuan X., Bencheng Y., Zhifeng W. and Zhihao Y., "A Multimodal Gender Recognition Based on Bayesian Hierarchical Model, Intelligent", *5th International Conference on Human-Machine Systems and Cybernetics (IHMSC), 2013*, vol.1, p.410-413, 26-27 Aug. 2013, doi: 10.1109/IHMSC.2013.104

[16] Savran, A., Cao H., Nenkova A. and Verma, R., "Temporal Bayesian Fusion for Affect Sensing: Combining Video, Audio, and Lexical Modalities," *IEEE Transactions on Cybernetics*, 2014, p.1, doi: 10.1109/TCYB.2014.2362101

[17] AT&T "The Database of Faces" (formerly "The ORL Database of Faces") Collected from the web documentation : http://www.cl.cam.ac.uk/research/dtg/attarchive/facedatabase.html.

[18] Rafael C. Gonzalez and Richard E Woods (2002), *Digital Image Processing*, Second edition, Prentic Hall.

[19] William K. Pratta(2001), *Digital Image Processing,* 3rd Edition, A Wiley-Interscience Publication, John Wiley & Sons, Inc.

[20] Pearson K., "On lines and planes of closest fit to systems of points in space," Philosophical magazine,2, pp. 559-572, 1901.

[21] Matthew Turk and Alex Pentland, "Eigenfaces for recognition," Journal of Cognitive Neuroscience, Vol. 3, No. 1, pp. 71–86 , 1991.

[22] Peter N. Belhumeur, Joao P. Hespanha, and David J. Kriegman, "Eigenfaces vs. Fisherfaces: recognition using class specific linear projection," IEEE Transactions on Pattern Analysis and Machine Intelligence, Vol. 19, No. 7, July 1997.

[23] David E. Goldberg, "Genetic algorithms in search, optimization and machine learning", Aaison-Wesley Professional, 1989.

[24] S, Rajasekaran and G. A. Vijayalakshmi pal, "Neural networks, fuzzy logic, and genetic algorithms synthesis and applications," PHI Learning Pvt. Ltd, ISBN- 81-203-2186-3, 2004.

International Conference on Electrical, Computer & Telecommunication Engineering (ICECTE)
8-10 December 2016, Rajshahi-6204, Bangladesh

Transformational Generative Grammar (TGG): An Efficient Way of Parsing Bangla Sentences

Mohammad Kamrul Huq Maroof, Lamia Alam and Mohammed Moshiul Hoque*
Dept. of Computer Science & Engineering
Chittagong University of Engineering & Technology,
Chittagong, Bangladesh.
Email: kamrulhuqmaroof@gmail.com, lamiacse09@gmail.com and moshiulh@yahoo.com*

***Abstract*— Natural language processing (NLP) refers to the ability of systems to process sentences in a natural language such as Bangla, rather than in a specialized artificial computer language. Computer processing of Bangla language is a challenging task due to its varieties of words formation and way of speaking. The same meaning can be expressed in different ways which is a great challenge to face for translation by an automatic machine translation system. With the advent of internet technology and e-commerce, the demand of automatic machine translation has been increased. Parsing is essential for any type of natural language processing. Parsing of Bangla natural language can be used as a subsystem for Bangla to another language machine aided translation. A parser usually checks the validity of a sentence using grammatical rule. In this paper, we propose a set of transformational generative grammar (TGG) in conjunction with phrase structure grammar to generate parse tree and to recognize assertive, interrogative, imperative, optative and exclamatory sentences of Bangla language. It is applicable for many sentences that cannot be parsed using only phrase structure grammars. The process involves analysis of Bangla sentence morphologically, syntactically where tokens and grammatical information are passed through parsing stage and finally output can be achieved. A dictionary of lexicon is used which contains some syntactic, semantic, and possibly some pragmatic information. We have tested our system for different kinds of Bangla sentences and experimental result reveals that the overall success rate of the proposed system is 84.4%.**

Keywords— natural language processing; machine translation; lexical analysis; syntactic analysis; transformational generative grammar; parse tree; lexicon.

I. INTRODUCTION

Bangla is the native language of millions of Bangladeshi people. Bangla is spoken by about 210 million people of Bangladesh and two states of India [1]. Today, most of the computer based resources and technical journals are in English. Due to the language barrier, the common masses face difficulties to obtain the optimum benefits out of the vast store house of information through internet. Bangla Language Processing (BLP) can help the way to remove this barrier. The success of BLP may have a huge impact particularly to learn and use information and communications technology (ICT) in Bangla for the common people. Without computerization of the language, it can't be achieved. Today internet communication is emerging rapidly. In this revolution, if Bangla language is not properly digitized, this language can't cope with the entire world.

Syntactic analysis is one of the most important phases in NLP. The result of syntactic analysis yields a syntactic representation in a grammar; this form is often displayed in a tree diagram or a particular way of writing it out as text. Sequences of words are transformed into structures that show how the words relate to each other in this analysis. It verifies the validity of a sentence of natural language. Syntactic analysis uses grammar rules such as Context-free grammars (CFG), Context-sensitive grammars (CSG), and Transformational generative grammar (TGG) for identifying whether an input sentence structure is correct or not. An input sentence is separated into phrases and the phrases are separated into tokens which are the constituent part of the sentence.

TGG as the name suggests that the grammar it provides is both transformational and generative. Transformation is a method of stating how the structures of many sentences in languages can be generated or explained formally as the result of specific transformations applied to certain basic sentence structures. The other characteristics of TGG are that it is generative. In other words, a grammar must generate all and only the grammatical sentences of a language. To generate is thus to predict what can be sentences of the language or to specify precisely what are the possible sentences of the language

The main contribution of this work is to develop an effective parser that can parse the five types of Bangla sentences such as, assertive, interrogative, imperative, optative and exclamatory sentences by proposing a set of TGG rules.

II. RELATED WORK

A significant number of parser was developed previously which can be mainly categorized into three categories such as CFG Based Parsing, CSG Based Parsing and TGG base Parsing.

978-1-5090-5785-6/16/$31.00 ©2016 IEEE

Some works have been done in syntax analysis Bangla simple sentences using CFG in [1-6]. In [1,2], a comprehensive approach for Bangla syntax analysis was developed where a formal language is defined as a set of strings. A parsing methodology for Bangla natural language sentences is proposed in [3] and shows how phrase structure rules can be implemented by top-down and bottom-up parsing approach to parse simple sentences of Bangla. In [4,5] a predictive parser was introduced which is effective for detecting a paragraph contains of almost all types of traditional and non -traditional Bangla sentences. The accuracy rate was in between 70-80%. In [6], English to Bangla machine translation (MT) system was built using context free grammar (CFG) which was able to translate only assertive sentence.

Quite a few works have been done using CSG. Among them, the most notable is a method to analyze syntactically Bangla sentence using context-sensitive grammar rules in [7,8]. The parser developed in [7] accepted almost all types of Bangla sentences, including simple, complex and compound sentences and then interpret the input Bangla sentence into English using the NLP conversion unit. But the limitation of that work was it couldn't handle the ambiguity of a sentence. In the work [8], 28 decomposition rules were used and the success rate was around 90%. It proposed a technique to parse Bangla sentences in a new approach using context-sensitive grammar rules and then convert them to English by NLP conversion unit. The principal goal was to design a parser that is capable of accepting all types of Bangla sentences, from the structural viewpoint. Arefin et. al proposed a set of CSG's to parse the Bangla sentences, including assertive, interrogative and imperative [8]. The proposed framework can parse Bangla of sentences with over 80% accuracy, but when sentence length increases the success rate decreases.

TGG based parsing is still a new concept to the natural language processing. Only a single work [9] relates to this type of parsing. In that work, they dealt with assertive sentence, interrogative sentence and imperative sentence. But in their work, they focused solely on the transformational aspects of TGG rather than handling variation of a sentence, besides, they didn't implement the parser for those TGG rules which confined their work to the theoretical concept only.

In [10] authors proposed a structure for detecting Bangla grammar which recognizes correct Bangla sentences and rejects incorrect ones based on Head-Driven Phrase Structure Grammar (HPSG). They used the Linguistic Knowledge Building (LKB) system for implementing their designed Bangla Grammar and it works only for simple assertive sentences.

In contrast to these, we proposed a set transformational generative grammar which is applicable for many usable sentences that cannot be parsed using only phrase structure grammars. In this paper, we developed a framework for the parser to parse five types of Bangla Sentence based on intonation i.e. assertive, interrogative, imperative, optative and exclamatory sentence. We considered simple sentences only in this paper.

III. PROPOSED SYSTEM

The proposed Bangla natural language parser is shown in fig. 1. The proposed parser module is capable of parsing of five types of Bangla sentence based on purpose, i.e. assertive, interrogative, imperative, optative and exclamatory sentences in syntactic pattern respectively. Details processing of this sentence by using this module is given in the following subsections.

A. Input sentence

Bangla sentences are taken as input for the proposed framework. In this system, only assertive, interrogative, imperative, optative and exclamatory sentences are considered as input for implementation.

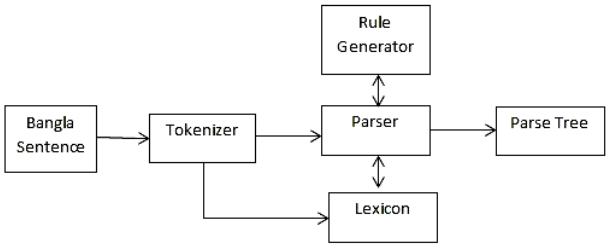

Fig. 1. Proposed Parser

B. Tokenizer

Tokenizer is the program module that accepts a sentence to be parsed as an unbroken string and breaks it into individual words called tokens. Tokens are stored in the list for further access. The token is then checked into the lexicon for the validity. From input sentence, tokenizer will generate tokens. For example:

Input Sentence: একটি মেয়ে বই পড়ছে

Output of tokenizer: ("এক", "টি", "মেয়ে", "বই", "পড়ছে")

The outputs of tokenizer are used as input of parsing to get the source language structure.

C. Lexicon

A lexicon is a dictionary of words where each word contains some syntactic, semantic, and possibly some pragmatic information. The information in the lexicon is needed to help determine the function and meanings of the words in a sentence. The entries in a lexicon could be grouped and given by word category (by determiner, nouns, verbs, and so on), and all words contained within the lexicon listed within the categories to which they belong. Entries in a dictionary will be equivalent to collections of attributes and values (i.e. features).

D. Rule Generator

The rule generator generates a set of phrase structure (PS) rules that relate to the sentence structure. List of used rule of Bangla to parse different type of sentences are given in table I.

E. Parser

Parsing is a process of taking tokens of input sentence and producing a parse tree or structural representation (SR) according to TGG rules.

1) Parsing Algorithm

The input Bangla sentence is parsed by bottom-up parsing. The steps are given below:

Step-1: The input string is separated into tokens and tokens are stored in a list for further access. For example, Bangla sentence "একটি মেয়ে বই পড়ছে" will be tokenized in to "এক", "টি", "মেয়ে", "বই", and "পড়ছে".

TABLE I. LIST OF PS RULES

Rule No.	TGG Rules	Example
1.	S→NP VP	রহিম পড়ছে
2.	NP→N_{animal}/N_{object}/$N_{creator}$	ছেলে/বই/আল্লাহ
3.	NP→(Det) NP	একটি বল
4.	NP→NP (Det)(Biv)	বলটি,স্কুলে,লোকটি কে
5.	NP→NP Biv NP	আমার বই
6.	Det→(Qtfr) Art	দুইটি, টি
7.	NP→ AP NP (EM)	সুন্দর পাখি
8.	NP→Person	সে, আমি
9.	Person→FP/SP/TP	আমি/তুমি/সে
10.	SP→SPHF/SPNHF/SPP	তুমি/ আপনি/ তুই
11.	TP→TPHF/TPNHF	সে, তারা / তিনি, তাঁরা
12.	VP→(IW)(NP) VF	ফুটবল খেলে
13.	VF→VR AUX (IM)	খেয়েছ, খেয়েছ?"
14.	Aux→ Aspect Tense Con	খেয়েছিলাম
15.	Aspect→ Imperative/Indefinite/Continuous/Perfect	
16.	Tense→ Past/ Present/Future	করলাম, করেছিলাম,করব
17.	Con→Con-FP/Con-SPHF/Con-SPNHF/Con-SPP/Con-TPHF/Con-TPNHF	ই(করি),এন,উন(করেন/করুন),অ, ও (কর/করো)
18.	NP→Null	
19.	NP→ (Adj) NP	গভীর সমুদ্র, বিশাল আকাশ
20.	VP→VF VF	খেলতে □াও, খেতে আসো
21.	VF→ VR Biv	খেতে, খেয়ে, □তে, খেলে, খেলতে
22.	AP→Ad Ads	কী চমৎকার, আশ্চর্য সুন্দর

[Abbreviations: S: Sentence, NP: Noun phrase, N: Noun, PN: Pronoun, VP: Verb phrase, VF: Verb form, V: Verb, Qntfr: Quantifier, PP: Preposition, Biv: Bivokti (inflection), AP: Adjective phrase, Adj: Adjective, Con: Concord, Aux: Auxiliary, Det: Determiner, Gr: Gerund, IW: Interrogative word, IM:Interrogative marker, FP: First Person SP: Second Person, TP: Third Person, SPNHF: Second person non-honorific , SPHF: Second Person Honorific, SPP: Second person pejorative, TPHF: Third person non-honorific , TFNHF: Third person honorific]

Step-2: The tokens are checked in the lexicon for the validity. Tokens ("এক", "টি", "মেয়ে", "বই", "পড়ছে") will be checked for validity

Step-3: The tokens are matched with the grammar. If a rule whose right hand side matches with a token, then the token is assigned with the appropriate category. This is equivalent to looking up the words in Bangla dictionary. For example, Qtfr->এক, Art->টি, TPNHF ->মেয়ে, N->বই, VR->পড়, Biv->ছে will produce a partial structure.

Step-4: Starting from left to right hand side of token list, check every rule whose right hand side will match one or more of the parts of speech. If a right hand side of a rule matches with appropriate parts of speech, then we have to select that rule.

Step-5: Finally, generate the corresponding parse tree.

The parser output for the example will be: NP[Det[Qtfr[এক]Art[টি]]N[Person[TP[TPNHF[মেয়ে]]]]VP[NP[N[বই]Biv[]]VF[V[পড়]Aux[Aspect[Cotinuous[ছ] Tense[Present[] Con[Con-TPNHF[এ]]]]]. Figure 2 illustrates the corresponding parse tree.

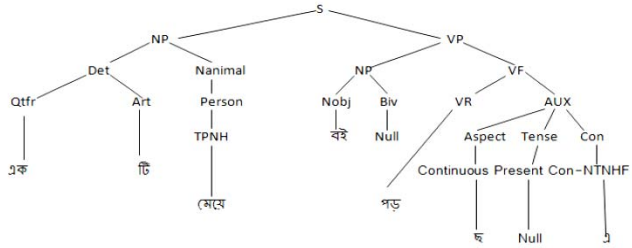

Fig. 2. Parse tree of "একটি মেয়ে বই পড়ছে"

F. Parsing Sentences with TGG

In this paper, we have used PS rules to represent deep structure of a sentence. Some transformational rules (TR) rule is applied over the deep structure(DS) to yield surface structure(SS) of other sentence. List of some used TR to parse different type of Bangla sentences are given in table II.

For example,let us consider a assertive sentence of ambigus SS:

i) একটি মেয়ে বই পড়ছে
ii) মেয়ে একটি বই পড়ছে
iii) মেয়েটি বই পড়ছে

TABLE II. LIST OF TRANSFORMATIONAL RULES (TR)

Type of Sentence	Transformational Rule
Assertive Sentence	i. #Qtfr+Art+N_{animal}#→ #N_{animal}+Qtfr+Art# ii. #N_{animal}+Qtfr+Art#□#N_{animal}+Art# Condition: if Qtfr=এক
Interrogative Sentence	iii.#Person+IW+NP+VF+IM#→#Person+NP+VF+IM# iv. #Person+NP+VF+IM#→#NP+VF+IM# Condition: Person=SP v. #Person+IW+NP+IM# → #NP+IW+Person+IM#
Imperative Sentence	vi. #Person+N+Biv+VF#→#N+Biv+VF# Condition: Person=SP
Optative Sentence	PS rules are adequate, No TR required
Exclamatory Sentence	vii. #N+Art+AP+EM→AP+N+EM#

[a] # (hash) symbol represents the end of string.

All these three sentences have the same deep structure. Among these three, the elementary sentence is "একটি মেয়ে বই পড়ছে",which is parsed using the PS rules described in table I and fig. 2 illustrates the parse tree.

Our system gnerates the parese tree for for sentence (ii) and (iii) using TR(i) and(ii) described in table II.

Applying TR (i) structure of "একটি মেয়ে" is transformed to structure of "মেয়ে একটি" which is shown in fig. 3.

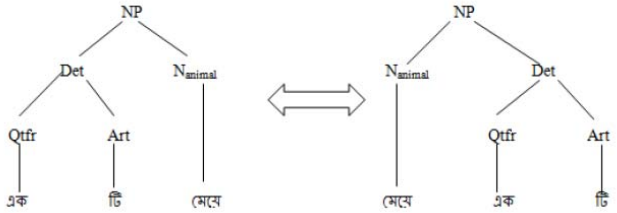

Fig. 3. Position Interchange Transformation applied in sample sentence

Applying TR (ii) structure of is transformed to structure of which is shown in fig. 4.

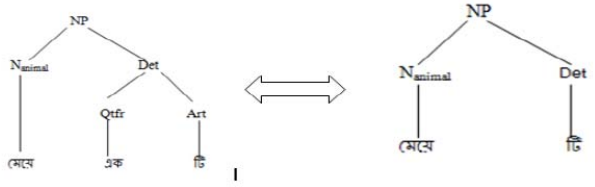

Fig. 4. Subractive Transformation applied in sample sentence

The transformation yields parse tree for sentence (ii) and (iii) which are shown in figure 5 and 6 respectively.

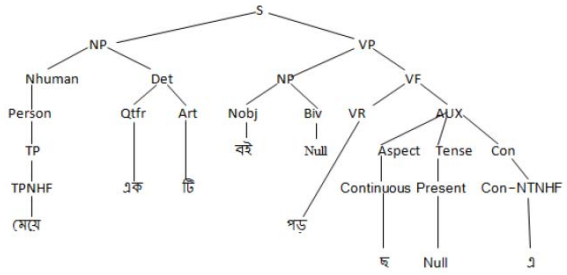

Fig. 5. Parse tree for "মেয়ে একটি বই পড়ছে"

IV. IMPLEMENTATION

We developed this system to parse for assertive, interrogative, imperative, optative and exclamatory sentences. Fig. 7 represent the implementation snapshots of our proposed parser for assertive sentence. The parser detects the sentence type and it shows the syntactic structure of input sentence as list of tokens. The PS rules used to generate the list of token is shown in PS rules field. Applied TR is shown in TR field.

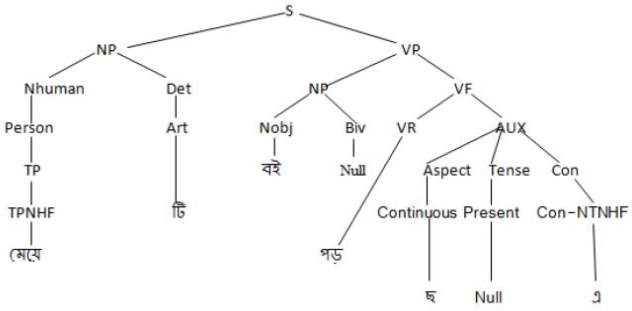

Fig. 6. Parse tree for" মেয়েটি বই পড়ছে"

V. EXPERIMENTAL RESULTS

In order to evaluate the effectiveness of our proposed system, we have tested the system for about 770 different kinds. These sentences were collected from Bangla grammar book [10] and the book in reference [11]. We measure the overall success rate of the proposed framework and expressed in terms of percentage.

A. Success Rate

From our analysis, we have found that total 650 of generated outputs are correct among them about 210 sentences are assertive, 190 sentences are interrogative, 80 sentences are imperative, 79 sentences are optative and 100 sentences are exclamatory. Success rate denotes the ratio between total no. of correctly parsed sentences and total no of input sentences. We have calculated success rate for

assertive, interrogative, imperative, optative and exclamatory sentences separately and finally we have calculated the overall success rate of our system. The success rate for assertive, interrogative, imperative, optative sentences and exclamatory sentences are 84%, 90.5%, 80%, 87.5% and 77% respectively. Overall success rate of proposed system is 84.4%. Table III illustrates the success rate of different types of sentence. From the table, we can see that our proposed system parses Bangla interrogative sentence most successfully, whereas parsing exclamatory sentence has the least success rate. This is due to the fact that we used a limited number of PS rules and TRs' listed in table II, which are not able to reflect the linguistic competence and knowledge of a native speaker. In order to increase the success rate, we need to introduce more PS rules and TRs'. We are optimistic about future research in this regard.

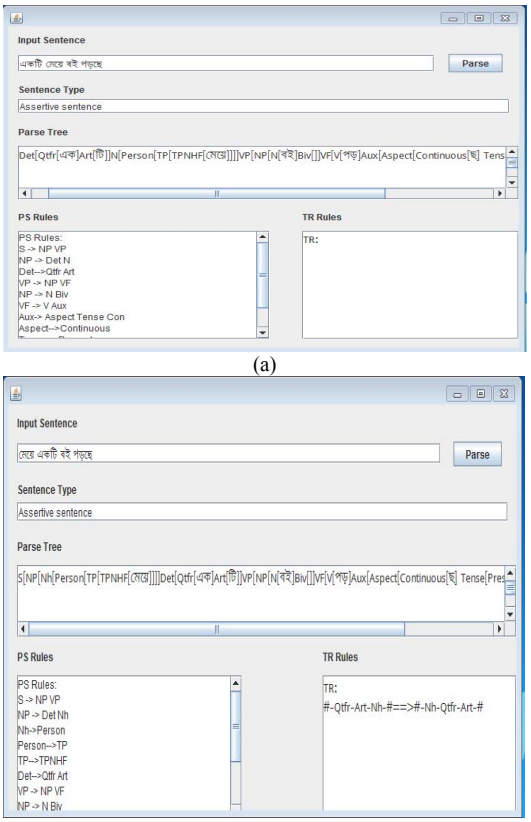

Fig. 7. Parsing of of the assertive sentence (a)"একটি মেয়ে বই পড়ছে" and (b) "মেয়ে একটি বই পড়ছে"

TABLE III. SUCCESS RATE OF DIFFERENT SENTENCE TYPES

Type of Sentence	Total no. of Sentence	Correctly performed syntax analysis	Success Rate (%)	Overall Success Rate (%)
Assertive	250	210	84	84.4
Interrogative	210	190	90.5	
Imperative	100	80	80	
Optative	80	70	87.5	
Exclamatory	130	100	77	

VI. Discussion

All sentences of a language cannot be generated using only PS rules, that's why we proposed a set transformational generative grammar. Let's take a Bangla interrogative sentence "তুমি কি ভাত খেয়েছ?": a parser can detect the sentence using PS rules as an interrogative sentence, but sentences such as "তুমি ভাত খেয়েছ?" and "ভাত খেয়েছ?" are not possible to be detected let alone using PS rules.

VII. Conclusion

Use of TGG in BLP is still at its rudimentary stage. Our implemented system can parse those sentences which was not possible to parse by PS rules only. It can analyze assertive, interrogative, imperative, optative & exclamatory sentences and generate parse tree for those input sentences efficiently. It can also detect the sentence category to which it belongs. It can parse those sentences having identical meaning, but of different surface structure. We have tested a good amount of sentence in our system and the testing result indicates, 84.4% of success rate.Our system mainly deals with parsing structurally simple sentences. Parsing of complex and compound sentence are left as future issues.

Reference

[1] Bengali language [Online]. Available: https://global.britannica.com/topic/Bengali-language

[2] L. Mehedy, S. M. Arefin and M. Kaykobad, "Bangla Syntax Analysis: A Comprehensive Approach", in Proc. *International Conference on Computer and Information Technology* (*ICCIT'03)*, Dhaka, Bangladesh, vol. 5, pp. 287-293, 2003.

[3] M. S. Islam, "*Research on Bangla Language Processing in Bangladesh: Progress and Challenges*", in Proc. 8th International Language & Development Conference, Dhaka, Bangladesh,pp. 527-533, 2009.

[4] M. M. Hoque and M. M. Ali, "A Parsing Methodology for Bangla Natural Language Sentences", in Proc. *International Conference on Computer and Information Technology* (*ICCIT'03)*, Dhaka, Bangladesh, vol. 2, pp. 277-282, 2003.

[5] K. M. A. Hasan, Al-Mahmud, A. Mondal and A.Saha, "*Recognizing Bangla Grammar using predictive parser*", International Journal of Computer Science and Network Security (IJCSNS), Vol. 3, No. 6, ,pp.61-73, Dec. 2011.

[6] K. M. A. Hasan, A. Mondal, A.Saha, "A Context Free Grammar and its Predictive Parser for Bangla Grammar Recognition", in Proc. *13th International Conference on Computer and Information Technology (ICCIT '10)*, Dhaka, Bangladesh,pp.87-95,2010.

[7] S. S. Ashrafi, M. H. Kabir, M. M. Anwar and A. K. M. Noman, *"English to Bangla Machine Translation System Using Context-Free Grammars"*, International Journal of Computer Science and Network Security(IJCSNS), Vol.10, Issue 3, No. 2, pp. 144-153 May 2013.

[8] M. M. Hoque and M. M. Ali, "Context-sensitive Phrase Structure rules for Structural Representation of Bangla Natural Language Sentences ", in Proc. Int. Conf. on Computer and Information Technology (ICCIT'04), pp. 615-620, 2004.

[9] M. S. Arefin, L. Alam, S. Sharmin and M. M. Hoque, "An empirical framework for parsing Bangla assertive, interrogative and imperative sentences," *in Proc. International Conference on Computer and Information Engineering (ICCIE'15)*, Rajshahi, 2015, pp. 122-125.

[10] M. M. Anwar, M. Z. Anwar and Md. A. Bhuiyan, "*Syntax Analysis and Machine Translation of Bangla Sentences*", International Journal

of Computer Science and Network Security (IJCSNS), Vol.9, Issue 8, pp. 317-326, Aug. 2009..

[11] M. A. Islam, K. M. A. Hasan and M. M. Rahman, "Basic HPSG structure for Bangla grammar," in Proc. *15th International Conference on Computer and Information Technology (ICCIT'12),* Chittagong, pp. 185-189, 2012.

[12] M. R. Selim and M. Z. Iqbal, "*Transformational Generative Grammar for Various Types of Bengali Sentences*", SUST Studies, Vol. 12, No. 1, pp. 99-105, 2010.

[13] বাংলা ভাষার ব্যাকরণ, জাতীয় শিক্ষাক্রম ও পাঠ্যপুস্তক বোর্ড, ঢাকা।

[14] H. Azad, "*Bakkyatotto* (বাক্যতত্ত্ব)", Dhaka University, Dhaka, Second Edition, 1994

Biocompatibility Analysis of a Battery Less Back- mountable DBS Device

Senjuti Rahman, Farha Khushi, Dr. Md. Kamal Hosain
Electronics and Telecommunication Engineering, Rajshahi University of Engineering and Technology Rajshahi-6204
CORRESPONDING AUTHOR: Senjuti Rahman (senjuti321@gmail.com)

***Abstract*— In this paper, the biocompatibility of a battery less back-mountable deep brain stimulation (DBS) device is analyzed. To conduct the work, a circular planar inverted F antenna (PIFA) at the resonance frequency of 915 MHz is proposed. The dimension of the antenna is $20\times 19.8904\times 1.5mm^3$. In the proposed antenna, the radiating layer is meandered, and FR-4 material with ε_r = 4.18, $tan\delta$ = 0.02 is used as the substrate with a thickness of 1.5 mm. The bandwidth of the designed antenna is 56.71 MHz at a return loss of -10 dB in free space. Functional and biological aspects are considered here. The functional aspect includes input impedance, resonance frequency, gain pattern, radiation efficiency of the antenna, and the biological aspect involves electric field distribution, and SAR value. A complete rat model is used here. Safety regulation is verified in this paper by the specific absorption rate (SAR) distribution in tissues surrounding the back-mountable passive DBS device. The finite difference time domain (FDTD) based EM simulation software XFdtd is used to determine the electric field distributions which has an impact on the SAR value.**

***Keywords*— Deep brain stimulation, battery less device, back-mountable device, planar inverted *F* antenna, biocompatibility, specific absorption rate, electric field distribution.**

I. INTRODUCTION

Deep brain stimulation (DBS) refers to a technique that involves implanting electrodes in target brain regions, and exciting the electrodes with an electrical pulse train generated by a stimulating device [1]. It is useful for a range of neurological and psychiatric disorders including Parkinson's disease, essential tremor, dystonia, chronic pain, major depression, obsessive-compulsion disorder, epilepsy, and Tourette's syndrome [2]. DBS system consists of three components: the implanted pulse generator (IPG), the lead, and the programmer. The IPG sends electrical pulses to the brain to interfere with neural activity at the target site. The lead is connected to the IPG by the extension. To change the IPG settings, the programmer can be used. The programmer can be used to adjust amplitude, frequency, duration, and polarity of the generated signals by communicating with the IPG [3-5].

Finite battery life time, battery size, and battery replacement difficulty in back mountable DBS devices, plus some generic environmental concerns associated with the use of batteries [6] are encouraging researches to develop battery less DBS devices. Energy can be harvested in two ways, near field and far field coupling. The far field technique is used here. Electromagnetic energy can be harvested by using the feeding sources. Since the required power by the DBS device is lower, the energy harvesting technique is preferable.

When an antenna is mounted on the back of a rat model for wireless energy harvesting, the dielectric tissues of the back not only affects the antenna performance, but also the antenna may have harmful effects on the rat back due to RF radiation. The analysis of the effects is required which is known as biocompatibility analysis. One of the biocompatibility analysis factors is SAR. The amount of the EM energy absorbed by the biological tissue can be measured by the SAR [7].

The pre-clinical research is done before implementing the DBS device practically. Preclinical studies on animal are essential because of their validity of the simulation parameters and brain targets. Different animals can be used in different study; rats are the most commonly used laboratory animals because of their availability and similarity with human neurons [8]. So in this study, a back-mountable energy harvested DBS is considered here. In the considered model, the back mounted antenna will transmit the same amount of power if it works as receiving antenna in the practical situation.

This paper presents the design of a meandered circular PIFA and the performance analysis in both free space and with the rat model. By employing the proposed antenna and the rat model, this paper provides the biocompatibility of the DBS device. Moreover, for maintaining safety regulation, electric field distribution and specific absorption of EM energy density in the rat model are assessed.

II. ANTENNA CONFIGURATION

The configuration of the proposed antenna is shown in the Fig.1. EM simulation software XFdtd is used for designing and optimizing the antenna dimension using an iterative method. The PIFA is best suited for this purpose because of its low profile, small size, built-in structure [9], easy fabrication, low manufacturing cost, and simple structure [10]. PIFA is also demanded because of its directional flexibility [11]. The volume of designed antenna is $20\times 19.8904\times 1.58\,mm^3$. The radius of the antenna is 10 mm. The thickness of dielectric substrate FR-4 is 1.58 mm. The loss tangent of FR-4

978-1-5090-5785-6/16/$31.00©2016 IEEE

is δ = 0.02 and the relative permittivity $is\ \varepsilon_r = 4.18$. The top metallic patch consists of a meandering structure to increase the length of the current flow path and cut down the physical size of the antenna [12], [13]. The feed point is located at 5.5 mm distant from the shorting pin. The input impedance of the antenna depends on the separation between the shorting pin and the feed point. The iterative simulation method is used to match the antenna impedance with the coaxial feed cable impedance of 50Ω.

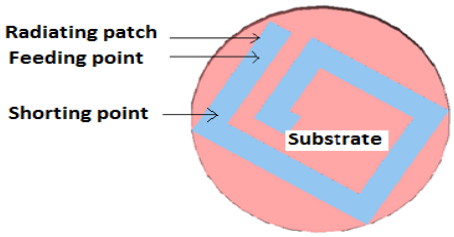

Fig.1 The configuration of the circular PIFA

III. ANTENNA PERFORMANCE

A. Antenna Performance in the Free Space

The designed antenna is simulated in free space to get the results of return loss, 3-D gain, input impedance, and directivity. Fig. 2 shows the simulated return loss of the antenna. This figure shows that the antenna resonates at around 915 MHz and the minimum simulated value of the reflection coefficient is -20.422 dB. The input impedance of the antenna is $Z_i = 68.001 - j29.732$ at 915 MHz. Thus the antenna is capacitive in nature. The antenna bandwidth of 56.71 MHz is obtained at a return loss of -10 dB. The recorded value of maximum gain is -24.8982 dBi at θ=70° and ϕ=120° as shown in Fig.3. The radiation efficiency of the antenna in the free space is 0.22%.

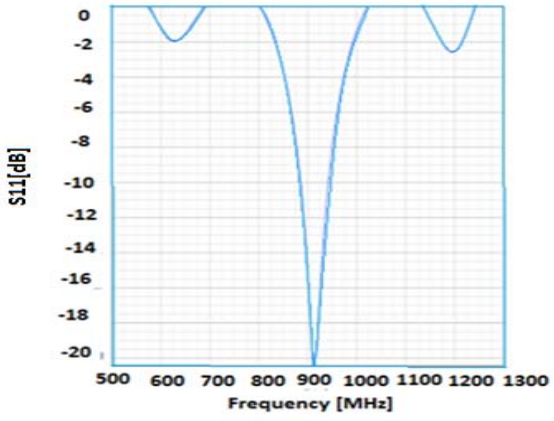

Fig.2 The return loss of the circular PIFA in free space.

B. Antenna Performance with the Rat Model

The dielectric properties of the thirteen tissues used in the complete rat model at 915 MHz are shown in the Table I. The complete rat model is collected from the Remcom XFdtd EM supporting software. The complete Rat model with the

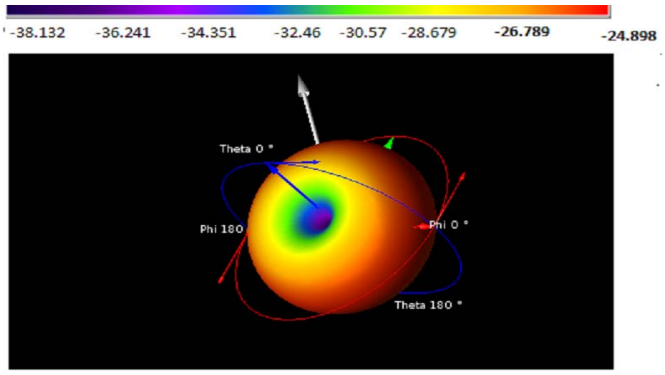

Fig.3 The 3-D gain of the circular PIFA in free space.

proposed PIFA and incident sine wave is given in Fig. 4. Then, the antenna is simulated with the rat model which is shown in Fig.4 to get the results. The simulated result is that the antenna resonates at around 926.65 MHz. The minimum value of the reflection coefficient is -23.795 dB. So, the resonant frequency is moved toward the upper frequency. In order to solve the problem of shifting the resonant frequency, the length of the meandering antenna patch is increased slightly and the position of the shorting pin is changed. The input impedance of the modified antenna is $Z_i = 78.349 - j22.874$. Thus it is capacitive in nature. The recorded value of maximum gain is -19.113 dBi at θ=85° andϕ=50°.The radiation efficiency of the antenna with the rat body is 1.34%. The comparison between the performance of the antenna in free space and with the rat model is given in TABLE II.

TABLE I: DIELECTRIC PROPERTIES OF A RAT MODEL AT 915 MHz[14-16]

Layer name	**Relative permittivity**	**Conductivity (s/m)**	**Mass density(kg/ mm^3)**
1.Inner lung	22	0.459	260
2.blood	60.4	1.86	1050
3.liver	46.8	0.861	1037
4.skin	49.1	0.888	1109
5.tooth	12.4	0.145	1730
6.nerve	37.6	0.684	1085
7.gray matter	57.1	1.22	1041
8.body fluid	67.5	1.75	1019
9.bone	20.8	0.344	1920
10.fat	5.48	0.048	978
11.aorta	42	0.776	1040
12.muscle	57.8	1.08	1045
13.bladder	18.9	0.385	1030

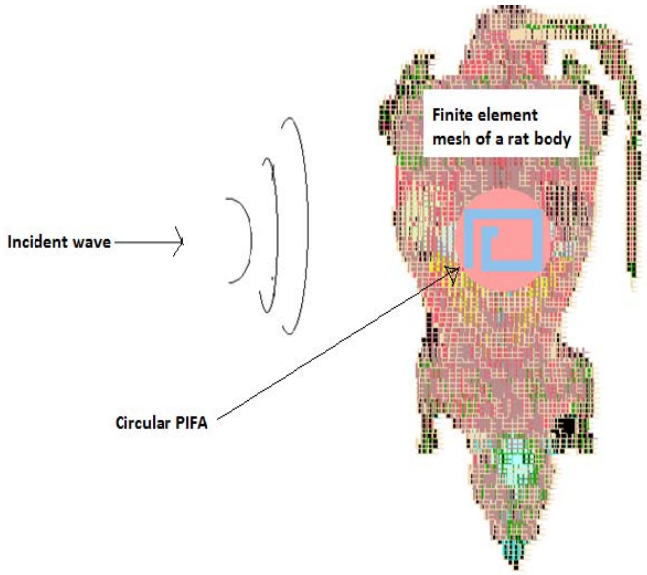

Fig.4 Complete rat model with proposed circular PIFA

TABLE II: PERFORMANCE COMPARISON AT 915 MHz

Antenna Position	Maximum gain (dBi)	Input impedance(Ω)	Resonance Frequency(MHz)
In free space	-23.795	68.00 - j29.732	915
With Rat Model	-19.113	78.34 – j22.874	926.65

IV. BIOCOMPATIBILITY ANALYSIS

Biocompatibility refers to the ability of a material to perform with an appropriate host response in a specific situation. One of the biocompatibility analysis factors is SAR. EM field distributions in different slices of the rat models and average SAR value, Maximum SAR value and the local SAR value in the rat model can be determined based on the simulations of the software. According to IEEE standards, the maximum 1-g and 10-g average SAR to a value of less than 1.6 W/kg and 2W/kg respectively [17], [18].

SAR can determine the amount of heat absorption. SAR is the time derivation of the incremental energy (dU) deposited in an incremental mass (dm) contained in a volume element of density, ρ:

$$SAR = \frac{\mathrm{d}}{\mathrm{dt}}\left(\frac{\mathrm{dU}}{\mathrm{dm}}\right) = \frac{\sigma}{\rho}|\mathrm{E}|^2 \ [\mathrm{W/Kg}] \quad (1)$$

Equation (1) can be written as:

$$SAR = \frac{\mathrm{J2}}{\rho\sigma}[\mathrm{W/kg}] \quad (2)$$

where, σ is the electrical conductivity of the body tissue[S/m], ρ is the material density of the body tissue[Kg/m^3], E is the rms value of the electric field strength in the tissue [V/m], and J is the current density [A/m]. The unit of SAR is watts per kilogram. Fig.5 displays the slice of the electric field in the time domain through the rat body which is at a distance of -4.5 mm from the antenna.

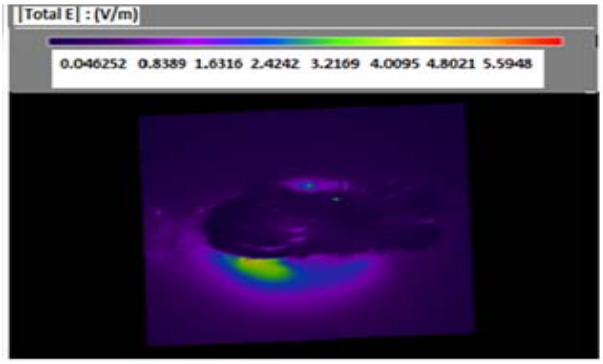

Fig.5 Electric field distribution of a slice at a distance of -4.5 mm from the antenna.

The CAD display of the body tissues and patch antenna is turned off to view the internal fields which are shown in Fig.5and Fig.7.

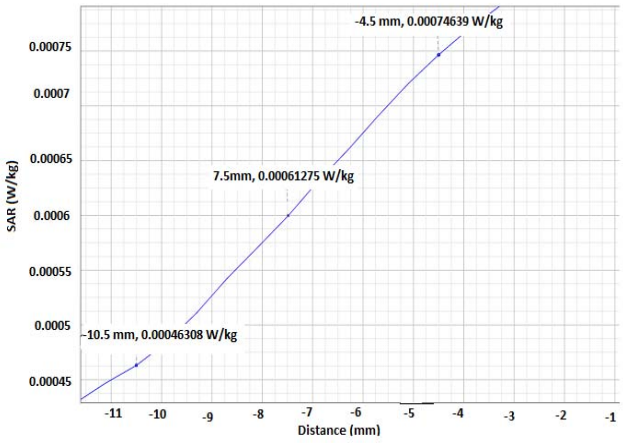

Fig.6 10-g SAR variations at different distances from the antenna.

Fig. 6 shows the plot of 10-g average SAR with the distance from the antenna. The calculation is done by using the distribution of the electric field according to equation (1). It indicates that the SAR is higher near the antenna and then rapidly decreases with the distance. The maximum 1-g average SAR value of 0.0060296 W/kg and 10-g average SAR value of 0.0015845 W/kg are obtained which are both lower than the IEEE C95.1-1999(1-g average SAR< 1.6 W/kg) [17] and IEEE C95.1-2005(10-g average SAR<2 W/kg) [18]. Fig.7 illustrates the average -1g and 10-g SAR values. The hotspot corresponds to the maximum absorption inside Rat model. The hotspot for the 1-g and 10-g is (-1.5,-3.29) and (9.9, 3.29) in mm respectively which indicates the position of the maximum absorption.

Finally, the proposed work can be compared with some other research work associated with it. Bakogianni et al.[19] has proposed a planar dipole antenna which was implanted into the skin of a three-layered human arm model. The stimulated maximum 1-g and 10-g average SAR values are 426.5 W/kg and 96.8 W/kg, respectively if the implantable antenna is delivering 1W.Kim and Samii [20] have designed microstrip patch antenna and PIFA which were implanted in the human chest. The peak SAR of the microstrip antenna and

the PIFA were recorded at the skin tissue in front of the antenna and were 182 W/kg and 209 W/kg respectively. The

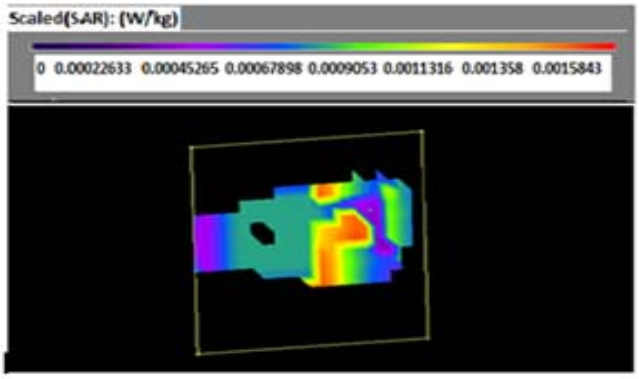

(a)

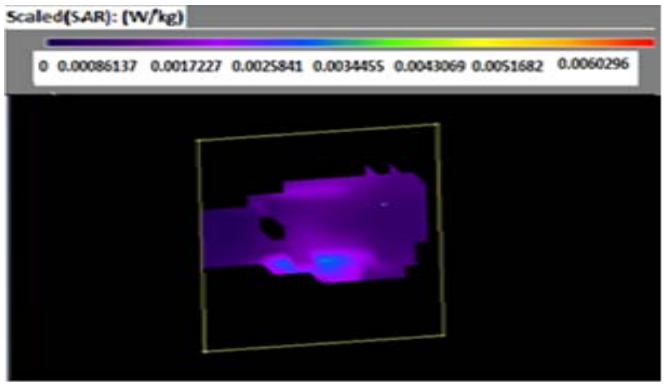

(b)

Fig.7 The scaled, (a) 10-g average SAR values, (b) 1-g average SAR values in the plane of the proposed antenna at the slice of maximum value.

values of the SARs are much higher than the standard value in both above mentioned research. But, the SAR values of the proposed work are lower than the standard value.

V. CONCLUSION

A circular PIFA was designed and the performance of the antenna in the free space as well as with the rat body was presented in this paper. The maximum stimulated gain of the antenna in free space and with the rat body are -23.795 dBi and -19.113 dBi respectively. Biocompatibility was also analysed for the energy harvested DBS device by calculating the SAR in this study.As the distance from the antenna increased the electric field distribution decreased gradually. Hence, the SAR value decreased with the distance from the antenna.The simulation result indicated that at -4.5mm, -7.5 mm and -10.5 mm distance the values of 10-g SAR were 0.00074639 W/kg, 0.00061275 W/kg, and 0.00046308 W/kg respectively.From the above simulation results, it is clear that the electric field and the SAR distribution are maximum near the antenna and theses values gradually decreases with the distance from the antenna. However, the SAR is within the regulated safety limits if the received power of the proposed harvested antenna is few miliwatts.

REFERENCES

[1] Liker, M.A., Won D.S., Rao, V.Y., Hua, S.E.: Deep brain stimulation: An evolving technology. *Proceedings of the IEEE 96(7), 1129-1141* (2008).

[2] R. J. Anderson, M. A. Frye, O. A. Abulseoud, K. H. Lee, J. A. McGillivray, M. Berk, and S.J Tye, "Deep brain stimulation for treatment-resistant depression: Efficacy, safety and mechanisms of action," Neuroscience & Biobehavioral Reviews, vol. 36, pp. 1920-1933, 2012.

[3] M. A. Liker, D. S. Won, V. Y. Rao, and S. E. Hua, *"Deep Brain Stimulation : An Evolving Technology,"Proceedings of the IEEE,*vol.96*, pp. 1129-1141,2008.*

[4] C. R. Butson and C. C. McIntyre, "Role of electrode design on the volume of tissue activated during deep brain stimulation," *Journal of Neural Engineering*, vol.3, p.1, 2006.

[5] N. Yousif and X. Liu, "Modeling the current distribution across the depth electrode-brain interface in deep brain stimulation," Expert Review of Medical Devices, vol.4, p.623, 2007.

[6] H. Jabbar, Y. S. Song, and T. T. Jeong, "RF energy harvesting system and circuits for charging of mobile devices," Consumer Electronics, *IEEE Transactions on* vol.56, pp. 247-253, 2010.

[7] A. Andújar, J. Anguera, C. Picher, and C. Puente, "Human Head Interaction Over Ground Plane Booster Antenna Technology: Functional and Biological Analysis," PIER B, vol. 41, pp. 153-185, 2012.

[8] M. K. Hosain, A. Kouzani, and S. Tye, "Multi-layer implantable antenna for closed loop deep brain stimulation system," in 2012 International Symposium on Communications and Information Technologies (ISCIT), Queensland, Australia, 2012, pp. 643-648.

[9] F. Wang, Z. Du, Q. Wang and K. Gong, "Enhanced-bandwidth PIFA with T-shaped ground plane", *Electronic Letters*, vol. 40, no. 23, pp. 1504 – 1505, Nov. 2004.

[10] B. Kim, J. Hoon and H. Choi, "Small wideband PIFA for mobile phones at 1800 MHz," *Vehicular Technology Conference*, vol. 1, pp. 27-29, May 2004.

[11] B. Merabet, L. Cirio, H. Takhedmit, F. Costa, C. Vollaire, B. Allard, and O. Picon, "Low-cost converter for harvesting of microwave electromagnetic energy," in Energy Conversation Congress and Exposition, ECCE 2009, San Jose, CA,pp.2592-2599, 2009.

[12] M. Hosain, A. Z. Kouzani, S. Tye, K. Walder, and L. Kong, "Design of a miniature UHF PIFA for DBS implants," in 2012 ICME International Conference on Complex Medical Engineering(CME), pp. 485-489, 2012.

[13] K. L. Wong, Compact and broadband microstripanrennas, First Ed. New York: John Wiley &Sons, Inc., 2002.

[14] C. Gabriel, S. Gabriel, and E. Corthout, "The dielectric properties of biological tissues: I. Literature survey," *Physics in medicine and biology,* vol. 41, pp. 2231, 1996.

[15] R. Pethig, "Dielectric properties of body tissues," *Clinical Physics and Physiological Measurement,* vol. 8, pp. 5-12, 1987.

[16] S. Bri, S. Kassimi, H. Habibi, and A. Mamouni, "Specific absorption rate (SAR) distribution in the human head at global system mobile (GSM) frequencies," *European Journal of Scientific Research*, vol. 49, pp. 590-600, 2011.

[17] IEEE standard for safety levels with respect to human Exposure to Radio frequency Electromagnetic fields, 3 KHz to 300 GHz, *IEEE Standard* C95.1, 1999.

[18] IEEE standard for safety levels with respect to human exposureto radiofrequency electromagnetic fields, 3 KHz to 300 GHz, *IEEE Standard* C95.1, 2005.

[19] Sofia Bakogianni, Stavros Koulouridis," An Implantable Planar Dipole Antenna for Wireless MedRadio-Band Biotelemetry Devices," *IEEE Antenna and Wireless Propagation Letters*, vol.15, pp. 234-237, June, 2015.

[20] Jaehoon Kim, YahyaRahmat-Samii, "Implanted Antennas inside a Human Body: Simulations, Designs, and Characterizations," *IEEE Transactions on Microwave Theory and Techniques*, vol.52, no.8, August, 2004.

International Conference on Electrical, Computer & Telecommunication Engineering (ICECTE)
8-10 December 2016, Rajshahi-6204, Bangladesh

Effect of low cost metal contact on the performance of Perovskite Solar Cell

Najmin Ara Sultana[1], Md Obidul Islam[2], Md. Faruk Hossain[3], Hiroyuki Okada[4]
[1,3]Department of EEE, Rajshahi University of Engineering & Technology, Rajshahi, Bangladesh
[2]Department of EEE, University of Dhaka, Dhaka, Bangladesh
[4]University of Toyama, Japan
E-mail: najmineee@gmail.com, obidulapece@gmail.com, dr.faruk_eee@ruet.ac.bd, okada@eng.u-toyama.ac.jp

***Abstract*—Organic-inorganic halide perovskite solar cells have attracted a great interest due to their superior optoelectronic behavior, high efficiency and low fabrication cost. A better understanding of the relationships between material parameters, device architectures and performances is still required for the continued development of the solar cell. This paper represents how the work function of metals can affect their photovoltaic characteristics. Comparatively cheap metals such as Al, Ag and C have been studied as the back contact electrodes for perovskite solar cell. The general trend observed is that the shunt resistance and open-circuit voltage of the devices decrease with the decreasing work function of the contact metal. Spiro-OMeTAD and TiO_2 have been used as HTM and ETM respectively in this solar cell. The results have showed that the materials of high work function can produce good ohmic contact with HTM. Maximum efficiency of 27.67% have been found for C-based TiO_2/$MAPbI_3$/spiro-OMeTAD cell.**

Keywords—Perovskite solar cell; back contact; simulation; wx-AMPS.

I. INTRODUCTION

The perovskite solar cell is a new category of solar cell using organic-metal halide perovskite materials as the light absorber. Owing to its excellent optoelectronic behaviour, good stability, easy fabrication process and high photoconversion efficiency (PCE) organometal halide based hybrid perovskite has been attracting the great attention to the recent solar cell researcher. Perovskite, a crystal structure, is usually represented as ABX3 where A is an organic/inorganic cation, B is divalent small metallic cation (Pb/Sn) and X is halide ion(I/Cl/Br) that binds to both cations [1]. In 1979, Salau recognized that the perovskite is a good absorber for solar cells[2] due to its extremely good electron and hole diffusion ability, very wide absorption wavelength range[3]. In 2009, Miyasaka remigrated perovskite in photovoltaics and obtained efficiency 3.81% and 3.13% for $MAPbI_3$ and $MAPbBr_3$ based solar cells, respectively [4]. It has been upgraded to 22.1% at KRICT/UNIST recently [5].

978-1-5090-5785-6/16/$31.00 ©2016 IEEE

One vital issue in the build-out of perovskite solar cells was moving from the liquid-electrolyte-based dye sensitized solar cell (DSSC) towards a solid state device to overcome the drawbacks of using liquid electrolyte and dye[6]. Unlike DSSC, in perovskite solar cell, the liquid electrolyte is replaced by a solid state hole transporting material alternative and the absorber material perovskite is used instead of dye to create a fully solid state electronic dye sensitized solar cell. The absorber material is used in centre of the solar cell to harvest the solar energy[7]. Immense knowledge and optimal use of all layers of solar cells are the very important matter in the solar cells fabrication. Dopant concentration, mobility of charge carrier, surface properties of the electron transporting material (ETM) and hole transporting material (HTM) and energy band alignment with absorber are vital factors to conduct the charge carriers to the front and back contacts.[8] Efficient collection of the charge carriers would be obtained only when work function of the front contact material is almost equal to or somewhat greater than conduction band minimum of ETM and at the mean time there would be barrier for holes. Likewise, high work function material as back contact can produce an ohmic contact for holes and electrostatic barrier for electrons in HTM[7].

The structure of the employed device is p-i-n type with low p-type doped $CH_3NH_3PbI_3$ sandwiched between a n-type material (TiO_2) and p-type 2,20,7,70-tet-rakis(N,N0-di-methoxyphenylamine)–9,90-spirobifluorene (spiro-OMeTAD) layer. TiO_2 is a semiconducting material as well to harvest a portion of the solar spectrum and spiro-OMeTAD is an organic hole transporting material.

In perovskite solar cells, Au and Ag are usually used as back contact metal. Ag is used in the form of thin film layer [9], embedded mesh in the PET substrate covered by a conductive polymer [10] and in an alloy form as a substrate for HTM or ETM. In 2013, efficiency of 15.4% have been reported for PSC with Ag-contact by vapour diposition [11]. But until now Au/spiro-OMeTAD structure contributes higher efficiency. Recently Krishna et al investigated that efficiency of 22.35% can be achieved for similar structure of PSC with Au-contact [12]. However high price of Au is a drawback to commercialization of PSCs. Aim of this study is optimizing a

comparatively low cost metal contact for PSC with high efficiency. On the other hand, chemical and photochemical stability is also an important factor in selection of a metal. Relatively low cost materials Al, Ag and C, normally used in optoelectronic devices have been investigated to analysis the performances of the PSC here. This study helps to optimize and improve the modules as well as to realize the role of work function of back contact.

II. Model and Simulation

The structure a of perovskite solar cell is shown in Fig. 1. It consists of about 90 nm(TiO_2) ETM layer over an FTO film, followed by a 400 nm erovskite over-layer, 400 nm spiro-OMeTAD (HTM) and a metal contact. To study the role of different metal contacts, performances of the PSC have been simulated.

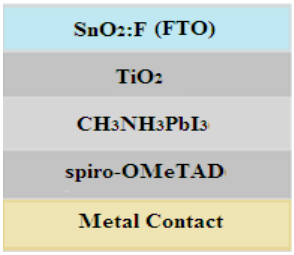

Fig. 1. Model of Perovskite Solar Cell. *(TiO2 as ETM, Perovskite (MAPbI3) as absorber and spiro-OMeTAD as HTM).*

TABLE I. Work Function of Metals Used in Simulation

Metal	Work Function (eV)
Al	4.06
Ag	4.26
C	5

TABLE II. Material Parameters Used in Simulation

Electrical properties	TiO_2	$MAPbI_3$	spiro-MeOTAD
ε_r	100	30	3
μ_n (cm^2/v-s)	0.006	50.0	0.0002
μ_p (cm^2/v-s)	0.006	50.0	0.0002
N_A , N_D (cm^{-3})	5.0×10^{19}	2.1×10^{17}	3.0×10^{18}
Eg (eV)	3.2	1.5	2.91
N_C (cm^{-3})	1.0×10^{21}	2.5×10^{20}	2.5×10^{20}
N_V (cm^{-3})	2.0×10^{20}	2.5×10^{20}	2.5×10^{20}
Affinity(eV)	4.0	3.93	2.2

In this study one-dimensional numerical analysis tool, wx-AMPS, has been used to modeling perovskite solar cell and obtained the results. Table 1 shows the work functions of different low cost metals which can be utilized as back contact with HTM in the PSC.[13,14] Table 2 shows the simulation parameters of different materials used in PSC layers.[12,15,16] The work function of 4.4 eV has been used for front contact (FTO).[12] For simulation, temperature has been used 300K as default and to get all the results, AM1.5 illuminations have been used.

A. wx-AMPS

The wx-AMPS program is an update of the very well-known solar cell simulation tool AMPS-1D (Analysis of microelectronic and photonic structures-1D) [18]. This program is designed based on three basic semiconductor equations and it is well adapted to modeling various hetero- and homo-junctions, multi-junction, and Schottky barrier devices. It is a computer aided numerical analysis of solar cells by solving Poisson's equation and the hole and electron continuity equations.[17] Generally the Poisson's equation is:

$$\frac{dy}{dx}\left(-\mathcal{E}(x)\frac{d\Psi}{dx}\right) = q\left[p(x) - n(x) + N_D^+(x) - N_A^-(x) + p_t(x) - n_t(x)\right] \quad (1)$$

where, N_D^+,N_A^- are the concentrations of ionized donors and acceptors, n, p are the concentrations of free electrons and holes, n_t, p_t are the concentrations of trapped electrons and holes, $\mathcal{E}$ is the dielectric permittivity of semiconductor, Ψ is the electrostatic potential, and q is the electron charge.

The transport characteristics of an electronic device can be derived by the continuity equation for the holes and electrons. The continuity equations in steady state conditions are:

$$\frac{1}{q}\frac{dJ_n}{dx} = R_n(x) - G(x) \quad (2)$$

$$\frac{1}{q}\frac{dJ_p}{dx} = G(x) - R_p(x) \quad (3)$$

where, R_n, R_p are electrons and holes recombination velocities for direct band-to-band and indirect transitions, J_n, J_p are electron and hole current density, and G is the optical generation rate which is expressed as a function of x is,

$$G(x) = -\frac{d}{dx}\sum_i \Phi_i^{FOR}(\lambda_i) + \frac{d}{dx}\sum_i \Phi_i^{REV}(\lambda_i) \quad (4)$$

where, Φ_i^{FOR} and Φ_i^{REV} are, respectively, the photon flux of the incident light and the light reflected from the back surface at a wavelength, λ of i at some point x, depending on the light absorption coefficient, and the light reflectance in the forward and reverse direction. The governing equations (1), (2), and (3) must hold at every position in a device, and the solution to these equations involves determining the state variables $\Psi(x)$, the n-type quasi-Fermi level E_{Fn}, and the p-type quasi-Fermi level E_{Fp} or, equivalently, $\Psi(x)$, $n(x)$, and $p(x)$, which completely defines the system at every point x. Because the governing equations for $\Psi(x)$, E_{Fn}, and E_{Fp} are non-linear and coupled. They cannot be analytically solved. There must be boundary conditions imposed on the set of equations. The Newton- Raphson technique is used in AMPS. To be specific, the solutions to equations (1), (2), and (3) must satisfy the

following boundary conditions:

$$\begin{gathered}\Psi(0) = \Psi_0 - V \\ \Psi(L) = 0 \\ J_p(0) = -qS_{po}[p_o(0) - p(0)] \\ J_p(L) = qS_{pL}[p(L) - p_o(L)] \\ J_n(0) = qS_{no}[n(0) - n_o(0)] \\ J_n(L) = -qS_{nL}[n_o(L) - n(L)]\end{gathered} \quad (5)$$

S_{po}, S_{pL}, S_{no}, and S_{nL} appearing in those conditions are effective interface recombination speeds for holes and electrons at $x = 0$, and $x = L$.

wx-AMPS solves three coupled differential equations each subject to boundary conditions (equ. 5) and then calculates the electrostatic potential and the quasi-Fermi level for holes and electrons at all point in the solar cell. Once these values are known as a function of depth, it is straight forward to calculate the carrier concentrations, electric fields and currents, and device parameters like the open-circuit voltage (*Voc*), short circuit current density (*Jsc*), fill-factor (FF), and the efficiency (η). The performance of a solar cell is defined by these parameters.

III. Result and Discussion

Figure 2 exibits the Current density versus voltage curve of perovskite cell with Al, Ag and C metal contacts. A considerable effect of using different metal is found here. The carbon contact performs better as compared to alluminium and silver cantacts, due to its larger open circuit voltage and stiffer J-V curve. Table III presents the photovoltaic performances of PSC with Al, Ag and C metal contacts.

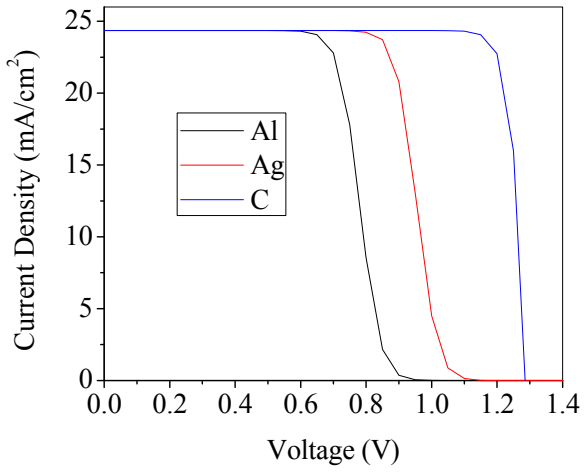

Fig. 2. Current density versus Voltage curves for $TiO_2/CH_3NH_3PbI_3$/spiro-OMeTAD cell using different metal contacts.

TABLE III. Photovoltaic characteristics of $TiO_2/MAPbI_3$/spiro-OMeTAD cell

Work Function	Open Circuit Voltage	Short Circuit Current Density	Fill Factor	PCE
eV	V	mA/cm^2	%	%
4.06	1.0698	24.3681	61.2389	15.964
4.26	1.2416	24.3682	66.6389	20.1625
5.00	1.2859	24.3685	88.33	27.6782

Figure 3 depicts the variation of open circuit voltage and Short circuit current density with work function of metal contacts. For work functions greater than 3.5eV, there is almost no change of short circuit current density and for work functions greater than 4.4eV, slight variation of open circuit voltage is observed. It is seen that both Voc and Jsc are maximum at the larger range of work function. Carbon contact leads to larger value of open-circuit voltage (Voc) and short-circuit current density (Jsc) for its larger work function than aluminum and silver contacts.

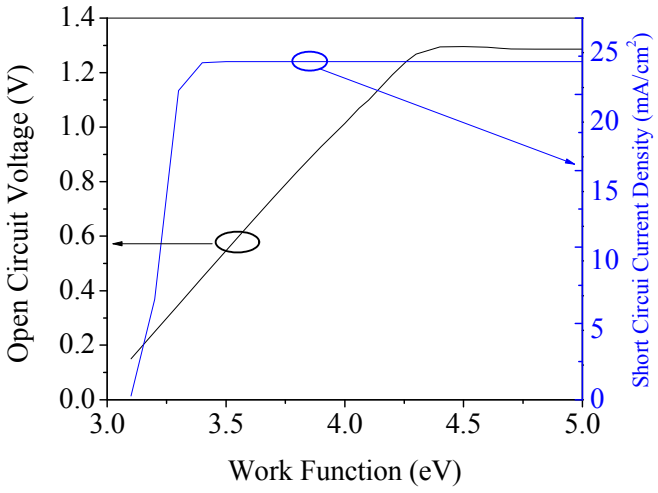

Fig. 3. Variation of Open Circuit Voltage & Short Circuit Current Density with Work Function.

Fill factor and Photovoltaic conversion efficiency versus work function of metal contacts are displayed in Figure 4. Both fill factor and efficiency are increased with increasing work function. But as we observed this is not true always. From the figure it is seen that at some perticular range of work function, fill factor slightly decreses with increase of efficiency. This is because performance of a solar cell also depends on V_{oc} and J_{sc}. Photovoltaic conversion efficiency of PSC increases almost linearly with work function up to 4.6eV. But work functions larger than 4.6eV causes small changes of efficiency.

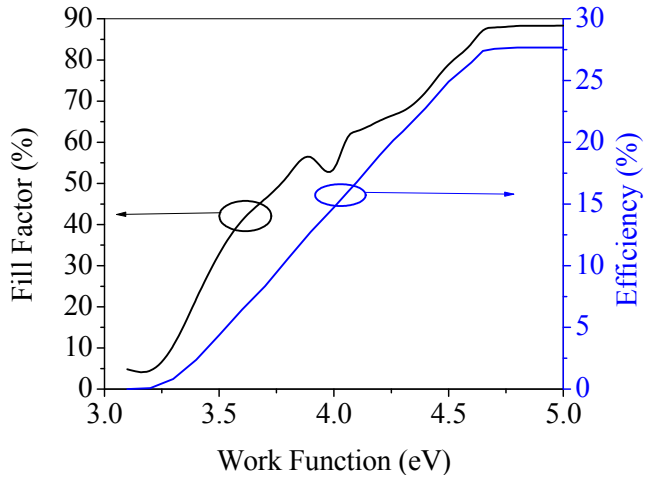

Fig. 4. Photovoltaic performances of PSC with the variation of work function.

IV. Conclusion

The role of different metals as a back contact electrode on the performance of PSCs has been studied. Results show that C is the optimum metal for use with spiro-OMeTAD as the back contact. This is due to the high stability and high work function of C (about 5.00 eV). It is very low cost material as compare to others metals used in PSCs. At the same time Ag provides the better performance compared to Al electrode. High work function led to suitable band bending at the HTM-metal interface. For solid state perovskite solar cells, carbon forms low interfacial resistance with the HTM. Although Ag is the second-most used metal contact, it has a stability problem [20]. On the other hand, C has a very good performance with spiro-OMeTAD. Efficiencies of 15.96%, 20.16% and 27.67% have been obtained for Al, Ag and C-based (TiO_2/$MAPbI_3$/spiro-OMeTAD) cells. In future, perovskite cell with carbon contact can be fabricated in laboratory for commercialization instead of gold or silver.

Acknowledgements

The authors thank Bernabé Marí Soucase for a critical reading of the manuscript. Also thank Prof. Rockett, Dr. Yiming Liu of UIUC and Prof. Fonash of PSU for wx-AMPS simulator.

References

[1] S. Luo and W.A. Daoud. J. Mater. Chem. A. 3, 8992-9010.

[2] A.M. Salau, Sol. Eergy Mater. 2(3), 327-332, 1980.

[3] Yecheng Zhou and Angus Gray-Weale, "A numerical model for charge transport and energy conversion of perovskite solar cell", Phys. Chem. Chem. Phys.,2016, 18, 4476.

[4] T. Miasaka, A. Kojima, K. Teshima and Y. Shirai, J.Amer. Chem Sovc. 131(17), 6050-6051, 2009.

[5] NREL: https://en.wikipedia.org/wiki/Perovskite_solar_cell.

[6] W. Tress, N. Marinova, T. Moehl, S. M. Zakeeruddin, Mohammad Khaja Nazeeruddinand M. Gr¨atzel , "Understanding the rate-dependent J–V hysteresis,slow time component, and aging in CH3NH3PbI3 perovskite solar cells: the role of a compensatedelectric field," Energy Environ. Sci., 2015, 8,995

[7] S. Fonash, Solar Cell Device Physics, 2nd ed. (Elsevier, 2012).

[8] W. J. Yin, J. H. Yang, J. Kang, Y. Yan and S. H. Wei, J. Mater. Chem A 3, 8926-8942,2015.

[9] K. Hwang, Y.S.Jung, Y.J.Heo, F.H.Scholes, S.E.Watkins, J. Subbiah, D.J.Jones,D.Y.Kim and D. Vak, Adv. Mater.,2015,27,1241-1247.

[10] Y.Li, L.Meng, Y.M.Yang, G.Xu, Z.Hong, Q.Chen,J.You, G.Li,Y.Yang and Y.Li, Nat.Commun.,2016,7,10214.

[11] Mingzhen Liu, Michael B. Johnston & Henry J. Snaith "Efficient planar heterojunction perovskite solar cells by vapour deposition", 9september2013/vol501/nature/395

[12] Krishna R. Adhikari, Shekhar Gurung, Binod K. Bhattarai and Bernabe Mari Soucase, " Comparative study on MAPbI3 based solar cells using different electron transporting materials," P hys. Status Solidi C 13, No. 1, 13– 17 (2016).

[13] Herbert B. Michaelson, "The work function of the elements and its periodicity," J. Appl. Phys. 48, 4729-4733 (1977).

[14] The 84th Edition of the CRC Handbook of Chemistry and Physics. 12-124.

[15] https://wiki.illinois.edu//wiki/display/solarcellsim/Simulation+Software

[16] Md. Sharafat Hossain, Nowshad Amin and Takhir Razykov , "Prospects of back contacts with back surface fields in high efficiency $zn_xcd_{1-x}s$ /cdte solar cells from numerical modeling," Vol. 8, No. 3, March 2011, p. 187 – 198

[17] "A Manual for AMPS-1D", The center for Nanotechnology Education and Utilization, The Pennsylvania State University, PA 16802

[18] Yiming Liu, Yun Sun and Angus Rockett , "A new simulation software of solar cells—wxAMPS," Solar Energy Materials & Solar Cells 98 (2012) 124–128.

[19] refractiveindex.info/?shelf=main&book=C&page=Peter

[20] F. Behrouznejad, S. Shahbazi, N. Taghavinia, Hui-Ping Wud and Eric Wei-GuangDiau, J. Mater. Chem. A, 2016, 4,13488

Device modeling and performance analysis of perovskite solar cells based on similarity with inorganic thin film solar cells structure

Dr. Md. Faruk Hossain[1], Mohammad Faisal[1], Hiroyuki Okada[2]
[1]Department of Electrical and Electronic Engineering
Rajshahi University of Engineering and Technology
Rajshahi-6204, Bangladesh
[2]Graduate School of Science and Engineering for Research
University of Toyama
3190 Gofuku, Toyama 930-8555, Japan
*mdfaisal.ruet11@gmail.com

***Abstract*— The photovoltaic cells are the best way to use solar energy by absorbing the photons radiation. The aim of this paper work is to simulate perovskite solar cell and finding the optimum thickness of the absorber layer. Here we run a simulation of perovskite solar cells on SCAPS-1D simulator software. The cell structure employs similarity with other inorganic solar cells such like CIGS, CdTe and Cu(In,Ga)Se_2. The absorber layer is $CH_3NH_3PbI_{3-x}Cl_3$ used here for its great attention as highly efficient absorber. A high open circuit voltage of 1.112 V achieved here and the efficiency is more than 22%. The effect of work function of front and back contact also has a great influence over the fill factor and on the efficiency. By varying the thickness of different layers optimum result has been achieved and demonstrates that in I-V characteristics and quantum efficiency (QE).**

Keywords—Perovskite solar cell, Scaps-1D, $CH_3NH_3PbI_{3-x}Cl_3$, Thickness, Conversion efficiency, Quantum efficiency.

I. INTRODUCTION

The perovskite solar cells recently attracted most of the researchers for its high absorption and tunable bang-gap energy. It has achieved high open circuit voltage and efficiency[1]-[6]. The organic-inorganic perovskite solar cells normally employ mesoporous TiO_2 as the buffer layer to increase light absorption [2][3][5]. But ZnO can also be successfully employed as a replacement of TiO_2 which also have good electrical properties to use as a buffer layer[7]. In recent years, the efficiency of 17.9% achieved using $CH_3NH_3PbI_{3-x}Cl_3$ as absorber and TiO_2 as buffer in perovskite solar cell simulation[8].

For the improvement of efficiency level it is required to understand the operation mechanism of perovskite solar cell, but unfortunately there has insufficient data about this. For better understanding of operation, device simulation is widely used for others inorganic cells like silicon [9]-[11]. CdTe, [12][13] $Cu_2ZnSn(S,Se)_4$[14] etc. The perovskite solar cells also have the structural similarity with them which allows to study about it with numerical analysis of performance parameters and operation using simulator. In this study we have used the Solar Cell capacitance Simulator (SCAPS). The device is modeled by comparison with real device and then performs the analysis for optimum design. We also have examined the effects of layer thickness of the absorber, effects of doping concentration variation on the cell performance.

II. PEROVSKITE SOLAR CELL MODEL

To study the performance analysis of solar cell with ZnO as buffer layer in simulator we have used structure as given below-

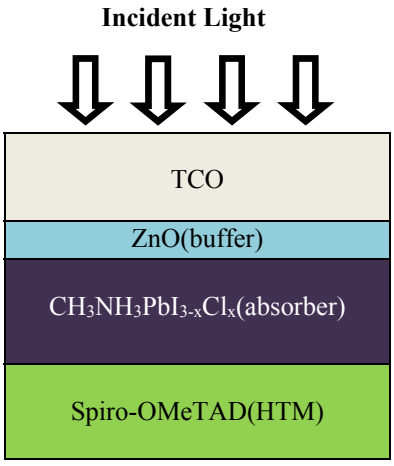

Fig. 1: Proposed structure of perovskite solar cell.

The cell structure consists of transparent conductive oxide (TCO)/buffer/absorber/hole transport material (HTM)/Au. The TCO is based on SnO_2:F (FTO) material which have the working function of 4.4 eV. The buffer used in the simulation is ZnO which is often called as "blocking layer". The absorber used here is $CH_3NH_3PbI_{3-x}Cl_3$ and the HTM used is 2,2′,7,7′-

978-1-5090-5785-6/16/$31.00 ©2016 IEEE

tetrakis(N,N-p-dimethoxy-phenylamino)–9,9′-spirobifluorene (Spiro-OMeTAD) respectively. The aim of this work is to study the performance analysis by changing absorber thickness and doping concentration using ZnO material as buffer layer. The cell structure has similarity with the inorganic solar cell CIGS (TCO/buffer/CIGS/back contact/substrate). The device performance is mainly based on electrical parameters, optical parameters and material parameters of each layers used in the simulation.

III. PARAMETERS FOR DEVICE SIMULATION

For the study of device performance SCAPS simulator is used. The cell structure was given in *Fig. 1*. The parameters used in the simulation are taken from different literatures. For the HTM and absorber layer parameters are taken from the standard value [7]. The band diagram of the cell structure is given below in *Fig. 2*. From the band diagram of the cell structure it can be seen that it can absorb more sunlight for lower bandgap of absorber. So, more free electrons and holes can generate which will lead to generate more current i.e. increasing fill factor and efficiency.

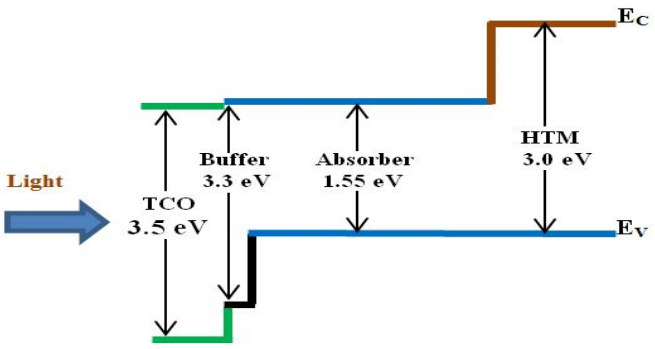

Fig. 2: Cell structure using bandgap energy in device simulation.

The parameters used in this study are given below. Table I summarizes the device parameters used in the simulation. The electrical and optical properties are taken from the literature [7] for HTM, Absorber and TCO materials. The buffer layer used here is ZnO and the parameters are taken from another literature [6].

The parameters are taken from these literatures are given in Table I below. Here, N_A and N_D are for acceptor and donor concentration. ε_r is relative permittivity, E_G is bangap energy, χ is electron affinity, μ_n and μ_p are for electron and hole mobility respectively. The conduction band offset and valence band offsets among buffer/absorber and absorber/HTM layers are set to be 0.0 eV by adjusting the electron affinity of the buffer and HTM respectively. The optimum choice of buffer and HTM will be discussed elsewhere. In the simulation the thermal velocity of electron and hole is 10^7 cm/s. The absorption constant is used as the default value of 10^5. The absorber is n-type carrier and the density is set to 10^{13} cm^{-3}. So, the layer is nearly intrinsic type. For achieving more practical result we have count defect density N_t in each layers. The N_t for the absorber layer is set to 2.5×10^{13} which gives the carrier diffusion lengths of electron and hole of 1.0 µm. The defect type is neutral and energetic distribution is Gaussian type which has characteristic value of 0.1 eV. The electron and hole's cross section area is selected as 2×10^{-14} cm^2. The simulation was done under AM1.5 G standard photon flux and the temperature was set at 300 K.

TABLE I. Parameters of perovskite solar cell used in the simulation process.

Parameters	TCO	ZnO	$CH_3NH_3PbI_{3-x}Cl_x$	Spiro-OMeTAD
Thickness (nm)	200	80	600	350
$N_A(cm^{-3})$	---	---	---	2×10^{18}
$N_D(cm^{-3})$	1×10^{18}	5×10^{17}	10^{13}	---
ε_r	9.0	9.0	6.5	3
X(eV)	4.0	3.9	3.9	2.45
$N_c(cm^{-3})$	2.2×10^{18}	1×10^{19}	2.2×10^{18}	2.2×10^{18}
$N_v(cm^{-3})$	1.8×10^{19}	1×10^{19}	1.8×10^{19}	1.8×10^{19}
E_g(eV)	3.5	3.3	1.55	3.0
$\mu_n(cm^2/Vs)$	20	50	2	2×10^{-4}
$\mu_p(cm^2/Vs)$	10	5	2	2×10^{-4}
$N_t(cm^{-3})$	10^{15}	10^{15}	2.5×10^{13}	10^{15}

IV. RESULTS ANALYSIS AND DISCUSSIONS

The simulation was done and achieved higher efficiency more than 22%. The high open circuit voltage of 1.112 V have been found which indicates successful reproduction of results achieved practically.[3] The fill factor achieved is about 82% indicates better absorption in absorber layer. The I-V characteristics curve is given below in *Fig. 3* calculated with the parameters given in TABLE I.

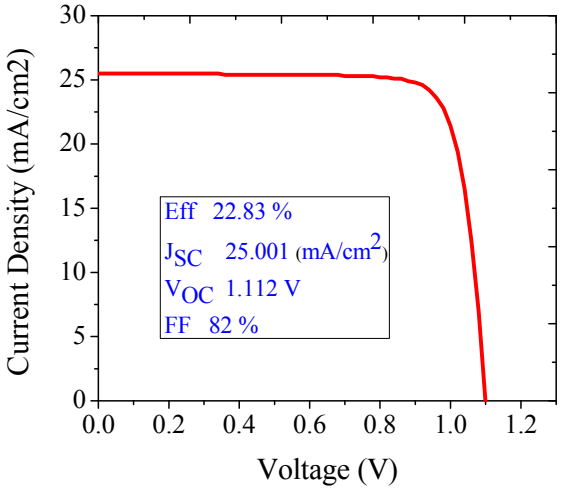

Fig. 3: I-V characteristics curve of perovskite solar cell.

The thickness of the absorber layer is very important parameter to achieve high efficiency. The performance parameters change tremendously within a certain level and after that increasing the thickness of the absorber cause decrease in efficiency. The absorber quality i.e. carrier diffusion length must be high enough for good collection of proto-generated carrier. The performance parameters of the solar cell have more impact on the thickness of the absorber layer. With the variation of the thickness the changes in different parameters are given below in *Fig. 4*.

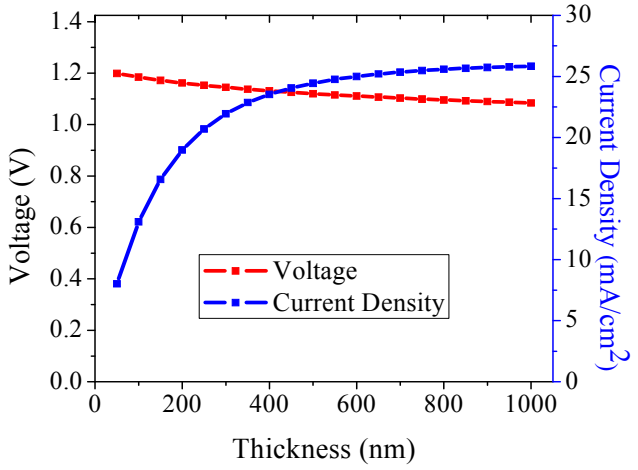

(a)

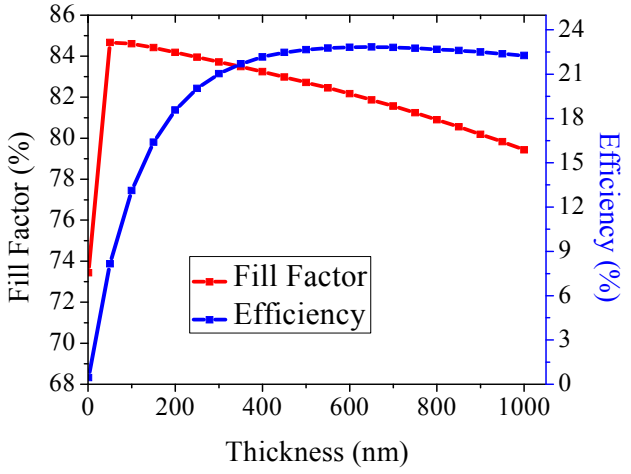

(b)

Fig. 4: Simulation result of (a) open-circuit voltage and current density, (b) fill factor and efficiency; as a function of thickness variation in absorber layer.

From the *Fig. 4(a)* it is seen that with the increase in the absorber thickness the performance parameters are changed and the cell obtained better results. With the increase in thickness, the cell absorbs more photon energy which produces more carriers in absorber layer. The open-circuit voltage obtained high with less layer thickness and decreases with the increase in thickness. The V_{OC} becomes saturated after 700 nm thickness. The current density at also saturated after attaining a value about 25 mA/cm^2 and the maximum value is 25.84 mA/cm^2. For thicker absorber the current density decreases less because of reduction of the electric field in the absorber. If the absorber quality is not good enough, the increase in thickness in absorber will results in more recombination current. Thus small absorber thickness is needed but less thickness also decrease the generation current. The *Fig. 4(b)* demonstrates that the FF decrease monotonically with the increase in the absorber layer thickness. It is generally occurred in every absorber even if it's a good quality absorber. The cell structure shows maximum FF for 50 nm layer thickness and decrease in small scale after that. This happened because the forward bias voltage reduces the electric field including the increase in recombination of current in absorber. The efficiency curve trend is mostly similar to that of the FF. With the increase in the thickness the efficiency decreases in small values after 600 nm and can be said to be saturated.

The *Fig. 4* describes the output of performance parameters as a function of thickness variation and indicates the optimum thickness of the absorber layer. The performance is saturated nearly at 600 nm which is almost similar to the practical observation. The absorber must be in good quality for good collection of current even at lower electric field.

The doping concentration of the absorber also has important impact on the efficiency. The cell efficiency reaches its maximum value when it is nearly intrinsic material. With the increase in doping concentration the efficiency decreases according to *Fig. 5*. In our study we use doping concentration of 1×10^{13} cm^{-3} which gives better performance and also shows similarity with the practical results.

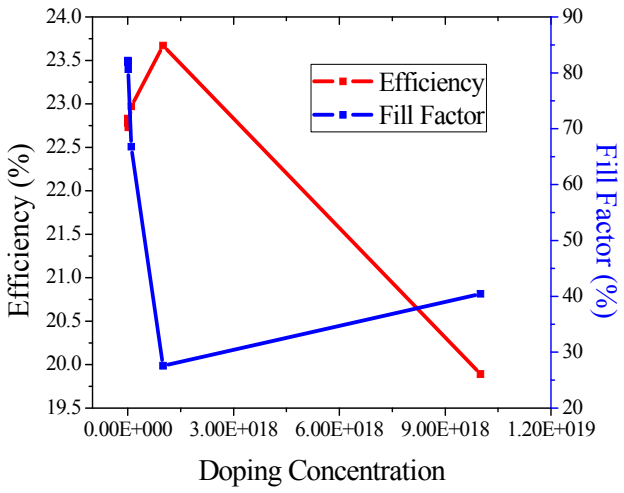

Fig. 5: Change in efficiency and fill factor with doping concentration.

The quantum efficiency is very important parameters that expose the quality of solar cell's active layer. The cell structure we have studied here has excellent quantum efficiency explained with *Fig. 6*. The quantum efficiency versus wavelength curve is given below-

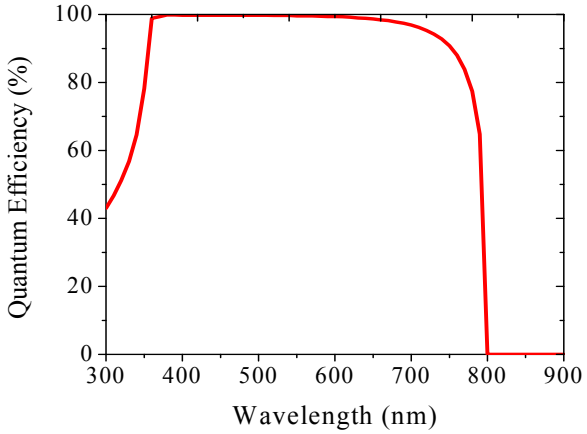

Fig. 6: QE characteristics calculated in device simulation.

The simulation study in this literature will lead mutual understanding of the operation mechanism which will helps in further improvement in performance of perovskite solar cells.

V. CONCLUSION

In this paper work device simulation of perovskite solar cells was performed using SCAPS-1D simulator widely used for inorganic solar cells. In our study we have used ZnO material which also shows very similar characteristics as TiO_2. Using ZnO as buffer obtained high efficiency of 22.83 % with FF of 82 % indicates better quality as buffer material. The simulation result of perovskite solar cell will help in further improvement in organic cell's performance. We observed the effect of absorber thickness on the performance parameters like V_{OC}, I_{SC}, FF and η of the perovskite cell. The result analysis shows importance of absorber thickness for optimum performance.

ACKNOWLEDGEMENT

We would like to acknowledge the use of SCAPS simulator which was developed by Professor Marc Burgelman, Department of Electronics and Information Systems, University of Gent.

REFERENCES

[1] H. Kim, S. Im and N. Park, "Organolead Halide Perovskite: New Horizons in Solar Cell Research", *J. Phys. Chem. C*, vol. 118, no. 11, pp. 5615-5625, 2014.

[2] S. Stranks, G. Eperon, G. Grancini, C. Menelaou, M. Alcocer, T. Leijtens, L. Herz, A. Petrozza and H. Snaith, "Electron-Hole Diffusion Lengths Exceeding 1 Micrometer in an Organometal Trihalide Perovskite Absorber", *Science*, vol. 342, no. 6156, pp. 341-344, 2013.

[3] J. Burschka, N. Pellet, S. Moon, R. Humphry-Baker, P. Gao, M. Nazeeruddin and M. Grätzel, "Sequential deposition as a route to high-performance perovskite-sensitized solar cells", *Nature*, vol. 499, no. 7458, pp. 316-319, 2013.

[4] M. Lee, J. Teuscher, T. Miyasaka, T. Murakami and H. Snaith, "Efficient Hybrid Solar Cells Based on Meso-Superstructured Organometal Halide Perovskites", *Science*, vol. 338, no. 6107, pp. 643-647, 2012.

[5] J. Noh, S. Im, J. Heo, T. Mandal and S. Seok, "Chemical Management for Colorful, Efficient, and Stable Inorganic–Organic Hybrid Nanostructured Solar Cells", *Nano Letters*, vol. 13, no. 4, pp. 1764-1769, 2013.

[6] F. Liu, J. Zhu, J. Wei, Y. Li, M. Lv, S. Yang, B. Zhang, J. Yao and S. Dai, "Numerical simulation: Toward the design of high-efficiency planar perovskite solar cells", *Appl. Phys. Lett.*, vol. 104, no. 25, p. 253508, 2014.

[7] Ray, J. R., C. J. Panchal, M. S. Desai, and U. B. Trivedi, "Simulation of CIGS thin film solar cells using AMPS-1D." *Journal of Nano-and Electronic Physics*, vol. 3, no. 1, p. 747, 2011.

[8] T. Minemoto and M. Murata, "Device modeling of perovskite solar cells based on structural similarity with thin film inorganic semiconductor solar cells", *J. Appl. Phys.*, vol. 116, no. 5, p. 054505, 2014.

[9] X. Sun, R. Asadpour, W. Nie, A. Mohite and M. Alam, "A Physics-Based Analytical Model for Perovskite Solar Cells", *IEEE Journal of Photovoltaics*, vol. 5, no. 5, pp. 1389-1394, 2015.

[10] P. Basore, "Numerical modeling of textured silicon solar cells using PC-1D", *IEEE Transactions on Electron Devices*, vol. 37, no. 2, pp. 337-343, 1990.

[11] P. Altermatt,"Models for numerical device simulations of crystalline silicon solar cells", *Journal of Computational Electronics*, vol. 10, no. 3, pp. 314-330, 2011.

[12] H. Yuan, V. Yost, M. Page, P. Stradins, D. Meier and H. Branz, "Efficient black silicon solar cell with a density-graded nanoporous surface: Optical properties, performance limitations, and design rules", *Appl. Phys. Lett.*, vol. 95, no. 12, p. 123501, 2009.

[13] A. Niemegeers and M. Burgelman, "Effects of the Au/CdTe back contact on IV and CV characteristics of Au/CdTe/CdS/TCO solar cells", *J. Appl. Phys.*, vol. 81, no. 6, p. 2881, 1997.

[14] D. Hironiwa, M. Murata, N. Ashida, Z. Tang and T. Minemoto, "Simulation of optimum band-gap grading profile of Cu 2 ZnSn(S,Se) 4 solar cells with different optical and defect properties", *Jpn. J. Appl. Phys.*, vol. 53, no. 7, p. 071201, 2014.

Biocompatibility Analysis of a Battery Less Back- mountable DBS Device

Senjuti Rahman, Farha Khushi, Dr. Md. Kamal Hosain
Electronics and Telecommunication Engineering, Rajshahi University of Engineering and Technology Rajshahi-6204
CORRESPONDING AUTHOR: Senjuti Rahman (senjuti321@gmail.com)

***Abstract*— In this paper, the biocompatibility of a battery less back-mountable deep brain stimulation (DBS) device is analyzed. To conduct the work, a circular planar inverted F antenna (PIFA) at the resonance frequency of 915 MHz is proposed. The dimension of the antenna is $20\times 19.8904\times 1.5mm^3$. In the proposed antenna, the radiating layer is meandered, and FR-4 material with ε_r = 4.18, $tan\delta$ = 0.02 is used as the substrate with a thickness of 1.5 mm. The bandwidth of the designed antenna is 56.71 MHz at a return loss of -10 dB in free space. Functional and biological aspects are considered here. The functional aspect includes input impedance, resonance frequency, gain pattern, radiation efficiency of the antenna, and the biological aspect involves electric field distribution, and SAR value. A complete rat model is used here. Safety regulation is verified in this paper by the specific absorption rate (SAR) distribution in tissues surrounding the back-mountable passive DBS device. The finite difference time domain (FDTD) based EM simulation software XFdtd is used to determine the electric field distributions which has an impact on the SAR value.**

***Keywords*— Deep brain stimulation, battery less device, back-mountable device, planar inverted *F* antenna, biocompatibility, specific absorption rate, electric field distribution.**

I. INTRODUCTION

Deep brain stimulation (DBS) refers to a technique that involves implanting electrodes in target brain regions, and exciting the electrodes with an electrical pulse train generated by a stimulating device [1]. It is useful for a range of neurological and psychiatric disorders including Parkinson's disease, essential tremor, dystonia, chronic pain, major depression, obsessive-compulsion disorder, epilepsy, and Tourette's syndrome [2]. DBS system consists of three components: the implanted pulse generator (IPG), the lead, and the programmer. The IPG sends electrical pulses to the brain to interfere with neural activity at the target site. The lead is connected to the IPG by the extension. To change the IPG settings, the programmer can be used. The programmer can be used to adjust amplitude, frequency, duration, and polarity of the generated signals by communicating with the IPG [3-5].

Finite battery life time, battery size, and battery replacement difficulty in back mountable DBS devices, plus some generic environmental concerns associated with the use of batteries [6] are encouraging researches to develop battery less DBS devices. Energy can be harvested in two ways, near field and far field coupling. The far field technique is used here. Electromagnetic energy can be harvested by using the feeding sources. Since the required power by the DBS device is lower, the energy harvesting technique is preferable.

When an antenna is mounted on the back of a rat model for wireless energy harvesting, the dielectric tissues of the back not only affects the antenna performance, but also the antenna may have harmful effects on the rat back due to RF radiation. The analysis of the effects is required which is known as biocompatibility analysis. One of the biocompatibility analysis factors is SAR. The amount of the EM energy absorbed by the biological tissue can be measured by the SAR [7].

The pre-clinical research is done before implementing the DBS device practically. Preclinical studies on animal are essential because of their validity of the simulation parameters and brain targets. Different animals can be used in different study; rats are the most commonly used laboratory animals because of their availability and similarity with human neurons [8]. So in this study, a back-mountable energy harvested DBS is considered here. In the considered model, the back mounted antenna will transmit the same amount of power if it works as receiving antenna in the practical situation.

This paper presents the design of a meandered circular PIFA and the performance analysis in both free space and with the rat model. By employing the proposed antenna and the rat model, this paper provides the biocompatibility of the DBS device. Moreover, for maintaining safety regulation, electric field distribution and specific absorption of EM energy density in the rat model are assessed.

II. ANTENNA CONFIGURATION

The configuration of the proposed antenna is shown in the Fig.1. EM simulation software XFdtd is used for designing and optimizing the antenna dimension using an iterative method. The PIFA is best suited for this purpose because of its low profile, small size, built-in structure [9], easy fabrication, low manufacturing cost, and simple structure [10]. PIFA is also demanded because of its directional flexibility [11]. The volume of designed antenna is $20\times 19.8904\times 1.58\,mm^3$. The radius of the antenna is 10 mm. The thickness of dielectric substrate FR-4 is 1.58 mm. The loss tangent of FR-4

978-1-5090-5785-6/16/$31.00©2016 IEEE

is δ = 0.02 and the relative permittivity $is\ \varepsilon_r = 4.18$. The top metallic patch consists of a meandering structure to increase the length of the current flow path and cut down the physical size of the antenna [12], [13]. The feed point is located at 5.5 mm distant from the shorting pin. The input impedance of the antenna depends on the separation between the shorting pin and the feed point. The iterative simulation method is used to match the antenna impedance with the coaxial feed cable impedance of 50Ω.

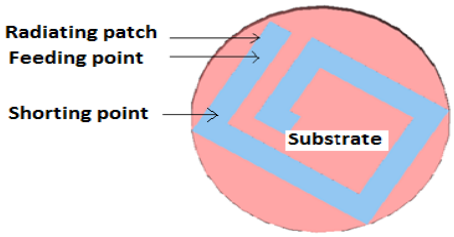

Fig.1 The configuration of the circular PIFA

III. ANTENNA PERFORMANCE

A. Antenna Performance in the Free Space

The designed antenna is simulated in free space to get the results of return loss, 3-D gain, input impedance, and directivity. Fig. 2 shows the simulated return loss of the antenna. This figure shows that the antenna resonates at around 915 MHz and the minimum simulated value of the reflection coefficient is -20.422 dB. The input impedance of the antenna is $Z_i = 68.001 - j29.732$ at 915 MHz. Thus the antenna is capacitive in nature. The antenna bandwidth of 56.71 MHz is obtained at a return loss of -10 dB. The recorded value of maximum gain is -24.8982 dBi at θ=70° and ϕ=120° as shown in Fig.3. The radiation efficiency of the antenna in the free space is 0.22%.

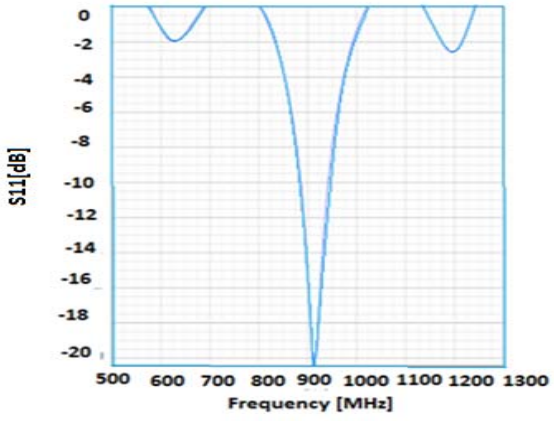

Fig.2 The return loss of the circular PIFA in free space.

B. Antenna Performance with the Rat Model

The dielectric properties of the thirteen tissues used in the complete rat model at 915 MHz are shown in the Table I. The complete rat model is collected from the Remcom XFdtd EM supporting software. The complete Rat model with the

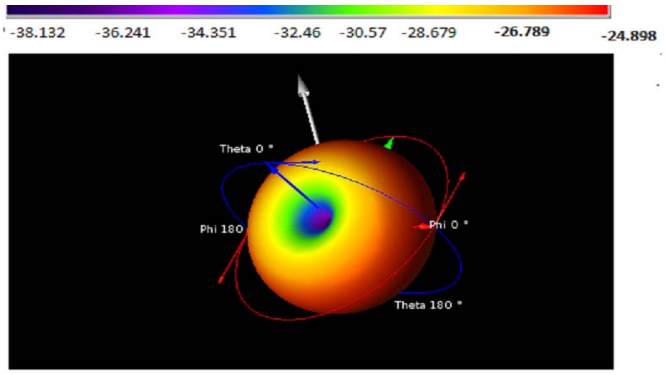

Fig.3 The 3-D gain of the circular PIFA in free space.

proposed PIFA and incident sine wave is given in Fig. 4. Then, the antenna is simulated with the rat model which is shown in Fig.4 to get the results. The simulated result is that the antenna resonates at around 926.65 MHz. The minimum value of the reflection coefficient is -23.795 dB. So, the resonant frequency is moved toward the upper frequency. In order to solve the problem of shifting the resonant frequency, the length of the meandering antenna patch is increased slightly and the position of the shorting pin is changed. The input impedance of the modified antenna is $Z_i = 78.349 - j22.874$. Thus it is capacitive in nature. The recorded value of maximum gain is -19.113 dBi at θ=85° andϕ=50°.The radiation efficiency of the antenna with the rat body is 1.34%. The comparison between the performance of the antenna in free space and with the rat model is given in TABLE II.

TABLE I: DIELECTRIC PROPERTIES OF A RAT MODEL AT 915 MHz[14-16]

Layer name	**Relative permittivity**	**Conductivity (s/m)**	**Mass density(kg/ mm^3)**
1.Inner lung	22	0.459	260
2.blood	60.4	1.86	1050
3.liver	46.8	0.861	1037
4.skin	49.1	0.888	1109
5.tooth	12.4	0.145	1730
6.nerve	37.6	0.684	1085
7.gray matter	57.1	1.22	1041
8.body fluid	67.5	1.75	1019
9.bone	20.8	0.344	1920
10.fat	5.48	0.048	978
11.aorta	42	0.776	1040
12.muscle	57.8	1.08	1045
13.bladder	18.9	0.385	1030

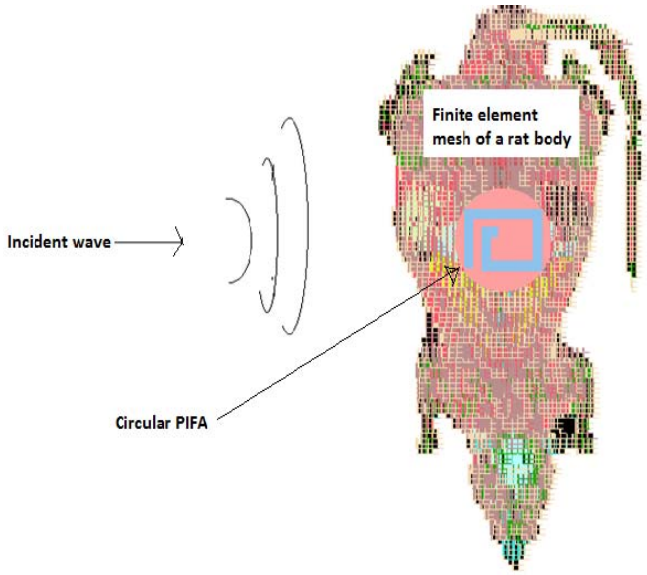

Fig.4 Complete rat model with proposed circular PIFA

TABLE II: PERFORMANCE COMPARISON AT 915 MHz

Antenna Position	Maximum gain (dBi)	Input impedance(Ω)	Resonance Frequency(MHz)
In free space	-23.795	68.00 - j29.732	915
With Rat Model	-19.113	78.34 – j22.874	926.65

IV. BIOCOMPATIBILITY ANALYSIS

Biocompatibility refers to the ability of a material to perform with an appropriate host response in a specific situation. One of the biocompatibility analysis factors is SAR. EM field distributions in different slices of the rat models and average SAR value, Maximum SAR value and the local SAR value in the rat model can be determined based on the simulations of the software. According to IEEE standards, the maximum 1-g and 10-g average SAR to a value of less than 1.6 W/kg and 2W/kg respectively [17], [18].

SAR can determine the amount of heat absorption. SAR is the time derivation of the incremental energy (dU) deposited in an incremental mass (dm) contained in a volume element of density, ρ:

$$SAR = \frac{\mathrm{d}}{\mathrm{dt}}\left(\frac{\mathrm{dU}}{\mathrm{dm}}\right) = \frac{\sigma}{\rho}|\mathrm{E}|^2 \ [\mathrm{W/Kg}] \quad (1)$$

Equation (1) can be written as:

$$SAR = \frac{\mathrm{J2}}{\rho\sigma}[\mathrm{W/kg}] \quad (2)$$

where, σ is the electrical conductivity of the body tissue[S/m], ρ is the material density of the body tissue[Kg/m^3], E is the rms value of the electric field strength in the tissue [V/m], and J is the current density [A/m]. The unit of SAR is watts per kilogram. Fig.5 displays the slice of the electric field in the time domain through the rat body which is at a distance of -4.5 mm from the antenna.

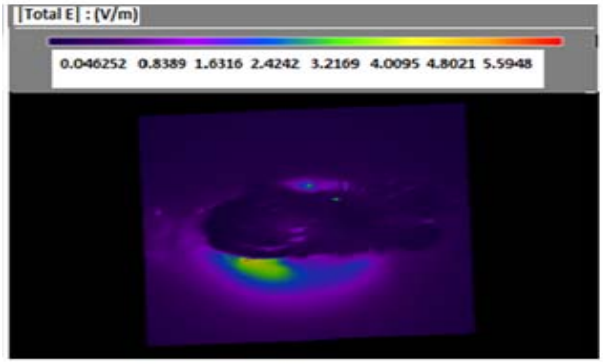

Fig.5 Electric field distribution of a slice at a distance of -4.5 mm from the antenna.

The CAD display of the body tissues and patch antenna is turned off to view the internal fields which are shown in Fig.5and Fig.7.

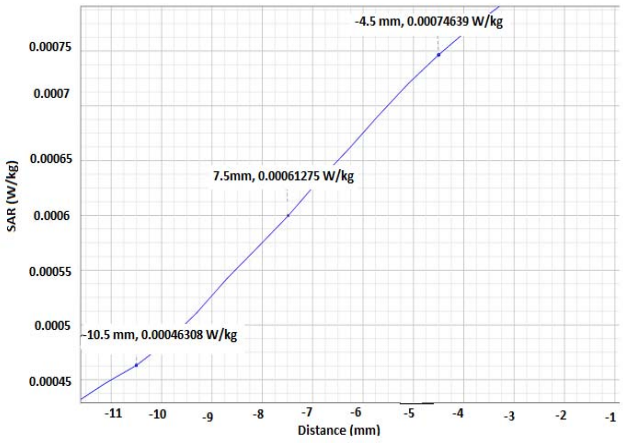

Fig.6 10-g SAR variations at different distances from the antenna.

Fig. 6 shows the plot of 10-g average SAR with the distance from the antenna. The calculation is done by using the distribution of the electric field according to equation (1). It indicates that the SAR is higher near the antenna and then rapidly decreases with the distance. The maximum 1-g average SAR value of 0.0060296 W/kg and 10-g average SAR value of 0.0015845 W/kg are obtained which are both lower than the IEEE C95.1-1999(1-g average SAR< 1.6 W/kg) [17] and IEEE C95.1-2005(10-g average SAR<2 W/kg) [18]. Fig.7 illustrates the average -1g and 10-g SAR values. The hotspot corresponds to the maximum absorption inside Rat model. The hotspot for the 1-g and 10-g is (-1.5,-3.29) and (9.9, 3.29) in mm respectively which indicates the position of the maximum absorption.

Finally, the proposed work can be compared with some other research work associated with it. Bakogianni et al.[19] has proposed a planar dipole antenna which was implanted into the skin of a three-layered human arm model. The stimulated maximum 1-g and 10-g average SAR values are 426.5 W/kg and 96.8 W/kg, respectively if the implantable antenna is delivering 1W.Kim and Samii [20] have designed microstrip patch antenna and PIFA which were implanted in the human chest. The peak SAR of the microstrip antenna and

the PIFA were recorded at the skin tissue in front of the antenna and were 182 W/kg and 209 W/kg respectively. The

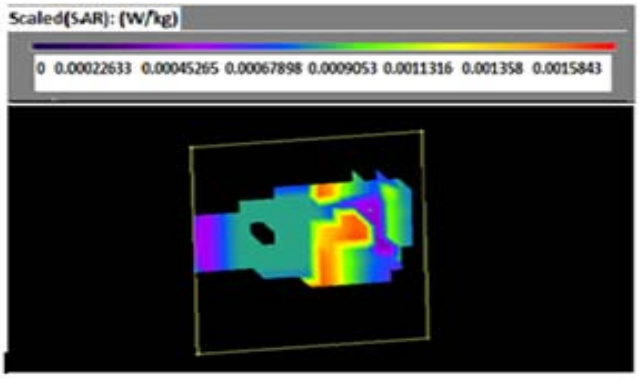

(a)

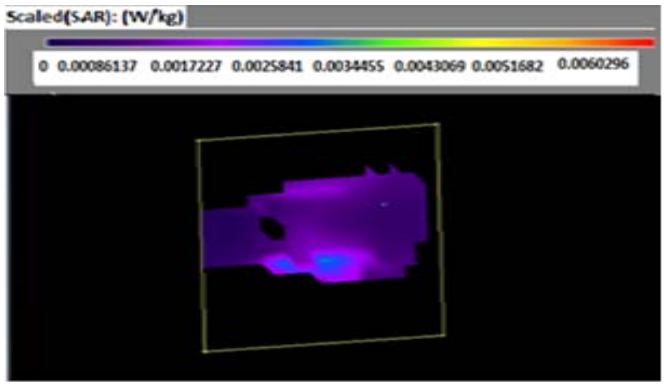

(b)

Fig.7 The scaled, (a) 10-g average SAR values, (b) 1-g average SAR values in the plane of the proposed antenna at the slice of maximum value.

values of the SARs are much higher than the standard value in both above mentioned research. But, the SAR values of the proposed work are lower than the standard value.

V. CONCLUSION

A circular PIFA was designed and the performance of the antenna in the free space as well as with the rat body was presented in this paper. The maximum stimulated gain of the antenna in free space and with the rat body are -23.795 dBi and -19.113 dBi respectively. Biocompatibility was also analysed for the energy harvested DBS device by calculating the SAR in this study.As the distance from the antenna increased the electric field distribution decreased gradually. Hence, the SAR value decreased with the distance from the antenna.The simulation result indicated that at -4.5mm, -7.5 mm and -10.5 mm distance the values of 10-g SAR were 0.00074639 W/kg, 0.00061275 W/kg, and 0.00046308 W/kg respectively.From the above simulation results, it is clear that the electric field and the SAR distribution are maximum near the antenna and theses values gradually decreases with the distance from the antenna. However, the SAR is within the regulated safety limits if the received power of the proposed harvested antenna is few miliwatts.

REFERENCES

[1] Liker, M.A., Won D.S., Rao, V.Y., Hua, S.E.: Deep brain stimulation: An evolving technology. *Proceedings of the IEEE 96(7), 1129-1141* (2008).

[2] R. J. Anderson, M. A. Frye, O. A. Abulseoud, K. H. Lee, J. A. McGillivray, M. Berk, and S.J Tye, "Deep brain stimulation for treatment-resistant depression: Efficacy, safety and mechanisms of action," Neuroscience & Biobehavioral Reviews, vol. 36, pp. 1920-1933, 2012.

[3] M. A. Liker, D. S. Won, V. Y. Rao, and S. E. Hua, *"Deep Brain Stimulation : An Evolving Technology,"Proceedings of the IEEE,*vol.96*, pp. 1129-1141,2008.*

[4] C. R. Butson and C. C. McIntyre, "Role of electrode design on the volume of tissue activated during deep brain stimulation," *Journal of Neural Engineering*, vol.3, p.1, 2006.

[5] N. Yousif and X. Liu, "Modeling the current distribution across the depth electrode-brain interface in deep brain stimulation," Expert Review of Medical Devices, vol.4, p.623, 2007.

[6] H. Jabbar, Y. S. Song, and T. T. Jeong, "RF energy harvesting system and circuits for charging of mobile devices," Consumer Electronics, *IEEE Transactions on* vol.56, pp. 247-253, 2010.

[7] A. Andújar, J. Anguera, C. Picher, and C. Puente, "Human Head Interaction Over Ground Plane Booster Antenna Technology: Functional and Biological Analysis," PIER B, vol. 41, pp. 153-185, 2012.

[8] M. K. Hosain, A. Kouzani, and S. Tye, "Multi-layer implantable antenna for closed loop deep brain stimulation system," in 2012 International Symposium on Communications and Information Technologies (ISCIT), Queensland, Australia, 2012, pp. 643-648.

[9] F. Wang, Z. Du, Q. Wang and K. Gong, "Enhanced-bandwidth PIFA with T-shaped ground plane", *Electronic Letters*, vol. 40, no. 23, pp. 1504 – 1505, Nov. 2004.

[10] B. Kim, J. Hoon and H. Choi, "Small wideband PIFA for mobile phones at 1800 MHz," *Vehicular Technology Conference*, vol. 1, pp. 27-29, May 2004.

[11] B. Merabet, L. Cirio, H. Takhedmit, F. Costa, C. Vollaire, B. Allard, and O. Picon, "Low-cost converter for harvesting of microwave electromagnetic energy," in Energy Conversation Congress and Exposition, ECCE 2009, San Jose, CA,pp.2592-2599, 2009.

[12] M. Hosain, A. Z. Kouzani, S. Tye, K. Walder, and L. Kong, "Design of a miniature UHF PIFA for DBS implants," in 2012 ICME International Conference on Complex Medical Engineering(CME), pp. 485-489, 2012.

[13] K. L. Wong, Compact and broadband microstripanrennas, First Ed. New York: John Wiley &Sons, Inc., 2002.

[14] C. Gabriel, S. Gabriel, and E. Corthout, "The dielectric properties of biological tissues: I. Literature survey," *Physics in medicine and biology,* vol. 41, pp. 2231, 1996.

[15] R. Pethig, "Dielectric properties of body tissues," *Clinical Physics and Physiological Measurement,* vol. 8, pp. 5-12, 1987.

[16] S. Bri, S. Kassimi, H. Habibi, and A. Mamouni, "Specific absorption rate (SAR) distribution in the human head at global system mobile (GSM) frequencies," *European Journal of Scientific Research*, vol. 49, pp. 590-600, 2011.

[17] IEEE standard for safety levels with respect to human Exposure to Radio frequency Electromagnetic fields, 3 KHz to 300 GHz, *IEEE Standard* C95.1, 1999.

[18] IEEE standard for safety levels with respect to human exposureto radiofrequency electromagnetic fields, 3 KHz to 300 GHz, *IEEE Standard* C95.1, 2005.

[19] Sofia Bakogianni, Stavros Koulouridis," An Implantable Planar Dipole Antenna for Wireless MedRadio-Band Biotelemetry Devices," *IEEE Antenna and Wireless Propagation Letters*, vol.15, pp. 234-237, June, 2015.

[20] Jaehoon Kim, YahyaRahmat-Samii, "Implanted Antennas inside a Human Body: Simulations, Designs, and Characterizations," *IEEE Transactions on Microwave Theory and Techniques*, vol.52, no.8, August, 2004.

2nd International Conference on Electrical, Computer & Telecommunication Engineering (ICECTE)
8-10 December 2016, Rajshahi-6204, Bangladesh

Performance Analysis of 4×4 FBG-OC-Based Bidirectional Optical Cross Connects Using Ten-Port ROC in WDM Networks

Nirupam Das[1], Pejush Chandra Sarker[1], Punab Chandra Kundu[2] and Md. Rabiul Islam[1]
[1]Department of Electrical and Electronic Engineering, Rajshahi University of Engineering & Technology, Rajshahi, Bangladesh
[2]Bangladesh Power Development Board, Bangladesh
nirupamruet@gmail.com, pejush01@yahoo.com, punabkundu97@yahoo.com, rabiulbd@hotmail.com

***Abstract*—In this paper, the crosstalk performance of a 4×4 fiber bragg grating optical circulator based bidirectional optical cross connects using ten-port rotatable optical circulator (ROC) in wavelength division multiplexing networks has been investigated. The bit-error rate and power penalty due to intraband crosstalk are also evaluated. Ten-port ROC provides better performance than that of four-port and five-port.**

Keywords—Bidirectional optical cross connect crosstalk; Fiber bragg grating; Wavelength division multiplexing;

I. INTRODUCTION

Bidirectional wavelength division multiplexing (WDM) ring networks (BWRNs) have attracted much attention and offer a cost-effective network topology with self-healing capability for metropolitan area network (MANs). Bidirectional optical cross connects (BOXCs) are the key switching element in BWRNs, which could selectively interchange wavelength channels among the BWRNs in both direction [1]. Different types of BOXCs were reported in [1]–[5]. They have their own merits and limitation such as polarization beam splitters (PBS). In gratings based BOXC, polarization state of input signals needs to be controlled to avoid induced polarization mode dispersion (PMD). In arrayed-waveguide gratings (AWGs) based BOXC, insertion loss is relatively high. In [1], fiber bragg grating optical circulator (FBG-OC) based BOXC has been proposed by dynamic and independent wavelength switching. A small tuning range equal to wavelength channel spacing can be achieved by operating it in the interleaving wavelength mode and thus increases the number of wavelength channels without imposing stringent constraint on the tuning range of tunable FBGs [1]. In [1], it is analyzed how to extend a 2×2 BOXC to a large N×N BOXC based on the benes network structures. In addition, it is proposed two types of 4×4 BOXC configurations, one is using FBG and four or five-port optical circulator (OC) and other is using FBG and ten-port OC. Insertion loss is lower in the second configuration.

In [6], crosstalk performance of a 4×4 FBG-OC based bidirectional optical cross connects using four-port or five-port rotatable optical circulator (ROC) has been analyzed. In [7], a 7×7 reconfigurable multiwavelength optical cross connect (RM-OXC) based on tunable fiber bragg grating (T-FBG) and optical circulator (OC) has been analyzed. So far in the literature, no study has been done on the crosstalk performance of a 4×4 FBG-OC based bidirectional optical cross connects using ten-port ROC.

The one of the main limiting factor of optical cross connect (OXCs) in optical network is crosstalk [8], [9]. Therefore, the network performance is limited due to the intraband crosstalk which gives an increase of a significant single degradation leading to a bit error probability. The effect due to intraband crosstalk has been studied in this paper.

In this paper, the crosstalk performance of a 4×4 FBG-OC based bidirectional optical cross connects using ten-port ROC in WDM networks has been also investigated and its crosstalk performance has been compared with the previously analyzed 4×4 FBG-OC based bidirectional optical cross connects using four-port and five-port ROC.

II. ARCHITECHTURE OF FBG-OC-BASED BOXCS

A schematic diagram of a feasible metro network composed of BWRNs is shown in Fig. 1, where smaller access ring networks are connected to a big metro-core ring network via BOXCs. In such a scheme, each ring network contains bidirectional add or drop multiplexer (BOADM) nodes within a local area [6]. A 4×4 BOXC using ten-port ROCs as shown in Fig. 2 is investigated. Two different sets of wavelength channels {A} and {B} propagate in opposite directions in each BWRN. Fig. 2 shows the configuration of BOXCs using ten-port ROC. To circumvent the constraint on the tuning range of FBGs, the interleaved wavelength scheme is carried out in this paper. In the following analysis, it is assumed that a set of wavelengths $\{\lambda_{2n-1}\}$ (1, 2,……., *m*), denoted as group A, and another set of wavelengths $\{\lambda_{2n}\}$ (1, 2,……., *m*), denoted as group B, are transmitted in opposite directions. A 4×4 BOXC using ten-port ROCs is more complex than a 2×2 and a 4×4 BOXC using four port ROCs. There are four ten-

978-1-5090-5785-6/16/$31.00 ©2016 IEEE

port ROCs as well as twelve sets of tunable FBGs and eight sets of fixed FBGs used in 4×4 BOXC. The OCs are nonreciprocal or fully rotatable.

III. Crosstalk Analysis of BOXCs

For crosstalk analysis, BOXCs configuration as shown in Fig. 2 has been considered. The insertion loss of the BOXCs is ignored and only the first-order crosstalk fields that arise in the BOXCs are considered. Since the higher-order crosstalk fields are very weak, it can be ignored [1]. λ_{2n} and λ_{2n-1} (n = 1, 2, …….., m) are used to denote the main WDM channels with odd and even wavelength numbers respectively. Similarly, λ'_{2n-1}, (λ''_{2n} , λ''_{2n-1}) , (λ''_{2n} , λ'''_{2n-1}) and λ'''_{2n} are used to denote the corresponding crosstalk channels with the same odd and even wavelength numbers as the main WDM channels respectively.

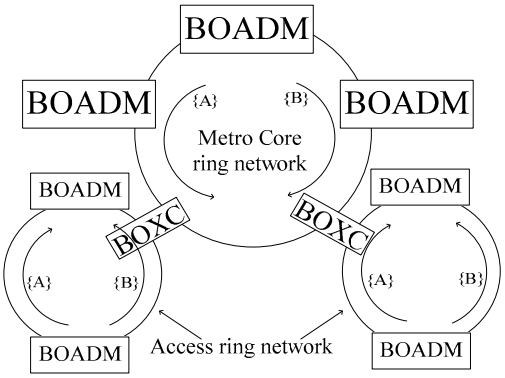

Fig. 1. A bidirectional WDM ring networks interconnected by BOXCs [1]

TABLE I. Number of Crosstalk Fields Generated in the 4×4 BOXC and Combined with the Main Signal for the Bar State (Port I to Port V)

Crosstalk type	Light source	Number of crosstalk
Coherent crosstalk	λ_{2n-1}	m-n
		n-1
		n-1
		m-n
Incoherent crosstalk	λ'_{2n-1}	1+1
	λ'_{2n-1}	1
	λ'_{2n-1}	0

Tables I, II, III, IV and V list the number of coherent and incoherent crosstalk fields generated in the 4×4 BOXC and combined with the main signal λ_{2n-1} for the bar and cross states respectively, where m is the number of channels entering the BOXCs for each direction and n is the position number of each channel. Since BOXCs are symmetric for both directions and fully rotatable, each row in tables is also applicable to the main signal with the even wavelength number λ_{2n}. The last column of Tables III, IV, and V have several sub-columns for the number of crosstalks which are combined with main signal λ_{2n-1} and follow either of the two paths to reach the destination port either of VI or VII or VIII during the cross state of the 4×4 BOXC.

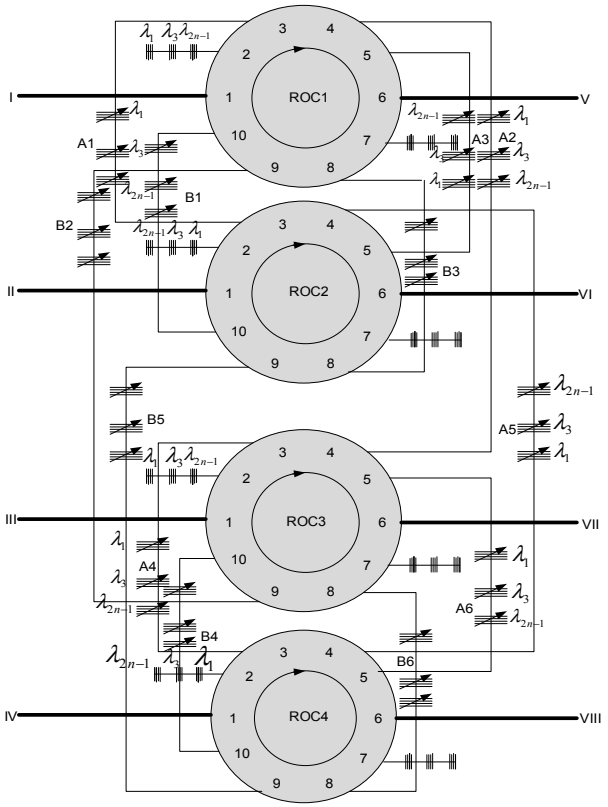

Fig. 2. A 4×4 rearrangeably nonblocking BOXC using ten-port ROCs [1].

TABLE II. Number of Crosstalk Fields Generated in The 4×4 BOXC and Combined with the Main Signal for the Bar State (Port I to Port V)

Crosstalk type	Light source	Number of crosstalk
Coherent crosstalk	λ_{2n-1}	m-n
		m-n
Incoherent crosstalk	λ'_{2n-1}	m+m
	λ''_{2n-1}	m
	λ'''_{2n-1}	1

TABLE III. Number of Crosstalk Fields Generated in the 4×4 BOXC and Combined with the Main Signal for the Cross State (Port I to Port VI)

Crosstalk type	Light source	Number of crosstalk	
Coherent crosstalk	λ_{2n-1}	m-n	m-n
		m-n	n-1
		n-1	n-1
Incoherent crosstalk	λ'_{2n-1}	m	1
		1	m
	λ''_{2n-1}	0	1
	λ'''_{2n-1}	1	1

TABLE IV. NUMBER OF CROSSTALK FIELDS GENERATED IN THE 4×4 BOXC AND COMBINED WITH THE MAIN SIGNAL FOR THE CROSS STATE (PORT I TO PORT VII)

Crosstalk type	Light source	Number of crosstalk	
Coherent crosstalk	λ_{2n-1}	*m*-*n*	*m*-*n*
		n-1	
		n-1	
Incoherent crosstalk	λ'_{2n-1}	1	*m*
	λ''_{2n-1}	*m*	*m*
	λ'''_{2n-1}	1	*m*

TABLE V. NUMBER OF CROSSTALK FIELDS GENERATED IN THE 4×4 BOXC AND COMBINED WITH THE MAIN SIGNAL FOR THE CROSS STATE (PORT I TO PORT VIII)

Crosstalk type	Light source	Number of crosstalk	
Coherent crosstalk	λ_{2n-1}	*m*-*n*	*m*-*n*
		m-*n*	*n*-1
Incoherent crosstalk	λ'_{2n-1}	*m*	1
	λ''_{2n-1}	1	*m*
	λ'''_{2n-1}	*m*	1

BER of any amplified system can be calculated as [6]

$$BER \cong \frac{1}{2} erfc\left(\frac{1}{2\sqrt{2}} \frac{GP_s}{\sigma_1}\right) \quad (1)$$

where, G is the amplifier gain, P_s is optical power of the main signal, and σ_1 is the total noise power of the receiver in optically amplified system. Since all crosstalk elements of same optical power are mixed with the signal, the maximum system power penalty, (PP) is calculated as [4]

$$PP = -5\log_{10}[1 - 4(N_1 + N_2)(X_F + X_R)Q^2] \quad (2)$$

where, X_F and X_R are the crosstalk coefficients of FBG and RB, and Q is the Q factor where $Q = 6$ at (BER) of 10^{-9} [4].

IV. RESULT AND DISCUSSION

Numerical computations are carried out based on (1) and (2) to evaluate the BER and PP performance of BOXCs. Fig. 3 shows BER with respect to change of received power at the bar-state of the 4×4 BOXC using ten-port ROCs with the different number of wavelength channels, *m*. It is observed that BER increases with the increases of *m*.

Power penalty as a function of component crosstalk the bar state of the 4×4 BOXC using ten-port ROCs with different number of wavelength channels, *m* is shown in Fig. 4. It is found that power penalty increases with the increases of *m*. Fig. 5 shows BER with respect to change of received power at the cross-state of the 4×4 BOXC using ten-port ROCs with the various position of wavelength channels, *n*. It is also seen that BER increases with the increases of *n*, while the number of wavelength channels, *m* is fixed. Fig. 6 shows power penalty as a function of component crosstalk of the cross state of the 4×4 BOXC using ten port ROCs with the various position of wavelength channels, *n*. It is seen that power penalty increases with the increase of *n*.

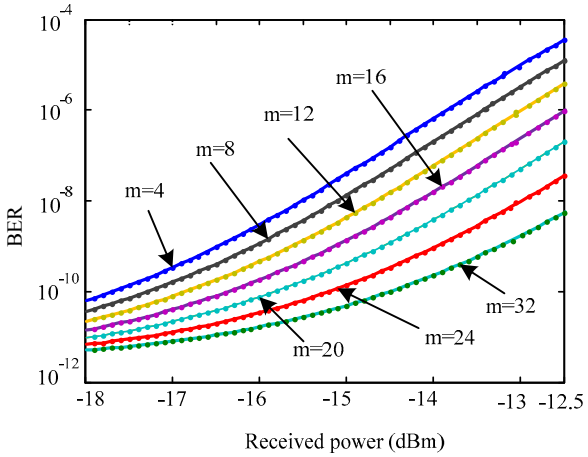

Fig. 3. BER with respect to change of received power at the bar-state of BOXC using ten-port ROCs with the different number of wavelength channels, *m*.

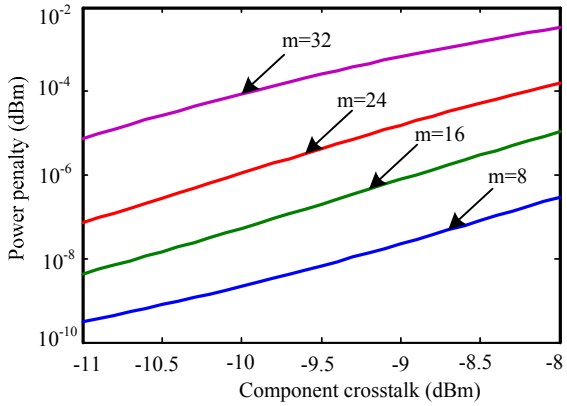

Fig. 4. WDM power penalty as a function of component crosstalk at the bar state of the 4×4 BOXC using ten-port ROCs with different number of wavelength channels, *m*.

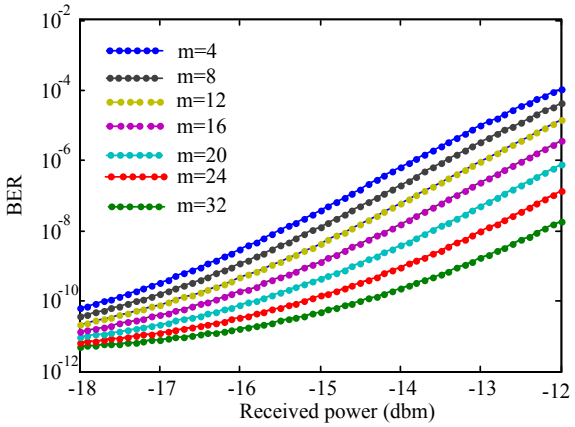

Fig. 5. BER with respect to change of received power at the cross-state of BOXC using ten-port ROCs with the various positions of the wavelength channels, *n* while number of wavelength channel, *m* is fixed.

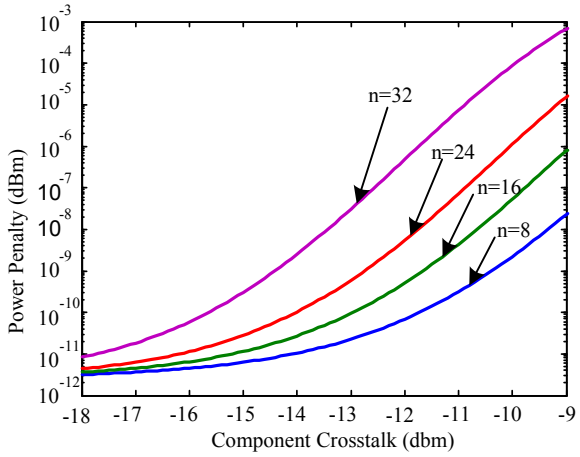

Fig. 6. Power penalty as a function of component crosstalk at the cross state of the 4×4 BOXC using ten-port ROCs with the various positions of wavelength channels, *n* while the number of wavelength channels, *m*=32 is fixed.

V. Conclusion

Both BER and power penalty increases in bar-state and cross-state BOXCs with the increase of the number of wavelength channels. The main problem of such kind of BOXCs is that the BER and power penalty also increase significantly as the position number of channel increases in the cross state. But, with the change of the position of wavelength channel does not affect on BER and power penalty in the bar-state. It is obtained that less amount of crosstalk generated in ten-port ROC than the existing four-port and five-port ROC.

References

[1] H. Yuan, W. Zhong and W. Hu, "FBG-Based Bidirectional Optical Cross Connects for Bidirectional WDM Ring Networks," *J. Lightwave Technol.*, vol. 22, pp. 2710–2721, Dec. 2004.

[2] S. K. Park and J. W. Park et al., "Multiwavelength bidirectional optical cross connect using fiber Bragg gratings and polarization beam splitters," *IEEE Photon. Technol. Lett.*, vol. 12, pp. 888–890, July 2000.

[3] J. Kim and B. Lee, "Independently switchable bidirectional optical cross connects," *IEEE Photon. Technol. Lett.,* vol. 12, pp. 693–695, June 2000.

[4] S. Kim, "Bidirectional optical cross connects for multiwavelength ring networks using single arrayed waveguide grating router," *J. Lightwave Technol.*, vol. 20, pp. 188–194, Feb. 2002.

[5] Y.Shen, K. Lu, and W. Gu, "Coherent and incoherent crosstalk in WDM optical networks," *J. Lightwave Technol.*, vol. 17, pp. 759–764, May 1999.

[6] M. R. Karim and S. P. Majumder, "Crosstalk modeling and analysis of FBG-OC-based bidirectional optical cross connects for WDM networks," *In: proc. IEEE TENCON* 2009, Singapore, Nov. 23–26, 2009.

[7] P. C. Kundu. M. R. Islam, P. C. Sarker and S. P. Majumber, "Cross-talk analysis of wavelength switch and MWSF limimted wavelength interchanging cross-connects (L-WIXC) in a WDM network," *In: Proc. 1st ICEEE*, 04–06 Nov. 2015, RUET, Rajshahi, Bangladesh.

[8] P. C. Kundu. M. R. Islam, P. C. Sarker and S. P. Majumder, "Performance analysis of DCS-based limited wavelegth interchanging cross-connects in WDM network," *In: Proc. 1st ICCIE*, 26–27, Nov. 2015, RUET, Rajshahi, Bangladesh.

2nd International Conference on Electrical, Computer & Telecommunication Engineering (ICECTE)
8-10 December 2016, Rajshahi-6204, Bangladesh

Developing a Framework for Analyzing Social Networks to Identify Human Behaviours

Khandakar Tareq Alam
Department of CSE,
CUET, Bangladesh
Email: ktareq024@gmail.com

Syed Mohammod Minhaz Hossain
Department of CSE,
BGC Trust University, Bangladesh
Email: minhaz_cse@yahoo.com

Mohammad Shamsul Arefin
Department of CSE,
CUET, Bangladesh
Email: sarefin_406@yahoo.com

Abstract— **Nowadays, online social networks become an important part in people's everyday life. Most of the people share their feelings, views, likings and disliking using social networks. By analysing social networks' data properly, it is possible to identify the behavioural patterns of the users. Considering this fact, in this paper we present a framework to analyse social networks' data to identify human behaviours. We have developed a framework for the collection and analysis of large data by crawling public data obtained from the users of online social networks. The system can analyze data posted by the users in two different languages. Experimental results show that social network is a good resource for estimating attitudes of the people.**

***Keywords*—Social networks, data crawling, behavior analysis.**

I. INTRODUCTION

Social network is a medium where users interact with several groups of users. Online social networks are useful to analyze the user behaviour from the data crawled from the social networks. Generally, the methods of user behaviour characterization, based on users' individual features, are not appropriate for online networking sites. Because users interact with the sites and with other users through a series of multiple interfaces that let them to upload photos and posts, view content, choose friends, rank favourite contents, subscribe to users and do many other interactions. Different interaction patterns can be observed for different groups of users.

The importance of analyzing users' behaviour let us to know the actual interest of the users. We can determine the users long time behaviours from the crawled data. The categorization of the user is very important for knowing the type of users. It will help to determine in which type of contents they are interested in, how they interact with other users, and by the place they visited we can know their interest. Identifying different user behaviours has the potential to improve business and resource management in online social networks.

Although there are many systems for analyzing social networks' data to identify users' behaviours, most of them are unilingual in nature and none of them considers the analysis of data of Bangla and English. Considering this fact, in this paper, we develop a system that can analyze social networks data of both languages to identify users' behaviours.

We decompose our behaviour analysis task into three parts. These are crawling data from social networks, storing crawled data into databases, analyzing stored data to identify users' behaviours.

The remainder of this paper is organized as follows. Section II provides a brief review of related work. In section III, we detail the computation framework of our proposed approach. Section IV presents the experimental results. Finally, we conclude and sketch future research directions in Section V.

II. RELATED WORK

Recently behaviour analysis from social networks has immense attention from the researchers and different methods have been proposed to accomplish the analysis procedure in different relevant fields. Mislove et al. [1] developed a system for measurement and analysis of online social networks where they examine data gathered from four popular online social networks: Flickr, YouTube, LiveJournal, and Orkut. They crawled publicly accessible user links on each site, obtaining a large portion of each social network's graph. They discussed the implications of these structural properties for the design of social network based systems. Maia et al. [2] propose a methodology for characterizing and identifying user behaviors in online social networks. They use a clustering algorithm to group users with similar behavioural pattern. They show that attributes that stem from the user social interactions are good discriminators and allow the identification of relevant user behaviours efficiently However, the main limitation of their approach is that the analysis is based on only with the measure of friendship relation. Benevenuto et al. [3] present an analysis of user workloads in online social networks. In their analysis they consider HTTP sessions of 37,024 users who accessed four popular social networks: Orkut, MySpace, Hi5, and LinkedIn. Based on their analysis, they designed a system for identifying influential users and their network impact.

Wilson et al. [4] propose the use of interaction graphs to impart meaning to online social links by quantifying user interactions. They analyze interaction graphs derived from Facebook user traces and show that they exhibit significantly lower levels of the "small-world" properties shown in their social graph counterparts. Perer et al. [5] presents techniques to help structural analysts understand social networks more effectively. They present a system known as SocialAction that uses attribute ranking and coordinated views to help users systematically examine numerous SNA measures. Nowell et al. [6] develop approaches to link prediction based on measures for analyzing the "proximity" of nodes in a network. Chau et al. [7] developed a framework of parallel crawlers for online social networks, utilizing a centralized queue.

Gjoka et al. [8] perform an analysis on a data set collected from Facebook and Adonomics. Based on their analysis they conclude that the popularity of Facebook applications has a

978-1-5090-5785-6/16/$31.00 ©2016 IEEE

highly skewed distribution. Felt et al. [9] address privacy related issues associated with social networking APIs. Viswanath et al. [10] studied the evolution of activity between users in the Facebook social network and found that links in the activity network tend to come and go rapidly over time, and the strength of ties exhibits a general decreasing trend of activity as the social network link ages.

III. SOCIAL NETWORK ANALYSIS: SYSTEM ARCHITECTURE AND DESIGN

The system architecture of behaviour analysis framework is shown in Fig. 1.

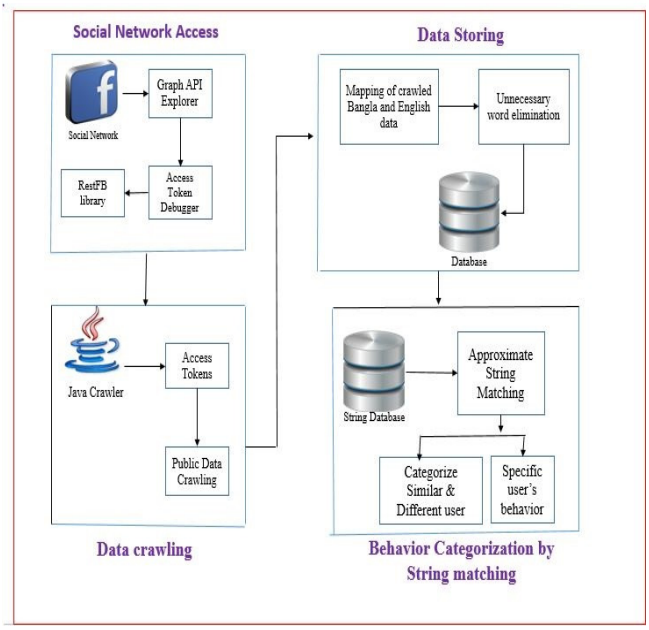

Fig.1 System architecture of the proposed system

First of all we have to establish network connection to get access from the social networks. The network connection will allow us to get access from the Graph API. Then from the Graph API we need to download the RestFB package in order to get access from the Graph API. The Graph API gave the pathway to get access tokens for collecting data from social network.

Algorithm *KeywordExtraction*

```
1.  begin
2.  for each independent word do
3.        initialize a 2D matrix with value=0;
4.  end for
5.  count=0;
6.  for each independent word do
7.      if word match with the sentence's word then
8.          count++;
9.      else
10.         do nothing;
11.     put the counted value in corresponding index;
12.   end if
13. end for
14. Determine the maximum value
15.     define the keyword;
16.  End
```

Fig 2 Algorithm for extracting keywords

Then, with the Java crawler we crawled data simultaneously from social network more than 30 days. The data then categorized into Bangla and English. We stored Bangla and English data into two different databases. We used mySQL database to store these data. Before storing data we mapped the data into reliable data by JSON Parser. After storing data into databases, we eliminated unnecessary words to make our dataset more reliable. After eliminating unnecessary words, we select many words as keywords and stored these keywords into another database for further analysis. Algorithm for selecting keywords is given in Fig. 2. The keywords we selected were categorized into several categories for behaviour analysis of the users of online social networks. Table I shows some of the categories and their corresponding categories. We also consider sub-categories within each main category. As for example, in movie loves category, we consider three sub-categories of movies such as action, horror, and romantic sub-categories.

The strings were matched with the Bangla and English datasets. When we found more than one keywords in one user's dataset, we assume that user into the defined category. After that we check for another match to perform further analysis.

TABLE I
KEYWORDS FOR DIFFERENT CATEGORY

S.N	Categorization	Keywords
1.	Movie lovers	Watching, film, , eating, movie, , reading, novel, book, poem
2.	Journey lover	Travelling, visiting, tour, ভ্রমন, নৌকা, পাহাড়, সমুদ্র, sea, hills, nature, beauty, bus, train
3.	Music lovers	Listening,music, song, গান, শুনতছি, গাই, সুর, কণ্ঠ, মায়া, guiter, chords, drum,সঙ্গীত, art,
4.	Food lovers	খাবার, ডমি, মুরগি, meat, eating, drinking, alcohol, smoking, chips, burger, chocolate, cake, pancake, pizza, পোলাও, ভাত
5.	Sports lovers	ক্রকিটে, ফুটবল, cricket, football, tenis, play, playing, match, fixing, schedule, ground, stadium, umpire, refree, toss, draw, win, lose, tournament, worldcup, test, one day, practice, olimpic

IV. SYSTEM IMPLEMENTATION AND EXPERIMENTS

In this section, we provide the implementation procedure and performance analysis of our developed system.

A. *Experimental Setup*

The behaviour analysis framework has been developed on a machine having the windows 7, 2.50 Core 2 duo processor with 2GB RAM. The system has been developed in JAVA in the front end and SQLite manager in the back end for storing

related data. For coding, we have used the latest version of NetBeans which is 7.3.

B. Implementation

The system architecture following illustrates the internal and external structure of system modules integrated together in one package to form one system. The following subsections provide a brief background overview of the tools used and the implementation details of the different modules of the developed system starting from the back-end to the front-end. The whole system was developed on windows operating system and Netbeans IDE platforms because they are open source technologies.

Fig. 3 Welcome screen of behaviour analysis framework

Fig. 3 shows the initial screen of our system. Any user who wants to use the system must have to login to the system. Fig. 4 shows the crawled data. From Fig. 4 we can see that

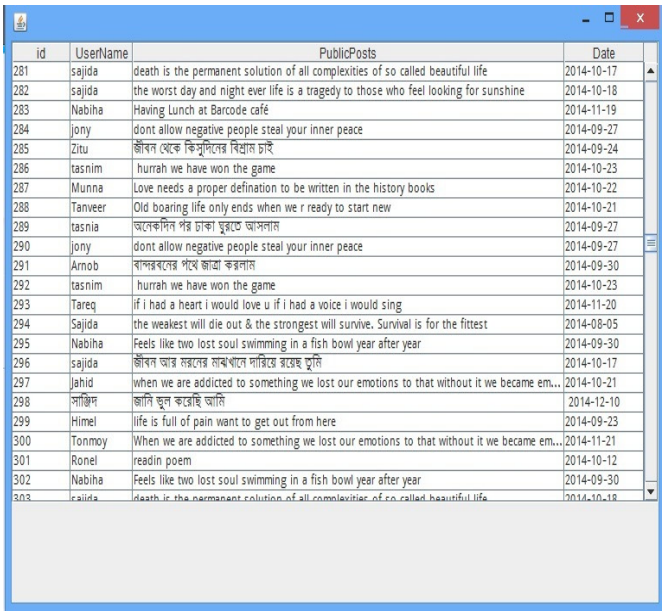

id	UserName	PublicPosts	Date
281	sajida	death is the permanent solution of all complexities of so called beautiful life	2014-10-17
282	sajida	the worst day and night ever life is a tragedy to those who feel looking for sunshine	2014-10-18
283	Nabiha	Having Lunch at Barcode café	2014-11-19
284	jony	dont allow negative people steal your inner peace	2014-09-27
285	Zitu	জীবন থেকে কিসুদিনের বিশ্রাম চাই	2014-09-24
286	tasnim	hurrah we have won the game	2014-10-23
287	Munna	Love needs a proper defination to be written in the history books	2014-10-22
288	Tanveer	Old boaring life only ends when we r ready to start new	2014-10-21
289	tasnia	অনেকদিন পর ঢাকা ঘুরতে আসলাম	2014-09-27
290	jony	dont allow negative people steal your inner peace	2014-09-27
291	Arnob	বান্দরবনের পথে জাত্রা করলাম	2014-09-30
292	tasnim	hurrah we have won the game	2014-10-23
293	Tareq	if i had a heart i would love u if i had a voice i would sing	2014-11-20
294	Sajida	the weakest will die out & the strongest will survive. Survival is for the fittest	2014-08-05
295	Nabiha	Feels like two lost soul swimming in a fish bowl year after year	2014-09-30
296	sajida	জীবন আর মরনের মাঝখানে দারিয়ে রয়েছ তুমি	2014-10-17
297	Jahid	when we are addicted to something we lost our emotions to that without it we became em...	2014-10-21
298	সাজিদ	জানি ভুল করেছি আমি	2014-12-10
299	Himel	life is full of pain want to get out from here	2014-09-23
300	Tonmoy	When we are addicted to something we lost our emotions to that without it we became em...	2014-11-21
301	Ronel	readin poem	2014-10-12
302	Nabiha	Feels like two lost soul swimming in a fish bowl year after year	2014-09-30
303	sajida	death is the permanent solution of all complexities of so called beautiful life	2014-10-18

Fig. 4 Portion of crawled data from social networks

crawled data contains the information of two different languages: English and Bangla. Fig. 5 presents the snapshot of categorization of the users' behaviours based on the crawled data. For identifying specific user's behaviour, we need to select corresponding user's name from the box.

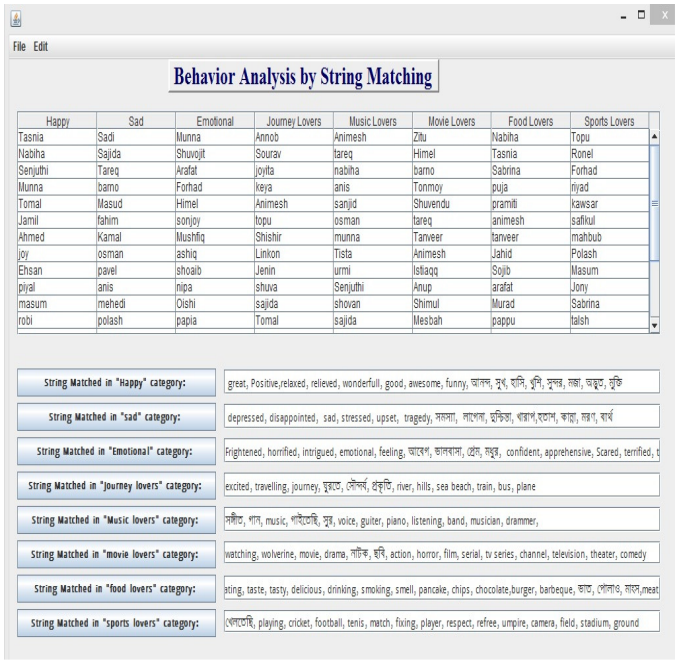

Fig. 5 Snapshot of the system showing the categorization

Then by approximate string matching, we can find out the behavioural pattern of each user. Fig. 6 shows the result.

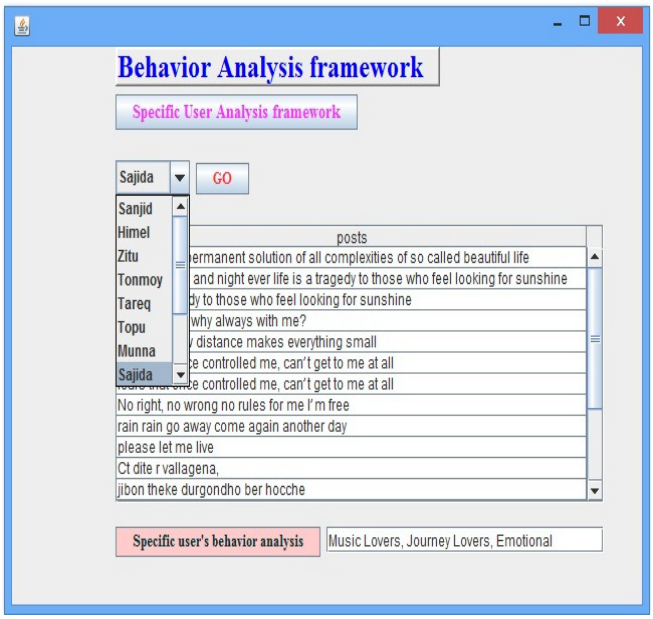

Fig.6 Snapshot showing a specific user's behaviour

C. Experimental Results

We performed the crawling of English and Bangla posts and comments. However, all the crawled information was not accurately processed. We ignored such incorrect information for the analysis. Fig. 7 shows the experimental results of the behavioural patterns of the users.

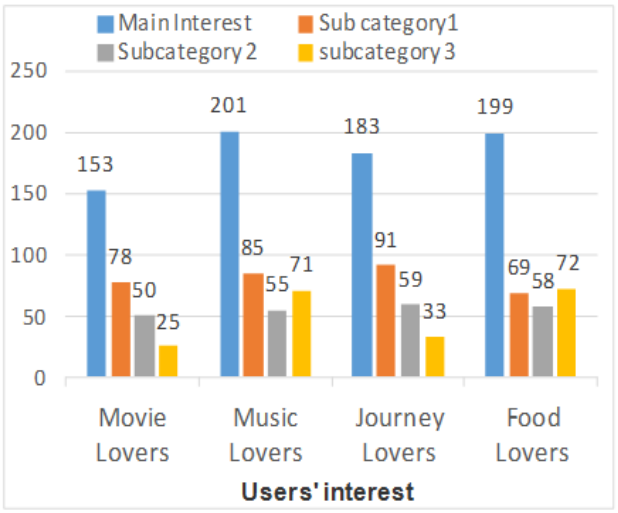

Fig. 7 Behavioural patterns of the users

V. Conclusion

We have developed a bilingual behaviour analysis framework that can categorize users based on their posts and comments in social networks. Online Social Networks are among the most intriguing phenomena of the last few years. As data relative to users and relationships among users are not publicly accessible, so we resorted to exploit some techniques derived from web data extraction in order to extract a significant sample of users and their publicly accessible posts. Future developments involve the implementation of parallel codes in order to speed-up the data extraction process and the evaluation of network metrics.

References

[1] A. Mislove, M. Marcon, K. P. Gummadi, P. Druschel, and B. Bhattacharjee, "Measurement and analysis of online social networks", In Proc. of the 7th ACM SIGCOMM Conference on Internet Measurement, pp. 29-42, 2007.

[2] M. Maia, J. Almeida, and V. Almeida, "Identifying user behavior in online social networks", In Proc. of the 1st Workshop on Social Network Systems, pp. 1-6, 2008.

[3] F. Benevenutoy, T. Rodriguesy, M. Cha, and V. Almeiday, "Characterizing user behavior in online social networks", In Proc. of the 9th ACM SIGCOMM Conference on Internet Measurement, pp. 49-62, 2009.

[4] C. Wilson, B. Boe, A. Sala, K. P. N. Puttaswamy and B. Y. Zhao, "User interactions in online social networks and their implications", In Proc. of the 4th ACM European Conference on Computer Systems, pp.205-218, 2009.

[5] A. Perer and B. Shneiderman. "Balancing systematic and flexible exploration of social networks", IEEE Transactions on Visualization and Computer Graphics, vol.12, issue 5, pp. 693-700, 2006.

[6] D. L. Nowell and J. Kleinberg, "The link-prediction problem for social networks", Journal of the American Society for Information Science and Technology, vol. 58, no. 7, pp. 1019-1031, 2007.

[7] D. Chau, S. Pandit, S. Wang, and C. Faloutsos, "Parallel crawling for online social networks", In Proc. of the 16th International Conference on World Wide Web, pp. 1283-1284, 2007.

[8] M. Gjoka, M. Sirivianos, A. Markopoulou, and X. Yang, "Poking facebook: characterization of osn applications", In Proc. of the 1st Workshop on Online Social Networks, pp. 31-36, 2008.

[9] A. Felt and D. Evans, "Privacy protection for social networking APIs", In Proc. of the 1st Workshop on Social Network Security Systems, pp. 1-6, 2008.

[10] B. Viswanath, A. Mislove, M. Cha, K. P. Gummadi, "On the evolution of user interaction in Facebook", In Proc. of the 2nd ACM Workshop on Online Social Networks, pp. 37-42, 2009.

[11] S. Catanese, P. De Meo, E. Ferrara, and G. Fiumara, "Analyzing the Facebook friendship graph", In Proc. of the 1st Workshop on Mining the Future Internet, pp. 14-19, 2010.

[12] S. A. Catanese, P. D. Meo, E. Ferrara, and G. Fiumara "Crawling Facebook for social network analysis purposes", In Proc. of the International Conference on Web Intelligence, Mining and Semantics, 2011.

[13] M. Bosnjak, E. Oliveira, J. Martins, E. Mendes and R. L. Sarento, "A distributed focused crawler to support open research with twitter data", In Proc. of ACM SIGMOD International Conference on Management of Data, pp. 791-792, 2012.

[14] P. Berger, P. Hennig, T. Klingbeil, and M. Kohnen, "Mining the boundaries of social networks: crawling social network and twitter", In Proc. of the 21st International Conference on World Wide Web, pp. 1233-1240, 2013.

Smart Load Management by Dual Mode Energy Meter for Rational Use of Generated Power

Md. Alimul Islam Salim[1], M.R.I. Sheikh[2] & Md. Habibur Rahman[3]
[1,2,3]EEE Department, Rajshahi University of Engineering &Technology, Rajshahi – 6204, Bangladesh
Email: islamsalim111004@gmail.com[1]

***Abstract*— Unfortunately electricity cannot be stored and hence it is the most perishable commodity in the world, it must therefore be used at the same second it is produced. But somehow if we can control the load of consumer section then it will be possible to use generated power of a country rationally for both using traditional and renewable resources. By using Dual Mode Energy Meter in consumer section which typically demonstrates two tariff modes, will inspire them to use more loads on off-peak hours which consequently reduces the loads in the peaking hours.**

Keywords—rational use; load management; reverse effect; dual mode energy meter; generated power; save mode

I. INTRODUCTION

The demand of electricity is creating a revolutionary growth all over the world and it will always be a challenge for the power generation companies to cope with the increasing consumer demand. But the demand of load in the consumer section varies throughout the day as shown in Fig. 1.

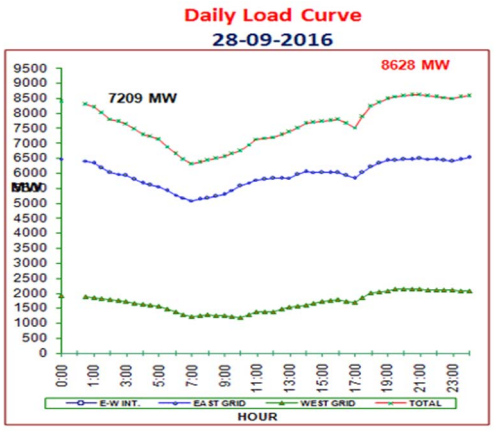

Fig. 1. A practical daily load curve of Bangladesh [1]

From out of the load connected, a consumer uses different fractions of the total load at various times of the day as per their requirements. Since a power system has to supply load to all such consumers, the load to be supplied varies continuously with time and does not remain constant.

From the load curve shown in Fig.1 we can see that the daily load curve of 28th September, 2016 was a highly variable one. The
low off-peak demand happened on nearly 5.00am to 9.00am (at morning hours) and high Peak hour demand happened on 7.00pm to 11.00pm (at evening hours). And Load shedding technique is currently being used in Bangladesh to balance the system.

The objective of this study is to shift non critical loads of peak hours (in renewable case: when renewable resources are unavailable or less) to off-peak hours (in renewable case: when renewable resources are available in plenty) and this redistribute use of power consumption is termed as 'rational use'. The consumers will eagerly shift their non-critical loads to off-peak hours if they are provided with low cost tariff in those hours. And this privilege can be provided to the consumers by implementing 'Dual Mode Energy Meter' in consumer section. By shifting some of the non-critical loads to the off peak hours the load burden of the peak hours will essentially be reduced and thus percentage of availability of electricity will increase progressively.

A detailed description of rational use of electricity is presented in the section II. In section III how we can use generated power rationally by using Dual Mode Energy Meter in consumer section is discussed. Results are discussed in the next section IV. Finally conclusion is drawn in section V.

II. RATIONAL USE OF ELECTRICITY

A. Critical Loads

In power system by the term critical load we mean such type of loads which are so critical that there is a great demand for non-stop electric power.

Some critical loads are: vital digital communications networks, advanced medical therapies, financial transactions such as credit cards and bank operations, elevator service, refrigeration, other essential services.

B. Non-Critical Loads

In power system by the term non-critical load we mean such type of loads the use of which can be postponed or shifted or reduced when necessary. These loads are not used 24 Hours in a day.

Some non-critical loads are:

978-1-5090-5785-6/16/$31.00 ©2016 IEEE

Washing Machine, Water Pumping Machine, Ironing, Laundry, Hot Water Heater, Room Heater, Air Conditioner, Dish Washer, Clothes dryer, Tumble Dryer, Electric Oven, Electric Cooking, Any charging devices

C. Peak Hours

Electricity usage fluctuates constantly due to weather conditions, commercial and industrial business hours and residential electricity usage. During the summer months, demand is usually greater as electricity is used to cool homes and businesses when it is really hot outside, especially during weekday afternoon hours between 3pm to 5pm. Generally, when we speak of "peak hours", we are referring to the times of highest electricity use over the course of the day. In general, Peak events are declared when demand for electricity threatens to outpace supply.

In Bangladesh generally peak hour occurs in between 5.00pm to 11.00pm. [2]

D. Off-Peak Hours

Generally, when we speak of "off-peak hours", we are referring to the times of lowest electricity use over the course of the day. In general, Off-Peak events are declared when demand for electricity comes to the lowest point of supply.

In Bangladesh generally off-peak hour occurs in between 1.00am to 11.00am. [2]

E. Electric Power Generation in Bangladesh and Fuel Cost

From TABLE I it is seen that the power plants which are based on natural gas, coal and hydro (Almost 8000MW) of Bangladesh are very cheap in fuel cost but due to the high cost peaking power plants, which has been a compulsory option on peaking hours, the total generation cost has gone far beyond the ability of normal average people of Bangladesh.

TABLE I. POWER GENERATION IN BANGLADESH AND FUEL COST (AS ON SEPTEMBER, 2016) [3-4]

TYPE	INSTALLED CAPACITY (MW)	GENERATION CAPACITY (MW)	PER UNIT FUEL COST (TK)
Gas	7988	7529	0.95
Hydro	230	230	--
Coal	250	200	2.91
Power Import	600	600	
Diesel	1528	1499	20.01
Furnace Oil	2684	2627	12.62
Total	13280	12685	

For this reason Bangladesh Energy Regulatory Commission (BERC) under Bangladesh government has subsidize the consumer bill and categorize them into following categories:

Category A: Residential; Category B: Agricultural pumping; Category C: Small Industries; Category D: Non-Residential (Light & Power); Category E: Commercial & Office; Category F: Medium Voltage, General Purpose (11 kV); Category G-2: Extra High Voltage, General Purpose (132 kV); Category H: High Voltage, General Purpose (33 kV); Category J: Street Light and Water Pumps [5]

TABLE II. NEW TARIFF PER UNIT RATE (TK.) EFFECTIVE FROM BILL MONTH SEPTEMBER, 2015 [5]

Customer Category and Slabs	NEW TARIFF PER UNIT RATE (TK.) EFFECTIVE FROM BILL MONTH SEPTEMBER, 2015
Category A: Residential	
Life Line: 1-50 Units	3.33
From 00 to 75 units	3.80
From 76 to 200 units	5.14
From 201 to 300 units	5.36
From 301 to 400 units	5.63
From 401 to 600 units	8.70
From 601 to above	9.98

F. Rational Use of Generated Power

From the TABLE II (only category A is shown) we can see that Residential consumers have to pay their bills from 3.33Tk/unit to 9.98Tk/unit. But on the other hand generation cost of electricity using Gas, Hydro and Coal is very less as shown in the TABLE I.

In the load curve as shown in Fig. 1 we can see that consumer load varies throughout the day. In the off-peak hours the load demand is low i.e. consumer side demanding low power. In this time of period consumer side demand varies in between 6500MW to 7000MW and which can be spontaneously supplied by the low cost base power plants as mentioned in TABLE I and the remaining 1000MW capacity are kept idle at that period. Practically this practice is being done by our National Load Dispatch Center (NLDC) of Bangladesh.

But in the peaking hours when load demand of the consumer side go beyond the capacity of low cost power plants then the high cost power plants as mentioned in TABLE I are brought into operation (i) which are acutely responsible for the increase in tariff and (ii) even by implementing them power generation of Bangladesh is hardly coping with the demand.

So to reduce the price of the electricity the utilization of power plants which are based on costly diesel or furnace oil is to be reduced. To reduce the use of peaking power plants the peak of the daily load curve is to be reduced.

For this reason, this study focuses on the rational use of electricity. Rational use of electricity does not mean that we need to stop or reduce the utilization of electricity, it simply means that we only need to be a bit more disciplined on using electricity. Rational use means we need to shift our non-critical loads to off-peak hours (providing consumers with an incentive of low cost tariff as this study proposes) and redistribute the use of this power consumption.

And for this purpose Bangladesh Power Development Board (BPDB) is promoting many advertisements to raise public

awareness to reduce the use of loads in peaking hours. But no change is noticeable yet in the peaking hours.

III. Dual Mode Energy Meter and Reverse Effect

So for the rational use of electricity, this study suggests a new format of energy meter which is called Dual Mode Energy Meter. This Dual Mode Energy Meter typically contains two tariff modes. They are: Save Mode and Normal Mode.

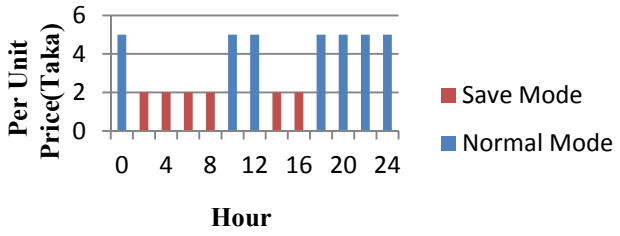

a.

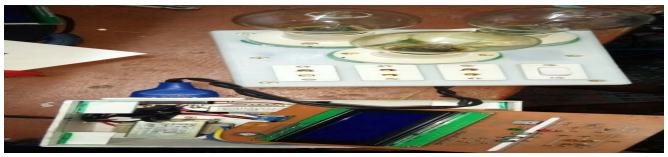

b.

Fig. 2. a. Two Tariff Modes for the rational use of generated power. b. Practical implementation of Dual Mode Energy Meter

A. Save Mode

This mode is declared for a certain period of off-peak hours containing low peak of the daily load curve with an incentive of low cost tariff; such as 2Tk instead of 5Tk as suggested in Fig. 2a. and figure of practical implementation of Save Mode in Dual Mode Energy Meter is shown in Fig. 3a.

a.

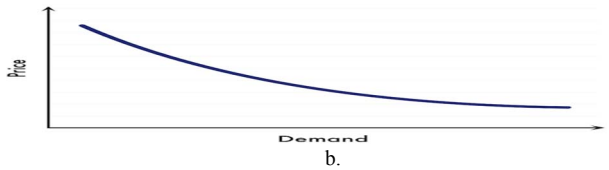

b.

Fig. 3. a. Practical implementation of Save Mode in Dual Mode Energy Meter ('S' stands for Save Mode; 'N' stands for Normal Mode) b. Demand Curve illustrating the increase in demand of electricity as the price falls [6]

From the demand curve it can be said that if the price of the electricity at save mode hours falls, then there will be considerable amount of increase in load in the consumer side as they are getting the same quality electricity at the lower price.

B. Reverse Effect

When consumers will consume some of their additional loads in the save mode hours then they will not have the same need of power in the peaking hours what they would have needed before.

There is a noticeable fact that the non-critical or shift able loads (Electric Ovens, Water Pumps etc.) are not needed to be operated 24hrs in a day.

So, when the non-critical loads are shifted to off-peak hours, there will be a certain reduction of loads in the peak hours.

This factor will aid to the saving of electricity and increase efficiency.

So, the term 'Reverse Effect' suggests 'Consumption of load reduces load'.

.

C. Normal Mode

The hours except the Save Mode hours are declared as Normal Mode hours typically contain the high peak of the daily load curve.

Fig. 4. Practical implementation of Normal Mode in Dual Mode Energy Meter ('N' stands for Normal Mode)

D. Dual Mode Energy Meter in Power Generation By Renewable Energy Resources

In power system generation side and load side are to be balanced in order to maintain the desirable frequency range. In wind power generation Stall Control and Pitch Control method are typically used for the balancing when generation is higher than the demand thus missing the chance of extracting the available wind energy rather using a certain portion of it.

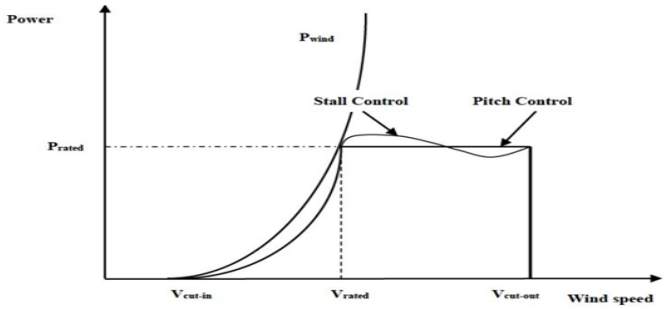

Fig. 5. Power content in the wind and the extractable rated power for pitch controlled and stall controlled wind turbines, as a function of wind speed [7]

In solar power generation system the excessive power is stored in the costly and environment unfriendly energy saving devices.

But with the application of Dual Mode Energy Meter the excessive power in both wind and solar power generation system can be simultaneously consumed at a low tariff rate by giving save mode to the consumers.

IV. Results

When save mode is applied then the consumers will manipulate to use some additional loads at that period and which will considerably reduce the peak hour loads as the reverse effect suggests. The results are shown in Fig. 6.

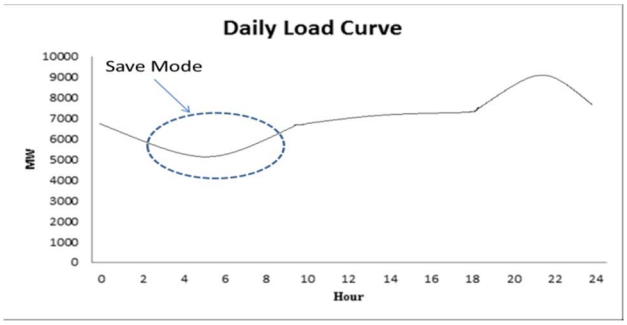

a.

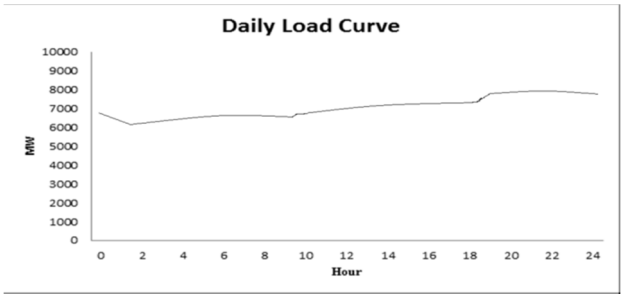

b.

c.

Fig. 6. a. Daily Load Curve before applying the Save Mode. b. Daily Load Curve after applying the Save Mode. c. Practical LCD output of Dual Mode Energy Meter ('S' stands for 'Save Mode'; 'N' stands for 'Normal Mode')

V. Conclusion

A detailed analysis and study of load curve, power generating plants and tariff rates of Bangladesh has been done. Different type of consumers and loads such as critical and non-critical were taken into consideration. Practical circuit implementation has been done and significant data have been being collected. Finally the study reveals that by applying 'Dual Mode Energy Meter' in consumer section will considerably reduce the energy wastage and increase the availability of electricity both for renewable and conventional power generation respectively.

References

[1] Bangladesh Power Development Board, [Online] Available: http://www.bpdb.bd/generation/daily generation archive (Accessed - 29 September, 2016)

[2] Bangladesh Power Development Board, [Online] Available: http://www.bpdb.gov.org

[3] Bangladesh Power Development Board, [Online] Available: http://www.bpdb.bd/generation/Zonewise generation (Accessed - 29 September, 2016)

[4] 'Annual Report 2010-2011' of Bangladesh Power Development Board, Chapter-7, pp. 90-91

[5] Bangladesh Energy Regulatory Comission, [Online] Available: http//www.berc.gov.bd (Accessed - 28 September, 2016)

[6] Florian Kugler, 'The Economics of App Store Pricing', April 5, 2013

[7] Professor M. Ragheb, 'wind energy converter concept', University of Illonois urbana champaign study resources

Sensitivity Analysis of a Graphene based Surface Plasmon Resonance Biosensor in Terms of Number of Graphene Layers

Md. Mushfequl Bari[1,2], Ajay Krishna Sarkar[1], Member, IEEE, Sakhawat Hossain[1]
[1]Department of Electrical and Electronic Engineering,
Rajshahi University of Engineering and Technology, Rajshahi-6204, Bangladesh.
Email: [2]barimdruet@gmail.com

***Abstract*— This research paper introduces the advantage of using graphene as a sensitivity enhancing material for the Surface Plasmon Resonance (SPR) Biosensor. Fresnel's four layer model has been used here for analyzing the performance parameters of SPR biosensor. The analysis shows that Surface Plasmon Resonance Frequency (SPRF) increases with the increasing concentration of target molecule for every graphene layer. It is found that the sensitivity curve for different graphene layer with respect to conventional SPR biosensor is non-linear. How the sensitivity increases with increasing graphene layer was studied in this work. The basic polynomial fitting is used and found that sensitivity increases nonlinearly with the increasing layers and the degree of nonlinearity also increases.**

Keywords—graphene layer; surface plasmon resonance; sensitivity; biosensor

I. INTRODUCTION

The Surface Plasmon Resonance (SPR) biosensor is a very flexible and powerful tool for detecting a wide diversity of bimolecular interactions. SPR monitors molecular interactions in real time and provides significant advantages over optical of calorimetric methods for systems with strong binding and low spectroscopic signals or reaction heats. The label free detection method of SPR technique makes it possible to measure interactions in real time with high sensitivity and without the need of labels. SPR has the application in life science, electrochemistry, gas phase detection, food & environment safety etc.

The use of Graphene has been attracted to researchers for its high surface area [3], electrical conductivity [4] and biocompatibility [4]. Graphene monolayer is sandwiched between metal films and sensing medium as a biomolecular recognition elements. Many researchers have been paying attention on graphene to work with. In [1] numerical modeling on SPR biosensor was carried out for detecting DNA-DNA hybridization by monitoring Resonance Frequency Characteristics (RFC). The results of that work showed the variations of RFC for using graphene sublayers. In that work the output of the biosensor is taken as resonance frequency instead of SPR angle. The work reported 95% of increasing of sensitivity in a linear equation of sensitivity and number of layers. I. e. the sensitivity increases linearly with the increasing number of graphene layers. The same type of results has been achieved in [2]. That research showed that the sensitivity of the biosensor (proposed in that work) is in 2.5% increase with the increase of graphene layers and also linear with respect to the number of layer. In both [1], [2] the analysis regarding the resonance frequency variation was not categorized, I mean, how the Surface Plasmon Resonance Frequency (SPRF) is varying with the number of layers. In case of sensitivity, both [1] and [2] did not show the analysis with respect to each increasing layers separately. Only a equation relating to the sensitivity and number of layers are reported and comments are drawn from that equation.

In this work the change in SPRF with respect to target concentrations was studied separately for increasing each graphene layers. Sensitivity for different number of graphene layers with respect to conventional SPR biosensor was also studied separately after increasing each layer. This work found different results those reported in [1] and [2], that is, the sensitivity is not concretely linear function of number of grapheme layers. This work included the geometric mean of refractive index of interface between the sensing layers for calculating SPRF.

II. METHODOLOGY

A. Numerical modeling for sensitivity analysis

The sensitivity of the optical SPR sensor is defined as the ratio of output parameters (SPRF, θ_{SPR}) to the change in concentration of biomolecules, (sensor input) as given below:

$$S = \frac{\Delta\theta_{SPR}}{\Delta c_a} \quad or \quad S = \frac{\Delta SPRF}{\Delta c_a} \tag{1}$$

In this analysis SPRF is taken as sensor output instead of SPR angle because of its improved advantage [1]. The SPR biosensor uses Kretschmann, prism configuration [5,6] as shown in Fig. 1 [2], where the first layer is a SF10 glass prism (Refractive index (RI) η_P = 1.723), second layer is gold film (thickness and RI are d_{Au} = 50 nm and η_{Au} = 0.726 + j3.4218

978-1-5090-5785-6/16/$31.00 ©2016 IEEE

respectively [5]). Third layer is graphene (thickness and RI are d_G = 0.34 nm and η_G = 3 + j1.14916 respectively [5]), and the final layer is water (RI, η_S = 1.33 [6]).

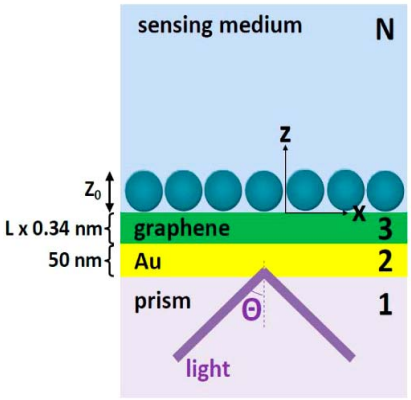

Fig. 1. The N-Layer model for surface plasmon resonance (SPR) biosensor: prism | Au (50 nm) | graphene (L× 0.34 nm) | sensing medium, where L is the number of graphene layers, and z_0 = 100 nm is the thickness of biomolecule layer [2].

A TM polarized He-Ne (wavelength, λ = 633 nm) light wave is used, which passes through the prism and some portion is reflected at the prism gold interface. For achieving SPRF we need to find out the Surface Plasmon Resonance Point (SPRP). The point at which optical wave propagation constant equals Surface Plasmon Wave (SPW) propagation constant is known as SPRP [5]. At this point, the frequency is called SPRF and the angle of incidence is called SPR angle (θ_{SPR}) that is given in [7] and can be shown as follows:

$$\theta_{SPR} = \sin^{-1}\sqrt{\frac{n_{Au}^2 n_s^2}{n_p^2\left(n_{Au}^2 + n_s^2\right)}} \qquad (2)$$

For the binding between target molecule and probe molecule the RI of sensing medium changes as follows [8,9]

$$n_s^d = n_s + c_a \frac{dn}{dc} \qquad (3)$$

Here n_s^d is the RI of the sensing dielectric after absorption of molecules and n_s is the RI of sensing dielectric before absorption of molecules, c_a is the concentration of absorbed molecules and $d\eta/dc$ is the RI increment due to the absorbate. The change in SPR angle changes the propagation constant of SPW (k_{SPW}) which has been explained in [5,10,11] and can be shown as follows:

$$k_{SPW} = \frac{2\pi}{\lambda} n_p \sin\theta_{SPR} \qquad (4)$$

The change in the propagation constant of SPW changes the SPRF which can be explained as follows:

$$SRF = \frac{c_0}{n_{geo}} \frac{k_{SPW}}{2\pi} \qquad (5)$$

Where $\frac{c_0}{n_{geo}}$ is the propagation velocity of SPW that is perpendicularly confined evanescent electromagnetic wave [12,5] and n_{geo} is the geometric mean of the interfaces of the sensing medium ($n_{ge0} = \sqrt[3]{n_{Au} n_s n_G}$, omitting imaginary part that is essential to real world design [7]). To generate a SPRF curve we used Fresnel's equations [13] for four layered hetero-optical system to determine transmitted light intensity [7].

III. Analytical Results and Discussion

Numerical result of SPRF as a function of molecular concentration without using layer (L = 0) and using different number of graphene layers (L = 1 to L = 6) is given in Table I, where c_a is the concentration of absorbed molecules and L is the number of graphene layer. L= 0 denotes no graphene layer exists in the SPR sensor.

TABLE I. SPRF for Different Layers

c_a (nM)	SPRF (THz)						
	L=0	L=1	L=2	L=3	L=4	L=5	L=6
1000	91.78	738.79	740.84	743.03	745.21	747.45	749.83
1010	91.87	739.42	741.46	743.57	745.83	748.06	750.44
1020	91.97	740.08	742.12	744.31	746.48	748.79	751.17
1030	92.09	740.86	742.98	745.09	747.33	749.57	751.94
1040	92.23	741.77	743.89	746.07	748.23	750.54	752.91
1050	92.38	742.90	744.93	747.11	749.35	751.65	754.01
1060	92.57	744.08	746.19	748.36	750.60	752.90	755.25
1070	92.78	745.58	747.69	749.85	752.08	754.37	756.72

From Table I it is comprehended that SPRF increases with the increase in target concentration for all the number of layers. The regression lines for each layer shows that (Fig. 2) there is a linear relationship between SPR and target

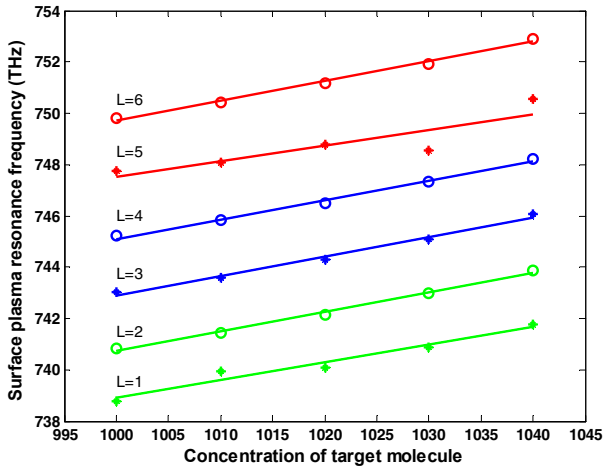

Fig. 2. Changes in Surface Plasmon Resonance Frequency with respect to target concentration.

concentration. However, higher number of layer contributes more SPR as expected. The reason behind it is that, the more absorption of the biomolecules occur by the more number of graphene layers [2].

The sensitivity curve for different number of graphene layers with respect to conventional SPR biosensor was analyzed. It has been seen that the sensitivity curves for one layer to up to three layers follows third degree equation and for four layers to eight layers it follows fourth degree equation, which can be shown from the following two figures (Fig. 3 & 4). Other figures are not shown to avoid overcrowding figures.

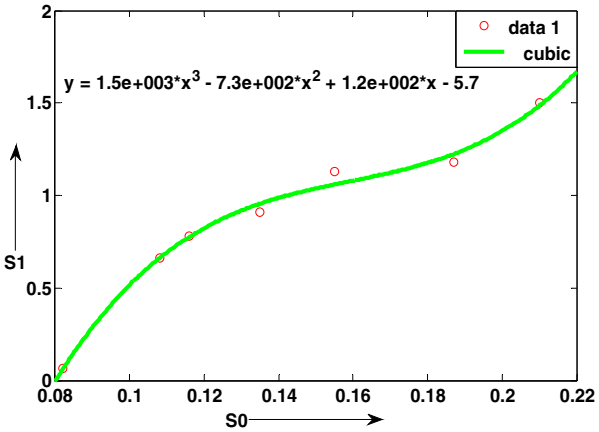

Fig. 3. S1 vs S0 curve where S0 is sensitivity of conventional SPR biosensor & S1 is sensitivity of Graphene based SPR biosensor for single layer.

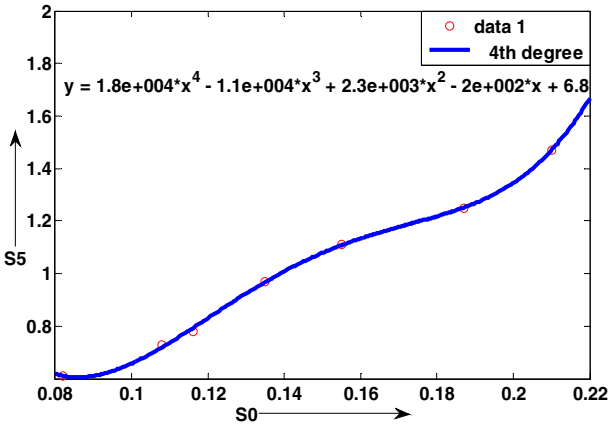

Fig. 4. S5 vs S0 curve where S0 is sensitivity of conventional SPR biosensor & S5 is sensitivity of Graphene based SPR biosensor for five layer.

From these figures (Fig. 3 and Fig. 4) it can be concluded that the sensitivity of SPR biosensor is not linear with respect to the increasing number of layers, whereas in [1]&[2] it has been said that sensitivity increases linearly with the increasing number of graphene layers. It could be guessed that the absorption happens nonlinearly with the increasing layer. So the increase in sensitivity with respect to number of layers follows nonlinear relationship.

The coefficients of the equations of sensitivity curve which have been achieved from basic fitting are listed in Table II. It is comprehended from Table II that up to L = 3 (three layers) the basic fitting needs only third degree poplynomials fitting but for more number of layers the degree increases for reasonable basic fitting. It indicated increasing level of nonlinearity of the sensitivity with respect to the number of layers. However, the sensitivity analysis is carried in this work from the basic fitting tools in the Matlab software platform which may not be the best fitting. For getting more accurate results the Least Square Method or some other fitting method could be carried out manually upon the data.

TABLE II. COEFFICIENTS OF DIFFERENT SENSITIVITY CURVES FOR BASIC FITTING

Layer	coefficient of x^4	coefficient of x^3	coefficient of x^2	coefficient of x	constant
L=1	0	1500	-730	120	-5.7
L=2	0	87	-20	6.8	0.14
L=3	0	370	-160	29	-0.96
L=4	19000	-11000	2400	-220	7.4
L=5	18000	-11000	2300	-200	6.8
L=6	19000	-11000	2400	-210	7.1
L=7	11000	-6800	1500	-140	5
L=8	20000	-11000	2400	-210	7

IV. CONCLUSION

The several Hundred THz frequency could be achieved by using increasing number of graphene layers. The previous researches showed that the sensitivity of graphene based SPR biosensor increases linearly with the increase of graphene layer. But from the analysis in this work it is found that sensitivity follows non-linear relationship for the increasing number of graphene layers. However, SPRF follows linear relationship with the change of molecular concentration for each layer. Also, more number of layers contributes higher values in SPRF. Then future research needs to adapt innovative fabrication techniques within the graphene-metal sandwiched layers to attain linearly increased sensitivity with linearly increased SPRF by increasing the number of graphene layers.

REFERENCES

[1] Md. Biplob Hossain, Md. Masud Rana, "DNA Hybridization Detection Based on Resonance Frequency Readout in Graphene on Au SPR Biosensor," *Journal of sensors*, Article ID 347595, October 2015.

[2] L. Wu, H. S. Chu, W. S. Koh and E. P. Li., "Highly sensitive Graphene biosensors based on surface plasmon resonance," *Optic Express*, Vol. 18, Issue 14, pp. 14395-14400, July 2010.

[3] B.Song,D. Li,W.Qi,M. Elstner, C. Fan, andH.Fang, "Graphene on Au(111): a highly conductive material with excellent adsorption

properties for high-resolution bio/nanodetection and identification," *ChemPhysChem*, vol. 11, no. 3, pp. 585–589, 2010.

[4] M. B. Hossain and M. M. Rana, "An effective compact-FDTD wideband modeling of graphene conductivity," in Proceedings of the IEEE International Conference on Electrical Engineering and Information Communication Technology (ICEEICT '15), pp. 1–3, IEEE, Dhaka, Bangladesh, May 2015.

[5] T.-J. Wang, C.-W. Tu, and F.-K. Liu, "Integrated-optic surface plasmon-resonance biosensor using gold nanoparticles by bipolarization detection," *IEEE Journal on Selected Topics in Quantum Electronics*, vol. 11, no. 2, pp. 493–499, 2005.

[6] S. H. Choi, Y. L. Kim, and K. M. Byun, "Graphene-on-silver substrates for sensitive surface plasmon resonance imaging biosensors," *Optics Express*, vol. 19, no. 2, pp. 458–466, 2011.

[7] R. L. Earp Jr., Multiwavelength surface plasmon resonance sensor designs for chemical and biochemical detection [Ph.D. thesis], 1998.

[8] L. Di´eguez, N. Darwish, M. Mir, E. Mart´ınez, M. Moreno, and J. Samitier, "Effect of the refractive index of buffer solutions in evanescent optical biosensors," *Sensor Letters*, vol. 7, no. 5, pp. 851–855, 2009.

[9] L. Di´eguez, D. Caballero, J. Calderer, M. Moreno, E. Mart´ınez, and J. Samitier, "Optical gratings coated with thin Si3N4 layer for efficient immunosensing by optical waveguide lightmode spectroscopy," *Biosensors*, vol. 2, no. 2, pp. 114–126, 2012.

[10] R. Boruah, D. Mohanta, A. Choudhury, P. Nath, and G. A. Ahmed, "Surface plasmon resonance based protein biosensing using a Kretschmann configured double prism arrangement," *IEEE Sensors Journal*, vol. 15, no. 12, pp. 6791–6796, 2015.

[11] R. Otupiri, E. K. Akowuah, S. Haxha, H. Ademgil, F. Abdel-Malek, and A. Aggoun, "A novel birefrigent photonic crystal fiber surface plasmon resonance biosensor," *IEEE Photonics Journal*, vol. 6, no. 4, 2014.

[12] N.-F. Chiu, W.-C. Lee, and T.-S. Jiang, "Constructing a novel asymmetric dielectric structure toward the realization of high performance surface plasmon resonance biosensors," *IEEE Sensors Journal*, vol. 13, no. 9, pp. 3483–3489, 2013.

[13] A. Ishimaru, ElectromagneticWave Propagation, Radiation, and Scattering, Prentice Hall, Upper Saddle River, NJ, USA, 1991.

Nonlinear Modeling and Control of DC Machines: A Partial Feedback Linearization Approach

Subroto K. Sarkar
Department of Mechatronics Engineering
Rajshahi University of Engineering & Technology
Rajshahi-6204, Bangladesh
Email: skshuvo138008@gmail.com

Sajal K. Das
Department of Mechatronics Engineering
Rajshahi University of Engineering & Technology
Rajshahi-6204, Bangladesh
Email: das.k.sajal@gmail.com

***Abstract*— This paper presents the design of a partial feedback linearization controller for speed control of DC machines. The design of the controller is presented based on the nonlinear modeling of the plant. The model of the plant is obtained from differential dynamic equations. A stability analysis is presented to guarantee the stability of the proposed design. To validate the effectiveness of the controller, DC machine systems are simulated. Simulation studies show that the proposed controller provides the accuracy and high performance of DC machines.**

Keywords*— Nonlinear Controller, DC Machines and Partial Feedback Linearization.

I. INTRODUCTION

Electrical machines are the devices that convert electrical energy into mechanical energy or vice versa [1]. Examples of electrical machines are transformers, generators and motors. Electrical machines are classified into two categories depending on the type of input and those categories are AC machines and DC machines. Example of DC machines are separately excited, shunt wounded, series wounded, compound wounded, permanent magnet, servo, and universal and brushless DC machine [1-4]. DC machine is important for different applications including industry, robotics, nanotechnology [4], hard disk drive [5], power system, electric vehicle, steel rolling, electric cranes, robotic manipulation and paper machines. Because it has simple mechanical structure and it offers simple mechanism and continuous control [6].

A number of researches have been done to model the dynamics of the electrical machines. Modeling and control of electrical machines has been an area of active research over the decades. In the different types of application accurate control of speed in DC machines is a great challenge for control engineers. Different controllers have been proposed to control the speed of DC machines. The Proportional-Integral-Derivative (PID) controller [6] is designed to control the speed in control industries. It provides reliable performance if PID parameter is identified properly. Otherwise it provides undesirable speed overshoot, sluggish response.

Adaptive control techniques such as LQR controller [3], model reference adaptive controller [7] have been proposed for speed control. These control techniques are dependent on the parameter and related to linearization of this model at operating time interval. As a result produces an error because of linearization of nonlinear model and cannot control the speed accurately.

When the control of systems is difficult due to their high nonlinearity properties fuzzy logic controller (FLC) [3] can be designed for speed control. It provides logical relationships between the system modelling and parameter and is used to obtain robust performance for large number of parameter. Although FLC provides flexibility in speed control, it makes complicated to design controller. A model predictive controller [7] is considered in for accurately control of speed. This controller is popular in control applications because it's controlling action. However its operation principle is computationally complex.

Direct Feedback linearization (DEL) and exact feedback linearization (EFL) controllers [6] have been proposed for nonlinear system. The implementation of DFL and EFL controllers require all the parameters to measure for a system and it is essential to design differentiator which reduces the robustness of the controller. Partial feedback linearization controller [8] is another control technique which does not require measuring all states. The motivation to design this controller is its ability to reduce the number of differentiators to control the system. The reduction of the number of differentiators allows us to control the DC machines with less complexity and more stability. This paper presents the design of a partial feedback linearization controller for DC machines.

The rest of this paper is organised as follows. Section 2 presents the preliminary definitions, Section 3 shows the dynamics modeling and partial feedback linearization control law of DC machines. Section 4 describes stability analysis of the internal dynamics and Section 5 presents the evaluation of the proposed controller using simulation. The paper is concluded in Section 6.

II. PRELIMINARY DEFINITION

In this section some definitions related to partial feedback linearization technique [8-9,11] are presented. Let a nonlinear system is defined as follows

$$\dot{x} = f(x) + g(x)u \tag{1}$$

$$y = h(x) \tag{2}$$

where $x \in R^n$ is the state vector; $u \in R$ is the control input vector; $y \in R$ is the output vector; $f(x)$ and $g(x)$ are n

978-1-5090-5785-6/16/$31.00 ©2016 IEEE

dimensional vector fields in the state space; $h(x)$ is scalar function of x.

Definition 1: Let $h: R^n \to R$ is a smooth scalar function and $f: R^n \to R$ be a smooth vector field on R^n, then the Lie derivative of $h(x)$ with respective to f is a scalar function defined by

$$L_f h(x) = \nabla h(x) f = \frac{\partial h(x)}{\partial x} f$$

Definition 2: Let a nonlinear system is defined as in (1) and (2)

$$\overset{r}{y} = L_f^r h(x) + L_g L_f^{r-1} h(x) u$$

where $L_f h(x)$ and $L_g h(x)$ represent the Lie derivative of $h(x)$ with respect to $f(x)$ and $g(x)$ respectively. If $L_g L_f^{r-1} h(x) \neq 0$, then r is called the relative degree of the system.

Definition 3: A nonlinear coordinate transformation for a system which can be written as

$$z = \phi(x) \qquad x = \phi^{-1}(z)$$

where z and x are the same dimensional vector and ϕ is the nonlinear function of x. Substituting (1) into the above equation for $\dot{x}$

$$\dot{z_1} = \frac{\partial h(x)}{\partial x} f(x) + \frac{\partial h(x)}{\partial x} g(x) u \tag{3}$$

$$\dot{z_1} = L_f h(x) + L_g L_f^{1-1} h(x) u$$

Since the first derivative of the output is not influenced by input signal u i.e. $L_g h(x) = 0$

and

$$\dot{z_1} = L_f^{2-1} h(x) = z_2$$
$$\vdots$$
$$\dot{z_n} = v = L_f h(\phi^{-1}(z)) + L_g L_f^{n-1} h(\phi^{-1}(z)) u$$

If $\alpha(x) = L_f h(\phi^{-1}(z))$ and $\beta(x) = L_g L_f^{n-1} h(\phi^{-1}(z))$

Then we can write the in the following way

$$v = \alpha(x) + \beta(x) u$$

$\beta(x)$ refers to the decoupling matrix. If $\beta(x)$ is non-singular then the input transformation can be obtained as:

$$u = \beta^{-1}(x)[v - \alpha(x)] \tag{4}$$

Hence the linear differential relation between the output z and u.

$$\begin{bmatrix} z_1^{r_1} \\ \vdots \\ z_m^{r_m} \end{bmatrix} = \begin{bmatrix} u_1 \\ \vdots \\ u_m \end{bmatrix}$$

The above input output relation is decoupled, in addition to being linear.

Therefore the fully linearized system with new co-ordinates $z = [z_1 \quad \cdots \quad z_n]^T$ where $n = r$ = relative degree

$$\dot{z} = Az + Bv \tag{5}$$
$$y = cz \tag{6}$$

where

$$A = \begin{bmatrix} 0 & 1 & 0 & \cdots & 0 \\ 0 & 0 & 1 & \cdots & 0 \\ \vdots & & & & \\ 0 & 0 & 0 & 0 & 0 \end{bmatrix}, \quad B = \begin{bmatrix} 0 \\ \vdots \\ 1 \end{bmatrix}, \quad z = \begin{bmatrix} z_1 \\ \vdots \\ z_r \end{bmatrix}$$

v is the control input for linearization system.

III. Dynamics Modeling and Partial Feedback Linearization Control Law

A. *Separately Excited DC Motor (SEDM)*

The complete model of a separately excited DC motor [2] for (1)-(2) is

where

$$f(x) = \begin{bmatrix} \frac{1}{L_a}(-R_a i_a - k i_f \omega \\ -\frac{1}{L_f} R_f i_f \\ \frac{1}{j}(k i_a i_f - T_L - B\omega) \end{bmatrix}; \quad g = \begin{bmatrix} \frac{1}{L_a} & 0 \\ 0 & \frac{1}{L_f} \\ 0 & 0 \end{bmatrix}$$

$$u = [v_a \quad v_f]^T; \quad x = [i_a \quad i_f \quad \omega]^T;$$

L_a = Armature inductance; v_a = Armature voltage

L_f = Field inductance; R_a = Armature resistance

R_f = Field resistance; T_L = Load Torque

v_b = Back EMF = $k i_f \omega$, B = Viscous Damping

T_e = Develop Torque = $k i_a i_f$

ω = Mechanical speed; j = Inertia moment

Since two variables are multiplied with each other, so this models is known as nonlinear model. The output of the above model is

$$y = h(x) = \omega \tag{7}$$

Now differentiating (7) by means of Lie derivative until the input appears.

$$\dot{y} = L_f h(x) + L_{g1} h(x) v_a + L_{g2} L_f h(x) v_f \tag{8}$$

Now $L_f h(x) = \frac{\partial h(x)}{\partial x} f = \frac{\partial \omega}{\partial x} f = \frac{1}{j}(T_e - T_L - B\omega)]$

Hence $L_{g1} h(x) = \frac{\partial h(x)}{\partial x} g_1 = 0 \quad L_{g2} h(x) = \frac{\partial h(x)}{\partial x} g_2 = 0$

$$\ddot{y} = L_f^2 h(x) + L_{g1} L_f h(x) v_a + L_{g2} L_f h(x) v_f$$

$$L_f^2 h(x) = \frac{k}{jL_a} i_f(-R_a i_a - v_b) - \frac{R_f}{jL_f} T_e - \frac{B}{j^2}(T_e - T_L - B\omega)$$

Hence $L_{g1} L_f h(x) = \frac{ki_f}{jL_a}$ and $L_{g2} L_f h(x) = \frac{ki_a}{jL_f}$

Since $L_{gi} L_f^{2-1} h(x) \neq 0$ at least one i, according to the Definition (2), the relative degree of the system is 2.

According to the (5) and (6)

$$A = \begin{bmatrix} 0 & 1 \\ 0 & 0 \end{bmatrix}, B = \begin{bmatrix} 0 \\ 1 \end{bmatrix}, C = \begin{bmatrix} 1 & 0 \end{bmatrix}, z = \begin{bmatrix} z_1 \\ z_2 \end{bmatrix}$$

From (4) the control input can be written as

$$u = \frac{v - L_f^2 h(x)}{\begin{bmatrix} L_{g1} L_f h(x) & L_{g2} L_f h(x) \end{bmatrix}}$$

B. Shunt DC Motor

The dynamic model of shunt motor [10] given below:

Using (1) and (2) $x = \begin{bmatrix} i_f & \omega & \theta \end{bmatrix}^T = \begin{bmatrix} x_1 & x_2 & x_3 \end{bmatrix}^T \quad u = v_T;$

$$f(x) = \begin{bmatrix} -A_2 x_1 \\ -A_4 x_1^2 x_2 - A_5 x_2 - A_6 T_L \\ x_2 \end{bmatrix}; g(x) = \begin{bmatrix} A_1 & A_3 x_1 & 0 \end{bmatrix}^T;$$

Where

θ = angular position; R_{adj} = Adjustable resistance

$T_e = \frac{ki_f}{R_a} v_T - \frac{k^2 i_f^2 \omega}{R_a} =$ Developed torque and other parameter are the same as separately excited DC motor.

$$A_1 = \frac{1}{L_f}; A_2 = \frac{R_{adj} + R_f}{L_a}; A_3 = \frac{k}{jR_a}; A_4 = \frac{k^2}{jR_a} \quad A_5 = \frac{B}{j}; A_6 = \frac{1}{j}$$

Hence $\dot{y} = L_f h(x) + L_g h(x) u$

Now $L_f h(x) = \frac{\partial x_2}{\partial x} f = -A_4 x_1^2 x_2 - A_5 x_2 - A_6 T_L$

$$L_g h(x) = \frac{\partial x_2}{\partial x} g = A_3 x_1$$

Since $L_{gi} L_f^{1-1} h(x) \neq 0$ at least one i. Hence the relative degree of the system is 1.

According to (5) and (6)

$$A = [0]; z_i = [z_1]; B = [1]; C = [1]$$

and the control input is defined by (4)

$$u = \frac{v + A_4 x_1^2 x_2 + A_5 x_2 + A_6 T_L}{A_3 x_1}$$

IV. Stability Analysis of Internal Dynamics

In this section we present the stability analysis [8-9] of the plant using partial feedback linearization controller. The analysis shows that the proposed controller is stable for all DC machines.

Let η be a stability factor and $\eta_1 \cdots \eta_{n-r}$ needs to be selected in such a way that it satisfies, $L_{g1} \eta_i(x) \cdots L_{gN} \eta_i(x) = 0$

$$\dot{\eta}_i(x) = L_f \eta_i(x) + L_{gi} \eta_i(x) u_i$$

$$\vdots$$

$$\dot{\eta}_{n-r} = L_f \eta_{n-r} + L_{gi} \eta_{n-r} u_i$$

If it is satisfied, then $\dot{\eta}_i(x) = L_f \eta_i(x)$ where $i = 1,2, \quad n-r$

In general, the control low needs to be chosen so that

$$\lim_{t \to \infty} h_i(x(t)) \to 0 \quad , \quad \dot{z}_1 = 0$$

Since $y_i = h_i(x) \to 0$ as $t \to \infty$, the above equation is defined as follows $\dot{\eta}_i(x) = 0$

which serves the internal dynamics of the ith subsystem. If the internal dynamics of the system is zero, it provides the stability of the system.

A. Separately Excited DC Motor (SEDM)

Let us consider

$$\eta(x) = \omega \tag{9}$$

Now differentiating (9) according to Lie derivative,

$$\dot{\eta}(x) = L_f \eta(x) + L_{g1} \eta(x) v_a + L_{g2} \eta(x) v_f = \frac{1}{j}(T_e - B\omega - T_L) = h(x)$$

Since $y = h(x) = 0$ as $t \to \infty$, the above equation can be written $\dot{\eta}(x) = 0$

Similar results can be obtained for shunt motor as well.

V. Performance Evaluation

The performance of the proposed controller is presented in this section. The simulation results of the proposed controller

using Matlab. Matlab simulink model is used to measure the dynamics of the DC machines. The results are presented for individual machine. The simulation results show that the proposed controller provides a significant improvement of the performance of the DC machine. The values of the parameters for the machines used in simulation results are listed in table 1. For shunt motor R_{adj}=44 ohm and other parameter values are same as separately excited DC motor. The results of the closed-loop system using partial feedback linearization controller are given from Fig. 1 and Fig. 2.

Table 1: Parameter values for separately excited DC motor

Parameter	Value
L_a	0.01 H
L_f	60 H
R_a	1 Ohm
R_f	60 Ohm
K	0.1238 Nm/A^2
B	0.0011 Nms/rad
J	0.00208 Kgm^2

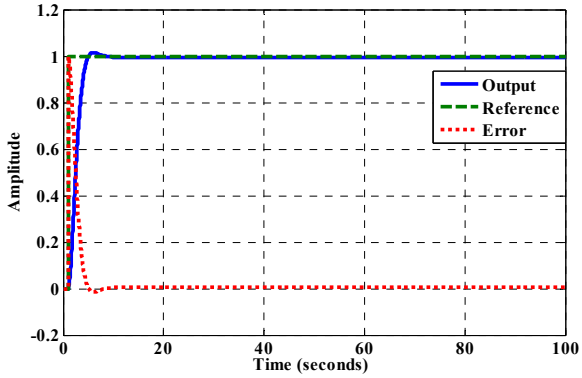

Fig.1. Reference tracking for SEDM

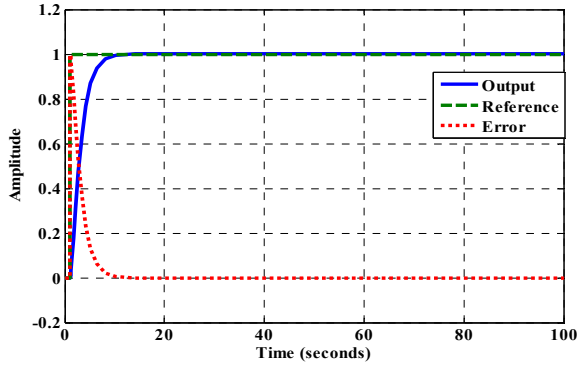

Fig.2. Reference tracking for shunt DC motor.

VI. CONCLUSION

The design of partial feedback linearization controller for speed control of DC machines is presented. The performance of proposed controller in DC machines is shown by simulation result. Simulation is done by using MATLAB. The simulation results show that the proposed controller provides reliable and accurate speed control of DC machines.

References

1. *S.* J. Chapman, "Electric Machinery Fundamentals*"* McGraw-Hill, 1985.
2. Zuo Zong Liu, Fang Lin Luo, and Muhammad H. Rashid, "Speed Nonlinear control of DC Motor Drive With Field Weakening", *IEEE Transactions on Industry Applications,* vol. 39, No. 2, March/April 2003.
3. Jason T. Teetor, Mo-yuen Chow, and James J. Brickley "A Novel Fuzzy Friction Compensation Approach to Improve the Performance of a DC Motor Control System*", IEEE Transaction on Industrial Electronics,* pp.113 – 120,vol. 43, no. 1, February 1996.
4. Sajal K. Das, Hemanshu R. Pota and Ian R. Petersen ''Damping Controller Design for Nanopositioners: A Mixed Passivity, Negative-Imaginary and Small-Gain Approach" *IEEE/ASME Transactions on Mechatronics* · pp. 416 – 426,Vol.2, Feb. 2015
5. Md. Arifur Rahman, Abdullah Al Mamun, Kui Yao and Sajal K. Das, "Design and Implementation of Feedback Resonance Compensatorin Hard Disk Drive Servo System: A Mixed Passivity,Negative-Imaginary and Small-Gain Approach in Discrete Time" *J Control Autom Electr Syst* August 2015, Vol. 26, pp 390–402
6. S.K. Das, N. Mondol, M.S.Rana and P.Das"Genetic algorithm based optimal PI controller for position control of Maxon S-DC motor with dSPACE" *IEEE/OSA/IAPR International Conference on Informatics, Electronics & Vision,* 04 October 2012.
7. Saverio Bolognani, Silverio Bolognani, Luca Peretti, and Mauro Zigliotto, "Design and Implementation of Model Predictive Control for Electrical Motor Drives*", IEEE Transactions on Industrial Electronics,* vol. 56, no. 6, June 2009.
8. M. A. Mahmud, H. R. Pota, M. Aldeen, and M. J. Hossain, "Partial Feedback Linearizing Excitation Controller for Multimachine Power Systems to Improve Transient Stability", *IEEE Transactions on Power systems, pp.* 561 - 571vol. 29, no. 2, March 2014.
9. Khalil HK. "Nonlinear systems" New York: Prentice-Hall; 1996.
10. J. Chiasson and M. Bodson, "Nonlinear control of a shunt DC motor", *IEEE Trans. Automat. Contr.*, vol. 38, pp. 1662–1666, Nov. 1993.
11. Sajal K. Das, N. Mondal and N. A. Sultana, "Design and Implement of a State Feedback Position Output Controller for a Maxon S-Dc Motor with dSPACE", *Proc. of the International Conference on Mechanical Engineering,*18-20 December 2011, Dhaka Bangladesh.

Sensitivity Enhancement of Porous Silicon Waveguide Sensor Using Graphene by FDTD with Lumerical Software

Dr. Md. Faruk Hossain[1], Tanzila Noushin[2]
Department of Electrical and Electronic Engineering
Rajshahi University of Engineering and Technology
Email: faruk94_ruet@yahoo.com[1], tnsupti@gmail.com[2]

Abstract— The aim of this paper is to analyze the effect of adding graphene layer on the porous silicon waveguide sensor. From rigorous theoretical calculations it is found that the resonant porous silicon sensor shows a 60-fold improvement in sensitivity over conventional SPR technology [1]. This paper proposes a Psi waveguide sensor designed in FDTD Lumerical software[2] with graphene layer. Due to having extraordinary properties, the added graphene layer increases the sensitivity of the sensor. This designed Psi waveguide sensor can be used as DNA detector[1], Optical gas sensor[3], Novel liquid sensor[4], Vapour sensor[5] with better sensitivity.

Keywords—Porous silicon resonant waveguide sensor, Graphene, High Sensitivity ,Lumerical Software, FDTD solution.

I. INTRODUCTION

Porous silicon is the perfect material for biosensing due to having a large surface area to volume ratio (~100m^2/cm^3) which facilitates both the substantial infiltration of biomolecules and the capability of molecular size selection [6]. Biomolecules infiltrated into the PSi waveguide increase the effective refractive index of the waveguide and the incident angle of light at waveguide mode is changed. The advantages of the Psi waveguide biosensor over other biosensors are: thin and resonant structure, minimized infiltration time, minimized requisite volume of the target material, strong field confinement and a sharp resonance feature which leads to a substantial increase in sensitivity of the porous silicon waveguide sensor with a low detection limit, enhanced interaction between electromagnetic field and biological molecules [3]. Fabrication of resonant waveguides can be possible by using a two-layer porous silicon based structure. In this sensor the light is coupled into the waveguide only at a particular angle of incidence and it induces an increase in the effective Psi refractive index. Due to biomolecular bindings inside the pores, the angle at which light is coupled into the waveguide is changed. The porous silicon waveguide is consists of pores which are of an average diameter 20nm [7]. In order to achieving further improvement in the performance of biosensor, a porous silicon waveguide sensor coated with graphene layer has been proposed in this paper which is designed in the Lumerical software by FDTD solutions. Lumerical FDTD solution employs the high performance 3D FDTD-method Maxwell solver for the design, analysis and optimization of nanophotonic devices, processes and materials involving wavelength scale structures. It solves arbitrary geometries and materials over any source bandwidth. The Lumerical FDTD simulation shows a few inherent approximations (=accurate). It is a very general technique that can deal with many types of problems. It solves Arbitrarily complex geometries. It's one simulation gives broadband result, takes less time to run and has less complex designing process. Graphene is a single layer of graphite. It is one atom thick 2-D thin planar sheet of carbon atoms, perfectly arranged in a honeycomb lattice. It possesses a lot of superior optical, electrical, thermal, chemical, mechanical and structural property such as high surface area [8], electrical conductivity [9], and biocompatibility [9, 10], which stably absorb biomolecules with carbon based ring structures, thus giving a large change in the refractive index near the sensing medium interface [11]. By using graphene, the RI will be changed, which in turn will lead to the change in the resonance angle that will translate a change in the propagation constant of SPW [11]. So, the graphene layer will increase the waveguide resonance angle and the sensitivity will be enhanced.

II. Sensor Fabrication

We introduce a numerical model using Kretschmann prism arrangement [12,13] described in Fig.1(a) and Fig. 1(b) that shows the schematic configuration of the proposed graphene-on-porous silicon waveguide biosensor,

9781509057856/16/$31.00©2016 IEEE

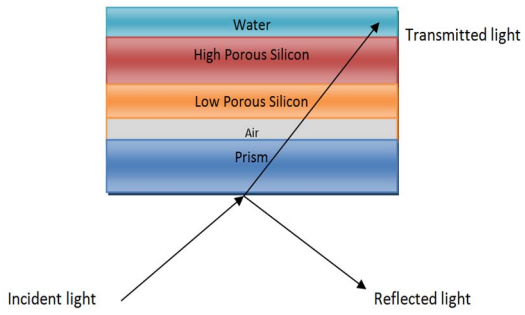

Fig.1(a):Schematic Configuration of Porous Silicon waveguide sensor without graphene

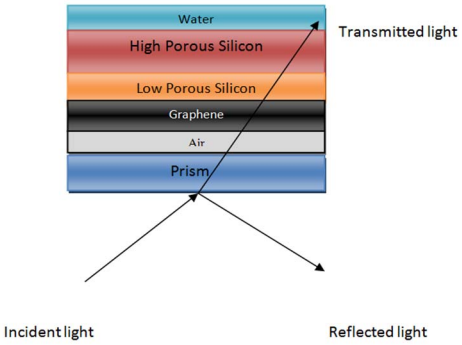

Fig.1(b) : Schematic configuration of Porous Silicon Waveguide sensor with graphene

where the first layer is a Metricon 2010 prism coupler (RI n_p=2.125,d_p=1000nm) after oxidation using 1550 nm light, second layer is air gap(d_a=500 nm and RI n_a=1), third layer is graphene (thickness variable and RI is $n_G = 3 + i1.149106$ [12]), and the fourth layer is Low porosity layer of silicon (RI n_L = 2.167 ,d_L=300nm , Porosity 52%[1]) and the fifth layer is High porosity layer of silicon (RI n_H=1.618,thickness d_H=1333nm, porosity=76%[1]) and the final layer is water (RI n_w = 1.33,d_w=181 nm) .Then, a light wave of wavelength, λ = 1550 nm is used [1], which passes through the prism and some portion is reflected at the prism- porous silicon interface. While impinging light energy to prism-porous silicon interface, an evanescent wave is generated which propagates with the different propagation constant from optical wave which is defined in [12, 14].Equation (1) suggests that SPR angle is a dependent parameter on RI of sensing medium.The angle of incidence,called SPR angle can be shown as follows[14]:

$$\theta_{SPR} = \sin^{-1}\sqrt{\frac{n_L^2 n_H^2 n_a^2 n_w^2}{n_p^2(n_L^2+n_H^2+n_a^2+n_w^2)}} \quad \text{.....} \quad (1)$$

then the RI of sensing medium is mathematically modified as [15],

$$\boldsymbol{n_s^d = n_w + c_a \frac{dn}{dc}} \quad \text{.....} \quad (2)$$

Here, $\boldsymbol{n_s^d}$ is the RI of the sensing dielectric after adsorption of sample molecules , $\boldsymbol{n_w}$ is RI of the sensing dielectric before adsorption of sample molecules, c_a is the concentration of adsorbed sample molecules, and dn/dc is the RI increment due to the adsorbate. If angle changes, the propagation constant of SPW also changes which is

$$\boldsymbol{k_{SPW} = \frac{2\pi}{\lambda} n_p \sin\theta_{SPR}} \quad ..(3) \quad [12, 16, 17]$$

And finally if propagation constant of SPW changes it makes the surface resonance frequency (SRF) change which can be explained by the following equation:

$$SRF = \frac{c_0}{n_{geo}} \frac{k_{SPW}}{2\pi} \quad \text{.....} \quad (4)$$

where, $c_0$is the propagation velocity of SPW that is a perpendicularly confined evanescent electromagnetic wave[12,18] and n_{geo} is the geometric mean of interface between Porous silicon and sensing medium, $n_{geo} = \sqrt[3]{n_L n_H n_w n_G}$ ..(5) If the incident angle of optical wave is tuned, SPR condition is achieved in which reflectance (R) of reflected wave is minimum and transmittance (T) is maximum. We define a plot "Reflection versus surface resonance angle (R~θ)," as resonant waveguide sensor curve. To calculate the sensitivity of the curve found by the simulation in Lumerical 2016a software, we used Fresnel equations [19] for four-layered heterooptical system to determine transmitted light intensity. The sensitivity of the proposed optical sensor is defined as the ratio of the SRF change, ΔSRF^T (sensor output), to the change happened in concentration of biomolecules , Δc_a (sensor input),[10] as given in the following:

$$S^G = \frac{\Delta SRF^T}{\Delta c_a} = \frac{\Delta SRF^0 + \Delta SRF^G}{\Delta c_a} = \frac{\Delta SRF^0 + (\Delta\theta)\Delta SRF^0}{\Delta c_a} = (1+\Delta\theta)\frac{\Delta SRF^0}{\Delta c_a}$$

$$or \quad S^G = (1+\Delta\theta)S^0 \quad \text{.....} \quad (6)$$

Where, ΔSRF^T is the SRF change of sensor summing with and without graphene layers, S^0 is the sensitivity of the devices without graphene film, S^G is the sensitivity for different thickness of graphene layers and Δθ is the difference

between the angles with graphene and without graphene porous silicon waveguide sensor and given by,

$\Delta\theta = \theta_G - \theta_0$…….(7) Where, θ_G= Resonance angle of porous silicon waveguide sensor with graphene layer, θ_0=Resonance angle of waveguide sensor without graphene layer. Layout of the sensor in the Lumerical Software is shown in Fig. 2.

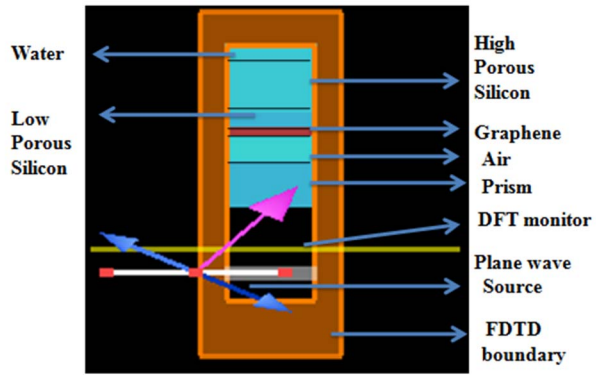

Fig. 2: Layout of the Sensor in Software

III. Result & Discussion

The Reflection intensity vs Angle output found from the designed sensor is shown in Fig.3(a) where 68nm, 100nm and 200nm thickness of graphene is used and Fig.3(b) shows the output ranging from 27° to 46° and in the Fig.3(c) the zoomed output of the waveguide resonance curve is shown where we can clearly see that the curve without graphene is at 40.25° and the curve with 68nm, 100nm, 200nm graphene is at 40.30°, 40.5°, 40.9°,so the enhanced sensitivity becomes 5%, 25% and 65% For 68nm, 100nm and 200nm graphene. The waveguide resonance curve with graphene 1000nm is shown in Fig.3(d) where the increased internal angle can be seen clearly. Fig.3(e) shows waveguide resonance with Graphene 100nm, 200nm, 300nm, 400nm, 500nm, 600nm in one curve where the zoomed output in Fig.3(f) shows that the increased sensitivity is respectively 55%, 13%, 12%, 11% for 300nm, 400nm, 500nm , 600nm graphene. So this result says that with increased thickness of graphene the sensitivity doesn't increase much.

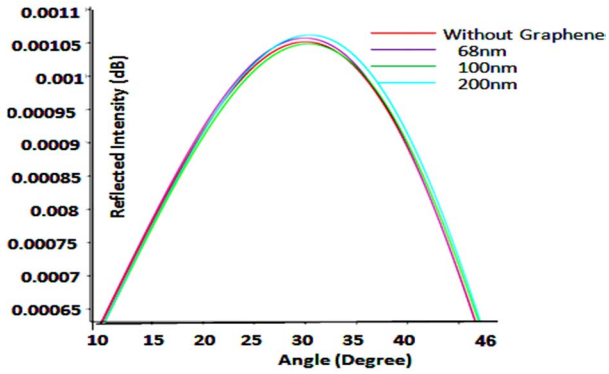

Fig. 3(a) : Waveguide Resonance Curve with 34nm, 68nm, 100nm and 200nm Graphene

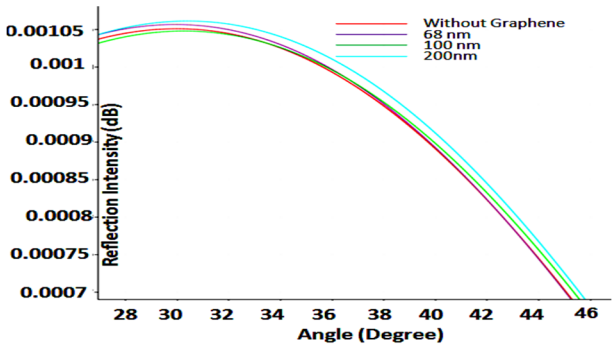

Fig. 3(b): Waveguide Resonance Curve angle ranging from 27° to 46°

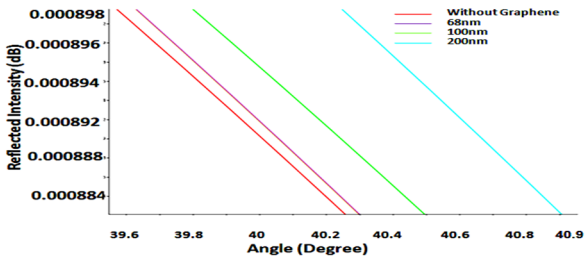

Fig. 3(c): Clear view of angle difference in waveguide resonance curve with 68nm, 100nm and 200nm Graphene

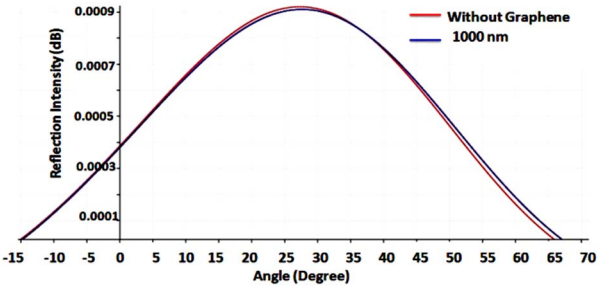

Fig. 3(d): Waveguide Resonance Curve with 1000nm Graphene

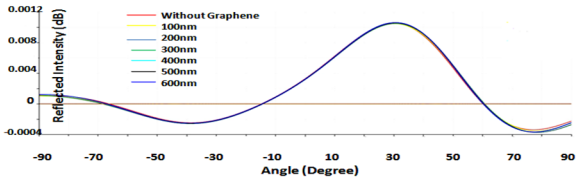

Fig. 3(e): Waveguide Resonance curve with 100nm, 200nm, 300nm, 400nm, 500nm and 600nm Graphene

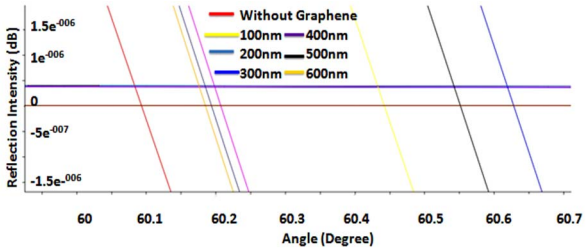

Fig. 3(f): Clear View of angle difference in waveguide resonance curve with 100nm, 200nm, 300nm, 400nm, 500nm, 600nm Graphene

To confirm this decrease of sensitivity with increased thickness, more simulation with graphene thickness 700nm,800nm,1000nm was done the curves of which is not shown here but the enhanced sensitivity(%) with different graphene thickness is shown in Table 1.

Thickness	Enhanced Sensitivity	Thickness	Enhanced Sensitivity
100nm	25%	600nm	11%
200nm	65%	700nm	26%
300nm	55%	800nm	25.98%
400nm	13%	900nm	25.96%
500nm	12%	1000nm	25.93%

Table 1: Enhanced Sensitivity at Diffferent Thickness (%)

IV. Conclusion

In this paper, a porous silicon waveguide sensor model based on graphene material was proposed. The graphene layer was sandwiched between metal film and sensing medium for enhancing sensor sensitivity. The sensor was designed in the Lumerical software. By using graphene layer the resonance angle was increased, which in turn increased the propagation constant, as a result of which sensitivity was enhanced. From the analysis it was observed that the increasing thickness of graphene layer up to 1000nm doesn't has much effect on sensitivity enhancement and just a thin layer of graphene say 200nm is enough to increase the sensitivity up to 65%.

References:

[1]G. Rong, A. Najmaie,J. E. Sipe, S. M. Weiss," Porous silicon waveguides for DNA detection",IEEE,2006.

[2] www.lumerical.com OR www.novadownloads.com

[3] J. J. Saarinen, S. M. Weiss, P. M. Fauchet, and J. E. Sipe, "Optical sensor based on resonant porous silicon structures,"Optics Express, vol. 13,pp. 3754-3764, May 2005.

[4]H. F. Arrand, T. M. Benson, A. Loni, R. Arens-Fischer, M. Kruger, M. Thonissen , H. Luth, and S. Kershaw," Novel Liquid Sensor Based on Porous Silicon Optical Waveguides", IEEE PHOTONICS TECHNOLOGY LETTERS, VOL. 10, 1998.

[5]Tanya Hutter, Nikos Bamiedakis and Stephen R. Elliott "Theoretical Study of Porous Silicon Waveguides and Their Applicability for Vapour Sensing" COMSOL Conference,2010.

[6] M. P. Stewart, and J. M. Buriak, "Chemical and biological applications of porous silicon technology," in Adv. Mater., vol. 12, pp. 859-869, 2000.

[7]Guoguang Rong,Ali Najmaie,John E. Sipe,Sharon M. Weiss," Nanoscale porous silicon waveguide for label-free DNA sensing", Elsevier B.V,2008.

[8]B. Song, D. Li, W. Qi, M. Elstner, C. Fan, and H. Fang, "Graphene on Au(111): a highly conductive material with excellent adsorption properties for high-resolution bio/nanodetection and identification," *ChemPhysChem*, vol. 11, no. 3, pp. 585–589, 2010.

[9]M. B. Hossain and M. M. Rana, "An effective compact-FDTD wideband modeling of graphene conductivity," *ICEEICT,* pp. 1–3,2015.

[10]H. Karimi, R. Yusof, R. Rahmani, H. Hosseinpour, and M. T. Ahmadi, "Development of solution-gated graphene transistor model for biosensors," *Nanoscale Research Letters*, vol. 9, no. 1, pp. 1–11, 2014

[11]Md. Biplob Hossain,Md. Masud Rana,"DNA Hybridization Detection Based on Resonance Frequency Readout in Graphene on Au SPR Biosensor", Hindawi Publishing Corporation Journal of Sensors,pp 2,2015

[12]L. Wu, H. S. Chu, W. S. Koh, and E. P. Li, "Highly sensitive graphene biosensors based on surface plasmon resonance,"*Optics Express*, vol. 18, pp. 14395–14400, 2010.

[13] S. H. Choi, Y. L. Kim, and K. M. Byun, "Graphene-on-silver substrates for sensitive surface plasmon resonance imaging biosensors," *Optics Express*, vol. 19, no. 2, pp. 458–466, 2011. [

[14] R. L. Earp Jr., *Multiwavelength surface plasmon resonance sensor designs for chemical and biochemical detection [Ph.D. thesis]*,1998.

[15] L. Dieguez, N. Darwish, M. Mir, E. Mart ´ ´ ınez, M. Moreno, and J. Samitier, "Effect of the refractive index of buffer solutions in evanescent optical biosensors," *Sensor Letters*, vol. 7, no. 5, pp.851–855,2009.

[16] R. Boruah, D. Mohanta, A. Choudhury, P. Nath, and G. A. Ahmed, "Surface plasmon resonance based protein biosensing using a *Kretschmann* configured double prism arrangement,"*IEEE Sensors Journal*, vol. 15, no. 12, pp. 6791–6796, 2015.

[17] R. Otupiri, E. K. Akowuah, S. Haxha, H. Ademgil, F. AbdelMalek, and A. Aggoun, "A novel birefrigent photonic crystal fiber surface plasmon resonance biosensor," *IEEE Photonics Journal*, vol.6,no.4,2014.

[18]N.-F. Chiu, W.-C. Lee, and T.-S. Jiang, "Constructing a novel asymmetric dielectric structure toward the realization of highperformance surface plasmon resonance biosensors," *IEEE Sensors Journal*, vol. 13, no. 9, pp. 3483–3489, 2013.

[19] A. Ishimaru, *Electromagnetic Wave Propagation, Radiation, and Scattering*, Prentice Hall, Upper Saddle River, NJ, USA, 1991.

Robust Uniform Concentric Circular Array Beamforming in the Existence of Look Direction Disparity

M. F. Reza*, M. S. Hossain, M. T. Hossein and M. M. Rashid
Department of Electrical and Electronic Engineering
Rajshahi University of Engineering and Technology (RUET), Rajshahi-6204, Bangladesh
*E-mail: farhamdur@gmail.com

***Abstract*- The concentric circular array with robust algorithm is addressed in this paper. A uniform concentric circular array antenna (CCAA) geometry is targeted due to its symmetrical configuration which enables the phased array antenna to scan azimuthally with minimal changes in its beam width and sidelobe levels. This paper first compares the performances of CCAA configuration with existing uniform circular arrays (UCA) to validate the suitability of the presented beamformer. Then the performance of CCAA based optimal beamformer is compared with delay-and-sum beamformer in the presence of interfering signals. The performance of optimal CCAA processor is reduced if signal of interest is deviate from the look direction. This paper also presents a diagonal loading technique to make the system robust for resolving the degradation problem and compare the performance with existing beamforming technique. MATLAB software is used to analyze the performance of proposed CCAA processor.**

Index Terms—Beamforming, Optimal beamforming, Delay-and-Sum beamformer, Diagonal Loading, Robust algorithm.

I. INTRODUCTION

Smart antenna systems have increased widespread interest in the communications industry due to their adaptive characteristics over the last decennary. Switched beam array and phased array antennas are the two main techniques of smart antennas. The direction of the beam is chosen from a set of predetermined beams in a switched beam array, while the main beam is steered towards a particular direction in a phased array. Instead of changing the structure mechanically, electronic manipulation is used in a phased array antenna to steers its beam towards a desired angle. This manipulation involves changes in both the amplitude and phase excitation of the antenna elements [1-2].

A ring antenna array is a planar array with elements are placed on a circle and an array is called concentric circular array, if several of these ring antenna arrays with different radii share a common center. Concentric ring arrays are used for direction finding and applications requiring main beam symmetry [3]. In contrast to linear antenna arrays, the radiation patterns of concentric circular antenna arrays inherently cover the entire space and the main lobe could be oriented in any desired direction.

The beamformers using uniform concentric circular array antenna (CCAA) are discussed in [4–7] and references there in. The overall dimension required for uniform circular array (UCA) [8-10] is much larger than the concentric array geometries to transmit or receive same amount of power. For practical applications with size limitations, the dimension of the UCA can be prohibitive for actual implementation. To overcome those problems CCAA is used [1-2].

CCAA with delay-and-sum beamforming technique can't detect and remove interference signal. But if optimal beamformer is used, it can detect and attenuate the interference signal. If there is any disparity occur between the direction of actual signal and the direction at which the array is steered, optimal beamformer consider the actual signal as interference signal and highly attenuate the signal [11-12]. The performance degradation problem can be minimized by using robust techniques with the existing CCAA processor. To overcome the aforementioned difficulties, CCAA processor is presented with following desirable properties.

- It is able to steer the main beam in any arbitrary direction.
- It is capable to cancel directional interference.
- CCAA is able to scan the entire space i.e. -180^0 to 180^0.
- Proposed CCAA processor is robust against look direction disparity.

This paper is divided into four Sections. Section 2 introduces the array geometries and signal model used in this work. Section 3 discusses about different beamforming techniques. Section 4 analyses and discusses the simulated results, and finally Section 4 concludes the paper.

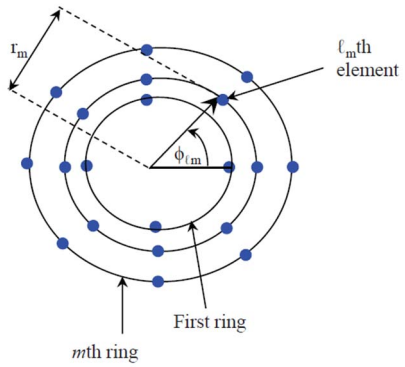

Fig. 1. Organization of broadband concentric circular antenna array.

978-1-5090-5785-6/16/$31.00 ©2016

II. SIGNAL MODEL

The linear antenna array can able to scan the object between 0^o – 180^o but many applications it is essential to scan the object between 0^o – 360^o. The general geometry of concentric circular antenna array is shown in Fig. 1. This geometry consists of several ring antenna arrays each of them with different radius, shared a common center and uniformly distributed antenna elements, either equal or unequal in number. Referring to Fig. 1, the geometry comprises M circular arrays. Each of them consists of L isotropic elements equally spaced with the center as the origin and having a radius r_m, where r_m is the radius of the m[th] ring. The position of each element of the geometry is described by two indices, $m = 1, 2, \ldots\ldots M$ and $l = 1, 2, \ldots\ldots L$, where increases from inwards to outwards. Clearly, for the case of M = 1 the CCAA geometry reduces to the regular UCA.

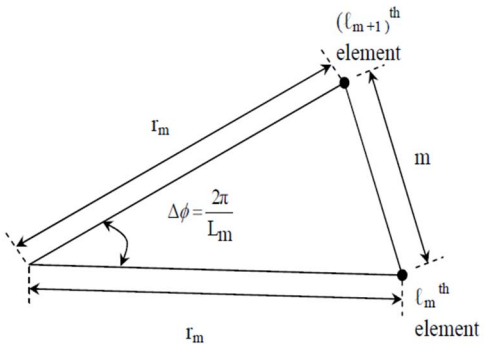

Fig. 2. Correlation between inter sensor spacing and the radius of the m[th] ring of CCAA processor [13].

The correlation between spacing of the elements and the radius of the m[th] ring of the CCAA is shown in Fig. 2 where the array element spacing in each ring is λ/2, λ is the smallest wavelength of the array to be operated and is denoted by λ_{min}. The radius of m[th] ring of the broadband CCAA is given by [3]

$$r_m = \frac{\lambda_{min}}{4\sin\left(\frac{\pi}{L_m}\right)}, \quad m = 1, 2, 3 \ldots\ldots M \tag{1}$$

For convenience, the radius is represented as its normalized version,

$$\widetilde{r_m} = \frac{r_m}{\lambda_{min}} = \frac{\lambda_{min}}{4\sin\left(\frac{\pi}{L_m}\right)} \tag{2}$$

III. BEAMFORMING TECHNIQUE

More than one ring with different antenna elements in each ring is used in a concentric circular array antenna. The output of an array is the combination of the signals from different elements of the array. Beamforming is a technique of combining the signals from different elements. Beamforming technique is mainly categorized into two types as Delay-and-sum and Optimal beamforming technique.

A. Delay-and-Sum Beamformer:

The delay-and-sum beamformer has weights of equal magnitudes. The phases are selected to steer the array in a particular direction (φ_0, θ_0) known as look direction. With denoting the steering vector in the look direction, Then the array weights, with steering vector ($\mathbf{S}_0$) in the look direction, are given by [2]

$$W_C = \frac{1}{L} S_0 \tag{3}$$

By taking the dot product of the weight vector with the steering vector S(φ, θ), the response of a delay-and-sum beamformer in the direction (φ, θ) is obtained. With the weights W_C the response y(φ, θ) is given by[2]

$$y(\varphi, \theta) = W_C^H S(\varphi, \theta)$$

$$= \frac{1}{L} S_0^H(\varphi, \theta) \tag{4}$$

B. Optimal Beamformer:

The delay-and sum beamformer described in the preceding section needs information about the directions of interfering signals, and the beamformer using the weights are calculated by this scheme does not maximize the output SNR. Those deficiencies can overcome using the optimal beamformer discussed in this section. The optimal beamforming method maximizes the output SNR in the absence of errors. It should be noted that the optimal beamformer, also known as the minimum variance distortion less response (MVDR) beamformer, discussed in this section does not require knowledge of directions and power levels of interferences as well as the level of the background noise power to maximize the output SNR. It only requires the direction of the desired signal [2].

We now discuss an optimal beamformer with its weights with constraints. Let the array weights be constrained to have a unit response in the look direction, that is,

$$\hat{W}^H S_0 = 1 \tag{5}$$

Thus it follows from unconstrained beamformer that constant μ_0 is given by

$$\mu_0 = \frac{1}{S_0^H R_n^{-1} S_0} \tag{6}$$

Substituting this for unconstrained beamformer results in the expression for weights of the constrained processor for the case is given by [3]

$$\hat{W} = \frac{R^{-1} S_0}{S_o^H R^{-1} S_0} \tag{7}$$

C. Proposed Robust Technique:

The optimization of weight vector can be done using adaptive beamforming techniques to localize targets via correlation with the data in a noisy environment. If any unwanted signal is present in the environment, these weight vectors generate a beam-pattern that places nulls in the direction of unwanted signal (i.e., signals, called interference, from directions other than the direction of interest). On the other hand, the weight vector is constant and independent of incoming data in case of delay-and-sum beamforming technique. The output in all directions can be optimized using an adaptive algorithm

minimum variance distortion less response subject to the condition that gain in the steering direction is unity. The direction in which the array is steered towards the signal of interest is called steering direction. This algorithm gives optimum performance by steering nulls in the direction of unwanted signal and also offers better performance in the case of correlated noise sources. But the MDVR beamformer treat the signal of interference as interference, if there is a little mismatch between the original signal and look direction.

A common way to increase robustness of the MVDR beam former is by using fixed diagonal loading (FDL) technique, in which a constant λ is added to the diagonal of the covariance matrix [11].

$$R_{new} = R + \lambda I \quad (8)$$

Adding a constant to the diagonal of the covariance matrix can be seen as increasing the noise level in the recorded data before finding the optimal aperture shading, assuming the noise is white. As white noise becomes dominant, the minimum variance solution approaches conventional beam forming with uniform shading. It is a challenging problem to select a fixed loading factor λ. One way to determine λ is to set it to a fixed value with reference to the background noise or equal to the standard deviation of the diagonal entries of the correlation matrix as discussed in [12]. However, it is not clear how to relate the parameters of the background noise gain constraint and the level of uncertainty of the direction of actual signal. Furthermore, the relationship between the diagonal loading factor and the parameters of the background noise gain constraint is not simple, and to satisfy this constraint, a multistep iterative procedure is required to adjust the diagonal loading factor [12]. Each step of this iterative procedure involves an update of the inverse of the diagonally loaded covariance matrix, and as a result, the total computational complexity of adaptive beamforming with the background noise gain constraint may be higher than that of the sample matrix inversion algorithm. Because of this, the diagonal loading factor is usually chosen in a more adhoc way, typically about 10 σ_n^2, where σ_n^2 is the background noise power at a single sensor.

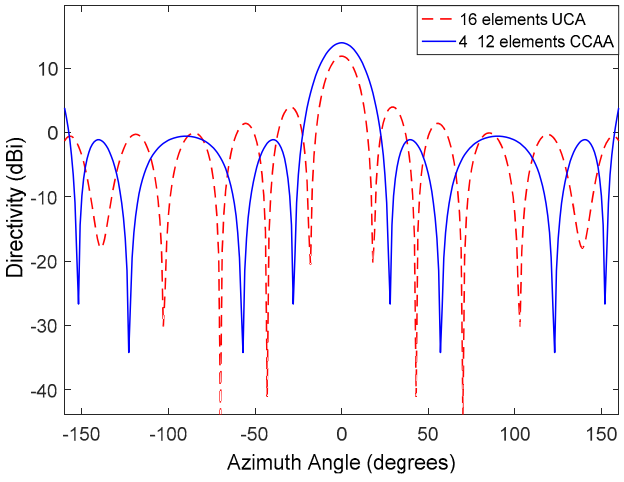

Fig. 3. Directivity comparison between UCA and CCAA with equal elements and unequal used space.

IV. Performance Evaluation

In this section, the performance processor of CCAA with equidistance spaced elements have analyzed using a number of example. It is assumed that the desired signal source broadside to the array is present with a unity power and the directional interferences are assumed to be uncorrelated with the look direction signal. The signal frequency is taken as 3MHz.

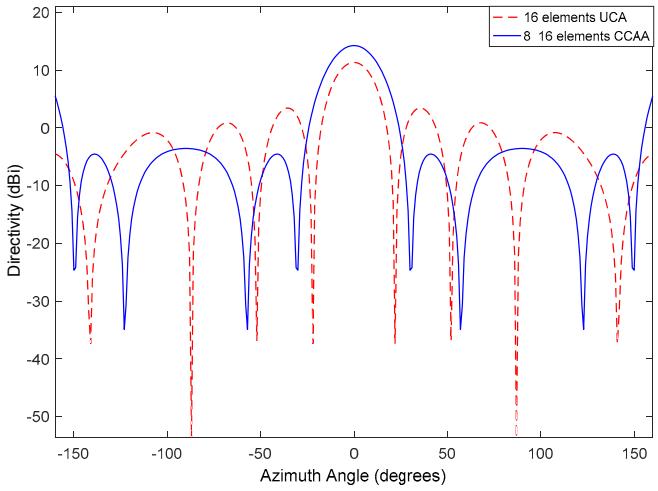

Fig. 4. Directivity comparison between UCA and CCAA with unequal elements and equal used space.

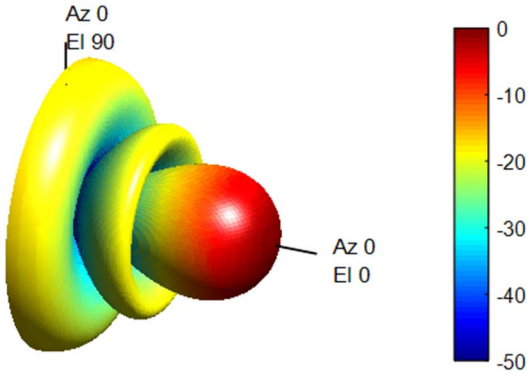

Fig. 5. 3-D response pattern for CCAA processor steered at 0 Az, 0 EL.

Fig. 3 and Fig. 4 shows a comparison between UCA and CCAA processor. Fig. 3 is plotted for equal number of antenna elements (16 elements) in both processors but the outer ring radius of CCAA processor not equal to the UCA processor. The radius of the 2 rings of CCAA processor used are 0.4λ and 1λ, on the other hand 1.2λ is used for UCA processor. From the Fig. 3, we can see that though the space required for CCAA is less compared to UCA the directivity gain of the CCAA (13.98 dB) is larger than UCA (11.9 dB) with same number of antenna elements. Again Fig. 4 is plotted for unequal number of antenna elements but outer ring radius of CCAA processor is equal to the radius of UCA (1λ) processor. Though the both antenna

system use same radial space but from the above figure we can observe that directivity of the CCAA (14.2532 dB) is large compared to UCA (11.3404 dB). So one can observe from those figure that the performance of CCAA processor is better than UCA processor using less antenna elements and radial space. The 3-D response of a CCAA processor is shown in Fig. 5. One can be easily observed that the main beam maintained the desired signal power in the assumed signal direction.

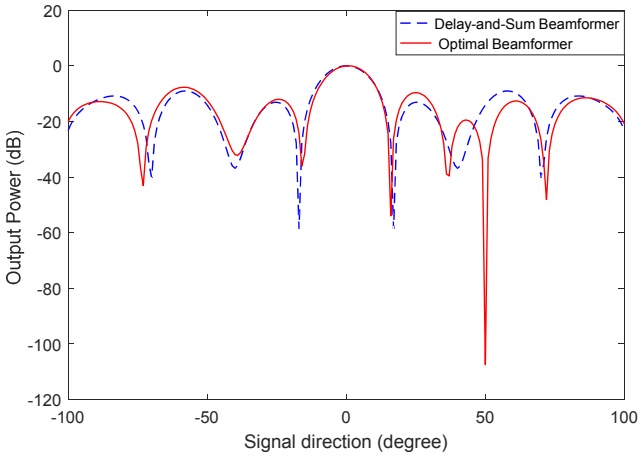

Fig. 6. Comparison between CCAA based optimal beamformer and delay-and-sum beamformer in the presence of an interfering signal at 50^0.

Fig. 6 compares the performance of optimal CCAA processor with delay-and-sum beamformer. An interfering signal is assumed for both the beamformer at an angle 50 degree. From Fig. 6, it can be observed that there is a large attenuation at an angle 50^0 for optimal beamformer. So it is cleared from the above figure that optimal beamformer has the interference cancellation capability and beamwidth is narrower than delay-and-sum beamformer.

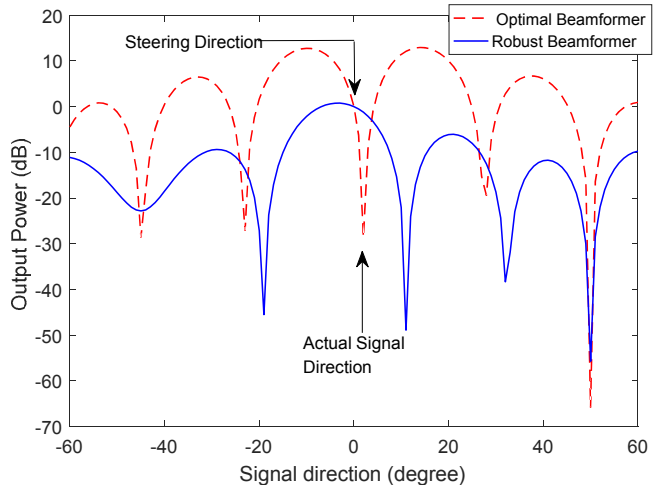

Fig. 7. Power pattern of CCAA based robust beamformer and optimal beamformer with assume signal direction=0^0 and actual signal direction=1^0.

Fig. 7 shows the radiation pattern of robust beamformer and optimal beamformer, and compares the performance robust beamformer with robust beamformer in the presence of 1 degree look direction error. If the array is steered at 0 degree but the actual signal direction is 1 degree, optimal beamformer considered the actual signal as interference and highly attenuate the original signal. From the Fig. 7 one can observe that robust beamformer can make the system robust enough to receive the mismatch signal with look direction.

V. CONCLUSION:

The performance of CCAA structure has been address in this paper. First the performance is compared with UCA processors. Then the relative comparison in radiation pattern of delay-and-sum beamformer, optimal beamformer and robust beamformer for CCAA processor have been discussed in the presence of interference, noise and look direction error. Fixed diagonal loading method is used to make the system robust. It has exposed using computer model that robust CCAA beamformer has the ability to identify signals in the presence of look direction error.

REFERENCES

[1]. N. Tohme, J.M. Paillot, D. Cordeau, S. Cauet, Y. Mahe, and P. Ribardiere, "A 2.4 GHz 1-dimensional array antenna driven by vector modulators", *IEEE MTT-S International Microwave Symposium Digest,* 2008, pp. 803-805.

[2]. L. C. Godara, Smart Antenna, CRC Press, 2004.

[3]. R. L. Haupt, "Optimized element spacing for low sidelobe concentric ring arrays," *IEEE Transactions on Antennas and Propagation,* vol. 56, no. 1, pp. 266–268, 2008.

[4]. G. Ram, D. Mandal, R. Kar, and S. P. Ghoshal, "Cat Swarm Optimization as Applied to Time Modulated Concentric Circular Antenna Array: Analysis and Comparison with Other Stochastic Optimization Methods" *IEEE Transaction on Antenna and Propagation* Vol. 63, pp. 4180-4183,2015.

[5]. M. A. Mangoud, H. M. Elragal, M. T. Alsharal, "Design of time modulated concentric circular and concentric hexagonal antenna array using hybrid enhanced particle swarm optimization and differential evolution algorithm" *IET Microwaves, Antennas & Propagation,* 2014

[6]. Z. Xiaowen, Y. Qingshan, Z. Yunhua, "Application of TLBO to Synthesis of Sparse Concentric Ring Arrays", *10th European Conference on Antennas and propagation,* 2016.

[7]. M. Carlin, G. Oliveri, and A. Massa, "Hybrid BCS-Deterministic Approach for Sparse Concentric Ring Isophoric Arrays" *IEEE transactions on antenna and propagation,* vol 63, No. 1, January 2015.

[8]. A. R. Kulaib, R. M. Shubair, M. Al-Qutayri, and J. Ng, "Accurate and Robust DOA Estimation Using Uniform Circular Displaced Antenna Array" *2015 IEEE International Symposium on Antennas and Propagation,* pp. 1552-1553, 2015.

[9]. M. Askari, M. Karimi, Z. Atbaee, "Robust beamforming in circular arrays using phase-mode transformation", IET Signal Processing, Vol. 7, Issue: 8, pp.693- 703, Year: 2013.

[10]. M. S. Hossain, G. N. Milford and M. C. Reed, "Efficient Robust Broadband Beamforming Using Circular Antenna Arrays", *2012 International Symposium on Communications and Information Technologies (ISCIT),* pp. 746 - 751, 2012.

[11]. M. S. Hossain, L. C. Godara, and M. R. Islam, "Efficient Robust Broadband Beamforming Algorithms Using Variable Loading", *IEEE Latin America Transactions*, Vol. 10,pp. 1697 - 1702, 2012.

[12]. M. S. Hossain, G. N. Milford, M. C. Reed and L. C. Godara, "Efficient Robust Broadband Antenna Array Processor in the Presence of Look Direction Errors*", IEEE Transactions on Antennas and Propagation*, Vol. 61, no.2, pp. 718-727, Feb. 2013.

[13]. M. S. Hossain, M. F. Reza, M. M. Rashid and M. F. Ali, "Performance Analysis of Broadband Concentric Circular Antenna Array Processor", *6th International Conference on Informatics, Electronics & Vision (*ICIEV*)* , page 1-4, May 2016.

2nd International Conference on Electrical, Computer & Telecommunication Engineering (ICECTE)
8-10 December 2016, Rajshahi-6204, Bangladesh

A Comparative Study of Optimization of Solid State Dye Sensitized Solar Cell Technologies for Power Grid Integration and Off-Grid Operation

Salman A. Chowdhury[1], Mobasseer M. Hossain[2], Md. Abu Sayem[3] and Md. Rafiqul Islam Sheikh[4]*

[1]*Department of Electrical & Electronic Engineering, TMSS Engineering College, Bogra, Bangladesh*
[2,3,4]*Department of Electrical and Electronic Engineering, Rajshahi University of Engineering & Technology, Bangladesh*
*Corresponding Author E-mail: salman.ananda.chowdhury@gmail.com

***Abstract*—In this paper, the performance analyses of Solid State Dye Sensitized Solar Cells (SSDSSCs) are carried out with power grid integration and off-grid operation in the intertropical region being the main focus. It has been observed that electrodes of different compositions such as: TiO_2 and ZnO, surface morphology of the thin films used in SSDSSCs, use of different types of dyes as photo sensitizers, use of Nanorods/Nanoparticles as photoanodes – all correspond to different photoelectric conversion efficiencies (PCEs) in SSDSSCs. As the SSDSSCs are free of leakage and corrosion related problems prevalent in conventional liquid-based Dye Sensitized Solar Cells (DSSCs), it has the potential to lower the maintenance cost and improving longevity of a system, so far however SSDSSCs suffer from low PCEs when compared with conventional DSSCs, with a maximum efficiency record of approximately 15 per cent set in 2013 by using solid-state mesoscopic TiO_2 solar cells sensitized with lead iodide perovskite ($CH_3NH_3PbI_3$) pigments[1-4], in early 2014 which was further lifted to 16.7 per cent[26]. Careful selection of highly photosensitive dye in conjunction with proper nanotube photonic crystals can optimize the efficiency of SSDSSCs for the intertropicsl region.**

Keywords—Dye Sensitized Solar Cells; Solid State Dye Sensitized Solar Cells; Nanotube Photonic Crystals; Photosensitizers

I. INTRODUCTION

Solar energy, being an abundant and free source of energy, has sparked much interest in the scientific community since the past century. With worldwide reserves of fossil fuels inevitably heading towards depletion and the alarming effects of global warming primarily driven by the usage of fossil fuels, the whole world is much more inclined towards cleaner, greener, and more environmentally friendly sources of energy. One of the main drawbacks of using solar energy as a viable alternative to fossil fuels has been the relatively much higher installation expenses and poor efficiency. However, with the advent of DSSCs as a third generation photovoltaic device in the 1990s pioneered by O'Reagan and Grätzel[7], with usage of low cost materials and manufacturing processes, a window of opportunity for low cost implementation of solar power has been opened. With the majority of the developing economies of the world being from the intertropical region, the need for low cost usage of solar cells optimized for use in the aforementioned region is now greater than ever. A nanostructured, mesoporous metal oxide film which is photosensitized to the visible spectrum of light using adsorbed molecular dyes, form the basis of a DSSC. The dye molecules absorb visible light, exciting the electrons and inject those from the excited state into the metal oxide conduction band. The injected electrons travel through the nanostructured film to the current collector, and the dye is regenerated by an electron donor in the electrolyte solution in liquid-based DSSCs [8] and in case of SSDSSCs, in the several solid hole transporting materials (HTMs). In recent times DSSCs based on TiO_2 have been intensively investigated by researchers [9-11]. ZnO has many features such as its band gap, electron affinity, and electron injection efficiency. These features enable ZnO to be an alternative photoelectrode in DSSCs [12]. Recently, ZnO has been widely investigated as a DSSC photo electrode[13-16]. Compared to DSSCs based on TiO_2, the efficiencies of ZnO based cells are still low. ZnO based cells have reached efficiencies in the 5 per cent range [17]. Despite offering relatively high conversion efficiencies for solar energy, typical DSSCs suffer from durability problems that result from their use of organic liquid electrolytes containing the iodide/tri-iodide redox couple, which causes serious problems such as electrode corrosion and electrolyte leakage[18]. Device instability and the need for good device packaging have become major hurdles for commercial application of DSSCs [19]. Furthermore, liquid electrolyte based solar cells cannot be easily fabricated into multicell modules [20]. One way to address this manufacturing difficulty is to replace the liquid redox electrolyte by a solid-state hole transport material, typically a p-type conjugated polymer. In this paper, the manufacturing methods and performance analyses of SSDSSCs optimized for use in intertropical regions are explored.

II. CONSTRUCTION OF DSSCS

As schematically illustrated in Fig. 1, a DSSC typically consists of a several micron thick semiconductor (e.g. TiO_2, ZnO and SnO_2) film served as a photoanode that is coated or grown on a conductive substrate, a sensitizer (i.e. dye; e.g. N719, N3 or organic dyes by monolayer adsorption or quantum dots (e.g. CdS, CdSe and PbS)), an electrolyte (e.g. I_3^-/I^- and Co^{2+}/Co^{3+} redox couples) injected between the sensitizer and counter electrode, and a counter electrode (e.g.

978-1-5090-5785-6/16/$31.00 ©2016 IEEE

Pt and carbon materials) deposited on another conductive substrate [21]. Illumination by visible light irradiation on the photoanode causes photo-excitation of the absorbed dye molecules to generate excited electrons which are subsequently injected into the conduction band of the semiconductor and quickly shuttled to the external circuit through the conductive substrate, producing an electric current. The original state of the dye is subsequently restored by electron donation from the redox electrolyte. The counter electrode returns charge from the external circuit back to the cycling circuit in the cell [21].

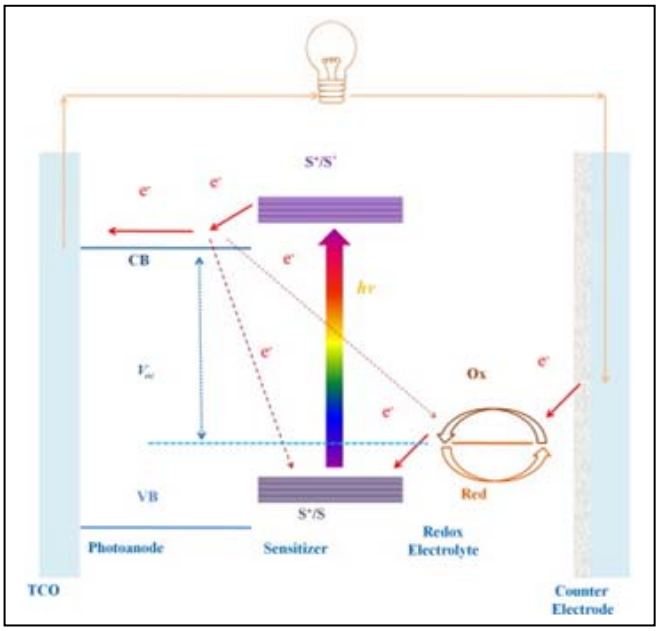

Fig. 1. *Schematic diagram of the electron-transfer processes occurring at the interfaces between each component in a DSSC.*

A. Maintaining the Integrity of the Specifications

The Each part of the device heavily determines the cost and efficiency of DSSCs. Areas of interest on the modification of each component of DSSCs for practical applications have included the construction of nanostructured semiconductor photoanodes with effective architectures for high dye loading and fast electron transport, the exploitation of versatile sensitizers with strong visible light harvesting ability, the utilization of redox electrolytes with useful compositions for efficient hole transport, the optimization of the Pt counter electrode as well as the development of other equivalent alternatives at lower costs[22-25]. In 2013, a new milestone for solid state mesoscopic TiO2 solar cells sensitized with lead iodide perovskite ($CH_3NH_3PbI_3$) was reported to achieve an exciting power conversion efficiency of more than 15 per cent [1-4], with expected future values as high as 20 per cent [5,6].

III. Solid State HTMs

Before The basic of SSDSSC is to replace the liquid electrolytes in DSSC with solid-state electrolytes, including various hole transporting materials (HTMs) [27].Several inorganic p-type materials (e.g. CuI/CuSCN and $CsSnI_3$) and organic polymers (e.g. poly (3,4-ethylenedioxythiophene) (PEDOT), 2,2',7,7'-tetrakis(N,N-di-4-methoxyphenylamino)-9,9'-spirobifluorene (spiro-MeOTAD), and poly (3-hexylthiophene) (P3HT)) have been successfully used in SSDSSCs[5,27-29]. Among these CuI/CuSCN HTMs possess high hole mobility. However, fast crystallization rates result in poor filling into photoanode films, and thus SSDSSCs show relatively low PCE of approximately 3.8per cent [28]. $CsSnI_3$, possessing high hole mobility, low cost, abundant raw materials, and low-cost processing, is another promising p-type semiconductor HTM. Pristine $CsSnI_3$ cell gives very good photocurrent density–voltage characteristics, open circuit voltage, fill factor, short circuit current density (J_{SC}) and overall power conversion efficiency as a solid state solar cell. Such electrolyte based devices have yielded a PCE of up to 10.2 per cent for SSDSSC in 2012[30]. Spiro-MeOTAD is much better than other types of organic HTMs [31] and in 2013 produced a high PCE of nearly 15 per cent when used in perovskite based SSDSSCs [1].Early in 2014, such PCE of perovskite $CH_3NH_3PbX_3$-based solar cells was further lifted to 16.7 per cent[26]with PCEs of 20 per cent expected in the near future [5, 6].However, low hole mobility and high manufacturing costs still inhibit the application of spiro-MeOTAD in SS-DSSCs. Good diffusion of HTMs into photoanode films and high conductivity for effective hole transfer are key issues for solid-state electrolytes in high-performance SSDSSCs.

IV. Effect of Solar Elevation Angle

The focus of this paper is to optimize the use of SSDSSC in the intertropical region, thus to maximize solar power generation in between 23°26'14.0" North and South latitude. Almost all types of solar cells suffer from a decreased power output when the incident light is tilted away from normal since the incident intensity generally follows a cosine law of the incident angle. It has been demonstrated experimentally that the use of nanotube photonic crystals (NT PC) can partially compensate the cosine power loss of a DSSC. The strategy used is to purposely choose the Bragg position of the NT PC to be at the longer wavelength side of the dye absorption peak. When the incident light is tilted, the blue shift of the Bragg position results in more overlap with the dye absorption peak, generating a higher efficiency that partially compensates the reduced photon flux due to light inclination. Moreover, the unique structure of the vertically aligned TiO2 nanotubes contributes an additional scattering effect when the incident light is tilted. As a result, the power output of a DSSC coupled with the NTPC layer shows a much flatter angular dependence than a DSSC without the NT PC. The figure 2 shown below shows the enhancements of normalized short circuit current after using NT PC of varying thicknesses, where the numbers preceding NT PC denotes the lattice constants in nanometers [32].

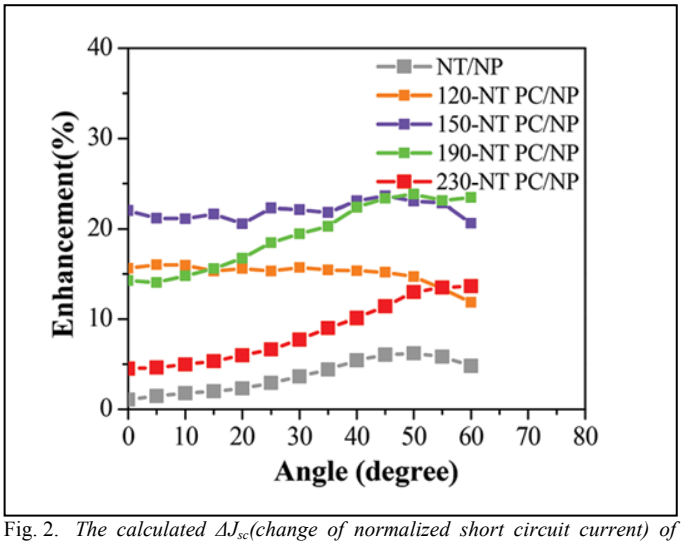

Fig. 2. *The calculated ΔJ_{sc}(change of normalized short circuit current) of different types ofDSSCs, as a function of incident angle [33].*

From the figure above, the 120, 150 and 190 nm NT PCs are of most importance here as these perform the best within the range of inclinations relevant for the tropics, namely from 0°-23.5° approximately. With NT PC compensation in place, the solar panels would be needed to only account for the daily East to Westward motion of the Sun and the reduction in power level due to the annual Southward motion of the Sun in Northern hemisphere in winter (and the opposite in Southern hemisphere) would be partially mitigated, making the implementation of this technology viable for domestic use.

V. Conclusion

This review summarizes recent advances in the components of DSSCs. These include the photoanode, sensitizer, electrolyte, and counter electrode. The slow progress of DSSCs based on iodide-electrolytes and ruthenium-sensitizers in the past ten years has necessitated the need for other novel, efficient and low-cost materials for the practical commercialization of DSSCs. Thus, a series of organic/inorganic materials have been explored for the production of the cost-effective DSSCs. It is expected that a reduction in the loss-in-potential to 500 mV by well matching the energy levels at the interface of photoanode/sensitizer/electrolyte, and the further extension of the light harvesting region to 920 nm by using strongly absorbing sensitizers, the PCE of DSSCs can be boosted to 19% [33].For the TiO2 NT PCs,by making use of the blue shift of the Bragg peak and the enhanced light scattering from TiO2 NT PC under oblique incidence, the photovoltaic performance of DSSCs can be made less sensitive to irradiance, an attractive feature for applications requiring less micromanagement [32]. With low cost and low maintenance SSDSSCs with built in Solar angle compensation close to commercial realization, it is this authors' understanding that in the near future such solar cells will play a crucial role in helping to boost the economy and supply the power demands of developing intertropical countries around the world.

References

[1] J. Burschka *et al.*, "Sequential deposition as a route to high-performance perovskite-sensitized solar cells," *Nature*, vol. 499, no. 7458, pp. 316–319, Jul. 2013.

[2] D. Liu and T. L. Kelly, "Perovskite solar cells with a planar heterojunction structure prepared using room-temperature solution processing techniques," *Nature Photonics*, vol. 8, no. 2, pp. 133–138, Dec. 2013.

[3] M. Liu, M. B. Johnston, and H. J. Snaith, "Efficient planar heterojunction perovskite solar cells by vapour deposition," *Nature*, vol. 501, no. 7467, pp. 395–398, Sep. 2013.

[4] J. T.-W. Wang *et al.*, "Low-temperature processed electron collection layers of Graphene/TiO 2 Nanocomposites in thin film Perovskite solar cells," *Nano Letters*, vol. 14, no. 2, pp. 724–730, Feb. 2014.

[5] M. Ye *et al.*, "Recent advances in dye-sensitized solar cells: From photoanodes, sensitizers and electrolytes to counter electrodes," *Materials Today*, vol. 18, no. 3, pp. 155–162, Apr. 2015.

[6] N.-G. Park, "Organometal Perovskite light absorbers toward a 20% efficiency low-cost solid-state Mesoscopic solar cell," *The Journal of Physical Chemistry Letters*, vol. 4, no. 15, pp. 2423–2429, Aug. 2013.

[7] N. F. Atta, A. Galal, and H. M. A. Amin, "Synthesis and Photoelectrochemical Behavior of a Hybrid Electrode Composed of Polyaniline Encapsulated in Highly Ordered TiO2 Nanotubes Array," *Int. J. Electrochem. Sci.*, vol. 7, no. 4, pp. 3610–3626, Apr. 2012.

[8] Yahia Chergui, N. Nehaoua, and D. E. Mekki, *Solar cells: Dye-sensitized devices*, L. A. Kosyachenko, Ed. InTech, 2011, ch. 3.

[9] Q. Dai and J. Rabani, "Photosensitization of nanocrystalline TiO2 films by anthocyanin dyes," *Journal of Photochemistry and Photobiology A: Chemistry*, vol. 148, no. 1-3, pp. 17–24, May 2002.

[10] R. Espinosa *et al.*, "Nanocrystalline TiO2 photosensitized with natural polymers with enhanced efficiency from 400 to 600nm," *Solar Energy Materials and Solar Cells*, vol. 85, no. 3, pp. 359–369, Jan. 2005.

[11] H. Zhou, L. Wu, Y. Gao, and T. Ma, "Dye-sensitized solar cells using 20 natural dyes as sensitizers," *Journal of Photochemistry and Photobiology A: Chemistry*, vol. 219, no. 2-3, pp. 188–194, Apr. 2011.

[12] A. M. Al-Kahlout, H. S. El-Ghamri, N. A. Dahoudi, T. M. El-Agez, S. A. Taya, And M. S. Abdel-Latif, "A comparative study: Synthetic dyes as photosensitizers for dye-sensitized solar cells," *Turkish Journal of Physics*, vol. 39, pp. 272–279, 2015.

[13] H. Chen, Z. Duan, Y. Lu, and A. Du Pasquier, "Dye-sensitized solar cells combining ZnO Nanotip arrays and Nonliquid gel Electrolytes," *Journal of Electronic Materials*, vol. 38, no. 8, pp. 1612–1617, Apr. 2009.

[14] T. W. Hamann, A. B. F. Martinson, J. W. Elam, M. J. Pellin, and J. T. Hupp, "Aerogel Templated ZnO dye-sensitized solar cells," *Advanced Materials*, vol. 20, no. 8, pp. 1560–1564, Apr. 2008.

[15] Z. Longyue, D. Songyuan, X. Weiwei, and W. Kongjia, "Dye-sensitized solar cells based on ZnO films," *Plasma Science and Technology*, vol. 8, no. 2, pp. 172–175, Mar. 2006.

[16] T. M. El-Agez, A. A. El Tayyan, A. Al-Kahlout, S. A. Taya, and M. S. Abdel-Latif, "Dye-sensitized solar cells based on ZnO films and natural dyes," *International Journal of Materials and Chemistry*, vol. 2, no. 3, pp. 105–110, Aug. 2012.

[17] N. Hongsith, *et al.*, *J. Nat. Sci.*, vol. 7, pp. 171-176, 2008

[18] S. Yanagida, Y. Yu, and K. Manseki, "Iodine/iodide-free dye-sensitized solar cells," *Accounts of Chemical Research*, vol. 42, no. 11, pp. 1827–1838, Nov. 2009.

[19] M. Grätzel, "Dye-sensitized solar cells," *Journal of Photochemistry and Photobiology C: Photochemistry Reviews*, vol. 4, no. 2, pp. 145–153, Oct. 2003.

[20] W. C. Sinke and M. M. Wienk, *Nature*, vol. 395, no. 6702, pp. 544–545, Oct. 1998.

[21] A. Hagfeldt, G. Boschloo, L. Sun, L. Kloo, and H. Pettersson, "Dye-sensitized solar cells," *Chemical Reviews*, vol. 110, no. 11, pp. 6595–6663, Nov. 2010.

[22] N. Tétreault, et al., *Energy Environ. Sci.*, vol. 5, pp. 8506–8516, 2012

[23] S. Zhang, et al., *Energy Environ. Sci*., vol. 6, pp. 1443–1464, 2013.

[24] M. Wang, et al., *Energy Environ. Sci*., vol. 5, pp. 9394–9405, 2012.

[25] M. Wu, et al., *ChemSusChem*, vol. 5, pp. 1343–1357, 2012.

[26] N. J. Jeon *et al.*, "O -Methoxy Substituents in Spiro-OMeTAD for efficient Inorganic–Organic hybrid Perovskite solar cells," *Journal of the American Chemical Society*, vol. 136, no. 22, pp. 7837–7840, Jun. 2014.

[27] D. Li, D. Qin, M. Deng, Y. Luo, and Q. Meng, "Optimization the solid-state electrolytes for dye-sensitized solar cells," *Energy Environ. Sci.*, vol. 2, no. 3, pp. 283–291, 2009.

[28] G. Hodes and D. Cahen, "All-solid-state, semiconductor-sensitized Nanoporous solar cells," *Accounts of Chemical Research*, vol. 45, no. 5, pp. 705–713, May 2012.

[29] D. Bi, L. Yang, G. Boschloo, A. Hagfeldt, and E. M. J. Johansson, "Effect of different hole transport materials on recombination in CH 3 NH 3 PbI 3 Perovskite-Sensitized Mesoscopic solar cells," *The Journal of Physical Chemistry Letters*, vol. 4, no. 9, pp. 1532–1536, May 2013.

[30] I. Chung, B. Lee, J. He, R. P. H. Chang, and M. G. Kanatzidis, "All-solid-state dye-sensitized solar cells with high efficiency," *Nature*, vol. 485, no. 7399, pp. 486–489, May 2012.

[31] J. H. Heo *et al.*, "Efficient inorganic–organic hybrid heterojunction solar cells containing perovskite compound and polymeric hole conductors," *Nature Photonics*, vol. 7, no. 6, pp. 486–491, May 2013.

[32] M. Guo, K. Xie, X. Liu, Y. Wang, L. Zhou, and H. Huang, "A strategy to reduce the angular dependence of a dye-sensitized solar cell by coupling to a TiO 2 nanotube photonic crystal," *Nanoscale*, vol. 6, no. 21, pp. 13060–13067, Sep. 2014.

[33] B. E. Hardin, H. J. Snaith, and M. D. McGehee, "The renaissance of dye-sensitized solar cells," *Nature Photonics*, vol. 6, no. 3, pp. 162–169, Feb. 2012.

2nd International Conference on Electrical, Computer & Telecommunication Engineering (ICECTE)
8-10 December 2016, Rajshahi-6204, Bangladesh

Performance Analysis of Acoustic Microphone Array Beamformer in the Presence of Interfering Signal

M. T. Hossein*, M. S. Hossain, and M. F. Reza
Department of Electrical and Electronic Engineering
Rajshahi University of Engineering and Technology (RUET), Rajshahi-6204, Bangladesh
*E-mail: tarek101008@gmail.com

Abstract—The acoustic beamformer is an important tool which is used in many environments to focus on a specific sound among many reverberations. This paper presents an acoustic microphone array beamformer in the presence of unwanted signal. Time delay and Frost beamforming techniques are used with microphone array to reduce the noise and cancel the interfering signal respectively. The presented beamformers can be able to increase the system SNR without array mismatch. The performance of the time delay and Frost microphone arrays will degrade in the presence of array imperfections. To improve the system performance a robust algorithm is addressed in this paper. The extensive computer simulation is presented to analyze the performance of the acoustic beamformer with different scenarios.

IndexTerms—Acoustic beamformer, array, time delay beamforming, Frost beamforming, SNR, robust algorithm, array gain

I. INTRODUCTION

Microphone arrays are widely used for their enhanced performances in signal detection and identification [1], source localization [2], noise and interference suppression [3]. Microphone array processing falls into two basic categories: One is array beamforming and another is source localization and tracking [4].The microphone array beamformer has recently become an important research subject since flexible 3D beam pattern synthesis can be realized [5]. But the difficulty for a microphone system is to scan and localize the desired single person's voice amidst other conversations and background noises [6]. So, the clarity of the desired person's voice can be greatly improved where the microphone array systems can be able to reduce the noise and cancel the interfering signals. This paper presents microphone array beamforming technique to extract desired speech signal in interference dominant noisy environment. The beamformer operation is used to enhance the received speech signal quality by increasing SNR and by suppressing the interference signal. Conventionally two types of time domain beamformers are used in microphone array signal processing which are time delay beamformer and Frost beamformer. The first one compensates the arrival time differences for the array elements signal in order to increase SNR and the latter one is used to obtain better beamformer performance by attaching FIR filters to each sensor. It is an adaptive algorithm that uses distortionless constraints to ensure desired signals are not suppressed.

The microphone array beamformer addressed in [7], where the optimum array observation is achieved by receiving signals that are physically de-correlated between microphones and an array structure based on implementing minimum variance distortion-less response beamforming. But it is not robust against array imperfections. The processor addressed in [8-9] is presented a comparison between Frost beam former and conventional time delay beamformer using wiener filter.

To overcome the aforementioned difficulties a robust beamforming technique for acoustic microphone array beamformer is presented in this paper. The diagonal loading technique improves the robustness of the frost beamformer by adding a small quantity to the elements so that performance does not suffer from inaccurate steering direction. To observe the performance of the proposed acoustic microphone array beamformer, a number of examples are demonstrated using computer simulation.

II. SYSTEM MODEL

Let us consider a uniform linear array (ULA) to receive the interference, echo, reverberation, noise and desired signal. A simple microphone array signal processor is shown in Fig 1.

It follows from Fig.1 that an expression for the array output is given by

$$y(t) = \sum_{l=1}^{L} w_l^* x_l(t) \tag{1}$$

where * denotes the complex conjugate. The conjugate of complex weights is used to simplify the mathematical notation. Denoting the weights of the array system using vector notation as

$$w = [w_1 \quad w_2 \quad w_3 .... \quad w_L]^T \tag{2}$$

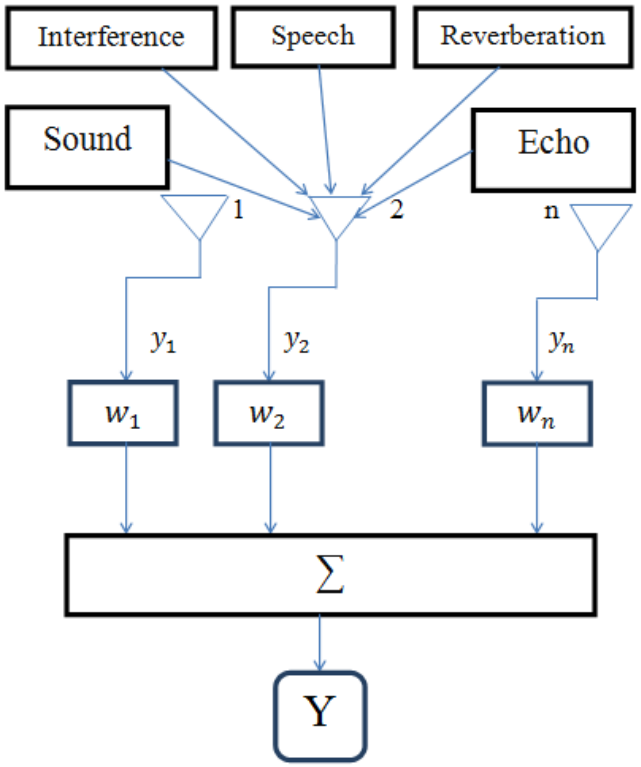

Fig 1: Microphone array signal processor.

The signals induced on all elements are

$$x(t) = [x_1(t) \quad x_2(t) \quad x_3(t)..... \quad x_L(t)]^T \tag{3}$$

and output of the array system becomes

$$y(t) = w^H x(t) \tag{4}$$

where superscript T and H, respectively, denote transposition and the complex conjugate transposition of a vector or matrix [10]. The array correlation matrices due to the signal source, unwanted interference, and random noise is define as

$$R = E[x(t)x^H(t)] \tag{5}$$

The robust loading technique adds a fixed value diagonally with the correlation matrix to reduce the signal cancellation for look direction errors. The robust correlation matrix is given by

$$R_{(new)} = R + \xi I \tag{6}$$

where ξ is the fixed diagonal loading factor taken to be equal to σ_n^2 which denoting the background noise power at the and I is the identity matrix.

III. PERFORMANCE ANALYSIS

A number of examples are presented in this section to evaluate the performance of the proposed acoustic microphone array. This array contains omnidirectional microphones with 5cm element spacing. We consider three types of signal in this array. At first, two recorded speech signals and a laughter signal are loaded. Here the laughter signal is considered as interference signal. Our concern is to reduce this interference signal to enhance the clarity of the speech signal at the beamformer output. The audio signal simulates and processed in a streaming fashion which is by breaking the audio signal into small blocks at the input and then assembling them at the output as the audio signal is too large to read the entire signal into the memory. The sampling frequency of the audio signals is 8 kHz. The first speech signal direction is -40^0 in azimuth and 0^0 in elevation and the second signal is -20^0 in azimuth and 20^0 in elevation. The direction of interference signal is varied to observe the performance of proposed processor. The power of the white noise is also varied for performance variance observation. A wideband collector is used in order to simulate a 3-second signal received by the array where each input single-channel signal is received at the origin of the array by a single microphone. For the time delay beamformer, number of sample per frame is 1000, propagation speed is 340 m/s and the direction of the first speech signal is taken as the steering angle. For the Frost beamformer, an FIR filter of order 20 is used for each microphone with 0 diagonal loading. Again, second speech signal direction is steered with taking estimated direction of the second speech signal as -17^0 in azimuth and 17^0 in elevation. Then to improve the robustness of the Frost beamformer, a diagonal loading is added with the correlation matrix. The received signal quality is adjudicated with listening the output received signal of the microphone array, array gain and also input, output SINR.

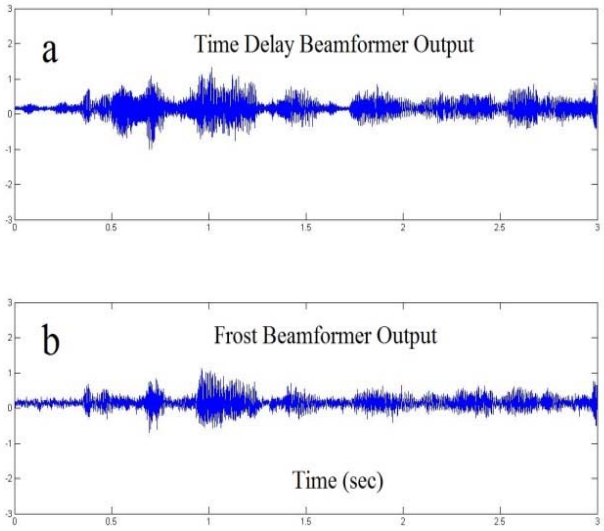

Fig. 2: Received signal for (a) time delay beamformer and (b) Frost Beamformer for 10 elements.

Fig. 2 shows the received signals for time delay and Frost beamformer. It is observed from Fig. 2 that the noise and interference reduction quality is better for Frost beamformer

than the time delay beamformer. The array gain is also better for Frost (8.4281 dB) than time delay (6.4402 dB) beamformer.

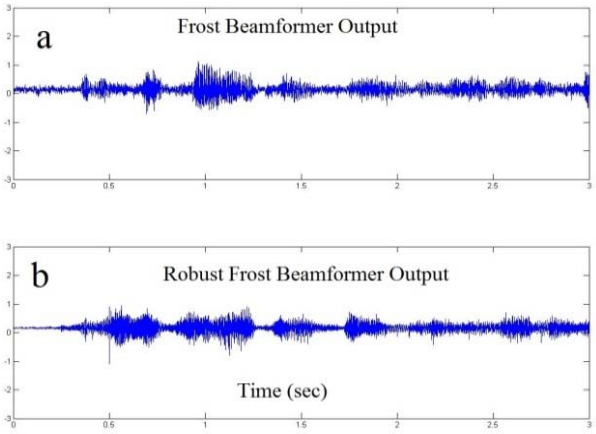

Fig. 3: Received signal for (a) Frost Beamformer and (b) robust Frost Beamformer for 10 elements

The received signal from conventional Frost and robust beamformer is shown in Fig. 3. One can observe from this figure that the noise and interference reduction quality is better for Robust Frost than conventional Frost beamformer and array gain is also better for Robust Frost (10.9572 dB) than Frost (8.4281 dB) beamformer. So, robust Frost is better than both time delay and Frost beamformer. The parametric variations of the three processors are given below:

A. *Variation of number of array elements*

Tab. I showed output SNR, input SNR and array gain for different beamformers with number of sensor elements variation for microphone array. The direction of interference signal is 30^0 in azimuth and 0^0 in elevation and the white noise power is $1e^{-4}$ watts.

Table I: Characteristic parameters of the received signals

Types	Number of Array Elements	Output SINR	Input SINR	Array Gain (dB)
Time Delay Beamformer	8	0.1578	0.0396	6.0090
	10	0.1578	0.0358	6.4402
	12	0.1578	0.0336	6.7211
Frost Beamformer	8	0.1578	0.0232	8.3199
	10	0.1578	0.0227	8.4281
	12	0.1578	0.0233	8.3106
Frost Beamformer (Estimation angle)	8	0.1440	0.0168	9.3396
	10	0.1440	0.0185	8.9104
	12	0.1440	0.0190	8.7854
Robust Frost (Diagonal loading)	8	0.1440	0.0126	10.5780
	10	0.1440	0.0115	10.9572
	12	0.1440	0.0110	11.1576

One can observed from table that the array gain is increased of the proposed beamformer compared to other existing processor for the same number of array elements. The gain is increased an approximate of 4.51dB than the time delay beamformer.

From Fig. 4 and Fig. 5, one can see that the noise and interference reduction quality is better for Robust Frost beamformer than both time delay and Frost beamformer and array gain is also better for Robust Frost (11.0304 dB) than both time delay (6.5046 dB) and Frost beamformer (8.4030 dB).

B. *Variation of Interference Directions*

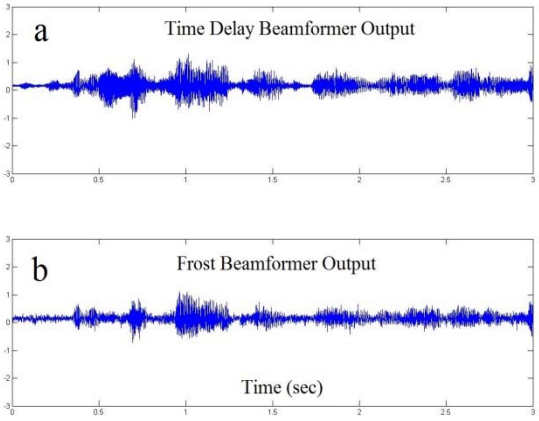

Fig. 4: Received signal for time delay beamformer and Frost Beamformer when azimuth angle is 30^0.

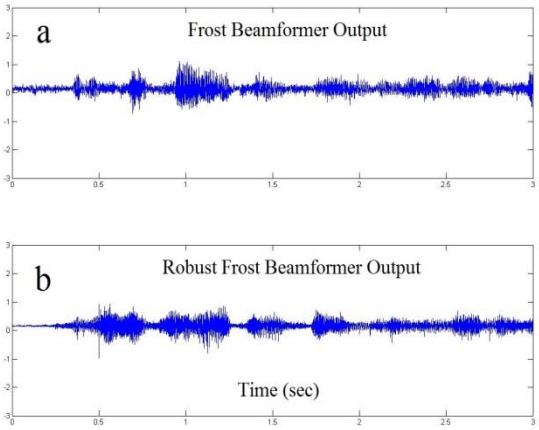

Fig. 5: Received signal for Frost Beamformer and robust Frost Beamformer when azimuth angle is 30^0.

Table II : Characteristics of the received signals.

Types	Azimuth Angle (Degrees)	Output SINR	Input SINR	Array Gain (dB)
Time Delay Beamformer	25	0.1578	0.0358	6.4402
	30	0.1578	0.0353	6.5046
	35	0.1578	0.0350	6.5371
Frost Beamformer	25	0.1578	0.0227	8.4281
	30	0.1578	0.0228	8.4030
	35	0.1578	0.0229	8.3930
Frost Beamformer (Estimation angle)	25	0.1440	0.0185	8.9104
	30	0.1440	0.0184	8.9283
	35	0.1440	0.0185	8.8995
Robust Frost (Diagonal loading)	25	0.1440	0.0115	10.9572
	30	0.1440	0.0114	11.0304
	35	0.1440	0.0112	11.0739

Tab. II shows the characteristics of the received signal for 10 elements array and noise power is $1e^{-4}$watts. Interference direction is varied. It is observed from Tab. II that the output

SNR, input SNR and array gain for different beamformers with interference signal variation. The robust technique approximately achieved array gain 4.53dB higher than the time delay beamformer.

C. *Variation of Noise Power*

The effect of noise power in the beamformer is significant for the system performance. From Fig. 6 and Fig. 7, it is observed that the noise and interference reduction quality is better for Robust Frost beamformer than both time delay and Frost beamformer and array gain is also better for Robust Frost (10.9766 dB) than both time delay (6.4899dB) and Frost beamformer (8.4281dB).

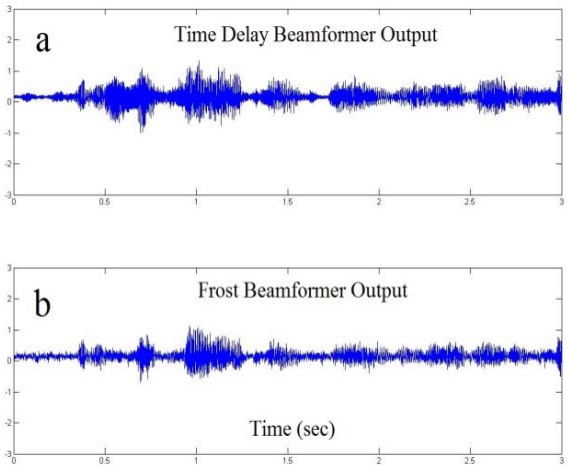

Figure 6: Received signal for time delay beamformer and Frost Beamformer when noise power is $0.5e^{-4}$watts

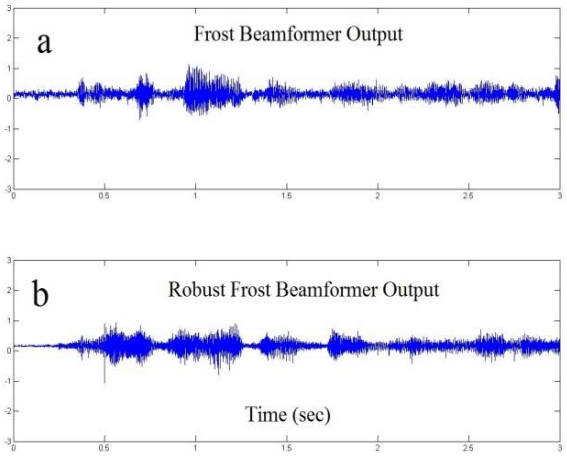

Figure 7: Received signal for Frost Beamformer and robust Frost Beamformer when noise power is $0.5e^{-4}$watts

Tab.III shows the noise power variation for different beamformer. It is clear that the array gain reduction is better for robust Frost than both time delay and Frost beamformer with the increase of noise power.

Table III: Characteristics of the received signals.

Types	Noise Power (watts)	Output SINR	Input SINR	Array Gain (dB)
Time Delay Beamformer	0.5e-4	0.1578	0.0354	6.4899
	1e-4	0.1578	0.0358	6.4402
	2e-4	0.1579	0.0364	6.3708
Frost Beamformer	0.5e-4	0.1578	0.0223	8.4972
	1e-4	0.1578	0.0227	8.4281
	2e-4	0.1579	0.0232	8.3332
Frost Beamformer (Estimation angle)	0.5e-4	0.1439	0.0190	8.7898
	1e-4	0.1440	0.0185	8.9104
	2e-4	0.1441	0.0181	9.0170
Robust Frost (Diagonal loading)	0.5e-4	0.1439	0.0115	10.9766
	1e-4	0.1440	0.0115	10.9572
	2e-4	0.1441	0.0116	10.9290

IV. CONCLUSION

With the aforementioned variations the performance of the acoustic microphone array beamformer output is observed. We perceived that with the increase of array elements, time delay beamformer and Frost beamformer output with diagonal loading is increased and with the variations of azimuth angle of interference signal, time delay beamformer and Frost beamformer output with diagonal loading is also increased. As array gain is the ratio of output SINR to input SINR,so here reduction of interference signal is better and so the output desired signal clarity is also better. Again, with the increase of noise power both the time delay beamformer and Frost beamformer with diagonal loading output is decreased and so the output desired signal clarity is not satisfactory.

V. REFERENCES

[1] H. Wang and L. Y. Wang, "Multi-sensor adaptive heart and lung sound extraction", in *Proc. IEEE Sensors Conf.*, Toronto, ON, Canada, pp. 1096–1099, Oct. 2003.

[2] A. A. Handzel and P. S. Krishnaprasad, "Biomimetic sound-source localization," *IEEE Sensors J.*, vol. 2, no. 6, pp. 607–616, Dec. 2002.

[3] C. Marro, Y. Mahieux, and K. U. Simmer, *IEEE Transaction on Speech Audio Processing,* vol. 6, no3, pp.240–259, May 1998.

[4] Y. R. Zheng, R. A. Goubran ,M.Tanany, and H. Shi, "A Microphone Array System for Multimedia Applications With Near-Field Signal Targets",IEEE sensors journal, vol. 5, no. 6, Dec. 2005.

[5] H. Sun, S. Yan, and U. P. Svensson, "Optimal Higher Order Ambisonics Encoding With Predefined Constraints", IEEE Trans. Audio, Speech & Language Processing 20(3): 742-754 (2012)

[6] M. S. Hossain, M. M. Rashid, M. R. Islam and M. F. Ali "Convolution constrained robust beamforming techniques for broadband microphone array", International Conference on Electrical & Electronic Engineering (ICEEE), 2015.

[7] K. Niwa, Y. Hiokaand and K. Kobayashi, "Optimal Microphone Array Observation for Clear Recording of Distant Sound Sources", IEEE Transactions on Audio, Speech, and Language Processing Volume: 24, Issue: 10, Oct. 2016.

[8] A. Hussain, K. Chellappan, SitiZamratol M, "Evaluation of multichannel speech signal separation with beamforming techniques", IEEE Conference on Biomedical Engineering and Sciences IECBES, Malaysia, 2014.

[9] Y. Hioka, M. Kingan, G. Schmid and K. A. Stol, "Speech enhancement using a microphone array mounted on an unmanned aerial vehicle", IEEE 15th International Workshop on Acoustic Signal Enhancement (IWAENC), China, Sept. 13-16, 2016.

[10] L. C. Godara, Smart Antennas, CRC Press, USA, 2004.

International Conference on Electrical, Computer & Telecommunication Engineering (ICECTE)
8-10 December 2016, Rajshahi-6204, Bangladesh

Performance Analysis of Grid Connected PV array with H-Bridge Inverter controlled by angular modulation scheme.

M.A. Munjer
Department of EEE,
RUET
Rajshahi, Bangladesh
abulmunjer@yahoo.com

Dr. Md. Faruk Hossain
Department of EEE,
RUET
Rajshahi, Bangladesh
faruk94_ruet@yahoo.com

Md. Akramul Alim
Department of EEE,
RUET
Rajshahi, Bangladesh
eaar@ymail.com

***Abstract*— This paper presents a modular cascaded H-bridge multilevel photovoltaic (PV) inverter for three-phase grid-connected solar cell. An angular controlled modulation scheme has been proposed for Modular Multilevel Converter in this application. To maximize the solar energy extraction in various irradiance, Incremental Conductance algorithm for maximum power point tracking is used, which allows independent control of each solar cell voltage. The performance of the system has also been analyzed at variable irradiance on the each cell. A simulation model of three-phase seventeen-level cascaded H-bridge inverter has been built by using twenty four number of H-bridge modules (eight modules per phase). Each H-bridge module is connected to a 270-W solar panel. Simulation results are presented to verify the feasibility of the proposed approach where on an average 1.5% THD is achieved in load phase voltage.**

Keywords*— Cascaded multilevel inverter, maximum power point (MPP) tracking (MPPT), photovoltaic (PV).

I. INTRODUCTION

Renewable energy, particularly solar energy, has become very popular due to the shortage of fossil fuels and environmental problems caused by conventional power generation. Solar-electric-energy demand has grown consistently by 20%–25% per annum over the past 20 years [1], and the growth is mostly in grid-connected applications. With the extraordinary market growth in grid-connected photovoltaic (PV) systems, there are increasing interests in grid-connected PV configurations.

Five inverter families can be defined, which are related to different configurations of the PV system: (i) Central inverters; (ii) String inverters; (iii) Multi string inverters (iv) AC-module inverters; and (v) Cascaded inverters[2]–[7]. Cascaded inverters consist of several converters connected in series; thus, the high power and/or high voltage from the combination of the multiple modules would favor this topology in medium and large grid-connected PV systems [8]–[10].

In cascaded dc/dc converter connection of PV modules each PV module has its own dc/dc converter, and the modules with their associated converters are still connected in series to create a high dc voltage, which is provided to a simplified dc/ac inverter [11],[12]. This approach combines aspects of string inverters and ac-module inverters and offers the advantages of individual module maximum power point (MPP) tracking (MPPT), but it is less costly and more efficient than ac-module inverters.

Another cascaded inverter each PV panel is connected to its own dc/ac inverter, and those inverters are then placed in series to reach a high-voltage level [13]–[16]. This cascaded inverter would maintain the benefits of "one converter per panel," such as better utilization per PV module, capability of mixing different sources, and redundancy of the system.

In addition, this dc/ac cascaded inverter removes the need for the per-string dc bus and the central dc/ac inverter, which further improves the overall efficiency.

The modular cascaded multilevel inverter, which requires an isolated dc source for each H-bridge, is one dc/ac cascaded inverter topology. The separate dc links in the multilevel inverter make independent voltage control possible [17]. As a result, individual MPPT control in each PV module can be achieved, and the energy harvested from PV panels can be maximized. Meanwhile, the modularity and low cost of multilevel converters would position them as a prime candidate for the next generation of efficient, robust, and reliable grid connected solar power electronics.

For better understand about the necessity of individual MPPT control, a brief discussion about panel mismatch is added. In the modulation of MMC, an angular controlled modulation algorithm has been proposed. A three-phase modular cascaded multilevel inverter prototype has been built in MATLAB

"978-1-5090-5785-6/16/$31.00 ©2016 IEEE"

simulation software. Each H-bridge is connected to a 270-W solar panel.

II. System Description

Fig.1 shows the Modular cascaded H- bridge multilevel inverters for three phase grid connected PV array where cascaded multilevel inverter is connected through RL filters for the reduction of the switching harmonics. Three phase load of 10 KVAR get coupled with the back to back connection of 3 phase PV array to 25kv transmission line from 120kv, 2500MVA grid.

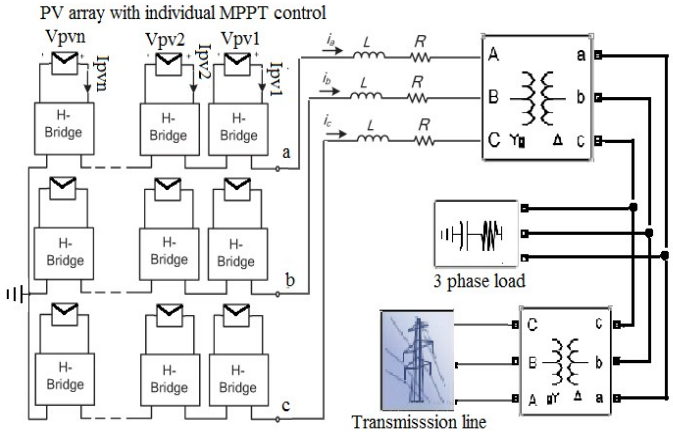

Fig. 1. Grid connected PV arry with individual MPPT control.

Each H-bridge module consists of four switching devices to generate three output voltage level as 0, +*v*dc and –*v*dc. For n number of module as well as solar cell in each phase, there will have (2n+1) number of level at the output voltage.

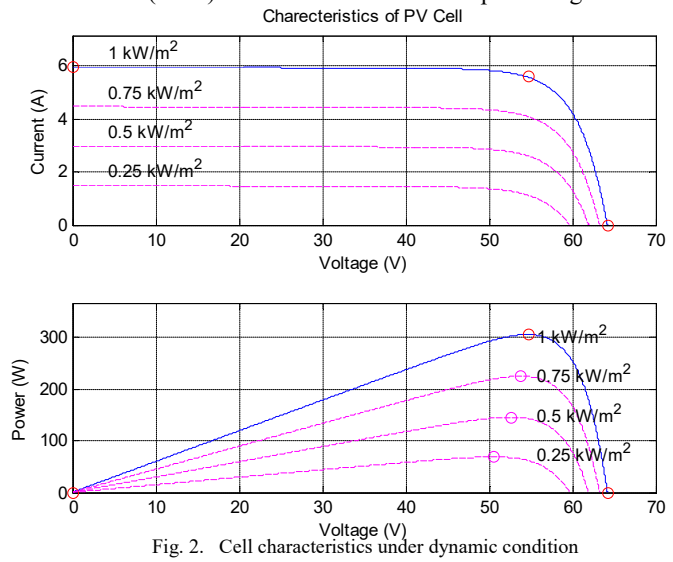

Fig. 2. Cell characteristics under dynamic condition

With the increase in level the harmonics of the output current is reduced and the voltage stress on the semiconductor device is also reduced, hence the efficiency can be higher in comparison with other converter topologies [18].

Due to the unequal received irradiance, different temperatures, and aging of the PV panels, the MPP of each PV module may be different. If each PV module is not controlled independently, the efficiency of the overall PV system will be decreased [17]. So before feeding the solar output to the converter, distributed MPPT control is used in this system.

The P-V characteristic of each cell used for this simulation is shown in fig.2. For a different irradiation from the sun on the two PV cell, for an example, panel 1 has irradiance S =1 kw/m^2, and panel 2 has S = .5 kw/m^2.

If power of each cell is tracked by individual MPPT controller, the power extracted from panel 1 would be 300 W, and the power from panel 2 would be 150 W, so the total power harvested from the PV system is 450 W. But If only panel 1 is tracked and its MPPT controller determines the average voltage of the two panels, the power extracted from panel must be lower than individual MPPT control [17].

III. Modulation For Gate Pulses

As shown in fig.3, three phase per unit voltage is fed to the PLL to determine the operating frequency of the line or grid to which PV array would be connected with. From this parameter δ and ξ signals will be generated to compare through three comparator in various criteria for having signals, composition of three magnitude of pulse. The frequency of each signals are same but the width of the containing pulses varies as shown in fig.5-6.

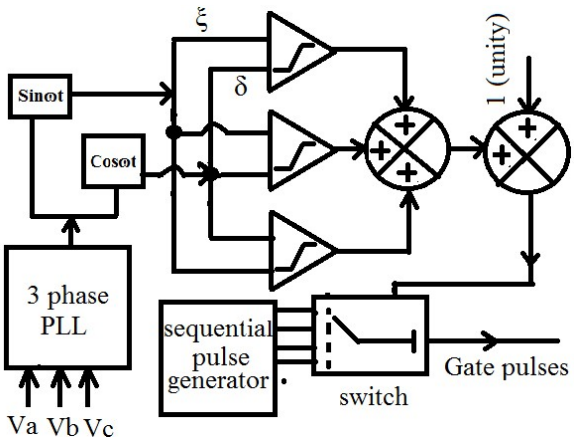

Fig. 3. Gate signals generation for the switching device of H-bridge module

Sequential pulse generator, actually a number of four pulse generator, generates four signals according to the pre-defined value to make them as gate pulses for the switching device of the H-bridge module through a pulse controlled switch.

TABLE I. PARAMETERS

Parameter	Value
Coupling inductor	250mH
Coupling resistor	2mΩ
Transmission line	
Line voltage	25kv/120kv
Feeder length	19km
Resistance per unit length (Ohms/km)	0.1153Ω
Inductance per unit length (H/km)	1.05mH
Capacitance per unit length (F/km)	11.33nF

IV. SIMULATION RESULT

Simulation is carried out to validate the angular controlled modulation scheme for the inverter in grid connected PV application. A three-phase seventeen-level cascaded H-bridge inverter is simulated and tested. Each H-bridge has its own 270-W PV panel (Suntech STP270S-24_Vb) connected as an independent source. The inverter is connected to the grid through a transformer, and the phase voltage of the secondary side is 260 Vrms. The system parameters are shown in Table I.Two conditions have considered on the irradiance for each cell. Firstly the output has taken in same irradiance S= 1000w/m^2 at a constant temperature and thereafter system is simulated at dynamic irradiance conditions.

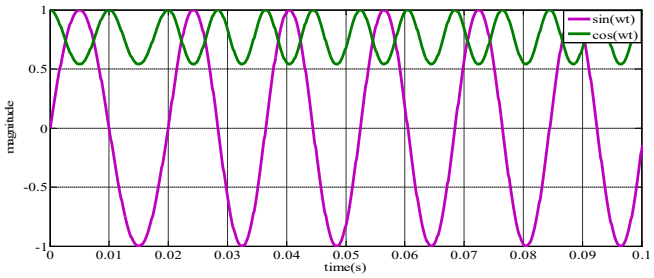

Fig. 4. ξ and δ signal output

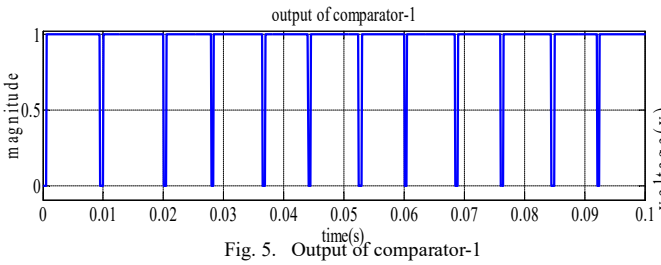

Fig. 5. Output of comparator-1

The gate signals of the transistor in the H-bridge are shown in fig.7, before that four comparators output (as shown in fig.5 & fig.6) combined through summer to take in operation of the sequential switch.

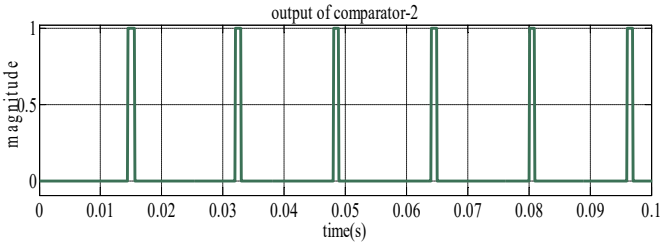

Fig. 6. Output of comparator-2

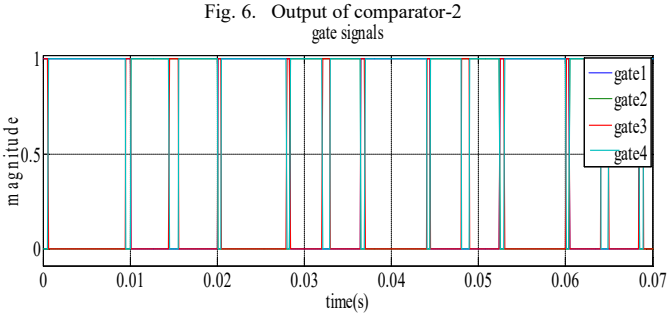

Fig. 7. Gate signals for the switching device of H-bridge module

The inverter output has shown in fig.8. where time t=0 to t=.02 was the initial periode of voltage rising for the PV array to attain the stability. In the next time of the simulatioin periode, the output of the inverter indicates, the system drives well to maintain 17 level (2n+1) of output voltage.

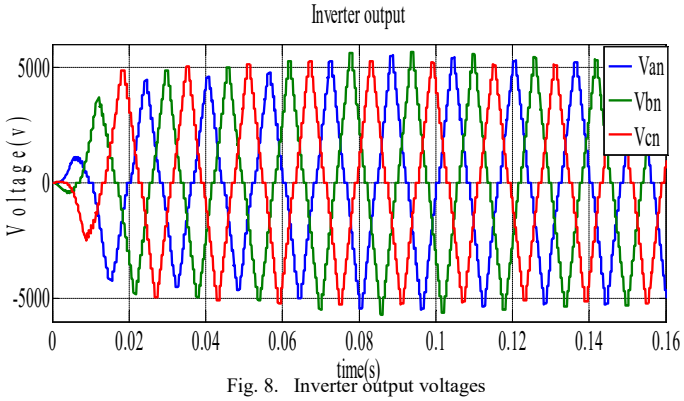

Fig. 8. Inverter output voltages

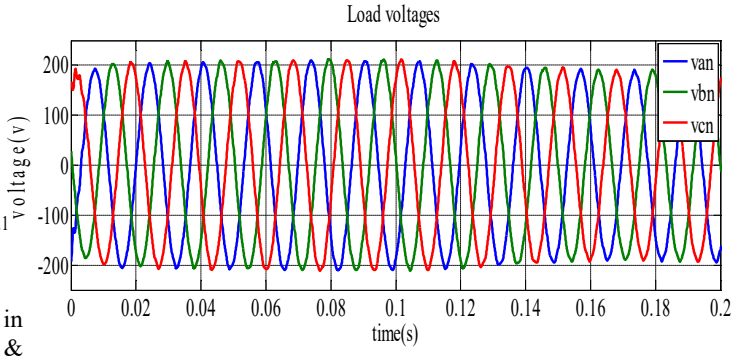

Fig. 9. Three phase load voltage

Fig.9 represents the three phase voltages of the load. It can be seen here that the maximum value of the phase voltage is 210V although 5kv/260v transformer was used to drive the load. On the other hand the variation of the inverter output can be observed from fig.10 where the value of irradiance was changed from S=1000w/m^2 to S=600 w/m^2 between t=0.01 to t=0.015s.

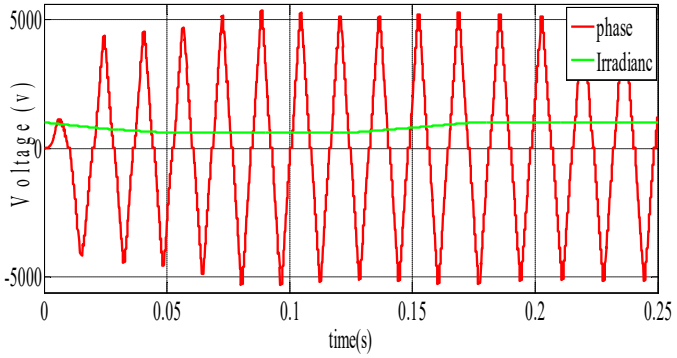

Fig. 10. Output of the inverter at dynamic condition.

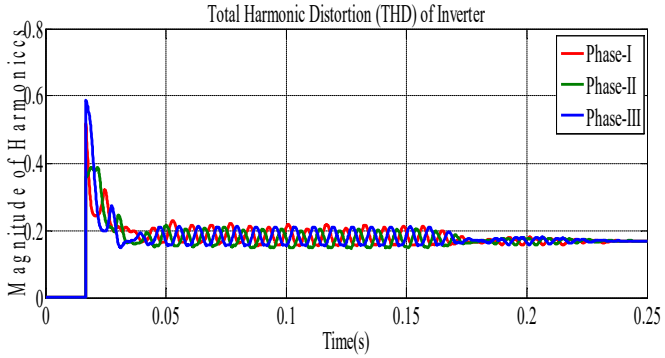

Fig. 11. (a) Total harmonic distortion of the inverter output

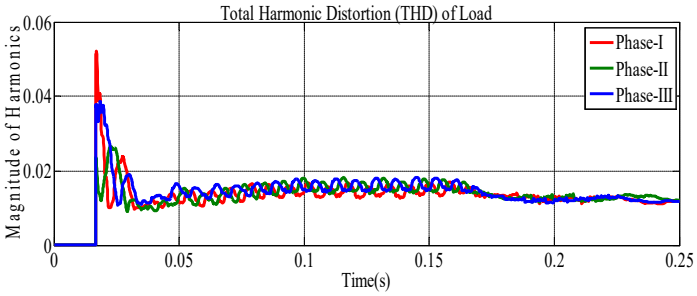

Fig.11. (b) Total harmonic distortion of the Load output

The total harmonic distortion of the inverter output was about 18%, shown in fig.11(a), and in the load side it is about 1.5% presented in fig.11(b).

V. Conclusion

In this paper, a modular cascaded H-bridge multilevel inverter for grid-connected PV applications has been presented. Power extracted from the PV cell has been tracked by individual MPPT control to have better power harvesting in save and variable irradiance condition. A gate signal generation procedure has been added here which will not increase the complexity of the control system but generate gate pulses to have successful outcome. Connecting the three phase PV array with the live transmission line was a great challenge after meeting with lower harmonic distortion (1.2%) in the load voltage. Furthermore, there might have a great opportunity for the further research of this work is to track the fault H-bridge module and the real and reactive power injection issue.

References

[1] J.M.Carrasco, "Power-electronic systems for the grid integration of renewable energy sources: Asurvey,"IEEETrans.Ind.Electron.,vol.53, no. 4,pp. 1002–1016,Jun. 2006.
[2] S. B. Kjaer, J. K. Pedersen, and F. Blaabjerg, "A review of single-phase grid connected inverters for photovoltaic modules," IEEE Trans. Ind. Appl., vol. 41, no.5,pp. 1292–1306,Sep./Oct. 2005.
[3] M. Meinhardt and G. Cramer, "Past, present and future of grid connected photovoltaic- and hybrid power-systems," in Proc. IEEE PES Summer Meet., 2000,vol. 2,pp.1283–1288.
[4] M.Calais, J.Myrzik, T.Spooner, and V.G.Agelidis, "Inverter for single phase grid connected photovoltaic systems—An overview, "in Proc. IEEE PESC, 2002,vol. 2, pp.1995–2000.
[5] J.M.A.Myrzik and M.Calais, "String and module integrated inverters for single-phase grid connected photovoltaic systems—A review," in Proc. IEEE Bologna Power Tech Conf.,2003,vol. 2,pp. 1–8.
[6] F. Schimpf and L. Norum, "Grid connected converters for photovoltaic, state of the art, ideas for improvement of transformer less inverters," in Proc. NORPIE, Espoo, Finland, Jun. 2008,pp.1–6.
[7] B. Liu, S. Duan, and T. Cai, "Photovoltaic DC-building-module-based BIPV system Concept and design considerations," IEEE Trans. Power Electron., vol.26, no.5, pp.1418–1429,May2011.
[8] L. M. Tolbert and F. Z. Peng, "Multilevel converters as a utility interface for renewable energy systems," in Proc. IEEE Power Eng. Soc. Summer Meet., Seattle, WA, USA, Jul. 2000,pp.1271–1274.
[9] H. Ertl, J. Kolar, and F. Zach, "A novel multi cell DC–AC converter for applications in renewable energy systems," IEEE Trans. Ind. Electron., vol. 49, no.5,pp. 1048–1057,Oct. 2002.
[10] S.Daher, J.Schmid, and F.L.M.Antunes, "Multi level inverter topologies for stand-alone PV systems," IEEE Trans. Ind. Electron., vol. 55, no. 7, pp. 2703–2712,Jul. 2008.
[11] G. R. Walker and P. C. Sernia, "Cascaded DC–DC converter connection of photovoltaic modules," IEEE Trans. Power Electron., vol. 19, no. 4, pp. 1130–1139,Jul. 2004.
[12] E. Roman, R. Alonso, P. Ibanez, S. Elorduizapatarietxe, and D. Goitia, "Intelligent PV module for grid-connected PV systems," IEEE Trans. Ind. Electron., vol.53, no.4, pp.1066–1073,Jun. 2006.
[13] F. Filho, Y. Cao, and L. M. Tolbert, "11-level cascaded H-bridge grid tied inverter interface with solar panels," in Proc. IEEE APEC Expo., Feb. 2010,pp.968–972.
[14] C. D. Townsend, T. J. Summers, and R. E. Betz, "Control and modulation scheme for a cascaded H-bridge multi-level converter in large scale photovoltaic systems," inProc. IEEEECCE, Sep. 2012,pp.3707–3714.
[15] B. Xiao, L. Hang, and L. M. Tolbert, "Control of three-phase cascaded voltage source inverter for grid-connected photovoltaic systems," in Proc. IEEE APEC Expo., Mar. 2013,pp.291–296.
[16] Y. Zhou, L. Liu, and H. Li, "A high-performance photovoltaic module integrated converter (MIC) based on cascaded quasi-Z-source inverters (qZSI) using eGaN FETs," IEEE Trans. Power Electron., vol. 28, no. 6, pp. 2727–2738, Jun.2013.
[17] Bailu Xiao, Lijun Hang, JunMei, Cameron Riley.LeonM.Tolbert, Fellow, and Burak Ozpineci, "Modular Cascaded H-Bridge Multilevel PV Inverter With Distributed MPPT for Grid-Connected Applications" IEEE Transaction on industry applications, vol.51, no.2, pp. 1722-1731, March/April 2015.
[18] J. Rodriguez, J. S. Lai, and F. Z. Peng, "Multilevel inverters: A survey of topologies, controls, and applications," *IEEE Trans. Ind. Electron.*, vol. 49, no. 4, pp. 724–738, Aug. 2002.

Improved Robustness of 3D CT to 2D Fluoroscopy Image Registration Using Log Polar Transforms

Masuma Akter[1], Andrew J. Lambert[2], Mark R. Pickering[3], Jenne M. Scarvell[4], Paul N. Smith[5], Fariha Tabassuma[6], and Mahamud Tariq Rashid[7]

[1]EEE, Dhaka University of Engineering and Technology, Gazipur, Bangladesh

[2-3]SEIT, University of New South Wales, Canberra, Australia

[4-5]Trauma and Orthopaedic Research Unit, Canberra Hospital, Australia

[6]EEE, Ahsanullah University of Science and Technology, Dhaka, Bangladesh

[7]Teshmont Consultants LP, Calgary , Canada.

***Abstract*—Automatic image registration algorithms that rely on a gradient descent based approach may fail when the initial misalignment between objects is large. The registration task is even more difficult for multi-modal images because of the non-linear relationship between the pixel intensities in the images to be aligned. In this paper we will present a multi-modal image registration algorithm which successfully registers 3D CT to 2D fluoroscopy data for large initial displacements between the images. The approach uses the conditional means (CM) of the joint probability distribution of the images to establish a model linear relationship between the pixel intensities of the images and then applies log-polar transforms (LPT) in the frequency domain to estimate the in-plane scale and rotation changes between the images. Our experimental results show that the proposed approach can increase the range of initial displacements for which the algorithm is able successfully register images by a factor of 4 when compared to the best of the existing gradient-descent based approaches.**

I. Introduction

Many medical applications require multi-modal 3D-2D registration [1], [2], [3] to align 3D pre-intervention data, such as computed tomography (CT) and Magnetic Rresonance (MR) images to, 2D intra-intervention data, including ultrasound and fluoroscopy. These applications include image guided surgery (IGS) and pre-, post-operative measurement of joint kinematics [4]. The knowledge of 3D joint kinematics is useful for understanding the function of the joint and for the diagnosis of pathology including ligament injury and osteoarthritis [4], and also for evaluating the stability and flexibility of treatments for rehabiliatation after injury [5], [6] and knee replacement surgery [4].

To date, the procedures which perform the best for multi-modal 3D-2D registration use a gradient-descent (GD) approach and are iterative in nature as explained in [7], [8]. However, a major limitation of such gradient-descent (GD) approaches is the limited range of initial displacements (typically less than $\pm 5\ mm$ translation and $\pm 5^{\circ}$ rotation)s for which the algorithms successfully converge to the global minimum of the similarity measure. For large initial displacements these algorithms tend to converge to a local minimum of the similarity measure which may provide a very poor alignment of the anatomical structures in the images. However the best of the GD approaches are able converge relatively quickly from small displacements and provide accurate results as described in [8].

Alternatively, the log-polar transform (LPT) has been used to estimate large scale and rotation changes between images [9]. However, this process always assume that the characteristics of the images are the same except for a rigid-body transform between them [10]. This assumption does not hold in multi-modal registration scenarios. Thus LPT based methods have had limited success for multi-modal registration [1], [11]. In this paper we will argue that, to extend the range of initial displacements using the LPT for multi-modal global registration, it is first necessary to establish a linear relationship between the pixels of the images to be registered.

There are a number of methods to provide this linear mapping such as using a joint intensity scatter plot (JISP) [12] or a polynomial intensity corrected sum of square difference (PIC-SSD) [13], [14] as the similarity measure. Polynomial based methods are used for non-rigid registration in which the coefficients are found in an iterative way. This is computationally expensive and can often lead to the algorithm becoming unstable. A numerical approximation based approach was proposed in [15] for combining the intensity and geometric transformation in which the higher order polynomial coefficients are estimated in an iterative process. Histogram-based techniques similar to mutual information have also been proposed to find the mutual information (MI) and global variation of the image intensities [16]. MI has a number of drawbacks including producing a non-convex and non-linear optimization with many local minima [15]. Since MI itself is a non-linear technique, it increases the non-linearity of the registration problem. More recently, the conditional mean based approach [17] was shown

978-1-5090-5785-6/16/$31.00

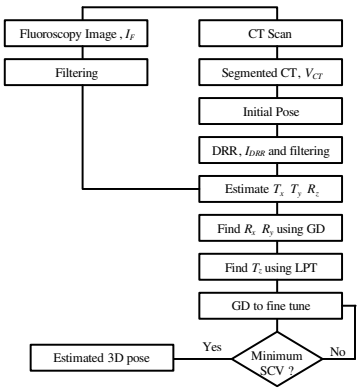

Fig. 1: The general flow chart of the proposed algorithm

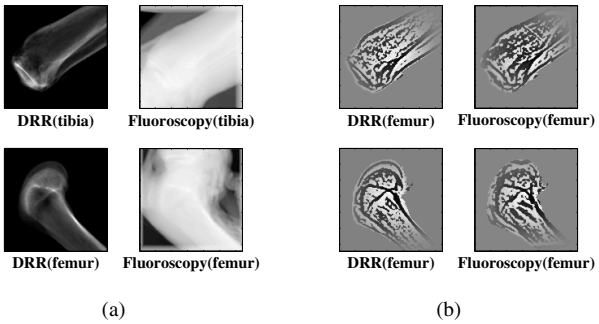

Fig. 2: (a) Input images (tibia and femur) used in this paper. Here, it is shown that I_F contains a large amount of extra soft tissue surrounding the bones and the resolution of the images is low. (b) Regenerated images for I_{DRR} and I_F using CPD after preprocessing. The effect of the soft tissue is minimized using this pre-processing method.

to be a better choice over mutual information (MI) as explained in [8].

In the application addressed in this paper, the goal of the registration algorithm is to define the 3D pose of the bones in a knee joint which best match the pose depicted in a 2D fluoroscopy projection of the same knee. We propose a new method to create a linear relationship between the image intensities by employing the CM of the joint probability distributions of the images. An LPT approach is then used to perform a global rigid-body 3D CT to 2D fluoroscopy registration. In this approach, the linear intensity mapping is used to regenerate the images which are used for the LPT based algorithm. Our experimental results show that the use of our proposed approach allows the registration of initial displacements of up to $\pm 20\ mm$ translation and , $\pm 20^\circ$ rotation while the state-of-the-art GD approach fails to converge from the same initial poses. An additional benefit of our approach is the reduced computational complexity, since four out of the six 3D rigid body transform parameters are effectively estimated using only two updates of the 3D CT volume.

II. The Proposed Methodology

In 3D-2D image registration, the 3D volume of the CT image V_{CT} is first converted into a 2D DRR, I_{DRR}, as described in [5], and then registered with the fluoroscopy image, I_F. In the application addressed in this paper, the goal of the registration algorithm is to calculate the six 3D rigid body transform parameters, $m = [T_x\ T_y\ T_z\ R_x\ R_y\ R_z]$, that define the 3D pose of the bones in a knee joint which best match the pose depicted in a 2D fluoroscopy projection of the same knee.

The general flow of the proposed LPT based 3D-2D registration process is shown in Fig. 1. The segmented CT data is first used to generate a DRR image I_{DRR} for each of the bones. Both the I_{DRR} and I_F images, are filtered using a LoG filter to enhance the image edges and remove the soft tissues surrounding the bones. Then, R_z is estimated using the method presented in [1] which makes use of the LPT in the spectral domain as proposed in [9]. After rectification of R_z, the masked registration approach proposed in [11] is used to estimate T_x and T_y. Estimating the values of T_x, T_y, and R_z as described here is very efficient since only a single iteration is required and V_{CT} is only updated two times. In the next stage, the estimation of R_x and R_y is performed using a GD approach to minimizse the sum of conditional variance (SCV) similarity measure as in [8].

A. Pre-processing

A novel approach to pre-processing the images is applied in this algorithm to successfully register real-world images where I_F is unsegmented and contains extra spectral information due to the presence of the soft-tissue of a normal knee joint as shown in Fig. 2(a). The images are thresholded to remove noise and highlight the most dominant edges. A Kaiser window is used to avoid the effects caused by the boundary of the image. Then the image is filtered using a Laplacian-of-Gaussian (LoG) filter in a multi-resolution frame-work (three stages). This filtering process is used to highlight the edges of the standard LoG filtered version images.

B. Estimate T_z

The out-of-plane translation T_z can be estimated by measuring the small amount of zoom that must be applied to the DRR to register it with the fluoroscopy. This change in scale is usually difficult to measure precisely as a large translation in the z-direction will result in only a very small scale change in the fluoroscopy frame [5]. To measure T_z using the LPT approach, a linear relationship between the pixel intensities of the two images is required.

For the target image I_{DRR} and the reference image I_F, the joint probability distribution is defined by

$$F(u, v) = P(I_{DRR} = u, I_F = v) \tag{1}$$

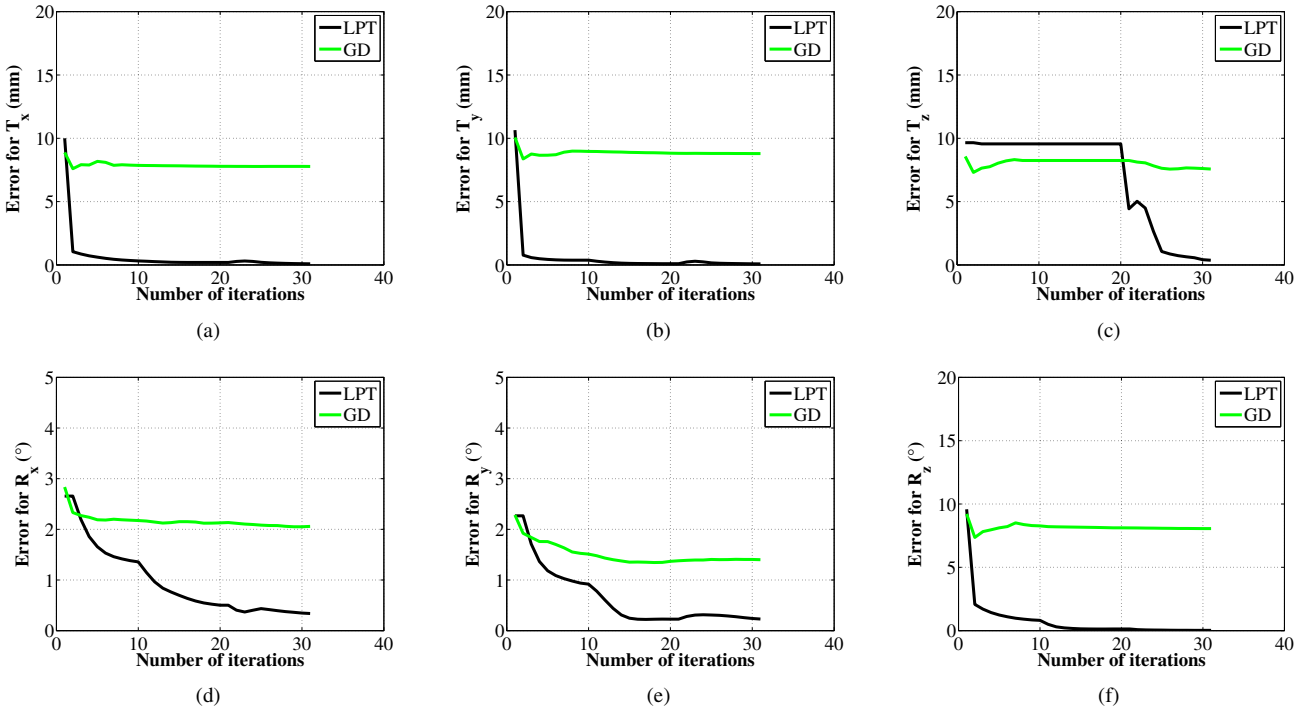

Fig. 3: The mean absolute registration errors at each iteration for the 3D rigid-body transform parameters, (a) T_x (b) T_y (c) T_z (d) R_x (e) R_y (f) R_z. The translation and rotations are measured in mm and ($^\circ$) respectively.

The contribution of unwanted pixels is removed from this joint distribution using the following

$$F' = \begin{cases} F(u,v) & \text{if } u > 0 \text{ and } v > 0 \\ F(u,v) & \text{if } u < 0 \text{ and } v < 0 \\ 0 & \text{otherwise} \end{cases}$$

The conditional mean for each value of v in I_F is given by

$$E(I_{DRR}|I_F = v) = \frac{\sum_u u \times F'(I_{DRR} = u|I_F = v)}{\sum_u F'(I_{DRR} = u|I_F = v)} \quad (2)$$

Given these conditional mean (CM) values, an estimate of I_F can be found which has pixel values that correspond linearly to the pixel values in I_{DRR}. This estimate is found by replacing the pixel values in I_F with the conditional mean of I_{DRR} for that value of I_F and is given by

$$\hat{I}_F = E(I_{DRR}|I_F = v) \qquad \text{when } I_F = v$$

Similarly, an estimate of I_{DRR} can be found which has pixel values that correspond linearly to the pixel values in I_F as follows:

$$\hat{I}_{DRR} = E(I_F|I_{DRR} = u) \qquad \text{when } I_{DRR} = u$$

The image $\hat{I}_F$ now has pixel values which correspond linearly to those in $\hat{I}_{DRR}$. However, the geometric transform that maps $\hat{I}_{DRR}$ to $\hat{I}_F$ will be the same as that which maps I_{DRR} to I_F. The spectral domain LPT approach is now applied on $\hat{I}_{DRR}$ and $\hat{I}_F$ instead of on I_{DRR} and I_F to estimate the scale change between the fluoroscopy image and the DRR as described in [1], [9].

The regenerated images, $\hat{I}_{DRR}$ and $\hat{I}_F$, with the linear relation between the pixel intensities are shown in Fig. 2(b). The LPT based approach provides a value that is close to the global minimum of T_Z but the value of this parameter will also be affected by the values of the other parameters. Hence, in the final stage, the GD approach from [8] is employed to fine-tune all six parameters simultaneously to find the global minimum of the similarity measure.

III. Experimental Results

The proposed LPT algorithm is compared with the approach which used only Gauss-Newton GD based optimization [8] to minimise the SCV similarity measure for 3D CT to 2D fluoroscopy registration. This GD approach was shown to provide the best performance among several competing approaches [18], [7] for the application addressed in this paper.

As in [8], the two algorithms were used to register a segmented CT volume of a tibia and a femur to synthetic fluoroscopy images that were generated using the unsegmented CT volume. The exact 3D position of the CT volume that was used to produce the fluoroscopy images is known and is used as the gold standard for measuring registration errors.

To test the robustness and accuracy of the algorithm, 100 randomly generated sets of 3D rigid body transforms were

TABLE I: Mean±SD of the registration errors for large initial displacements of the average values of the femur and the tibia bones. The translation and rotations are measured in mm and $(^\circ)$ respectively.

		Error	
	range	LPT	GD
T_x	±20	-0.06± 0.43	1.35±9.50
T_y	±20	-0.02±0.32	1.01±10.17
T_z	±20	-0.25±0.76	-0.22±8.96
R_x	±5	0.30±0.20	0.67±2.45
R_y	±5	-0.13±0.32	0.99±1.51
R_z	±20	-0.00±0.02	-0.22±10.05

applied to the segmented CT volumes of the bones. The range of initial values for the transform parameters were $\pm 20\ mm$ for T_x, T_y and T_z, $\pm 20^\circ$ for R_z and $\pm 5^\circ$ for R_x and R_y away from the true pose (gold standard position). Each algorithm was then used to register this data to the fluoroscopy images. The values of the transform parameters for the true registered position are all exactly zero, so the goal of the registration algorithms was to produce a final set of parameters that are as close to zero as possible. Hence, the registration error was calculated as the mean and standard deviation (SD) of the errors between the known and estimated parameters. Here the value of mean and SD indicate the bias and precision of the algorithm respectively.

For a better understanding of the robustness of the proposed algorithm, the mean absolute registration errors for each of the transform parameters at each iteration is shown in Fig.3. Here, the values of the transform parameters are taken as the average of the values that are measured for both the tibia and the femur bones. These results show that, in all cases, the proposed algorithm provides much better stability when compared to the existing GD approach. Note that four out of the six transform parameters ($T_x \quad T_y \quad T_z \quad R_z$) are estimated efficiently in a single iteration as shown in Fig.3(a) , Fig.3(b), Fig.3(c) and Fig.3(f). Notice also that the proposed regeneration process for the I_{DRR} and I_F images using their CM allows convergence to the global minimum from $\pm 20\ mm$ displacement for T_z as shown in Fig.3(c) and that the value of T_z is reduced very sharply from a large initial distance in a single iteration (after iteration 20) using the LPT based approach. Convergence from this large range of initial values of T_z has not been demonstrated for this application by any other single plane 2D-3D registration approach.

Table I shows the final mean±SD of the registration errors for each of the six rigid body parameters for the LPT and GD algorithms. The magnitude of mean±SD for the average of femoral-tibial pose error were less than $0.06 \pm 0.43\ mm$ for T_x and T_y and $0.30^\circ \pm 0.32^\circ$ for all rotations while the corresponding values for the GD algorithm were $1.35 \pm 10.17\ mm$ and $0.99^\circ \pm 10.05^\circ$. The average error in T_z for the LPT and GD approach was $0.25 \pm 0.76\ mm$ and $0.22 \pm 8.96\ mm$ respectively.

These results demonstrate that the LPT approach with the new regeneration process increases the range of initial poses for which the proposed algorithm can successfully register the DRR and fluoroscopy images while maintaining the overall accuracy of the algorithm.

IV. Conclusion

In this paper, we have presented a 3D-2D image registration technique for 3D kinematic analysis of knee joints. Reducing the non-linearity between the images using the joint probability distribution has allowed us to develop a robust 3D-2D registration algorithm that can produce accurate estimates for out-of-plane translation in a single iteration. Our experimental results show that the proposed approach can successfully register images with a range of initial displacements of up to $\pm 20\ mm$ and $\pm 20^\circ$. This range is significantly greater than any previously proposed single plane multi-modal 3D-2D registration algorithm. Since this algorithm extends the range of initial poses while maintaining the high accuracy of GD approaches, this approach can be used to automatically follow the position of the bones in a knee joint from one frame to the next in a fluoroscopy video.

V. Relation to Prior Work

The work presented is focused on developing a 3D-2D multi-modal image registration algorithm which uses the benefit of the LPT in the spectral domain to measure the very small amount of scale change using logarithm scale. The LPT based approaches are popular for mono-modal image registration [9] and the algorithm in [11] is used to calculate in-plane translations for the same modality. In [10], [1], it is mentioned that the LPT is not suitable for multi-modal registration because of the non-linear mapping between pixel intensities in the two images. There are a number of methods [12], [13], [14], [16], [17] to estimate a linear mapping. In the present work, the conditional means of the joint probability distribution are used to create the images with linear intensity mappings for a subsequent LPT-based multi-modal registration, which is a new approach for the application addressed in this paper.

References

[1] M. Akter, A. J. Lambert, M. R. Pickering, J. M. Scarvell, and P. N. Smith, "A 2D-3D Image Registration Algorithm using Log-Polar Transforms for Knee Kinematic Analysis," *IEEE conference on Digital Image Computing: Techniques and Applications*, pp. 1–8, Fremantle, Western Australia, 3-5th December, 2012.

[2] ——, "A non-invasive method for kinematic analysis of knee joints," *IEEE International Symposium on Signal Processing and Information Technology.*, pp. 386–391, Athens, Greece, 12-15th December 2013.

[3] ——, "Robust initialisation for single-plane 3D CT to 2D fluoroscopy image registration," *Computer Methods in Biomechanics and Biomedical Engineering: Imaging & Visualization*, no. ahead-of-print, pp. 1–25, 2014.

[4] P. Markelj, D. Tomazevic, B. Likar, and F. Pernus, "A review of 3D/2D registration methods for image-guided interventions," *Journal of Medical Image Analysis*, vol. 16(3), pp. 642 – 661, 2012.

[5] J. M. Scarvell, M. R. Pickering, and P. N. Smith, "New registration algorithm for determining 3D knee kinematics using CT and single-plane fluoroscopy with improved out-of-plane translation accuracy," *Journal of Orthopaedic Research*, vol. 28, pp. 334–340, 2010.

[6] M. Akter, A. J. Lambert, M. R. Pickering, J. M. Scarvell, and P. N. Smith, "3d ct to 2d low dose single-plane fluoroscopy registration algorithm for in-vivo knee motion analysis," pp. 5121–5124, 2014.

[7] F. Maes, D. Vandermeulen, and P. Suetens, "Comparative evaluation of multiresolution optimization strategies for multimodality image registration by maximization of mutual information," *Journal of Medical Image Analysis*, vol. 3, pp. 373–386, 1999.

[8] M. Pickering, A. Muhit, J. Scarvell, and P. Smith, "A new multi-modal similarity measure for fast gradient-based 2D-3D image registration," *IEEE conference on Engineering in Medicine and Biology System*, pp. 5821 –5824, Hilton Minneapolis, Minnesota, September 2-6, 2009.

[9] R. Gonzalez, "Robust Image Registration via Cepstral Analysis," *IEEE conference on Digital Image Computing: Techniques and Applications*, pp. 45 –50, dec. Queensland, Australia, 6-8 December, 2011.

[10] J. Orchard, "Efficient Least Squares Multimodal Registration With a Globally Exhaustive Alignment Search," *IEEE Transactions on Image Processing*, vol. 16(10), pp. 2526 –2534, 2007.

[11] D. Padfield, "Masked Object Registration in the Fourier Domain," *IEEE Transactions on Image Processing*, vol. 21(5), pp. 2706–2718, 2012.

[12] J. Orchard, "Multimodal image registration using floating regressors in the joint intensity scatter plot," *Journal of Medical Image Analysis*, vol. 12(4), pp. 385–396, 2008.

[13] W. Ou and C. Chefd'Hotel, "Polynomial intensity correction for multi-modal image registration," *IEEE International Symposium on Biomedical Imaging*, pp. 939–942, Boston, Massachusetts, USA, June 28 - July 1, 2009.

[14] A. Guimond, A. Roche, N. Ayache, and J. Meunier, "Three-dimensional multimodal brain warping using the Demons algorithm and adaptive intensity corrections," *IEEE Transactions on Medical Imaging*, vol. 20(1), pp. 58 –69, 2001.

[15] N. Chumchob and K. Chen, "Improved variational image registration model and a fast algorithm for its numerical approximation," *Journal of Numerical Methods Partial Differential Equations*, vol. 28, pp. 1966–1995, 2012.

[16] C. Guetter, C. Xu, F. Sauer, J. Hornegger, J. Duncan, and G. Gerig, "Learning Based Non-rigid Multi-modal Image Registration Using Kullback-Leibler Divergence Medical Image Computing and Computer-Assisted Intervention ," *Medical Image Computing and Computer Assisted Intervention Society*, vol. 3750, pp. 255–262, California, USA, October 26-29, 2005.

[17] M. R. Pickering, "A new similarity measure for multi-modal image registration," *IEEE International Conference on Image Processing*, pp. 2273 –2276, Brussels, Belgium, September 11-14, 2011.

[18] F. Wang and B. Vemuri, "Non-Rigid Multi-Modal Image Registration Using Cross-Cumulative Residual Entropy," *International Journal of Computer Vision*, vol. 74, pp. 201–215, 2007.

2nd International Conference on Electrical, Computer & Telecommunication Engineering (ICECTE)
8-10 December 2016, Rajshahi-6204, Bangladesh

Mitigation of Frequency Disturbance in Power Systems during Cyber-Attack

Mehedi Hassan[1,*], N. K. Roy[1], Md. Sahabuddin[2]
1Department of Electrical and Electronic Engineering, KUET, Khulna, Bangladesh
2Department of Electrical and Electronic Engineering, JUST, Jessore, Bangladesh

* E-mail: mhj24.jsr@gmail.com

***Abstract*—This article investigates the impact of cyber-attack on a power station in frequency disturbing aspects during sudden changes of load of the system and proposes a solution method to make it stable. Stable limit of the speed regulation for load frequency control (LFC) and integral controller gain for automatic generation control (AGC) is derived from their characteristic equations. Depending upon the nature of cyber-attack (positive biased or negative biased attack) simulations are performed to show the frequency deviations and oscillations of the power system. Finally a feedback LFC block with a three input switch is designed to remove these oscillations.**

***Index Terms*— Automatic Generation Control (AGC); cyber-attack; cyber-security; Load Frequency Control (LFC); smart grid**

I. Introduction

Starting from generation to consumer, modern power system is going to be smarter, intelligent and reliable that leads to motivate the concept of smart grid. With the incorporation of cyber space such as information and communications technology (ICT), advanced controllers are increasingly integrated into power systems that introduce potential threats in terms of cyber attacks [1]–[8].

The Stuxnet virus found recently is considered as one of the first pieces of malware targeting Supervisory Control and Data Acquisition (SCADA) systems that has alarmed many by its sophistication [9],[10]. Once a Programmable Logic Controller (PLC) of PC was successfully infected through USB, the worm would open communication links to the attacker's computers in other parts of the world. When the data for different parameters of a power system are sending from sensing section to control section using communication network, the attacker can access the confidential data and change the action of automatic controller that results in malfunctioning of the controller with changed set value, thereby causing an impact on the system stability whose output consequences cannot be neglected [11].

To ensure power system frequency stability, LFC plays a major role. LFC sets the prime mover speed according to the signal sensed from frequency sensor to compensate system frequency [12]. Prime mover speed varies with the governor speed regulator (R) which is identified as the vulnerable quantity of cyber attack in this paper. Malfunctioning of the governor speed regulator due to cyber-attack causes the speed of the prime mover out of control and results in making the system frequency unstable.

An AGC is nothing but the LFC system with the addition of a secondary loop (integral controller). It changes the governor speed set point by acting on the load reference setting and forces the final frequency deviation to zero [13]. To get satisfactory transient response, the integral controller gain K_I must be adjusted properly which is considered as another vulnerable threat of cyber attack.

To minimize frequency deviation and ensure system stability, cyber-attack impact should be analysed properly; which is the aim of this paper. A three input switch in the feedback LFC loop is designed to make the system stable during any unauthorized attack

The rest of the paper is organized as follows. Related work is given in Section II, speed regulation vulnerability on LFC in Section III, integral controller vulnerability on AGC in Section IV, mitigation of frequency disturbance in Section V and conclusions are given in Section VI.

II. Literature Survey

The authors of reference [14] introduced the impact of intelligent data integrity attacks into a power network voltage control loop. The impacts of data integrity and denial of service attacks are presented in [15], where authors have used a chemical reactor system. The impact of cyber-attack on FACTS is discussed in [16] and [17]. In [18], a numerical framework is developed to access into a 2-Area power network for ensuring safety. In [19], the authors analyzed the impact of cyber attack on wind farms power networks.

The authors of [20] have investigated the construction of false data injection, its impact on electricity market and way of defense against attack. Using graph technique, relationship between electrical and cyber grid is synthesized to analyze the impact of cyber attack in [21]. None of this work deeply analyzes the impact of cyber attack on power system frequency stability relating the vulnerable parameters of LFC and AGC, which is investigated in this paper.

III. Speed Regulation Vulnerability on LFC

For stability of the system frequency, speed regulation setting plays important role. Due to cyber-attack, the LFC may not be able to set the regulation properly and if this occurs then the system frequency will oscillate and make the system unstable.

978-1-5090-5785-6/16/$31.00 ©2016 IEEE

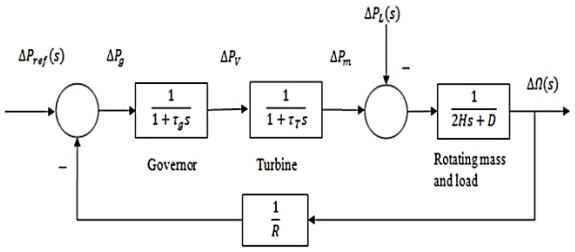

Fig. 1 LFC block diagram [12]

Stable limit of the speed regulation (R) can be derived from the characteristic equation of the LFC loop using Routh-Hurwitz array. The transfer function of the LFC is the following.

$$\frac{\Delta\Omega(s)}{-\Delta P_L(s)} = \frac{(1+\tau_g s)(1+\tau_T s)}{(2Hs+D)(1+\tau_g s)(1+\tau_T s)+ {}^{1}/_{R}} (1)[12]$$

This paper considers an isolated power station that has the following parameters with 250MW turbine output power at a nominal frequency of 50Hz and a sudden load change of 50MW [12].

TABLE I. POWER SYSTEM PARAMETERS

Parameter	Value
Turbine time constant (τ_T)	0.2 sec
Governor time constant (τ_g)	0.5 sec
Generator inertia constant (H)	5.0 sec
Variation of load for 1% change in frequency (D)	0.8

From equation (1) and Routh-Hurwitz array, the stability limit of speed regulation is determined as R> 0.0135 using the assumed data in Table I. Frequency deviation for different values of R is shown in Fig. 2. It is seen that when R=0.05, the system frequency deviation is in stable condition which signifies that for stable operation of this power station the set value of R (speed regulation) should be 0.05. Any fluctuation from this set value causes oscillations in the system. The deviation of the speed regulation from set value is due to cyber- attack on LFC (unauthorized access to the controller). In this work, the cyber-attack is classified into two types, one is positively biased attack and the other one is negatively biased attack depending on the affected value of speed regulation (R).

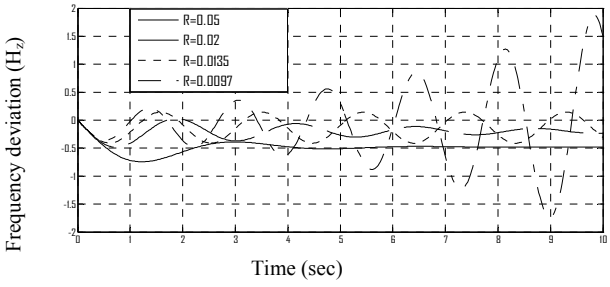

Fig. 2 Performance curve of LFC for different values of R

A. Result of positively biased attack

Positively biased attack is caused when the value of speed regulation increases due to cyber-attack. From Fig. 3, it is clear that in case of positive biased attack, the system frequency can be restored without disturbing the stability of the system. However, large deviation of system frequency may allow the governor taking more time to set the desired position for restoring that frequency.

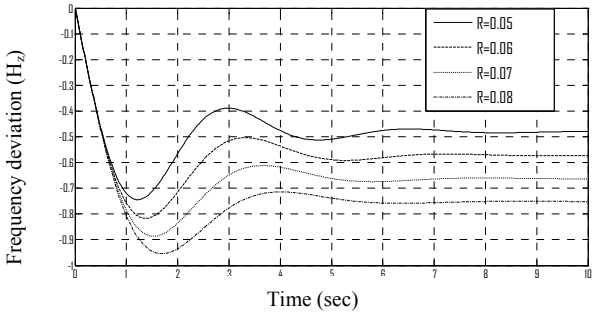

Fig. 3 Frequency deviation in case of positively biased attack.

B. Result of negatively biased attack

The decreasing of speed regulation value due to cyber-attack is termed as negative biased attack. Due to attack, if the speed regulation value falls below the stable condition (R>0.0135), the frequency deviation will be oscillating in nature as shown in Fig. 4 and governor fails to restore the system frequency.

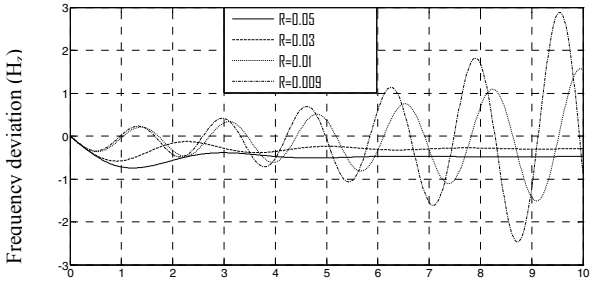

Fig. 4 Frequency deviation in case of negatively biased attack.

IV. INTEGRAL CONTROLLER VULNERABILITY ON AGC

In Fig. 5, various functional parts of AGC are shown. The addition of integral controller allows the governor to set appropriate point to increase the speed of turbine in case of sudden load rise and to restore the system frequency quicker than primary LFC loop. Any change of integral controller gain (K_I) due to unauthorized access to the AGC loop may cause oscillations in the system frequency.

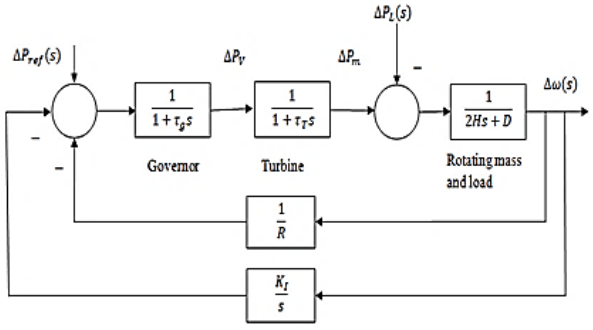

Fig. 5 Block diagram of AGC [12].

The appropriate value of K_I is determined using the characteristic equation of AGC loop. The closed loop transfer function of the control system shown in Fig. 5 is

$$\frac{\Delta\Omega(s)}{-\Delta P_L(s)} = \frac{(1+\tau_g s)(1+\tau_T s)}{(2Hs+D)(1+\tau_g s)(1+\tau_T s)+K_I+{}^{s}/_{R}} \quad (2)[12]$$

Fig. 6 shows the frequency deviation step response to determine the right value of K_I at which frequency deviation is zero and here it is seen that for K_I =7 frequency deviation goes to zero quickly which is the limiting value of K_I.

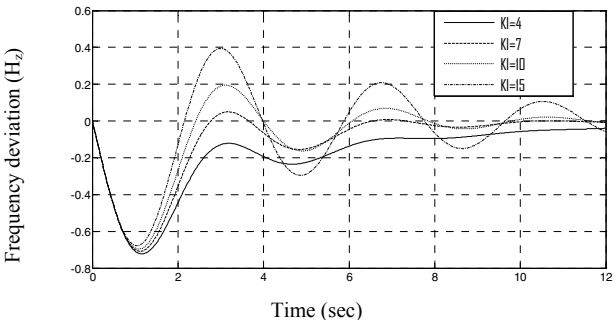

Fig. 6 Frequency deviation step response for different values of K_I.

A. Result of positively biased attack on AGC

Unauthorized access to AGC may lead to the system frequency deviation and sometimes make the deviation oscillating in nature. Moreover, the attack on AGC may cause unwanted delay to restore the frequency. Fig. 7 shows that more the positive biased attack is caused, more serious impact on the system's frequency is appeared.

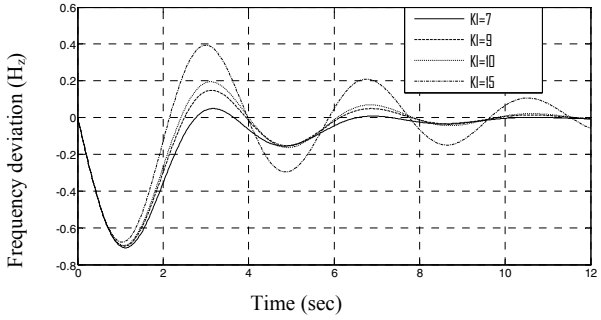

Fig. 7 Frequency deviation in case of positively biased attack.

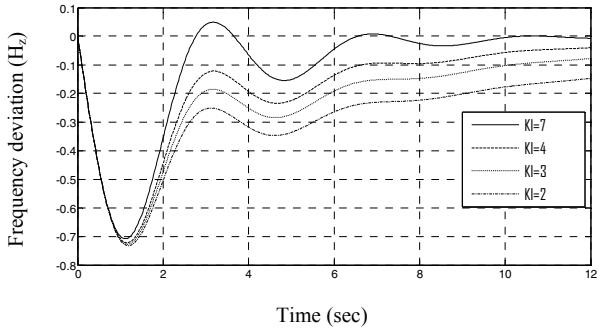

Fig. 8 Frequency deviation in case of negatively biased attack.

B. Result of negatively biased attack on AGC

A negative biased attack makes the integral controller ineffective so as to oppose the objective of the use of integral controller. It leads to the unwanted delay of restoring the system frequency. Negative biased attack on AGC is not so serious like positive one because it does not make the frequency deviation oscillating in nature that shown in Fig. 8.

V. Mitigation of Frequency Disturbance

The governor is capable of restoring the system frequency by increasing or decreasing the fuel supply if the frequency deviation is stable (sudden rising or falling). But when the frequency deviation is oscillating in nature, then governor will fail to restore system frequency.

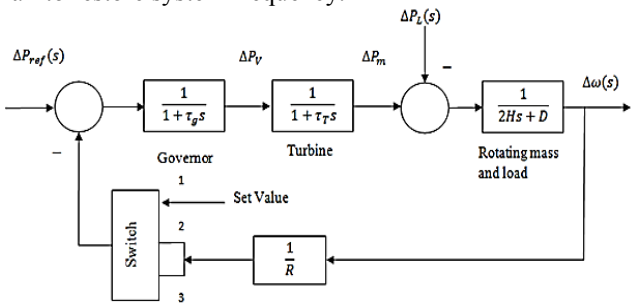

Fig. 9 LFC with a three input switch.

The frequency disturbance may collapse the whole system stability. A solution is proposed in Fig 9 to reduce the oscillating frequency deviation by connecting a three input switch in the feedback path of LFC block. The mathematical description of the switch is given below.

$$S.P = \begin{cases} U_1,\ U_2 \geq \text{threshold} \\ U_3,\ \text{else} \end{cases} \quad (3)$$

where, S.P = Switch passing terminal, U_1 = Input terminal 1, U_2 = Input terminal 2, U_3 = Input terminal 3.

The switch property is shown in Fig 10.

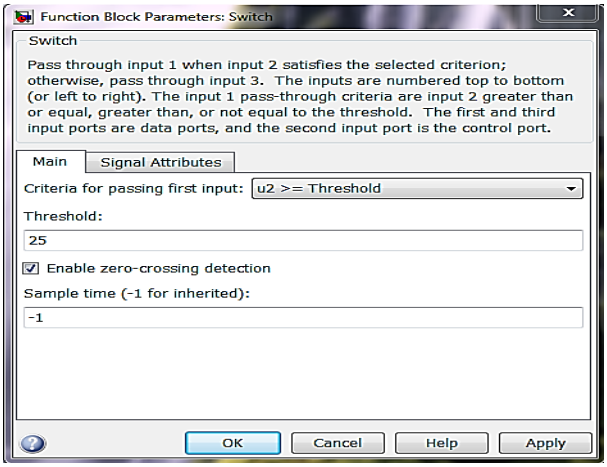

Fig. Fig. 10 Switch properties [10].

From Fig. 4 it is seen that as the value of R decreasing from 0.05(1/R=1/.05=20), the frequency deviation is moving towards instability. That is why, threshold value is chosen as (1/R=1/.04) 25 for injecting the set value after cyber-attack. The attack may be occurred due to unauthorized access to control system and also by injecting bad data to the system. When the value at input terminal 2 is greater than the threshold value that means R is less than 0.04 then the system tends to become unstable. At this moment the switch activates the input terminal 1 to forcely inject the set value to achive system stability. When the input value at terminal 2 is less than the threshold , it seems that the system is stable and the switch allows input 3. Fig. 11 clearly represents the deviation of frequency during cyber attack before and after using the switch. Due to sudden load increase, the frequency deviates without any switch during the attack. Whereas, using the proposed switch the deviation of frequency can be minimized significantly.

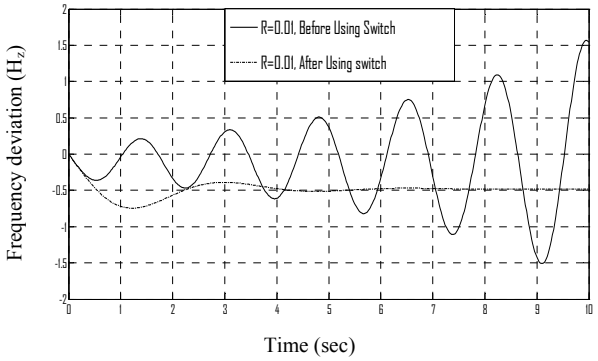

Fig. 11 Frequency deviation before and after using the switch

VI. CONCLUSION

To ensure the frequency stability of power systems, this paper analyses the impact of cyber-attack on LFC and AGC by considering their individual set value or stable limit parameter which can be a suitable source of unauthorized access. A positive biased attack on LFC causes the system frequency falls down; however, the system becomes stable quickly. On the other hand, a positive biased attack on AGC causes large oscillations on the system's frequency that makes the governor unable to set the appropriate point to restore its frequency. For AGC, negative biased attack is not as serious as like positive one but frequency deviates highly with large oscillations for an attack in LFC. A proper connection of a three input switch in the feedback loop of LFC and appropriate determination of its threshold value can efficiently mitigate the frequency disturbance during cyber hazard. Developing frameworks to identify false data injection (FDI) vulnerabilities and determining the way of self- healing process to ensure cyber security of the control system against unauthorized access is the future aim of this work.

REFERENCES

[1] Y. Mo, T.-H. Kim, K. Brancik, D. Dickinson, H. Lee, A. Perrig, and B. Sinopoli, "Cyber–physical security of a smart grid infrastructure," Proceedings of the IEEE, vol. 100, no. 1, pp. 195–209, 2012.

[2] J. Liu, Y. Xiao, S. Li, W. Liang, and C. P. Chen, "Cyber security and privacy issues in smart grids," IEEE Communications Surveys & Tutorials, vol. 14, no. 4, pp. 981–997, 2012.

[3] Y. Yan, Y. Qian, H. Sharif, and D. Tipper, "A survey on cyber security for smart grid communications," IEEE Communications Surveys & Tutorials, vol. 14, no. 4, pp. 998–1010, 2012.

[4] W. Wang and Z. Lu, "Cyber security in the smart grid: Survey and challenges," Computer Networks, vol. 57, no. 5, pp. 1344–1371, 2013.

[5] Y. Yamaguchi, A. Ogawa, A. Takeda, and S. Iwata, "Cyber security analysis of power networks by hypergraph cut algorithms," in Proc. IEEE International Conference on Smart Grid Communications (SmartGridComm), 2014, pp. 824–829.

[6] S. Mousavian, J. Valenzuela, and J. Wang, "A probabilistic risk mitigation model for cyber-attacks to PMU networks," IEEE Transactions on Power Systems, vol. 30, no. 1, pp. 156–165, 2015.

[7] H. Zhang, P. Cheng, L. Shi, and J. Chen, "Optimal DoS attack scheduling in wireless networked control system," IEEE Transactions on Control Systems Technology, vol. 24, no. 3, pp. 843–852, 2016.

[8] Z. Li, M. Shahidehpour, A. Alabdulwahab, and A. Abusorrah, "Bilevel model for analyzing coordinated cyber-physical attacks on power systems," IEEE Transactions on Smart Grid, vol. 7, no. 5, pp. 2260–2272, 2016.

[9] J. F. Keith Stouffer and K. Kent, "Guide to supervisory control and data acquisition (SCADA) and industrial control systems security—Recommendations of the national institute of standards and technology," Special Publication 800-82, Initial Public Draft Sept. 2006.

[10] Chen, T.M.,"Stuxnet, the real start of cyber warfare?", IEEE Network 2010.

[11] S. Sridhar, A. Hahn, and M. Govindarasu, "Cyber-physical system security for the electric power grid," Proc. IEEE, vol. 100, no. 1, pp.210–224, Jan. 2012.

[12] Hadi Saadat, Power System Analysis. McGraw-Hill, New York, 1999.

[13] Abdallah K. Farraj, Eman M. Hammad, Ashraf Al Daoud and Deepa Kundur, "A Game-Theoretic Control Approach to Mitigate Cyber Switching Attacks in Smart Grid Systems," IEEE International Conference on Smart Grid Communications, pp. 958-963, 2014.

[14] Sridhar and G.Manimaran, "Data integrity attacks and their impacts on scada control system," in Proc. IEEE Power Eng. Soc. General Meeting, Jul. 2010, pp. 1–6.

[15] Y.-L. Huang, A. A. Cardenas, S. Amin, Z.-S. Lin, H.-Y. Tsai, and S. Sastry, "Understanding the physical and economic consequences of attacks on control systems," Int. J. Critical Infrastructure Protection, vol. 2, no. 3, pp. 73–83, 2009.

[16] L. R. Philips, M. Baca, J. Hills, J. Margulies, B. Tejani, B. Richardson, and L. Weiland, "Analysis of Operations and Cyber Security Policies for a System of Cooperating Flexible Alternating Current Transmission System (FACTS) Devices," Sandia National Lab., Dec. 2005.

[17] S. Sridhar and G.Manimaran, "Data integrity attack and its impact on voltage control loop in power grid," in Proc. IEEE Power Eng. Soc.General Meeting, Jul. 2011, pp. 1–6.

[18] P.Mohajerin Esfahani, M. Vrakopoulou, K.Margellos, J. Lygeros, and G. Andersson, "Cyber attack in a two-area power system: Impact identification using reachability," in Proc. American Control Conference (ACC), 2010, Jul. 2010, pp. 962–967.

[19] J. Yan, C.-C. Liu, and M. Govindarasu, "Cyber intrusion of wind farm SCADA system and its impact analysis," in Proc. Power Systems Conference and Expo. (PSCE), Mar. 2011, pp. 1–6.

[20] Ruilong Deng ; Gaoxi Xiao ; Rongxing Lu ; Hao Liang ; Athanasios V. Vasilakos, "False Data Injection on State Estimation in Power Systems -Attacks, Impacts, and Defense: A Survey," IEEE Transactions on Industrial Informatics, Volume: PP, Issue: 99 , September 2016

[21] D. Kundur, X. Feng, S. Liu, T. Zourntos, and K. Butler-Purry, "Towards a framework for cyber attack impact analysis of the electric smart grid," in 2010 First IEEE International Conference on Smart Grid Communications (Smart Grid Comm), Oct. 2010, pp. 244–249.

Existing, Emerging and Future Solar Energy Applications: A Bangladesh Perspective

Md. Ashib Rahman* and Md. Rabiul Islam†
*†Department of Electrical and Electronic Engineering, Rajshahi University of Engineering & Technology, Rajshahi, Bangladesh
Email: m.rahman.bd@ieee.org and rabiulbd@hotmail.com

***Abstract*—This article presents the most up-to-date scenario of utilizing solar energy based applications across the country, Bangladesh. As, Bangladesh geographically situated in a region to harness solar energy most effectively, prospects and opportunities of solar energy based appliances are investigated here, along with the present energy situation of Bangladesh. Initiatives taken by Bangladesh government and non-government organizations to harness solar energy to fulfill the future energy demand of Bangladesh are also reviewed. Diverse utilization of solar energy in terms of off-grid or grid tied conditions are also presented.**

***Keywords*—Solar and renewable energy; Bangladesh.**

I. Introduction: Bangladesh

Located near the 'Bay of Bengal', Bangladesh is a developing country in South Asia, having estimated population of about 170 million with an area of 147,570 km^2 and geographical location is between 24°34′ to 26°38′ north latitude and 88°01′ to 92°42′ east longitude [1]. Being world's eighth most populous country with 1319/km^2 population density, Bangladesh is continuously craving for better energy status than other South Asian countries. Electricity accessing rate in Bangladesh is 76% of total households with 371 kWh per capita energy consumption where, national grid serves 62% (urban 91%, rural 51%) [2]. Solar energy technology is accessible to 11% of households (urban 3%, rural 15%) and continuous progress is going on in this field in Bangladesh [2]. Present 'Gross Domestic Product' (GDP) growth rate in Bangladesh, which signifies socio-economic progress of any country, is 7.05% and expected to be 7.40% in 2020 [3]. 0.23% of per capita GDP increasing happens if per capita energy consumption increases by 1% [4]. Therefore, Government of Bangladesh (GOB) put all the efforts to increase the generation and distribution of energy, either by public or private sectors to meet the long term energy demand.

II. Bangladesh Present Energy Scenario

Bangladesh expects to become a middle income country by 2021 and developed country by 2041. Energy is the inevitable benchmark of socioeconomic development of a country. Bangladesh's energy demand is increasing day by day and GOB is also taking different initiatives to meet this growing demand. The present energy scenario is best summarized in Table I, based on the data extracted on September, 2016.

III. Solar Energy Potential in Bangladesh

Majority of world's energy is extracted from fossil fuels, which leads to production of CO_2 – a greenhouse gas and vital factor for global warming. 1 kW of energy production from fossil fuels produces 1000g of CO_2 [6]. So, men are shifting focus from fossil fuel to renewable based energy harnessing. Abundance, flexibility, cleanliness make solar energy predominant in renewable energy realm. 3.8×10^{23} kW is the rate at which sun radiates light and 1.8×10^4 kW is captured by earth [1]. 1h of capturing energy at this rate can satisfy yearly worldwide energy demand [6]. The daily solar energy intercepted by Bangladesh is about 4-6.5 kWh/m^2, which is equivalent to 1018×10^{18} J of energy and country's present energy utilization is 1.12×10^{18} J, which is only 0.11% of total solar energy interception in Bangladesh [4].

IV. Planning and Initiatives Taken to Harness Solar Energy in Bangladesh

According to 'Renewable Energy Policy', Bangladesh has a plan to produce 10% (2000 MW) of total energy generated, from the renewable energy by 2020 and 20% (4000 MW) by the year 2030 [2]. Now, the total share of renewable energy is 2.97%. To improve and promote renewable energy based applications, in 2012, GOB approves 'Sustainable Renewable Energy Development Authority (SREDA) Act' and started its journey on May 22, 2014 [7]. Under this initiative '500 MW Solar Energy Plan' is undertaken. Table II represents the year wise targeted plan to utilize solar energy.

V. Solar Energy Based Projects

Solar energy can be efficiently harnessed by using basically, two technologies, such as: Concentrating solar power (CSP) or solar thermal technology and Photovoltaic cells (PV) technology. In Bangladesh, CSP technology has not been considered yet, in comparison with PV technology. Though, CSP technology has tremendous potential in Bangladesh. In this section, PV based projects are given priority for their diverse application in Bangladesh and later CSP technology is presented in a concise way.

A. Solar Home System (SHS)

SHS has proven to be the most viable and effective off-grid power system in feeding power to the rural households with the highest installation rate in the world. Started by 'Infrastructure

978-1-5090-5785-6/16/$31.00 ©2016 IEEE

TABLE I
BANGLADESH'S PRESENT ENERGY SCENARIO WITH THE ESTIMATED DATA [2], [5]

Installed capacity	12780 MW	Public Private	0.54% 0.46%
Generation capacity	Year	megawatt (MW)	
	Sept. 2016	12185	
	2020 [est.]	24000	
	2030 [est.]	40000	
Peak demand	Year	megawatt (MW)	Maximum demand Served 9,036 MW (June 30, 2016)
	Sept. 2016	11405	
	2020 [est.]	17304	
	2030 [est.]	33708	
No. of power plants	101 (March, 2016)		
No. of electricity customer	21.80 million		
Per capita energy consumption	371 kWh		
Access to electricity (percentage of total population)	76% (including off-grid renewable energy and captive)		

TABLE II
YEAR WISE SOLAR ENERGY GENERATION (TARGETED PLAN) [7]

Description	2015	2016	2017	2018	2019	2020	2021	Total (MW)
SHS (MW)	30	30	30	30	8	6	6	140
Solar mini/micro grid (MW)	6	6	32.25	0	0	0	0	44.25
Solar irrigation (MW)	30	30	162.5	0	0	0	0	222.5
Solar park (MW)	3	263	190	200	180	190	195	1221
Solar PV in govt. installations (MW)	2	3	3	3	3	3	3	20
Solar PV in private installations (MW)	4	4	4	4	4	4	4	28
Total (MW)	75	336	421.75	237	195	203	208	1675.8

Development Company Limited (IDCOL)' and designed by 'Prokaushali Sangsad Limited (PSL)', SHS program faced considerable boost after undertaking 'Rural Electrification and Renewable Energy Development Project (REREDP)' in 2003. Up to September 2016, 4.5 million SHSs (175 MW) have been installed and expected to install 6.0 million (220 MW) by 2017 [8]. Typically SHS operates at 12V dc and consists of one or more crystalline Si solar PV module (10-120 Wp with 20 years warranty), a rechargeable flooded lead acid battery (12V dc, 50-130 Ah, DOD 70% at discharge rate of 10h with 5 years of useful life), a charge controller (with low and high voltage detection, 90% efficiency) to control and protect against abnormal conditions among the modules, battery, loads etc. and the loads may be fluorescent lamps (5W, 45 lum/W), radio, TV, fan (15W) etc.

B. Solar School Boats

The non-profit organization 'Shidhulai Swanirvar Sangstha (SSS)' invented solar-powered floating schools at 'Chalan-beel' regions of northwestern Bangladesh in 2002, to help children's undisturbed education during flooding seasons, to give recharge facilities to their low cost solar lanterns and to improve socio-economic conditions of the families of that area [9]. The boats are 55 feet long and 11 feet wide fitting 30 children and a teacher. PV modules are installed on the boat rooftops, providing between 200 Wp - 2 kWp of power, depending on demand [9]. Up to 2013, SSS has 111 boats, bringing services to more than 90,000 families and 70,000 children [10], solar powered lights, internet linked laptops, 10 libraries, 20 schools, 7 adult education centers, 5 floating health clinics, employing more that 200 staff members including 61 teachers, 48 boat drivers and 300 volunteers [11].

C. Solar Battery Charging Station

In Bangladesh, three wheeler easy bikes carry 5 to 6 passengers and auto rickshaws carry 2 to 3 passengers. 4-5 batteries with capacity 12V, 60-120 Ah are used in easy bikes to operate 400-1000 W dc motor, which makes them able to run 100-150 km at a stretch. Solar based charging station will be a definite benefit and so, first ever solar power station is implemented at Rohitpur, Keraniganj, Dhaka on January, 2016. It was funded by 'Palli Bidyut Samity (PBS)' and contracted with RREL to have capacity of about 21.0 kWp, no. of vehicle charging capability is 15-20, cost was BDT 51.704 lakh, daily grid power saving expected is 50-60 kWh and tariff is BDT 50-60 for charging [12].

D. Solar PV Drinking Water

Due to saline intrusion, people of coastal areas of Bangladesh like Khulna, Bagerhat, Satkhira, depend on unsafe pond water, causing water borne diseases. 'Solar Energgy Development (SED)' program of 'GIZ Bangladesh' initiated installing solar PV for drinking water supply since 2020 [13]. Up to now SED helped to implement 139 solar water pumping units haivng capacity to supply around 2.18 million liters of drinking water daily [13]. Recently UN supported to bring 500 solar powered water purification units, manufactured by Swedish firm 'Watersprint' having capability to purify 600 liters of water per hour and run on PV generated 12V energy. In 2015, 'Watersprint' and the 'Yunus Centre' distributed 10 portable water purification systems throughout Bangladesh [14].

E. Solar Water Heater

After the approval of 'Renewable Energy Policy 2002', research works started going on to fabricate and install solar water heater (SWH) technology in different parts of Bangladesh. At first, 'Local Govt. Engineering Department (LGED)' installed three, 200 litre, vacuum tube SWHs and one, 200 litre, flat plate SWH at LGED offices [15]. In 2010, 'Rahimaafrooz Renewable Energy Ltd. (RREL)' implemented 12 SWHs all over the country. First time, SWH technology introduced on the rooftop of tanneries of Hazaribagh area of Dhaka, by 'United Nation Industrial Development Organization (UNIDO)', under the pilot project titled as 'Projects for Improvement of Tannery Sectors in Bangladesh' on March, 2016 [16]. 150000 m^3 of natural gas can be saved by supplying SWHs to 25 small, 20 medium and 6 large tanneries of Hazaribagh area on yearly basis [16]. The typical cost of 1000 litre system is around BDT 175000. SWH normally heats up water upto 60-80° and comprised of four parts - solar collector, insulated hot water tank, backup electric heater and mounting structure [17].

F. Solar Pipe Lights

GIZ Bangladesh's SED program introduced a project to use solar pipe lights to harness solar energy for industry applications. Under this project, this technology is applied to small ice cream and cottage factories and result shows that this initiative is helping industries to use natural lighting during daytime for 10-12h covering around 750-800 square feet factory area, illuminating equivalent light of 500W compact fluorescent light (CFL) bulb, saving monthly energy cost of around BDT 1800 and reducing almost 77 kgs of CO_2 [13].

G. Solar Powered Auto-rickshaw

To release burden on national grid from recharging batteries of auto-rickshaws, on May 2014, a solar powered rickshaw was designed jointly by JU and MIST, where four 12V solar panels (total 48V) were fixed on the hood of the rickshaw to charge the battery and run 300 W dc motor with a micro-controller to regulate the speed [18]. The was equipped with hydraulic brakes, claimed to run 11-12 hours with full charging of battery and total cost was BDT 70,000. On December 2014, another group from 'Khulna University of Science and Technology (KUET)', designed a rickshaw with an extra 12V, 6W dynamo. 4 pieces of 40W solar panels are used to recharge a 6V, 14Ah dry cell battery and 4 pieces of 12V, 30Ah super start dry charged batteries to run a 48V, 500W brushless dc motor [19].

H. Solar Mini-grid and Solar Park Projects

The first commercial 220V 100 kWp ac solar mini-grid with 40 kW diesel backup was installed in coastal island of Sandwip, Bangladesh on September, 2016. Assisted by PSL and installed by 'Energy Systems (Bangladesh)', the plant acquired 0.6 acre of land with 60kW PV modules, bi-directional inverters, total of 96 batteries with 12000 Ah capacity, at a cost of BDT 56.780 million [20]. Till March 2014, it has 457 consumers (average bill BDT 531/month), monthly production is 12110.64 kWh with monthly 8477.45 kg of CO_2 reduction [20]. So far IDCOL have approved 18 'Solar Mini-Grid Projects', among which 7 are operational while the rest are under construction [8] and targets to install 50 solar mini-grid by 2018. 4 ongoing projects conducted by BPDB, equivalent to 42 MW and 2 grid tied 1 MW and 0.5 MW projects and 2 solar 500 kW projects are under planning [5]. Moreover, 16 solar park projects equivalent to approximately 325 MW are under construction in different locations of the country.

I. Solar Irrigation Pumps

Agriculture is the largest employment sector in Bangladesh. As of 2016, it employs 47.5% of total labor force and comprises 16.33% of the GDP [21]. According to the 'Ministry of Agriculture', there are around 15.183 million families which depend on agriculture. Bangladesh has 8.505 million hectares cultivable land and total cropped area is 14.943 million hectares [21]. This large amount of land is cultivated by 1.61 million irrigation pumps of which, 1.34 millions are diesel run and 0.27 millions are run by electricity [22]. Diesel irrigation pumps use approximately 1 million tons/year of diesel fuel (USD 900 million), which is definitely a costly amount. Moreover, electricity run pumps utilize huge amount of power and create burden on national grid. In this regard, IDCOL has approved 459 solar irrigation pumps till now, of which 324 are already in operation and has a target to finance 1550 pumps by 2017 [8]. All the pumps have capacity ranging from 2.2 kW to 15 kW and PV power capacity is, from 1.68 kWp to 36.04 kWp.

J. Solar Rooftop System

First, rooftop solar power system was installed at the office of the Prime Minister on December 2009 by BPDB with capacity of 20.16 kWp. Till then BPDB installed in total of 43.37 kWp, 63.86 kWp, 97 kWp rooftop solar system in 2010-11, 2011-12, 2012-13 fiscal year respectively [5]. More than 223 kWp solar rooftop system have already been installed by BPDB and installation about 407 kWp solar PV system are

under planning and implementing stages. Govt. has a plan to generate about 30 MW of power from rooftop solar system. Govt. has installed the biggest solar power plant on the rooftop of the 11 storeyed 'Bureau of Statistics' building in Dhaka on July 6, 2013 with capacity 200 kWp, equivalent to 5000 bulbs of 40 W. Plant comprises of 670 panels of 300 W will meet around 40% of the electricity demand of the building.

K. Solar Powered Fish Pond Aeration

Fish farms contribute around 5% of GDP in Bangladesh [23] and around 1.3 million fish ponds aerate using diesel and electricity run pumps in Bangladesh [22]. Solar powered aerator devices concentrate solar energy using solar collectors and send them to the deep water of the pond. Thus the water gets heated and risen up, which results in equal distribution of oxygen in pond and fish can grow healthy.

L. Solar Street and Traffic Lighting System

BPDB is implementing a solar street lighting project in six city corporations of the country. It is designed to replace 1000 km of streetlights across the six city corporations at the expense of USD 37.03 million. Solar street light was first installed in Dhaka city as a pilot program at Arambagh area at the expense of BDT 39 million on September 2011, funded by Bangladesh Municipal Development Fund (BMDF). Under this program, 122 poles were set up in the area, each pole having two street lights of 250 W each. On June 2012, Dhaka South City Corporation installed 122 solar LED lights, 75 W each on 61 lamp post at the Notre Dame College area, along 1.8 km road at the expense of BDT 22.5 million. A project is also undergoing of solarizing 100 traffic intersection points in Dhaka city at a cost of BDT 265 million, funded by World Bank and will be implemented jointly by Rahimafrooz Ltd. and CMS traffic system of India.

M. Concentrated Solar Power (CSP) or Solar Thermal

For large scale power generation, CSP technology utilizes lenses or mirrors to concentrate large area solar radiation into small area to heat up stored water into 300°C-1000°C steam, which runs a turbine to produce electricity. CSP technology has huge prospect in Bangladesh, as direct normal irradiance (DNI) of 2000 kWh/m^2/year is considered as economical for CSP and Bangladesh gets 1500-2300 kWh/m^2/year, 4-6.5 kWh/m^2/day (5 kWh/m^2/day economical) [24]. CSP technology exists mainly in four forms: parabolic through, linear fresnel reflectors, parabolic dish and solar power tower. Among those, parabolic through type CSP technology is more experienced, matured and the cost with energy storage system is USD 9800/kW [24].

VI. Conclusion

This article is all about how solar energy can be harnessed and utilized in respect of Bangladesh. Here, a brief picture of present solar energy situation in Bangladesh is over-viewed. Present energy situation of Bangladesh, GOB's initiatives and planning regarding meeting the need of future power demand with either conventional or renewable energy is also presented. It is clear from the above sections that Bangladesh has a huge potential to harness solar energy, though in present situation, we could not utilize solar energy up to the mark. But, with the latest advancement and adoption of low cost, innovative solar cell technology, solar energy will be a definite solution for meeting the future energy demand of Bangladesh.

References

[1] H. S. Das, A. Yatim, C. W. Tan, and K. Y. Lau, "Proposition of a pv/tidal powered micro-hydro and diesel hybrid system: A southern bangladesh focus," *Renewable and Sustainable Energy Reviews*, vol. 53, pp. 1137 – 1148, 2016.

[2] Power division. Government of People's Republic of Bangladesh. Accessed: September 14, 2016. [Online]. Available: www.powerdivision.gov.bd/

[3] (2016) Bangladesh survey on power system master plan. Power Division. [Online]. Available: www.powerdivision.gov.bd/

[4] P. Halder, N. Paul, M. Joardder, and M. Sarker, "Energy scarcity and potential of renewable energy in bangladesh," *Renewable and Sustainable Energy Reviews*, vol. 51, pp. 1636 – 1649, 2015.

[5] Bangladesh power development board. Accessed: September 15, 2016. [Online]. Available: www.bpdb.gov.bd/

[6] W. X. Md. Rabiul Islam, Faz Rahman, *Advances in Solar Photovoltaic Power Plants*. Springer-Verlag Berlin Heidelberg: Springer, 2016.

[7] Sustainable and renewable energy development authority. Accessed: September 10, 2016. [Online]. Available: www.sreda.gov.bd/

[8] Infrastructure development company limited. Accessed: September 14, 2016. [Online]. Available: www.idcol.org

[9] Shidhulai swanirvar sangstha. Accessed: Sept. 10, 2016. [Online]. Available: www.shidhulai.org/

[10] E. Epstein. (2015, July 22) How one architect transformed education in flood-ravaged bangladesh through 'floating schools'. [Online]. Available: http://mashable.com/2015/07/21/bangladesh-floating-schools/

[11] A. Yee. (2013, June 30) Floating schools bring classrooms to stranded students. [Online]. Available: http://www.nytimes.com/2013/07/01/world/asia/floating-schools-in-bangladesh.html

[12] Solar power charging station at keraniganj. Accessed: Sept. 10, 2016. [Online]. Available: www.reb.gov.bd/

[13] (2016) Sustainable energy for development (sed) programme. [Online]. Available: www.giz.de/en/downloads/giz2014-en-sustainable-energy.pdf

[14] A. Rees. (2016, Feb. 25) Smart solar powered units providing clean water in bangladesh. [Online]. Available: https://en.reset.org/blog/smart-solar-powered-units-providing-clean-water-bangladesh-02252016

[15] Local government engineering department. Accessed: October 1, 2016. [Online]. Available: www.lged.gov.bd/

[16] M. Sadi. (2016, March 16) Solar solutions. [Online]. Available: http://archive.dhakatribune.com/feature/2016/mar/16/solar-solutions-0

[17] (2009) Application of renewable energy technologies in bangladesh. [Online]. Available: http://www.academia.edu/download/38979233/2009-RET-Full-Paper-Zaman.pdf

[18] K. U. Kamal. (2014, May 07) Solar powered rickshaw in bangladesh. [Online]. Available: https://hifipublic.com/2014/05/07/solar-powered-rickshaw-in-bangladesh/

[19] W. S. Mohammad, M. S. Hossain, M. N. Hasan, and M. T. I. Gias, "Design a solar and pedaling powered rickshaw."

[20] H. J. Khan and A. Huque. (2014, May 25) The first solar mini-grid service in bangladesh. [Online]. Available: http://progressbangladesh.com/the-first-solar-mini-grid-service-in-bangladesh/

[21] Ministry of agriculture. Government of People's Republic of Bangladesh. Accessed: September 14, 2016. [Online]. Available: http://www.moa.gov.bd/

[22] Dh infrastructure, economics and finance. Accessed: Sept. 10, 2016. [Online]. Available: https://dhinfrastructure.com/

[23] Field evaluation of a passive aeration system for aquaculture. Accessed: Sept. 10, 2016. [Online]. Available: https://poweringag.org/innovators/field-evaluation-passive-aeration-system-aquaculture

[24] A. Barua, S. Chakraborti, D. Paul, and P. Das, "Analysis of concentrated solar power technologies, feasibility, selection and promotional strategy for bangladesh," *Journal of Mechanical Engineering*, vol. 44, no. 2, pp. 112 – 116, 2015.

Electromagnetic Field Radiation Measurement for Occupational Settings using Three Axis Tesla Meter

M. A. Raquib and M. S. Hossain
Department of Electrical and Electronic Engineering
Rajshahi University of Engineering & Technology
Rajshahi-6204, Bangladesh
Raquib966.rpi@gmail.com; engg.selim@gmail.com

***Abstract*— This paper presents an assessment of exposure to extremely low power frequency (ELF) magnetic field in general and occupational settings using three-axis Tesla meter. The measurements are performed at the exposure level of PF magnetic field in some typical places where general public and occupational workers are subjected to the fields. In the occupational settings, high value of current radiates strong magnetic field that might exceed the safe limit of creating possible adverse health effects if proper shielding is not made. Radiated magnetic field from welding machines are measured and compared with international guidelines. In order to obtain space distribution, the work place is divided into meshes and fields are measured in the grid points. The measurements are performed using a single axis and three axis EMF meter (Gauss meter). Readings are taken in three axes to obtain a mean squared value for single axis EMF meter. The three axis EMF meter can directly measure the radiated field value without any calculation.**

Keywords— Radiated Field; Occupational exposure measurement; Three axis EMF meter.

I. INTRODUCTION

The use of electricity in our everyday life is growing in such a way that we cannot think to live without using it even for a moment. Whenever electricity flows, it produces electric and magnetic fields in the proximity of the supply line or near the appliances that utilize electricity. The magnetic fields from man-made sources generally have higher intensities than the naturally occurring fields. In the home and public places, magnetic flux densities that range from 0.03μT to 30 μT are produced around household appliances, and up to 35 μT near transmission lines, depending on the current carried and the distance from the line [1]. If the magnitude of the induced current exceeds certain threshold value it may cause stimulation to the excitable cells and may cause adverse health effects or radiation hazard [2-4]. The Occupational exposure to magnetic fields is mainly encountered in industrial processes involving high electric current equipment, in certain new technologies for energy production and storage, and in specialized research facilities and the exposure level is in general higher. Around various types of welding machines, furnaces, and induction heaters, the magnetic flux densities at the operator location range from about 1 μT to more than 10 mT [4-6].

The magnetic field radiation measurement for general and occupational setting is addressed in [7] using single axis Tesla meter. The problem of using single axis Tesla meter is to find out the exact mean square magnetic field. To overcome the aforementioned difficulties, the electromagnetic field radiation is measured using 3-axis Tesla meter and finally compared with the calculated and International Commission of Non-ionizing Radiation protection (ICNIRP) guidelines. The value of current density also obtained from the measured value to estimate biological effect for electromagnetic field radiation. At the center of the body, induced current is negligible and is maximum at the periphery of the body.

II. METHODOLOGY

The basic vector quantities describing a magnetic field are field strength, H (A/m) and magnetic flux density, B (T or G). These quantities are related through $B = \mu H$, where μ is the magnetic permeability of the medium. B is measured in this paper using 3-axis Tesla meter which is capable of measuring B in mG and μT. The measured values are used to calculate the magnetically induced current in the human body using very simple model. The calculated or predicted quantities are compared with the guidelines suggested by the ICNIRP [6]. Fig.1 shows the block diagram of the proposed study.

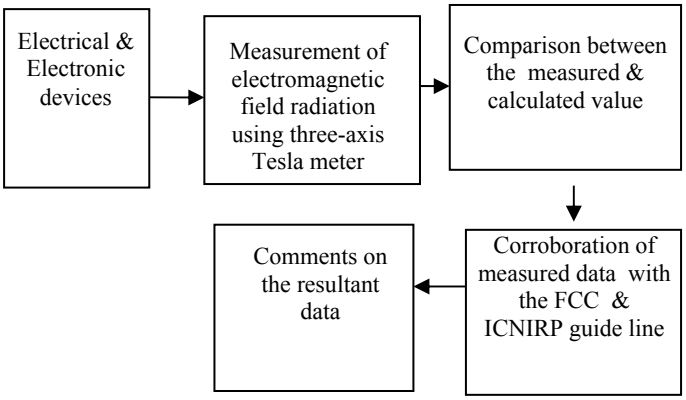

Fig.1. Block diagram of the proposed measurement system

978-1-5090-5785-6/16/$31.00 ©2016 IEEE

Measurement of a linearly polarized magnetic field consists of recording the maximum magnetic flux density in three orthogonal directions. Three axis Gauss meter can measure and calculate the B values automatically. Fig. 2 shows the experimental setup to measure the electromagnetic field radiation from a welding spot.

The voltages and currents induced directly into human body are of great concern if they are high enough to cause health effects. If the conductive object is grounded, the induced current that travels through the object to the ground is called the short-circuit or body current $\mathbf{I_{sc}}$ that can be fairly approximated using the following formula when measured in micro-Amperes (μA) [7]

$$I_{SC} = 5.4h^2E \quad (1)$$

Fig.2: Measurement setup for welding spot.

Where h is the height in meter and E is in kV/m. The validity of equation (1) was tested in [5] by actual measurement.

Magnetically induced body current can be estimated by assuming homogeneous and isotropic conductivity in human body. Faradays law can be applied to calculate the induced electric field around the head. The integral form of the Faradays law is [7];

$$\oint_C \vec{E} \bullet d\vec{l} = -\frac{\partial}{\partial t}\oint_\Omega \vec{B} \bullet d\vec{S} \quad (2)$$

where C is path of integration around head and Ω is the head cross-section. For the time harmonic field with angular frequency ω, the magnitude of induced electric field E can be derived by equation 3 as

$$E_{ind} = \pi RfB \quad (3)$$

and the corresponding induced current density

$$J_{ind} = \sigma E_{ind} \quad (4)$$

Where **R** is the mean radius of head and **σ** is the conductivity of head tissue. It is seen from the equation that the current density is directly proportional to **f**, **B** and **R**. This implies that at the center of the body, induced current is negligible and is maximum at the periphery of the body. The power loss in the periphery of the body due to this body current could also be calculated using as $\frac{1}{2}\sigma|E|^2$ Watt/m^2.

III. Results and Discussion

Using 3-axis Tesla meter, the radiated magnetic flux densities are measured at the welding spot. Fig. 3 shows the measured result of **B** at a welding spot for different distances from welding spot to welder. The measured results are compared with the calculated to check the validation of the proposed measurement system. One can observed from Fig.3 that the both results are nearly same for the different distance variations.

As it is expected, **B** is an increasing function of current. Fig. 4 depicts the current density for different current setting of welding machine. One can observed from the Fig. 4 that the current density is higher at 250 Amp compared to 225 Amp for the same distances from the welding spot.

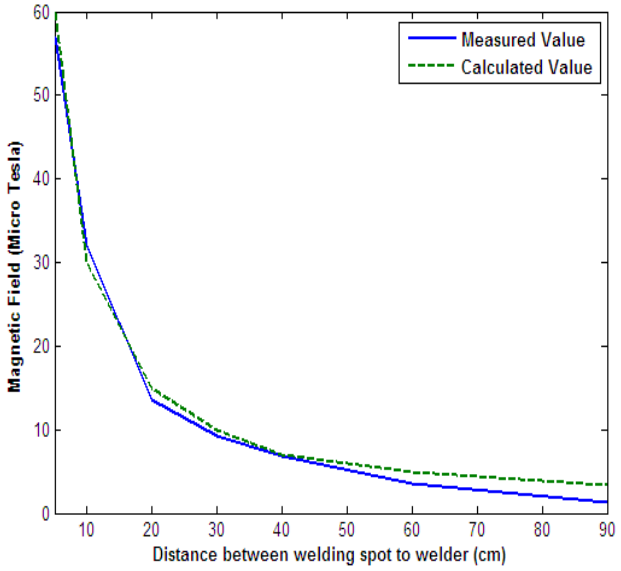

Fig. 3: Comparison between measured and calculated value from a welding spot.

TABLE I. ICNIRP GUIDELINES OF ELF EXPOSURE [6]

		Public	Occupational
Basic Restriction	J(mA/m^2)	2.00	10.00
Reference Level	E(kV/m)	5.00	10.00
	B (μT)	100.00	500.00

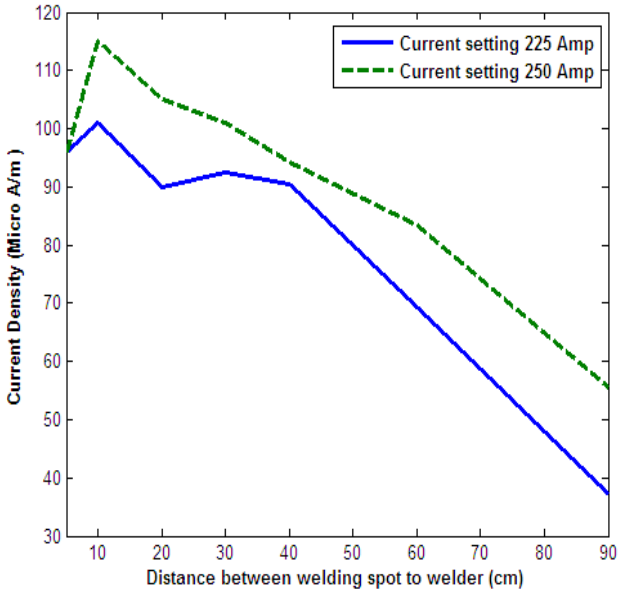

Fig. 4: Current Density for different current setting of a welding machine.

The ICNIRP guidelines are shown in Table I. The magnetic field and current density for public and occupational settings are different which is mentioned in the guidelines. The measurement of magnetic field radiation for occupational settings is highly important and sometimes occupational works are done publicly.

The results obtained using 3-axis Tesla meter are compared with the results presented in [7]. The magnetic field B at 30cm distance from welding spot to welder for 250 Amp current setting is around 20 µT in [7]. For the same scenario the presented field value B is around 10 µT which is near equal to calculated value.

IV. CONCLUSION

The measured results of power frequency radiated magnetic field have been presented in this paper for welding spot. These measurements are necessary to estimate the magnitude of the induced electric and magnetic fields in the human body and that are required to assess their contributions to the possible adverse health effects. This types of measurements are made worldwide to insure the ICNIRP guidelines for safe use of electrical accessories. The guidelines of ELF exposure as suggested by ICNIRP are shown in Table I. It is expected that the preliminary results presented in this paper would help visualizing the present scenario of the magnetic field radiation in the occupational welding spot. This research is conducted in specific and limited situations, so that more systematic analysis and Precise measurements are necessary to formulate an empirical relationship to estimate the exposure level considering other variables such as operating conditions, measurement position, and frequency band, as well as actual exposure data in different occupational settings. It is observed that the presented results and analysis is more accurate than the existing literature, which used single axis Tesla meter.

TABLE II. RADIATED MAGNETIC FIELD AT WELDING SPOT

Current settings=225 (Amp) Line current=12amp average at welding condition				**Current settings=250 (Amp) Line current=18 amp average at welding condition**			
Distances between welding spot and welder (cm)	Measuring value using Three axis Tesla meter (µT)	Calculated value (µT)	Current density J (µA/m)	Distances between welding spot and welder (cm)	Measuring value using Three axis Tesla meter (µT)	Calculated value (µT)	Current density J (µA/m)
5	57	60	96	5	58	72	96
10	32	30	101	10	34	36	115
20	13.5	15	89.91	20	21.41	18	105.1
30	9.3	10	92.5	30	10	12	101.11
40	6.78	7	90.5	40	7.0	9.0	94.3
60	3.48	5	69.4	60	4.1	6.0	83.3
90	1.24	3.33	37.2	90	1.81	4.0	55.4

Table.II shows the measurement data from a welding spot. It is observed from the Table that the EMFs are strongest near the welding spot. This means we are exposed to stronger EMFs when standing close to welding spot and exposed to weaker fields as move away. The 5cm distance is considered as minimum distance from the welding spot to welder. Usually the current carrying conductor is attached to the limb of the welder. The effect of electromagnetic field radiation on biological tissue also to be considered in this case.

REFERENCES

[1] A. Barchanski, M. Clemens, H. D. Gersem and T. Weiland, "Efficient Calculation of Current Densities in The Human Body Induced By Arbitrarily Shaped, Low-Frequency Magnetic Field Sources", *Journal of Computational Physics*, Volume 214, Issue 1 pp. 81-95, 2006.

[2] P. Gajšek, P. Ravazzani, J. Grellier, T. Samaras, J. Bakos and G. Thuróczy, "Review of Studies Concerning Electromagnetic Field (EMF) Exposure Assessment in Europe: Low Frequency Fields (50 Hz–100 kHz)", *International Journal of Environmental Research and Public Health*,13 (875), pp.1-4,2016.

[3] I.Vilcane, T. Koppel, J. Bartusauskis, V. Urbane, J. Ievins, H. Kalkis, and Z. Roja, "Electromagnetic Fields Exposure to Head, Torso And Limbs in Office Workplaces", *Agronomy Research* 14(Z), xxx–ccc, 2016.

[4] P. Slottje, L. J. Schouten, R.A. Goldbohm, H. Kromhout and R. Vermeulen, "Occupational Extremely Low-Frequency Magnetic Field Exposure and Selected Cancer Outcomes in a Prospective Dutch Cohort", *springer*, Volume 25, Issue 2, pp 203–214, Feb. 2014.

[5] M. Bereta, L. Janoušek, M. Cifra and K. Červinková, "Low Frequency Electromagnetic Field Effects On Ultra-Weak Photon Emission From Yeast Cells," *IEEE conference ELEKTRO*, pp. 478-481, May 16-18, 2016.

[6] ICNIRP Evaluation of Carcinogenic Risks To Human From Exposures To Electric And Magnetic Fields" http://www.icnirp.org/ 2001.

[7] M. S. Hossain and M. R. Amin, "Power Frequency Magnetic Field Exposure Assessmentin General and Occupational Settings: A Case Study",*International Journal of Research in IT, Management and Engineering*, Vol. 1, Issu.3, ISSN: 2249- 1619, pp. 54-67, 2012.

Improvement of antenna performance using Stacked Microstrip Patch Antenna

Md. Bappy Hossain
ETE Department
Rajshahi University of Engineering & Technology, Rajshshi
(bappyeteruet@gmail.com)

Sham Datto
Lecturer, Department of ETE
Rajshahi University of Engineering & Technology, Rajshshi
(shamdatto@ruet.ac.bd)

***Abstract*—A rectangular stacked microstrip antenna has been designed in this paper to increase the performance of the conventional microstrip antenna. The antenna performances such as bandwidth, gain, directivity and return loss of the conventional and stacked antenna have been examined using coaxial probe feed and transmission line feed techniques. A comparative study has been also made between these two techniques. The antenna has been designed using ansoft HFSS software to operate in the C-band having resonant frequency 5.3 GHz.**

Keywords— Microstrip patch antenna, stacked Antenna, return loss, bandwidth, gain, ansoft HFSS.

I. INTRODUCTION

The demand of microstrip patch antenna is increasing day by day with the rapid growth of wireless communications because of their advantages such as low-profile, small size, light weight, simple and inexpensive to manufacture using modern printed-circuit technology, mechanically robust, ease of integration with feed networks etc. It is used in high-performance aircraft, spacecraft, satellite and missile applications, mobile radio and wireless communications. However, conventional microstrip antennas suffer from many operational disadvantages such as low efficiency, low power, poor polarization purity, spurious feed radiation, low gain and very narrow frequency bandwidth.

Many efforts have been taken to overcome the drawbacks of the microstrip patch antenna. These efforts include the use of low dielectric substrate, the use of various impedance matching and feeding techniques, increase the substrate thickness, the use of multiple resonators, the use of slot antenna geometry and stacking.

II. THE MICROSTRIP PATCH ANTENNA

Microstrip patch antenna consists of a metal strip called the radiating element on a dielectric substrate covered by a ground plane on the other side. The dielectric substrate retains most of the power because the shielding ground plane is spaced a few substrate thicknesses away. The radiating patch may be square, rectangular, thin strip, circular, elliptical, triangular or any other configuration.

There are many configurations that can be used to feed the microstrip antennas. The four most popular are the microstrip line, coaxial probe, aperture coupling, and proximity coupling.

The microstrip line feed is a conducting strip, usually of much smaller width compare to the patch. It is easy to fabricate, simple to match by controlling the inset position and rather simple to model.

In coaxial line feeds the inner conductor of the coax is attached to the radiation patch while the outer conductor is connected to the ground plane are also widely used. The coaxial probe feed is also easy to fabricate and match and it has low spurious radiation. However it is more difficult to model.

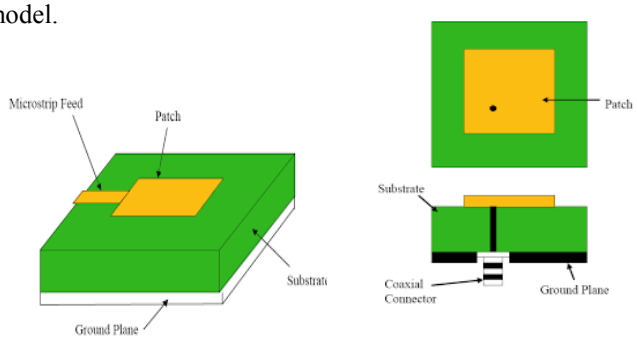

(a) (b)

Fig. 1. (a) Microstrip line feed, (b) Coaxial probe feed.

III. THE STACKED PATCH ANTENNA

In this antenna two patches are vertically stacked and builted like a multilayer printed circuit board. It is also called a dual patch antenna or multilayer antenna. The top and bottom patches are referred to as the radiating patch and the feeding patch respectively. The radiating patch is excited via an electromagnetic coupling from the feeding patch.

There are three ways to connect to this antenna as given below:

- Connecting to both patches individually (dual band)
- Connecting to the upper patch only: series fed (dual band)

978-1-5090-5785-6/16/$31.00 ©2016 IEEE

- Connecting to the lower patch only: shunt fed (wide band)

Fig 2. Shows the three connection.

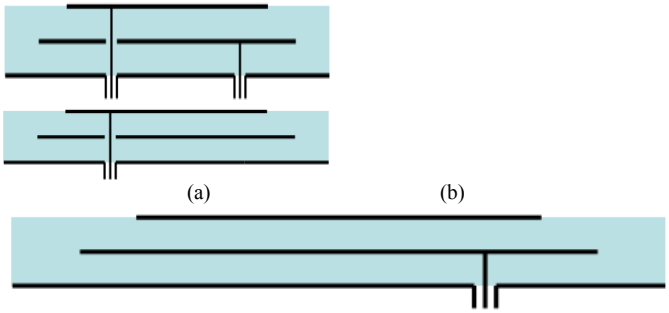

Fig. 2. (a) Dual feed, (b) Series feed, (c) Shunt feed.

IV. ANTENNA DESIGN

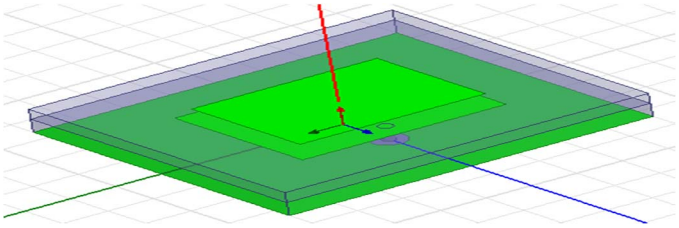

Fig. 3. Stacked microstrip antenna with coaxial probe feed.

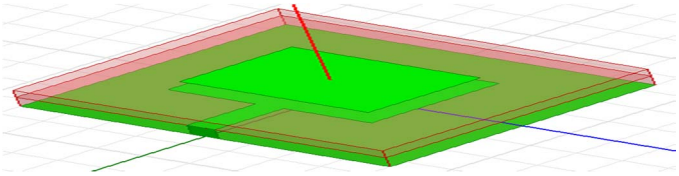

Fig. 4. Stacked microstrip antenna with microstrip line feed.

The design parameters for the two proposed antennas are given below-

1. Antenna with coaxial probe feed:
   - Ground : L=34 mm, W=40 mm
   - Lower substrate : (RT/Duroid, Relative permittivity = 2.2) L=34 mm, W=40 mm, H(Height)=2.9 mm
   - Upper substrate : (Foam, Relative permittivity=1.07) L=34 mm, W=40 mm, H=2.2 mm
   - Feeding patch : L=17 mm, W=22.4 mm
   - Radiating patch : L=14.4 mm, W=20.4 mm
   - Coaxial feed position (x,y)= (0 mm, 6 mm)
     - Inner cylinder : (pec) r=0.7 mm, H=7.9 mm
     - Outer cylinder : (vaccum) r=1.8 mm, H=5mm

2. Antenna with microstrip line feed:

The size of the ground, lower substrate and upper substrate is same.

- Feeding patch : L=16.4 mm, W=22 mm
- Radiating patch : L= 14.4 mm, W=20.4 mm
- Microstrip line : L=8.8 mm, W=3mm
- Port : W=3 mm, H=2.9 mm

V. ANTENNA DESIGN EQUATION

- The width of the patch antenna can be calculated as

$$w = \frac{C}{2f_r} \times \sqrt{\frac{2}{\varepsilon_r + 1}}$$

Where, c = velocity of light.
= 3×10 m/sec.
ε_r = Dielectric constant of the substrate.
f_r = Resonant frequency.

- The effective dielectric constant is

$$\varepsilon_{eff} = \frac{\varepsilon_r + 1}{2} + \frac{\varepsilon_r - 1}{2\sqrt{1 + 12\frac{h}{w}}}$$

Where, h = Height or thickness of the dielectric.
w = Width of the patch.

- The length extension ΔL on each side is

$$\Delta L = 0.41h \times \frac{(\varepsilon_{eff} + 0.3)}{(\varepsilon_{eff} - 0.258)} \times \frac{(\frac{w}{h} + 0.264)}{(\frac{w}{h} + 0.8)}$$

- Effective length of the patch is

$$L_{eff} = \frac{C}{2f_r\sqrt{\varepsilon_{eff}}}$$

- The actual length of the patch is

$$L = L_{eff} - 2\Delta L$$

- The ground plane dimensions would be given as

$L_g = 6h + L$
$W_g = 6h + w$

VI. RESULTS AND DISCUSSION

The performance of our antenna has been observed in terms of the return loss, directivity, gain, impedance bandwidth and impedance matching. The optimization is gained by using the method of design of variables.

A. Return loss and Bandwidth

Fig 5. And Fig 6. Illustrates the return loss plot of the stacked antenna with coaxial probe feed and microstrip line feed respectively. It has been observed that the stacked antennas resonate exactly at the frequency of operation (5.3

GHz) as compared to the single patch antennas. The return loss and bandwidth have been increased by both techniques but the increment is higher for the coaxial probe feed.

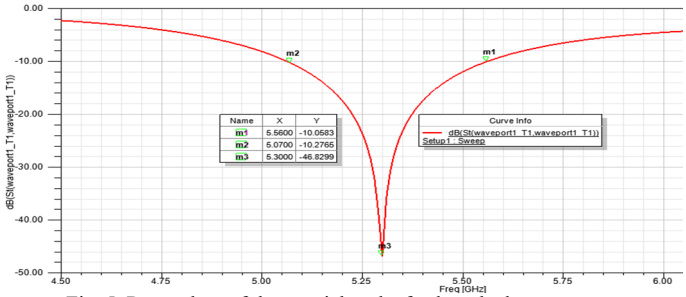

Fig. 5. Return loss of the coaxial probe feed stacked antenna.

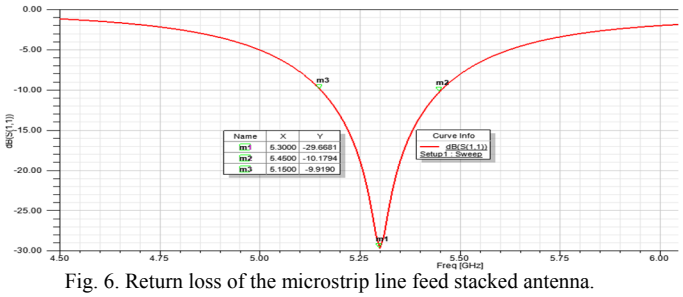

Fig. 6. Return loss of the microstrip line feed stacked antenna.

B. Gain

The gain plot of the two antennas has been given in Fig 7. and Fig 8. It has been observed that the gain of the microstrip line feed antenna is higher.

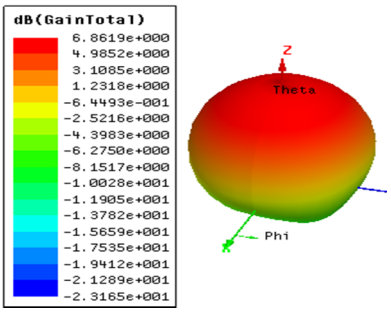

Fig. 7. Gain of the coaxial probe feed stacked antenna.

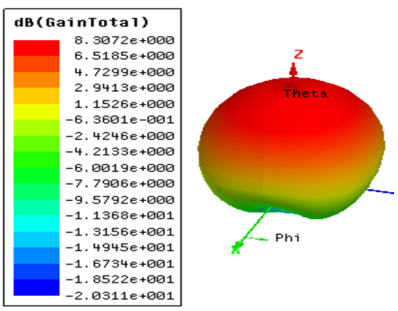

Fig. 8. Gain of the microstrip line feed stacked antenna.

C. Radiation pattern

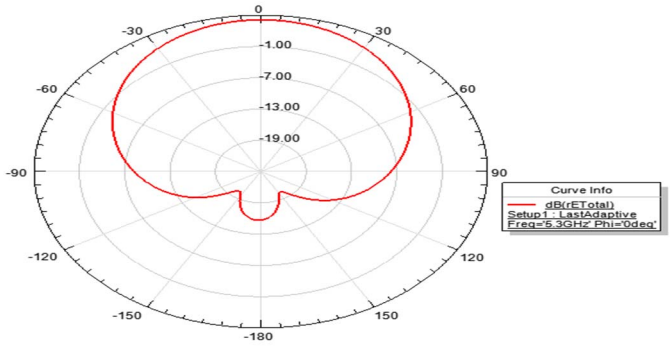

Fig. 9. Radiation pattern of the coaxial probe feed stacked antenna.

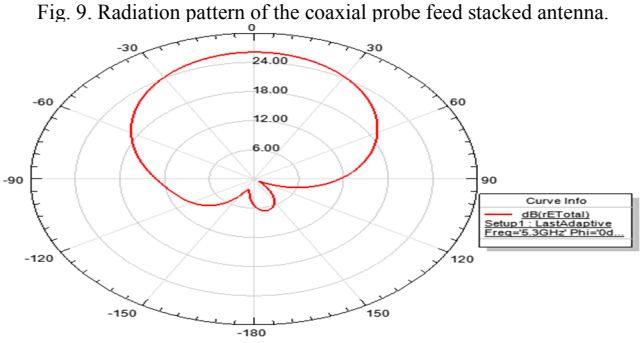

Fig. 10. Radiation pattern of the microstrip line feed stacked antenna.

D. Smith chart

The Smith chart shows that the coaxial probe feed stacked antenna has a better impedance match than the micristrip line feed antenna.

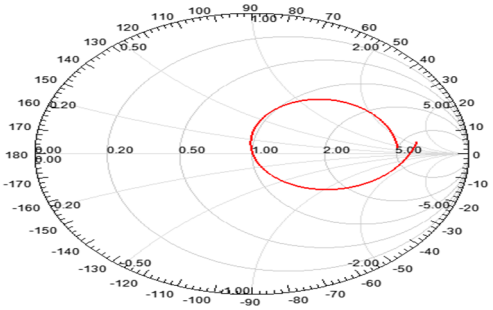

Fig. 11. Smith chart of the probe feed antenna shows a good impedance match at 5.3 GHz.

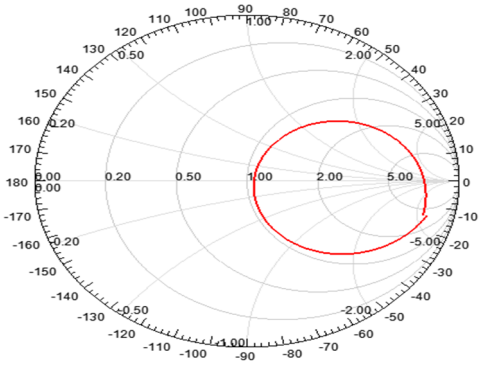

Fig. 12. Smith chart of the microstrip line feed antenna shows a less impedance match at 5.3 GHz

E. VSWR

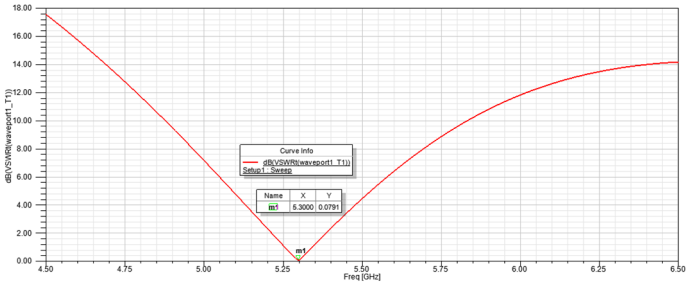

Fig. 13. VSWR plot coaxial probe feed antenna showing resonant frequency of 5.3 GHz.

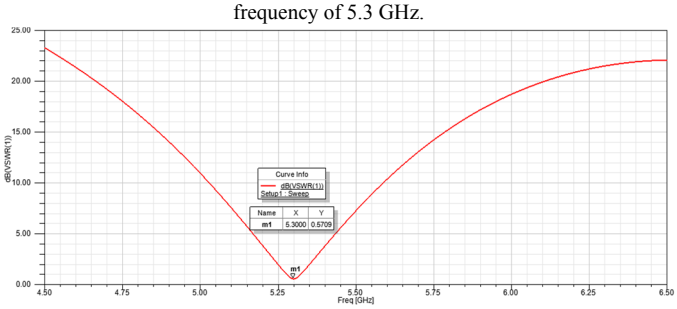

Fig. 14. VSWR plot of microstrip line feed antenna showing resonant frequency of 5.3 GHz.

TABLE I. COMPARISON OF RESULTS

Parameters	Coaxial probe feed		Microstrip line feed	
	Single	***stack***	***Single***	***stack***
Return loss(dB)	-18.54	-46.83	-23.33	-29.67
Bandwidth (MHz)	220	490	280	300
VSWR (dB)	2.0656	0.0791	1.1864	0.5709
Gain (dB)	6.777	6.862	8.169	8.307
Directivity (dB)	6.780	6.870	8.128	8.275

VII. CONCLUSION

A coaxial probe feed and a microstrip line feed stacked antennas are proposed in this paper. The ansoft HFSS software is used to design the antennas. It is observed that the performance of the antenna is increased by both the techniques. The return loss and bandwidth are increased greatly by the probe feed technique. The coaxial probe feed stacked antenna shows a better impedance matching than the microstrip line feed antenna. From the vswr plot we have observed that the stacked antennas are exactly operate at the resonant frequency as compared to the single patch antenna. The antennas can be used in C-band operation.

REFERENCES

[1] Mr. G.Sreedhar Kumar, Mr. J. Anil kumar, Mr. C. Mahesh babu, Mr. Md. Furqan ahmed, Mr. K. Harinath, Mr. P. Guru Prasad, “Bandwidth enhancement techniques using stacked microstrip patch antennas,” International Journal of Computer Systems (ISSN: 2394-1065), Volume 03– Issue 04, April, 2016

[2] Rushit D Trivedi, Vedvyas Dwivedi, “Stacked microstrip patch antenna: gain and bandwidth improvement, effect of patch rotation,” 2012 International Conference on Communication Systems and Network Technologies

[3] J. Chandrasekhar Rao and A. K. Chaitanya, “Performance analysis of double layer stacked patch antenna with edge feed,” International Journal of Energy, Information and Communications Vol.4, Issue 5 (2013), pp.15-24

[4] K. Shahida Salma and P. Jothilakshmi, “Performance enhancement of modified multiband stackedmicrostrip patch antenna for wireless communication,” Middle-East Journal of Scientific Research 24 (Special Issue on Innovations in Information, Embedded and Communication Systems): 120-125, 2016

[5] Naresh Kumar Joshi, Manisha Uttamrao Birare, Neeraj nahata, “Design of microstrip stacked square patchantenna,” International Journal of Engineering and Innovative Technology (IJEIT) Volume 2, Issue 3, September 2012

[6] Jennifer, B.T and Carolyn, T.J, "Resonant frequencies of rectangular microstrip antennas with flush and spaced dielectricsuperstrates," IEEE Transactions on Antennas and Propagation, vol. 47, No. 2, 1999, pp. 302-308.

[7] Balanis, C.A, "Antenna theory, analysis and design," 3rd Ed. John Wiley & Sons, NY, 2005, pp 811-882.

[8] Manfred, K; Rolf, J.H; Koster, H.L, "Accurate model for open end effect of microstrip lines," Electronic Letters, vol.17, 1981, pp. 123-125.